Fatigue and Fracture Mechanics

28TH VOLUME

John H. Underwood,

Bruce D. Macdonald, and

Michael R. Mitchell, editors

ASTM

STP 1321

STP 1321

Fatigue and Fracture Mechanics: 28th Volume

John H. Underwood, Bruce D. Macdonald, and Michael R. Mitchell, editors

ASTM Publication Code Number (PCN):
04-013210-30

ASTM
100 Barr Harbor Drive
West Conshohocken, PA 19428-2959

Printed in the U.S.A.

ISBN: 0-8031-2410-4
PCN: 04-013210-30
ISSN: 1040-3094

Peer Review Policy

Each paper published in this volume was evaluated by two peer reviewers and at least one editor. The authors addressed all of the reviewers' comments to the satisfaction of both the technical editor(s) and the ASTM Committee on Publications.

To make technical information available as quickly as possible, the peer-reviewed papers in this publication were prepared "camera-ready" as submitted by the authors.

The quality of the papers in this publication reflects not only the obvious efforts of the authors and the technical editor(s), but also the work of the peer reviewers. The ASTM Committee on Publications acknowledges with appreciation their dedication and contribution of time and effort on behalf of ASTM.

Printed in Ann Arbor, MI
July 1997

Foreword

This publication, *Fatigue and Fracture Mechanics: 28th Volume,* contains papers presented at the 28th National Symposium on Fatigue and Fracture Mechanics, held in Saratoga Springs, New York, on 25–27 June 1996. The sponsor of the event was ASTM Committee E-08 on Fatigue and Fracture and the Army Research Office. The symposium chairmen were John H. Underwood, U.S. Army Armament R D & E Center, Bruce D. Macdonald, Knolls Atomic Power Laboratory, and Michael R. Mitchell, Rockwell International Science Center.

Contents

WELD APPLICATIONS

FRACTURE ANALYSIS

Overview

The 28th National Symposium on Fatigue and Fracture Mechanics included research and application papers on a broad range of fatigue and fracture topics to match the intended wide scope of the symposium. Thirty-seven papers are published here on topics including general overview papers, constraint effects on fracture toughness, technology and applications of fatigue, weld applications, and analysis of fracture in various materials and components. These five topics were used to group the papers, but it is clear that there is considerable overlap of these topics in many of the papers.

The National Symposium on Fatigue and Fracture Mechanics has become an annual review of new research and technology in this broad technical area for presentation and discussion before leading practitioners in fatigue and fracture from the United States and abroad. Much of the work is included in this archival publication following a thorough peer review process. Many basic concepts and results in fatigue and fracture are well understood and have been documented in prior technical literature, so that the problems now being addressed are often the difficult and complex questions. Nearly every paper here addresses an unproven material or manufacturing process or a set of severe service conditions that requires very careful testing or analysis. To the extent that the problems and solutions are complex, this Symposium and its papers are intended for those who have some experience with the field of fatigue and fracture. Nevertheless, the introductory and reference materials contained in the papers can be used by those with less experience to gain some understanding of subtopics within the overall field. In addition, the three keynote papers and the many papers dealing with industrial applications will also be useful for those with limited experience in fatigue and fracture.

General Topics

The Jerry L. Swedlow Memorial Lecture by J. C. Newman, Jr. of NASA Langley Research Center opened the Symposium with a critical review of the past four decades of technical development of fatigue and fracture mechanics concepts. Included are discussions on the development of fatigue damage and crack formation and growth concepts, crack growth analysis, material inhomogeneities and nonlinear behavior, crack-closure mechanisms, small crack growth behavior, and safe-life and damage-tolerance concepts. Hamada et al. studied the influence of fiber surface treatment on the Mode I delamination toughness and fatigue resistance of glass fabric/vinyl ester composite laminates. The static toughness of the laminates before treatment showed consistent differences in the two main fabric directions. Treatment with high concentrations of aqueous silane solutions increased both the fatigue resistance and the static fracture toughness of the laminates. Saxena gave a critical assessment of the state-of-the-art of time-dependent fracture mechanics concepts, tests and analysis procedures—particularly in relationship to maintenance of high-temperature equipment. Creep deformation and time-dependent damage accumulation in components subjected to elevated temperature were emphasized. Chang described the results of a research program conducted to establish the fracture control requirements for composite overwrap pressure vessels used in space programs. Important findings include fatigue and fracture analysis methods for metallic liners, nondestructive evaluation techniques, and impact damage effects on the composite overwrap.

Fourspring and Pangborn (in a student paper) used X-ray diffraction to characterize cyclic microstructural deformation in polycrystalline steels. They studied the distribution of deformation at certain fractions of fatigue life and at various surface and interior locations of fatigue samples. Changes in deformation were noted for different levels of cycling and at different locations. Ye et al. modeled damage initiation and growth at holes and notches in fiber-reinforced metal laminates and polymer matrix composite laminates. Damage and damage growth were modeled using fictitious cracks with a cohesive stress acting on the crack surfaces. The effect of hole/notch size on residual strength of the laminates was determined from the models and compared with experimental results from the literature. Reuter et al. report the results of an international cooperative test program on fracture toughness of high-strength steel specimens containing surface cracks. It was determined that the maximum load cannot be used to calculate toughness when significant stable cracking occurs. However, the load at which stable cracking initiates, obtained by NDT methods, provided a useful comparison to K_{Ic}. Miyata et al. investigated a relationship for upper shelf fracture toughness degradation of low-carbon steel due to cold working. The product of yield stress and critical strain for microvoid coalescence (based on material tests and the HRR model) is related to J_{Ic}. The critical strain is also correlated with the slope of the tearing resistance curve.

Constraint Effects

Nine contributions deal with constraint effects on transition regime and upper shelf fracture toughness of structural alloys, a general topic of active fracture mechanics research in recent years. In the Session Keynote Paper by Dodds et al. from the University of Illinois, Urbana, micro-mechanics modeling of material failure near the crack front is combined with constraint modeling through finite element analysis to examine constraint effects on ductile tearing. J-T and J-Q analyses are used to describe stationary crack stress fields. The advantages and limitations of this approach in correlating fracture toughness data are described. McCabe and Merkle describe a computational procedure that couples order statistics, weakest link statistics, and a constraint model to determine a lower bound value of fracture toughness. This approach is utilized when data are too sparse to use conventional statistics.

Two papers deal with constraint effects in surface-cracked configurations. Chao and Reuter compare surface and through-crack fracture toughness results for high-strength D6-AC steel. Strains at a critical distance ahead of the crack front were related to K and T-stress in a data set of bend specimens with through cracks. Initiation sites and fracture loads were predicted for a second data set containing surface flaws. Joyce and Link used surface-cracked specimens loaded in combined tension and bending to characterize the transition regime of ASTM A515 Grade 70 steel. Three-dimensional elastic-plastic finite element analysis was used to determine the maximum value of J along the crack front at fracture. Comparison was made with previous results from the same alloy tested in different configurations.

Sokolov et al. compared precracked Charpy-size-corrected results for irradiated and unirradiated reactor vessel steel with results from large specimen databases. The master curve placement from the small specimens agreed with the large specimen EPRI and ASME data fits. This work supports the use of surveillance Charpy specimens to define the irradiation damage transition temperature shift in fracture mechanics terms. Landes and Sakalla developed a technique to estimate the fracture mechanics transition temperature from a single specimen. Order statistics were used to generate a single temperature fracture distribution. This led to an estimate of fracture mechanics transition temperature with a 20°C scatter for sets of six specimens taken one at a time. Yan et al. used a simplified local damage statistical approach, in conjunction with the *J*-*Q* stress field, to account for scatter in transition regime fracture toughness of structural steel. Use of the *J*-*Q* stress field removes the need for large deformation finite element calculations that are generally needed to determine the effective stress used in the local damage approach. Dawicke et al. performed a numerical and experimental study of thickness effects on stable tearing of 2324-T7351 aluminum alloy. Three-dimensional elastic-plastic finite element modeling of side-grooved compact tension specimens was performed. The crack tip opening angle results were compared with those from microtopographic experiments to support a steady state ductile tearing fracture criterion.

Fatigue Technology

Four of the seven papers in the fatigue technology grouping deal with applications, and the remainder have to do with assessment of certain types of fatigue behavior. Applications include the session keynote paper on ground vehicle design, railway components, and cannon components. Assessments of fatigue behavior include methods for representing lifetime, thermomechanical test methods, and crack growth in fully plastic conditions.

The Session Keynote Paper by Landgraf of Virginia Polytechnic Institute reviews the development and implementation of fatigue technology in automotive design. Examples are given, including the complexities of real engineering structures and service environments, along with probabilistic approaches for dealing with variability and uncertainty. Marquis et al. describe the results of a series of fatigue tests on railway boggie components in Finland and Sweden, with attention to the relationship between test loads and the actual field service loads. Results showed that design and testing should include the large amount of fatigue damage that can be contributed by the small cycles in the loading spectrum. Parker and Underwood describe an analysis that represents fatigue lifetime as a single expression which is a simple function of local stress range and initial crack size. Existing experimental life data are used to define the expression, and examples are given of its application to the ordering of several potential fatigue failure locations within a complex cannon component. Cook and Huang describe the development of a rapid thermomechanical fatigue test method for application to the hot components of a gas turbine. They use an integrated air-cooling-induction heating chamber for developing the test method. The test equipment and the associated heat transfer analysis and stress analysis required to analyze the test data are described.

Endersby et al. present elastic-plastic numerical analysis and fatigue lifetime predictions for shrink-fit compound thick cylinders containing multiple, axial holes at the interface between the inner and outer tube. As the shrink-fit interference is increased, the fatigue lifetime increases, and the axial holes become the critical location rather than the bore of the inner tube. The lifetime is superior to that of autofrettaged compound tubes with similar axial holes. Troiano et al. describe a fatigue and fracture case study of a prototype cannon pressure vessel that failed prematurely following cannon firings that involved both pressure oscillations and an aggressive chemical environment. Analysis showed that most of the pressure oscillation cycles were below the fatigue threshold, and environmental cracking was the more likely cause of the premature failure. Kin and Baik evaluate the elevated temperature fatigue cracking behavior of nickel base Alloy 718 under plastic loading conditions, using ΔK and ΔJ correlations of crack growth rate. At 538°C, ΔK gives the better description of growth rate, whereas at 649°C the description is poor for both approaches. Finite element analysis shows that crack closure diminishes as the crack tip plasticity increases.

Weld Applications

Welding adds considerable complexity to the already difficult fracture mechanics problems associated with flaw tolerance assessment of structural alloys. The six papers on weld applications address some of these complexities, including weld inhomogeneities, weld/base metal strength mismatch, residual stresses, and shallow and irregularly shaped flaws at welds.

Kenney et al. (in a student paper) showed that structural steel multi-pass weld cross sections demonstrate considerable variation in fracture toughness. In particular, the coarse-grain heat-affected zone may include brittle zones that seriously degrade the resistance to fracture initiation. The nature of these regions of limited cleavage resistance and the comparison with superior weld regions provide a compelling argument to adhere to recommended interpass temperatures. Yee et al. suggest that mismatching base metal and weld strength can affect joint efficiency and the applicability of standard fracture toughness test methods. To test these hypotheses, 15-mm-thick HSLA-100 steel plate was heat treated to various strength levels and joined with the same weld wire and process. For yield strength mismatches from -30% to $+16\%$, bend specimens showed no significant variation in weld toughness in either the transition regime or upper shelf. Cross-weld tensile testing revealed no loss of joint efficiency for yield strength mismatches greater than -9%. Wang et al. presented improvements in J-integral and CTOD formulas used to interpret test results with various weld/base metal strength mismatch. The range of applicability of the formulas was extended to $0.05 < a/w < 0.7$. Results were checked by comparing the predicted residual plastic component of CTOD with that from interrupted fracture toughness tests.

Keeney et al. describe finite-element analyses of full-thickness weld-cladding beam test specimens containing through-clad flaws. A description of the test program is provided. Comparison is made with previous analyses of unclad, flawed beams. Michaleris et al. show how undue conservatism regarding weld residual stresses can be overcome by finite element simulation of the weld process. Redistribution and relaxation of stresses during ductile crack growth were also modeled. Weld process simulation temperatures agreed with thermocouple data, and predicted residual stresses agreed with measurements from test components. Irizarry-Quiñones et al. investigated flawed beams with and without weld cladding, using both numerical calculations and experiments to quantify weld-cladding benefits to crack driving force. Three-dimensional elastic-plastic finite element analysis included cooling from stress relief heat treatment and modeling the resulting tensile residual stress in the cladding due to its different thermal expansion. Stress intensity factor solutions were found to agree with the finite element solution up to complete yielding of the cladding.

Fracture Analysis

The remaining eight papers in the volume address computational and experimental analysis of fracture for application to a variety of materials and structural components. Included are papers dealing with fracture critical applications such as nuclear reactors and cannon barrels, calculation of stress intensity factors for general application, analysis of fracture in general classes of materials such as aluminum alloys and brittle materials, and fracture of specific materials such as a brittle steel with a thermal gradient and a rubber-toughened polymer.

Davies determined critical crack lengths for nuclear reactor pressure tubes using small-scale curved compact tension specimens. These small-scale test results were compared with results from other small-scale tests of different configuration. Scaling factors based on a volume-controlled fracture model for the deformation J-integral were key to these studies. Chang and Cordes describe a computational model for predicting fracture in flawed or cracked specimens of aluminum alloys. Finite element calculations using nonlinear spring elements are used to predict the crack initiation load, the extent of material damage, and the crack growth behavior. No experimental fracture toughness data are required to make fracture predictions, only material tensile stress-strain data. Baratta summarizes three experimental works by him and other authors that investigate the effects of crack stability on the measured values of fracture toughness—in a brittle polymer, a brittle tungsten alloy, and a silicon nitride ceramic. Comparisons of the experimental results with his stability analysis show that stable fracture resulted in a lowering of the measured K_{Ic} for the three materials. Vigilante et al. (in a student paper) conducted hydrogen-cracking tests on high-strength steels and nickel-iron base alloys using a bolt-load specimen in acid and electrolytic cell environments. In general the steels showed much higher crack growth rates and thresholds than the nickel-iron base alloys. In both material types strength level was the predominant factor in controlling cracking, with a 10% increase in strength often causing a drastic decrease in cracking resistance.

Machida et al. proposes a fracture mechanics model for dynamic elastic-plastic crack propagation and arrest based on Achenbach's asymptotic singular stress field approach. The model simulates acceleration, deceleration, and arrest of a crack in a wide plate in biaxial tension with a temperature gradient (ESSO wide plate test). They conclude that the crack arrest toughness is heavily dependent on the temperature gradient. Toor presents stress intensity solutions from a finite element analysis that accounts for the curvature effects of circumferential cracks at the inner surface of thick wall cylinders. Results are given for a wide range of cylinder radius to wall thickness ratio and crack depth to wall thickness ratio. Zhao et al. showed that damage tolerance analysis of surface and corner cracks emanating from holes can be implemented by a three-dimensional weight function method. The K3D computer program can be run on a personal computer to determine the stress intensity factor along the entire crack front in complicated (uncracked) stress fields. Wu et al. investigated the effects of rubber particles on the constitutive relation and the fracture toughness of polymers. Stress analysis showed that the hydrostatic stress inside the particles is similar to that in the matrix, whereas rubber particle cavitation releases the constraint and allows significant plastic strain to occur.

Acknowledgments

We thank Dr. Kalisam Iyer and the Army Research Office for financial support for the Symposium. We thank the authors for their efforts in presenting and publishing their technical work. The student authors and their sponsors deserve special thanks:

Patrick M. Fourspring	Lockheed Martin Corporation, KAPL Inc.
Kevin L. Kenney	Idaho National Engineering Laboratory
Gregory N. Vigilante	Army Armament RD&E Center

Finally, we pay great tribute to the technical reviewers of these papers. They take the time to provide thoughtful comments and suggestions, with no thought of remuneration or rec-

ognition. There is no question that the technical quality of this volume has been significantly raised by the efforts of the peer reviewers.

John H. Underwood

Army Armament RD&E Center,
Watervliet, NY 12189;
Symposium Chairman and Editor

Bruce D. Macdonald

Knolls Atomic Power Laboratory,
Schenectady, NY 12301;
Symposium Chairman and Editor

Michael R. Mitchell

Rockwell International Science Center,
Thousand Oaks, CA 91358;
Symposium Chairman and Editor

Jerry L. Swedlow Memorial Lecture

J. C. Newman, Jr.[1]

THE MERGING OF FATIGUE AND FRACTURE MECHANICS CONCEPTS: A HISTORICAL PERSPECTIVE *

REFERENCE: Newman, J. C., Jr., "**The Merging of Fatigue and Fracture Mechanics Concepts: A Historical Perspective,**" Fatigue and Fracture Mechanics: 28th Volume, ASTM STP 1321, J. H. Underwood, B. D. Macdonald, and M. R. Mitchell, Eds., American Society for Testing and Materials, 1997.

ABSTRACT: The seventh Jerry L. Swedlow Memorial Lecture presents a review of some of the technical developments, that have occurred during the past 40 years, which have led to the merger of fatigue and fracture mechanics concepts. This review is made from the viewpoint of "crack propagation." As methods to observe the "fatigue" process have improved, the formation of fatigue micro-cracks have been observed earlier in life and the measured crack sizes have become smaller. These observations suggest that fatigue damage can now be characterized by "crack size." In parallel, the crack-growth analysis methods, using stress-intensity factors, have also improved. But the effects of material inhomogeneities, crack-fracture mechanisms, and nonlinear behavior must now be included in these analyses. The discovery of crack-closure mechanisms, such as plasticity, roughness, and oxide/corrosion/fretting product debris, and the use of the effective stress-intensity factor range, has provided an engineering tool to predict small- and large-crack-growth rate behavior under service loading conditions. These mechanisms have also provided a rationale for developing new, damage-tolerant materials. This review suggests that small-crack growth behavior should be viewed as typical behavior, whereas large-crack threshold behavior should be viewed as the anomaly. Small-crack theory has unified "fatigue" and "fracture mechanics" concepts; and has bridged the gap between safe-life and durability/damage-tolerance design concepts.

KEYWORDS: fatigue, fracture mechanics, microstructure, cracks, surface cracks, stress-intensity factor, J-integral, fatigue crack growth, crack closure, elasticity, plasticity, finite element method, constraint

In 1965, ASTM Committee E24 on Fracture Testing of Metallic Materials was formed to promote the rapid growth of the field of Fracture Mechanics. Committee E09 on Fatigue had already been in existence for nearly two decades. With the recent merger of Committees

* Seventh Annual Jerry L. Swedlow Memorial Lecture

[1] Senior Scientist, NASA Langley Research Center, Hampton, Virginia, 23681-0001.

E09 and E24 to form Committee E08 in 1993, it seems appropriate to explore the merging of fatigue and fracture mechanics concepts in a forum that honors and remembers Professor Jerry L. Swedlow, who incidentally completed his Ph.D. Thesis also in 1965 [*1*].

Since the 1950's, events in the naval, nuclear, and aircraft industries have fostered the development of the field of fracture mechanics. The failure of the Comet transport jet aircraft [*2*] from fatigue cracks gave rise to treatments of crack propagation using notch-root parameters and the stress-intensity factor concept of Irwin [*3*] and Paris et al. [*4,5*]. Crack propagation theories would eventually form the bridge that would link fatigue and fracture mechanics concepts. The notch-root local-stress approach hinged upon the Neuber [*6*] or Hardrath-Ohman [*7*] equations which related local plastic stresses and strains to the elastic stress concentration. Later, Hutchinson [*8*] and Rice [*9*] noted some similarities between Neuber's elastic-plastic relation for notches and their solutions for elastic-plastic behavior of cracks. Using a notch-root parameter, $K_{tn}S_{net}$, for a sharp notch or crack, McEvily and Illg [*10*] correlated fatigue-crack-growth rates in a very similar manner to the current ΔK-rate concept. Years later, this notch-root parameter was shown to be directly related to the stress-intensity factor [*5*]. But the elegance and simplicity of the stress-intensity factor concept rapidly developed into the durability and damage tolerance concepts currently used today to design fatigue- and fracture-critical components. The next major link between fatigue and fracture mechanics was the discovery of fatigue-crack closure by Elber [*11*]. The crack-closure concept put crack-propagation theories on a firm foundation and allowed the development of practical life-prediction methods for variable-amplitude and spectrum loading, such as experienced by modern-day commercial aircraft.

In the mid-1970's, Pearson [*12*] and Kitagawa [*13*] showed that short cracks (less than about 0.5 mm in length) grew much faster than long cracks when correlated against the stress-intensity factor range. During the next two decades, short- or small-crack research formed the final link between fatigue and fracture mechanics. These studies, conducted by many world-wide organizations [*14,15*], the AGARD Structures and Materials Panel [*16-18*], ASTM Committees E9 and E24 [*19*], NASA and the CAE [*20*] provided experimental databases and analysis methods to perform fatigue analyses on notch components using "crack propagation" theories. The small-crack theory (treatment of fatigue as the growth of micro-cracks, 1 to 20 μm in length) has been applied to many engineering materials with reasonable success. Although this review will concentrate mainly on a fracture-mechanics viewpoint, the local notch-root stresses and strains from classical fatigue analyses are the driving forces behind the initiation and growth of small cracks at material discontinuities or manufacturing defects. The merging of fatigue and fracture mechanics concepts will provide industries with a unified approach to life prediction. Small-crack theory can now be used to assess the influence of material defects and manufacturing or service-induced damage on fatigue life behavior. This approach will ultimately improve the reliability and economic usefulness of many structures.

The review will begin with some fatigue and fatigue-crack growth observations that have set the stage for the treatment of fatigue from a fracture-mechanics viewpoint. This treatment hinges strongly upon whether fracture-mechanics parameters can be used to model micro- or small-crack growth rate behavior. The development of the stress-intensity factor and some nonlinear fracture-mechanics parameters, such as the J and T* integrals, and their application to small-crack behavior will be discussed. The application of linear elastic fracture mechanics, i.e. the stress-intensity-factor range, ΔK, to the "small or short" crack-growth regime has been actively studied and questioned for more than two decades. Various nonlinear crack-tip parameters and crack-closure effects were introduced to help explain the differences between small- and large-crack growth rate behavior. A key element in these nonlinear crack-tip parameters is crack closure. A brief survey of the finite-element and finite-difference analyses that have been conducted to study the fatigue-crack growth and closure processes; and some typical results will be given. A review of some of the more popular yield-zone models, empirical crack-closure models, and the analytical crack-closure (modified Dugdale or strip-yield) models will be discussed. The application of some of these models to predict crack growth under aircraft spectrum load histories will be presented. Constraint or three-dimensional stress state effects play a strong role in the fatigue initiation and crack-growth process. For example, plasticity-induced crack closure (yielded material at the crack tip and in the wake of the advancing crack) is greatly affected by plane-stress or plane-strain behavior. The most common constraint parameters, and their use in fatigue-crack growth relations, will be discussed. The evolution of some of the proposed fatigue-crack-growth rate relations will then be reviewed. Some observations on the effects of microstructure, environment, and loading on fatigue-crack-growth rate behavior will be discussed. These observations are important in developing the intrinsic crack-growth-rate relations to calculate crack growth under general cyclic loading. The small-crack growth rate data presented by Pearson [*12*], and enlarged upon by Lankford [*21*], will be presented and discussed. An analysis of the Pearson and Lankford small-crack data reveals an important conclusion about the relevance of the large-crack thresholds. The prediction of fatigue life, on the basis of crack propagation from microstructural features, such as inclusions or voids, will be presented for several materials and loading conditions. A design concept using "small-crack theory" will be discussed.

This review is necessarily limited in scope and will not be able to fully cover the vast amount of research that has been conducted over the past 40 years in the fields of fatigue and fracture mechanics. Several excellent books and articles on the "merging of fatigue and fracture mechanics concepts" have helped set the stage for this paper. The book by Fuchs and Stephens [*22*] presents a brief history on the subject, the book entitled "Fatigue Crack Growth -- 30 Years of Progress" edited by Smith [*23*] gives excellent reviews on a variety of technical subjects, and the paper on "History of Fatigue" by Schütz [*24*] gives a historical perspective. The author request the readers indulgence and forgiveness if some major events have been omitted unintentionally, or if reference is not made to all of those who have made significant contributions to the subject. As pointed out by Paris in the Third Swedlow Lecture [*25*], "History has a strong tendency to be one man's personal recollection of important events ...". This review is no different.

FATIGUE AND FATIGUE CRACK GROWTH OBSERVATIONS

The fatigue life, as presented by Schijve [*26*], is divided into several phases: crack nucleation, micro-crack growth, macro-crack growth, and failure, as shown in Fig. 1. Crack nucleation is associated with cyclic slip and is controlled by the local stress and strain concentrations, and notch constraint. Although the slip-band mechanism of crack formation may be necessary in pure metals, the presence of inclusions or voids in engineering metals will greatly affect the crack-nucleation process. Micro-crack growth, a term now referred to as the "small-crack growth" regime, is the growth of cracks from inclusions, voids, or slip bands, in the range of 1 to 10 μm in length. Schijve [*27*] has shown that for polished surfaces of pure metals and for commercial alloys, the formation of a small crack to about 100 μm in size can consume 60 to 80 % of the fatigue life. This is the reason that there is so much interest in the growth behavior of small cracks. Macro-crack growth and failure are regions where fracture-mechanics parameters have been successful in correlating and in predicting fatigue-crack growth and fracture. This review will highlight the advances that have been made in the use of the same fracture-mechanics parameters in the treatment of micro- or small-crack growth using continuum-mechanics approaches.

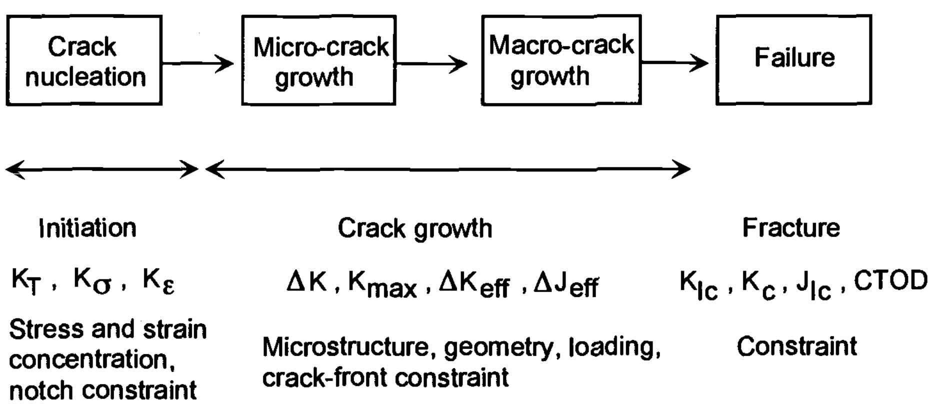

FIG. 1--Different phases of fatigue life and relevant factors (modified after Schijve, 1979 [*27*]).

One of the earliest observations on the mechanism of small-crack growth was made by Forsyth [*28*]. He showed that the initiation and early growth of small cracks can occur at a single slip system (Stage I crack growth) in a favorably oriented surface grain, as shown in Fig. 2(a). Slip-band cracking is promoted by high stresses and higher alloy purity, such as observed in cladding on aluminum alloys. The transition from Stage I to a crack-growth mechanism involving multiple slip systems at the crack tip (Stage II) can occur at or near the first grain boundary encountered by the crack. As might be expected, grain boundaries can have a significant effect on the growth of small cracks. The grain boundaries contribute greatly to the scatter that is observed in small-crack growth rate behavior.

All materials are anisotropic and inhomogeneous when viewed at a sufficiently small scale. For example, engineering metals are composed of an aggregate of small grains. Inhomogeneities, see Fig. 2(b), exist not only due to the grain structure, but also due to the presence of inclusion particles or voids. These inclusion particles are of a different chemical composition than the bulk material, such as silicate or alumina inclusions in steels. Because of the nonuniform microstructure, local stresses may be concentrated at these locations and may cause fatigue cracks to initiate. Crack initiation is primarily a surface phenomenon because: (1) local stresses are usually highest at the surface, (2) an inclusion particle of the same size has a higher stress concentration at the surface than in the interior, (3) the surface is subjected to adverse environmental conditions, and (4) the surfaces are susceptible to inadvertent damage. The growth of "natural" surface initiated cracks in commercial aluminum alloys has been investigated by Bowles and Schijve [*29*], Morris et al. [*30*] and Kung and Fine [*31*]. In some cases, small cracks initiated at inclusions and the Stage I period of crack growth was eliminated, as shown in Fig. 2(b). This tendency toward inclusion initiation rather than slip-band (Stage I) cracking was found to depend on stress level and inclusion content [*31*]. Similarly, defects (such as tool marks, scratches and burrs) from manufacturing and service-induced events will also promote initiation and Stage II crack growth, as shown in Fig. 2(c).

In 1956, Hunter and Fricke [*32*] conducted rotating beam tests on chemically-polished un-notched specimens made of 6061-T6 aluminum alloy. Testing was interrupted periodically in order to obtain plastic replicas of the specimen surface. These replicas reproduced the surface details and provided direct measurement of cracks. The stress-

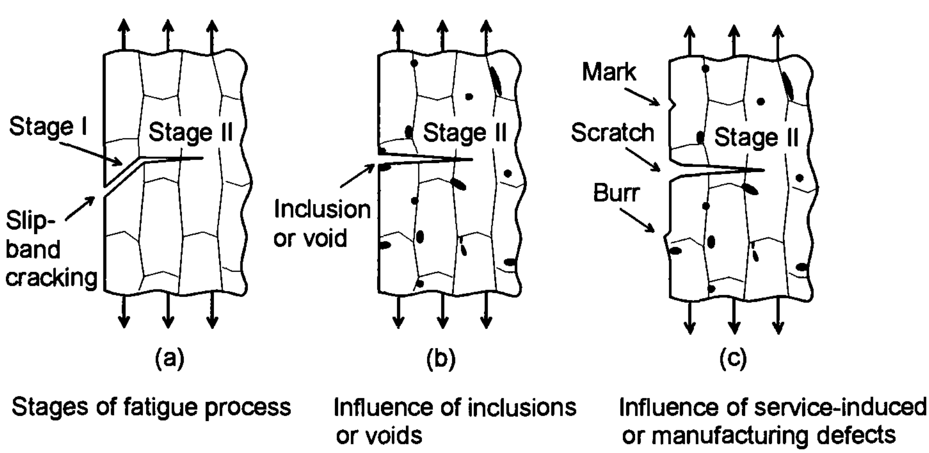

FIG. 2--Stages of the fatigue-crack-growth process (after Forsyth, 1962 [*28*]; after Morris, Buck and Marcus, 1976 [*30*]).

cycles (S-N) relation between the "first" crack observed and failure is shown in Fig. 3. (No crack length was defined for the first crack, but crack length data was presented for lengths greater than about 0.1 mm.) These tests revealed that at high stresses, crack propagation was a dominate part of life, whereas at low stresses, near the endurance limit, crack nucleation was dominant. Their results on crack-length-against-cycles from 0.1 to 1 mm did not show any abnormal behavior (i.e., rates were a monotonically increasing function of crack length).

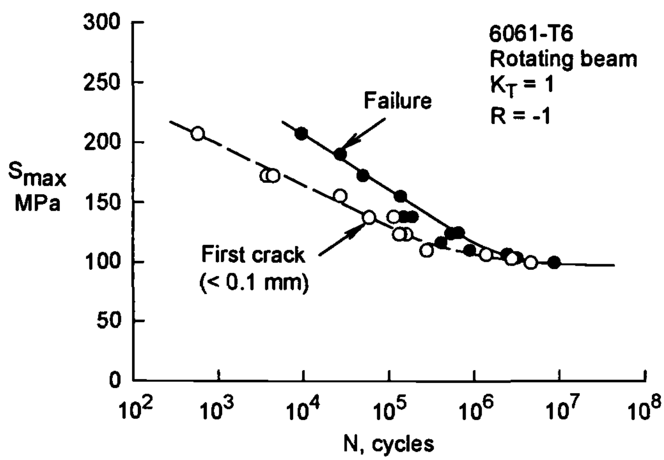

FIG. 3--Stress-life curves for rotating beams under constant-amplitude loading (after Hunter and Fricke, 1956 [*32*]).

Newman and Edwards [*17*], in an AGARD cooperative test program involving several laboratories, found similar results under an aircraft load spectrum, FALSTAFF, on chemically-polished notched specimens made of 2024-T3 aluminum alloy. Replicas were also used to monitor crack initiation and crack growth from 10 μm to 2.3 mm. The stress-life curves for lives to a given crack length are shown in Fig. 4. These results show that crack growth is the dominant part of life (about 90 %) for the limited range of stress levels tested. Similar results were also found for the Gaussian load spectrum and various constant-amplitude loading conditions (R = -2, -1, 0 and 0.5) with stress levels above and near the endurance limit. For all loading conditions, 80 to 90 percent of the fatigue life was spent as crack growth from a crack length of 20 μm to failure (inclusion-particle cluster sizes at the initiation sites ranged from 2 to 7 μm in length). How much of the fatigue life is consumed by crack growth from a crack of the inclusion-particle size to 20 μm is left to conjecture, but it could easily account for 5 to 10 percent of the total life.

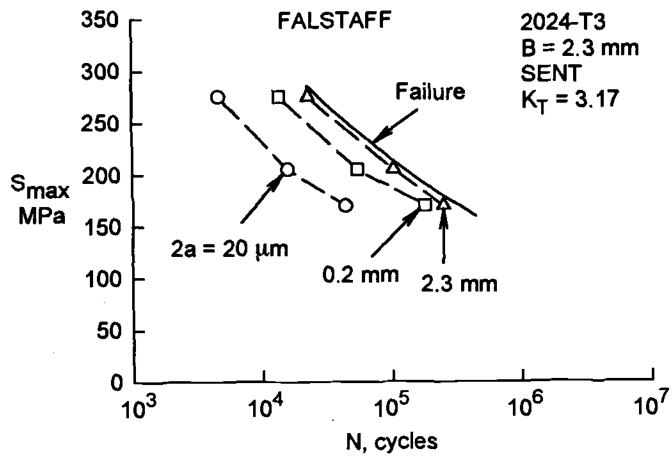

FIG. 4--Stress-life curves for single-edge-notch tensile (SENT) specimens under aircraft spectrum loading (after Newman and Edwards, 1988 [*17*]).

Elber [*33*], in 1968, observed that fatigue-crack surfaces contact with each other even during tension-tension cyclic loading. This contact is due to residual plastic deformation that is left in the wake of an advancing crack, as illustrated in Fig. 5(a). This deformed material contacts during unloading. It is surprising that this observation appeared so many years after crack growth was first studied. But this simple observation and the explanation of the crack-closure mechanism (or more properly crack-opening) began to explain many crack-growth characteristics almost immediately. Since the discovery of plasticity-induced closure, several other closure mechanisms, such as roughness- and oxide/corrosion/fretting product-induced closure, have been identified. The roughness mechanism, discovered by Beevers and his coworkers [*34, 35*], appears to be most prevalent in the near-threshold regime of large-crack growth where the maximum plastic-zone sizes are typically less than the grain size [*36*]. At these low stress levels, crack extension is primarily along a single slip system resulting in a Stage I-like mechanism and a serrated or zig-zag ($\pm\,\theta$ deg.) crack-growth path, as shown in Fig. 5(b). These cracks will have mixed-mode (Mode I and II) crack-surface deformations, which provide the mechanism for contact between the surfaces during cyclic loading. Cracks growing along a non-planar path, such as during overloads in aluminum alloys, will develop surface contact and create debris due to fretting and the growth of oxides from the newly created crack surfaces, see Fig. 5(c). This debris will cause premature contact, as discussed by Paris et al. [*37*] and Suresh et al. [*38*]. These new closure mechanisms, and the influence of the plastic wake on local crack-tip strain field, have greatly advanced the understanding of the fatigue-crack growth process. A brief review of some of the numerical analyses and models of the crack-closure phenomenon will be presented later.

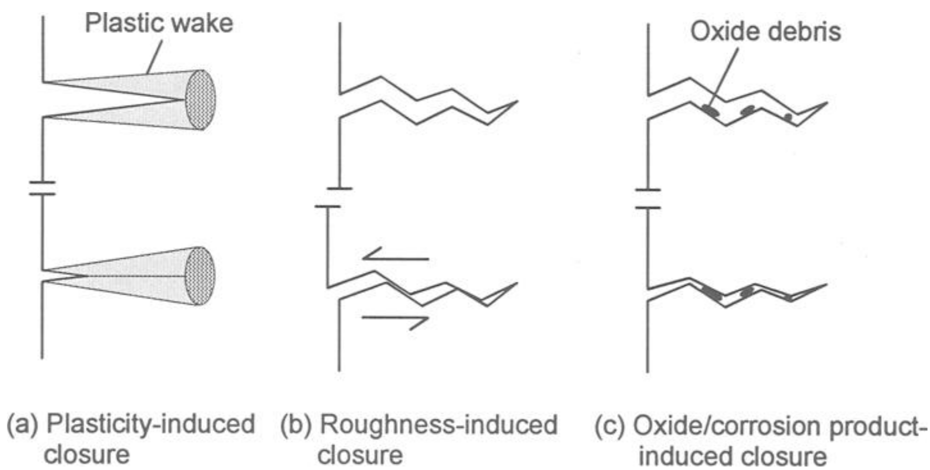

FIG. 5--Dominant fatigue-crack-closure mechanisms (after Suresh and Ritchie, 1982 [*36*]).

STRESS-INTENSITY FACTORS

The essential feature of fracture mechanics is to characterize the local stress and deformation fields in the vicinity of a crack tip. In 1957, Irwin [*3, 39*] and Williams [*40*] recognized the general applicability of the field equations for cracks in isotropic elastic bodies. Under linear elastic conditions, the crack-tip stresses have the form:

$$\sigma_{ij} = K\,(2\pi\, r)^{-1/2}\, f_{ij}(\theta) + A_2\, g_{ij}(\theta) + A_3\, h_{ij}(\theta)\, r^{1/2} + \ldots \qquad (1)$$

where K is the Mode I stress-intensity factor; r and θ are the radius and polar angle measured from the crack tip and crack plane, respectively; A_i are constants; $f_{ij}(\theta)$, $g_{ij}(\theta)$ and $h_{ij}(\theta)$ are dimensionless functions of θ. The stress fields for both two- and three-dimensional cracked bodies are given by equation (1). After some 30 years, the stress-intensity factors for a large number of crack configurations have been generated; and these have been collated into several handbooks (see for example Refs. *41* and *42*). The use of K is meaningful only when small-scale yielding conditions exist. Plasticity and nonlinear effects will be covered in the next section.

Because fatigue-crack initiation is, in general, a surface phenomenon, the stress-intensity factors for a surface- or corner-crack in a plate or at a hole, such as those developed by Raju and Newman [*43, 44*], are solutions that are needed to analyze small-crack growth. Some of these solutions are used later to predict fatigue-crack growth and fatigue lives for notched specimens made of a variety of materials.

ELASTIC-PLASTIC OR NONLINEAR CRACK-TIP PARAMETERS

Analogous to the stress field for a crack in an elastic body, Hutchinson, Rice and Rosengren (HRR) [*8*, *45*] derived the asymptotic stress and strain field for a stationary crack in a nonlinear elastic body. The first term for a power-hardening solid was given by:

$$\sigma_{ij} = [E'\ J/(\sigma_o^2\ r)]^{n/(n+1)}\ \sigma_o\ f_{ij}(\theta,n) \tag{2}$$

$$\varepsilon_{ij} = [E'\ J/(\sigma_o^2\ r)]^{1/(n+1)}\ g_{ij}(\theta,n) \tag{3}$$

where J is the path-independent integral of Rice [*9*], E' is the elastic modulus (E' = E for plane stress or E' = E/(1-ν^2) for plane strain), σ_o is the flow stress, n is the strain-hardening coefficient (n = 0 is perfectly plastic and n = 1 is linear elastic), r and θ are the radius and polar angle measured from the crack tip and crack plane, respectively, and $f_{ij}(\theta,n)$ and $g_{ij}(\theta,n)$ are dimensionless functions depending upon whether plane-stress or plane-strain conditions are assumed.

J and T* Path Integrals

The J-integral appeared in the works of Eshelby [*46*], Sanders [*47*], and Cherepanov [*48*], but Rice [*9*] provided the primary contribution toward the application of the path-independent integrals to stationary crack problems in nonlinear elastic solids. The J-integral, defined in Fig. 6, has come to receive widespread acceptance as an elastic-plastic fracture parameter. Landes and Begley [*49*] and others have used the J-integral as a nonlinear crack-tip parameter to develop crack initiation J_{Ic} values and J-R curves for a variety of materials. However, because deformation theory of plasticity, instead of incremental theory, was used in its derivation, the J-integral is restricted to limited amounts of crack extension in metals.

In 1967, Cherepanov [*48*, *50*] derived an invariant integral (denoted Γ) that is valid for the case of a moving crack with arbitrary inelastic properties, such as an elastic-plastic material. (Both Rice and Atluri have used the symbol Γ to denote a contour around the crack tip. This should not be confused with Cherepanov's definition of his Γ-integral.) Atluri and his co-workers [*51*, *52*] overcame experimental and numerical difficulties in evaluating the Γ-parameter (denoted as T*, see Fig. 6) for a moving crack. The T*-integral is beginning to receive more attention in the literature.

Cyclic Crack-Tip Parameters

Both the J- and T*-integrals have been extended to apply to applications involving cyclic loading. Dowling and Begley [*53*] developed an experimental method to measure the cyclic J values from the area under the load-against-deflection hysteresis loop that accounted for the effects of crack closure. The ΔJ_{eff} parameter has been successfully used to correlate fatigue-crack-growth rate data from small- to large-scale yielding conditions for tension and bending loads [*54*]. Similarly, Atluri et al. [*52*] have derived the ΔT^* integral (see Fig. 6) for cyclic loading and others [*55*] are beginning to evaluate the parameter under cyclic loading.

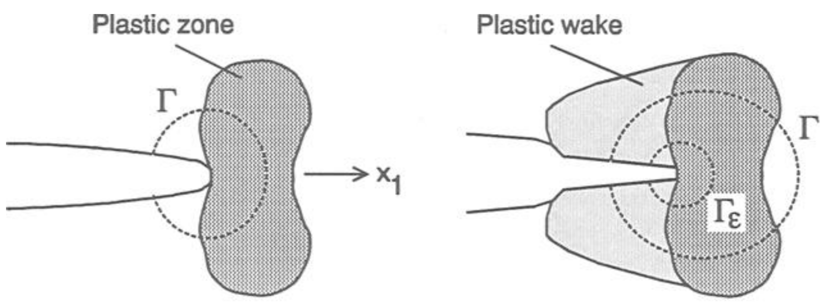

Rice (1968):

$$J = \int_{\Gamma} (W n_1 - t_i \, u_{i,1})\, d\Gamma$$

Atluri (1982):

$$T^* = J - \int_{V-V_\varepsilon} [W_{,1} - (\sigma_{ij} \, \varepsilon_{ij,1})]\, dV$$

Dowling and Begley (1976):

$$\Delta J_{eff} = 2\, A_c \,/\, B\, b$$

Atluri, Nishioka and Nakagaki (1984):

$$\Delta T^* = \int_{\Gamma_\varepsilon} (\Delta W n_1 - (t_i + \Delta t_i)\, \Delta u_{i,1} - \Delta t_i \, u_{i,1})\, d\Gamma$$

FIG. 6--Elastic-plastic crack-tip parameters.

Plastic Stress-Intensity Factors and the Dugdale Model

In 1960, Irwin [*56*] developed a simple approach to modify the elastic stress-intensity factor to "correct" for plastic yielding at the crack tip. The approach was to add the plastic-zone radius to the crack length and, thus, calculated a "plastic" stress-intensity factor at the "effective" crack length ($c + r_y$). The size of the plastic zone was estimated from equation (1) as

$$r_y = \alpha_i \, (K/\sigma_{ys})^2 \tag{4}$$

where $\alpha_i = 1/(2\pi)$ for plane stress and $\alpha_i = 1/(6\pi)$ for plane strain. The term α_i is Irwin's constraint parameter that accounts for three-dimensional stress state effects on yielding. Note that equation (4) gives approximately the "radius" of the plastic zone because of a redistribution of local crack-tip stresses due to yielding, which is not accounted for in the elastic analysis. The actual plastic-zone size is roughly $2r_y$. Based on test experience, the fracture toughness, K_c, calculated at the effective crack length remained nearly constant as a function of crack length and specimen width for several materials until the net-section stress exceeded 0.8 times the yield stress (σ_{ys}) of the material [57].

Many researchers have used the Dugdale-Barenblatt (DB) model [*58, 59*] to develop some nonlinear crack-tip parameters (see Refs. *60* and *61*). Drucker and Rice [*62*] presented some very interesting observations about the model. In a detailed study of the stress field in the elastic region of the model under small-scale yielding conditions, they reported that the model violates neither the Tresca nor von Mises yield criteria. They also found that for two-dimensional, plane-stress, perfect-plasticity theory, the DB model satisfies the plastic flow rules for a Tresca material. Thus, the model represents an exact two-dimensional plane-stress solution for a Tresca material even up to the plastic-collapse load. Therefore, the J-integral calculations from Rice [*9*] and ΔJ estimates may be reasonable and accurate under certain conditions. Of course, the application of the DB model to strain-hardening materials and to plane-strain conditions may raise serious questions because plane-strain yielding behavior is vastly different than that depicted by the model.

Rice [*9*] evaluated the J integral from the DB model for a crack in an infinite body and found that

$$J = \sigma_o\,\delta = 8\sigma_o^{\,2} c/(\pi E)\,\ell n[\sec(\pi S/2\sigma_o)] \tag{5}$$

where σ_o is the flow stress, δ is the crack-tip-opening displacement, c is the crack length, E is the elastic modulus, and S is the applied stress. An equivalent plastic stress-intensity factor K_J is given as

$$K_J^{\,2} = JE/(1 - \eta^2) \tag{6}$$

where $\eta = 0$ for plane stress, and $\eta = \nu$ (Poisson's ratio) for plane strain. DB model solutions for plastic-zone size, ρ, and crack-tip opening displacement, δ, are available for a large number of crack configurations (see Ref. *41*). Thus, J and K_J can be calculated for many crack configurations. However, for complex crack configurations, such as a through crack or surface crack at a hole, closed-form solutions are more difficult to obtain. A simple method was needed to estimate J for complex crack configurations. A common practice in elastic-plastic fracture mechanics has been to add a portion of the plastic zone ρ to the crack length, like Irwin's plastic-zone correction [*56*], to approximate the influence of crack-tip yielding on the crack-driving parameter.

Newman [*63*] defined a plastic-zone corrected stress-intensity factor as

$$K_p = S\,(\pi d)^{1/2}\,F(d/w, d/r, \ldots) \tag{7}$$

where $d = c + \gamma\rho$ and F is the boundary-correction factor evaluated at the effective crack length. The term γ was assumed to be constant and was evaluated for several two- and three-dimensional crack configurations by equating K_p to K_J. From these evaluations, a value of 1/4 was found to give good agreement up to large values of applied stress to flow stress ratios. To put the value of one-quarter in perspective, Irwin's plastic-zone corrected stress-intensity factor [*56*] is given by γ equal to about 0.4 and Barenblatt's cohesive modulus [*59*] is given by $\gamma = 1$. A comparison of K_e (elastic stress-intensity factor) and K_p, normalized by K_J and plotted against S/σ_o (applied stress to flow stress) for two symmetrical through cracks emanating from a circular hole is shown in Fig. 7. The dashed curves show K_e and the solid curves show K_p for various crack-length-to-hole-radii (c/r). The elastic curves show significant deviations while the results from the K_p equation (eqn. 7) are within about 5% of K_J up to an applied stress level of about 80% of the flow stress.

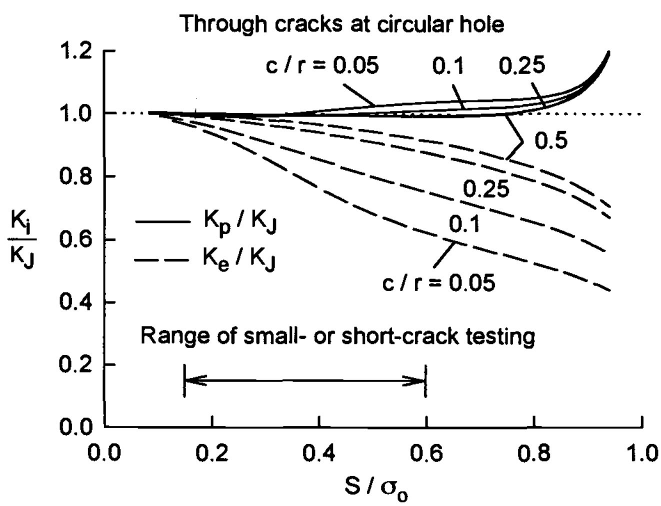

FIG. 7--Ratio of elastic K_e and plastic K_p values to equivalent K_J values (after Newman, 1992 [*63*]).

This matches well with the 80%-limit established for Irwin's plastic-zone corrected stress-intensity factor, as discussed by McClintock and Irwin [*57*]. To convert K_p to ΔK_p in equation 7, the applied stress and flow stress are replaced by ΔS and $2\sigma_o$, respectively, and ρ is replaced by the cyclic plastic zone ω (see Ref. *64*). Thus, Fig. 7 would be identical for cyclic behavior if K_p/K_J, is replaced by $\Delta K_p/\Delta K_J$ and S/σ_o is replaced by $\Delta S/(2\sigma_o)$, again, with $\gamma = 0.25$. Thus, ΔK_p is evaluated at a crack length plus one-quarter of the cyclic plastic zone. An application using this parameter to predict the fatigue life under high stresses will be presented later.

NUMERICAL ANALYSES AND MODELS OF CRACK GROWTH AND CLOSURE

Since the early 1970's, numerous finite-element and finite-difference analyses have been conducted to simulate fatigue-crack growth and closure. These analyses were conducted to obtain a basic understanding of the crack-growth and closure processes. Parallel to these numerical analyses, simple and more complex models of the fatigue-crack growth process were developed. Although the vast majority of these analyses and models were based on plasticity-induced crack-closure phenomenon, a few attempts have been made to model the roughness- and oxide-induced crack-closure behavior (see for example Refs. *36* and *65*). This section will briefly review: (1) finite-element and finite-difference analyses, (2) yield-zone and empirical crack-closure models, and (3) the modified Dugdale or strip-yield models. In each category, an example of the results will be given.

Finite-Element and Finite-Difference Analyses

A chronological list of the finite-element and finite-difference analyses [*66-88*] is given in Table 1. The vast majority of these analyses were conducted using two-dimensional analyses under either plane-stress or plane-strain conditions. Since the mid-1980's, only a few three-dimensional finite-element analyses have been conducted. Newman and Armen [*66-68*] and Ohji et al. [*69*] were the first to conduct two-dimensional finite-element analyses of the crack-closure process. Their results under plane-stress conditions were in quantitative agreement with the experimental results of Elber [*11*] and showed that crack-opening stresses were a function of R ratio (S_{min}/S_{max}) and stress level (S_{max}/σ_o). Nakagaki and Atluri [*70*] conducted crack-growth analyses under mixed-mode loading and found that cracks did not close under pure Mode II loading. In the mid-1980's, there was a widespread discussion on whether fatigue cracks would close under plane-strain conditions, i.e. where did the extra material to cause closure come from in the crack-tip region, since the material could not deform in the thickness direction, like that under plane-stress conditions. Blom and Holm [*72*] and Fleck and Newman [*76, 79*] studied crack-growth and closure under plane-strain conditions and found that cracks did close but the crack-opening levels were much lower than those under plane-stress conditions. Sehitoglu and his coworkers [*74, 85*] found later that the residual plastic deformations that cause closure came from the flanks of the crack (i.e., the material was plastically stretched in the direction parallel to the crack surfaces). Nicholas et al. [*77*] studied the closure behavior of short cracks and found that at negative R ratios the crack-opening levels were negative, i.e. the short cracks were open at a negative load.

In 1992, Llorca [*84*] was the first to analyze the roughness-induced closure mechanism using the finite-difference method. He found that the key controlling factor in roughness-induced closure was the tilt angle (θ) between the crack branches (as the crack zig-zags $\pm\theta$ degrees). Crack-opening loads as high as 70% of the maximum load were calculated and these results agree with the very high opening loads measured on the 2124-T351 aluminum alloy.

TABLE 1-- Finite-element analyses of fatigue crack growth and closure.

• Two-Dimensional Cracks	• Three-Dimensional Cracks
Newman 1974-76	Chermahini 1986
Newman and Armen 1975	Chermahini et al. 1988-93
Ohji, Ogura and Ohkubo 1975-77	Dawicke et al. 1992
Nakagaki and Atluri 1980	Newman 1993
Anquez 1983	
Blom and Holm 1985	
Kobayashi and Nakamura 1985	
Lalor, Sehitoglu and McClung 1986-87	
Fleck 1986	
Bednarz 1986	
Nicholas et al. 1988	
Fleck and Newman 1988	
Llorca and Galvez (a) 1989	
Anquez and Baudin 1988	
McClung et al. 1989-94	
Llorca (a) 1992	
Sehitoglu et al. 1993-96	

(a) Finite-difference method of analysis.

McClung [*80-82*] performed extensive finite-element crack-closure calculations on small cracks, crack at holes, and various fatigue-crack growth specimens. Whereas Newman [*68*] found that S_{max}/σ_o could correlate the crack-opening stresses for different flow stresses (σ_o) for the middle-crack tension specimen, McClung found that K-analogy, using K_{max}/K_o could correlate the crack-opening stresses for different crack configurations for small-scale yielding conditions. The term $K_o = \sigma_o \sqrt{(\pi a)}$ where σ_o is the flow stress. (K-analogy assumes that the stress-intensity factor controls the development of closure and crack-opening stresses, and that by matching the K solution among different cracked specimens, an estimate can be made for the crack-opening stresses.) Some typical results are shown in Fig. 8. The calculated crack-opening stress, S_{op}/S_{max}, is plotted against K_{max}/K_o for three crack configurations: middle-crack tension M(T), single-edge-crack tension SE(T) and bend SE(B). The symbols show the finite-element calculations for three crack-length-to-width ratios (c/w). At high values of K_{max}/K_o, the crack-opening values became a function of crack configuration. A similar approach using "plastic-zone analogy" may be able to correlate the crack-opening stresses under large-scale yielding. The dashed curve shows the crack-opening stress equation, from the strip-yield model, developed by Newman [*89*] and recast in term of K-analogy. The dashed curve gives a lower bound to the finite-element results. The reason for the differences between the finite-element and strip-yield model results must await further study.

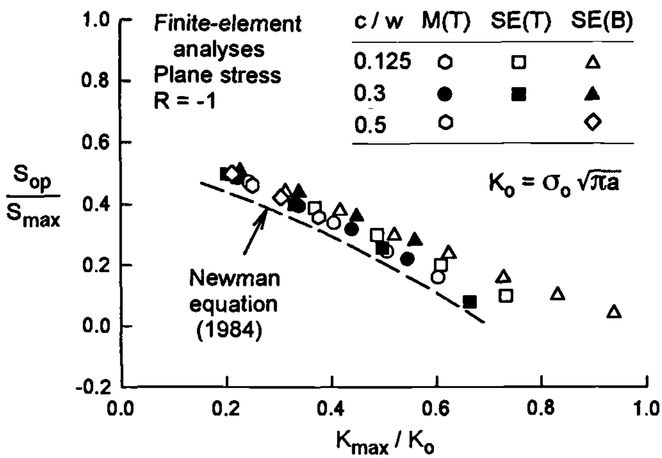

FIG. 8--Configuration effects on crack-opening stresses (after McClung, 1994 [*82*]).

Very little research on three-dimensional finite-element analyses of crack closure has been conducted. In 1986, Chermahini et al. [*86-88*] was the first to investigate the three-dimensional nature of crack growth and closure. He found that the crack-opening stresses were higher near the free surface (plane stress) region than in the interior, as expected. Later, Dawicke et al. [*90*] obtained experimental crack-opening stresses, similar to Chermahini's calculations, along the crack front using Sunder's striation method [*91*], backface-strain gages, and finite-element calculations.

In reviewing the many papers on finite-element analyses, a few analysts were extending the crack at "minimum" load, instead of at maximum load for various reasons. Real cracks do not extend at minimum load and crack-closure and crack-opening behavior calculated from these analyses should be viewed with caution. As is obvious from Table 1, further study is needed in the area of three-dimensional finite-element analyses of crack growth and closure to rationalize the three-dimensional nature of closure with respect to experimental measurements that are being made using crack-mouth and backface-strain gages. Because the measurements give a single value of crack-opening load, what is the relation between this measurement and the opening behavior along the crack front? Is the measurement giving the free surface value, i.e. the last region to open? The crack-opening value in the interior is probably the controlling value because it is dominant over a large region of the crack front [*87, 90*]. Also, more analyses are needed on the other forms of closure, such as roughness-induced closure. From the author's point of view, plasticity- and roughness-induced closure work together to close the crack and the phenomena are difficult to separate. In Llorca's analyses [*84*] in the near-threshold regime, the plastic-zone size was smaller than the mesh points in the finite-difference method. Is the method able to accurately account for the mixed-mode deformation under these conditions? Residual plastic deformations in the normal and shear directions are what causes the crack surfaces to prematurely contact during cyclic loading.

Yield-Zone and Empirical Crack-Closure Models

A list of some of the more popular yield-zone models [*92-97*] and empirical crack-closure models [*98-102*] is given in Table 2. The Wheeler [*92*] and Willenborg et al. [*93*] models were the first models proposed to explain crack-growth retardation after overloads. These models assume that retardation exists as long as the current crack-tip plastic zone is enclosed within the overload plastic zone. The physical basis for these models, however, is weak because they do not account for crack-growth acceleration due to underloads or immediately following an overload. Chang and Hudson [*103*] clearly demonstrated that retardation and acceleration are both necessary to have a reliable model. Later models by Gallagher [*94*], Chang [*95*] and Johnson [*96*] included functions to account for both retardation and acceleration. A new generation of models was introduced by Bell and Wolfman [*98*], Schijve [*99*], de Koning [*100*], Baudin et al. [*101*] and Aliaga et al. [*102*] that were based on the crack-closure concept. The simplest model is the one proposed by Schijve, who assumed that the crack-opening stress remains constant during each flight in a flight-by-flight sequence. The other models developed empirical equations to account for retardation and acceleration, similar to the yield-zone models.

TABLE 2-- Empirical yield-zone or crack-closure models.

• Yield-Zone Models	• Crack-Closure Models
Willenborg et al. 1971	Bell and Wolfman 1976
Wheeler 1972	Schijve 1980
Gallagher (GWM) 1974	de Koning (CORPUS) 1981
Chang (EFFGRO) 1981	Baudin et al. (ONERA) 1981
Johnson (MPYZ) 1981	Aliaga et al. (PREFAS) 1985
Harter (MODGRO) 1988	

Lazzeri et al. [*104*] conducted fatigue-crack growth tests on a middle-crack tension specimen under a flight-by-flight load history (ATR-spectrum) at a mean flight stress level (S_{1g}) of 75 MPa. Tests results are shown in Fig. 9. These results show an initial high rate of growth followed by a slowing down of crack growth from 7 to 10 mm and then a steady rise in the overall growth rates until failure. This behavior is what Wanhill [*105*] calls "transient crack growth" under spectrum loading. Lazzeri et al. then made comparisons of the predicted crack length against flights from four of the empirical models (CORPUS, PREFAS, ONERA, and MODGRO, see Table 2) and one strip-yield model (FASTRAN-II, to be discussed later). The predicted results are shown with symbols in Fig. 9. The MODGRO model was very conservative, while the other three empirical models gave essentially the same results but under predicted the flights to failure. The FASTRAN-II model predicted failure at about 15 % shorter than the test results, but this model came closer to modeling the "transient crack growth" behavior, as discussed by Wanhill. This behavior has been traced to the "constraint-loss" regime in thin-sheet materials by Newman [*106*].

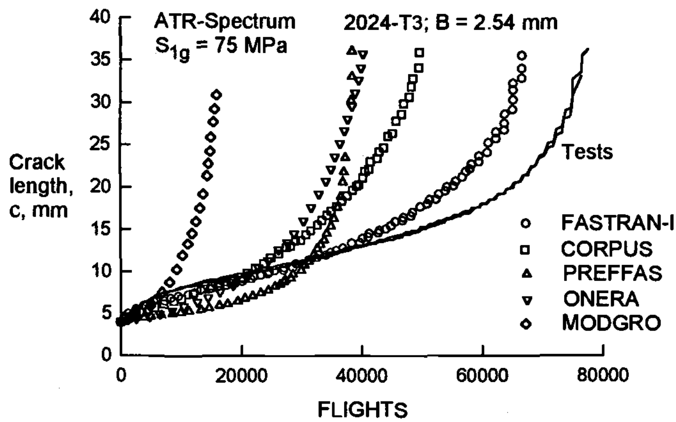

FIG. 9--Comparison of predictions from various models on aircraft spectrum (after Lazzeri et al., 1995 [*104*]).

<u>Modified Dugdale or Strip-Yield Models</u>

A chronological list of the modified Dugdale or strip-yield models [*107-125*] is given in Table 3. Shortly after Elber [*33*] discovered crack closure, the research community began to develop analytical or numerical models to simulate fatigue-crack growth and closure. These models were designed to calculate the growth and closure behavior instead of assuming such behavior as in the empirical models. Seeger [*107*] and Newman [*66*] were the first to develop two types of models. Seeger modified the Dugdale model and Newman developed a ligament or strip-yield model. Later, a large group of similar models were also developed using the Dugdale model framework. Budiansky and Hutchinson [*109*] studied closure using an analytical model, while Dill and Saff [*108*], Fuhring and Seeger [*111*], and Newman [*112*] modified the Dugdale model. Some models used the analytical functions to model the plastic zone, while others divided the plastic zone into a number of elements. The model by Wang and

Blom [*118*] is a modification of Newman's model [*112*] but their model was the first to include weight-functions to analyze other crack configurations. All of the other models in Table 3 are quite similar to those previously described. The models by Nakai et al. [*113*], Tanaka [*116*] and Sehitoglu et al. [*85*] began to address the effects of microstructure and crack-surface roughness on crack-closure behavior.

TABLE 3--Modified Dugdale or strip-yield crack-closure models.

Seeger 1973	Tanaka 1985
Newman 1974	Ibrahim 1986
Dill and Saff 1976	Wang and Blom 1987, 1991
Budiansky and Hutchinson 1978	Chen and Nisitani 1988
Hardrath et al. 1978	de Koning and Liefting 1988
Fuhring and Seeger 1979	Keyvanfar and Nelson 1988
Newman 1981, 1990	Nakamura and Kobayashi 1988
Nakai et al. 1983	Daniewicz 1991
Sehitoglu 1985	ten Hoeve and de Koning 1995
Keyvanfar 1985	Sehitoglu et al. 1996

A typical modified Dugdale model is shown in Fig. 10. This model [*110, 112*] uses bar elements to model the plastic zone and the residual plastic deformations left as the crack grows. Three-dimensional constraint is accounted for by using the constraint factor, α. For plane-stress conditions, α is equal to unity and for plane-strain conditions, α is equal to 3. The constraint factor has been used to correlate constant-amplitude fatigue crack growth rate data, as will be discussed later.

CONSTRAINT EFFECTS ON CRACK-GROWTH BEHAVIOR

The importance of constraint effects in the failure analysis of cracked bodies has long been recognized by many investigators. Strain gradients that develop around a crack front cause the deformation in the local region to be constrained by the surrounding material. This constraint produces multiaxial stress states that influence fatigue-crack growth and fracture. The level of constraint depends upon the crack configuration and crack location relative to external boundaries, the material thickness, the type and magnitude of applied loading, and the material stress-strain properties. In the last few years, a concerted effort (see Refs. *126-128*) has been undertaken to quantify the influence of constraint on fatigue-crack growth and fracture. To evaluate various constraint parameters, two- and three-dimensional stress analyses have been used to determine stress and deformation states for cracked bodies. The constraint parameters that are currently under investigation are (1) Normal stress, (2) Mean stress, (3) T-

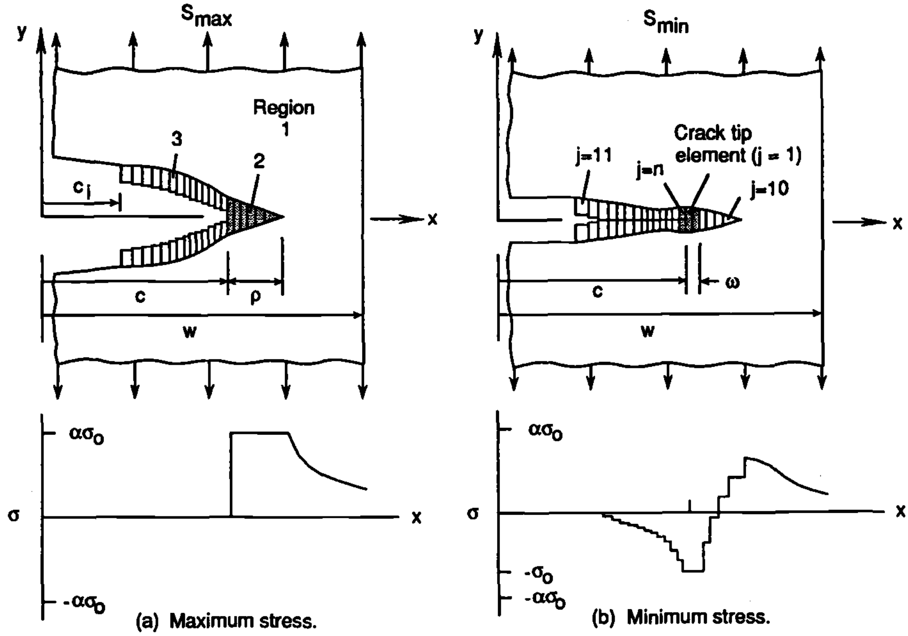

FIG. 10--A typical Dugdale or strip-yield model for plasticity-induced closure (after Newman, 1981 [*112*]).

stress, and (4) Q-stress. In 1960, an elevation of the "normal" stress was used by Irwin [*56*] in developing equation (4) using only the K solution. This is similar to the constraint factor used in the modified strip-yield models (see Ref. *112*). McClintock [*129*] and Rice and Tracey [*130*] considered the influence of the mean stress, $\sigma_m = (\sigma_1 + \sigma_2 + \sigma_3)/3$, on void growth to predict fracture. The mean stress parameter is currently being used in conjunction with three-dimensional (3D), elastic-plastic, finite-element analyses to characterize the local constraint at 3D crack fronts, see for example Reference *131*.

In the early 1970's, the fracture community realized that a single parameter, such as K or J, was not adequate in predicting the plastic-zone size and fracture over a wide range of crack lengths, specimen sizes, and loading conditions. At this point, "two-parameter" fracture mechanics was born. The second parameter was "constraint." The characterization of constraint, however, has been expressed in terms of the next term(s) in the series expansion of the elastic or elastic-plastic crack-tip stress fields. In 1975, Larsson and Carlsson [*132*] demonstrated that the second term, denoted as the T-stress (stress parallel to the crack surfaces), had a significant effect on the shape and size of the plastic zone. The effects of the elastic T-stress on J dominance for an elastic-plastic material under plane-strain conditions was studied by Betegon and Hancock [*133*] using finite-element analyses. Analytically, Li and Wang [*134*] developed a procedure to determine the second term in the asymptotic expansion of the crack-tip stress field for a nonlinear material under plane-strain conditions. Similarly, O'Dowd and Shih [*135, 136*] have developed the J-Q field equations to characterize the difference between the HRR stress field and the actual stresses. The Q-stress collectively represents all of the higher order terms for nonlinear material behavior. The J-Q field equations have been developed for plane-strain conditions. An asymptotic analysis that includes more terms for the stress and deformation fields at a crack embedded in a nonlinear material under Mode I and II loading for either plane-stress or plane-strain conditions has been developed by Yang et al. [*137, 138*]. Chao et al. [*138*] demonstrated that the first "three" terms in these series expansion (J, A_2, and A_3) can characterize the stress σ_{ij} for a large region around the crack tip for Mode I plane-strain conditions. The third term was subsequently shown to be directly related to the first and second terms, thus two amplitudes, J and A_2, were sufficient to describe the local stress field.

In 1973, the Two-Parameter Fracture Criterion (TPFC) of Newman [*139, 140*] was developed which used the additional term in the local stress equations for a sharp notch or a crack. The TPFC equation, $K_F = K_{Ie} / (1 - m\ S_n/\sigma_u)$, was derived using two approaches. (K_F and m were the two fracture parameters; K_{Ie} is the elastic stress-intensity at failure; S_n is the net-section stress and σ_u is the ultimate tensile strength.) In the first approach, the stress-concentration factor for an ellipsoidal cavity, $K_T = 1 + 2\ (a/\rho)^{1/2}/\Phi$ from Sadowsky and Sternberg [*141*], was used with Neuber's equation [6], $K_\sigma\ K_\varepsilon = K_T^2$, to derive a relation between local elastic-plastic stresses and strains and remote loading. This is similar to the way Kuhn and Figge [*142*] used the Hardrath-Ohman equation [7] many years earlier. Assuming that fracture occurred when the notch-root stress and strain was equal to the fracture stress and strain, σ_f and ε_f, respectively, and that a crack had a critical notch-root radius, ρ^*, the TPFC equation was derived. The second parameter, m, came from the "unity" term in the stress-concentration equation. The second approach [*140*], used the elastic stress field equation for a crack (eqn.(1)) and Neuber's equation to relate the elastic stresses to the elastic-plastic stresses and strains at a crack tip. In this approach, it was again assumed that fracture occurred at a critical distance, r*, in front of the crack tip when the local stress and strain was equal to the fracture stress and strain, σ_f and ε_f. The second parameter, m, came from the next higher-order term in the stress-field expansion. The TPFC has been successfully applied to a large amount of fracture data on two- and three-dimensional crack configuration and materials.

As pointed out by Merkle, in the Fifth Swedlow Lecture [*143*], "... estimation of constraint effects is best accomplished with three-dimensional analyses." With this in mind, Newman et al. [*144, 145*] conducted 3D elastic-plastic, finite-element analyses on a cracked plate with a wide range in crack lengths, thicknesses, and widths for an elastic-perfectly-plastic material under tension and bending loads. Because the previously discussed crack-closure models require information about constraint (elevation of the normal stress around the crack tip), an average normal stress in the plastically-deformed material normalized by the flow stress was evaluated from the 3D analyses. This normalized average stress was denoted as a global constraint factor, α_g. Some typical results of α_g plotted against a normalized K are shown in Fig. 11 for a thin-sheet material. The symbols show the results from the analyses for various specimen sizes. The upper dashed lines show the results under plane-strain conditions. The global constraint factor was nearly a unique function of the applied K level. Some slight differences were observed near the plane-stress conditions (high K levels). These results show that the global constraint factor rapidly drops as the K level increases (plastic-zone size increases) and approaches a value near the plane-stress limit. The solid line is a simple fit to the results and shows that the constraint-loss regime may be defined by a unique set of K values under monotonic loading. On the basis of some results from cyclic loading and conjecture, the constraint-loss regime may be defined by a unique set of ΔK_{eff} values under cyclic loading. This point will be discussed later.

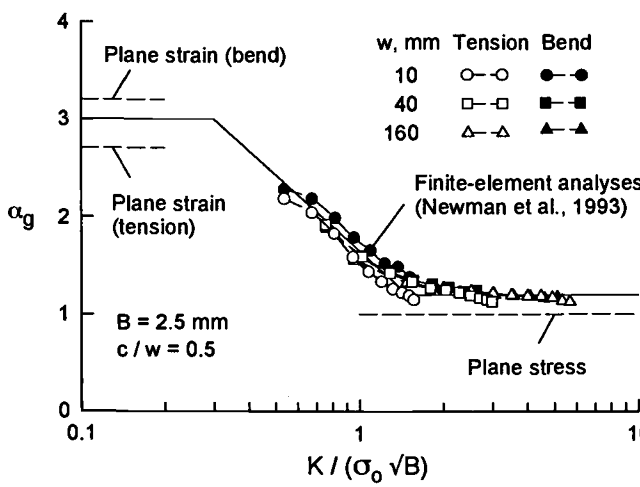

FIG. 11--Constraint variations from three-dimensional finite-element analyses (after Newman et al., 1994 [*145*]).

CRACK GROWTH RATE RELATIONS

The number of fatigue-crack growth rate relations in the literature is enormous. But the first such relation was attributed to Head in 1953 [*146*]. After the Comet accidents [*2*], which were caused by fatigue cracks growing from windows in the fuselage, the search for a reliable crack-tip parameter and growth rate relation was underway. Table 4 gives a very small list of some crack-growth rate relations that have been proposed since the early 1960's. This list is a summary of the major relations that are currently being used today in many damage-tolerance life-prediction codes. In 1961, Paris et al. [*4*] made a major step in applying the stress-intensity factor range to fatigue-crack growth. Donaldson and Anderson [*147*] demonstrated how this new concept could be applied to aircraft components. Very quickly it was found that ΔK alone would not correlate fatigue-crack growth rate data for different stress ratios, R, and other equations were proposed. Of these, the Forman et al. [*148*] and Walker [*149*] equations are commonly used in many life-prediction codes. The next major step in understanding fatigue-crack growth came when Elber [*11, 33, 150*] discovered crack closure and proposed that the ΔK_{eff} parameter should control crack growth. Prior to Elber's discovery, Tomkins [*151*] was using the BCS (Bilby, Cottrell and Swinden [*152*]) model to develop a local crack-tip displacement parameter for crack growth. After Rice [*9*] developed the J-integral, Dowling and Begley [*53, 54*], and others, began to explore the use of the ΔJ_{eff} parameter for fatigue-crack growth. Similarly, Ogura et al. [*153*] proposed to use the local cyclic hysteresis energy (W_{eff}). The relationship between ΔK, or any other parameter discussed here, plotted against crack-growth rate does not always fit the simple power laws that have been proposed. Miller and Gallagher [*154*] found that more accurate life predictions could be made if a table-lookup procedure was used. (The reason that the table-lookup procedure is more accurate will become apparent later.) A number of life prediction codes, such as NASA FLAGRO [*155*] and FASTRAN-II [*156*], have adopted this procedure.

TABLE 4--Evolution of some typical crack-growth rate relations.

- Paris, Gomez and Anderson (1961): $dc/dN = C\ \Delta K^n$
- Paris and Erdogan (1963): $dc/dN = C\ \Delta K^n\ (K_{max})^m$
- Forman, Kearney and Engle (1967): $dc/dN = f(\Delta K, R, K_c)$
- Tomkins (1968): $dc/dN = f(\Delta CTOD)$
- Elber (1970): $dc/dN = C\ (\Delta K_{eff})^n$
- Walker (1970): $dc/dN = f(\Delta K, R)$
- Dowling and Begley (1976): $dc/dN = C\ (\Delta J_{eff})^n$
- Ogura et al. (1985): $dc/dN = f(W_{eff})$
- Miller and Gallagher (1981): Table-lookup procedure $dc/dN = f(\Delta K, R)$

LARGE CRACK GROWTH BEHAVIOR

This next section will review some observations and present results on the effects of microstructure, environment, and loading on fatigue-crack growth rate behavior.

Microstructural Effects

As previously mentioned, fatigue-crack growth rate relations do not necessarily fit a simple power law because of sharp transitions in the ΔK-rate curves. In 1982, Yoder et al. [*157*], using data generated by Bucci et al. (1980), began to explain these transitions in terms of microstructural barriers to slip-band transmission, as shown in Fig. 12. The transition to threshold, T_1, appeared to be controlled by dispersoid spacing (cyclic plastic zone was about the size of the mean free path between dispersoid particles). Similarly, for T_2 and T_3, the cyclic plastic zone size appeared to correlate with the subgrain and grain size, respectively. Note that these tests were conducted at an R ratio of 0.33. Phillips (see Ref. *145*) tested 7075-T6 at R ratios of -1, 0 and 0.5 and found that these transitions were at different ΔK levels for each R ratio, but that each transition occurred at nearly the same crack-growth rate. Wanhill (Annex A in Ref. *17*) found similar transitions in 2024-T3 aluminum alloy and concluded that the transitions were controlled by the "effective cyclic plastic zones" based on ΔK_{eff} instead of the cyclic plastic zones computed from ΔK. Thus, the transitions in the two alloys appear to be controlled by ΔK_{eff} in laboratory air because the transitions occur at about the same rate.

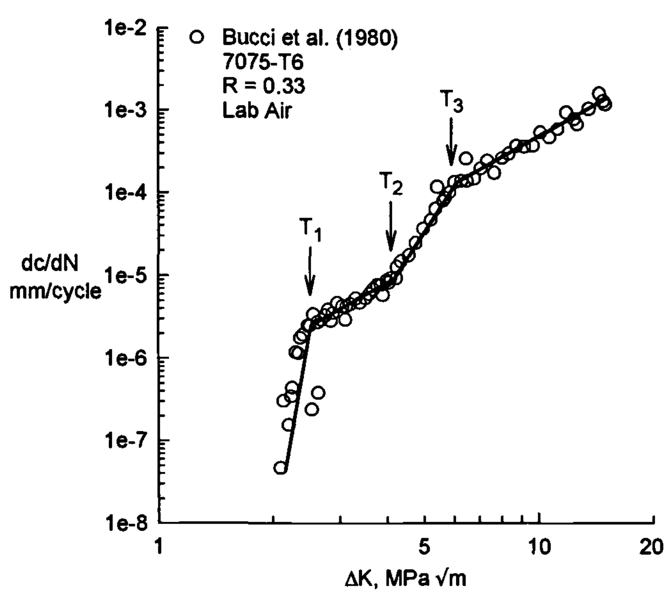

FIG. 12--Microstructural control of fatigue-crack growth (after Yoder et al., 1982 [*157*]).

Environmental Effects

Piascik and Gangloff [*158*] found that these transitions were affected by the environment in crack-growth rate tests on a 2090 aluminum-lithium alloy. Fig. 13 shows tests results in (1) moist air or water vapor, (2) NaCl solution, and (3) Oxygen, helium or vacuum. Test results in each category fell along a particular ΔK-rate relation. The results in moist air or water vapor show a similar characteristic as exhibited by the 7075 alloy in laboratory air (Fig. 12), that is, the sharp transitions at T_1 and T_2. But tests under the salt solution, eliminated the T_2 transition and moved the T_1 transition to a different values of ΔK. Under the inert environments, the transitions did not develop. Piascik and Gangloff attributed these behaviors at low crack-growth rates to fracture mode changes from cracking on the {100} plane in the salt solution to slip-band cracking in the inert environments.

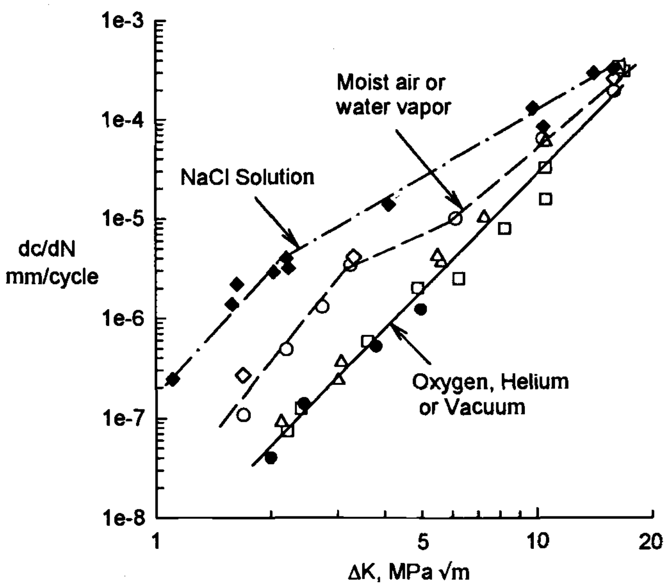

FIG. 13--Environmental fatigue-crack growth in aluminum-lithium alloy (after Piascik and Gangloff, 1993 [*158*]).

Results from Petit and Henaff [*159*, *160*], as shown in Fig. 14, demonstrate the intrinsic behavior of crack growth under the various fracture modes, Stage I, Stage II and Stage I-Like for a wide variety of materials and R ratios tested in high vacuum. When the Stage II crack-growth rate data is plotted against ΔK_{eff} normalized by the elastic modulus (E), all materials (aluminum alloys, aluminum-lithium alloys, steels and TA6V) fall along a unique relation. Similar results are shown for the Stage I and Stage I-Like behaviors. These results help explain why the fracture mode changes can produce transitions in the ΔK-rate relations. These results also demonstrate how new, metallic materials can be developed to have improved damage-tolerance properties. With many engineering metals falling together on a $\Delta K_{eff}/E$ plot, one way to improve the material is to produce a material that would have a large amount of closure either due to plasticity, roughness, or some other closure mechanism.

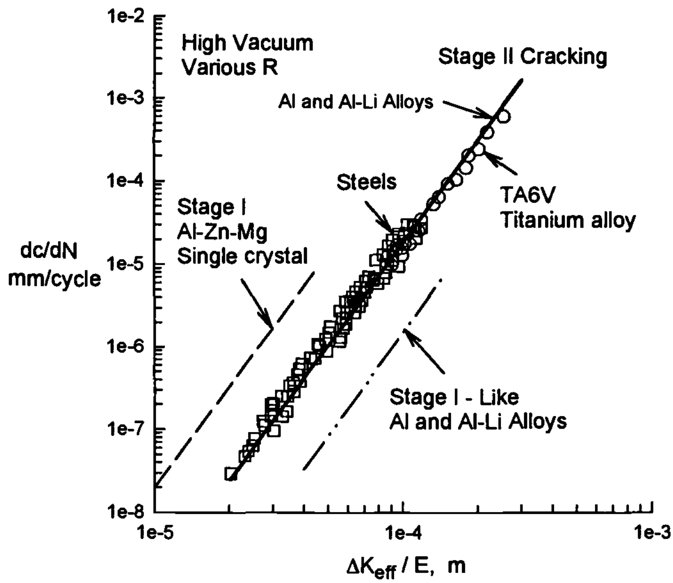

FIG. 14--Intrinsic fatigue crack growth for various material at high vacuum (after Petit and Henaff, 1991-93 [*159,160*]).

Loading Effects

Large-Crack Threshold--Because many of the comparisons between the growth of small and large cracks have been made in the near-threshold regime for large cracks, it is important to know whether the large-crack threshold is a material property or is caused by the load-reduction procedure. Several investigators have experimentally or numerically shown (see Ref. *161*) that the stress-intensity factor threshold under load-reduction schemes can be partly explained by the crack-closure behavior. Some typical results on an aluminum alloy are shown in Fig. 15. Minakawa and McEvily [*162*] conducted a threshold test on a compact specimen and measured the crack-opening loads as the ΔK level approached ΔK_{th}. The crack-opening loads were determined from a displacement gage at the crack mouth. For high ΔK levels, the P_o/P_{max} values ranged from 0.15 to

0.35. The horizontal line is the calculated P_o/P_{max} ratio from Newman's crack-closure model [112] under constant-amplitude loading with plane-strain conditions ($\alpha = 3$). The calculated ratios agreed fairly well with the experimental values. As ΔK approached ΔK_{th}, the P_o/P_{max} ratio rapidly rose and the ratio was nearly unity at threshold. Thus, the rise in crack-opening load explains why the threshold developed. But what caused the rise in crack-opening loads? A number of suggestions have been advanced to explain this behavior. Among these are the mismatch of crack-surface features observed by Walker and Beevers [34] in a titanium alloy; the corrosion product formation on the crack surfaces, as observed by Paris et al. [37]; the variation in the mode of crack growth with stress-intensity factor level as reported by Minakawa and McEvily [162]; and the plastic wake caused by the load-reduction procedure [161]. The usefulness of the large-crack threshold data for small-crack growth is in question, if the threshold development is caused by the activation of different fracture modes, such as roughness-induced closure, and these mechanisms are not activated for small cracks. If the large-crack threshold is affected by the load-reduction procedure, then the overall usefulness of ΔK_{th} for large-crack-growth behavior under variable-amplitude loading is also questionable.

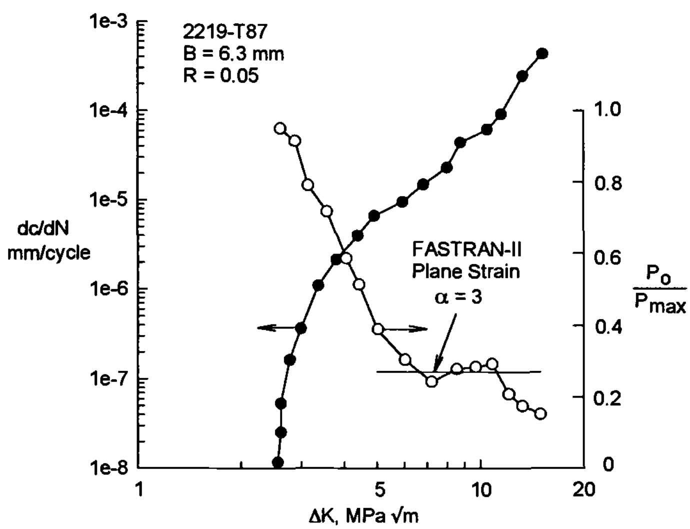

FIG. 15--Experimental crack-growth rates and opening levels near large-crack threshold (modified after Minakawa and McEvily, 1981 [161]).

<u>Transition from Tensile-to-Shear Mode Crack Growth</u>--The crack-growth regime where a crack grows from flat (tensile fracture) to slant (shear fracture), as shown in Fig. 16, is important to defining the constraint-loss regime from plane strain to plane stress. As

observed by Schijve [*26*], the end of transition from flat-to-slant crack growth appears to occur at the same fatigue crack-growth rate, independent of the stress ratio. Newman et al. [*163*] used this observation to control the constraint-loss regime in the analytical crack-closure model. Because the crack-closure concept is able to collapse crack-growth rate data onto nearly a single ΔK_{eff}-rate relation, Schijve [*164*] proposed that the effective stress-intensity factor should control the transition from flat-to-slant crack growth. To develop a simple estimate for the transitional region, Newman [*106*] proposed that the transition to complete slant crack growth occurs when the effective cyclic plastic-zone size calculated from ΔK_{eff} is a certain percentage of the sheet thickness. This relation is

$$\mu = (\Delta K_{eff})_T \,/\, (\sigma_o \sqrt{B}) \tag{8}$$

where σ_o is the flow stress and B is the sheet thickness. Using transitional data from the literature, the transitional coefficient (μ) is plotted against sheet thickness in Fig. 17. Although considerable scatter is evident in the data, the general trend is for μ to be about 0.5 for 1 to 6 mm-thick material. While the ΔK_{eff} at the end of transition is a function of specimen thickness, Wilhem [*165*] suggested that the beginning of the shear-lip development for aluminum and titanium alloys may be independent of specimen thickness. This is reasonable, considering that the material at the free surface is in a state of plane stress, regardless of thickness.

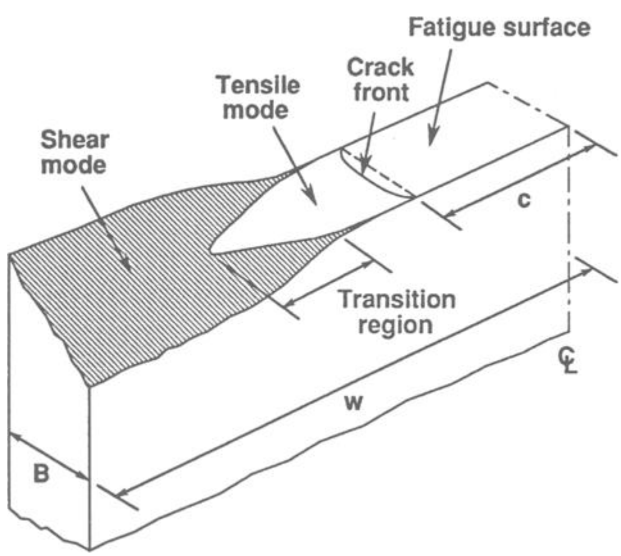

FIG. 16--Flat-to-slant fatigue-crack growth in metallic materials.

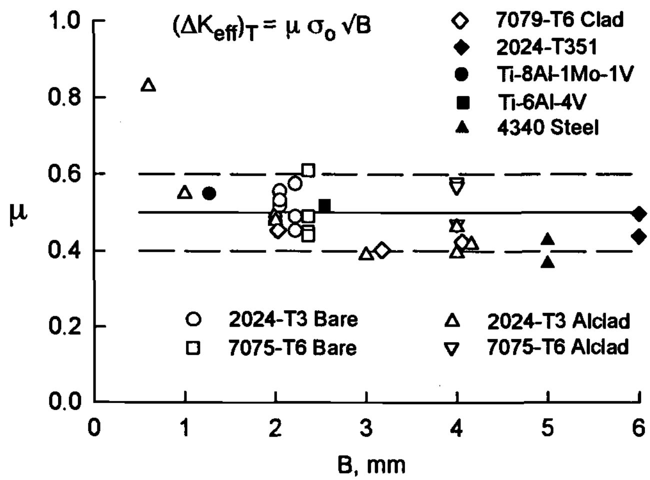

FIG. 17--Controlling parameter for flat-to-slant fatigue-crack growth (after Newman, 1992 [*106*]).

Constant-Amplitude Loading--In 1969, Hudson [*166*] produced fatigue-crack-growth-rate data for 2024-T3 and 7075-T6 aluminum alloy sheet over a wide range of stress ratios (R = -1 to 0.8) and stress-intensity factor ranges. Later, Phillips [*145, 167*] generated crack-growth data in the near-threshold regime for the same alloys; and Dubensky [*168*] conducted tests at extremely high remote stress levels (0.6 to 1.0 times the yield stress of the material). These tests produced crack-growth-rate data over 8-orders of magnitude in rates! These types of tests and data are needed to obtain the baseline crack-growth-rate relations that are needed to predict crack growth under variable-amplitude and aircraft spectrum loading, as will be discussed later.

Typical fatigue-crack growth rate data on 7075-T6 aluminum alloy sheet for various R ratios [*20*] and analyzed with Newman's closure model equations [*89*] are shown in Fig. 18. On the basis of ΔK_{eff}, the data collapsed into a narrow band with several changes in slope (transitions) occurring at about the same growth rate. For these calculations, a constraint factor (α) of 1.8 was selected for rates less than 7E-4 mm/cycle and α equal to 1.2 for rates greater than 7E-3 mm/cycle. The vertical dash line shows the calculation of $(\Delta K_{eff})_T$ from equation (8) with μ = 0.5. The T_4 location (defined herein) shows a sharp transition in the constraint-loss regime. The solid line is the baseline relation. In the low crack-growth rate regime, the large-crack threshold data has been neglected. The baseline relation near the large-crack threshold is an estimate based on small-crack data [*20*].

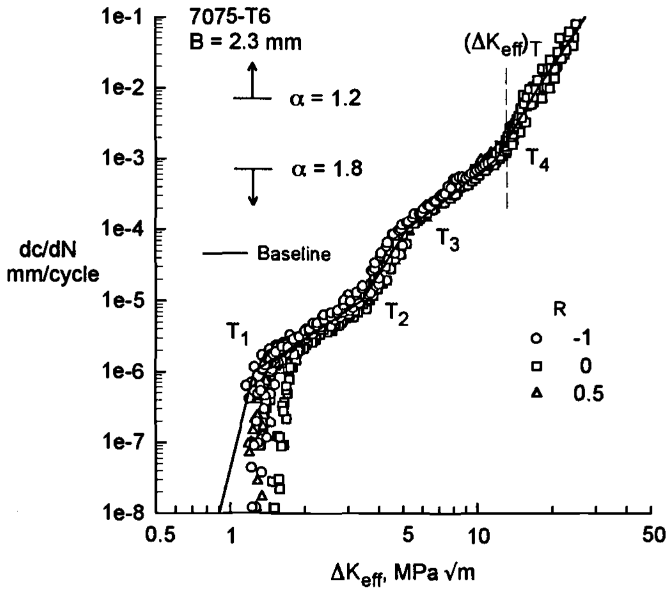

FIG. 18--Effective stress-intensity factor against crack-growth rate for an aluminum alloy (after Newman et al., 1994 [*20*]).

Spectrum Loading--Wanhill [*169*, *170*] conducted spectrum crack-growth tests on middle-crack tension specimens made of 2024-T3 Alclad material (B = 3.1 mm). Tests were conducted under the TWIST (transport wing spectrum) clipped at Level III with a mean flight stress of S_{mf} = 70 MPa. Fig. 19 shows a comparison of test results and calculated results from Newman's closure model [*112*] with the constraint-loss regime (α = 2 to 1) estimated from equation (8). The model used ΔK_{eff}-rate data like that shown in Fig. 18, but for the 2024-T3 alloy. To illustrate why the constraint-loss regime is necessary, example calculations were made for constant constraint conditions of either α = 1 or 2 (dashed curves). The model with a low constraint condition (α = 1) predicted much longer lives than the tests, whereas the model with the high constraint predicted much shorter lives than the tests. Thus, the correct constraint-loss regime is required to predict fatigue-crack growth under aircraft spectrum loading in thin-sheet materials.

SMALL CRACK GROWTH BEHAVIOR

The observation that small or short fatigue cracks can: (1) grow more rapid than those predicted by linear-elastic fracture mechanics (LEFM) based on large-crack data, and (2) grow at ΔK levels well below the large-crack threshold, has attracted considerable

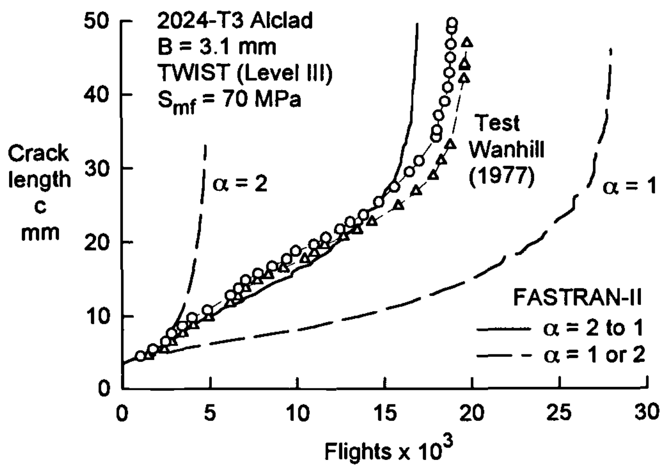

FIG. 19--Experimental and calculated crack length against flights for an aluminum alloy (after Newman, 1992 [*106*]).

attention in the last two decades [*12-21*]. Some consensus is emerging on crack dimensions, mechanisms, and possible methods to correlate and to predict small-crack behavior. A useful classification of small cracks has been made by Ritchie and Lankford [*171*] and these are summarized in Table 5. Naturally-occurring (three-dimensional) small cracks, often approaching microstructural dimensions, are largely affected by crack shape (surface or corner cracks), enhanced crack-tip plastic strains due to micro-plasticity, local arrest at grain boundaries, and the lack of crack closure in the early stages of growth. Whereas, two-dimensional short cracks, about 100 μm or greater, are through-thickness cracks which have been created artificially be removing the wake of material from large through cracks. Their behavior appears to be controlled by the plastic-wake history left by the large-crack growth process and the crack-growth rates are averaged over many grains through the thickness.

Over the last two decades, in the treatment of microstructurally-, mechanically-, and physically-small cracks, two basic approaches have emerged to explain the rapid growth and deceleration of small cracks when compared to large-crack growth behavior. The first is characterized by "grain-boundary" blocking and consideration of microstructural effects on small-crack growth rates (see for example Refs. *21* and *172*). The second is a "continuum mechanics" approach accounting for the effects of material nonlinearity on the crack-tip driving force and crack-closure transients (see for example Refs. *161* and *173*).

TABLE 5--Classes of small-fatigue cracks, dimensions, responsible mechanisms and potential crack-tip parameters (modified after Ritchie and Lankford, 1986 [*171*]).

Types of Small Cracks	Dimension	Mechanisms	Parameters
Microstructurally-small	$a < d_g$ [(a)] $2c < 5$ to $10\ d_g$	Crack-tip shielding enhanced $\Delta\varepsilon_p$ Crack shape	Probabilistic approach
Mechanically-small	$a < r_y$ [(b)]	Excessive (active) plasticity	ΔJ, $\Delta CTOD$ (ΔK_p)
Physically-small	$a < 1$ mm	Crack-tip shielding (crack closure)	ΔK_{eff}
Chemically-small	up to $\cong 10$ mm (c)	Local crack tip environment	

(a) d_g is critical microstructural dimension, such as grain size; a is surface-crack depth and 2c is surface-crack length
(b) r_y is plastic-zone size or plastic field of notch
(c) critical size is a function of frequency and reaction kinetics

The microstructural barrier model, developed by Miller and co-workers [*15, 172*], was conceived to separate regimes of "microstructurally-small" cracks and "physically-small" cracks. The regime of microstructurally-small cracks (MSC) occurs when crack lengths are less than a dominant microstructural barrier, such as the grain size. Various researchers consider this regime to be synonymous with growth of a crack across a single grain or several grain diameters. For example, a crack may initiate at an inclusion particle on a grain boundary, propagate, slow down, and stop at the next grain boundary. With further cycling, or if the stress level is increased, this barrier can be overcome and the crack will propagate to the next barrier. Several different microstructural barriers to crack growth may exist in a single material because of material anisotropy and texture. The physically-small crack (PSC) regime is defined for crack lengths greater than the spacing of these dominant barriers. Miller [*172*] suggests that the complexities near micro-structural barriers in the MSC and PSC regimes hinder theoretical analyses of small-crack growth behavior based on LEFM parameters and he emphasizes the development of empirical equations, based on extensive test data, to determine constants in these relations. However, progress has been made in the analyses of cracks growing from inclusions (see for example Ref. *174*) and interacting with grain boundaries [*113, 116*]. These analyses may be useful in developing the LEFM relations for cracks in complex microstructures.

As shown in Fig. 20, small-crack initiation and growth is a three-dimensional process with cracks in the depth, a, and length, c, directions interacting with the grain boundaries at different times in their cyclic history. Whereas, an observed crack in the length direction may have decelerated at or near a grain boundary, the crack depth may still be growing. As the crack grows in the depth direction, the rise in the crack-driving force at the c-location contributes to the crack penetrating that barrier. As the cracks become longer, the influence of grain boundaries become less as the crack front begins to average behavior over more grains. Small-crack growth deceleration may or may not occur depending upon the orientation of the adjacent grains [21]. A probabilistic analysis would be required to assess the influence of the variability of the grain structure on crack-growth rate properties. From an engineering standpoint, however, a weak-link or worst case scenario of grain orientation may provide a conservative estimate for the growth of small cracks through a complex microstructure. This is the basis for the continuum mechanics approach.

It has been argued that the calculation of ΔK for a small crack growing from an inclusion could be in error (Schijve [175]). For example, if crack initiation occurs at a subsurface inclusion with subsequent breakthrough to the surface, a considerable elevation

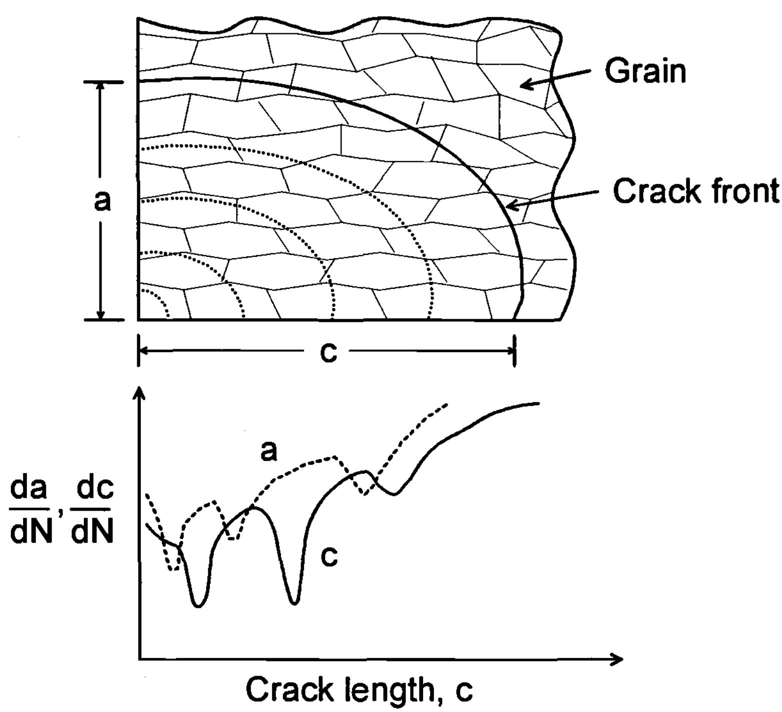

FIG. 20--Surface crack growth and an influence of grain boundaries.

in ΔK is possible over that calculated from surface observations. Although the use of ΔK to characterize the growth of small cracks has proved to be convenient, its universal application has been viewed with some skepticism. Despite the above qualifications, research work on the growth of naturally-initiated small cracks, notably by Lankford [*21, 176*] and AGARD studies [*17, 18*], has demonstrated the usefulness of the ΔK concept.

One of the leading continuum mechanics approaches to small-crack growth is that of Newman et al. [*161, 163*]. The crack-closure transient (or more correctly the lack of closure in the early stages of growth) has long been suspected as a leading reason for the small-crack effect. The Newman crack-closure model [*112*] has demonstrated the capability to model small-crack growth behavior in a wide variety of materials and loading conditions [*161*]. Difficulties still exist for large-scale plastic deformations at holes or notches but these are problems that can be treated with advanced continuum mechanics concepts. In the remaining sections, the application of the Newman model to predict or calculate fatigue life based solely on crack propagation will be reviewed.

Earlier work by Pearson [*12*] on fatigue-crack initiation and growth of small cracks from inclusion particles in two aluminum alloys (BS L65 and DTD 5050) set the stage for the development of small-crack theory. His results are shown in Fig. 21(a), as the dashed curve, along with additional small-crack data from Lankford [*21*] on 7075-T6 aluminum alloy. Pearson concluded that cracks of about the size of the average grain size, grew several times faster than large cracks at nominally identical ΔK values. The open symbols and dash-dot curve show the large-crack data and the development of the large-crack threshold at about 3 to 4 MPa $\sqrt{m}$. The solid symbols show the typical small-crack behavior with growth at ΔK levels as low as 1.5 MPa $\sqrt{m}$. The other solid curves show the behavior measured on other small cracks. Some general observations, by Lankford [*21*], were that the minimum in da/dN occurred when the crack depth, a, was about the minimum dimension of the pancake grain (subsurface grain boundary, as shown in Fig. 20) and that the magnitude of the lower rates was controlled by the degree of micro-plasticity in the next grain penetrated by the crack. If the next grain is oriented like the first, then no deceleration will occur, as indicated by the uppermost small-crack curves in Fig. 21(a).

At this stage, it would be of interest to compare the test results from Pearson and Lankford with the small-crack growth predictions made from a continuum-mechanics model based on crack closure [*156*]. The ΔK_{eff}-rate relation used in the closure model for the 7075-T6 alloy was generated in Ref. *20* and the relation is shown in Fig. 21(b) as the dotted lines. These results were generated from large-crack data for rates greater than about 2E-6 mm/cycle. The results are quite different from those shown for the Pearson-Lankford large-crack data in that the T_2 transition (at about 1E-5 mm/cycle) did not appear in their data. The lower section of the ΔK_{eff}-rate relation (below 2E-6 mm/cycle) was estimated on the basis of small-crack data, also generated in Ref. *20*. Because small cracks are assumed to be fully open on the first cycle, the ΔK_{eff}-rate relation is the starting point for small-crack analysis. The results of an analysis of the test specimen used by Lankford is shown by the heavy solid curve. The initial defect was selected as a 10 μm radius semi-circular crack, so that the 2a dimension (on the surface) would be 20 μm.

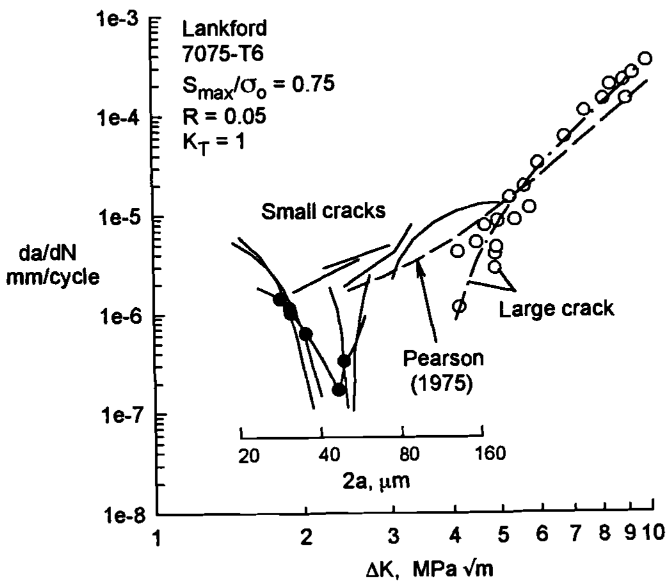

FIG. 21(a)--Measured and calculated small-crack growth in an aluminum alloy (after Lankford, 1982 [21]).

As the small crack grows, the closure level increases much faster than the ΔK level and a rapid decrease in rates is calculated. This rapid drop is a combination of the closure transient and the sharp change in slope at the T_1 location (at about 1E-6 mm/cycle). At about 30 μm, the crack-opening stresses have nearly stabilized and the effects of plasticity on the crack-driving force is quite small considering that the applied stress was 0.75 times the flow stress (see Fig. 6 in Ref. *63*). The predicted small-crack results are in excellent agreement with Pearson's data and agree with Lankford's data which do not exhibit a grain-boundary influence. Interestingly, the small-crack analysis shows a single dip in the small-crack curve, similar to the "single" dip observed in some of Lankford's small-crack data. Would the grain-boundary interaction always occur at the same crack length (40 μm)? Why aren't there other dips, or small indications of a dip, in the rate curve at 80, 120 or 160 μm? Further study is needed to help resolve these issues, but the fatigue life, or at least a lower bound fatigue life, can be calculated from continuum-mechanics concepts. The following sections will review the use of Small-Crack Theory to predict fatigue life for notch specimens under various load histories.

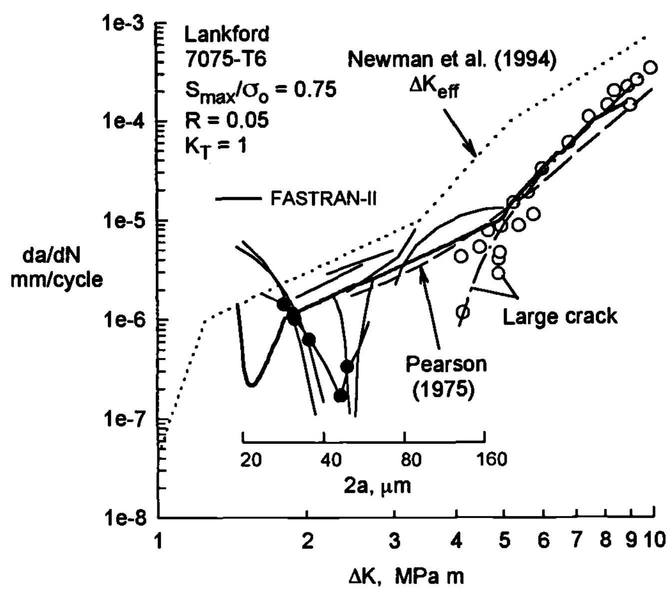

FIG. 21(b)--Measured and predicted small-crack growth in an aluminum alloy.

PREDICTION OF FATIGUE LIFE USING SMALL-CRACK THEORY

During the last decade, several international research programs have been conducted by the AGARD Structures and Materials Panel [*17, 18, 177, 178*], the National Aeronautics and Space Administration (NASA) [*20*] and the Chinese Aeronautical Establishment (CAE) [*179*] on small-crack effects in a wide variety of materials and loading conditions. A summary of the materials and loading conditions used to generate small-crack data on notched specimens is listed in Table 6. Most of these studies dealt with naturally-initiated cracks at notches but some studies [*177, 178*] used small electrical-discharged-machined notches to initiate cracks.

All materials listed in Table 6 were subjected to a wide range of stress ratios (R) under constant-amplitude loading. The 2024-T3 aluminum alloy [*17, 18*] was subjected to FALSTAFF, Inverted FALSTAFF, Gaussian, Felix-28, and TWIST loading; and the 7075-T6 alloy [*18, 20, 179*] was subjected to the Gaussian and Mini-TWIST load spectra. The Lc9CS (a clad equivalent of 7075-T6) [*20, 179*] was subjected to Mini-TWIST loading. Aluminum-lithium alloy 2090 [*18*] was subjected to the FALSTAFF, Gaussian, TWIST, and Felix-28 load sequences. The 4340 steel [*18*] was subjected to only the Felix-28 helicopter load sequence. The three titanium alloys (Ti-6Al-4V, IMI-685 and Ti-17) [*177, 178*] were subjected to only the Cold Turbistan spectrum. Details on these standardized spectra may be obtained from the appropriate references.

TABLE 6--Materials and loading conditions used in various small-crack programs.

Materials	Loading Conditions (a)
2024-T3	Constant-amplitude
7075-T6	FALSTAFF
Lc9CS (clad)	Inverted FALSTAFF
2090-T8E41	Gaussian
4340	TWIST
Ti-6Al-4V	Mini-TWIST
IMI-685	Felix-28
Ti-17	Cold Turbistan
	Commercial transport

(a) List of materials and loading conditions are not associated.

Newman and many of his coworkers [*17, 20, 163, 180*] used continuum-mechanics concepts with initial defect sizes, like those which initiated cracks at inclusion particles, voids or slip-bands, and the effective stress-intensity factor range (corrected for plasticity and closure) to predict the fatigue lives for many of the materials listed in Table 6. A summary of the initial defect sizes measured at numerous initiation sites is listed in Table 7. The baseline crack-growth rate data for these materials were obtained from the large-crack data, ignoring the large-crack threshold, and using small-crack growth rates at the extremely low rates. Small-crack thresholds were estimated from the endurance limit for the various materials. In the following, some typical examples of small-crack theory application will be presented.

Aluminum Alloy 2024

Landers and Hardrath [*181*] conducted fatigue tests on 2024-T3 aluminum alloy sheet material with specimens containing a central hole. The results are shown in Fig. 22 as symbols. Both elastic and elastic-plastic fatigue-crack growth analyses were performed. The solid and dashed curves show predictions using large-crack growth rate data (ignoring the large-crack threshold) and an initial crack size based on an average inclusion-particle size that initiated cracks [*17*]. The large-crack growth rate properties are given in Ref. *163* for the elastic stress-intensity factor analysis. The crack-growth rate properties using the elastic-plastic effective stress-intensity factor analysis were obtained from a re-analysis of the large-crack data [*182*]. Both predictions agreed near the fatigue limit but differed substantially as the applied stress approached the flow stress (σ_0 = 425 MPa). In these predictions, a ΔK-effective threshold for small cracks was selected as 1.05 MPa $\sqrt{m}$ (see Ref. *17*). Using this threshold value and the

TABLE 7--Average material defect sizes and equivalent area crack sizes (surface defect unless otherwise noted).

Material	Defect Half-length, μm	Defect Depth, μm	Equivalent Area Semi-Circular Crack Radius, μm
2024-T3	3	12	6
7075-T6	3	9	5.2
Lc9CS (clad)	77 (a)	77	77
2090-T8E41	3.5	11	6
4340	8	13	10
Ti-6Al-4V (sheet)	(b)	(b)	0.5 (c)
Ti-6Al-4V (forging)	(b)	(b)	15 (c)

(a) Corner crack at clad layer (clad thickness about 60-70 μm).
(b) No metallurgical examination of initiation sites was made.
(c) Value selected to fit fatigue data.

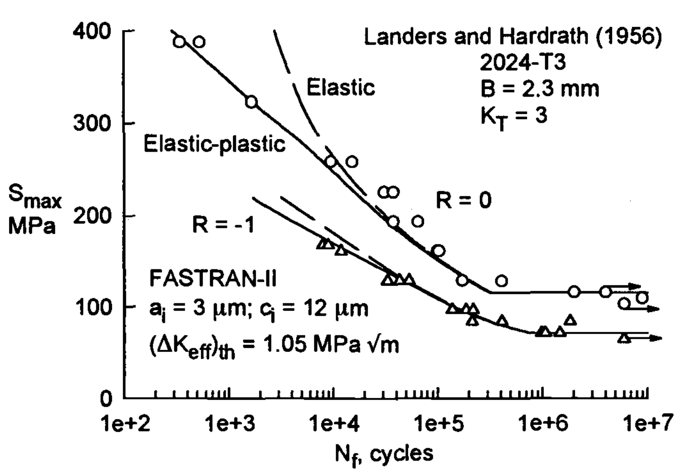

FIG. 22--Measured and predict fatigue lives for a hole in an aluminum alloy under constant-amplitude loading (after Newman, 1992 [*182*]).

initial defect size, the analysis were used to match the fatigue limits for the two R ratio tests. Above a stress level of about 250 MPa, the results from the elastic and elastic-plastic analyses differed substantially. The results from the elastic-plastic analyses agreed well with the test data and substantiated the use of the cyclic-plastic-zone corrected effective-stress-intensity-factor range [*63*]. Similar comparisons between measured and predicted S-N behavior for notched and un-notched aluminum alloy specimens subjected to either constant- or variable-amplitude loading are presented in Reference *183*.

Laz and Hillberry [*184*] conducted a study to address the influence of inclusions on fatigue-crack formation in 2024-T3 using a probabilistic model in conjunction with the FASTRAN-II code [*156*]. An examination of the microstructure produced data on nearly 3800 inclusions on the primary crack plane. A Monto Carlo simulation was conducted for 1000 trials. In each trial, an inclusion particle area is randomly selected and converted to an equivalent semi-circular initial crack size. The initial crack size, which was assumed to be located at the center of a single-edge-notch tension (SENT) specimen, was grown using the FASTRAN-II model. The probabilistic model produced a predicted distribution of fatigue lives. These results are presented in Fig. 23 as the solid curve and are compared with experimental data from the AGARD study [*17*] and other tests conducted by Laz and Hillberry. The probabilistic model accurately predicts both the mean and variation of the experimental results. Most importantly, however, the model predicted the critical lowest life values, which correspond to the largest, most damaging inclusions.

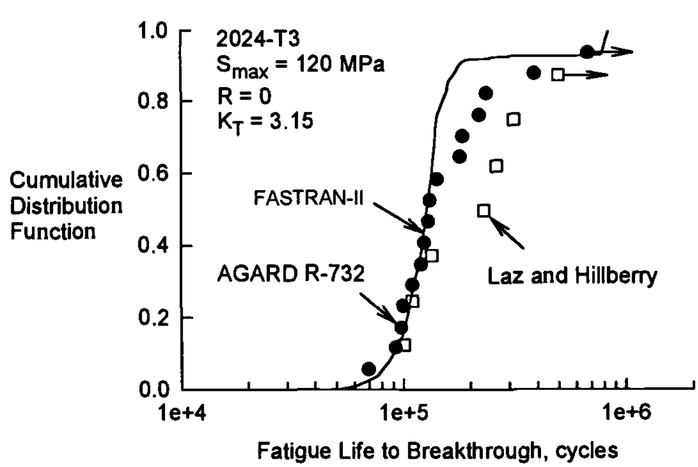

FIG. 23--Measured and predicted cumulative distribution function for a notched aluminum alloy under constant-amplitude loading (after Laz and Hillberry, 1995 [*184*]).

High-Strength 4340 Steel

Swain et al. [*185*] conducted fatigue and small-crack tests on 4340 steel, single-edge-notch tensile specimens. Tests were also conducted on large cracks to obtain the baseline crack-growth rate data. These tests were conducted under both constant-amplitude and spectrum loading. Only the results from the spectrum load fatigue tests will be discussed here.

The results of the fatigue life tests under the Felix-28 load sequence are shown in Fig. 24 as symbols. Inspection of the fracture surfaces showed that in each case a crack had initiated at an inclusion particle defect. Those specimens which had the shorter lives had cracks which initiated at spherical calcium-aluminate particle defects, whereas those with the longer lives had cracks which initiated at manganese sulfide stringer inclusion particle defects. Examination of the initiation sites for over 30 fatigue cracks produced information on the distribution of crack initiation site dimensions. The spherical particle defects range in size from 10 to 40 μm in diameter. The stringer particles were typically 5 to 20 μm in the thickness direction and range up to 60 μm in length. The median values of the defect dimensions measured were a_i = 8 μm and c_i = 13 μm.

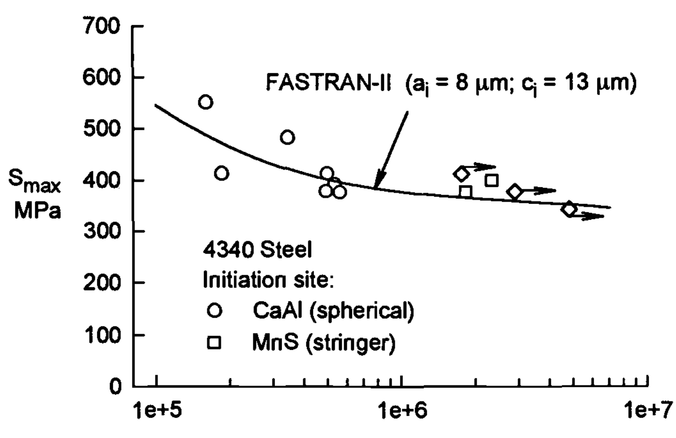

FIG. 24--Measured and predict fatigue lives for notched high-strength steel under helicopter spectrum loading, Felix/28 (after Swain et al., 1990 [*185*]).

Predictions of total fatigue life under the Felix-28 load spectrum were made using FASTRAN-II [*156*] by calculating the number of cycles necessary to grow a crack from the assumed initial defect size, located at the center of the notch root, to failure. The comparison between model predictions and experimental fatigue lives are shown in Fig. 24. The predicted results agreed well for those specimens which contained spherical defects as crack initiation sites. But, the predicted lives fell short for those specimens where cracks initiated from stringer inclusions or where no cracks of minimum size necessary for continued propagation were formed. Again, it is desirable to have good agreement for the larger spherical-inclusion particles because these particles will produce the minimum fatigue lives. For an engineering component, which may contain a large number of fastener holes or other areas of stress concentration, the likelihood of a critical sized inclusion particle being located at one of these sites is large.

Titanium Alloy Ti-6Al-4V

The titanium alloys listed in Table 7, the sheet and forging products, exhibited quite different behavior in terms of the equivalent initial flaw size (EIFS) required to fit the S-N data on notched specimens. For the sheet alloy, the EIFS was 0.5 μm [*180*], whereas the forging alloy required a defect 2 to 20 μm in depth to bound the scatter in tests on two different forgings. A comparison of the measured and calculated fatigue lives on the two titanium forgings are shown in Fig. 25. The fatigue test data generated on double-edge-notch tensile specimens made from the two forgings agreed well with each other. The FASTRAN-II life prediction code was used with large-crack growth rate data to calculate the fatigue lives from a selected initial semi-circular surface crack size, as shown by the solid curves (see Ref. *145*). An average defect size of about 10 μm would fit the mean of the experimental data quite well. (Note: An error was detected in the review process. The predicted S-N behavior, Fig. 20 in Ref. *145*, was calculated at R = 0 instead of 0.1. Fig. 25 is a re-analysis of the S-N behavior.)

Because no metallurgical examination of the fractured specimens was made to evaluate the initiation site in either References *178* or *186*, an attempt was made to relate the assumed initial crack size to some microstructural features (see Ref. *180*). Because titanium has a relatively high solubility for most common elements and when multiple vacuum arc melting is accomplished with high purity materials, the occurrence of inclusion-type defects is rare. In a mill-annealed titanium alloy, Eylon and Pierce [*187*] studied the initiation of cracks and found that cracks preferred to nucleate in the width direction of alpha needles, or colonies of alpha needles, along a shear band on the basal plane. The size of the alpha needles was not reported but was stated to be considerably smaller than the size of alpha grains (grains were about 8 μm in size). Thus, the alpha needle size may be close to the initial crack size needed to predict most of the fatigue life based solely on crack propagation. For the forging alloy, Wanhill and Looije [*188*] found that the primary α-grains and platelet α-packets ranged from 8 to 18 μm. Whether these α-grains or packets contributed to the early initiation of micro-crack growth in the titanium forgings must await further study.

DESIGN CONCEPT USING SMALL-CRACK THEORY

The research that has occurred over the last two decades on "small- or micro-" crack growth has evolved into a new design concept that provides an alternative to the traditional safe-life (or S-N) approach. The diagram in Fig. 26 shows the various design concepts: Safe-

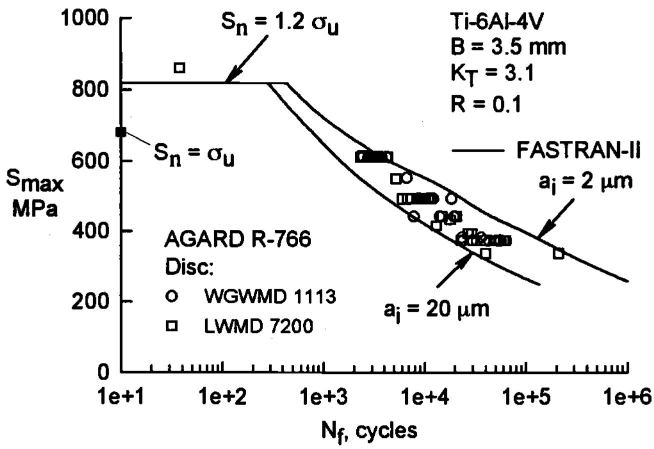

FIG. 25--Measured and calculated fatigue lives for a double-edge-notch tensile specimen under constant-amplitude loading (modified after Newman et al., 1994 [*145*]).

life, Small-crack theory, Durability, Damage tolerance, and Fail-safe, and their relative location with respect to flaw size. The flow in the diagram, from safe-life to the fail-safe concept, depicts crack formation, micro-crack growth, macro-crack growth, and fracture.

One of the original design concepts used in the aerospace industry was "safe-life", see Reference *22*. Here a structure was assumed to be defect free and the life was established by conventional S-N or ε-N approaches. A safe-life component is retired from service when its useful life has been expended. More recently, the total life has been calculated from a crack-initiation period (N_i) and a crack-propagation period (N_p), see Reference *189*. However, the crack size existing after the initiation period was debatable. In practice, however, it has been found that preexisting manufacturing defects (i.e., scratches, flaws, burrs, and cracks) or service induced damage (i.e., corrosion pits) are very often the source of structural cracking problems. The effect of these defects on the life of a component was dependent on the defects initial size, the rate of crack growth with service usage, and the critical crack size.

From these considerations, the "damage-tolerance" design philosophy [*190*] was developed. The damage-tolerance approach assumes that a component has prior damage or a flaw size that is inspectable. Useful service life is then some specified portion of the crack propagation life required to grow the crack from the inspectable size to failure.

The durability design concept [*191*] is economic-life extension to minimize in-service maintenance costs and to maximize performance. The durability analysis methodology, based on a probabilistic fracture mechanics approach, accounts for the initial fatigue quality (i.e., surface treatment, manufacturing defects), fatigue-crack growth in a population of structural details, load spectra, and structural design details. A statistical distribution of the "equivalent

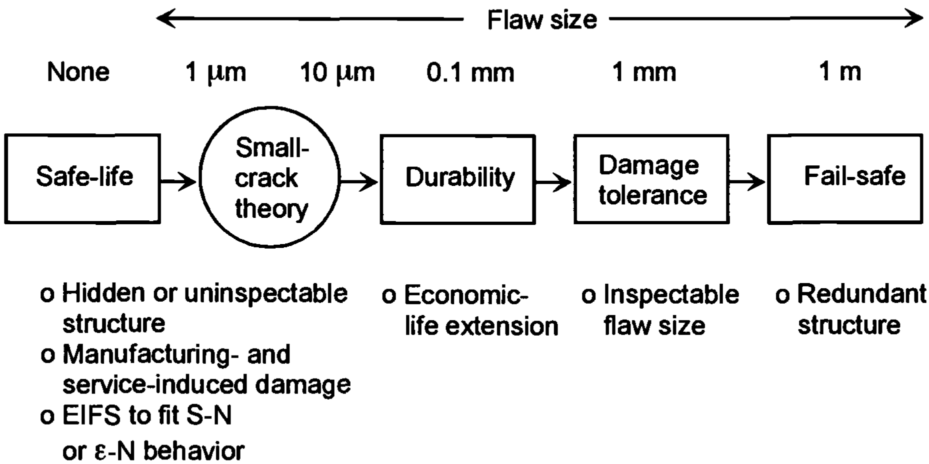

FIG. 26--Evolution of design concepts in relation to "small-crack theory."

initial flaw sizes" (EIFS) is used to represent the initial fatigue quality of structural details. In practice, the EIFS distributions have ranged from 0.1 to 0.5 mm. As the EIFS's become smaller (below about 1 mm), the question of small-crack effects is raised. The current durability methodology, which does not account for small-crack effects, masks the small-crack behavior by deriving an EIFS that predicts the desired crack-propagation life. However, EIFS variability with load spectra may be resolved if small-crack theory is implemented into the design practice.

The evolution of "safe-life" and "durability/damage-tolerance" design concepts have both moved in the direction of "small-crack behavior." As inspection techniques and manufacturing quality improves, smaller flaw sizes will be detected or produced in manufacturing. The design of uninspectable or hidden structures, or structures subjected to an extremely large number of cyclic loads (i.e., engines and helicopter components) must relie on approaches that deal with the growth of small cracks.

"Small-crack theory" is currently used to assess the structural fatigue life at two levels of initial flaw sizes. First, it is used to assess the initial design quality of a structure based solely on "material" microstructural properties, such as cracks growing from inclusion particles, voids, grains, grain boundaries or cladding layers. Of course, this crack-growth life is the best the current material can provide under the desired loading. In the second level of calculations, as in the durability analysis, a manufacturing or service-induced flaw size is used with small-crack theory. But the effects of small-crack growth are now accounted for in the analysis (i.e., faster growth rates at a given ΔK and growth below the large-crack threshold). Small-crack theory can now be used to evaluate EIFS for various spectra and structural details; and to characterize S-N or ε-N behavior. The impact of small-crack effects on design-life calculations have been discussed by Phillips and Newman [*192*].

SUMMARY – Past, Present and Future

A summary of the observations as well as past, present and potential future approaches concerning fatigue concepts, crack-propagation concepts, and small- (or micro-) crack growth behavior has been made. In the past, fatigue was characterized by stress-life (S-N) or strain-life (ε-N) curves; and crack propagation was characterized by the ΔK-rate concept. It was observed that small cracks initiated early in life at high stress levels, but initiated late in life at low stress levels (near the endurance limit). Thus, initiation life was dominate near the endurance limit. At present, fatigue is characterized by a crack initiation stage (N_i) and a crack-propagation stage (N_p); and crack propagation is characterized by the effective cyclic stress-intensity factor (ΔK_{eff}) or J-integral (ΔJ_{eff}). Small cracks grow faster than large cracks; and small cracks grow at stress-intensity factor (ΔK) levels well below the large-crack threshold (ΔK_{th}).

Proposed future approaches are: (1) fatigue damage is characterized by crack size and fatigue lives are calculated by crack propagation from a micro-crack size, (2) crack growth is characterized by a local nonlinear crack-tip stress or deformation parameter, such as J, T*, ΔCTOD or cyclic hysteresis energy, (3) small-crack growth is viewed as the typical behavior and large-crack growth near and at threshold is the anomaly on a ΔK basis, and (4) fatigue life prediction methods need to be developed to predict micro-crack growth, as influenced by microstructure and environment, under complex load histories. The proposed approaches will potentially bridge the gap between "safe life" and "durability/damage tolerance" concepts.

REFERENCES

[*1*] Swedlow, J. L., Ph.D. Thesis, California Institute of Technology, Pasadena, CA, 1965.

[*2*] Cohen, B., Farren, W., Duncan, W. and Wheeler, A., "Report of the Court of Inquiry into the Accidents to Comet G-ALYP on 10 January 1954 and Comet G-ALYY on 8 April 1954," HMSO, London, 1955.

[*3*] Irwin, G. R., *Journal of Applied Mechanics*, Vol. 24, 1957, pp 361-364.

[*4*] Paris, P., Gomez, M. and Anderson, W., *The Trend in Engineering*, Vol. 13, 1961, p 9.

[*5*] Paris, P. C. and Erdogan, F., *Journal of Basic Engineering*, Vol. 85, 1963, p 528.

[*6*] Neuber, H., *Journal of Applied Mechanics*, Vol. 28, No. 4, 1961, pp 544-550.

[*7*] Hardrath, H. F. and Ohman, L., NACA TR 1117, 1953.

[*8*] Hutchinson, J. W., *Journal of Mechanics and Physics of Solids*, Vol. 16, 1968, p 13.

[*9*] Rice, J. R., *Journal of Applied Mechanics*, June 1968, pp 379-386.

[*10*] McEvily, A. J., Jr. and Illg, W., NACA TN 4394, 1958.

[*11*] Elber, W., in ASTM STP 486, 1971, pp 230-242.

[*12*] Pearson, S., *Engineering Fracture Mechanics*, Vol. 7, No. 2, 1975, pp 235-247.

[*13*] Kitagawa, H. and Takahashi, S., in *Proceedings of 2nd International Conference on Mechanical Behavior of Materials*, Boston, MA, 1976, pp 627-631.

[*14*] Ritchie, R. O. and Lankford, J., eds., *Small Fatigue Cracks*, The Metallurgical Society, Inc., Warrendale, PA, 1986.

[15] Miller, K. J. and de los Rios, E. R., eds., *The Behaviour of Short Fatigue Cracks*, European Group on Fracture, Publication No. 1, 1986.
[16] Zocher, H., ed., AGARD CP-328, 1983.
[17] Newman, J. C., Jr. and Edwards, P. R., AGARD Report No. 732, 1988.
[18] Edwards, P. R. and Newman, J. C., Jr., eds., AGARD Report No. 767, 1990.
[19] Larsen, J. M. and Allison, J. E., eds., ASTM STP 1149, 1992.
[20] Newman, J. C., Jr.; Wu, X. R.; Venneri, S. L and Li, C. G., NASA RP-1309, 1994.
[21] Lankford, J., *Fatigue of Engineering Materials and Structures*, Vol. 5, 1982, p 233.
[22] Fuchs, H. and Stephens, R., *Metal Fatigue in Engineering*, John Wiley and Sons, 1980.
[23] Smith, R. A., ed., *Fatigue Crack Growth*, Pergamon Press, New York, 1986.
[24] Schütz, W., *Engineering Fracture Mechanics*, Vol. 54, No. 2, 1996, pp 263-300.
[25] Paris, P. C., in ASTM STP 1207, J. Landes, D. McCabe and J. Boulet, eds., 1994, p 5.
[26] Schijve, J., in ASTM STP 415, 1967, pp 415-459.
[27] Schijve, J., *Engineering Fracture Mechanics*, Vol. 11, 1979, pp 167-221.
[28] Forsyth, P. J. E., in *Proceedings of Crack Propagation Symposium*, Vol. I, Cranfield College of Aeronautics, Cranfield, UK, 1961, pp 76-94.
[29] Bowles, C. Q. and Schijve, J., *International Journal of Fracture*, Vol. 9, 1973, p 171.
[30] Morris, W., Buck, O. and Marcus, H., *Metallurgical Transactions*, Vol. 7A, August 1976, pp 1161-1165.
[31] Kung, C. Y. and Fine, M. E., *Metallurgical Transactions*, Vol. 10A, 1979, p 603.
[32] Hunter, M. S. and Fricke, W. G., Jr., in *Proceedings of the American Society for Testing and Materials*, Vol. 56, 1956, pp 1038-1046.
[33] Elber, W., Ph.D. Thesis, University of New South Wales, 1968.
[34] Walker, N. and Beevers, C. J., *Fatigue of Engineering Materials and Structures*, Vol. 1, No. 1, 1979, pp 135-148.
[35] Halliday, M. D. and Beevers, C. J., *International Journal of Fracture*, Vol. 15, p R27.
[36] Suresh, S. and Ritchie, R. O., *Metallurgical Transactions*, Vol. 13A, September 1982, pp 1627-1631.
[37] Paris, P. C., Bucci, R. J., Wessel, E. T., Clark, W. G. and Mager, T. R., in ASTM STP 513, 1972, pp 141-176.
[38] Suresh, S., Parks, D. and Ritchie, R., in *Proceedings Symposium on Fatigue Thresholds*, J. Backlund, A. Blom, and C. Beevers, EMAS Ltd., Warley, UK, 1982, pp 391-408.
[39] Irwin, G. R., in *9th International Congress Applied Mechanics*, Brussels, Vol. 8, 1956, p 245-251.
[40] Williams, M. L., *Journal of Applied Mechanics*, Vol. 24, 1957, pp 109-114.
[41] Tada, H., Paris, P. C. and Irwin, G. R., *The Stress Analysis of Cracks Handbook*, Del Research Corporation, Bethlehem, PA, 1985.
[42] Murakami, Y., ed., *Stress Intensity Factors Handbook*, Pergamon Press, 1987.
[43] Raju, I. S. and Newman, J. C., Jr., *Engineering Fracture Mechanics*, Vol. 11, No. 4, 1979, pp 817-829.
[44] Newman, J. C., Jr. and Raju, I. S., in *Computational Methods in the Mechanics of Fracture*, S. N. Atluri, ed., Elsevier, 1986, pp 311-334.

[*45*] Rice, J. R. and Rosengren, G. F., *Journal Mechanics and Physics of Solids*, Vol. 16, 1968, pp 1-12.

[*46*] Eshelby, J. D., *Solid State Physics*, Vol. 3, Academic Press, New York, 1956, p 79-144.

[*47*] Sanders, J. L., *Journal of Applied Mechanics*, Vol. 27, 1960, pp 352-353.

[*48*] Cherepanov, G. P., *Applied Mathematics and Mechanics*, Vol. 31, No. 3, 1967, pp 467-488.

[*49*] Landes, J. D. and Begley, J. A., in ASTM STP 514, 1972, p 1.

[*50*] Cherepanov, G. P., *International Journal Solids and Structures*, Vol. 25, 1989, p 1267.

[*51*] Atluri, S. N., *Engineering Fracture Mechanics*, Vol. 16, 1982, pp 341-364.

[*52*] Atluri, S. N., Nishioka, T. and Nakagaki, M., *Engineering Fracture Mechanics*, Vol. 20, No. 2, 1984, pp 209-244.

[*53*] Dowling, N. E. and Begley, J. A., in ASTM STP 590, 1976, pp 82-103.

[*54*] Dowling, N. E., in ASTM STP 601, 1976, pp 19-32.

[*55*] Kumar, K., Dattaguru, B., Ramamurthy, T., Prakash, R., and Raju, K., in *27th National Symposium on Fatigue and Fracture Mechanics*, Williamsburg, VA, 1996.

[*56*] Irwin, G. R., in *Proceedings 7th Sagamore Conference*, 1960, pp IV.63-IV.76.

[*57*] McClintock, F. A. and Irwin, G. R., in ASTM STP 381, 1965, pp 84-113.

[*58*] Dugdale, D. S., *Journal of the Mechanics and Physics of Solids*, Vol. 8, 1960, p 100.

[*59*] Barenblatt, G. I., *PMM*, Vol. 23, No. 3, 1959, pp 434-444.

[*60*] Newman, J. C., Jr., *Engineering Fracture Mechanics*, Vol. 1, 1968, pp 137-154.

[*61*] Chan, K. S., in *Small Fatigue Cracks*, The Metallurgical Society, Inc., Warrendale, PA, 1986, pp 407-426.

[*62*] Drucker, D. C. and Rice, J. R., *Engineering Fracture Mechanics*, Vol. 1, 1970, p 577.

[*63*] Newman, J. C., Jr., in ASTM STP 1149, J. Larsen and J. E. Allison, eds., 1992, p 6.

[*64*] Hudak, S. J., Jr. and Chan, K. S., in *Small Fatigue Cracks*, The Metallurgical Society, Inc., Warrendale, PA, 1986, pp 379-406.

[*65*] Hudak, S. J., Jr. and Page, R. A., *Corrosion - NACE*, Vol. 39, July 1983, pp 287-290.

[*66*] Newman, J. C., Jr., Ph.D. Thesis, VPI&SU, Blacksburg, VA, May 1974.

[*67*] Newman, J. C., Jr. and Armen, H., Jr., *AIAA Journal*, Vol. 13, Aug. 1975, p 1017.

[*68*] Newman, J. C., Jr., in ASTM STP 490, 1976, p 281.

[*69*] Ohji, K., Ogura, K. and Ohkubo, Y., *Engineering Fracture Mechanics*, Vol. 7, 1975, pp 457-464.

[*70*] Nakagaki, M. and Atluri, S. N., *AIAA Journal*, Vol. 18, 1980, pp 1110-1117.

[*71*] Anquez, L., La Recherche Aerospatiale, Report No. 1983-2, 1983.

[*72*] Blom, A. F. and Holm, D. K., *Engineering Fracture Mechanics*, Vol. 22, 1985, pp 997.

[*73*] Kobayashi, H. and Nakamura, H., in *Current Research on Fatigue Cracks*, The Society of Materials Science (Japan), 1985, pp 201-215.

[*74*] Lalor, P., Sehitoglu, H. and McClung, R. C., in *The Behavior of Short Fatigue Cracks*, EFG 1, Mechanical Engineering Publications, London, 1986, pp 369-386.

[*75*] Bednarz, E., Ph.D. Thesis, Air Force Institute of Technology, 1986.

[*76*] Fleck, N. A., *Engineering Fracture Mechanics*, Vol. 25, 1986, pp 441-449.

[*77*] Nicholas, T., Palazotto, A. N. and Bednarz, E., in ASTM STP 982, 1988, pp 361-379.

[78] Anquez, L. and Boudin, G., in ASTM STP 982, 1988, pp 380-397.
[79] Fleck, N. A. and Newman, J. C., Jr., in ASTM STP 982, 1988, pp 319-341.
[80] McClung, R. C. and Sehitoglu, H., *Engineering Fracture Mechanics*, Vol. 33, 1989, pp 253-272.
[81] McClung, R. C., in *Theoretical Concepts and Numerical Analysis of Fatigue*, A. Blom and C. Beevers, eds., Engineering Materials Advisory Services, Ltd., 1992, p 153.
[82] McClung, R. C., *Fatigue and Fracture of Engineering Materials and Structures*, Vol. 17, 1994, pp 861-872.
[83] Llorca, J. and Galvez, S., *Engineering Fracture Mechanics*, Vol. 37, 1990, p 185.
[84] Llorca, J., *Fatigue and Fracture of Engineering Materials and Structures*, Vol. 15, 1992, pp 655-669.
[85] Sehitoglu, H., Gall, K. and Garcia, A. M., *International Journal of Fracture*, Vol. 80, No. 2-3, 1996, pp 165-192.
[86] Chermahini, R. G, Ph.D. Thesis, Old Dominion University, Norfolk, VA, 1986.
[87] Chermahini, R. G., Shivakumar, K. N. and Newman, J. C., Jr., in ASTM STP 982, 1988, pp 398-413.
[88] Chermahini, R. G. and Blom, A. F., *Theoretical and Applied Fracture Mechanics*, Vol. 15, 1991, pp 267-276.
[89] Newman, J. C., Jr., *International Journal of Fracture*, Vol. 24, 1984, pp R131-R135.
[90] Dawicke, D., Shivakumar, K., Newman, J., and Grandt, A., in ASTM STP 1131, Vol. II, 1992, pp 46-57.
[91] Sunder, R. and Dash, P. K., *International Journal of Fatigue*, Vol. 4, 1982, pp 97-105.
[92] Wheeler, O. E., *Journal of Basic Engineering*, 1972, pp 181-186.
[93] Willenborg, J. D., Engle, R. M. and Wood, H. A., AFFDL-TM-71-1-FBR, Dayton, OH, January 1971.
[94] Gallagher, J. P., AFFDL-TM-74-28-FBR, Dayton, OH, January 1974.
[95] Chang, J. B., Engle, R. M. and Stolpestad, J., in ASTM STP 743, 1981, pp 3-27.
[96] Johnson, W. S., in ASTM STP 748, 1981, pp 85-102.
[97] Harter, J. A., AFWAL-TM-88-157-FIBE, February 1988 (Revised July 1994).
[98] Bell, P. D. and Wolfman, A., in ASTM STP 595, 1976, pp 157-171.
[99] Schijve, J., in ASTM STP 700, 1980, pp 3-34.
[100] De Koning, A. U., in ASTM STP 743, 1981, pp 63-85.
[101] Baudin, G. and Robert, M., in *Proceedings of the Fifth European Conference on Fracture*, Lisbon, Spain, 1984, pp 779-792.
[102] Aliaga, D., Davy, A. and Schaff, H., in *Durability and Damage Tolerance in Aircraft Design*, EMAS Ltd., Warley, UK, 1985, pp 605-630.
[103] Chang, J. B. and Hudson, C. M., eds., ASTM STP 748, 1981.
[104] Lazzeri, L., Pieracci, A. and Salvetti, A., in *18th Symposium of International Committee on Aeronautical Fatigue*, Melbourne, Australia, May 1995.
[105] Wanhill, R. J. H., *International Journal of Fatigue*, Vol. 16, 1994, pp 99-110.
[106] Newman, J. C., Jr., in *Fatigue of Aircraft Materials*, A. Beukers, T. deJong, J. Sinke, A. Vlot and L. B. Vogelesang, eds., Delft University Press, 1992, pp 83-109.

[*107*] Seeger, T., Institut fur Statik und Stahlbau, Report No. 21, Darmstadt, Germany, 1973.
[*108*] Dill, H. D. and Saff, C. R., in ASTM STP 595, 1976, pp 306-319.
[*109*] Budiansky, B. and Hutchinson, J. W., *Journal of Applied Mechanics*, Vol. 45, 1978, pp 267-276.
[*110*] Hardrath, H. F., Newman, J. C., Jr., Elber, W. and Poe, C. C., Jr., in *Fracture Mechanics*, N. Perrone, Liebowitz, H., Mulville, D. and Pilkey, W., eds., University of Virginia Press, 1978, pp 347-364.
[*111*] Fuhring, H. and Seeger, T., *Engineering Fracture Mechanics*, Vol. 11, 1979, p 99.
[*112*] Newman, J. C., Jr., in ASTM STP 748, 1981, pp 53-84.
[*113*] Nakai, Y., Tanaka, K. and Yamashita, M., *Journal Society of Material Science*, Japan, Vol. 32, 1983, pp 19-25.
[*114*] Sehitoglu, H., *Engineering Fracture Mechanics*, Vol. 21, No. 2, 1985, pp 329-339.
[*115*] Keyvanfar, F., Ph.D. Thesis, Stanford University, Stanford, CA, August 1985
[*116*] Tanaka, K., in *Small Fatigue Cracks*, The Metallurgical Society, Inc., 1986, p 343.
[*117*] Ibrahim, F. K., Ph.D. Thesis, University of Waterloo, Waterloo, Canada, 1986.
[*118*] Wang, G. S. and Blom, A. F., The Aeronautical Research Institute of Sweden, Report FFA TN 1987-79, 1987.
[*119*] Keyvanfar, F. and Nelson, D. V., in ASTM STP 982, 1988, pp 414-436.
[*120*] deKoning, A. U. and Liefting, G., in ASTM STP 982, 1988, pp 437-458.
[*121*] Nakamura, H. and Kobayashi, H., in ASTM STP 982, 1988, pp 459-474.
[*122*] Chen, D. H. and Nisitani, H., in ASTM STP 982, 1988, pp 475-488.
[*123*] Wang, G. S. and Blom, A. F., *Engineering Fracture Mechanics*, Vol. 40, 1991, p 507.
[*124*] Daniewicz, S. R., Ph.D. Thesis, Ohio State University, 1991.
[*125*] ten Hoeve, H. J. and de Koning, A. U., NLR CR 95399 L, The Netherlands, 1995.
[*126*] Blauel, J. G. and Schwalbe, K., eds., *Defect Assessment in Components - Fundamentals and Applications*, ESIS/EGF 9, Mechanical Engineering Publication Ltd., 1991.
[*127*] Hackett, E., Schwalbe, K. and Dodds, R., eds., ASTM STP 1171, 1993.
[*128*] Kirk, M. and Bakker, A., eds., ASTM STP 1244, 1995.
[*129*] McClintock, F. A., *Journal of Applied Mechanics*, June 1968, pp 363-371.
[*130*] Rice, J. and Tracey, D. M., *Journal of the Mechanics and Physics of Solids*, Vol. 17, 1969, pp 201-217.
[*131*] Sommer, E. and Aurich, D., in *Defect Assessment in Components - Fundamentals and Applications*, ESIS/EGF 9, J. G. Blauel and K. -H. Schwalbe, eds., 1991, pp 141-174.
[*132*] Larsson, S. G. and Carlsson, A. J., *Journal of the Mechanics and Physics of Solids*, Vol. 21, 1973, pp 263-278.
[*133*] Betegon, C. and Hancock, J. W., *Journal of Applied Mechanics*, Vol. 58, 1991, p 104.
[*134*] Li, Y. and Wang, Z., *Scientia Sinica* (Series A), Vol. 29, 1986, pp 941-955.
[*135*] O'Dowd, N. P. and Shih, C. F., *Journal of Mechanics and Physics of Solids*, Vol. 39, 1991, pp 989-1015.
[*136*] O'Dowd, N. P. and Shih, C. F., *Journal of Mechanics and Physics of Solids*, Vol. 40, 1992, pp 939-963.

[*137*] Yang, S., Chao, Y. J. and Sutton, M. A., *Engineering Fracture Mechanics*, Vol. 45, 1993, pp 1-20.

[*138*] Chao, Y. J., Yang, S. and Sutton, M. A., *Journal of Mechanics and Physics of Solids*, Vol. 42, 1994, pp 629-647.

[*139*] Newman, J. C., Jr., *Engineering Fracture Mechanics*, Vol. 5, 1973, pp 667-689.

[*140*] Newman, J. C., Jr., in *Proceedings of the Tenth Anniversary Meeting of the Society of Engineering Science*, Raleigh, N. C., 1973, pp 67-74.

[*141*] Sadowsky, M. and Sternberg, E., *Journal of Applied Mechanics*, Vol. 16, 1949, p 149.

[*142*] Kuhn, P. and Figge, I. E., NASA TN D-1259, 1962.

[*143*] Merkle, J. G., in ASTM STP 1256, 1995, pp 3-40.

[*144*] Newman, J. C., Jr., Bigelow, C. A. and Shivakumar, K. N., *Engineering Fracture Mechanics*, Vol. 46, No. 1, 1993, pp 1-13.

[*145*] Newman, J. C., Jr., Phillips, E. P. and Everett, R. A., Jr., in AGARD Report No. 797, 1994, pp 2.1-2.13.

[*146*] Head, A. K., *Philosophical Magazine*, Vol. 44, pp 925-928.

[*147*] Donaldson, D. R. and Anderson, W. E., in *Proceedings of the Crack Propagation Symposium*, Vol. II, Cranfield College of Aeronautics, 1962, pp 375-441.

[*148*] Forman, R. G., Kearney, V. E. and Engle, R. M., *Journal of Basic Engineering*, Vol. 89, No. 3, 1967, pp 459-464.

[*149*] Walker, K., in ASTM STP 462, 1970, pp 1-14.

[*150*] Elber, W., *Engineering Fracture Mechanics*, Vol. 2, No. 1, 1970, pp 37-45.

[*151*] Tomkins, B., *Philosophical Magazine*, Vol. 18, 1968, pp 1041-1066.

[*152*] Bilby, B. A., Cottrell, A. H. and Swinden, K. H., in *Proceedings of the Royal Society A*, Vol. 272, 1963, p 304.

[*153*] Ogura, K., Miyoshi, Y. and Nishikawa, I., in *Current Research on Fatigue Cracks*, T. Tanaka, M. Jono, and K. Komai, eds., Society of Materials Science, Japan, 1985, p 57.

[*154*] Miller, M. S. and Gallagher, J. P., in ASTM STP 738, 1981, pp 205-251.

[*155*] Forman, R., Shivakumar, V., Newman, J., Piotrowski, S. and Williams, L., in ASTM STP 945, 1988, pp 781-803.

[*156*] Newman, J. C., Jr., NASA TM-104159, February 1992.

[*157*] Yoder, G. R., Cooley, L. A. and Crooker, T. W., *Scripta Metallurgica*, Vol. 16, 1982, pp 1021-1025.

[*158*] Piascik, R. S. and Gangloff, R. P., *Metallurgical Transactions*, Vol. 24A, December 1993, pp 2751-2762.

[*159*] Petit, J. and Henaff, G., *Scripta Metallurgica*, Vol. 25, 1991, pp 2683-2687.

[*160*] Petit, J. and Henaff, G., in *Fatigue 93*, J. Bailon and Dickson, J., eds., 1993, p 503.

[*161*] Newman, J. C., Jr., in AGARD CP-328, 1983, pp 6.1-6.26.

[*162*] Minakawa, K. and McEvily, A. J., in *Proceedings International Conference on Fatigue Thresholds*, Vol. 2, Stockholm, Sweden, 1981, pp 373-390.

[*163*] Newman, J. C., Jr., Swain, M. H. and Phillips, E. P., in *Small Fatigue Cracks*, The Metallurgical Society, Inc., Warrendale, PA, 1986, pp 427-452.

[*164*] Schijve, J., Delft University of Technology, Report LR-287, Sept. 1979.

[165] Wilhem, D. P., in ASTM STP 415, 1967, pp 363-383.
[166] Hudson, C. M., NASA TN D-5390, 1969.
[167] Phillips, E. P., in ASTM STP 982, pp 505-515.
[168] Dubensky, R. G., NASA CR-1732, 1971.
[169] Wanhill, R. J. H., NLR TR 77092 U, July 1977.
[170] Wanhill, R. J. H., *Fatigue of Engineering Materials and Structures*, Vol. 1, 1979, p 5.
[171] Ritchie, R. O. and Lankford, J., in *Small Fatigue Cracks*, The Metallurgical Society, Inc., Warrendale, PA, 1986, pp 1-5.
[172] Miller, K. J., *Fatigue and Fracture of Engineering Materials and Structures*, Vol. 10, No. 1, 1987.
[173] El Haddad, M. H., Dowling, N. E., Topper, T. H. and Smith, K. N., *International Journal of Fracture*, Vol. 16, 1980, pp 15-30.
[174] Trantina, G. G. and Barishpolsky, M., *Engineering Fracture Mechanics*, Vol. 20, 1984, pp 1-10.
[175] Schijve, J., in *Proceedings 2nd International Conference on Fatigue and Fatigue Thresholds*, University of Birmingham, September 1984.
[176] Lankford, J., *Fatigue of Engineering Material and Structures*, Vol. 6, 1983, pp 15-32.
[177] Mom, A. J. A. and Raizenne, M. D., eds., AGARD Report 766, August 1988.
[178] *AGARD Engine Disc Cooperative Programme*, AGARD Report 766 (Addendum), April 1993.
[179] *Selected Papers in Scientific and Technical International Cooperation Program*, C. Zhihua, ed., Chinese Aeronautical Establishment, No. 5, Aviation Industry Press, 1994.
[180] Newman, J. C., Jr., Phillips, E. P., Swain, M. H. and Everett, R. A., Jr., ASTM STP 1122, 1992, pp 5-27.
[181] Landers, C. B. and Hardrath, H. F., NACA TN-3631, March 1956.
[182] Newman, J. C., Jr., in *Theoretical Concepts and Numerical Analysis of Fatigue*, A. F. Blom and C. J. Beevers, eds., EMAS, Ltd., 1992, pp 301-325.
[183] Newman, J. C., Jr., *Fatigue and Fracture of Engineering Materials and Structures*, Vol. 17, 1994, pp 429-439.
[184] Laz, P. J. and Hillberry, B. M., in *Fatigue 96*, Lutjering G. and Nowack, H., eds., Berlin, Germany, May 1996.
[185] Swain, M. H., Everett, R. A., Jr., Newman, J. C., Jr. and Phillips, E. P., in AGARD Report 767, 1990, pp 7.1-7.30.
[186] Lanciotti, A. and Galatolo, R., in AGARD Report 767, 1990.
[187] Eylon, D. and Pierce, C. M., *Metallurgical Transactions*, Vol. 7A, 1976, pp 111-121.
[188] Wanhill, R. and Looije, C., in AGARD Report 766 (Addendum), 1993, pp 2.1-2.40.
[189] Dowling, N. E., *Mechanical Behavior of Materials*, Prentice Hall, Inc., p 667.
[190] Gallagher, J., Giessler, F., Berens, A., and Engle, R., AFWAL-TR-82-3073, May 1984.
[191] Manning, S. D. and Yang, J. N., AFWAL-TR-83-3027, January 1984.
[192] Phillips, E. P. and Newman, J. C., Jr., *Experimental Mechanics*, June 1989, pp 221-225.

General Topics

Hiroyuki Hamada[1], Masaya Kotaki[1] and Adrian Lowe[2]

EFFECT OF INTERFACIAL CHARACTERISTICS ON MODE I FRACTURE BEHAVIOUR OF GLASS WOVEN FABRIC COMPOSITES UNDER STATIC AND FATIGUE LOADING

REFERENCE: Hamada, H., Kotaki, M. and Lowe, A., **''Effect of Interfacial Characteristics on Mode I Fracture Behaviour of Glass Woven Fabric Composites under Static and Fatigue Loading''**, Fatigue and Fracture Mechanics: 28th Volume, ASTM STP 1321, J. H. Underwood, B. D. Macdonald and M. R. Mitchell, Eds., American Society for Testing and Materials, 1997.

ABSTRACT: The influence of fibre surface treatment on the mode I delamination characteristics of a glass fabric/vinyl ester composite was studied. Five treatments were used: solutions containing 0.01wt%, 0.4wt% and 1.0wt% of γ-methacryloxy-propyltrimethoxysilane (MS); 0.4wt% of MS subsequently washed in methanol; and 0.4wt% of γ-glycidoxypropyltrimethoxysilane (ES). Static mode I tests were performed on specimens oriented in both the warp and weft fibre directions. The tests revealed that stable crack propagation was only observed with the ES-treated specimens and with the most dilute MS treatment. Invariably, fracture toughnesses were higher in the weft oriented specimens. The degree of unstable fracture observed under fatigue loading was generally significantly lower than under static loading. The specimens treated with the highest concentrations of MS possessed the highest fatigue resistance and had threshold toughness values in excess of the static toughness values. Fractographic examination was performed on both static and fatigue fracture surfaces, revealing markedly different fracture morphologies in relation to the degree of interfacial failure observed.

KEY WORDS: fabric composites; fibre surface treatments; fracture toughness; modelling; fatigue; fracture mechanisms

INTRODUCTION

In order to tailor the mechanical properties of composite materials towards specific applications, an understanding of the fibre/matrix interface is essential. There are many aspects to consider before reliable interfacial design can be attained. These aspects include determination of the type of fibre/matrix bond present; the influence of any interphase region present, and the effect of chemical coupling agents on the physical and mechanical properties of the interface. Perhaps the most important aspect to consider is how microstructural effects at the interface boundary ultimately translate into macro-scale effects in bulk

[1]Professor and Research Student, Kyoto Institute of Technology, Kyoto 606, Japan

[2]Lecturer, Engineering Department, Australian National University, Canberra Australia

composite structures. The use of single fibre microcomposite test methods to determine interfacial characteristics on a micro-level is well documented [1-10]. However, opinions differ as to how the data generated from these tests can be used to predict macro-scale mechanical properties in multifibre composites. The main difficulty is in the understanding of the interactive processes that occur when a large number of fibres are in proximity to each other. Perhaps the most successful method of realising an improvement in interfacial bonding is in the use of fibre surface treatments. These can be either dry treatments (e.g. plasma) or wet treatments (chemical silane coupling agents or chemical etchants).

A particularly poorly understood aspect of interfacial behaviour is the influence of different fibre surface treatments on the fatigue delamination behaviour of composite structures. As delamination in fabric composites invariably occurs around the interfacial regions, it is essential that the change in fatigue resistance caused by the use of fibre surface treatments is known. Also, the effect of the plastic zone around the crack tip needs to be understood.

The purpose of this study is to characterize the effect on composite fracture toughness in static and fatigue loading of various fibre treatments that are known to function on a microscale. Previous work on glass cloth/polyester composites [11-14] revealed that the geometry of the weave pattern directly influenced the resulting fracture toughness values, and so a model was proposed [14] that would express the bulk fracture toughness of a fabric composite (G_{woven}) in terms of the toughness of the fibre/matrix interface, the toughness of the matrix phase, toughness variations caused by the weave pattern and the percentage of the total fracture surface area that is interfacial, as described by equation (1):

$$G_{woven} = \alpha G_{int} + (1-\alpha) G_{res} + \alpha\left(\frac{m}{m+n}\Delta G_0 + \frac{n}{m+n}\Delta G_{90}\right) \qquad (1)$$

where

G_{int} =	fracture toughness of the interface
G_{res} =	fracture toughness of the resin
m and n =	fractions of fibre surface area in the 0° and 90° directions respectively
ΔG_0 and ΔG_{90} =	increments of fracture toughness derived from the bending of fibres in the 0° and 90° directions respectively
α =	parameter expressing the ratio of exposed interfacial region to the total surface area exposed on the fracture surface

The work presented in this paper attempts to use this model to explain the variation of fracture toughness with parameters such as weave orientation, fracture morphology and G_{int} using materials subjected to several different fibre treatments. In addition, the effect of fibre surface treatment on the fatigue response of the composite material will be established, and fractographic analysis will be used to identify any differences in fracture mechanisms between different materials and different loading types.

TEST MATERIALS

Glass fibre woven fabric of warp/weft ratio 44/34 (where warp and weft are measured in counts per inch), was used as the fibre phase. The fabric consisted of E-glass fibre bundles containing roughly 400 fibres of diameter 9μm. The fibre surface treatments used were γ-methacryloxypropyltrimethoxysilane (MS) and γ-glycidoxypropyltrimethoxysilane (ES). The fibre preforms were treated by immersion in aqueous silane solutions of predefined concentrations at a constant pH value of 4.0. Five different fibre treatment combinations were adopted, as detailed in Table 1. The purpose of the methanol washing was to remove any absorbed silane from the fibre surface. All wet materials were squeeze dried at 110°C for 10 minutes.

TABLE 1-- *Detailing the fibre surface treatments adopted for the test program.*

Fibre treatment	Aqueous solution	Finishing process
A	0.01wt% MS	
B	0.4wt% MS	
C	1.0% MS	
D	0.4wt% MS	washing in methanol
E	0.4% ES	

The matrix material was a vinyl ester-based resin (RipoxyR806), formed by the reaction of unsaturated polyester monomer with 0.7 parts per hundred of methylethylketone peroxide. This resin family chemically reacts with MS coupling agent far more readily than with the ES coupling agent. The hand lay-up technique was used to manufacture laminates, 20 plies thick, with a 40μm thick PTFE insert forming a pre-crack region between the 10th and 11th plies. This material was cured to a final laminate thickness of 4mm.

STATIC TEST DETAILS

Test geometry

All static mode I fracture toughness tests were performed using the Double Cantilever Beam (DCB) test geometry, as detailed in figure 1. Specimens were cut parallel to both warp and weft fibre directions and were 100mm long by 25mm wide. An Instron model 4206 test apparatus was used and tests were performed at a displacement rate of 1mm/min. A single loading cycle was used and the crack length periodically measured by means of a travelling microscope attached to the side of the test specimen.

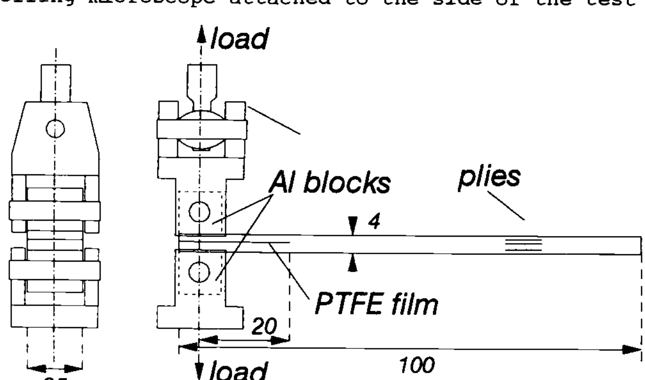

FIG 1-- *DCB test apparatus and specimen (all dimensions in mm).*

Corresponding values for applied load (P) and crack opening displacement (δ) were also recorded, and a compliance value (C) at each crack length calculated using

$$C = \frac{\delta}{P} \tag{2}$$

For each crack length, the mode I fracture toughness (G_{Ic}) was calculated using equation (3):

$$G_{Ic} = \frac{3P^2(BC)^{2/3}}{2(2H)B^2\xi} \tag{3}$$

where B = specimen width
H = specimen half-thickness
ξ = a correction factor

The value of ξ is defined in equation (4)

$$\frac{a}{2H} = \xi(BC)^{1/3} + \beta \tag{4}$$

where a = crack length
β = a constant

Hence a plot of $a/2H$ versus $(BC)^{1/3}$ will yield a value of ξ for each test specimen.

STATIC TEST RESULTS

Figure 2 shows typical plots of fracture toughness versus crack extension, Δa, for each of the five different test materials tested in the weft direction (5 tests per material). Material A to material E denote material fabricated using fibre surface treatments A to E respectively.

It is clear that only material A and material E exhibit stable crack propagation characteristics under static loading. These two materials also exhibited the smallest R-curve effect, especially during crack propagation. The "saw tooth" behaviour seen with materials B, C and D is characteristic of unstable crack propagation. Although material B is clearly failing in an unstable manner, there is a small region where stable crack propagation has occurred. This does not occur in material D, and so washing with methanol reduces the stability of crack propagation, as does increasing the MS content of the fibre treatment.

Figure 3 presents the same information as figure 2, but obtained in the warp direction (again, 5 tests per material). Clearly, changing the fabric orientation had no bearing on overall failure mechanisms, and only materials A and B experienced any variation in fracture toughness characteristics between warp and weft oriented specimens. In the case of material A (subjected to the most dilute surface treatment), the difference is most marked at the crack initiation stage and during the early stages of crack propagation, where a pronounced R-curve effect occurs. This results in G_{Ic} values substantially lower than in the weft direction. In the warp direction, material B is wholly unstable, and both materials A and B appear to be significantly less delamination resistant in this direction.

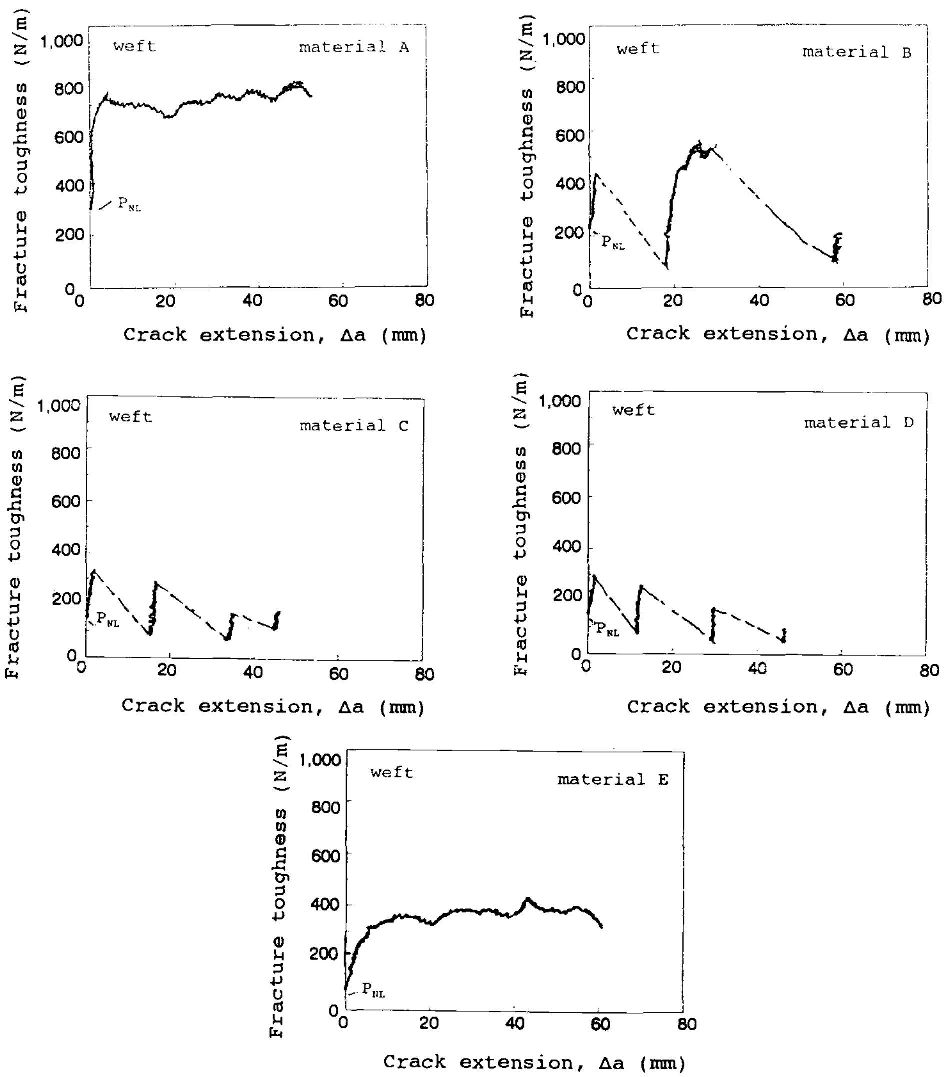

FIG 2-- Variation of fracture toughness with crack extension for weft oriented specimens under mode I loading: (a) 0.01wt% MS; (b) 0.4wt% MS; (c) 1.0wt% MS; (d) methanol washed 0.4wt% MS and (e) 0.4wt% ES. Also indicated are the points of non-linearity (P_{NL}) from which initiation fracture toughness values are taken.

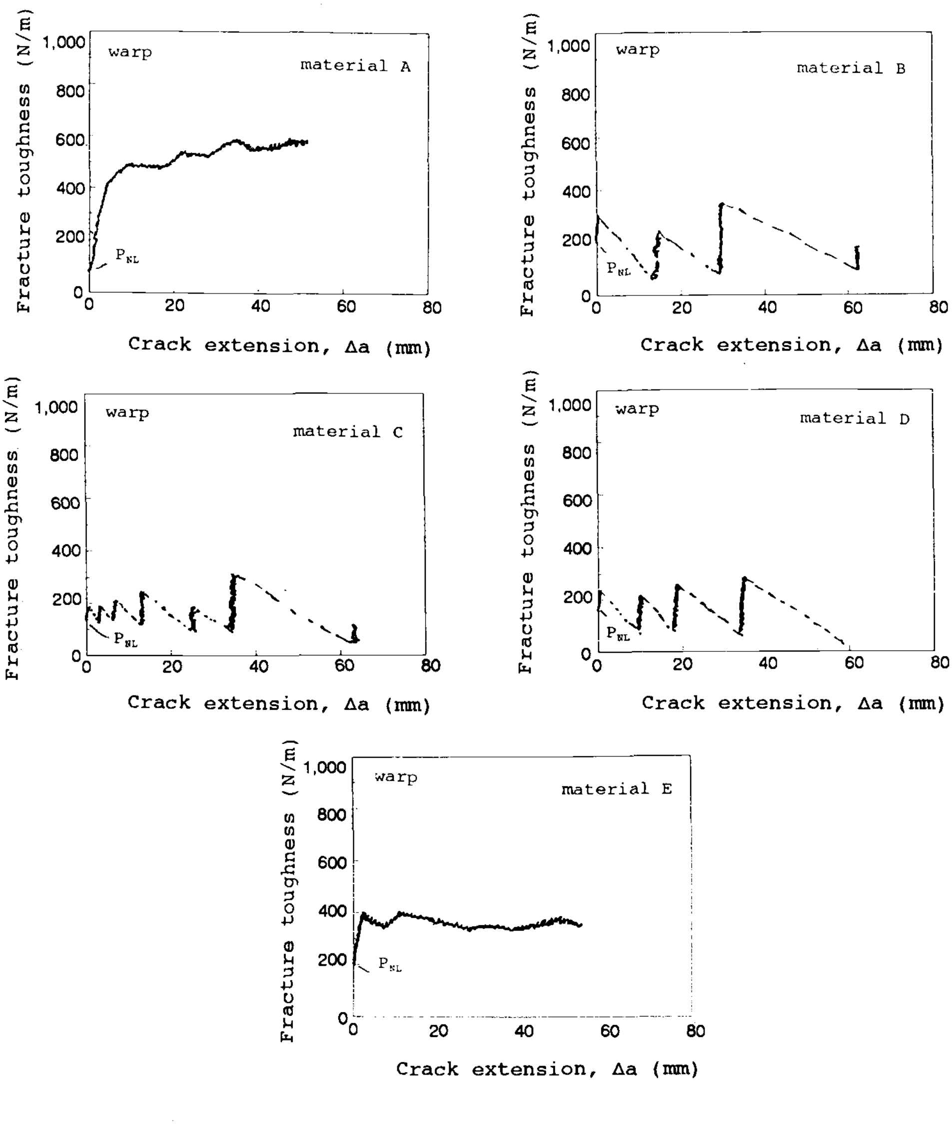

FIG 3-- *Variation of fracture toughness with crack extension for warp oriented specimens under mode I loading: (a) 0.01wt% MS; (b) 0.4wt% MS; (c) 1.0wt% MS; (d) methanol washed 0.4wt% MS and (e) 0.4wt% ES. Also indicated are the points of non-linearity (P_{NL}) from which initiation fracture toughness values are taken.*

Whenever an R-curve effect is apparent, it is important to quote the fracture toughness of the system as both an initiation value (the toughness when the crack begins to propagate from the PTFE insert) and as a propagation value (the toughness during steady state growth), as the crack growth mechanisms may be different. For instance, the initiation process originates from a crack tip that is equal in size to the thickness of the PTFE insert, whereas the propagation process originates from a crack front that is much thinner. The propagation toughness value is extremely important to designers from a viewpoint of structural stability [15]. Using figure 2 and figure 3, the initiation value of G_{Ic} is defined as the point of onset of non-linear behaviour, and is indicated by the points marked P_{NL}.

Figure 4(a) details the initiation fracture toughness values obtained for all test materials in both the warp and weft orientations and shows that specimens oriented with the weft direction parallel to the specimen axis were generally more resistant to mode I crack growth. The exception is the ES-treated material. The effect of washing in methanol appears to be a slight reduction in initiation fracture toughness. Interestingly, the influence of specimen orientation in the MS-treated specimens became significantly greater as the treatments became more dilute. Figure 4(b) details the propagation fracture toughness values obtained for all materials in both the warp and weft orientations after crack growth of approximately 20mm and clearly shows that the highest delamination resistance is obtained from the most dilute fibre treatment. Again, higher fracture toughness was obtained from specimens oriented in the weft direction.

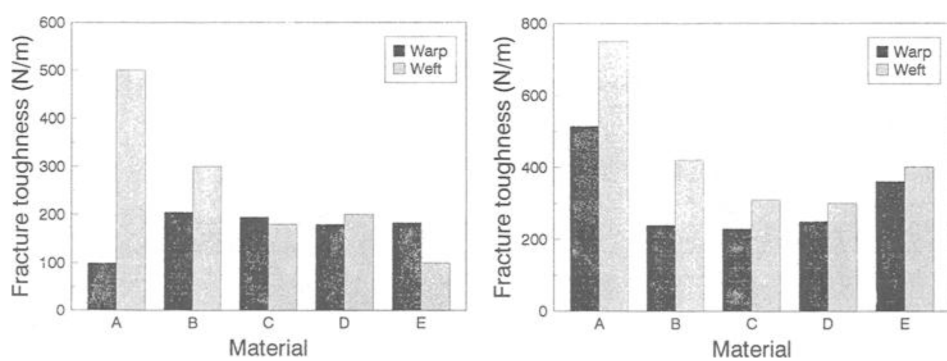

FIG 4-- *Showing the variation of (a) initiation fracture toughness and (b) propagation fracture toughness with fibre surface treatment in both the warp and weft orientations.*

STATIC FRACTOGRAPHIC ANALYSIS

Figure 5 presents mode I static fracture surfaces obtained for each test material in the weft direction from regions of crack growth. Clearly the fracture morphologies differ significantly between materials exhibiting stable crack propagation and those exhibiting unstable crack propagation. During stable crack growth (material A and material E) the crack path is totally interfacial, hence the value of α in equation (1) approaches unity, whereas during unstable crack propagation, large areas of resin cleavage are observed, indicating that the crack path has cleaved the resin-rich regions that exist between plies. These regions significantly reduce the value of α. Further fractographic analysis on warp oriented specimens showed that there was no difference in fracture profiles between warp and weft orientations. Therefore, the differences observed in fracture toughnesses are due to an effect other than variation in α values.

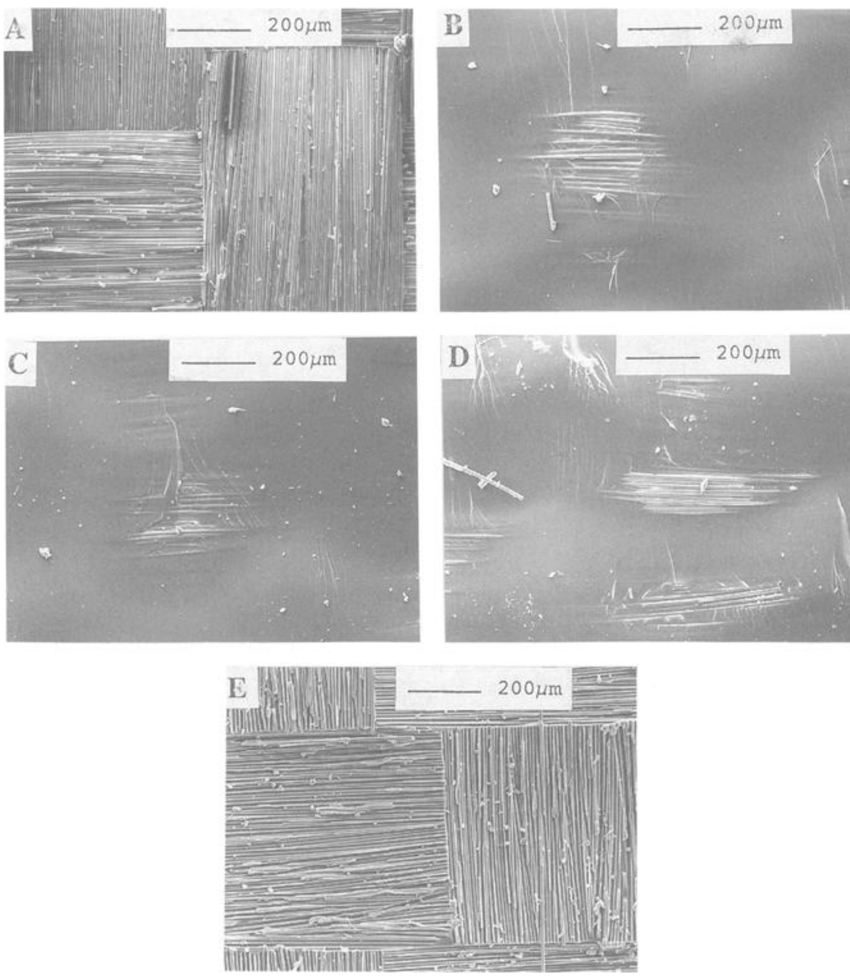

FIG 5-- *Scanning electron images of the fracture paths seen during static mode I crack propagation* (Δa=20mm) *for all materials.*

The results from the static test program have shown that the fracture toughness of glass/polyester woven cloth is dependent upon the fibre surface treatment and also upon the orientation of the test specimen relative to the warp and weft directions. More specifically, the fracture toughness during crack propagation decreased with increasing MS concentration in the fibre surface treatment, and the fracture path changed from being wholly interfacial (α=1) to being progressively more matrix dominated ($\alpha \Rightarrow 0$). According to equation (1), this correlation between toughness and fracture morphology should be expected, because the fracture toughness of the composite will decrease as the value of α decreases. The decrease in toughness caused by the methanol washing can also be explained, as the fractographic evidence shows that the value of α has been reduced. Despite having similar values of α, material A has a significantly higher toughness than material E. This is due to the fact that MS and ES react differently with the fibre surface, resulting in the value of G_{int} in equation (1) being lower in epoxy silane-treated materials.

Invariably, specimens tested in the weft direction possessed higher propagation toughness values than those tested in the warp direction. This is a consequence of the difference in weaving density between the two directions. As the weaving density of the weft fibres is smaller than that of the warp fibres, the crimp ratio is larger in the weft direction and hence the values of ΔG_0 and ΔG_{90} are larger in the weft direction. According to the model, this will give a higher fracture toughness in the weft direction. The disparity in warp and weft fracture toughness values increases with decreasing MS concentration in the fibre surface treatment. Fractographically, there is minimal difference between warp and weft α values, so the reason for this difference must be due to ΔG_0 and ΔG_{90} changing with MS concentration at different rates in different directions. This is assuming that G_{int} for each fibre surface treatment does not vary with orientation.

Most importantly, this work has shown that mode I fracture toughness testing of fabric composites does not give the fracture toughness of the fibre/matrix interface, as the crack front will occasionally travel through resin-rich regions. Additionally, even if the crack path is wholly interfacial, the nature of the irregular weaving structure in most fabric materials will give incorrect readings.

FATIGUE TEST DETAILS

The test specimen geometry used for the fatigue test program was identical to that shown in figure 1 for the static test program, although all specimens were cut parallel to the weft direction. The tests were performed using an Instron model 4505 test apparatus connected to an X-Y chart recorder and five specimens per material were tested. A sinusoidal waveform was generated under load control by cycling at a frequency of 0.2Hz between predefined upper and lower load values, P_{max} and P_{min} such that P_{min}/P_{max}=0.1. Because of the large beam deflections generated during the loading, a frequency of 0.2Hz represented the highest attainable frequency that still allowed for accurate sinusoidal waveform generation. The crack front generated by the fatigue loading was recorded using a travelling microscope located to the side of the test specimen and for an applied load range of ΔP, where $\Delta P = P_{max} - P_{min}$, the corresponding fracture toughness range, ΔG, was calculated using equation (5):

$$\Delta G = \frac{3\Delta P\delta}{2B(a+\Gamma)}\frac{F}{N} \tag{5}$$

where Γ, F and N are geometrical correction factors accounting for large beam deflections, moment effects caused by the blocks and the geometry of

the beam.
The parameter Γ is a crack modification factor and is calculated from a plot of $C^{1/3}$ versus a, as shown schematically in figure 6 and must be calculated for each material.

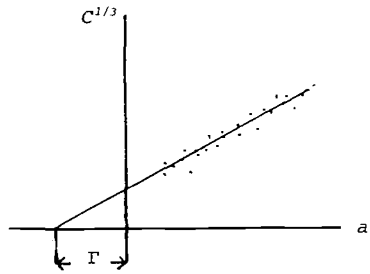

FIG 6-- *Calculation of the crack modification factor,* Γ *(the dots correspond to data points).*

The parameters F and N represent corrections made to the fracture toughness calculation to account for the geometry of the end blocks and are given by equation (6) and equation (7) respectively.

$$F = 1 - \frac{3}{10}\left(\frac{\delta}{a}\right)^2 - \frac{3}{2}\left(\frac{\delta l_1}{a^2}\right) \tag{6}$$

$$N = 1 - \left(\frac{l_2}{a}\right)^3 - \frac{9}{8}\left[1 - \left(\frac{l_2}{a}\right)^2\right]\frac{\delta l_1}{a^2} - \frac{9}{35}\left(\frac{\delta}{a}\right)^2 \tag{7}$$

The values of l_1 and l_2 are dependent upon the geometry of the blocks and are defined according to figure 7

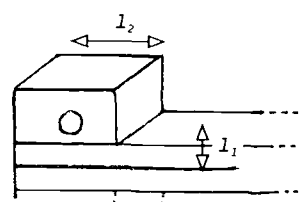

FIG 7-- *Definition of the parameters* l_1 *and* l_2

FATIGUE TEST RESULTS

All fatigue data obtained are presented in figure 8 as a logarithmic plot of crack growth rate (da/dN, measured in m/cycle) versus applied ΔG.

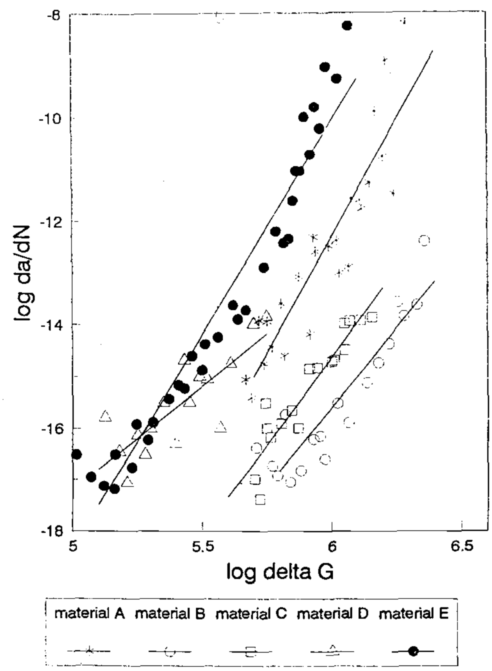

Fig 8-- *Logarithmic variation of fatigue crack growth rate with applied ΔG for materials A to E.*

Assuming all materials obey the Paris Law i.e.

$$\frac{da}{dN} = \eta \Delta G^{\phi} \tag{8}$$

the fatigue behaviour of each material can be characterised in terms of the fatigue constants η and ϕ. Table 2 details the parameters η and ϕ for each test material in addition to values for ΔG_{max}, the maximum (threshold) applied ΔG range that is possible before spontaneous unstable fracture occurs.

Figure 8 shows that fatigue resistance increases with increasing concentration of MS treatment (for a specified ΔG value, the lower the value of da/dN, the higher the fatigue resistance), suggesting that MS enhances the fatigue life of the composite.

TABLE 2-- *Values for the fatigue parameters η and ϕ and for the threshold fracture toughness range ΔG_{max} for materials A to E (* denotes threshold value not attained)*

Material	$\ln\eta$ (m/cycle)	ϕ (m^2/N/cycle)	ΔG_{max} (N/m)
A	-65.9	8.94	544
B	-52.1	6.09	590
C	-55.2	6.76	483
D	-37.3	4.02	323*
E	-59.5	8.23	433

FRACTOGRAPHIC ANALYSIS

Figure 9 presents corresponding scanning electron images obtained under mode I fatigue loading, and a direct comparison with the images in figure 5 reveals marked differences in failure mode. All materials exhibited a large degree of stable crack growth under fatigue loading and this is reflected in the fracture morphologies observed, as crack propagation under fatigue loading invariably follows the fibre/matrix interface. There are, however, substantial regions of resin fracture observed, especially with material C and material D which indicate that complete stability in the crack growth process has not been achieved. The exception is material A, where there are large areas of resin fracture that do not occur during static loading.

The fatigue test program has shown that the failure mechanisms observed are substantially different to the static failure mechanisms. With reference to the fracture toughness model, the higher degree of interfacial debonding observed results in a higher value for α, and this would explain why the threshold toughness values are higher than the static toughness values. The failure morphology of material A suggests that under a fatigue loading, the interface has become stronger than the bulk resin. This is surprising as material A was treated with the most dilute MS concentration and should in theory possess the weakest interfacial region, as confirmed by the static test results. The fundamental microstructural difference to occur when changing from a static to a fatigue loading is the formation of a much larger plastic zone at the crack tip, and consequently the strains experienced are much greater. Clearly material A possesses an interface capable of withstanding these strains and hence fatigue failure occurs within the matrix. Observation of figure 8 shows that there is a distinct difference in the values of ϕ (the rate of change of fatigue crack propagation with applied load) between each failure mode. For materials exhibiting interfacial fatigue failure, ϕ is approximately 8.5 whereas for materials exhibiting resin fatigue failure, ϕ is closer to 6.5. The scatter observed in the data for material D makes an accurate value for ϕ difficult to achieve. Therefore materials exhibiting fatigue failure at the fibre/matrix interface (material A and material E) are significantly more susceptible to changes in applied load.

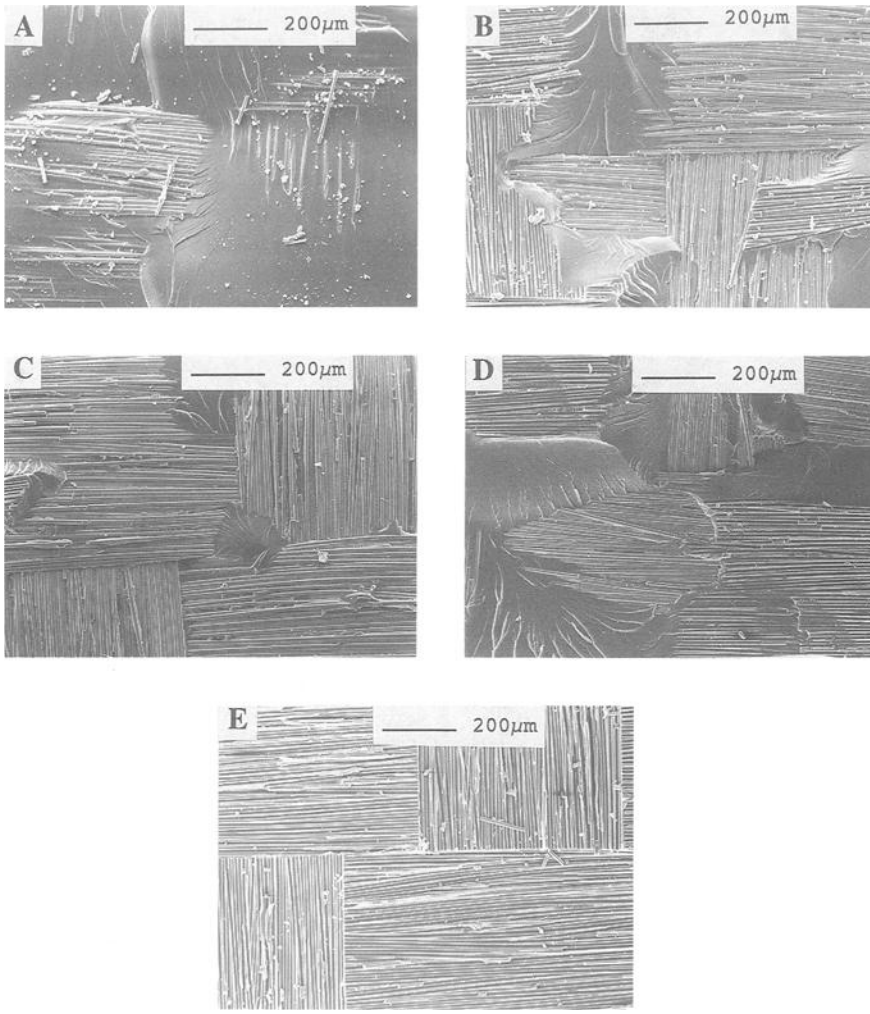

FIG 9-- *Scanning electron images of the fracture paths seen during mode I fatigue crack propagation (Δa=20mm) for all materials.*

CONCLUSIONS

The static and fatigue test programs detailed in this work have characterised the effect of fibre treatment, fabric geometry and loading mode on the interlaminar fracture characteristics of woven glass cloth/epoxy composite material, and have used the model previously proposed in [14] to explain this behaviour.

Under static loading, the nature of crack propagation becomes increasingly unstable with increasing concentration of MS fibre surface treatment, and the fibre/matrix interface becomes correspondingly stronger.

Static fracture toughness decreases with increasing MS concentration, and is dependent on the relative orientations of the warp and weft fibres.

The fracture toughness model has been successfully used to explain this behaviour in addition to explaining the relationship between fracture morphology and fracture toughness.

Varying the fibre treatments affects the R-curve behaviour of the composite, and so the fracture toughness must be characterized at both crack initiation and at crack propagation.

Under fatigue loading, the fatigue resistance of the composite increases with increasing MS concentration, and the level of interfacial bonding is far higher than under static loading conditions. The exception is the composite subjected to the most dilute fibre surface treatment, where the inherent ductility of the interfacial bond renders it resistant to the large plastic strains surrounding the crack tip.

The use of methanol washing and of ES fibre treatment effectively reduces the fracture toughness of the composite in both static and fatigue loading.

REFERENCES

[1] D.L.Caldwell and D.A.Jarvie - "Determination of the Interfacial Strength of Advanced Composites" in *33rd International SAMPE Symp.* pp.1268-1275 (1988).

[2] M.J.Rich and L.T.Drzal - "Interfacial Properties of Some High-Strain Carbon Fibers in an Epoxy Matrix" -in *41st Annual Conference of the Reinforced Plastics and Composites Institute*" the Society of the Plastics Industry, Inc. Jan.27-31 session 2-F (1986).

[3] B.Miller, P.Muri and L.Rebenfeld - "Microbond Method for Determination of the Shear Strength of a Fibre/Resin Interface" *Comp. Sci. & Tech.*, **28**, pp.17-32 (1987).

[4] L.T.Drzal - "Composite Interphase Characterization" *SAMPE Journal*, **19**, pp.7-13 (1983).

[5] E.Fitzer, K.H.Geigl, W.Huttner and W.Weiss - "Chemical Interactions Between the Carbon Fibre Surface and Epoxy Resins" *Carbon*, **18** pp.389-393 (1980).

[6] P.S.Chua and M.R.Piggott - "The Glass Fibre-Polymer Interface: 1 - Theoretical Consideration for Single Fibre Pull-Out Tests" *Comp. Sci. & Tech.*, **22**, pp.33-42 (1985).

[7] H.Hamada, N.Ikuta, Z.Maekawa, H.Ichihashi and N.Nishida - "Evaluation of the Interfacial Properties in the Embedded-Single-Fibre Coupon Test" *Comp. Sci & Tech.*, **48** pp.81-90 (1993).

[8] L.M.Zhou, J.K.Kim and Y.W.Mai - "On the Single Fibre Pull-Out Problem: Effect of Loading Method" *Comp. Sci. & Tech.*, **45** pp.153-164 (1992).

[9] M.R.Piggott and D.Andison - "Carbon Fibre-Epoxy Interface" *J. Reinf. Plast. & Comp.*, **6**, pp.290-299 (1987).

[10] K.P.McAlea and G.J.Besio - "Adhesion Between Polybutylene Terephthalate and E-Glass Measured with a Microdebond Technique" *Polym. Compos.*, **9**, pp.285-290 (1988).

[11] Y.Suzuki, Z.Maekawa, H.Hamada, M.Kibune, M.Hojo and N.Ikuta - "Influence of Adsorption Behaviour of a Silane Coupling Agent on Interlaminar Fracture in Glass Fibre Fabric-Reinforced Unsaturated Polyester Laminates" *J. Mat. Sci.*, 27 pp.6782-6790 (1992).

[12] Y.Suzuki, Z.Maekawa, H.Hamada, A.Kokoyama, T.Sugihara and M.Hojo - "Influence of Silane Coupling Agents on Interlaminar Fracture in Glass Fibre Fabric Reinforced Unsaturated Polyester Laminates" *J. Mat. Sci.*, **28** pp.1725-1732 (1993).

[13] M.Kotaki, M.Hojo, N.Tsujioka and H.Hamada - "Effect of Surface Treatment on Interlaminar/Intralaminar Crack Growth Behaviour of CFRP Laminates" *Proc. 4th Japan Int. SAMPE Symposium*, pp.1008-1013 (1995).

[14] M.Kotaki and H.Hamada - "Effects of Interfacial Properties and Weave Structure on Mode I Interlaminar Fracture Behaviour of Glass Satin Woven Fabric Composites" *submitted to Composites*, (1996).

[15] M.Hojo, K.Kageyama and K.Tanaka - "Prestandardization study on Mode I Interlaminar Fracture Toughness Test for CFRP in Japan" *Composites*, **26** pp.243-255 (1995)

Ashok Saxena[1]

APPLICATION OF FRACTURE MECHANICS IN MAINTENANCE OF HIGH TEMPERATURE EQUIPMENT - AN ASSESSMENT OF CRITICAL NEEDS

REFERENCE: Saxena, A., "**Application of Fracture Mechanics in Maintenance of High Temperature Equipment - An Assessment of Critical Needs**", Fatigue and Fracture Mechanics: 28th Volume, ASTM STP 1321, J. H. Underwood, B. D. Macdonald, and M. R. Mitchell, Eds., American Society for Testing and Materials, 1997.

ABSTRACT: Extending the operating life of power-plant, chemical reactor and land, sea and air based gas turbine components beyond their original design life has considerable economic advantages. Fracture mechanics is used extensively to predict the remaining life and safe inspection intervals as part of maintenance programs for these systems. The presence of creep deformation and time-dependent damage accumulation in these components present very significant challenges. Therefore, the emphasis of this paper is on the time-dependent fracture mechanics concepts.

A critical assessment of the current state-of-the-art of time dependent fracture mechanics concepts, test techniques, analytical procedures and application tools is made to demonstrate the potential of this technology in maintenance engineering. In addition, future developments that are needed to enhance the application of this technology are also described and limits of the current approaches are also discussed.

KEYWORDS: creep, cracks, fatigue, fracture, turbines, high-temperature, service behavior

---

Extending the life of existing power-plants, chemical reactor pressure vessels, and gas turbines for land, marine and aircraft applications beyond their original design life is a multi-billion dollar business. However, the economic advantages of saving or delaying capital investments must always be considered in the context of increased risk of catastrophic failures which can cause total shutdown and lead to loss of human lives. The recent public concern about the safety of aging aircraft is an example of such

---

[1]Professor and Chair, School of Materials Science and Engineering, Georgia Institute of Technology, Atlanta, GA 30332-0245

considerations. Never-the-less, extending the life of expensive equipment such as aircraft, power and chemical plant components etc. has tremendous economic benefits if accompanied by well defined and sound risk management strategies including periodic and thorough inspections for damage and by ensuring that the original designs are damage-tolerant.

Fracture mechanics based models are widely used in risk/remaining life applications in several industries which rely heavily on structural components. The focus of this paper is on high temperature components in which failures occur by creep damage and by other high temperature damage mechanisms such as environmental degradation and creep-fatigue-environment interactions. Particular emphasis is placed on power-plant components when choosing examples but the methodology applies to a much broader class of high temperature components.

Figure 1a shows cracks that were found in the interior of a steam header during an inspection after approximately 25 years of operation, at a maximum service temperature of 538°C. Figure 1b shows schematics of the stress-time histories of critical locations (locations where cracks are found) in the header similar to one in Fig. 1a through a complete operating cycle, including a cold-start, steady-state operation and shut-down. From the service temperatures and the stress-time histories, the role of creep and creep-fatigue crack growth is very apparent in the development and propagation of these cracks. Figure 2 lists the considerations in predicting the long-term high temperature performance of elevated temperature components. If we critically examine the service environment and the material used in fabricating the header, all factors listed in Fig. 2 can be considered relevant. However, only a subset of the factors listed dominate the cracking behavior in the component, making the analysis tractable.

In the following section, a brief description of the available time-dependent fracture mechanics (TDFM) concepts is provided followed by an assessment of the critical needs to further enhance this technology. The limitations of the approach, as appropriate, are also discussed.

TDFM CONCEPTS:

When a constant load is suddenly applied to a cracked body at elevated temperature, creep deformation accumulates in the crack tip region due to high stresses resulting from the stress concentration. In some materials, which are called creep-ductile materials, considerable creep deformation accumulates prior to any crack extension. Thus, the crack extension occurs in the presence of substantial creep strains and the cracktip lags considerably behind the advancing creep zone boundary. In other materials, which are called creep-brittle materials, the crack extends rapidly as creep strains accumulate and in the steady-state, the creep zone boundary and the crack tip move at equal rates. Thus, to an observer stationed at the moving crack tip, it appears that the stress distribution is constant ahead of the crack tip and is uniquely determined by the

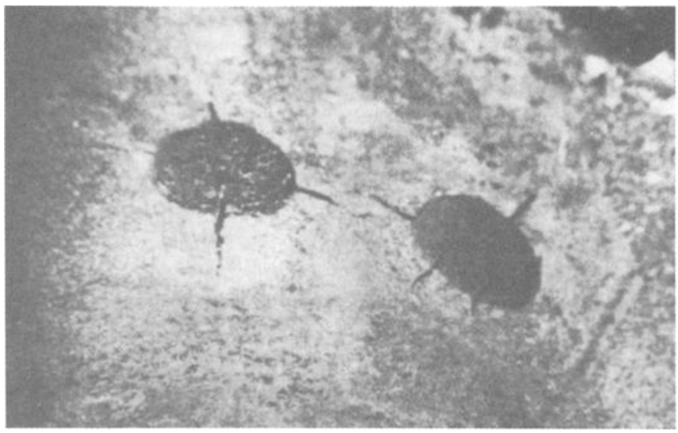

Fig. 1(a) - Cracks found in the interior of a steam header removed from service at 538°C after 25 years.

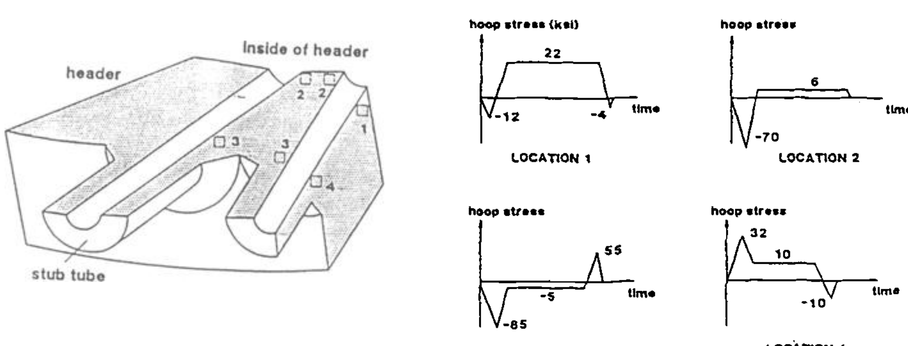

Fig. 1(b) - Schematic of Stress-time histories at various locations in headers where cracks are typically found.

Fig. 2 Considerations in predicting crack growth life in high temperature components

- Transients and steady-state thermal stresses
- Hold times and cyclic stresses due to external loading in fracture critical locations
- Environmental effects (oxidation)
- Creep deformation (primary, secondary and tertiary) and rupture
- Varying material properties due to temperature gradients
- Complex crack geometries
- Load interaction effects
- In-service degradation of material properties

applied magnitude of the crack tip stress intensity parameter, K. A necessary condition for an ideal steady-state to exist is that the size and shape of the creep zone be characterized uniquely by K. Prior to achieving steady-state, the crack tip region undergoes transient conditions in which the crack tip stress and the size and shape of the creep zone undergo changes with time even when the applied K remains constant. Except for these initial remarks explaining the differences between creep-ductile and creep-brittle materials, the discussion in this paper will exclusively deal with the creep-ductile materials which include the Cr-Mo and Cr-Mo-V steels and austenitic stainless steels used in power-plant and chemical reactor components. These class of problems are more complex and require the use of TDFM.

In applying fracture mechanics to creep-ductile materials, an assumption can be made that the crack tip is essentially stationary. This implies that the elastic stresses due to crack growth in the forward sector of the crack tip are overwhelmed by the creep strains which continue to accumulate due to the high stresses in that region. The assumption of a slowly moving crack makes it possible to use stationary crack tip parameters for correlating creep and creep-fatigue crack growth rates.

The uniaxial version of the creep constitutive law used for describing the materials is given by the following equations.

$$\dot{\varepsilon} = \frac{\dot{\sigma}}{E} + A_1 \varepsilon^{-p} \sigma^{n_1(1+p)} + A\sigma^n \qquad (1a)$$

or

$$\dot{\varepsilon} = \frac{\dot{\sigma}}{E} + [A_1(1+\rho)]^{\frac{1}{1+\rho}} \frac{\sigma^{n_1}}{(1+\rho)t^{\rho/(1+\rho)}} + A\sigma^n \quad (1b)$$

Equations (1a) and (1b) are equivalent forms in which σ = stress, ε = strain, t = time and dots indicate derivatives with respect to time, E = elastic modulus, A_1, n_1, ρ are regression constants which describe the primary creep behavior of the material and A and n are regression constants which describe the secondary creep behavior of the material.

CREEP CRACK GROWTH

In creep-ductile materials, the time-rate of crack growth da/dt, is characterized by the C_t parameter [1-3] for a wide range of creep conditions which include small-scale and extensive creep. These correlations are valid for primary, secondary and combined primary-secondary creep conditions [2]. Figure 3 shows a typical correlation between da/dt and C_t obtained from large compact type (CT) specimens (width = 254mm) in which substantial crack extension occurred under both small-scale and extensive creep

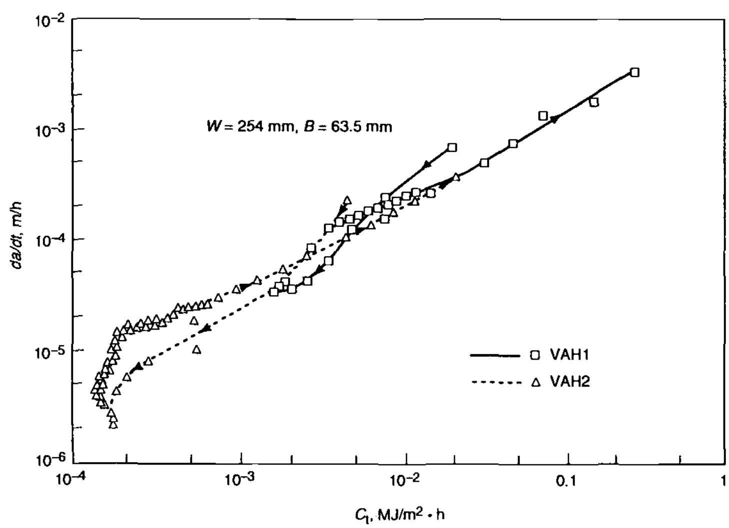

Fig. 3 - Creep crack growth rate as a function of the C_t parameter for 1Cr-1Mo-0.25V steel at 538°C using 254 mm wide (w) compact specimens. The arrows on the lines indicate the order in which crack growth data were collected. Note the initial decrease in da/dt due to small-scale creep and transient creep conditions and the subsequent increase in the crack growth rates for both specimens. The load for VaH1 was higher than the load for VAH2.

conditions [4]. In these tests, C_t initially decreases due to stress redistribution caused by creep deformation, attains a minimum value, and then increases. However, a unique relationship (within experimental scatter) between da/dt and C_t is obtained during the entire period, proving the validity of C_t as a characterizing parameter for a wide range of creep conditions. The crack growth rate is described by:

$$da/dt = b(C_t)^q \tag{2}$$

where b and q are regression constants obtained from the slope and intercept of the da/dt versus C_t relationship. The methods for estimating C_t in test specimens and in components are reviewed elsewhere [2]. Under extensive creep conditions, C_t becomes identical to the C^*-integral [5, 6] and it characterizes the amplitude of the crack tip stress field. In the small-scale-creep regime, C_t is directly related to the rate of expansion of the creep zone size [3]. Thus, direct relationships have been identified to uniquely relate the magnitude a globally measured parameter, C_t, to the local crack tip quantities which are expected to dominate the kinetics of the damage processes and determine the creep crack growth rate.

CREEP-FATIGUE CRACK GROWTH

The application of C_t has been extended to situations involving time-dependent crack growth rates during hold times between the loading and unloading events [7 - 10]. Crack extension under such conditions are classified as creep-fatigue crack growth. The average value of da/dt, $(da/dt)_{avg}$, and the average value of C_t during the hold time, $(C_t)_{avg}$, are shown to uniquely correlate with each other for different amounts of hold time. Figure 4 shows an example of $(da/dt)_{avg}$ versus $(C_t)_{avg}$ data for a Cr-Mo steel for various hold times and also includes the creep crack growth rate data. In this material, the creep-fatigue crack growth rates and creep crack growth rates are indistinguishable within the normal data scatter. Thus, it can be argued that the creep-fatigue interaction in this material consists of reinstatement of the stress redistribution which is included in the magnitude of the C_t parameter. This reinstatement occurs by reversing of the accumulated creep deformation during hold time by cyclic plasticity during the unloading portion of the cycle. The creep reversal can be partial or complete, depending on the size of the cyclic plastic zone compared to the size of the accumulated creep zone. As the creep zone size increases, the extent of creep reversal every cycle decreases [9].

The comparability between the creep and creep-fatigue crack growth rates shown in Fig. 4 also implies that no fundamental change occurs in the crack tip damage mechanisms due to loading/unloading. Noting that fatigue crack growth occurs by a transgranular mechanism and creep crack growth by grain boundary cavitation, one can argue that there is minimal interaction between fatigue and creep damage. Thus, when considering creep-fatigue interactions during fatigue cycling with hold time, it is reasonable to choose the dominant-damage hypothesis in which,

$$\frac{da}{dN} = \max\left[\left(\frac{da}{dN}\right)_{cycle}, \left(\frac{da}{dN}\right)_{time}\right] \tag{3}$$

in contrast with the damage summation hypothesis which states,

$$\frac{da}{dN} = \left[\left(\frac{da}{dN}\right)_{cycle} + \left(\frac{da}{dN}\right)_{time}\right] \tag{4}$$

where, da/dN = total crack growth per cycle including loading, unloading and the hold time, $(da/dN)_{cycle}$ = crack growth rate for the same cyclic stress intensity parameter, ΔK, value except with no hold time and $(da/dN)_{time}$ = crack growth during the hold time.

While the above arguments are primarily for considering the influence of cyclic loading on crack growth during sustained loading, we must also consider the influence of creep deformation on crack growth rate during cyclic loading. This becomes relevant during short hold times (<100 seconds). It can be argued that creep deformation can blunt the crack substantially and decrease the amount of the cyclic crack growth. Indeed, studies have shown that at low ΔK values, the da/dN for a cycle with hold time is less than the da/dN for the corresponding ΔK without a hold time [8, 10].

CRACK GROWTH IN WELDMENTS

Several high temperature cracking problems originate in weldments. For example, among power-plant components, steam header and pipe constructions rely heavily on welding, and major failures in these components are reported to have originated at the weldments [11]. The creep deformation rates in weldmetal and base metal can be substantially different and as a result, the analysis of cracks which lie along the base metal/weld metal interface is much more complicated than for homogeneous materials. Also, special test methods must be utilized to obtain the high temperature crack growth behavior in these composites. Figure 5 shows the da/dt versus C_t behavior of the various regions of weldments showing that the crack growth rates along the fusion line can be higher than the crack growth rates in the base metal and the weld metal [12]. Thus, in applications, an appropriate distinction must be made between the properties of the various regions of the weldments. In a later section of this paper, we will critically examine the conceptual limitations of homogeneous body fracture mechanics for addressing cracking in weldments in high temperature components.

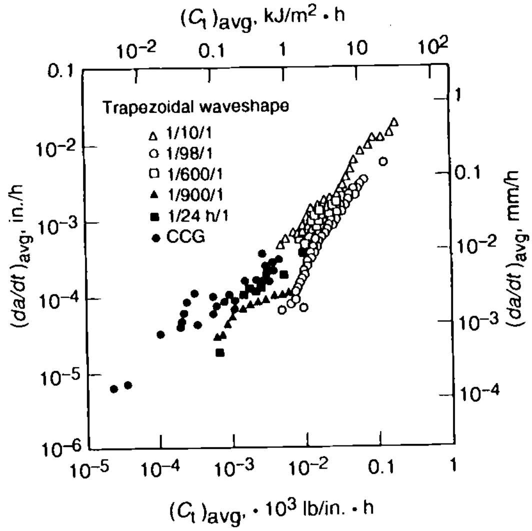

Fig 4 - Fatigue crack growth rate for various hold times in seconds for 1.25Cr-0.5Mo steel at 538°C [Ref.8].

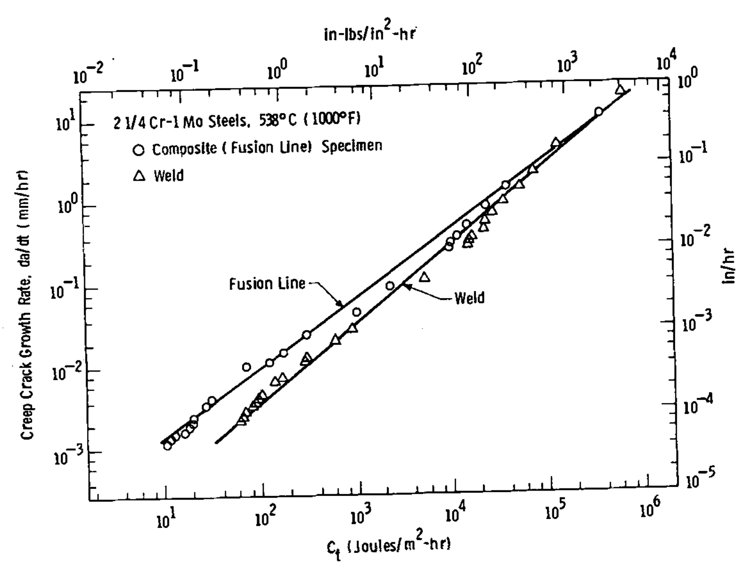

Fig. 5 - Comparison between creep crack growth rates for base metal and the fusion line regions in a 2.25Cr-1Mo steel [Ref.12].

APPLICATION OF CRACK GROWTH MODELS IN REMAINING LIFE ASSESSMENT

The material data needed to apply the crack growth models for predicting remaining life include tensile properties, elastic constants, creep deformation constants, the constants representing the material's fatigue, creep and creep-fatigue crack growth behavior and the fracture toughness of the material. Once the material properties are identified, using the stress analysis of the component and the crack/component geometry, an appropriate crack geometry is selected. The appropriate expressions for K and C^* must be identified for the geometry. The remaining life, t_R, for components subjected to sustained loading can be estimated by integrating equation (2). For components subjected to cyclic loading, the following equation can be integrated to estimate the remaining life cycles, N_R.

$$\frac{da}{dN} = c(\Delta K)^m + b_1\left[(C_t)_{avg}\right]^{q_1} t_h \qquad (5)$$

where C and m are regression constants describing the fatigue crack growth behavior, t_h is the hold time, and b_1 and q_1 are regression constants describing the creep-fatigue crack growth behavior. For some materials as seen in Fig. 4, $b = b_1$ and $q = q_1$, but this result should not be generalized.

In writing equation (5), we have assumed the damage summation hypothesis for representing creep-fatigue interactions which is in apparent contradiction with the previously mentioned preference for the dominant damage hypothesis. However, the former is more conservative in predicting component behavior while the other is more conservative (and also accurate) in analyzing test data. Therefore, for predicting remaining life, equation (5) is preferred.

LIFE ASSESSMENT OF HOT REHEAT PIPING

Due to the occurance of two major failures in 1985 and 1986, there is considerable interest in inspecting seam welded piping and assessment of its remaining life [11]. These pipes are produced from 1.25Cr-0.5Mo and from 2.25Cr-1Mo steels. The weldments in these systems include girth welds, seam welds and occasionally repair welds. All three types of welds are at risk for cracking due to creep and fatigue. The creep cracks observed in steam pipes are quite likely to be service induced. Fabrication flaws such as lack of fusion defects or inclusion clusters can also be present and can potentially cause failures.

A major concern in evaluating large weldments is the variability in the weld metal creep deformation resistance, the geometry of the weld and microstructural variations.

For example, variations in trace element content and microstructure can significantly reduce creep ductility, creep deformation resistance or both. An alloy which is ductile in the ferritic condition can become brittle in the coarse grain bainitic condition. Likewise, base metals and weld metals which look very similar microstructurally can exhibit quite different creep resistance due to minor variations in chemical composition. Variations in creep deformation resistance between base metal and weld metal can often cause strain concentrations in the weaker metal and accelerate crack formation and the growth rate.

Creep and creep-fatigue crack growth analysis is performed to evaluate fabrication flaws (or flaw indications), slag inclusions, hot tears and toe cracks. If evidence of cavitation damage is uncovered in the form of creep cracking, crack growth analysis should not be conducted. If it is necessary to estimate crack growth life under these circumstances, very conservative crack growth behavior must be used. Figure 6 shows the remaining life of a 750 mm diameter steam pipe, subjected to an internal pressure of 5.03 MPa, as a function of initial crack depth for various operating times between start ups and shut downs. As expected, remaining life decreases as the average operating time between start up and shut down decreases [13]. Figure 7 shows a comparison between the remaining lives for flaws located in the base metal/weld metal interface with those located in the base metal. This clearly shows the advantages of seamless versus seam welded piping, because flaws in the latter will more likely be in the interface region. In the presence of flaw indications, other operating options very often include reducing the operating temperature and/or pressure to increase remaining life.

LIFE ASSESSMENT OF TURBINE CASINGS

A recent workshop sponsored by the Electric Power Research Institute (EPRI) has documented cracking problems in turbine casings [14]. Turbine casings are made from 1.25Cr-0.5Mo steel, 2.25Cr-1Mo steel and from 1Cr-1Mo-0.25V steel. Cracking in turbine casings occurs in sections where the local thermal stresses are high, for example, at the steam inlets of the high pressure and intermediate pressure sections of the turbine. Cracks are often found in the interior sections of the steam chests, valve bodies and bolt holes. The primary cause of cracking in turbine casings is fatigue due to high fracture appearance transition temperatures (FATT). The fatigue and creep-fatigue cracking occurs due to thermal stresses. Creep contributes to cracking in regions exposed to temperatures in excess of 427°C (800°F). Frequent cycling and rapid thermal ramp rates decrease the crack initiation time and increase the crack growth rates. Typically, the crack growth rates are slow and can be detected during the five year inspection interval without much risk of becoming critical size.

Figure 8 shows the results of the calculations of remaining life as a function of initial crack size for ship's service turbine generator casing [15]. In this case, cracks were considered to have initiated early in life and the majority of the life was spent in crack propagation. The life calculations were made for cracks lying in regions exposed to 538°C where creep effects are large and in regions exposed to 427°C where creep effects

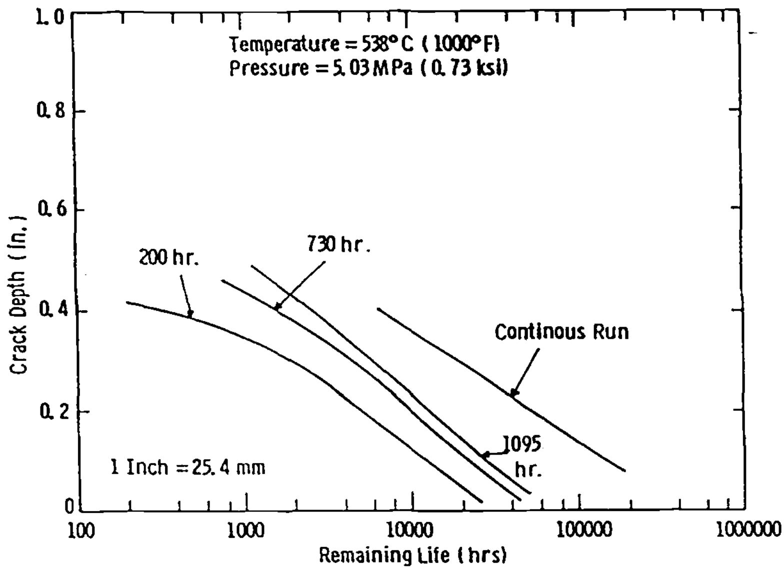

Fig. 6 - The relationship between crack depth and remaining life for different operating times between successive starts and stops in high temperature steam pipes [Ref. 13].

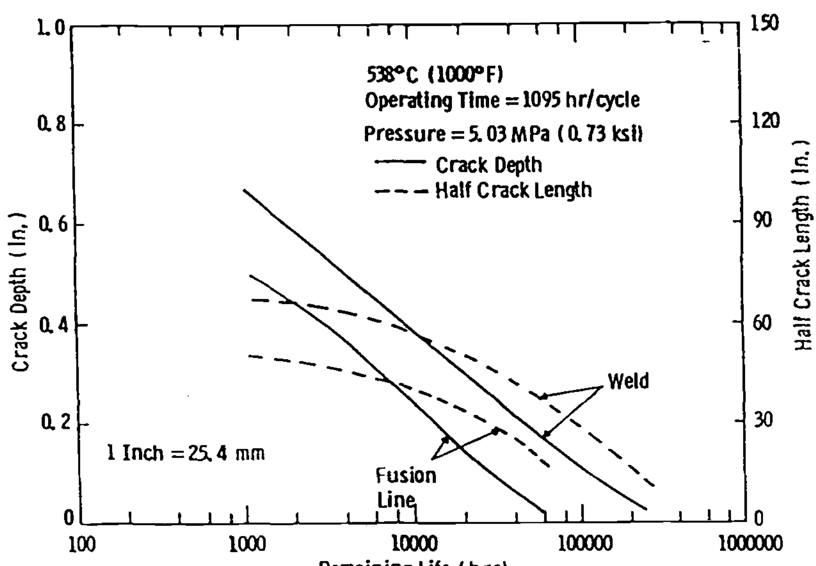

Fig. 7 - The relationship between crack depth and remaining life for cracks lying in the weld metal and those lying along the fusion line in steam pipes. The dotted lines refer to maximum allowable half crack length that will lead to leak-before-rupture conditions [Ref. 13].

are marginal. The operating history of the casing consists of 50 cycles per year. Therefore, even in the presence of 5mm deep cracks, the predicted remaining life was approximately 900 cycles (or 18 years) which is quite significant. These predictions are in general agreement with the trend that at the time of inspection, the crack growth rates were slow.

In making the above life predictions, several simplifying assumptions were necessary to proceed with the calculations. Thus, the accuracy of these predictions is somewhat uncertain. Wherever possible, conservative assumptions were made but in several instances it cannot be argued with confidence that the assumptions were conservative. For details, the readers are referred to the earlier paper [15].

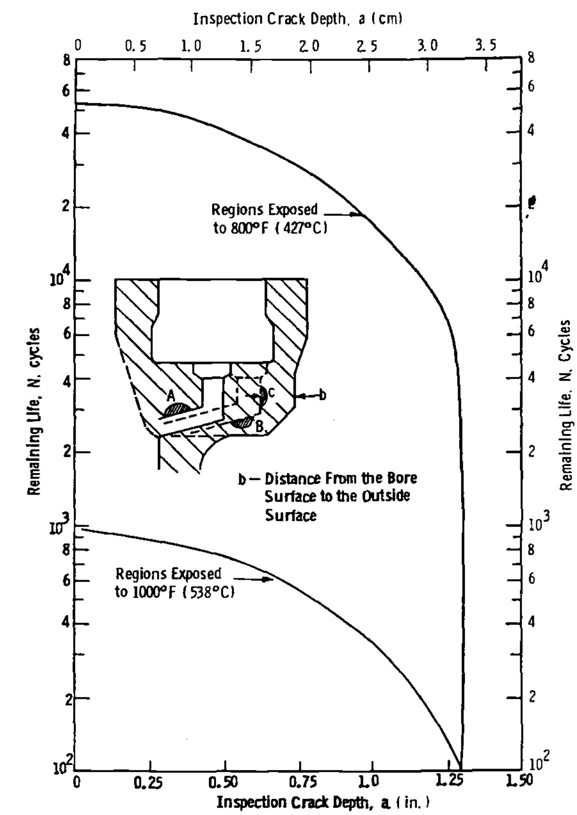

Fig. 8- The relationship between crack depth and remaining life for steam turbine casings for regions exposed to 538°C and 427°C [Ref.15]

ASSESSMENT OF FUTURE NEEDS

The potential of time-dependent fracture mechanics (TDFM) in establishing safe maintenance practices and quantifying the risk of operating aging components of power plants and chemical reactors is quite obvious from the examples considered in the previous section. There are several areas in which fruitful research can be performed to support such analysis, including opportunities for ASTM to contribute by developing new test standards. A brief description and justification of these areas is provided in this section.

High temperature components are usually subjected to varying temperatures that can range from temperatures well into the creep range to temperatures where creep damage may be either marginal or not significant. A majority of tests and analyses are performed assuming isothermal conditions in which the influence of environment is not explicitly included. When temperatures below the creep regime are encountered, the dominant role of environment cannot be discounted. Even Cr-Mo steels, which are considered to be resistant to oxidation, exhibit a cracking phenomenon known as oxide notching [16]. The cracks found in service in steam headers are frequently accompanied by oxide spikes in the crack tip region underscoring the role of environment. Very little fundamental understanding exists in modelling crack growth due oxidation and its transition into creep dominance as the temperature is increased. Thus, more research into creep-fatigue-environment interactions is necessary.

The cracking in a large number of high temperature components including steam headers, turbine casings and turbine rotors is due to transient thermal stresses. Again, all life prediction analysis assume isothermal conditions. Considerable research is needed in analytical methods for treating crack growth under thermal-mechanical loading and also new test methods are needed which more closely resemble the service conditions. It must be noted that in the presence of temperature gradients, the monotonic and cyclic flow properties of the materials can vary significantly. Thus, the limitations of crack tip parameters, such as the ΔJ under thermal gradients must be explored.

Another area which has not been investigated is that of load interactions during crack growth at elevated temperature. In the presence of transient thermal stresses, it becomes quite important to treat the effects of overload on the crack growth rate during the subsequent hold time. A recent study by Yoon et.al [17] has clearly shown that for steels, overload can accelerate the time rate of crack growth during the subsequent hold time. The role of crack closure during high temperature fatigue crack growth has not been investigated in any systematic experimental studies.

There are significant opportunities for developing standard methods for creep-fatigue crack growth testing. These tests are highly specialized and require precise controls and measurements. The data analysis is also cumbersome. Thus, standard test methods for creep-fatigue crack growth can be quite useful in promoting such testing in support of remaining life analyses for critical components.

A very important area for future research is the evaluation of the high temperature performance of advanced materials including nickel base alloys, intermetallics, titanium alloys, ceramics and their composites and high temperature aluminum alloys. These materials are creep-brittle in nature, and in the temperature regimes in which they are likely to operate are quite resistant to creep deformation. Therefore, the crack extension in these materials is not accompanied by significant creep deformation. It is, therefore, necessary to explicitly account for crack growth in the search for suitable crack tip parameters. With the understanding that currently exists in TDFM, very rapid progress can be made in developing analysis methods for characterizing creep crack growth in these materials.

Another important area for research is that of predicting crack growth in the interface regions of weldments in which the weld metal and base metal have dissimilar creep deformation properties. A lot of ground work has been laid for developing this area through analytical studies in the elastic-plastic fracture regime. This area also provides opportunities for creative test method development.

The role of constraint on creep crack growth has not yet been investigated. Often, creep cracks in pipes originate on the surfaces with crack sizes being about 2 to 5 percent of the uncracked ligament. The applicability of the data developed on deeply cracked compact type specimens with a high degree of constraint to components subjected to largely uniform stresses and containing shallow cracks (low constraint) needs to be investigated. Such studies will have a direct bearing on the confidence level in our ability to predict remaining lives of elevated temperature components.

Good analytical solutions for determining the J-integral and C^*-integral for 3-d crack geometries subjected to nonuniform stress field needs to be investigated. Similarly, the relationship between crack size and the J and C^* integrals must be determined for the conditions of transient thermal stresses.

Monitoring of the service experience is a very important step in developing confidence in the life prediction models. Crack size data from inservice inspections performed at different times can be very helpful in the verification of the life prediction models. Programs to regularly inspect and record the inspection data must be established for each critical component. Thus, the predictions can be compared with actual experience.

CONCLUSIONS

Considerable progress has occurred in the recent past in the area of predicting crack growth behavior in elevated temperature components. Crack tip parameters for correlating high temperature fatigue crack growth, creep crack growth and creep-fatigue crack growth in homogeneous metals under isothermal conditions are available. Similarly, well developed test methods are available for characterizing the crack growth behavior in such materials. The use of these methods was illustrated by examples involving remaining life assessment of high pressure steam pipes and turbine casings. By contrast, similar concepts for treating high temperature gradients are not available. Several other areas in which fruitful research can be performed to further the state-of-the-art for predicting remaining life of high temperature components are also outlined.

ACKNOWLEDGEMENTS

The author wishes to acknowledge several years of financial support from the Electric Power Research Institute (EPRI) under the direction of Dr. R. Viswanathan and for recent support from NASA under the direction of Dr. R. Piascik for the studies leading to this paper. He also acknowledges the contribution of numerous co-workers from Georgia Tech including Prof. D. L. McDowell, Drs. N. Adefris, K. B. Yoon, R. H. Norris, P. Grover, David Hall and Mr. B. Carter Hamilton.

REFERENCES

1. Saxena, A., "Creep Crack Growth Under Non-Steady State Conditions", Fracture Mechanics: Seventeenth Conference, ASTM STP 905, 1986, ASTM Philadelphia, pp 185-201.

2. Saxena, A., "Creep Crack Growth in High Temperature Ductile Materials", Eng. Fracture Mechanics, Vol. 40, 1991, pp 721-736.

3. Bassani, J. L., Hawk, D. E. and Saxena, A., "Evaluation of the C_t-Parameter for Characterizing Creep Crack Growth in the Transient Regime", in Nonlinear Fracture Mechanics: Time-Dependent Fracture, ASTM STP 995, 1989, ASTM, Philadelphia, pp 7-29.

4. Saxena, A., Yagi, K. and Tabuchi, M., "Crack Growth Under Small Scale and Transient Creep Conditions in Creep-Ductile Materials", in Fracture Mechanics: Twenty Fourth Volume, ASTM STP 1207, ASTM Philadelphia, pp 481-497.

5. Landes, J. D. and Begley, J. A., "A Fracture Mechanics Approach to Creep Crack Growth", in Cracks and Fracture, ASTM STP 590, 1976, ASTM, Philadelphia, pp 128-148.

6. Saxena, A., "Evaluation of C^* for Characterizing Creep Crack Growth in 304 Stainless Steel", in Fracture Mechanics: Twelfth Conference, 1980, ASTM STP 700, ASTM, Philadelphia, pp 131-151.

7. Saxena, A. and Gieseke, B., "Transients in Elevated Temperature Crack Growth", Seminar Proceedings of MECAMAT: Int. Seminar on High Temperature Fracture Mechanics and Mechanisms, 1987, Dourdan, France, pp 19-36.

8. Yoon, K. B., Saxena, A., and Liaw, P. K., "Characterization of Creep-Fatigue Crack Growth Behavior Under Trapezoidal Waveshape Using the C_t Parameter", International Journal of Fracture, Vol. 59, 1993, pp 95-114.

9. Adefris, N., Saxena, A. and McDowell, D. L., "Creep-Fatigue Crack Growth Behavior in 1CR-1Mo-0·25V Steels, Part I: Estimation of Crack Tip Parameters", Fatigue and Fracture of Engineering Materials and Structures, Vol. 19, 1996, pp 387-399.

10. Adefris, N., Saxena, A. and McDowell, D. L., "Creep-Fatigue Crack Growth Behavior in 1Cr-1Mo-0·25V Steels, Part II: Crack Growth Behavior and Models, Fatigue and Fracture of Engineering Materials and Structures, Vol. 19, 1996, pp 401-411.

11. Foulds, J. R. and Viswanathan, R. "Guidelines for Assessment of Seam-welded High Energy Piping", Proceedings of the American Power Conference, Vol. 57-III, 1995, pp 1835-1854.

12. Liaw, P. K., Saxena, A. and Schaefer, J, "Estimating Remaining Life of Elevated-Temperature Steam Pipes-Part I. Materials Properties", Engineering Fracture Mechanics, Vol. 32, 1989, pp 675-708.

13. Liaw, P. K., Saxena, A. and Schaefer, J., "Estimating Remaining Life of Elevated-Temperature Steam Pipes-Part II. Life Prediction Analysis", Engineering Fracture Mechanics, Vol. 32, 1989, pp 709-721.

14. "Workshop Proceedings - Life Assessment and Repair of Steam Turbine Casings", EPRI-CS-4676-SR, July 1986, Electric Power Research Institute, Palo Alto, CA.

15. Saxena, A., Liaw, P. K., Logsdon, W. A. and Hulina, V. E., "Residual Life Prediction and Retirement for Cause Criteria for SSTG Casings-II. Fracture Mechanics Analysis", Engineering Fracture Mechanics, Vol. 25, 1986, pp 289-303.

16. Nakoneczny, G. J. and Schultz, C. C., "Life Assessment of High Temperature Headers", Proceedings of the American Power Conference, Vol. 57-III, 1995, pp 1855-1884.

17. Yoon, K. B., Saxena, A. and McDowell, D. L., "Effect of Cyclic Overload on the Crack Growth Behavior During Hold Period at Elevated Temperature", International Journal of Fracture, Vol. 59, 1993, pp 199-211.

James B. Chang[1]

ON SPACE FLIGHT PRESSURE VESSEL FRACTURE CONTROL

REFERENCE: Chang, J. B., ''**On Space Flight Pressure Vessel Fracture Control,**'' Fatigue and Fracture Mechanics: 28th Volume, ASTM STP 1321, J. H. Underwood and B. D. Macdonald, M. R. Mitchell, Eds., American Society for Testing and Materials, 1997.

ABSTRACT: Pressure vessels (PVs) are classified as fracture critical items in most space systems including the space shuttle, launch vehicles, and spacecraft. Fracture control requirements specified in MIL-STD-1522A are being implemented to the metallic PVs used in most of the space programs. However, requirements in "-1522A" are not applicable to composite overwrapped pressure vessels (COPVs), which are widely used in current space programs. A research, development, test, and evaluation (RDT&E) program is being conducted to generate database needed for establishing fracture control requirements for the COPVs. This paper provides an overview of the fracture control of the metallic PVs and reports important findings obtained from this RDT&E program. The important COPV findings include fatigue and fracture analysis methods used for the metallic liners, nondestructive evaluation techniques, and impact damage effects on the composite overwraps.

KEY WORDS: fracture control, metallic pressure vessel, composite overwrapped pressure vessel, impact damage, leak-before-burst failure mode, fatigue, fracture mechanics, crack growth safe-life analysis

Space systems such as the space shuttle, launch vehicles, and spacecraft use propellant tanks and pressurant bottles in their propulsion/reaction control subsystems. This hardware, commonly referred to as pressure vessels (PVs), is usually made of titanium, steel, and Inconel. Due to the weight restriction in most space systems, these PVs are normally designed to a 1.5 burst factor, which is much smaller than the factor of 4 required by ASME code[1] for ground use PVs. Consequently, the ability of the space flight PVs to tolerate pre-existing flaws or defects is much less. Furthermore, to replace or repair a defective PV in space is very difficult if not impossible. If the failure mode of a defective PV is brittle fracture instead of leak-before-burst (LBB), it could cause a mishap. On the other hand, a defective PV with LBB failure mode could jeopardize the mission if it develops leakage. Hence, it is extremely important to implement fracture control on space flight PVs to prevent premature failure due to the propagation of undetected cracks or crack-like defects. A military standard, MIL-STD-1522A, "Standard General Requirements for Safe Design and Operation of Pressurized Missile and Space Systems,"[2] specifies the fracture control requirements and procedures for metallic PVs and is being widely adopted by the space industry for domestic and

[1] Senior Engineering Specialist, The Aerospace Corporation

international space programs[3,4]. In part 1, this paper briefly describes the requirements specified in this standard, including the criteria for determining failure mode, nondestructive inspection (NDI), acceptance proof testing, and safe-life analysis methods.

Fracture control procedures for composite PVs are not as well developed. Yet, in recent years, carbon composite overwrapped pressure vessels(COPVs) have been used in space systems such as the Centaur Upper Stage vehicle[5] and the Hughes 601 spacecraft[6] because of their light weight and low cost. The major differences between COPVs and all metallic PVs are: analysis methods, NDE techniques, impact damage effects, and stress rupture characteristics.

Recently, a research, development, test and evaluation (RDT&E) program, "Enhanced Technology for Composite Overwrapped Pressure Vessels"[7], was initiated at The Aerospace Corporation. The primary objective of this RDT&E effort is to generate the necessary database for establishing fracture control requirements and procedures for COPVs. The following tasks are being conducted:

- Task 1. Data Review and Program Plan Development
- Task 2. Sample Selection/Specimen Validation
- Task 3. Database Extension
- Task 4. NDE Techniques Assessment
- Task 5. Material Requirements Development
- Task 6. Fabrication/Process Control Enhancement
- Task 7. Design Analysis Methodology Validation
- Task 8. Impact Damage Effects/Control
- Task 9. Technology Consolidation

Task 3 is to generate the needed test data such that safety related characteristics of carbon COPVs including impact damage effects, stress rupture life, and material compatibility can be understood. Task 4 is primarily to assess the applicability of the state-of-the-art NDI techniques to COPVs, while task 7 is to evaluate the validity of using conventional fatigue and fracture mechanics to determine the failure mode of a COPV and to demonstrate that a COPV has adequate safe-life. In part 2, this paper will summarize the findings obtained to date.

PART 1 - METALLIC PRESSURE VESSEL FRACTURE CONTROL, A REVIEW

Background

According to MIL-STD-1522A, there are two acceptable approaches to design and to qualify a metallic PV for military space programs. As shown in Fig. 1, Approach A allows the design not to meet ASME Code while Approach B is the ASME Code design. Two paths in Approach A can be selected based on the failure mode and the usage of a specific vessel. If the vessel contains non-hazardous fluids and the failure mode is LBB, fracture control is not required. Conventional fatigue analysis is acceptable to demonstrate its safe-life. The acceptance test and qualification test requirements are shown in the left hand path of Approach A. On the other hand, if a PV contains hazardous fluids or if its failure mode is brittle fracture, fracture control is required. NDI and fracture mechanics safe-life demonstration are needed. Other requirements are shown in the right hand path of Approach A. For the

ASME Code designed PVs, the random vibration and pressure cycle testing are also required.

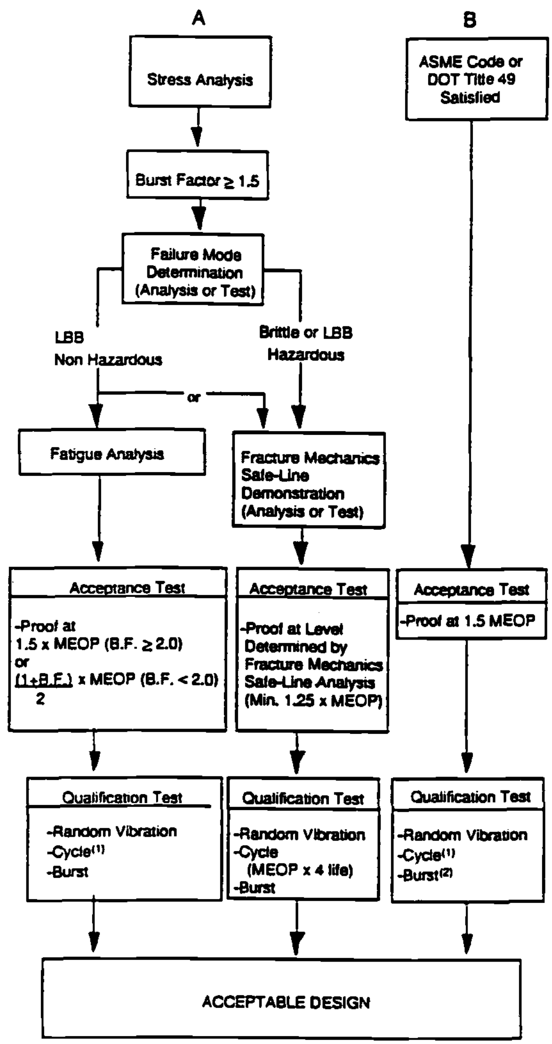

(1) Cycle test at either MEOP x 4-life or 1.5 MEOP x 2 life
(2) Burst or disposition vessel with approval of the procuring agency

FIG. 1--Space flight metallic pressure vessel design and testing requirements per MIL-STD-1522A

Leak-Before-Break Failure Mode Determination

There are several ways to determine whether the failure mode of a specific PV design is LBB. In the space industry, two approaches are allowed. They are the Air Force "Ductile Fracture" criterion as recommended in MIL-STD-1522A, and the NASA "10t" criterion. The ductile fracture criterion was proposed by Au and originally used for screening non-fracture critical parts for DOD space shuttle payloads[8]. It can be expressed as:

$$K_{IC}/\ \sigma_{op} \geq 2\ \alpha\sqrt{t}$$

$$(\alpha\ \sigma_{op}\ \leq F_{ty},\ \alpha > 1)$$

where K_{Ic} is the plane strain fracture toughness, σ_{op} is the operating stress, α is the proof test factor, F_{ty} is the tensile yield strength of the vessel material, and t is the vessel thickness.

The 10t criterion was introduced at NASA Johnson Space Flight Center. It can be expressed in the following simple form:

$$K(2c= 10t)\ <\ K_c$$

where K(2c=10t) is the stress intensity factor of a through-the-thickness crack with a crack length 2c equal to 10 times the vessel wall thickness and K_c the fracture toughness of the vessel material.

Example--The following example illustrates the use of these two criteria: A space system used a 5.8 in. diameter spherical pressure vessel to store highly pressurized gaseous nitrogen (GN_2) in its reaction control subsystem. The cross section of this GN_2 tank is shown in Fig. 2. The tank was made of titanium alloy, Ti- 6Al-4V, in solution treat and aged (STA) condition. Its maximum expected operating pressure (MEOP) was 8,000 psi and the proof test factor α was 1.5.

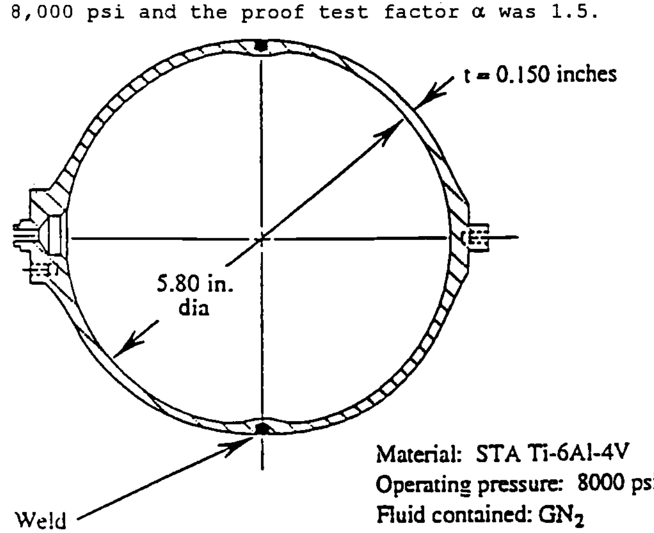

FIG. 2--GN_2 pressure vessel cross section

To apply the ductile fracture criteria, the maximum operating stress, σ_{op} corresponding to MEOP at critical locations should be determined first. In general, three locations should be considered: membrane section, membrane-boss transition, and girth weld region. For illustration, only the membrane section is considered here. The maximum operating stress is calculated to be σ_{op} = 77.3 ksi. To meet ductile fracture criteria, one must show that $K_{Ic}/\sigma_{op} \geq 2\alpha\sqrt{t}$. Since the plane strain fracture toughness (K_{Ic}) of the tank material is 42 ksi -$\sqrt{in}$[11], the value of (K_{Ic}/σ_{op} = 0.543) is less than ($2\alpha\sqrt{t}$=1.16). Hence, it does not meet the ductile fracture criteria for LBB failure mode. The failure mode of this GN_2 tank is classified as brittle fracture.

To apply the 10t criterion, the calculated stress intensity factor for a through-the-thickness crack with a crack length (2c=1.5 in.) in the membrane region of the tank is calculated as:

$$K = \beta\,\sigma_{op}\sqrt{\pi c} \cong 220\ \text{ksi}\text{-}\sqrt{\text{in.}}$$

The value of K exceeds the mixed mode fracture toughness (Kc= 56.2 ksi-$\sqrt{in}$) for this material for a thickness, t = 0.15 in. Hence, to apply "10t" criterion, the failure mode of this GN_2 tank is also non-LBB.

Proof test factor determination--Based on MIL-STD-1522A, if a PV exhibits brittle fracture failure mode or if it contains hazardous fluids such as hydrazine, monomethylhydrazine(MMH), unsymmetrical dimethylhydrazine(UDMH) and oxidizer, the acceptance proof test shall be conducted at a pressure level $P_p = \alpha \times$ MEOP. The proof test factor, α, shall be determined by linear elastic fracture mechanics (LEFM). For simplicity, the following relationship can be used to determine the proof test factor[10]:

$$\alpha = \left(\sqrt{a_{cr} / a^*_i}\right)\left(\beta_{cr} / \beta_i\right)$$

where a_{cr} is the critical crack size and a^*_i is the maximum allowable initial crack size determined by fatigue crack growth analysis, β_{cr} and β_i are the geometrical correction function corresponding to a_{cr} and a^*_i respectively. Fig. 3 shows schematically how to determine the maximum allowable initial crack size. It is backtracked four life-times (4L/T) from the critical crack size (a_{cr}) along the crack growth curve calculated by LEFM principles. The pressure/load spectrum defined for the service life of a PV, which includes the pressure/loads induced by ground handling, transportation and testing, and launch and in-orbit operation, is used in establishing the crack growth curve.

Safe-life initial crack size determination--For PVs under fracture control, it is necessary to perform NDI and safe-life demonstration. MIL-STD-1522A specifies that "*a complete inspection by the selected NDI technique(s) shall be performed prior to proof pressure test to establish the initial condition of the hardware.*" and "*...Safe-life of each pressure vessel covering the maximum expected operating loads and environments, shall be performed under the assumption of pre-existing initial flaws or cracks in the vessel. In particular, the analysis shall show that the pressure vessel with the flaws placed in the most* *unfavorable orientation with respect to the applied stress and material properties, of sizes defined by the acceptance proof test or NDI ...".*

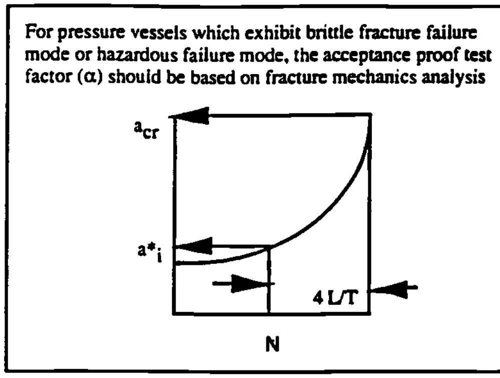

FIG. 3--Fracture mechanics based proof test factor determination

Proof test logic--The use of proof pressure level to determine the initial flaw size of a PV relies on the so-called "proof test logic" [10, 12]. As shown in Fig. 4, if a PV has successfully passed the proof test, the maximum possible initial flaw size, a_i , for a flaw which might still exist in the vessel can be determined by the following relationship:

$$a_i \leq a_{cr} = (Q K^2_c) / (\beta^2 \pi \sigma^2_p)$$

where Q is the shape factor of an elliptical crack, K_c is the fracture toughness of the vessel material, β is the geometrical correction factor, and σ_p is the stress corresponding to the proof pressure.

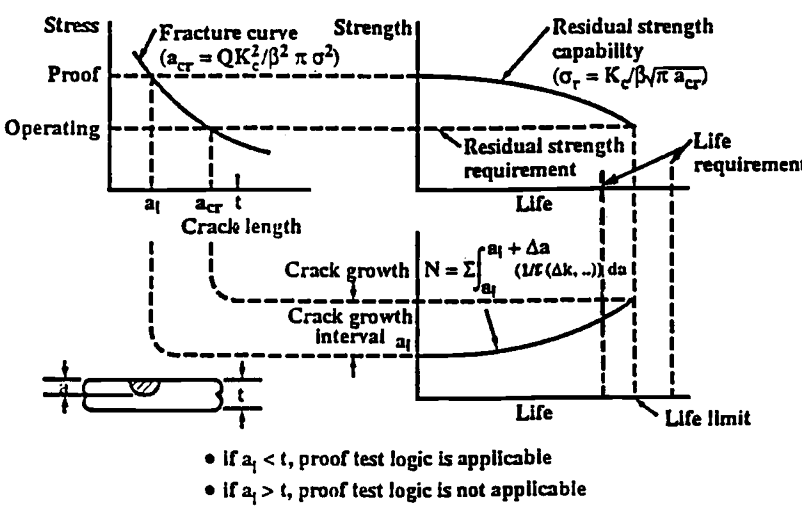

FIG. 4--Proof test logic

"a_i" is considered as the initial flaw size used in the safe-life calculation. However, for most space programs, the current trend is to use relative high strength and high fracture toughness materials such as cryostretched 301 stainless steels and annealed 6Al-4V titanium alloys; the typical vessel thickness is less than 0.05 in. Thus the calculated a_i is usually greater than the vessel wall thickness, t. In such cases, the proof test logic is considered not applicable for determining the initial flaw size. To increase proof pressure and/or conduct the proof test at cryogenic temperature are the alternatives. However, the proof pressure should be kept below a maximum level such that no gross yielding will occur as the result of the proof test.

NDI techniques--When the proof test logic is not applicable, the determination of the initial sizes used in the safe-life analysis has to rely on NDI. In general, radiography (x-ray) is typically used to detect weld defects such as lack of penetration, voids, and cracks. Dye penetrant is usually used to detect surface flaws while ultrasound is commonly used to detect subsurface (embedded) flaws. However, one form of ultrasonic technique, the Lamb Wave ultrasound, has been used to detect surface flaws in space flight propellant tanks with very small wall thicknesses (in the vicinity of 0.015 in.).

In the last two decades, government agencies have funded many research and development programs to determine the probability of detection (POD) for various NDI techniques. The so-called "standard" NDI detectable flaw sizes have been established by NASA for space shuttle payload fracture control. Table 1[3] shows the detectable sizes for various NDI techniques and different crack geometries as shown in Fig. 5. According to NASA's requirements, if a fracture critical part is subjected to a specific NDI by a qualified inspector and nothing is detected, then a safe-life analysis with an initial flaw size based on the detection limits specified in Table 1 for that NDI method shall be performed using a computer code. Currently, several codes are available for predicting fracture mechanics safe-life. CRACKS[13], CRKGRO,[14] and NASA/FLAGRO [15]are typical examples.

Concluding Remarks

Fracture control has been implemented on metallic PVs used in the military and NASA space programs for many years. As a result, there are no in-service mishaps caused by the failure of metallic PVs. However, there is an urgent need to develop NDI techniques which can be reliably used for thin-walled PVs.

PART 2 - COMPOSITE OVERWRAPPED PRESSURE VESSEL FRACTURE CONTROL

Background

There are two types of non-metallic PVs: all composite vessels and COPVs. Fracture control requirements for all composite PVs are not specified in MIL-STD-1522A. It only states that for this class of vessels, the requirements specified in ASME Boiler and Pressure Vessel Code, Section X[16], shall be met. For COPVs with metallic liners, the fracture control requirements specified in "-1522A" are identical to that for all metal vessels. However, there are no requirements for the composite overwraps. Since the analysis methods and NDI techniques which are currently used for metallic PVs might not be applicable to COPVs, the RDT&E effort described previously is aimed at generating the needed data such that requirements for composite overwraps can be established. Furthermore, since carbon composite materials are susceptible to impact damage, the effect of impact potentially induced during testing, ground handling and transportation, launch pad assembly and integration, and launch preparation needed to be investigated. Some of the findings in these areas generated from this RDT&E program are briefly reported here.

TABLE 1--Minimum initial crack sizes for fracture analysis based on NDE method

U. S. CUSTOMARY UNITS (inches)

Crack Location	Part Thickness, t (inches)[1]	Crack Type	Crack Dimension a (inches)	Crack Dimension c (inches)
		Eddy Current NDE		
Open Surface	$t \leq 0.050$	Through	t	0.050
	$t > 0.050$	PTC[2]	{ 0.020 0.050	{ 0.100 0.050
Edge or Hole	$t \leq 0.075$	Through	t	0.100
	$t > 0.075$	Corner	0.075	0.075
		Penetrant NDE		
Open Surface	$t \leq 0.050$	Through	t	0.100
	$.050 < t \leq .075$	Through	t	$0.15 - t$
	$t > 0.075$	PTC	{ 0.025 0.075	{ 0.125 0.075
Edge or Hole	$t \leq 0.100$	Through	t	0.100
	$t > 0.100$	Corner	0.100	0.100
		Magnetic Particle NDE		
Open Surface	$t \leq 0.075$	Through	t	0.125
	$t > 0.075$	PTC	{ 0.038 0.075	{ 0.188 0.125
Edge or Hole	$t \leq 0.075$	Through	t	0.250
	$t > 0.075$	Corner	0.075	0.250
		Radiographic NDE		
Open Surface	$.025 \leq t \leq 0.107$	PTC	$0.7t$	0.075
	$t > 0.107$		$0.7t$	$0.7t$
		Ultrasonic NDE		
Open Surface	$t \geq 0.100$	PTC	{ 0.030 0.065	{ 0.150 0.065

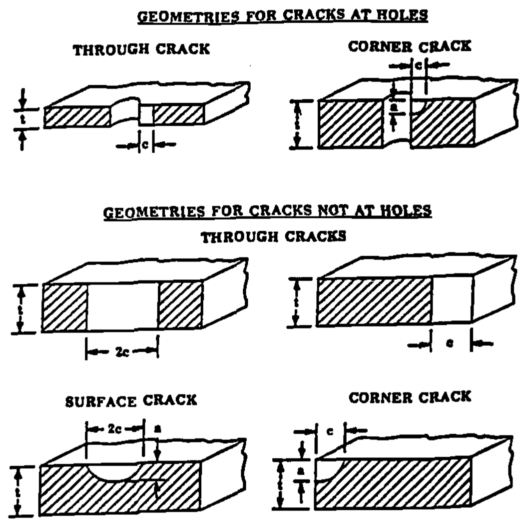

FIG. 5--Standard crack geometries

Fatigue and Fracture Mechanics Analysis Methods Validation

Literature survey results indicate that for the metal liners of COPVs, the failure mode prediction criteria, conventional fatigue analysis, and fracture mechanics safe-life analysis are based on the methods used for all metal PVs. However, these analytical tools have not been systematically assessed for their validity to apply on COPVs. In the current RDT&E program, one of the nine tasks is to assess these analytical tools. Three COPV designs which are thin aluminum liners with graphite/epoxy composite overwraps were used for the preliminary assessment. These COPVs have been flown in different space programs[7]. The failure mode of each COPV design was predicted by using both the "ductile fracture" and the "10t" criterion, and the safe-life prediction was done by using the "universal slope" approach[17]. Table 2 summarizes the prediction results. It can be seen that both these failure mode criteria predicted that all COPV designs exhibit LBB failure mode. An LBB demonstration test conducted on the large cylindrical COPV showed that the failure mode is indeed LBB [5].

TABLE 2--Predicted COPV liners failure mode and safe-life

COPV Type	Liner Mat'l	Liner Thk (in)	MEOP (psi)	σ_{op} (ksi)	K_{Ic} (a)	Kc (a)	K(10t) (a)	K_{Ic}/σ_{op} ($\sqrt{in}$)	$2\alpha\sqrt{t}$ ($\sqrt{in}$)	Predicted Failure Mode	Predicted Safe-Life (cyc)	Tested Safe-Life	Test ed Failure Mode
Small Sphere	5086-0	0.05	6,000	35.3	45	49.5	39.4	1.27	0.56	LBB	250	>50 (b)	N/A
Small Cylinder	6061-T62	0.04	6,000	41.1	26	46.8	42	0.634	0.5	LBB	3,000	>50	N/A
Large Cylinder	6061-T62	0.04	6,000	45.8	26	46.8	43	0.567	0.5	LBB	200	>50	LBB

Notes: (a) Ksi-$\sqrt{in}$
(b) Fatigue Tests stopped after 50 MEOP cycles

Since all three COPVs are used to store gaseous helium, which is considered nonhazardous, and their failure modes are LBB, conventional fatigue analysis can be used to demonstrate the required safe-life. The results of the fatigue analysis, shown in Table 2, exceed 200 MEOP cycles. Since all these COPVs have successfully completed 50 MEOP pressure cycle testing, the analytical prediction results appear to be reasonable.

NDE Techniques Assessments

In the COPV RDT&E program, the following state-of-the-art NDE methods have been assessed for their applicability to COPVs [18,19]: ultrasound, IR-thermography, shearography, acoustic emission, and eddy current.

The primary purpose for using NDE is to detect the impact damage potentially introduced during transportation and ground handling of a COPV which has been successfully subjected to acceptance proof test and leak check. The following briefly describe each NDI technique assessed to date.

Ultrasound--Both through-transmission and pulse-echo ultrasonic techniques were applied on various type of COPVs. In both cases, the COPVs were immersed in and filled with water. For the through-transmission technique, a sound pulse generated by one transducer was received by a second passing completely through the COPV. For the pulse-echo technique, a reflection rod was inserted into the center of the vessel. The amplitude of the 5 MHz pulse was recorded in each case as a function of position after passing through the pressure vessel wall. A pulse-echo C-Scan of a small cylindrical COPV after a 4 ft-lb impact is shown in Fig. 6. The impact area was not visually detectable, but is clearly indicated by a low amplitude (dark) region in the scan.

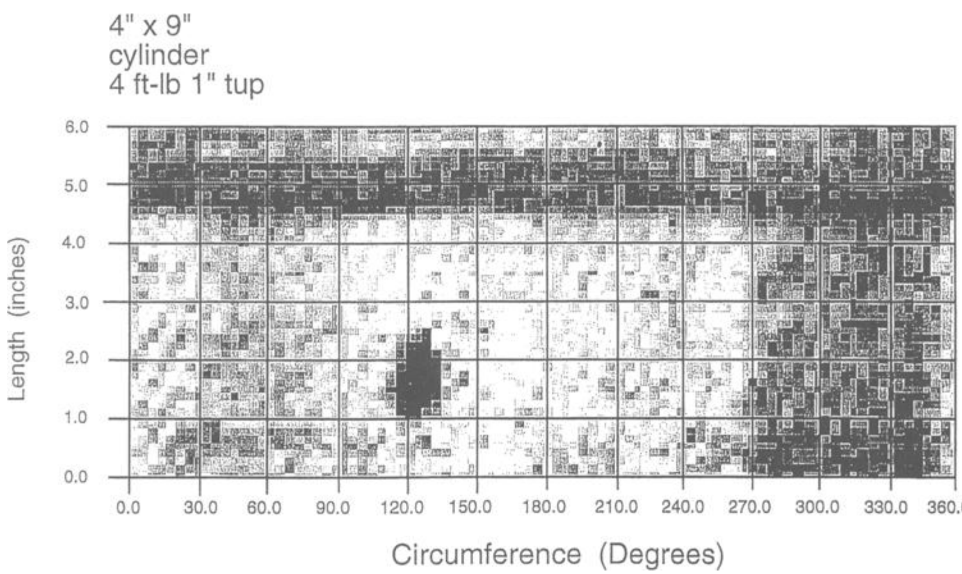

FIG. 6--Pulse-echo C-Scan of a COPV after 4 ft-lb impact

Thermography--A thermography instrument with an infrared (IR) camera is used to measure the surface temperature of the impacted COPV based on its emission of the IR radiation. Fig. 7 shows a schematic diagram of the setup. Using the IR camera, the complete temperature profile of a COPV was recorded at video frame rates (30 Hz). The impact on a COPV created a disbond between the liner and the composite overwrap thus having a significant higher thermal impedance than an undamaged area. An increase in the thermal impedance translates into higher surface temperature when the COPV is exposed to a transient heat source. The location of the surface hot spots can thus be mapped. An image obtained during the thermography inspection of the same impacted COPV is shown in Fig. 8.

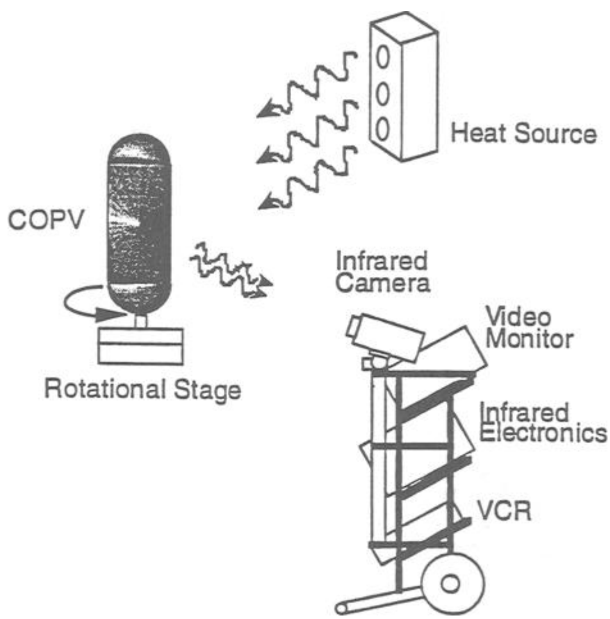

FIG. 7--Schematic of thermography setup

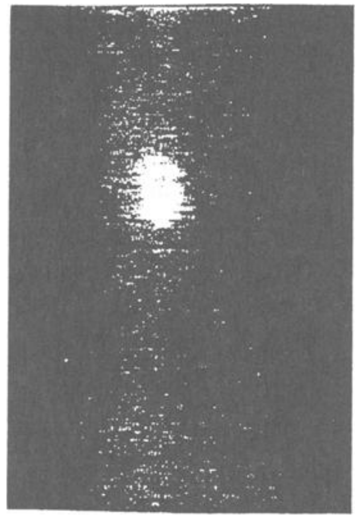

FIG. 8--Pulse thermography results from a Bales Scientific IR camera for a 4 ft-lbs impact, 0.25 sec after the thermal pulse.

Shearography--Electronic shearography, a non-contacting interferometric method which measures changes in the out-of-plane slope of a surface, was tried on the cylindrical COPV subjected to impact. The application of shearography to the COPV requires an initial image of the vessel to be acquired and stored in the digital memory of the computer. After storing the initial image, a small internal pressure was applied to the COPV and a second image was acquired and subtracted from the initial image, thus creating a family of high contrast fringes as shown in Fig. 9a, which indicates the deformations due to the pressure differential of the two images acquired conditions for an undamaged COPV. Since impacts to the COPV cause subtle changes in the deformation contours, the contrast fringes shown in Fig. 9b indicate the location of a 15 ft-lb impact.

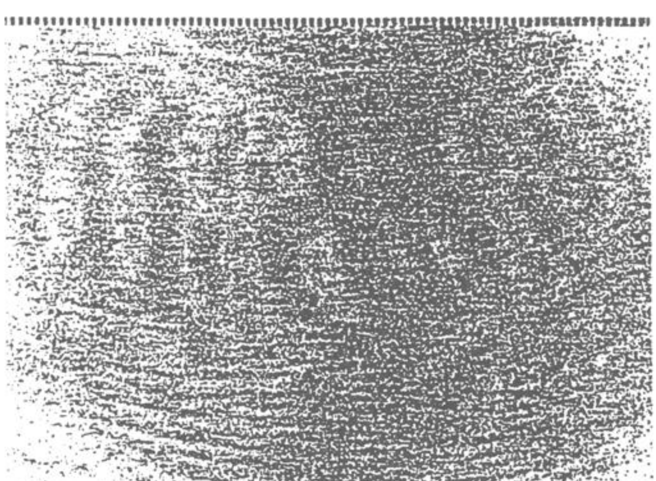

FIG. 9a--Initial shearographic image of a spherical COPV using a 40 psi pressure differential

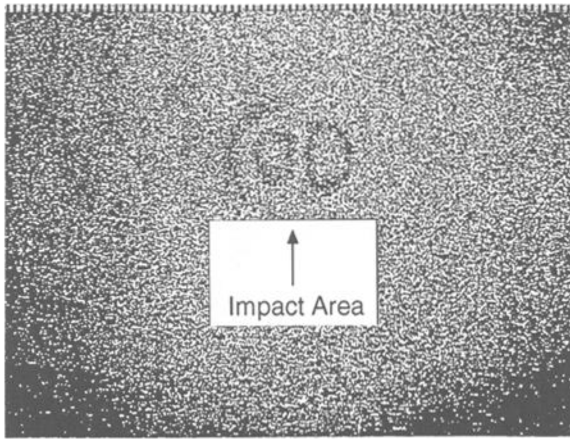

FIG. 9b--Post-impact shearographic image of the spherical COPV of Figure 9a following a 15 ft-lb impact with a 1 in. diameter tup. A 40 psi pressure differential was employed to create the image.

Acoustic emission--An array of six acoustic emission (AE) sensors was used to record the acoustic activity of a COPV during pressurization. To detect impact damage, the COPVs were subjected to an initial AE screening, and then pressurized again after being subjected to an impact. Changes in the acoustic activity were noted with COPVs exhibiting significantly more AE events after impact which exceeded a particular energy threshold. Test results show that the impact energy threshold varies significantly depending on COPV types and sizes.

Eddy current--Eddy current (EC) is a mapping technique which has been widely used for detecting cracks or crack-like defects in metallic structures with well established detectable sizes shown in Table 1. For COPVs, EC detects impact damage by the lift-off effect associated with the liner deformation. A 400 kHz EC probe driven by an analyzer was used to map the damage-affected zone of the COPV.

Summary of NDE Results

Table 3 summarizes the preliminary results of the assessment conducted at Aerospace. It shows that most of the NDE techniques can detect an impact event. However, there are not enough data to establish the POD vs. impact damage size relationship.

TABLE 3--NDE Assessment Summary

Inspection Technique	Assessment Comments
Visual	Sensitive to outer layer composite overwrap fiber breakage and debanding, the visible thresholds are higher than other NDI
Ultrasound	Sensitive to delamination in composite overwrap of COPVs
IR Thermography	A fast screening method for detecting delaminations in COPVs
Shearography	Sensitive to anomalies in the surface displacement of COPVs
Acoustic Emission	Current techniques are suited for use as screening procedure
Eddy Current	Sensitive to deformation in linear of COPVs

Impact Damage Testing

The literature survey showed that the impact damage test data for COPVs are almost non-existent. Hence,an extensive test program was initiated at NASA Johnson Space Center(JSC)/White Sands Test Facility (WSTF), Las Cruces, New Mexico. The test program consists of the following five test series: Baseline Burst, Failure Mode/Safe-Life, Impact Damage, Sustained Load/Impact Effect, and Material Compatibility Testing.

The Impact Damage Testing series is being conducted using four different types of graphite/epoxy COPVs as test articles. To avoid the ambiguity of scaling and the initial conditions of the test articles, it was decided that only the full-scale flight qualified COPVs would be used in the test program, except for the screening tests conducted in the Material Compatibility Testing Series. Table 4 summarizes the pertinent information of the test articles.

TABLE 4--Test Articles Characteristics

COPV Type	Size (in.)	Composite Thickness (in.)	Liner Thickness (in.)	Volume V (in^3)	Weight W (lb)	MEOP (psi)	Burst Strength P_b (psi)	Perform. Factor P_bV/W (in.)
Large Spherical	19 dia.	0.168	0.03	3,157	24.5	4,500	7,280	938,000
Small Spherical	10.25 dia.	0.162	0.05	484	5.3	6,000	10,600	968,000
Small Cylindrical	6.6x20	0.104	0.05	500	5.3	6,000	10,700	1,009,000
Large Cylindrical	13x25	0.147	0.05	2,650	16.7	4,500	7,850	1,246,000

Impact test--An instrumented mechanical impact tester (IMIT) with semiconductor strain gages is used to create impact and to record high-speed, real-time response of the impactor and the test articles. A special I-beam frame supports the IMIT to allow placement of the tested COPVs under the impact tup. Fig. 10 shows a sketch of the IMIT. A typical impact test data sheet is shown in Fig. 11.

Pre-and post-impact NDE--Prior to the impact testing, each test article is examined by a qualified inspector. The pre-impact inspection consists of visual, radiography (x-ray), and IR-theromography. Test articles that show abnormal appearance or defects will not be used in the test program. After impact, visual inspections are performed first by three inspectors to establish the visibility of the damage. The damaged COPV is then photographically documented. The indentation size and depth are measured and recorded. IR-thermography, ultrasound, and eddy current are then used to make quantified measurements of the damage area.

Burst testing--After the post-impact inspection, the damaged COPV is installed in the burst test facility and filled with deionized water. Air is purged from the system and the pressure is increased at a nominal ramp rate of 50 psi/sec. At MEOP of the vessel, the pressure in the system is held constant for 60 sec. The pressure in the vessel is then ramped at the same rate until the vessel fails. The burst pressure, identified as burst-strength after impact (BAI), is recorded.

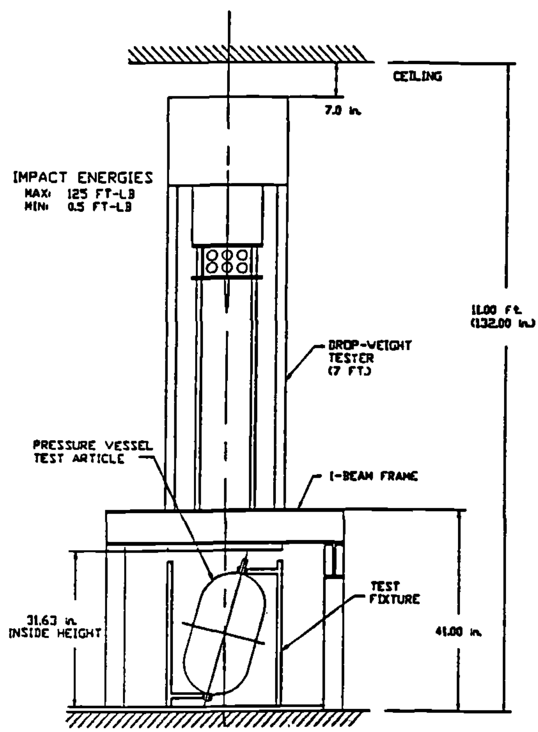

FIG. 10--WSTF-instrumented mechanical impact tester

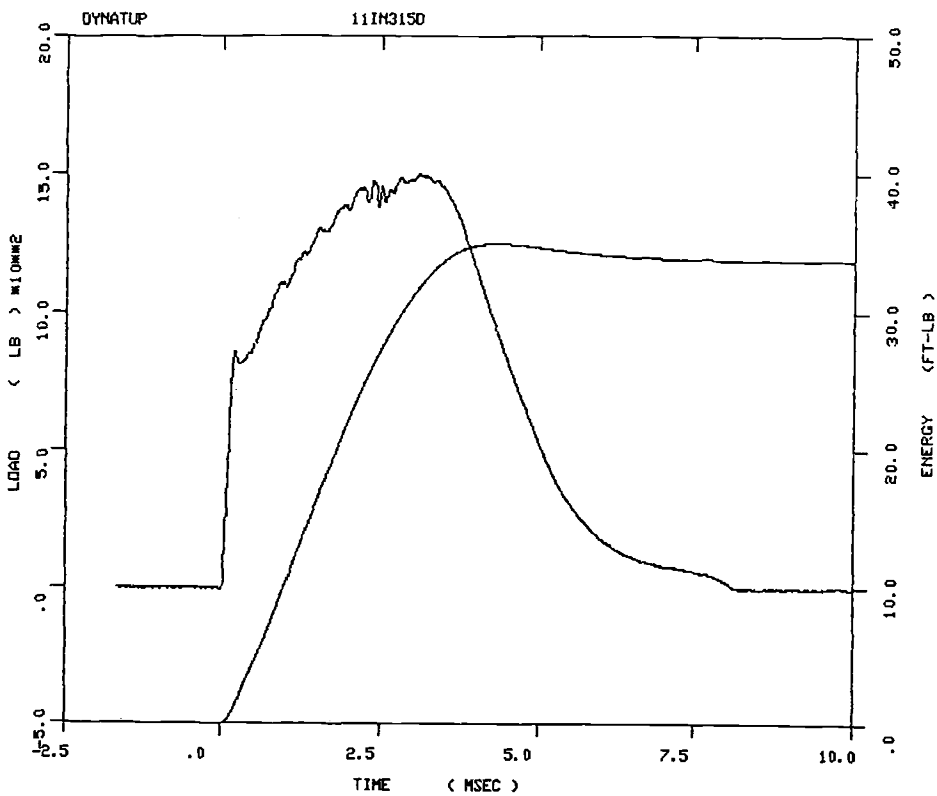

Dynatup
Batch:11in315d

MANUFACTURER :BRUNSWICK
MODEL NO. :220088-1
SERIAL NO. :93-27518-061
TUP NO. :7023

Date of Test: JAN 6, 1995 Time of Test: 10:32:24

1. Comments:
10.25" BRUNSWICK IMPACTED AT 35 FT/LB
W/ 12.85 LB. FROM 32.75 INCHES IMPACTED
@ 11 3/8" AND 315 DEGREES.

Sp #	Impact Energy (ft-lb)	Impact Velocity (ft/sec)	Maximum Load (lb)	Energy to Max.Ld (ft-lb)	Time to Max. Ld (msec)	Deflection at Max. Ld (inch)	Total Energy (ft-lb)
1	34.65	13.17	1503.37	31.71	3.07	.34	33.85

Fig. 11--Impact test data sheet

Test results--Results of the impact damage testing conducted to date are summarized in Table 5. The impact energy level applied to the small spherical COPVs ranged from 25 to 50 ft-lb with the majority of the tests conducted at 35 ft-lb level. The invisible impact damage threshold is approximately 25 ft-lb. For the small cylindrical COPVs, the impact energy level ranged from 5 to 20 ft-lb. The invisible impact damage threshold is around 15 ft-lb. The general trend is that BAI reduces as the impact energy level increases.The BAI scatter for three replicas at a specific impact level and test condition was approximately 15%, [20] which is much larger than that of 3% for the undamaged ones. Among the most important findings so far is the effect of internal pressurization condition during impact to the BAIs. For the small spherical COPVs, the increase of the internal pressure seems to improve the tolerance to the impact. The BAIs only reduced 5 to 10% from the baseline(burst strength of the undamaged vessel). There is no apparent difference between the conditions whether the vessels were pressurized with water or with gas. For the small cylindrical COPVs, the effect was similar when they were pressurized at 0.5 MEOP. However, for those COPVs which were pressurized with water to their MEOP level during impact, the BAIs reduced by an average of 25% for three repeated tests. When the pressure was gas, the effect was even more drastic. One COPV lost its burst strength by 30%; another exploded in the impact test cell immediately after impact and damaged the test facility.

TABLE 5--Impact Damage Testing Results

COPV Type & Size	Impact Energy Level (ft-lb)	BAI* (psi)	Normalized BAI	Remarks
Small Sphere 10.6" Dia.	0	10,600	N/A	Average of 3 tests, no impact applied
	25	10,676	1.0	Average of 2 tests, two locations
	35	9,005 ± 832	0.85	Average of 14 tests, many variables
	40	8,145	0.77	One test
	50	7,399	0.7	One test
Large Sphere 19" Dia.	0	7,280	N/A	One test, no impact applied
	65	7,256	99.7	One test
	100	6,256	85.9	One test
Small Cylinder 6" x 20"	0	10,700	N/A	Average of 3 tests, no impact applied
	5	9,800	0.92	One test
	10	8,884	0.83	One test
	15	8,517 ± 1,185	0.79	Average of 11 tests, many variables
	20	7,764	0.77	One test
Large cylinder 13" x 25"	0	7,850	N/A	One test, no impact applied
	25	7,263	92.5	One test
	35	5,953	75.8	One test
	50	5,401	68.6	One test

*Burst Strength after impact

Concluding Remarks

Fracture control for COPVs has not been well established. From the test results generated in the RDT&E program, it is apparent that COPVs using graphite/epoxy as overwrap materials are susceptible to impact damage. It is important to assess the impact damage effects on the burst strength of a specific COPV design and to develop an impact protection system if the COPV designed with a small safety factor is to be used in any space program.

REFERENCES

[1] "ASME Boiler and Pressure Vessel Code, Section VIII," The American Society of Mechanical Engineers

[2] MIL-STD-1522A(USAF), "Standard General Requirements for Safe Design and Operation of Pressurized Missiles and Space Systems," 1984.

[3] NHB 8071.1, "Fracture Control Requirements for Payloads Using The National Space Transportation Systems (NSTS)," National Aeronautical and Space Administration, 1988

[4] ESA PSS-01-401, "ESA Fracture Control Requirements," European Space Agency, 1989.

[5] Craig, G.W., "Preliminary Stress Analysis for Titan/Centaur 18-inch Helium Sphere," BCL-87-011, Brunswick Corp. 1987.

[6] Braun, C. A., "Innovative Features Providing Proven Solutions for Integration of Composite Pressure Vessels into Aerospace Systems," AIAA Paper 93-2099, 1993

[7] Chang, J.B. et al., "Enhanced Technology for Composite Overwrapped Pressure Vessels", The Aerospace Corp., 1993.

[8] Au, N. N., SD-YV-0068, "Fracture Control Requirements for DOD Shuttle Payloads," Air Force Space Division, 1981

[9] Ecord, GM, "Fracture Control Plan for JSC Flight Hardware," JSC 25863, National Aeronautics and Space Administration, Johnson Space Center, 1992.

[10] Chang, J.B., "Space Flight Pressure Vessel Design," PVP-Vol. 277, *Rectification and Stress Classification Issues*, American Society of Mechanical Engineers, 1994.

[11] "Fatigue Crack Growth Computer Program, NASA/FLAGRO," JSC-22267, National Aeronautics and Space Administration, Johnson Space Center, 1986.

[12] Tiffany, C.F. and Masters, V.N., "Applied Fracture Mechanics," *ASTM STP 381, Fracture Toughness Testing and Its Applications,* American Society for Testing and Materials, 1965.

[13] Engle, R.M., "CRACKS, A FORTRAN IV Digital Computer Program for Crack Propagation Analysis," AFFDL-TR-70-107, Air Force Flight Dynamics Laboratory, 1970.

[14] Chang, J.B., and Szamossi, M., "A Manual for a Detailed Level Fatigue Crack Growth Analysis Computer Code: The CRKGRO Program," AFWAL-TR-81-3093, Vol. 1, Air Force Wright Aeronautical Laboratories, 1981.

[15] JSC-2226 "Fatigue Crack Growth Computer Program, (NASA/FLAGRO)" NASA, Johnson Space Center, Houston, TX, 1988.

[16] "ASME Boiler and Pressure Vessel Code, Section X. Fiber-Reinforced Plastic Pressure Vessels," The American Society of Mechanical Engineers, 1989.

[17] Fuchs, H.O., and Stephens, R. I., Metal Fatigue in Engineering, John Wiley and Sons, 1980.

[18] Nokes, J.P., and Johnson, E.C., "Inspection Techniques for Composite Overwrapped Pressure Vessels," *PVP-Vol.318, Structural Integrity of Pressure Vessels*, American Society of Mechanical Engineers, 1995.

[19] Tapphorn, R.M., Starrit, L., and Beeson, H.D., "Nondestructive Evaluation Techniques Applied to Impact-Damage Testing of Carbon Overwrapped Pressure Vessels," Presented at JANNAF Meeting, 1995.

[20] Chang, J.B. and Beeson, H.D., "Composite Overwrapped Pressure Vessel (COPV) Program Review," NASA/DOD Pressure Systems Seminar, 1996.

Patrick M. Fourspring[1] and Robert N. Pangborn[2]

AN X-RAY DIFFRACTION STUDY OF MICROSTRUCTURAL DEFORMATION INDUCED BY CYCLIC LOADING OF SELECTED STEELS

REFERENCE: Fourspring, P. M., Pangborn, R. N., "**An X-Ray Diffraction Study of Microstructural Deformation Induced by Cyclic Loading of Selected Steels,**" Fatigue and Fracture Mechanics: 28th Volume, ASTM STP 1321, J. H. Underwood, B. D. Macdonald, and M. R. Mitchell, Eds., American Society for Testing and Materials, 1997.

ABSTRACT: X-ray double crystal diffractometry (XRDCD) was used to assess cyclic microstructural deformation in a face centered cubic (fcc) steel (AISI304) and a body centered cubic (bcc) steel (SA508 class 2). The objectives of the investigation were to determine if XRDCD could be used effectively to monitor cyclic microstructural deformation in polycrystalline Fe alloys and to study the distribution of the microstructural deformation induced by cyclic loading in these alloys. The approach used in the investigation was to induce fatigue damage in a material and to characterize the resulting microstructural deformation at discrete fractions of the fatigue life of the material. Also, characterization of microstructural deformation was carried out to identify differences in the accumulation of damage from the surface to the bulk, focusing on the following three regions: near surface (0-10 μm), subsurface (10-300 μm), and bulk. Characterization of the subsurface region was performed only on the AISI304 material because of the limited availability of the SA508 material. The results from the XRDCD data indicate a measurable change induced by fatigue from the initial state to subsequent states of both the AISI304 and the SA508 materials. Therefore, the XRDCD technique was shown to be sensitive to the microstructural deformation caused by fatigue in steels; thus, the technique can be used to monitor fatigue damage in steels. In addition, for the AISI304 material, the level of cyclic microstructural deformation in the bulk material was found to be greater than the level in the near surface material. In contrast, previous investigations have shown that the deformation is greater in the near surface than the bulk for Al alloys and bcc Fe alloys.

KEY WORDS: fatigue damage, cyclic microstructural deformation, X-ray diffraction, X-ray double crystal diffractometry, AISI304, stainless steel, SA508, pressure vessel steel

Prior to fatigue crack nucleation, microstructural deformation occurs in an engineering material as the result of cyclic loading. X-ray diffraction is one of several techniques that have been used and are being used to assess cyclic microstructural deformation. This information can be used to monitor fatigue damage and, as a result, to

[1]Engineer, Lockheed Martin Corporation, POB 1072, Schenectady, NY 12301-1072.

[2]Professor of Engineering Mechanics, The Pennsylvania State University, 101 Hammond Building, University Park, PA 16802.

enhance the safety and the economy of a wide range of mechanical components and structures. In addition, an understanding of the response of a material to cyclic loading can be used to develop materials that are more resistant to fatigue damage.

In the past, various X-ray diffraction techniques have been used successfully to assess cyclic microstructural deformation in Al, Ni, and Fe alloys. Furthermore, one technique, that uses a double crystal diffractometer to assess this deformation, has been proposed for and validated on aircraft structural alloys (Al alloys) and aircraft engine alloys (Ni alloys). To build on these results, X-ray double crystal diffractometry (XRDCD) was used in the investigation reported in this paper to assess cyclic microstructural deformation in a face centered cubic (fcc) steel (AISI304) and a body centered cubic (bcc) steel (SA508 class 2).

The objective of this investigation was twofold. The first objective was to determine if XRDCD could be used to effectively monitor cyclic microstructural deformation in polycrystalline Fe alloys. The second objective was to study the distribution of the microstructural deformation induced by cyclic loading in these alloys.

TECHNICAL BASIS

Cyclic loading induces microstructural deformation in a material prior to the subsequent nucleation of microcracks that lead to macrocrack formation and propagation to failure. The first step in the fatigue failure process, microcrack initiation, typically comprises three critical processes [1-9]:

1. cyclic microstructural deformation,
2. near surface deformation, and
3. microcrack nucleation.

Microcrack initiation begins with the microstructural deformation of a material in response to cyclic loading. This deformation, referred to as cyclic microstructural deformation, results in dislocations, either existing or generated, rearranging into lower strain energy states. The resulting dislocation configurations decrease the ductility of the material by hampering dislocation motion [10]. Microstructural deformation in the near surface (0-10μm) and the subsurface (10-300μm) region develops differently than in the bulk as a result of the influence of the free surface. This unique deformation leads to geometric discontinuities that can become localized stress risers on the microstructural scale. Therefore, the decreased ductility together with the localized stress risers results in microcrack nucleation. At these geometric discontinuities, microcracks nucleate as a result of the inability of the microstructure to accommodate the strain energy that arises as a result of the discontinuity.

During cyclic microstructural deformation, groups of interacting dislocations evolve from random clusters within volumes that are nearly free of dislocations to bands of interacting dislocations surrounding volumes that are nearly free of dislocations. For cubic materials, the following three general categories of dislocation configurations have been observed and evolve in the order shown[1-9]:

1. dislocation patches and planar arrays,
2. walls and channels (including the labyrinth variation), and
3. cells.

Furthermore, cyclic microstructural deformation will lead to a change in the dislocation density from the initial density. Several microstructural processes can increase or decrease the dislocation density. For example, if the initial dislocation density is insufficient to accommodate the imposed cyclic loading, then dislocation multiplication can lead to an increase in the dislocation density allowing the material to accommodate the loading. The initial dislocation density varies with the fabrication process. A cold worked material will have a high dislocation density, and an annealed material will have a low dislocation density.

In a laboratory environment, X-ray diffraction has been shown to be sensitive to cyclic microstructural deformation in engineering materials [11-23]. In general, the level of lattice distortion in the diffracting grains changes the shape of the X-ray diffraction profiles. XRDCD can provide additional information by indicating the formation of dislocation cell configurations that result in multimodal diffraction peaks, i.e. peaks with multiple maxima. For example, if the initial state of a material is annealed, then cyclic loading will most likely increase lattice distortion and lead to the formation of dislocation cells. The increase in the lattice distortion is caused by the increase in the dislocation density from dislocation multiplication. As a result, the diffraction peaks will, in general, "broaden" and become multimodal.

EXPERIMENTAL APPROACH AND PROCEDURES

The approach for the experimental investigation was to induce fatigue damage in selected materials and to characterize the resulting microstructural deformation at discrete fractions of the fatigue life. Characterization of microstructural deformation was also carried out to identify differences in the accumulation of damage from the surface to the bulk. In the near surface region (0-10μm), the procedure was to interrupt the cyclic loading of the test bars at various estimated fractions of life and then characterize the near surface of the test bars at each stage. Once the test bar failed and the number of cycles to failure became known, the exact fraction of life at each interruption was calculated by dividing the number of accumulated cycles by the total number of cycles at failure. For the study of the subsurface region (10-300μm), the procedure was to halt the cyclic loading of the test bars at various estimated fractions of life and then characterize the surface of the test bars. A layer of material was then removed from the surface by electropolishing to permit characterization of the newly exposed surface. Therefore, by repeating this procedure several times at varying depths into the material, a profile of the microstructural deformation within the subsurface region emerged. Finally, for the bulk characterization, the Ishikawajima-Harima Heavy Industries Company (IHI) provided samples from fatigued test bars as part of a parallel research project [24]. IHI exposed the bulk material by cutting the gage section of the test bars perpendicular to the longitudinal axis to produce disk shaped samples.

The experimentation included two different steels. One steel was an annealed austenitic stainless steel, AISI304, that is widely used in power systems for piping and piping support structures. The second steel was a vacuum treated (degassed), quenched, and tempered alloy steel, SA508, class 2, that is used for nuclear reactor pressure vessels. Figure 1 contains a sketch of the test bar configuration, and Table 1 provides a description of the composition, heat treatment, surface preparation, and cyclic loading for each material. The microstructure of the AISI304 is face centered cubic (fcc) austenite, and the microstructure of the SA508 is a body centered cubic (bcc) granular bainite. Microscopy showed that the grain size of the AISI304 was approximately 80 to 90μm and the grain size of the SA508 was approximately 10 to 20μm. For both materials, an electropolishing procedure insured a smooth surface and removed any near surface microstructural deformation caused by machining.

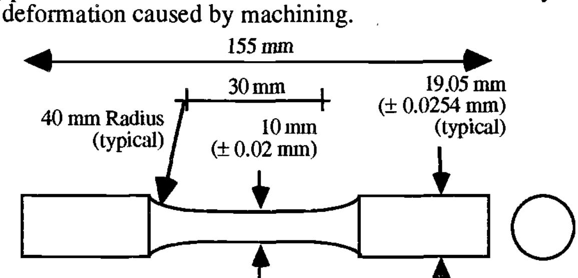

Figure 1 Test bar configuration

TABLE 1-- Composition, Heat Treatment,, Surface Preparation, and Cyclic Loading

AISI304	**SA508 class 2**
Composition	
(test bars) 0.052%C; 1.64% Mn; 0.36%Si; 18.48%Cr; 9.10%Ni; 0.027%P; 0.022%S (samples*) 0.04%C; 1.09%Mn; 0.67%Si; 18.87%Ci; 8.73%Ni; 0.034%P; 0.009%S	(test bars and samples*) 0.21%C; 1.53%Mn; 0.08%P; 0.03%S; 0.28%Si; 1.02%Ni; 0.21%Cr; 0.53%Mo; 0.004%V
Heat Treatment	
(test bars) Annealing: 1060°C in Argon Environment for 60 minutes; Quenching: room temperature in Argon Environment for 60 minutes (samples*) Annealing: 1060°C in air for 54 minutes; Quenching: water	(test bars and samples*) Normalizing: 890-905°C/12.3hrs.; Air Cool; Tempering: 645-650°C/12.5hrs.; Furnace Cool; Reheating 870-890°C/6.5hrs.; Water Quench; Tempering: 650-670°C/6.5hrs.; Furnace Cool; Stress Relieving: 608-631°C/45.4hrs.; Furnace Cool
Surface Preparation	
(test bars) Electropolish: Hydrite 4000™ (50% H_3PO_4 & 50% H_2SO_4); 3.0 amps/sq.in.; 55-60°C; time varied (samples*) Electropolish: 100 ml $HClO_4$; 400 ml Ethanol; 1.785 - 7.65 amps/sq. in.; 0-10°C; 6 minutes	(test bars and samples*) Electropolish: Hydrite 4000™ (50% H_3PO_4 & 50% H_2SO_4); 3.0 amps/sq.in.; 55-60°C; time varied
Cyclic Loading	
Strain Controlled with Extensometer; Tension-Compression Load Ratio (R=-1); Triangle Wave; Temperature: 24°C; Failure Criterion: 10% load drop set1: $\Delta\varepsilon$ = 0.60%; 2Hz (test bars) set1: $\Delta\varepsilon$ = 0.60%; 0.0833Hz (samples*) set2: $\Delta\varepsilon$ = 1.20%; 2Hz (test bars)	Strain Controlled with Extensometer; Tension-Compression Load Ratio (R=-1); Triangle Wave; Temperature: 300°C; Failure Criterion: 10% load drop set1: $\Delta\varepsilon$ = 0.48%; 2Hz (test bars) set1: $\Delta\varepsilon$ = 0.48%; 0.1042Hz (samples*) set2: $\Delta\varepsilon$ = 0.78%; 2Hz (test bars) set2: $\Delta\varepsilon$ = 0.78%; 0.0641Hz (samples*)

* These samples refer to the disk shaped material that was removed from the gage section of test bars by Ishikawajima-Harima Heavy Industries Company (IHI). Refer to the text on the previous page for a description of these samples.

The X-ray double crystal diffractometer system used in the experimentation consisted of three primary components: an X-ray generator, a double crystal diffractometer, and a position sensitive, proportional X-ray detector. A Rigaku X-ray generator was equipped with a chromium target X-ray tube to reduce fluorescence from the steel specimens. A Blake Industries double crystal diffractometer with a silicon single crystal wafer of (111) orientation was employed to produce a parallel, monochromatic incident beam. An MBraun position sensitive, proportional X-ray detector with a multichannel analyzer (MCA) intercepted the diffraction cone from the specimen and converted the X-ray intensities into electronic data. Auxiliary components in the X-ray double crystal system included a microcomputer for data acquisition and control and a stepping motor with a controller. Table 2 lists the XRDCD settings used for the test bars and the samples of both the AISI304 and the SA508 materials. For both materials, the approximate penetration depth of the Cr wavelength X-rays for the planes characterized in this investigation is on the order of 10μm. This value is based on the assumption that 95% of the incident intensity is reflected [25].

TABLE 2-- XRDCD Settings and Data Acquisition Regime

Parameter	**AISI304**	**SA508 class 2**
Plane	(111)	(110)
X-ray Target	Cr, $K\alpha_1K\alpha_2$, 30kV/15mA	Cr, $K\alpha_1K\alpha_2$, 30kV/15mA
First Crystal	Silicon single crystal, (111)	Silicon single crystal, (111)
Beam Size	3 mm horizontal 12 mm vertical for test bars 10 mm vertical for samples	3 mm horizontal 12 mm vertical for test bars 8 mm vertical for samples
Detector Window (per channel on the MCA)	0.5 mm horizontal 0.0455 mm vertical	0.5 mm horizontal 0.0455 mm vertical
Detector Distance	85 mm (minimum)	85 mm (minimum)
Specimen Orientation	Test Bars: vertical Samples: flat against holder	Test Bars: vertical Samples: flat against holder
Surface Locations	Two, 180° apart	Two, 180° apart
Rotations per Surface Location	80 at 4.1667 minutes each	40 at 4.1667 minutes each
Dwell Time	8 minutes	8 minutes

ANALYSES OF THE XRDCD DATA

Two quantitative analyses of the XRDCD data were used in this investigation. The first method is referred to as variance analysis, and the second method is referred to as individual peak analysis. The same data sets were used in both analyses. The form of these data sets is a matrix of intensities of diffracted X-rays.

XRDCD allows the unique capability to analyze individual diffraction peaks from individual diffracting entities in a material, usually the population of metallic grains oriented for diffraction for the selected (hkl) reflection. However, identification and deconvolution of the individual diffraction peaks require several mathematical operations. As a minimum, this analysis requires data smoothing to allow peak identification and peak modeling to allow deconvolution of overlapping peaks. Furthermore, the XRDCD data from materials with a very small grain size ($\approx$10μm) have overlapping peaks that are difficult to model. As an alternative to individual peak analysis of the XRDCD data, an aggregate analysis of the same data provides a mathematically simple, but less sensitive approach. For this investigation, the variance of the XRDCD data was used as an aggregate parameter.

Variance is a statistical measure of the variability in data. As the diffraction peaks broaden or contract with the introduction of microstructural deformation in a material, the deviation of each data point from the mean intensity of all the data points will also change. The variance analysis of the XRDCD data involved normalizing the data to remove instrumental influences and calculating the statistical variance, specifically the sample variance, of the normalized data.

The individual peak analysis of the XRDCD data focuses on each diffraction peak within the data set instead of the data set as a whole. For assessing fatigue damage, the analysis of each peak is used in the traditional approach to analyze these data [11-18, 26]. These references refer to the individual peak analysis of the XRDCD data as computer aided rocking curve analysis (CARCA). The basic approach of the individual peak analysis is to identify an individual diffraction peak and to calculate a quantitative measure of the peak's shape, the integral breadth, as an indication of the microstructural deformation within the diffracting entity. The integral breadth is the volume under the peak divided by the height of the peak.

RESULTS

The as-collected XRDCD data show discernible changes between the initial and the failure states for both the near surface and the bulk regions. Figures 2 and 3 display representative, as-collected XRDCD data from the fcc (AISI304) and the bcc (SA508) material, respectively. For these figures, the diffraction cone arc is the angular distance along the Debye-Scherrer diffraction cones, and the rocking curve arc is the angular distance that the test bar is rotated through the Bragg angle [11-18, 25, 26]. From the near surface region of the fcc material, Figure 2 shows a dramatic broadening of the diffraction peaks from the test bar cycled continuously to failure with an 1.20% strain range. As shown in Figure 3, the asperity of the diffraction peaks increases from the initial state to the failure state for the near surface region of the SA508 material cycled with a 0.78% strain range.

The results of the quantitative analyses of the XRDCD data provide coherent trends with accumulated fatigue damage and into the depth. The coherent trends indicate a measurable change induced by fatigue from the initial state to subsequent states. The results are juxtaposed with one another to allow comparison of the trends with the factors that were varied in the experimentation.

The data from the individual peak analysis of the XRDCD data are presented in two forms to emphasize the unique character of the XRDCD data that allows culling the less deformed diffracting entities (grains) from the more deformed diffracting entities. The cyclic microstructural deformation will vary from grain to grain, and therefore, the ability to quantify the deformation of individual grains is critical. First, Figure 4 shows representative histograms of the integral breadths from the bulk of the AISI304 material fatigued with a 0.60% strain range. These distributions show that some of the peaks, that is the diffracting entities, have remained virtually unchanged while other peaks have broadened, increasing the magnitude of the integral breadth. Generally, the histograms indicate left skewed distributions for the initial state and early in the fatigue life; whereas, they indicate right skewed distributions for more advanced fatigue and the failure states. Second, Figures 5 and 6 show the trends in results from the individual peak analysis of the XRDCD data with accumulated fatigue damage for the near surface and the bulk. The population proportion estimator was used on the results of this analysis to quantify the change in the integral breadth distributions [27]. For this analysis, the estimator is the proportion of integral breadths that exceed 25 arc minutes. This value of the integral breadth is approximately the mean of all the initial state integral breadths for the AISI304 material. Figures 5 and 6 contain plots of this estimator against the corresponding fraction of life. To test for statistical significance between the initial state of each test bar, or sample, and any subsequent state, the large sample z test for population proportions was used. The null hypothesis used was p_1-p_2=0, and the significance level used was 0.05. No results from the individual peak analysis for the SA508 materials were obtained, due to the difficulty in deconvoluting the small diffraction peaks.

The results from the variance analysis of the XRDCD data show coherent trends for both the fatigued fcc material (AISI304) and the fatigued bcc material (SA508). Figure 7 shows the results of the variance analysis for the bcc material. In this figure, the variance of each data set of X-ray intensities is plotted against the corresponding fraction of life. No statistical significance testing was completed on the variance estimator, since only two data points were available per state.

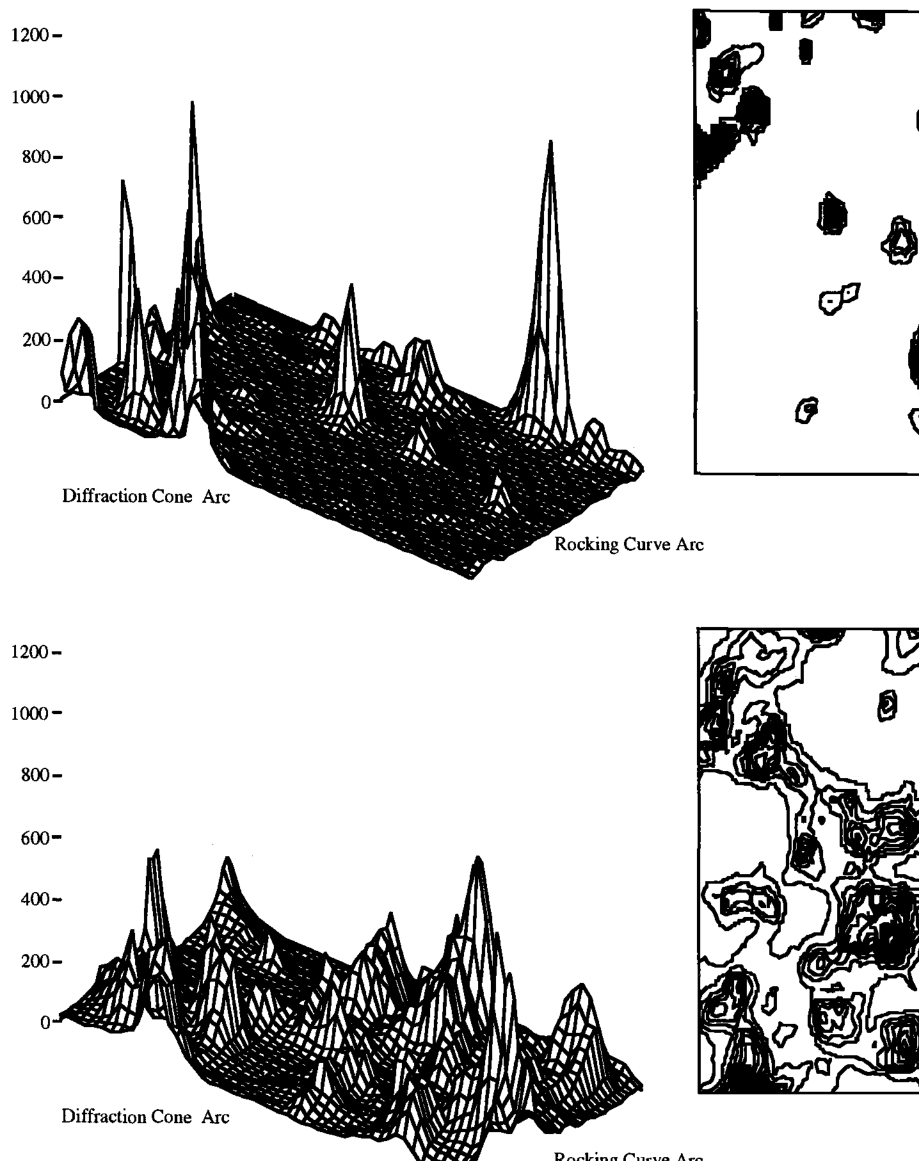

Figure 2 Surface and contour plots of XRDCD data: AISI304, $\Delta\varepsilon = 1.20\%$, near surface, top plots: initial state, bottom plots: failure state. range of axes: vertical: (as shown) total X-ray counts, diffraction cone arc: $\approx 12°$, rocking arc: 5.49°.

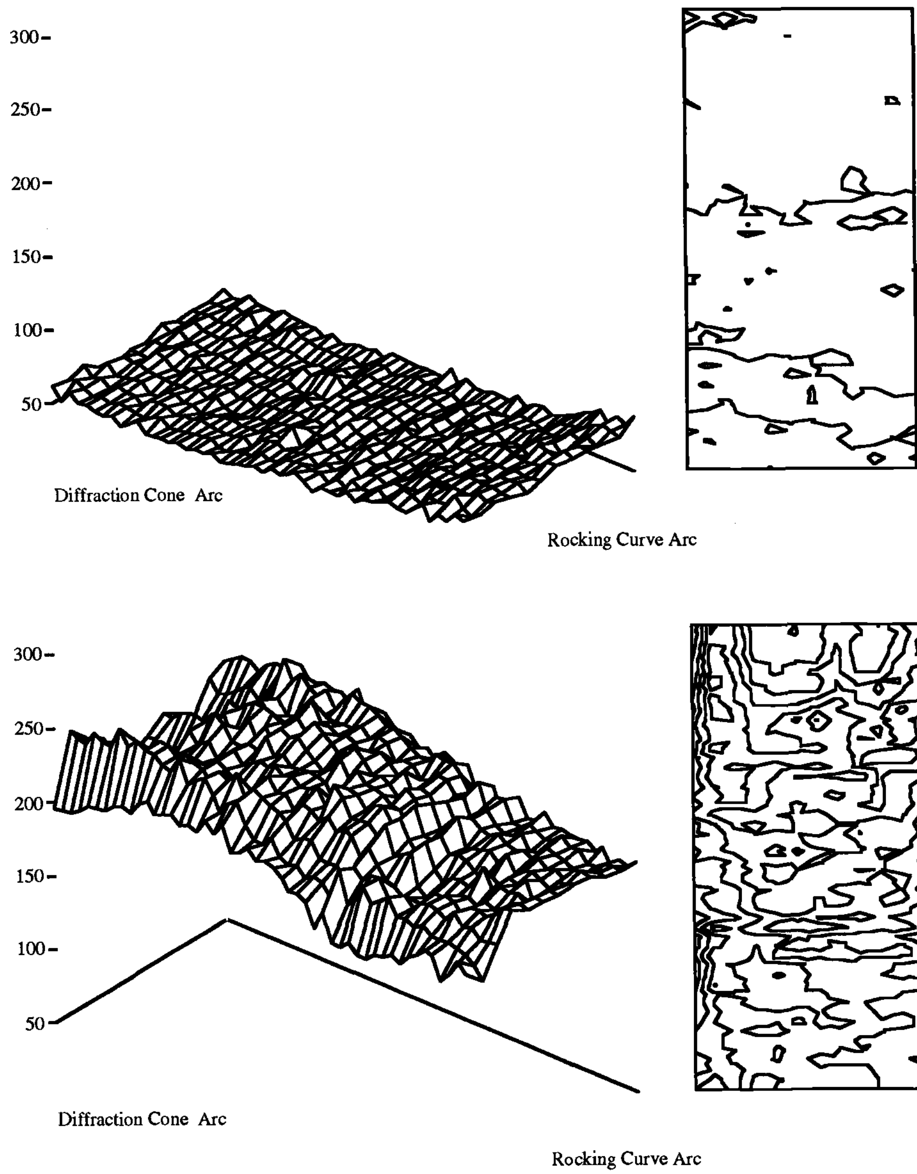

Figure 3 Surface and contour plots of XRDCD data: SA508, $\Delta\varepsilon$ = 0.78%, near surface, top plots: initial state, bottom plots: failure state. range of axes: vertical: (as shown) total X-ray counts, diffraction cone arc: ≈12°, rocking arc: 1.647°.

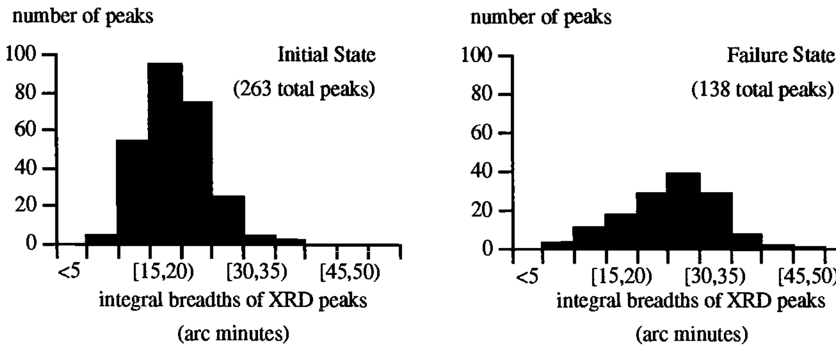

Figure 4 Histograms of the integral breadths from the XRDCD data.
AISI304, $\Delta\varepsilon$ = 0.60%, bulk

For all the quantitative analyses (Figures 5-7), the plots in the left column show the absolute magnitudes of the estimator (either proportional or variance); whereas, the plots in the right column show the value of the estimator normalized with a value that was based on the initial state estimator for the test bars or the samples. The absolute magnitudes are useful for comparing trends from the same analysis of other data. The relative magnitudes are useful for comparing the trends from various analyses, as well as from other studies, that use X-ray diffraction and other techniques to measure fatigue damage. To facilitate comparison between the results from the individual peak analysis and the variance analysis, the normalized values were equal either to the value of each estimator divided by the initial state value or vice versa; thus the normalized value always increased with accumulated damage. The proportional estimator is dimensionless as is the normalized value of the estimator. The variance estimator is in units of X-ray counts, and the normalized value of the estimator is dimensionless. The appropriate units are shown on the x axes. For the proportional estimator, the solid symbols represent results which have a statistically significant difference from the initial state; and, the outlined symbols represent results which have no statistically significant difference from the initial state. The error bars indicate plus and minus one standard error and are only shown on the plots of the absolute magnitudes (plots in the left column). For the trends in the subsurface region (Figure 6), a horizontal line is shown to indicate the initial state of the material. This line is based on the initial state of the near surface region and implies that the deformation prior to cyclic loading is uniform from the surface to the bulk, that is the measured values for the surface apply also to the initial state of subsurface and bulk regions.

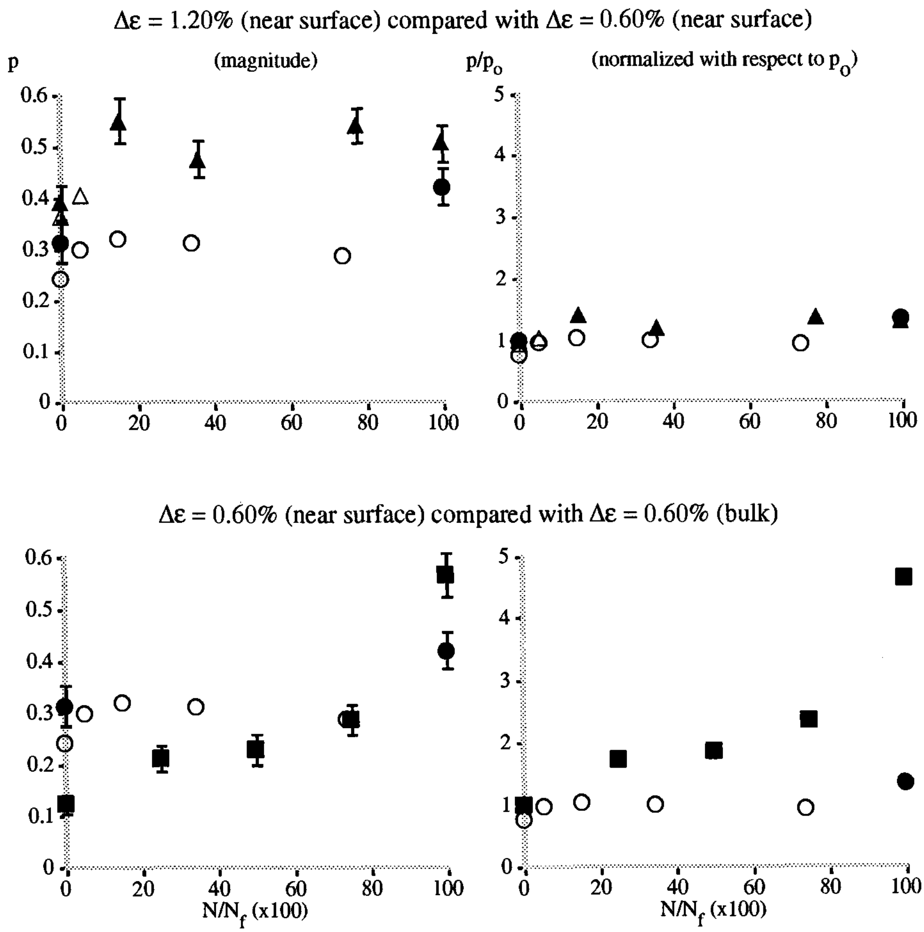

● (O) Δε = 0.60% (near surface) ■ (□) Δε = 0.60% (bulk)
▲ (Δ) Δε = 1.20% (near surface)

(The solid symbols represent results which have a statistically significant difference from the initial state; and, the outlined symbols represent results which have no statistically significant difference from the initial state.)c

Figure 5 Individual peak analysis of the XRDCD data for AISI304 for the near surface and bulk.

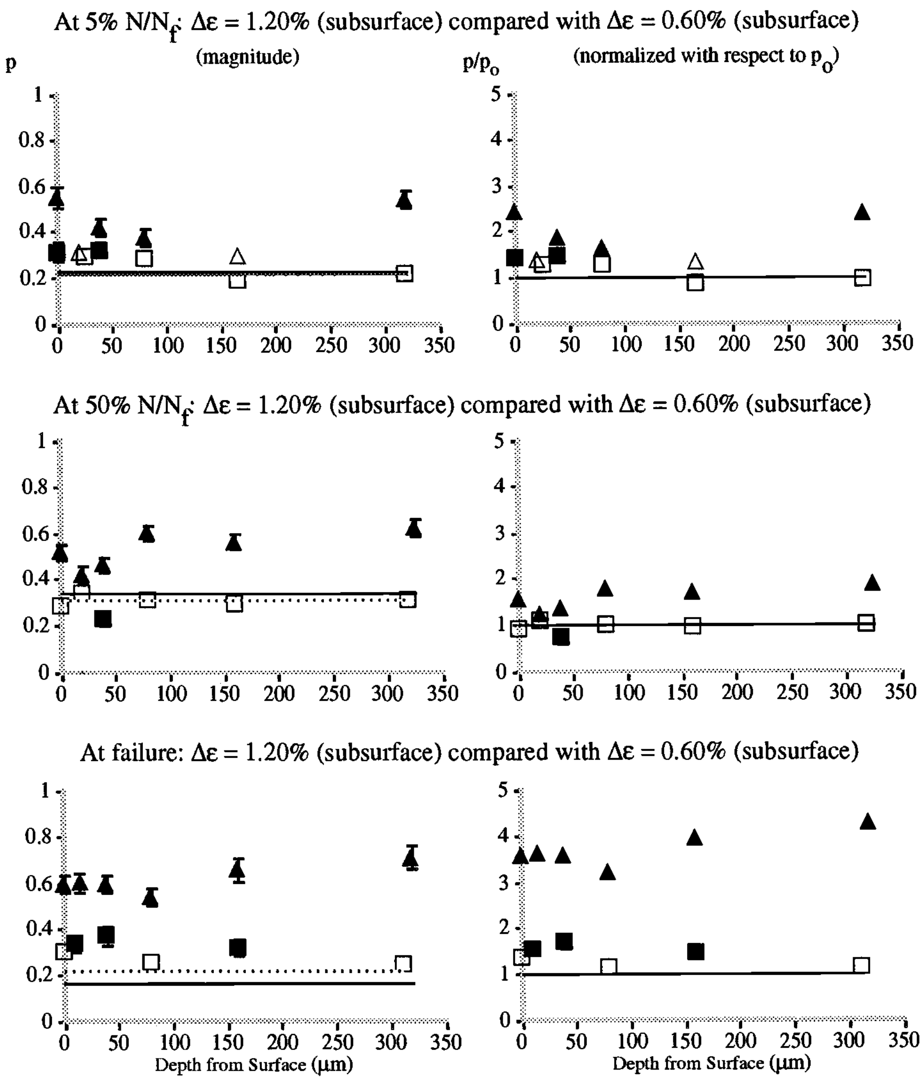

■ (□) $\Delta\varepsilon$ = 0.60% (subsurface) ▲ (Δ) $\Delta\varepsilon$ = 1.20% (subsurface)

. . . . initial state for $\Delta\varepsilon$ = 0.60% test bars ____ initial state for $\Delta\varepsilon$ = 1.20% test bars

(The solid symbols represent results which have a statistically significant difference from the initial state; and, the outlined symbols represent results which have no statistically significant difference from the initial state.)c

Figure 6 Individual peak analysis of the XRDCD data for AISI304 for the subsurface.

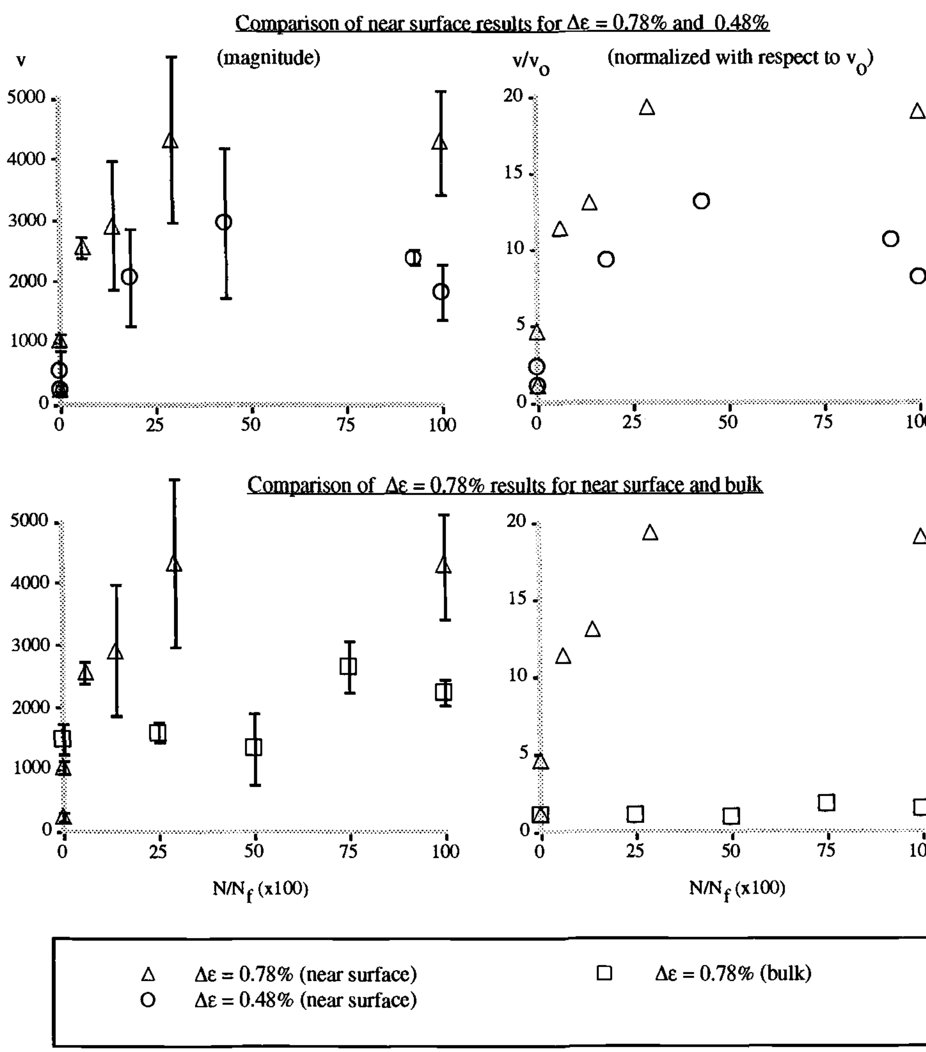

Figure 7 Variance analysis of the XRDCD data for SA508 for the near surface and the bulk.

DISCUSSION

The results of this investigation indicate that the XRDCD technique is sensitive to the microstructural deformation caused by fatigue in steels. Therefore, this XRD technique can be used to monitor fatigue damage as it is accumulated during cycling to failure. The XRDCD data indicate a measurable change from the initial state to subsequent states induced by fatigue of both the fcc material (AISI304) and the bcc material (SA508). For the fcc material, Figures 5 and 6 for the individual peak analysis of the XRDCD data show coherent trends in the results with fatigue damage accumulation or into the depth. For the bcc material, Figure 7 for the variance analysis of the XRDCD data shows coherent trends in the results as the fatigue damage accumulates. A discussion of specific features of the results and the underlying microstructural deformation follows.

For the fcc material, lattice distortion increased as fatigue damage accumulated in the near surface, subsurface, and bulk regions. Figures 5 and 6 show an increase in the integral breadths with fatigue damage. The increase in the integral breadth indicates that the diffraction profiles from the XRDCD data "broadened." The integral breadth is a quantitative measure of the broadening in the diffraction profiles, as shown in Figure 2. It is assumed that, prior to cyclic loading, the annealed, fcc material had a low dislocation density as compared to a cold worked material. During cyclic loading, dislocation multiplication is thought to have occurred to accommodate the imposed strains. The increase in the dislocation density enhanced the development of the cell dislocation configuration as the dislocations reconfigured into lower energy states. As a result, the X-ray diffraction profiles broadened in general. Furthermore, multimodal peak formation, indicating cell dislocation configurations, is evident in the XRDCD data shown in Figure 2.

Comparison of the results from the near surface and the subsurface shows that the level of lattice distortion increased as the strain amplitude increased. The increase in the integral breadths (Figures 5 and 6) was greater for the material fatigued with a 1.20% strain range than the material cycled with a 0.60% strain range. The larger strain amplitude would likely cause a more pronounced rate of dislocation multiplication. With a higher dislocation density, the development of the cell dislocation configuration is more complete [10]. Therefore, the level of lattice distortion and cell development was greater in the fcc material cycled at the larger strain amplitude.

For the fcc material, the level of lattice distortion was greater in the bulk material than the near surface material. Figure 5 shows a comparison between the near surface and the bulk for the material cycled with a 0.60% strain range. The change in the integral breadths from the bulk material is greater than the change in the integral breadths from the near surface material. The following description of the microstructural processes that lead to this result is inferred from related microscopy results from other investigators[28-33]. Initially, the free surface both attracts dislocations and allows them to egress, until the increase in the near surface strain energy due to the dislocation density increase begins to repel dislocations rather than attract them[5, 34, 35]. In contrast, no reduction in dislocation density due to egress occurs in the bulk, although mutual annihilation still occurs. Even though the dislocation multiplication rate in the near surface may exceed the bulk because of the decreased dislocation density in the near surface, the multiplication rate in both regions would still be low as compared to a fcc material that cross slips easily. Austenitic stainless steel, such as AISI304, exhibits restricted cross slip; and, as a result, the dislocation multiplication rate is low. Therefore, the dislocation density in the bulk would remain greater than the density in the near surface, even with dislocation multiplication occurring there at a greater rate. With the higher dislocation density, the development of the cell dislocation configuration in the bulk would be more complete. Hence, the broadening of the diffraction profiles and the formation of multimodal profiles would be more pronounced in the bulk as indicated by the results.

Similarly, although less apparent, the lattice distortion and the development of cell dislocation configurations were greater in the subsurface than the near surface (Figure 6).

In contrast to the cyclic microstructural deformation caused by the cyclic loading of the fcc material, the lattice distortion decreased in the bcc material. The increase in the variance parameter indicates that the diffraction profiles from the XRDCD data became increasingly acicular. As for the formation of cell dislocation configurations, the high density of diffraction peaks in the XRDCD data from the bcc material (see Figure 3) preclude distinguishing multimodal peaks that indicate cell dislocation configurations. As a quenched, bainitic steel, the bcc material contains ferrite laths that begin with a high density of randomly oriented dislocations [36]. Although bainite consists of ferrite laths that are embedded with several different phases, the XRDCD data was gathered primarily from the ferrite phase, because of the diffraction angle used [25, 35]. The externally applied cyclic loading provides the energy for the dislocations to glide and reconfigure into lower strain energy configurations. During this process, mutual annihilation of dislocations and dislocation egress at the free surface occur. Therefore, the dislocation density decreases; and, as a result, the lattice distortion decreases.

For the bcc material, the decrease in the lattice distortion was greater in the near surface material than in the bulk material, in contrast to the results for the fcc material. Figure 7 shows a comparison between the results from the near surface and the bulk regions for the material cycled with a 0.78% strain range. The change in the variance estimator from the near surface material is greater than the change in the variance estimator from the bulk material. The variance estimator increased with fatigue damage in both regions. Like the fcc material, dislocation egress at the free surface may have occurred in the bcc material. However, as a material that cross slips with ease, the bcc material has a greater rate of dislocation multiplication than the fcc material. Therefore, the dislocation density reduction in the near surface of the bcc material due to egress at the free surface was quickly reversed as dislocation multiplication occurred to allow the material to accommodate the imposed strains. With the higher dislocation density, the reconfiguration of the dislocations into lower strain energy states is more complete.

Finally, in the near surface of the bcc material, the magnitude of the lattice distortion change increased as the strain amplitude increased. The increase in the variance parameter (Figure 7) was greater for the material fatigued at a strain range of 0.78% than the material cycled with a strain range equal to 0.48%. As the strain amplitude increases, the number of gliding dislocations increase. As a result, dislocation egress at the free surface increases, and subsequent dislocation multiplication is more effective. As already discussed for the fcc material, the reconfiguration of the dislocations into lower strain energy states is more complete as the number of dislocations involved in the cyclic microstructural deformation process increases.

CONCLUSIONS

The general conclusion of the research presented in this paper is that X-ray double crystal diffractometry (XRDCD) was shown to be sensitive to the microstructural deformation caused by fatigue in steels and can be used to monitor fatigue damage. This conclusion is significant because assessing fatigue damage with XRDCD had yet to be demonstrated on steels. Specifically referring to the results from Pangborn et al. [37], Allen et al. stated, "It remains to be determined whether such a method [XRDCD] could be applied to steel." [38]. Other conclusions of the research are summarized as follows:

1. For the fcc material (AISI304), lattice distortion increased and cell dislocation configurations developed as fatigue damage accumulated in the near surface, subsurface, and bulk regions. In contrast, the lattice distortion decreased with advancing fatigue in the near surface and bulk regions of the bcc material (SA508).

2. In both materials, cyclic microstructural deformation increased as the strain amplitude increased.
3. For the fcc material, the level of lattice distortion was greater in the bulk material than the near surface material. In contrast, the level of lattice distortion was greater in the near surface region than the bulk for the bcc material. This conclusion supports previous investigations that also showed greater microstructural deformation in the near surface than the bulk for bcc Fe alloys [39, 40]. The results from the fcc material, however, are contrary to the results from previous investigations of near surface deformation in fcc alloys, specifically Al alloys and Ni alloys [14, 17]. The difference is that the austenitic stainless steel (AISI304) cross slips with difficulty. As a result, the cyclic microstructural deformation develops differently in the near surface region.
4. XRDCD was shown to be useful on an engineering material with a complex microstructure, that is the bainitic pressure vessel steel, SA508.

ACKNOWLEDGMENTS

The authors wish to recognize Ishikawajima-Harima Heavy Industries Company (IHI) for its' support of this work and for providing the SA508 test bars and the samples of both alloys used to characterize the bulk material behavior.

REFERENCES

[1] Grosskreutz, J. C., "The Mechanisms of Metal Fatigue (I)," Physica Status Solidi (B), Vol. 47, 1971, pp. 11-31.

[2] Grosskreutz, J. C., "The Mechanisms of Metal Fatigue (II)," Physica Status Solidi (B), Vol. 47, 1971, pp. 359-396.

[3] Mughrabi, H., "A Surface Effect Specific to Cyclically Deformed B.C.C Metals - The Surface Roughening of Polycrystalline alpha-Iron During Cyclic Deformation," in Surface Effects in Crystal Plasticity, R. M. Latanision and J. T. Fourie, Editors, Noordhoff International Publishing, 1977, pp. 479-485.

[4] Mughrabi, H., "Microscopic Mechanisms of Metal Fatigue," in Strength of Metals and Alloys, Proceedings of the Fifth International Conference on the Strength of Metals and Alloys, P. Haasen, V. Gerold, and G. Kostorz, Editors, Pergamon Press, Aachen, Federal Republic of Germany, 1980, pp. 1615-1638.

[5] Mughrabi, H., et al., "Fatigue Crack Initiation by Cyclic Slip Irreversibilities in High-Cycle Fatigue," in Fatigue Mechanisms: Advances in Quantitative Measurement of Physical Damage, ASTM STP 811, J. Lankford, et al., Editors, ASTM, Philadelphia, 1983, pp. 5-45.

[6] Mughrabi, H., "Dislocations in Fatigue," in Dislocations and Properties of Real Materials, Proceedings of the Conference to Celebrate the Fiftieth Anniversary of the Concept of Dislocation in Crystals, Vol. 323, Institute of Metals, London, 1985, pp. 244-262.

[7] Sudarshan, T. S. and M. R. Louthan, Jr., "Gaseous Environment Effects on Fatigue Behaviour of Metals," International Materials Review, Vol. 32, No. 3, 1987, pp. 121-151.

[8] Sudarshan, T. S., T. S. Srivatsan, and D. P. Harvey, II, "Fatigue Processes in Metals: Role of Aqueous Environments," Engineering Fracture Mechanics, Vol. 36, No. 6, 1990, pp. 827-852.

[9] Laird, C., "Recent Advances in Understanding the Cyclic Deformation of Metals and Solid Solutions," in Work Hardening in Tension and Fatigue, A. W. Thompson, Editor, AIME, 1977, pp. 150-176.

[10] Kuhlmann-Wilsdorf, D., "Theory of Plastic Deformation:--properties of low energy dislocation structures," Materials Science and Engineering, Vol. A113, 1989, pp. 1-41.

[11] Pangborn, R. N. and B. L. Peterson, "Precision Measurement of Microplasticity by Computer-Aided Rocking Curve Analysis," Crystal Properties and Preparation, Vol. 16, 1988, pp. 185-200.

[12] Mayo, W. E., "Microscopic-Damage-Based Criterion for Fatigue Failure Prediction," International Journal of Fatigue, Vol. 9, No. 4, 1987, pp. 203-209.

[13] Mayo, W. E. and S. Weissmann, "Characterization and Failure Prediction of Fatigued Alloys by Computer-Aided X-ray Rocking Curve Analyzer," in Microstructural Characterization of Materials by Non-Microscopical Techniques, N. H. Andersen, et al., Editors, Risø National Laboratory, Roskilde, Denmark, 1984, pp. 391-396.

[14] Khatri, R. P., et al., "Surface Features and Plasticity Induced by Tension-Tension Fatigue of Inconel 718," Journal of Materials Science, Vol. 21, 1986, pp. 511-521.

[15] Mayo, W. E. and S. Weissmann, "Nondestructive Failure Prediction in Cycled Commercial Alloys by Computer Aided X-ray Rocking Curve Analysis (CARCA)," in Fatigue 84, Proceedings of the Second International Conference on Fatigue and Fatigue Thresholds, Vol. 2, Engineering Materials Advisory Services Ltd, Birmingham, England, 1984, pp. 1161-1170.

[16] Pangborn, R. N., S. Weissmann, and I. R. Kramer, "Measurement of Cumulative Fatigue Damage by X-Ray Double Crystal Scanning Diffraction Methods," Advances in X-Ray Analysis, Vol. 24, 1981, pp. 203-208.

[17] Pangborn, R. N., S. Weissmann, and I. R. Kramer, "Dislocation Distribution and Prediction of Fatigue Damage," Metallurgical Transactions A, Vol. 12A, 1981, pp. 109-120.

[18] Pangborn, R. N., S. Weissmann, and I. R. Kramer, "Work Hardening in the Surface Layer and in the Bulk During Fatigue," Scripta Metallurgica, Vol. 12, No. 2, 1978, pp. 129-131.

[19] Zamrik, S. Y. and R. N. Pangborn, "Fatigue Damage Assessment Using X-Ray Diffraction and Life Prediction Methodology," Nuclear Engineering and Design, Vol. 116, 1989, pp. 407-413.

[20] Weiss, V. and Y. Oshida, "Fatigue Damage Characterization by X-Ray Diffraction Line Analysis," in Fatigue 84, Proceedings of the Second International Conference on Fatigue and Fatigue Thresholds, Vol. 2, Engineering Materials Advisory Services Ltd, Birmingham, England, 1984, pp. 1151-1160.

[21] Field, J. L., F. Behnaz, and R. N. Pangborn, "Characterization of Microplasticity Developed During Fatigue," in Fatigue Mechanisms: Advances in Quantitative Measurement of Physical Damage, ASTM STP 811, J. Lankford, et al., Editors, ASTM, Philadelphia, 1983, pp. 71-94.

[22] Evans, W. P., R. E. Ricklefs, and J. F. Millan, "X-ray and Fatigue Studies of Hardened and Cold-Worked Steels," in Local Atomic Arrangements Studied by X-Ray Diffraction, J. B. Cohen and J. E. Hilliard, Editors, Metallurgical Society Conferences, Vol. 36, Gordon and Breach, Science Publishers, Inc., New York, 1966, pp. 351-377.

[23] Taira, S. and K. Honda, "X-ray Investigation on the Fatigue Damage of Metals," Bulletin of JSME, Vol. 4, No. 14, 1961, pp. 230-237.

[24] Nakagawa, H., H. Yoshizawa, and M. E. Lapides, "Measurement of Fatigue Accumulation in High-Strength Steels by Microstructural Examination," Metallurgical Transactions A, Vol. 21A, 1990, pp. 1989-1996.

[25] Cullity, B. D., Elements of X-Ray Diffraction, 2nd ed, Addison-Wesley Publishing Company, Inc, Reading, Massachusetts, 1978.

[26] Pangborn, R. N., Surface Layer and Bulk Plasticity of Tensile Deformed and Fatigue Cycled Metals and Prediction of Fatigue Life by X-ray Diffraction, Ph.D., Rutgers University, The State University of New Jersey (New Brunswick), 1979.

[27] Devore, J. L., Probability and Statistics for Engineering and the Sciences, 3rd ed, Brooks/Cole Publishing Company, Monterey, California, 1991.

[28] Gerland, M., et al., "Evolution of Dislocation Structures and Cyclic Behaviour of a 316L-type Austenitic Stainless Steel Cycled in vacuo at Room Temperature," Materials Science and Engineering, Vol. A118, 1989, pp. 83-95.

[29] Ghafouri, S. N., R. G. Faulkner, and T. E. Chung, "Microstructural Developments in Type 316L Stainless Steel During Low-cycle Fatigue at 350-550°C and Their Effects on Cyclic Strength and Life," Materials Science and Technology, Vol. 2, 1986, pp. 1223-1232.

[30] Ermi, A. M. and J. Moteff, "Microstructural Development and Cracking Behavior of AISI 304 Stainless Steel Tested in Time Dependent Fatigue Modes," Journal of Engineering Materials and Technology, Vol. 105, 1983, pp. 21-30.

[31] Jin, N., C. Zhong, and X. Chen, "Cyclic Deformation of AISI-310 Stainless Steel--II. Saturation Dislocation Structures," Acta Metallurgica Materiala, Vol. 38, No. 11, 1990, pp. 2141-2148.

[32] L'Espérance, G., J. B. Vogt, and J. I. Dickson, "The Identification of Labyrinth Wall Orientations in Cyclically Deformed AISI-SAE 316 Stainless Steel," Materials Science and Engineering, Vol. 79, 1986, pp. 141-147.

[33] Magnin, T., et al., "Low-Cycle Fatigue Damage Mechanisms of F.c.c. and B.c.c. Polycrystals: Homologous Behaviour?," Materials Science and Engineering, Vol. A118, 1989, pp. 41-51.

[34] Hull, D. and D. J. Bacon, Introduction to Dislocations, 3rd ed, International Series on Materials Science and Technology, Vol. 37, Pergamon Press, Oxford, 1984.

[35] Jastrzebski, Z. D., The Nature and Properties of Engineering Materials, 2nd ed, John Wiley & Sons, Inc., 1976.

[36] Edmonds, D. V. and R. C. Cochrane, "Structure-Property Relationships in Bainitic Steels," Metallurgical Transactions A, Vol. 21A, 1990, pp. 1527-1539.

[37] Pangborn, R. N., S. Weissmann, and I. R. Kramer, "Fatigue Failure Prediction by X-ray Double Crystal Diffractometry and Topography," Proceedings of the Fifth International Conference on the Strength of Metals and Alloys, Vol. 2, Pergamon Press, Toronto, 1979, pp. 1279-1284.

[38] Allen, A. J., et al., *Microstructural Examination of Fatigue Accumulation in Critical LWR Components.* Final Report for Electric Power Research Institute. No. NP-5590. January 1988, United Kingdom Atomic Energy Authority.

[39] Kramer, I. R., "Surface Layer Effects on the Mechanical Behavior of Metals," in Advances in the Mechanics and Physics of Surfaces, R. M. Latanision and T. E. Fischer, Editors, Vol. 3, Harwood Academic Publishers, Chur, Switzerland, 1986, pp. 109-248.

[40] Lee, W. J., Y. W. Chung, and M. E. Fine, "Effect of Environment and Grain Size on Cyclic Deformation and Surface Hardening of Iron," Metallurgical Transactions A, Vol. 19A, 1988, pp. 337-344.

Lin Ye[1] *, Akbar Afaghi-Khatibi[1], Yiu-Wing Mai[1]

PROGRESSIVE DAMAGE AND RESIDUAL STRENGTH OF NOTCHED COMPOSITE LAMINATES: A NEW EFFECTIVE CRACK GROWTH MODEL

REFERENCE: Ye L., Afaghi-Khatibi A., and Y.-W. Mai, **"Progressive Damage and Residual Strength of Notched Composite Laminates: A New Effective Crack Growth Model,"** Fatigue and Fracture Mechanics: 28th Volume ASTM STP 1321, J. H. Underwood and B. D. Macdonald, M. R. Mitchell, Eds., American Society for Testing and Materials, 1997.

ABSTRACT: The main objective of this study was to evaluate the residual strength of fibre reinforced metal laminates (FRMLs) and polymer matrix composite laminates (PMCLs) with a circular hole or sharp notch using an effective crack growth model (ECGM). Damage is assumed to initiate when the local normal stress at the hole edge/notch tip reaches the tensile strength or yield strength of the composite and metal layers, respectively. The damage in the constituent materials was modelled by fictitious cracks with cohesive stress acting on the crack surfaces, and the damage growth was simulated by extension of the fictitious cracks step by step and reduction of the cohesive stress with crack opening. The apparent fracture energy of composite layers and fracture toughness of metal layers were used to define the relationships between the tensile/yield strength and the critical crack opening. Based on the global equilibrium, an iterative technique was developed to evaluate the applied load required to produce the damage growth. The residual strength of notched composite laminates was defined by instability of the applied load with damage growth. The effect of hole/notch size on the residual strength was studied and the stress redistribution with damage growth was discussed. The residual strength simulated from ECGM correlated well with experimental data in the open literature.

[1] Senior Lecturer, Postgraduate and Professor, respectively. Centre for Advanced Materials Technology, Department of Mechanical and Mechatronic Engineering, University of Sydney, NSW 2006 Australia.

[*] To whom all the correspondence should be addressed.

KEYWORDS: residual strength, damage growth, notched composite laminates, effective crack growth, cohesive stress, failure criterion.

Nomenclature

a	Crack length
R	Hole radius
A_{ij}	In-plane laminate stiffness
a_{tot}	Total crack length (a+c)
c	Fictitious crack length in laminate
c_A	Fictitious crack length in metal layer
c_{Com}	Fictitious crack length in composite layer
COD	Crack Opening Displacement
CTOD	Crack Opening Displacement at crack tip or hole edge
E_{11}	Young's modulus of composite layer in the fibre direction
E_{22}	Young's modulus of composite layer in the transverse direction
E_A	Young's modulus of metal
FWC	Finite width correction factor
$F_{coh}(n)$	Cohesive force acting on individual increment of fictitious crack
F_{coh}^{A}	Cohesive force in metal layer
F_{coh}^{Com}	Cohesive force in composite layer
G_c^{A}	Fracture toughness of metal
G_c^{Com}	Apparent fracture energy of composite layer
G_c^{*}	Apparent fracture energy of composite laminate
K_I	Mode I stress intensity factor
k_T^{∞}	Stress concentration factor
t	Thickness of laminate
t_A	Total thickness of metal layers
t_{Com}	Total thickness of composite layers
$v_{(n)}$	Crack opening displacement
$v_{\sigma_{coh}(n)}$	COD due to the cohesive stress

$v_{\sigma_{app}(n)}$	COD due to the applied stress
v_c^A	Critical CTOD for metal layer
v_c^{Com}	Critical CTOD for composite layer
W	Specimen width
x	Distance from hole centre
Y(a/W)	Linear elastic calibration function for stress intensity factor
Δc	Fictitious crack increment
σ_c	Residual strength of composite laminate
σ_o	Unnotched strength of composite laminate
$\sigma_{coh}(n)$	Cohesive stress
$\sigma_{app}(i)$	Applied stress in *the* *i*th step
σ_y^*	Modified elastic stress distribution ahead of fictitious crack tip
σ_y	Elastic stress distribution
σ_y^A	Yield strength of metal
σ_{uts}^{Com}	Tensile strength of composite
σ_{coh}^{A}	Cohesive stress in metal layer
σ_{coh}^{Com}	Cohesive stress in composite layer

INTRODUCTION

The prediction of residual strength of composite laminates containing sharp notches or holes has been proven to be rather difficult because of complex failure mechanisms [1-7]. The previous models developed for evaluating residual strength of notched polymer matrix composite laminates (PMCLs) normally adopted a characteristic dimension, such as the Point and Average Stress Criteria [1, 8], the Inherent Flaw Criterion [2], the Three-Parameter Model [9], the Mar-Lin Model [10] and the Damage Zone Criterion [11]. The most essential limitation of these models is that the characteristic dimension is not a physical parameter and needs to be empirically determined through fitting experimental data. Furthermore, this characteristic dimension is not a material constant and it is dependent on the geometry of the specimens [3].

In addition, the most common way to evaluate the residual strength of fibre reinforced metal laminates (FRMLs) is to extend the current residual strength models developed for notched polymer matrix composite laminates [12]. Only a few models have been developed for evaluating the fracture behaviour of FRMLs, e.g. Modified Net Section (MNS) criterion [13], and an R-curve approach proposed by Macheret and Bucci [14].

Generally speaking, the essential characteristics of failure mechanisms, such as stress redistribution, damage initiation and growth etc, are not addressed in previous "characteristic-dimension" models. This paper presents a study on effective crack growth and residual strength of PMCLs and FRMLs with a sharp notch or circular hole. First, the effective crack growth model (ECGM), developed in the previous work [15], is briefly described and the basic concepts of the model for simulating damage growth and stress redistribution are addressed. Then, based on the failure mechanisms, ECGM is extended to simulate residual strength of some notched FRMLs and PMCLs. Various laminates with a circular hole or sharp notch are evaluated using this new approach, and the results are compared with both experimental data and the evaluations from other models.

EFFECTIVE CRACK GROWTH MODEL

For a composite laminate with a central circular hole of radius R or a sharp notch of size 2a, damage is assumed to initiate when the local normal tensile stress at the hole edge or notch tip reaches the unnotched strength of the composite laminate. The damage is simulated by a fictitious crack with cohesive stress acting on its surface, as shown in Fig. 1. Upon further loading, the fictitious crack is assumed to open and grow, step by step, by a length of Δc, simulating progressive damage in the composite laminate. The cohesive stress profile can be correlated with the crack opening displacement, v, using the apparent fracture energy, G_c^*,

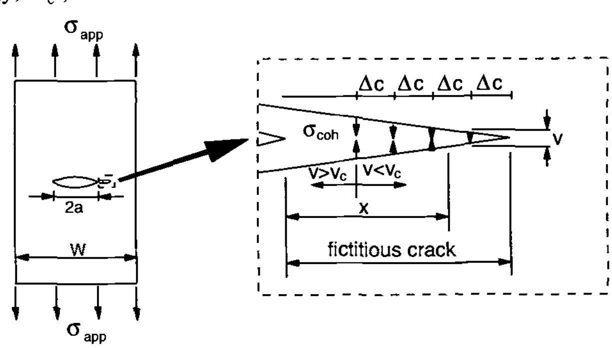

FIG. 1--Effective crack growth in ECGM.

$$\sigma_{coh} = f(v_{(n)}, G_c^*) \tag{1}$$

The applied load associated with the fictitious crack growth in the notched composite laminate can be evaluated from the global equilibrium condition, i.e. the applied load is in equilibrium with the cohesive stress acting on the surface of the fictitious crack and the modified elastic stress acting on the undamaged section plane [15, 16],

$$f(\sigma_{coh}\ ,\ \sigma_y^*\ ,\ \sigma_{app}\ ,\ W\ ,\ t)\ =\ 0 \tag{2}$$

To evaluate the crack opening displacement, $v_{(n)}$, associated with the applied stress and the cohesive stress, an appropriate equation is proposed [15, 16],

$$v_{(n)}\ =\ f(\sigma_{app}\ ,\ \sigma_{coh}) \tag{3}$$

Using an iterative technique the applied load corresponding to a specific fictitious crack length is evaluated with Eqs. 1-3. In such an approach, the residual strength of notched composite laminates is defined by the unstable point of the applied load with damage growth.

RESIDUAL STRENGTH OF NOTCHED FRMLS AND PMCLS

For a FRML with a circular hole or sharp notch and tensile loads applied on its ends, damage first initiates by local yielding in the metal layers and fibre breakage in the composite layer in the region ahead of the hole edge or notch tip due to stress concentration. As a result, delamination between the metal and composite layers is induced by the shear stress at the interface. These fracture mechanisms cause stress redistribution/relaxation ahead and behind the crack tip, associated with apparent fibre bridging due to non-coplanar cracking of composite layers in the wake of the crack tip [17].

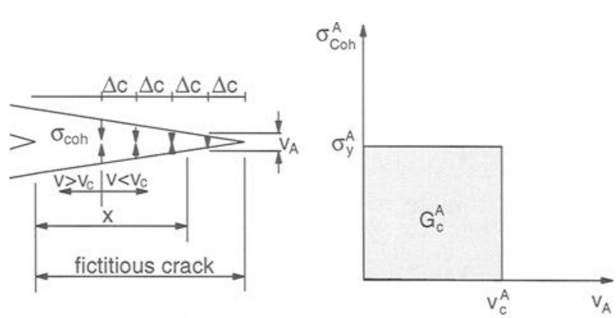

FIG. 2--Fictitious crack and Dugdale model for metal layer.

Damage is assumed to initiate in the metal layers when the normal tensile stress at the hole edge or notch tip reaches the yield strength of the metal, σ_y^A. With increasing applied load, the extension of the yielding zone is simulated using a fictitious crack with cohesive stress, σ_{coh}^{A}, acting on the crack surfaces, i.e. the Dugdale model [18] as shown in Fig. 2. The fracture toughness of the metal, G_c^A, is used to define the critical crack opening, v_c^A, associated with the yield strength σ_y^A. When the crack opening displacement, v, is larger than v_c^A, a real crack initiates and propagates stably.

It is assumed that damage in the fibre composite layers initiates when the normal tensile stress at the hole edge or notch tip reaches the ultimate tensile strength of the composite layer, σ_{uts}^{Com}. With increasing applied load, the damage grows, associated with stress relaxation due to fibre breakage and pullout. The material degradation within the damage region is simulated by a fictitious crack with cohesive stress σ_{coh}^{Com} acting on the crack surfaces as shown in Fig. 3. A linear relationship between the crack opening displacement and the cohesive stress has been proven to provide a good description of the damage behaviour of composite materials [19]. The apparent fracture energy, G_c^{Com}, is used to correlate the critical crack opening, v_c^{Com}, and cohesive stress, σ_{coh}^{Com}.

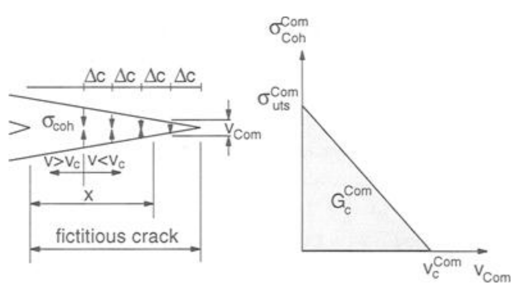

FIG. 3--Fictitious crack and linear relationship between cohesive stress and crack opening in composite layer.

Residual Strength Evaluation

At each step of effective crack growth, the cohesive force along the fictitious crack is the sum of the cohesive forces [15, 16], acting on the individual metal and composite layers.

$$F_{(n)}^{coh} = F_{coh}^{A} + F_{coh}^{Com} = vol_A \, \sigma_{coh}^{A} \, \Delta c \; t + vol_{Com} \, \sigma_{coh}^{Com} \, \Delta c \; t \tag{4}$$

and

$$\sigma_{(n)}^{coh} = vol_A \sigma_{coh}^{A} + vol_{Com} \sigma_{coh}^{Com} \tag{5}$$

where

The local stress distribution, σ_y^*, ahead of the damage zone in the undamaged ligament of the laminate, as shown in Fig. 4, is described by a modified linear elastic stress

$$vol_A = \frac{t_A}{t_A + t_{Com}}$$
$$vol_{Com} = \frac{t_{Com}}{t_A + t_{Com}} \tag{6}$$

distribution. For the reason of stress continuity, the value of σ_y is modified by $\Delta\sigma_y$ [11],

$$\sigma_y^* = \sigma_y + \Delta\sigma_y \tag{7}$$

where

$$\Delta\sigma_y = \sigma_{coh}(i) - \sigma_y \Big|_{x=a+c_i} \tag{8}$$

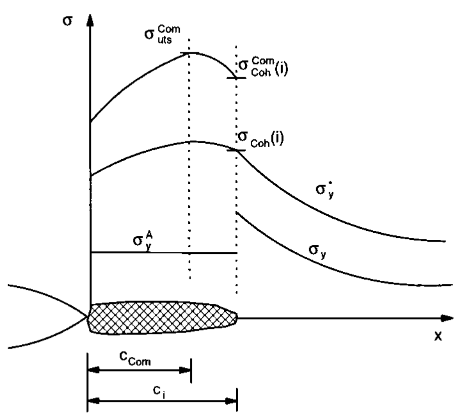

FIG. 4--Stress distribution in metal and composite layers along the net-section plane for a FRML containing a sharp notch.

The applied load is in equilibrium with the resultant axial force acting on the net-section plane of the laminate. The equilibrium condition in the global approach can be expressed as:

$$\sum_{n=1}^{i} F_{(n)}^{coh} + \int_{a+c_i}^{W/2} (\sigma_y + \Delta\sigma_y)\, t\, dx = \sigma_{app}(i)\, \frac{W}{2}\, t \tag{9}$$

The linear elastic stress distribution, σ_y, along the net-section plane (x-axis) for an infinite orthotropic plate containing a sharp notch of length 2a is given by [1, 8],

$$\sigma_y = K_I \frac{x}{\sqrt{\pi a\,(x^2 - a^2)}} \tag{10}$$

The stress intensity factor, K_I, for a plate with a finite width can be described as:

$$K_I = \sigma_{app}\, Y(\frac{a}{W}) \sqrt{\pi a} \tag{11}$$

where Y(a/W) is the finite-width calibration function, neglecting the effect of orthotropy, given by [20],

$$Y(\frac{a}{W}) = \sqrt{\frac{W}{\pi a} \tan(\frac{\pi a}{W})} \tag{12}$$

In addition, the linear elastic stress distribution, σ_y, along the net-section plane (x-axis) for an infinite orthotropic plate containing a circular hole of diameter 2R, is given by [21],

$$\sigma_y = \left\{ 2 + (\frac{R}{x})^2 + 3(\frac{R}{x})^4 - (K_T^{\infty} - 3)\left[5(\frac{R}{x})^6 - 7(\frac{R}{x})^8\right]\right\}\frac{\sigma_{app}}{2} \tag{13}$$

For a symmetric laminate with orthotropic in-plane stiffness, the stress concentration factor can be expressed as [21],

$$K_T^{\infty} = 1 + \sqrt{\frac{2}{A_{11}}\left(\sqrt{A_{11}A_{22}} - A_{12} + \frac{A_{11}A_{22} - A_{12}^2}{2A_{66}}\right)} \tag{14}$$

Artificial Crack Opening

The total crack opening profile can be described by

$$v_{(n)} = v_{\sigma_{coh}(n)} + v_{\sigma_{app}(n)} \tag{15}$$

It is obvious that $v_{\sigma_{coh}(n)}$ is of negative value, indicating crack closure under the cohesive stress. The crack opening profile for metal or composite layers of FRML containing a sharp notch is given by [22],

$$v_{(n)} = \frac{4\sigma_{app}}{E}\sqrt{a_{tot}^2-x^2} + \frac{4\sigma_{coh}^{equ}}{\pi E}\left[a \log\left|\frac{\sqrt{a_{tot}^2-a^2}+\sqrt{a_{tot}^2-x^2}}{\sqrt{a_{tot}^2-a^2}-\sqrt{a_{tot}^2-x^2}}\right| \right. \tag{16}$$

$$\left. -x\log\left|\frac{a\sqrt{a_{tot}^2-x^2}+x\sqrt{a_{tot}^2-a^2}}{a\sqrt{a_{tot}^2-x^2}-x\sqrt{a_{tot}^2-a^2}}\right| -2\sqrt{a_{tot}^2-x^2}\arccos\left(\frac{a}{a_{tot}}\right)\right]$$

where for the metal layers $E = E_A$ and $a_{tot} = a + c_A$; while for the composite layers $E = E_{11}^{Com}$ (for applied load in the longitudinal or fibre direction) or $E = E_{22}^{Com}$ (for applied load in the transverse direction) and $a_{tot} = a + c_{Com}$. σ_{coh}^{equ} is given by $\sigma_{coh}^{equ} = \frac{\Sigma\sigma_{coh}^{A}}{c_A}$ for the metal layer and $\sigma_{coh}^{equ} = \sigma_{uts}^{Com}\frac{\sum_{1}^{i}\left(1-\frac{v_{(n)}}{v_c}\right)}{c_{Com}}$ for the composite layer [22].

For a FRML with a circular hole, if the ratio of the fictitious crack length to the hole radius is less then 1.8, the COD formulations for edge cracks [23] can be used to simulate the crack opening displacement of the fictitious crack [24],

$$v = \frac{4\,\sigma}{E}\sqrt{c^2-x^2}\;D\left(\frac{x}{c}\right) \tag{17}$$

where for the metal layers $E = E_A$ and $c = c_A$; while for the composite layers $E = E_{11}^{Com}$ (for applied load in the longitudinal or fibre direction) or $E = E_{22}^{Com}$ (for applied load in the transverse direction) and $c = c_{Com}$; with

$$D\left(\frac{x}{c}\right) = 1.454 - 0.727\left(\frac{x}{c}\right) + 0.618\left(\frac{x}{c}\right)^2 - 0.224\left(\frac{x}{c}\right)^3 \tag{18}$$

for $v_{\sigma_{coh}(n)}$, $\sigma = \sigma_{coh}^{com}$ for the composite layer and $\sigma = \sigma_{coh}^{A}$ for the metal layer; for $v_{\sigma_{app}(n)}$, $\sigma = \sigma_{app}\,FSC$ for both layers. The Finite Size Correction (FSC) factor for COD calculation of cracks emanating from a circular hole is given by [25],

$$FSC = \frac{0.6865}{(0.2772 + c/R)} + 0.9439 \tag{19}$$

Because the cohesive force depends on the crack opening displacement, an iterative approach has to be applied to solve Eqs. 4-9 and 15. In this case with an initial value of $v_{(n)} = 0.0$

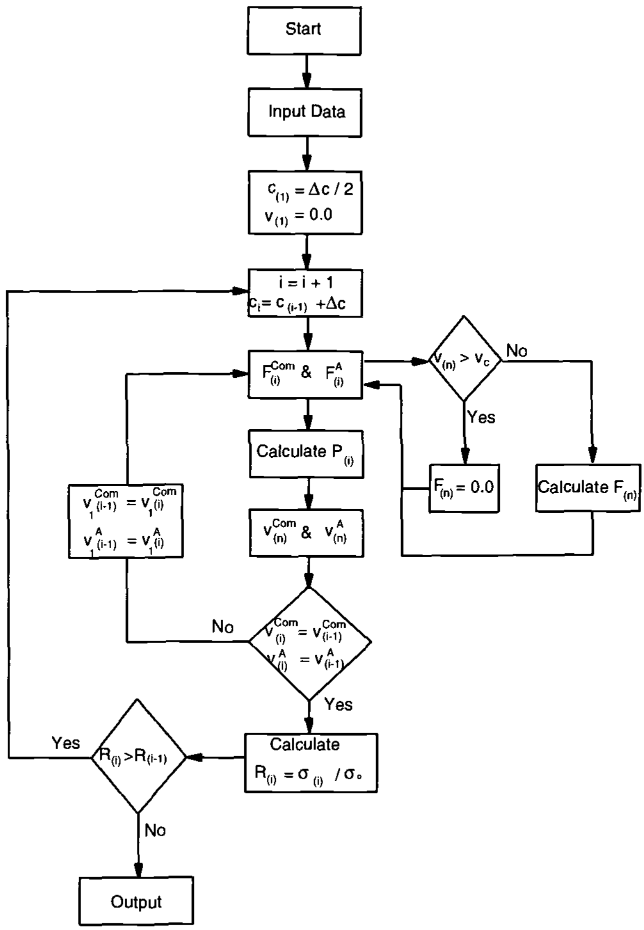

FIG. 5--Flow chart for residual strength evaluation by ECGM.

for both metal and composite layers, $F_{(n)}^{coh}$ is solved from Eq. 4, whereafter $\sigma_{app}(i)$ is obtained from Eq. 9. This procedure is repeated until the convergent value of $v_{(n)}$ is obtained, as shown in the flow chart of Fig. 5. Then a new damage increment (or fictitious crack length) is further introduced. Therefore, a new crack opening profile is produced in each step. Repeating the procedure described above, a relationship between the applied stress $\sigma_{app}(i)$ and steps of the fictitious crack growth is obtained. It should be noted that similar concepts have been applied for residual strength evaluation of polymer matrix composite laminates [15, 16]. Typical results for an ARALL1x laminate [26] with a circular hole (2R = 6.35 mm and W = 50.8 mm) and a CF/Epoxy $[0/\pm45/90]_{4S}$ laminate

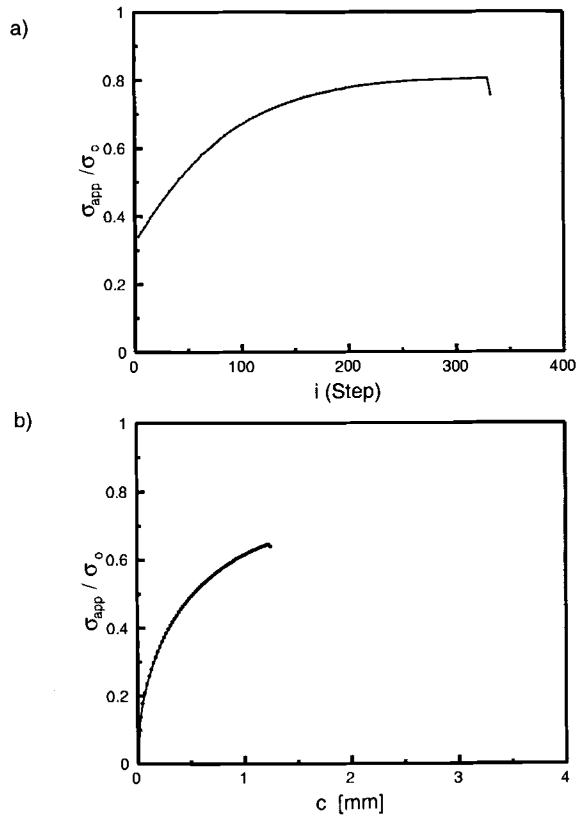

FIG. 6--Normalised applied stress versus fictitious crack length: (a) for ARALL1x laminate with circular hole, and (b) for CF/Epoxy composite laminate with centre crack.

[11] with a centre crack (2a = 6 mm and W = 36.2 mm) are illustrated in Fig. 6a and 6b, respectively. For these examples Δc = 0.01 mm was selected in the simulation. The maximum value of the evaluated applied load is the critical failure load of the notched fibre reinforced composite laminate, and the corresponding fictitious crack length(s) is the critical damage zone length(s) in the metal and composite layer, respectively.

To study the effect of the fictitious crack increment Δc on the convergence of simulations, the residual strengths of various specimens were evaluated with Δc = 0.1 mm and 0.01 mm, respectively. The normalised residual strengths simulated for these two different Δc are illustrated in Fig. 7a and 7b for an ARALL1x [3/2] laminate [26] (2R = 6.35 mm and W = 50.8 mm) and a AS4/948A1 $[0/90]_{4S}$ laminate [15] (2R=10 mm and W = 83.6 mm), respectively. It can be clearly seen that the difference between the simulations is very small when Δc is changed from 0.1 mm to 0.01 mm, and the maximum deviation is only about 1%.

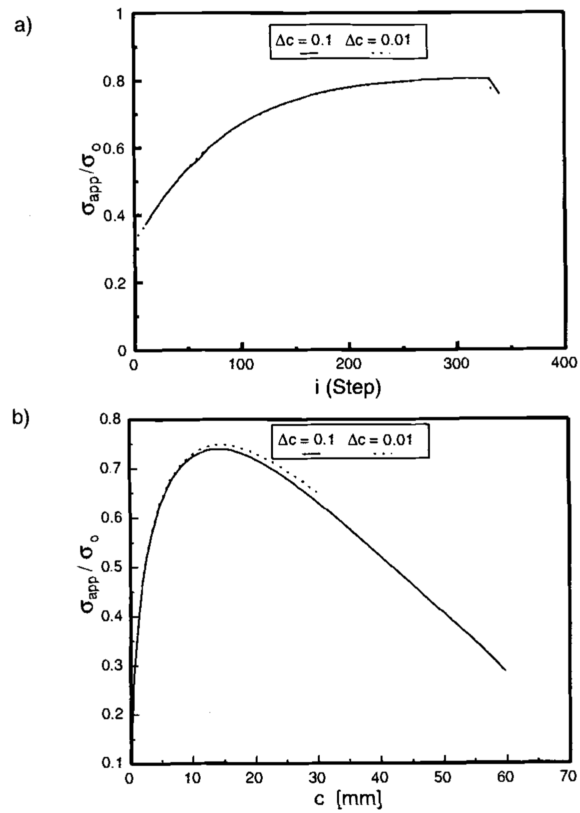

FIG. 7--Effect of Δc on applied load simulation: (a) for ARALL1x laminate with circular hole, and (b) for AS4/948A1 laminate with circular hole.

EVALUATION OF RESIDUAL STRENGTH

The residual strengths of various FRMLs and PMCLs containing a circular hole or a sharp notch are evaluated using the effective crack growth model (ECGM) in this section. The simulations are compared with experimental results in the open literature and predictions from other models, including Point Stress Criterion (PSC) proposed by Whitney and Nuismer [1, 8] and Damage Zone Criterion (DZC) developed by Eriksson and Aronsson [11]. To evaluate the residual strength of notched composite laminates from these two models, "characteristic dimensions" have to be determined, i.e. a characteristic distance d_0 for PSC and a critical damage length d_I^* for DZC. Using one set of experimental data for each laminate, these two parameters were determined. Using the procedure described by Eriksson and Aronsson [11], the apparent fracture energy of each composite laminate was determined to define the relationship between the critical crack opening and the cohesive stress acting on the fictitious crack surfaces. G_c^* represents the sum of all energies dissipated in various fracture mechanisms. Since from the macroscopic point of view the fracture process of composite laminates of one lay-up configuration is different to another, G_c^* is a laminate property. However, it can be dependent on either laminate geometry or notch size to some extent. In practice notched three-point bend specimens can be used to determine the apparent fracture energy [27]. From a parametric study, it was found that the change of G_c^* from 50 to 150 kJ/m^2 for a PMCL has a certain influence, but not remarkable, on the residual strength evaluated by the ECGM, as shown in Fig. 8.

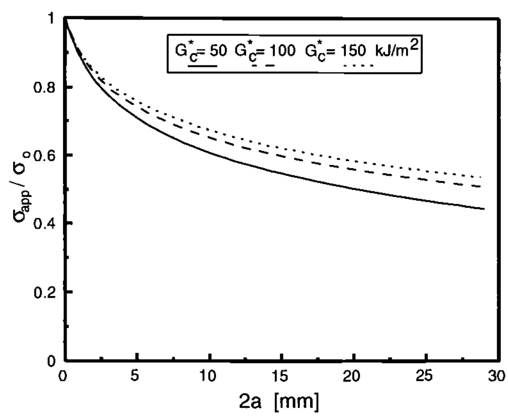

FIG. 8--Effect of apparent fracture energy on residual strength for T300/914C laminate with W = 1000 mm.

Furthermore, the approximate finite width correction (FWC) factor for the stress concentration factor of orthotropic laminates with a circular hole [28] is applied in the evaluations.

$$\frac{K_T^\infty}{K_T} = \frac{3(1 - D/W)}{2 + (1 - D/W)^3} + \frac{1}{2}\left(\frac{D}{W}M\right)^6 (K_T^\infty - 3)\left[1 - \left(\frac{D}{W}M\right)^2\right] \tag{14}$$

where

$$M^2 = \frac{\sqrt{1 - 8\left[\frac{3(1 - D/W)}{2 + (1 - D/W)^3} - 1\right]} - 1}{2\,(D/W)^2} \tag{15}$$

Comparison with Previous Models

The effect of notch size on the residual strength of ARALL1x laminates [26] with various notch/width ratios are shown in Fig. 9. For ARALL1x loaded in the longitudinal direction (Fig. 9a), and the transverse direction (Fig. 9b) with the width of specimens of W = 50.8 mm. The simulations from ECGM are in good agreement with experimental results. Good agreement is also obtained for PSC and DZC because of the curve fitting characteristics. Keeping the same geometry, the residual strength versus the hole size for ARALL3 laminates [29] is illustrated in Fig. 9c for the longitudinal loading and in Fig. 9d for the transverse loading, respectively. Again, it can be seen that simulations from ECGM agree well with experimental data.

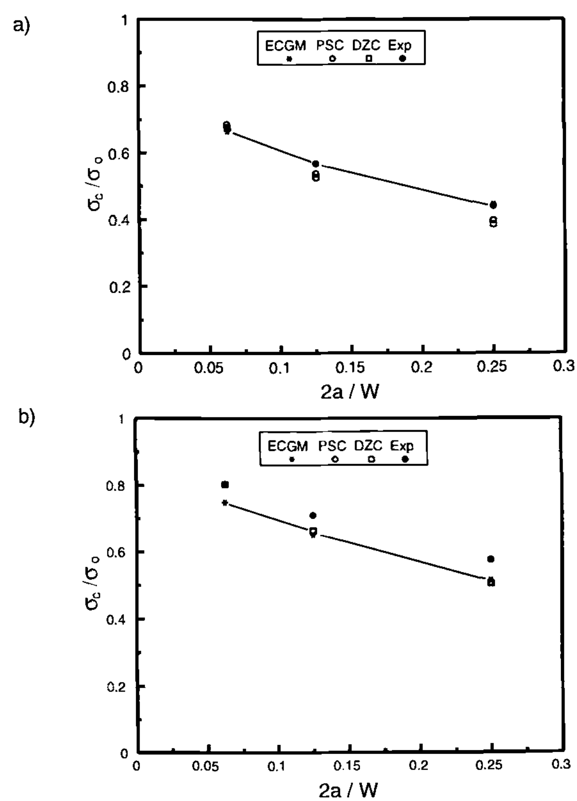

FIG. 9-- Effect of notch/hole size and load direction: (a) ARALL1x with centre crack, loaded in longitudinal direction, (b) ARALL1x with centre crack, loaded in transverse direction.

The effect of the crack length on the residual strength of PMCLs with different notch/width ratios is illustrated in Fig. 10 for T300/914C $[(\pm45/0/90)_3\ /0/90\pm45]_S$

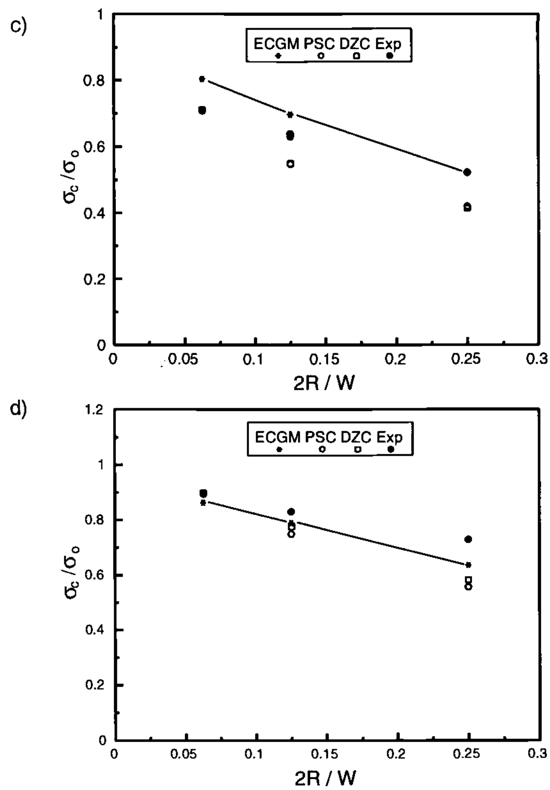

FIG. 9--*Continued:* (c) ARALL3 with circular hole, loaded in longitudinal direction, (d) ARALL3 with circular hole, loaded in transverse direction.

laminates [11] (the notch/width ratio was 0.2 and the crack length varied from 6 to 10 mm, Fig. 10a) and for AS4/948A1 $[0/90]_{4S}$ laminates [15] (the width was 83 mm and the hole diameter varied from 6 to 60 mm, Fig. 10b). The ECGM provides predictions with good accuracy and similar characteristics are observed for evaluations from other approaches.

Stress redistribution

For the reason of equilibrium, stress redistribution occurs with damage growth and increasing applied load. The distribution of stress in the *nth* step of effective crack growth should be clearly very different from that when the damage initiates from the hole edge. This point has been taken into account in evaluating the applied load from the equilibrium

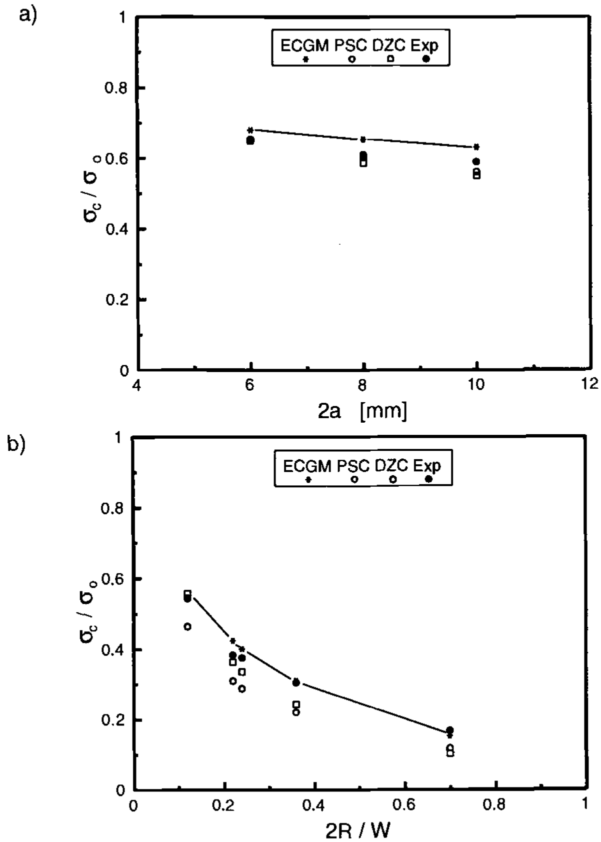

FIG. 10--Effect of notch/hole size on residual strength of PMCLs: (a) T300/914C with centre crack and (b) AS4/948A1 with circular hole.

condition at each step of the effective crack growth. The stress profiles along the fictitious crack (i.e. stress defined by Eq. 5) and the undamaged ligament length are illustrated in Fig. 11 for an ARALL1x laminate [26] (2R = 6.35 mm and W = 50.8 mm) and a T300/N5208 $[0/90]_{4S}$ laminate [8] (W = 25.1 mm, 2a = 2.8 mm). It can be clearly identified that the distribution of σ_y^* varies significantly after certain steps of effective crack growth, i.e. stress relaxation and redistribution occur with damage growth.

Critical Damage Zone Length

As described in the previous section, when the applied load reaches its critical value, the corresponding fictitious crack length can be referred to as the critical damage zone length. In Fig. 12a, the critical damage zone length is plotted versus the crack length for T300/N5208 $[0/90]_{4S}$ laminates [8] with a centre crack. It is of interest to see that the

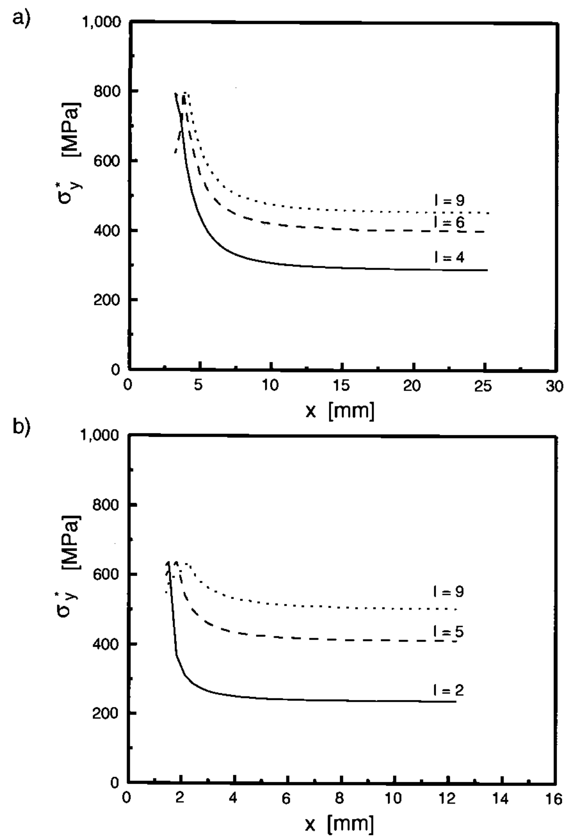

FIG. 11--Redistribution of normal stress σ_y^*, with damage growth: (a) for ARALL1x laminate and (b) for T300/N5208 laminate.

damage zone length evaluated by the ECGM is the same order of magnitude as d_0 and d_l^* [16] . However, it is found that a larger crack length is correlated to a longer critical damage zone length. In Figs. 12b and 12c, the effects of the specimen width and the hole size on the critical damage zone length of the glass/epoxy laminates [8] are illustrated. When the hole diameter is 2 mm, it can be clearly identified that the critical damage zone size increases with the specimen width (Fig. 12b). This is attributed to the fact that the specimen with a larger width has a higher residual strength which induces more significant damage before unstable fracture. In addition, the critical damage zone size enlarges with an increase in the hole radius (Fig. 12c), due to the fact that more serious damage is present in specimens with a large hole, associated with a large field of stress concentration. Based on these results, one can state that the critical damage zone size is not a laminate constant and it is highly dependent on the notch size and the specimen geometry.

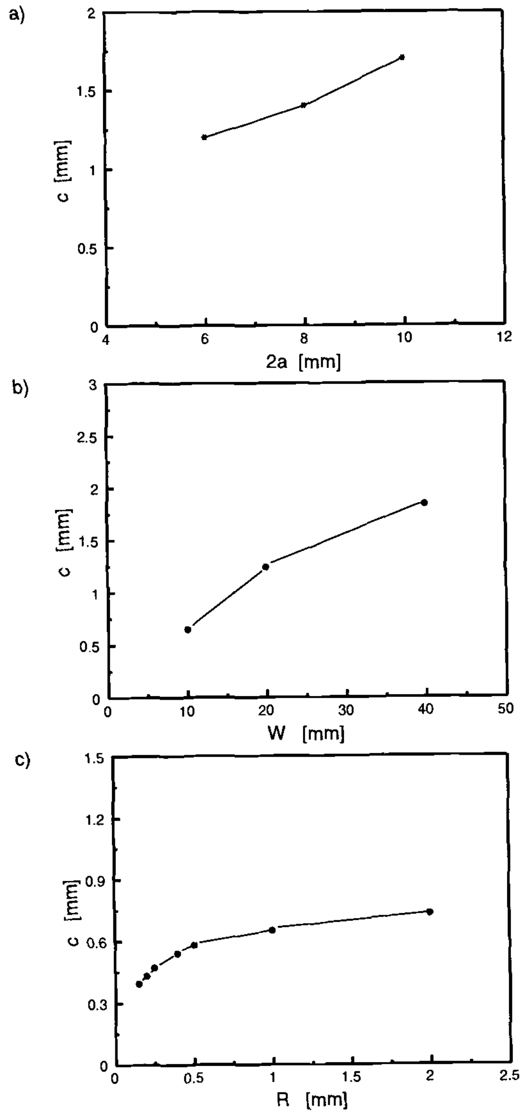

FIG. 12--Effect of notch/hole size on critical damage zone length of PMCLs: (a) for T300/N5208 laminates, (b) for glass/epoxy with 2R = 2 mm, (c) for glass/epoxy with W = 10 mm.

From the simulations, it is found that for fibre reinforced metal laminates with a circular hole, damage normally initiates first in the composite layer. The crack opening displacement at the hole edge (CTOD) versus steps of effective crack growth is shown in Fig. 13a for an ARALL1 laminate [26] with 2R = 3.18 mm and W = 50.8 mm, loaded

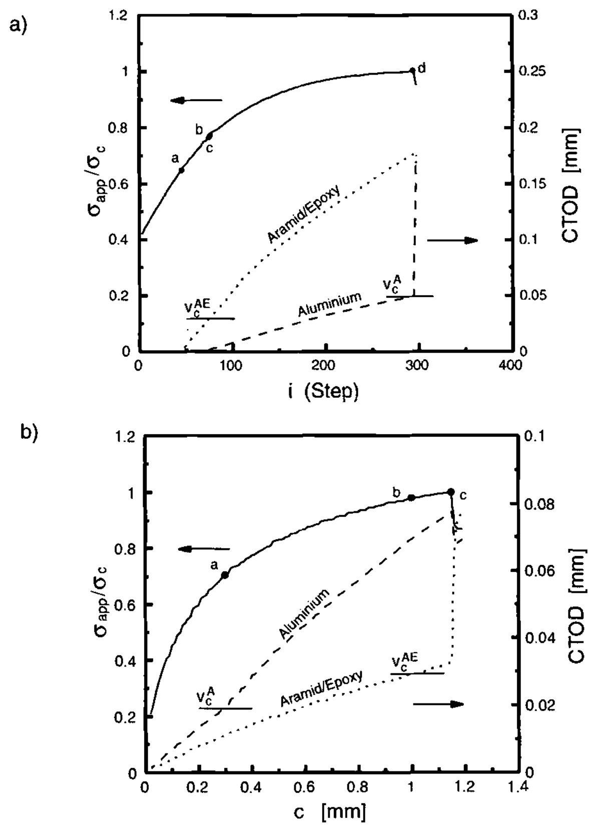

FIG. 13--Effect of notch/hole size on critical damage zone length of FRMLs: (a) for ARALL1 laminate with circular hole, (b) for ARALL1x laminate with centre crack.

in the longitudinal direction. It can be identified that the damage in the composite layer initiates when the applied load reaches about 65% of the ultimate failure stress (symbol a) and the total damage zone length in the composite layer is 2.5 mm at ultimate failure. In particular, CTOD in the composite layer exceeds its critical value at about 76% (symbol b) of the ultimate failure stress, i.e. the transition from the fictitious crack to a real crack occurs, which is an indication of stable crack growth in the composite layer. However, for the aluminium layer, damage (or yielding) occurs at about 75% (symbol c) of the ultimate failure stress, and the transition (symbol d) happens exactly at laminate ultimate failure, which is in agreement with experimental observations for a carbon fibre reinforced metal laminate [17]. Furthermore, it is found that the damage zone size in the composite layer is larger than that in the aluminium layer.

The crack tip opening displacement (CTOD) versus effective crack length for an ARALL1x laminate [26] with 2a = 3.18 mm, W = 50.8 mm, loaded in the longitudinal direction is shown in Fig. 13b. Clearly, CTOD for the aramid/epoxy layer is smaller than that for the aluminium layer. In addition, CTOD in both the aluminium and composite layers exceeds its critical value at 70% (symbol a) and 95% (symbol b) of the ultimate fracture stress, respectively, i.e. the transition from the fictitious crack to real crack occurs before laminate failure, which indicates stable crack growth in both aluminium and composite layers. In this case, the total length of stable crack growth in the aluminium layer is 0.85 mm before ultimate failure.

CONCLUSION

The effective crack growth model (ECGM) has been applied to evaluate the tensile residual strength of fibre reinforced metal or polymer matrix composite laminates with a circular hole or a sharp notch. It was found that the simulations from the ECGM correlated very well with the experimental data in the open literature. Stress redistribution and relaxation were identified with damage growth, which is well correlated with the failure mechanisms of notched composite laminates.

The effect of fictitious crack increment on convergence of the residual strength simulations was investigated. The maximum deviation was only about 0.5-1% when the increment was changed from 0.1 mm to 0.01 mm.

The major differences between the ECGM and the previous residual strength models can be illustrated by two important characteristics, i.e. stress redistribution and damage growth, which were not involved in most of the previous models. From the evaluation of the effective crack growth model, it has been found that for the notched composite laminates, larger notch sizes or wider specimens result in greater damage zone sizes, i.e. the critical damage zone size is not a laminate constant and it is dependent on the notch size and specimen geometry.

From the simulations, it has also been identified that stable crack growth occurs in both aluminium and composite layers for the ARALL laminates with a sharp notch before ultimate fracture. In addition, it has been found that damage occurs in composite layers followed by stable crack growth well before ultimate failure of ARALL laminates containing a circular hole.

REFERENCES

1. Whitney, J. M. and Nuismer, R. J., "Stress Fracture Criteria for Laminated Composites Containing Stress Concentrations," Journal of Composite Materials, Vol. 8, 1974, pp. 253-265.

2. Waddoups, M. E., Eisenmann, J. R., and Kaminski, B. E., "Macroscopic Fracture Mechanics of Advanced Composite Materials," Journal of Composite Materials, Vol. 5, 1971, pp. 446-454.

3. Awerbuch, J. and Madhukar, M. S., "Notched Strength of Composite Laminates: Predictions and Experiments - A Review," Journal of Reinforced Plastics and Composites, Vol. 4, 1985, pp. 3-159.

4. Harel, H., Marom, G., Fischer, S., and Roman, I., "Effect of Reinforcement Geometry on Stress Intensity Factor Calibration in Composites," Composites, Vol. 11, 1980, pp. 69-72.

5. Lagace, P. A., "Notch Sensitivity and Stacking Sequence of Laminated Composites," Composite Materials: Testing and Design (Seventh Conference) STP 893, J. M. Whitney, Ed., American Society for Testing and Materials, 1986, pp. 161-176.

6. Harris, C. E. and Morris, D. H., "Effect of Laminate Thickness and Specimen Configuration on the Fracture of Laminated Composites," Composite Materials: Testing and Design (Seventh Conference), STP 893, J. M. Whitney, Ed., American Society for Testing and Materials, 1986, pp. 177-195.

7. Harries, C. E. and Morries, D. H., "Fracture Behaviour of Thick, Laminated Graphite/Epoxy Composites," NASA Contract Report 3784, National Aeronautics and Space Administration, Washington, DC, 1984.

8. Nuismer, R. J. and Whitney J. M., "Uniaxial Failure of Composite Laminates Containing Stress Concentrations," Fracture Mechanics of Composites, STP 593, G. P. Sendeckyj, Ed., American Society for Testing and Materials, 1975, pp. 117-142.

9. Pipes, R. B., Wetherhold, R. C. and Gillespie, J. W. Jr., "Notched Strength of Composite Materials," Journal of Composite Materials, Vol. 12, 1979, pp. 148-160.

10. Mar, J. W. and Lin, K. Y., "Characterisation of Splitting Process in Graphite/Epoxy Composites," Journal of Composite Materials, Vol. 13., 1979, pp.278-287.

11. Eriksson I. and Aronsson, C. G., "Strength of Tensile Loaded Graphite/Epoxy Laminates Containing Cracks, Open and Filled Holes," Journal of Composite Materials, Vol. 24, 1990, pp. 456-482.

12. Rijn, van J. C. F. N., "The Use of Composite Fracture Models to Describe the Blunt Notch Behaviour of Metal Laminates," NLR Technical Publication, TP 92061L, The Netherlands, 1992.

13. Macheret, Y., Bucci, R. J. and Kulak, M., "Metal Plasticity and Specimen Size Effects in Evaluation of ARALL Laminates Notched Panel Residual Strength," Fracture Behaviour and Design of Materials and Structures - Proceedings of 8th

European Conference on Fracture, Vol. I, 1990, pp. 288-295.

14. Macheret, J. and Bucci, R. J., "A Crack Growth Resistance Curve Approach to Fibre/Metal Laminate Fracture Toughness Evaluation," Engineering Fracture Mechanics, Vol. 45, 1993, pp. 729-739.

15. Afaghi-Khatibi, A., Ye, L. and Mai, Y.-W., "An Effective Crack Growth Model for Residual Strength Evaluation of Composite Laminates with Circular Holes," Journal of Composite Materials, Vol. 30, 1996, pp. 142-163.

16. Afaghi-Khatibi, A., Ye, L. and Mai, Y.-W., "Progressive Damage and Residual Strength of Composite Laminates with a Sharp Notch," Journal of Composite Materials, (in press 1996).

17. Lawcock, G., Ye, L. and Mai, Y.-W., "Progressive Damage and Residual Strength of a Carbon Fibre Reinforced Metal Laminate," submitted to Journal of Composite Materials, 1995.

18. Dugdale D. S., "Yielding of Steel Sheets Containing Slits," Journal of Mechanics & Physics of Solids, Vol. 8, 1960, pp. 100-108.

19. Bäcklund J. and Aronsson, C. G., "Tensile Fracture of Laminates with Holes," Journal of Composite Materials, Vol. 20, 1986, pp. 259-286.

20. Irwin, G. R., "Fracture," Handbuch der Phsik. Vol. 6, Springer, 1958, pp. 551-590.

21. Konish, H. J. and Whitney, J. M., "Approximate Stresses in an Orthotropic Plate Containing a Circular Hole," Journal of Composite Materials, Vol 9, 1975, pp.157-166.

22. Afaghi-Khatibi, A., Ye, L. and Mai Y.-W., "Evaluation of Effective Crack Growth and Residual Strength of Fibre Reinforced Metal Laminates with a Sharp Notch," submitted to Composite Science and Technology, 1995.

23. Tada, H., Paris, P. C. and Irwin, G., "The Stress Analysis of Crack Handbook," 2nd Edition, Paris Production Incorporated (and Del Research Corporation), St. Louis, Missouri, 1985, p. 8.1a.

24. Boström, L. A., "The Dugdale Model Used for Short Radial Cracks Emanating From a Circular Hole in an Infinite Sheet," Engineering Fracture Mechanics, Vol. 34, 1989, pp. 823-829.

25. Grandt Jr. A. F., "Stress Intensity Factors for some Through-Cracked Fastener Holes," International Journal of Fracture, Vol. 11, 1975, pp. 283-294.

26. Hidde, J. S. and Harakovich C. T., "Notch Sensitivity of ARALL Laminates," Proceedings of the 7th International Conference on Composite Materials, China, 1989, pp. 435-440.

27. Aronsson, C.-G. and Bäcklund, J., "Damage Mechanics Analysis of Matrix Effects in Notched Laminates," Composite Materials: Fatigue and Fracture STP 907, H. T. Hahn, Ed., American Society for Testing and Materials, 1986, pp. 134-157.

28. Tan, S. C. "Finite-Width Correction Factors for Anisotropic Plate Containing a Circular Opening," Journal of Composite Materials, Vol. 22, 1988, pp. 1080-1097.

29. Prasad, K. S., Gürdal, Z. and Herakovich C. T., "An Experimental and Numerical Study of Notch Sensitivity of ARALL Laminates with Holes," Proceedings of the 4th Japan-US Conference on Composite Materials, Washington, DC, 1989, pp. 179-188.

Walter G. Reuter,[1] Norman C. Elfer,[2] D. Allan Hull,[3] James C. Newman, Jr.,[4] Dietrich Munz,[5] and Tina L. Panontin[6]

FRACTURE TOUGHNESS RESULTS AND PRELIMINARY ANALYSIS FOR INTERNATIONAL COOPERATIVE TEST PROGRAM ON SPECIMENS CONTAINING SURFACE CRACKS

REFERENCE: Reuter, W. G., Elfer, N., Hull, D. A., Newman, J. C., Jr., Munz, D., and Panontin, T. L., **"Test Results and Preliminary Analysis for International Cooperative Test Program on Specimens Containing Surface Cracks,"** *Fatigue and Fracture Mechanics: 28th Volume, ASTM STP 1321,* J. H. Underwood, B. D. Macdonald, and M. R. Mitchell, Eds., American Society for Testing and Materials, 1997.

ABSTRACT: Specimens containing surface cracks were tested in either tension or bending to compare the stress intensity factor at failure with plane strain fracture toughness (K_{Ic}) in an International Cooperative Test Program. The material was heat treated to σ_{ys} = 1 587 MPa and K_{Ic} = 54 MPa$\sqrt{}$m$^{1/2}$. Because substantial stable crack growth occurred for some specimens, the test plan was modified to include detecting the onset of crack growth. It is shown that P_{max} and the original fatigue precrack size cannot be employed to calculate K_{max} for comparison with K_{Ic} when significant stable crack growth occurs. However, using P_{init} (load at which stable crack growth is initiated) and the original fatigue precrack size to calculate K_{max} or $K_{\phi=30°}$ provides a very useful comparison with K_{Ic}. The influence of variations in fatigue precrack configuration on test results are also discussed.

---

[1]Consulting Engineer, Idaho National Engineering Laboratory, Lockheed Martin Idaho Technologies Company, P.O. Box 1625, Idaho Falls, ID 83415-2218.

[2]Senior staff engineer, Lockheed Martin Corporation, Manned Space System, New Orleans, LA.

[3]Engineer, Engineering Material Research, Downsview, Ontario, Canada.

[4]Senior scientist, NASA Langley Research Center, Hampton, VA 23681-0001.

[5]Professor, University of Karlsruhe, Karlsruhe, Federal Republic of Germany.

[6]Group leader, NASA Ames Research Center, Moffet Field, CA 94035-1000.

KEYWORDS: surface cracks, tensile or bending loads, crack growth initiation, K_{Ic}

INTRODUCTION

One of the major uses of fracture mechanics is to predict the fitness for service of structural components containing known or assumed natural defects. These natural defects are primarily surface cracks that form during fabrication of a component or as a result of exposure to operating conditions (such as stress-corrosion cracking and fatigue); they also may be embedded flaws that formed during fabrication (welding). In developing models to assess fitness for service, it is necessary to compare predictions of failure with test results. The cost of fabricating structural components for testing is usually excessive; therefore, an alternative approach based on testing specimens containing surface cracks is needed.

For materials and test conditions that satisfy linear elastic fracture mechanics (LEFM) requirements, as defined in ASTM E399 [1], the anticipated approach is to use plane strain fracture toughness (K_{Ic}) and applicable equations to predict fracture for the loading conditions and the defect configurations of interest. However, verifying the adequacy of equations available for calculating the applied stress intensity factor (K) as a function of defect size, loading condition (tensile and/or bending), and position (θ) or (ϕ) (see Fig. 1) around the perimeter of the surface-crack front is a major problem. Initially, it was assumed that failure occurs when $K_{max} = K_{Ic}$; the maximum value of applied stress intensity factor (K_{max}) occurs at either the free surface or at the maximum crack depth.

The ability of the Newman-Raju equations [2], in conjunction with K_{Ic}, to predict fracture of surface-cracked specimens has been investigated [3],[4],[5]. For tests on a high-strength β-titanium alloy and a monolithic ceramic, failure was synonymous with catastrophic fracture, which occurred very soon after crack growth initiation was detected by acoustic emission. It was observed that the ratio K_{max}/K_{Ic} ranged from 1.0 to 1.4 for specimens loaded in tension and from 1.0 to 2.0 for the metal specimens loaded in bending. These results were discussed in ASTM Task Group E24.01.03 (now E08.07.03) in an attempt to use them to modify ASTM E740 [6]. Because these data [3],[4],[5] were developed at a single laboratory, the task group suggested that a larger test program be conducted that included a different material and more investigators.

An International Cooperative Test Program was established to develop data for modifying ASTM E740 to include bending stresses and specimen configuration effects (thickness

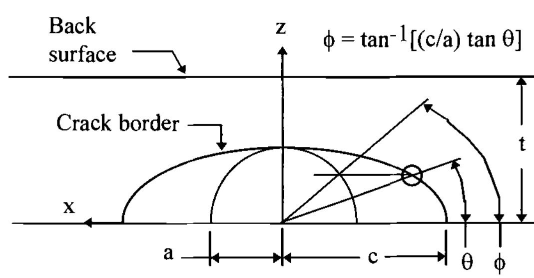

FIG. 1--Schematic of the surface crack.

and remaining ligament relative to plastic zone size, crack depth relative to 2.5 $(K/\sigma_{ys})^2$, 2c relative to W, etc.). Specimen configuration effects must be quantified for cases where predictions based on K_{Ic} are specimen dependent. This information will be used in techniques for employing surface-crack specimen test data to predict fracture of a structural component. The information will also provide limits of applicability for predicting structural behavior based on K_{Ic}.

A call for participants in the International Cooperative Test Program was sent to the membership of ASTM E24 in January 1991. Help was solicited in machining of test specimens, precracking, and/or testing of specimens containing surface cracks. The test material (D6-aC) was supplied by Morton Thiokol, Inc., in the form of a segment from a rocket motor case; material specifications are listed in Table 1. The authors of this paper, representing six laboratories, agreed to collaborate in the testing.

The test matrix selected was to determine if failure is a function of

- maximum K_I (K_{max})
- K_I at ϕ = 30° (from free surface) (K_{30}) or
- K_{ave} (integrated average based on ϕ).

Participants were urged to investigate other possible failure conditions. To quantify anisotropy effects, E399 procedures were used to measure K_{Ic} as a function of crack tip location and orientation.

This paper describes the results of the International Cooperative Test Program and provides some discussion of the relevance of the data.

TEST PROGRAM

The D6-aC steel motor case was cut into segments, annealed to R_c 28-32, and sent to the participants for fabricating surface-cracked and single-edge-notch bend (SEB) specimens. The protocol for the test program requested that the specimens conform to the dimensions in Table 2 with a gauge length ≥2W. It was requested that each participant measure K_{Ic} per E399 using four replicate specimens in each of the L-S and L-T orientations, with the motor case curvature being the long transverse direction. (Specimens containing surface cracks were oriented in the LS/LT directions depending on whether crack growth occurred in the "a" or "2c" direction.) A schematic of the plate was supplied to each participant, indicating the orientation and possible locations of surface-cracked specimens, fracture toughness specimens, and tensile specimens. The curved piece was not to be straightened. It was possible to use

TABLE 1--Specifications for D6-aC steel received from Thiokol Corporation.[a]

Republic heat number: 864 1373
Ingot number: 382 5634
Vacuum arc remelted
Ladish forging number: DUU 128
Thiokol part number: IU50717-02 S/N 035
Renumbered to: 7U52821-01
Chemistry: 0.460C, 0.80Mn, 0.010P, 0.001S, 0.23Si, 0.12Cu, 0.47Ni, 1.07Cr, 0.99Mo, 0.10V, balance Fe.

a. D. W. Sutherland

TABLE 2--Test matrix for 6.35 mm thick surface cracked specimens.

Specimen and crack dimensions (mm)						Number of Specimens per Participant	
W	a	2c	a/2c	a/t	Loading		
50.0	1.57	3.3	0.5	0.25	Tension	1	
50.8	1.57	3.3	0.5	0.25	Bending	1	if material available
50.8	1.57	15.8	0.1	0.25	Tension	1	
50.8	1.57	15.8	0.1	0.25	Bending	1	
50.8	2.84	5.8	0.5	0.45	Tension	1	
50.8	2.84	5.8	0.5	0.45	Bending	1	
50.8	2.84	28.4	0.1	0.45	Tension	1	
50.8	2.84	28.4	0.1	0.45	Bending	1	
50.8	4.11	8.4	0.5	0.65	Tension	1	
50.8	4.11	8.4	0.5	0.65	Bending	1	
50.8	4.11	20.6	0.2	0.65	Tension	1	
50.8	4.11	20.6	0.2	0.65	Bending	1	
101.6	4.11	41.1	0.1	0.65	Tension	1	
101.6	4.11	41.1	0.1	0.65	Bending	1	
50.8	5.38	10.7	0.5	0.85	Tension	1	
50.8	5.38	10.7	0.5	0.85	Bending	1	
50.8	5.38	26.9	0.2	0.85	Tension	1	
50.8	5.38	26.9	0.2	0.85	Bending	1	
101.6	5.38	53.8	0.1	0.85	Tension	1	
101.6	5.38	53.8	0.1	0.85	Bending	1	

machine flat, 102 mm wide, specimens with a minimum thickness of 10.6 mm for the grip section.

All the specimens were sent to Engineering Materials Laboratory in Santa Fe Springs, California, USA, for heat treating and then returned to the participants for fatigue precracking and testing. To identify a suitable thermal cycle for heat treating this steel, various thermal cycles were performed on fracture toughness specimens that were then tested to measure K_{Ic}. Based on these results, the heat treatment selected was to austenitize at 900°C for 30 min, oil quench, and temper at 204°C for 2 h plus 2 h (Batch 1 in Tables 3 and 4). It was recommended that 0.13 to 0.25 mm be removed from each specimen surface after heat treatment. It was intended that all of the remaining specimens be heat treated in a single batch, but it was necessary to perform the heat treatment in two batches (Batches 2 and 3 in Tables 3 and 4).

TABLE 3--Tensile properties for specified heat treat cycle measured at Engineering Materials Laboratory

	Yield Strength[a] (MPa)	Ultimate Tensile Strength[a] (MPa)	Elongation (%)	Reduction in Area (%)
		Batch No. 1		
	1 560	1 600[b]	1[b]	21[b]
	1 570	1 900	8	20
	1 550	1 880	9	19
Average	1 560	1 890	8	20
		Batch No. 2[c]		
	1 700	2 160	15	40
	1 680	2 220	14	28
	1 740	2 150	12	38
Average	1 700	2 180	14	35
		Batch No. 3[d]		
	1 560	2 060	12	36
	1 530	1 960	11	38
Average	1 540	2 010	12	37

Note: All specimens were austenitized at 900°C, 30 min; oil quenched; and tempered at 204°C for 2 + 2 h.
a. Rounded to nearest 10 MPa.
b. Not included in average.
c. These specimens were sent to NASA-Langley, Engineering Material Research, NASA-Ames, Martin Marietta, and the University of Karlsruhe.
d. These specimens were sent to an organization that has been unable to complete their testing and to the INEL.

Fatigue precracking was to be performed per E399, with the fatigue starter notch contained within a 30° included angle from the crack tip. The test protocol noted that if a triangular electric discharge machined (EDM) notch is used, the fatigue precrack generally grows beyond the starter notch. When an elliptical starter notch is used, the fatigue precrack often does not grow much beyond the starter notch. It was suggested that the participants use a triangular EDM starter notch, but other configurations and procedures were acceptable.

Testing was to be performed at room temperature by loading monotonically to failure using a load rate consistent with ASTM E399. If a COD gauge was used, it was necessary to describe how and where it was attached to the specimen, and explain why the attachment did not influence the results. For the bend tests, 4-point loading with a span(s) $\geq$W, preferably S = 2W, was requested. For tensile testing, two specimen configurations were provided as guidelines.

TABLE 4--Fracture Toughness[a]

		Fracture Toughness, K_{Ic} (MPa·m$^{1/2}$)	
Heat Treat Batch No. 1			
Specimens were 10.0 (B) x 10.0 mm (W)		LT Orientation	LS Orientation
		60.9	61.6
		59.7	62.3
		60.4	63.0
		62.4	62.0
	Average	60.8	62.2
Heat Treat Batch No. 2[b]			
Specimens were 10.0 (B) x 10.0 mm (W)			LS Orientation
			55.7
			54.6
			54.0
			56.8
		Average	55.3
TL specimens were 11.5 x 12.5 mm and TS specimens 6.4 x 11.8 mm		TL Orientation	TS Orientation
	NASA-Ames	62.9	53.0
		59.2	56.8
		57.6	52.2
	Average	59.9	54
LT specimens were 6.4 x 11.84 mm and LS specimens 11.46 x 25.5 mm		LT Orientation	LS Orientation
	Engineering Material Research	51.3	46.2
		47.9	49.6
		50.1	49.3
		49.6	48.2
		50.7	48.6
	Average	49.9	48.4
Heat Treat Batch No. 3[c]			
		LT Orientation	LS Orientation
LT specimens were 12.7 x 12.1 mm		60.5	—
		59.8	—
	Average	60.2	—
LT, LS specimens were 12.7 x 12.1 mm;	INEL	54.5	51.8
		56.5	56.8
	Average	55.5	54.3

TABLE 4--Fracture Toughness[a]

LT and LS specimens were 6.4 x 12.1 mm	46.1	50.1
	51.9	56.3
Average	49.0	53.2

a. Except where specifically noted, tests performed by the Engineering Materials Laboratory.
b. These specimens were sent to NASA-Langley, Engineering Material Research, NASA-Ames, Martin Marietta, and the University of Karlsruhe.
c. These specimens were sent to an organization that has been unable to complete their testing and to the INEL.

The test records required were

- For fatigue precracking, starter notch configuration and size (including width), load sequence and corresponding number of cycles, and the included angle from crack tip to fatigue crack starter notch measured at θ = 0, 45, 90, 135, and 180°.
- For testing, specimen and precrack geometry, load, test temperature, load versus cross head displacement, load versus CMOD gauge, and a nominally 200 x 250 mm photograph of the fracture surface showing complete surface crack configuration and size plus thickness of specimens. (Photographs were to include a scale.) It was requested that other measurements such as load versus acoustic emission, electric potential, etc., be used to verify that little or no subcritical crack growth occurred.

RESULTS

Tensile Tests

Test results from specimens in each heat treatment batch are provided in Table 3. Some variation in the tensile properties is evident. The tensile and yield strength values for Batches No. 1 and No. 3 were in reasonable agreement, and those for Batches No. 2 and No. 3 were within ±10% of the mean.

SEB Tests

Fracture toughness (K_{Ic}) measurements are provided in Table 4 as a function of heat treatment batch number, orientation, and participant. Based on these results, it is apparent that K_{Ic} varied somewhat from batch to batch. For Batch No. 1, K_{Ic} averaged 60.8 MPa·m$^{1/2}$ for the LT orientation and slightly higher, 62.2 MPa·m$^{1/2}$, for the LS orientation. Batch No. 3's K_{Ic} values determined by the Engineering Materials Laboratory were the same as for Batch No. 1, but the INEL test values and Batch No. 2 values ranged from 10 to 20% lower than Batch No. 1 values. The test results were used to determine a nominal K_{Ic} of 53 MPa·m$^{1/2}$ for both Batch No. 2 and Batch No. 3.

The value of K_{Ic} chosen for Batch No. 2 was based primarily on the average of the five test averages, even though two of these were from a different orientation. The average value of K_{Ic}, 53.5 MPa·m$^{1/2}$, was reduced to 53 MPa·m$^{1/2}$ because of the lower values measured with the smallest specimen sizes, which are closer to the thickness of the specimens containing surface cracks.[1]

The value of K_{Ic} = 53 MPa·m$^{1/2}$ for Batch No. 3 was based primarily on the average (53.0 MPa·m$^{1/2}$) of the four INEL test averages. (A more extensive series of tests was conducted at the INEL where K_{Ic} was measured to be 54 MPa·m$^{1/2}$, in very close agreement to the above estimates.)

Surface Cracks

Test data from four participants are summarized in Tables 5 and 6. Each of these participants observed that considerable subcritical crack growth occurred in many specimens (a photograph of the fracture surface of a typical specimen is shown in Fig. 2). Thus, the calculated results of K_{max} in Tables 5 and 6, which are based on the initial flaw size and the maximum load, have no relevance to K_{Ic} and depend on specimen geometry and system compliance. (Note the large values of K_{max}/K_{Ic}.) Therefore, the test plan was modified to identify the load and location around the perimeter of the fatigue precrack associated with initiation of subcritical crack growth. This revised procedure was followed by two of the participants. Acoustic emission and d.c. potential drop techniques were used to detect the onset of subcritical crack growth. A nominal 5% change in d.c. potential drop was associated with initiation of crack growth. The intent was not to detect the initiation event, but rather to allow sufficient subcritical crack growth to occur so that subsequent fatigue cycling would show the extent and location of subcritical crack growth (see Fig. 3).

The loads associated with a 5% change in d.c. potential drop are provided in Tables 7 and 8. The Newman-Raju equations [2] were used to calculate K_{max} at the loads associated with crack growth initiation. Crack growth initiation took place somewhat before the loads in Tables 7 and 8 were reached, as indicated in Fig. 3.

DISCUSSION

Fig. 4 presents plots of the ratio K_{max}/K_{Ic} for specimens loaded in tension or in bending versus cF^2. The parameter cF^2, a term used to quantify the severity of the

---

[1]For Batch No. 2, there are test results where K_{Ic} = 59.9 and 49.9 MPa·m$^{1/2}$ for the TL orientation and K_{Ic} = 54.0 and 48.4 MPa·m$^{1/2}$ for the TS orientation. As these average K_{Ic} measurements are primarily for comparison with surface-cracked specimen test results obtained at NASA-Ames, the K_{Ic} values measured at NASA-Ames were given greater emphasis. These two sets of K_{Ic} results are in general agreement with the LS measured values; therefore, K_{Ic} = 53 MPa·m$^{1/2}$.

TABLE 5--Data from SC(B) specimens

Specimen ID	W[a] (mm)	t (mm)	a (mm)	2c (mm)	a/2c	a/t	σ_{max}[b] (MPa)	K_{max}[c] (MPa√m)	K_{max}/K_{Ic}
				Engineering Material Research					
SB-1	51.0	6.43	1.66	3.66	0.45	0.26	1 806	82.6	1.56
SB-2	50.8	6.29	3.31	30.32	0.11	0.53	864	61.0	1.15
SB-3	50.8	6.29	3.78	9.15	0.41	0.60	1 211	76.8	1.45
SB-4	50.9	6.26	6.26	12.64	0.50	1.00	1 742	Thru crack	—
SB-5	50.8	6.34	3.58	16.25	0.22	0.56	1 103	79.3	1.50
SB-6	51.0	6.42	4.04	25.76	0.16	0.63	712	84.3	1.59
SB-7[d]	50.8	6.41	4.66	37.28	0.12	0.73	860	73.9	1.39
SB-8	51.0	6.35	4.96	36.14	0.14	0.78	645	77.6	1.46
SB-9[e]	50.9	6.43	5.13	40.0	0.13	0.80	575	75.0	2.42
WB-1	102.0	6.38	5.03	42.8	0.12	0.79	1 688	148	2.79
WB-2[e]	102.0	6.42	5.26	61.8	0.08	0.82	1 252	129	2.43
				Martin-Marietta					
1A1-02	50.9	6.38	1.57	3.43	0.46	0.25	2 010	75.3	1.42
1A1-04	50.9	6.40	2.87	21.49	0.13	0.45	1 150	72.9	1.38
1A1-06A	50.9	6.30	3.00	5.87	0.51	0.48	1 944	96.3	1.82
1A1-08	50.9	6.38	3.96	28.45	0.14	0.62	953	85.6	1.62
1A1-10	50.9	6.38	4.32	8.41	0.51	0.68	1 736	112.4	2.12
1A1-12	50.9	6.38	3.99	20.62	0.19	0.62	1 176	101.0	1.91
1A1-14[f]	101.6	6.40	4.80	41.25	0.12	0.75	1 032	103.7	1.96
1A1-16	50.9	6.40	4.80	10.72	0.45	0.75	1 504	120.6	2.28
1A1-18	50.9	6.38	4.45	27.64	0.16	0.70	867	87.5	1.65
1A1-20	101.6	6.38	5.33	53.34	0.10	0.84	815	98.3	1.85
1A1-22	50.9	10.19	4.70	10.85	0.43	0.46	1 287	104.5	1.97
				University of Karlsruhe					
B-1[e]	51.1	6.35	5.00	29.43	0.17	0.79	879	101.7	1.92
B-5	51.0	6.35	3.09	19.76	0.16	0.49	1 257	86.3	1.63

TABLE 5--Data from SC(B) specimens

Specimen ID	W[a] (mm)	t (mm)	a (mm)	2c (mm)	a/2c	a/t	σ_{max}[b] (MPa)	K_{max}[c] (MPa$\sqrt{m}$)	K_{max}/K_{Ic}
B-12	51.0	6.35	3.54	19.86	0.18	0.56	1 265	98.2	1.85
B-17a[e]	50.0	6.35	1.86	6.39	0.29	0.29	1 578	81.9	1.55
B-18a	50.5	6.35	1.94	5.17	0.37	0.30	1 657	84.2	1.59
B-18b	50.5	6.35	2.86	9.23	0.31	0.45	1 644	103.8	1.96
B-19[e]	50.5	6.35	3.85	9.67	0.40	0.61	1 710	118.1	2.23
B-20[e]	50.5	6.35	5.03	11.92	0.42	0.79	1 533	128.6	2.43
B-21[e]	50.5	6.35	1.89	11.04	0.17	0.30	1 637	84.3	1.59
B-22[e]	102.0	6.35	5.05	54.73	0.09	0.80	772	88.2	1.66
B-23	101.9	6.35	4.55	40.44	0.11	0.72	888	84.4	1.59

a. W = plate width, t = plate thickness, a = maximum crack depth, 2c = crack length at surface.
b. Maximum plate bending stress (far-field, from beam theory) when $\sigma_{max} > \sigma_{ys}$ = 1 587 MPa; the applied stress was limited to 1 587 MPa.
c. Maximum stress intensity around perimeter at maximum stress level.
d. Tunnel developed, crack extended in 2c direction but did not extend to free surface.
e. Fatigue precrack did not extend beyond EDM notch in "a" direction.
f. Fatigue precrack did not extend sufficiently beyond the EDM notch in all directions.

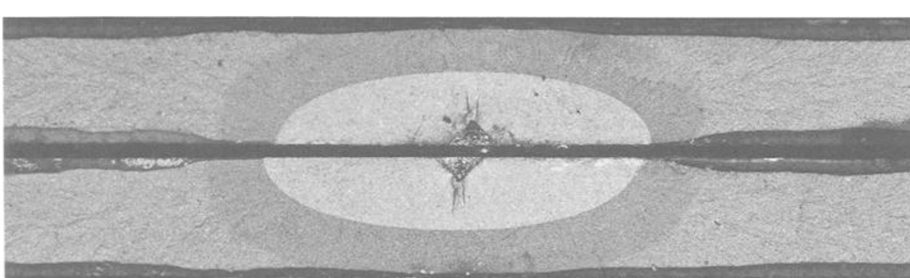

FIG. 2--Example of stable crack growth (shaded area surrounding the shiny precrack). Specimen No. 17.

TABLE 6--Data from SC(T) specimens

Specimen ID	W[a] (mm)	t (mm)	a (mm)	2c (mm)	a/2c	a/t	σ_{max}[b] (MPa)	K_{max}[c] (MPa$\sqrt{m}$)	K_{max}/K_{Ic}
				NASA Langley Research Center					
ST-1	51.3	6.42	2.08	4.62	0.45	0.32	1 077	67.8	1.28
ST-2	51.0	6.35	2.97	14.27	0.21	0.47	634	68.6	1.29
ST-3	51.0	6.40	3.15	6.76	0.47	0.49	835	69.1	1.30
ST-4	51.0	6.32	3.20	28.91	0.11	0.51	350	54.4	1.03
ST-5	51.0	6.38	3.99	9.07	0.44	0.62	648	65.6	1.24
ST-6[d]	51.0	6.38	3.45	22.45	0.15	0.54	485	69.5	1.31
ST-7[e]	51.0	6.40	4.67	10.82	0.43	0.73	614	72.0	1.36
ST-8[d]	51.0	6.43	5.36	29.72	0.18	0.83	420	92.8	1.75
WT-1	101.8	6.27	4.22	45.19	0.09	0.67	295	63.5	1.20
WT-2	101.8	6.40	4.88	60.25	0.08	0.76	251	74.3	1.40
				Martin-Marietta					
1A1-01	50.9	6.30	1.78	2.97	0.60	0.28	1 333	67.4	1.27
1A1-03	50.9	6.35	2.74	15.77	0.17	0.43	757	82.6	1.56
1A1-05	50.9	6.38	3.12	5.84	0.53	0.49	984	75.8	1.43
1A1-06	50.1	6.38	3.30	5.89	0.56	0.52	931	72.4	1.37
1A1-07	50.9	6.38	3.71	28.55	0.13	0.58	401	68.6	1.29
1A1-09	50.9	6.38	4.19	8.05	0.52	0.66	813	80.2	1.51
1A1-11	50.9	6.40	3.99	20.47	0.20	0.62	513	75.1	1.42
1A1-13	101.7	6.38	4.50	41.15	0.11	0.70	359	76.0	1.43
1A1-15[e]	50.8	6.35	4.78	11.68	0.41	0.75	616	75.5	1.43
1A1-17	50.9	6.38	4.45	26.92	0.16	0.70	420	78.0	1.47
1A1-19	101.7	6.40	5.72	54.61	0.10	0.89	261	80.6	1.52
1A1-21	50.9	10.13	4.88	10.72	0.46	0.48	743	77.1	1.45
1A1-T2B[e]	50.9	6.35	5.13	10.69	0.48	0.81	712	89.2	1.68
1A1-T3B	50.9	6.40	4.39	10.62	0.41	0.69	736	82.4	1.55
				University of Karlsruhe					
Z-2	51.0	6.35	1.98	4.16	0.48	0.29	1 000	60.8	1.15
Z-3[f]	51.0	6.35	5.54	24.44	0.23	0.81	430	81.1	1.53
Z-4	51.0	6.35	2.57	6.36	0.40	0.38	877	64.1	1.21
Z-6	51.0	6.35	4.17	8.74	0.48	0.61	642	64.5	1.22
Z-7[f]	51.0	6.35	3.27	22.14	0.15	0.48	578	79.8	1.51
Z-8[e]	51.0	6.35	5.00	10.26	0.49	0.73	671	81.5	1.54
Z-10[f]	51.0	6.35	1.59	10.16	0.16	0.23	865	65.6	1.24
Z-11	51.0	6.35	5.32	19.63	0.27	0.78	486	75.8	1.43
Z-13[f]	102.0	6.35	4.79	33.95	0.14	0.70	341	67.7	1.28

TABLE 6--Data from SC(T) specimens

Specimen ID	W[a] (mm)	t (mm)	a (mm)	2c (mm)	a/2c	a/t	σ_{max}[b] (MPa)	K_{max}[c] (MPa$\surd$m)	K_{max}/K_{Ic}
Z-14[f]	102.0	6.35	4.52	34.20	0.13	0.66	374	71.9	1.36
Z-15[f]	102.0	6.35	5.34	43.25	0.12	0.78	306	75.3	1.42
Z-16[f]	102.0	6.35	5.41	43.42	0.12	0.79	326	81.0	1.53

a. W = plate width, t = plate thickness, a = maximum crack depth, 2c = crack length at surface.
b. Maximum tensile stress (far-field).
c. Maximum stress intensity around perimeter at maximum stress level.
d. Fatigue precrack did not extend beyond the EDM notch in "a" direction.
e. Fatigue precrack did not extend sufficiently beyond EDM notch in all directions.
f. Fatigue precrack did not extend beyond EDM notch in 2c direction.

TABLE 7--Data from W = 50.9 mm wide SC(B) specimens (modified procedure).

Specimen ID	t[a] (mm)	a (mm)	2c (mm)	a/2c	a/t	σ_{max}[b] (MPa)	K_{max}[c] (MPa$\surd$m)	K_{max}/K_{Ic}
			Idaho National Engineering Laboratory					
2[d]	3.25	0.86	1.73	0.50	0.27	1 980	68.0	1.28
4	3.15	1.75	7.82	0.22	0.56	1 381	72.6	1.36
6[d]	3.15	1.32	2.84	0.46	0.42	1 768	74.5	1.41
8	3.15	2.36	20.96	0.11	0.75	1 093	77.1	1.45
8A	3.15	2.11	14.22	0.15	0.67	1 269	77.9	1.47
10[d]	3.15	1.85	4.27	0.43	0.59	1 637	81.8	1.55
12	3.12	2.41	20.82	0.12	0.77	1 093	79.2	1.49
14	3.18	2.29	5.31	0.43	0.72	1 689	93.4	1.76
16	3.23	2.34	26.92	0.09	0.72	1 125	81.0	1.53
18[d]	3.18	1.85	9.86	0.19	0.58	1 263	69.0	1.30
20	3.28	1.96	13.21	0.15	0.60	1 456	82.2	1.55
			NASA-Ames Research Center					
B-1	6.32	1.38	3.48	0.40	0.22	1 378	62.2	1.17
B-2	6.38	3.51	17.60	0.20	0.55	1 044	79.9	1.51
B-3	6.38	3.34	6.88	0.49	0.52	1 278	84.1	1.59
B-4	6.38	3.41	29.3	0.12	0.53	902	68.7	1.30
B-5	6.25	4.61	11.06	8.42	0.74	1 187	95.7	1.81
B-6[e]	6.38	3.63	20.49	0.18	0.57	820	65.1	1.23
B-7[f]	6.50	4.82	11.46	0.42	0.74	1 085	89.4	1.69
B-8	6.38	4.78	36.50	0.13	0.75	488	60.6	1.14

TABLE 7--Data from W = 50.9 mm wide SC(B) specimens (modified procedure).

a. t = plate thickness, a = maximum crack depth, 2c = crack length at surface.
b. Maximum plate bending stress (far-field, from beam theory).
c. Maximum stress intensity around perimeter at maximum stress level.
d. Two planes, a_{max}.
e. Fatigue precrack does not extend to EDM depth in "a" direction.
f. Fatigue precrack barely beyond EDM notch in "2c" direction.

crack size and shape relative to the specimen size, was originally proposed by Newman [7] and later verified by statistical analysis [8]. F is related to the geometry correction term in Newman-Raju equations [2] by

$$F = M \sqrt{\frac{a}{cQ}} \left(\frac{1 - \pi ac}{Wt} \right) .$$

where Q is the shape factor for an elliptical crack, M is a geometry correction factor [2], and F is the combined net section conversion, shape, and magnification factor for the front and back faces. K_{max} was calculated using the original precrack size and the load associated with a 5% change in d.c. potential drop.

For tensile loads (Fig. 4a), K_{max}/K_{Ic} ranged from 0.91 to 1.61, whereas for bending (Fig. 4b) K_{max}/K_{Ic} ranged from 1.14 to 1.81. There is a difference in the relation between K_{max}/K_{Ic} and cF^2 for the two loading modes since for tensile loads K_{max}/K_{Ic} decreased with increasing cF^2. At this time, there is no explanation for the observed behavior but it would be beneficial to perform tensile tests of specimens with $cF^2 \geq 3$ mm to see if K_{max}/K_{Ic} continues to decrease. For bending loads, the ratio K_{max}/K_{Ic} continued to increase with increasing cF^2. The difference in the relation between K_{max}/K_{Ic} and cF^2 for tensile and bend tests suggests that tensile test data could become nonconservative, while bend test data could become overly conservative. Fig. 4 suggests negligible effects from whether K_{max} occurred at the free surface or at maximum crack depth or from irregularities in the fatigue precrack.

Results of 113 tests are presented in Tables 5 through 8. Unfortunately, there were instances of irregular fatigue precracks; the major concerns are:

- Fatigue precrack does not extend sufficiently beyond the EDM notch. This may occur in the "a" or "2c" direction, or in all directions
- Irregularities exist in the fatigue precrack so that the configuration is not elliptical
- Fatigue precracks grow from two different planes of the EDM starter notch.

When K_{max} occurred at maximum crack depth, some test results were influenced by the fatigue precrack not extending beyond the EDM starter notch. Specimen ST-8 (Table 6) had K_{max}/K_{Ic} = 1.75, and the fatigue precracks extended only about 56% in the "a" direction of the EDM notch. Specimen ST-6 had K_{max}/K_{Ic} = 1.31 and a fatigue precrack that extended about 86% in the "a" direction. Fig. 5a shows specimens in which the fatigue precrack did not extend beyond the depth of the EDM notch. The test results show an increase in K_{max} when the fatigue precrack did not extend beyond 56% of the "a" direction of the EDM notch and K_{max} occurred at the maximum crack

TABLE 8--Data from SC(T) specimens (modified procedure).

Specimen ID	W[a] (mm)	t (mm)	a (mm)	2c (mm)	a/2c	a/t	σ_{max}[b] (MPa)	K_{max}[c] (MPa$\sqrt{m}$)	K_{max}/K_{Ic}
				Idaho National Engineering Laboratory					
1	50.86	3.16	1.51	3.56	0.42	0.48	1 484	85.5	1.61
3	50.93	3.15	1.77	7.90	0.22	0.56	777	65.1	1.23
5	50.90	3.18	1.52	3.05	0.50	0.48	1 224	69.0	1.30
7	50.95	3.20	2.09	13.81	0.15	0.65	644	75.0	1.42
9	50.88	3.20	1.90	4.57	0.42	0.59	907	62.4	1.17
11	50.95	3.15	2.16	13.24	0.16	0.68	527	61.5	1.16
13	50.95	3.20	2.76	5.66	0.49	0.86	803	74.3	1.40
17	50.90	3.20	1.94	10.74	0.18	0.61	601	59.9	1.13
19	50.95	3.23	1.78	12.85	0.14	0.55	529	54.3	1.02
21	50.87	3.25	2.49	32.84	0.08	0.77	351	80.4	1.52
23	50.95	3.12	2.35	29.10	0.08	0.75	326	65.4	1.24
24	50.93	3.23	2.48	30.66	0.08	0.77	335	71.9	1.36
25	76.40	6.40	3.87	47.87	0.08	0.60	258	56.6	1.06
26	76.38	6.45	4.58	56.82	0.08	0.71	233	70.8	1.33
27	76.38	6.40	4.67	61.89	0.08	0.73	218	76.9	1.45
28[d,e]	50.98	3.25	2.17	50.98	0.04	0.67	215	80.4	1.52
29[e]	50.88	3.20	1.57	50.88	0.03	0.49	390	78.3	1.47
30[e]	50.93	3.25	1.60	41.29	0.04	0.49	389	63.4	1.19
31	50.97	3.12	1.65	35.81	0.05	0.52	372	59.2	1.12
32[e]	50.90	6.43	3.72	50.90	0.07	0.58	160	48.4	0.91
33[d,e]	50.93	6.43	1.40	46.42	0.01	0.10	658	62.0	1.17
34	50.90	6.40	2.11	40.38	0.05	0.33	469	59.8	1.13
				NASA-Ames Research Center					
T-2	50.95	6.38	2.11	14.22	0.148	0.33	736	68.7	1.30
T-3	50.72	6.48	2.57	5.74	0.448	0.40	1 035	74.6	1.41
T-6	50.90	6.17	5.47	22.02	0.248	0.89	452	78.7	1.48

a. W = plate width, t = plate thickness, a = maximum crack depth, 2c = crack length at surface.
b. Maximum plate tensile stress (far-field).
c. Maximum stress intensity around perimeter at maximum stress level.
d. Crack front is irregular, difficult to identify a_{max}.
e. a_{max} is skewed from center line of specimen.

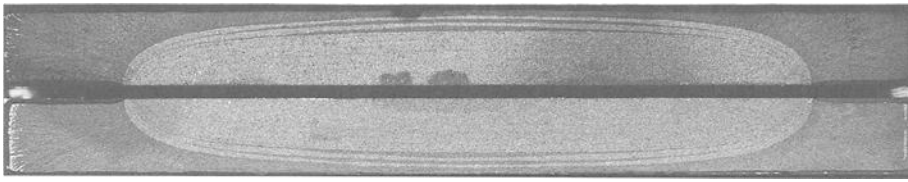

a. Specimen No. 26 showing stable growth (darker) followed by fatiguing (lighter); two sequences and then failure.

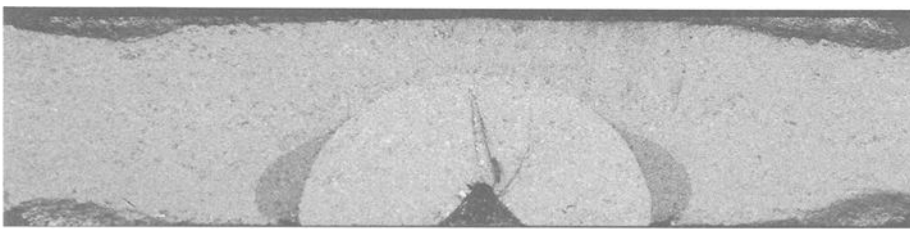

b. Specimen No. 14 tested in bending. The stable crack growth region is the darker coloration bounded on both sides by lighter-colored fatigue precrack.

FIG. 3--Fracture surfaces of two D6-aC surface-cracked specimens.

depth. When the fatigue precrack exceeded 86% of the "a" direction EDM notch, there was no significant effect on K_{max}.

A number of instances were encountered in which the precrack did not extend beyond the EDM notch in the 2c direction (see footnote f in Table 6 and Fig. 5b). The amount of fatigue crack growth at the free surface of the EDM notch ranged from 70 to 96% for these specimens. All of these specimens had K_{max} occurring at a_{max}, and the ratios of K_{max}/K_{Ic} averaged 1.40. For these specimens, the lack of a fatigue precrack extending beyond the EDM notch at the free surface had negligible effect on the measured K_{max} values. Therefore, it appears that the fatigue precrack is not required to exceed 1.27 mm at each of the two EDM corners making up 2c when K_{max} occurs at a_{max}. For the few specimens that had minimal fatigue precrack in all directions around the EDM notch (see footnote e in Table 6), there was a tendency for K_{max}/K_{Ic} to be somewhat higher.

When the crack front at maximum crack depth was irregular and the cracks were skewed relative to the specimen center line, it was difficult to measure K_{max}. Five specimens (footnote e in Table 8; Fig. 6) had fatigue precracks that were irregular and/or were skewed from the center line of the specimen. This complicated the ability to identify the appropriate a_{max}, which was where K_{max} occurred in these specimens. The K_{max}/K_{Ic} values were 1.52, 1.47, 1.19, 0.91, and 1.17 for these specimens. There is no clear-cut relation between these difficulties and K_{max}/K_{Ic}, see the plots of K_{max}/K_{Ic}

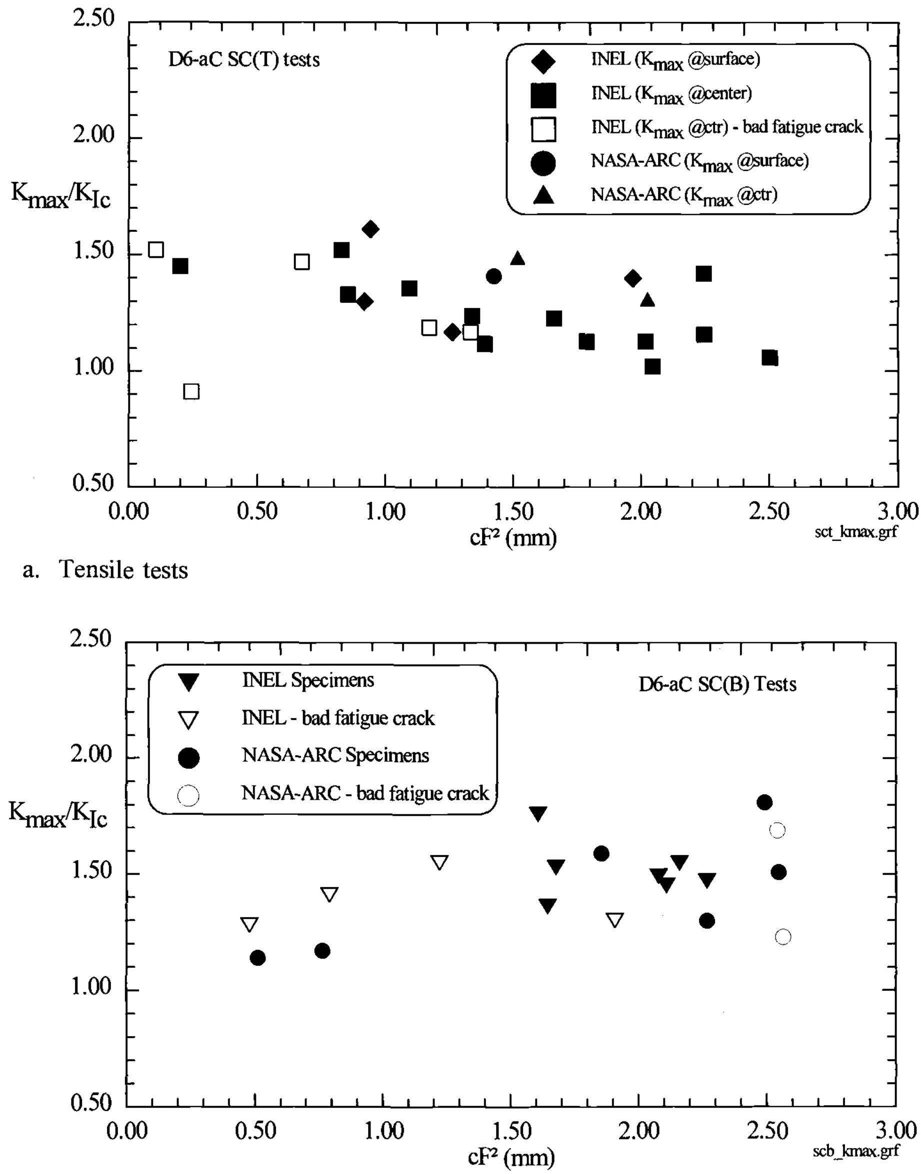

a. Tensile tests

b. Bend tests

FIG. 4--K_{max}/K_{Ic} versus cF^2 for load corresponding to crack growth initiation (d.c. potential drop).

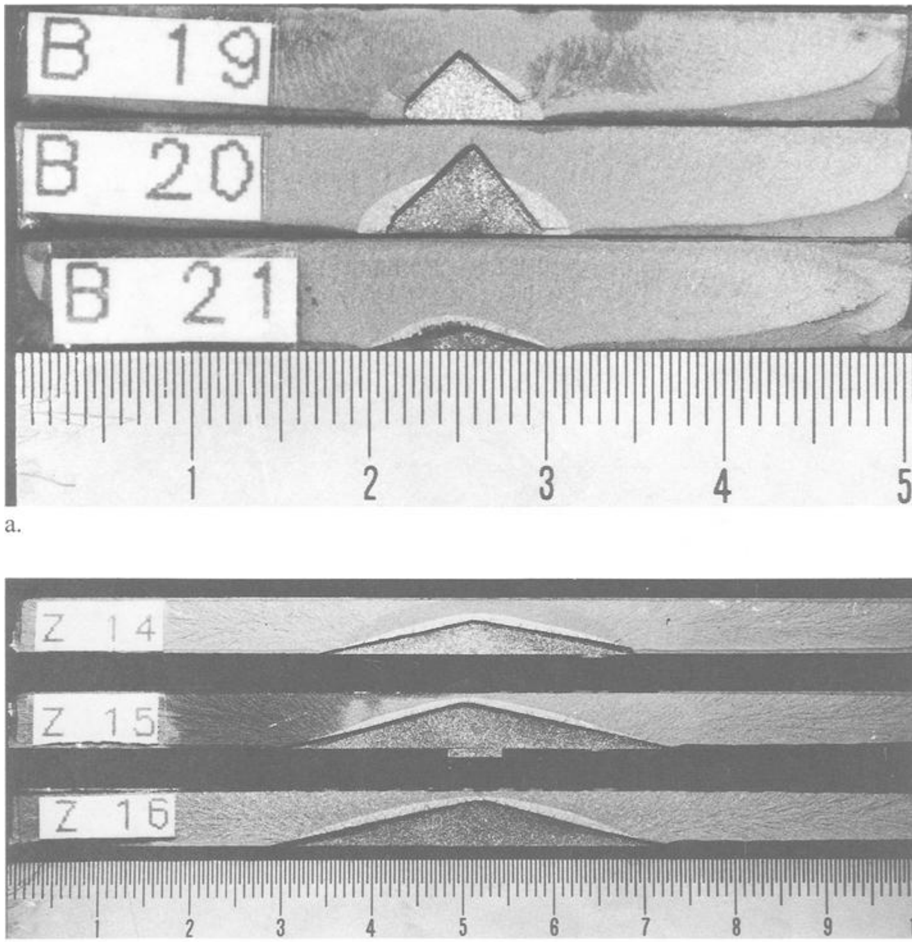

FIG. 5--Specimens in which fatigue precrack did not extend beyond the EDM notch (a) in the "a" direction, and (b) in the 2c direction at free surface.

vs. cF^2 (Fig. 4). Other irregularities in the fatigue precrack had negligible influence on K_{max}/K_{Ic} (see Fig. 4).

An approach based on K calculated for a constant angle of $\phi = 30°$ has been found to provide good correlations with K_{Ic}—$K_{\phi=30°}/K_{Ic}$ is substantially reduced from K_{max}/K_{Ic} (Fig. 4). These calculations were performed on the data in Tables 7 and 8; the results are plotted in Fig. 7. For the tensile results in Fig. 7a, the ratio $K_{\phi=30°}/K_{Ic}$ ranges from nominally 0.69 to 1.46. A comparison between tensile results in Figs. 4a and 7a shows a higher K_{max}/K_{Ic} than $K_{\phi=30°}/K_{Ic}$.

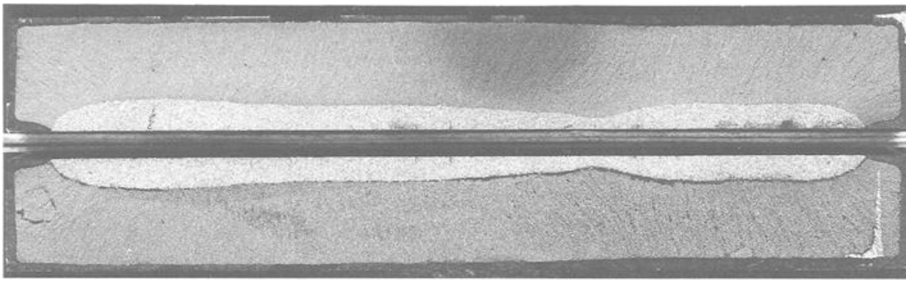

FIG. 6--Fatigue precrack irregularities, such as the considerable variation in crack depth shown here (Specimen 33), caused difficulties.

A comparison between bend test results in Figs. 4b and 7b shows that K_{max}/K_{Ic} is substantially higher than $K_{\phi=30°}/K_{Ic}$, which ranges between 0.83 and 1.39. This strongly suggests that it is not necessary to locate the origin of crack growth initiation and that $K_{\phi\text{-}30°}$ can be used as the critical condition. Fig. 7 shows a reasonably constant $K_{\phi=30°}/K_{Ic}$ value of 1.05, no variation with cF^2, and no influence of fatigue precrack irregularities. This observation appears to be true for both tensile and bending loads. (Work presently underway at INEL shows that crack growth initiation did not occur at ϕ = 30° for specimens loaded in tension.)

For the bend tests, one of the participants provided measurements of the specimen and crack sizes as well as photographs of the fracture surfaces. Measurements were made at the INEL using these photographs, and the calculated values of K_{max} were compared with the measured ones—the photograph-based values ranged from 0.80 to 1.40 times the measured values. A large part of this difference was because some of the photographs were taken at low magnification, the lighting was not uniform, or only one surface of the fracture was provided.

CONCLUSIONS AND RECOMMENDATIONS

Substantial crack growth occurred in many of the specimens fabricated from D6-aC, a high-strength steel. If K_{max} is calculated using the surface-cracked specimen failure load and Newman-Raju equations [2], the results range from 1 to 1.6 times K_{Ic} for tensile loading and from 1 to 2.4 times K_{Ic} for bending loads. These ranges are functions of the crack size, specimen size, and compliance of the test system. The amount of stable crack growth varied with specimen size, crack size and shape, and loading condition. K_{max} calculated from the initial flaw size and maximum load has no relation to K_{Ic} but depends upon specimen geometry and system compliance.

Detecting the load corresponding to initiation of stable crack growth (using d.c. potential drop, acoustic emissions, etc.) simulates the definition of K_{Ic} (related to a 2% change in crack length). Therefore, the use of K_{Ic} plus Newman-Raju solutions will predict a value K_{max} associated with crack growth initiation that is conservative, ranging from K_{max}/K_{Ic} of 0.91 to 1.61 for tensile loads and from 1.17 to 1.81 for bending loads.

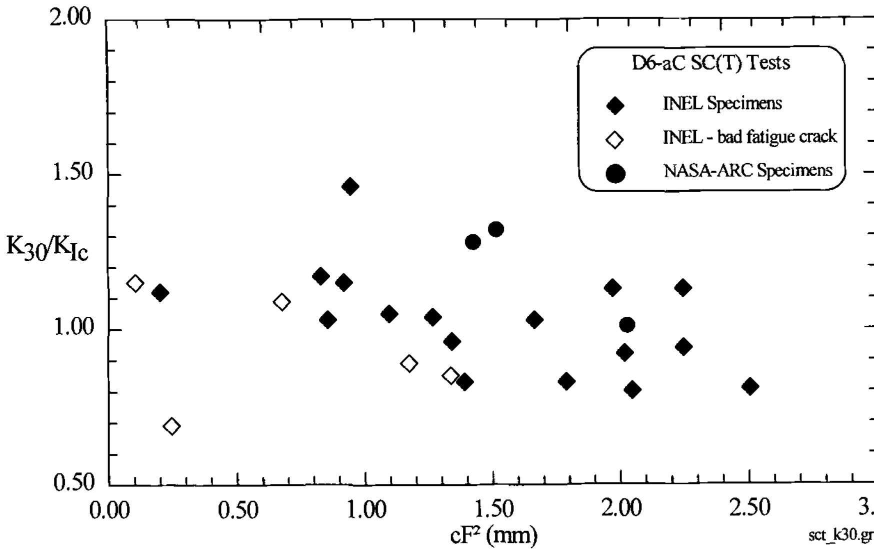

a. Tensile tests

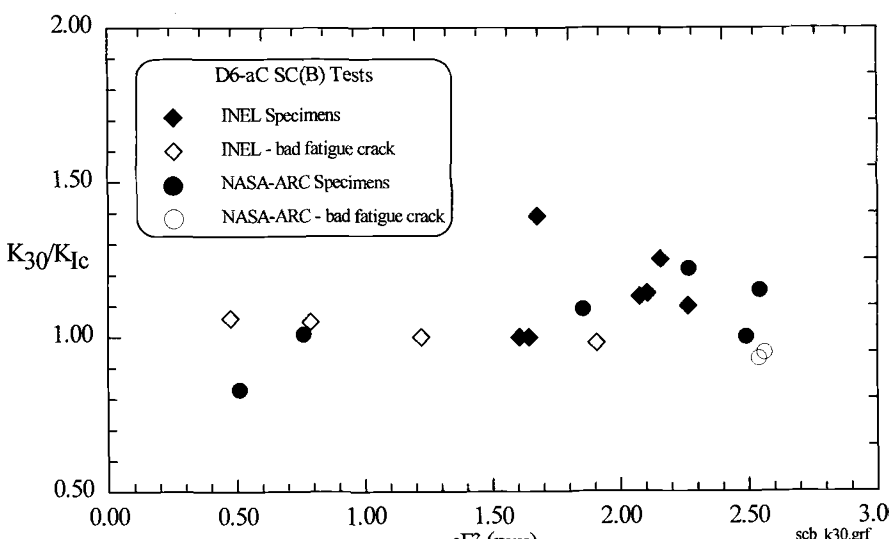

b. Bend tests

FIG. 7--$K_{\phi=30°}/K_{Ic}$ versus cF^2 for load corresponding to crack growth initiation (d.c. potential drop) at ϕ = 30°.

These results show that substantial errors may occur if surface-cracked specimens are used to estimate K_{Ic} and that the magnitude of the error is greater for bending loads.

The use of $K_{\phi=30°}/K_{Ic}$ instead of K_{max}/K_{Ic} yields a nominal average value of 1.05 and tends to eliminate any influence of cF^2. For tensile loading, $K_{\phi=30°}/K_{Ic}$ ranges from 0.69 to 1.46, and for bending loads $K_{\phi=30°}/K_{Ic}$ ranges from 0.83 to 1.39. For practical purposes, it appears that using $K_{\phi=30°}$ will provide very useful predictions of structural/specimen failure when K_{Ic} is used with the Newman-Raju equations [2]. However, additional results at INEL show that crack growth initiation occurs at ϕ = 90° and not at ϕ = 30° for surface-cracked specimens loaded in tension.

A number of difficulties were observed with the fatigue precracks. When K_{max} occurred at maximum crack depth, these test results suggest that K_{max}/K_{Ic} was not adversely influenced when:

- Shallow fatigue precracks exceeded 90% of the EDM notch in the "a" direction.
- The fatigue precrack did not extend beyond the EDM notch in the 2c direction.

K_{max}/K_{Ic} was adversely influenced only when the fatigue precrack depth did not exceed 50% of the EDM notch in the "a" direction. This resulted in an increase in K_{max}. When K_{max} occurred at the free surface, these test results suggest that K_{max}/K_{Ic} was not adversely influenced by:

- A tunnel in 2c direction.
- Shallow fatigue precracks that did not exceed the EDM notch in the "a" direction.

For specimens in which the fatigue precrack extended only a short distance in all directions around the EDM notch, there was a tendency for K_{max} to be somewhat higher than that obtained from specimens with substantial fatigue precrack growth.

When measurements are made from photographs of the fracture surface, considerable error may result if sufficient magnification is not used, suitable lighting is not provided, and both fracture surfaces are not considered.

It is recommended that additional studies include:

- Tensile tests where $cF^2 > 3$ mm to see if K_{max}/K_{Ic} continues to decrease.
- Bend tests where $cF^2 > 3$ mm to see if K_{max}/K_{Ic} continues to increase.
- Development of models to identify the conditions controlling the fracture process in specimens containing surface cracks.
- Another series of tests using cylinders and spheres with various crack orientations.

ACKNOWLEDGMENTS

This work was supported in part by the U.S. Department of Energy, Office of Energy Research, Office of Basic Energy Sciences, and Office of Industrial Technology under DOE Idaho Operations Office Contract DE-AC07-94ID13223. The authors express their appreciation to Dorothy Cullen for typing the manuscript and to Myrtle Siefken for editing it.

REFERENCES

[1] "Standard Test Method for Plane-Strain Fracture Toughness of Metallic Materials," E399-90, *1996 Annual Book of ASTM Standards*, Section 3, Vol. 0.3.01.

[2] Newman, J. C., Jr. and Raju, I. S., *Analysis of Surface Cracks in Finite Plates Under Tension and Bending Loads*, NASA Technical Paper 1578, National Aeronautics and Space Administration, Washington, D.C., December 1978.

[3] Reuter, W. G. and Epstein, J. S., "Experimental Evaluation of an Equation Applicable for Surface Cracks Under Tensile and Bending Loads," *Fracture Mechanics: Nineteenth Symposium, ASTM STP 969*, T. A. Cruse, Ed., American Society for Testing and Materials, Philadelphia, 1987, pp. 597-619.

[4] Reuter, W. G., Epstein, J. S., and Haggag, F. M., "Comparison Between 'Standard' Fracture Toughness Results and Surface Flaw Data for Silicon Carbide," *International Journal of Fracture*, Vol. 47, 1991, pp. 181-200.

[5] Reuter, W. G., Newman, J. C., Jr., Macdonald, B. D., and Powell, S. R., "Fracture Criteria for Surface Cracks in Brittle Materials," *Fracture Mechanics: Twenty-Fourth Volume, ASTM STP 1207*, John D. Landes, Donald E. McCabe, and J.A.M. Boulet, Eds., American Society for Testing and Materials, Philadelphia, 1994, pp. 617-635.

[6] "Fracture Testing with Surface-Crack Tension Specimens," E740-95, *1996 Annual Book of ASTM Standards*, Section 3, Vol. 03.01.

[7] Newman, J. C. Jr., "Fracture Analysis of Various Cracked Configurations in Sheet and Plate Materials," *Properties Related to Fracture Toughness*, ASTM STP 605, American Society for Testing and Materials, 1976, pp. 104-123.

[8] Reuter, W. G., Matthew, S. D., and Smith, F. W., "Critical Parameters for Ductile Fracture of Surface Flaws," *Eng. Fract. Mechanics, Vol. 19*, No. 1, 1984, pp. 159-179.

Takashi MIYATA [1], Tetsuya TAGAWA[2] and Syuji AIHARA[3]

INFLUENCE OF PRE-STRAIN ON FRACTURE TOUGHNESS AND STABLE CRACK GROWTH IN LOW CARBON STEELS

REFERENCE: Miyata, T., Tagawa, T., and Aihara, S., ''**Influence of Pre-stain on Fracture Toughness and Stable Crack Growth in Low Carbon Steels**'', Fatigue and Fracture Mechanics: 28th Volume, ASTM STP 1321, J. H. Underwood and B. D. Macdonald, M. R. Mitchell, Eds., American Society for Testing and Materials, 1997.

ABSTRACT: Experimental investigations demonstrate a significant effect of pre-strain on fracture toughness and stable crack growth resistance of a low carbon structural steel. Fracture toughness, J_i for the onset of stable ductile crack growth is decreased to one half with a 9% pre-strain due to cold rolling. The characteristic distance model for ductile crack initiation was applied to analyze parameters affecting the degradation of fracture resistance. The model predicts that value of J_i is given as a linear function of yield strength and ductility of the material. In order to confirm the theoretical prediction, notched round bar tensile tests were performed and ductility under a high triaxial stress state was measured. Critical plastic strain for micro-void coalescence is significantly decreased with increasing pre-strain. Degradation in J_i due to pre-strain can be well explained by the characteristic distance model.

To clarify micro-mechanisms of degradation in ductility due to pre-strain, fracture process in notched round bar specimens was investigated emphasizing the role of micro-void nucleation and growth. Experimental observation indicates that the significant decrease of the critical strain due to pre-strain is attributed to the increase of void nucleation sites under a high triaxial stress state.

KEYWORDS: pre-strain, J_{IC}, stable crack growth, characteristic distance model, critical plastic strain, micro-void nucleation

---

The great earthquake in the Kobe area, Japan in January, 1995, revealed the necessity of considering the fracture toughness of materials for buildings and the possibility of degradation in toughness due to large plastic deformations. Reliability of structural components and gas line pipe damaged plastically by the earthquake is now being discussed in the technical community. On the other hand, cold working of structural elements becomes nowadays familiar with increase in scale of steel constructions. For an assessment of structural integrity, the effect of plastic damage due to construction on fracture toughness and crack growth of materials should be verified.

Pre-straining or cold working causes hardening of materials and it should also cause degradation of ductility and toughness. However, micro-mechanisms of the degradation are not evident. Incorporation of local micro-mechanistic fracture criteria to an analytical or numerical solution for the stress/strain distribution at the crack tip can derive an expression of fracture toughness in terms of flow and fracture properties of the materials as

[1]Professor, Department of Materials Science and Engineering, Nagoya University, 464-01 Japan
[2]Associate Professor, Department of Materials Science and Engineering, Nagoya University, 464-01 Japan
[3]Senior Researcher, Nagoya Research Laboratories, Nippon Steel Corp., 476 JAPAN

shown by Ritchie, Knott and Rice [1], Pineau [2] and Beremin [3]. This local approach gives us a way for quantitative prediction of variance in the fracture toughness that arises from variance in mechanical and metallurgical factors.

Micro-void coalescence type of fracture is a process of void nucleation, growth and coalescence. That is dependent on stress triaxiality [4-6]. Analytical descriptions of fracture toughness for onset of stable crack growth have been developed by several authors [7-17]. The local criterion in the characteristic distance model [7-9, 12,16] has been proposed as a critical plastic strain value or critical void growth ratio is exceeded over some distance ahead of the crack tip. The Rice-Johnson model [10] describes toughness and crack growth resistance in terms of radius and spacing of nonmetallic inclusions [11,14,15]. Gurson's constitutive equation for porous materials [18] introduces additional numerical methodology to analyze ductile fracture toughness and crack growth [17,19-23].

The purpose of this work is to clarify the effect of pre-strain on fracture toughness of steels on the basis of the local fracture criterion approach with particular reference to micro-void coalescence type of fracture. Additionally, micro mechanisms of degradation in toughness and ductility are investigated. For cleavage, brittle type of fracture, formulations of the fracture toughness have been successfully derived [6,24]. The hardening induced by pre-straining causes a remarkable decrease in cleavage fracture toughness since the fracture toughness is in inverse proportion to the power of yield strength of materials. Details of the mechanisms of degradation in cleavage fracture toughness of steels will be shown elsewhere [24].

LOCAL CRITERION APPROACH FOR MICRO-VOID COALESCENCE TYPE OF FRACTURE

Since void growth rate is exponentially dependent on stress triaxiality, σ_m / σ_{eq} [4,25], where σ_m and σ_{eq} are mean stress (average of three principle stresses) and equivalent Mises stress, respectively, the critical plastic strain for void coalescence shows strong dependence on stress triaxiality [5]. The dependency is different for individual materials, because the significance of void growth in the whole process of the ductile fracture is dependent on the spacing of void nucleation sites and the size of inclusions [6]. Nonuniform distribution of strain and stress triaxiality at the crack tip region requires rigorously continuous and spatial analysis for micro-voids nucleation and voids growth [19-23]. However, the value of the critical plastic strain, $\varepsilon_{p,i}$ for void coalescence takes an almost constant value for highly triaxial stress state, though it is decreased sharply with an increase in stress triaxiality for low triaxial stress state [5,6]. As a first approximation, therefore, the constant strain criterion for a high stress triaxial state can be adopted and such simplified criterion will satisfy the purpose of the present work to identify the significant parameters controlling the degradation in toughness.

The characteristic distance model for the ductile fracture, where plastic strain is locally exceeded over some distance, λ ahead of the crack tip, gives the following expression of the ductile fracture toughness for the materials having HRR (Hutchinson, Rice and Rosengrain) singularity [9,12,14,16].

$$J_i = D\, \lambda\, \sigma_{ys}\, \varepsilon_{p,i} \tag{1}$$

where D and λ are the materials constant, σ_{ys} is the yield strength of the material and $\varepsilon_{p,i}$ is the critical plastic strain for void coalescence in a high triaxial stress state.

EFFECT OF PRE-STRAIN ON J_i AND CRACK GROWTH

The effect of pre-strain induced by cold rolling on the ductile fracture toughness and the stable crack growth were investigated for a low carbon structural steel. Critical strain in notched specimens was measured for the same materials to confirm the analytical prediction induced by the characteristic distance model.

TABLE 1-*Chemical composition of the low carbon, 500MN/m² class medium strength steel.*

C	Si	Mn	P	S
0.16	0.44	1.42	0.02	0.04

TABLE 2-*Mechanical properties of steels and test results on ductile fracture.*

Steel	Yield Strength (σ_{ys}) MN/m^2	Tensile Strength (σ_{uts}) MN/m^2	Critical Plastic Strain,(ε_{pi})	Fracture Toughness (Ji) MN/m	Critical Stretched Zone Width (SZWcr) mm
Normalized	350	519	0.51	0.17	0.18
2.3%C.W.	414	566	0.36	0.13	0.15
9.2%C.W.	590	619	0.18	0.08	0.11

Experimental Procedure

Material tested was a low carbon, 500MN/m² class medium strength steel received in the normalized condition with 40mm thickness. Pre-strains of 2.3% and 9.2% in equivalent plastic strain were induced by cold rolling. Chemical composition of the steel and mechanical properties of materials tested are given in Table 1 and Table 2. All specimens were cut from the center region in thickness of cold rolled plate, because of possible variation in plastic strain through the thickness. Pre-strain values were estimated from the variation in plate length before and after cold rolling, and these values agreed with the offset strain in stress-strain relations before and after cold rolling. All test specimens were oriented so that the tensile axis coincided with the rolling direction of the plates. Ductile fracture toughness, Ji and crack growth resistance were measured for half inch CT specimens in accordance with ASTM E813 and JSME S001[26]. Stretched zone width on the fracture surface was measured by SEM for all specimens. Critical plastic strain, $\varepsilon_{p,i}$ was obtained from circumferentially notched round bar tensile specimen with 1mm notch radius, 6mm diameter in notched section and 12mm outer diameter. Macroscopic coalescence of voids at the center of the minimum cross section was defined as the point when the load dropped sharply prior to final failure of the specimen. Diameter of the minimum cross section was continuously measured during testing, and effective plastic strain at that point was evaluated from the change of the minimum diameter as an average in the cross section. Dimple sizes on the fracture surface at the center of notched round bar specimens are measured from the observation by SEM and image analyzer.

Results and discussion

Relations between J values and stable crack extension are shown in Fig.1, and relations between J values and stretched zone width are shown in Fig.2. It should be noticed that the pre-strain decreases the crack growth resistance and the critical stretched zone size which is constant after the onset of ductile crack growth. Figure 3 shows the decrease in Ji for the onset of stable crack growth with the increase of the pre-strain. The values of Ji were evaluated from the intersection points of the blunting line with the critical stretched zone in accordance with JSME S001[26] as shown in Fig.2 because of insufficient data for the multi-specimen R curve procedure in ASTM E813. The value of Ji for 9.2% cold worked material is decreased to less than one half of the value of the normalized material as shown in Fig.3 and Table 2.

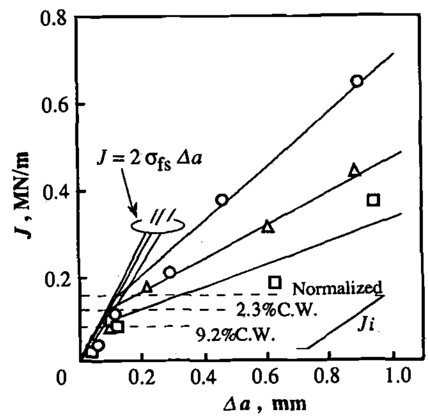

FIG. 1-*Relations between J value and stable crack extension.*

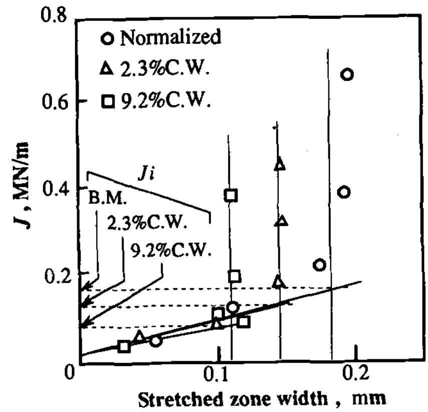

FIG. 2-*Relations between J value and stretched zone width.*

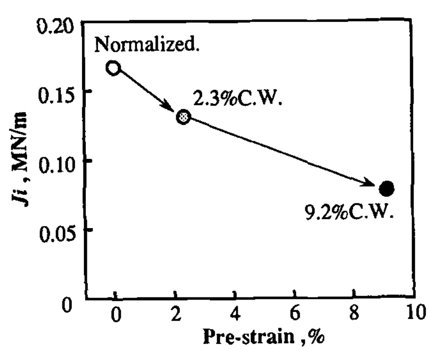

FIG. 3-*Effect of pre-strain on fracture tougness Ji.*

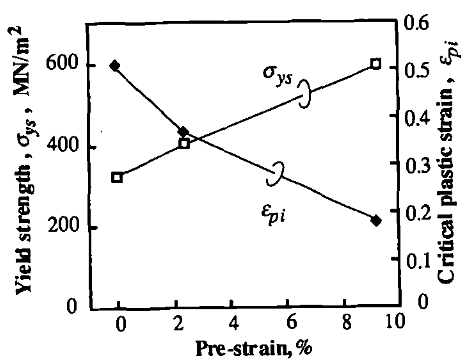

FIG. 4-*Effect of pre-strain on yield strength and critical plastic strain.*

Figure 4 shows the variance of the yield strength and the critical strain, $\varepsilon_{p,i}$ for the notched specimens with the pre-strain. With the increase of the pre-strain, the value of yield strength increases and $\varepsilon_{p,i}$ decreases to less than 40 % of that for the normalized material. Even in comparison for the total strain involving the pre-strain, the ductility in notched specimen shows a large degradation due to the cold working.

The value of J_i is predicted in Eq. 1 to be proportional to the product of the yield strength and $\varepsilon_{p,i}$, if the material constants D and λ are not changed by the pre-straining. The value of λ is related to the distance between nonmetallic inclusions, and D is a function of strain hardening exponent of the material. The pre-straining should have little influence on these constants. Correlation between J_i and the product of σ_{ys} and $\varepsilon_{p,i}$ that are obtained in the round bar specimens is shown in Fig. 5. Experimental data in the previous work, investigating the effect of temperature and microstructure on J_i for several low carbon steels [6], are also shown. The value of J_i is decreased along linearly proportional relation with the increase of the pre-strain. This result indicates the validity of the characteristic distance model and the effect of pre-strain on J_i can be discussed through the effects on σ_{ys} and $\varepsilon_{p,i}$ of the materials.

The reason of significant decrease in $\varepsilon_{p,i}$ due to pre-strain can be explained with the mechanisms of void

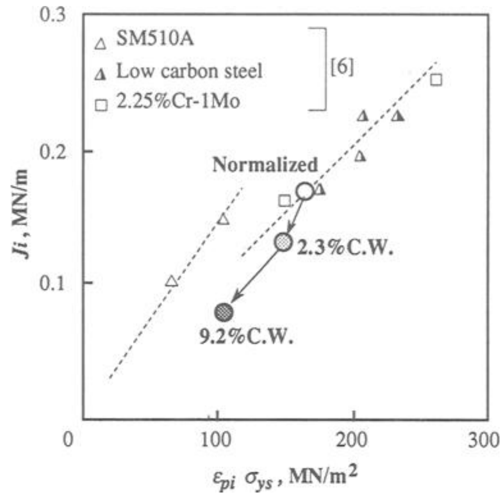

FIG. 5-*Correlation between fracture touhgness Ji and critical strain obtained by 1mmR notched round bar specimen.*

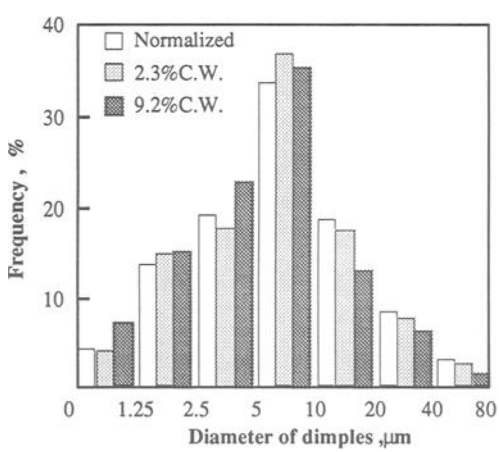

FIG. 6-*Dimple size distributions in terms of area ratio of particular dimple size in the center of fracture surface of notched specimens.*

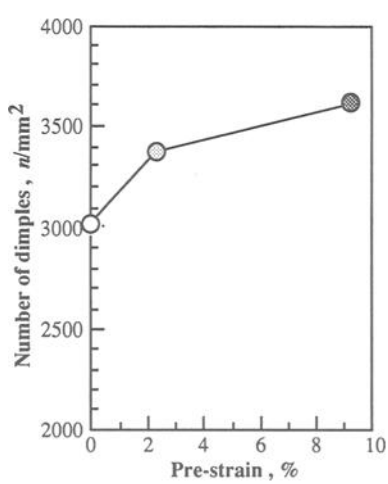

FIG. 7-*Number of dimples in the center of fracture surface of notched specimens.*

nucleation and coalescence, since void growth is independent on flow stress of matrix [4, 25]. Distributions of dimple size on the fracture surface at the center of notched specimens are shown in Fig. 6 in terms of the percentage of area that is occupied with dimples of particular sizes. The frequencies of small dimples with a diameter up to 5μm are larger in the pre-strained materials. Fig.7 shows number of dimples in a specified area for each material. Total number of dimples in 9.2% cold worked material is 20% more than that of the normalized material. This suggests that the hardening of matrix due to pre-straining causes the increase of void nucleation sites, since void nucleation is considered to be governed by interfacial stress between matrix and inclusions [27].

EFFECT OF PRE-STRAIN ON MICRO-VOID COALESCENCE TYPE OF FRACTURE

The effect of pre-strain on fracture process of micro-voids coalescence type of ductile fracture was investigated to confirm the fact that the hardening induced by pre-strain causes a large number of small voids in early stage of deformation under a high triaxial stress state.

Experimental Procedure

Material tested in this investigation was a low carbon mild steel (JIS SS400), with a yield strength of 300MN/m^2 and an ultimate tensile strength of 460MN/m^2, of which chemical composition is given in Table 3. The microstructure contained equiaxied ferrite and pearlite, and the size of non-metallic inclusions were relatively small and uniform in comparison with the steel investigated in the previous section. Pre-strains in the range of 10% to 40% in effective plastic strain were given in uniaxial tension using a smooth round bar of 20mm diameter. Straining for 20% and 40% pre-strain was repeated to a specified strain after smoothing the local necking away with re-machining. Process of the void nucleation, void growth and coalescence were observed metallographically in circumferentially notched round bar specimens with a notch radius of 1mm, of which outer diameter and diameter of notched section were 12mm and 6mm, respectively.

TABLE 3-*Chemical composition and mechanical properties of the low carbon mild steel (JIS SS400) tested.*

C	Si	Mn	P	S
0.16	0.23	0.48	0.03	0.02

Yield Strength (σ_{ys}) MN/m^2	Tensile Strength (σ_{uts}) MN/m^2	Reduction of area %
297	459	66

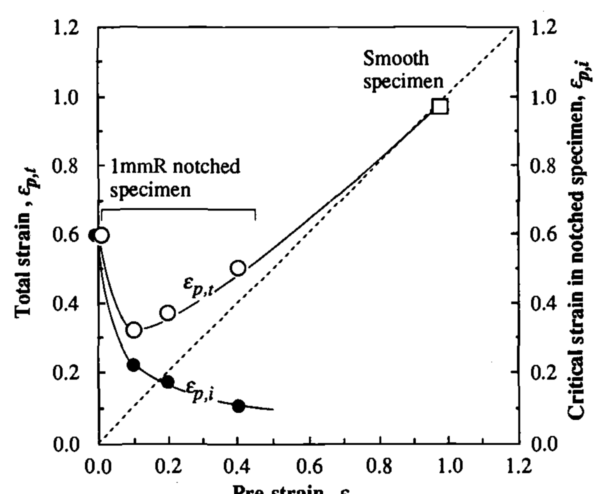

FIG. 8-*Effect of pre-strain on critical strain for micro-voids coalesence.*

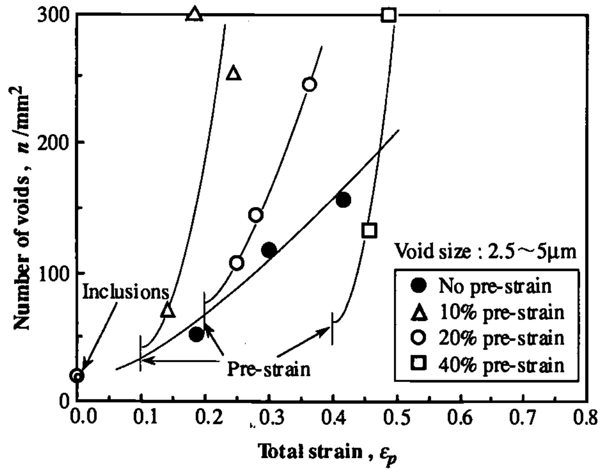

FIG. 9-*Variance in number of voids in notched specimens with plastic strain.*

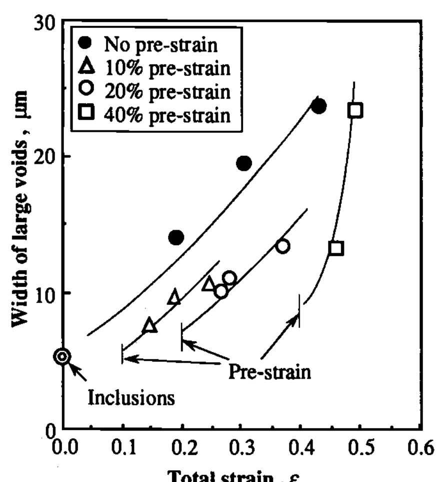

FIG. 10-*Variance of void size in notched specimens with plastic strain.*

Results and Discussion

Figure 8 shows the critical plastic strains for void coalescence at the center of notched specimens. Definition of the strain is the same with the previous section. The pre-strain deteriorates significantly the critical strain in the notched specimens, especially in the range of small pre-strain. Metallographic observation at the longitudinal mid section of the notched specimens subjected to various levels of strain revealed that the pre-strain has a strong influence on the void nucleation as shown in Fig. 9, though a little influence is observed on the rate of the void growth as shown in Fig. 10. Figure 9 shows the variance in the number of voids with a diameter of 2.5μm to 5μm as a function of the total strain involving the pre-strain. Figure 10 shows the relation between the

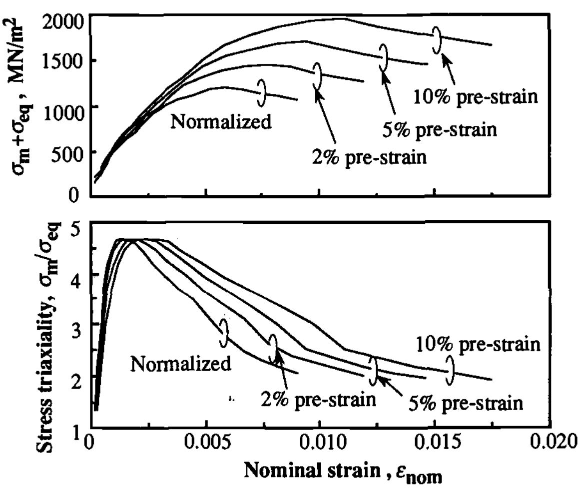

FIG. 11-*Interfacial stress, $\sigma_m+\sigma_{eq}$, and stress triaxiality, σ_m/σ_{eq} , calculated by FEM for the center of 1mmR notched specimens.*

average width of voids for the largest 5 voids in observed area and the total strain. The pre-strain significantly increases the number of small voids in small plastic strain.

Goods and Brown [28] reviewed a number of theoretical and experimental investigations on void formation in metallic materials. From those results it is generally assumed for steels that the nucleation of micro-voids takes place from debonding of interface between inclusion and matrix, and debonding is controlled by interfacial normal stress. Argon and Im [27] give the interfacial stress, σ_{rr} as :

$$\sigma_{rr} = \sigma_m + k\,\sigma_{eq} \tag{2}$$

where k is a constant depending on the shape of inclusions, and is unity for spherical inclusions. Figure 11 shows the numerical results by FEM on the sum of stresses, $\sigma_m + \sigma_{eq}$ and the stress triaxiality, σ_m / σ_{eq} at the center of the 1mm R notched specimen for the material tested in the previous section. Both the sum of σ_m and σ_{eq}, and the stress triaxiality are increased in the larger pre-strained materials. Although the results are depending on the location from the crack tip, similar results were obtained for the cracked specimen.

From above results, it can be said that under a high triaxial stress state, the increase in flow stress due to pre-straining is amplified than the stress sufficient to nucleate the micro-voids. The size and type of inclusions are distributed in a material, and the critical strength at interface for debonding should be different from each inclusion, resulting statistical distribution of the void nucleation rate [29]. The increase of the interfacial stress due to pre-strain causes the early nucleation of voids and the increase of void nucleation sites, and results low ductility in a high triaxial stress state. The hardening due to pre-straining can be eliminated by annealing, and annealing repeated during deformation process give a large ductility and a few number of voids with tremendous dimple size [30]. These results indicate that the void nucleation is controlled by the stress as is proposed by Argon and Im [27].

CONCLUSIONS

Influence of pre-strain on ductile fracture toughness, stable crack growth and ductile fracture process in low carbon structural steels was investigated. Small amounts of pre-strain due to cold rolling deteriorates fracture toughness for the onset of stable crack growth, J_i and crack growth resistance. The local strain criterion model for pre-cracked specimens, so called the characteristic distance model, predicts a linearly proportional relation between ductile fracture toughness and the product of yield strength and critical plastic strain for micro-void coalescence. Experimental results showed the validity of this prediction and that the degradation in J_i due to pre-strain is caused by the decrease of the critical plastic strain. Fractographic observation revealed that number of small dimples was increased in the pre-strained materials. Experimental results on the notched specimen and finite element calculation demonstrated that void nucleation from small inclusions was acceleratively induced by the high flow stress due to pre-straining and high mean stress amplified through the high stress triaxiality. The increase of the void nucleation sites in small applied strain results the low ductility of the pre-strained materials under a high stress triaxiality.

REFERENCES

[1] Ritchie, R. O., Knott, J. F., and Rice, J. R., *Jour. of the Mechanics and Physics of Solids*, Vol.21, 1973, pp. 395-410.

[2] Pineau, A., In: *Advances in Fracture Research, Proc. of ICF 5*, Vol.2, 1981, pp.553-577.

[3] Beremin, F. M., *Met. Trans. A*, Vol. 14A, 1983, pp.2277-2287.

[4] McClintock, F. A., *Jour. of Applied Mechanics, Trans. ASME*, Vol. 34, 1968, pp.363-371.

[5] Hancock, J. W. and Mackenzie, A. C., *Jour. Mechanics and Physics of Solids*, Vol.24, 1976, pp.147-169.

[6] Miyata, T., Otsuka, A., Mitsubayashi, M., Haze, T., and Aihara, S., *Fracture Mechanics: Twenty-First Symposium, ASTM STP 1074*, J. P. Gudas, J. A. Joyce and E. M. Hackett, Eds., American Society for Testing and Materials, 1990, pp.361-377.

[7] Kraft, J. M., *Appl. Mater. Res.*, Vol.3, 1964, p.88.

[8] Sailors, R. H., In: *Properties Related to Fracture Toughness, ASTM STP 605*, J. B. Wheeler, Ed., American Society for Testing and Materials, 1976, pp.34-61.

[9] Hahn, G. T. and Rosenfield, A. R., *Met. Trans. A*, Vol.6A, 1975, pp.653-668.

[10] Rice, J. R. and Johnson, M. A., In: *Inelastic Behavior of Solids*, M. F. Kanninen, W. G. Adler, A. R. Rosenfield, and R. J. Jaffe, Eds., McGraw-Hill, 1970, pp.641-672.

[11] McMeeking, R. M., *Jour. Mechanics and Physics of Solids*, Vol.25, 1977, pp.357-381.

[12] Mackenzie, A. C., Hancock, J. W., and Brown, D. K., *Engineering Fracture Mechanics*, Vol.9, 1977, pp.167-188.

[13] Amar, E. and Pineau, A., *Engineering Fracture Mechanics*, Vol. 22, 1985, pp.1061-1071.

[14] Garrison, W. M. and Thompson, A. W., *Met. Trans. A*, Vol.17A, 1986, pp.2249-2253.

[15] Garrison, W. M. and Moody, N. R., *Met. Trans. A*, Vol.18A, 1987, pp.1257-1263.

[16] Lee, S., Majno, L., and Asaro, R. J., *Met. Trans. A*, Vol.16A, 1985, pp.1633-1648.

[17] Tvergaard, V. and Hutchinson, J. W., *Jour. Mechanics and Physics of Solids*, Vol.40, 1992, pp.1377-1397.

[18] Gurson, A. L., *Jour. Engineering Materials and Technology*, Vol.99, 1977, pp.2-15.

[19] Needleman, A. and Tvergaard, V., *Jour. Mechanics and Physics of Solids*, Vol.32, 1984, pp.461-490.

[20] Needleman, A. and Tvergaard, V., *Jour. Mechanics and Physics of Solids*, Vol.35, 1987, pp.151-183.

[21] Shih, C. F. and Xia, L., In: *Constraint Effects in Fracture Theory and Applications: Second Volume, ASTM STP 1244*, M. Kirk and A. Bakker, Eds., American Society for Testing and Materials, 1995, pp.163-190.

[22] Koers, R. W. J., Krom, A. H. M., and Bakker, A., In: *Constraint Effects in Fracture Theory and Applications: Second Volume, ASTM STP 1244*, M. Kirk and A. Bakker, Eds., American Society for Testing and Materials, 1995, pp.191-208.

[23] Brocks, W. and Schmitt, W., In: *Constraint Effects in Fracture Theory and Applications: Second Volume, ASTM STP 1244*, M. Kirk and A. Bakker, Eds., American Society for Testing and Materials, 1995, pp.209-252.

[24] Miyata, T. and Tagawa, T., submitted to *EUROMECH-MECAMAT '96, Local Approach to Fracture 86-96*, Fontainebleau, France, Spetember, 1996.

[25] Rice, J. R. and Tracey, D. M., *Jour. Mechanics and Physics of Solids*, Vol.17, 1969, pp.201-217.

[26] Japanese Society for Mechanical Engineering, Standard Method of Test for Elastic-Plastic Fracture Toughness J_{IC}, JSME S 001-1992.

[27] Argon, A. S., Im, J., and Safoglu, R., *Met. Trans. A*, Vol.6A, 1975, pp.825-837.

[28] Goods, S. H. and Brown, L. M., *Acta Metallugica*, Vol.27, 1979, pp.1-15.

[29] Chu, C. C. and Needleman, A., *Jour. Engineering Materials and Technology*, Vol.20, 1980, pp.249-256.

[30] Miyata, T. and Tagawa, T., to be submitted to *Jour. of Testing and Evaluation, JTEVA*.

Constraint Effects

Robert H. Dodds, Jr.[1], *Claudio Ruggieri*[1] *and Kyle Koppenhoefer*[1]

3-D Constraint Effects on Models for Transferability of Cleavage Fracture Toughness

REFERENCE: Dodds, Jr., R.H., Ruggieri, C., and Koppenhoefer, K.C., "**3-D Effects on Models for Transferability of Cleavage Fracture Toughness**," Fatigue and Fracture Mechanics: 28th Volume, ASTM STP 1321, J. H. Underwood and B. D. Macdonald, M. R. Mitchell, Eds., American Society for Testing and Materials, 1997.

ABSTRACT: Since the late 1980s there has been renewed interest and progress in understanding the effects of *constraint* on transgranular cleavage in ferritic steels. Research efforts to characterize the complex interaction of crack tip separation processes with geometry, loading mode and material flow properties proceed along essentially two major lines of investigation: (1) multi-parameter descriptions of stationary crack-tip fields under large-scale yielding conditions, and (2) rational micromechanics models for the description of cleavage fracture which also reflect the observed scatter in the ductile-to-brittle transition (DBT) region. This article reviews the essential features of a specific example representing each approach: the J-Q extension to correlative fracture mechanics and a local approach based on the Weibull stress. Discussions focus on the growing body of 3-D numerical solutions for common fracture specimens which, in certain cases, prove significantly different from long-established plane-strain results.

KEY WORDS: fracture mechanics, constraint, cleavage, statistical effects, Weibull stress, scaling models, finite elements

NOMENCLATURE

f_{ij}	Non-dimensional angular functions
h	Constraint parameter, $h = \sigma_h/\sigma_e$
q	Constraint parameter, $q = \sigma_e/\sigma_h$
(r, θ, z)	Cylindrical coordinates
CTOD	Crack Tip Opening Displacement
J	J-contour integral
J_{avg}	J-value that would be reported from experimental work using a plastic η-factor
J_{local}	J-value at a specific location along the crack front

[1] Professor, Visiting Assistant Professor, and Graduate Research Assistant respectively, Department of Civil Engineering, University of Illinois, Urbana, IL 61801

Q Non-dimensional hydrostatic stress parameter

K_{I} Mode I stress intensity factor

T Elastic stress expressed by the second term of Williams' linear elastic solution

δ_{ij} Kronecker delta

η Non-dimensional factor relating the measured plastic work and the plastic component of J

σ_e Mises stress, $\sigma_e = (3S_{ij}S_{ij}/2)^{1/2}$

σ_h Hydrostatic stress, $\sigma_h = \sigma_{ii}/3$

σ_0 Yield stress

INTRODUCTION

Since the late 1980s there has been renewed interest and progress in understanding the effects of "constraint" on transgranular cleavage fracture in ferritic steels at temperatures in the ductile-to-brittle transition (DBT) region. For these materials, the interaction of crack tip plastic zones with nearby traction-free surfaces and with global plastic zones affects strongly the near tip strain-stress fields. Stresses relax below the values determined uniquely by the J-integral [1] for the high constraint condition of small-scale yielding (SSY) [2] which exists early in the loading of common fracture specimens. This loss of a unique relationship between the crack tip fields and J underlies the *constraint loss* phenomenon and contributes to the observed specimen geometry and loading mode dependence on measured values of cleavage fracture toughness (J_c, CTOD). Research efforts to characterize the complex interaction of crack tip separation processes with global loading, geometry and material flow properties proceed along essentially two major lines of investigation: (1) multi-parameter descriptions of stationary crack tip fields applicable under large-scale yielding conditions, and (2) rational micromechanics models, i.e., local approaches, for the description of cleavage fracture which may also address the randomness of material characteristics at the microlevel.

The two-parameter J-T, J-Q theories [3-7] and higher-order asymptotics [8-12] extend a fundamental concept of fracture mechanics in the use of scalar parameter(s) to quantify the strain-stress fields ahead of a stationary crack tip. The J-integral sets the size scale over which high stresses develop while the second parameter quantifies the level of stress triaxiality at distances of a few CTODS ahead of the crack tip. The addition of a second parameter (T, Q, ...) leads to the construction of experimentally derived fracture toughness loci, rather than conventional, single-valued definitions of toughness. The *correlation* of fracture conditions across different crack geometries/loading modes of the same material (and temperature) then proceeds without recourse to detailed features of the crack tip separation processes. At identical values of the scalar parameters (J, Q, T..), the crack tip strain-stress fields that drive the local fracture process have identical values as well. Efforts adopting this approach focus primarily on cleavage fracture under large-scale yielding prior to significant ductile tearing. While successes have been achieved (see [3,13,14] for examples) each of these characterizing parameters derive from a two-dimensional viewpoint, i.e., J, Q, T vary pointwise along a crack front. Extensions and applications within a fully 3-D framework to treat these crack front variations remain elusive, as does their integration into a systematic treatment of strong statistical effects on cleavage toughness in the DBT region.

By coupling macroscopic measures of fracture toughness (J, CTOD) with micromechanics models for material failure ahead of the crack tip, researchers endeavor to *predict*, rather than correlate, constraint effects on fracture toughness. Weakest link models [15-22] have proven effective for the essentially stress-controlled, transgranular cleavage mechanism. Various levels of complexity introduced into descriptions of the microscale fracture process lead to differing versions of the so-called *local approach* (see review articles by Mudry [23] and Pineau [24]). In each such model, constraint loss in fracture specimens under large-scale yielding generates a complex coupling relationship between J and the local parameter. The key to this approach lies in the assumption that fracture occurs at material dependent, critical values of the local parameter (irrespective of the J-value). Since various fracture specimens generate different coupling relationships between J and the local parameter, dissimilarities in measured J-values at fracture may be resolved. Perhaps more importantly, predictions of critical J-values for other configurations become possible once stress analyses provide their J–local parameter relationship. Since evaluation of the local parameter occurs over a relevant (volume) of near-tip material termed the process zone, this approach reflects a 3-D formulation from the outset. The treatment of statistical effects on cleavage toughness enters through the process model adopted for microscale fracture. For example, a local approach model based on the Weibull stress [16,23] can be adopted to predict the effects of constraint variations on critical J-values, *and* to assign numerical values for fracture probability over the spectrum of J-values [25-27]. Simpler models of the microscale fracture process, e.g., the Dodds-Anderson stressed-volume approach [28,29], lead to predictions of relative constraint variations on critical J-values at similar, but unspecified, fracture probabilities.

The objectives of this brief paper focus on a summary of the correlative and local approaches to characterize constraint effects on cleavage fracture toughness. Discussions emphasize features of representative 3-D solutions which, in certain cases, prove strongly different from long-established plane-strain results. The plan of the paper is as follows. The next section discusses the notion of constraint and the utility of small-scale yielding reference solutions. This is followed by a very brief description of the J-Q approach to extend correlative fracture mechanics; emphasis is placed on differences between plane-strain and recently computed 3-D, J-Q trajectories. Illustrative toughness loci demonstrate both the appealing simplicity and practical difficulties of this correlative approach. The presentation then turns to a local approach for cleavage fracture based on the Weibull stress. Our recently computed small-scale yielding reference solutions for the Weibull stress are described; these enable assessment of constraint loss in fracture specimens using a local approach. Newly available results illustrate the magnitude of differences in evolution of the Weibull stress for a deep notch SE(B) specimen modeled in plane-strain, in 3-D as a plane-sided geometry and in 3-D as a side-grooved geometry.

MEASURES OF CONSTRAINT AND SSY

Constraint most generally refers to the evolving level of stress triaxiality ahead of the crack front under increased remote loading. When comparing differences in constraint between crack configurations, questions arise about the precise definition of stress triaxiality and about the relevant position(s) ahead of the crack front at which to make such comparisons. Two approaches to address these issues may be identified: (1) use of a direct triaxiality measure (e.g., h, q) computed pointwise ahead of the crack, and (2) use of full "reference" fields constructed for small-scale yielding (SSY) conditions; fields computed for finite bodies are compared to SSY fields to define *relative* constraint differences. We briefly outline the first approach then provide a more complete discussion of the reference field approach.

A widely cited example of the first approach defines a constraint parameter, h (or its reciprocal), as the ratio of hydrostatic stress (σ_h) to current Mises stress (σ_e), i.e., $h = \sigma_h/\sigma_e$, where values of h reach 3-4 ahead of a stationary crack tip in deep-notch bend specimens of moderately hardening materials. Since h varies with position (r, θ) ahead of the crack and at each position along the front (z), researchers have advanced various proposals for the location to compare h which reflect the mechanism of fracture (cleavage *vs.* ductile tearing, each with different, *relevant* distances from the tip) and modeling details (small-strain *vs.* large-strain). Brocks and Schmidt [30] review these issues and describe representative computations of h for stationary cracks; also see Roos et al. [31] for a discussion of the h-like parameter, q.

The motivation to consider plane-strain, SSY "reference" fields for stationary cracks derives from the existence of such fields in finite bodies when the plastic zones remain vanishingly small compared to the relevant physical dimension, e.g., crack length, thickness or remaining ligament [2]. Under such restricted conditions, the elastic-plastic fields along the crack front at locations away from traction free surfaces may be characterized by a loading parameter (K_I or J) and the non-singular, elastic stress (T) acting parallel to the crack front outside the immediate plastic zone [3-5,32]. Current asymptotic solutions for stationary cracks in SSY employ remote loading described by K_I and T but remain limited to idealized power-law material behavior and (nonlinear elastic) small-strain theory. The HRR [33,34] fields represent the first such solutions with $T \equiv 0$ and fully incompressible material behavior. Subsequent researchers derived asymptotic solutions for stationary cracks to include non-zero T-stresses, material elasticity and two or more terms for the elastic-plastic fields [8-12].

Finite element analyses of the modified boundary layer (MBL) problem enable construction of SSY fields for general material response and admit the option to include finite-strain (blunting) effects at the crack tip [6,7,35]. The plane-strain element mesh represents a single-ended crack in an infinite body where specified values for K_I and T uniquely define the linear-elastic remote field enclosing a vanishingly small plastic zone at the tip (i.e., compared to the finite extent of the element mesh). Incremental plasticity theory, viscoplasticity and arbitrary material flow properties, for example, introduce no difficulties. Such general FE solutions retain the powerful concepts of similarity fields and length-scales found in the more restricted asymptotic solutions. Distances, for example, all scale with $(K_I/\sigma_0)^2$, J/σ_0 and CTOD.

At increasing loads in finite bodies, the initially strong SSY fields gradually diminish at varying rates as plastic zones sense nearby traction free boundaries, which increasingly violates the conditions of SSY. The one-to-one correspondence of K_I (or J) and T to the crack-tip fields diminishes gradually as well in this process. The differences between the actual finite-body field and those of the comparison SSY field (having the applicable elastic T-stress), quantify the extent of large-scale yielding (LSY) effects. Such comparisons led directly to development of the J-Q theory described subsequently for stationary cracks. In the local approach, the FE analyses provide numerical values of the SSY fields needed to compute the evolution of a crack tip parameter (e.g. Weibull stress) with K_I and T. For a fixed set of material dependent constants in the microscale fracture criterion, these relationships constitute the SSY reference conditions for the local approach. In finite bodies, the gradual deviations from these reference conditions quantify the loss of constraint, but from the viewpoint of an explicit, local criterion for cleavage fracture, rather than from deviations of specific field components, mean stress, etc.

CORRELATIVE FRACTURE MECHANICS: *J-Q* Toughness Locus

Details of J-Q Theory

The J-Q description of mode-I, plane-strain crack tip fields derives from consideration of the MBL model for small-scale yielding. Crack tip stresses for linear elastic conditions have the form [36]

$$\sigma_{ij} = \frac{K_{\mathrm{I}}}{\sqrt{2\pi r}} f_{ij}(\theta) + T\delta_{1i}\delta_{1j} \ . \tag{1}$$

Here r and θ are polar coordinates centered at the crack tip with $\theta = 0$ corresponding to a line ahead of the crack and $K_{\mathrm{I}} = \sqrt{EJ/(1-\nu^2)}$, E is Young's modulus and ν is Poisson's ratio. Crack tip fields differing in stress triaxiality are generated by varying the non-singular stress, T, parallel to the crack plane (which does not affect the value of J). In the computational model for SSY, the conditions defined by Eq. (1) are imposed incrementally via displacements on the remote outer boundary of a symmetrically constrained, semi-circular mesh of elements focused on the crack tip (see Fig. 1(a)).

O'Dowd and Shih [6,7] (OS) employed asymptotic analyses and detailed finite element analyses to propose the approximate two-parameter description of the crack tip fields which applies rigorously under SSY conditions and *approximately* under large-scale yielding conditions

$$\sigma_{ij} = \sigma_0 \, f_{ij}\left(\frac{r}{J/\sigma_0}, \theta; Q\right) \ , \qquad \epsilon_{ij} = \epsilon_0 \, g_{ij}\left(\frac{r}{J/\sigma_0}, \theta; Q\right) \ . \tag{2}$$

The dimensionless second parameter, Q, in Eq. (2) defines the amount by which σ_{ij} and ϵ_{ij} in fracture specimens differ from the adopted $\mathrm{SSY}_{T=Q=0}$ reference solution at the same applied-J. For non-zero values of the T-stress, Q exhibits a simple (unique) dependence on T in SSY that varies only with the material flow properties [7].

To a good approximation, OS showed that $Q\sigma_0$ represents the *difference* in hydrostatic stress over the forward sector ahead of the crack tip between the $\mathrm{SSY}_{T=0}$ and fracture specimen fields, i.e.,

$$\sigma_{ij} = (\sigma_{ij})_{\mathrm{SSY;T=0}} + Q\sigma_0\delta_{1i}\delta_{1j} \ ; \quad |\theta| < \frac{\pi}{2}, \ J/\sigma_0 < r < 5J/\sigma_0 \ . \tag{3}$$

Operationally, Q is defined by

$$Q \equiv \frac{\sigma_{\theta\theta} - (\sigma_{\theta\theta})_{\mathrm{SSY;T=0}}}{\sigma_0}, \qquad \text{at } \theta = 0, \ r = 2J/\sigma_0 \tag{4}$$

where finite element analyses containing sufficient mesh refinement to resolve the fields at this length scale provide the finite body stresses ($\sigma_{\theta\theta}$). Construction of a J-Q *trajectory* follows by the evaluation of Eq. (4) at each stage in loading of the finite body. Again, this procedure imposes no restrictions on models to describe material flow properties or incremental *vs.* deformation plasticity. Large geometry changes (LGC) may be included although values of Q derived from small geometry change (SGC) analyses prove satisfactory in applications which make use of stresses sufficiently outside the

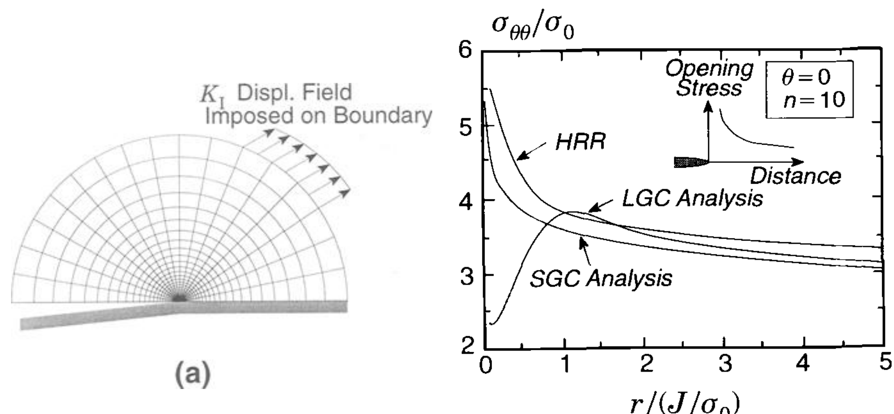

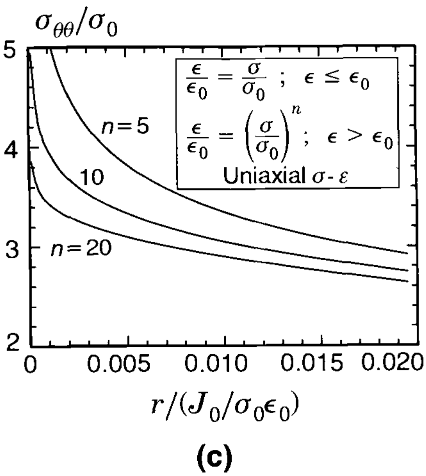

	Hoop Stress: $\frac{\sigma_{\theta\theta}}{\sigma_0}$		
n	a	β	γ
5	1.5144	–0.17669	–2.0260
10	2.0600	–0.095105	–4.4849
20	2.4904	–0.047627	–6.6943

Fitting Function: $\frac{\sigma_{\theta\theta}}{\sigma_0} = a\hat{r}^{\beta}\exp(\gamma\hat{r})$

(d)

FIG. 1 (a) Finite element mesh for SSY model; (b) HRR, small geometry change and large geometry change opening mode stresses for SSY, $T=0$; (c) Example of SSY, $T=0$ stresses used to compute J-Q trajectories; (d) Fitting coefficients for SGC stresses shown in (c).

near tip blunting region. To incorporate loading rate (i.e., strain rate) effects on material response in the boundary layer model, the K_I $(T=0)$ displacement field is imposed over prescribed time increments. The strain-rate dependence of material flow properties then have a strong influence on near-tip stresses [37].

Figure 1(b) compares the opening mode stresses on the crack plane of the $T=0$ reference field obtained using (1) the HRR field, (2) a SGC boundary layer analysis and (3) a LGC boundary layer analysis. The boundary layer analyses employ a description of the material's uniaxial stress-strain response represented by an elastic power-law model having the form

$$\epsilon = \begin{cases} \sigma/E & \text{if } \sigma \le \sigma_0 \\ \epsilon_0(\sigma/\sigma_0)^n & \text{if } \sigma > \sigma_0 \end{cases} \quad ; \quad \epsilon_0 = \sigma_0/E \tag{5}$$

with values of $E/\sigma_0 = 500$, $\nu = 0.3$ adopted in the computations. Outside the blunting zone, the LGC and SGC stresses converge to very similar values (note that LGC values represent *true* stresses in the figure). Reference fields determined from SGC analyses prove adequate for most applications. However, accurate descriptions of fields near the zone of finite strains may be desirable in some applications, e.g. for computation of the Weibull stress in the local approach. LGC analyses eliminate numerical difficulties arising with integration of the singular stress fields present in the SGC solutions.

Figure 1(c) provides the SGC reference solutions for $T=0$ over a range of strain hardening exponents (n). For convenience in post-processing the 3-D finite element solutions, continuous functions are constructed to fit these SSY stresses which take the form

$$\frac{\sigma_{\theta\theta}}{\sigma_0} = \alpha \hat{r}^{\beta} exp(\gamma\hat{r}); \quad \hat{r} = \frac{r}{J/\sigma_0\epsilon_0} \tag{6}$$

and α, β, γ are curve fitting parameters. The table included in Fig. 1(d) lists the values of these parameters for $n = 5$, 10 and 20. Note: these fits apply for all E/σ_0 ratios; $\hat{r}$ as defined above is the similarity length-scale of the HRR fields.

At low deformation levels, fracture specimens experience SSY conditions and Q remains very nearly zero (Q and T are uniquely related under SSY, and T varies linearly with K_I). Once large-scale yielding conditions prevail, hydrostatic stresses at the crack tip have substantially smaller values than those in $\text{SSY}_{T=0}$ at the same J-value. This difference produces *negative* Q values once the specimen deviates from SSY conditions. For deeply notched SE(B) and C(T) specimens, their positive T-stress causes Q to take on slightly positive values at low deformation levels before constraint loss occurs.

For 3-D, mode-I configurations, the near tip fields at locations sufficiently far from external surfaces approach the form of Eq. (3) as $r \rightarrow 0$. The use of Eq. (4) provides Q values at locations (x_3) along a 3-D crack front using local J-values and stresses in planes perpendicular to the crack front. Alternatively, the direct interpretation of Q as the hydrostatic (mean) stress suggests a definition in 3-D as

$$Q_m \equiv \frac{\sigma_{kk} - (\sigma_{kk})_{\text{SSY;T=0}}}{\sigma_0}, \quad \text{at } \theta = 0, \; r = 2J/\sigma_0 \; . \tag{7}$$

Previous studies by Faleskog [14] and Dodds, et al. [38] demonstrate the negligible differences between Q and Q_m for through-crack and surface crack configurations.

3-D Effects on J-Q Trajectories in Conventional Test Specimens

Nevalainen and Dodds [39] (ND) performed detailed 3-D analyses of SE(B) and C(T) specimens, plane-sided and side-grooved, to derive J-Q trajectories at locations across the crack front. Selected key results described here illustrate the strong interaction of in-plane and through-thickness effects on crack front fields not captured in plane-strain analyses. Figure 2 shows an example of a finite element model constructed for analyses of C(T) specimens. Meshes typically have 15 variable thickness layers defined over the half-thickness. In each layer, the level of mesh refinement equals or exceeds levels used in previous plane strain analyses. Typical 3-D models for the SE(B) and C(T) specimens contain 6500-8500 elements. The complete analysis matrix includes plane-sided SE(B) specimens with $a/W = 0.1$ and 0.5, $W/B = 1$, 2, 4 and plane-sided C(T) specimens with $a/W = 0.6$, $W/B = 1$, 2, 4. To investigate the potential effects of 20% side grooves (10% each side) on standard $W/B = 2$ configurations, ND analyzed a C(T) having $a/W = 0.6$

and SE(B)s having $a/W = 0.1$ and 0.5. The material model employs deformation plasticity theory (nonlinear elasticity) in a conventional SGC formulation. The uniaxial (tension) stress-strain curve follows the model in Eq. (5) with $E/\sigma_0 = 500$, $\nu = 0.3$. Figure 1(c) shows the SSY reference fields.

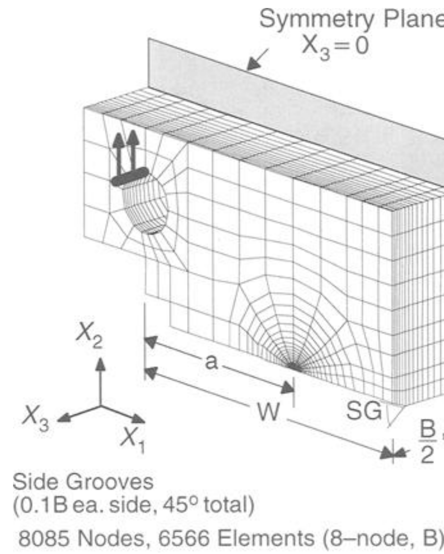

FIG. 2 3-D finite element mesh of side-grooved C(T) specimen to compute J-Q trajectories

Figures 3 (a) and (b) show the J-Q trajectories generated under increased loading at locations over the crack front for plane-sided, deep and shallow notch SE(B) specimens having $W/B = 1$ and $n = 10$. Q is defined by Eq. (4) at the normalized distance ahead of the crack front given by $r/(J_{local}/\sigma_0) = 2$. However, we plot the evolution of Q values against specimen deformation described by J_{avg} rather than J_{local}. For the deep notch in Fig. 3 (a), Q-values are positive at low loads (corresponding to the positive elastic T-stress for this geometry) except near the outside surface. Over the center portion of the specimen thickness, SSY conditions ($Q \geq 0$) exist *strictly* for deformation levels $b > 140\, J_{avg}/\sigma_0$, where b denotes the remaining ligament length; at larger deformations Q takes on negative values. To simplify the description of levels of constraint loss, we use the expression $b > M\, J_{avg}/\sigma_0$, where M represents a non-dimensional deformation limit. Note that σ_0 here denotes the proportional limit of the idealized stress-strain curve. The plane-strain result for this configuration shown in Fig. 3 (a) indicates constraint loss at lower-levels of deformation, $b > 170\, J_{avg}/\sigma_0$. The difference between plane-strain and 3-D (centerplane) trajectories increases with continued loading. Q-values at various distances ahead of the tip on the midplane, see Fig. 3 (c), show steadily increasing radial dependence under increasing load which reflects the strong gradient of the bending field acting on the small remaining ligament. All deep notch SE(B) and the C(T) specimens exhibit similar levels of Q dependence on r at large deformations.

In Fig. 3 (b), Q-values for the $a/W = 0.1$ configuration reveal an immediate loss of constraint upon loading. Crack front locations maintaining highest constraint are $x_3/(B/2) \sim 0.3$-0.68 rather than at the midplane for all other configurations examined. Strong anticlastic bending in the square cross-section contributes to this different behavior. The plane-strain result agrees reasonably well with the 3-D analysis over this portion of the crack front. Fig 3 (d) demonstrates the much stronger radial independence of Q-values for the $a/W = 0.1$ configuration. The global bending field impinges less strongly on the crack-tip fields in the shallow notch geometry. However, no practical size/deformation limit exists to maintain SSY conditions in this specimen; constraint loss occurs upon initial loading (the T-stress is negative for this a/W ratio).

Figure 4 provides additional J-Q trajectories for SE(B) specimens showing the effects of W/B ratios and side grooves, for $a/W = 0.5$ and $n = 5$, 10. Examination of these

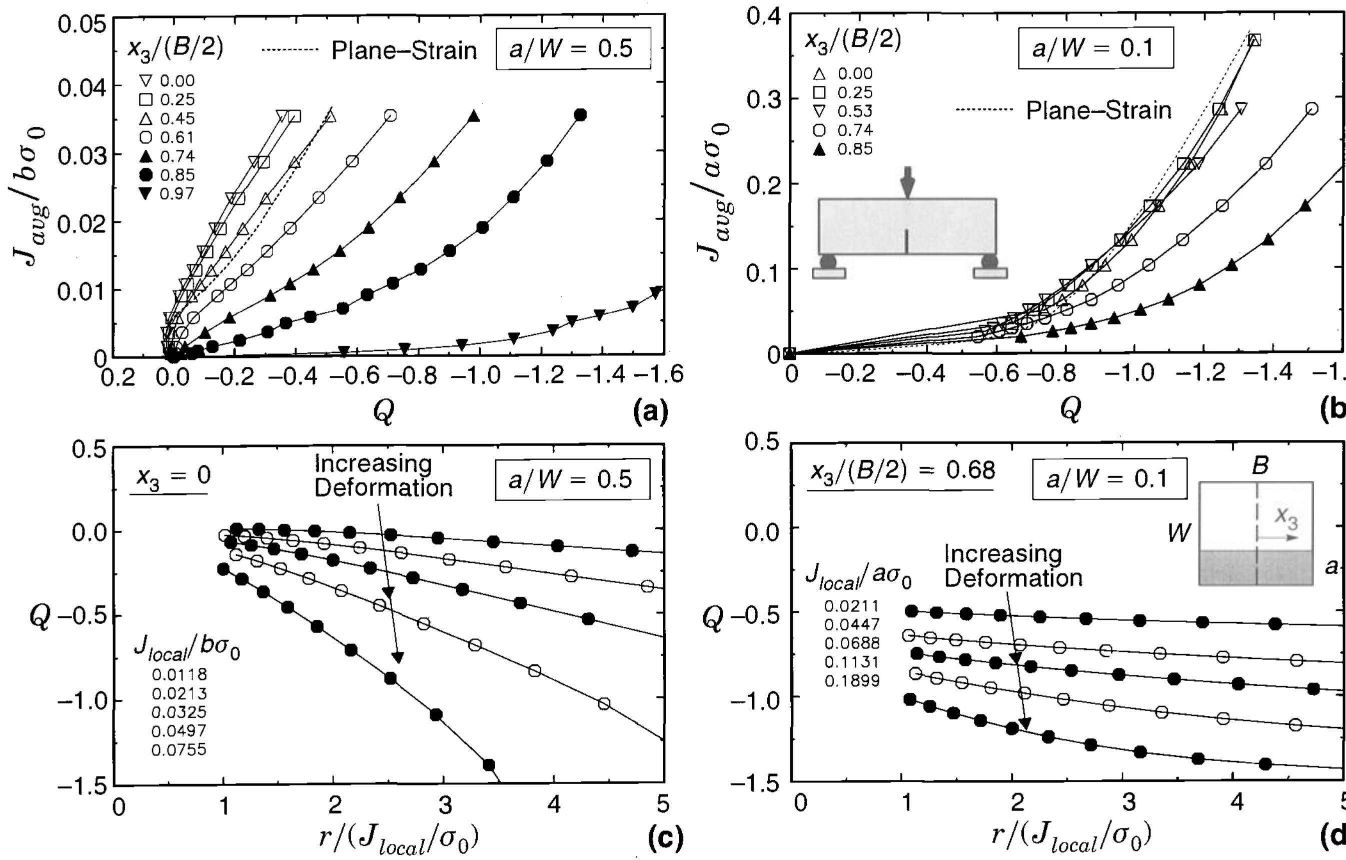

FIG.. 3 Constraint in terms of Q triaxiality parameter for plane–sided, deep and shallow notch SE(B) specimens having $W/B = 1$, $n = 10$. (a) and (b) show variations across crack front for Q defined at $r/(J/\sigma_0) = 2$. (c) and (d) show typical dependence of Q on distance ahead of crack tip. $E/\sigma_0 = 500$, $\nu = 0.3$ in all analyses.

results leads to the following observations: (1) the $W/B = 1$ and 2 trajectories are nearly identical; (2) side grooves in the $W/B = 2$ configurations provide small increases of constraint on the midplane at high deformation levels and have insignificant effect early in the loading; (3) specimens having $W/B = 4$ show a severe constraint loss on the midplane upon initial loading; (4) strain hardening variations from $n = 5 \rightarrow 10$ have a small effect on the 2-D and 3-D J-Q trajectories at higher loads—for a specified J-value, reduced hardening does make Q more negative.

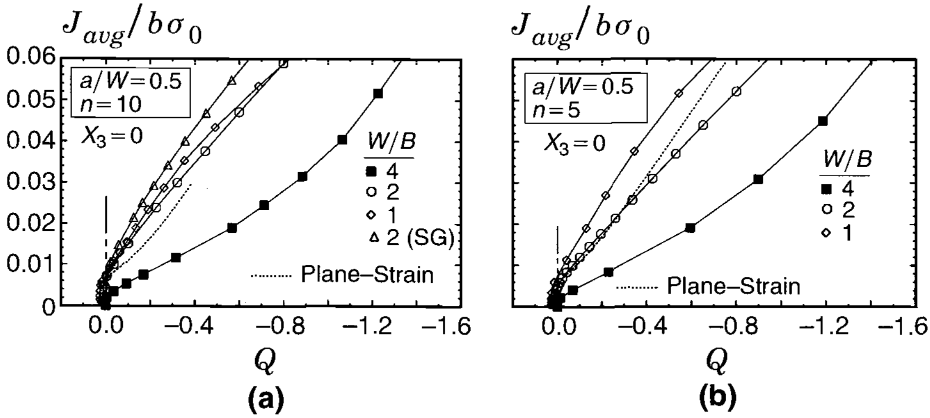

FIG. 4 J-Q trajectories for SE(B) with $a/W = 0.5$ showing effect of W/B, side-grooves and strain hardening.

Figure 5 provides J-Q trajectories for deep notch C(T) specimens. These results lead to the following observations: (1) in contrast to the SE(B) specimens, the plane-strain model now predicts the maintenance of high constraint to larger deformation levels; (2) side grooves have a slight effect of lowering constraint at high load levels on the midplane, see Fig. 5 (a); (3) side-grooves increase constraint significantly at other front locations relative to the plane-sided specimen, compare Figs. 5 (b) and (d); (4) strain hardening affects constraint somewhat for the standard $W/B = 2$ specimen at high loads with a larger effect for the thin specimen $W/B = 4$; (5) SSY conditions in 3-D exist *strictly* for deformation levels $M \approx 100$ in the standard $W/B = 2$ configuration. The increased elastic T-stress of the C(T) specimen relative to the deep notch SE(B) specimen leads to the 25% increase in deformation (3-D) before SSY conditions breakdown; $\beta = T\sqrt{\pi a}/K_I = 0.58$ for the C(T) with $a/W = 0.6$ compared to $\beta = 0.15$ for the SE(B) with $a/W = 0.5$.

Toughness Locus: 3-D Effects

Testing of fracture specimens enables construction of J-Q *toughness loci* to characterize a material's cleavage resistance over a range of crack tip stress triaxiality at a fixed temperature in the DBT range. Experimentally measured J-values at cleavage fracture are plotted on the trajectories computed by finite element analyses for the specimens, such as those shown in Fig. 6(a). The Q-value at fracture is thus not measured; rather it is inferred by the J controlled location on the appropriate J-Q trajectory. The usual scatter in results observed for multiple tests of the same specimen configuration defines points that lie along the loading trajectory for that specimen. By connecting, separately, the upper-most fracture value on all loading trajectories tested and then the lower-most

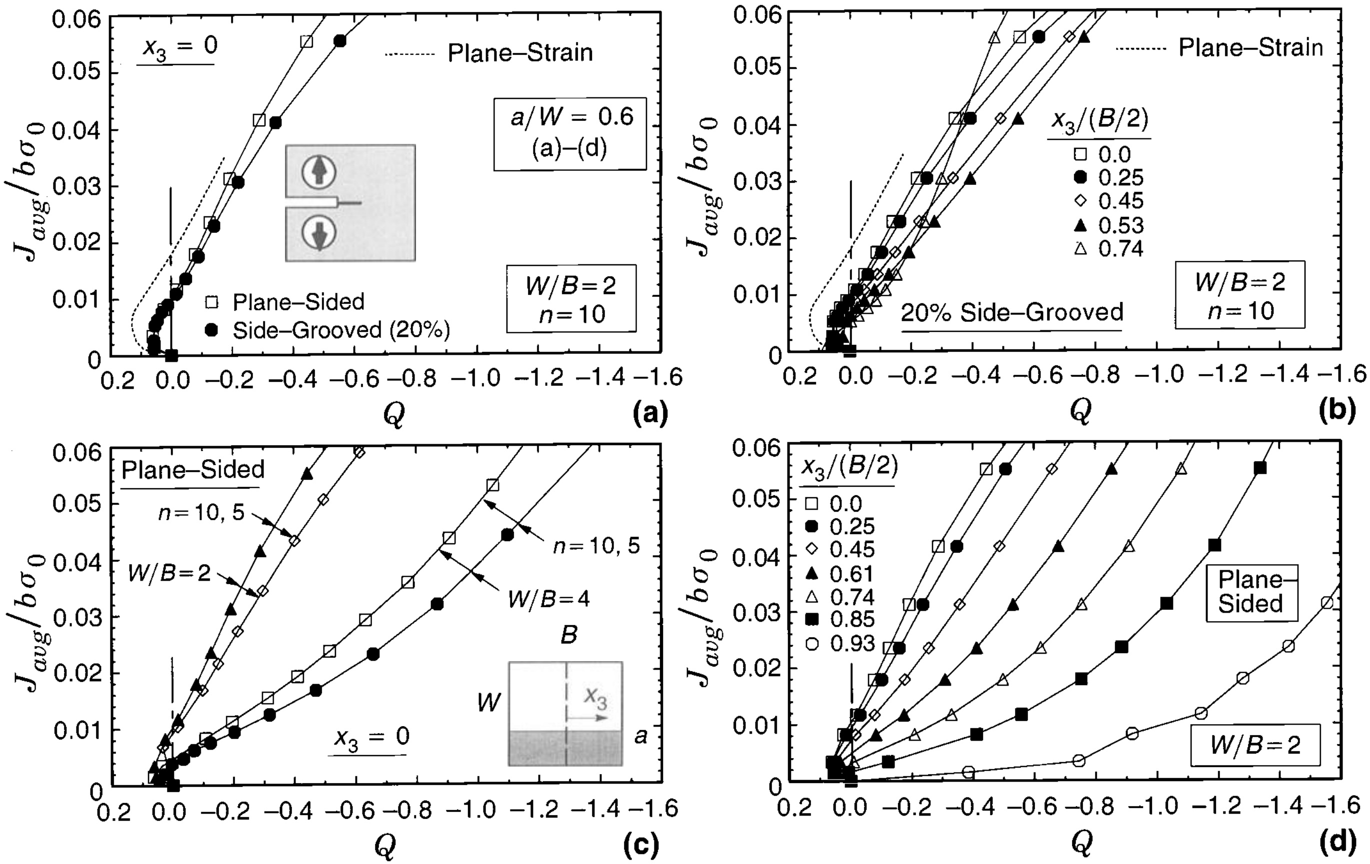

FIG.. 5 *J-Q* trajectories for C(T) specimens showing effects of B/W ratio, side-grooves and strain hardening. Q defined at $r/(J/\sigma_0) = 2$ and $E/\sigma_0 = 500$, $\nu = 0.3$ in all analyses.

fracture values, measured envelopes of toughness may be constructed. Utilization of the toughness locus in fracture assessments is illustrated in Fig. 6(b). The driving force curve for a highly constrained geometry (structure A) rises rapidly in the J-Q space. Consequently, cleavage fracture occurs when it intersects the failure locus for cleavage. In contrast, a low constraint geometry (structure B) induces a gradually rising driving force so that ductile tearing is the likely event at overload.

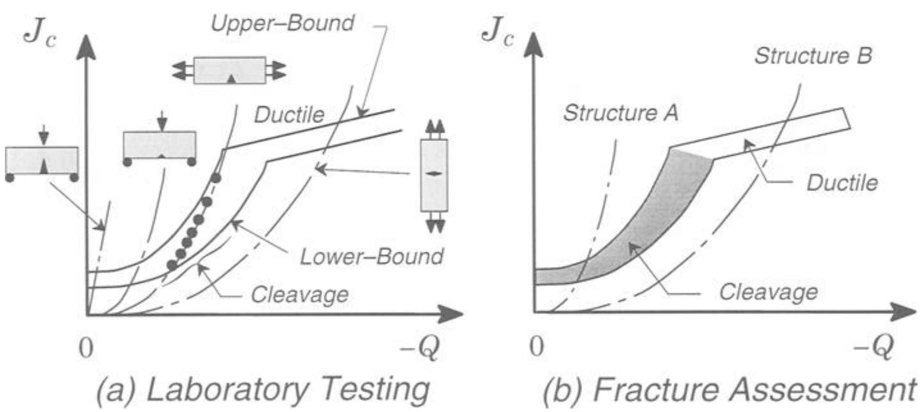

FIG. 6 Application of the J-Q methodology in fracture assessments.

The analyses described here show clearly the strong 3-D effects on J-Q trajectories required for construction of the toughness loci. Trajectories derived from plane-strain and 3-D analyses differ for deep notch SE(B) and C(T) specimens. For the SE(B) results shown in Fig. 3, the 3-D centerplane trajectory lies above the one for plane strain at all loading levels. The difference shown in J-values at fixed Q increases further when the 3-D, J_{local} values are considered, rather than J_{avg}. ND [39] showed that $J_{local} \approx 1.35 \times J_{avg}$ for $W/B = 2$ (plane-sided) and $\approx 1.15 \times J_{avg}$ for $W/B = 1$ (plane-sided) and $W/B = 2$ (side-grooved). Similar differences between J_{local} and J_{avg} are found for the C(T) specimens, which exhibit reversed trends; the use of J_{local} rather than J_{avg} nows brings the 3-D centerplane and plane strain trajectories into closer agreement. The strong (positive) T-stress present in the C(T) promotes this behavior.

For the plane-sided specimens, the 3-D analyses reveal nearly identical J-Q trajectories over the center 50% of the specimen thickness, before the sharp constraint reduction near the outside surfaces. This result greatly simplifies applications and agrees with experimental observations which show a clustering of cleavage trigger sites over this portion of the thickness. Side-grooves simply eliminate material over which fracture seldom initiates and promote a more uniform J-Q trajectory over the crack front (compare Figs. 5 (b), (d)). Unfortunately, in low constraint specimens, the upper and lower J-values on the toughness loci increase dramatically with decreasing constraint (more negative Q) due to the very large scatter of measured toughness data. Formal approaches to address this key issue in a toughness locus framework remain unavailable.

MICROMECHANICAL (LOCAL) APPROACH

The Weibull Stress (σ_w) as a Probabilistic Fracture Parameter

Extensive work on cleavage fracture in ferritic steels demonstrates that cracking of grain boundary carbides in the course of plastic deformation and subsequent extension of these cracks into the surrounding matrix governs failure [40,41]. This type of fracture is a highly localized phenomenon which exhibits strong sensitivity to material characteristics at the microlevel. The inherent random nature of cleavage fracture prompted the development of a model to couple macroscopic fracture behavior with random micro-scale events. As previously noted, existing probabilistic models most often adopt weakest link arguments to yield asymptotic distributions for the fracture strength of brittle materials. In the local approach to cleavage fracture, the probability distribution for the fracture stress of a cracked solid is a monotonically increasing function of loading (represented by the J-integral) given by the two-parameter Weibull distribution [16,26,27]

$$\mathcal{P}(J) = 1 - \exp\left[-\frac{1}{V_0}\int_{\Omega}\left(\frac{\sigma_1}{\sigma_u}\right)^m d\Omega\right] = 1 - \exp\left[-\left(\frac{\sigma_w}{\sigma_u}\right)^m\right] \tag{8}$$

where Ω denotes the volume of the (near-tip) fracture process zone and σ_1 is the maximum principal stress acting on material points inside the fracture process zone. Here, the loci $\sigma_1 \geq \lambda\sigma_0$, with $\lambda \approx 2$ defines the fracture process zone. Parameters m and σ_u appearing in Eq. (8) denote the Weibull modulus and the scale parameter of the Weibull distribution. In particular, m defines the *shape* of the probability density function describing the microcrack size, a, which is of the form $f(a) \propto a^{-\beta}$ with $m = 2\beta - 2$. Now, following Beremin [16], the Weibull stress is defined as the stress integral

$$\sigma_w = \left[\frac{1}{V_0}\int_{\Omega}\sigma_1{}^m d\Omega\right]^{1/m} \tag{9}$$

In the context of probabilistic fracture mechanics, the Weibull stress, σ_w, emerges as a near-tip parameter to describe the coupling of remote loading with a micromechanics model which incorporates the statistics of microcracks (weakest link philosophy). Unstable crack propagation (cleavage) occurs at a critical value of σ_w; under increased remote loading (J or CTOD), differences in evolution of the Weibull stress reflects the potentially strong variations of near-tip stress fields due to the effects of constraint loss. Equation (8) implicitly defines a zero threshold stress for fracture; consequently, stresses vanishingly small compared to the fracture stress yield a non-zero (albeit small) probability for fracture. A more refined form of the limiting distribution for the fracture stress of a cracked solid using a threshold stress, σ_{th}, has been explored by Bakker and Koers [42,43] and Ruggieri and Dodds [26] (RD). The threshold stress has the physical interpretation of a lower-bound strength for fracture; the failure probability for the material volume element becomes zero for any stress below σ_{th}. However, RD [26] show that such refinement does not appear to provide significant improvements in the fracture behavior predicted by the present methodology in an application using an high strength low alloy (HSLA) steel.

Weibull Stress Under Small-Scale Yielding: Reference Solutions

Small-scale yielding analyses with $T/\sigma_0 = 0$ provide the reference fields to assess effects of crack-tip constraint on fracture resistance based upon the Weibull stress. These SSY results also demonstrate important features of σ_w as a crack tip parameter broadly applicable to describe brittle fracture behavior across different structural crack configurations (i.e., transferability of cleavage fracture toughness). Finite element solutions using LCG formulation (note that analyses presented in previous sections employ a SGC formulation) are generated for power-law hardening materials having two levels of strain hardening ($n = 5$, 10) with $E/\sigma_0 = 500$ and $\nu = 0.3$. For the case $n = 10$, numerical results are also obtained for $E/\sigma_0 = 250$, 1000. These properties characterize the plastic behavior for commonly utilized structural and pressure vessel steels with moderate-to-high strength. In each analysis, a *reference* unit thickness, $B = 1$, is adopted.

In evaluating the Weibull stress, Eq. (9), under increased loading, two values of the shape parameter are considered: $m = 10$ and 20, which represent a range of values for ferritic steels reported in previous work [16,22,25,]. In particular, $m \approx 20$ characterizes the distribution of Weibull stress at cleavage fracture for a nuclear pressure vessel steel (ASTM A508) [16]. These values of m reflect different microcrack densities thereby defining different fracture behavior for these materials.

Figure 7(a) shows the variation of Weibull stress under increasing deformation for the two levels of hardening $n = 5$, 10 and with $m = 10$, 20. Figure 7(b) shows the variation of Weibull stress with increasing deformation for $n = 10$, $m = 20$ and varying mechanical properties, $E/\sigma_0 = 250$, 500, 1000. In these plots, $J/(\sigma_0 \epsilon_0 R)$ describes the far-field loading with the Weibull stress normalized by the yield stress, σ_0. The evolution of σ_w with increasing loading displayed in Fig. 7(a) depends markedly on the degree of strain hardening and the shape parameter. However, for fixed strain hardening, n, and shape parameter, m, are fixed, the σ_w-values become invariant of E/σ_0 as shown in Fig. 7(b) which greatly simplifies development of "handbook" reference solutions. Furthermore, the values of Weibull stress scales with K_I in accordance with $\sigma_w = \beta_m K_I^{4/m}$ [23], where the proportionality constant, β_m, depends on m, for fixed n, E/σ_0.

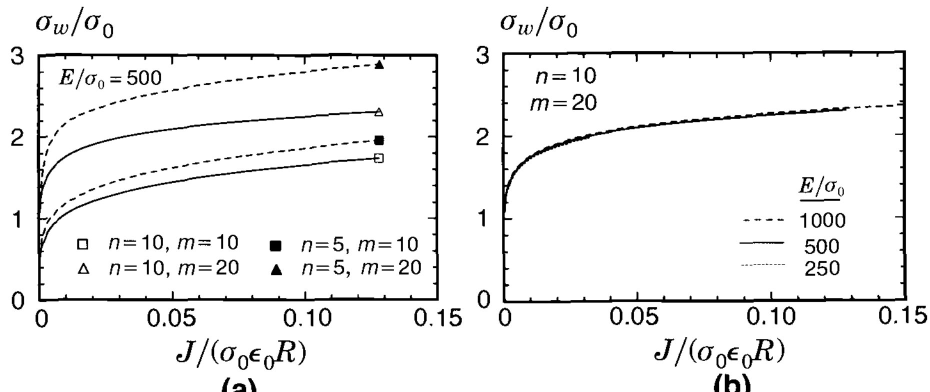

FIG. 7 Evolution of the Weibull stress with increasing loading for varying mechanical properties and microcrack distributions. (a) $E/\sigma_0 = 500$. (b) $n = 10$ and $m = 20$. R is radius of SSY model.

The key feature of these results lies in the interpretation of σ_w as a *macroscopic* crack driving force. Because the Weibull stress reflects the fracture strength at the microlevel, it seems plausible to assume that cleavage fracture occurs when σ_w reaches a critical value, σ_{wc}, which becomes a material property independent of stress triaxiality, temperature (within a wide range in the transition region) and possibly strain rate, radiation, etc. Under increased remote loading, development of the Weibull stress provides a link between the local conditions upon which fracture takes place and the macroscopic fracture parameter (J). Further, a probabilistic interpretation is readily established upon examining Eq. (8): increasing σ_w-values with loading correspond to increasing values for the failure probability of cleavage fracture. The analysis results shown in Fig. 7(a) demonstrate that attainment of σ_{wc} for lower hardening materials occurs only at much greater deformation levels (J) relative to higher hardening materials. These results also demonstrate the strong effect of the shape parameter, m (which characterizes the microcrack distribution), on fracture behavior.

3-D Effects on Evolution of Weibull Stress in Standard Test Specimens

Figure 8 shows a typical finite element model constructed for analyses of $a/W = 0.5$ SE(B) specimens (the model shown contains a V-notch to accommodate the CVN geometry). Meshes have 14 variable thickness layers defined over the half-thickness. In each layer, the level of mesh refinement equals levels used in plane strain analyses. The quarter-symmetric 3-D models for the SE(B) specimens typically have 23000 nodes and 2000 elements. The analysis matrix includes plane-sided and 20% side grooved (10% each side) SE(B) specimens with $a/W = 0.5$, $W/B = 1$. The material model employs incremental plasticity theory with a linear, power-law hardening uniaxial (tension) stress-strain curve ($E/\sigma_0 = 500$, $\nu = 0.3$). The analyses include the LGC formulation which eliminates numerical issues in computation of σ_w at the crack tip.

Figure 9 (a) shows the evolution of Weibull stress, as defined by Eq. (9), under increased loading for SSY and for the deep notch SE(B) specimen (plane strain and 3-D). As in the description of J-Q results, we plot the evolution of σ_w against J_{avg} rather than J_{local} for the 3-D analyses. Fig. 9 (a) shows that σ_w-values for the SE(B) models coincide with SSY at low loads. As deformation levels increase the plane strain SE(B) results diverge from SSY followed by the 3-D, plane sided results. This deviation from SSY defines the *loss of constraint* in SE(B) specimens. To more easily define the deformation levels at constraint loss, the results in Fig. 9 (a) may be interpreted as shown in Fig. 9 (b). Cleavage fracture occurs at a critical values of σ_w. Therefore, the ratio of J-values (J_{avg}/J_0) necessary to obtain a specified critical σ_w-value becomes the quantitative measure of deviation from SSY.

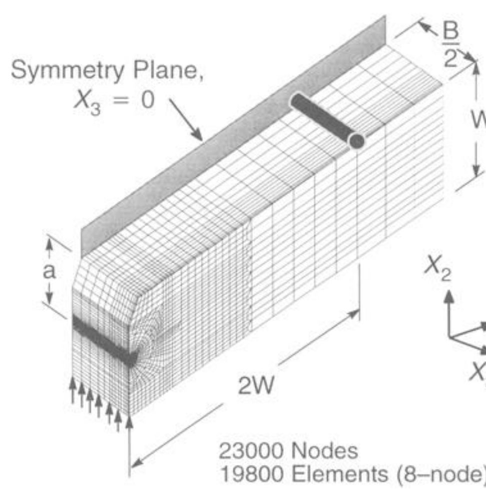

FIG. 8 3-D finite element mesh of SE(B) specimen to compute Weibull Stress.

Figures 10 (a) and (b) show the relationship between J-ratios (J_{avg}/J_0) and normalized deformation in the SE(B) ($M = b\sigma_0/J_{avg}$) for the $n = 10$ case . This normalization of J_{avg} yields values of the deformation limit (M) along the abscissa with deformation in-

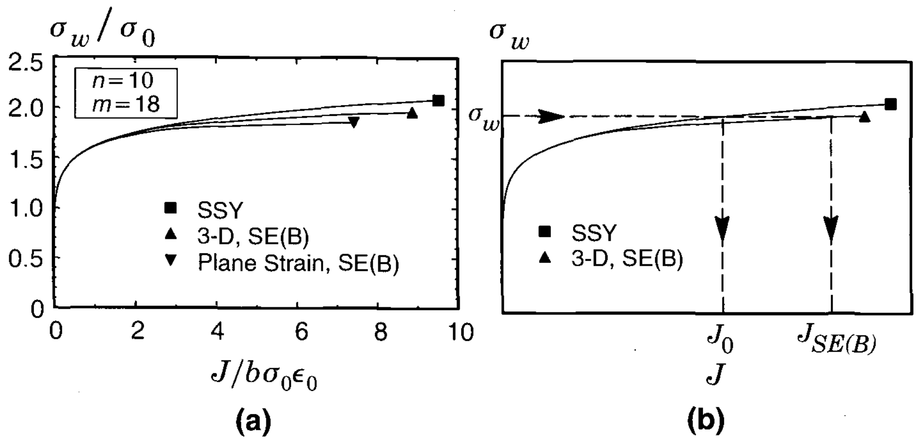

FIG. 9 Weibull stress for SSY and SE(B). (a) Comparison of plane strain and 3-D Weibull stress to SSY. (b) Schematic representation of method used to develop SE(B) deformation limits.

creasing as *M decreases.* The Weibull stress, Eq. (9), is evaluated using a typical value of $m = 18$. Extensive analyses [44] show that M depends weakly on m over typical ranges ($m = 10 \sim 20$). At low loads, the J-ratios all equal 1.0, and SSY conditions exist within the three SE(B) models (plane strain, 3-D plane sided, 3-D side-grooved). As deformation increases, J_{avg}/J_0 deviates from 1.0 and the models indicate a loss of constraint. Allowing a deviation from strict SSY conditions of $J_{avg}/J_0 = 1.2$, Fig. 10 (a) indicates a deformation level of $M = 85$ for the side-groove model. This same deviation from SSY yields a deformation level of $M = 145$ in the 3-D, plane sided model and $M = 180$ for the plane strain model. While these M-values are somewhat dependent on the J-ratios, we observe that adopting $J_{avg}/J_0 = 1.2$ implies only a 10% deviation in the corresponding values of K_I. This choice of J-ratio requires engineering judgement; we proceed with $J_{avg}/J_0 = 1.2$ based upon our experience in previous analyses. The decreasing deformation limits (smaller M values) in 3-D exhibit the same *trend* determined by ND [39]. However, the M values here are significantly less generous than those determined by the Toughness Scaling Model (TSM) (see ND). The TSM M-values are determined at the mid-plane of deeply notched SE(B) whereas M-values from σ_w (as shown in Fig. 10 (a)) effectively represent a through-thickness average. Figure 10 (b) indicates deformation limits from σ_w calculated at the centerplane of the 3-D SE(B), and these limits ($M = 85$, 100 for the plane-side and side-groove models, respectively) show good agreement with the TSM.

CONCLUDING REMARKS

Characterization of constraint effects on cleavage fracture toughness using a correlative approach involves a two-parameter description of crack tip fields. The paper shows that parameters J and Q suffice to quantify a wide range of near-tip constraint states at the onset of fracture. J sets the size scale of the zone of high stresses and large deformations while Q scales the near-tip stress level relative to a high triaxiality reference stress state. The J-Q methodology serves as a basis for extending fracture mechanics methodology and enables construction of experimentally derived fracture toughness

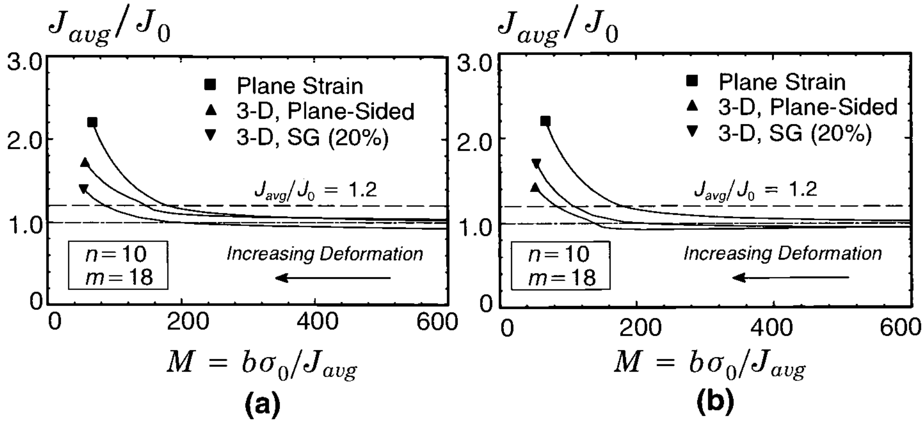

FIG. 10 Deformation limits based on Weibull stress computed (a) as a through thickness average, (b) at the centerplane of the model.

loci, rather than conventional, single-valued definition of toughness. The representative 3-D solutions and associated toughness loci presented in the paper demonstrate the utility and relative simplicity of this approach.

The success in correlating fracture conditions across different crack geometries/loading modes of the same material depends on how well the experimental toughness locus represents the *actual* fracture process in J-Q space (see Fig. 6). The experimental determination of a toughness locus can become very costly, requiring considerable material and testing time, especially if toughness data are needed for varying test temperatures. Additional complications related to the inherent scatter of measured values of fracture toughness also introduce difficulties in the correlative methodology. Furthermore, because the J-Q parameters are essentially 2-D quantities, extension of this correlative approach within a 3-D framework still remains a open issue.

To model the statistics of microcracks and the pronounced effects on scatter of measured J_c-values in the transition region for ferritic materials, a local approach based upon the Weibull stress, σ_w, appears very promising. This near-tip, or *local,* fracture parameter reflects the different rates at which near-tip stresses increase with applied J (and the corresponding reduction in the size of the process zone for cleavage fracture) due to constraint loss in different specimen geometries or crack configurations with varying levels of crack-tip stress triaxiality. Micromechanics considerations permit establishing a simple fracture criterion: unstable crack propagation occurs when σ_w attains a critical value.

Applications of this methodology in fracture assessments require mechanical testing, fracture testing and nonlinear finite element analyses for the cracked structure. In contrast to the J-Q approach, the σ_w-based local approach provides a means to *predict* the effects of constraint variations and the distribution of measured values of fracture toughness across different geometries and structures; it enables quantifying the probability of failure of structural components. However, the use of local approaches in fracture assessments is not without limitations. It is essential that parameters characterizing the micromechanics model, particularly the Weibull modulus (m,) be sufficiently representative of the actual fracture process. Unfortunately, adequate calibration of the parameter m is not a simple task, especially when only limited number of fracture toughness data are available. Further refinements of the model, such as the use of a threshold stress, are necessary to establish a realistic, robust local approach for cleavage fracture.

Acknowledgments

This investigation was supported by grants principally from the U.S. Nuclear Regulatory Commission, the Naval Surface Warfare Center-Annapolis Detachment and the NASA-Ames Research Center. Access to the Cray C-90 was provided by the National Aerodynamic Simulator facility (NAS) at NASA-Ames and by a grant of HPC resources from the DoD HPC Centers at the Waterways Experiment Station and the Stennis Space Center.

References

[1] Rice, J.R., "A Path Independent Integral and the Approximate Analysis of Strain Concentration by Notches and Cracks," *Journal of Applied Mechanics*, Vol. 35, pp. 379-386, 1968.

[2] Hutchinson, J.W., "Fundamentals of the Phenomenological Theory of Nonlinear Fracture Mechanics," *Journal of Applied Mechanics*, Vol. 50, pp. 1042-1051, 1983.

[3] Betegon, C., and Hancock, J.W., "Two-Parameter Characterization of Elastic-Plastic Crack Tip Fields," *Journal of Applied Mechanics*, Vol. 58, pp. 104-113, 1991.

[4] Du, Z.-Z., and Hancock, J.W., "The Effect of Non-Singular Stresses on Crack-Tip Constraint," *Journal of Mechanics and Physics of Solids*, Vol. 39, pp. 555-567, 1991.

[5] Parks, D.M., "Advances in Characterization of Elastic-Plastic Crack-Tip Fields," in *Topics in Fracture and Fatigue*, A. S. Argon, Ed., Springer Verlag, pp. 59-98, 1992.

[6] O'Dowd, N.P., and Shih, C.F., "Family of Crack-Tip Fields Characterized by a Triaxiality Parameter: Part I - Structure of Fields," *Journal of the Mechanics and Physics of Solids*, Vol. 39., No. 8, pp. 989-1015, 1991.

[7] O'Dowd, N.P., and Shih, C.F., "Family of Crack-Tip Fields Characterized by a Triaxiality Parameter: Part II - Fracture Applications," *Journal of the Mechanics and Physics of Solids*, Vol. 40, pp. 939-963, 1992.

[8] Li, Y.C., and Wang, T.C., "Higher-Order Asymptotic Field of Tensile Plane-Strain Nonlinear Crack Problem," *Scientia Sinica (Series A)*, Vol. 29, pp. 941-955, 1986.

[9] Sharma, S.M. and Aravas, N. *Journal of Mechanics and Physics of Solids*, Vol. 39, pp. 1043-1072, 1991.

[10] Xia, L., Wang, T.C. and Shih, C.F., "Higher-Order Analysis of Crack-Tip Fields in Power Law Hardening Materials," to appear in *Journal of Mechanics and Physics of Solids.*

[11] Yang, S., Chao, Y.J. and Sutton, M.A., "Higher Order Terms in Two-Dimensional Analysis of Crack Tip Fields in Elastic-Plastic Bodies", *Engineering Fracture Mechanics*, Vol. 45, pp. 1-20, 1993.

[12] Chao, Y.J. and Sutton, M.A., "On the Fracture of Solids Characterized by One or Two Parameters", *Journal of Mechanics and Physics of Solids*, Vol. 42, pp. 629-647, 1994.

[13] Sumpter, J., "An Experimental Investigation of the *T*-Stress Approach," *Constraint Effects in Fracture, ASTM STP 1171*, E.M. Hackett, K.H. Schwalbe, and R.H. Dodds, Eds., American Society for Testing and Materials, Philadelphia, pp. 492-502, 1993.

[14] Faleskog, J., "Effects of Local Constraint Along Three Dimensional Crack Fronts—A Numerical and Experimental Investigation," *Journal of the Mechanics & Physics of Solids*, V. 43, pp. 447-493, 1995.

[15] Evans, A. G., "A General Approach for the Statistical Analysis of Multiaxial Fracture," *Journal of American Ceramic Society*, Vol. 61, pp. 302–308, 1978.

[16] Beremin, F.M, "A Local Criterion for Cleavage Fracture of a Nuclear Pressure Vessel Steel," *Metallurgical Transactions*, Vol. 14A, pp. 2277-2287, 1983.

[17] Brückner-Foit, A. and Munz, D., "Prediction of Failure Probabilities for Cleavage Fracture From The Scatter of Crack Geometry and of Fracture Toughness Using the Weakest Link Model", *Engineering Fracture Mechanics*, V18, N2, pp. 359-375, 1983.

[18] Wallin, K., Saario, T., and Torronen, K., "Statistical Model for Carbide Induced Brittle Fracture in Steel," *Metal Science*, Vol. 18, pp. 13-16, 1984.

[19] Wallin, K. "The Scatter in K_{Ic} Results," *Engineering Fracture Mechanics,* Vol. 19, pp. 1085-1093, 1984.

[20] Lin, T., Evans, A. G. and Ritchie, R. O., 1986, "A Statistical Model of Brittle Fracture by Transgranular Cleavage", *Journal of Mechanics and Physics of Solids,* Vol. 21, pp. 263–277, 1986.

[21] Brückner–Foit, A., Ehl, W., Munz, D. and Trolldenier, B., "The Size Effect of Microstructural Implications of the Weakest Link Model", *Fatigue and Fracture of Engineering Materials and Structures,* Vol. 13, pp. 185–200, 1990.

[22] Ruggieri, C., Minami, F. and Toyoda, M.,"The Local Approach to the Effect of Notch Depth on Fracture Toughness" in *9^{th} European Conference on Fracture (ECF9)*, Vol.I, pp. 621–626, Varna, Bulgaria, 1992.

[23] Mudry, F., "A Local Approach to Cleavage Fracture," *Nuclear Engineering and Design,* Vol. 105, pp. 65-76, 1987.

[24] Pineau, A., "Global and Local Approaches to Fracture-Transferability of Laboratory Test Results to Components," in *Topics in Fracture and Fatigue,* A. S. Argon, Ed., Springer Verlag, pp. 197-234, 1992.

[25] Minami, F., Brückner–Foit, A., Munz, D.and Trolldenier, B., "Estimation Procedure for the Weibull Parameters Used in the Local Approach," *International Journal of Fracture,* Vol. 54, pp. 197–210, 1992.

[26] Ruggieri, C., and Dodds, R. H., "A Transferability Model for Brittle Fracture Including Constraint and Ductile Tearing Effects: A Probabilistic Approach," *International Journal of Fracture,* Vol. 79, pp. 309–340, 1996.

[27] Ruggieri, C. and Dodds, R. H., "WSTRESS: Numerical Computation of Probabilistic Fracture Parameters". *Structural Research Series (SRS) 608,* UILU–ENG–95–2013, University of Illinois at Urbana–Champaign, 1996.

[28] Dodds, R.H., Anderson, T.L.,and Kirk, M.T., "A Framework to Correlate a/W Ratio Effects on Elastic-Plastic Fracture Toughness (J_c)," *International Journal of Fracture,* Vol. 48, pp. 1-22, 1991.

[29] Anderson, T.L. and Dodds, R.H., "Specimen Size Requirements for Fracture Toughness Testing in the Ductile-Brittle Transition Region," *Journal of Testing and Evaluation,* Vol. 19, pp. 123-134, 1991.

[30] Brocks, W., and Schmidt, W., "Quantitative Assessment of the Role of Crack Tip Constraint on Ductile Tearing," *Constraint Effects in Fracture, ASTM STP 1171,* E.M. Hackett, K.H. Schwalbe, and R.H. Dodds, Eds., American Society for Testing and Materials, Philadelphia, pp. 64-78, 1993.

[31] Roos, E., Eisele, U., and Silcher, H., "Effect of Stress State on Ductile Fracture behavior of Large-Scale Specimens," *Constraint Effects in Fracture, ASTM STP 1171,* E.M. Hackett, K.H. Schwalbe, and R.H. Dodds, Eds., American Society for Testing and Materials, Philadelphia, pp. 41-63, 1993.

[32] Bilby, B.A., Cardew, G.E., Goldthorpe, M.R. and Howard, I.C., "Size Effects in Fracture," *Institution of Mechanical Engineers,* London, England, pp. 36-46, 1986.

[33] Rice, J.R., and Rosengren, G.F., "Plane Strain Deformation Near a Crack Tip in a Power-Law Hardening Material," *Journal of Mechanics and Physics of Solids,* Vol. 16, pp. 1-12, 1968.

[34] Hutchinson, J.W., "Singular Behavior at the End of a Tensile Crack in a Hardening Material," *Journal of Mechanics and Physics of Solids,* Vol. 16, pp. 13-31, 1968.

[35] McMeeking, R.M., and Parks, D.M., "On Criteria for J-Dominance of Crack-Tip Fields in Large-Scale Yielding," *Elastic-Plastic Fracture, ASTM STP 668,* J.D. Landes, J.A. Begley, and G.A. Clark, Eds., American Society for Testing and Materials, Philadelphia, Pennsylvania, pp.175-194, 1979.

[36] Williams, M.L., *Journal of Applied Mechanics,* Vol. 24, pp. 109-114, 1957.

[37] Koppenhoefer, K., Dodds, R. H., "Constraint Effects on Fracture Toughness of Impact Loaded, Pre-Cracked Charpy Specimens", *Nuclear Engineering and Design,* Vol. 162, pp. 145–158, 1996.

[38] Dodds, R. H., Shih, C. F., and Anderson, T. L. "Continuum and Micro–Mechanics Treatment of Constraint in Fracture," *International Journal of Fracture,* Vol. 64, pp. 101–133, 1993.

[39] Nevalnien, M., and Dodds, R. H. "Numerical Investigation of 3–D Constraint Effects on Brittle Fracture in SE(B) and C(T) Specimens," *International Journal of Fracture,* Vol 74, pp. 131–161, 1995.

[40] Tetelman, A. S. and McEvily, A. J., *Fracture of Structural materials,* John Wiley & Sons, New York, 1967.

[41] Smith, E., "Cleavage Fracture in Mild Steel", *International Journal of Fracture Mechanics,* Vol. 4, pp. 131–145, 1968.

[42] Bakker, A. and Koers, R. W. J., "Prediction of Cleavage Fracture Events in the Brittle-Ductile Transition Region of a Ferritic Steel" in *Defect Assessment in Components – Fundamentals and Applications, ESIS/EG9,* Blauel and Schwalbe, Eds., Mechanical Engineering Publications, London, pp. 613–632, 1991.

[43] Koers, R. W. J., Krom, A. H. M. and Bakker, A. "Prediction of Cleavage Fracture in the Brittle to Ductile Transition Region of a Ferritic Steel" in *Constraint Effects in Fracture – Theory and Applications, ASTM STP 1244,* Kirk and Bakker, Eds., American Society for Testing and Materials, Philadelphia, pp. 191–208, 1995.

[44] Koppenhoefer, K., Dodds, R. H., Manuscript in preparation.

Donald E. McCabe[1] and John G. Merkle[1]

ESTIMATION OF LOWER-BOUND K_{Jc} ON PRESSURE VESSEL STEELS FROM INVALID DATA

REFERENCE: McCabe, D. E., and Merkle, J. G., **"Estimation of Lower-bound K_{Jc} on Pressure Vessel Steels from Invalid Data,"** *Fatigue and Fracture Mechanics: 28th Volume, ASTM STP 1321*, J. H. Underwood, B. D. Macdonald, and M. R. Mitchell, Eds., American Society for Testing and Materials, 1997.

ABSTRACT: Statistical methods are currently being introduced into the transition temperature characterization of ferritic steels. The objective is to replace imprecise correlations between empirical impact test methods and universal K_{Ic} or K_{Ia} lower-bound curves with direct use of material-specific fracture mechanics data. This paper will introduce a computational procedure that couples order statistics, weakest-link statistical theory, and a constraint model to arrive at estimates of lower-bound K_{Jc} values. All of the above concepts have been used before to meet various objectives. In the present case, the scheme is to make a best estimate of lower-bound fracture toughness when resource K_{Jc} data are too few to use conventional statistical analyses. The utility of the procedure is of greatest value in the middle-to-high toughness part of the transition range where specimen constraint loss and elevated lower-bound toughness interfere with the conventional statistical analysis methods.

KEYWORDS: fracture toughness, K_{Ic}, K_{Jc}, lower bound, constraint, order statistics, weakest link

---

INTRODUCTION

Good progress is being made relevant to the problem of defining the transition temperature of ferritic steels. The problem has been in learning how to deal with excessive scatter in fracture mechanics data based on K_{Ic} and/or K_{Jc} values. Statistical methods are now being used to model the data scatter patterns and to pinpoint the

---

[1]Metals and Ceramics and Engineering Technology Divisions, respectively, Oak Ridge National Laboratory, P.O. Box 2008, Oak Ridge, TN, 37831-6151, managed by Lockheed Martin Energy Research Corp. under contract DE-AC05-96OR22464 for the U.S. Department of Energy.

characteristics that can be used to more accurately compare one material or material condition with another.

Values of K_{Jc} are now being used that imply elastic-plastic stress intensity factors determined at the point of onset of cleavage fracture. Such instabilities are triggered by minute microstructural impurities that are almost always present in commercially produced steels. These can be carbides and/or nonmetallic inclusions of varied sizes that are scattered randomly throughout the microstructure [1]. To trigger cleavage, a particle must be of a critical size and by chance be located within the highly stressed volume of material local to the crack tip [2]. The resulting scatter of K_{Jc} data due to this probabilistic phenomenon usually produces ratios of from 2 to 3 times between the lowest to the highest values; assuming, of course, that data replication is sufficient to demonstrate this. It follows that crack tip volume sampling effects that produce data scatter can also lead to a statistical thickness effect in which large specimens tend to exhibit lower toughness than small specimens. This can be explained by using a statistical weakest-link theory.

In general, statistical methods have been able to explain much of what has been observed experimentally. However, there are other influential conditions that need to be taken into account as well. As already mentioned, cleavage fracture is triggered by particles of a critical size exposed to a critical tritensile combination of stress and plastic strain that develops along the crack front. The stress ratios and plastic strain magnitudes are controlled by the degree of crack tip constraint. Therefore, constraint must be well managed to successfully use statistical models on the data. Constraint is a function of material strength, specimen thickness, and specimen or component geometry. This aspect of transition range behavior has generated a second and somewhat independent focal point for research work [3]. Care can be taken to control constraint in laboratory tests, but the application of laboratory-generated data to engineering problems requires added attention to possible constraint differences.

This paper uses both statistical and constraint modeling to deal with the special problems sometimes encountered in engineering applications. We will consider the case where the background data are too few to use conventional statistics, and show a method of imposing extrapolation limits on the weakest-link size effect model to generate an estimate of the lower bound of fracture toughness.

Background information will be covered first that applies to the more precise determination of median K_{Jc} and standard deviation that is possible when a sufficient data sampling plan is used. This approach will provide benchmark information for comparison to the backup method of lower certainty proposed here.

BACKGROUND ON STATISTICAL MODELS

The three-parameter Weibull statistical model has been chosen as the best one to fit K_{Jc} data distributions [4]. It has the versatility to fit a wide variety of data distributions, one of which is the typical fracture mechanics-based fracture toughness data distribution.

Cumulative probability for failure, P_f, at or before stress intensity driving level, K_{Jc}, is calculated by the following modification of the three-parameter Weibull equation:

$$P_f = 1 - \exp\left\{ - \left[\frac{(K_{Jc} - K_{min})}{(K_o - K_{min})} \right]^b N \right\} . \tag{1}$$

Parameters K_o, K_{min}, and b are three Weibull data population fitting constants obtained from data sampling. The model of Eq. (1) also shows a fourth parameter, N, that describes the phenomenon of weakest-link behavior that develops only in the low-to-middle part of the transition range of fracture toughness. Term N is a size ratio and, for test specimens of different sizes where all dimensions are scaled proportionally, specimen thickness is used; i.e., $N = B_2/B_1$. In theory, the dimension B_1 is arbitrary and once B_1 is selected, K_o is determined by the order statistics of sample data. For example, when replicate tests are made on specimens of thickness B_1 and median $K_{Jc(1)}$ has been determined, median $K_{Jc(2)}$ for specimens of thickness B_2 can be calculated using the following relationship:

$$K_{Jc(2)} = (K_{Jc(1)} - K_{min})(1/N)^{1/b} + K_{min} . \tag{2}$$

Equation (2) is derived from Eq. (1) and it models the weakest-link size effect described earlier. The trend set by Eq. (2) has been extended outside the range covered by typical test specimen sizes for predicting large flaw effects in engineering applications [5]. Crack size ratio instead of thickness is then used in term N. The end point of extrapolation on Eq. (2) is 20 MPa√m and the present work will propose an existence of a truncation point at higher K_{Jc} values based on a constraint limit rationale. To obtain the three Weibull parameters of Eq. (1) that represent the total data population, it is important to know how large the data sampling must be. Early Weibull parameter fitting work was done without such consideration [4]. Subsequently, Wallin [6] conducted a much-needed sensitivity study and it was determined that parameters K_{min} and Weibull slope, b, require huge numbers of replicate tests; of the order of 50 to 100. However, in this same study, it was determined that when K_{min} is set to 20 MPa√m, Weibull slope for ferritic steels tended to centralize to a constant value of 4. Data were taken from several experiments to demonstrate the centralizing tendency with increased sample size described above. This discovery has been used to convert what had been an interesting technical observation into a practical engineering tool that is amenable to standardization practices. Hence, Eqs. (1) and (2) become more consistent and universally reproducible. To determine the Weibull scale parameter, K_o, requires only 6 replicate tests. With Weibull slope known and essentially constant, the standard deviation, σ, on data scatter is precisely characterized from the following [7]:

$$\sigma = 0.28\ K_{Jc(med)} \left(1 - \frac{20}{K_{Jc(med)}} \right) \quad MPa\sqrt{m}\ , \tag{3}$$

where $K_{Jc(med)}$ is the calculated median toughness value.

Equations (1) through (3), used with the two fixed Weibull parameters, have been tested repeatedly with experimental results and, although small data samplings cannot always accurately match and confirm the two fixed parameters, the evidence of the centralizing tendency to these values is quite convincing.

Finally, Wallin [6] has determined that the median of K_{Jc} fracture toughness for ferritic steels will fit a common transition curve; namely, 1T compact and bend bar specimens (25 mm thick) will fit the following curve:

$$K_{Jc(med)} = 30 + 70\ \exp\ [0.019(T - T_o)] \quad MPa\sqrt{m}\ . \tag{4}$$

This curve is known as the "master curve," and it can be noted that Eq. (4) is of the same mathematical form as the American Society of Mechanical Engineers (ASME) *Boiler and Pressure Vessel Code* equations for static lower-bound K_{Ic} and crack arrest K_{Ia}. In those cases, the curves are positioned using reference temperature, RT_{NDT} [8]. For the master curve, reference temperature is T_o and, when test temperature, T, is set at the reference temperature, $K_{Jc(med)}$ is 100 MPa√m.

Again, the concepts presented to this point will be used to set the more exact characterization of fracture toughness. The following sections deal with an application that is specialized toward seeking a lower bound of K_{Jc} fracture toughness for the data distribution of the material. It will be assumed that sample size is insufficient. A constraint-based model is then applied to a lower-bound K_{Jc} estimate to find a safe K_{Jc} value for use in engineering applications.

ORDER STATISTICS

Steinstra et al. [9] have described how lower-bound tolerance estimates on K_{Jc} can be made from small data samplings. The method is aided by having prior knowledge of the Weibull slope of the data population. When K_{Jc} values are arranged in order of increasing magnitude, the cumulative probability value can be estimated independently from each datum using the so-called "Beta distribution estimator." These estimates are determined for a discretionally selected value of cumulative probability. For example, $P_f = 0.10$ will be used predominantly here. At the same time, one must choose a confidence level on the determination. The concept involves the development of a set of coefficients, η, that, when multiplied by ranked data, will provide estimates of $K_{Jc(0.1)}$

values that are expected to reside in the 10% lower tail of the population distribution. The process of developing the multiplier coefficients is explained in detail elsewhere [8]. Table 1 is an example of such coefficients, set up to cover from one to six data sample sizes.

TABLE 1--Coefficient, "η," for $P_f = 0.10$ and 90% confidence on the estimate.

K_{Jc} rank	Number of tests 1	2	3	4	5	6
1	0.4625	0.550	0.6087	0.6541	0.6916	0.7239
2		0.434	0.5042	0.5516	0.5888	0.6198
3			0.4206	0.4822	0.5238	0.5564
4				0.4122	0.4686	0.5062
5					0.4062	0.4587
6						0.4016

A hypothetical example will be used here to illustrate the use of order statistics (see Fig. 1). Assume three 1T compact specimens had been tested at 100°C, giving K_{Jc} values of 165, 190, and 235 MPa√m. These are ranked as shown in Table 2 and the appropriate coefficients from Table 1 are assigned (column 3).

TABLE 2--Estimates of K_{Jc} at or below the $P_f = 0.10$ level.

Rank	K_{Jc} (MPa√m)	Coefficient (η)	$K_{Jc(0.1)}$ (MPa√m)
1	165	0.6087	108
2	190	0.5042	106
3	235	0.4026	110

The Beta distribution estimation assumes two-parameter Weibull with a slope of 4; so for a three-parameter model, the following equation was used:

$$K_{Jc(0.1)} = (K_{Jc} - 20)\,\eta + 20 \quad \text{MPa}\sqrt{\text{m}}\ . \tag{5}$$

The solid and dashed curves in Fig. 1 represent the assumed master curve characteristic of the material population. The true K_{Jc} at the 10% tolerance bound of the data population is about 140 MPa√m and the filled square datum approximates the order statistic placement of all three order statistic estimates. Such values, when based on few data, carry the potential of being overly conservative. The following order statistic example will be based on actual experimental data.

Figure 2 shows a master curve and tolerance bound developed from the testing of about 150 1T compact specimens. The data came from a round-robin activity sponsored by the Materials Properties Council and the Japanese Society for the Promotion of Science [10]. Eighteen laboratories were involved. A 508 class 2 steel was tested at three test temperatures: −50, −75, and −100°C. Duplication for each variable (test temperature and laboratory) was five specimens. In this case, the order statistic exercise was to determine how well each data set could predict the lower tolerance bound of the master curve. The 10% tolerance bound on the master curve was margin adjusted 16°C to cover the uncertainty in reference temperature, T_o, from the five-specimen sample size. A 95% confidence level is imposed.[2] The same tolerance bound and confidence level was imposed on the order statistic estimates. Clearly, the order statistics estimates related well to the more rigorous determinations of the three-parameter Weibull method.

ADJUSTMENT TO LOWER-BOUND TOUGHNESS

Equation (2) can follow the size effect trend of median K_{Jc} values suitably for data obtained from test specimens. However, some questions arise when the test temperature is high in the transition range and when the equation is used on in-service flaws that could perhaps be an order of magnitude or more larger than that of the test specimens. Observe that predicted $K_{Jc(2)}$ in Eq. (2) will tend toward 20 MPa√m as size ratio tends to infinity. It is argued here that such a trend will cease to be maintained as upper-shelf temperature is approached and the model should break down. It seems only reasonable to expect that real K_{min} must rise to J-R curve levels at the upper-shelf part of the transition range. In addition, it is important to recognize that K_{min} = 20 MPa√m is used as a deterministic parameter of the Weibull model and there must be some departure between the model and real material behavior at temperatures high in the transition range [11,12]. Figure 3 depicts how this departure is envisioned. Here, 1T compact specimens are tested at a test temperature where the median K_{Jc} is 300 MPa√m. The distribution for 10T compact specimens is calculated using weakest-theory. A constraint-based data truncation point is calculated to be at 144 MPa√m using a procedure that is to be covered presently. K_{Jc} data to the left of the vertical line cannot be developed experimentally, irrespective of the specimen size used. To experimentally demonstrate the phenomenon at such temperatures as depicted here is difficult for more than one reason. In Fig. 3, it appears that the smaller 1T specimens have an advantage against data truncation because only 3% of the possible test data are influenced. However, small specimens will develop severe top-end K_{Jc} data loss due to excessive loss of constraint; a subject not addressed in this paper. On the other hand, an experiment with adequate numbers of 10T specimens would never be considered practical.

---

[2]Test Method for the Determination of Reference Temperature, T_o, for Ferritic Steels in the Transition Range, Appendix C, Draft 12, American Society for Testing and Materials, January 31, 1996.

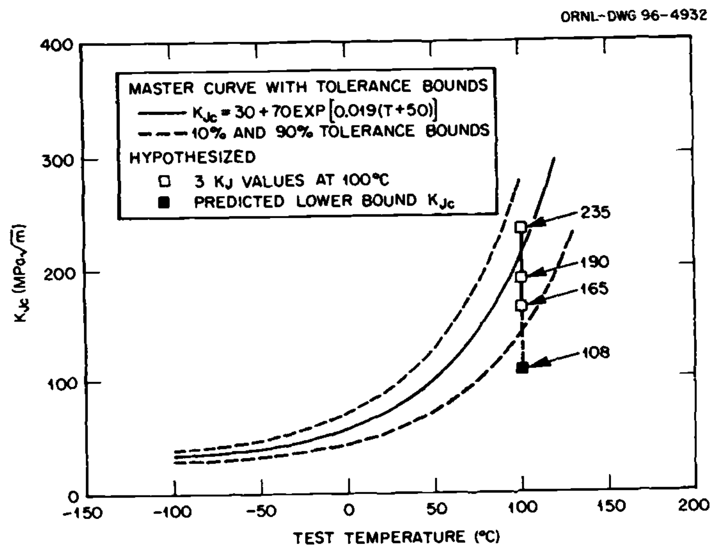

FIG. 1--Schematic representation of a three-specimen sample from material defined by the master curve with 10% and 90% tolerance bounds.

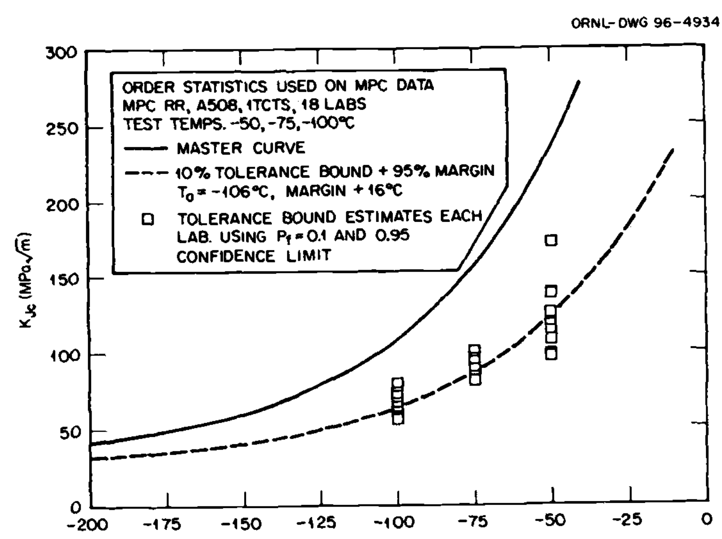

FIG. 2--Data for A 508 class 2 steel from 18 participating laboratories from a round robin sponsored by the Materials Properties Council and the Japanese Society for the Promotion of Science. Each data point represents an estimate of the 10% tolerance bound from five replicate tests.

DETERMINATION OF LOWER-BOUND K_{Jc} TOUGHNESS

The constraint model to be applied here emanates from the most senior model used in the technology of fracture mechanics [13]. We assume that the critical maximum constraint is achieved when thickness, B_2, satisfies the following inequality:

$$B_2 > \alpha_o \, (K_{Jc}/\sigma_{ys})^2 \, . \tag{6}$$

The right side of Eq. (6) can be input into ratio N of Eq. (2) to project the trend of K_{Jc} decrease with increased thickness. Then an equation of the following cubic form results:

$$\left(\frac{K_{Jc(2)}}{K_{min}}\right)^{3/2} - \left(\frac{K_{Jc(2)}}{K_{min}}\right)^{1/2} - 2G = 0 \, , \tag{7}$$

$$\text{where } 2G = \left(\frac{K_{Jc(0.1)}}{K_{min}} - 1\right)\left(\frac{\sqrt{B_1/\alpha_o}}{K_{min}/\sigma_{ys}}\right)^{1/2} . \tag{8}$$

The following simple steps will produce a K_{Jc} of maximum constraint if $G > \sqrt{1/(3)^3}$:

$$M_1 = G + \sqrt{G^2 \, (-1/3)^3} \, .$$

$$M_2 = G - \sqrt{G^2 \, (-1/3)^3} \, .$$

$$\text{Let } y = M_1^{1/3} + M_2^{1/3} \, .$$

$$\text{Then } K_{Jc(2)} = y^2 \, (K_{min}) \, . \tag{9}$$

Alternatively, the following empirical power law can be used:

$$K_{Jc(2)} = 44.78(G)^{0.538} \quad MPa\sqrt{m} \ . \tag{10}$$

Substitution of $K_{Jc(2)}$ into Eq. (6) will define the limiting thickness of full constraint where increased specimen thickness will not further reduce K_{Jc}. The choice of α_o to be used in Eqs. (6) and (8) can be based on experimental evidence. If $\alpha_o = 2.5$ were used, $K_{Jc(2)}$ and B_2 would satisfy the validity limits for K_{Ic} [13] in the American Society for Testing and Materials (ASTM) Standard Test Method for Plane-Strain Fracture Toughness of Metallic Materials (E 399). However, experimental work on ferritic steels has indicated that $\alpha_o = 1$ is the more accurate coefficient [14]; this is the value selected to be used in the examples that follow.

Figure 4 is again a schematic example of specimen size effects. It shows the three-parameter Weibull trend of median fracture toughness (solid line), with open squares for 1/2T, 1T, 2T, 4T, and 6T compact specimens, the $P_f = 0.10$ (dotted line) curve is calculated using Eqs. (1) and (2). The open-diamond points represent exact $P_f = 0.1$ predictions for lower-bound K_{Jc} at each specimen thickness. When these lower-bound values, $K_{Jc(0.1)}$, are adjusted using Eqs. (8) and (9), the $K_{Jc(2)}$ values shown as filled squares result. The lower bound of K_{Jc} toughness is defined and the separation between the dashed line and the dotted line indicates the extent of K_{Jc} lower-bound adjustment applied to data distributions.

The Heavy-Section Steel Irradiation Program Fifth Irradiation Series can be used as a challenging example application of the proposed procedure [15]. Test data replications varied from two to nine specimens and specimen sizes varied from 1T to 8T. There were nominally eight test temperatures selected along the transition range. Two materials were submerged-arc welds in A 533 grade B plate (72W and 73W) that differed only in copper content. The ASME reference temperatures (RT_{NDT}) were known precisely (±5°C) for both unirradiated and irradiated conditions.

Figures 5 and 6 show unirradiated K_{Jc} data for 73W (0.31% Cu) material as tabulated (Fig. 5) and then after order statistics and constraint adjustments for lower-bound K_{Jc} have been applied (Fig. 6). Again, the fracture toughness truncation used corresponds to $\alpha_o = 1.0$ in Eq. (6). The ASME lower-bound K_{Ic} curve shown in Fig. 6 is reputed to correspond to a 2% confidence limit (short dash). The 2% cumulative probability tolerance bound line (long dash) based on the master curve is also shown.

Figures 7 and 8 are the same as Figs. 5 and 6, except that the material is weld 72W (0.23% Cu). In this case, lower-bound predictions tend to be a little nonconservative at the low test temperatures.

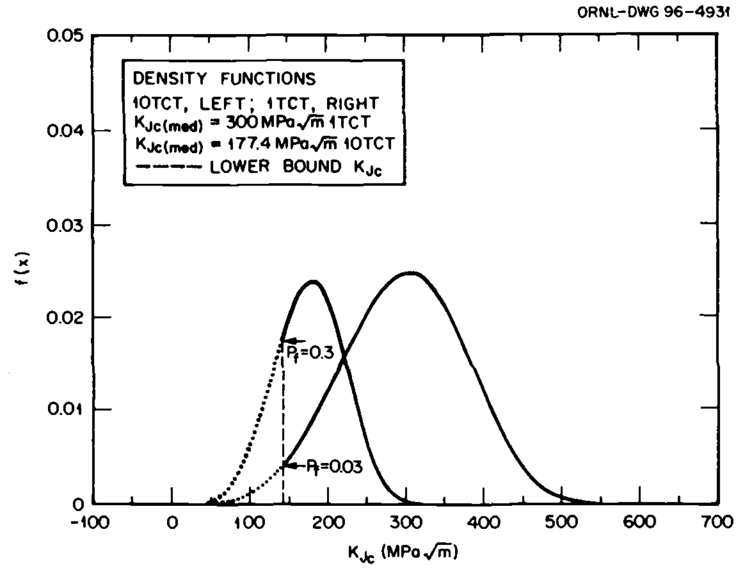

FIG. 3--Density function distributions for 1T C(T) and 10T C(T) specimens showing the effect of a true lower bound on distribution shape.

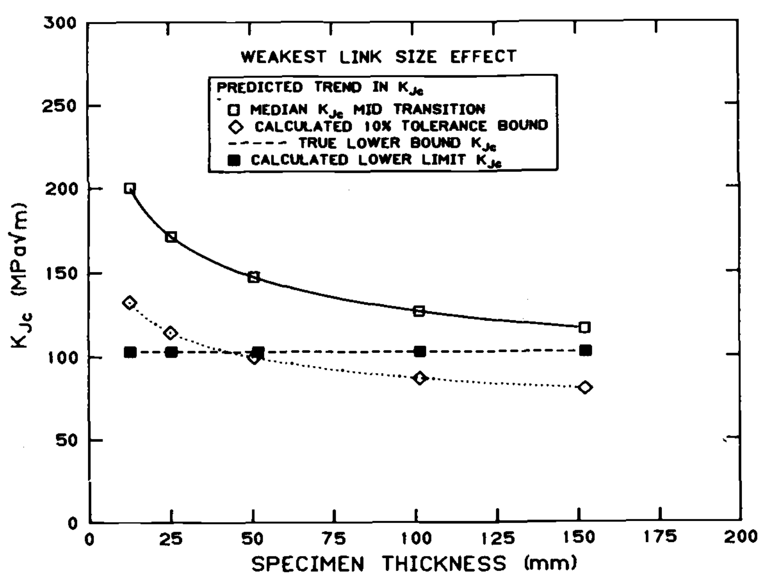

FIG. 4--Three toughness versus specimen size trends showing K_{Jc} median trend by weakest link (open squares), K_{Jc} 10% tolerance bound trend by weakest link (open diamonds), and lower-bound K_{Jc} (dashed line).

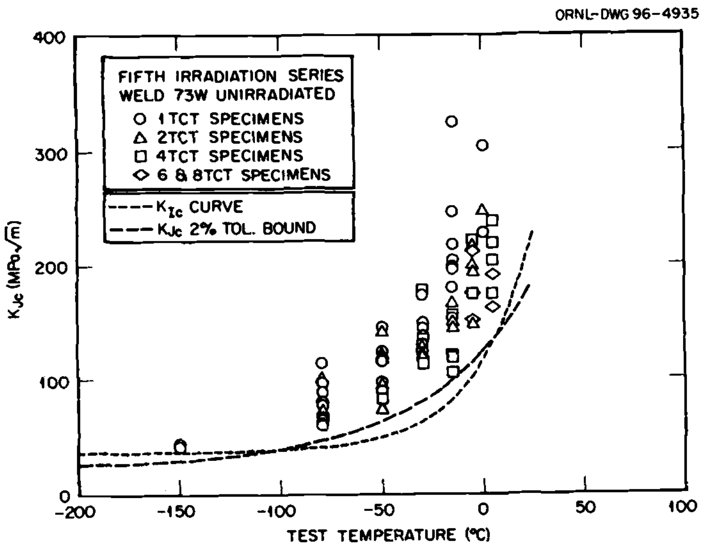

FIG. 5--Unadjusted data, American Society of Mechanical Engineers lower-bound K_{Ic} curve (dotted), and 2% tolerance bound curve (dashed), for weld 73W (A 533 grade B) of the Heavy-Section Steel Irradiation Program Fifth Irradiation Series.

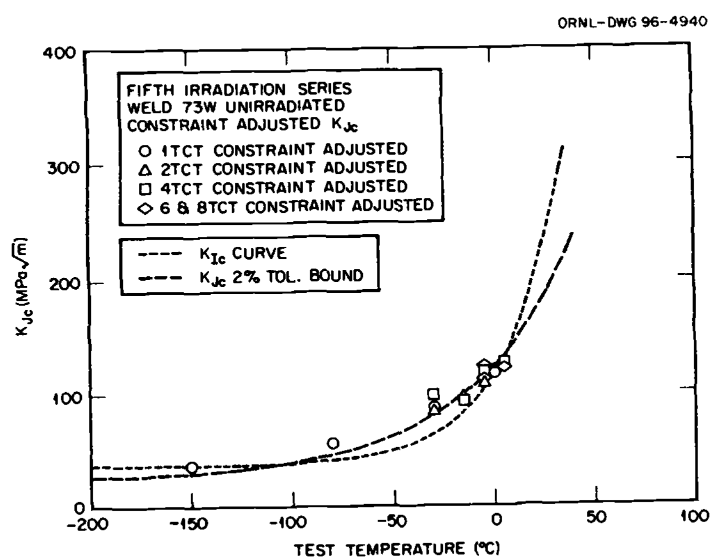

FIG. 6--American Society of Mechanical Engineers K_{Ic} curve (dotted), 2% tolerance bound curve (dashed), and procedurally adjusted lower-bound estimates (data) for Heavy-Section Steel Irradiation Program weld 73W.

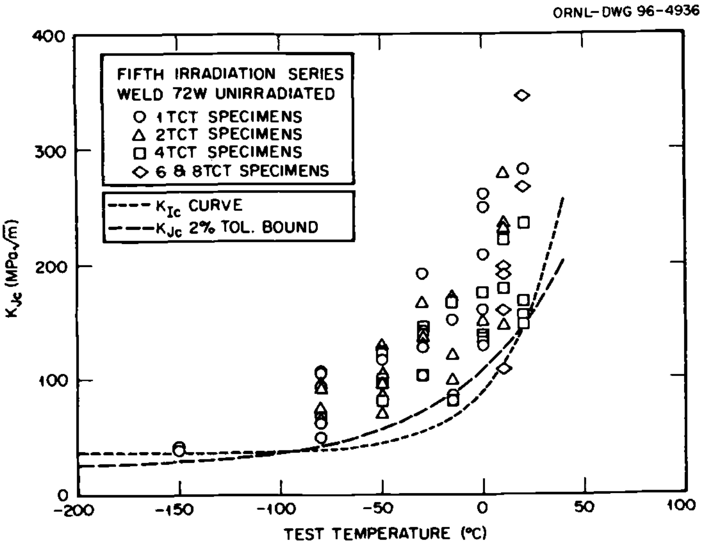

FIG. 7--Unadjusted data, American Society of Mechanical Engineers lower-bound K_{Ic} curve (dotted), and 2% tolerance bound curve (dashed) for Weld 72W of the Heavy-Section Steel Irradiation Program Fifth Irradiation Series.

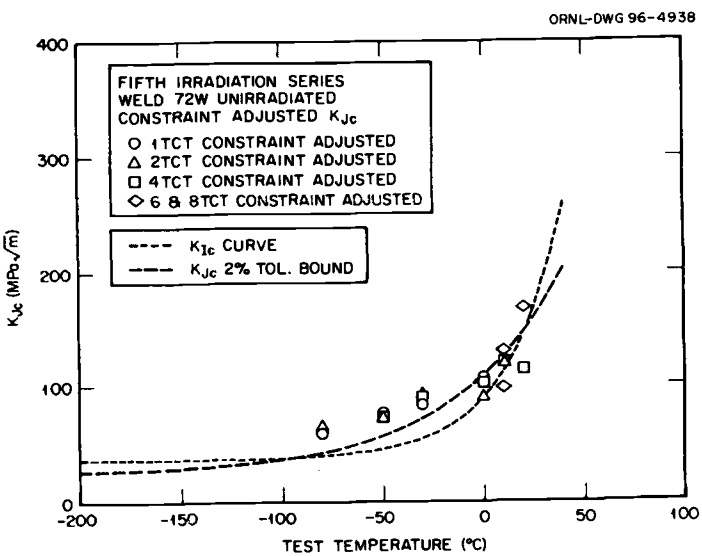

FIG. 8--American Society of Mechanical Engineers K_{Ic} curve (dotted), 2% tolerance bound curve (dashed), and procedurally adjusted lower-bound estimates (data) for Heavy-Section Steel Irradiation Program weld 72W.

Figures 9 and 10 present the same comparison for both materials in the irradiated condition. In this case, 72W and 73W data were combined because the two materials ended up with the same irradiated RT_{NDT} temperature. The adjusted data of Fig. 10 are quite similar to those of Fig. 6, both of which tend to favor the 2% tolerance bound curve.

CONCLUSIONS

This paper proposes a method of analysis that represents a best effort at predicting lower-bound fracture toughness K_{Jc} values when the supporting data are sparse. Order statistics can be used to estimate a K_{Jc} toughness value that is near to lower bound when the data sample is small. The resulting K_{Jc} estimate can be adjusted for specimen size to large flaw size equivalence. A constraint model is used to truncate the statistical weakest-link size effect trend at a size where constraint will cease to increase with increased crack size. This model is of most value in the middle-to-high toughness part of the transition range, where the weakest-link size effect begins to vanish. The lower-bound K_{Jc} estimate may or may not be precisely the same as lower-bound K_{Ic} but, at the same time, it is preferred as an estimate of that value as opposed to the alternative use of impact tests with an assumed correlation to the universal K_{Ic} lower-bound curve.

The methodology presented is flexible in terms of the value of α_0 and/or confidence limits selected and can be adjusted to various levels of conservatism chosen at the discretion of the user. The levels chosen for this paper were selected to follow the transition K_{Ic} lower-bound curve. However, this practice is not proposed to replace the more rigorous statistical practices.[3] The applications are for circumstances where source information is sparse or for engineering applications where the conditions are such that the weakest-link theory cannot properly model the fracture toughness/size effect trend.

ACKNOWLEDGMENTS

This research is sponsored by the Office of Nuclear Regulatory Research, U.S. Nuclear Regulatory Commission, under Interagency Agreement DOE 1886-8011-9B with the U.S. Department of Energy under Contract No. DE-AC05-96OR22464 with Lockheed Martin Energy Research Corp. The authors would like to thank Shafik K. Iskander and Mikhail A. Sokolov for peer review and Julia L. Bishop for preparation of the manuscript.

---

[3]Test Method for the Determination of Reference Temperature, T_o, for Ferritic Steels in the Transition Range, Appendix C, Draft 12, American Society for Testing and Materials, January 31, 1996.

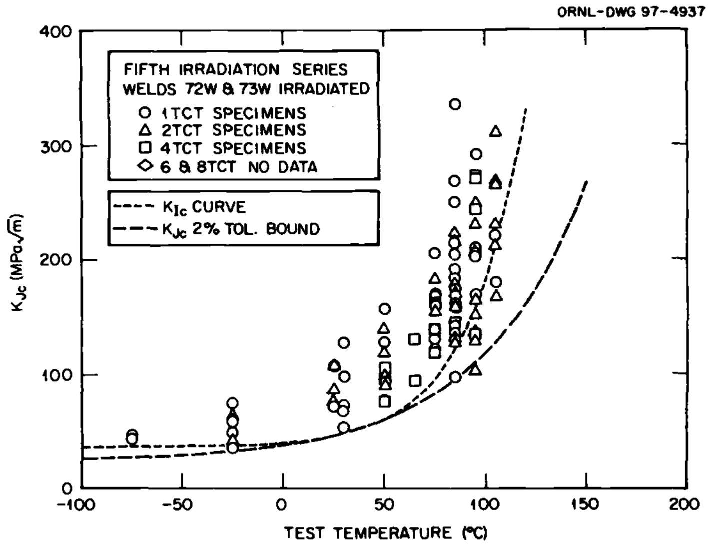

FIG. 9--Unadjusted data, lower-bound K_{Ic} curve (dotted), and 2% tolerance bound curve (dashed) for Heavy-Section Steel Irradiation Program welds 72W and 73W irradiated to a fast neutron fluence of 1.5×10^{19} n/cm^2 (>1 MeV).

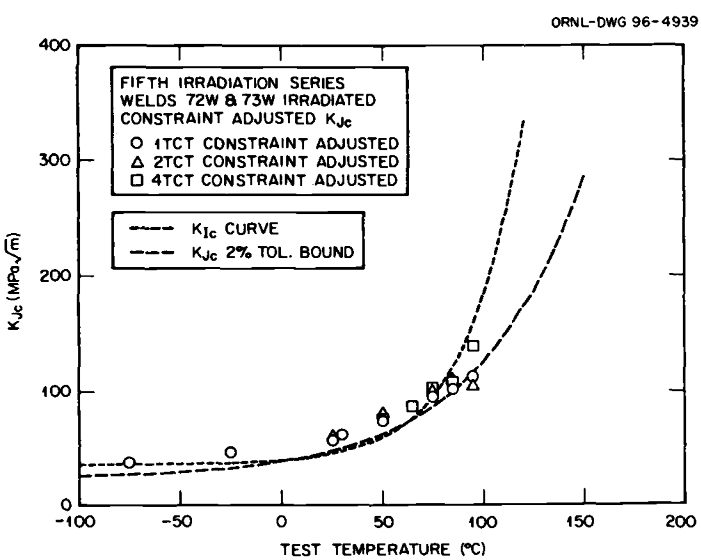

FIG. 10--American Society of Mechanical Engineers K_{Ic} curve (dotted), 2% tolerance bound curve (dashed), and procedurally adjusted to lower-bound data for Heavy-Section Steel Irradiation Program welds 72W and 73W irradiated to a fast neutron fluence of 1.5×10^{19} n/cm^2 (>1 MeV).

REFERENCES

[1] Heerens, J., Read, D. T., Cornec, A., and Schwalbe, K.-H., "Interpretation of Fracture Toughness in the Ductile-to-Brittle Transition Region by Fractographical Observations," pp. 659-678 in *Defect Assessment in Components – Fundamentals and Applications*, ESIS/EGF9, J. G. Blauel and K.-H. Schwalbe, Eds., Mechanical Engineering Publications, London, 1991.

[2] Anderson, T. L. Stienstra, D., and Dodds, R. H., Jr., "A Theoretical Framework for Addressing Fracture in the Ductile-Brittle Transition Region," pp. 186-214 in *Fracture Mechanics: Twenty-Fourth Volume, ASTM STP 1207*, J. D. Landes, D. E. McCabe, and J. A. M. Boulet, Eds., American Society for Testing and Materials, Philadelphia, 1994.

[3] Hackett, E. M., Schwalbe, K.-H., and Dodds, R. H., Jr., Eds., *Constraint Effects in Fracture, ASTM STP 1171*, American Society for Testing and Materials, Philadelphia, 1993.

[4] Landes, J. D., and McCabe, D. E., "Effect of Section Size on Transition Temperature Behavior of Structural Steels," pp. 378-392 in *Fracture Mechanics: Fifteenth Symposium, ASTM STP 883*, R. J. Sanford, Ed., American Society for Testing and Materials, Philadelphia, 1984.

[5] *French Verification of PWR Vessel Integrity*, EPRI NP-6713, Electric Power Research Institute, Palo Alto, Calif., February 1990.

[6] Wallin, K., "The Scatter in K_{Ic}-Results," *Engineering Fracture Mechanics*, 19(6), 1085-1093 (1984).

[7] Johnson, L. G., "Operations Research in Life Testing," pp. 1-16 in *Industrial Mathematics*, Vol. 8, 1957.

[8] "Material Properties," Sect. XI, Article A-4000, *ASME Boiler and Pressure Vessel Code. An American National Standard*, American Society of Mechanical Engineers, New York, 1994.

[9] Steinstra, D. Anderson, T. L., and Ringer, L. J., "Statistical Inferences on Cleavage Fracture Toughness Data," *Journal of Engineering Materials and Technology*, 112/31, 31-37 (January 1990).

[10] Van Der Sluys, W. A., and Miglin, M. T., "Results of MPC/JSPS Cooperative Testing Program in the Brittle-to-Ductile Transition Region," pp. 308-324 in *Fracture Mechanics: Twenty-Fourth Volume, ASTM STP 1207*, J. D. Landes, D. E. McCabe, and J. A. M. Boulet, Eds., American Society for Testing and Materials, Philadelphia, 1994.

[11] McCabe, D. E., Merkle, J. G., and Nanstad, R. K., "A Perspective on Transition Temperature and K_{Jc} Data Characterization," pp. 215-32 in *Fracture Mechanics: Twenty-Fourth Volume, ASTM STP 1207*, J. D. Landes, D. E. McCabe, and J. A. M. Boulet, Eds., American Society for Testing and Materials, Philadelphia, 1994.

[12] McCabe, D. E., Zerbst, U., and Heerens, J., *Development of Test Practice Requirements for a Standard Method on Fracture Toughness Testing in the Transition Range*, GKSS Report 93/E/81, GKSS Forschungszentrum, Geesthacht GmbH, Geesthact, Germany, 1993.

[13] Jones, M. H., and Brown, W. F., Jr., "The Influence of Crack Length and Thickness in Plane Strain Fracture Toughness Tests," pp. 63-101 in *Review of Developments in Plane Strain Fracture Toughness Testing, ASTM STP 463*, W. F. Brown, Jr., Ed., American Society for Testing and Materials, Philadelphia, 1970.

[14] Rolfe, S. T., and Novak, S. R., "Slow-Bend K_{Ic} Testing of Medium-Strength High-Toughness Steels," pp. 124-159 in *Review of Developments in Plane Strain Fracture Toughness Testing, ASTM STP 463*, W. F. Brown, Jr., Ed., American Society for Testing and Materials, Philadelphia, 1970.

[15] Nanstad, R. K., et al., *Irradiation Effects on Fracture Toughness of Two High-Copper Submerged-Arc Welds, HSSI Series 5*, NUREG/CR-5913, Vol. 1 (ORNL/TM-12156/V1), Oak Ridge National Laboratory, Oak Ridge, Tenn., October 1992.

Y.J. Chao[1] and W. G. Reuter[2]

FRACTURE OF SURFACE CRACKS LOADED IN BENDING

REFERENCE: Chao, Y. J. and Reuter, W. G., "**Fracture of Surface Cracks Loaded in Bending,**" *28th National Symposium on Fatigue and Fracture, ASTM STP 1321,* J. H. Underwood, B. Macdonald, and M. Mitchell, Eds., American Society for Testing and Materials, West Conshohocken, 1997.

ABSTRACT: Theoretical background of the constraint effect in brittle fracture of solids is reviewed. Fracture test data from D6-aC, a high strength steel, using three-point-bend (SE(B)) specimens and surface cracked plate (SC(B)) specimens under bending are presented. It is shown that the SE(B) data has an elevated fracture toughness for increasing a/W, i.e. a crack geometry with a larger T/K corresponds to a higher K_c which is consistent with the theoretical prediction. The fundamental fracture properties, i.e. the critical strain and the critical distance, determined from the SE(B) test data are then applied to the interpretation and prediction of the SC(B) test data. Reasonable agreement is achieved for the crack growth initiation site and the load.

KEYWORDS: brittle fracture, constraint effect, fracture toughness, linear elastic fracture mechanics, crack tip stress fields, fracture stress, size effect, surface crack

---

Introduction

The purpose of the development of fracture mechanics is to interpret and predict, if possible, the growth of a crack-like flaw in a structure under service loads. A surface crack presents the most common type of flawed geometry in structures. Consequently, extensive studies have been devoted to the fracture behavior of specimens containing surface cracks (e.g. see [1-3]). Note that surface cracks in a structure are three-dimensional (3D) in geometry. On the other hand, most fracture mechanics theories and the ASTM fracture testing standards are based on two-dimensional (2D) assumptions. The fracture toughness data for a given material from standard testing methods may be valid in the interpretation of fracture of a two-dimensional, through crack in a plate, but the validity becomes unclear when applied to 3D cracks, such as a surface crack. Thus,

[1] Professor, Department of Mechanical Engineering, University of South Carolina, Columbia, SC 29208
[2] Consulting Engineer, Idaho National Engineering Laboratory, P. O. Box 1625, Idaho Fall, ID 83415

one of the main topics in the study of the fracture behavior of a surface crack is transferability, i.e. how to apply the fracture toughness data determined from specimens of two-dimensional nature to three-dimensional surface cracks.

For some materials, initiation of crack growth is synonymous with catastrophic failure. For instance, Reuter, et al. [3] attempted to interpret several groups of test data from surface cracks using K_{IC} determined from the standard ASTM procedures. The results for surface cracked specimens tested under tensile loading (where K_{max} occurred at maximum crack depth) were generally consistent with K_{max}/K_{IC} ranging from 1.0 to 1.4. But for specimens tested under bending loads (where K_{max} occurs at the free surface) the results varied from reasonable to substantial conservatism (K_{max}/K_{IC} ranging from 1.0 to 2.0). For the material used in this study stable crack growth often preceded catastrophic failure. At this time the ability to predict catastrophic failure after stable crack growth occurs does not exit; therefore, the measured values of K_{IC} (per ASTM E399) is often used to predict conditions (load for a specific specimen geometry including the flaw size) associated with initiation of crack growth.

Recent advances in constraint effects in fracture mechanics have revealed that the critical stress intensity factor, or the apparent fracture toughness K_c, is a function of crack depth, specimen size, and loading configuration [4,5]. This behavior is commonly attributed to the term "constraint effect", i.e. flawed specimens or structures of different constraint level at the crack tip exhibit different K_c. In the current paper, we first review the theoretical basis of the constraint effect in the brittle fracture of solids; then we present the test data from three-point-bend (SE(B)) specimens and surface cracked plate (SC(B)) specimens made of the high strength steel D6-aC; and finally we apply the constraint theory to interpret and predict the fracture of the SC(B) using the SE(B) test data. It is shown that (1) the SE(B) data display an elevated fracture toughness for increasing a/W, i.e. a crack geometry having higher constraint (defined here as higher T-stress, e.g. a specimen having T-stress = -10 MPa has higher constraint than a specimen having a T-stress = -200 MPa) has a higher K_c, (2) the fracture properties for this material may be characterized by the two mechanics parameters, K and T, and (3) when the material fracture properties are applied to the SC(B) specimens, the load and location along the crack front corresponding to the crack growth initiation can be interpreted and predicted.

It should be noted that the level of constraint, defined by the T-stress, for a specimen/structure identified in this paper follows the commonly adopted notion, e.g. a CCP specimen has a lower constraint than a SE(B) specimen; a specimen with shallow crack has lower constraint than a specimen with deep cracked. In other words, high constraint means larger T-stress at the crack tip at the fracture initiation load.

Constraint Effect in Brittle Fracture

In a previous report, Chao and Zhang [4] investigated the constraint effect, i.e. variation of apparent fracture toughness, in brittle fracture of solids within the context of linear elastic fracture mechanics. Williams' asymptotic series solutions including higher order terms are used to characterize the crack tip stress and strain fields for various specimen geometries. It was demonstrated that the material's resistance to fracture can be quantified by two mechanics parameters K and T for strain controlled fracture or K and A_3 for stress controlled fracture. A fracture assessment procedure was proposed. Constraint related issues such as size, crack depth, and biaxial stress effect were discussed. The theoretical basis of the constraint effect in relation to the fracture of brittle materials from ref. 4 is reviewed in this section.

Theoretical Background

In 1924, Griffith [6,7] stated ".... The general condition for rupture will be the attainment of a specific tensile stress at the edge of the crack". Obviously, the critical, specific tensile stress at rupture differs from material to material. Thus, this critical stress may be regarded as one of the material mechanical properties. Furthermore, in one of his early papers, Irwin [8] has explicitly pointed out that two mechanics parameters K and T are needed to characterize the crack tip stress fields for various test configurations, loads, and crack lengths. Consequently, if the brittle fracture event is controlled by the local stress or strain fields at a crack tip, *two* critical mechanics parameters, K and T, are required to characterize the fracture event.

With this prelude, we now examine the mechanics and physics at a crack tip. For a crack embedded in a linear elastic medium, it was shown by Williams [9] that the stress and strain near the crack tip can be written as

$$\sigma_{ij} = \sum_{n=1}^{\infty} A_n \, r^{\frac{n}{2}-1} \, f_{ij}^{(n)}(\theta)$$
$$\varepsilon_{ij} = \sum_{n=1}^{\infty} A_n \, r^{\frac{n}{2}-1} \, g_{ij}^{(n)}(\theta) \tag{1}$$

where a polar coordinate system (r,θ) with origin at the crack tip is used for the indices i and j and $f_{ij}^{(n)}(\theta)$ and $g_{ij}^{(n)}(\theta)$ are the angular functions of the n-th term. Note that equation (1) is from an asymptotic analysis and has infinite number of terms. The first term is the singular term with the coefficient A_1 related to the stress intensity factor K by $A_1 = \dfrac{K}{\sqrt{2\pi}}$.

Let us now examine the realistic distribution of the opening stress in front of a crack tip. Figure 1 shows the schematic of the opening stress distribution in front of a crack tip along with the first term, K-stress, determined from eqn.(1). Note that the K-stress differs from the actual stress because the former only includes the first term of eqn.(1). The K-stress and the actual stress only asymptotically approach each other as

$r \to 0$. Furthermore, the actual stress drops off in the region immediately near the crack tip where the fracture process takes place. Following Griffith [6,7] and Ritchie, et al [10,11], it is postulated that fracture of material is controlled by the attainment of a critical stress (e.g. for cleavage fracture) or strain (e.g. for dimple rupture) at a critical distance $r = r_c$. The critical stress and distance r_c may depend on the composition of the material, temperature and environment and can also be treated as a material property in the fracture criterion. Note that this fracture criterion (i.e. σ_c and r_c) has been used by Ritchie, et al [10,11] in the interpretation of fracture of nuclear reactor pressure vessel steels and also adopted by Chao, et al. [12] for the study of fracture under large scale yielding conditions.

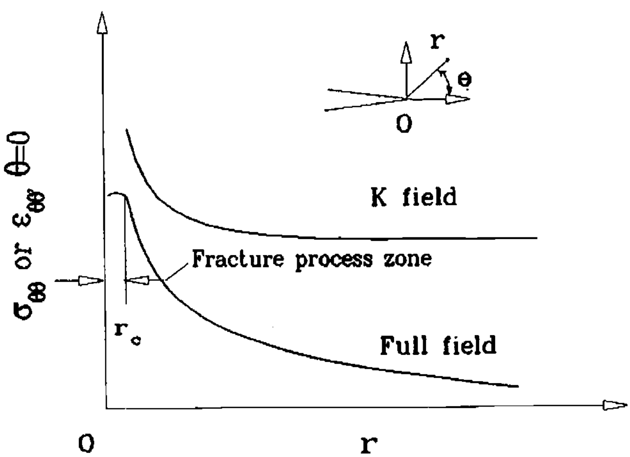

Figure 1 -- Opening stress/strain ahead of a crack tip

Since the controlling stress/strain for fracture is at a *finite* distance, r_C , from the crack tip in contrast to $r \to 0$, the stress level may or may not be properly characterized by the K-stress as demonstrated in fig.1. For a given material, if the K-fields at a crack tip dominate in the area $r=r_C$, then the actual stress at r_C is close to the K-stress. Thus, using a critical stress σ_C as the fracture criterion is equivalent to using a critical K, such as K_{IC}, since σ_c can be characterized by K. On the other hand, if the K-dominant zone is smaller than r_C , then the stress at $r = r_C$ cannot be completely characterized by K alone. Under these conditions, using K alone to characterize the fracture event is not sufficient. Since the size of the K-dominant zone depends upon the specimen geometry, size, crack length, and loading configuration, it leads to the constraint effect in brittle fracture, i.e. the dependence of fracture toughness, K_C , on these factors. It should be noted that if the stress/strain fields near $r = r_C$ are dominated by plasticity, i.e. the plastic zone size $r_y >> r_C$, the elastic-plastic asymptotic solution [13] should be used to describe the constraint effect [12,14] since the Williams solution, eqn.(1) or the K field, losses its validity under these conditions. In this paper, we only discuss the case of $r_c > r_y$ and the stress/strain at r_C can be characterized by the Williams' linear elastic solution.

To describe the stress (strain) level at a finite distance (such as r_c) from the crack tip, higher order terms from eqn.(1) may be used. In this discussion, our primary emphasis is Mode I fracture and thus we shall only examine the opening stress and strain ahead of the crack tip, i.e. along $\theta=0^0$. Furthermore, we assume that two non-vanishing terms from Williams' series expansion are sufficient to characterize the stress and strain at the critical distance r_C. It is demonstrated in [4] that a material's resistance to fracture can be quantified by two mechanics parameters, K and T, for strain controlled fracture or by K and A_3 for stress controlled fracture, where A_3 is the coefficient of the third term in eqn.(1). The (K,T) criterion is adopted here because (a) the results in [4] indicate a similar trend by using either (K,T) or (K, A_3), and (b) the values of T for various specimen geometries and the calculation method of T are readily available in the literature.

It follows from (1)

$$\varepsilon_{\theta\theta}\big|_{\theta=0^0} = \frac{(1+\upsilon)(1-2\upsilon)}{\mathrm{E}}\frac{K_I}{\sqrt{2\pi \mathrm{r}}} - \frac{(1+\upsilon)\upsilon}{\mathrm{E}}\mathrm{T} \qquad \text{(plane strain)} \qquad (2)$$

where $T = 4A_2$ and is the so-called T-stress. Equation (2) shows that the opening strain is controlled by two mechanics parameters K_I and T. K_I can be interpreted as the applied loading level and T a function of specimen geometry and loading configuration. Note that T is linearly proportional to the applied load for a given geometry due to the linearity of the problem. Adopting the fracture criterion of a critical strain at a critical distance r_c, (2) becomes

$$\varepsilon_c = \frac{(1+\upsilon)(1-2\upsilon)}{\mathrm{E}}\frac{K_c}{\sqrt{2\pi \mathrm{r_c}}} - \frac{(1+\upsilon)\upsilon}{\mathrm{E}}\mathrm{T_c} \qquad (3)$$

where K_c and T_c are the critical K_I and T , respectively, corresponding to the critical load. Eqn.(3) can be stated as : the fracture event occurs when the opening strain at r_c in front of the crack tip reaches a critical value ε_c . It indicates that the critical strain at r_c is controlled by the two mechanics parameters K_c and T_c. Furthermore, the two local *material* fracture properties, ε_c and r_c, are now replaced by the two *mechanics* parameters, K and T to quantify the fracture event. Since T_c can be either positive or negative depending upon specimen or structural geometries, then the magnitude of K_c varies with specimen geometry in order to achieve the same fracturing strain ε_c for the material to fail.

Eqn. (3) can be rewritten as

$$K_c = \frac{\nu\sqrt{2\pi r_c}}{1-2\nu}T_c + \frac{E\sqrt{2\pi r_c}}{(1+\nu)(1-2\nu)}\varepsilon_c \qquad (4)$$

Thus for a given material, i.e. fixed ε_c, r_c, E, and ν, eqn.(4) is a straight line with the slope $\frac{\nu\sqrt{2\pi r_c}}{1-2\nu}$ in the (K,T) space with K as the ordinate and T as the abscissa. Since r_c is positive and $\nu < 0.5$, the slope is positive. Thus, a specimen of higher T should fail with higher K. In addition, a material with larger (smaller) fracture process zone, r_c, has a higher (lower) slope or the constraint effect is more (less) pronounced.

It is noted that the two local fracture properties, ε_c and r_c, are assumed as material properties in the current discussion. They are consequently invariant with respect to crack geometry (e.g. 2D or 3D) and loading configuration (e.g. bending or tension). For instance, these two material fracture properties can be determined from 2D specimens and then applied to 3D structures. The next section outlines the basic steps in performing such a task.

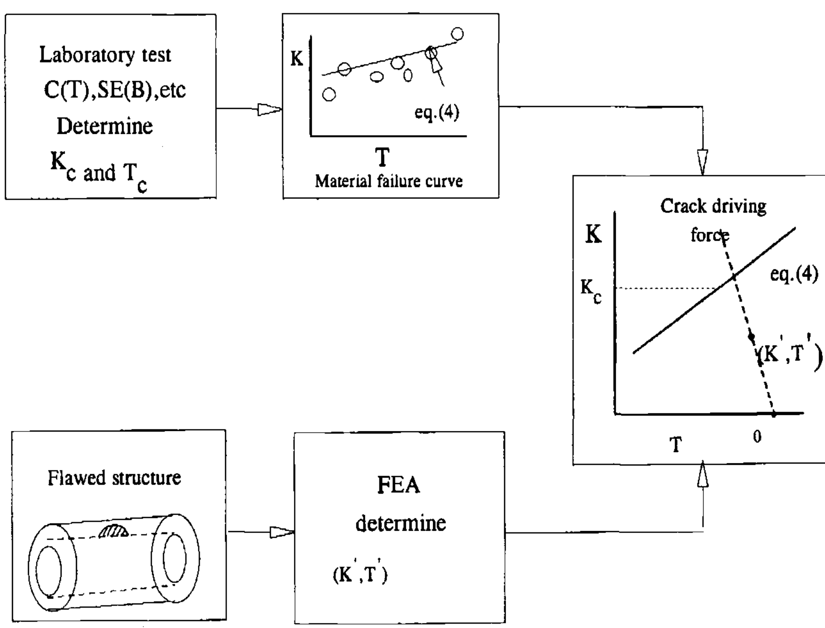

Figure 2 – Fracture assessment procedures based on a critical strain concept

Fracture Assessment of Specimen or Structures

Based on eqn.(2) and (3), a fracture assessment procedure for prediction of the onset of crack propagation in a specimen or structure is depicted in fig.2 and formulated as follows.

(1) Determine (K_c, T_c) material failure data for the material of interest. This can be accomplished by using laboratory test specimens and obtaining the critical load (P_Q) at fracture. Finite element analysis (FEA), handbook, or ASTM fracture toughness testing procedures may be used to obtain the critical stress intensity factor, K_c. Numerical methods, such as weight function method and FEA, can then be used to determine T_c, i.e. the T value corresponding to the particular specimen geometry and the critical load. A best fit to the data consisting (K_c, T_c) using eqn.(3) forms the material failure curve. Note that eqn.(3) is a linear equation of K_c and T_c. Therefore, a minimum of two test data are required to determine ε_c and r_c although more data points are needed in practice due to scatter in the test data. It should be pointed out that there is no need for in-plane size and geometry requirements for the laboratory test specimens as specified in E399 because the two sets of data (K,T) develop a straight line relation according to eqn.(4). The effect of specimen size and crack length is reflected by the magnitudes of K_c and T_c from tests.
(2) For safety assessment of a structure against fracture, perform FEA for the (postulated) crack in the service structure to determine the crack driving force at a crack tip which is the trace of (K, T) for different applied K. Since T is linearly proportional to K for a given geometry, *one* elastic FEA with the applied load at any level (e.g. K' and T' shown in fig.2) is sufficient to obtain the crack driving force.
(3) Superimpose the two straight lines obtained in steps (1) and (2). The point of intersection of these two lines determines the failure parameter (K_c, T_c). The applied load corresponding to this failure K_c is the failure load.

Material Properties and Fracture Test Results of D6-aC

The high strength steel, D6-aC, was austenitized at 913 ^{0}C, oil quenched and tempered at 204 ^{0}C for 2 plus 2 hours. The resulting yield stress is σ_{ys} = 230 ksi (1587 MPa). The Young's modulus E and Poisson's ratio ν are assumed as 30×10^6 psi and 0.3, respectively, for this steel. The chemical composition of the material is 0.46 C, 0.80 Mn, 0.01 P, 0.001 S, 0.23 Si, 0.12 Cu, 0.47 Ni, 1.07 Cr, 0.99 Mo, 0.10 V, balance Fe. The material was tested using SE(B) and SC(B) specimen geometries. The SE(B) specimens cover the a/W ratio from 0.1 to 0.85. The tests followed the ASTM E399 procedures [15] except P_Q was obtained at 2% of a_0, the initial crack length. Table 1 presents the specimen dimensions and test results. Additional test data were developed from SE(B) specimens by the participants in the international cooperative test program (see reference 16). T_Q in Table 1 is obtained using the tabulated results by Sham [18]. Note that the subscript Q for K_Q and T_Q here follows the notation in E399 and K_Q and T_Q is equivalent to K_C and T_C, respectively, for the current discussion. Table 1 has four groups of data with first two groups being the TS-orientation and the later two groups TL-orientation. The first and the third groups have B (thickness) = 12.70 mm and the second and the fourth groups B=6.37 mm. These thicknesses satisfy the thickness requirement, i.e. B $\geq 2.5\,(K_{IC}/\sigma_{ys})^2$ by E399; and thus the specimens can be regarded as plane strain

Specimen No.	Crack length a (mm)	width W (mm)	a/W	thickness B (mm)	offset	P_Q KN	f(a/W)	K_Q $MPa \cdot m^{1/2}$	T_Q MPa
TS01	1.778	12.14	0.146	12.69	0.022	16.7	1.005	47.5	-247.57
TS02	1.88	12.12	0.155	12.71	0.022	16.5	1.034	48.3	-218.37
TS03	2.057	12.14	0.169	12.69	0.022	17.29	1.078	52.7	-198.14
TS04	2.489	12.12	0.205	12.71	0.025	16.66	1.192	56.2	-119.16
TS05	3.048	12.11	0.252	12.71	0.027	13.86	1.344	52.8	-51.51
TS06	3.150	12.14	0.259	12.69	0.028	12.76	1.372	49.5	-43.91
TS07	5.944	12.13	0.490	12.69	0.053	7.11	2.579	51.9	77.71
TS08	6.223	12.12	0.514	12.71	0.0562	7.33	2.783	57.7	113.45
TS09	9.017	12.12	0.74	12.71	0.124	2.554	7.446	53.8	178.50
TS10	9.144	12.14	0.75	12.69	0.130	2.359	7.854	52.4	187.64
TS11	9.881	12.12	0.816	12.71	0.188	1.27	12.25	44.0	225.71
TS12	10.084	12.14	0.831	12.69	0.199	1.182	13.94	39.4	259.59
TS25	1.44	12.08	0.119	6.37	0.020	8.665	0.915	45.0	-281.36
TS26	1.60	12.08	0.133	6.29	0.021	7.925	0.962	43.8	-249.43
TS27	2.057	12.07	0.171	6.37	0.022	7.85	1.084	48.4	-177.25
TS28	1.961	12.07	0.163	6.37	0.022	8.425	1.059	50.7	-207.54
TS29	3.124	12.07	0.259	6.37	0.028	6.72	1.370	52.3	-46.60
TS30	3.048	12.08	0.253	6.37	0.028	6.92	1.349	53.0	-50.99
TS31	5.918	12.07	0.492	6.37	0.053	3.388	2.596	50.0	76.99
TS32	6.096	12.07	0.504	6.37	0.056	3.66	2.706	56.3	99.72
TS33	9.263	12.08	0.768	6.37	0.142	1.075	8.633	52.7	203.73
TS34	9.144	12.07	0.758	6.37	0.135	1.127	8.101	51.9	191.09

Table 1 SE(B) test specimen configuration and test results, S(Span) = 48 mm

Specimen No.	Crack length a (mm)	width W(mm)	a/W	thickness B (mm)	offset	P_Q KN	f(a/W)	K_Q $MPa\cdot m^{1/2}$	T_Q MPa
TL13	1.44	12.71	0.113	12.16	0.02	19.08	0.894	47.0	-293.57
TL14	16.76	12.71	0.132	12.15	0.021	20.55	0.958	54.3	-303.92
TL15	2.128	12.70	0.168	12.14	0.022	14.19	1.074	42.1	-157.05
TL16	2.306	12.71	0.182	12.16	0.023	17.55	1.118	54.1	-163.85
TL17	2.87	12.69	0.226	12.14	0.026	11.6	1.258	40.4	-58.08
TL18	3.122	12.71	0.246	12.16	0.027	15.56	1.326	56.8	-58.91
TL19	5.804	12.70	0.457	12.14	0.048	8.75	2.333	56.4	45.51
TL20	5.748	12.71	0.453	12.15	0.048	8.4	2.305	53.4	38.94
TL21	9.119	12.71	0.718	12.16	0.113	3.07	6.427	54.4	169.14
TL22	9.246	12.71	0.728	12.16	0.118	3.018	6.791	56.4	180.05
TL23	10.447	12.71	0.823	12.16	0.179	1.506	12.951	53.7	280.91
TL24	10.726	12.71	0.845	12.16	0.190	1.224	15.823	53.4	312.87
TL-35	1.626	12.71	0.128	6.37	0.021	9.15	0.945	45.4	-262.46
TL-36	1.524	12.70	0.120	6.37	0.020	8.42	0.917	40.7	-247.03
TL-37	1.974	12.51	0.158	6.37	0.022	8.85	1.042	49.7	-213.30
TL-38	2.083	12.71	0.164	6.37	0.022	8.3	1.062	46.4	-182.48
TL-39	3.023	12.71	0.238	6.37	0.026	7.61	1.299	52	-61.05
TL-40	2.946	12.71	0.231	6.37	0.026	7.1	1.289	48.1	-62.82
TL-41	6.223	12.71	0.489	6.37	0.053	3.415	2.572	46.2	66.61
TL-42	1.266	12.71	0.492	6.37	0.054	3.8	2.596	51.9	77.88
TL-43	9.754	12.71	0.768	6.37	0.141	1.182	8.633	53.7	202.35
TL-44	9.474	12.51	0.757	6.37	0.134	1.209	8.048	51.2	188.40

Table 1 SE(B) test specimen configuration and test results, S (Span)=48 mm (continued)

specimens. All SE(B) specimens tested had fast, brittle crack propagation when fracture occurred.

In addition to the data shown in Table 1, three groups of larger SE(B) specimens (B=17 mm, W (width) = 34 mm, and S (span) = 102 mm with a TS-orientation were tested with a/W=0.5 in an attempt to obtain the fracture toughness K_{IC} as defined in ASTM E399. Each group contains four specimens and the average K_C from the three groups are 62.3 MPa·m$^{1/2}$, 55.2 MPa·m$^{1/2}$, and 54 MPa·m$^{1/2}$. A similar test from four larger specimens for the TL-orientation yields 60.8 MPa·m$^{1/2}$ and four larger specimens for the LT-orientation yields 59.9 MPa·m$^{1/2}$.

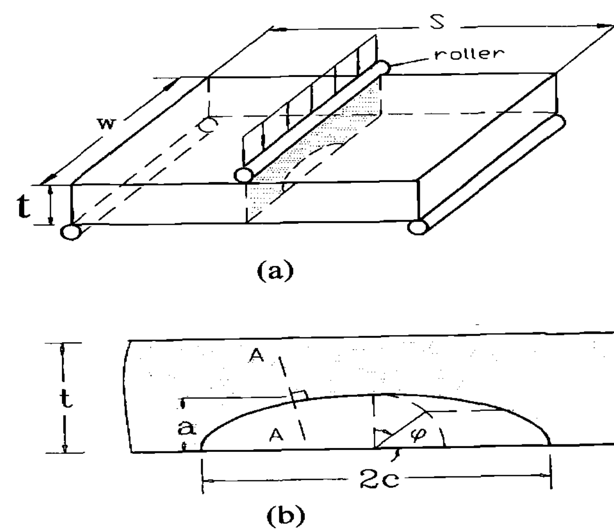

Figure 3 --- (a) Test configuration for the surface cracked panel (SC(B))
(b) Nomenclature of a surface crack

Four SC(B) tests were performed using the three-point-bend configuration, as shown in fig.3. A constant displacement across the width of the specimen is applied through the roller from the testing machine to the specimen. The cracks are semi-elliptical shape and the detailed crack dimensions are shown in fig. 4. Relatively, the crack in specimen B-1 is shallow and very small; the crack in specimen B-6 is large; the crack in specimen B-7 is deep and specimen No.4 is thinner. DC potential drop method and acoustic emission were used in the tests to detect the initiation of crack growth. The test was stopped and the load was recorded as the crack initiation load when a five percent DC potential change was observed. The load was then reduced and this SC(B) specimen was fatigue cycled to identify and outline the amount of the stable crack growth. After some fatigue crack growth the specimen was loaded to failure. It is assumed that at five percent DC potential drop a small amount of crack growth has initiated somewhere along the crack front. Thus, by examining the post-test fractured surface, the crack initiation site can be located. The observed fracture initiation sites and the fracture loads for the four specimens are indicated in fig. 5. In fig. 5, the elliptical angle ϕ is defined the standard way for semi-elliptical curve as shown in fig. 3 and the nominal bending stress σ is equal to $\frac{MC}{I} = \frac{3PS}{2Wt^2}$ where P is the fracture load of the specimen. Note that the initiation sites for the crack growth are all near the free surface of the crack. More details of the test procedures, crack growth initiation sites, etc. are provided in reference 17.

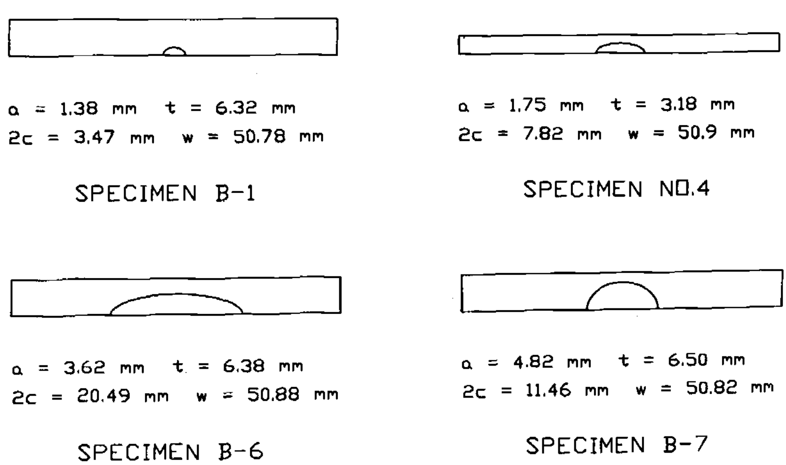

Figure 4 Surface crack dimensions

Analysis of the Test Results

K_Q vs. the crack depth a/W from the SE(B) specimens is presented in fig.6 which shows a slightly upward trend for K_Q as a/W is increased (this relationship is discussed in more detail in ref. 17). Careful examination of the test data shown in fig.6 reveals that the last two specimens in the first group, TS11 and TS12, obviously do not follow the trend, i.e. their K_Q are too low. It was therefore decided that only the data from the other three groups would be used in the following analysis. It is expected that the omission of the first group of data will be negligible since these data, except for TS11 and TS12, compare well with other results. A discussion will be given later for these specimens that have large a/W ratios.

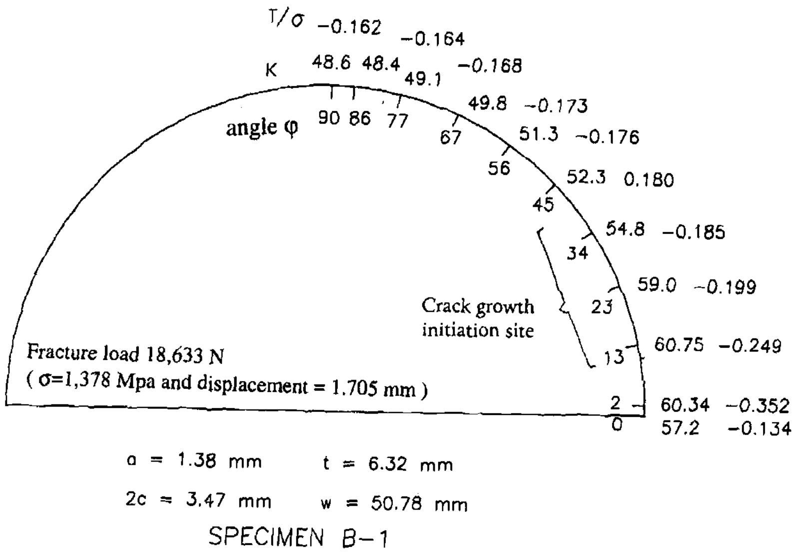

Figure 5(a) --- The observed fracture initiation site and the K and T distribution along the crack front corresponding to the fracture load; specimen B-1

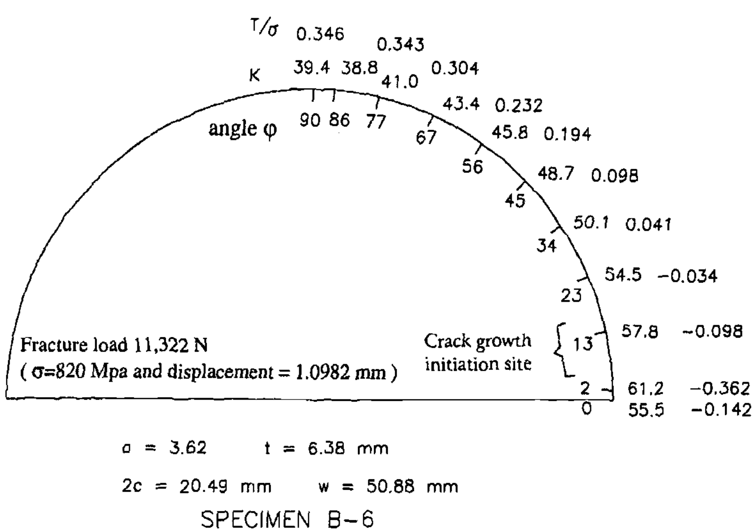

Figure 5(b) --- The observed fracture initiation site and the K and T distribution along the crack front corresponding to the fracture load; specimen B-6

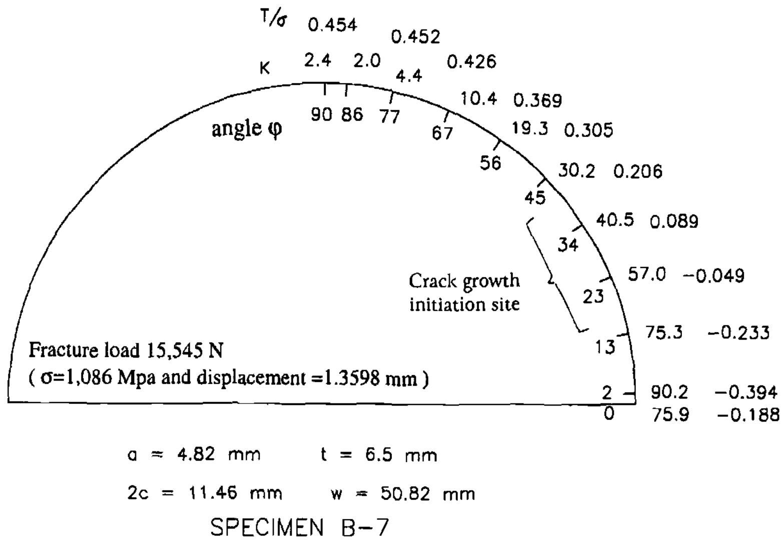

Figure 5(c) --- The observed fracture initiation site and the K and T distribution along the crack front corresponding to the fracture load; specimen B-7

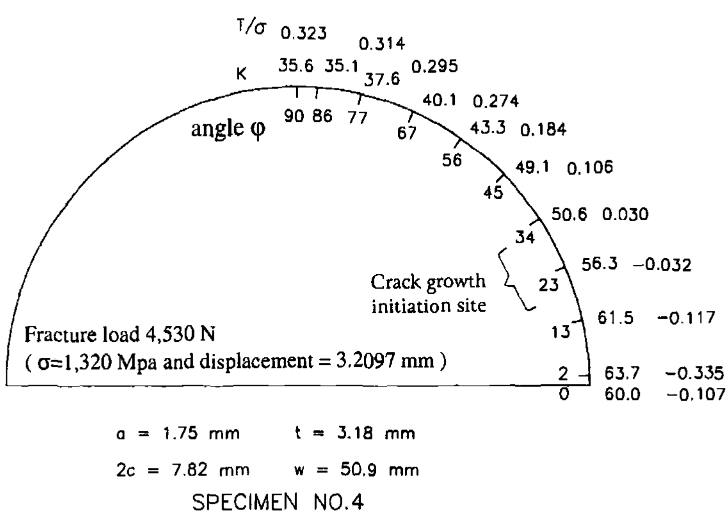

Figure 5(d) --- The observed fracture initiation site and the K and T distribution along the crack front corresponding to the fracture load; specimen No. 4

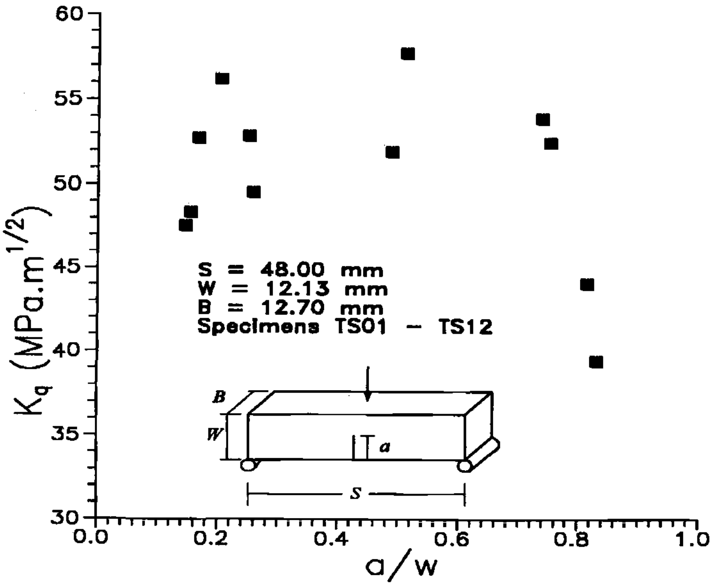

Figure 6(a) ---Variation of fracture toughness K_Q with a/W

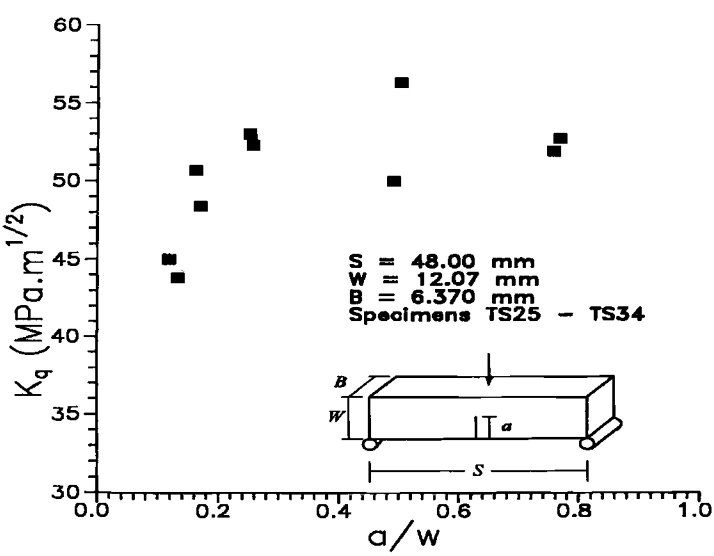

Figure 6(b) ---Variation of fracture toughness K_Q with a/W

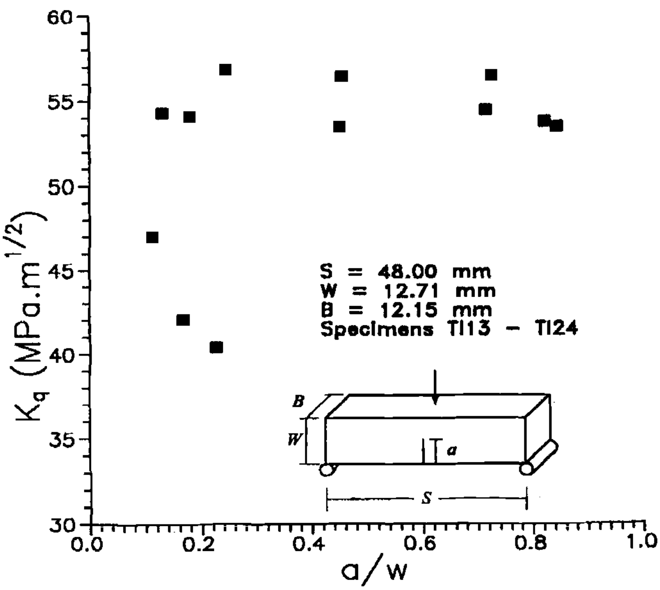

Figure 6(c) ---Variation of fracture toughness K_Q with a/W

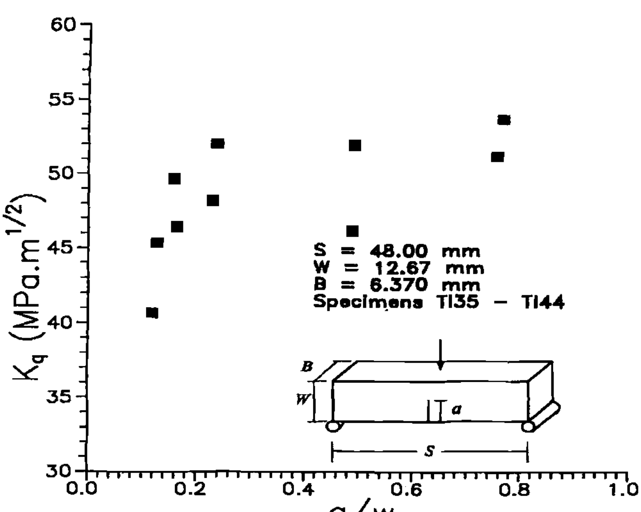

Figure 6(d) ---Variation of fracture toughness K_Q with a/W

Following the fracture assessment procedures outlined in the previous sections, we proceed to first plot the K and T pairs from Table 1 in the K-T space and a straight line is fitted to the data points as shown in fig.7. It is noted from the test data and fig.7 that (a) there is no obvious difference among the data from the three groups, and (b) specimens of increasing a/W, thus larger T_Q, have higher K_C as predicted by eqn.(3). Using eqn.(3) as the formula for a best-fit straight line, we obtain $\varepsilon_c = 0.0002224 = 0.02224\%$ and $r_c = 0.052$ mm. Note that using $r_Y = \frac{1}{8\pi}(\frac{K}{\sigma_{YS}})^2$ and the maximum K_Q in Table 1, 56.8 MPa·m$^{1/2}$, the maximum size of the plastic zone r_y is estimated as 0.051 mm. Comparing this r_y with r_c it appears that the critical distance r_c is slightly larger than the plastic zone, i.e. the fracture process zone encompasses the plastic zone. Thus, using a linear elastic mechanics solution, eqns.(1) and (2), to describe the stress and strain at r_c is justified.

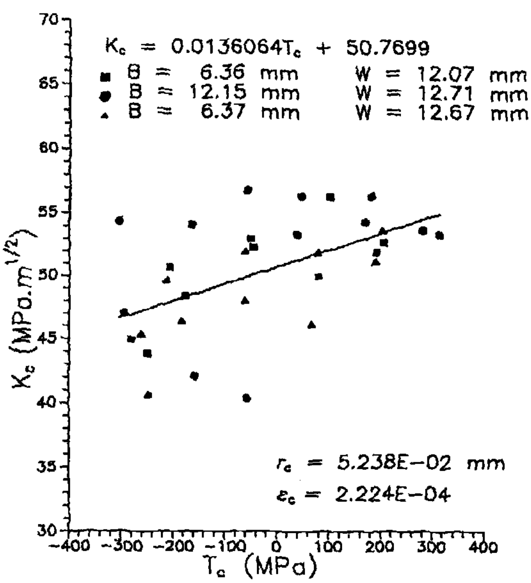

Figure 7 --- D6-aC material failure curve obtained from the SE(B) specimens using a critical strain fracture criterion

To predict the fracture of a specimen of another geometry or size, we follow the fracture assessment procedures outlined in the previous section. Here, we use the large SE(B) with the TS-orientation (W=34 mm) as an example. This specimen geometry with a/W = 0.5 has a T/K = 0.9381 and it is plotted in fig. 8 as the dashed line along with the test data. In fig. 8, the test data from smaller SE(B) (W=6.37 mm) are also presented with a straight line fit according to eqn.(4). The predicted K_C is 51.73 MPa·m$^{1/2}$ from the intersection of the two lines in fig.8 as compared to the test data 62.3 MPa·m$^{1/2}$, 55.2 MPa·m$^{1/2}$, and 54 MPa·m$^{1/2}$. If T/K = 0.9381 is used in fig.7 with the three groups of data, K_C = 51.43 MPa·m$^{1/2}$ is predicted. Thus, the predicted K_C is about 9.5 percent lower than the average of the three data. Note that the large specimen is about three times larger in any linear dimension of the small SE(B) specimen. The reasonable agreement between the test and the prediction indicates that the size effect can be properly addressed by the proposed fracture assessment procedures. In addition, the effect of the material orientation seems to be very minimum. Thus, the data shown in fig.7 which includes test data from both TL- and TS-orientation are used in the next section for the SC(B) specimens.

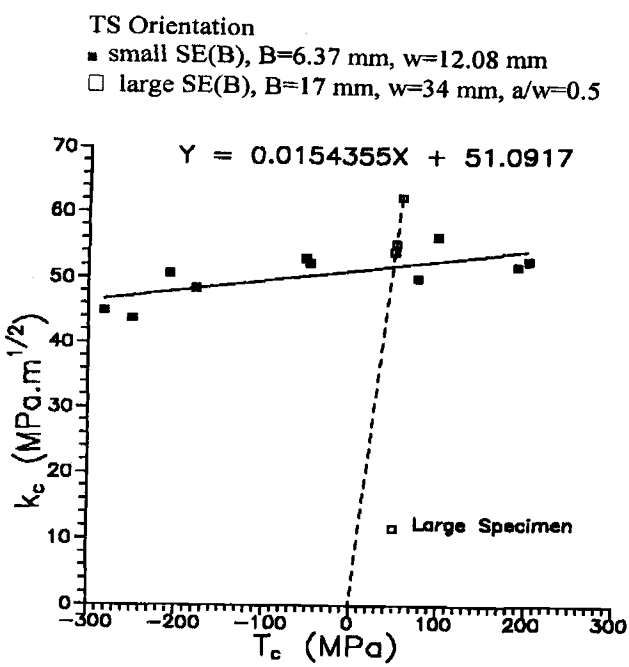

Figure 8 --- Size effect: a comparison of predicted with test data

(K, T) Determination for SC(B)

For a surface crack, the crack front is a curved line. A (K, T) pair and a crack driving force at each point along the crack front are present as the far field load is increased. By putting all the crack driving forces along the crack front together, the crack driving force for the surface crack becomes a curved front as depicted in fig. 9, since (K,T) varies from point to point along the crack front for a given far field load. Each point on the curve represents the condition of the opening strain at a particular point in front of the crack front of the surface crack. For instance, the right end point of the curve may represent the condition of the opening strain at the deepest point of the surface crack and the left point corresponding to the point where the crack front intersects with the plate surface. In fig. 9, (0,0) represents the condition of no applied load. As the applied K increases, the crack driving force front develops and moves upward with increasing K, as indicated by the dashed line with the arrow head in fig. 9. The shape of the crack driving force front depends upon the geometry of the surface crack and the loading configuration, and is self-similar as it develops upward (see fig. 9) due to the linearity of the problem. When the crack driving force front first contacts the material failure curve as the load increases, shown in fig. 9 using the current D6-aC, SE(B) data as an example, crack growth initiation is predicted to occur at that corresponding point on the crack front of the surface crack and at that particular applied far field load. Note that this K-T fracture criterion is based on the critical strain concept, that is, fracture occurs as the opening strain at r_c at any point on the crack front reaches the critical strain ε_c of the material. And this fracture criterion is demonstrated in fig.9 as the crack driving force reaches the material failure curve as the load increases.

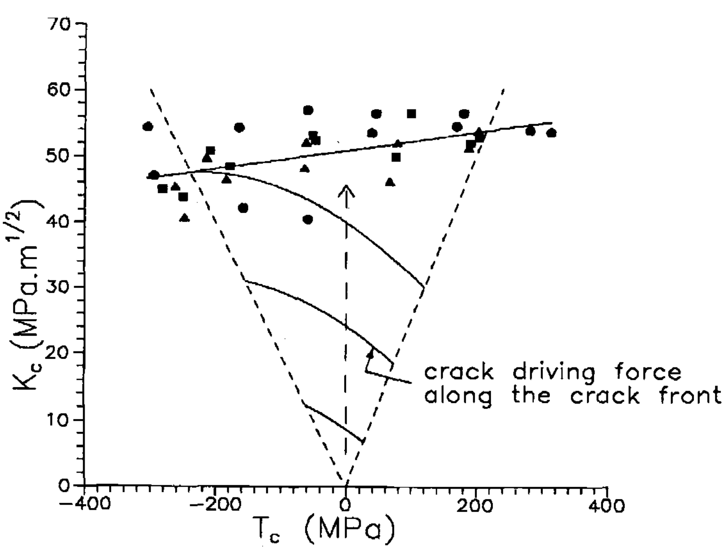

Figure 9 --- Crack driving force front for a surface crack

In order to obtain the K and T-stress for points along the crack front, finite element analysis (FEA) was used for the SC(B)'s. Three-dimensional mesh was first generated using ORMGEN [19], a program for finite element mesh generation of 3D cracked geometries. A circular fan-type arrangement of the mesh around the crack tip was adopted. The generated mesh with proper boundary conditions assigned was then combined with the ABAQUS [20] finite element code. Twenty node isoparametric elements were used for the 3D model. The quarter-point wedge element is used at the crack front to simulate the $1/\sqrt{r}$ singularity for the stress and strain fields. A total of 1794 elements with 8426 nodes was used. Figure 10 shows the mesh for specimen B-6; fig. 10(a) is the complete mesh for one quarter of the specimen (due to symmetry) and fig. 10(b) is the enlarged view of the crack tip region. In the FEA, a uniform displacement boundary condition is applied along the nodes where the central roller was placed in the actual test (see fig. 3(a)) to simulate the loading situation. The displacement is applied up to the level such that the summation of all the nodal forces along this line is equal to the fracture initiation load from the test.

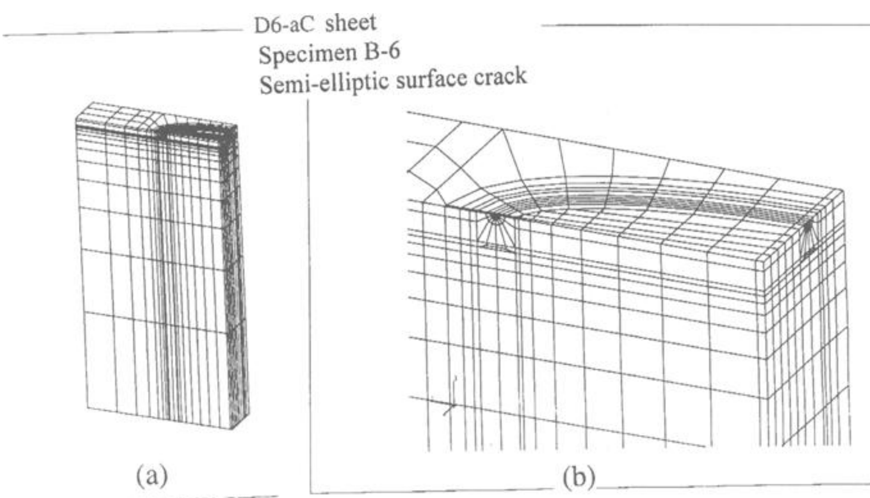

Figure 10 --- Finite element mesh for specimen B-6
(a) the ¼ model, (b) detailed crack tip region

After the finite element analysis, post processing of the computer output determines the K and T as follows. The stress intensity factor K was determined using a modified nodal force method [21]. In [21], Raju and Newman adopted two terms of $\sigma_{\theta\theta}\big|_{\theta=0^0}$ from eqn.(1) and converted these stresses to forces at the finite element nodes. Since the crack tip elements may have different sizes, approximations are involved when converting the stress to force. In addition, accurate results can only be achieved when the few nodes used in the curve fit are within the two-term dominated zone. Because of these reasons, we proceeded using three terms of $\sigma_{\theta\theta}\big|_{\theta=0^0}$ and the opening stress directly since the stress is readily available from the computer output. Note that using the near tip stress to obtain the stress intensity factor has been a standard practice in the experimental method of photoelasticity (see, e.g. [22]). Thus, adopting the first three terms from eqn.(1) for $\sigma_{\theta\theta}\big|_{\theta=0^0}$, we obtain

$$\sigma_{\theta\theta}\big|_{\theta=0^0} = \frac{K}{\sqrt{2\pi r}} + 3A_3 r^{1/2} + 5A_5 r^{3/2} \tag{4}$$

Let $$K_{app.} = \sigma_{\theta\theta}\big|_{\theta=0^0} \cdot \sqrt{2\pi r} \tag{5}$$

We obtain

$$K_{app.} = K + B_3 r + B_5 r^2 \tag{6}$$

where $B_3 = 3\sqrt{2\pi}\,A_3$ and $B_5 = 5\sqrt{2\pi}\,A_5$. The K_{app} is first determined using $\sigma_{\theta\theta}\big|_{\theta=0^0}$ from FEA output at near tip nodes along the plane normal to the crack front (e.g. A-A plane in fig. 3(b)) and eqn.(5). A parabola curve is fitted to several data points according to eqn. (6). The K is determined as K= K_{app} at r=0 or from eqn.(6). A typical case is presented in fig.11 where the solid points are used to fit eqn.(6). Note that ABAQUS calculates J-integral directly. However, when converting this J to K a plane stress or plane strain state has to be assumed. It is not clear which one is more appropriate for points along a surface crack front especially for points near the free surface. Nevertheless, the K evaluated using eqn.(6) is close to the K converted from the J using the plane strain formula for points near the deepest region of the surface crack and is about three to five percent lower for points near the free surface.

Using eqn.(1), along $\theta = 180^0$, σ_{rr} can be written as,

$$\begin{aligned}\sigma_{rr}\big|_{\theta=180^0} &= 0 + 4A_2 + 0 - 8A_4 r + \dots\dots\dots \\ &= T - 8A_4 r + \dots\dots\end{aligned} \tag{7}$$

Note that the odd number terms vanish and $4A_2$=T. Thus, the T-stress can be determined directly by examining the σ_{rr} at nodes on the crack flank near the crack tip and on a plane normal to the crack front. Since the singular and the third terms are not present, the T-stress dominated region is normally not small.

Figure 5 shows the K and T distributions along the crack front for the four test specimens at the critical load. It is shown that K is maximum near the free surface of the crack and decreases rapidly to the deepest point and the trend for T is reversed. Raju and Newman [22] and others have studied the "boundary layer" effect, i.e. K value at the intersection of the elliptical crack front and the free surface. They reported a sharp drop of K at this point as the FEA mesh is refined. This trend is also observed in our analysis. The boundary layer effect is out of the scope of the current analysis. However, it is safe to say that the maximum K occurs near, but not at, the free surface. A very thin layer of elements is used in our FEA. The K values at ϕ=0 shown in fig.5 are therefore not reliable since further drop of K is anticipated if finer mesh was used. It is consistent with the experimental observation that fracture initiation site is close to, but not at, the free surface.

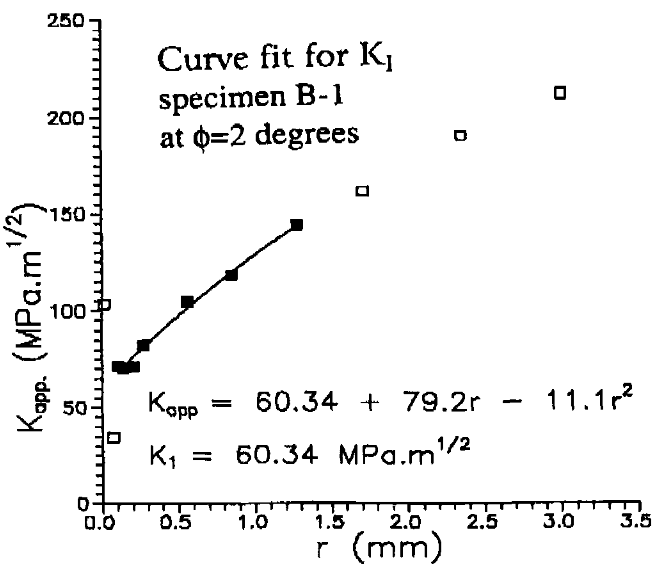

Figure 11 --- Determination of K using a parabolic curve fit to the opening stress in front of the crack tip

Prediction of Crack Initiation Site and Load

The (K,T) pairs along the crack front corresponding to the fracture initiation load for the four SC(B) cases are plotted in the K-T space along with the SE(B) data in fig.12(a) to (d). The results indicate that for these specimens under far field bending the maximum crack depth (free surface) position is on the right (left) end of the crack driving front. The data points shown by * in fig. 12 are from the corresponding angles shown in fig. 5. A detailed map of these angles is provided in fig.12(b) for specimen B-6. Following the fracture assessment procedures outlined previously, it can be seen that (a)

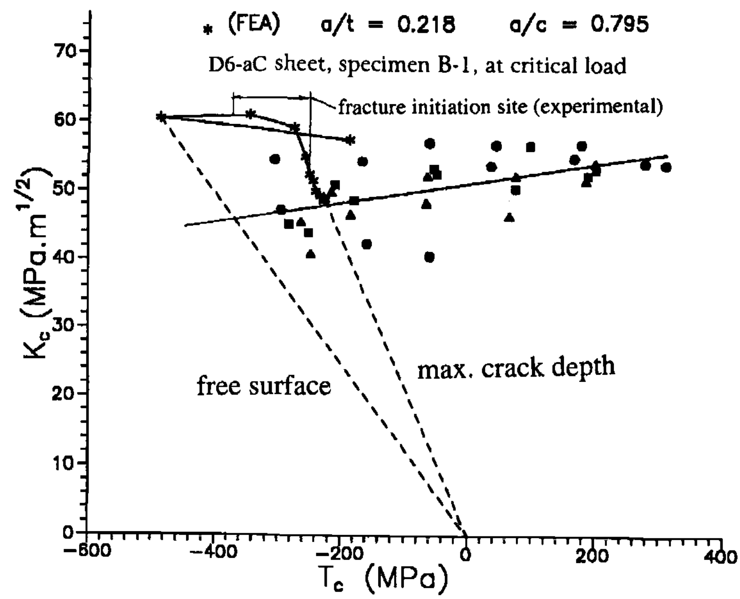

Figure 12(a) ---Crack driving front for SC(B); specimen B-1

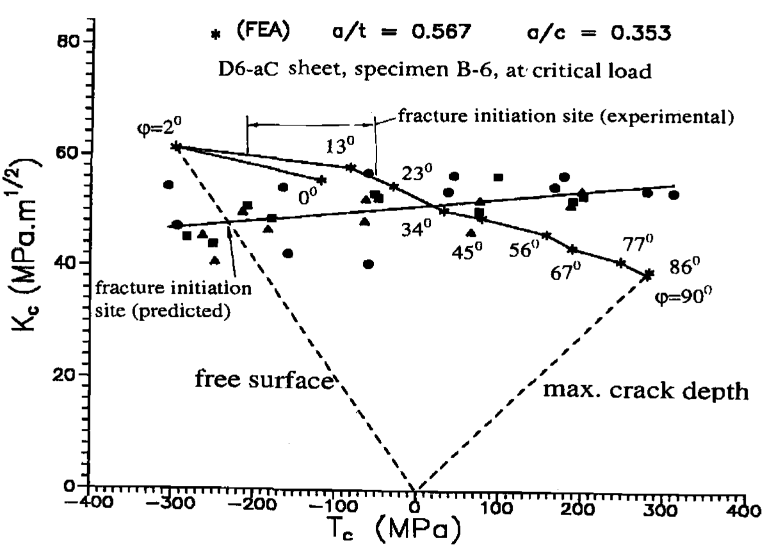

Figure 12(b) --- Crack driving front for SC(B); specimen B-6

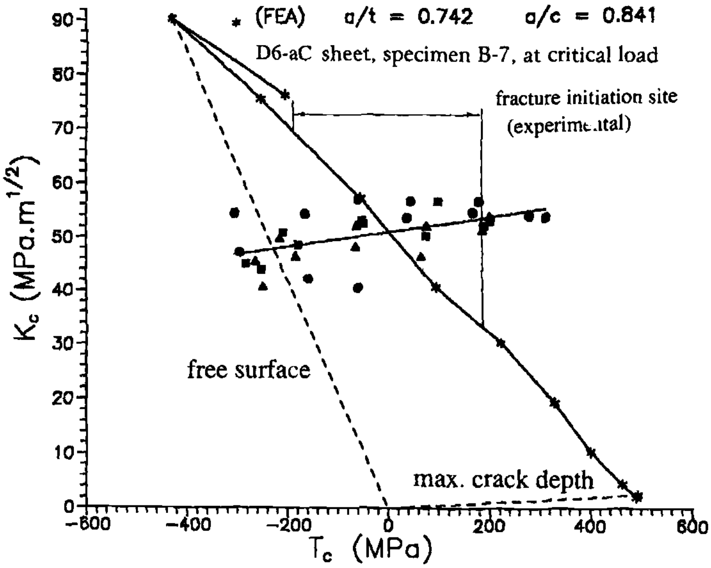

Figure 12(c) --- Crack driving force front for SC(B); specimen B-7

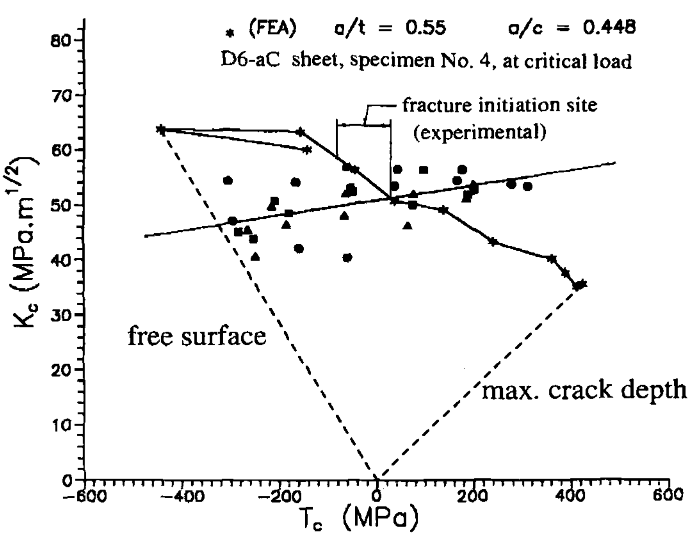

Figure 12(d) --- Crack driving force front for SC(B); specimen No.4

the crack growth initiation sites are closely predicted by the theory in that all four cases occur in an area near the free surface of the surface crack (see the observed crack growth initiation sites in fig. 5), and (b) the predicted fracture loads appear to be lower than the measured by about twenty-two percent (specimen B-1 and B-6) to forty-eight percent (specimen B-7) using the Kc values shown in the figures.

To be more specific, specimen B-6 is used here to demonstrate the methodology. Referring to fig.5 for specimen B-6, the predicted fracture initiation site is near the free surface and at the recorded fracture load the fracture event should have been incurred in the area from ϕ=0 to 31 degrees (noting that each data point on the crack driving front in fig.12(b) corresponds to a particular elliptical angle shown in fig.5). The test results indicate that the fracture initiation site is from ϕ=5 to 18 degrees. The applied K is 61.5 $MPa{\cdot}m^{1/2}$ at ϕ=2 degrees from the FEA. Since this point on the crack driving front reaches the material failure curve first as the load increases, the predicted fracture initiation K at this location is 47.7 $MPa{\cdot}m^{1/2}$ from fig. 12 (b). Since K is linearly proportional to the applied load, the predicted load is about twenty-two percent lower than the measured, i.e. (61.5-47.7)/61.5=0.22.

It should be noted that the fracture loads reported here were recorded at the instant when the change of the potential drop is five percent. It is known that the crack growth has initiated before the potential drop value reaches five percent. The precise amount of overestimate for the recorded fracture load based upon this testing practice is not known at this time. All four predicted loads shown in fig.12 are lower than the recorded loads at fracture initiation which is consistent with this argument.

The analysis and prediction are based on plane strain assumptions, it is known that the plane strain assumptions are not valid near the free surface of the SC(B). More detailed studies using both plane stress and plane strain in conjunction with test data from thinner specimens may shed light on the detailed fracture behavior near the free surface of the SC(B), such as the precise fracture initiation site.

Discussion

As shown in reference 17, it is possible that K_Q remains essentially constant for a/W ranging from 0.25 to 0.77 for the TS orientation and for a/W ranging from 0.13 to 0.85 for the TL orientation. Thus, designating K_Q as K_{IC} and using this K_{IC} as a constant or increasing as a function of a/W will have negligible impact on the approach used in this paper. It will however change the magnitude of the prediction error versus experimental results.

In this paper, the critical strain ε_c and the critical distance r_C determined from through cracks in two dimensional plates are assumed to be material constants to interpret the test results from surface cracks. Further experimental and analytical studies are needed to investigate these assumptions, e.g. the effect of thickness and specimen geometry on the ε_c and r_c .

In this work we only considered the opening strains along the zero degree direction ahead of the crack tip. That is, we assumed that the crack would propagate along the zero degree direction. It should be pointed out that the maximum opening strain $\varepsilon_{\theta\theta}$, for pure Mode I condition, may be at an angle other than zero degree when more than one term are retained from eqn.(1). This normally occurs as the T-stress becomes very large such that the K-term is not dominant at $r = r_C$. Under this situation, the corresponding K_C is anticipated to be lower than predicted by eqn.(3). Note that SE(B) specimen of high a/W have large T/K; thus a lower K_C is possible. This could partially attribute to the low K_C for specimens TS11 (a/W=0.814) and TS12 (a/W=0.831). A slightly lower K_C for TL23 (a/W=0.823) and TL24 (a/W=0.845) are also observed. Detailed analysis and results will be reported later.

The four cases analyzed in this paper are SC(B) under bending load. The crack initiation site and load may be different for other SC(B) geometries and loading configuration since the crack driving force (see fig. 9) may be different for other cases. For example, test data has shown that the crack growth initiation site for SC(B) under remote tension is at the deepest point of the surface crack in most cases. We used B-6 specimen geometry and ran a FEA with far field tension as a postulated case. The crack driving force is shown in fig. 13. Note that for this specimen under tension the maximum crack depth (free surface) position is on the left (right) end of the crack driving front. Thus, fig.13 would predict that the crack growth initiation site is at $\phi=90^0$ or the maximum crack depth of the surface crack which is consistent with the available test data.

It should be reiterated that

(a) It appears that the apparent constraint effect in fracture of solid is due to the fact that a single mechanics parameter K is used to interpret the fracture event while the crack tip stress and strain fields may not be characterized by the K-term alone. On the other hand, a fracture criterion using a local critical stress or strain is more fundamental and physically sound.

(b) Fracture is a phenomenon that the material separates at the crack tip. Thus, a one-dimensional failure theory, i.e. a critical stress or strain at the crack tip, appears to be reasonable. When the local critical stress or strain at a crack tip can be represented by mechanics solutions, presumably from a pure mathematical analysis, mechanics parameters, other than material's parameters, may be used to quantify the fracture. In this paper and [4] two terms from the Williams' mechanics solution, eqn.(3), are used to characterize the critical stress and strain at the critical distance near the crack tip. Thus, we are able to use the two mechanics parameters K and T to replace the two fundamental material fracture properties, the critical strain and critical distance for the characterization of the fracture event.

As a final note, the analysis presented in this paper is based upon the Williams *elasticity* solution for the stress/strain fields at a crack tip. The application of the theory is only valid for brittle fracture with negligible plastic deformation at the crack tip at the

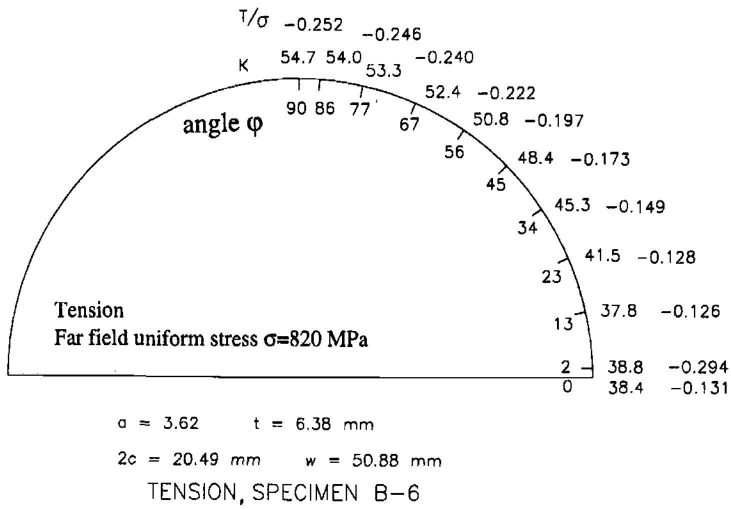

Figure 13(a) --- SC(B) specimen B-6 under remote tension; K and T distributions along the crack front

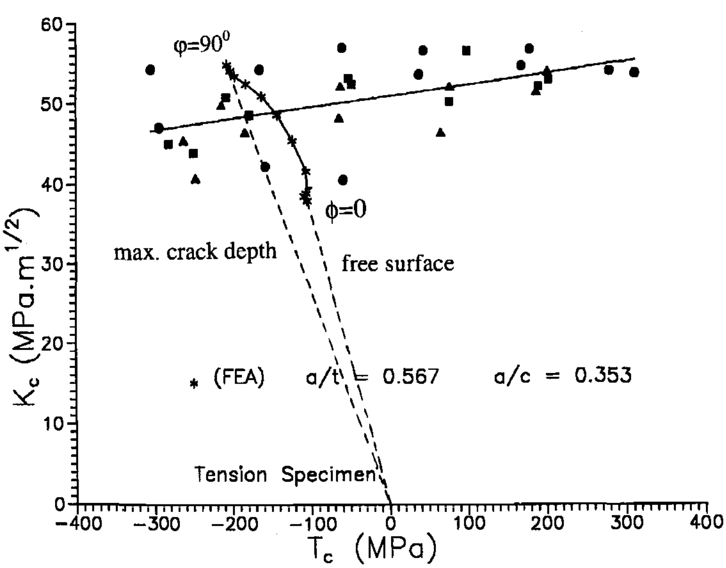

Figure 13(b) --- SC(B) specimen B-6 under remote tension; crack driving force front incipient of fracture. Therefore, the necessary condition for this analysis to be valid is $r_C > r_Y$ and the Williams mechanics solution is sufficient to characterize the stress/strain fields at r_C . Furthermore, as stated after eqn. (4) in the text, the theory predicts a higher K_c for a higher T_c which appears to be consistent with the experimental data shown in fig.7 and $r_C > r_Y$ is justified in the paper for the data.

There have been extensive studies using K and T as the two parameters for the characterization of *elastic-plastic* crack tip fields, e.g. Parks [24], Hancock [25], Kirk and Dodds [26]. In that case, a correlation between the *elastic* (K,T) boundary layer fields and the *elastic-plastic* crack tip deformation is obtained by FEA. Consequently, the T-stress is also used to interpret the constraint effect in the elastic-plastic fracture. Readers are reminded that the theory presented in the current paper and the K,T approach in ref. 24-26 are intended for two completely different types of fracture, i.e. one with negligible plastic deformation and one with extensive plastic deformation at the crack tip. Furthermore, both the theory and test data have indicated that the constraint effect in the brittle fracture with large plasticity (e.g. cleavage fracture of steels) has opposite trend to the constraint effect in the brittle fracture with negligible plasticity. For example, a shallow cracked specimen would fail with a higher K_C than a deep cracked specimen if the deformation mode at the crack as the fracture commences is large scale plasticity. More detailed discussion can be found in Chao and Zhang [4].

Acknowledgment

This work was supported in part by the Office of Basic Energy Sciences, Department of Energy, Contract DE-A507-761D01670 with the Idaho National Engineering Laboratory. The interest and support of Dr. O.P. Manley is deeply appreciated. The authors also wish to thank B. R. Bass and J. A. Keeney of the Oak Ridge National Laboratory by providing the mesh generation program ORMGEN-3D. In addition, the authors would also like to acknowledge the support from the Air Force Office of Scientific Research (AFOSR), Program Director Dr. Walter F. Jones. Finite element analysis was performed by M. X. Zhao of the University of South Carolina.

Reference

[*1*] Papers from the Symposium on the Surface Crack, *Experimental Mechanics*, 28(2), June 1988.

[*2*] Reuter, W.G., Lloyd, W.R., and Graham, S.M., "Evaluation of Capabilities of Fracture Mechanics to Predict Structural Integrity," *Proceedings of the Ninth International Conference on Offshore Mechanics and Arctic Engineering*, Vol. III, Part B, American Society for Mechanical Engineers, New York, 1990, pp.261-268.

[*3*] Reuter, W. G., Newman, J.C., MacDonald, B.D., and Powell, S.R., "Fracture Criteria for Surface Cracks in Brittle Materials," Fracture Mechanics: Twenty-Fourth Volume, ASTM STP 1207, J. D. Landes, D. E. McCabe and J.A.M. Boulet, eds., American Society for Testing and Materials, Philadelphia, 1994, pp.617-635.

[4] Chao, Y.J. and Zhang, F., "Constraint Effect in Brittle Fracture" *Fatigue and Fracture Mechanics : 27th National Symposium on Fatigue and Fracture, ASTM STP 1296,* Robert Piascik Ed., American Society for Testing and Materials, Philadelphia, 1996, to appear.

[5] Richardson, D. E. and Goree, J. G., "Experimental Verification of a New Two-Parameter Fracture Model," *Fracture Mechanics: Twenty-third Symposium,* ASTM STP 1189, R. Chona, Ed., American Society for Testing and Materials, Philadelphia, 738-750, 1993.

[6] Griffith, A. A., "The Phenomena of Rupture and Flow in Solids," *Philosophical Transactions of the Royal Society of London*, A221, pp.163-197, 1921.

[7] Griffith, A. A., "The Theory of Rupture," *Proceedings of the First International Conference of Applied Mechanics*, Delft, 1924.

[8] Irwin, G. R., "Analysis of Stresses and Strains Near the End of a Crack Tip Traversing a Plate," *ASME Journal of Applied Mechanics*, vol.79, 1957, 361-364.

[9] Williams M. L., "On the Stress Distribution at the Base of a Stationary Crack," *ASME Journal of Applied Mechanics*, 24, 109-114, 1957.

[10] Ritchie, R. O., Server, W. L., and Wullaert, R. A., "Critical Fracture Stress and Fracture Strain Models for the Prediction of Lower and Upper Shelf Toughness in Nuclear Pressure Vessel Steels," *Metallurgy Transaction*, 10A, 1557, 1979.

[11] Ritchie, R. O., Knott, J. F., and Rice, J. R., "On the Relationship Between Tensile Stress and Fracture Toughness in Mild Steel," *Journal of the Mechanics and Physics of Solids*, 21, 395-410, 1973.

[12] Chao, Y.J., Yang, S., and Sutton, M. A., "On the Fracture of Solids Characterized by One or Two Parameters: Theory and Practice," *Journal of Mechanics and Physics of Solids*, 42(4), 1994, pp.629-647.

[13] Yang, S., Chao, Y.J. and Sutton, M. A., "Higher Order Asymptotic Crack Tip Fields in a Power-Law Hardening Material," *Engineering Fracture Mechanics*, 45(1), 1-20, 1993.

[14] Chao, Y.J. and Lam, P. S., "Effects of Crack Depth, Specimen Size, and Out-of Plane Stress on the Fracture Toughness of Reactor Vessel Steels," to appear in ASME *Journal of Pressure Vessel Technology.*

[15] "Standard Test Method for Plane-Strain Fracture Toughness of Metallic Materials," ASTM E399-90, 1993 Annual Book of ASTM Standards.

[16] Reuter, W.G., Elfer, N., Hull, D. A., Newman, Jr. J. C., Munz, D., and Panontin, T. L., "Test Results and Preliminary Analysis for International Cooperative Test Program on Specimens Containing Surface Cracks," presented in the 28th National Symposium on Fatigue and Fracture Mechanics, Saratoga Springs, New York, June 25-27, 1996.

[17] Reuter, W.G., Lloyd, W.R., Kenney, K. L., Parks, D. M., McClintock, F. A., and Ganti, S., "Predicting Crack Growth Initiation for Surface Cracks in High Strength Steel," presented in the 28th National Symposium on Fatigue and Fracture Mechanics, Saratoga Springs, New York, June 25-27, 1996.

[18] T. -L. Sham, "The Determination of the Elastic T-term Using Higher Order Weight Function," *International Journal of Fracture*, **48**: 81-102, 1991.

[*19*] Bass, B. R. and Bryson, J. W., "Applications of Energy Release Rate Techniques to Part-Through Cracks in Plates and Cylinders: Volume 1. ORMGEN-3D: A Finite Element Mesh Generator for 3-Dimensional Crack Geometries," NUREG/CR-2997, ORNL/TM-8527/V1, Oak Ridge National Laboratory, December 1982.

[*20*] *ABAQUS User's Manual*, Version 5.4, Hibbit, Karlson, and Sorensen, 1995.

[*21*] Raju, I. S. and Newman, J.C. Jr., "Three-dimensional Finite Element Analysis of Finite-Thickness Fracture Specimen," NASA Technical Note, NASA TN D-8414, NASA Langley Research Center, 1977.

[*22*] Smith, C. W. and Olaosebikan, "On the Extraction of Stress-Intensity Factors from Near-Tip Photoelastic Data," *Experimental Mechanics*, 26(4), 1986, pp.313-318.

[*23*] Raju, I. S. and Newman, J.C. Jr., "Stress-Intensity Factors for a Wide Range of Semi-elliptical Surface Cracks in Finite-Thickness Plates," *Engineering Fracture Mechanics*, 11, 1979, pp.817-829.

[*24*] Parks, D. M., "Advances in Characterization of Elastic-Plastic Crack-Tip Fields," *Topics in Fracture and Fatigue*, Editor: A.S. Argon, pp. 59-98, Springer-Verlag, 1992.

[*25*] Hancock, J. W., "Constraint and Stress State Effects in Ductile Fracture," *Topics in Fracture and Fatigue*, Editor: A.S. Argon, pp. 99-144, Springer-Verlag, 1992.

[*26*] Kirk, M. T. and Dodds, R.H., "Approximate Techniques for Predicting Size Effects on Cleavage Fracture Toughness (Jc)," NUREG/CR-5970, 1992.

James A. Joyce[1] and Richard E. Link[1]

DUCTILE-TO-BRITTLE TRANSITION CHARACTERIZATION USING SURFACE CRACK SPECIMENS LOADED IN COMBINED TENSION AND BENDING

REFERENCE: Joyce, J.A. and Link, R.E., "**Ductile-to-Brittle Transition Characterization Using Surface Crack Specimens Loaded in Combined Tension and Bending,**" *Fatigue and Fracture Mechanics: 28th Volume, ASTM STP 1321,* J.H. Underwood, B.D. Macdonald and M.R. Mitchell, Eds., American Society for Testing and Materials, 1997.

ABSTRACT: Surface cracked tension specimens of ASTM A515, Grade B steel plate were tested to failure in the ductile-to-brittle transition region. Two different specimen configurations were used: one configuration was loaded in tension except for the natural bending resulting from the presence of the surface crack, the second configuration had an offset test section and was pin-loaded to provide a strong bending component in addition to the tension load. For each configuration, at least seven repeat tests were conducted at each of two temperatures. All specimens failed by cleavage and the critical J-integral, J_c, was obtained using three-dimensional finite element analysis of the specimen. The FEM analysis was validated by comparison with experimental strain gage and displacement measurements taken during the tests. The results were compared with previous fracture toughness measurements on the same plate using 2T SE(B) specimens and surface cracked bend SC(B) specimens. The present results exhibited the expected elevation in fracture toughness and downward shift in the transition temperature compared to the highly constrained, deeply cracked SE(B) specimens. The master curve approach was used to characterize the transition curves for each specimen geometry and the shift in the transition temperature was characterized by the associated reference temperature.

KEYWORDS: surface crack, fracture toughness, constraint, A515 steel, J-integral, master curve

[1]Professor and Assistant Professor, respectively, U.S. Naval Academy, Annapolis, MD 21402.

OBJECTIVE

The fracture toughness of ferritic steels in the ductile-to-brittle transition remains one of the principal concerns in guaranteeing the structural integrity of nuclear reactors, submarines, surface ships, and many other large steel structures. Most testing in the ductile-to-brittle regime has been done with Charpy specimens or with ASTM standard fracture toughness geometries like compact specimens or single edge notched bend specimens. In structural applications, however, the common flaw is a surface crack with a roughly semi-elliptical shape, a depth to length ratio, 2c/a, from 2 to 8, and a depth to plate thickness ratio, a/t, from 0.1 to 0.5. The crack-tip constraint in surface cracked specimens is lower than in deeply-cracked fracture specimens[1]. It is generally believed that fracture assessments of structures containing surface cracks which are based on fracture toughness data from deeply-cracked, bend-type specimen geometries such as those in ASTM standards will result in conservative estimates of the flaw tolerance of the structure. Indeed, some users would argue that such an assessment is unduly conservative and is overly pessimistic. Others take a more cautious approach and rely on the conservatism as an extra factor of safety. The degree of conservatism in these assessments has not been well quantified and it is not a trivial matter to quantify the conservatism present in the analysis when one considers the scatter in fracture toughness data in the ductile-brittle region. Statistical approaches to describe the scatter in fracture toughness data have been under development for some time and are showing progress [2-5]. A new standard test method to define a reference temperature that describes the toughness in the ductile-brittle transition regime is under development within ASTM[2]. Experimental data on the fracture behavior of surface cracked structural elements is needed in order to better quantify the degree of conservatism in fracture assessments based on laboratory specimen data and to develop appropriate guidelines for performing such assessments.

In this experimental work a series of fracture toughness tests were conducted on a ferritic structural pressure vessel steel in the ductile-to-brittle regime using surface cracked specimens. For each temperature and loading condition 6 to 8 repeat tests were conducted allowing a probabalistic analysis of the results. Fracture toughness data on sets of standard test geometries is also available for the test material for comparison with the results of the surface crack specimens.

The test results were analyzed using the recently proposed ASTM T_0 reference temperature procedure, and a master curve and confidence bounds were developed using a Weibull statistical approach. The median of the surface crack results is shown to be elevated in comparison to the median of the high constraint results obtained from the standard ASTM specimens.

---

[2] Draft 12 of the proposed "Test Method for the Determination of Reference Temperature, T_0, for Ferritic Steels in the Transition Range." ASTM Task Group E08.08.03, Philadelphia, 1996.

EXPERIMENTAL DETAILS

The material used in this study was an ASTM A515 Grade 70 steel which is a C-Mn alloy pressure vessel steel that is in the ductile-to-brittle transition at room temperature. The product form of the material was a 127 mm (5 inch) thick plate that had been normalized and the microstructure consisted of a mixture of ferrite and pearlite with an average grain size of approximately 75 micrometers. This material was used in previous studies [6,7] and fracture toughness data developed on standard ASTM bend geometries and on surface cracked bars loaded in bending from these studies is available. The quasi-static, uniaxial tensile properties of the A515 material, determined from duplicate tests are given in Table 1. This steel exhibits an upper and lower yield point as well as yield point elongation behavior as shown in the stress-strain curve shown in Figure 1. Upper shelf fracture toughness properties developed in accordance with ASTM E 813 resulted in J_{Ic} = 112 kJ/m^2 at a temperature of 93°C.

Table 1 Average tensile mechanical properties of ASTM A515, Gr. 70 steel plate.

Temperature °C	Yield Strength MPa	Ultimate Strength MPa	Flow Strength MPa	Elongation %	Reduction of Area %
21	288.	555.	476	25	45
-5	288.	572.	493.	24	41
-40	315.	603.	521.	24	41

Previous Test Geometries

Experimental work by Kirk et al.[6] on this material used ASTM SE(B) geometries with W/B=1 and with the crack oriented in the T-S direction. Crack depths from a/W = 0.1 to a/W = 0.5 were used as well as specimen thicknesses, B, of 10 mm, 25.4 mm, and 50.8 mm. All specimens in this study were tested at 20° C where A515 fails predominantly by cleavage. Experimental work by Porr et al.[7] used this same material but tested surface cracked bend (SC(B)) specimens with the crack again oriented in the T-S direction. Specimen dimensions were 50.8 mm x 203.2 mm x 584 mm, and the specimens were tested in four point bending. Surface cracks were produced from plunge electric discharge machine (EDM) starter slots which were then extended by fatigue precracking in bending to give starter cracks with 2c/a = 2.8 and 6.0, and a depth to thickness ratio, a/t, of 0.25.

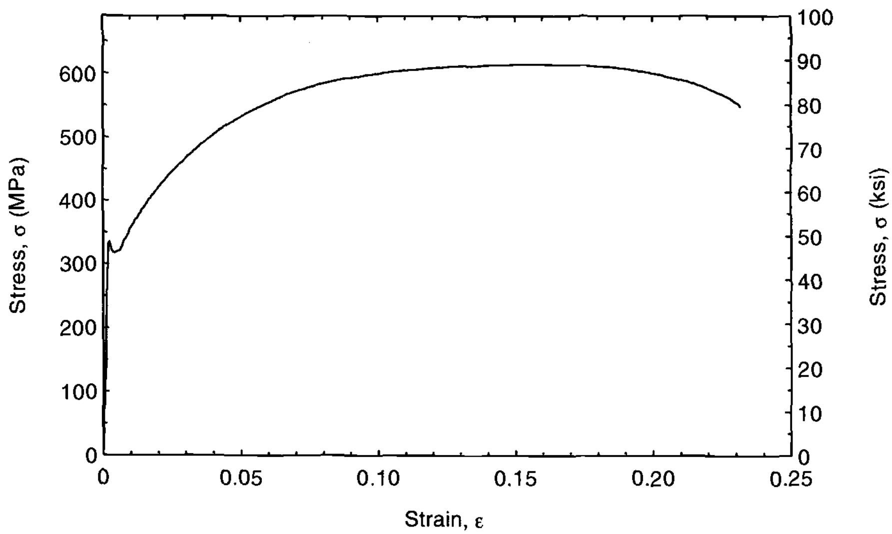

Figure 1 Typical quasi-static stress-strain curve for ASTM A515, Grade 70 (-40°C) steel plate examined in this study.

Present Specimen Geometries

The specimen geometries tested in this project are shown in Figure 2. For the pin-loaded geometry the centerline of the pin is aligned with the cracked surface of the specimen test section which causes a large bending moment to be superimposed on the axial tensile loading in this case. The bolt-loaded specimen is symmetrical and only has the bending component that is generated by the presence of the surface crack. Large, rigid grips were used in this case to provide a predominantly tensile loading. This flaw geometry was obtained by using a plunge EDM process to obtain a starter notch which was then fatigue precracked in bending to obtain the desired $a/t = 0.25$ test crack configuration. Due to the variation in the stress intensity factor along the crack front, the precrack extended more at the deepest part of the crack front than near the crack surface. The EDM notch shape was adjusted to compensate for this effect. The EDM slot had a height of 0.5 mm (0.020 in). At least 1 mm (0.040 in.) of fatigue crack extension was present at all points along the crack front prior to the fracture test. A computer-controlled system was used to precrack the specimens to obtain as repeatable a crack geometry as possible. The compliance equation used for precracking was obtained from 3D elastic finite element analysis of the test geometries using the ABAQUS finite element code. The results of nine separate finite element analyses over the a/t region of interest is shown in Figure 3 and compared to results from Newman and Raju[8].

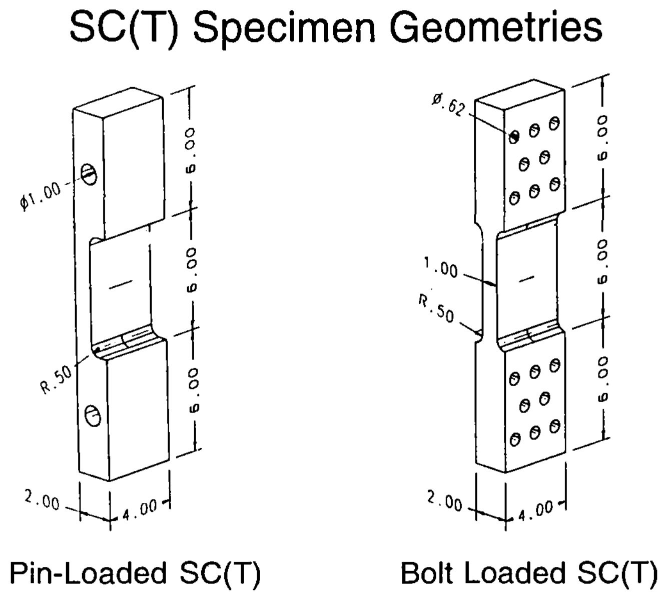

Figure 2 Pin and bolt-loaded surface crack (SC(T)) specimen geometries used in this investigation (Dimensions are in inches).

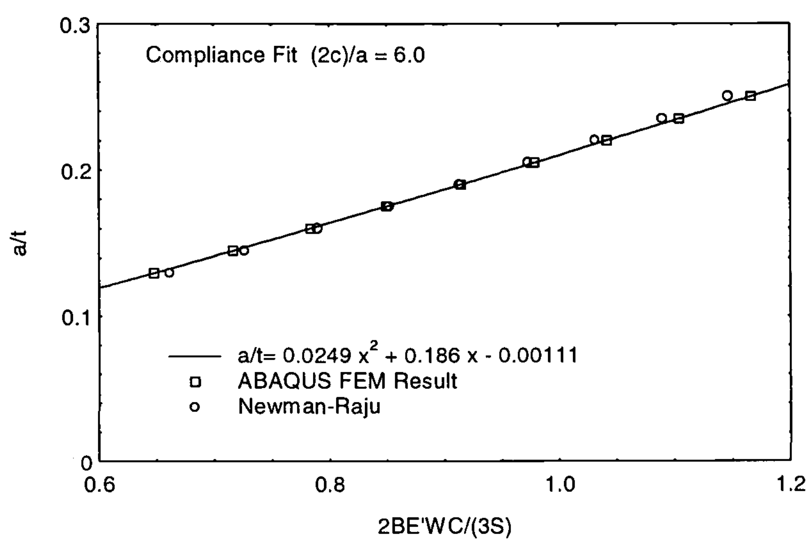

Figure 3 Crack opening compliance for SC(T) specimen loaded in four-point bending.

It was found that a second order polynomial fit of the ABAQUS results adequately fit the compliance results over the region $0.1 \leq a/t \leq 0.25$ giving:

$$a/t = 0.0248\, x^2 + 0.186\, x - 0.00122 \tag{1}$$

with: $x = 2BE'WC/3S$

S = Bend span,
C = v/P = Specimen COD compliance,
$E' = E/(1 - \nu^2)$,
E = Material elastic modulus,
ν = Poisson ratio,
B, W = specimen width and depth respectively.

Equation 1 fits the ABAQUS results within 0.1% and agrees with the Newman- Raju results within 0.5%.

A ring-type COD gage with a gage length of 1.5 mm (0.060 in.) was mounted on the centerline of the surface crack and used for COD measurement during precracking. The stress intensity was controlled during precracking such that $K_{max} \leq 20$ MPa$\sqrt{m}$ (18 ksi-$\sqrt{in}$) with a stress ratio of 0.1. The stress intensity factor at the point of maximum crack depth was evaluated from the FEM analysis and the results are shown in Figure 4. The present FEM results are compared with results of Newman and Raju [8] and the present results are approximately 10% lower. The reason for the discrepancy between the stress intensity calculations for two sets of results is not known. The ABAQUS results were used here and fit as a function of a/t with a second order polynomial which was then used to define the stress intensity during the precracking process. The computer-controlled servohydraulic test system was programmed to maintain constant K conditions as the precrack grew, and shut down the precracking process at the final desired crack length. Since several nominally identical tests were to be run at each condition, it was important that similar crack geometries be obtained in a relatively large number of surface crack specimens at a reasonable cost. Repeatability was found to be very good using the above described method as will be shown later in this paper. A typical notch and precrack is shown in the photograph of Figure 5.

Experimental Testing

All tests were conducted under quasi-static loading in a 2.5 MN (500 kip) servohydraulic test machine running in displacement control. Specimens were installed in an environmental chamber and the temperature was controlled using a liquid nitrogen spray system. The pin-loaded specimens were loaded with clevises similar to those used to test large compact specimens. The bolt-loaded specimens were loaded as rigidly as possible using large block clevises, see Figure 6, approximately 200 mm × 200 mm × 330 mm threaded onto 127 mm studs which were threaded in turn into the machine load cell and actuator. For all specimens, load, COD at the crack centerline, a load-line

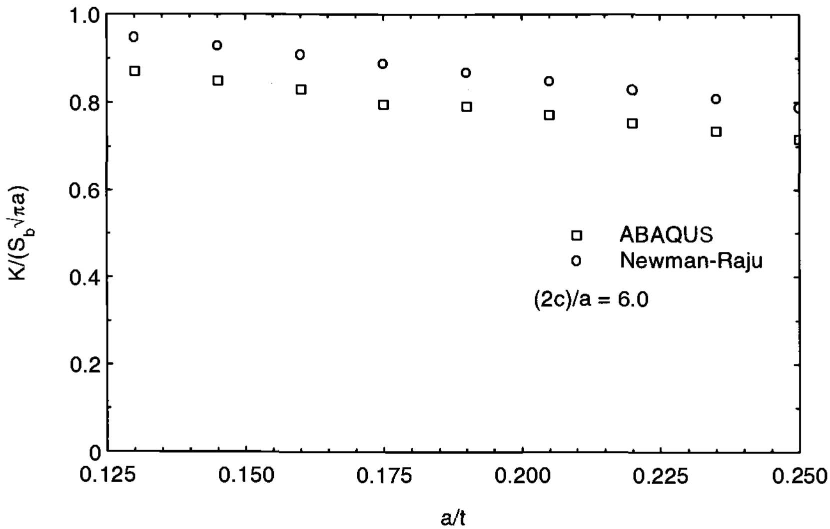

Figure 4 **Stress intensity factor at the point of maximum crack depth for SC(T) specimens loaded in four-point bending.**

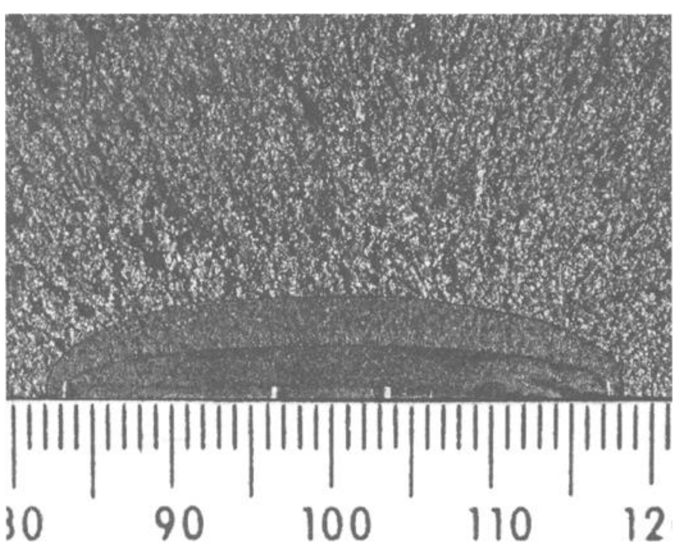

Figure 5 **Photograph of the fracture surface of a typical SC(T) specimen showing EDM notch and fatigue precrack. Small divisions on scale are in mm.**

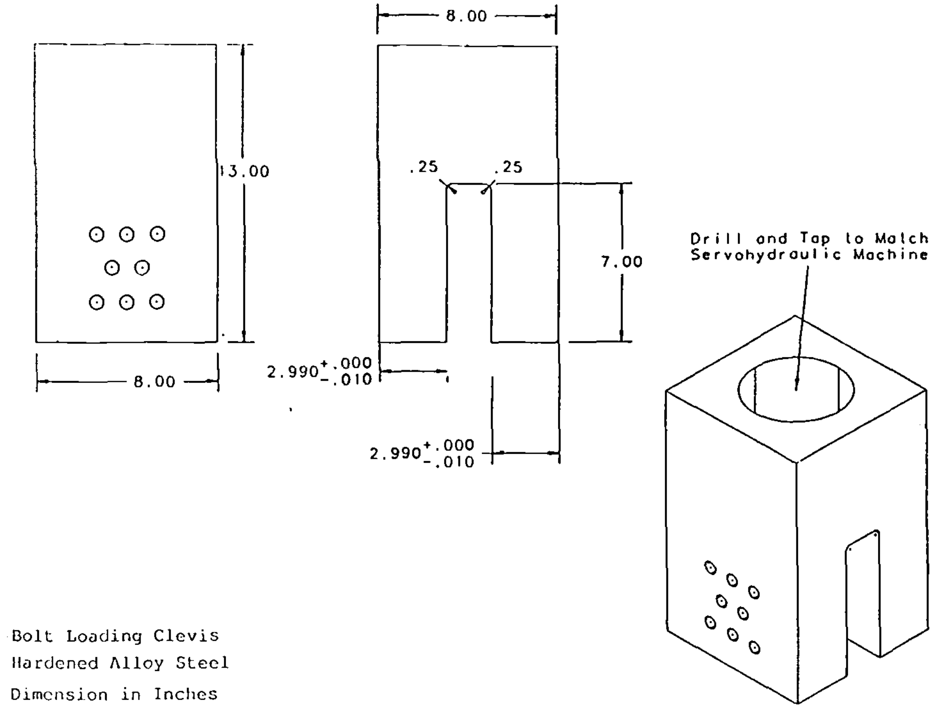

Figure 6 Clevis used for gripping bolt-loaded SC(T) specimens.

displacement, and the test machine actuator displacement were recorded using a digital data acquisition system. Additionally four strain gages were attached to most specimens to allow a post test comparison of the experimental strains and 3D finite element calculations. It was not the purpose of these strain measurements to experimentally evaluate the J-integral, only to verify the finite element analysis, which then could confidently be used to evaluate J. The temperature in each test was measured using a thermocouple attached to the specimen surface. This information was recorded on a separate analog strip chart recorder.

Test temperatures were established carefully using an approximately 3 hour soak time, and the specimens were tested to failure with a slow ramp loading requiring approximately 5 minutes to failure.

ANALYSIS

A matrix of the tests conducted in this study is shown in Table 2. All specimens failed by cleavage fracture with little or no prior ductile crack extension. The only specimens that exhibited any noticeable ductile crack extension were four of the bolt-loaded specimens tested at 10°C. The maximum extent was approximately 0.9 mm and no account of ductile tearing has been made in any of the subsequent analyses. The precracks were measured by digitizing photographs of the fracture surface after the specimen had been tested. The precrack size and shape was very consistent from specimen to specimen and profiles for a set of seven specimens are plotted in Figure 7. Load versus crack opening displacement records for the set of pin-loaded and a set of bolt-loaded specimens tested at -7° C are shown in Figure 8. The load and COD at fracture instability for the specimens tested here are summarized in Table 3. Also tabulated is the length and depth of the precrack for each specimen, and of course the test temperature. The initiation sites for the cleavage failures in these specimens will be located and reported, but that has not yet been completed.

Table 2 Matrix of test conditions examined in this study.

SC(T)	Temperature		
Specimen Type	-40° C	-7° C	10° C
Pin-loaded	7	7	---
Bolt-loaded	---	7	8

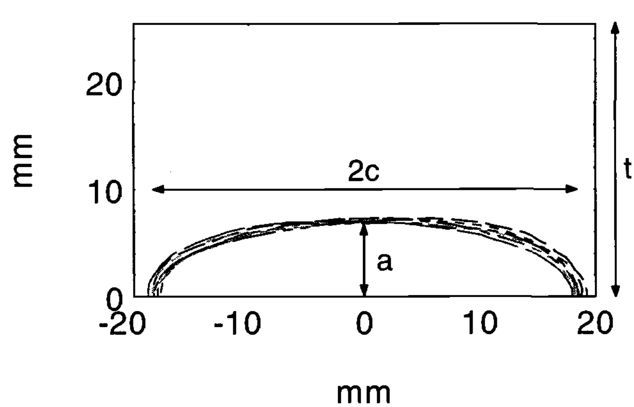

Figure 7 Fatigue crack front profiles from a series of seven SC(T) specimens tested at -7°C.

Table 3 Results of fracture toughness tests of ASTM A515, Gr. 70 pin- and bolt-loaded SC(T) specimens tested in the transition region.

Specimen ID	Test Temperature (°C)	Crack Depth, a (mm)	Crack Length, 2c (mm)	Failure COD (mm)	Failure Load (kN)	J_c (kJ/m^2)
		Pin-Loaded C(T) Specimens				
GGS-1	-40	7.29	37.08	0.09	295.0	15.6
GGS-8	-40	7.34	36.98	0.14	333.1	28.2
GGS-14	-40	7.19	36.83	0.16	338.0	32.4
GGS-16	-40	6.83	36.17	0.15	316.7	32.3
GGS-18	-40	7.16	36.43	0.16	333.8	34.5
GGS-19	-40	7.04	36.81	0.17	323.8	35.3
GGS-20	-40	6.93	36.44	0.18	348.0	38.2
GGS-2	-7	7.11	36.09	0.58	*	138.7
GGS-5	-7	6.93	36.35	0.22	342.7	49.3
GGS-6	-7	7.06	36.32	0.46	506.4	109.1
GGS-7	-7	7.37	37.95	0.23	332.7	50.5
GGS-11	-7	7.87	37.64	0.34	404.9	78.0
GGS-12	-7	7.42	37.72	0.20	338.0	43.8
GGS-13	-7	7.34	39.02	0.37	441.2	85.8
		Bolt-Loaded SC(T) Specimens				
GGS-3	-7	6.48	35.87	0.41	834.9	107.9
GGS-17	-7	7.19	36.67	0.31	744.4	79.1
GGS-22	-7	7.16	36.69	0.43	832.0	116.2
GGS-24	-7	6.65	36.53	0.40	798.5	107.1
GGS-26	-7	6.40	36.15	0.33	761.5	84.2
GGS-27	-7	7.49	37.92	0.41	761.5	110.1
GGS-36	-7	7.34	37.10	0.39	764.3	101.9
GGS-32	10	7.26	38.15	0.27	733.9	70.2
GGS-30	10	7.11	37.42	0.39	765.6	105.6
GGS-25	10	6.91	36.99	0.41	795.8	111.3
GGS-31	10	6.93	36.90	0.49	879.7	135.9
GGS-21	10	6.76	36.92	0.72	895.0	212.6
GGS-35	10	6.99	37.54	0.89	875.6	265.6
GGS-28	10	7.11	37.38	0.75	906.6	217.7
GGS-33	10	6.93	36.42	1.04	1001.1	319.2

* Failure load not recorded

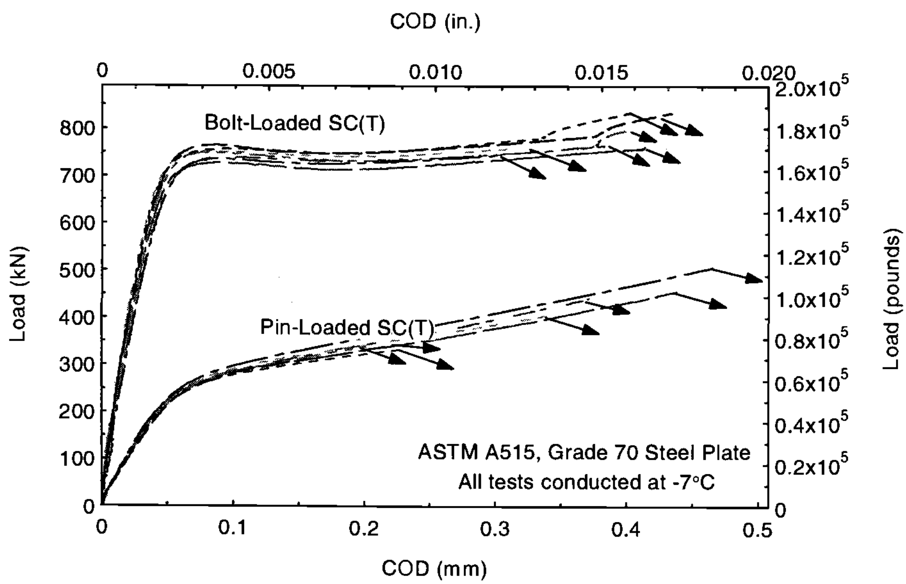

Figure 8 Load versus COD for a series of pin- and bolt-loaded SC(T) specimens tested at -7°C.

Standard equations do not exist to obtain the J-integral at instability for these surface crack geometries as tested in this work. It is known that the J-integral will depend on the position along the crack front and it will be largest at the deepest point along the crack front, i.e. at the crack centerline. In this work 3-D, elastic-plastic finite element analyses were conducted on eight different geometries, the two basic test geometries were analyzed at four a/t ratios each, that is, a/t = 0.225, 0.250, 0.275, and 0.300. The crack length to crack depth ratio (2c/a) was kept at 6 to 1 for each case.

The finite element meshes used were developed from the work of Faleskog[9] who supplied a FORTRAN code to generate the 3D meshes from specimen size and crack size input data. A typical mesh shown in Figure 9 had 1296 elements and 19230 degrees of freedom. All analyses were run on the ABAQUS general purpose finite element code. The stress-strain curve used in the analysis had to include the yield point elongation behavior of the A515 steel in order to accurately capture the load-displacement behavior of the SC(T) specimens. The large rotations exhibited by the specimens made it necessary to incorporate non-linear geometric modeling in the analysis. The variation of J along the crack front for each of the specimen geometries is nearly identical as shown in Figure 10 and it can be seen that J is a minimum at the specimen surface (ϕ=0°) and is a maximum at the deepest point on the crack front (ϕ=90°). A second order polynomial was fit to the normalized results for the bolt-loaded specimen as shown in Figure 11.

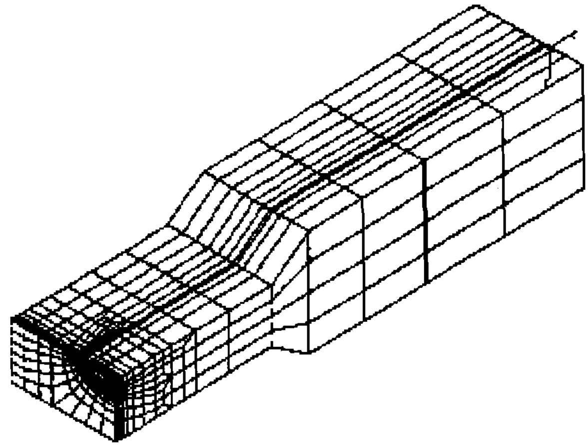

Figure 9 Typical quarter-symmetric finite element mesh employed in elastic-plastic FEM analysis of SC(T) specimens.

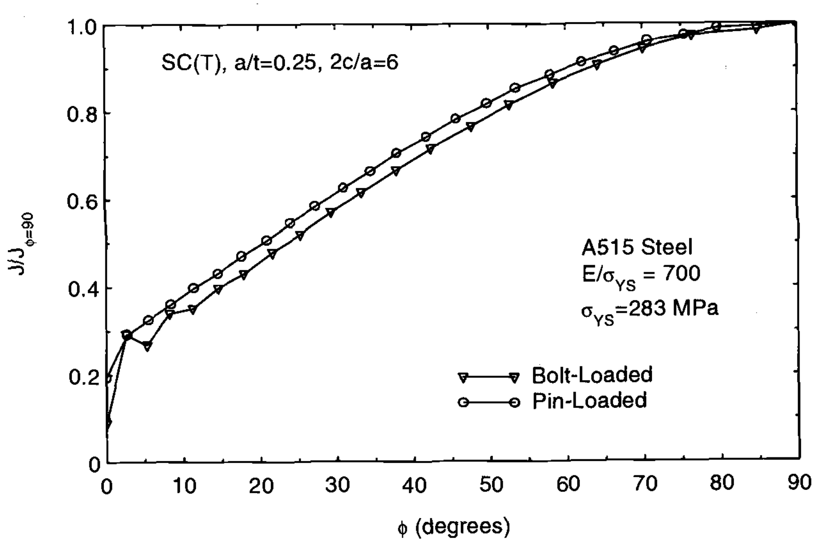

Figure 10 Variation of J around the crack front as a fuction of the elliptic angle (ϕ=0° at surface, 90°at maximum depth) for the SC(T) specimens with a/t=0.25 and 2c/a=6.

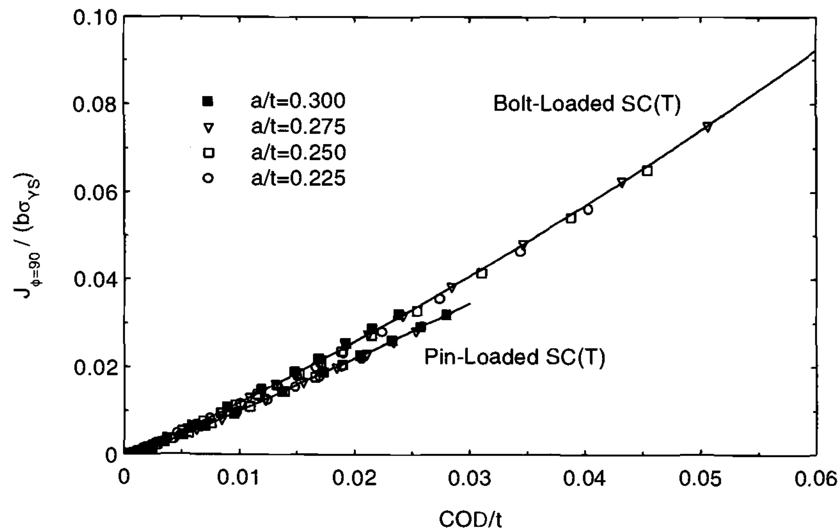

Figure 11 J as a function of COD for the pin- and bolt-loaded SC(T) specimens with 2c/a=6, 0.225 ≤ a/t ≤ 0.300.

The resulting function valid over the range 0.225 ≤ a/t ≤ 0.300 and 0.001 ≤ COD/t ≤ 0.05 was

$$\frac{J_{\phi=90}}{b\sigma_{YS}} = 5.50\left(\frac{COD}{t}\right)^2 + 1.22\left(\frac{COD}{t}\right) - 7.45\times 10^{-4} \tag{3}$$

where t is the specimen thickness, b= (t - a), and σ_{YS} is the yield strength. Similar results for the pin-loaded specimen geometry are also shown in Figure 11 and the expression for this specimen, valid over the range 0.225 ≤ a/t ≤ 0.300 and 0.001 ≤ COD/t ≤ 0.03, was

$$\frac{J_{\phi=90}}{b\sigma_{YS}} = 2.75\left(\frac{COD}{t}\right)^2 + 1.11\left(\frac{COD}{t}\right) - 1..25\times 10^{-3} \tag{4}$$

The measured crack length and the COD at failure were used to determine the critical value for J_c using Eq. 3 or Eq. 4 as applicable. The resulting critical J integral values are presented in Table 3.

Verification of the finite element analyses was done by comparing the load, COD, and strain predictions of the finite element analyses to those obtained experimentally. The comparison of experimental and computational load versus COD records for each specimen type is shown in Figure 12. Clearly these results show excellent agreement between the computations and the experiments.

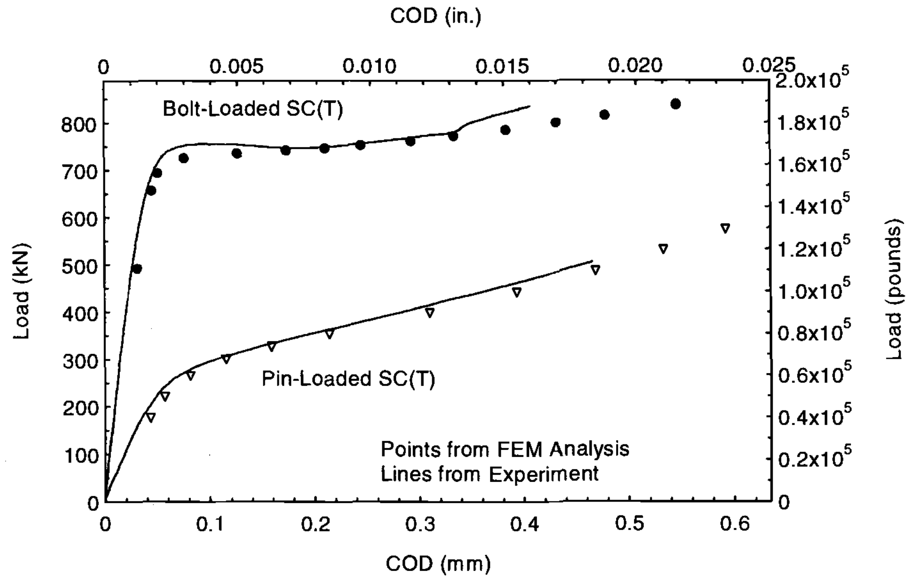

Figure 12 Comparison of predicted load versus COD behavior of the SC(T) specimens with experimental measurements.

In order to further validate the FEM analyses, strain gages were placed at several positions on many of the specimens for comparison with the predicted strain response. Strain gages were located on the crack plane on the back face and on the edge of the specimen as well as on the front and back face along the specimen centerline at a distance of 38 mm above the crack plane. Figure 13 shows the strain gage measurements from a pin-loaded specimen tested at -7°C compared to the FEM predictions, while Figure 14 shows the corresponding comparison for a bolt-loaded specimen. Again, these results show excellent agreement, lending confidence to the FEM results.

DISCUSSION

The critical J at instability, J_c, is presented as a function of test temperature in Figure 18, and the results are compared with the previous results of Kirk et al. and Porr et al. Several observations can be made regarding the critical fracture behavior of the A515 steel in the transition region. Clearly, as the test temperature is increased, the scatter in the fracture toughness increases markedly. The 2T SE(B) specimens tested at 20°C have slightly lower toughness than the SC(B) specimens tested at the same temperature and the scatter appears more or less the same between the two specimen geometries. Comparing the SC(T) results at -7°C, the bolt-loaded specimens have a slightly higher median toughness and lower scatter than the pin-loaded SC(T) specimens. It would be expected

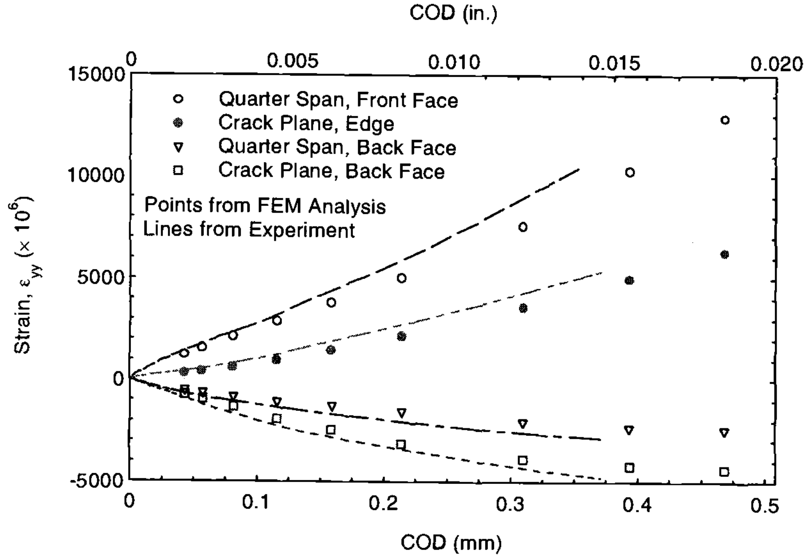

Figure 13 Predicted versus experimentally measured strains in the pin-loaded SC(T) specimen tested at -7°C.

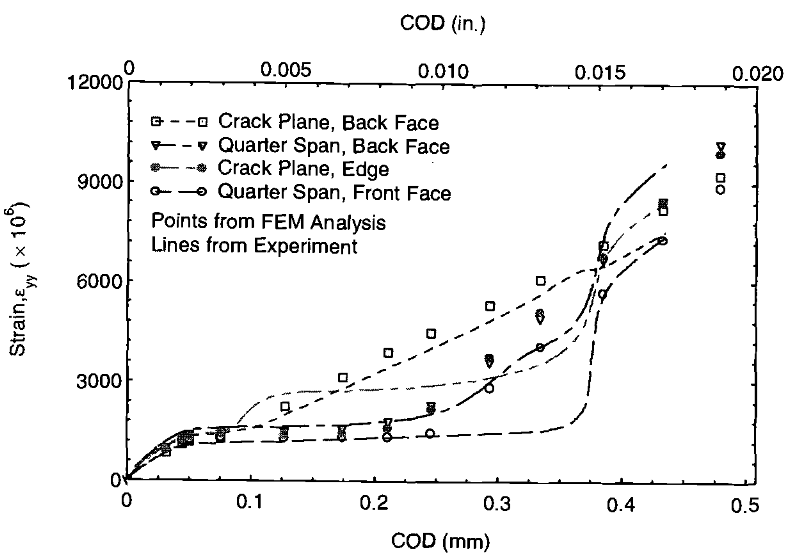

Figure 14 Predicted versus experimentally measured strains in the bolt-loaded SC(T) specimen tested at -7°C.

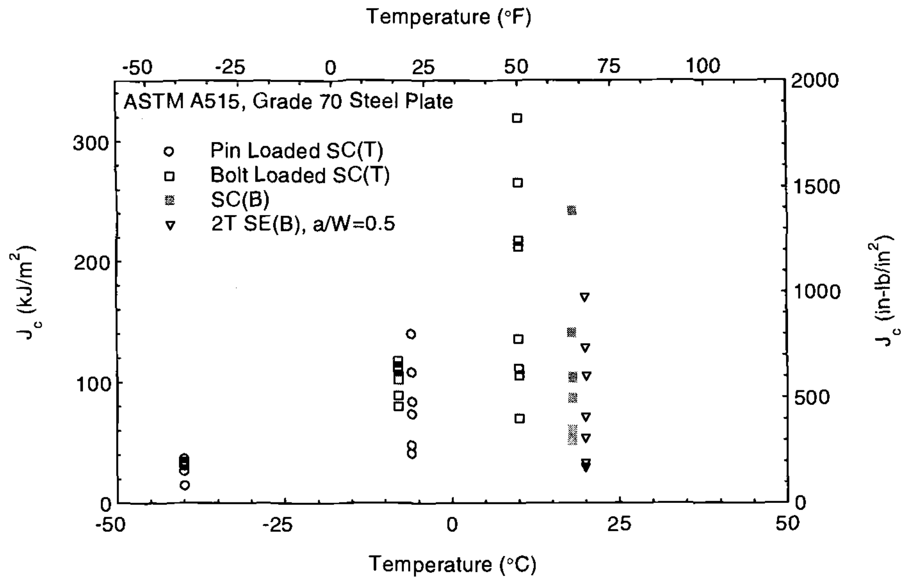

Figure 15 J_c versus test temperature for ASTM A515, Gr. 70 SC(T) and a/W=0.5 SE(B) specimens.

that the constraint in the pin-loaded specimen is greater than the bolt-loaded specimen due to the large bending component in the pin-loaded specimen. The increased toughness in the bolt-loaded specimen makes sense in this regard, but the reduced scatter seems counter intuitive.

Variations in the fracture toughness can be attributed to changes in constraint between various specimen geometries and loading modes (in-plane effects) as well as the thickness of the specimen or structure (statistical size effect). Wallin [3] has developed a model to account for the statistical size effect on fracture toughness and that model is employed here in order to make a more meaningful comparison between the various test results. Specifically, the model relates the fracture toughness expected from various size specimens by the following relationship:

$$K_{B_2} = K_{\min} + \left(K_{B_1} - K_{\min}\right)\left(\frac{B_1}{B_2}\right) \qquad (5)$$

where B_1 and B_2 are the thicknesses (length of crack front) for two different specimens, K_{min} is some assumed minimum fracture toughness level and K_{B1} and K_{B2} are the respective fracture toughnesses of the samples. The critical J values are converted to K_{Jc} values using the relationship $K_{Jc} = \sqrt{(J_c E)}$, and then adjusted to a size corresponding to a 1T specimen (25mm thick) using equation (5) where K_{min} is taken as 20 MPa$\sqrt{m}$ and the length of the crack front is used as B for the surface cracked specimens. Furthermore, the SE(B) results can be used to develop a "master curve" which describes the variation in the fracture toughness of relatively high constraint, deeply cracked specimens over the ductile-brittle transition region. The master curve proposed by Wallin is a function which approximates the shape of the fracture toughness vs. temperature curve for a wide range of ferritic steels in the ductile-brittle regime [10]. The median fracture toughness as a function of temperature is described by the master curve which has the form:

$$K_{J_c(med)} = 30 + 70\exp\left[0.019\left(T - T_0\right)\right] \qquad \textbf{(6)}$$

where T_0 is the temperature at which the median fracture toughness is 100 MPa$\sqrt{m}$. The reference temperature was determined in accordance with the proposed ASTM standard method for determining the reference temperature of ferritic materials using the Kirk et al. SE(B) data [6] as representing the highest constraint data set available for this material. The resulting reference temperature, T_0, was evaluated to be -9°C and the resulting equation for the master curve was thus $K_{Jc(med)}$ = 30 + 70 exp (T+9°C), where T is the temperature in °C and $K_{Jc(med)}$ is the median fracture toughness in MPa$\sqrt{m}$ for a 25 mm thick (1T) specimen at a temperature, T.

All results from Table 3 are compared again in Figure 16 after conversion to K_{Jc} and correction for the statistical size effect. The master curve and the 5% and 95% confidence limits for the SE(B) specimens are plotted as well. In this figure, it becomes clear that the surface crack specimen geometries have a significantly higher toughness than the SE(B) specimens. The minimum toughness exhibited by the surface cracked specimens is nearly equal to the median toughness of the SE(B) specimens represented here by the master curve.

Using the same procedure the reference temperature was determined for each of the surface crack geometries and the results are listed in Table 4. The resulting master curves for the various specimen types are plotted along with the data in Figure 17. Among the surface crack specimens there is now a clear ranking of the toughness exhibited by each geometry with the SC(B) specimens being the lowest, followed by the pin-loaded SC(T) specimens and then the bolt-loaded SC(T) specimens. There is a shift in the reference temperature of about 9°C between each of the various specimen types and the effect on the fracture toughness becomes apparent from the master curves plotted in Figure 17.

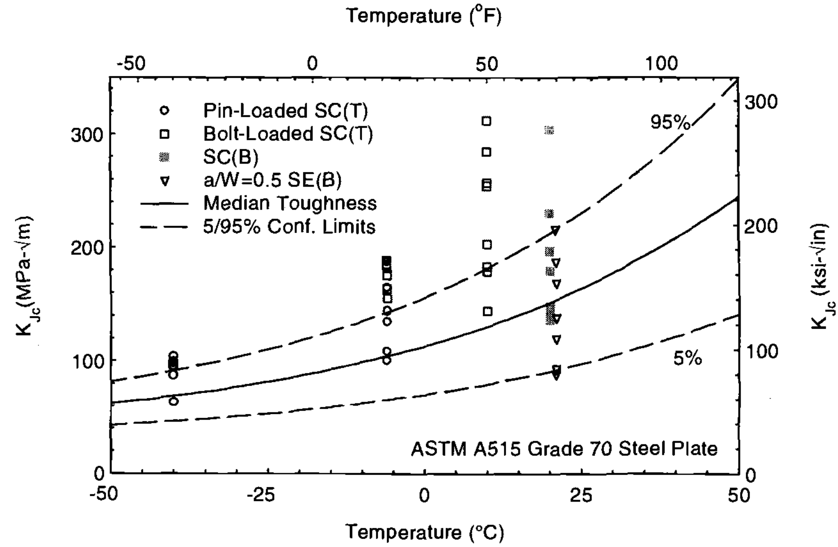

Figure 16 K_{Jc} **as a function of temperature for ASTM A515, Gr. 70 SC(T) and SE(B) specimens. All toughness values adjusted to an equivalent 1T (25 mm) size.**

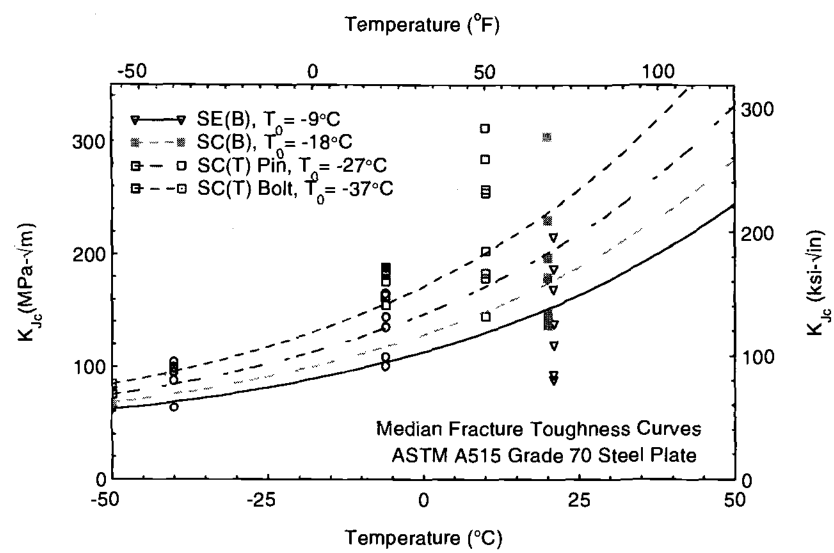

Figure 17 Comparion of the master curves for each of the various specimen geometries along with the 1T size-adjusted fracture toughness values.

Table 4 Reference temperatures determined for each specimen type.

Specimen Geometry	Ref. Temp. T_0
SE(B) tested at 20°C	-9°C
SC(B) tested at 20°C	-18°C
Pin-loaded SC(T) tested at -40°C	-25°C
Bolt-loaded SC(T) tested at -7°C	-29°C
Pin-loaded SC(T) tested at -7°C	-34°C
Bolt-loaded SC(T) tested at 10°C	-39°C

CONCLUSIONS

This program has shown that surface crack specimens can be efficiently tested in the ductile-to-brittle transition regime. A total of 29 specimens were successfully tested in this program out of 31 attempts. The surface cracks were very repeatable and sets of seven repeat tests were generated for each temperature and loading condition allowing a statistical treatment of the results. A 3D finite element analysis was used to evaluate the critical J integral J_c at instability so that a comparison could be made between the results of this study and standard results obtained on this A515 material by previous researchers. The finite element models included piecewise linear models of the material stress-strain curve and a non-linear geometric model to account for the large specimen rotations that occurred. The experimentally measured load displacement records and strain measurements made during the experiments were found to correspond closely to the predictions of the 3D finite element analyses.

Application of the new ASTM master curve approach shows that the surface crack geometries do result in higher effective toughness measurements due, it is felt, to the lower constraint present in these specimens in comparison to that present in deeply cracked SE(B) specimens. Quantification of this effect is not yet possible, though it does appear from these results that the lowest constraint case among those investigated is that of the bolt loaded surface crack geometry, that is, the geometry with the largest relative tension loading component.

REFERENCES

[1] Dodds, R.H., Jr, Anderson, T.L. and Shih, C.F., "Continuum and Micromechanics Treatment of Constraint in Fracture," U.S. Nuclear Regulatory Commission, NUREG/CR-5971, Washington, D.C., 1993.

[2] Landes, J.D. and Shaffer, D.H., "Statistical Characterization of fracture in the transition region," *Fracture Mechanics: Twelfth Conference, ASTM STP 700*, pp. 368-382, American Society for Testing and Materials, Philadelphia, 1980.

[3] Wallin, K., "The Size Effect in K_{Ic} Results," *Engineering Fracture Mechanics*, **22**, No. 1, 149-163, 1985.

[4] Anderson, T.L. and Stienstra, D., "A Model to Predict the Sources and Magnitude of Scatter in Toughness Data in the Transition Region," *Journal of Testing and Evaluation*, **17**, pp. 46-53, 1989.

[5] Ruggierri, C. and Dodds, R.H., Jr., "A Transferability Model for Cleavage Fracture: A Probabalistic Approach," *International Journal of Fracture*, to appear.

[6] Kirk, M.T., Koppenhoeffer, K.C., and Shih, C.F., "Effect of Constraint on Specimen Dimensions Needed to Obtain Structurally Relevant Toughness Measures," *Constraint Effects in Fracture, ASTM STP 1171*, E.M. Hackett, et al., Eds., American Society for Testing and Materials, Philadelphia, pp. 2-20, 1993.

[7] Porr, W.C., Jr., Link, R.E., Waskey, J.P., and Dodds, R.H., Jr., "Experimental Application of Methodologies to Quantify the Effect of Constraint on J_c for a 3-D Flaw Geometry," *Fracture Mechanics: 26th Volume, ASTM STP 1256*, W.G. Reuter, J.H. Underwood and J.C. Newman, Eds., American Society for Testing and Materials, Philadelphia, pp. 107-125, 1995.

[8] Newman, J.C., Jr., and Raju, I.S., "Stress-Intensity Factor Equations for Cracks in Three-Dimensional Finite Bodies Subjected to Tension and Bending Loads," NASA Technical Memorandum 85793, Langley Research Center, April 1984.

[9] Faleskog, J. "Crack Growth in Elastic-Plastic Material," PhD Dissertation, The Royal Instutute of Technology, Stockholm, 1994.

[10] Wallin, K., "A Simple Theoretical Charpy-V - K_{Ic} Correlation for Irradiation Embrittlement," *Innovative Approaches to Irradiation Damage and Fracture Analysis, PVP-Vol. 170*, D.L. Marriott, et al., Eds., The American Society of Mechanical Engineers, New York, pp. 93-100, 1989.

Mikhail A. Sokolov,[1] Kim Wallin,[2] and Donald E. McCabe[1]

APPLICATION OF SMALL SPECIMENS TO FRACTURE MECHANICS CHARACTERIZATION OF IRRADIATED PRESSURE VESSEL STEELS

REFERENCE: Sokolov, M. A., Wallin, K., McCabe, D. E., "**Application of Small Specimens to Fracture Mechanics Characterization of Irradiated Pressure Vessel Steels,**" *Fatigue and Fracture Mechanics: 28th Volume, ASTM STP 1321,* J. H. Underwood, B. D. Macdonald, and M. R. Mitchell, Eds., American Society for Testing and Materials, 1997.

ABSTRACT: In this study, precracked Charpy V-notch (PCVN) specimens were used to characterize the fracture toughness of unirradiated and irradiated reactor pressure vessel steels in the transition region by means of three-point static bending. Fracture toughness at cleavage instability was calculated in terms of elastic-plastic K_{Jc} values. A statistical size correction based upon weakest-link theory was performed. The concept of a master curve was applied to analyze fracture toughness properties. Initially, size-corrected PCVN data from A 533 grade B steel, designated HSST Plate 02, were used to position the master curve and a 5% tolerance bound for K_{Jc} data. By converting PCVN data to 1T compact specimen equivalent K_{Jc} data, the same master curve and 5% tolerance bound curve were plotted against the Electric Power Research Institute valid linear-elastic K_{Ic} database and the ASME lower bound K_{Ic} curve. Comparison shows that the master curve positioned by testing several PCVN specimens describes very well the massive fracture toughness database of large specimens. These results give strong support to the validity of K_{Jc} with respect to K_{Ic} in general and to the applicability of PCVN specimens to measure fracture toughness of reactor vessel steels in particular. Finally, irradiated PCVN specimens of other materials were tested, and the results are compared to compact specimen data. The current results show that PCVNs demonstrate very good capacity for fracture toughness characterization of reactor pressure vessel steels. It provides an opportunity for direct measurement of fracture toughness of irradiated materials by means of precracking and testing Charpy specimens from surveillance

---

[1]Metals and Ceramics Division, Oak Ridge National Laboratory, P.O.Box 2008, Oak Ridge, TN 37831-6151, managed by Lockheed Martin Energy Research Corp. under contract DE-AC05-96OR22464 for the U.S. Department of Energy.

[2]Technical Research Centre of Finland, P.O.Box 1704, FIN-02044, Finland.

capsules. However, size limits based on constraint theory restrict the operational test temperature range for K_{Jc} data from PCVN specimens.

KEYWORDS: precracked Charpy, fracture toughness, master curve, reconstitution, reactor pressure vessel

---

INTRODUCTION

The American Society of Mechanical Engineers (ASME) K_{Ic} curve is based upon data acquired by testing large specimens of unirradiated reactor pressure vessel (RPV) steels and weld metals that satisfy the validity requirements of the American Society for Testing and Materials (ASTM) Standard Test Method for Plane-Strain Fracture Toughness of Metallic Materials (E 399-90). Currently, the provisions for determination of the upward temperature shift of the ASME K_{Ic} curve due to irradiation of reactor pressure vessel steels are based on the Charpy 41-J shift, and the shape of the fracture toughness curve is assumed not to change as a consequence of irradiation. The main reason for such assumptions was that it is not practicable to accumulate the equivalent linear-elastic K_{Ic} data base for irradiated material in the transition region. In fact, the maximum size of compact specimens for irradiation studies is limited to 4T (101.6 mm) simply due to through-thickness fluence gradients. With testing of small specimens in the transition region, some amount of local crack tip plasticity is unavoidable and fracture toughness up to cleavage instability is calculated in terms of size-dependent elastic-plastic K_{Jc} values. Therefore, for a ductile-to-brittle transition region a statistical size correction based upon weakest-link theory has been proposed [1].

In this study, precracked Charpy V-notch (PCVN) specimens were used to characterize fracture toughness of unirradiated and irradiated reactor pressure vessel steels in the transition region by means of three-point slow bending. The PCVN specimens were fatigue precracked to a/W ratio of about 0.5. A method employing Weibull statistics was applied to model fracture toughness data distributions in the transition region and a master curve concept was used to describe the temperature dependence of fracture toughness. The PCVN specimen has exceptional application for reactor pressure vessels. The Charpy V-notch specimen is the most commonly used specimen geometry in surveillance programs. Precracking and testing of irradiated Charpy surveillance specimens would allow one to determine and monitor directly actual fracture toughness of an irradiated vessel instead of indirect evaluations using correlations established with impact data.

How well PCVN K_{Jc} data compare to compact specimen K_{Jc} data and how well a PCVN specimen generated master curve lower tolerance bound compares to the ASME lower-bound K_{Ic} curve, will be examined in this paper.

ANALYSIS PROCEDURE

The fracture toughness data were analyzed by a procedure based on earlier work described in Ref. [2] and developed in a proposed ASTM draft standard, [3], by applying the statistical model of Weibull [4]. The analysis procedure is based on fitting replicated fracture toughness data to a three-parameter Weibull cumulative distribution function at the test temperature. It was determined in Ref. [2], at least for reactor pressure vessel steels, that among these three parameters, the shape parameter (Weibull slope) is equal to 4 and the location parameter, K_{min}, is about 20 MPa$\sqrt{m}$. Fixing the slope b = 4 and K_{min} = 20 gives the Weibull cumulative probability distribution function as:

$$P_f = 1 - \exp\left[-\left(\frac{K_{Jc}-20}{K_o-20}\right)^4\right], \tag{1}$$

where P_f is the cumulative fracture probability for $K \leq K_{Jc}$ and K_o is a specimen thickness and temperature-dependent scale parameter. Thus, only the scale parameter, K_o, needs to be determined. As a consequence, only a few replicate tests are needed to obtain this parameter with good accuracy. The proposed ASTM practice, Ref. [3], requires at least six replicated tests. The procedure employs the maximum likelihood concept regarded as the most accurate method of obtaining K_o:

$$K_o = \left[\frac{\sum_{i=1}^{N}(K_{Jc(i)}-20)^4}{N-1+\ln 2}\right]^{1/4} + 20,\ MPa\sqrt{m} \tag{2}$$

where $K_{Jc(i)}$ represents each datum obtained at the given test temperature. The term N is the total number of replicate data at that test temperature. Occasionally with the testing of small specimens, a data set may contain an invalid K_{Jc} value, and, in such cases, Eq. (2) is modified to handle censored (invalid) data. This procedure is described in Ref. [3] and requires at least six valid data to proceed. Additionally, weakest-link theory is used [1] to explain statistical specimen size effects so that data, for example, equivalent to that for a 1T size specimen, $K_{Jc(1T)}$, can be calculated from data measured with specimens of different sizes, $K_{Jc(xT)}$:

$$K_{Jc(1T)} = 20 + [K_{Jc(xT)}-20]\left[\frac{B_{(xT)}}{B_{(1T)}}\right]^{1/4},\ MPa\sqrt{m} \tag{3}$$

where $B_{(xT)}$ and $B_{(1T)}$ are the test specimen and 1T size specimen thicknesses, respectively. Statistical size correction is based on the fact that the cleavage fracture in the transition range is initiated by small microstructural defects that are always present in commercially produced reactor pressure vessel steels. Thus, the thicker the specimen being tested, the higher the probability of encountering the trigger point of a critical size on the crack tip front at a critical stress state and, as result, measuring lower fracture toughness than with a specimen of smaller thickness. Equation (3) is the mathematical expression for these statistical effects. Finally, knowing all of the parameters of the distribution allows one to determine the median K_{Jc} toughness for a specimen of chosen reference size, usually a 1T C(T), $K_{Jc(med)}$, at a given temperature; the K_{Jc} value at $P_f = 0.5$.

Thus, the current procedure provides a tool to describe the scatter of fracture toughness data in the transition region and to determine median K_{Jc} (1T) value by means of performing a few replicate tests. However, the application of this procedure to small specimens has some limitations. On the high-temperature side small specimens are limited by specimen capacity to maintain constraint. As the lower-shelf toughness at low temperatures is approached, the statistical size effects diminish since the fracture becomes more and more propagation controlled and Eq. (3) becomes inapplicable because the initiation criterion is no longer dominant. These mean that the test temperature range for small specimens is quite narrow in order to provide data acceptable for the current analysis procedure. Practically, PCVN specimens provide reliable data at $K_{Jc(med)}$ values equal to or slightly below 100 MPa$\sqrt{m}$.

For structural ferritic steels however, $K_{Jc(med)}$ values tend to form transition temperature curves of the same universal shape which is known now as the "master curve." The master curve of $K_{Jc(med)}$ for 1T size specimens in the transition region is described by:

$$K_{Jc(med)}^{1T} = 30 + 70\exp[0.019(T - T_{100})],\ MPa\sqrt{m} \tag{4}$$

where T_{100} is the reference temperature at which $K_{Jc(med)}{}^{1T}$ is 100 MPa$\sqrt{m}$. Thus, having the temperature dependence of fracture toughness fixed by Eq. (4) permits obtaining a reliable value of $K_{Jc(med)}$ from PCVN specimens at one temperature and then estimating the whole transition region curve by means of the master curve.

TEST OF HSST PLATE 02

Initial tests were performed on ASTM A 533 grade B class 1 plate, designated HSST Plate 02. PCVN specimens were tested in three-point slow bending. Load versus load-point displacement was measured. The 1T compact specimens of the same orientation (T-L) and location in the plate have been previously tested as a part of the Heavy-Section Steel Technology Program (HSST) performed at Oak Ridge National Laboratory (ORNL) [5]. Table 1 summarizes test and analysis results for this plate. Four test temperatures were selected based on 1T specimen data. The lowest test temperature was $-50°$C. Seven PCVN specimens were tested at this temperature and the parameter K_o is equal to 91.9 MPa$\sqrt{m}$, see Table 1. The median toughness value adjusted to 1T equivalence by Eq. (3) is reported in Table 1. Finally, the reference transition temperature, T_{100}, as determined by rearranging Eq. (4) was $-23°$C. Seven specimens were tested at $-30°$C and, although this test temperature was only 20° higher, one K_{Jc} value slightly exceeded the constraint limit currently set in Ref. [3] by the following:

$$K_{Jc(limit)} = \left(\frac{E b_o \sigma_y}{30}\right)^{1/2},\ MPa\sqrt{m} \tag{5}$$

where E is elastic modulus, b_o is the initial remaining ligament dimension, and σ_y is the yield strength. The yield strength for HSST Plate 02 was calculated by $\sigma_y = 492 - 0.842T + 0.00234T^2$ from Ref. [5]. According to the proposed ASTM draft standard [3], the invalid data point was censored and assigned the $K_{Jc(limit)}$ toughness value. Then, the K_o was determined by:

$$K_o = \left[\frac{\sum_{i=1}^{N}(K_{Jc(i)} - 20)^4}{r - 1 + \ln 2}\right]^{1/4} + 20,\ MPa\sqrt{m} \tag{6}$$

where r is the number of valid data (six in this case) and N is the total number of valid and invalid K_{Jc} values. The reference fracture toughness temperature determined from this data set is −26°C. The difference between two estimates is only 3°C, which indicates that median toughness values determined by PCVNs fit very well to the shape of the master curve. The average of these two values, −25°C, is used as the reference fracture toughness temperature determined by testing of PCVN specimens in following evaluations of HSST Plate 02 properties. The third data set illustrates how narrow the operational test temperature range is for PCVN specimens based on the constraint limit set by Eq. (5). Although the test temperature was increased by 15°C only, all seven tests gave invalid K_{Jc} results. Finally, seven specimens were tested at 15°C and only six of them cleaved after some slow-stable crack extension. Results from the last two sets of data are included in Table 1 for information only.

Figure 1 reviews fracture toughness data for HSST Plate 02 derived by testing 1T compact [5] and precracked Charpy specimens. The PCVN data, both valid and invalid, are plotted after adjustment to 1T size. Dotted lines represent the upper-shelf validity limits by Eq. (5) for corresponding specimen sizes assuming $b_o = 0.5W$. The validity limit for PCVN specimens is also adjusted to 1T size. The master curve and 5 and 95% tolerance bounds evaluated from testing of PCVN specimens ($T_{100} = -25$°C) are presented on the same plot, see Fig. 1. Tolerance bounds are calculated using following [3]:

$$K_{Jc(0.95)} = 34.6 + 102.2\exp[0.019(T - T_{100})],\ MPa\sqrt{m} \tag{7}$$

$$K_{Jc(0.05)} = 25.4 + 37.8\exp[0.019(T - T_{100})].\ MPa\sqrt{m} \tag{8}$$

Figure 1 shows that the analysis procedure described here provides a powerful tool to describe fracture toughness K_{Jc} properties in the transition region by testing limited numbers of PCVN specimens. Together with the advantages, these data also highlight the limitation on PCVN specimens due to the constraint limit imposed by Eq. (5). In other words, K_{Jc} values from PCVN specimens can be as good as those from larger compact

TABLE 1--Results of PCVN specimen data analysis of HSST Plate 02.

T_{test} (°C)	K_{Jc} (MPa√m)	b_o (mm)	$K_{Jc(limit)}$ (MPa√m)	K_o (MPa√m)	$K_{Jc(med)}^{1T\,adj}$ (MPa√m)	T_{100} (°C)
−50	79.23	4.94	136.66	91.90	72.17	−23
	82.21	4.69	133.16			
	85.77	4.76	134.15			
	92.99	4.84	135.27			
	93.44	4.13	124.96			
	94.56	5.14	139.40			
	101.67	4.78	134.43			
−30	96.20	4.86	132.58	122.88	94.65	−26
	101.83	4.52	127.86			
	109.37	5.01	134.61			
	121.46	5.14	136.34			
	121.66	5.20	137.14			
	126.57	4.75	131.07			
	147.63	4.77	131.35			
−15	141.85	4.48	125.28	N/A	N/A	N/A
	149.24	4.73	128.73			
	152.04	5.20	134.97			
	163.07	4.78	129.41			
	173.68	4.91	131.15			
	174.65	4.91	131.15			
	178.36	4.86	130.49			
15[a]	238.93	5.05	129.11	N/A	N/A	N/A
	242.79	5.43	133.88			
	268.93	5.39	133.38			
	280.91	5.46	134.25			
	281.00	5.35	132.89			
	300.30	5.05	129.11			
	304.29[b]	4.81	126.00			

[a] All specimens tested at this temperature were 20% side-grooved.
[b] End of test value; specimen did not cleave.

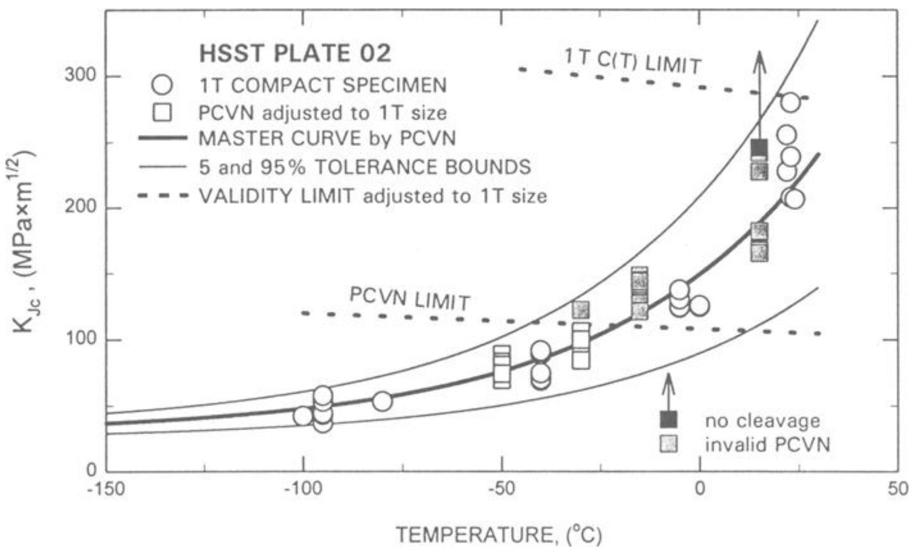

FIG. 1--Elastic-plastic fracture toughness, K_{Jc}, of A 533 grade B HSST Plate 02 determined by 1T compact and precracked Charpy specimens.

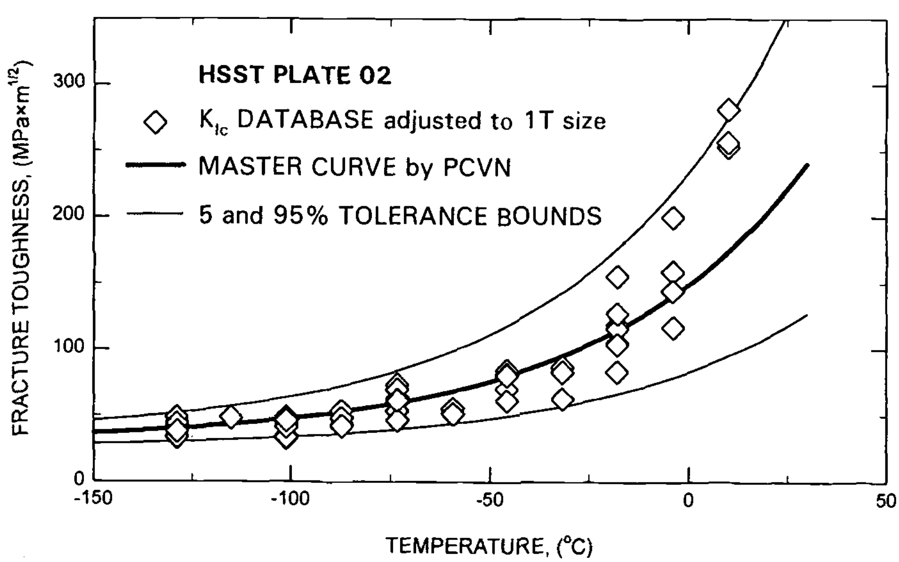

FIG. 2--Comparison of the HSST Plate 02 linear-elastic K_{Ic} database relative to the master curves with 5 and 95 % margin-adjusted tolerance bound curves derived by testing of several PCVN specimens.

specimens but caution needs to be applied in the selection of a test temperature in order to have valid K_{Jc} data.

RELEVANCE TO THE ASME K_{Ic} CURVE

The ASME K_{Ic} curve was constructed as a lower bound to its respective linear-elastic K_{Ic} database for reactor pressure vessel steels [6] plotted as a function of test temperature (T) normalized to a reference nil-ductility temperature, RT_{NDT}, namely, $T - RT_{NDT}$. The RT_{NDT} is derived from a combination of drop-weight and Charpy impact test results. The majority of the ASME database is represented by the HSST Plate 02.

Obviously none of the K_{Jc} values from PCVN specimens reported in Table 1 could satisfy the validity requirements for linear-elastic K_{Ic} stated in ASTM E 399-90. Lower bound fracture toughness has, for many years, been believed to be achievable only through valid K_{Ic} data. Therefore, a question remains regarding the relevance of properties evaluated by the "master curve" procedure to the ASME lower-bound K_{Ic} curve. We will approach this question in two steps. First, the same master curve evaluated by testing PCVN specimens will be compared to the linear-elastic K_{Ic} data of HSST Plate 02 from Ref. [6], see Fig. 2. These K_{Ic} data have been obtained by testing of seventy specimens of different sizes up to 11T thickness. The statistical size correction by Eq. (3) is applied to adjust the data to 1T size equivalence. In order to cover uncertainty in T_o due to testing only a few specimens, a margin, ΔT_{100}, is added to tolerance bounds. The margin is equal to:

$$\Delta T_{100} = \sigma(Z_{85}) \tag{9}$$

were σ is standard deviation and Z_{85} is the tabulated two-tail normal deviate for the specified probability (we used 85%). Standard deviation for estimates on T_{100} is approximated as $\sigma = 18°C/\sqrt{N}$, where N is the total number of specimens that were used to obtain T_{100}. In our case N = 14. Z_{85} is of 1.44. Thus, ΔT_{100} is equal to 7°C. Figure 2 shows that the master curve and the 5 and 95% margin-adjusted tolerance bounds derived from testing of several PCVN specimens represents very well the large K_{Ic} database accumulated by testing of massive specimens.

Having success in describing the K_{Ic} database by the master curve from PCVN specimens of the same material, the next step is the direct comparison between the ASME lower bound curve and the 5% margin-adjusted tolerance bound curve, see Fig. 3. All 174 K_{Ic} data from the EPRI database were re-examined and checked for accuracy in Ref. [7] and these data are also plotted on this figure. The top and right axes are in English units which is usual when relative temperature, $T - RT_{NDT}$, is expressed in °F. The first ASME curve was manually constructed as the lower boundary to all K_{Ic} values available at that time in a normalized temperature range, $T - RT_{NDT}$, from −100 to +100°F. More recently, such graphical representation has been replaced by the so-called EPRI equation which in SI units is as follows:

$$K_{Ic} = 36.5 + 3.083\exp[0.036(T - RT_{NDT} + 55.6)].\ MPa\sqrt{m} \tag{10}$$

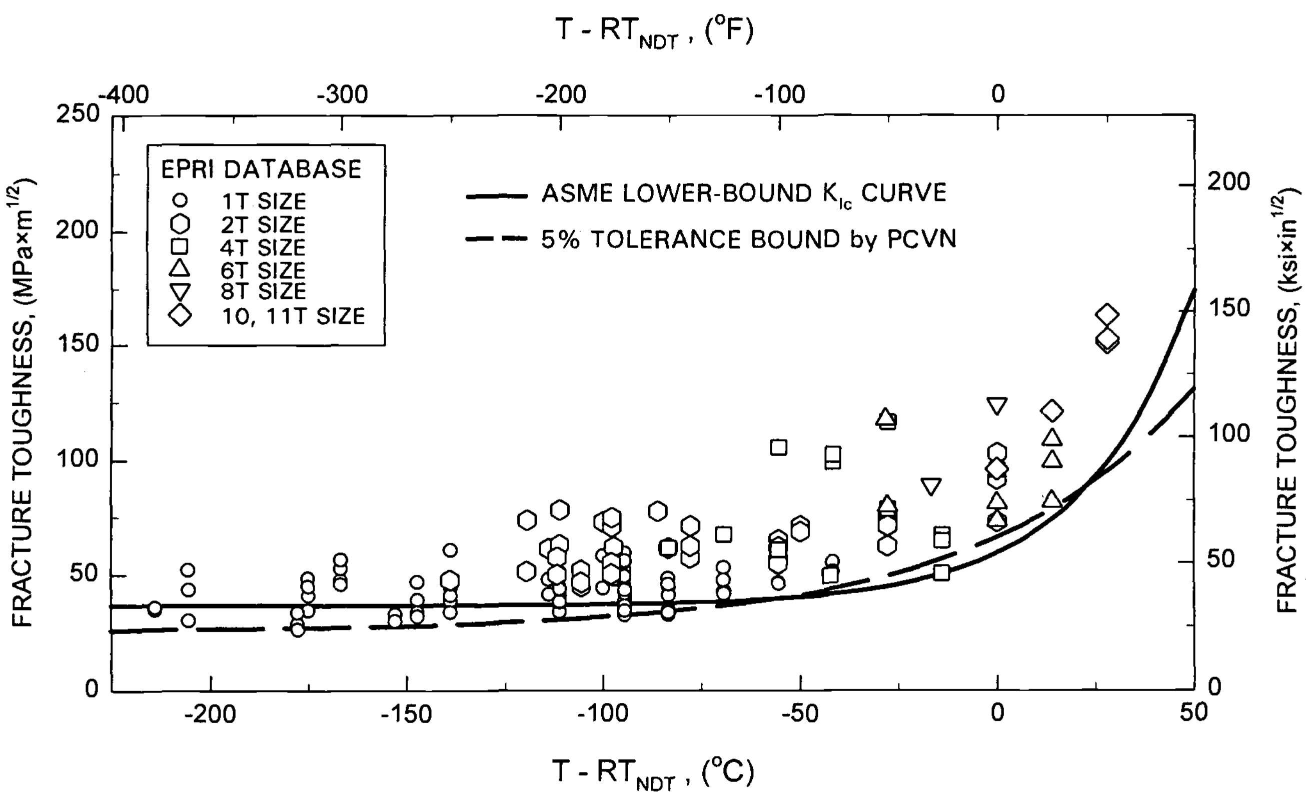

FIG. 3--Comparison of the K_{Ic} EPRI database and ASME lower-bound curve relative to the 5% margin-adjusted tolerance bound curve derived by testing of several PCVN specimens of HSST Plate 02.

For a comparison, the 5% margin-adjusted tolerance bound curve derived from testing of PCVN specimens of HSST Plate 02 in the temperature coordinate normalized to RT_{NDT},[3] including the effect of ΔT_{100}, is equal to:

$$K_{Jc(0.05)} = 25.4 + 37.8\exp[0.019(T - RT_{NDT})],\ MPa\sqrt{m} \tag{11}$$

In Fig. 3, Eqs. (10) and (11) are both plotted over the full temperature range of the K_{Ic} data. The first observation is that Eq. (10) is only a fitting function for the data in the temperature range −100°F to +100°F, hence it is not a true lower bound to all of the data. In fact, the 5% tolerance bound curve from the present study suits better as the lower-bound to the total EPRI database. In the transition region, the ASME K_{Ic} curve rises more rapidly than the tolerance bound to the master curve. The deviation starts at $T - RT_{NDT}$ above 25°C. On the other hand, this is the region where almost no K_{Ic} data are available. Thus, the shape of the ASME curve at $T - RT_{NDT}$ above 25°C reflects rather a postulated shape, while the master curve concept has been experimentally proven to describe the scatter of elastic-plastic-based fracture toughness values in the transition region. In this discussion however, the caution regarding the necessity for using only valid K_{Ic} data is relaxed by applying the master curve based on K_{Jc} data to describe the scatter of K_{Ic} data of the same material and also the total K_{Ic} database. The specific advantage of the present results is that the master curve was developed from PCVN specimens.

TEST OF RECONSTITUTED PCVN SPECIMENS

Recent progress in reconstitution by welding of Charpy-size specimens from previously broken surveillance specimen halves [8] opens a new area for the PCVN specimen application. Reconstituted surveillance PCVN specimens can be used for direct measurements of fracture toughness of reactor pressure vessels in the irradiated condition and/or, for example, for an evaluation of benefits from possible thermal annealing. Reconstituted PCVN specimens are also good candidates for a supplemental surveillance program. In the present study, PCVN specimens were reconstituted by a welding technique described in Ref. [9] from the broken halves of previously tested crack-arrest specimens of a RPV submerged-arc weld, designated as HSSI weld 73W.

The HSSI weld 73W has been well characterized as a part of the Heavy-Section Steel Irradiation (HSSI) Program Fifth Irradiation Series [10]. Seventy-eight compact specimens ranging in sizes from 1T to 8T were tested in the unirradiated condition at ORNL and Materials Engineering Associates to characterize the transition region. These data are compared to reconstituted PCVN specimen data from the present study in Fig. 4. The scatter of fracture toughness data is well described by the master curve with 5 and 95% margin-adjusted tolerance bounds obtained only from PCVN specimen data. Eleven PCVN specimens were tested over the temperature range. Utilizing the postulates already discussed [Eqs. (1) through (4)], each K_{Jc} value was used to calculate T_{100} from individual data points and then the maximum likelihood estimate of T_{100} for this set was determined

[3]In this case, $T_{100} = -25$°C, $RT_{NDT} = -18$°C(0°F), and $\Delta T_{100} = 7$°C.

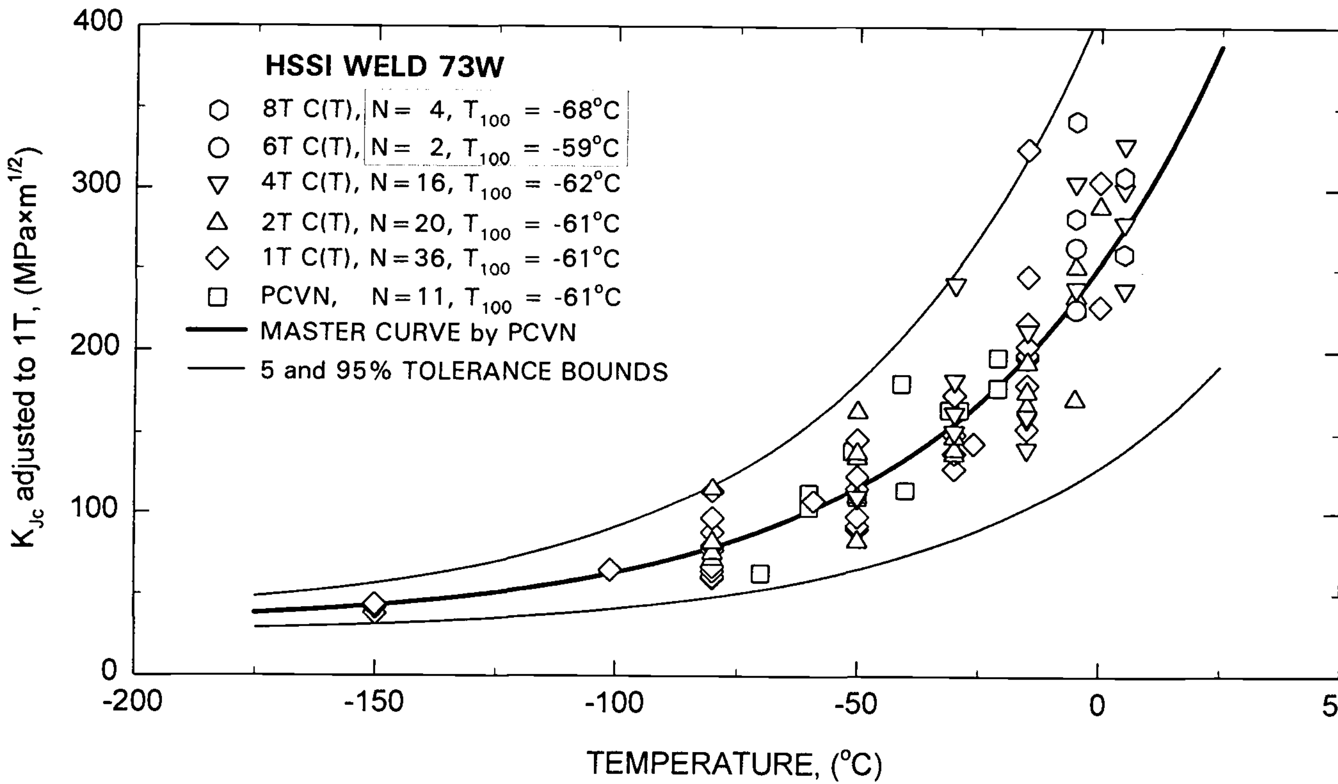

FIG. 4--Fracture toughness of HSSI weld 73W measured with different specimens relative to the master curve with 5 and 95% margin-adjusted bounds obtained only from tests of several reconstituted PCVN specimens.

by a procedure described in Ref. [11]. The constraint limit imposed by Eq. (5) was not applied to qualify data for this analysis. In order to perform the comparison, K_{Jc} data from specimens of each size were separately analyzed to determine T_{100}. The result of each analysis is also presented in Fig. 4. There were only two 6T C(T) and four 8T C(T) tested. Thus, T_{100} estimates from these two data sets are unreliable and are presented as supplementary information only.

The comparison of T_{100} values obtained from specimens of different sizes clearly proves the applicability of reconstituted PCVN specimens to characterize fracture toughness of RPV steels in the transition region. Some unresolved issues may remain regarding quality of welding reconstitution, minimum length of the inserts, etc., but such matters are outside of the scope of this paper.

CHARACTERIZATION OF IRRADIATED STEELS

PCVN specimens were used to characterize fracture toughness of an A 533 grade B plate and submerged-arc weld in both the unirradiated and irradiated conditions. The PCVN data are compared to compact specimens data.

An A533 grade B plate, designated JRQ, is the new International Atomic Energy Agency (IAEA) correlation monitor material. This plate was widely used in the IAEA Coordinated Research Programme Phase 3 (CRP-3). The analysis of K_{Jc} data from CRP-3 has revealed a T_{100} value gradient in the plate thickness direction [12]. Based on this observation, only specimens from about the same depth in the plate can be compared. PCVN specimens, 0.5T round compact (RCT) specimens, and 1T compact specimens of L-T orientation were tested in the unirradiated condition. PCVN and 0.5T RCT specimens were also studied after irradiation in the surveillance position of Loviisa Nuclear Power Plant to a neutron fluence of approximately 2×10^{19} n/cm^2 (>1 MeV) at 265°C.

Fracture toughness data from specimens of different sizes are summarized in Figs. 5 and 6 for the unirradiated and irradiated conditions, respectively. In both Figs. 5 and 6, the master curve with 5 and 95% tolerance bounds obtained only from testing of PCVN specimens are used to describe the scatter of all K_{Jc} data. The plate JRQ data show that the master curve with tolerance bounds from tests of only PCVN specimens adequately characterize the scatter of K_{Jc} data from compact specimens. As in the case with HSSI weld 73W, PCVN specimens from the JRQ plate were tested over the transition temperature range. Thus, estimation of the T_{100} values was performed by the procedure described in Ref. [11]. The constraint limit imposed by Eq. (5) was not applied. This issue will be addressed next.

The HSSI Program at ORNL has a task to characterize the properties, before and after irradiation, of the submerged-arc welds from the Midland Unit 1 pressurized water reactor vessel. This vessel was built for a nuclear unit to be operated by Consumers Power of Midland, Michigan, that was canceled prior to startup. The beltline weld from that vessel has the designation WF-70 which stands for a specific heat of copper-coated weld wire used with a specific lot of Linde 80 flux. A thorough characterization [13] has demonstrated that this weld is distinguished by inhomogeneity of fracture toughness, mechanical properties, and copper content within the weld. Therefore, this weld was

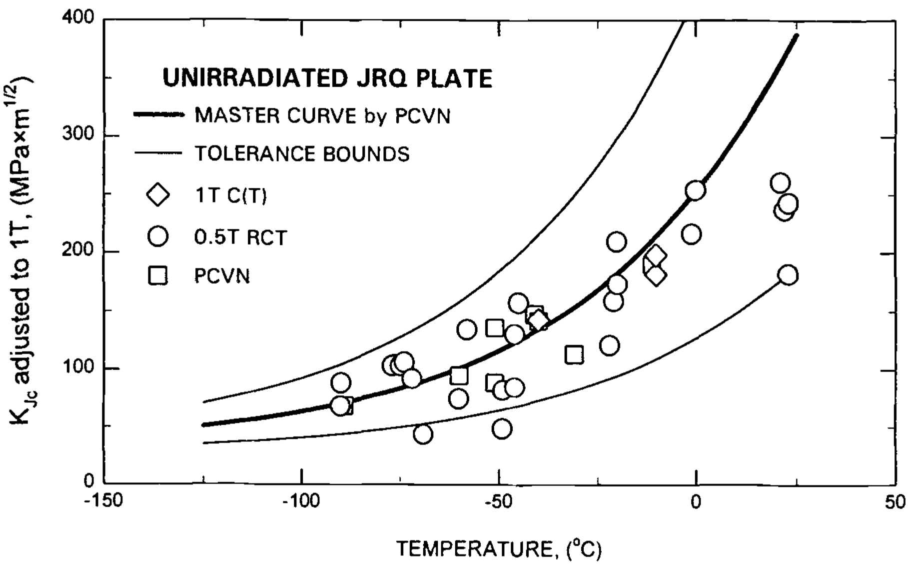

FIG. 5--Fracture toughness of A 533 grade B JRQ plate measured with different specimens relative to the master curve with 5 and 95% margin-adjusted bounds evaluated only from tests of several PCVN specimens.

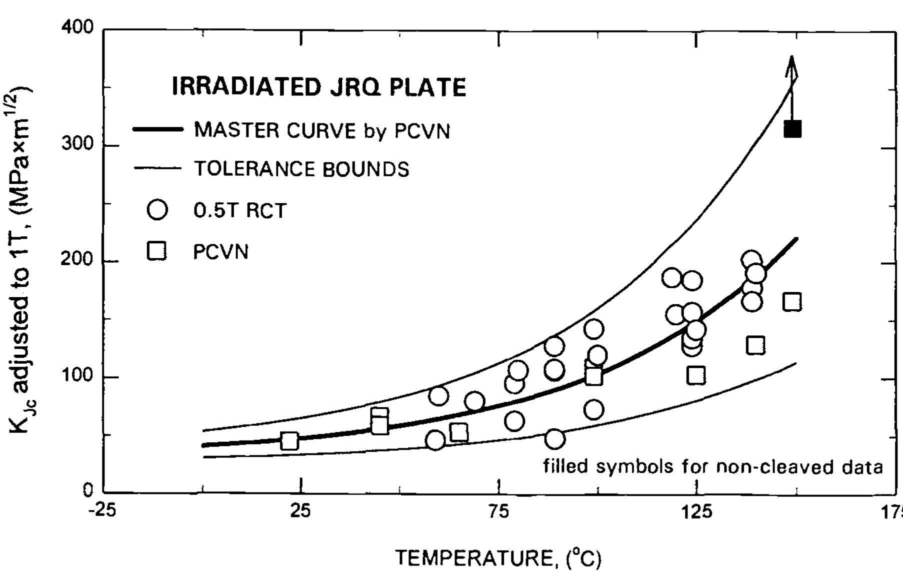

FIG. 6--Fracture toughness of JRQ plate after irradiation to 2×10^{19} n/cm^2 measured with different specimens relative to the master curve with 5 and 95% margin-adjusted bounds obtained only from tests of several PCVN specimens.

selected to be a good trial to study the ability of PCVN specimens to establish the transition region fracture toughness of an actual reactor pressure vessel weld both before and after irradiation. Irradiation of this weld was performed at 288°C to the target neutron fluence of 1×10^{19} n/cm^2 (>1 MeV) at the University of Michigan Ford Reactor.

The PCVN specimens were tested together with compact specimens before and after irradiation. The results were processed using the analysis procedure described in the present study. The master curves and 5/95% margin-adjusted tolerance bounds obtained from testing PCVN specimens were employed to predict compact specimen data in the transition region. Compact specimens ranging in size from 0.5T to 4T were tested in the unirradiated condition, while only 0.5T and 1T irradiated compact specimens were tested.

Figures 7 and 8 present K_{Jc} values of the beltline weld in the unirradiated and irradiated conditions, respectively. Irradiation-hardening results in an increase of the K_{Jc} validity limit, which is a critical aspect in an application of PCVN specimens. In general, master curves derived from PCVN specimens describe very well the wide scatter of fracture toughness of weld studied, as can be seen in Figs. 7 and 8.

The capacity of PCVN specimens to provide valid K_{Jc} before losing constraint is restricted by the extremely small remaining ligament, see Eq. (5). This penalizes the PCVN geometry more compared to, for example, the 0.5T compact specimen, although both are about the same thickness. In order to have valid PCVN data, the test temperature needs to be selected to be in the lower part of the transition region (below 100 MPa$\sqrt{m}$). Due to the exponential nature of the master curve as it approaches the lower shelf, median K_{Jc} must be determined with more accuracy than the median K_{Jc} determined at the T_{100} temperature. The accuracy of PCVN-derived K_{Jc} values on the lower part of transition region is also somewhat reduced because the statistical size effect implied by Eq. (3) is tending to vanish in this region. Thus, it may become necessary to recommend an increase in the number of PCVN specimens to be tested in the lower transition region. Ten to twelve PCVN specimens per curve may be necessary.

CONCLUSIONS

In this paper, the applicability of small specimens to characterize the fracture toughness of pressure vessel steels has been examined by the testing of precracked Charpy specimens. Weibull statistical concepts were applied to analyze K_{Jc} values and the master curve approach was used to describe the temperature dependence of fracture toughness in the transition region. Conclusions are summarized as follows:

1. The Weibull statistic/master curve approach provides a powerful tool to describe the fracture toughness properties in the transition region of unirradiated and irradiated reactor pressure vessel steels enabling the testing of limited numbers of PCVN specimens.

2. However, the "valid" test temperature range for PCVN specimens is very narrow. The capacity of PCVN specimens is restricted on the high-temperature side by constraint control requirements and on the lower-temperature side by accuracy of statistical effects.

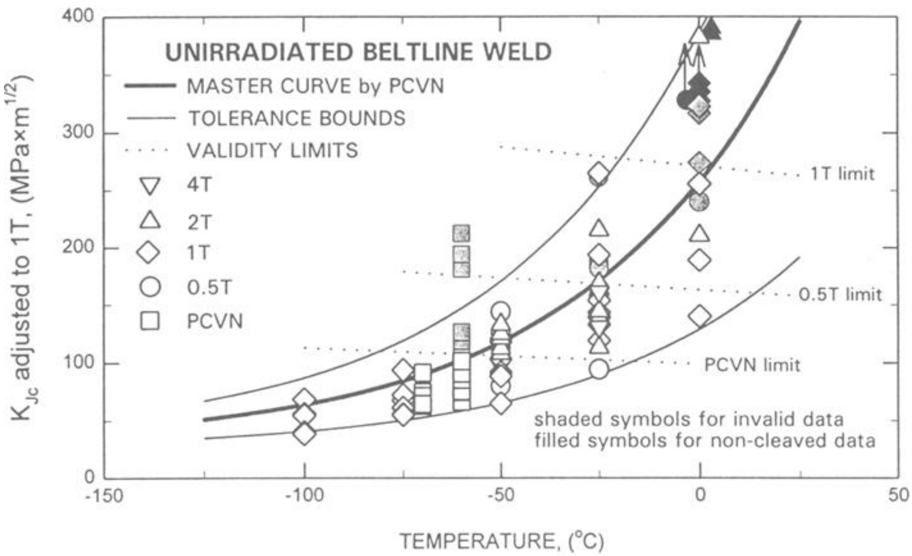

FIG. 7--Fracture toughness of Midland beltline weld measured with different specimens relative to the master curve with 5 and 95% margin-adjusted bounds obtained only from tests of several PCVN specimens.

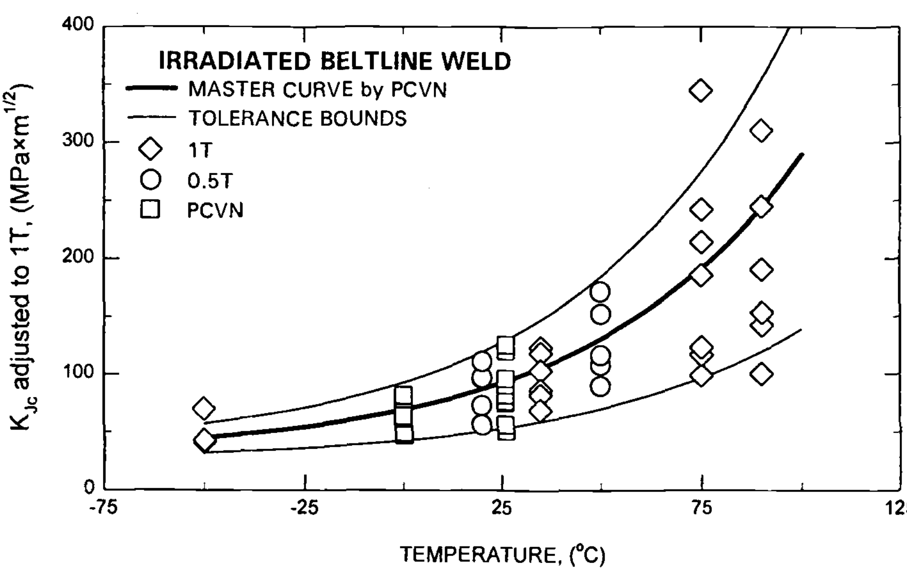

FIG. 8--Fracture toughness of Midland beltline weld after irradiation to 1×10^{19} n/cm^2 measured with different specimens relative to the master curve and 5 and 95% margin-adjusted tolerance bounds obtained only from tests of several PCVN specimens.

3. It is shown that the master curve derived from the testing of several PCVN specimens of HSST Plate 02 represents very well the large linear-elastic K_{Ic} database (adjusted to 1T C(T) size) accumulated by the testing of massive specimens needed for K_{Ic} validity. Also the 5 and 95% margin-adjusted tolerance bounds of the master curve describe successfully the scatter in K_{Ic} results of this same material.

4. The 5% margin-adjusted tolerance bound derived from the testing of several PCVN specimens of HSST Plate 02 was compared to the EPRI K_{Ic} database. It is shown that the 5% tolerance bound from the present work is more accurate as a lower bound curve to the K_{Ic} database than the ASME K_{Ic} curve itself.

5. PCVN specimens of HSSI weld 73W were manufactured by means of welding reconstitution from the broken halves of previously tested specimens. The master curve obtained from testing these reconstituted PCVN specimens fits perfectly within a large K_{Jc} database for compact specimens in sizes ranging from 1T to 8T.

6. The fracture toughnesses of Plate JRQ and the Midland reactor vessel weld, in both the unirradiated and irradiated conditions, were adequately characterized by PCVN specimens. The accuracy of characterization of fracture toughness in the transition region by PCVN specimens will probably have to be improved by increasing the number of specimens tested.

ACKNOWLEDGMENTS

This research is sponsored by the Office of Nuclear Regulatory Research, U.S. Nuclear Regulatory Commission, under Interagency Agreement DOE 1886-8109-8L with the U.S. Department of Energy under Contract DE-AC05-94OR22464 with Lockheed Martin Energy Research Corp. The authors would like to thank John G. Merkle and Roger E. Stoller for peer review and Julia L. Bishop for final preparation.

REFERENCES

[1] Wallin, K., "The Size Effect in K_{Ic} Results," *Engineering Fracture Mechanics*, Vol. 22, No.1, 1985, pp. 149-163.

[2] Wallin, K., "The Scatter in K_{Ic}-Results," *Engineering Fracture Mechanics*, Vol. 19, No.6, 1984, pp. 1085-1093.

[3] "Test Method for the Determination of Reference Temperature, T_0, for Ferritic Steels in the Transition Range," Proposed ASTM Test Practice, Draft 12, ASTM Task Group E08.08.03, American Society for Testing and Materials, 1996.

[4] Weibull, W., "A Statistical Theory of the Strength of Materials," *Proceedings of Royal Swedish Institute for Engineering Research*, Stockholm, No.151, 1939.

[5] McGowan, J. J., Nanstad, R. K., and Thoms, K. R., *Characterization of Irradiated Current-Practice Welds and A 533 Grade B Class 1 Plate for Nuclear Pressure Vessel Service*, NUREG/CR-4880, Vol. 1, (ORNL/TM-6484/V1), Oak Ridge National Laboratory, Oak Ridge, Tenn., 1988.

[6] Marston, T. U., Ed., *Flaw Evaluation Procedures: Background and Application of ASME Section XI Appendix A*, EPRI NP-719-SR, Electric Power Research Institute, Palo Alto, Calif., 1978.

[7] Nanstad, R. K., Keeney, J. A., and McCabe, D. E., *Preliminary Review of the Bases for the K_{Ic} Curve in the ASME Code*, ORNL/NRC/LTR-93/15, Oak Ridge National Laboratory, Oak Ridge, Tenn., 1993.

[8] Van Walle, E., "Reconstitution: Where do we Stand?" *Effects of Radiation on Materials: 17th Symposium, ASTM STP 1270*, D. S.Gelles, R. K.Nanstad, A. S.Kumar, and E. A.Little, Eds., American Society for Testing and Materials, 1997, pp. 415-441.

[9] Valo, M., and Ahlstrand, R., "Application of Reconstitution Welding Technique for Studying Base Metal of a Novovoronezh Unit-1 Trepan Sample," *Small Specimen Test Techniques Applied to Nuclear Reactor Vessel Thermal Annealing and Plant Life Extension, ASTM STP 1204*, W. R.Corwin, F. M.Haggag, and W. L.Server, Eds., American Society for Testing and Materials, Philadelphia, 1993, pp. 440-456.

[10] Nanstad, R. K., McCabe, D. E., Haggag, F. M., Bowman, K. O., and Downing, D.J., "Statistical Analyses of Fracture Toughness Results for Two Irradiated High-Copper Welds," *Effects of Radiation on Materials: 15th International Symposium, ASTM STP 1125*, R. E. Stoller, A. S. Kumar, and D. S. Gelles, Eds., American Society for Testing and Materials, Philadelphia, 1992, pp. 270-291.

[11] Wallin, K., "Validity of Small Specimen Fracture Toughness Estimates Neglecting Constraint Corrections," *Constraint Effects in Fracture: Theory and Applications, ASTM STP 1244*, M. Kirk and A. Bakker, Eds., American Society for Testing and Materials, 1996.

[12] Wallin, K., "Summary of the IAEA/CRP 3 Fracture Mechanical Results," *VTT Report for the IAEA contract 8251/RB*, VTT Manufacturing Technology, Espoo, Finland, 1996.

[13] Nanstad, R. K., McCabe, D. E., and Swain. R. L., "Evaluation of Variability in Material Properties and Chemical Composition for Midland Reactor Weld WF-70," *Effects of Radiation on Materials: 18th International Symposium, ASTM STP 1325*, R. K. Nanstad, M. L. Hamilton, F. A. Garner, and A. S. Kumar, Eds., American Society for Testing and Materials, 1997.

John D. Landes[1] and Khalled Sakalla[2]

SINGLE SPECIMEN METHOD FOR DETERMINING THE MASTER CURVE IN THE TRANSITION

REFERENCE: Landes, John D. and Sakalla, Khalled, **"Single Specimen Method for Determining the Master Curve in the Transition"**, Fatigue and Fracture Mechanics: 28th Volume, ASTM STP 1321, J. H. Underwood, B. D. Macdonald and M. R. Mitchell, Eds., American Society for Testing and Materials, 1997.

ABSTRACT: A single specimen method was developed to predict the fracture toughness behavior for steels in the transition. The prediction is based on a single specimen estimate of lower bound toughness in the transition and order statistics. A fracture toughness from a single test is subjected to a lower bound estimate to generate a single lower bound value. This value is transformed into a fictitious distribution of toughness values using order statistics. From this a median value of toughness, $K_{Jc(med)}$, is determined and hence T_0 where T_0 is the temperature at which the master curve reaches a median toughness of 100 MPa$\sqrt{m}$. With the determination of T_0 the entire distribution of toughness in the transition is determined.

The single specimen method of T_0 determination was evaluated for transition toughness tests where a large number of fracture toughness values were available at a single temperature. Single specimen values of T_0 were compared with the T_0 from the entire population of fracture toughness values and from random selections of six toughness values taken one at a time. The result of the evaluation shows that the single specimen could estimate T_0 to within a reasonable value if the test temperature was close to T_0. Compared with the result of a random selection of six values to determine T_0 the single specimen method gave similar results.

KEYWORDS: fracture toughness, transition, steels, master curve, single specimen, order statistics

---

[1] Professor, Mechanical and Aerospace Engineering and Engineering Science, University of Tennessee, Knoxville, TN 37996-2030

[2] IIT Technical institute, 10208 Technology Dr., Knoxville, TN 37932

INTRODUCTION

The concept of a master curve has allowed an easy characterization of the entire fracture toughness transition curve for steels [1, 2]. The master curve requires the testing of a number of fracture toughness specimens in the transition at a single temperature and subsequent statistical characterization of the data. Once the toughness at one temperature has been characterized statistically, the entire transition is specified by the master curve which uses the reproducible pattern of transition toughness behavior. The master curve concept uses a three parameter Weibull statistical distribution to characterize the distribution of toughness values at a single temperature. This is given by

$$1 - P = \exp\left[-\left(\frac{K_{Jc} - 20}{K_o - 20}\right)^4\right] \tag{1}$$

where P is to probability that a fracture has occurred at or below toughness K_{Jc} with K in MPa√m. K_o is a fitting parameter and 20 is a lower bound for the Weibull equation, given in MPa√m. A distribution of transition fracture toughness values is fit by eq. 1 and from that a median value of toughness is found, labeled $K_{Jc(med)}$. This median toughness value is part of the master curve of median toughness values. The master curve has a fixed equation which uses a reference temperature, T_o, to give the distribution of toughness throughout the transition [3]. The expression for the master curve is given by

$$K_{Jc(med)} = 30 + 70 \exp[0.019(T - T_o)] \tag{2}$$

where $K_{Jc(med)}$, the median value of transition fracture toughness, is given in MPa√m and temperatures T and T_o in °C. The temperature, T, is T_o when the value of $K_{Jc(med)}$ is 100 MPa√m. The master curve is illustrated in graphical form in Fig. 1. At a different temperature from that of the test temperature the median toughness is found by taking the appropriate point on the master curve. The distribution at the new temperature follows the same three-parameter Weibull model, Eq. 1, that was used at the test temperature. Hence, once the master curve can be found, the toughness distribution at any temperature in the transition is known.

To determine a master curve for transition fracture toughness, a draft test method has been developed [3]. In this method at least six results are required at a single test temperature. This is easy to do for characterizing a given heat of steel when there is sufficient material available. In some cases, however, there may be a limit to the amount of material available. This might be the case for nuclear surveillance specimens, for evaluation of fracture toughness on a failed component or for cases where the material may be too expensive to produce several specimens. For these cases it would be good to be able to develop the master curve from fewer specimens. A technique is developed in this paper to

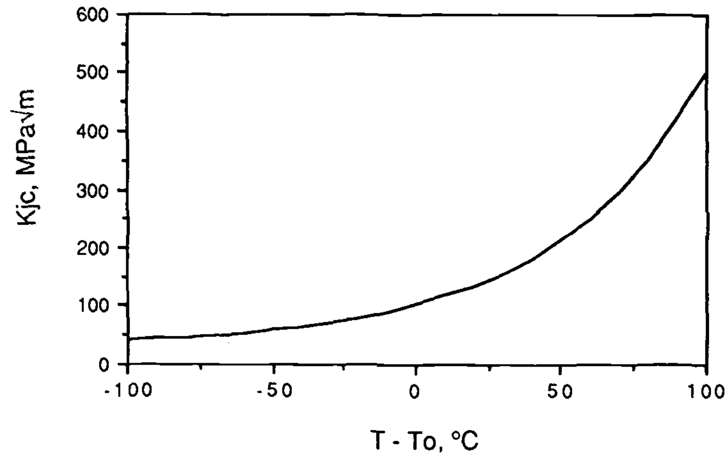

Fig. 1 - Master Curve for Transition Toughness

estimate T_0 and hence the master curve from the test result of a single specimen.

To develop the single specimen T_0 a lower bound estimate of fracture toughness from a single test result is used. This lower bound is then taken with order statistics to generate a fictitious fracture toughness distribution for multiple specimens at the test temperature. The fictitious distribution is fitted with the three-parameter Weibull statistical model, eq. 1, to determine a median toughness value at the temperature of the single result. From this median toughness estimate, and eq. 2, the value of T_0 and the entire master curve can be determined.

LOWER BOUND TOUGHNESS

The concept of a lower bound fracture toughness for a distribution of fracture toughness values in the transition was discussed by Stienstra and Anderson [4]. They used order statistics to determine the lower bound for a small sample of toughness values, typically a sample size that was not sufficient to determine a reliable statistical distribution of toughness values using the Weibull three parameter model. The order statistics could be used to generate k multiplying factors that would result in a given percentage lower bound with a fixed confidence level. For example, a 10 percent lower bound could be found with a 95 percent confidence level. The order statistics were used with a Weibull model that had a slope of 2 based on J for the toughness characterization. The k multiplying factors were fixed values that were multiplied times the toughness values in the small sample. For example, in Table 1 the k factors that would give 10 percent lower bound estimates with 95 percent confidence are given for a few sample sizes. The toughness values are ordered from smallest to largest and the k values are multiplied, the first with the smallest toughness, etc. The result is a narrow range of lower bound fracture toughness estimates.

Table 1 - k Multipliers for 10 percent confidence and 95 percent lower bound

Point no.	3 points	5 points	7 points	10 points
1	.3248	.4193	.4962	.5930
2	.2295	.3136	.3785	.4585
3	.1607	.2516	..3131	.3860
4		.2024	.2659	.3360
5		.1516	.2267	.2973
6			.1896	.2648
7			.1465	.2361
8				.2083
9				.1791
10				.1413

In a later work Landes, et al used [5] an empirical method to determine a lower bound from a single value of toughness in the transition. The method is summarized here. A standard ASTM specimen like the compact is tested until a cleavage failure results and a J_c value at the cleavage point is determined. No adjustment is made for constraint and no data are eliminated by a size or other criteria. The method uses both a size criterion and a statistical model. First the size criterion is applied to the value of the J_c toughness value. This is based on the model of Iwadate et. al. [6] for determining the number of specimens that should comprise an adequate sample for determining a lower bound toughness.

$$N = 1000\,(J_c/\sigma_Y)/B \qquad (3)$$

where N is the number of tests in a data set needed for an adequate sampling. An effective yield stress or flow stress, σ_Y, is used and the size is based upon the thickness, B. From the number of specimens, N, needed for an adequate sample, a statistical analysis is made with the test result, J_c, representing the top of a scatterband and the lower bound toughness, J_{LB}, representing the bottom of a scatterband. The scatterband is represented by a Weibull plot which is distributed as i/(N+1) where i takes the values of 1 through N for determining the probability of fracture for each test result taken in increasing order of toughness. In this case the specimen test result, J_c, occupies the probability position N/(N+1) and the J_{LB} the position 1/(N+1). The statistical part of the analysis is illustrated in Fig. 2. The Weibull model is a two-parameter distribution with a slope of 2. This is given by

$$1 - \text{Prob} = \exp\{-(J/\theta)^2\} \qquad (4)$$

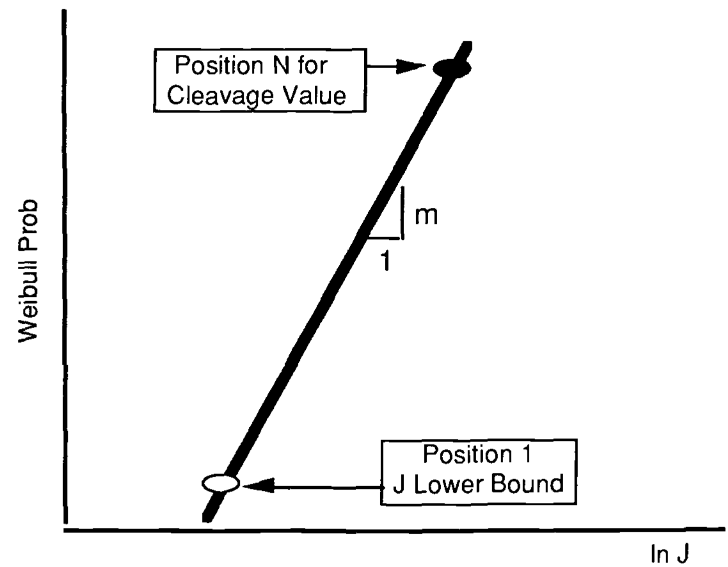

Fig. 2 - Lower Bound J Estimate from Single Specimen Test

Putting the probability position into equation 4 gives the relationship for J_c of

$$J_c = \theta \, [-\ln\{N/(N+1)\}]^{1/2} \qquad (5)$$

and J_{LB} of

$$J_{LB} = q \, [-\ln\{1/(N+1)\}]^{1/2} \qquad (6)$$

solving equations 5 and 6 gives

$$J_{LB} = J_c \, [\{\ln(N/[N+1]\}/\{\ln(1/[N+1]\}]^{1/2} \qquad (7)$$

This value J_{LB} then represents a lower bound estimate to the fictitious scatterband of N toughness values where J_c is the highest toughness value in the scatterband.

In calculating lower bound estimates using eq. 7 it was found the the J_{LB} estimate was similar in magnitude to the lower bound estimate from the order statistics of Stienstra and Anderson [4]. The idea then occurs that if order statistics can be used to estimate a lower bound from a distribution of toughness values; a single lower bound could be used with order statistics in reverse to estimate a distribution of toughness values. With this distribution the standard Weibull three-parameter statistical model could be used to determine $K_{Jc(med)}$

and hence T_o and the entire distribution of toughness values in the transition. The detailed description of the method is given in the next section.

SINGLE SPECIMEN T_o PROCEDURE

The sequence of the method to predict T_o from a single specimen is as follows. The toughness value is subjected to the single specimen lower bound estimate procedure of Landes et al, [5] producing a single lower bound estimate, J_{LB}, of the toughness as well as a suggested sample size, N. The lower bound toughness estimate is divided by the k multipliers of that sample size to produce a distribution of toughness values. The distribution of toughness values is analyzed with the three-parameter Weibull statistics to determine a median toughness value. From the median toughness the value of T_o is determined, hence the entire distribution of toughness values is known.

An example is given for a 20MnMoNi50 steel (Appendix 1). Sixteen fracture toughness values were measured at a temperature of -90 °C in the transition. To illustrate the method two points are randomly chosen, one near the low end of the distribution and the other near the high end, to get a single specimen estimate of the T_o value. The toughness is measured as a J_c value so the Weibull distribution with a slope of 2 is used. A toughness value of 82.3 kJ/m^2.was chosen from the lower end of the scatterband. For this the single specimen lower bound estimate is 28.06 kJ/m^2 with a sample size of five specimens. Using the k multipliers of Table 1 for a sample size of five gives a toughness distribution of 66.9, 89.5, 111.6, 138.5, 185.1 kJ/m^2. For these five points the values must be converted to K_{Jc} values to determine the master curve T_o value. The plane stress relationship

$$K_{Jc} = \sqrt{E\,J_c} \tag{8}$$

is used, where E is the elastic modulus. After converting to K_{Jc}, the median toughness value can be calculated from the distribution. This is determined to be 149 MPa$\sqrt{m}$ and the corresponding T_o is -117.9 °C. A second value of J_c in the distribution, 153.9 kJ/m^2, chosen from the higher end for comparison gives a lower bound of 34.2 kJ/m^2 and a sample size of nine specimens. Going through the procedure requires that this value is divided by the k multipliers for nine specimens resulting in a fictitious toughness distribution with nine values. These nine values are converted to K_{Jc} values. A median toughness value of 154 MPa$\sqrt{m}$ and a T_o of -120.3 °C is then determined. Using all 16 points in the distribution gives a median value, $K_{Jc(med)}$ of 149.0 MPa$\sqrt{m}$ and T_o of -117.9 °C. This value of T_o is close to both single specimen estimates of T_o.

SINGLE SPECIMEN METHOD EVALUATION

The single specimen method for determining T_o was evaluated on five data sets for two steel alloys. They are all nuclear grade pressure vessel steels and had sample sizes ranging from 11 to 20 specimens. The two steels are a 20MnMoNi50 steel and an A533B steel [7]. The first had a room temperature yield strength of 450 MPa and the second a room temperature yield strength of 444 MPa. Some details of the data sets are given in Table 2 and all of the values of J_c from all data sets used are given in Appendix 1. For each set all of the toughness values in the distributions were subjected to a single specimen evaluation of T_o. The values of T_o determined by the single specimen method were compared with T_o values determined from the entire distribution. In the draft standard for T_o determination the minimum number of specimens that can be tested to determine a statistical distribution is six [3]. The test sample distributions all had more than six specimens in the entire sample, therefore, groups of six specimens were chosen to determine T_o to give a comparison with a result which might be obtained by the draft standard [3]. First samples of six specimens were first chosen randomly and then the absolute lowest six and highest six were chosen to make the comparison. In addition the value of T_o that would result from choosing the single specimen as the median value was evaluated to show what would happen if only a single test value were available and no procedure was applied.

Table 2 - Summary of data sets analyzed

Material	Test Temp. °C	No. of tests	T_o °C	High J_c kJ/m^2	Low J_c kJ/m^2	$K_{Jc(med)}$ MPa$\sqrt{m}$
20MnMoNi50	- 90	16	- 117.9	270	49.4	149
20MnMoNi50	- 90	20	- 127.9	357	16.9	174
A533B	- 75	16	- 79.9	133	5.6	106.9
20MnMoNi50	- 60	11	- 124.2	661	178	267
A533B	- 150	17	- 50.7	13.0	5.4	40.6

The results are given in Figs. 3 through 7. Determinations of T_o were made for five conditions on each data set. They are: 1) using all points in the data set, labeled all points; 2) using six points in the set randomly chosen, labeled six points random; 3) using the highest and lowest six points in the data set, labeled six point absolute; 4) using the method for the single specimen estimation, labeled 1 point order; 5) using a single point as $K_{Jc(med)}$ to determine T_o with no additional analysis applied, labeled 1 point absolute. For condition 2 where six points are randomly chosen, about 12 trials were taken and the lowest and highest values of T_o were plotted. For condition 4, using the single specimen procedure with order statistics, only the highest and lowest values of T_o are plotted. These correspond to the lowest and highest values respectively of toughness in the distribution. The intermediate values of toughness would give intermediate values of T_o.

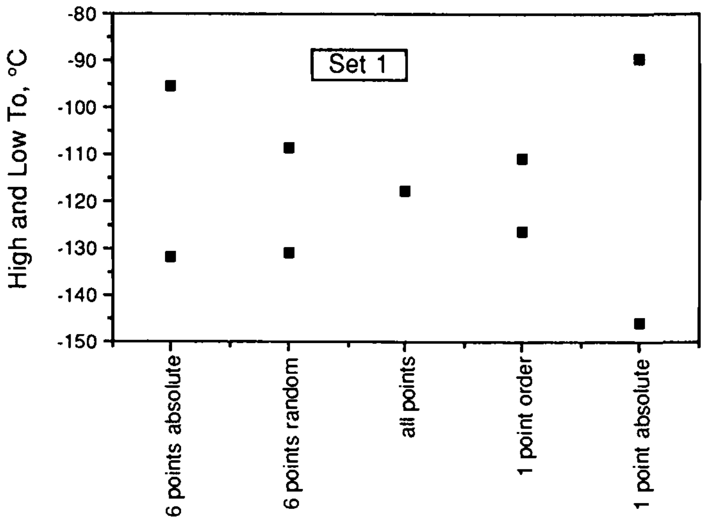

Fig. 3 - Set 1 Values of To

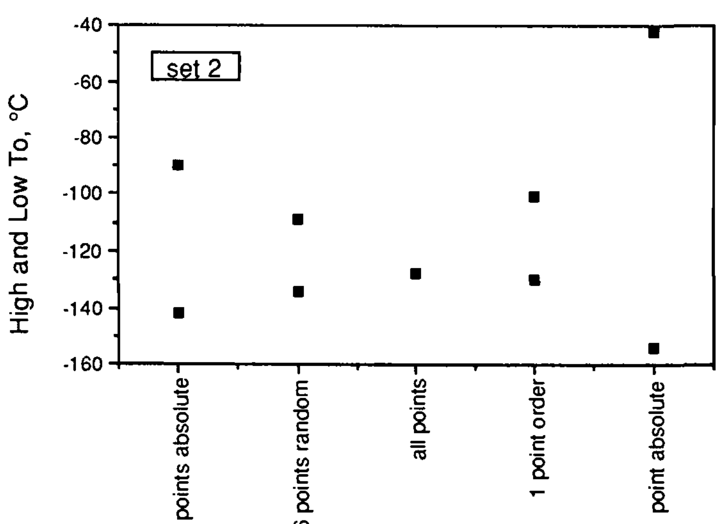

Fig. 4 - Set 2 Values of To

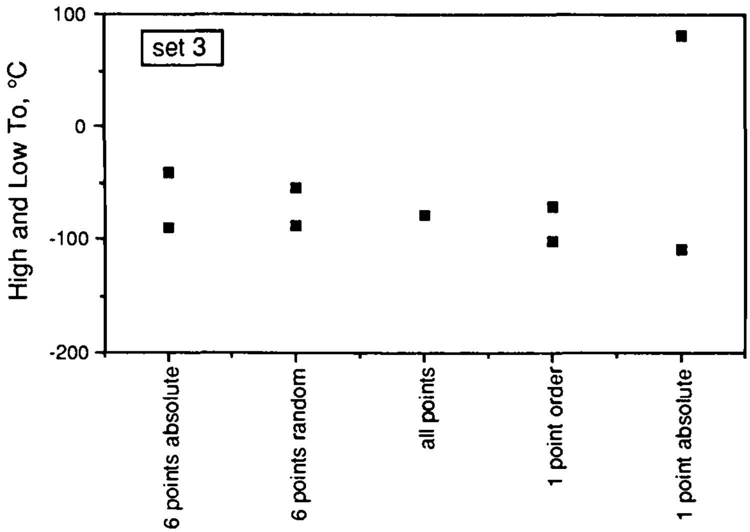

Fig 5 - Set 3 Values of To

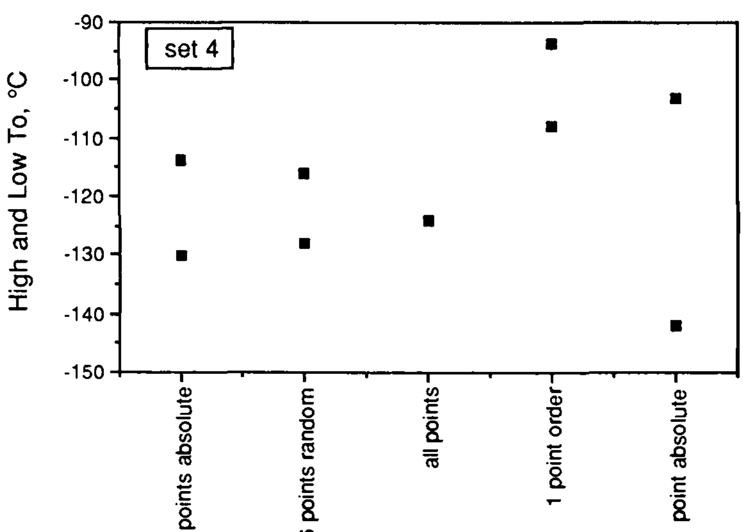

Fig. 6 - Set 4 Values of To

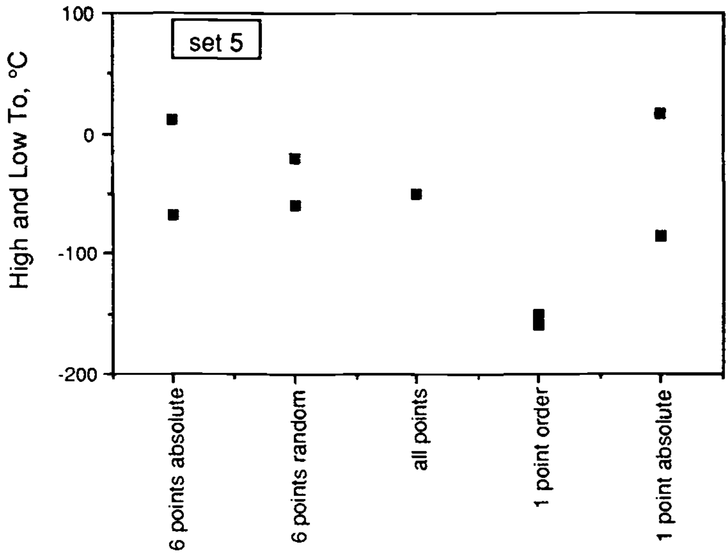

Fig. 7 - Set 5 Values of To

DISCUSSION

The results in Figs. 3 through 7 show a varied success for the single specimen method of determining T_0. For the first three sets the values of T_0 from the single specimen procedure are in the range of the T_0 determined for all points and for the T_0 determined from randomly taking six points at a time. In some cases the single specimen T_0 are closer to the all points value than the one determined from six points taken randomly and always better than the six points taken from the top and bottom of the distribution. For the last two data sets the single specimen values of T_0 are not at all accurate and do not fall in the range of the all points T_0. To get a better feeling for the accuracy involved, the error in the T_0 determination is plotted for each method of evaluation. This is a plot of the absolute difference between T_0 from a given method and the all points T_0. These are shown for the five data sets in Figs 8 through 12. The important factor in the success of the single specimen evaluation seems to depend on where the data set lies on the master curve; that is, the range of toughness values in the data set. A better feeling for this can be gotten by looking at the range of toughness values in Table 2. The first three sets have a range in toughness values that gives a $K_{Jc(med)}$ between 100 to 200 MPa$\sqrt{m}$. For the fourth data set $K_{Jc(med)}$ is well above 200 and for the fifth is well below 100. To show where these data sets line up on the master curve, Fig. 1 is replotted with the position of each set in Fig. 13 . From this it is obvious that the

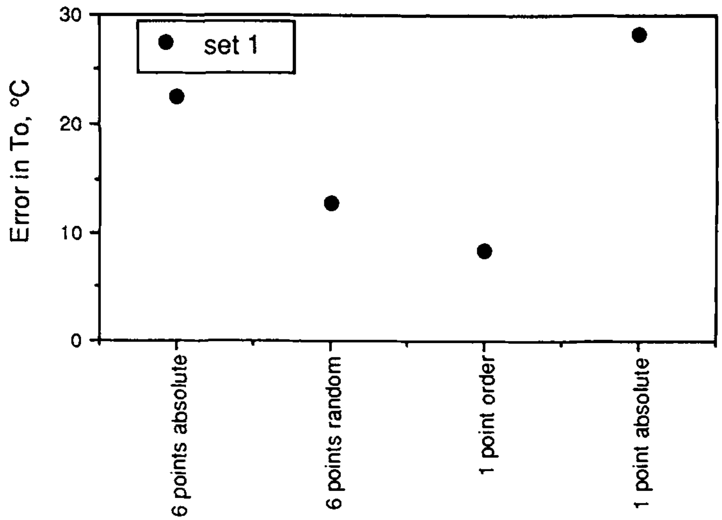

Fig. 8 - Set 1 Error in To

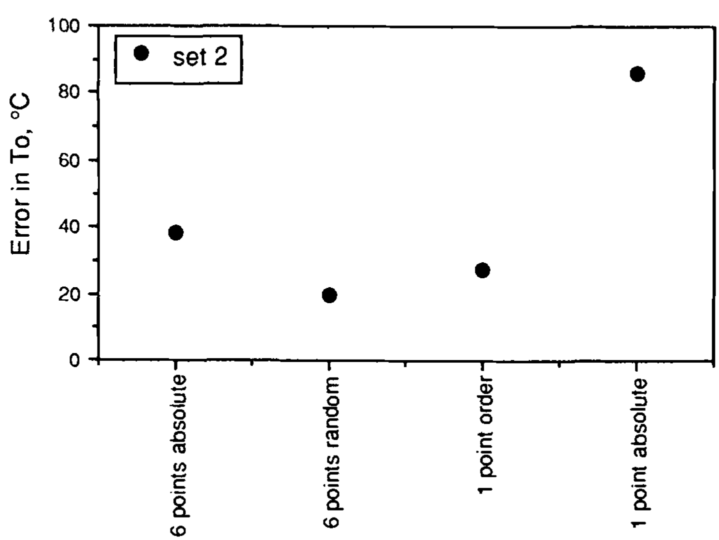

Fig. 9 - Set 2 Error in To

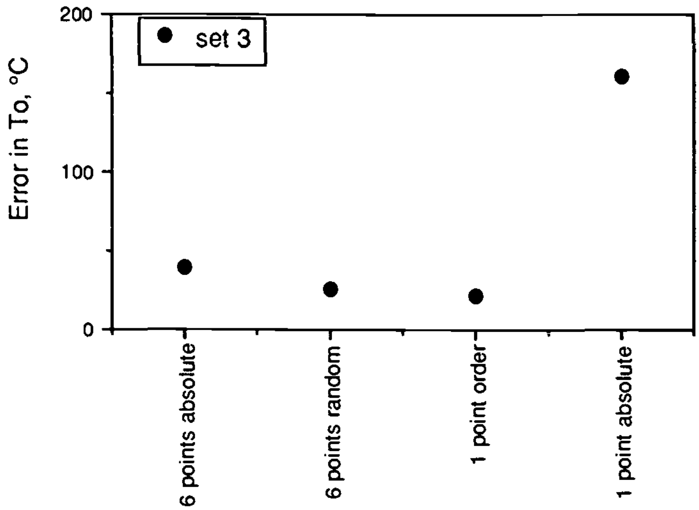

Fig. 10 - Set 3 Error in To

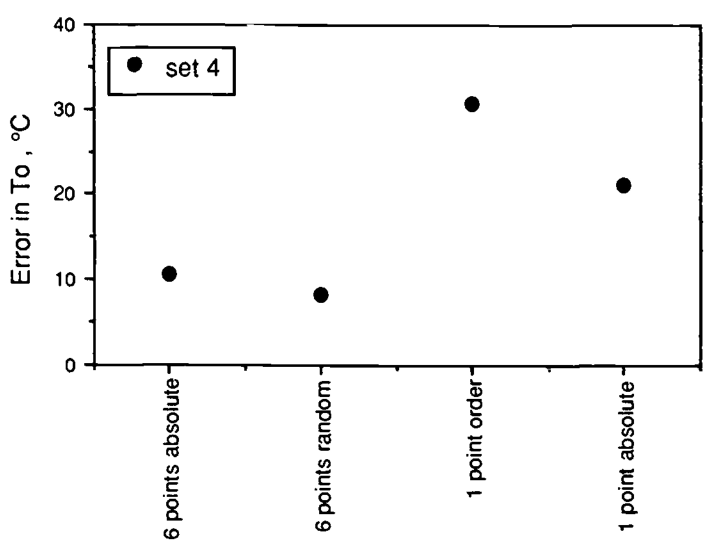

Fig. 11 - Set 4 Error in To

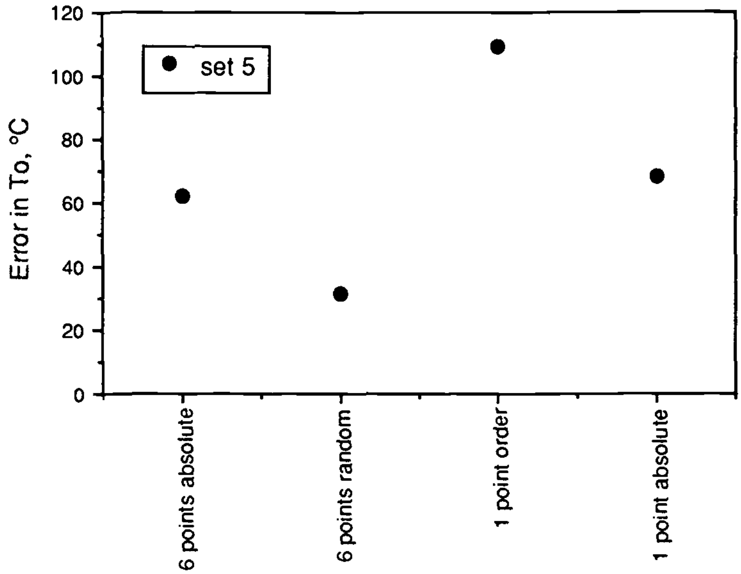

Fig. 12 - Set 5 Error in To

first three sets lie in a middle range of the curve whereas the fourth set is at the high end and the fifth set at the low end. It appears that the single specimen method will not work if the data sets do not lie in this middle range. The method works well when the toughness values in terms of J_c are between 30 to 300 kJ/m^2 and the test temperature within ± 50 °C of T_o. If the data are not in this range it is not wise to apply the method.

It could be noted that data sets 3 and 5 are the same material and the T_o values do not agree well for the all points calculation. Tests conducted at a temperature well below T_o are on the flat part of the master curve and do not give an accurate measure of T_o regardless of the method used. Data sets 1, 2, and 4 are the same steel and the values of T_o agree well between data sets.

Some speculation could be made about how to determine the position of the data set relative to T_o from only a single value of toughness. The low values of sets two and three are below 30 kJ/m^2 and they give reasonable estimates of T_o. This is presumably because the overall data set lies in the middle range of the master curve. When a single value of toughness exists that is in the range of 30 to 300 MPa√m, it is impossible to tell whether it is a middle value in a data set that is tested near T_o where the method works or whether it is a high or low value of a set that is far from T_o, where the method does not work. More study is needed to extend the range of applicability of the method. In the meanwhile if a single specimen is to be tested it would be wise to try to do the test at a temperature near T_o perhaps within ± 50 °C of T_o. For the testing of six specimens as required by the draft standard it is also good to test near T_o.

There are techniques available to try to estimate the range of T_0 for a given steel [3]. These techniques could be applied for choosing an appropriate test temperature for a single specimen test.

This single specimen method for estimating T_0 has been applied only to a limited type of steel, namely nuclear grade pressure vessel steel. Nothing can be said about whether or not it might apply to steels that have radically different properties such as steels subjected to irradiation damage or thermal aging.

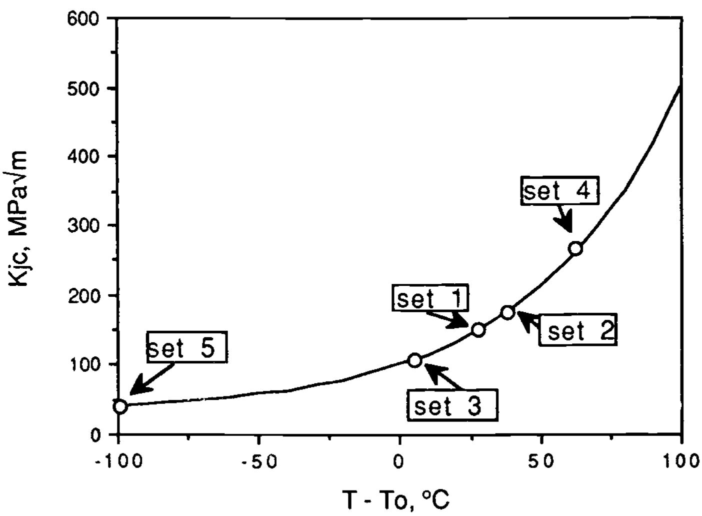

Fig. 13 - Data Set Positions on Master Curve

SUMMARY

A method was developed to determine the master curve and T_0 from the fracture toughness result of a single specimen test. The method can be used to predict fracture toughness of steels in the transition. The method uses a lower bound estimate of toughness from the single specimen fracture toughness. This lower bound is used with order statistics to predict a distribution of toughness values from which $K_{Jc(med)}$ is determined and hence T_0. The method could be useful for cases where a sufficient number of specimens are not available to apply the draft standard procedure.

The method was applied to five sets of fracture toughness data where for each set many toughness values had been measured at a single temperature. The results showed that the method worked well for data sets that lay in the middle range of the master curve where the test temperature was near T_0. For data sets at the low and high end of the master curve the method did not work at all. More study is required to make the method applicable to a wider range of fracture toughness test results.

REFERENCES

1. Wallin, K., "Fracture Toughness Transition Curve Shape for Ferritic Structural Steels", Proceedings of the Joint FEFG/ICF International Conference on Fracture of Engineering Materials, Singapore, August 6-8, 1991, pp. 83-88.

2. Stienstra, D., "Stocastic Micromechanical Modelling of Cleavage Fracture in the Ductile-Brittle Transition Region", MM6013-90-11, PhD Dissertation, Texas A&M University, College Station, Texas, August 1990.

3. "Test Method for the Determination of Reference Temperature T_0, for Ferritic Steels in the Transition Range", (Draft 12) American Society for Testing and Materials, 1996.

4. Stienstra, D., Anderson, T. L., and Ringer, L. J., "Statistical Inferences on Cleavage Fracture Toughness Data", Journal of Engineering Materials and Technology, Vol. 112, January 1990, pp. 31-37.

5. Landes, J. D. , Zerbst, U., Heerens, J., Petrovski, B., and Schwalbe, K-H., "Single-Specimen Test Analysis to Determine Lower Bound Toughness in the Transition, Fracture Mechanics:Twenty-fourth Volume, ASTM STP 1207, John D. Landes, Donald McCabe and J. A. M. Boulet,Eds.,American Society for Testing and Materials, Philadelphia, 1994, pp. 171-185.

6. Iwadate, T., Tanaka, Y., Ono, S., and Watanabe, J., "An Analysis of Elastic-Plastic Fracture Toughness Behavior of J_{Ic} Measurement in the Transition Region", Elastic-Plastic Fracture: Second Symposium, Volume II-Fracture Resistance Curves and Engineering Applications, ASTM STP 803, C. F. Shih and J. P. Gudas, Eds., ASTM 1983, pp. II-531-II- 561.

7. McCabe, D. E. "A Comparison of Weibull and β_{Ic} Analysis of the Transition Range", Fracture Mechanics: Twenty-third Symposium, ASTM STP 1189, R. Chona Ed., American Society for Testing and Materials, 1993, Philadelphia, pp 80-94.

Appendix 1 - Data Used in the Evaluation of the Single Specimen T_0

The fracture toughness values from all five data sets used in the analysis of the single specimen T_0 are given here. All values are J_c given in kJ/m^2
Sets 1, 2 and 4 are from Heerens, J., and Petrovski, B (1991).
Sets 3 and 5 anre from Ref. 7

	Set 1	Set 2	Set 3	Set 4	Set 5
1	49.4	16.9	5.6	178.2	5.4
2	49.7	29.6	13.2	211.8	6.0
3	50.6	40.6	18.0	241.2	6.2
4	63.8	66.2	24.2	286.9	6.4
5	82.3	72.4	32.0	340.3	6.5
6	84.4	74.8	34.8	408.9	6.8
7	85.2	75.3	37.8	424.1	7.4
8	121.2	83.8	39.9	447.5	7.4
9	121.3	89.4	41.4	483.4	7.6
10	129.2	94.7	46.9	582.3	8.2
11	135.2	148.7	48.3	660.8	8.3
12	153.9	149.6	51.9		8.6
13	176.0	172.8	61.7		9.4
14	179.2	182.7	68.3		10.1
15	233.6	215.0	73.0		11.4
16	270.2	218.8	78.3		12.9
17		232.8	82.0		13.0
18		278.7	89.8		
19		288.4	112.6		
20		357.4	133.3		

Cheng Yan[1], Shang-Xian Wu[1], and Yiu-Wing Mai[1]

Application of J-Q Theory to the Local Approach Statistical Model of Cleavage Fracture

REFERENCE: Yan, C., Wu, S. X., and Mai, Y. W., **"Application of J-Q Theory to the Local Approach Statistical Model of Cleavage Fracture,"** Fatigue and Fracture Mechanics: 28th Volume, ASTM STP 1321, J. H. Underwood, B. D. Macdonald, and M. R. Mitchell, Eds., American Society for Testing and Materials, Philadelphia, 1997

ABSTRACT: A statistical model has been established to predict the fracture toughness in the lower-shelf and lower transition regions. It considers the in-plane constraint effect in terms of the two-parameter J-Q stress field. This model has been applied to predict the effect of crack depth and specimen geometry on fracture toughness and there is good agreement with experimental data. The specimens with lower in-plane constraints have a large toughness scatter due to the significant constraint loss during the loading process. The lower-bound toughness is not sensitive to crack depth and specimen geometry and this is attributed to the fact that all specimens have a similar in-plane constraint at small loads.

KEYWORDS: cleavage fracture, lower-shelf and lower-transition regions, in-plane constraint, local approach theory, toughness scatter, lower-bound toughness.

The effect of crack depth and specimen geometry on fracture toughness in the lower-shelf and ductile-brittle transition regions have been widely investigated [1-6]. The work of Sorem et al [3] indicated that the higher toughness of specimens with shallow cracks can be attributed to the lower opening stress ahead of the crack tip. Also, in Ref 2, finite element analysis has indicated that the variation of fracture toughness associated with different specimen geometries is consistent with the magnitude of the in-plane constraint.

By slip-line analysis of non-hardening materials, McClintock [7] and Wu [8] have shown that the stress state ahead of a crack depends strongly on the specimen geometry and crack depth. For a power-law hardening material in plane-strain condition, it is commonly accepted that the single parameter characterization of stress-strain fields ahead of a crack tip, J or crack-tip opening displacement (CTOD), is valid only for specimens with large in-plane constraint. The size requirement for cleavage fracture to be size independent has been proposed by Anderson et al [5]. Recently, O'Dowd and Shih [9-11] have shown that the stress field at the crack tip can be characterized by two parameters J

[1] Research student, ARC research fellow and professor respectively, Centre of Advanced Materials Technology, Department of Mechanical and Mechatronic Engineering, University of Sydney, NSW 2006, Australia.

and Q. The J integral characterizes the intensity of HRR stress and Q describes the stress triaxiality or constraint. The J-Q theory has been applied to correlate the variation in toughness with constraint levels [12]. However, it cannot describe the scatter of toughness data.

To predict the scatter of fracture toughness in the lower-shelf and transition regions, many statistical models have been developed [13-17]. However, most of these models do not consider the variation in constraint for different specimens and at different load levels. The local approach statistical theory has been proposed [18-20] in which an 'effective stress', i.e., Weibull stress, is defined to characterize the cleavage fracture process. Recently, based on this approach and considering the constraint effect, Minami et al [21] employed three-dimensional finite element analysis to study the effect of thickness on the critical J-integral. Their results gave an improved estimation of the size effect on the critical J compared to a simple weakest link model in which the variation in constraint is not taken into account. However, the shortcoming of this method is that a large deformation finite element analysis must be conducted to obtain the Weibull stress. In this study, based on the local approach and J-Q stress field, a simple statistical model to predict toughness scatter in the lower-shelf and lower-transition regions is proposed.

Theoretical Model

Local Approach Theory

In the three-parameter Weibull model, considering a structure with volume V stressed by a non-uniform maximum normal stress distribution σ_{yy}, the fracture probability P_f can be expressed by

$$P_f = 1 - \exp\left(-\int_{V_{th}} \left(\frac{\sigma_{yy} - \sigma_{th}}{\sigma_u - \sigma_{th}}\right)^m \frac{dV}{V_o}\right) \tag{1}$$

where m is the Weibull shape parameter, σ_u is the characteristic (63% probability) of the distribution, σ_{th} is the threshold stress below which cleavage cannot occur, V_o is a reference volume and V_{th} is the volume where $\sigma_{yy} \geq \sigma_{th}$. The Weibull stress is defined as [20]

$$\sigma_w = \sigma_{th} + \left(\int_{V_{th}} \left(\sigma_{yy} - \sigma_{th}\right)^m \frac{dV}{V_o}\right)^{\frac{1}{m}} \tag{2}$$

Then, equation (1) may be written as

$$P_f = 1 - \exp\left(-\left(\frac{\sigma_w - \sigma_{th}}{\sigma_u - \sigma_{th}}\right)^m\right) \quad for \quad \sigma_w \geq \sigma_{th}$$

$$P_f = 0 \qquad\qquad for \quad \sigma_w < \sigma_{th} \tag{3}$$

If $\sigma_{th}=0$ equation (3) becomes a two-parameter Weibull model. Bakker et al [20] have compared the two-parameter and three-parameter models for toughness prediction. They concluded that a three-parameter model with a threshold value was physically reasonable and more suitable for predicting failure at small probabilities. For these reasons, we chose the three-parameter model.

J-Q Stress Field

According to the J-Q theory proposed by O'Dowd and Shih [9-11], for a power-law hardening material, the stress-strain fields at the crack tip, within the forward sector ($|\theta|<\pi/2$) of the annulus $J/\sigma_o < x < 5\, J/\sigma_o$, can be characterized by two parameters, J and Q. Therefore, the opening stress along the line directly ahead of the crack tip is

$$\frac{\sigma_{yy}}{\sigma_o} = \left(\frac{J}{\alpha \varepsilon_o \sigma_o I_n x}\right)^{\frac{1}{n+1}} \hat{\sigma}(\theta = 0, n) + Q \tag{4}$$

where σ_o is yield stress, n is hardening exponent, α and I_n are constants, ε_o is yield strain, $\hat{\sigma}$ is angular factor and x is distance ahead of the crack tip. The definition of Q is [11]

$$Q = \frac{\sigma_{yy} - (\sigma_{yy})_{HRR}}{\sigma_o}, \qquad \theta = 0, \quad x = \frac{2J}{\sigma_o} \tag{5}$$

A negative Q is associated with a low constraint specimen geometry, while a zero or positive Q corresponds to a high constraint level. The variation of Q with load, hardening exponent and a/W ratio for centre-cracked panel, three-point bend bar and double-edge cracked panel can be found in Ref 11. Furthermore, an approximate expression of Q for compact tension and three-point bend specimens has been proposed by Wu et al [22] where

$$Q=\frac{1}{C_1+C_2\left(\log\hat{J}\right)^2+C_3\left(\log\hat{J}\right)^4+C_4\left(\log\hat{J}\right)^6} \quad (6)$$

and $\hat{J}=J/b\sigma_o$, b is the remaining ligament, C_1, C_2, C_3 and C_4 are numerical constants and have been given in Ref 22

Active Volume V_{th}

The active volume is that part of material ahead of the crack tip where cleavage fracture can be initiated. In some statistical models, the active volume was taken as the whole crack tip plastic zone. Actually, the cleavage fracture path does not deviate to a great extent from the plane of the precrack. In this study, the simplified active volume has a constant width of l, as shown in Fig.1.

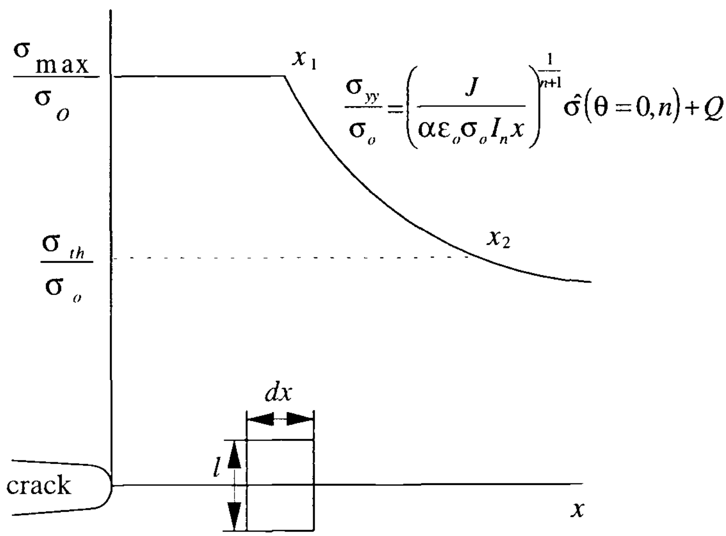

Fig.1-*Definition of active volume ahead of crack tip*

This is similar to the active volume used by Godse and Gurland [17] and Anderson [23]. Therefore, the unit integral volume is

$$dV = lBdx \quad (7)$$

where B is the thickness of the crack front, i.e., thickness of the specimen. It is assumed that σ_{yy} remains constant along l and B directions. Godse and Gurland assumed l and B equalled two ferrite grain diameter. Actually, l and B are scale parameters and their magnitudes only affect the absolute value of the Weibull stress rather than the shape parameter m. For actual specimens, due to crack tip blunting upon loading, the maximum opening stress in the vicinity of the crack tip is not infinite. In Fig. 1, for a given load, the stress distribution from the crack tip to the maximum opening stress point (x_1) is less than σ_{max}. However, when calculating the cumulative failure probability by equation (3), σ_{yy} must be taken as the maximum stress the material point has experienced. Therefore, the magnitude of the opening stress from the crack tip to the maximum opening stress (point x_1) is regarded as constant, which depends on n and σ_o. The positions of points x_1 and x_2 can be determined by substituting selected values of σ_{max}/σ_o and σ_{th}/σ_o in equation (4) respectively. Thus, the Weibull stress can be calculated by

$$\sigma_w = \sigma_{th} + \left\{ \frac{lB}{V_o} \left(\left(\sigma_{max} - \sigma_{th}\right)^m x_1 + \int_{x_1}^{x_2} \left[\sigma_o \left(\frac{J}{\alpha \varepsilon_o \sigma_o I_n x} \right)^{\frac{1}{n+1}} \hat{\sigma}(\theta = 0, n) + Q\sigma_o - \sigma_{th} \right]^m dx \right) \right\}^{\frac{1}{m}} \quad (8)$$

Determination of Weibull Parameter m

From equation (1), to establish the statistical model, it is necessary to determine σ_{th}, m, σ_u, and V_o. In Refs 16 and 20, σ_{th} was assumed to be about $2.5\sigma_o$. McMeeking [24] has employed deformation plasticity theory to calculate the stress distribution ahead of a blunted crack. His results indicated that the magnitude of the maximum opening stress depends on the yield stress σ_o and the hardening exponent n, *e.g.*, for n=5, σ_{max}/σ_o=5. Beyond the crack tip region, McMeeking's calculation is basically the same as the HRR stress field. In this study, we choose HRR field as the reference stress field and consider crack tip blunting (Fig. 1). The threshold stress $\sigma_{th}=2.5\sigma_o$ seems to be too conservative for fracture probability estimation. In the study of Chen et al [25], the measured cleavage fracture stress was in the range of $3.1\sim3.9\sigma_o$ for a material with hardening exponent n=5. Therefore, we choose the threshold stress $\sigma_{th}=3.5\sigma_o$. m and σ_u can be optimized by the least squares method. At first, for a set of experimental data, assuming an initial m, the Weibull stress σ_w at every cleavage fracture point can be obtained from equation (8). Then, a linear regression of the $\ln\ln(1/1\text{-}P_f)$ versus $\ln\sigma_w$ plot gives a slope m' and the characteristic stress σ_u. P_f is taken as the rank probability of the fracture points within the experimental data set. This iterative routine is repeated with an adjusted m until $m' \cong m$. As pointed out by Bakker and Koers [20], the choice of the reference volume V_o does not affect the iterative process and the Weibull parameter m. It only affects the absolute value of σ_w and σ_u. In this study, we assume V_o=1 mm^3.

m is basically a material constant and is independent of crack depth and specimen geometry. In this study, the parameter m is not sensitive to the choice of σ_{th}. Therefore, according to equation (3), the Weibull stress σ_w at any fracture probability should also be the same irrespective of crack depth or specimen geometry. In equation (8), at the same load (J) level, the specimens with a lower constraint have a lower σ_w, thereby having a lower fracture probability (equation(3)). In other words, to achieve the same σ_w, specimens with a lower in-plane constraint need a higher load (J) level.

Experimental Verification

Some data have been collected from the literature to examine the validity of the statistical model. To show the effect of crack depth (a/W) on toughness, the results of Kirk et al [12] on an ASTM A515 steel in three-point bend (SE(B)) specimens are analyzed. From the results of specimens with a/W=0.15, Weibull parameter m=1.02 and characteristic stress σ_u=1128MPa are obtained by the iteration process referred to above. Based on these m and σ_u values, the failure probability as a function of Weibull stress σ_w can be calculated from equations (3) and (8) for any given loads. Fig. 2(a) shows the variation of failure probability with σ_w for specimens with a/W=0.15. Because m is a material constant, the variation of Weibull stress σ_w with applied load (J) for specimens with different a/W can be obtained from equation (8), as shown in Fig. 2(b). From equation (3), the Weibull stress σ_w at any failure probability should be the same irrespective of crack depth and specimen geometry. For a given range of cleavage probability, two critical σ_w can be obtained from the relationship between cleavage probability and σ_w. The dash lines in Fig. 2(a) give two critical σ_w corresponding to 5% and 95% cleavage probability. Then, from Fig. 2(b), based on the two critical σ_w, the lower bound and upper bound toughnesses can be determined for specimens with different a/W. Fig. 2(c) gives the predicted statistical variation of toughness (P_f=5% and 95%) together with the experimental data from Ref. 12. The shallow crack specimens have a higher mean toughness but a larger scatter band compared to the deep crack specimens.

According to the calculation of Q [11] at small J, i.e., small scale yielding condition, Q in both shallow and deep crack specimens are similar and close to zero, Fig. 3, i.e., shallow and deep crack specimens have similar in-plane constraint and the stress distribution at the crack tip can be approximately described by HRR stress field. From the data of Kirk et al (Fig.2), at small J (below 10 KJ/m^2), the specimen thickness (B=25.4mm), crack depth (a=7.6, 15.2 and 25.4mm) and ligament (b=43.2, 35.5 and 25.4mm) all satisfied the condition for cleavage to be size independent [5], i.e.,

$$B,b,a \geq \frac{200J_c}{\sigma_o} \tag{9}$$

where σ_o=300MPa and $200J_c/\sigma_o$=6.67. In Fig. 2(b), when J<10KJ/m^2, specimens with different a/W have a similar Weibull stress, i.e., a similar in-plane constraint level.

With increasing J, the constraint decreases rapidly in the shallow crack specimens (Q becomes negative) and the difference of Q between shallow and deep crack specimens becomes remarkable (Fig.3). The work of Sorem et al [3] has indicated that in the lower-transition region, with increasing load, plasticity spreads to the backface behind the crack tip in shallow crack specimens. However, plasticity remains confined to the crack tip for

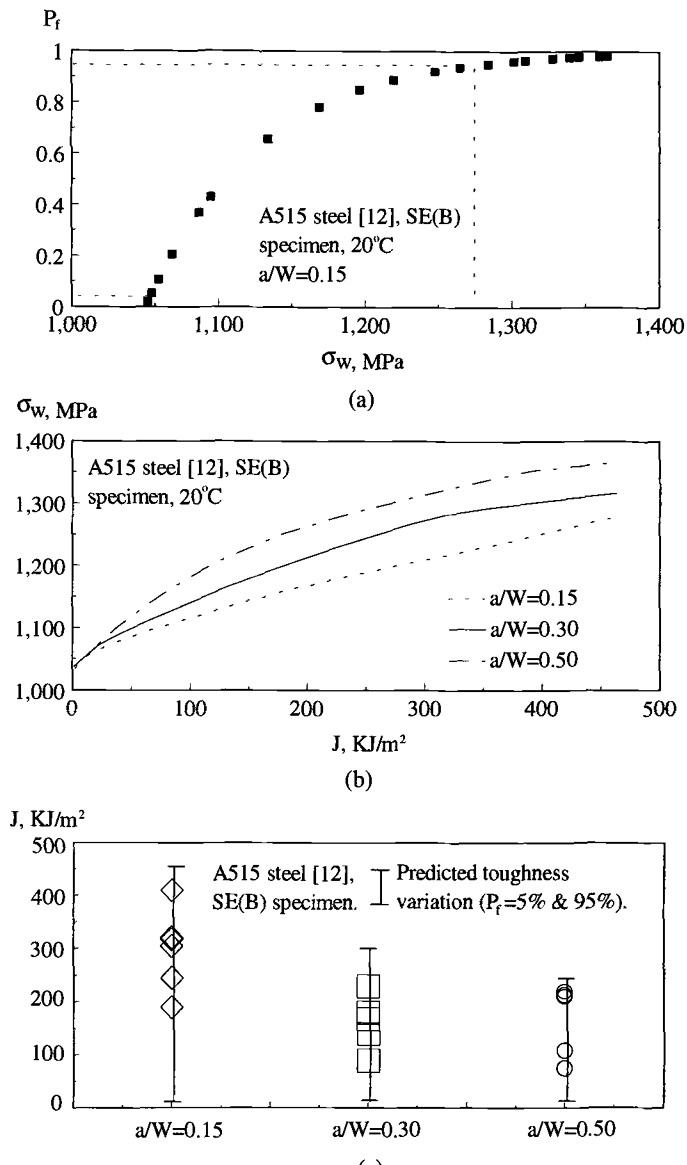

FIG. 2— (a) *Statistical distribution of Weibull stress,* (b) *computed Weibull stress Versus load, and* (c) *predicted toughness variation* (P_f*=5% & 95%) compared with experimental data (m=1.02,*σ_u*=1128MPa & n=4).*

the deep crack specimens. In Fig. 2(b), at large J, the shallow crack specimen have a lower Weibull stress compared to the deep crack specimen due to the loss of constraint.

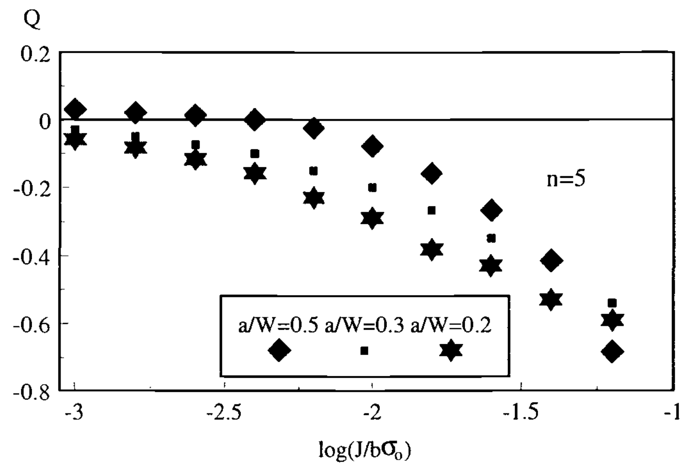

Fig. 3-Evolution of Q with increasing J for three-point bend specimen [11].

For the data of Sorem et al [3], m=0.96 and σ_u=1122 MPa are obtained from the data set of specimens with a/W=0.15. Then, the anticipated statistical variation of toughness (P_f=5% and 95%) for specimens with a/W=0.15 and 0.5 is shown in Fig. 4. The prediction process is the same as illustrated in Fig. 2. It can be seen that all the experimental points fall within the range of predicted toughness variation. Fig. 4 also includes the toughness prediction (P_f=5% and 95%) for the data of Theiss et al [6], where m=0.8 and σ_u=2054 MPa.

Also, this model can be applied to predict the toughness variation in different specimen geometries. Fig. 5(a) indicates the variation of Weibull stress with load for the central-cracked panel (CCT) and compact tension (CT) specimens. The data is from the work of Heerens et al [26]. The CCT specimens have a lower σ_w than that of CT specimens due to a lower constraint level. Fig. 5(b) shows a comparison of predicted fracture toughness (P_f=5% and 95%) with experimental points.

It is important to note that there is a larger scatter for the specimens with lower in-plane constraint compared to those with higher constraint. In Fig. 2(c) and Fig. 4, for both predicted and experimental toughness data, the specimens with shallow precracks (a/W) have a significantly larger scatter compared to the specimens with deep precracks. A similar trend can be found in Fig. 5(b), in which the data scatter for CCT specimens is larger than that for CT specimens. Therefore, it can be concluded that a large data scatter is an inherent characteristic of specimens with lower in-plane constraints. The reason is the large loss of constraint at large deformation, which leads to a decrease of the slope of the Weibull stress with loading (Fig.2 (b)). For the same failure probability, the specimens with a lower constraint therefore have a lower Weibull stress to initiate cleavage fracture.

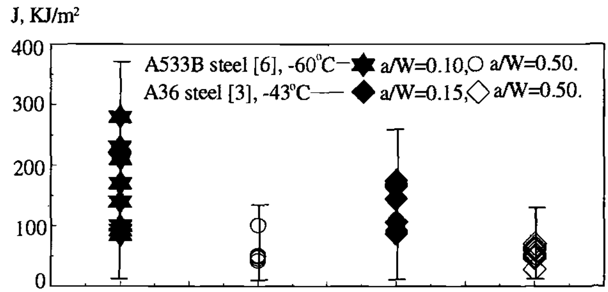

FIG. 4-*Predicted toughness variation* (P_f=5% & 95%) *compared with experimental data.*

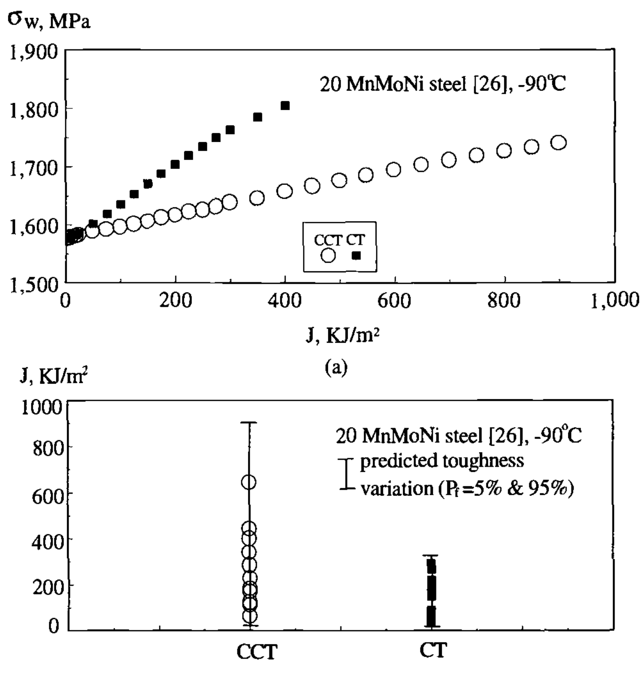

FIG. 5-(a) *Calculated Weibull stress versus load, and* (b) *predicted toughness variation* (P_f=5% *and* 95%) *compared with experimental data* (m=0.82, σ_u =1624 MPa & n=5).

Discussion

The validity of this model has been examined by predicting the effect of crack depth and specimen geometry on toughness scatter in the lower-shelf and lower-transition regions in which there is no ductile crack growth. The advantage of the model is characterized by both a clear physical meaning and simplicity. Cleavage fracture is a competition process between the distribution of brittle cracks and opening stress ahead of the crack tip. The Weibull stress, which is related to the stressed volume, is a reasonable parameter to describe the fracture probability. The effect of crack depth and specimen geometry on toughness can be unified in terms of the in-plane constraint, which results in a different Weibull stress. Also, the extent of toughness scatter is related to the loss of constraint during loading.

Because of the large data scatter, the lower-bound toughness becomes more critical in estimation of structure reliability. Usually, the toughness value corresponding to small fracture probability is chosen as an estimation of the lower-bound. With the results of Kirk et al [12] at P_f=5%, the lower-bound toughnesses are about 3.0, 2.5, and 2.4 KJ/m^2 for the specimens with a/W=0.15, 0.30, and 0.50, respectively (Fig. 2(c)). In Fig. 5(b), the data of Heerens et al [26] show the lower-bound toughnesses for CCT and CT specimens to be 5.0 and 4.8 KJ/m^2, respectively, at P_f=5%. Therefore, crack depth and specimen geometry have little effect on the lower-bound toughness. This may be because all the specimens having a similar in-plane constraint (Q) at small loads. Zerbst, Heerens and Schwalbe [27] employed six different procedures to examine the lower-bound toughness in the ductile-brittle transition region. They have found that the lower-bound toughness corresponding to 5% fracture probability is basically independent of specimen geometry, hence supporting the above finding.

From equations (2) and (3), the condition for P_f=0 is σ_{yy}-σ_{th}=0. Substituting this condition into equation (4), the toughness corresponding to P_f=0 (J_{min}) is

$$J_{\min} = \alpha\ \varepsilon_o \sigma_o I_n x \left[\frac{1}{\hat{\sigma}} \left(\frac{\sigma_{th}}{\sigma_o} - Q \right) \right]^{n+1} \qquad (10)$$

At small load (J) level, Q approaches zero and equation (10) can be simplified to

$$J_{\min} = Cx \frac{\sigma_{th}^{n+1}}{\sigma_o^n} \qquad (11)$$

where $C = \alpha\, \varepsilon_o I_n / \hat{\sigma}^{n+1}$.

Therefore, J_{min} is mainly determined by σ_{th} and x. σ_{th} can be related to the well-known Griffith equation

$$\sigma_{th} = \left[\frac{2E\gamma_p}{\pi(1-v^2)c_o} \right]^{\frac{1}{2}} \tag{12}$$

where γ_p is fracture surface energy, c_o is maximum flaw size, E and ν are Young's modulus and Poisson's ratio. Also, σ_{th} can be measured using single-edge notch bend specimen [28].

In equation (11), when x approaches zero, J_{min} also approaches zero. This means that cleavage may occur at a vanishingly small load. Hence, it seems necessary to supplement cleavage criterion by the additional requirement that critical stress σ_{th} be achieved over a characteristic distance. In the work of Ritchie et al [29], the minimum x (x_{min}) was assumed to be twice the grain diameter. For ASTM A515 steel, assuming σ_{th}/σ_o=3.5, n=4 [12] and x_{min} =two grain diameters=100μm [30], J_{min} was about 3.2 KJ/m^2 using equation (11). This value is similar to the lower-bound toughness corresponding to 5% fracture probability, i.e., 2.4-3.0 KJ/m^2 (Fig. 2). Therefore, the lower-bound toughness can be estimated by the value corresponding to 5% fracture probability or by equation (11). However, further work on determining the minimum initiation distance should be carried out.

Conclusions

Based on the local approach theory in conjunction with the J-Q stress field, a statistical model has been established, which can be used to predict the effect of crack depth and specimen geometry on the toughness in the lower-shelf and lower-transition regions. The validity of the model has been proven by some experimental data. The crack depth and specimen geometry have little effect on the lower-bound toughness due to a similar in-plane constraint for all specimens at small loads. Specimens with a lower in-plane constraint (shallow crack bend bar and centre-cracked panel) have a larger toughness scatter compared to those specimens with a higher constraint (deep crack bend and compact tension). This is caused by the significant loss of constraint when the specimens with a lower constraint are being loaded.

Acknowledgments

The authors thank the Australian Research Council (ARC) for the continuing support of this project. Cheng Yan acknowledges the OPRS and UPRA awards by the University of Sydney.

References

[1] Wu, S. X., Mai, Y. W., Cotterell, B., and Le, C. V., "Ductile-Brittle Fracture Transition due to Increasing Crack Length in a Medium Carbon Steel," *Acta Metallurgica Mater.*, Vol.39, 1991, pp. 2527-2532.

[2] Wu, S. X., Mai, Y. W., and Cotterell, B., "Ductile-Brittle Fracture Transition as a Result of Increasing In-Plane Constraint in a Medium carbon Steel," in *Fracture Mechanics, ASTM STP 1207*, J.D. Landes, D.E. McCabe and J.A.M. Boulet, Eds., American Society for Testing and Materials, Philadelphia, 1994, p. 376-386.

[3] Sorem, W. A., Dodds, R. H., Jr., and Rolfe, S. T., "Effect of Crack Depth on Elastic-Plastic Fracture Toughness," *International Journal of Fracture*, Vol. 47, 1991, pp.105-126.

[4] Dodds, R. H., Jr., Anderson, T. L., and Kirk, M. T., "A Framework to Correlate a/W Ratio Effect on Elastic-Plastic Fracture Toughness (J_c)," *International Journal of Fracture*, Vol. 48, 1991, pp. 1-22.

[5] Anderson, T. L., and Dodds, R. H., Jr., "Specimen Size Requirement for Fracture Toughness Testing in the Transition Region," *Journal of Testing & Evaluation*, Vol. 18, 1991, pp.123-134.

[6] Theiss, T. J., and Bryson, J. W., "Influence of Constraint on Fracture Toughness of Reactor Pressure Vessel Steel," *Constraint Effect in Fracture, ASTM STP 1171*, E.M. Hackett, K.H. Schwalbe and R.H. Dodds, Eds., American Society for Testing and Materials, Philadelphia, 1993, pp. 104-119.

[7] McClintock, F. A., in *Fracture: An Advanced Treaties*, Vol.3, H. Liebowitz, Eds., Academic Press, New York, 1971, p. 47.

[8] Wu, S. X.,"Fracture Analysis and Toughness Measurement of Specimens with Deep and Shallow Crack", Ph.D. thesis, The University of Sydney, Sydney, Australia, 1990.

[9] O'Dowd, N. P., and Shih, C. F., "Family of Crack-Tip Fields Characterized by a Triaxiality Parameter-I. Structure of Fields," *Journal of Mechanics and Physics of Solids*, Vol.39, 1991, pp. 898-1015.

[10] O'Dowd, N. P., and Shih, C. F., "Family of Crack-Tip Fields Characterized by a Triaxiality Parameter-II. Fracture Application," *ibid*, Vol. 40, 1992, pp. 939-963.

[11] O'Dowd, N. P., and Shih, C. F., "Two-Parameter Fracture Mechanics: Theory and Applications," in *Fracture Mechanics, ASTM STP 1207*, J.D. Landes, D.E. McCabe, and J.A.M. Boulet, Eds., American Society for Testing and Materials, Philadelphia, 1994, pp. 21-47.

[12] Kirk, M. T., Koppenhoefer, K. C., and Shih, C. F., "Effect of Constraint on Specimen Dimensions Needed to Obtain Structurally Relevant Toughness Measures," in *Constraint Effect in Fracture, ASTM STP 1171*, E.M. Hackett, K.-H. Schwalbe and R.H. Dodds, Eds., American Society for Testing and Materials, Philadelphia, 1993, pp. 79-103.

[13] Landes, J. D., and Shaffer, D. H., "Statistical Characterization of Fracture in the transition region," in *Fracture Mechanics, ASTM STP 700*, American Society for Testing and Materials, 1980, pp. 368-382.

[14] Wallin, K., "The Scatter in K_{IC}-Results," *Engineering Fracture Mechanics*, Vol. 19, 1984, pp.1085-1093.

[15] Wallin, K., "The Size Effect in K_{IC} Results," *Engineering Fracture Mechanics*, Vol. 20, 1985, pp. 149-163.

[16] Lin, T., Evans, A. G.,and Ritchie, R. O., "Statistical Analysis of Cleavage Fracture ahead of Sharp Cracks and Round Notches," *Acta Metallurgica*, Vol. 34, 1986, pp. 2205-2216.

[17] Godse, R.,and Gurland, J., "A Statistical Model for Low Temperature Cleavage Fracture in Mild Steel," *Acta Metallurgica*, Vol. 37, 1989, pp. 541-548.

[18] Beremin, F. M., "A Local Criterion for Cleavage Fracture of a Nuclear Pressure Vessel Steel," *Metallurgical Transactions A*, Vol. 14A, 1983, pp. 2277-2287.

[19] Mudry, F., "A Local Approach to Cleavage Fracture," *Nuclear Engineering and Design*, Vol. 105, 1987, pp. 65-76.

[20] Bakker, A., and Koers, R. W. J., "Prediction of Cleavage Fracture Events in the Brittle-Ductile Transition Region of a Ferrite Steel," in *Defect Assessment in Components-fundamentals and Applications, ESIS Publication 9*, J.G. Blauel and K.H. Schwalbe, Eds., Mechanical Engineering Publ. Ltd., London, UK, 1991, pp. 613-632.

[21] Minami, F., Bruckner-Foit, Munz, A. D., and Trolldenier, B., "Estimation Procedure for the Weibull Parameter Used in the Local Approach," *International Journal of Fracture*, Vol. 54, 1992, pp. 197-210.

[22] Wu, S. X., Mai, Y. W., and Cotterell, B., "Prediction of the Initiation of Ductile Fracture," *Journal of Mechanics and Physics of Solids*, Vol. 43,1995, p. 793

[23] Anderson, T. L., "A Combined Statistical and Constraint Model for the Ductile-Brittle Transition Region," in *Nonlinear Fracture Mechanics: Volume-II-Elastic-Plastic Fracture, ASTM STP 995*, J.D. Landes, A. Saxena and J.G. Merkle, Eds., American Society for Testing and Materials, Philadelphia, 1989, pp. 563-583.

[24] McMeeking, R. M., "Finite Deformation Analysis of Crack-Tip Opening in Elastic-Plastic Materials and Implications for Fracture," *Journal of the Mechanics and Physics of Solids*, Vol.25, 1977, pp. 375-381.

[25] Chen, J. H., Yan, C., and Sun, J., "Further Study on the Mechanism of Cleavage Fracture at Low Temperature," *Acta Metallurgica. Mater*, Vol. 42, 1994, pp. 251-261.

[26] Heerens, J., Zerbst, U., and Schwalbe, K.-H., "Strategy for Characterizing Fracture Toughness in the Ductile to Brittle Transition Regime," *Fatigue and Fracture of Engineering Materials and Structure*, Vol. 16, 1993, pp. 1213-1230.

[27] Zerbst, U., Heerens, J., and Schwalbe, K.-H., "Estimation of Lower Bound Fracture Resistance of Pressure Vessel Steel in the Transition Regime," *Fatigue and Fracture of Engineering Materials and Structure*, Vol. 16, 1993, pp. 1147-1160.

[28] Griffith, J. R., and Owen, D. R. J., "An Elastic-Plastic Stress analysis for a Notched Bar in Plane Strain Bending," *Journal of Mechanics and Physics of Solids*, Vol. 19, 1971, pp. 419-431.

[29] Ritchie, R. O., Knott, J. F., and Rice, J. R., "On the Relationship between Critical Tensile Stress and Fracture Toughness in Mild Steel," *Journal of Mechanics and Physics of Solids*, Vol. 21, 1973, pp. 395-410.

[30] *Metal Handbook*, Ninth Edition, Vol. 9, American Society for Metals, Metals Park, Ohio, 1992, p. 205.

D. S. Dawicke,[1] R. S. Piascik,[2] J. C. Newman, Jr.[2]

ANALYSIS OF STABLE TEARING IN A 7.6 MM THICK ALUMINUM PLATE ALLOY

REFERENCE: Dawicke, D. S., Piascik, R. S. and Newman, J. C., Jr., **"Analysis Of Stable Tearing In A Thick Aluminum Alloy"**, Fatigue and Fracture Mechanics: 28th Volume, ASTM STP 1321, J. H. Underwood, B. D. Macdonald, and M. R. Mitchell, Eds., American Society for Testing and Materials, 1997.

ABSTRACT: The behavior of a 7.6 mm thick 2000 series aluminum plate alloy was investigated. Fracture tests were conducted on 304.8 mm and 101.6 mm wide M(T) specimens and 152.4 mm and 101.6 C(T) specimens (the 101.6 mm wide C(T) specimen had 10% side grooves). Two-dimensional and three-dimensional, elastic-plastic finite element simulations used the critical CTOA criterion to simulate the fracture behavior. A plane strain core was used in the two-dimensional analyses to approximate the three-dimensional constraint. The results from this study indicate: (A) The three-dimensional finite element analyses required a critical CTOA of 5.75° to simulate the fracture behavior of the 101.6 mm and 304.8 mm wide M(T) specimens and the 152.4 C(T) specimen. This angle was about the upper limit of the surface CTOA measurements. (B) The three-dimensional finite element analyses required a critical CTOA of 3.6° to simulate the fracture behavior of the 101.6 mm C(T) specimen with side grooves. This angle was about the upper limit of the microtopography through-thickness CTOA measurements. (C) A plane strain core height of PSC = 4 mm was required for the two-dimensional analyses to match the fracture behavior obtained from the three-dimensional analyses. This height agreed with the distance that a three-dimensional analysis indicated was the start of plane strain like behavior. (D) For large M(T) specimens (W > 1000 mm) the two-dimensional plane strain core analysis predicted a failure stress between the plane stress and plane strain conditions and provided a good approximation of the three-dimensional analyses. (E) The experimental measurements and analytical results show good agreement when the specimens sizes meet the uncracked ligament to thickness ratio (b/B > 4) determined by Newman et. al [14]. This indicates that there is a minimum size "laboratory specimen" that can be used to determine the material behavior needed to predict fracture in large specimens and structures.

KEYWORDS: Fracture, stable crack growth, CTOA, aluminum, plate

NOMENCLATURE

CTOA	Crack-tip opening angle
P	Load, KN

---

[1]Senior Scientist, Analytical Services and Materials, Hampton, VA 23666
[2]Senior Scientist, NASA LaRC Research Center, Hampton, VA 23665

Δa	Crack extension, mm
S	Stress, MPa
B	Thickness, mm
b	Uncracked ligament length, mm
a	Crack length (half crack length in M(T) specimens), mm
PSC	Plane strain core height, mm
W	Specimen width, mm
ψ_c	Critical CTOA, degrees
R	Stress ratio
ΔK	Stress intensity factor, MPa $\sqrt{m}$

INTRODUCTION

The NASA Aircraft Structural Integrity Program [1] is developing analysis tools and investigating fracture criteria for applications on the aging commercial aircraft fleet. The wing structure of these aircraft contain wide, aluminum components machined from thick plates and require a fracture methodology to predict residual strength. Several fracture mechanics parameters have been proposed to characterize stable crack growth: crack-tip strain [2], energy release rate [3], the J-integral [4], average crack opening angle (COA) [5], crack-tip opening displacement (CTOD) [6-8], and crack-tip opening angle (CTOA) [9,10].

The prediction of residual strength for large aircraft components requires a fracture criterion that ascertains the material behavior from small laboratory coupons and predicts the behavior of the larger structures. The critical CTOA criteria has been shown to successfully predict the fracture behavior in a wide range of crack configurations for thin-sheet (2.3 mm) aluminum alloys [11, 12] and in 7.6 mm thick aluminum plate [13]. Newman, et. al found that the CTOA criteria was independent of crack geometry if the ratio of uncracked ligament to thickness (b/B) exceeded 4 [14]. This criteria assumes that stable crack growth will occur when an angle made by a point (at a fixed distance behind the crack-tip) on the upper surface of a crack, the crack-tip and a point (again at a fixed distance behind the crack-tip) on the lower surface reaches a "critical" angle. This CTOA is a mild function of the distance behind the crack-tip where the angle is measured and a distance of 1 mm has been used for consistency between experimental measurements and analyses [11].

The objective of this study was to evaluate the effectiveness of the CTOA criterion on a 7.6 mm thick 2000 series aluminum plate alloy. Fracture tests were conducted on 101.6 mm and 304.8 mm wide M(T) specimens and 152.4 mm and 101.6 mm wide C(T) specimens (the 101.6 mm wide C(T) specimen had 10% side grooves). CTOA measurements were made using an optical microscope [15] and a microtopographic technique [13, 16-17]. Two-dimensional and three-dimensional, elastic-plastic finite element simulations were performed for all experiments and predictions were made for M(T) specimens as wide as 1500 mm.

EXPERIMENTAL PROCEDURE

Fracture tests were conducted on M(T) and C(T) specimens machined from a 7.6 mm thick, 2000 series aluminum plate. The material was machined from the center (T/2) of a plate more than 30 mm thick, simulating the processing history and microstructure present in the aircraft wing structure. The tests are summarized in Table 1. Critical

CTOA measurements were made using an optical method and using a microtopography technique.

Table 1
Summary of Fracture Tests

Specimen Type	Width (mm)	Precrack Length (mm)	Uncracked Ligament to Thickness Ratio
M(T)	101.6	33.0	2.3
M(T)	101.6	33.0	2.3
M(T)	304.8	114.3	12.5
M(T)	304.8	119.4	12.2
C(T)	152.4	64.6	11.5
C(T)	101.6*	40.6	8.0
C(T)	101.6*	40.8	8.0

* 10% side grooved

Fracture Tests

Each specimen was fatigue precracked at a stress level that resulted in a stress intensity factor range of $\Delta K = 8$ MPa $\sqrt{m}$. The tests were conducted under displacement control and measurements of load, crack extension, crack opening displacement, and critical CTOA were made. The 101.6 mm wide C(T) specimens had a 10% side groove that prevented surface measurements of crack extension and CTOA. In one side groove specimen test, the stable tearing was stopped after 6 mm of crack growth. The specimen was then fatigue cracked at a high stress ratio (R=0.8) until failure, marking the fracture surface with three distinct regions: fatigue precrack, stable tearing, and fatigue crack growth.

CTOA Measurement Techniques

Two techniques were used to measure the critical CTOA: optical surface and microtopographic through-thickness. The optical technique [15] used a long focal length microscope to capture images of the crack-tip while the crack was growing. For each image, the surface CTOA was measured 5-10 times at distances of between 0.5 - 1.5 mm behind the crack-tip. The measurements for each image were averaged to give a measurement of the CTOA at a distance of 1 mm behind the crack-tip.

The microtopographic technique [17] measures the through-thickness CTOA by digitizing the topography of the two fractures surfaces. A computer then reconstructs the fracture process from the digitized values. Slices, perpendicular to the plane of the crack, are made for several through-thickness locations and crack lengths. The CTOA is measured from the slices in the same manner as used to obtain the CTOA in the optical technique.

FINITE ELEMENT ANALYSES

The elastic-plastic finite element codes ZIP2D [18] and ZIP3D [19] used the critical CTOA criterion to simulate fracture. The critical CTOA was always evaluated at a distance of 1.0 mm behind the crack-tip. Convergence studies were conducted to ensure that the crack-tip element were small enough and for the three-dimensional analysis, that a sufficient number of elements were used to model the through-thickness behavior.

Three-Dimensional Analyses

The three-dimensional analyses used 8-noded brick elements to model the crack geometries. Symmetry conditions required that only a quarter of the C(T) specimens and an eighth of the M(T) specimens were needed to be modeled. The size of the meshes ranged from 1695 nodes for the 101.6 mm wide M(T) specimen to 8856 nodes for the 304.8 mm wide M(T) specimen. The critical CTOA was evaluated at the middle of the specimen, 1 mm behind the crack front.

Two convergence studies were conducted to determine the minimum element size along the crack plane and the number of elements required to model the thickness. First, single layer through-the-thickness meshes were analyzed with crack-plane element sizes of 1 mm and 0.5 mm (the former required that the CTOA be analyzed at the first node behind the crack-tip and the latter required it to be analyzed at the second node behind the crack-tip). Both analyses produced nearly the same applied load at failure, indicating that convergence was achieved. Thus, the 1mm element size (with CTOA evaluated at the first node behind the crack-tip) was chosen for the three-dimensional analyses.

For the second convergence study, one-, two-, and three-layer meshes were used to model the half thickness. The failure load of the two-layer model was about 5% larger than the one-layer model and was nearly the same as the three-layer model, indicating that convergence was achieved with two or more layers. Thus, the half thickness was modeled with two-layers for all of the three-dimensional analyses.

Two-Dimensional Analyses

The two-dimensional analysis used 3-noded constant strain triangular elements. Symmetry conditions required that only a quarter of the M(T) specimens and half of the C(T) specimens were needed to be modeled. The size of the meshes ranged from 1095 nodes for the 101.6 mm wide M(T) specimen to 4322 nodes for the 304.8 mm wide M(T) specimen. The critical CTOA was evaluated 1 mm behind the crack front.

Meshes with crack-plane element sizes of 1.0 mm, 0.5 mm, and 0.25 mm (evaluating the critical CTOA an the 1st, 2nd, and 3rd node behind the crack-tip, respectively). The mesh with the 1.0 mm crack-plane elements had a 4.2% larger failure stress than the mesh with the 0.5 mm crack-plane elements. That mesh, in turn had a 1.9% larger failure stress than the mesh with the 0.25 mm crack-plane elements. The difference between the 0.5 mm and 0.25 mm meshes was small enough to consider the 0.5 mm mesh to be converged. This mesh size was used in all other two-dimensional analyses.

The finite element analyses were conducted for plane strain and plane stress conditions and using a plane strain core. The plane strain core analyses forced a "core" of elements along the crack plane to be under plane strain conditions, while the rest of the specimen was under plane stress conditions. The plane strain core was intended to approximate the three-dimensional constraint that develops at the crack-tip [20]. The height of the plane strain core (PSC) generally increases with specimen thickness and was obtained through comparison with three-dimensional analyses.

RESULTS AND DISCUSSION

Fracture tests were conducted on a 7.6 mm thick, 2000 series aluminum plate alloy in both M(T) and C(T) configurations. An optical technique was used to measure the critical CTOA at the surface and a microtopography technique was used to measure the through-thickness critical CTOA. Two- and three-dimensional, elastic-plastic finite element analyses were conducted to simulate the fracture experiments.

Critical CTOA Measurements

The number of surface CTOA values that can be measured in a fracture test depends on the amount of stable crack extension experienced during the test. As the ratio of uncracked ligament to specimen thickness decreases, the amount of stable crack extension also decreases. The 7.6 mm thick material produced 3-5 CTOA measurements for the 101.6 mm wide M(T) specimens and 5-15 CTOA measurements for the 304.8 mm wide M(T) and 152.4 mm wide C(T) specimens, as shown in Fig. 1. The trends of the surface CTOA values were similar to that seen in 2.3 mm thick 2024-T3 [15,21]: (1) initially the CTOA was high and decreased during a transient period, (2) after a small amount of stable crack growth the CTOA oscillated about a constant value, and (3) the scatter in the measurements was as about ±1°. The upper limit of the scatter in the CTOA measurements for the 7.6 mm thick 2000 series aluminum plate alloy was about 5.75°.

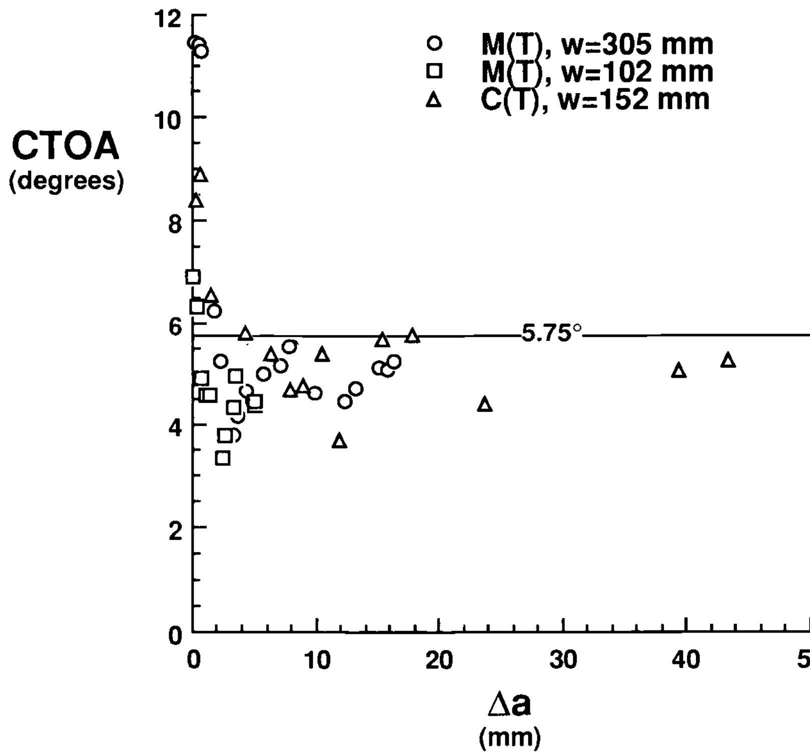

FIG. 1--Surface CTOA measurements from the M(T) and C(T) specimens.

The CTOA measured along the crack front was determined by analyzing cross sectional slices of matched conjugate fracture surfaces at several locations through the thickness [17]. The values of CTOA noted in Fig. 2, a plot of crack extension (Δa) against distance from mid-plane, are determined along two crack fronts during the early stages of a fracture test. Using slices perpendicular to the crack plane, the CTOA was calculated in a similar manner as established for the optical microscope (OM) technique [15, 17]. Fig. 2 shows CTOA values for two tunneled crack fronts with crack extensions from Δa = 0.81

mm to 4.06 mm. Similar average CTOA values of 2.7° (circles) and 2.8° (squares) were observed for both crack fronts.

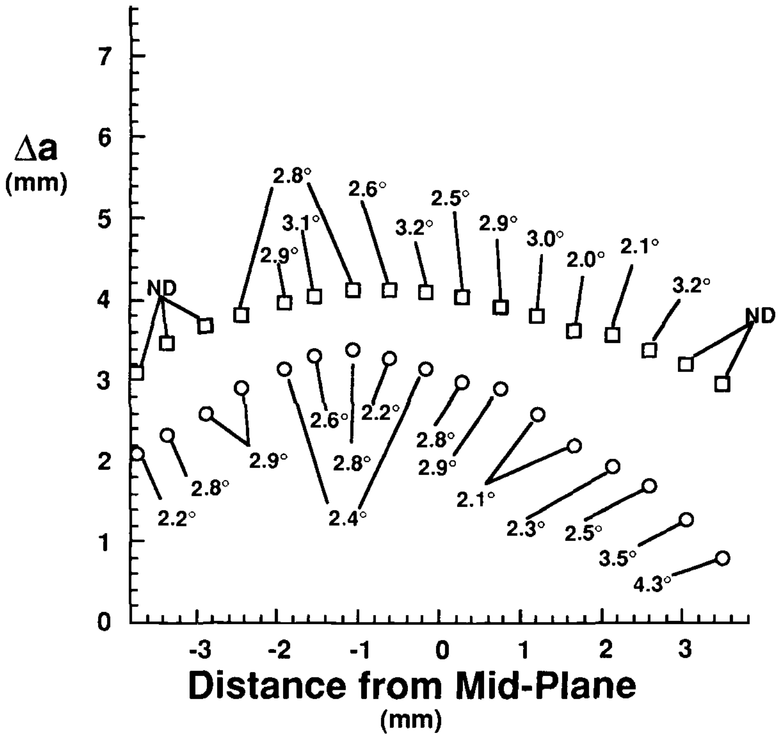

FIG. 2--Microtopography CTOA measurements along two stable tearing crack fronts.

A comparison of CTOA determined by OM surface measurements (shaded region) and microtopography measurements along the centerline (solid symbols) is shown in Fig. 3. The OM measurements were obtained from 7.6 mm thick M(T) and C(T) fracture tests and the microtopography results were from the fracture test on the 7.6 mm thick side grooved C(T) specimen. The microtopography CTOA values along the centerline ranged from 1.6° to 3.8° for crack extensions of Δa = 1.4 mm to 3.7 mm. This range of CTOA values is significantly less that observed from the surface measurements of the non-side grooved specimens, but the ±1° scatter band is about the same.

Plane Strain Core Determination

The plane strain core height (PSC) was determined through a comparison of the two-dimensional and three-dimensional finite element analyses. A critical CTOA criteria was used to simulate stable tearing and a critical CTOA of ψ_c = 5° was assumed. Analyses were conducted for the 304.8 mm and 101.6 mm wide M(T) specimens and 152.4 mm and 101.6 mm wide C(T) specimens, as shown in Figs. 4-7. In the three-dimensional analyses, the specimens were modeled with 2 layers through-the-thickness and a minimum element size along the crack plane of 1 mm. In the two-dimensional analyses, the minimum element size along the crack plane was 0.5 mm and a range of plane strain core heights from 0 (plane stress) to full height (plane strain) were analyzed.

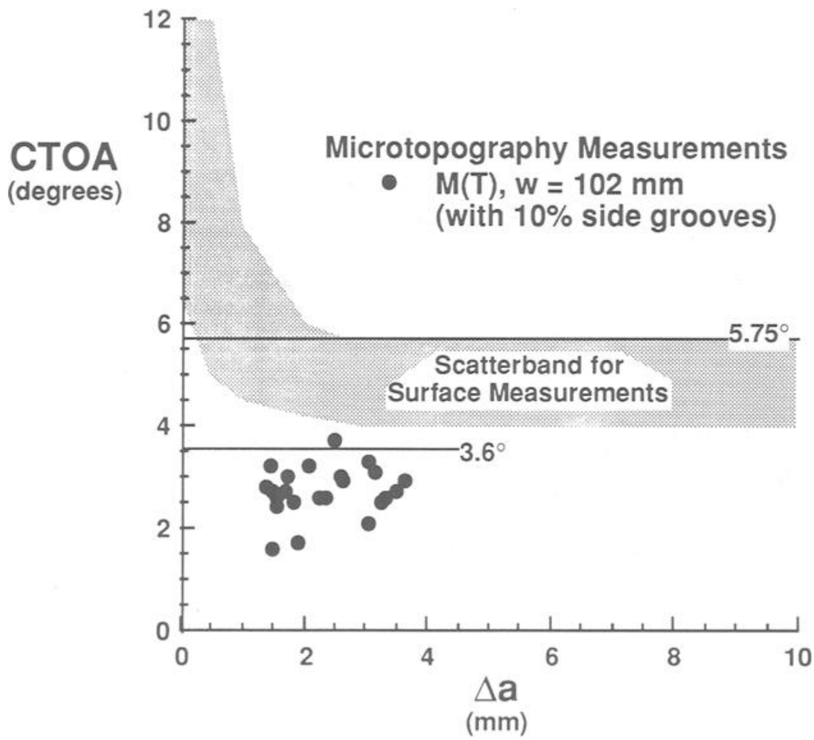

FIG. 3--Surface and Microtopography CTOA measurements from the M(T) and C(T) specimens.

The three-dimensional finite element simulations for the larger M(T) specimen and the two C(T) specimens was best approximated by the two-dimensional analysis with a plane strain core height of PSC = 4 mm. However, a plane strain core height of PSC = 20 mm was required to match the three-dimensional finite element simulation for the 101.6 mm wide M(T). This smaller M(T) specimen had an uncracked ligament to thickness ratio (b/B) of about 2.3, not meeting the requirement of b/B = 4 obtained from the three-dimensional analyses of Newman et. al [14].

Fracture Results and Finite Element Simulations

The three-dimensional, elastic-plastic finite element analyses were used to determine the critical CTOA that best simulated the fracture behavior observed in the experiments. For the 304.8 mm and 101.6 mm wide M(T) specimens and the 152.4 mm wide C(T) specimen, an angle of 5.75° was needed for the simulations to match the experimental results, as shown in Figs. 8-10. This CTOA value was about the upper range of the scatter band of the surface CTOA measurements (Fig. 1). The three-dimensional simulation for the 152.4 mm wide C(T) specimen and the 304.8 mm wide M(T) specimens were 6% higher and 4% lower, respectively, than the experimental

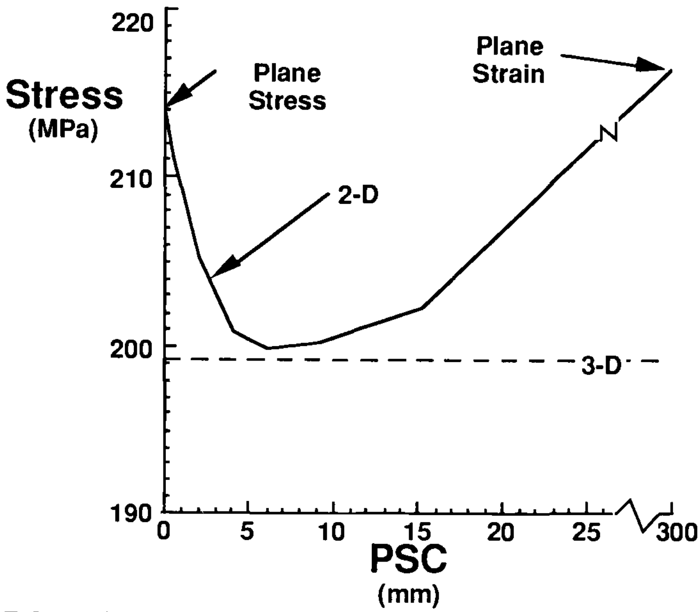

FIG. 4--Three-dimensional and two-dimensional plane strain core analyses for the 304.8 mm wide M(T) specimen.

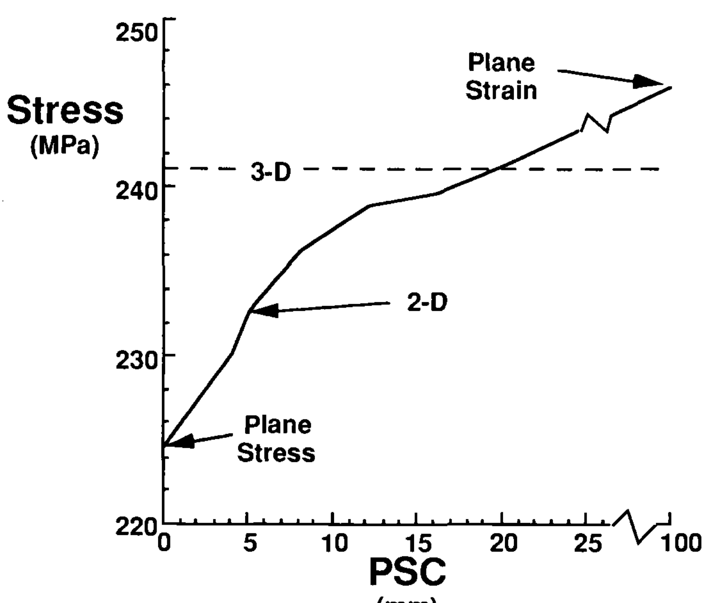

FIG. 5--Three-dimensional and two-dimensional plane strain core analyses for the 101.6 mm wide M(T) specimen.

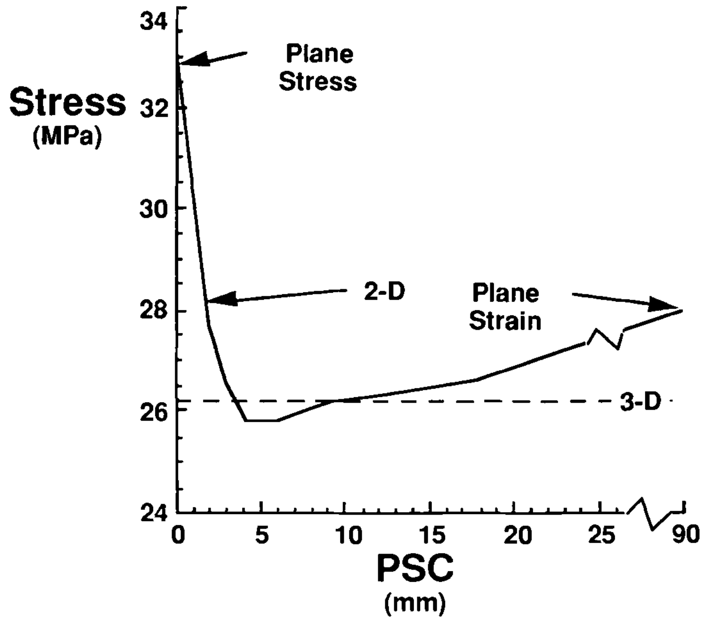

FIG. 6--Three-dimensional and two-dimensional plane strain core analyses for the 152.4 mm wide CT) specimen.

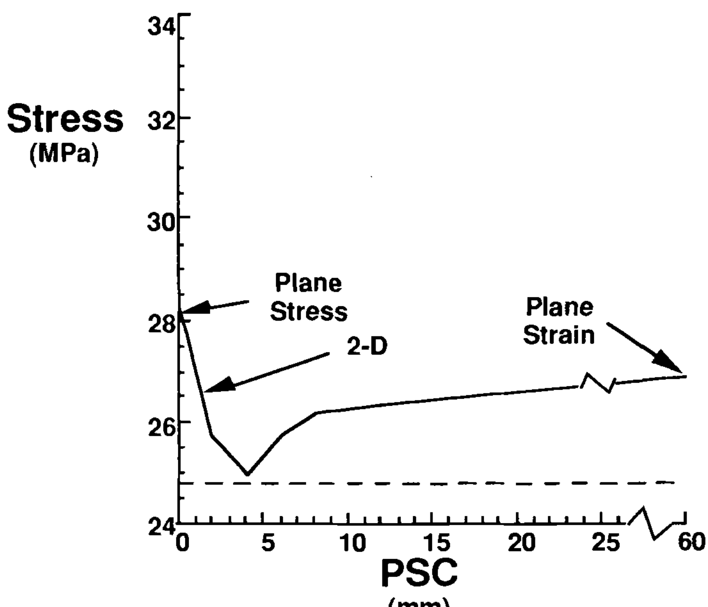

FIG. 7--Three-dimensional and two-dimensional plane strain core analyses for the 101.6 mm wide CT) specimen.

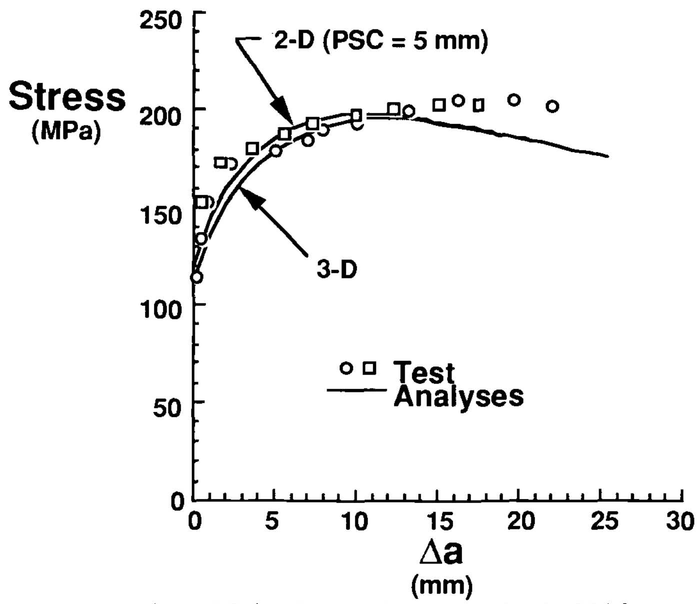

FIG. 8--Fracture test results and finite element simulations for the 304.8 mm wide M(T) specimen.

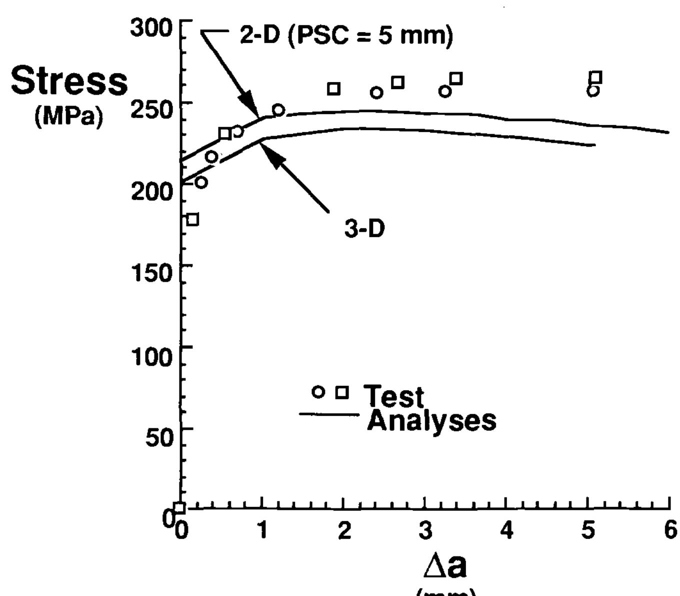

FIG. 9--Fracture test results and finite element simulations for the 101.6 mm wide M(T) specimen.

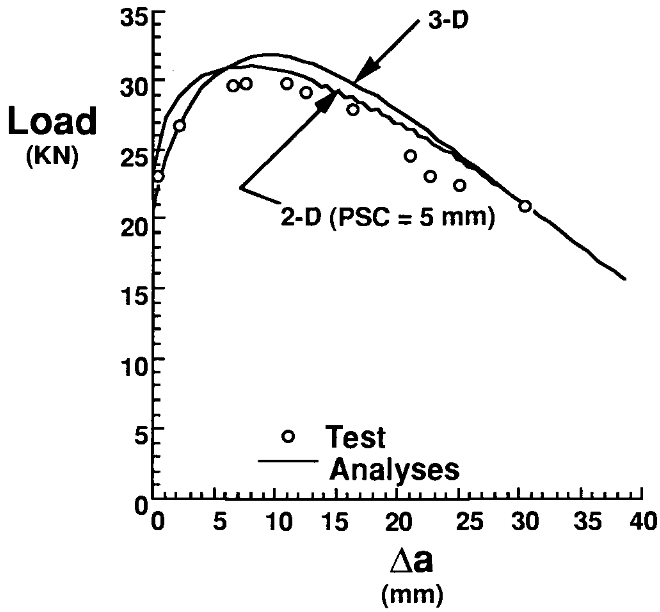

FIG. 10--Fracture test results and finite element simulations for the 152.4 mm wide C(T) specimen.

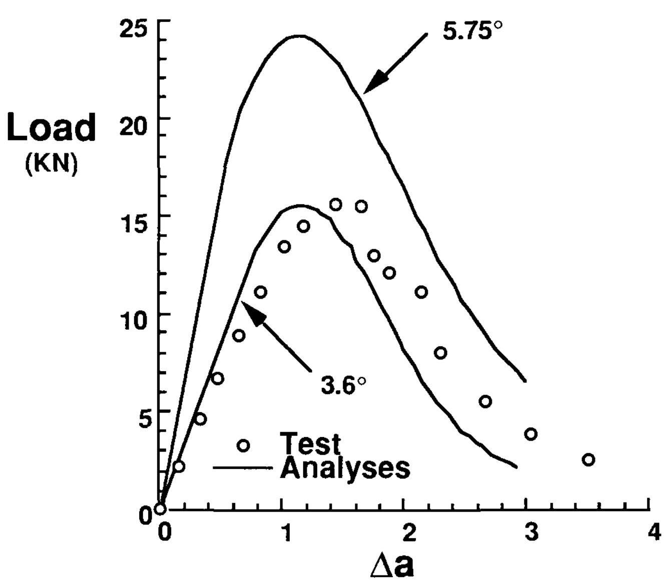

FIG. 11--Three-dimensional finite element simulations and fracture test results for the 101.6 mm wide C(T) specimen with side grooves.

measurements. For the 101.6 mm wide M(T), the three-dimensional finite element simulation was about 12% below the observed failure stress, however, this specimen failed to meet the CTOA thickness requirements (b/B > 4). The two-dimensional analyses with a plane strain core height of PSC = 4 mm was within 5% of the three-dimensional analyses in all cases.

The 101.6 mm wide C(T) specimen with side grooves was simulated with a three-dimensional finite analysis that modeled the side groove region with a single layer of elements. The remainder of the thickness was modeled with two layers of elements. Using a critical CTOA value of 5.75° resulted in a failure load that was about 60% greater than that observed in the experiment, as shown in Fig. 11. The angle required to simulate the fracture behavior was 3.6°. This angle was about the upper range of the scatter band of the microtopography measurements made through-the-thickness of the specimen.

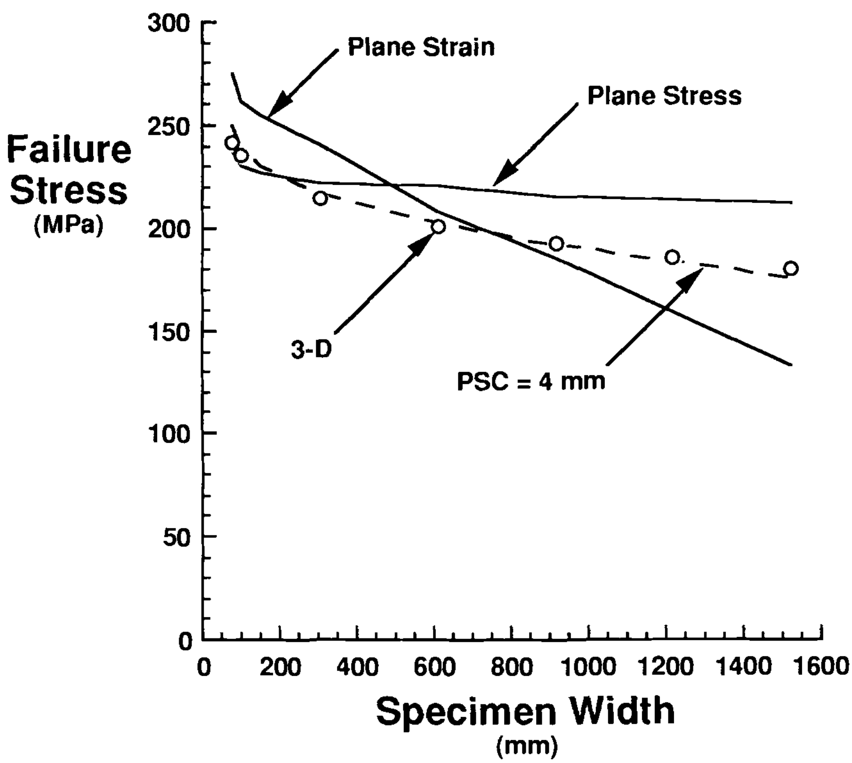

FIG. 12--Two-dimensional finite element simulations (critical CTOA = 5.75°) for M(T) specimens with a crack length to width ratio of a/W = 1/3.

Finite Element Predictions

The two- and three-dimensional finite element analyses (critical CTOA = 5.75°) were used to predict the behavior of larger M(T) specimens. Simulations were performed using full three-dimensional, plane strain, plane stress, and plane strain core (PSC = 4 mm) conditions for M(T) specimens with crack length to width ratios of 2a/W = 1/3. The thickness used in the simulations was 7.6 mm.

The two-dimensional plane stress simulation displayed only a slight influence of specimen width on the stress at failure, as shown in Fig. 12. However, the failure stress obtained from the two-dimensional plane strain simulation decreased sharply with increasing specimen width. For specimen widths less than 250 mm, the plane strain simulations produced higher failure stresses than the plane stress simulations. For larger specimens, the plane stress simulations produced higher failure stresses, with a 40% difference between the plane strain and plane stress failure stresses at a specimen width of 1500 mm. The failure stresses obtained from the three-dimensional analyses and the two-dimensional plane strain core analyses were nearly identical and generally between the plane stress and plane strain results, except near the crossover point where both analyses fell below the plane strain and plane stress results.

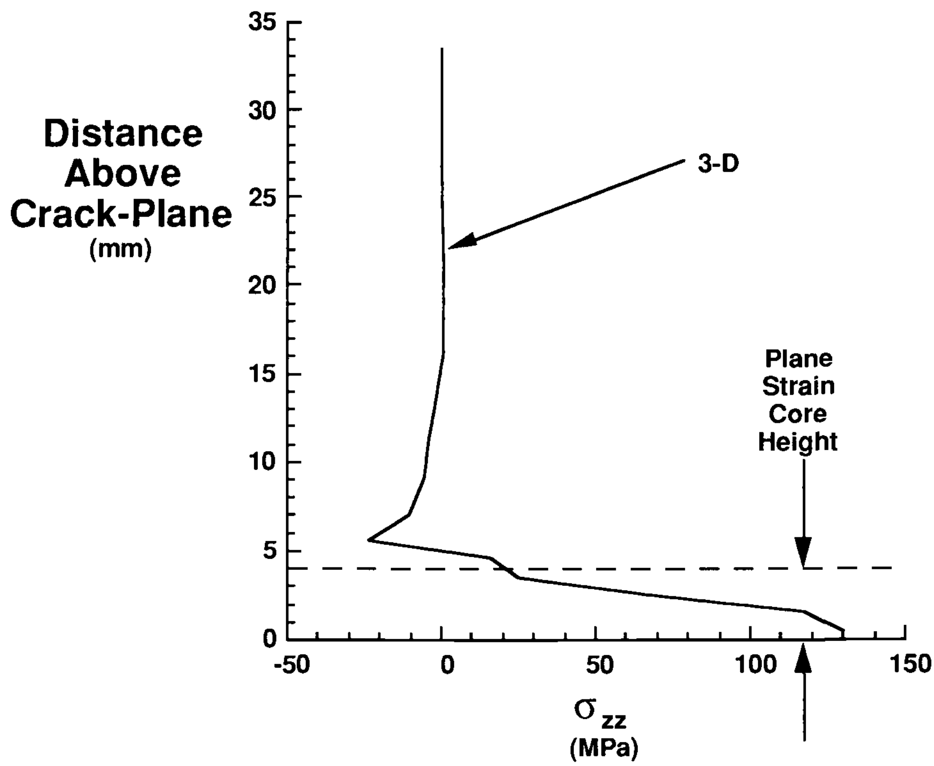

FIG. 13--The σ_{zz} stresses along a line perpendicular to the crack-plane and 1 mm ahead of the crack front for a 304.8 mm M(T) specimen after 10 mm of stable tearing.

The plane strain core approximation assumes that the material in the region of the crack is under plane strain conditions. A three-dimensional elastic-plastic finite element analysis was conducted to investigate this assumption. A simulation was performed on a 304.8 mm wide M(T) specimen with an initial crack length of 50.8 mm. The crack was extended using the CTOA criteria for 10 mm and the centerline σ_{zz} stresses were determined along a line perpendicular to the crack plane and 1 mm ahead of the crack tip. Figure 13 contains a plot of the σ_{zz} stresses against the distance above the crack plane. Away from the crack plane the σ_{zz} stresses were small (plane stress), but around 4 - 5 mm above the crack plane, the σ_{zz} stresses increased sharply (plane strain). This distance is close to the plane strain core height used in the two-dimensional simulations.

The failure stress of large structures (W > 1000 mm) will probably fall somewhere between the plane stress and plane strain results. If a plane stress analysis is used to find a CTOA that matches the experimental measurements of small laboratory specimens (W < 200 mm), the predicted failure stress will likely greatly overpredict the failure of the larger structure. If a plane strain analysis is used, the predicted failure stress will greatly underestimate the failure stress of the larger structure. A three-dimensional analysis would be able to account for the constraint variation that drives the size effects, but would be too computer intensive to run for the larger structures. The two-dimensional analysis with the plane strain core provides an approximation of the three-dimensional constraint effects, and retains the computational efficiency required to analyze the larger structures.

CONCLUDING REMARKS

The behavior of a 7.6 mm thick 2000 series aluminum plate alloy was investigated. Fracture tests were conducted on 101.6 mm and 304.8 mm wide M(T) specimens and 101.6 mm and 152.4 C(T) specimens. The 101.6 mm wide C(T) specimen had 10% side grooves. The critical CTOA criteria was used in elastic-plastic finite element simulations. Two-dimensional and three-dimensional, elastic-plastic finite element simulations were conducted to simulate the fracture behavior. A plane strain core was used in the two-dimensional analyses to simulate the three-dimensional constraint. The results from this study indicate:

A. The three-dimensional finite element analyses required a critical CTOA of 5.75° to simulate the fracture behavior of the 101.6 mm and 304.8 mm wide M(T) specimens and the 152.4 C(T) specimen. This angle was about the upper limit of the surface CTOA measurements.

B. The three-dimensional finite element analyses required a critical CTOA of 3.6° to simulate the fracture behavior of the 101.6 mm C(T) specimen with side grooves. This angle was about the upper limit of the microtopography through-thickness CTOA measurements.

C. A plane strain core height of PSC = 4 mm was required for the two-dimensional analyses to match the fracture behavior obtained from the three-dimensional analyses. This height agreed with the distance that a three-dimensional analysis indicated was the start of plane strain like behavior.

D. For large M(T) specimens (W > 1000 mm) the two-dimensional plane strain core analysis predicted a failure stress between the plane stress and plane strain conditions and provided a good approximation of the three-dimensional analyses.

E. The experimental measurements and analytical results show good agreement when the specimens sizes meet the uncracked ligament to thickness ratio (b/B > 4) determined by Newman et. al [14]. This indicates that there is a minimum size "laboratory specimen" that can be used to determine the material behavior needed to predict fracture in large specimens and structures.

REFERENCES

1 Harris, C. E., "NASA Aircraft Structural Integrity Program," NASA TM-102637, April 1990.

2 Orowan, E., "Fracture and Strength of Solids," Report of Progress in Physics, Physical Society of London, Vol. 12, pp. 185-233, 1949.

3 Broberg, K.B., "On stable crack growth," Journal of the Mechanics and Physics of Solids, Vol. 23, 1975, pp. 215-237.

4 Rice, J.R., "A Path Independent Integral and the Approximate Analysis of Strain Concentration by Notches and Cracks," ASME Journal of Applied Mechanics, Vol. 35, 1968, pp. 379-368.

5 Kanninen, M.F., "The Analysis of Stable Crack Growth in Type 304 Stainless Steel," in Proceedings of the International Conference of Fracture, pp. 1759-1768 (1980).

6 Wells, A.A., "Unstable Crack Propagation in Metals: Cleavage and Fast Fracture," in Proceedings of the Cranfield Crack Propagation Symposium, Vol. 1, 1961, pp. 210-230.

7 Wells, A.A., "Application of Fracture Mechanics at and Beyond General Yielding," British Welding Journal, Vol. 11, 1961, pp. 563-570.

8 Wells, A.A., "Notched Bar Tests, Fracture Mechanics and Brittle Strengths of Welded Structures," British Welding Journal, Vol. 12, 1963, pp. 2-13.

9 Anderson, H., "Finite Element Representation of Stable Crack Growth," Journal of Mechanics and Physics of Solids, Vol. 21, 1973, pp. 337-356.

10 de Koning, A.U., "A Contribution to the Analysis of Quasi Static Crack Growth in Steel Materials," in Fracture 1977, Proceedings of the 4th International Conference on Fracture, Vol. 3, pp. 25-31.

11 Dawicke, D. S., Newman, J. C., Jr., Sutton, M. A., and Amstutz, B. E., "Influence of Crack History on the Stable Tearing Behavior of a Thin-Sheet Material with Multiple Cracks," NASA Conference Publication 3274, pp. 193-212, September 1994.

12 Newman, J. C., Jr. and Dawicke, D. S., "Fracture Analysis of Stiffened Panels Under Biaxial Loading with Widespread Cracking," AGARD-CP-568, pp. 3-1 - 3-16, December 1995.

13 Dawicke, D. S., Piascik, R. S., and Newman, J. C., Jr., "Prediction of Stable Tearing and Fracture of a 2000-Series Aluminum Alloy Plate Using a CTOA Criterion," Fracture Mechanics: 27 Volume , ASTM STP 1298, to be published 1996.

14 Newman, J. C., Jr., Crews, J. H., Jr., Bigelow, C. A., and Dawicke, D. S., "Variations of a Global Constraint Factor in Cracked Bodies Under Tension and Bending Loads," NASA TM-109119, May 1994.

15 Dawicke, D. S. and Sutton, M. A., "Crack-Tip Opening Angle Measurements and Crack Tunneling Under Stable Tearing in a Thin Sheet 2024-T3 Aluminum Alloy, NASA-CR 191523, September 1993.

16 Kobayashi, T., Irwin, G. R., and Zhang, X., J., "Topographic Examination of Fracture Surfaces in Fibrous-Cleavage Transition Behavior," ASTM STP 827, 1989, pp. 234-251.

17 Lloyd, W. R. and Piascik, R. S., "Three-Dimensional Crack Growth Assessment by Microtopography Examination," Fracture Mechanics: 26th Volume, ASTM STP 1256, W. G. Reuter, J. H. Underwood, and J. C. Newman, Jr., Eds., American Society for Testing and Materials, Philadelphia, 1995.

18 Newman, J. C., Jr., "Finite-Element Analyses of Fatigue Crack Propagation--Including the Effects of Crack Closure," Ph.D. Thesis, VPI & State University, Blacksburg, VA, May 1974.

19 Shivakumar, K. N., and Newman, J. C., Jr., "ZIP3D - An Elastic and Elastic-Plastic Finite-Element Analysis Program for Cracked Bodies," NASA TM-102753, 1990.

20 Hom, C.L. and McMeeking, R.M., "Large Crack Tip Opening in Thin, Elastic-Plastic Sheets," International Journal of Fracture, Vol. 45, pp. 103-122, 1980.

21 Sutton, M. A., Dawicke, D. S., and Newman, J. C., Jr., "Orientation Effects on the Measurement and Analysis of Critical CTOA in an Aluminum Alloy Sheet," Fracture Mechanics: 26th Volume, ASTM STP 1256,W. G. Reuter, J. H. Underwood, and J. C. Newman, Jr., Eds., American Society for Testing and Materials, Philadelphia, 1995.

Fatigue Technology

Ronald W. Landgraf[1]

FATIGUE TECHNOLOGY IN GROUND VEHICLE DESIGN

REFERENCE: Landgraf, R. W., "**Fatigue Technology in Ground Vehicle Design,**" Fatigue and Fracture Mechanics: 28th Volume, ASTM STP 1321, J. H. Underwood, B. D. Macdonald, and M. R. Mitchell, Eds., American Society for Testing and Materials, 1997.

ABSTRACT: With the continuing trends toward structural weight reduction, performance optimization, and the application of improved materials, fatigue analysis has become an essential and integral part of the ground vehicle design process. The roots of contemporary life prediction methods, dating back over 100 years, are first identified followed by a review of their development and implementation in automotive design. Examples of the application of fatigue technology in product development and evaluation are presented to demonstrate current capabilities. The complexities of real engineering structures and service environments are emphasized along with probabilistic approaches for dealing with variability and uncertainty.

KEYWORDS: fatigue, durability, reliability, design methods, automotive structures, sensitivity analysis, probabilistic design

Over the last three decades substantial progress has been made in improving and refining fatigue life prediction procedures, in developing design methods based on these procedures, and, finally, in integrating these methods into the product development process. Noting that fatigue is a mature field with roots going back well over one hundred years, it is perhaps surprising that is has taken so long to tap effectively this potentially beneficial body of knowledge. Much of the recent success can be attributed to parallel developments in experimental and computational tools. Thus, modern closed-loop, servo-hydraulic test systems have allowed for the detailed documentation of cyclic deformation responses, the systematic generation of relevant cyclic material properties, and the laboratory simulation of material and structural responses to irregular loading sequences. Similarly, computer technology has provided powerful tools for structural analysis, damage analysis, test system programming and control, data acquisition, and information manipulation and visualization.

[1] Professor, Engineering Science and Mechanics, Virginia Tech, Blacksburg, VA 24061

These developments come at an opportune time for the ground vehicle industry which continues to experience intense global pressure to develop more efficient and durable products at reduced cost and in an accelerated time frame. The challenge today is to package and effectively integrate contemporary fatigue technology into the robust design and development methods used increasingly by the industrial sector.

It is the plan of this paper to briefly trace the development of modern life prediction methods, to review their implementation in automotive design, and to demonstrate, through case studies, their application in product development and evaluation. The complexities of real engineering structures and service environments are emphasized along with probabilistic approaches for dealing with variability and uncertainty.

DEVELOPMENTS IN FATIGUE TECHNOLOGY

Early Studies

While the pioneering work of Wöhler [1] receives considerable attention, equally significant are the efforts of Bauschinger [2] who performed meticulous studies of cyclic deformation responses in metals in an effort to identify a material's "natural elastic limit" that, in his view, would correlate with Wöhler's "endurance limit." Because it was not the practice at that time to display results graphically, the value of this work has not been fully appreciated. The plot of some of Bauschinger's data is shown in Fig. 1 provides evidence of his testing capabilities and his knowledge of cyclic plasticity.

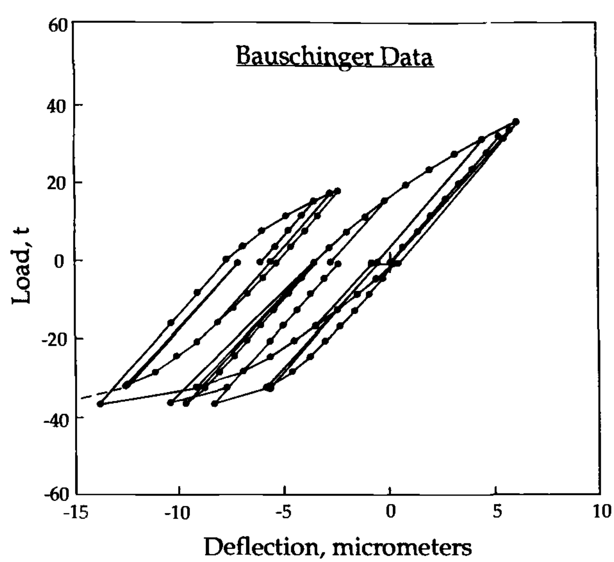

Fig. 1--Example of Bauschinger's cyclic deformation studies (adapted from [2]).

Subsequent deformation studies by Bairstow [3] and Smith and Wedgwood [4] provided further documentation of real cyclic material behavior and helped motivate Jenkin [5] to develop what is likely the first spring-slider model for simulating material cyclic stress-strain response. Rheological models of this type are now used in computer simulations of material response. Thus, by the early 1920's, the essential behavioral patterns providing the basis for what has come to be called the "local stress-strain approach" to fatigue were well in-hand.

Recent Progress

A resurgence of interest in cyclic deformation aspects of fatigue damage accumulation occurred in the early 1950's through the low-cycle fatigue studies of Coffin [6] and Manson [7]. Efforts in the 1960's and early 70's led to important developments in notch analysis [8], material characterization schemes [9], cycle counting [10], and computer simulation [11]. The 70's also saw the development of engineering design methods that were applied, in increasingly effective ways, to product development and evaluation in the 80's. Finally in the 90's, fatigue technology has become an integral part of the engineering design process.

Key features of the local stress-strain approach to damage analysis, as implemented in contemporary automotive fatigue analysis methods, are shown in Fig. 2. Here the material response at a critical location to the applied loading is developed using simulation models of the type presented by Jenkin. From this response, individual events are identified based on the concept of closed hysteresis loops—the underlying principle of rainflow cycle counting [10]—and damage assessed.

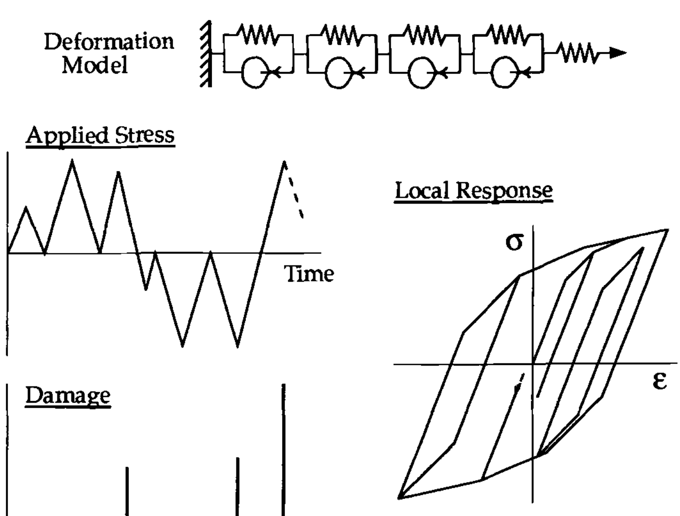

Fig. 2--Example of local stress-strain simulation and damage analysis.

The stress-strain and fatigue-life relations used in these analyses are listed in Table 1 and are seen to involve a set of standard cyclic material properties [9]—E, K', n', σ_f', b, ε_f', c—relating strain amplitude, ε_a, stress amplitude, σ_a, and fatigue life, $2N_f$.

TABLE 1--Cyclic stress-strain and fatigue relations

Cyclic stress-strain curve	$\varepsilon_a = \frac{\sigma_a}{E} + \left(\frac{\sigma_a}{K'}\right)^{\frac{1}{n'}}$
Strain-life curve	$\varepsilon_a = \frac{\sigma_f'}{E}(2N_f)^b + \varepsilon_f'(2N_f)^c$
Mean stress (Morrow)	$\varepsilon_a = \frac{(\sigma_f' - \sigma_m)}{E}(2N_f)^b + \varepsilon_f'(2N_f)^c$
Mean stress (Smith/Watson/Topper)	$\sigma_{max}\,\varepsilon_a\,E = \sigma_f'^2(2N_f)^{2b} + \sigma_f'\,\varepsilon_f'\,E\,(2N_f)^{b+c}$

The crucial role played by professional societies in the development of contemporary fatigue technology is particularly noteworthy. Through the efforts of dedicated members, ASTM Committees E-9 on Fatigue and E-24 on Fracture, along with the SAE Fatigue Design and Evaluation Committee, have made important contributions in developing standard practices, in conducting experimental verification programs, and in publishing research findings and design guidelines for practicing engineers.

FATIGUE METHODS FOR GROUND VEHICLE STRUCTURES

Nature of the Problem

Ground vehicle designers face unique challenges in the context of durability assurance. Complicating issues include:

- automobiles are produced in large volumes with emphasis on manufacturing feasibility and cost,
- structures are generally non-redundant with relatively thin sections,
- vehicles experience wide variations in service usage, and
- vehicles are not subject to regular structural inspections.

These circumstances have fostered a design philosophy that concentrates on crack initiation and early growth coupled with extensive testing of hardware in the laboratory or on captive durability routes. Because of the high production volumes and uncertainties in usage, there is also considerable interest in design methods that can account for the effects of variations in design, loading, and material parameters on the fatigue performance of a population of vehicles. Such considerations are especially relevant to the establishment of performance targets and to warranty issues, and have taken on increased significance with the trend toward global manufacturing and marketing.

Durability Design Procedures

Historically, the automotive industry has relied heavily on field testing of prototype and production vehicles to assure adequate structural integrity. This rather costly and time-consuming process is being rapidly supplanted by a host of newer experimental and analytical tools and procedures. As shown in Fig. 3, the process of life estimation entails a determination of systems loads, an analysis of component stresses and strains, followed by cumulative damage analyses. To the left of the figure is presented an experimental approach involving full-scale laboratory simulation testing of instrumented vehicles, the determination of component strains by means of strain gages, followed by the testing of material specimens under measured strain histories to determine crack initiation lives. While providing valuable design assistance, these techniques have also been remarkably effective in validating and refining life prediction methods.

More recently, emphasis has been productively directed to analytical approaches, based on computer modeling and simulation, as shown to the right of Fig. 3. Here, vehicle dynamics models are employed to develop loading information, finite element models provide critical component stresses, and fatigue damage is assessed through

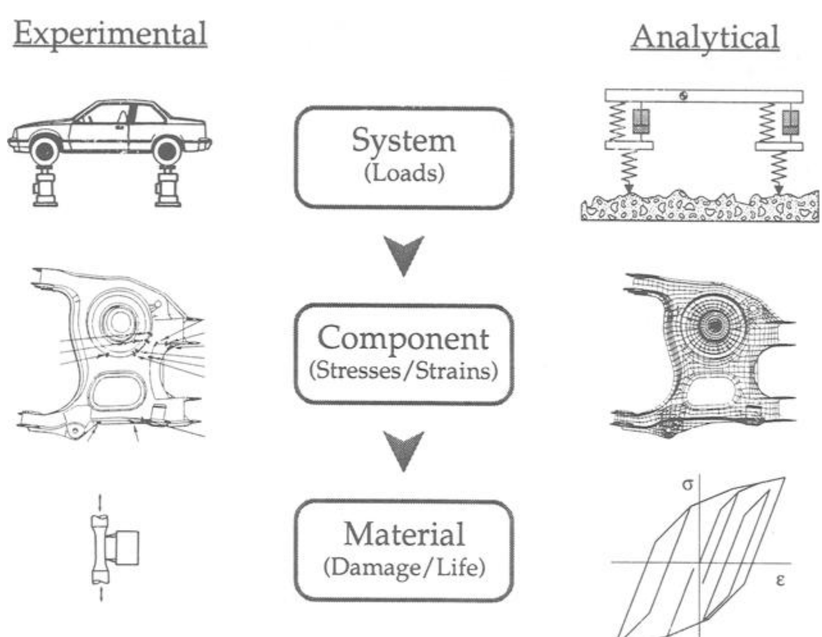

Fig. 3--Experimental and analytical approaches to durability assurance.

cyclic plasticity modeling of local material response (Fig. 2). In addition to obtaining life estimates, the relative damage associated with specific events can be quickly determined to assist in problem solving or in the development of realistic laboratory simulation tests.

With such procedures in place, it is possible to consider, quickly and systematically, a greater array of design options and possibilities and, thus, to more effectively anticipate durability problems in the course of achieving more optimized structures. The sensitivity of fatigue life to variations in design, material, and loading parameters is an area of considerable current interest with a view to establishing probabilistic design methods that provide estimates of failure probability for specified design scenarios.

Fatigue Technology In Product Development

As a result of the ready availability of durability related technologies, fatigue issues can now be addressed throughout the product development process. Table 2 provides a summary of fatigue analysis activities at various phases of the development process. In progressing from the concept stage through prototype development, product validation, and product improvement, the methods employed are seen to move from the analytical, computer simulation world toward the experimentally based data acquisition and testing world.

TABLE 2--Fatigue analysis in product development

Phase	Loading	Stresses	Applications
Concept (preprototype)	Vehicle dynamics model	Finite element model	Design iterations Sensitivity analysis
Prototype development	Instrumented vehicle	Instrumented components	Design refinement Mat'l./proc. selection
Product validation	Test routes Lab simulation	Instrumentation FEA	Design targets Customer correlation
Product improvement	Historical database	Computer simulation	Optimization (geom., mat'l., proc.)

Perhaps the most significant trend in durability design is the employment of fatigue analysis early in the development process. It is here that the greatest benefits can be realized through the rapid and systematic consideration of a range of design alternatives prior to prototype development. The combination of finite element modeling and fatigue analysis provides a particularly powerful development tool. The flow chart in Fig. 4 serves to illustrate such a procedure in which finite element modeling provides unit load stresses, that is, the contribution of individual load inputs to the stress state of each element. Using this information, the fatigue analysis program then combines, by elastic superposition, the various load channels to obtain resultant stress components that, after transformation to an equivalent axial stress, are processed through a damage assessment model to obtain a life estimate [12].

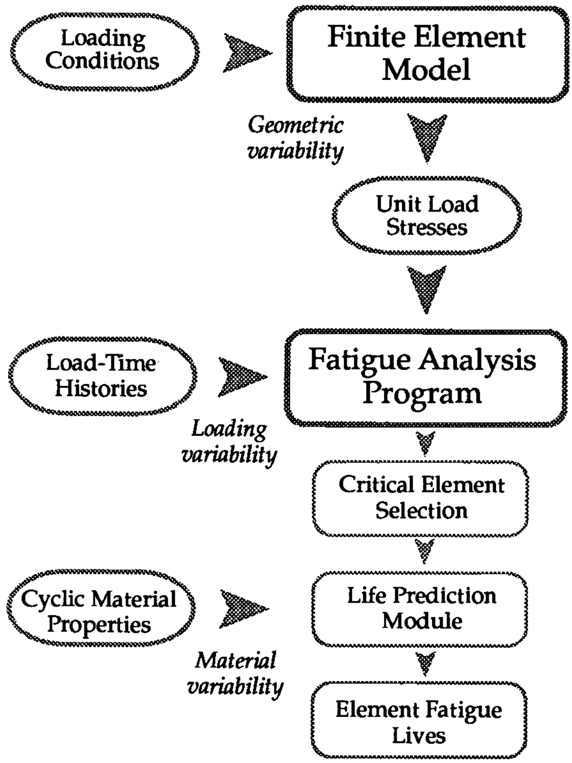

Fig. 4--Flow chart of fatigue durability procedure.

Also indicated in Fig. 4 are the points in the analysis procedure when variations in design parameters can be accounted for. Geometric variations are conveniently handled through the finite element model; certain commercial codes can provide sensitivity derivatives, the rate of change of stress with change in component geometry, for such purposes. Loading variations can be assessed by scaling the input load channels or by appropriate statistical procedures. Material variations are accounted for through statistical analysis of fatigue data sets that provide standard deviations for the cyclic properties. Such information, when integrated with reliability methods, provides valuable inputs regarding expected variations in structural durability in expected service situations [13]. Examples of these applications are presented in the next section.

EXAMPLE APPLICATIONS

This section will highlight some representative case studies of fatigue analysis in component development and validation with emphasis on methods for dealing with the complexities associated with real structures operating in actual service environments.

Multiaxial Loading Analysis

Automotive structures are typically subjected to multiple, time-varying load histories. Fatigue analysis under such circumstances requires that the combined effect of all load-time channels on potential failure locations be properly assessed. Using the procedure outlined in Fig. 4, analysis results for a suspension control arm are shown in Fig. 5. Six of the 13 load channels are shown along with the local stress component histories obtained using the unit load calibrations from finite element analysis.

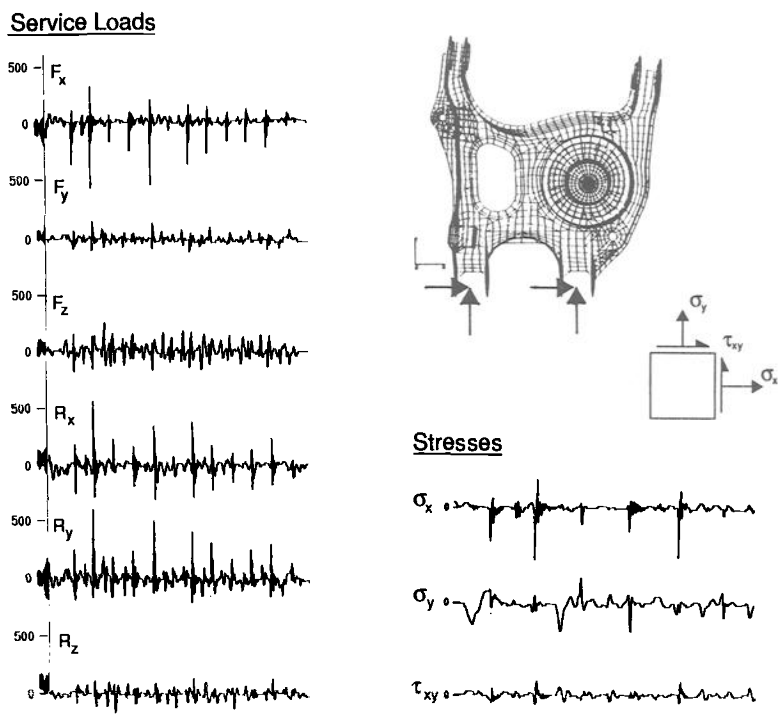

Fig. 5--Suspension arm load-time histories and resulting local stress-time histories.

The local stress components must next be transformed into an equivalent stress parameter for inclusion in life prediction procedures. A number of multiaxial cumulative damage models have been developed to handle such situations[14], however, none has yet achieved wide acceptance. Many of the available approaches involve identifying the orientation of a critical plane that experiences the maximum cyclic shear stress. A computational aid for such determinations is shown schematically in Fig. 6 [15]. On the left are displayed time histories for stress components referenced to a local x-y coordinate system. As a cursor is moved along the time axis, the instantaneous stress components, either on the principal stress plane or a user defined plane, are displayed along with a dynamic Mohr's circle portrayal of the stress state. This provides a convenient tool for evaluating and refining candidate damage models. Research efforts continue in this area.

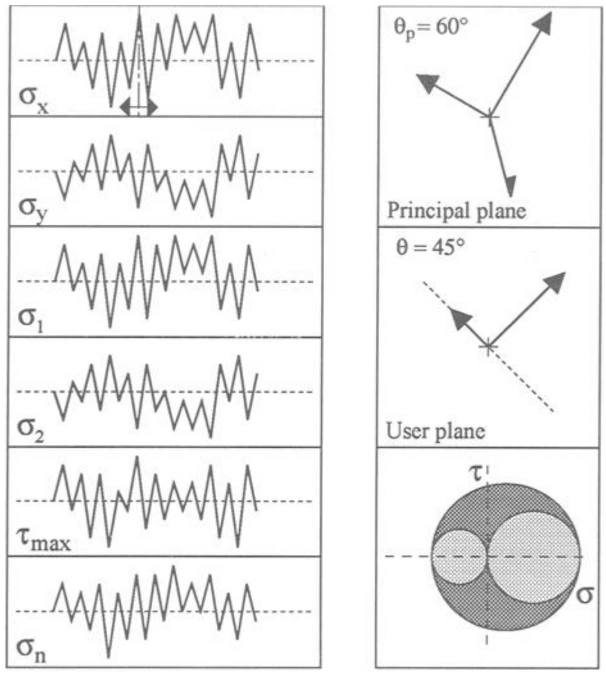

Fig. 6--Interactive graphics screen for multiaxial stress analysis.

Component Processing Optimization

Selective surface processing is a commonly used method for enhancing the performance of bending and torsional members. For induction hardened components, it is important to determine the optimum case depth to maximize fatigue resistance. This will be a function of component geometry, loading histories, and material properties, as influenced by the near-surface residual stresses, and is amenable to detailed fatigue analysis using the methods described. The performance concept entails achievement of an equal likelihood of failure in the case and core.

In Fig. 7 are shown estimated performance curves for an induction hardened transmission shaft subjected to a torsional loading history. Fatigue life (in blocks of the history to failure) is plotted as a function of history scaling factor. Surface fatigue response is shown along with subsurface failure curves for three case depths. Here it can be seen, for example, that for the history as recorded (magnification factor = 1), a fractional case depth of 0.3 results in optimum resistance—failure is equally likely at the surface and subsurface. Such portrayals allow for rapid determination of optimum conditions for any loading profile and also provide estimates of the effects of varying case depths relating to process control strategies.

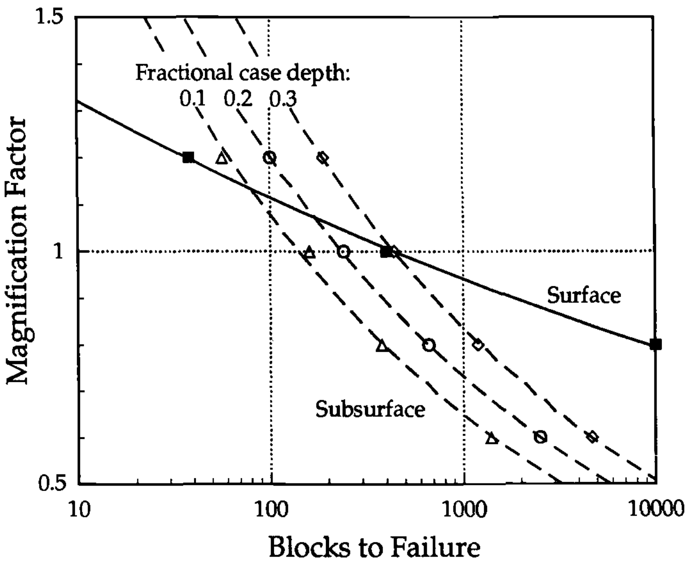

Fig. 7--Optimization scheme for induction hardened shaft.

Fatigue Sensitivity Analysis

Early in the development cycle, when design iterations can be more easily accomplished, it is useful to have available indications of the sensitivity of component fatigue performance to changes in design and material and processing variations. Because many performance targets must be met simultaneously, it is usually not possible to optimize for a single attribute, e.g., fatigue life.

Results of a fatigue sensitivity analysis of an automotive wheel assembly is shown in Fig. 8. In this example, a low-carbon steel wheel is evaluated under a mountainous test route giving a mean lifetime of 100,000 miles. At the bottom of the figure is shown the change in relative fatigue life to changes in material thickness and applied loading (bending moment). It can be seen that a 10% increase in thickness will increase life by two and one-half times while a 10% increase in bending moment will decrease life by a factor-of-two. Through use of a sensitivity index, S.I., changes in fatigue life due to variations in any design parameter can be determined by means of the following relation:

$$\text{Relative Life} = (\text{Relative Parameter})^{\text{S.I.}} \quad (1)$$

In general, the sensitivity of fatigue life, L, is a function of the variation of applied stress, S, with a particular design variable, V, and the variation in life with stress, or in differential form:

$$\frac{\partial L}{\partial V} = \frac{\partial S}{\partial V} \cdot \frac{\partial L}{\partial S} \quad (2)$$

The rate of change of stress with geometric parameters is conveniently determined by finite element analysis, while the rate of change of life with stress is provided by appropriate fatigue curves.

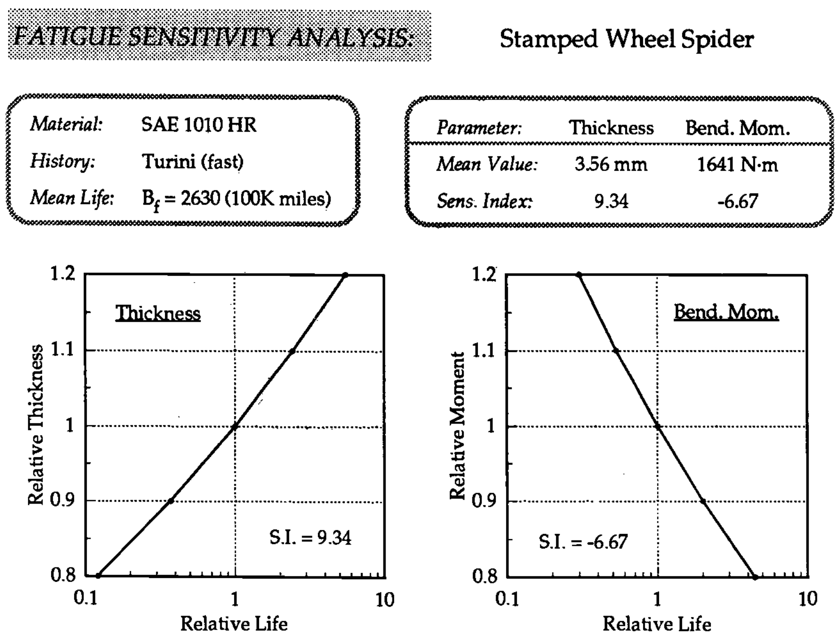

Fig. 8--Sensitivity analysis of wheel spider.

Failure Probabilities

Because of the exceptionally high production volumes and uncertainties in product use, automotive designers must be concerned with anticipating "worst case scenarios"—what is the likelihood of a minimum thickness component, made from a lower-bound material, getting into the hands of a particularly aggressive driver? In attacking such problems, an approach combining durability and reliability methods can be usefully employed.

The basic steps involved in such a procedure are outlined in Fig. 9. Here, the loading, geometric, and material parameters are treated as random variables with specified statistical distributions. The appropriate design data are accessed and separated into "stress" and "strength" elements. These, in turn, are combined into a performance function, $G(R,S)$, that is called repeatedly by the reliability analysis program in order to arrive at the design point by an iterative scheme [16]. Once iteration is complete, the probability of failure for the component, subject to the specified distribution functions, can be calculated.

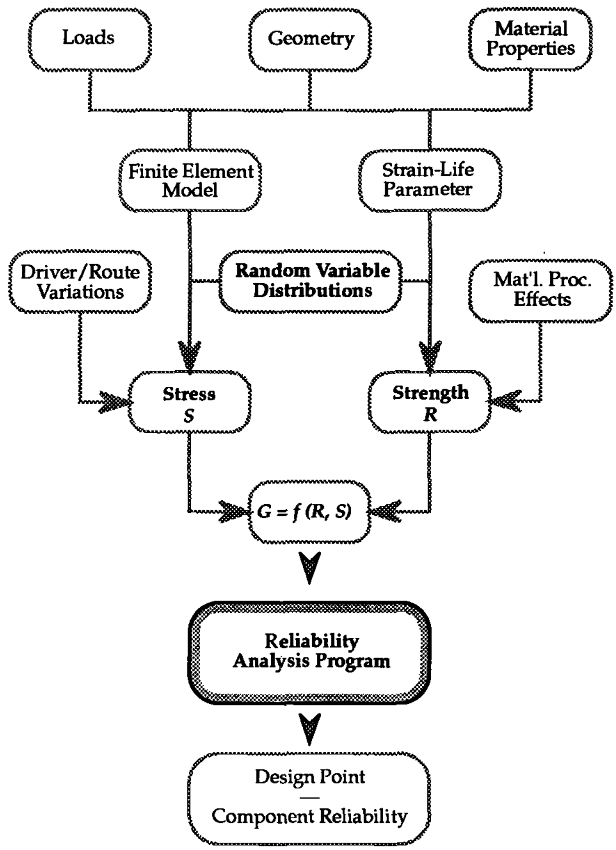

Fig. 9--Flow chart for combined durability/reliability analysis.

Again using the wheel assembly as an example, the results of a probabilistic analysis of component performance under anticipated service conditions are presented in Fig. 10. Curves of failure probability versus fatigue life are shown for three driver percentiles (3, 50, and 99), as well as a reference test driver. The analysis accounts for variations in material thickness and cyclic properties for the SAE 1010 steel. Driver severity data was generated by sampling the patterns of a cross section of drivers using an instrumented vehicle driven over a standard test route. Results indicate that at a lifetime of 100,000 miles, average drivers (50%) would be expected to experience a failure rate of slightly over 1 in 10,000, while the failure rate for the more aggressive 99% driver would be 2 in 1,000.

Portrayals of this type can be of considerable value in the product validation process in arriving at more optimum designs and in selecting and controlling material and processing parameters to assure a given safe level of performance.

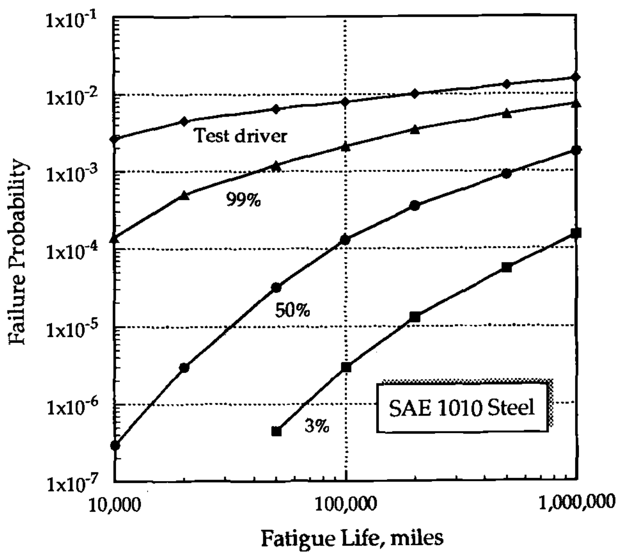

Fig. 10--Failure probability estimates for a wheel assembly.

CONCLUDING REMARKS

While significant progress has been made in developing and implementing durability design tools to help assure, with high confidence, the structural integrity of ground vehicle structures, opportunities remain for further improvements. Just as the integration of fatigue technology with finite element and reliability methods has greatly extended analysis capabilities, equally important advancements can be anticipated through the inclusion of additional simulation packages such as system dynamics models to develop more realistic vehicle loading profiles early in the design cycle.

In the longer term, it is conceivable that, with the availability of a highly integrated tool set, designers could quickly arrive at structural configurations and material choices to meet a specified level of system reliability—that is, an actual design tool would be created from analysis modules. Complete integration would also allow simultaneous consideration of all relevant design issues including, for example, fatigue, crashworthiness, and vibration.

The addition of more comprehensive prediction modules for dealing with surface processed components, welded structures, and components subjected to wear would provide valuable enhancements. Finally, improved methods for managing and displaying analysis results to increase accessibility and utility are needed. Here, ongoing developments in scientific visualization, using interactive computer graphics, hold great promise.

REFERENCES

[1] Wöhler, A., "Versuche zur Ermittelung der auf die Eisenbahnwagen-Achen einwirkenden Kräfte und der Widerstandsfähigkeit der Wagen-Achsen," Zeitschrift für Bauwesen, Vol. 10, 1860.

[2] Bauschinger, J., "Über die Veränderung der Elasticitätsgrenze und der Festikeit des Eisens und Stahls durch Strecken und Quetschen, durch Erwärmen und Abkühlen und durch oftmal Wiederholte Beanspruchung," Mitt. Mech.-Tech. Lab. Munich, Vol. 13, No. 8, 1886, pp. 1-115.

[3] Bairstow, L., "The Elastic Limits of Iron and Steel under Cyclical Variations of Stress," Phil. Trans., Royal Soc. (A), Vol. 210, 1909-10, pp. 35-55.

[4] Smith, J. H., and Wedgwood, G. A., "Stress-Strain Loops for Steel in the Cyclic State," Jrn., Iron & Steel Inst., Vol. 91, No. 1, 1915, pp. 365-397.

[5] Jenkin, C. F., "The Fatigue Failure of Metals," Proc., Royal Soc. (A), Vol. 103, 1923, pp. 121-138.

[6] Coffin, L. F., Jr., "A Study of Cyclic Thermal Stresses on a Ductile Metal' Trans., ASME, Vol. 76, 1954, pp. 931-950.

[7] Manson, S. S., "Behavior of Materials under Conditions of Thermal Stress," NASA TN 2933, National Aeronautical and Space Administration, Washington, D.C., 1953.

[8] Neuber, H., "Theory of Stress Concentration for Shear-Strained Prismatical Bodies with Arbitrary Nonlinear Stress-Strain Law," Trans., ASME, J. Appl. Mechs., Vol. 8, 1961, pp. 544-550.

[9] Morrow, J., "Cyclic Plastic Strain Energy and Fatigue of Metals," Internal Friction, Damping, and Cyclic Plasticity, ASTM STP 378, Amer. Society for Testing & Materials, Philadelphia, 1965, pp. 45-87.

[10] Matsuishi, M., and Endo, T., "Fatigue of Metals Subjected to Varying Stress," Japan Soc. of Mech. Engrs., 1968.

[11] Martin, J. F., Topper, T. H., and Sinclair, G. M., "Computer Based Simulation of Cyclic Stress-Strain Behavior with Applications to Fatigue," Mat'l. Research & Standards, Vol. 11, No. 2, 1970, pp. 23-29.

[12] Conle, F. A., and Mousseau, C. W., "Using Vehicle Dynamics Simulations and Finite Element Results to Generate Fatigue Life Contours for Chassis Components," Int'l. Jrn. of Fatigue, Vol. 13, No. 3, 1991, pp. 195-205.

[13] Thangjitham, S., and Landgraf, R. W., "Probability-Based Methods for Fatigue Analysis," Fatigue Research and Applications, SAE SP-1009, Society of Automotive Engineers, Warrendale, PA, 1993, pp. 81-85.

[14] Leese, G., and Socie, D. F., eds., Multiaxial Fatigue: Analysis and Experiments, AE-14, Society of Automotive Engineers, Warrendale, PA, 1989.

[15] Landgraf, R. W., and Conle, F. A., "Vehicle Durability Analysis," Concurrent Engineering of Mechanical Systems, DE-Vol. 22, American Society of Mechanical Engineers, New York, 1990, pp. 111-121.

[16] Ridder, R. L., Landgraf, R. W., and Thangjitham, S., "Reliability Analysis of an Automotive Wheel Assembly," Fatigue Research and Applications, SAE SP-1009, Society of Automotive Engineers, Warrendale, PA, 1993, pp. 225-235.

Gary Marquis[1], Tormod Dahle[2], Jussi Solin[1]

SERVICE LOAD FATIGUE TESTING OF RAILWAY BOGIE COMPONENTS

REFERENCE: Marquis, G., Dahle, T., and Solin J., "**Service Load Fatigue Testing of Railway Bogie Components**", Fatigue and Fracture Mechanics: 28th Volume, ASTM STP 1321, J. H. Underwood, B. D. Macdonald and M. R. Mitchell, Eds., American Society for Testing and Materials, 1997.

ABSTRACT: A series of fatigue tests on railway bogie (undercarriage) components has been completed in Finland and Sweden. Tests were designed to evaluate the high cycle fatigue behavior of welded constructions. The loading was based on in-service field measured data. A standard test procedure for evaluating the fatigue integrity of bogies is based on an assumption of infinite life and in-phase interaction between four load actuators. The relationship between the standardized loads and the actual field service loadings is examined. Results showed that design and testing procedures should be based on a long but finite life concept that recognizes the large amount of fatigue damage that can be contributed by small cycles in a spectrum that contains only a small portion of large cycles that exceed the constant amplitude fatigue limit.

KEYWORDS: spectrum fatigue, high cycle fatigue, bogie, fatigue testing, load spectra, railway components, welded structures

Designers employ a variety of fatigue prevention philosophies into the design of structures subject to dynamic loads. One possible choice is the *infinite life* concept which recognizes that for many materials there exists a stress threshold below which macroscopic fatigue damage is not observed. By ensuring that all alternating stresses are below this threshold, fatigue failure can be avoided regardless of how long a component is used. Another common approach is the *safe life* concept that allows a structure to have a finite service life. In this case design parameters are chosen so that failure is expected only after the useful life of the structure is exhausted. Both of these approaches have been used in the design and testing of railway bogies.

[1] Research Scientist, VTT Manufacturing Technology, PO Box 1704, FIN-02044 VTT, Finland

[2] Senior Research Engineer, ABB Corporate Research, Laboratory for Applied Mechanics, S-72183 Västerås, Sweden

If service loads are considered, the infinite life concept focuses attention on the loads that produce the maximum range of stress during operation. The goal is to design a structure in which the maximum stress range is below a threshold stress. The number of applications of the stress need not be considered since they will all be non-damaging. In theory stresses below the threshold could be applied an infinite number of times without failure. The safe life concept, however, requires that some information about the entire spectrum of loads be known. In the case of rail vehicles, the maximum loads are usually of lesser importance because they are rare events and do not contribute significantly to fatigue damage. The effect of larger loads is to alter the fatigue limit behavior thus causing normal operating load cycles, that are far below the fatigue limit, to become damaging. Attention is thus drawn away from the rare events to the stresses that occur during normal operation.

SERVICE LOADS

Measured in-service stresses will depend on several factors, vehicle speed, track condition, payload, vehicle suspension [1], etc. Figure 1 shows eight spectra of rainflow counted cycles (ASTM Practices for Cycle Counting in Fatigue Analysis E 1049-85) representing vertical loads on different types of bogies and along different routes. The horizontal exceedance axis in this figure is obtained by dividing the number of cycles with stress ranges larger than ΔS_i by the total number of cycles during a measurement period. From these exceedance diagrams, profiles related to usage and track condition are formed and serve as valuable input to the design process. Vehicles ranged from suburban to high speed trains and measurement times were from 30 minutes to several days.

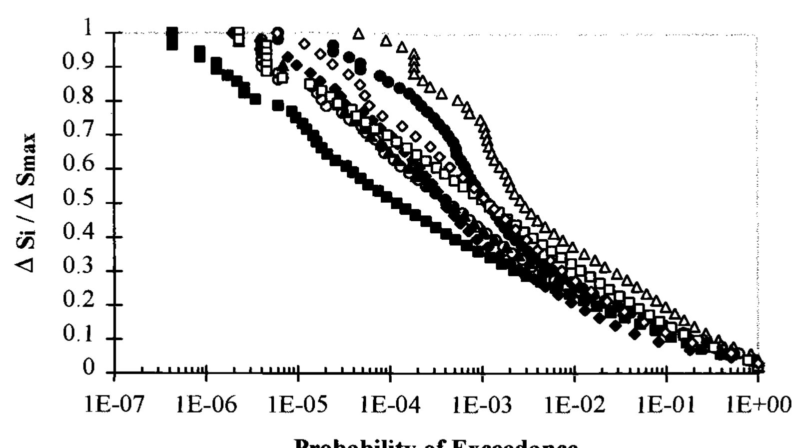

FIG. 1 -- Eight measured stress spectra representing vertical loads on different types of bogies and along different routes.

For longer term measurements it is often possible to describe the stress range spectra using a Weibull distribution

$$P\left(\frac{\Delta S}{\Delta S_{max}} \geq \frac{\Delta S_i}{\Delta S_{max}}\right) = \exp\left(-\left\{\frac{\Delta S_i}{\Delta S_{max}}\right\}^k \cdot \ln\{N_o\}\right), \tag{1}$$

where $\Delta S/\Delta S_{max}$ is the normalized magnitude of the cycle of interest, $\Delta S_i/\Delta S_{max}$ corresponds to the ordinate of Fig. 1, k is the shape parameter, and N_o is the number of cycles in the spectrum. Equation 1 can be extrapolated based on extreme value theory so that the peak stresses and the anticipated load spectrum during, for example, a one year period can be estimated. Peak stresses may be significantly larger than what was measured during a several day measurement period. This "truncation dilemma" has been addressed by Schütz [2].

To compare the severity of different spectra it is often convenient to represent a spectrum as a single number. This is can be done using the Palmgren-Miner linear damage rule and assuming a straight S-N line given by

$$C = N_f \cdot \Delta S^m, \tag{2}$$

where C is the fatigue capacity of a certain geometry of welded connection, N_f is cycles to failure under constant amplitude loading at a stress range ΔS. These two assumption yield an expression for *estimated specific life*

$$L = \frac{\Sigma n_i}{\Sigma\left(n_i \cdot \left\{\frac{\Delta S_i}{\Delta S_{max}}\right\}\right)^m}, \tag{3}$$

where n_i is the number of stress cycles of size ΔS_i.

Figure 2 shows measurements of transverse components of force for three different types of trains. Even though the relative frequency of the largest cycles are approximately the same for all spectra, the shape is quite different as is illustrated by the resulting estimated specific life. Assuming m = 3, the resulting values are L_{bogie1}= 332, L_{bogie2}=1023 and L_{bogie3}=495. This indicates that for a constant value of ΔS_{max}, a bogie loaded using spectrum 1 would have 30% the fatigue life of a bogie loaded using spectrum 2 and 60% the life of a bogie loaded using spectrum 3.

STANDARDIZED TEST

In 1993 the International Union of Railways, UIC, issued a code of practice concerning the fatigue testing of passenger train bogie frames [3]. In this code three modes of loading are considered: vertical forces due to the weight of the vehicle and passengers/cargo, transverse forces due to inertial effects as the vehicle encounters a curve in the track, and twisting forces such as would be experienced due to unevenness between the rails. Application location of these forces is shown in Fig. 3.

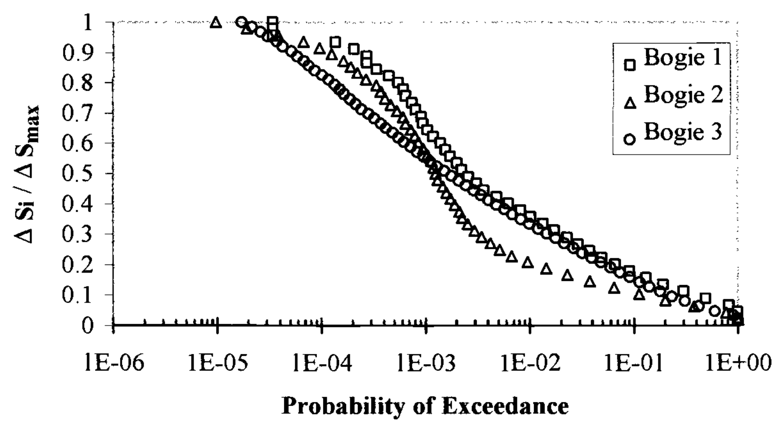

FIG. 2 -- Measured transverse load spectra for three bogies.

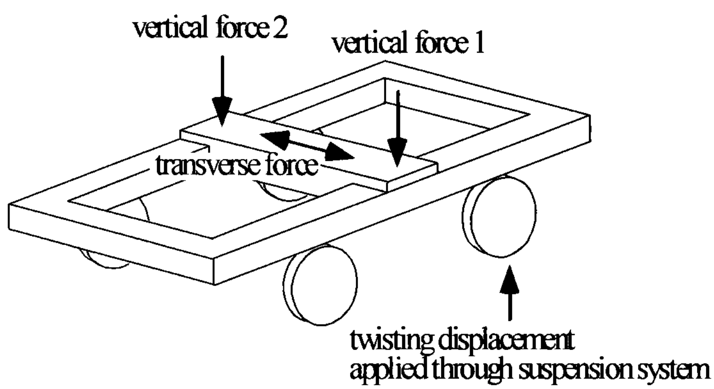

FIG. 3 -- Forces and displacements applied to bogie frame during fatigue testing according to UIC code of practice.

The vertical forces are divided in to static, quasi-static and dynamic components. Quasi-static loads are defined as fatigue loads having a period measured in tens of seconds such as might be induced when rounding a corner or during braking. Dynamic forces can be of much higher frequency and are associated with irregularities in the track or at turnouts. Vertical loads are applied by means of two actuators centered above each of the two longitudinal side beams. The static and dynamic load components applied by the two actuators are identical while the quasi-static load components are 180° out-of-phase. Transverse forces have only the quasi-static and dynamic components. Twisting loads are not applied in all cases but, when required, have only a low frequency dynamic component. The sequence and phase relationship between the four applied loads is shown in Fig. 4.

Prior to fatigue testing the static stress response at critical locations on the bogie is measured by applying 12 load combinations that represent the 12 extreme load cases occurring during one block of loading. These 12 load combinations are illustrated in Fig. 4. The mean stress and stress range at each location are compared to a Goodman diagram to evaluate if the bogie stresses are expected to result in infinite life [3,4].

Magnitudes of the vertical and transverse loads are computed based on the weights of the vehicle, bogie and expected payload. The magnitude of twist is given as 5°. Following an initial test of $6x10^6$ dynamic load cycles, quasi-static and dynamic load components are increased by 20% and an additional $2x10^6$ cycles are applied. The bogie must survive this portion of the test without noticeable fatigue cracking. Dynamic and quasi-static loads are then increased to 140% of the original value for a final $2x10^6$ dynamic cycles. Cracks are allowable at the completion of this test phase, but they cannot be so severe as would require immediate repair.

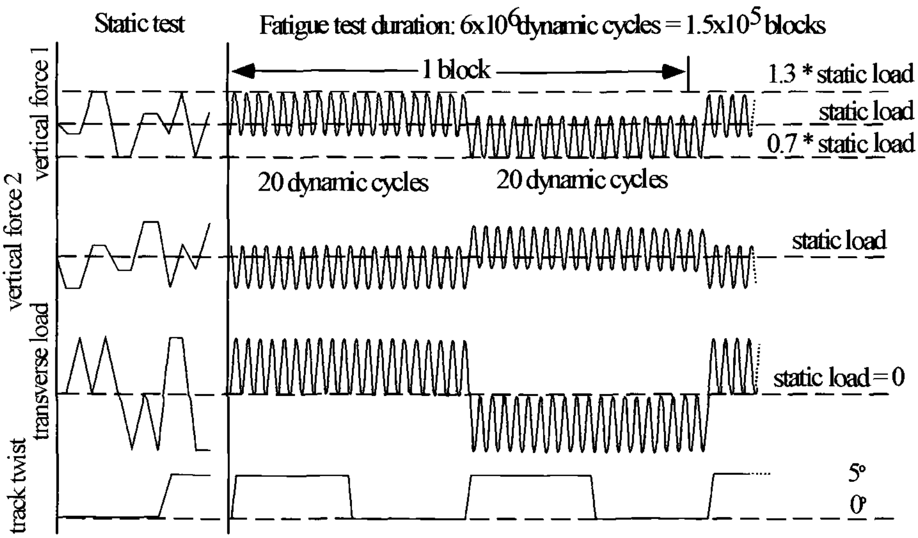

FIG. 4 -- Sequence and phase relationships between the four applied loads in the ORE standardized static and fatigue tests for passenger train bogies.

From the fatigue load history in Fig. 4, and if rainflow counted cycles rather that dynamic cycles are considered, it can be seen that the maximum stress range will be applied only once for every reversal of the quasi-static component of vertical and transverse load, i.e., once per block of 40 dynamic cycles. Therefore, even though the dynamic loads are applied a fairly large number of times, $6x10^6$, the maximum stress range will be applied only $1.5x10^5$ times during the initial fatigue test. For welded constructions, $1.5x10^5$ cycles is approximately a factor of ten to few to ensure infinite life. It is also clear that the stress exceedance diagrams resulting from the applied loads in Fig. 4 will not resemble any of the field measured histories shown in Fig. 1.

SPECTRUM LOAD TESTING

Full-scale bogie test

The existence of only one large cycle per block, as would be expected from the applied loads from the standardized fatigue test shown in Fig. 4, was observed during full-scale fatigue testing of a locomotive bogie at VTT Manufacturing Technology. At the start of testing, a standardized load spectrum was used to observe the resulting stress range exceedance history at critical locations on the bogie. The history showed no resemblance to the exceedance diagrams obtained during field strain measurements and after a few blocks of loading, the test was halted and loads based on the in-service measured strain histories were used. A schematic of the bogie and loading points during out-of-phase spectrum loading and a small sample of the applied loads are shown in Fig. 5. During fatigue testing, integrity of the applied loads was evaluated by means of several comparisons between laboratory and field measured stress histories:

- the overall shape of the exceedance diagrams
- calculated fatigue damage at 60 strain gage locations
- the distributions of fatigue damage between cycles of different sizes
- the values of calculated equivalent constant amplitude load

The test continued until nine million kilometers of operation had been simulated without failure thus satisfying the required design life of three million kilometers with the desired safety factor of 3. This represents a projected useful life of 30 years. Approximately 1.2×10^7 load cycles had been applied by each of the primary actuators [5].

Box beam components

Right angle beams -- Five large test specimens were manufactured at the Finnish State Railways (VR) Pasila workshop from Fe52 steel using the manual MAG process. Component size, geometry, and manufacturing method were similar to those found in rail-car bogies. The complex geometry is shown in Fig. 6. The large specimen size ensured that the magnitude of welding residual stresses and the weld quality would be similar to that found in actual bogies.

Longitudinal beams -- Twelve test beams were manufactured from a weldable micro-alloyed steel, SS 2134-01 according to the Swedish standard. The half scale by section and full thickness beams were manufactured at three local workshops. The beams were manually welded using ½ -V groove welds along the bottom flange and double fillet welds along the top flange. All beams were stress relieved at 580° C followed by slow cooling. Manufacturing processes were comparable to that used in bogies. Geometry of the test beams is shown in Fig. 7.

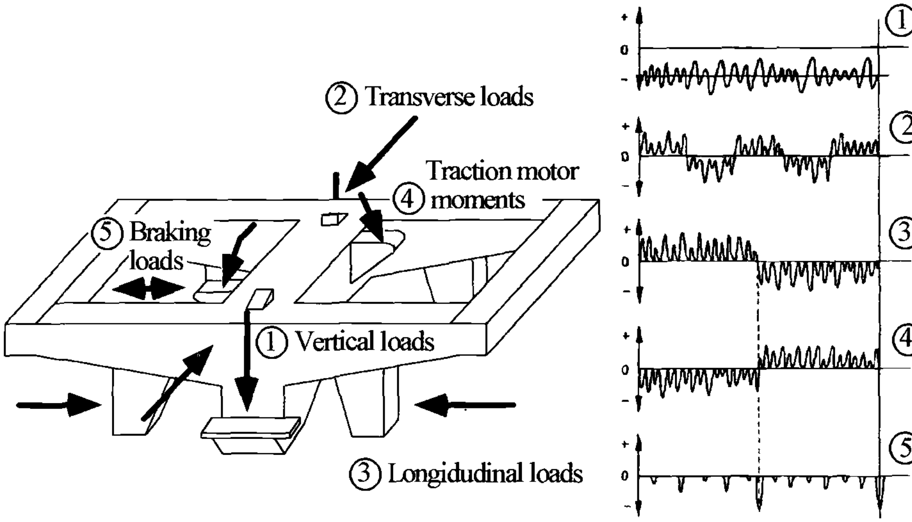

FIG. 5 -- External loads applied during the full-scale test of a locomotive bogie.

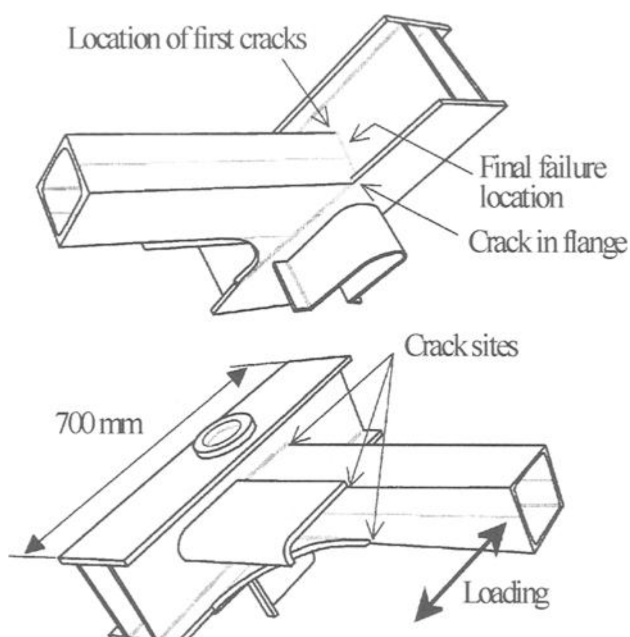

FIG. 6 -- Geometry of the right angle box beam components.

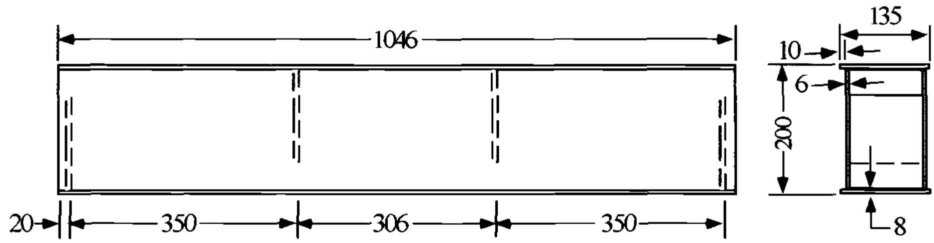

FIG. 7 -- Geometry of the longitudinal beams tested using four-point bending (dimensions mm).

Load Spectra -- The first load spectrum for the right angle component consisted of a total of 408,000 cycles with an irregularity factor of I=0.86. All cycles with ranges less than 10% of the maximum load range were omitted. Two other spectra were derived from the first spectrum by imposing omission levels of 16% and 31% for the small cycles. The peak-valley sequence that resulted in the largest rainflow counted load ranges remained the same for all three spectra. The mean load of the largest cycle was zero and smaller cycles had a varying mean stress. Constant amplitude loading was used for the first specimen. Based on the fatigue life and assuming that the fatigue limit would occur at a stress range corresponding to $5x10^6$ cycles, it was estimated that the 10% omission level represented the elimination of all cycles with stress ranges less than 50% of the fatigue limit. The 16% omission level is equivalent to the elimination of all cycles less than 80% of the constant amplitude fatigue limit [6].

Three of the longitudinal beams were tested using four-point bend constant amplitude loading, $\Delta S_{max} = 152$ MPa, R = 0.33. Spectrum loading was used for the remaining 9. Eight beams were tested using a load spectrum containing 268,200 cycles and one beam was tested using a shortened version of the spectrum obtained by eliminating all cycles with stress ranges less than 19% of the maximum stress range. Spectra were based on field measurements from a prototype railway bogie and the irregularity factor was approximately one [7].

Figure 8 shows the load range exceedance diagrams used in the two test series. As can be seen the spectra are nearly identical. The estimated specific lives were 380 and 530 respectively for the right angle and longitudinal beam components. Also shown in this figure are the load spectra used in two other test programs related to high cycle fatigue of welded components [8-10]. These were considered to be related to short span bridge spectra and are significantly different from the load histories based on rail vehicle measurements used here. The final stress range exceedance diagram is that produced by either of the two vertical actuators during the first 8 million dynamic cycles of the standardized test during which no fatigue damage is permitted. It should be noted, however, that during this sequence, the largest cycles are applied only during the final 25% of the test.

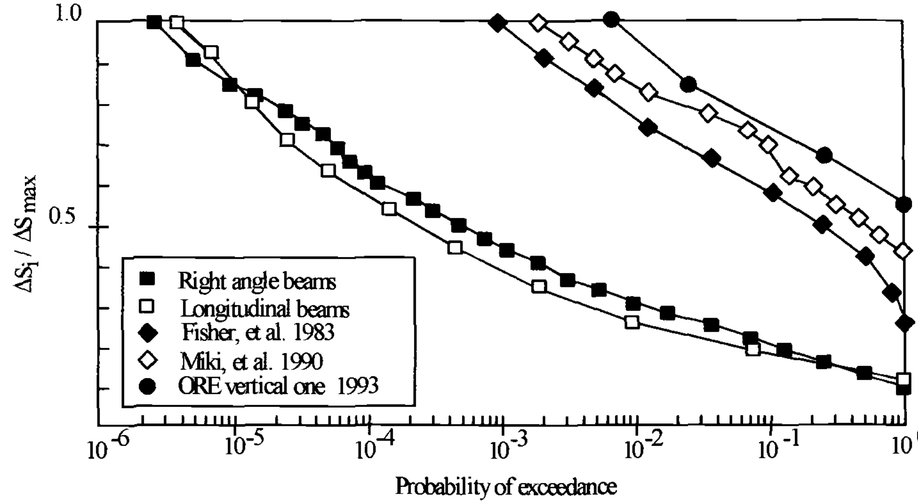

FIG. 8 -- Bogie load spectra for the two beam fatigue test series reported here, two spectra considered representative for highway bridges, and the spectrum produced by one vertical actuator in the standardized bogie test.

Fatigue test results -- Results from all box beam fatigue tests are shown in Fig. 9. In this figure the applied root mean cube stress range is plotted vs. component life. Stress in the right angle beams was measured 12 mm from the toe of the weld joining the two box members. Failure in the longitudinal beams was defined as a 10 mm deflection of the beam mid-section. For the right angle beams, failure was defined as the development of a 50 mm long surface crack. In all cases the failure crack initiated and propagated from the root of a partial penetration fillet weld that joined the two box members [6,7].

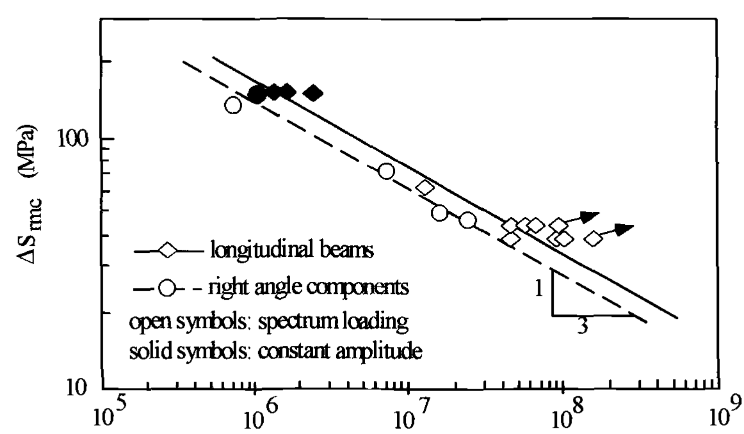

FIG. 9 -- Fatigue test results for the welded box beam components.

As seen from Fig. 9 there is no tendency toward a reduced slope S-N curve for fatigue lives as long as $3x10^7$ cycles for the right angle components and nearly 10^8 cycles for the longitudinal beams. This is in contrast to what is suggested by most design codes which specify that the damage contribution of cycles with ranges less that the fatigue limit be computed using a reduced damage slope line. It has been shown that cycles with stress ranges far below the fatigue limit contribute damage in welded structures as if the threshold stress did not exist and that the fatigue limit measured by constant amplitude loading is not a relevant parameter for spectrum loaded components [11-13].

DISCUSSION

Stresses in service and during testing

Long term field measurements of railway bogies often reveal a stress range exceedance diagram that can be adequately described using a Weibull type distribution. The Weibull distribution allows extrapolation based on extreme value theory so that expected peak stresses experienced during, for example, a year one period can be estimated. In some cases the expected cycles would be larger than the constant amplitude fatigue limit even if only cycles smaller than the fatigue limit were observed during field measurements. For rail vehicles there will be rare events like severe braking, operating with large payloads, or driving over a section of track in need of repair. Such situations do not arise often but occasionally they will occur and their effect on fatigue damage should be considered.

The load sequence given in the code of practice is not adequate for ensuring the infinite life of a bogie because the largest load range cycle is applied only 5×10^4 times during that portion of the test when fatigue damage is not permitted and occurs only during the final 25% of the load sequence. The largest cycle occuring during the first 75% of fatigue testing is repeated 1.5×10^5 times. For a finite life strategy to be retained, the fatigue test should be defined so that the maximum stress range associated with a change in direction of the transverse force is applied 5 - 10 million times. For example, the static load pattern shown in Fig. 4 could be repeated and other sub-cycles could be eliminated.

Structural testing according to actual measured load spectra is a well established technology in the automotive and aerospace industries. Railway bogies pose the additional challenge in that the service lives are very long and will involve hundreds of millions of load cycles; thus load histories must be highly edited for testing. It is not practical to simulate every load cycle expected during life so tests of smaller components should be done to measure the contribution of small cycles using spectra typical of those found in bogies. Rules or models for estimating the damage produced by small cycles as part of a spectrum are not fully established but cycles as small as 1/3 to 1/4 the constant amplitude fatigue limit may need to be considered in finite life calculations.

Small cycle damage

Larger stress cycles in a spectrum may themselves produce only a small amount of damage. Their major effect is that they change the fatigue limit behavior of the component so that cycles that would normally fall below the fatigue limit becoming damaging. It is therefore more appropriate to adopt a safe life philosophy in design and testing of bogies rather than the current infinite life strategy illustrated in the UIC code of practice for testing. Finite life does not imply a short life, and the typical design lives of $6x10^6$ kilometers over 30 years can still be achieved. A safe life strategy will direct attention toward defining service load spectra during normal use rather than only defining the maximum loads as is done with the infinite life strategy. An infinite life strategy will be adequate only if it can be shown with reasonable confidence that even the stresses produced by the rare events will be below the fatigue limit.

The tests reported here confirm the significant damage caused by small cycles when they are part of a spectrum with only a few cycles above the fatigue limit. This is in agreement with other researchers who have previously observed similar phenomena when using short span highway bridge load spectra [8,9,14]. Failure has been observed in laboratory tests of large welded structures where as few as 0.01% of the cycles exceeded the constant amplitude fatigue limit. An exceedance of 0.01% translates to an average of one cycle larger than the fatigue limit for approximately every 500 kilometers of bogie operation.

The tests described in this paper were performed using spectra considered representative of rail bogies. For bridge spectra, the majority of damage is contributed by cycles with ranges greater that half the fatigue limit. This is in contrast to the bogie spectra where the majority of fatigue damage is done by the large number of cycles with stress ranges less than half the constant amplitude fatigue limit [13]. As seen in Fig. 8, the load spectrum produced during the standardized fatigue test for bogies does not resemble the field measured spectra.

The best estimate of small cycle fatigue damage was found to be a straight line extension of the S-N curve below the fatigue limit. A bi-linear S-N curve that is a feature in many design codes for welded structures, is not supported by the test data generated in these experiments and is not generally supported by other published data. Small cycle damage should be computed based on a constant slope S-N line for stresses at least as low as 1/3 the fatigue limit. The fatigue limit observed under constant amplitude loading is related to fatigue crack initiation and not relevant to spectrum loading fatigue of welds which is dominated by crack growth.

CONCLUSIONS

Based on observations of actual service loads for a variety of railway bogies, experience from tests on full-scale bogie components and published high cycle spectrum fatigue test results for welded structures, the following conclusions can be made:

1. Fatigue load spectra as defined in the UIC code of practice will not produce stress exceedance diagrams in a test structure that resembles service loads.
2. The code is based on an infinite life strategy but does not apply the maximum stress range often enough to adequately test according to that strategy.
3. Only a small fraction of cycles exceeding the constant amplitude fatigue limit for welded joints can result in significant fatigue damage being caused by the large number of cycles below the fatigue limit.
4. A finite life strategy should be adopted in the design and testing of bogies unless it can be demonstrated that even rare event produce stress below the fatigue limit.

REFERENCES

[1] Leluan, A., "Fatigue test method and damage models used by the SNCF for railway vehicle structures," Automation in fatigue and fracture: Testing and analysis, ASTM STP 1231, C. Amzallag, Ed., ASTM, Philadelphia, PA, 1994, pp. 405 - 418.

[2] Schütz, W., "The significance of service load data for fatigue life analysis," Fatigue Design: ESIS Publication 16, J. Solin, G. Marquis, A. Siljander, and S. Sipilä, Eds., Mechanical Engineering Publications Ltd., London, 1993, pp. 1 - 17.

[3] UIC Code 515-4, "Passenger rolling stock: Trailer bogies-running gear: Bogie frame structure strength tests," International Union of Railways, Paris, 1993, 27 p.

[4] Leluan, A., "Bench testing of bogie frames," French Railway Review, vol. 1, no. 3, North Oxford Academic, Bordas-Dunod, 1983, pp. 223 - 240.

[5] Marquis, G., and Solin, J., "Spectrum fatigue testing using dedicated software," Automation in fatigue and fracture: Testing and analysis, ASTM STP 1231, C. Amzallag, Ed., ASTM, Philadelphia, PA, 1994, pp. 241 - 256.

[6] Dahle, T., and Larsson, B., "Spectrum fatigue data in comparison to design curves in the long life regime," Fatigue Design: ESIS Publication 16, J. Solin, G. Marquis, A. Siljander, and S. Sipilä, Eds., Mechanical Engineering Publications Ltd., London, 1993, pp. 63 - 71.

[7] Marquis, G., "High cycle spectrum fatigue of box beam components," Proceedings of the 3rd International Conference of the Engineering Integrity Society, ," Cawte, E. R., Draper, J. M., and Trigwell, N., Eds., EMAS, London, 1995, pp. 261 - 274.

[8] Fisher, J. W., Mertz, D. R., and Zhong, A. "Steel bridge members under variable amplitude long life fatigue loading," Washington: Transportation Research Board, National Research Council, 1983, 38 p. (NCHRP report 267).

[9] Miki, C., Toyoda, Y., Mori, T., and Enokido, N., "Fatigue of large-scale welded girders under simulated highway loadings," Structural Engineering / Earthquake Engineering, vol. 7, no. 2, 1990, pp. 283 - 291. (IIW-XIII-1459-92).

[10] Tilly, G. P., and Nunn, D. E., "Variable amplitude fatigue in relation to highway bridges," Proceedings of the Institute of Mechanical Engineers, vol. 194, 1981, pp. 259 - 267.

[11] Marquis, G., "Long-life spectrum fatigue of carbon and stainless steel welds," Fatigue and Fracture of Engineering Materials and Structures, in print, 1996.

[12] Dahle, T., "Long life spectrum fatigue tests of welded joints," International Journal of Fatigue, vol. 16, no. 6, 1994, pp. 392 - 396.

[13] Marquis, G., High Cycle Spectrum Fatigue of Welded Components, VTT Publications 240, Technical Research Centre of Finland, Espoo, Finland, 1995, 83 p.

[14] Fisher, J. W., Nussbaumer, A., Keating, P. B., and Yen, B. T., "Resistance of welded details under variable amplitude long-life fatigue loading," Washington: Transportation Research Board, National Research Council, 1993, 32 p. (NCHRP report 354).

Anthony P. Parker[1] and John H. Underwood[2]

SOME METHODS OF REPRESENTING FATIGUE LIFETIME AS A FUNCTION OF STRESS RANGE AND INITIAL CRACK SIZE

REFERENCE: Parker, A. P., Underwood, J. H., **"Some Methods of Representing Fatigue Lifetime as a Function of Stress Range and Initial Crack Size"**, Fatigue and Fracture Mechanics: 28th Volume, ASTM STP 1321, J. H. Underwood and B. D. Macdonald, M. R. Mitchell, Eds., American Society for Testing and Materials, 1997.

ABSTRACT: An analysis is developed which permits fatigue lifetimes of components with pre-existing crack-like defects to be represented by a single expression which is a function of stress range and initial defect size; this is designated the Fatigue Intensity Factor (FIF). A graphical representation indicates that all such failures will fall upon a single, flat surface. The conventional S-N curve is shown to be a special case of this surface. Outliers from this surface may indicate deficiencies in estimates of stress range, of initial crack length, or that the failure is not due solely to fatigue. An equivalent analysis based upon the concept of threshold stress intensity indicates that a second, flat, intersecting surface exists. The conventional 'fatigue limit' often shown on S-N plots is shown to be a special case of this surface. Existing experimental data are used to define the surface, and examples of its application to the ordering of several potential fatigue failure locations within a single system and to interpreting non-standard fatigue failure are described.

KEYWORDS: fracture, fatigue, fatigue intensity, fatigue lifetime, stress range, stress intensity, stress intensity threshold, crack size, S-N curve.

---

[1]Visiting Professor, Royal Military College of Science, Cranfield University, SWINDON, SN6 8LA, UK

[2]Research Engineer, Army Armament R D & E Center, Watervliet, NY 12189, USA

INTRODUCTION

Gun tubes develop bore cracks very early in their lifetime as a result of fatigue loading and severe thermal conditions that can cause so-called 'heat-checking'. There are also other potential failure locations, e.g. external notches and holes cut through the tube wall. It is important to have a clearly defined, well understood and easily presented design methodology to assess such potential failure locations and to identify the most critical.

Fatigue crack growth rates and associated lifetimes of components which contain pre-existing crack-like defects are frequently represented on a plot of log da/dn (crack growth per loading cycle) versus log ΔK (Positive Stress intensity factor range). A typical relationship between these two parameters is shown in Fig. 1(a). Much of a component's lifetime falls within region B, which can be represented by Paris' law, [1], as:

$$\frac{da}{dN} = C(\Delta K)^m \tag{1}$$

where C and m are determined experimentally. In the case of steels m is typically 3.

The more traditional representation of Fatigue lifetime as a function of stress range is via a plot of log (stress range) versus log (cycles to failure), the 'S-N curve'. Results for tests on components (such as welded joints) which contain pre-existing defects are generally of the form shown in Fig. 1(b). Maddox [2] has demonstrated that the slope of the line in the traditional S-N presentation is equal to (-1/m). Maddox includes an analysis, based upon Paris Law, retaining the full lifetime dependency upon initial and critical defect size and shape factor in order to develop a generalized effective stress range parameter. The purpose of this paper is to confine Maddox's analysis to variations of stress range and initial crack size , to produce graphical representations and to test their viability by comparing to existing experimental data relating to gun tubes.

ANALYSIS

Assume an edge or center-cracked geometry with remotely applied uniaxial elastic stress range, $\Delta\sigma^*$. Hence the stress intensity factor range, ΔK, for cracks small relative to the specimen width is given by:

$$\Delta K = Q\Delta\sigma^* \sqrt{\pi a} \tag{2}$$

where Q = 1 for a straight-fronted center crack and 1.12 for an edge crack.

(a)

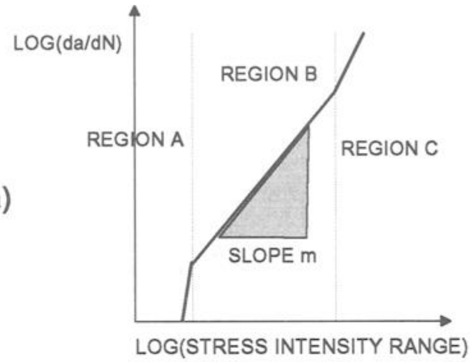

(b)

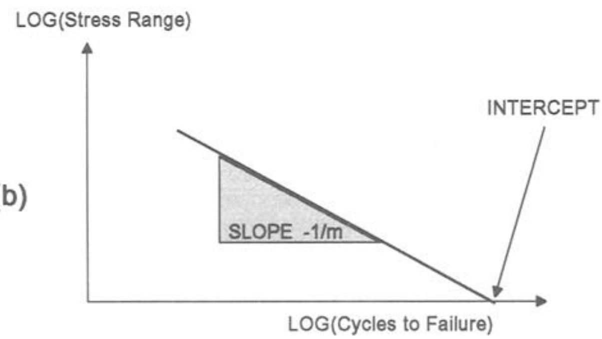

Fig. 1 : (a) Schematic Representation of Typical da/dN versus ΔK Plot (b) Conventional Lifetime Plot Showing Slope (related to Paris' exponent) and Intercept (related to initial Crack length)

Using Paris' Fatigue crack growth Law, Eqn. (1), defining $Q\Delta\sigma^*$ as $\Delta\sigma$ and substituting (2) into (1) and integrating between initial crack length a_i and final crack length a_c, for constant amplitude cyclic loading:

$$N = \int_{a_i}^{a_c} \frac{da}{C(\Delta\sigma\sqrt{\pi a})^m} = \left[\frac{a^{(1-m/2)}}{C\pi^{m/2}(1-m/2)(\Delta\sigma)^m}\right]_{a_i}^{a_c} \qquad (3)$$

$$N = \frac{1}{C\pi^{m/2}(1-m/2)(\Delta\sigma)^m}\left[a_c^{(1-m/2)} - a_i^{(1-m/2)}\right] \tag{4}$$

Eqn. (4) is the basis of the work by Maddox to relate Paris' law to the conventional log(stress range) versus log(Lifetime), 'S-N', presentation. Recognising that the square bracket is a constant for fixed initial crack size and $a_c >> a_i$ and taking logs of both sides leads to:

$$\log(N) = A - m\log(\Delta\sigma) \tag{5}$$

where A is a constant, or

$$\log(\Delta\sigma) = B - \left[\frac{1}{m}\right]\log(N) \tag{6}$$

where B is a constant.

Eqn. (6) may be plotted in the conventional S-N fashion as shown in Fig. 1(b), and it gives the familiar negative slope relationship. Maddox noted that this slope is the negative reciprocal of the Paris law exponent, m. However, if Eqn. (4) is simply modified to embody $a_c >> a_i$ so that the effect upon lifetime of a_c is negligible (an assumption which generally alters lifetime by 5% or thereabouts), we obtain:

$$N = \frac{a_i^{(1-m/2)}}{C\pi^{m/2}(m/2-1)(\Delta\sigma)^m} \tag{7}$$

Which, on taking logs, produces:

$$\log N = -m\log\Delta\sigma + (1 - m/2)\log a_i - \log\{C\pi^{m/2}(m/2 - 1)\} \tag{8}$$

or alternatively:

$$\log\Delta\sigma = (-1/m)\log N + (1/m - 1/2)\log a_i \\ -(1/m)\log\{C\pi^{m/2}(m/2 - 1)\} \tag{9}$$

Eqn. (8) indicates that a three-dimensional lifetime 'surface' exists, based upon axes logN, log$\Delta\sigma$ and log a_i, see Fig. 2.

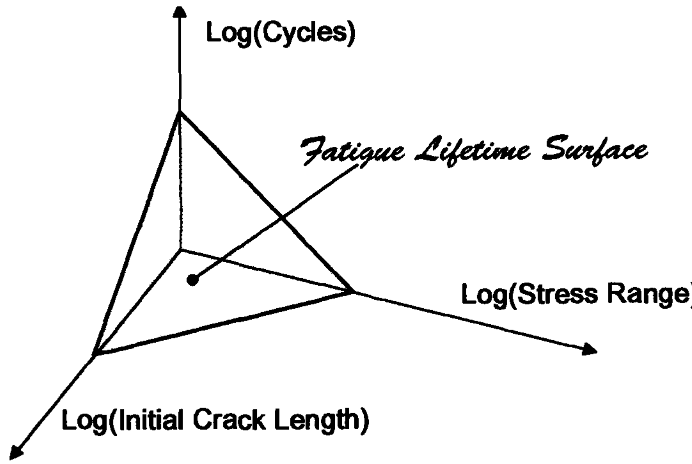

Fig. 2 : 3D Fatigue Lifetime 'Surface'

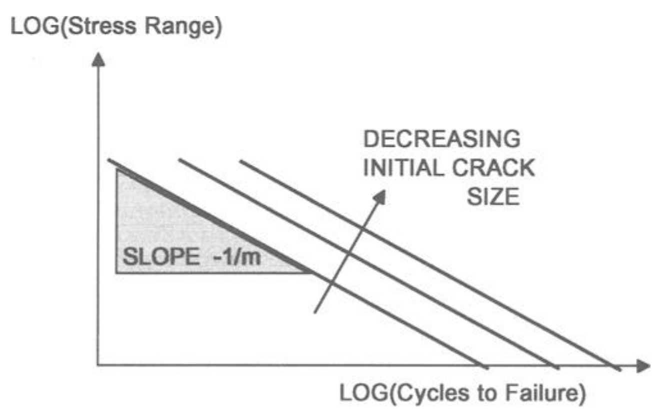

Fig. 3 : Family of Conventional Lifetime Plots Relating to Different Initial Crack Sizes

Eqn. (9) indicates the slope of the conventional 'S-N' plot; when viewed in the logN, $\log\Delta\sigma$ plane this becomes a series of parallel lines with slope (-1/m), see Fig. 3. Each line relates to a different value of initial crack size.

It is also possible to quantify the intercepts in Figures 2 and 3. From Eqn. (8), extrapolating to $\log \Delta\sigma = 0$ gives the value of the intercept as:

$$\log N = (1 - m/2)\log a_i - \log\{C\pi^{m/2}(m/2 - 1)\} \tag{10}$$

alternatively extrapolating to $\log a_i = 0$ gives:

$$\log N = -m\log \Delta\sigma - \log\{C\pi^{m/2}(m/2 - 1)\} \tag{11}$$

It is possible to force all results to fall on a single line by rearranging (9) to give:

$$\begin{aligned}\log \Delta\sigma + (1/2 - 1/m)\log a_i = &-(1/m)\log N \\ &-(1/m)\log\{C\pi^{m/2}(m/2 - 1)\}\end{aligned} \tag{12}$$

or

$$\log\left[\Delta\sigma . a_i^{(1/2-1/m)}\right] = -(1/m)\log N - (1/m)\log\{C\pi^{m/2}(m/2 - 1)\} \tag{13}$$

It is convenient to define the Fatigue Intensity Factor (FIF) as:

$$\textit{Fatigue Intensity Factor (FIF)} = \Delta\sigma \times a_i^{(1/2-1/m)} \tag{14}$$

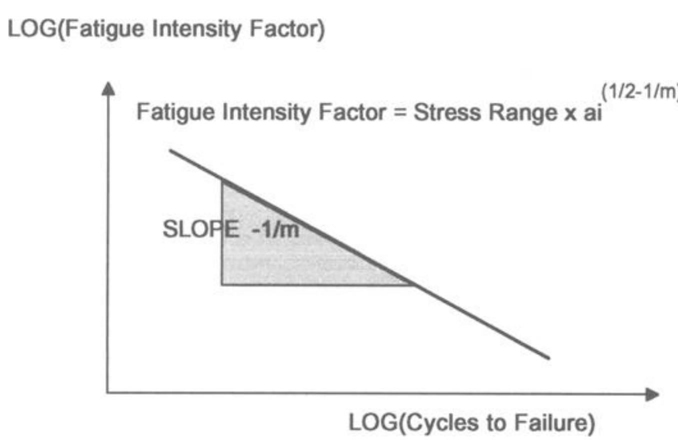

Fig. 4 : Single Line Plot of Lifetime for all Initial Crack Lengths

Fig. 4 shows a plot of the left hand side of Eqn. (13) versus logN,. Note that the last term on the right hand side is a material constant.

POSSIBLE APPLICATIONS

Somewhat surprisingly, if a single data point is plotted as in Fig. 4 and Paris' coefficient and exponent are known, it is possible to extrapolate to the logN axis and hence to calculate a value of a_i. Obviously such a procedure would be applied only when a significant number of data points was available.

The method of presentation employed in Fig. 4 makes possible a single line 'criticality' plot for a component or system which consists of a single material. In the case of a gun tube, for example, it is possible to plot each potential failure location and associated manufacturing process (such as the inclusion or exclusion of autofrettage) in order to assess the current and potential future critical fatigue failure locations.

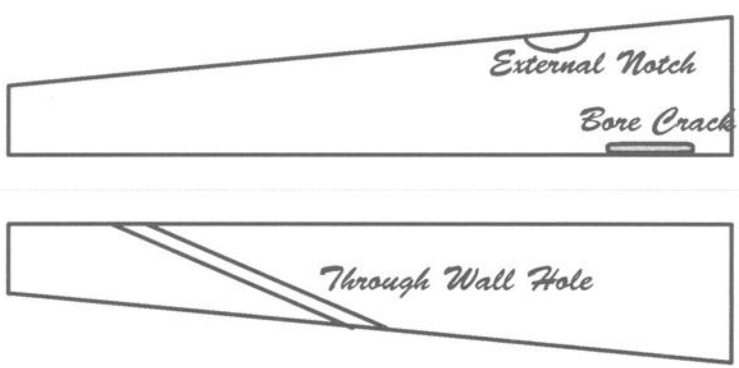

Fig. 5 : Potential Fatigue Failure Locations in a Gun Tube

Fig. 5 shows, schematically, potential fatigue failure locations in a typical gun tube. Each location may be assessed for initial defect size and cyclic stress range (taking account of residual stress contributions, in particular the presence or absence of autofrettage). These values, when plotted against the axes defined in Fig. 4, will produce a series of points as illustrated in Fig. 6, all of which should fall on a straight line. Any outliers from such a plot either indicate an error in stress range (perhaps due to incorrect assessment of residual stress or to incorrect assessment of stress concentration), in initial defect size, or that the failure is due to other factors in addition to conventional mechanical fatigue.

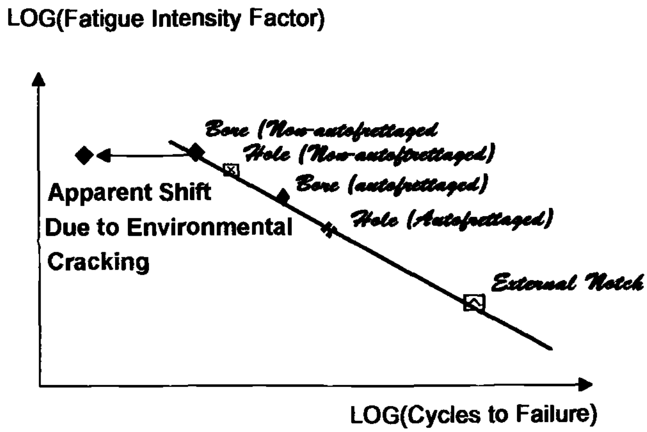

Fig. 6 : Schematic of Single Line Plot Used to Assess Location 'Criticality'

A possible outlier scenario related to environmental cracking is illustrated schematically.

A PRESENTATION WHICH ENCOMPASSES ALL STEELS

Thus far the Paris' law exponent (m) and coefficient (C) have been regarded as independent of one another. In the case of steels there is strong experimental evidence, for a range of microstructures, that C can be expressed as a function of m. Ref. [3], Chapter 2 indicates a simple relationship between C and m for steels, valid over the range m=1.8 to m=4, namely:

$$C = \frac{1.315x10^{-4}}{(895.4)^m} \quad \text{for crack growth in mm/cycle and } \Delta K \text{ in Nmm}^{-3/2} \qquad (15)$$

Converting units this provides (see [3], Appendix 3)

$$C = \frac{1.315x10^{-7}}{(28.3175)^m} \quad \text{for crack growth in m/cycle and } \Delta K \text{ in MNm}^{-3/2} \qquad (16)$$

Hence, substituting from Eqn. (16) into Eqn. (13):

$$\log\left[\Delta\sigma.a_i^{(1/2-1/m)}\right] = -(1/m)\log N - (1/m)\log\left\{\left[\frac{1.315x10^{-7}}{(28.3175)^m}\right]\pi^{m/2}(m/2-1)\right\} \qquad (17)$$

Plotting this relationship in the same way as Fig. 4 leads to a set of straight lines, slope (-1/m), as illustrated in Fig. 7 for the cases m=2.5, 3.0 and 3.5. Note that there is comparatively little difference between the three cases.

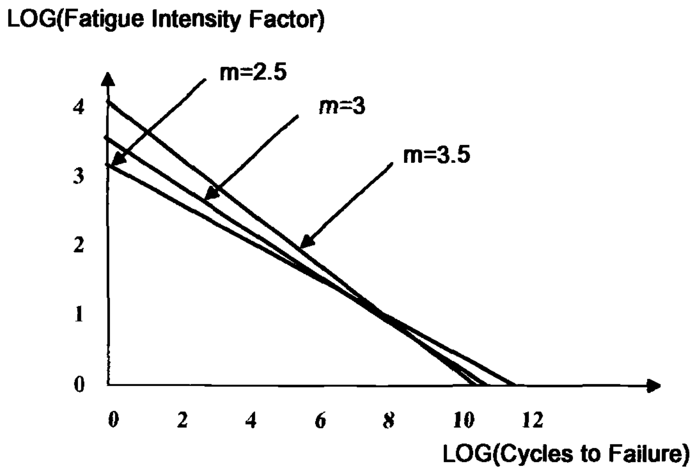

Fig. 7 : Straight Line Plot Presentation for all Steels

EFFECT OF FATIGUE LIMIT (STRESS INTENSITY RANGE THRESHOLD)

In the traditional (S-N) presentation for many materials there exists a so-called 'fatigue limit', i.e. a stress range below which the fatigue lifetime is infinite. The direct equivalent of this concept in conventional fracture and fatigue terms is a threshold value of stress intensity factor range, ΔK_{th} , [3], below which small crack-like defects will not grow under cyclic loading.

In order to define a Fatigue Limit 'surface' in $\log N - \log\Delta\sigma - \log a_i$ space for inclusion in a manner similar to Fig. 3 it is convenient to convert directly from Fracture/Fatigue to S-N presentation, retaining relevant parameters.

Since, at the Fatigue Limit:

$$\Delta\sigma\sqrt{\pi a_i} = \Delta K_{th} \tag{18}$$

taking logs

$$\log\Delta\sigma = \log(\Delta K_{th}/\sqrt{\pi}) - \log a_i \tag{19}$$

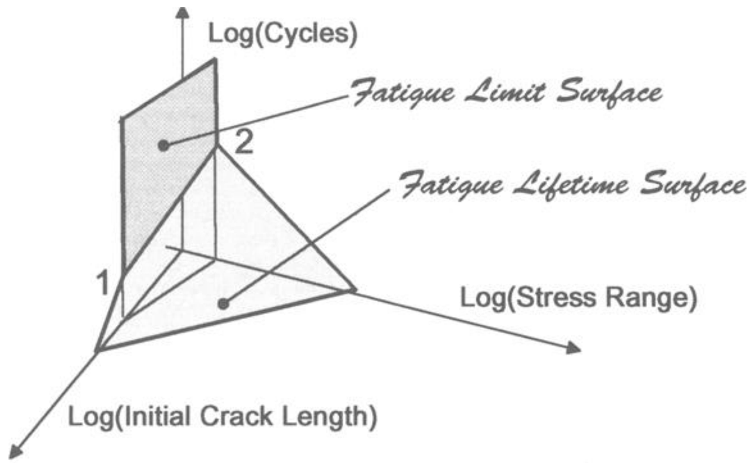

Fig. 8 : Intersection of Fatigue Limit and Fatigue Lifetime Surfaces

where the first term on the right hand side is a material constant.

Hence we see that we have defined a fatigue-limit 'surface' which lies parallel to the logN axis and intersects the lifetime surface along the straight line, 1 - 2, Fig. 8. This fatigue limit 'surface' may be defined in one of two ways:

a. **Via a conventional S-N curve.** A single value of the fatigue limit for any stress range permits the full definition of the fatigue limit 'surface'. Again we note a somewhat surprising result. Recall that it was noted earlier that initial crack length may be calculated from a single S-N point, via the intercept. In this case the initial crack size and the stress range at the fatigue limit onset are sufficient to define ΔK_{th} ; hence it is not necessary to undertake precise crack length observations to determine ΔK_{th}

b. **Via Fracture/Fatigue.** A known value of ΔK_{th} is sufficient to define the surface.

EXPERIMENTAL EVIDENCE AND EXAMPLES

The critical fatigue failure location within a cannon tube can vary depending upon the initial defect sizes, stress concentration effects of notches and holes, and the presence or absence of residual stress, typically due to autofrettage of the tube. Existing fatigue life test results from cannon tubes are available that can be used to demonstrate how well the fatigue intensity factor concept of Fig. 4 works in describing fatigue life for the various conditions mentioned above. Table 1 summarizes fatigue results from early and recent work, [4, 5 and 6].

The cannon tubes had various inner and outer radii and values of applied pressure, but the comparison was limited to tubes of the same type of high strength steel with yield strength of about 1200 MPa. Some of the tubes contained residual stresses due to autofrettage which, in the case of the plated bore and through-wall hole results, had an effect on fatigue life. The effects of applied and residual stress on fatigue life were determined by the following calculation of stress range:

$$\Delta\sigma = k_T\,[\sigma_P + \sigma_R] + P_{hole} + P_{crack} \tag{20}$$

Table 1 - Summary of Fatigue Life Information for Various Cannon Tubes

	Inner Rad $r1$ mm	Outer Rad $r2$ mm	Yield Strngth σ_Y MPa	Applied Pressure P MPa	Residual Stress σ_R MPa	Stress Range $\Delta\sigma$ MPa	Initial Crack a_i mm
Bore; fired	89	187	1250	345	0	890	0.50
Bore; unfired	89	187	1280	345	0	890	0.01
Bore; plated	89	142	1230	393	ID : -570	720	0.12
Thru-wall	53	76	1240	207	0	2210	0.01
	60	94	1170	297	ID : -460	2250	0.01
	78	107	1220	83	ID : -360	830	0.01
External Notch	78	142	1240	393	OD : +560	1200	0.01 0.03

where k_T is the stress concentration factor of the through hole or the external notch, σ_P and σ_R are the applied and residual hoop stresses determined from the well known expressions for pressure vessels [7, 8], and P_{hole} and P_{crack}, are the values of pressure that are applied to the inner surfaces of the through-hole and the growing crack, respectively. This implies, as before, that only the positive part of the stress range is included.

The values of the various parameters used to calculate $\Delta\sigma$ are listed in Table 2. The values of k_T are the usual 3.0 for the through wall holes and 3.3 for the external notch, calculated from [7]:

$$k_T = 1 + 2a/b \tag{21}$$

where a is the depth (7.6 mm) of the semi-elliptically shaped external notch and b is the half-width of the notch (6.7 mm). Regarding residual stresses, the chromium plated tubes were the only bore-initiated failure in which the tubes had a residual stress at the bore. This compressive stress lowered considerably the stress range and greatly extended the fatigue life over that which would have been measured with no autofrettage residual stress. Other than this, no residual stresses were directly used in the stress range calculations. Residual stresses were present in two of the three types of through-wall hole tests, but, as has been shown in [6], the residual stress causes the crack initiation site to move to a point near mid-wall thickness where the residual stress is zero and the applied stress is reduced. Thus the residual stresses indirectly cause an extension of fatigue life at the new initiation site, which has been used in the $\Delta\sigma$ calculation. Tensile residual stresses were present in the area of the external notch but were not considered because they did not add to the stress range. Finally, regarding pressure in the holes and cracks, note that the applied pressure has been added to the stress range as appropriate for the tube configuration and failure location.

Table 2 - Summary of Stress Range Calculations

	Stress conc. k_T	Applied Stress σ_P MPa	Residual Stress σ_R MPa	Pressure in hole P_{hole} MPa	Pressure in Crack P_{Crack} MPa
Bore; fired	1.0	547	0	n/a	345
Bore; unfired	1.0	547	0	n/a	345
Bore; plated	1.0	902	-547	n/a	393
Thru-wall					
R_1 = 53mm	3.0	599	0	207	207
R_1 = 60mm	3.0	552	0	297	207
R_1 = 78mm	3.0	221	0	83	83
External Notch	3.3	361	0	n/a	n/a

The fatigue life results based on Eqn. (20) and Tables I and 2 are shown in Fig. 9, using the type of single line plot in Fig. 4. The exponent of a_i is 1/6, for the case here of m = 3. The fatigue lives, N, were measured from full size cannon tubes which had been fired several hundred times prior to hydraulic testing, except as noted, and then hydraulically pressure cycled to failure in the laboratory. The stress range calculations have been discussed above. The initial crack size of 0.01 mm, from recent work [6], was used for most of the tests here, as a reasonable estimate of the inclusion size of the steel used in the tests, or alternatively, as an estimate of the roughness of the machined surface. In three cases metallographic measurements showed that a_i was larger than 0.01 mm. For the fired tubes with bore failure, heat check cracks of about 0.50 mm deep were observed. For the chromium plated tubes with bore failure, the cannon firing caused cracks in the plate to a depth equal to the plate thickness, 0.12 mm. For one of the externally notched tubes a rapid machining process resulted in an a_i of about 0.03 mm.

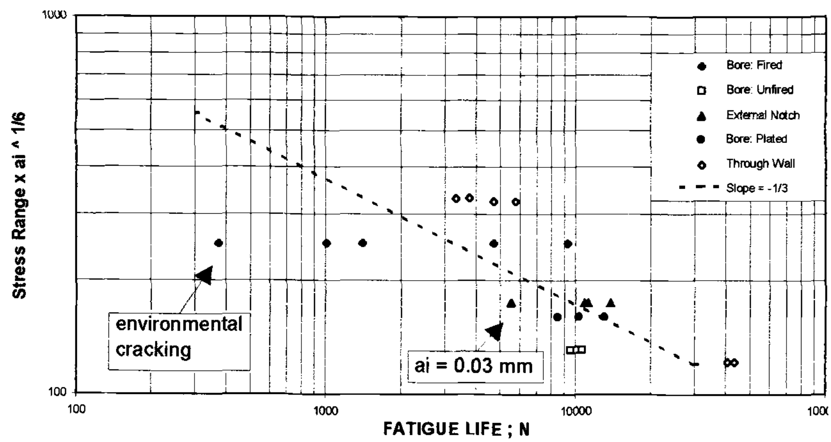

Fig. 9 : Fatigue Life as a Function of Stress Range and Initial Crack Size

The results plotted in Fig. 9 are in approximate agreement with a line of -1/3 slope as predicted in Fig. 4. The most significant deviations from the single line plot are some of the fired tubes with bore failure, particularly the tube that failedin less than 400 cycles. In the prior work, [4], intergranular fracture was noted for this tube, and environmental cracking, often associated with intergranular fracture, was considered to be possible. In light of the results here, it appears that environmental cracking did indeed contribute to the early failure. A clear advantage of the single line analysis of fatigue results - including as it does the three important variables, $\Delta\sigma$, N and a_i - is the identification of an apparent fatigue failure that has been affected by other than pure mechanical fatigue processes such as environmental cracking in the example just discussed.

Another advantage of the single line plot of fatigue results is that it provides a quantitative procedure to account for variations in a_i, which can be overlooked in a conventional $\Delta\sigma$ - N plot. For example if the external notch result in Fig. 9 with a_i = 0.03mm had been plotted with no account of its different value of a_i, it would have increased the apparent scatter and uncertainty of the results. Accounting for a_i gives a better understanding of the fatigue life results.

A final comment on the results is that without the inclusion of the effects of residual stresses described earlier, the agreement of the results with the single line analysis would have been affected. The results from the plated tubes and those with through-wall holes would have been in poorer agreement with the other results. This shows the important effect that residual stresses can have on $\Delta\sigma$ and thus on life.

SUMMARY AND CONCLUSIONS

An analysis has been developed which permits fatigue lifetimes of components with pre-existing crack-like defects to be represented by a single expression which is a function of stress range and initial defect size; this is designated the *Fatigue Intensity Factor (FIF)*. Graphical representation indicates that all such failures will fall upon a single, flat surface. Outliers from this surface may indicate deficiencies in estimates of stress range, of initial crack length, or that the failure is due to other factors in addition to mechanical fatigue.

An equivalent analysis links the so-called stress intensity threshold to the fatigue limit. This gives rise to a second, intersecting flat surface. The combination of these three-dimensional surface representations is shown to be the general, fully quantified case of the conventional S-N presentation with fatigue limit.

Existing experimental data are used to define the surface, and examples of its application are indicated in a two dimensional presentation. Cannon tube fatigue life results are shown to plot on a single line when the applied and residual stresses and known variations in initial crack size are accounted for. Fatigue lives known to be affected by environmental cracking are significant outliers from the single line plot, with lives reduced by up to a factor of ten from the lives due only to mechanical fatigue.

ACKNOWLEDGEMENT

Much of this work was undertaken during an attachment by one of the authors (APP) to the US Army Armament Research, Development and Engineering Center, Watervliet, NY. The attachment was arranged via the European Research Office of the US Army Research, Development and Standardization Group (UK).

REFERENCES

[1] Paris, P. C. and Erdogan, F., "A Critical Analysis of Crack Propagation Laws", Journal of Basic Engineering, Trans ASME, Vol 85, pp 528-534, 1963.

[2] Maddox, S. J., "Assessing the Significance of Flaws in Welds Subject to Fatigue", Welding Research Supplement, American Welding Society, Vol. 53, No. 9, pp 401-409, 1974.

[3] Gurney, T. R., "Fatigue of Welded Structures", 2nd Edition, Cambridge University Press, 1979.

[4] Davidson, T. E., Throop, J. F. and Underwood, J. H., "Case Studies in Fracture Mechanlcs", AMMRC MS 77-5, Army Materials and Mechanics Research Center, Watertown MA, 1977, pp 3.9.3 - 3.9.13.

[5] Audino, M J, "Fatigue Life Assessment of 155-MM M284 Cannon Tubes", ARCCB-TR-93036, Army Armament Research, Development and Engineerlng Center Report, Watervliet, NY, 1993.

[6] Underwood, J. H., Parker, A. P., Corrigan, D. J. and Audino M. J., "Fatigue Life Measurements and Analysis for Overstrained Tubes with Evacuator Holes", presented at ASME PVP Conference, Hawaii, 1995 and to be published in ASME Journal of Pressure Vessel Technology , 1996.

[7] Roark, R. J. and Young, W. C., Formulas for Stress and Strain, McGraw-Hill, New York, 1975, pp 590 - 606.

[8] Parker, A. P., "Stress Intensity and Fatigue Crack Growth in Multiply-Cracked, Pressurized, Partially Autofrettaged Thick Cylinders", Fatigue of Engineering Materials and Structures, Vol. 4, No. 4, pp 321-330, 1981.

Thomas S. Cook[1] and Hsin T. Huang[2]

DEVELOPMENT OF A RAPID THERMOMECHANICAL FATIGUE TEST METHOD

REFERENCE: Cook, T. S. and Huang, H. T., ''**Development of A Rapid Thermomechanical Fatigue Test Method**'', Fatigue and Fracture Mechanics: 28th Volume, ASTM STP 1321, J. H. Underwood, B. D. Macdonald, and M. R. Mitchell, Eds., American Society for Testing and Materials, 1997.

Abstract: Hot flowpath components of gas turbines can undergo thermomechanical fatigue (TMF), the simultaneous cycling of thermal and mechanical loads. The interactions between the two types of loads can produce damage mechanisms different than those observed during isothermal cycling. Models of this behavior, based on isothermal observations, need to be verified through TMF testing. In order to reduce temperature gradients, TMF tests are usually conducted at very slow frequencies, thereby requiring long testing duration to reach typical component lives. Given the expense and stability hazard of long tests, a method is needed to speed the production of TMF data. Such a method has been developed using an integrated air cooling-induction heating chamber. The test facility and the associated heat transfer and stress analysis required to analyze the test data are described.

Keywords: thermomechanical fatigue, low cycle fatigue, nonisothermal testing, time dependent fatigue, thermal stress analysis

INTRODUCTION

In structures used at elevated temperature, components can be subject to independent thermal and mechanical loads. When these loads fluctuate, the process is termed thermomechanical fatigue, and is often the life limiting condition. Life prediction for components undergoing TMF can be difficult since temperature variation during mechanical loading can produce an interaction that alters the isothermal fatigue mechanisms. To determine the extent of this synergism, TMF experiments must be conducted. Techniques for conducting tests in which temperature

[1]Lead Engineer, General Electric Power Generation, Schenectady, New York, 12345

[2]Engineer, General Electric Aircraft Engines, Cincinnati, Ohio 45215

and load are separately controlled have been developed, but such tests require sophisticated equipment and are expensive to perform because of the long time required to complete a test. In order to minimize the temperature gradients producing nonuniform stress fields in the specimens, cycle times of 3-8 minutes are usually employed. Reasonable test duration for such slow frequencies mandates large mechanical strains that are not usually present in the intended application. In order to complete tests in the nominally elastic strain regime, a new technique for rapid thermal cycling under controlled conditions has been developed. This method will allow data generation and model evaluation in a life regime, up to 100,000 cycles, that has been prohibitively expensive to explore in depth.

The research conducted in thermomechanical fatigue has been previously summarized [1,2] and only a few results will be cited here. As noted above, the slow test frequency used in TMF experiments means that the majority of test lives must necessarily be, due to economic constraints and the stability hazard during long tests, relatively short. Increasing the applied strain range into the plastic regime is usually done to insure reasonable test life. This makes the application of existing TMF knowledge to gas turbines difficult since the majority of turbine cyclic strains are nominally elastic. Material differences arise since crack initiation mechanisms in the nickel-base superalloys used in gas turbine components can be quite different from the lower strength, more ductile materials used in much of the previous research. Another consideration is the time dependent behavior of the superalloys which can be complex and distinct from ferrous alloys. There is some evidence in IN718 that at low strain levels, much of the time dependence of elevated temperature fatigue disappears [3].

A further complication is the effect of cycle shape and strain-temperature phasing. The majority of TMF tests have investigated only temperature-strain cycles that are in-phase or out-of-phase. While many applications can be approximated as in-phase or 180 degrees out-of-phase, other cycles are often encountered [4] and life prediction for these cycles is more difficult. For example, a strain-temperature cycle that is 90 or 270 degrees out-of-phase produces a diamond shape in strain-temperature space. However, in one case the diamond is traversed clockwise and in the other case, counterclockwise. Despite the maximum strain occurring at the same intermediate temperature for both cycles, the cyclic lives can be quite different [3]. The capability to understand the reason for this effect and whether it exists in the small strain region is required.

EXPERIMENTAL APPROACH

A variety of approaches to TMF testing have been developed over the years and have been reviewed by Carden [2]. The general methods might be loosely termed closed loop and open loop. In the former, test output is measured and a feedback loop used to update control parameters. The open loop method does not provide test output to the control system and is typified by the fluidized bed [5] or a thermal cycling furnace [6]. Flame impingement has been extensively used to evaluate fatigue properties of coatings [7] because of its high heating rate and environmental effects. These open loop tests provide a volume of results without large amounts of instrumentation. The tests tend to be relatively inexpensive but it is difficult to obtain quantitative data.

These tests are best suited to screening experiments and were not deemed appropriate for the proposed program.

In contrast to the simplicity of open loop testing, controlled approaches to thermomechanical fatigue require considerable instrumentation and a feedback system to provide independent control of the test variables [8]. These tests are run in servohydraulic machines so that quantitative data on temperature, strain, and load can be recorded. These tests are expensive to conduct and therefore should be part of a carefully planned experimental program.

The objective of this investigation was to develop a controlled test method that would provide measured data at a rate fast enough to economically test up to 10^5 cycles. The approach taken was to employ a conventional servomechanical test frame with an appropriate rapid heating and cooling system. It has been appreciated that specimen cooling is the controlling element in the cycle time for TMF testing. Natural convective cooling is frequently used as it generally minimizes temperature, and therefore stress, gradients within the specimen. However convective cooling can produce very long cycle times, particularly as the minimum temperature decreases. It becomes necessary to use forced air cooling to shorten cycle times and provide linear temperature ramps but this introduces two problems. One problem is the creation of thermal gradients in the specimen. Careful control of the air flow will minimize nonuniform temperatures but temperature gradients will still exist and the resulting stress must be accounted for. A second consideration is that the cooling air can affect the instrumentation associated with the test and cause stability problems with the extensometer, thermocouples, etc. This concern increases as test duration increases. This latter problem has led some researchers to employ hollow specimens with internal cooling [8].

Hollow specimens, while minimizing thermal mass, are difficult and expensive to manufacture. It is necessary to have a finish on the interior surface similar to that on the exterior of the specimen. The techniques used for machining internal surfaces are not the ones used externally, thereby yielding potential differences in finish and residual stress. This variation, combined with the cycle dependent stress and temperature fields, can lead to failure initiation at the interior surface. Data interpretation becomes more difficult in these cases. To be effective, internal cooling requires a mechanism to produce turbulent flow, thus further complicating the system. The flow, when rapidly cycled, could produce irregular temperature distributions. These distributions would be difficult to predict; the resulting stress could influence the TMF behavior in an unpredictable way. For these reasons, it was decided to employ solid specimens even though cycle time might be further reduced by hollow bars and internal cooling.

The type of heating method to use was the subject of considerable debate. Induction, flame impingement, direct resistance, and quartz lamps can all provide rapid specimen heating and can be controlled in a closed loop system. Extensive experience with induction heating led to it being the choice for the initial work. Preliminary tests showed that a cylindrical bar could be heated to 650-760C from 150C in under 10 seconds. Attention was therefore focused on designing a system to produce a controlled cool down cycle.

The TMF test specimen proposed was a solid cylindrical specimen with a reduced gage section and buttonhead grips. The reduced diameter and length were 6.35 and 31.75mm, respectively. The gage length was 12.70mm. This specimen is a variant of a standard fatigue specimen but the reduced diameter section is longer to help obtain a better temperature distribution.

A number of cooling designs were suggested but impingement airflow normal to the surface seemed to offer the most advantages. It is very effective in cooling, the air flow can be uniform, and axial gradients due to the flow are avoided. The obvious problem with impingement cooling is the disruption of the airflow by the induction coils and the extensometer. It was proposed that, by building an annular chamber, the induction coils could be placed inside the chamber and not interfere with the airflow. By constructing the chamber of a noncoupling material like Lexan plastic, only the test piece would be inductively heated. The chamber lid could be made removable to allow insertion and adjustment of the induction coil. Suitably spaced cylindrical ports extended through the annulus to provide extensometer or noncontacting temperature measurement access. An air line would be connected to the body to keep the chamber pressurized and the impingement airflow uniform and constant

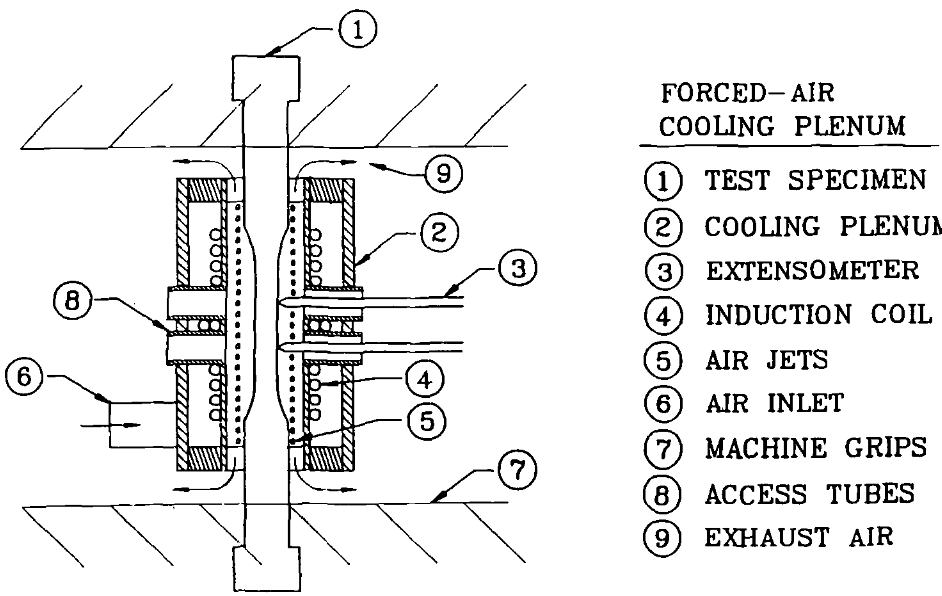

Fig. 1--Schematic of heating/cooling chamber design.

during cooling. The induction heater is always on but a solenoid valve would keep the airflow off during heating. Four axial rows of closely spaced cooling holes directed the cooling air at the cylindrical specimen. Based on this design, a preliminary heat transfer analysis was carried out. The calculations demonstrated that the cooling rate would be acceptable, as would be the tangential temperature distribution. An analysis involving six rather than four axial cooling arrays gave only a small improvement in thermal distribution, so the smaller array design was adopted.

A sketch of the heating-cooling system design is shown in Fig. 1. Based on the specimen used in this program, the cooling chamber was 82.6mm high, with an internal diameter of 25.4mm and external diameter of 127.0mm. The cooling was provided by four linear arrays of 1.5mm diameter holes, circumferentially ninety degrees apart. The linear arrays consisted of 25 holes and were located where they did not intersect the access ports.

The principal features of this system are:

1. The air impinges on the specimen at 90 degrees from a constant pressure source.
2. Four arrays of axial holes provide even specimen cooling.
3. The induction coil, inside the air plenum, does not interfere with the air flow.
4. Ports allow the extensometer to be positioned out of the air flow.

Once the design parameters were determined, a more detailed heat transfer analysis was conducted.

HEAT TRANSFER ANALYSIS

To demonstrate the design feasibility prior to fabrication, a transient heat transfer analysis was carried out. Subsequently a transient stress analysis was done. Since the nonuniform thermal stress produced by thermal cycling will influence the failure location in the specimen, the stress field needed to be included in the design and data analysis.

An axisymmetric finite element model of the specimen (minus the button heads) was constructed to perform the thermal analysis. This model was made with 25 elements and 45 nodes. The boundary conditions for the transient finite element heat transfer analysis consisted of heat transfer coefficients, heat input, and surface temperature at the grip area. The heat transfer coefficient, h, for the impingement flow was based on the work of Kercher and Tabikoff [9]. The values of h are obtained from

$$hD/K = \Phi_1\Phi_2 \ (R_e)^m \ P_r^{0.33} \ (Z/D)^{0.091}$$

where

Z is the axial distance from the specimen midplane,
D is the impingement hole diameter,
K is the thermal conductivity of air,
R_e is the Reynolds number,
P_r is the Prandtl number,
m, Φ_1, are functions of the hole spacing and diameter,
Φ_2 is a crossflow accumulation parameter

As the air passes the specimen shank, the duct area is reduced. This change in duct size was accounted for in the coefficients.

At the top of the chamber, the flow continues along the specimen but is no longer enclosed in a duct. When the air encounters the grip, it moves away from the specimen along the grip face. Once the air leaves the chamber, the heat transfer was taken as a constant over the top of the shank. The heat transfer coefficient was estimated from the wall jet analysis of Reference 10. The initial values of the heat transfer coefficients over the length of the specimen are shown in Fig. 2.

The specimen is loaded by the button heads in the water cooled grips. The temperature of the specimen was measured where the shank enters the grips and this temperature, 71C, was assumed to apply over the surface of the specimen within the grips.

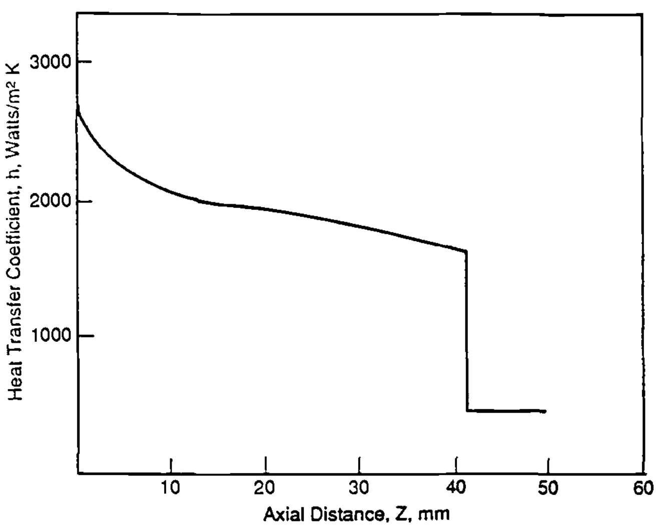

Fig. 2--Initial heat transfer coefficients used in transient thermal analysis.

The heating cycle was modelled by using an approximation to the induction heating process. High frequency induction heating produces heat in a shallow layer at the surface of the specimen. This was modelled by a surface heat flux rather than a heat generation effect since the heat generation would apply to the whole element rather than the surface layer.

Using the air flow and induction parameters, a transient heat transfer analysis was carried out. This analysis indicated that a superalloy bar could be thermally cycled between 204 and 593C in less than eight seconds. This cycle time indicated the feasibility of the proposed design.

Following fabrication of the system, temperature measurements were made to calibrate the thermal analysis. A number of thermocouples were applied to a specimen to obtain the axial and tangential temperature distribution. One specimen also had a blind 0.25mm axial hold drilled down the center of the specimen to attempt to measure the internal temperature.

There were a number of concerns about the test cycle, principally whether a triangular wave form could be achieved and whether it could be maintained over the duration of the test. It was found that by increasing the heating time to eight seconds and the cooling time to ten seconds, linear ramps with slight rounding at the turning points could be achieved. (The heating/cooling equipment is capable of a faster cycle time but the control system and the temperatures will determine the test limit.) Figure 3 shows an example of the ramps that were achieved, as well as the transition from turning the air off and bringing up the induction heat. The three thermocouples, at the center of the specimen, are spaced 45 degrees apart and show a minimal tangential temperature variation. The 0 degree output overlays the command signal, except at the maximum and minimum points. As expected, there is no angular variance during heating but a small variation during cooling exists. Another set of thermocouples, similarly spaced but at the top of the gage section, gave data that was indistinguishable among the three devices.

The collected thermocouple data was then used to calibrate the heat transfer model. A model more refined than the initial mesh was created; this second model had 355 nodes and 280 elements. A comparison with the earlier model gave a maximum temperature difference in the gage section during cool down of 4C. Heat up differences were half this value. In a series of analyses with the refined model, the heat transfer coefficients and heat flux were adjusted to match the predicted cycle time and the maximum and minimum temperatures with the test. Much better agreement between the experimental and analytical results could have been achieved if, instead of the derived heat transfer coefficients, an empirical temperature fit had been used. This was done but the monotonic curve of Figure 2 was replaced by a multivalued spline fit. Since there is no physical basis for such variability within the impingement zone, the choice was made to use the analytical heat transfer coefficients with limited data matching. At the center of the specimen, an adjustment in the coefficients of less than 10 percent was required. In the shank region where conditions are further from those assumed in the models, a maximum adjustment of thirty percent was necessary. A typical analysis result is shown in Figure 4. Note that the analysis has been carried out to almost 400 seconds to ensure that the computed cycle is stable.

Figures 5-7 compare the calculated and measured temperature profile at the surface of the bar at several locations along the bar. The comparison shows that the maximum and minimum points are closely matched but the intermediate times indicate the bar is responding more slowly than is calculated. A very uniform axial temperature distribution was achieved over the gage section as shown in Figure 5. Only data for the top half of the specimen is shown; temperatures in the lower half of the bar were identical.

Figure 7 illustrates one difficulty with a rapid cycle test. These tests are temperature controlled by thermocouples spot welded to the bar, but the thermocouples must not be applied to the constant diameter gage

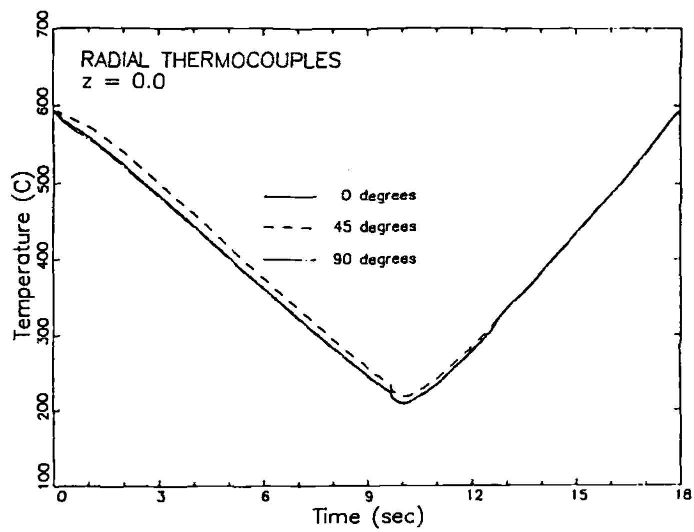

FIG. 3--Angular temperature variation measured at the center of the specimen.

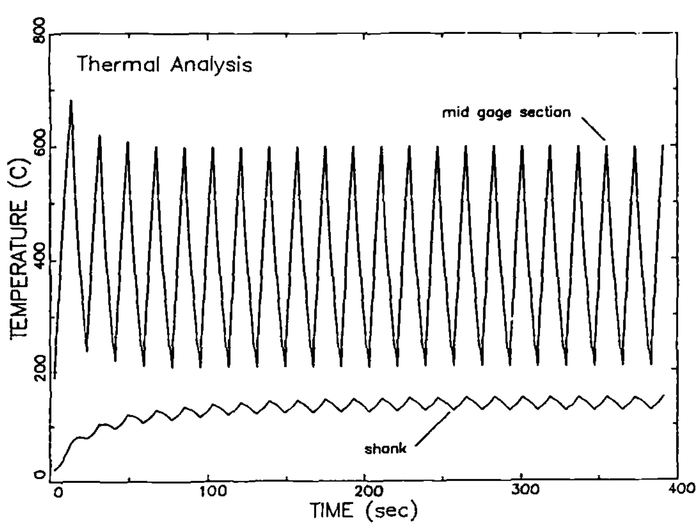

FIG. 4--Calculated temperatures at center and shank of TMF specimen.

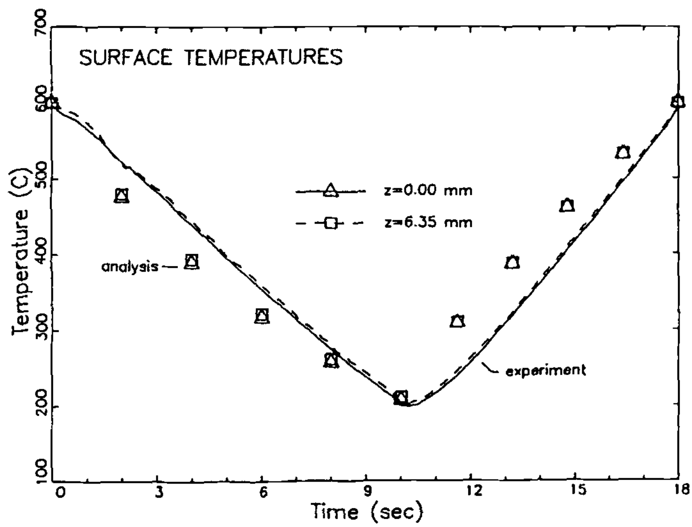

FIG. 5--Comparison of calculated and measured surface temperatures at center and top of gage section.

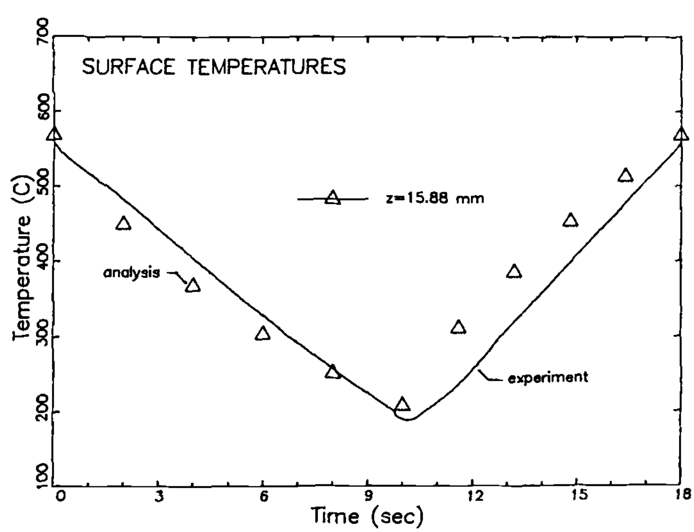

FIG. 6.--Comparison of calculated and measured surface temperatures at top of the constant diameter section.

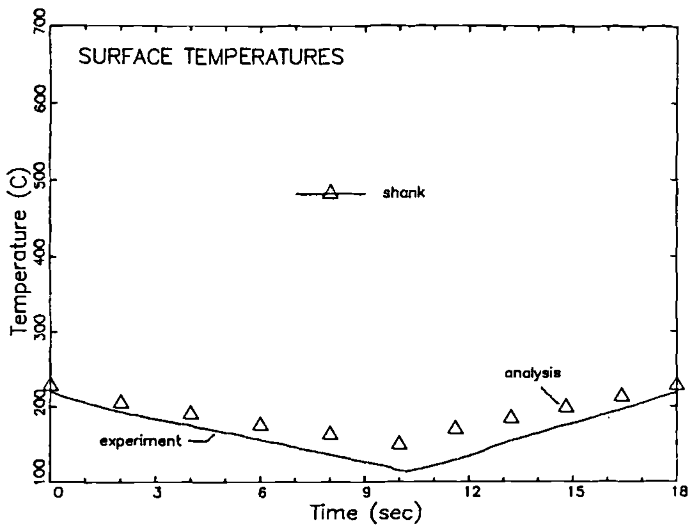

FIG. 7--Comparison of calculated and measured surface temperatures in the shank of the TMF specimen.

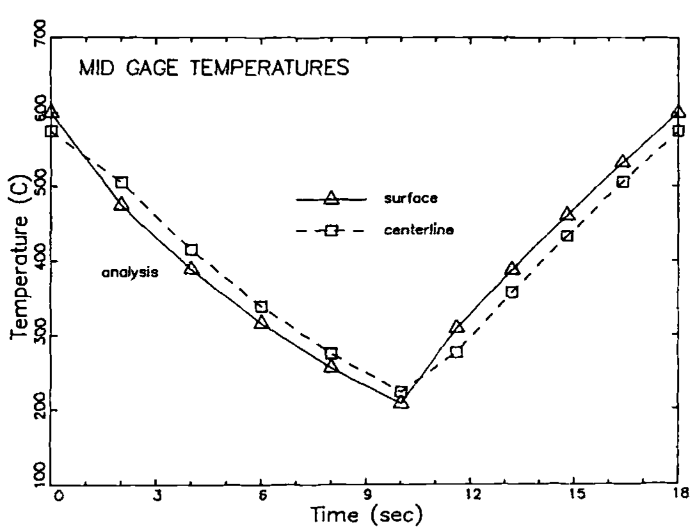

FIG. 8.--Calculated radial temperature gradient at the center of the specimen.

section. Crack initiation usually takes place at the weld but the lower stress and temperature of the shank can overcome this tendency. However, the rapid cycle does not provide much temperature fluctuation in the shank. A large change in gage section temperature corresponds to a small change at the shank. The control thermocouple was applied in the transition radius and by careful calibration and selection of signal ranges, a reproducible control signal was obtained that provided the uniform temperature profiles shown.

Figure 8 shows the computed temperatures at the center of the specimen at both the outer surface and the center line. There is a small radial gradient at the minimum temperature which increases to about 28C during the heating ramp. The cooling ramp has a slightly smaller gradient than does the heating portion. The comparison of measured and calculated surface temperatures is replotted from Figure 5. The experimental temperatures acquired at the centerline are not shown as they showed a very large, over 100C, radial temperature gradient. It is suspected that the thermocouple, which was just pushed down the centerline hole, was not making good contact with the hole surface and thus was giving an inaccurate temperature reading.

The temperatures at six locations from one heat transfer analysis are given in Table 1. The cooling ramp ends at 95.25 seconds and ramps to maximum temperature 8 seconds later. The origin of the axes is at the centerline and midpoint of the specimen length as shown in Figure 9. The temperature within gage at the specimen surface, R = 3.2mm, is calculated to be 212C, 95.25 seconds, and 601-602C, 103.25 seconds. This is about four percent above the target values of 204 and 593C but shows the absence of an axial temperature gradient within the gage. Outside the gage section, there is an axial variation of 11 and 39C at the minimum and maximum temperature, respectively. Within the gage section, the radial gradient from the centerline of the bar to the surface is approximately five percent. This value increases slightly as the transition radius is approached.

TABLE 1--Calculated temperatures at the beginning (95.25 sec) and end (103.25 sec) of a heating ramp-(distance in mm). Gage surface target temperatures are 204 and 593C, respectively.

	95.25 Seconds		103.25 Seconds	
	Temperature, C			
Z	R=0	R=3.2	R=0	R=3.2
0	224	212	575	602
6.4	228	212	574	601
15.9	214	201	534	563

STRESS ANALYSIS

Once the heat transfer analysis was complete, a stress analysis was carried out to determine the stresses due to the thermal cycle. The rapid thermal cycle produces cyclic thermal stresses within the test bar which must be included in the life assessment of the specimen. The

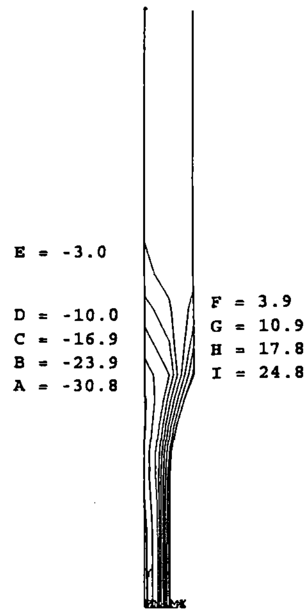

FIG. 9--Axial stress distribution at start of heating ramp at t = 95.25 seconds (stress in MPa).

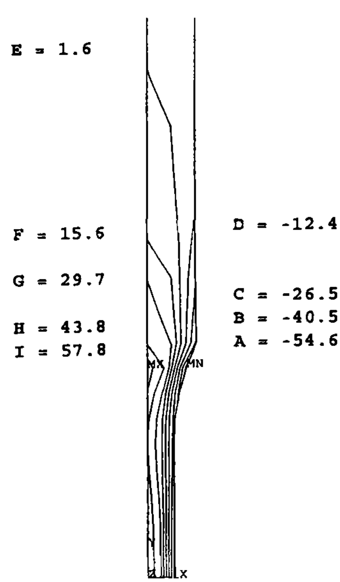

FIG. 10.-- Axial stress distribution at end of heating ramp at t = 103.25 seconds (stress in MPa).

analysis was carried out over a complete thermal cycle once it had reached stability. The results of this analysis are given in Figures 9 and 10. Figure 9 gives the axial stress at the end of the cooling cycle, 95.25 seconds, while Figure 10 is the corresponding plot at 103.25 seconds, the end of a heat up ramp. As would be expected from the temperature distribution, the constant stress contours are primarily axial. At 95.25 seconds, the surface of the bar is in tension, with a maximum value of axial stress approximately 34.5 MPa. The maximum axial stress is at the center of the gage section while the effective stress is a maximum on the surface at the start of the transition radius. This might cause cracking problems in a few types of cycles but this location will usually be cooler than other high stress regions. At the end of the heating ramp, 103.25 seconds, the interior of the bar is cooler and is in tension. At this time, the maximum axial and effective stress location has shifted to the interior of the specimen, again at the transition from the gage section to the shank section. The shifting of the location of maximum effective stress may also cause out of gage failures in certain cycles. The minimum axial stress in the bar is -62.1 MPa. These stresses are much smaller than the intended applied mechanical stress. It will be necessary, however, to include the effect of the thermal stress in the data analysis.

In addition to the stresses, the calculated strains were examined. An elastic finite element analysis was used in this program so the strain values did not provide any new insight. Since the strains are cycle and material dependent, they have not been included here. However, once the TMF cycle contains significant inelastic strains, it becomes necessary to use nonlinear analysis and strain based parameters to predict TMF behavior[11].

The thermal stress analysis was used to examine the potential for cracking at the welded thermocouple. A semicircular surface flaw, 0.13mm radius, was assumed to exist at the point of attachment in the transition radius and the thermal and mechanical stress range applied. Based on the fatigue crack growth rate in the material, the thermocouple should not pose a threat to test completion. However, cracking may pose a problem for other materials and TMF cycles. It will be necessary to estimate the life for a particular application to ensure that propagation of a weld initiated crack will not end the test prematurely.

PROOF OF CONCEPT TESTING

Following the completion of the thermal stress analysis, the test system was assembled and an Inconel 718 specimen inserted to ascertain whether the system would remain stable over a typical test duration. The specimen was thermally cycled and the free thermal strain captured. In the usual method for axial strain control TMF, this signal was combined with the desired mechanical strain range, 0.80 percent, to obtain the total strain signal [8]. An in-phase cycle, with a period of 18 seconds was run for 30,000 cycles. The cycle was changed to an out-of-phase cycle and the test continued. Further, since the anticipated cycle involves elastic cycling, the control mode was switched from strain to load. A total of over 50,000 cycles was accumulated during this exercise. There was no indication that the air currents were affecting the instrumentation. The load and strain signals remained stable. A fiber optic wire was used to monitor the temperature in the gage section and this also showed no thermal drift.

No cracking problems were found with the welded thermocouple. No attempt was made to measure the Lexan temperature at the inner diameter of the chamber but no cracking or distortion was seen.

This new TMF system is now undergoing further testing in which the TMF data will be generated and compared to the existing LCF and TMF data base.

SUMMARY

The goal of this investigation, the development of a closed loop system capable of carrying out rapid TMF cycling, has been achieved. The system combines a conventional servohydraulic TMF test facility with a specially designed heating/cooling chamber. This hollow annular chamber contains the induction coils and is pressurized. The chamber provides impingement cooling air to the specimen without interference from the induction heating system. The TMF cycle currently used is an eight second heating ramp and a ten second cooling ramp. A transient heat transfer and a stress analysis of the specimen have been carried out. These results show the thermal stresses produced in the specimen are acceptable and can be factored into the test data analysis. The test facility has been cycled sufficiently to conclude that there are no stability or control problems associated with the instrumentation and test environment. The system is being used to generate TMF data for comparison to existing test results.

ACKNOWLEDGMENT

The authors would like to acknowledge the contributions of Mr. Jack Luers in the development of the experimental facility and Mr. Ken Seitzer for help in conducting the heat transfer analysis. Dr. Robert Van Stone was the source for a number of helpful discussions.

REFERENCES

[1] Halford, G.R., Thermal Stresses II, R.B. Hetmorski, Ed., Elsevier Science Publishers B.V., New York, NY, 1987, pp. 330-428.

[2] Carden, A.E., "Fatigue at Elevated Temperatures: A Review of Test Methods", Fatigue at Elevated Temperatures, ASTM STP 520, American Society for Testing and Materials, 1973, pp. 195-223.

[3] Van Stone, R.H., McKnight, R.L., and Cook, T.S. "Crack Initiation and Crack Growth Under TMF Loading Conditions", presented at NASA Fifth Thermomechanical Fatigue Workshop, Cleveland, 10-11 October 1989.

[4] Embley, G.T. and Russell, E.S., "Thermal-Mechanical Fatigue of Gas Turbine Bucket Alloys", in Proceedings, First Parsons International Turbine Conference, Dublin, Institute of Mechanical Engineers, 1984, p. 157.

[5] Howes, M.A.H., "Evaluation of Thermal Fatigue Resistance of Metals Using the Fluidized Bed Technique", Fatigue at Elevated Temperatures, ASTM STP 520, American Society for Testing and Materials, 1973, pp. 242-254.

[6] Hillery, R.V., Pilsner, B.H., McKnight, R.L., Cook, T.S., and Hartle, M.S., "Thermal Barrier Coating Life Prediction Model Development", NASA CR-180807, Nov. 1988.

[7] Benn, R.C., Deb, P., and Boone, D.H., "Coatability of High Gamma-Prime ODS Superalloys", High Temperature Coatings, Kholaib, M. and Krutenat, R.C. Eds., The Metallurgical Society, Warrendale, Pa., 1986, pp. 1-79.

[8] Hopkins, S.W., "Low-Cycle Thermal Mechanical Fatigue Testing", Thermal Fatigue of Materials and Components, ASTM STP 612, American Society for Testing and Materials, 1976, pp. 157-169.

[9] Kercher, D.M. and Tabikoff, W., "Heat Transfer by a Square Array of Round Jets Impinging Perpendicular to a Flat Surface Including The Effect of Spent Air", ASME Paper 69-GT-4, April 1969.

[10] Akfirat, J.C., "Transfer of Heat From An Isothermal Flat Plate Due to a 2-D Wall Jet", Proceedings of Third International Heat Transfer Conference, Chicago, Vol. 2, 1966, pp. 274-279.

[11] Cook, T.S., Kim, K.S., and McKnight, R.L., "Thermal Mechanical Fatigue of Cast Rene 80", Low Cycle Fatigue, ASTM STP 942, H.D. Solomon, G.R. Halford, L.R. Kaisand, and B.N. Leis, Eds., American Society for Testing and Materials, Philadelphia, 1988, pp. 692-708.

Stephen N. Endersby[1], Anthony P. Parker[2], Timothy J. Bond[3] and John H. Underwood[4]

STRESS CONCENTRATION, STRESS INTENSITY AND FATIGUE LIFETIME CALCULATIONS FOR SHRINK-FIT COMPOUND TUBES CONTAINING AXIAL HOLES WITHIN THE WALL

REFERENCE: Endersby, S. N., Parker, A. P., Bond, T. J., Underwood, J. H., **"Stress Concentration, Stress Intensity and Fatigue Lifetime Calculations for Shrink-Fit Compound Tubes Containing Axial Holes Within the Wall",** Fatigue and Fracture Mechanics: 28th Volume, ASTM STP 1321, J. H. Underwood, B. D. Macdonald and M. R. Mitchell, Eds., American Society for Testing and Materials, 1997.

ABSTRACT: Elastic-plastic numerical stress analyses and fatigue lifetime predictions are presented for shrink-fit compound tubes containing multiple, axial holes at the interface between inner and outer tube. The holes, which are semi-circular, are introduced initially as periodic notches on the outer surface of the inner tube and an outer plain tube is heated, slid over the inner tube and allowed to cool to achieve the shrink-fit. Residual stresses resulting from interference and operational stress ranges arising from cyclic bore pressurization are calculated and fatigue lifetimes are predicted. Two potentially critical locations for fatigue failure are identified as the bore and the notch root. The predicted lifetimes are compared with earlier work on a similar overall geometry subjected to autofrettage. The critical location is shown to be at the bore and a clear improvement in overall fatigue lifetime is demonstrated for the shrink-fit tube compared with the autofrettaged tube. As the interface radius is reduced, there is a general reduction in the ratio of fatigue stress range at the bore to that at the hole and the possibility of the critical location moving to the notch root. A normalized presentation for design purposes is proposed.

KEYWORDS: crack growth, fatigue cracks, fatigue lifetimes, axial holes, channels, compound tubes, cylinders, compound cylinders, fracture, fracture mechanics, residual stress, shrink-fit, stress concentration factor, stress intensity factor.

[1]Research Student, University of Northumbria, NEWCASTLE, NE1 8ST, UK
[2]Visiting Professor, Royal Military Coll of Science, Cranfield University, SWINDON, SN6 8LA, UK
[3]Principal Lecturer, University of Northumbria, NEWCASTLE, NE1 8ST, UK
[4]Research Engineer, Army Armament R D & E Center, Watervliet, NY 12189, USA

INTRODUCTION

The use of autofrettage to enhance fatigue lifetimes of thick tubes subjected to internal cyclic pressurization is well known and relatively well understood. Recent work has addressed the problems associated with geometrical changes which remove the initial axi-symmetric nature of geometry and stressing of these tubes, namely:

a. Axial erosion grooves, *which arise after autofrettage,*along the bore of the tube, Ref [1].
b. Cross-bore holes normal to the tube axis [2] and inclined at an angle to the axis [3]. These holes likewise are *introduced after autofrettage.*
c. Periodic axial holes within the bore which are *introduced prior to autofrettage* of the tube [4].

The purpose of the work presented herein is to predict, using elastic and elastic/plastic stress analysis methods, the fatigue behavior of compound cylinders which contain a series of equally-spaced holes oriented parallel to the tube axis, the holes being created by the thermal shrink-fitting of an external (featureless) tube onto an externally-notched inner tube, Fig. 1 (schematic). Experience indicates that two potentially critical failure locations are on a radial line at the point on the hole closest to the bore and on the bore itself.

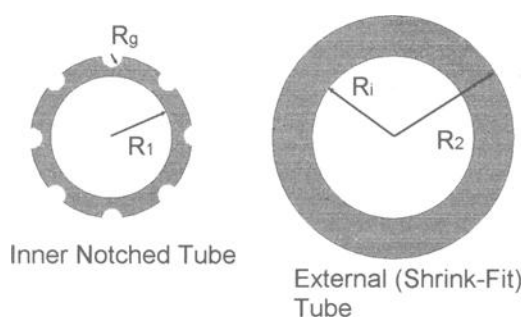

Fig. 1 : Schematic of Hole Geometries Analyzed with Finite Element Method

FINITE ELEMENT (FE) ANALYSIS

Several possible designs were analyzed using the NISA Finite Element program. In all cases they consist of a periodic array of 24 equally-spaced holes. The material typically has an Elastic Modulus, E, of 200GPa and a coefficient of thermal expansion, α, of 12×10^{-6}/degC. In cases of autofrettage used for comparison purposes, a yield strength of 1200MPa was employed.

Throughout the investigation the inner and outer radii (R_1 and R_2) were 84.5mm and 152.5mm respectively. The groove radius (R_g) was 6.35mm. Interface radii (R_i) for the cases considered are given in Table 1 below:

Table 1 : Interface Radii Examined

Case 1: Interface radius (R_i)	122.00 mm
Case 2: Interface radius (R_i)	114.00 mm
Case 3: Interface radius (R_i)	106.75 mm
Case 4: Interface radius (R_i)	100.65 mm

In order to construct an FE mesh for these configurations taking full advantage of symmetries it was only necessary to model some 360/(24x2) or 7.5 degrees of the tube. Essential symmetry conditions were ensured by imposing zero shear stress and zero tangential displacement on all radii of symmetry. The interference was simulated in the FE analysis by maintaining a constant temperature difference between material in each of the inner and outer tubes.

One particular objective of this work was to compare the shrink fit method with the autofrettage method examined in Ref [4]. Three different amounts of shrink fit were investigated for each of the four interface radii. The shrink fits were designed to give a hoop stress at the bore of two shrink-fit featureless cylinders equivalent to 40%, 50% and 60% autofrettage (overstrain) of a solid tube respectively.These temperature differentials were selected to give an appropriate spread of results for comparison purposes, while avoiding significant amounts of plasticity at the hole boundary. The relationships between equivalent autofrettage, interference and temperature differential are shown in Table 2.

Table 2 : Relationship Between Equivalent Autofrettage, Interference and Temperature Differential for Tubes Examined

	Equiv. Autofrettage	Interference	Temp diff
Case 1	40%	0.663 mm	453 deg C
	50%	0.783 mm	535 deg C
	60%	0.851 mm	581 deg C
Case 2	40%	0.500 mm	366 deg C
	50%	0.591 mm	432 deg C
	60%	0.642 mm	470 deg C
Case 3	40%	0.401 mm	313 deg C
	50%	0.474 mm	370 deg C
	60%	0.515 mm	402 deg C
Case 4	40%	0.351 mm	291 deg C
	50%	0.415 mm	344 deg C
	60%	0.451 mm	373 deg C

To simulate cyclic pressurization a pressure of 434 MPa was applied to the bore.

ELASTIC HOOP STRESSES DUE TO BORE PRESSURIZATION AND SHRINK FIT

Fig. 2 shows(upper curve) the elastic variation of hoop stress with radius from the bore to the notch root for an internal pressure of 434.4MPa. For comparison the standard (Lamé) solution for a pressurized, plain thick cylinder is also shown. This indicates the expected stress concentration effect of the notch and a slight variation at the bore resulting from the presence of the holes, see [4] for a discussion of this point.

Fig. 2 also illustrates (lower three curves) the compressive hoop stresses resulting from the shrink fitting process. These results were obtained from an elastic analysis using NISA, and it is clear that no compressive yielding is likely for Cases 1 and 2 since maximum hoop stress magnitude does not exceed yield strength (1200 MPa). Elastic/plastic analyses were also conducted for those cases of shrink-fitting in which yielding might occur; these results are referred to later in this paper. For comparison the more complex residual stress profiles resulting from an elastic/plastic FE analysis of autofrettage of the same geometry [4] are also presented in Figure 2 as the middle three curves; note that these results relate to equivalent overstrains of 40%, 60% and 80%.

HOOP STRESS RANGE AND FATIGUE LIFETIME

Superposition of the combinations of elastic stresses due to internal pressure and residual stresses arising from shrink-fitting provides an indication of the positive stress range during cyclic pressurization, Fig. 3.

There are two potential fatigue failure locations on a single radial line at the point on the hole closest to the bore and at the bore itself. The fatigue lifetime formulae, based upon Paris' law and governing lifetime for failure from different initial defect sizes with different stress ranges are developed in [5] . In summary the fatigue lifetime at a particular location depends principally upon initial defect size (a_i) and stress range ($\Delta\sigma$), the latter taking account of both residual stresses and any pressure acting upon the crack surfaces as a result of infiltration from the bore. The expression for lifetime, N, is:

$$N = \frac{a_i^{(1-m/2)}}{C\pi^{m/2}(m/2-1)(\Delta\sigma)^m} \qquad (1)$$

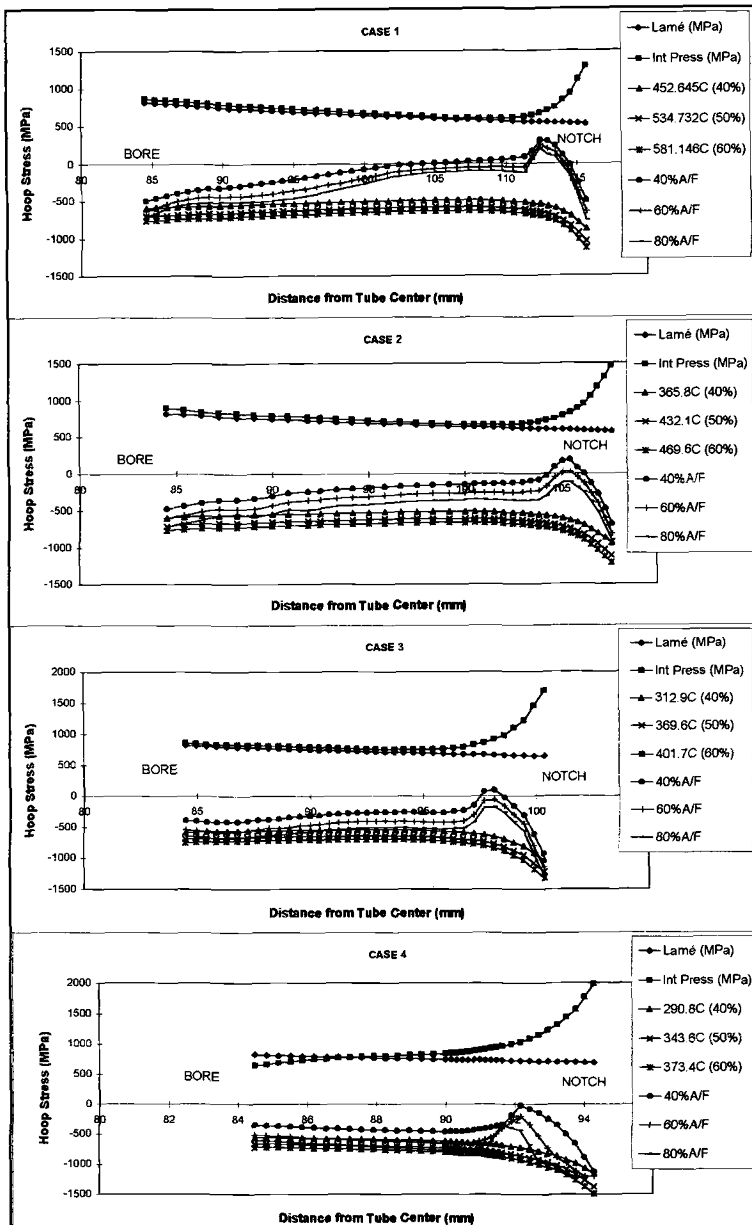

Fig. 2 : Elastic Variation of Hoop Stress from Bore to Hole due to Internal Pressure (upper two curves) ; Residual Hoop Stresses Arising from Shrink Fitting (lower three) and from Autofrettage (Ref [4]) (middle three curves).

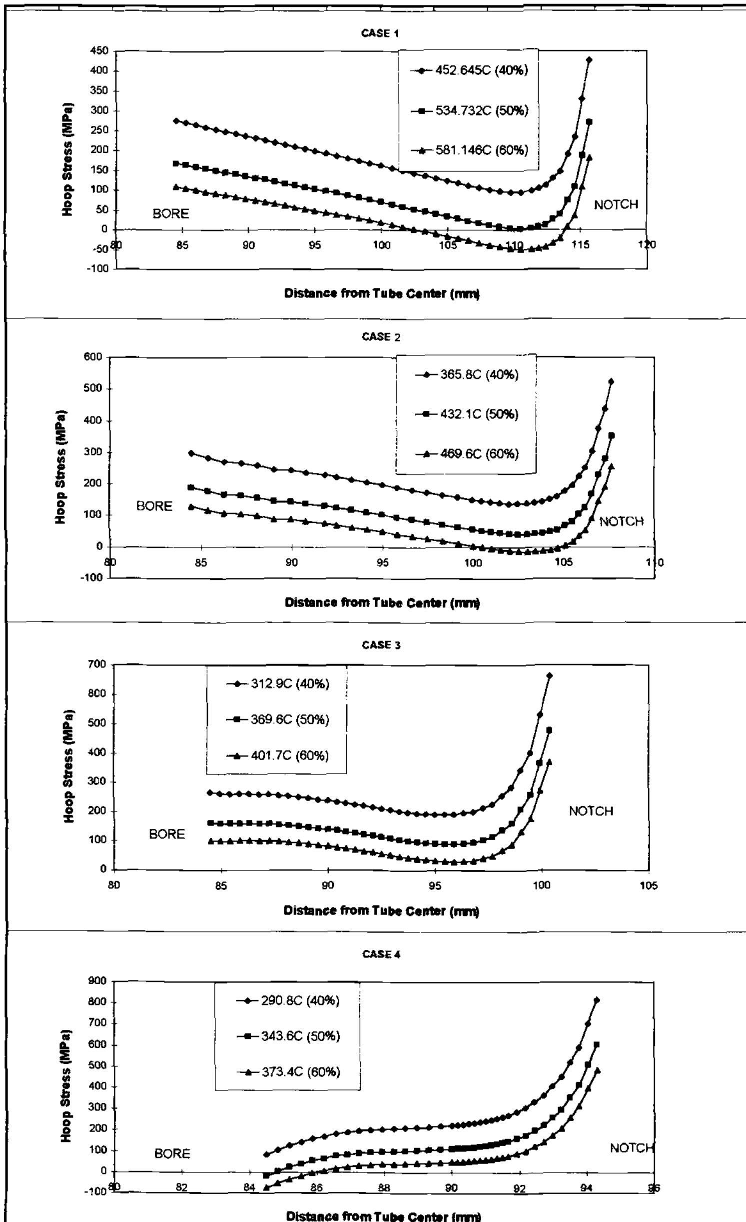

Fig. 3 : Positive Cyclic Stress Range of Shrink-Fit Arrangement Resulting from Pressurization of Bore

where C and m are Paris' Law coefficient and exponent respectively.

For design purposes, where there are two potential failure locations, it may be more useful to plot lifetime ratios. If we calculate the ratio of lifetimes with two different initial crack lengths and associated stress ranges, a_1 and $\Delta\sigma_1$, a_2 and $\Delta\sigma_2$, these combinations will, in general, yield two different lifetimes, N_1 and N_2. From Equation (1) the ratio of these lifetimes is:

$$\frac{N_2}{N_1} = \left[\frac{a_2}{a_1}\right]^{(1-m/2)} \left[\frac{\Delta\sigma_1}{\Delta\sigma_2}\right]^{m} \tag{2}$$

The effective stress range at the hole is given in Fig. 3 by the values at the far right of each plot, while the effective stress range at the bore is that given in Figure 3 at the left _plus the contribution from the bore pressure which infiltrates the fatigue crack_. Assuming at this stage equal length initial defects at the two locations, the more critical will be that with the higher effective stress range. Table 3 gives ratios, for all geometries analyzed, of effective stress range at bore/effective stress range at hole, designated Fatigue Stress Range Ratio, R_σ where:

$$R_\sigma = \frac{\text{(Hoop Stress Range at Bore + Bore Pressure in Crack)}}{\text{Hoop Stress Range at Hole}} \tag{3}$$

When R_σ is below unity this indicates a potential shift of failure location from bore to hole for the case of equal length initial defects at the two locations. In the general case where $a_B \neq a_H$ Equation (2) indicates that the shift will occur when:

$$R_\sigma = \left[\frac{a_B}{a_H}\right]^{(1/m-1/2)} \tag{4}$$

where a_B and a_H are the initial crack sizes at the bore and the hole respectively.

Table 3 shows the R_σ ratio for shrink-fitting for all cases considered. For all geometries the result of the elastic analysis is provided. In cases of shrink-fitting in which yielding occurs the value in parentheses refers to the equivalent elastic/plastic FE analysis result. For comparison Table 3 also includes full results of the elastic/plastic autofrettage FE analysis reported in detail in [4]. Furthermore, since there is experimental evidence that, for the autofrettage case, the residual stresses at the hole may be near to zero, a further set of ratios based on this assumption is included.

Table 3 : Fatigue Stress Range Ratios for Shrink Fit Analysis, Autofrettage Analysis and Autofrettage Experiment

	Equivalent Autofrettage	Shrink - Fit	Autofrettage (Analysis)	Autofrettage (zero residual stress)
Case 1	40%	1.62	1	1.21
	50%	2.19	_	_
	60%	2.96	1.02	1.01
	80%	_	1.10	0.89
Case 2	40%	1.40	1.10	0.59
	50%	1.77	_	_
	60%	2.20	1.13	0.50
	80%	_	1.12	0.43
Case 3	40%	1.06	1.17	0.53
	50%	1.25 (1.21)	_	_
	60%	1.44 (1.09)	1.35	0.44
	80%	_	1.53	0.38
Case 4	40%	0.64	0.85	0.37
	50%	0.69 (0.53)	_	_
	60%	0.74 (0.46)	0.72	0.28
	80%	_	0.61	0.24

Note 1: Shrink-fit results are predominantly elastic. Where yielding occurs the equivalent elastic/plastic result is given in parentheses.
Note 2: See Ref [4] for full details of autofrettage analyses

It is important to note that the differences between predicted and measured residual stresses at the hole reported in [4] arise from elastic/perfectly plastic assumptions which do not fully represent the actual notch effects. In the case of the shrink-fitting process, which is overwhelmingly elastic in nature and in which reversed yielding does not occur, such problems do not arise.

In fact the assumption of equal initial defect sizes at hole and bore is far from reality, since in the application under consideration (a large caliber gun tube) the initial crack depth at the bore due to heat-checking is likely to be several times larger than that at the hole.

In the case of autofrettage there is some evidence that failure may initiate from the hole in cases of over 60% autofrettage (overstrain) (Ref [4]). In the case of shrink-fit it appears that the critical location will undoubtedly be at the bore; there are two reasons for this assertion:

a. The fatigue stress range is higher at the bore for Cases 1, 2 and 3

b. The initial defect sizes are larger at the bore (at least twenty times greater than at the hole, [4]). Referring to Equation (4) it is noted that with such a ratio of initial defect sizes, failure will occur from the bore down to a fatigue stress ratio of 0.61, assuming a Paris law exponent, m = 3. Clearly such a figure is not achieved in any of the shrink-fit cases under consideration.

This observation leads to a straightforward prediction of fatigue lifetime for the shrink-fit design of Case 2 which has the same value of a_i as the autofrettage design. Since there are laboratory lifetime figures available for failures originating from the bore of heat-checked cannon tubes made of the same material, [4], Equation (2) indicates that, for such equal initial crack sizes, the predicted lifetime is given by:

Lab Lifetime x (Lab Effective Stress range / New Effective Stress range)^m (5)

Some existing data is provided in Table 4, and is used to predict lifetimes for Case 2. This is further compared with experimental data relating to failure from the hole in the autofrettaged design; in the latter case a ratio a_B/a_H = 58.8 is assumed in accordance with [4].

In the case of the 60% overstrain of a plain tube, the tube was subjected to a cyclic bore pressure of 393 MPa resulting in a positive bore stress range of 717.8 MPa. Prior to cyclic pressurization the tube had been fired sufficiently for initial bore heat-check cracking to be fully established. Thus the initial crack size at the bore may be assumed to be the same in other heat-checked tubes. In the case of shrink-fitting, with failure from the bore, a simple application of Equation (5) provides the predicted lifetimes shown in Table 4.

Turning to the case of autofrettage, with failure from the hole, Ref [4] contains details of the calculation of the ratio a_B/a_H where a_B relates to heat-checking and a_H relates to surface finish. The a_B/a_H ratio calculated in [4] is 58.8. Equation (2) then provides a lifetime prediction of 9,005 cycles with cyclic pressurization of 434 MPa. This lifetime is the same for all percentage overstrains since it is observed experimentally, [4], that residual hoop stress at the hole is near zero.

An additional objective of this work was to determine whether, by adjusting the semi-circular groove configuration, effectively making it a semi-ellipse with a reduced radius of curvature at the critical location, there would be any improvement in lifetime. The conclusion is clear, since the notch is not the primary fatigue failure location, any reduction in the local stresses will have no effect upon an overall lifetime which is governed by failure from a relatively remote location, namely the bore.

Table 4 : Predicted Lifetimes for Proposed Shrink-Fit design (Case 2)

60% overstrain of plain tube - Experimental result; (Ref 4)				
Stress range (MPa) (B)	717			
Life (Cycles)	10,873			
Shrink Fitting - Predicted Lifetimes of Perforated Tube;				
Equivalent Autofrettage (%)	40%	50%	60%	_
Stress range (MPa) (B)	732	624	562	_
Life (Cycles) (B)	10,234	16,549	22,570	_
Autofrettage - Predicted Lifetime for All % overstrains of perforated tube (based upon experimental result); Ref 4				
Equivalent Autofrettage (%)	40%	_	60%	80%
Stress Range (MPa) (H)	1511	_	1511	1511
Life (Cycles) (H)	9,005	_	9,005	9,005

Notes:
1. All predicted lifetimes are for Case 2 geometry and loading with cyclic bore pressure of 434 MPa
2. (B) indicates failure originating from bore
3. (H) indicates failure originating from hole
4. a_B/a_H = 58.8 throughout (Ref 4)

A NORMALIZED, PARAMETRIC DESIGN REPRESENTATION

For future design purposes it may be more appropriate to present the results herein in normalized form, since by varying the major parameters (amount of shrink-fit and radius of interface) the crucial fatigue stress range ratio, R_σ, will vary and may cause the critical location to shift from bore to hole. Fig. 4 shows the variation of R_σ with normalized interface radius, R_N, and normalized interface pressure, P_N, where:

$$R_N = (Ri - R1)/(R2 - R1) \qquad \text{and} \qquad P_N = E\alpha T/P$$

where P is pressure acting upon bore and bore crack surfaces. Note that all results presented in normalized form are based upon elastic analyses.

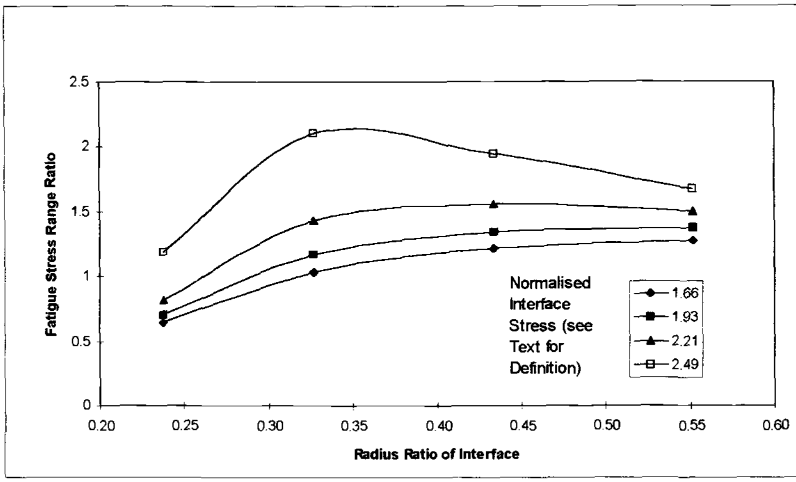

Figure 4 : Normalized Representation of Fatigue Stress Range Variation

As discussed earlier, the regions within which the R_σ surface shown in Fig. 4 dips below unity indicate a potential shift of failure location from bore to hole for the case of equal length initial defects at the two locations. In other cases the shift will occur in accordance with Equation (4).

SUMMARY AND CONCLUSIONS

This work addressed the fatigue lifetimes of thick cylinders containing multiple, axial holes within the wall. The holes are semi-circular and were created by thermally shrink-fitting an outer (plain) tube onto an inner tube which contains a periodic array of semi-circular notches. Finite Element analyses indicate that the residual stresses so introduced are compressive in the two principal potential failure locations, namely the bore and the notch root.

Superposition of an elastic stress field due to bore pressurization permits the calculation of positive cyclic stress ranges from bore to hole. This in turn may be used (after taking account of pressure infiltrating bore cracks) to calculate Fatigue Stress Ranges at the bore and hole. These indicate that, for most cases considered, the critical fatigue location is the bore and that there is no benefit in seeking to reduce the stress concentration at the notch root.

Further comparison of an alternative method of introducing advantageous residual stresses, namely autofrettage of two of the cases considered, indicates significant lifetime advantages for the shrink-fit design.

Finally, a normalized design presentation is proposed which permits a rapid assessment of the major design parameters, interference and shrink-fit radius.

ACKNOWLEDGMENTS

Three of the authors (SNE, APP, and TJB) acknowledge partial support for this work via the European Research Office of the US Army Research, Development and Standardization Group (UK).

REFERENCES

[1] Underwood, J. H., and Parker, A. P., "Fatigue Life Analysis and Tests for Thick-Walled Cylinders Including Effects of Overstrain and Axial Grooves", ASME Conference on Pressure Vessels & Piping , Hawaii ,1995 (In Press), Published in ASME J. Pressure Vessel Tech., Vol. 117, 222-226 (1995).

[2] Parker, A. P. and Underwood, J. H., "Stress Intensity, Stress Concentration, and Fatigue Crack Growth Along Evacuator Holes of Pressurized, Autofrettaged Tubes", ASME PVP Conference Proceedings, Hawaii, 1995 (In Press), Published in ASME J Pressure Vessel Tech., Vol 118, 336-342 (1996).

[3] Endersby, S. N., Bond, T. J. and Parker A. P., "Stress Concentration, Stress Intensity and Fatigue Crack Growth Along Angled Evacuators of Pressurized, Autofrettaged Tubes", (In preparation for publication, 1996).

[4] Parker, A. P., Endersby, S. N., Bond, T. J. and Underwood, J. H., Lee, S. L. and Higgins, J., "Stress Concentration, Stress Intensity and Fatigue Lifetime Calculations in Autofrettaged Tubes Containing Axial Perforations Within the Wall", ASME PVP Conference Proceedings, Montreal, July 1996 (In Press). (Submitted for publication in ASME J. Pressure Vessel Tech., 1996).

[5] Parker, A P, Underwood, J H, "Some Methods of Representing Fatigue Lifetime as a Function of Stress Range and Initial Crack Length", presented at ASTM 28th National Symposium on Fatigue and Fracture Mechanics, Saratoga Springs, June 1996 (Accepted for publication in Fatigue and Fracture Mechanics: 28th Volume, ASTM STP 1321, J. H. Underwood and B. D. MacDonald, M. R. Mitchell, Eds., American Society for Testing and Materials, 1997).

Edward Troiano[1], John H. Underwood[1], Anthony Scalise[1], G. Peter O'Hara[1], Daniel Crayon[2]

FATIGUE ANALYSIS OF A VESSEL EXPERIENCING PRESSURE OSCILLATIONS

REFERENCE: Troiano, E., Underwood, J.H., Scalise, A., O'Hara, G.P., Crayon, D., "**Fatigue Analysis of a Pressure Vessel Experiencing Pressure Oscillations**", Fatigue and Fracture Mechanics: 28th Volume, ASTM STP 1321, J.H. Underwood, B.D. Macdonald, M.R. Mitchell, Eds., American Society for Testing and Materials, 1997.

ABSTRACT: A pressure vessel, designed and tested under laboratory conditions for tens of thousands of cycles, failed in service after only a few cycles. Thousands of oscillatory pressure reversals have been measured at each loading. However, the predominance of the stress amplitudes were well below the critical threshold values necessary to initiate fatigue cracking.

Analysis has demonstrated that the disparity between lab cycling and field loading conditions cannot be explained simply by mechanical loading alone. Further investigation into the problem revealed that an extremely aggressive environment, the by-products of the internal combustion from within the pressure vessel, along with high temperatures, pressures, and other sources of high tensile loading all contribute to the short fatigue life of the vessel.

KEY WORDS: low cycle fatigue, pressure oscillation, pressure vessel, cumulative damage model, residual stresses, hoop stress, radial stress, fatigue cracks, Palmgren-Miner rule, environmentally assisted cracking

---

[1] Research Engineer, US Army Research Development and Engineering Center, Benet Laboratories, Watervliet, New York, 12189

[2] Mechanical Engineering Technician, US Army Research Development and Engineering Center, Benet Laboratories, Watervliet, New York, 12189

INTRODUCTION

Often it is necessary to connect sections of a pressure vessel in order to attain the required configuration of the overall component. This connection requires some form of sealing at the section interfaces in order to preserve continuity and to produce a leakproof joint (Figure 1). The oil and piping industries have sought various types of connectors that provide such a leakproof joint [1,2].

In the case of cannons, the sealing of the pressure vessel sections is further complicated by the presence of pressure oscillations associated with the combustion process. As many as two thousand pressure reversals have been observed during each firing cycle. This paper will address several important issues related to the sealing of such pressure vessels experiencing oscillations. They include;

1. The effect of the pressure oscillations on the overall life of the pressure vessel
2. The source of the tensile loads necessary to cause failure
3. The role of environmentally assisted cracking, and its impact on failures
4. Conclusions and recommendations necessary to prevent further failures

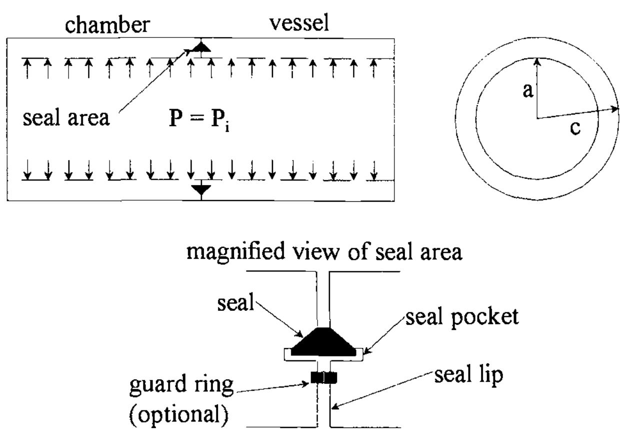

FIGURE 1 - Schematic of Seal Concept, Geometry and Loading

HISTORICAL PROSPECTIVE

Historically, large caliber thick walled cannon pressure vessels like the type investigated here required only a simple mechanical wedge block assembly that completely sealed the rear face of the pressure vessel. For various reasons which will not be explored here, the use of a wedge block was not deemed practical for this application, and forced the designers to pursue other means of sealing. The sections being sealed are hereafter referred to as the chamber and vessel (Figure 1). The chamber material is PH 13-8Mo stainless steel heat treated to 1 276 MPa, and the vessel is A723 Grade 2 steel heat treated to 1 172 MPa. Other mechanical properties are defined in Table 1. The seal is 17-4 PH stainless steel heat treated to 627 MPa. The vessel has been mechanically autofrettaged, so that the elastic/plastic boundary is 55% through the vessel wall. Basic geometric features include an internal radius of 78 mm and an outside radius of 162 mm. Internal peak pressures are nominally 405 MPa.

TABLE 1 -- Properties of Materials Investigated

Material	Tensile Strength, σ_{UTS} (MPa)	0.2%Yield Strength, σ_{YS} (MPa)	Young's Modulus, E (GPa)	strain @ 10^6 cycles [3] (%)	true fracture strain [4] (%)
PH 13-8Mo	1 344	1 276	200	0.241	15.0
A723	1 275	1 172	207	0.167	14.6

The detailed sealing concepts investigated in this study are described in Figure 2. The original sealing concept (configuration #1) included a two-surface wedge seal, encased in a rectangular shaped seal pocket at the radial wall location, r/c, of 0.68. Configuration #1 also included a guard ring located at the radial wall location of 0.62. The guard ring possessed four through holes located at 0, 90, 180 and 270 degrees from

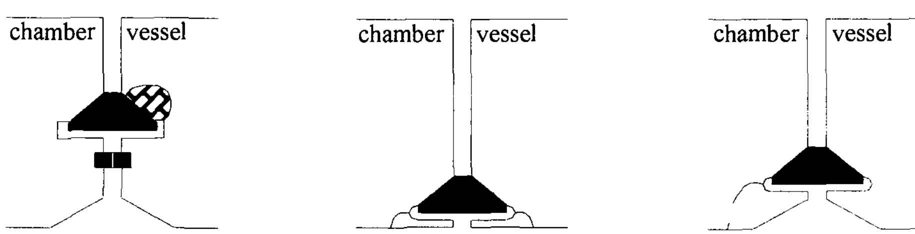

configuration #1
C-R crack orientation
5 cycles

configuration #2
R-L crack orientation
30 cycles

configuration #3
R-L crack orientation
100 cycles

FIGURE 2 - Historical Prospective of Seal Configurations

top center position of the pressure vessel. The guard ring's function is to provide a barrier between the internal combustion by-products and the seal. The through holes in the guard ring are necessary in order to allow pressure to enter the seal pocket and force the two seal surfaces against their mating surfaces on the chamber and vessel respectively.

Cracking of the vessel portion of configuration #1 was observed after only five loading cycles. Cracking initiated in the C-R orientation (a plane perpendicular to the circumferential direction, with crack growth predominately in the radial direction), at a mid-wall location emanating from the rectangular seal pocket. At the time of the failure very little was known about the nature of the pressure oscillations. The cracking was in an area of known tensile stresses, consisting of the applied hoop firing stresses and residual hoop autofrettage stresses. Although the combination of applied and residual stresses is well below the yield strength of the vessel material (see stress verses wall location plot in Figure 3), the sharp stress riser of the rectangular seal pocket may have concentrated the local stresses to about the level of the yield stress. At this time further investigation of configuration #1 was halted because it was felt that the source of the stresses and the failure had been characterized well enough to proceed to configuration #2.

The configuration #2 concept took the lessons learned in configuration #1 and made what were thought to be significant improvements to the seal area. Major changes included moving the seal closer to the inside diameter of the vessel and chamber to a radial wall location of 0.55, and removing the rectangular seal pocket in lieu of a semicircular (r=3.2 mm) seal pocket. As can clearly be seen in the plot in Figure 3, the configuration #2 seal and seal pocket is at a location of nearly zero hoop stresses. The semicircular seal pocket further reduced the local high stresses resulting from the sharp stress concentrator that may have contributed to the configuration #1 failure. Seal lips that were integral with both the chamber and vessel replaced the guard ring, for protection of the seal. Cracking of configuration #2 occurred after approximately 30 loading cycles. Cracking initiated at the root of the seal pocket notch, in the R-L orientation (a plane perpendicular to the radial direction, with crack growth predominately in the longitudinal direction), in both the chamber and vessel. Both seal pockets had nearly identical cracks which

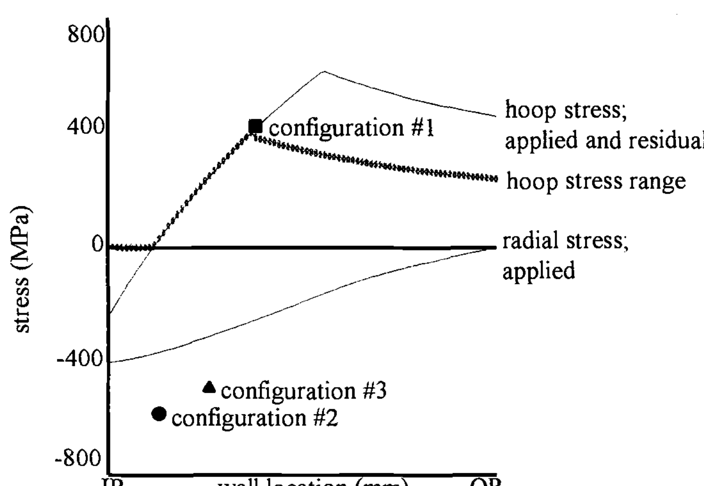

FIGURE 3 -Theoretical Stress Distribution taking into effect Lame Stresses and Autofrettage Stresses, Points Indicate Effects of K_t

occurred at the same radial location, and eventually grew approximately 50 mm in length along the root of the seal pockets. During testing of configuration #2 the presence of the pressure oscillations were becoming evident. However, as in configuration #1, the full extent of the pressure oscillation was not understood.

Configuration #3 had the same seal and seal pocket as configuration #2. The main difference in the two configurations was that the location of the seal was now at a radial wall location of 0.62. This wall location, although clearly not in as favorable a hoop stress region, was at a location that allowed the designers the opportunity to provide a stiffer seal lip while also providing the necessary protection of the seal itself. Configuration #3 failed in a similar fashion to configuration #2 after 100 loading cycles. A radial stress induced crack (R-L orientation) emanated from the root of the seal pocket on the chamber side, and grew approximately 50 mm in length until a section of the seal lip became dislodged. Unlike the failure of configuration #1, the source of the radial stress that initiated the crack at the roots of the seal lips was not known, and propritary concerns prevented any definitive investigation. Analysis of possible sources of radial stresses near the seal is given in a following section. During testing of configuration #3 the full extent of the pressure oscillations that were being experienced did become evident. The extent of these pressure oscillations will be discussed in the next section.

OSCILLATION BEHAVIOR

Typically, large caliber cannon pressure vessels like the one investigated here experience a pressure versus time trace that is relatively smooth and of a sinusoidal waveform, rising from zero to peak pressure and back to zero in approximately 0.05 seconds. Oscillations are often observed during a normal loading cycle. However, the relative number and magnitude of these oscillations are typically very small. The vessel and chamber investigated here experienced a different, more complex loading history. A strain range-time plot, as measured by hoop strain gages placed on the outside diameter of the chamber, can be seen in Figure 4. In this case, more than 1 400 strain reversals were measured, however in other cases as many as 2 000 strain reversals have been recorded. One of the major concerns with this loading history is that the magnitudes of some of the strain reversals exceed the average nominal strain that is typically experienced. The data depicted in Figure 4, for configuration #1, was analyzed, and a histogram of the number of occurrences at each strain range and R-ratio was made (these nominal strains were also used to calculate local strains for configuration #2 and configuration #3). The results can be seen in Figure 5. Analysis of the histogram shows that 68% of occurrences are in the 0% to 5% of maximum strain range, and 90% of the occurrences occur between 0% and 15% of the maximum strain range.

STRESSES IN THE SEAL AREA

Stresses in the vessel and chamber arise from two forms of loading, namely Lamé stresses [5] resulting from the internal pressure, and residual stresses resulting from the

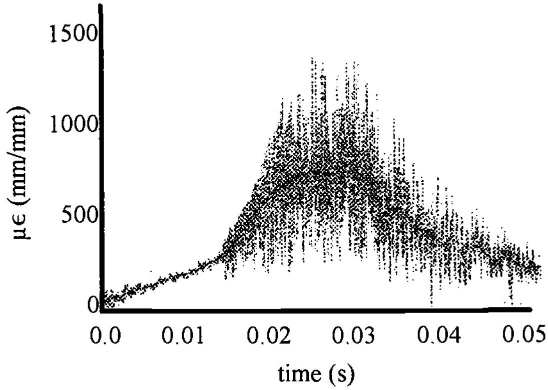

FIGURE 4 - Typical Strain verses Time Plot Showing Loading Oscillations

autofrettage process [6,7].

The resultant hoop stress includes the Lamé hoop stresses

$$\sigma_{hoop\text{-}Lame} = \frac{a^2 P_i}{c^2 - a^2}\left(1 + \frac{c^2}{r^2}\right) \tag{1}$$

and the autofrettage residual hoop stresses

$$\sigma_{hoop\text{-}autofrettage} = \sigma_{YS}\left[\left(\frac{a^2}{c^2-a^2}\right)\left(1+\frac{c^2}{r^2}\right)\left(\frac{\rho^2-c^2}{2c^2} - \ln\left(\frac{\rho}{a}\right)\right) + \left(\frac{\rho^2+c^2}{2c^2} - \ln\left(\frac{\rho}{r}\right)\right)\right] \tag{2}$$

which is valid in the range $a < r < \rho$, and

$$\sigma_{hoop\text{-}autofrettage} = \sigma_{YS}\left(1+\frac{c^2}{r^2}\right)\left[\frac{\rho^2}{2c^2} + \frac{a^2}{c^2-a^2}\left(\left(\frac{\rho^2-c^2}{2c^2}\right) - \ln\frac{\rho}{a}\right)\right] \tag{3}$$

which is valid in the range $\rho < r < c$. Where a is the inside radius, c is the outside radius, r is the radial location of interest, P_i is the internal pressure, σ_{YS} is the material yield strength and ρ, defined as the elastic/plastic interface is

$$\rho = (c-a) * \frac{\%autofrettage}{100} + a \tag{4}$$

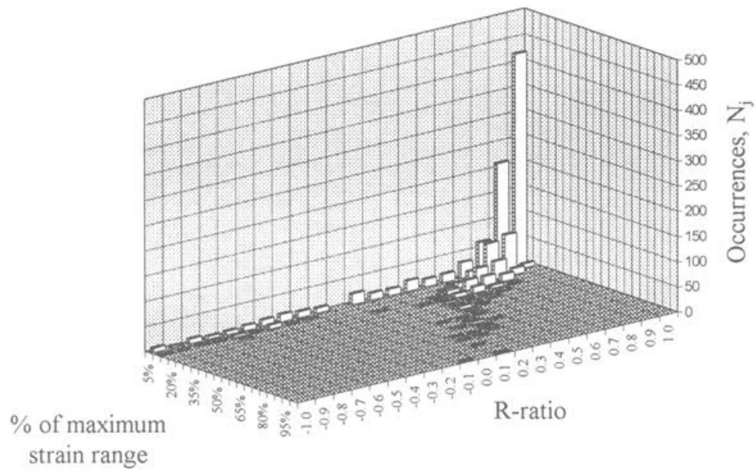

FIGURE 5 - Histogram of Occurrences, R-ratio, and Hoop Seal Area Strain Range

The superposition of these stresses results in the total hoop stress defined as

$$\sigma_{hoop-total}=\sigma_{hoop-autofrettatge}+\sigma_{hoop-Lame} \tag{5}$$

The total hoop stress (at maximum pressure) from Equation 5, and the resultant tensile hoop stress range is plotted in Figure 3 for configuration #1. The configuration #1 point lies directly on the hoop stress profile because there is no stress concentrator in the hoop orientation, so that Equation 5 does not require a K_t scaling factor.

In a similar fashion, the Lamé radial stress is expressed as

$$\sigma_{radial-Lame}=\frac{a^2P_i}{c^2-a^2}(1-\frac{c^2}{r^2}) \tag{6}$$

and the autofrettage residual radial stress is

$$\sigma_{radial-autofrettage}=\sigma_{YS}[(\frac{a^2}{c^2-a^2})(1-\frac{c^2}{r^2})(\frac{\rho^2-c^2}{2c^2}-\ln(\frac{\rho}{a}))+(\frac{\rho^2-c^2}{2c^2}-\ln(\frac{\rho}{r}))] \tag{7}$$

which is valid in the range $a < r < \rho$, and

$$\sigma_{radial-autofrettage}=\sigma_{YS}(1-\frac{c^2}{r^2})[\frac{\rho^2}{2c^2}+\frac{a^2}{c^2-a^2}((\frac{\rho^2-c^2}{2c^2})-\ln\frac{\rho}{a})] \tag{8}$$

which is valid in the range $\rho < r < c$.

At first glance it might seem that a typical stress concentration factor for configuration #2 and configuration #3 in the R-L orientation would be greater than 3.0, due to the fact that both configurations possess a semicircular seal pocket whose depth is greater than its radius. But this is not the case. Finite element modeling (FEM) of the seal and seal pocket areas was accomplished utilizing Lamé and autofrettage loading as well as a small preload on the seal which prevents gases from escaping during the lower pressure stages of loading. The results of the FEM indicate that the K_t associated with the internal pressure Lamé loading is approximately 1.0. Since the seal pocket is pressurized to the same pressure as the vessel and chamber, it makes sense that the resultant stress concentration at the seal pocket notch would be negligible. For the autofrettage loading case, the FEM predicts stresses which are 60% higher than those predicted for the unnotched case. Hence a K_t of 1.6 for the radial autofrettage stress was utilized. The resultant total radial stress can be represented as

$$\sigma_{radial-total}=1.6\ \sigma_{radial-autofrettatge}+\sigma_{radial-Lame} \tag{9}$$

The resultant radial stresses (at maximum pressure) for configuration #2 and configuration #3, accounting for the previously described stress concentrators are indicated in Figure 3. The maximum stress values (and stress ranges) from Equation 5 and Equation 9 are used to determine the local stress ranges at the failure locations in the next section.

LABORATORY MODELING OF SEAL AREA AND COMPARISON WITH FIELDED SYSTEM

Now that the stresses which are typically seen in this type of pressure vessel are known, and the oscillatory behavior of the loadings has been well characterized, the next logical step was to see what effects their combination had on the overall life of the component. The method of comparison utilizes the well known Palmgren-Miner rule [8].

$$B_f\ [\Sigma\frac{N_j}{N_{fj}}]_{one\ repetition}=1 \tag{10}$$

In Equation 10, N_j is the number of occurrences during the loading cycle at a particular strain level in the fielded system, N_{fj} is the experimentally derived life the component should survive at the given strain level in the laboratory, and B_f is the total number of cumulative repetitions to failure.

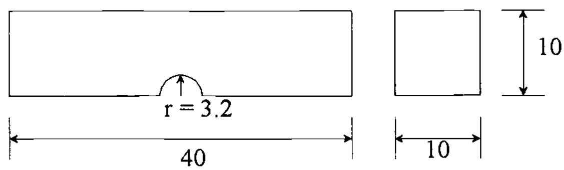

FIGURE 6 - Specimen Geometry Modeling Notch Detail, all Dimensions in millimeters

Since N_j is already known (Figure 5), the only quantity left to establish is N_{fj}. A simple three point bend specimen (Figure 6) with a semicircular notch that models the seal pocket was used. The notch detail is geometrically identical to the seal pocket notch in configuration #2 and configuration #3, and possesses a K_t of 3.0 in uniaxial bend loading (in this case). Testing was conducted in load control, for both A723 (Figure 7) and PH 13-8Mo (Figure 8) at three load ratios, R=0.1, R=0.25, and R=0.5. Laboratory modeling was concentrated in the 1 000 < N_{fj} < 25 000 cycles to failure region. The data generated was plotted and three distinct regions of fatigue were investigated. The data in the 1 000 < N_{fj} < 25 000 region was curve fit with a log-log equation of the form of the Coffin-Manson equation [8]. The data in the 1 < N_{fj} < 25 000 cycle region was then extrapolated to the true fracture strain for each material (at N_{fj} ~ 1 cycle), and curve fit with a similar log-log equation. The data in the 25 000 < N_{fj} < 1E+6 cycle region was extrapolated to the strain at a life of 1E+6 cycles, and curve fit with a similar log-log equation. The latter two regions are expressed as dotted lines on Figure 7 and Figure 8.

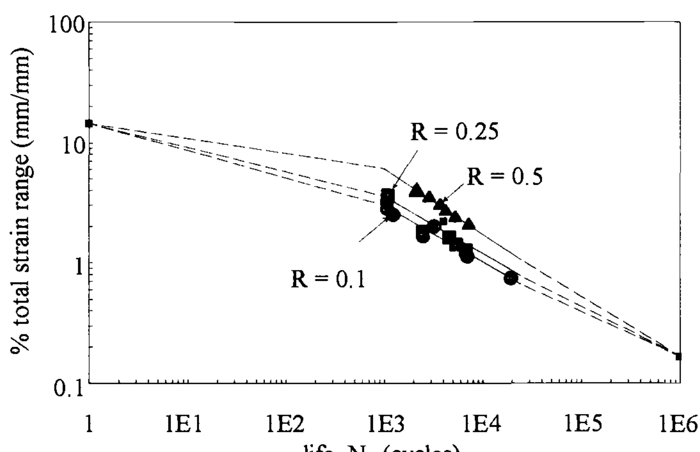

FIGURE 7 - Low Cycle Fatigue Data A723 Steel, σ_{YS} = 1 172 MPa, K_t = 3.0

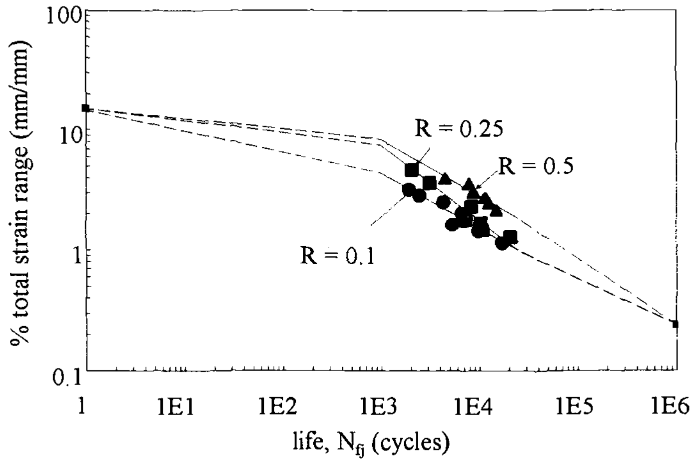

FIGURE 8 - Low Cycle Fatigue Data PH 13-8Mo Stainless Steel, σ_{YS} = 1 276 MPa, K_t = 3.0

The effects of the compressive residual stresses for R < 0 have not been properly analyzed in the laboratory. Although no attempt has been made to model these desirable residual stresses, it is known that their omission in the analysis will lead to conservative results [9]. In the analysis all of the N_j with R $\leq$ 0.1 were modeled in the laboratory at R = 0.1, those with 0.2 $\leq$ R $\leq$ 0.3 were modeled in the laboratory at R = 0.25, and those with R $\geq$ 0.4 were modeled at R=0.5. The stresses predicted by Equation 5 and Equation 9 are in the elastic region, therefor Hookes law ($\epsilon = \sigma/E$) was utilized to convert these seal pocket stresses into seal pocket strains. Once the conversion is made, the use of Figure 7 and Figure 8 allow the N_{fj} to be calculated. At this point B_f for each material and configuration can be determined.

Analysis of Configuration #1 - Because configuration #1 failed in the C-R orientation, and the hoop stresses in the seal pocket region (Equation 5) are known to be tensile, the use of Equation 10 predicts that the A723 steel vessel should survive a total of B_f = 9 400 repetitions before failure. The PH 13-8Mo chamber, which possesses better fatigue resistance than the A723 steel should survive B_f = 16 200 repetitions before failure. Both predictions are orders of magnitude higher than the five cycles to failure in the fielded system.

Analysis Configuration #2 and Configuration #3 - From Figure 2 we can see that each of these configurations failed in the R-L orientation as a result of a radial tensile stress, yet according to the results in Figure 3, the radial stresses in the area of the seal pocket are compressive. The type of analysis used for configuration #1 predicts infinite life for these configurations, which we know is not the case.

The analysis up to this point has concentrated on Lamé and autofrettage stresses only, and as can clearly be seen from the previous analysis, these loadings alone could not have caused these failures. It is obvious that some other loadings which induce tensile stresses in the seal pocket region must be present. The next section explores these other sources of loading.

OTHER SOURCES OF TENSILE LOADING

Since the previous section could not satisfactorily explain the source of radial tensile stresses, it was necessary to investigate other potential sources of loading. There is compression loading in this case that consists of two components (Figure 9A), namely the compressive distributed loading of the seal on the seal pocket face ($\sigma_{\text{seal contact}}$), and the contact loading between adjacent sections ($\sigma_{\text{adjacent sections}}$) of the chamber and vessel. This type of loading has a direct analogy to the Timoshenko and Goodier [10] analysis of a hole in a plate under remote compression loading (Figure 9B). This analysis shows that a hole in a plate under remote compressive loading will set up a tensile stress equal in magnitude to the remotely applied compressive stress, as shown in Figure 9B. Although the symmetry and loading are different in the two cases outlined in Figure 9A and 9B, the comparison of the two situations is logical. The correct way of modeling the stresses resulting from these end loads is through finite element analysis. This work is underway, but not yet completed.

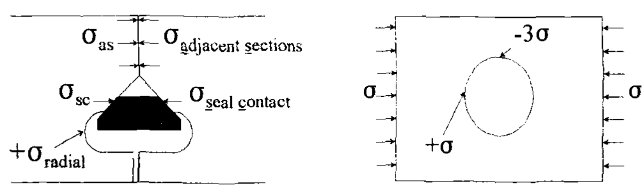

FIGURE 9 - (9A) Possible Source of Tensile Radial Loads
(9B) Hole in a Plate Analogy

Although the exact extent of the end loads is unknown, an approximate analysis of these stresses utilizing the shear strength of the thread that couples the chamber to the vessel, and the seal contact stresses was utilized. The stress resulting from the adjacent sections was approximated by assuming that the threads that couple the adjacent sections were loaded to 25% of their maximum shear load [5], and that there is a 20% loss of loading due to frictional effects. The seal contact stresses were approximated by assuming that a compressive stress equal in magnitude to the yield strength of the seal material was present [11]. Assuming these stresses along with the previously mentioned Lamé and autofrettage stresses, the radial stress distribution of Equation 9 can be modified to

$$\sigma_{radial\text{-}total} = 1.6\ \sigma_{radial\text{-}autofrettatge} + \sigma_{radial\text{-}Lame} + \sigma_{adjacent\ sections} + \sigma_{seal\ load} \tag{11}$$

The resultant stresses at the seal for configuration #2 and configuration #3 were calculated, along with the critical flaw size (a_c) approximated by

$$K_{applied}=1.12\ \sigma_{applied}\sqrt{\pi\ a_c} \tag{12}$$

The results can be seen in Table 2.

Note that the critical flaw sizes calculated by the previously outlined approach estimate that the flaws necessary to initiate fast cracking range from 6.5 mm to 12.4 mm. It is extremely unlikely that a flaw of this magnitude existed. Flaws of this size would certainly have been detected in the inspection process.

ENVIRONMENTAL FRACTURE

Thus far the investigation has: shown that the oscillations could not have caused the earlier than anticipated failure of all three configurations; identified the likely source of tensile loading in the seal region for configuration #2 and configuration #3; and clearly shown that a classic fast fracture is unlikely due to the extremely large critical flaw sizes needed. This section takes the classic fracture mechanics approach one step further, and investigates the possibility that environmentally assisted cracking caused the premature failures.

TABLE 2 -- Fracture Properties, Radial Stresses and Calculated Critical Flaw Sizes

Material	config.	K_{Ic}@ 25°C (MPa√m)	$\sigma_{radial\text{-}total}$ (MPa)	a_c (mm)	K_{IEAC}@ 25°C (MPa√m)	$\sigma_{radial\text{-}total\text{-}EAC}$ (MPa)	a_{EAC} (mm)
PH 13-8Mo	#2	148	670	12.4	15	950	0.063
	#3	148	766	9.5	15	961	0.062
A723	#2	123	670	8.5	15	950	0.063
	#3	123	766	6.5	15	961	0.062

Internal combustion gasses present in both the chamber and vessel are known to be high in hydrogen concentration. In the presence of hydrogen, materials such as PH 13-8Mo and A723 are highly susceptible to accelerated cracking, to the point where fracture toughness values drop to dangerously low levels. Environmentally assisted fracture toughness, K_{IEAC}, test results measured by Vigilante et al. [12] have indicated that the threshold fracture toughness for both PH 13-8Mo and A723 is approximately 15 MPa√m, a small fraction of the K_{Ic} value in Table 2. Another critical feature necessary to promote environmentally assisted cracking is the presence of tensile stress. The previous section identified the possible source of tensile stresses. It is believed that hydrogen may be present at the fracture site long after the Lamé stresses have dissipated, accompanied by tensile radial stresses arising from the autofrettage, adjacent section contact, and seal load contact. Modifying Equation 11 to reflect these changes results in

$$\sigma_{radial\text{-}total\text{-}EAC} = 1.6\ \sigma_{radial\text{-}autofrettatge} + \sigma_{adjacent\ sections} + \sigma_{seal\ load} \tag{13}$$

The resulting stresses ($\sigma_{radial\text{-}total\text{-}EAC}$), and calculated critical flaw sizes (a_{EAC}) are shown in Table 2. Observe that the calculated critical flaw sizes, in the presence of a hydrogen rich environment are 0.062 mm to 0.063 mm. These small flaw sizes are much more likely to have been present than the larger a_c previously predicted.

SUMMARY

1. The oscillations that are present in this pressure vessel were not the cause of the premature failures. They are an interesting oddity, but they had no significant effect on the failure of the pressure vessel. The predominance of the oscillations present are of such a small magnitude that they are below the level of strain necessary to induce fatigue cracking.

2. The driving force behind the C-R orientated failure in configuration #1 appears to be the autofrettage tensile hoop orientated stress. The recommendation to move the seal toward the inner radius, away from the tensile hoop stress region was justified. However, a deleterious tensile radial stress was encountered.

3. The driving force behind the R-L oriented failures in configuration #2 and configuration #3 is the tensile radial stress generated in the seal pocket notch. This stress is the result of the compressive end loading of the contacting chamber and vessel, and the compressive seal loading. Recommended corrective actions to eliminate this type of failure requires the removal of all compressive end loads. The end load associated with the adjacent sections contacting is easily corrected by making sure that the chamber and vessel do not contact during the assembly process. There is no obvious method of removing the seal end loads with this design. Corrective actions are likely to result in a complete redesign of the seal and seal pocket. FEM of this area is necessary before a detailed recommendation can be made.

4. Environmentally assisted cracking as a direct result of the hydrogen rich by-products of the combustion process is the likely candidate for premature failure of all three configurations. Calculation of the critical flaw sizes necessary to induce cracking in the presence of hydrogen are on the order of the size of flaws that could be present with this type of material and manufacturing process.

REFERENCES

(1) API Specification 6A, Specification for Wellhead and Christmas Tree Equipment, Seventeenth Edition, February 1996, Section 10.

(2) Owens, J.H. Seal Integrity and Connector Clamping Forces at the Subsea Wellhead, 15th Annual Offshore Technology Proceedings, 1983.

(3) Aerospace Structural Metals Handbook, Mechanical Properties Data Center, Belfour Stulen Inc. 1971.

(4) Troiano, E., Underwood, J.H., Crayon, D., "Low Cycle Notched Fatigue Behavior and Life Predictions of A723 High Strength Steel", Fatigue and Crack Growth: Environmental Effects, Modeling Studies and Design Considerations, PVP-Vol 306, 1995

(5) Shigley, J.E. and Mitchell, L.D., Mechanical Engineering Design, Fourth Edition, McGraw Hill, New York 1983.

(6) Prager, W. and Hodge, P.C., Theory of Perfectly Plastic Solids, J. Wiley and Sons, New York, 1951.

(7) Hill, R., The Mathematical Theory of Plasticity, Oxford University Press, 1967.

(8) Dowling, N.E., Mechanical Behavior of Materials, Prentice Hall, 1993.

(9) Parker, A.P., "Stress Intensity Factors, Crack Profiles and Fatigue Crack Growth Rates in Residual Stress Fields", Residual Stress Effects in Fatigue, ASTM STP 776, 1982.

(10) Timoshenko, S.P., and Goodier, J.M., Theory of Elasticity, McGraw Hill, 1970.

(11) Roark, R.J. and Young, W.C., Formulas for Stress and Strain, McGraw Hill, 1975.

(12) Vigilante, G.N., Tauscher, S., Underwood, J.H., Crayon, D., Sage, T., and Troiano, E., "K_{IEAC} Test of High Strength Steels and Nickel Based Alloys in Hydrogen Environments using the Bolt Loaded Compact Specimen", Fatigue and Fracture Mechanics 28th Volume, STP 1321, J.H. Underwood, B.D. Macdonald, M.R. Mitchell, Ed., American Society for Testing and Materials, Philadelphia, 1997.

K. S. Kim[1] and Y. M. Baik[1]

FATIGUE CRACK GROWTH IN THE HIGHLY PLASTIC REGIME

REFERENCE: Kim, K. S., Baik, Y. M., **''Fatigue Crack Growth in the Highly Plastic Regime''**, Fatigue and Fracture Mechanics: 28th Volume, ASTM STP 1321, J. H. Underwood, B. D. Macdonald and M. R. Mitchell, Eds., American Society for Testing Materials, 1997.

ABSTRACT: This paper evaluates the performance of ΔJ^*, $\Delta J^\wedge$ and ΔK as fracture parameters for center-cracked plate specimens of Alloy 718 under $R_\sigma=0$, nominally elastic and plastic loading at elevated temperatures. The parameters ΔJ^* and $\Delta J^\wedge$ are computed from the results of an elastic-plastic finite element analysis of crack growth. At 538°C the results show, in contrast to the previous results of $R_\varepsilon=-1$ strain control tests, that the correlation of crack growth rates with ΔJ^* or $\Delta J^\wedge$ deviates from the relation of the Paris law type while ΔK gives a satisfactory correlation. The correlation at 649°C is poor for all three parameters, The finite element analysis shows that the crack closing behavior diminishes and eventually disappears as the crack tip plasticity increases due to crack growth or increased applied stress.

KEYWORDS: integral parameters, stress intensity factor, Alloy 718, crack growth, crack closure

The crack growth under plastic loading may not be a desirable situation in reality, however it is often found that failure is initiated at sites where stresses are much higher than expected. These circumstances may occur in structural elements where engineering analysis can not be accurately performed due to various complexities. Stress raisers such as inclusions, porosities or other defects in materials often produce highly localized stress fields resulting in premature failure. Sometimes human errors in the assembly process or misuse of the parts cause high stresses leading to failure. Hot spots in high temperature components may undergo extra damage due to local material softening and stress concentration. In these circumstances it is possible that cracks initiate in the early stage of the component life, and the remaining life is determined by the crack propagation life. In this respect, it is meaningful to investigate methods for the prediction of crack propagation in the plastically loaded regime.

[1]Professor and Graduate student, respectively, Department of Mechanical Engineering, Pohang University of Science and Technology, Pohang, Korea 790-784.

The linear elastic fracture mechanics (LEFM) approaches are often reported to be unsuitable for prediction of crack growth in the plastic regime [1-4]. In the mean time, the fracture parameters in the nonlinear regime such as the J-integral and the crack tip opening displacement (CTOD) have not been used in applications involving cyclic loads as much as the LEFM parameters are utilized. The operationally defined ΔJ approaches, for instance Dowling et al. [1,2], McClung et al. [3], have been applied with some success to simple loading conditions, however the computation of the energy density from the hysteresis loop may be prohibiting its application to more complex loading. The CTOD approach is basically similar to ΔJ in view of their relationship.

In recent years Kim et al.[4,5] used integral parameters to correlate crack growth under strain control at elevated temperatures. A drawback of these parameters is that the physical meaning is ambiguous, while no restrictions are put on the scope of the constitutive relations where these parameters are applicable. Despite this drawback, it was found that Blackburn's integral J* [6] and Kishimoto et al.'s integral J^ [7] correlated satisfactorily Alloy 718 crack growth data at 538°C [4] and Hastelloy-X data at temperatures ranging from 427°C to 982°C [5]. The Alloy 718 data were obtained on single edge notch (SEN) specimens, and the Hastelloy-X data were generated by Jordan et al. [8] on tubular specimens. The nominal stresses applied on the specimens in [4,8] ranged from the elastic to plastic level. The loading condition was R_ε=-1 strain control in both studies. Certainly, these parameters need to be further examined in other situations before finding their places as fracture parameters. The purpose of this paper is to investigate if they can also correlate fatigue crack growth data for center-cracked plate (CCP) specimens under stress control conditions. The performance of the approach based on the stress intensity range (ΔK) is also examined with the crack growth data obtained in this study. The computation of J* and J^ (see the Appendix for the definitions of these parameters) requires a numerical analysis of the crack propagation process. The computational procedure and the results of analysis will be discussed along with the experimental data obtained on Alloy 718 specimens at 538°C and 649°C.

EXPERIMENT

The material tested in this study is the γ"-strengthened nickel-base superalloy Alloy 718. The material procured was round bars with diameter of 19mm produced by Teledyne Allvac Corporation. The bars were supplied as solution-treated at 982°C for 1 hour then quenched in the water. The ladle composition is as shown in Table 1, and the grain size as received was in the range of ASTM 9-10. The bars were cut into a length somewhat longer than the specimen size. They were then aged at 718°C for 8 hours, cooled at 0.8°C/min in the furnace to 631°C, where they

Table 1.-- Chemical Compositions of Alloy 718

Elements	C	S	Mn	Si	Cr	Mo	Co	T	Al
Wt%	0.024	0.0006	0.08	0.04	18.06	2.89	0.30	0.98	0.50
Elements	B	Fe	Cu	Ni	P	Cb	Ta	Nb+Ta	
Wt%	0.004	17.78	0.06	53.92	0.006	5.18	0.02	5.30	

were held for 8 hours, then cooled to room temperature. The surface hardness was R_C=15 and R_C=41 before and after aging, respectively.

The tests conducted in this study are tensile tests, fatigue tests and crack growth tests. The tensile and fatigue test specimens were solid specimens with a diameter of 6mm in the gage section. The CCP specimens for crack growth tests had threaded ends and a flat gage section that was electric-discharge machined (EDM) and then ground. The width of the gage section was 15mm, the length 50mm and the thickness 3mm. An EDM notch of length 3mm was introduced in the middle of the specimen. A thermo-couple wire was spot-welded near the center of the specimen. Tests were conducted on a closed loop servo-hydraulic testing machine equipped with an induction heating system. All tests were performed in air. Tension tests were performed at two strain rates (0.02%/s, 0.1%/s) at both 538°C and 649°C to examine the rate sensitivity. However, no significant difference was observed. Tensile stress-strain curves showed slight serrated yielding at both 538°C and 649°C. Fatigue tests were performed to generate cyclic stress-strain curves to use in the finite element analysis of crack growth and crack closure. The tests were conducted under R_ε=-1 strain control with strain amplitudes of 0.75% and 1.75%. The strain rates used in the fatigue tests were 0.1%/s and 0.02%/s. Slight reverse strain rate sensitivity was observed, however it was ignored in the finite element analysis because the code did not have the capability to handle strain rate effects. The material showed cyclic softening, as well known. The cyclic stress-strain curves approximated for use in the analysis are shown in Fig. 1.

The crack propagation tests were performed at 538°C and 649°C under R_σ=0 stress control. The maximum applied stresses, S_{max}, and its ratio to the yield stress, S_Y, (in the parenthesis) are as follows: for 538°C, 300MPa (0.6), 450MPa (0.9), 600MPa (1.2); for 649°C, 250MPa (0.55), 375MPa (0.83), 500MPa (1.11). Here, the yield stress is the stress where the stress-strain relation deviates from linearity. One can see that the stress level spreads over the nominally elastic and plastic range. The load was applied at a constant rate, 2.94kN/s. The crack length was measured using a traveling microscope with a magnification ratio of 40. The variation of the half crack length (a) with the number of cycle is shown in Fig. 2 for the six specimens tested. The crack growth rate (da/dN) versus crack length (a) relation was obtained using the secant modulus method. This relation was then used to find the crack growth rates at crack lengths corresponding to the crack tip nodes in the finite element model.

FINITE ELEMENT ANALYSIS

The crack propagation was analyzed for each specimen using an elastic-plastic finite element code used in [4,5]. The constitutive model in this code is based on the subvolume theory by Besseling [9] wherein the material is assumed to consist of several subvolumes of elastic-perfectly plastic materials with different yield stresses. The finite element method used for the plasticity iteration was the initial strain method in which the stiffness matrix is based on the elastic properties and the residual plastic force is updated in each plastic iteration.

A quarter of the gage section of the specimen was modeled in consideration of the symmetry. The element type is a 3 noded constant strain triangle. The number of nodes and elements were 638 and 1170, respectively. The crack path element size was 0.15 mm, which is 1/50 of the width (W/2) of the model. The load was uniformly distributed over

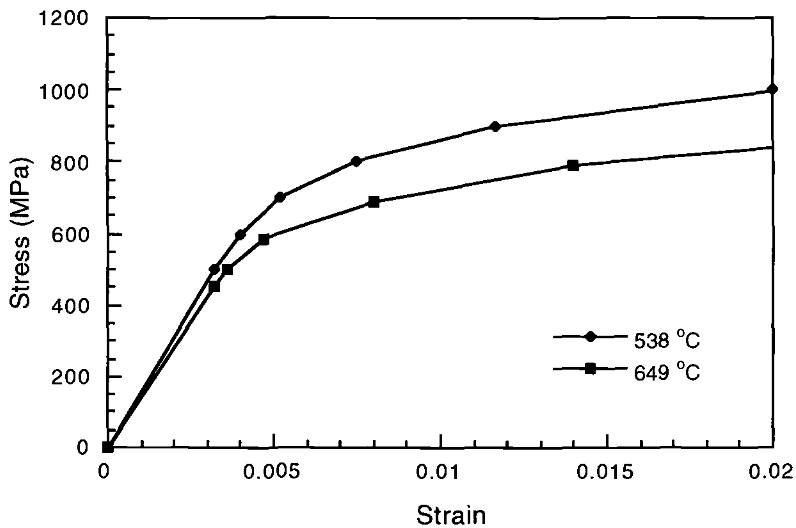

Fig. 1--Cyclic stress-strain curves of Alloy 718 used in the finite element analysis.

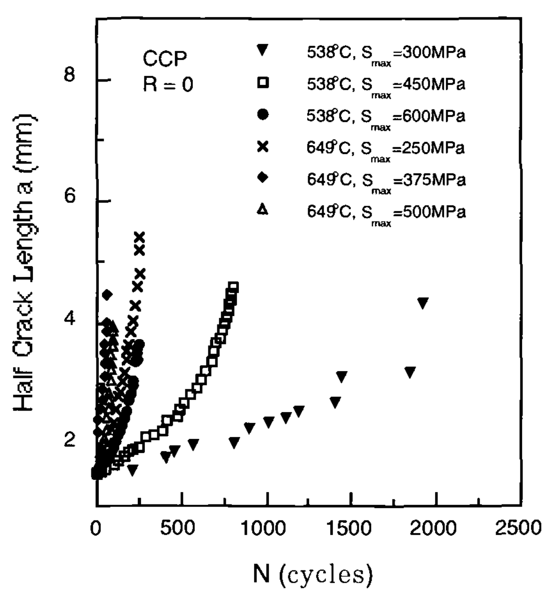

Fig. 2--Variation of crack length with the number of cycles

the width of the model at the upper boundary, and symmetry boundary conditions were used on the crack plane and on the mid-width center line; $\sigma_{12}=0$, $\sigma_{22}=0$ for $|x_1|<a$, $x_2=0$, $\sigma_{12}=0$, $u_2=0$ for $a \leq x_1 \leq W/2$, $x_2=0$, and $\sigma_{12}=0$, $u_1=0$ for $x_1=0$, where σ is stress, u is displacement, directions 1 and 2 are the crack direction and the loading direction, respectively, and a is the half crack length. The normal stress on the crack surface (σ_{22}) was automatically revised during analysis when contact stress was developed due to crack closure. The state of deformation was assumed to be plane stress. The load steps in the crack growth analysis are: (1) the load is increased to the maximum load, (2) the crack tip node is released, (3) the load is released. Then the sequence goes back to step (1) to load the model at an increased crack length. The input file was prepared such that the above cycle be repeated from the initial half crack length (1.5mm) to the final half crack length measured in the experiment. The largest number of loading steps was 87 that occurred for the test condition of 649°C, S_{max}=250MPa.

The contact of crack surface for analysis of crack closure was modeled by applying constraints on the contact nodes using a penalty method. The contact condition was evaluated for crack plane nodes in each plasticity iteration: if the reaction of a closed node is tensile, the node was released in the next iteration by removing the penalty constant in the stiffness matrix, and the nodes in the region of the overlap of crack surfaces were constrained in the subsequent iteration. The iteration was continued until all contact conditions were satisfied and the prescribed plasticity convergence criterion was satisfied for all elements in the model. The convergence criterion used for the plasticity iteration was based on the difference of the effective plastic strain between any two iterations. For most load steps, the difference of 5% or 1×10^{-5} in the absolute value of the strain was used. The tolerance was loosened somewhat, if necessary, toward the end of analysis where large plastic deformation occurred. The number of iterations varied from less than 10 to nearly 400 depending on the degree of plasticity. The convergence became harder to achieve as the crack approached to the final length, particularly when the maximum load was large. Four cases were stopped slightly short of the measured final crack length because of the convergence problem, and two cases ran to the final crack length (see Table 2).

A question may be raised on the load step size in this analysis and its cumulative effect on the accuracy of the field quantities at a later stage. Since the plastic deformation around the crack tip increases enormously as the crack propagates toward its final length, substantial nonproportional loading is expected to occur. In this situation, the large step size may introduce some inaccuracy in the results. One may suggest to carry out the computation cycle by cycle with small step sizes. This is extremely difficult due to the number of load steps involved. The scheme adopted here, despite the big step size, is thought to yield satisfactory results in view of the reasonably good comparison of the load and crack closure responses between analysis and experiment obtained in [4].

The crack closure analysis was carried out by restarting the crack growth run from the maximum load step, i.e., step (1). These analyses were done only at crack lengths where the crack closing and opening behavior was observed in the crack growth analysis. The total number of load steps in a cycle varied from 40 to 100. The load step sizes were made smaller toward the region where crack closing and opening were likely to occur.

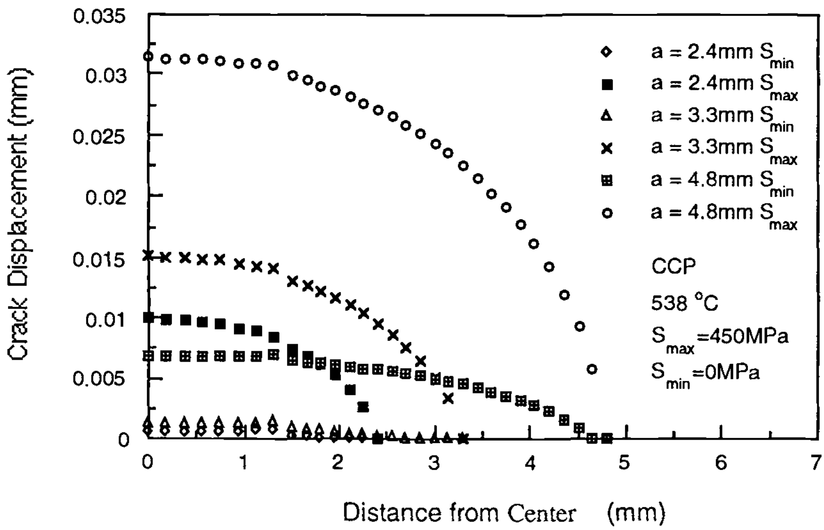

Fig. 3--Crack profiles during crack growth.

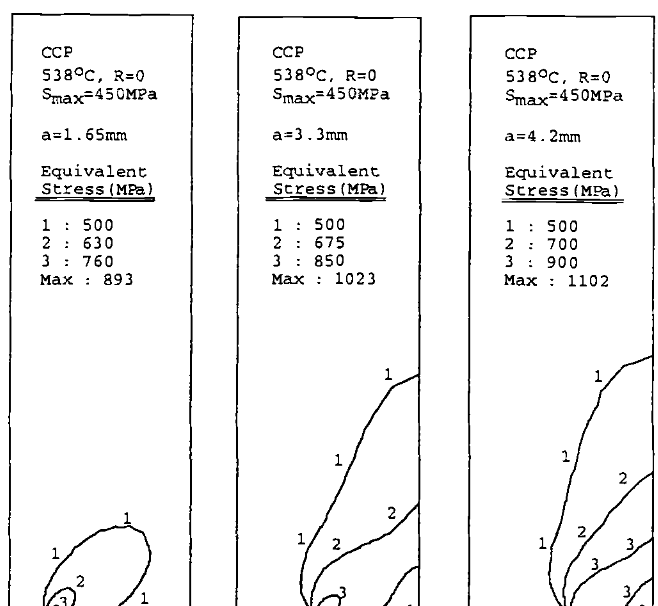

Fig. 4--Variation of the plastic zone during crack growth.

DISCUSSION OF RESULTS

Examples of crack profiles during crack growth are shown in Fig. 3 at three crack lengths for 538°C, S_{max}=450MPa. The profiles at both the maximum and minimum loads are shown for each crack length. One can find a discontinuity in the slope of the profile at the initial crack tip (1.5mm) as normally expected. One can also notice the crack closure behind the crack tip at the minimum load. The extent of crack closure is observed to vary with crack length. An example of the variation of the plastic zone (S_{eff}>S_Y =500MPa) with crack growth is shown in Fig. 4 for 538°C, S_{max}=450MPa. It is seen that the plastic zone is beyond the small scale yielding even at the smallest crack length shown. The shape of the plastic zone is consistent with those usually obtained for this type of specimen.

The crack closing was found for all three load levels at 538°C. The crack closing stress, S_c, and opening stress, S_o, increased with crack length in the initial part of crack growth and reached peak values. Then, as the crack grew further, the closing and opening behavior diminished rapidly and finally disappeared. Figure 5 illustrates this for 538°C, S_{max}=300MPa, 450MPa and 600MPa. The crack closing and opening behavior diminished also when the applied load increased. The observed trend of S_c and S_o with the load level agrees with the results of several papers [10-13]. However, the level of S_c and S_o in this research was found to be significantly lower for S_{max}=300MPa (S_{max}/S_Y=0.6). In [10-13] the mesh size was taken much smaller than that used in this study and the total lengths of crack propagation in these analyses were kept rather small. A separate analysis for S_{max}=300MPa with approximately a fourth of the original mesh size in the crack path yielded S_o and S_c values in the range found in [10-13]. This analysis was performed only for a few crack lengths. For S_{max}=450MPa and 600MPa, the results in Fig. 5 are believed to be good since the ratio of the mesh size to the plastic zone size in the crack plane was mostly within 5% [11]. It is also noteworthy that a bigger crack length increment than in the present study was used in [4] for SEN specimens of Alloy 718 at 538°C, and yet a fairly good correlation of the closure behavior with experimental data was obtained. A difference between the results of the SEN specimen and the CCP specimen is that the plastic zone is stretched along the crack path in the SEN specimen, while it is elongated in the off-axis direction in the CCP specimen. Thus, the plastic zone size measured on the crack plane tends to be much larger for the SEN specimen provided that other conditions are similar. This implies that a coarser mesh size can be used for the SEN specimen compared with the CCP specimen. It is also observed in Fig. 5 that the crack opening load is substantially higher than the closing load, which is consistent with other studies [4,10-12].

The stress intensity factor for the CCP specimen was calculated from Tada's equation [14]: $K = S(1-0.0025\alpha^2+0.06\alpha^4)[\pi a \sec(\pi\alpha)]^{1/2}$,where a is the half crack length, α is the ratio of a to the width of the specimen and S is the applied stress. The accuracy of this equation is ±0.2% for all α. The average K_c values obtained from CCP specimens were 71.3MPa-$\sqrt{m}$ at 538°C and 65.5MPa-$\sqrt{m}$ at 649°C. These values are somewhat lower than the data obtained from CT and CCP specimens of Alloy 718, but agree with data obtained using K_b specimens (round bar specimen with a semi-circular surface crack) [15]. The net section stress at fracture (see Table 2) was over 1150MPa for 538°C specimens, and it was over 1100MPa for 649°C specimens. It was surmised from this that the final failure was due to the net section stress rather than due to the fracture toughness. The range of the stress intensity factor was used to

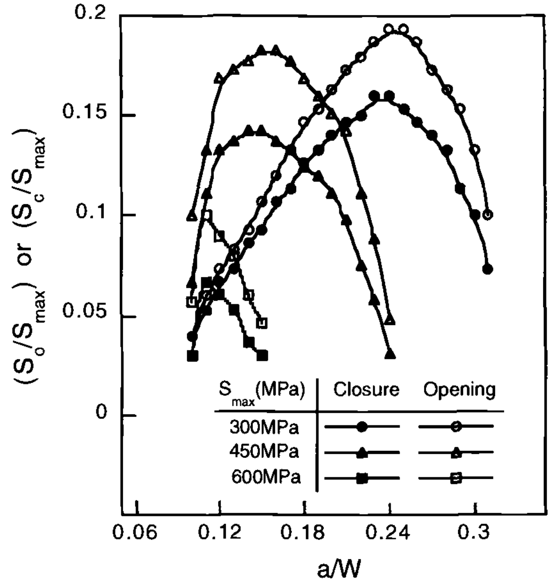

Fig. 5--Variation of crack closing and opening stresses with crack length at 538°C.

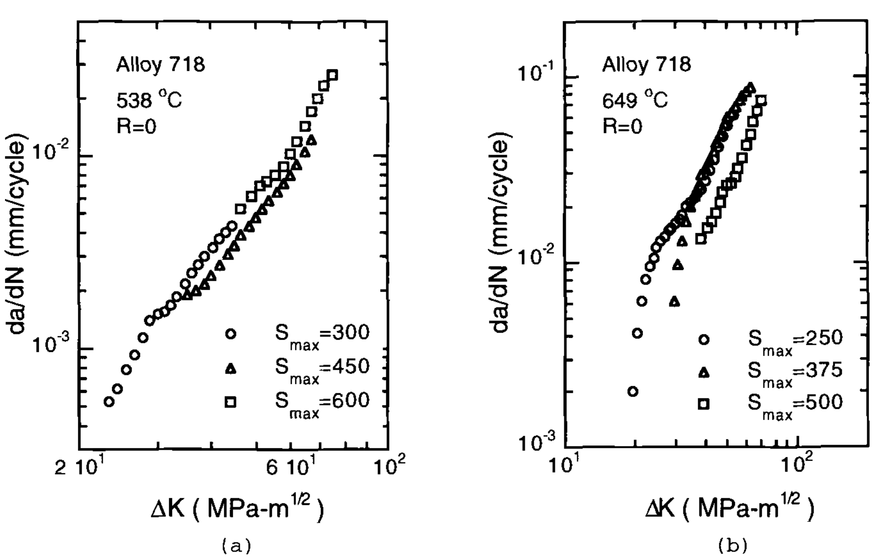

Fig. 6--Correlation of crack growth rates with ΔK (a) 538°C, (b) 649°C

correlate the measured crack growth rates. The results are shown in Fig. 6. The correlation at 538°C appears to be good, meaning that ΔK is useful even in the plastic loading regime. However, the correlation was poor at 649°C where the environmental effect may play a role and a different fracture mechanism may be operative. A point worth to note is that the correlation under stress control appears to be different from that obtained previously [4] under strain control, shown in Fig. 7. It is apparent that direct application of the da/dN-ΔK data from stress-control tests to strain-controlled crack growth analysis will not yield reliable results. Similar statement is also true when K_{max} is used instead of ΔK. The consideration of crack closure is expected to improve the results, however the decreasing crack growth rates at the later stage of crack growth would give some difficulties in correlation.

The results of finite element analysis were post-processed to compute the integral parameters J* and J^. The paths of integration were taken in a rectangular manner along the sides of elements such that the initial and final crack tip positions were within these paths. The computation was performed for four paths at each loading step. The results showed path-independence of these parameters. Figure 8 shows the variation of the integral parameter J^ with crack length at the maximum and minimum loads. The variation was slow for much of the crack growth, and there was a rapid change in both the maximum and minimum values near the final fracture. Similar trends were found for J* and for all other test conditions. The shapes of the curves in Fig.8 are in contrast with those of R_ε=-1 strain control SEN specimen [4] where the slope of dJ^/da at the maximum strain decreased with crack length and the minimum value remained almost constant. This is because the stress-strain field around the crack and in the whole specimen becomes more severe in stress control as the crack grows, while the load is relieved in strain control as the crack grows.

The variation of the integral parameter at a fixed crack length is depicted in Fig. 9. The load varies from the maximum value to the minimum, then back to the maximum in multiple load steps. When the cycle was completed, the values of the integral parameters increased somewhat. This increment varied with the amount of plasticity in the crack tip field. For small crack sizes and the lowest maximum load, the down-loading and up-loading parts of the loop were almost the same and the difference was negligible. The change was mostly within 10%. This increase could be in part due to non-proportional loading effect in

Table 2 -- Fracture toughness (K_c) and fracture stress (S_f) calculated from the experimental final crack length

Test Condtion	$2a_f$-exp (mm)	$2a_f$-anal (mm)	K_c (MPa-$\sqrt{m}$)	S_f (MPa)
538°C, 300MPa	11.1	9.6	64.2	1154
538°C, 450MPa	9.4	8.7	73.5	1205
538°C, 600MPa	7.4	7.5	76.3	1184
649°C, 250MPa	11.7	11.4	60.0	1136
649°C, 375MPa	9.9	9.9	64.7	1103
649°C, 500MPa	8.4	7.8	71.8	1136

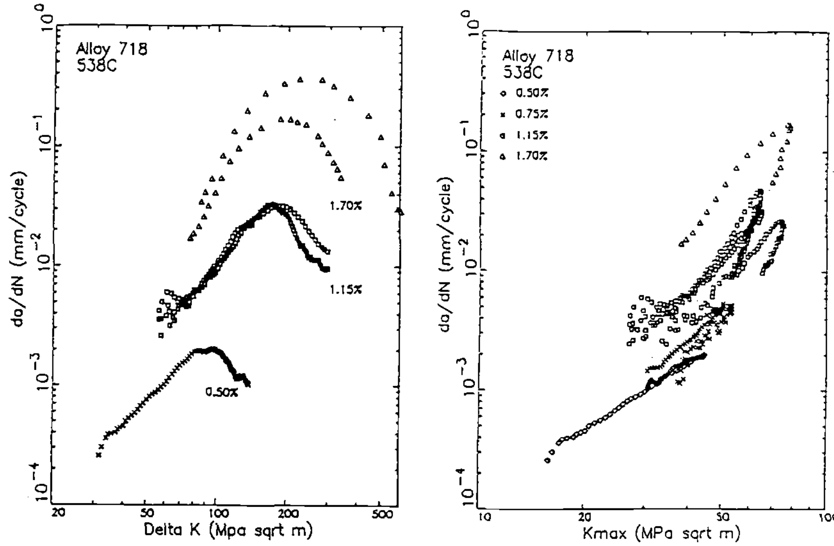

(a) (b)

Fig. 7--Crack growth rates versus (a) ΔK, (b) K_{max} of Alloy 718 tested at 538°C under R_ε=-1 strain control, from [4].

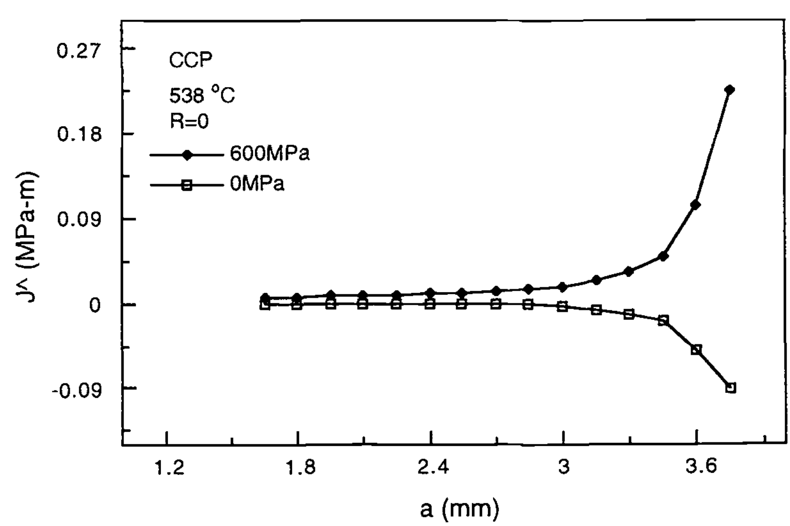

Fig. 8--Variation of J^ with crack length during crack growth.

connection with large step sizes in the crack propagation analysis as described earlier. This difference does not scatter data points significantly on the log-log plot of da/dN-ΔJ* or ΔJ^, where Δ represents the range from the minimum load to the maximum load. Another point to note is that the values of J* and J^ at the crack closing and opening points were small and close to the value at the minimum load. This was also observed for strain control cases [4]. The values of ΔJ* and ΔJ^ can be therefore viewed as the ranges from the crack opening point to the maximum load.

The correlation of da/dN with ΔJ* and ΔJ^ are shown in Figs. 10 and 11, for 538°C and 649°C, respectively. It appears that these parameters consolidate the crack growth data at 538°C excluding a few points at the far right of the data set where excessive plasticity is found. But the relation of da/dN - ΔJ* or ΔJ^ does not follow the Paris law. As in the case of ΔK, the correlation with ΔJ* or ΔJ^ at 649°C is not as good as at 538°C. It is also noted that the analyses in [4] and [5] were carried out only to a quarter of the specimen width. Thus, it is possible that the correlation of crack growth rates with ΔJ* or ΔJ^ is not as good as reported at larger crack lengths.

A requirement for a crack growth parameter is that it must have a characteristic value where the final fracture is onset. These values of J* and J^ for four test conditions were not determined because the analysis was terminated before the final crack length observed in the experiment. Even when the analysis proceeded to the fracture point in two cases, a substantial difference was found in the final values of the parameters. This could be due to the computational difficulties in plasticity iterations toward the fracture point.

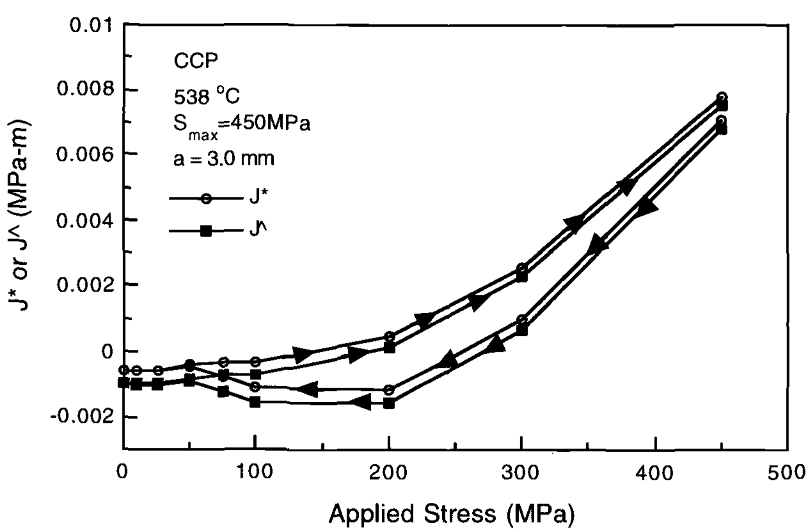

Fig. 9--Variation of J^* and J^ during a load cycle.

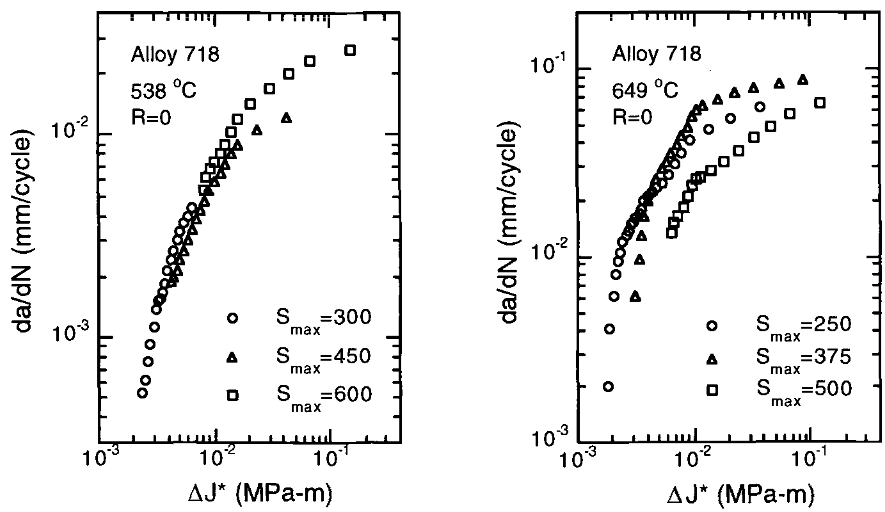

(a) (b)

Fig. 10--Correlation of da/dN with ΔJ^*, (a) 538°C, (b) 649°C.

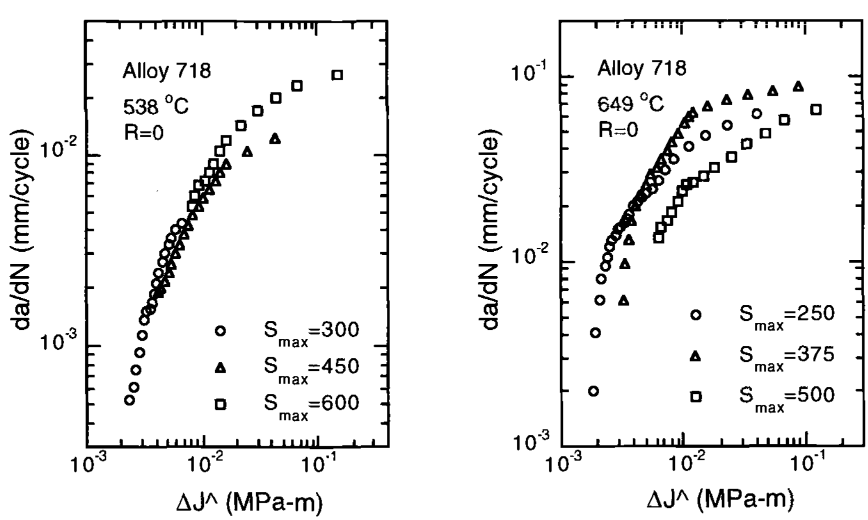

(a) (b)

Fig. 11--Correlation of da/dN with $\Delta J^\wedge$, (a) 538°C, (b) 649°C.

CONCLUSIONS

This research evaluated the ability of J* and J^ to correlate crack growth rates under R_σ=0 stress cycling for CCP specimens of Alloy 718. The performance of the ΔK approach was also examined. The applied maximum stresses ranged from the nominally elastic to nominally plastic level. Crack growth data were generated at 538°C and 649°C. The crack propagation and crack closure behavior were analyzed by use of an elastic-plastic finite element method. The parameters J* and J^ were computed by post-processing the results. The crack growth rates were correlated with ΔJ* and ΔJ^ as well as ΔK. The following conclusions were drawn from the results:

(1) The ΔJ* and ΔJ^ can consolidate the crack growth rates at 538°C, but the da/dN - ΔJ* or ΔJ^ deviates from the relation of the Paris law type. The correlation at 649°C is poor.
(2) The ΔK correlated crack growth data well with the Paris law at 538°C. However, it did not correlate the 649°C data.
(3) The crack closing and opening stresses increase with crack length for the initial part of crack growth. Then they arrive at peak values, and decrease fast as the crack propagates further. As the maximum applied stress increases from the nominally elastic to the nominally plastic region, the degree of crack closing diminishes rapidly.

ACKNOWLEDGMENT

This work was supported by Pohang University of Science and Technology, Pohang, Korea.

REFERENCES

[1] Dowling, N.E. and Begley, J.A., "Fatigue Crack Growth during Gross Plasticity, and the J-integral," Mechanics of Crack Growth, ASTM STP 590, ASTM, Philadelphia, pp. 82-103, 1976.

[2] Dowling, N.E. and Iyyer, N.S., "Fatigue Crack Growth and Closure at High Cyclic Strains," Materials Science and Engineering, Vol. 96, 1987, pp. 99-107.

[3] McClung, R.C. and Sehitoglu, H., "Closure Behavior of Small Cracks under High Strain Fatigue Histories," Mechanics of Fatigue Crack Closure, ASTM STP 982, J.C. Newmann, Jr. and W. Elber, Eds., ASTM, Philadelphia, 1987, pp. 342-360.

[4] Kim, K.S and Van Stone, R.H., "Application of Path-Independent Integrals to Elevated Temperature Crack Growth," Elevated Temperature Crack Growth, ASME MD-Vol. 18, 1990, pp. 155-167.

[5] Kim, K.S. and Van Stone, R.H., " Characterization of Elevated Temperature Crack Growth in Hastelloy-X Using Integral Parameters," ASME Journal of Engineering Materials and Technology, Vol.117, 1995, pp. 299-304.

[6] Blackburn, W.S., "Path-Independent Integrals to Predict Onset of Crack Instability in an Elastic Material," International Journal of Fracture Mechanics, Vol. 8, 1972, pp. 343-346.

[7] Kishimoto, K., Aoki, S., and Sakada, M., "On the Path-Independent Integral - J^", Engineering Fracture Mechanics, Vol. 13, 1980, pp. 841-850.

[8] Jordan, E.H. and Myers, G.J., "Fracture Mechanics Applied to Elevated Temperature Crack Growth," ASME Journal of Engineering Materials and Technology, Vol. 111, 1989, pp. 306-313.

[9] Besseling, J.F., "A Theory of Plastic Flow for Anisotropic Hardening in Plastic Deformation of an Initially Isotropic Material," Report S. 410, National Aeronautical Research Institute, Amsterdam, 1953.

[10] Lalor, P.L. and Sehitoglu, H., "Fatigue Crack Closure Outside a Small-Scale Yielding Regime," Mechanics of Fatigue Crack Closure, ASTM STP 982, J.C. Newmann, Jr. and W. Elber, Eds., ASTM, Philadelphia, 1987, pp. 342-360.

[11] McClung, R.C. and Sehitoglu, H., "On the Finite Element Analysis of Fatigue Crack Closure," Engineering Fracture Mechanics, Vol. 33, 1989, pp. 237-252.

[12] Nicholas, T., Palazotto, A.N. and Bednarz, E., "An Analytical Investigation of Plasticity Induced Closure Involving Short Cracks," Mechanics of Crack Closure, ASTM STP 982, J.C. Newmann, Jr. and W. Elber, Eds., ASTM, Philadelphia, 1988, pp. 361-379.

[13] Newmann, J.C., Jr., "A Finite-Element Analysis of Fatigue Crack Closure," Mechanics of Crack Growth, ASTM STP 590, ASTM, 1976, pp. 281-301.

[14] Tada, H., "A Note on the Finite Width Corrections to the Stress Intensity Factor," Engineering Fracture Mechanics, Vol. 3, No. 3, 1971, pp. 345-347.

[15] Domas, P.A., "Reduction and Comparison of Inconel 718 Crack Growth Rate Data from Multiple Sources & Test Specimen Configuration," General Electric Aircraft Engines TM 80-60, 1980.

APPENDIX

The J*-integral [6] and the J^-integral [7] are defined as follows:

$$J^* = \int_\Gamma (\sigma_{ij}u_{i,j}/2dx_2 - t_i u_{i,1}ds) + \int_A (\sigma_{ij}u_{i,j1}/2 - \sigma_{ij,1}u_{i,j}/2)dA$$

$$\hat{J} = - \int_\Gamma t_i u_{i,1}ds + \int_A \sigma_{ij}\varepsilon_{ij,1}dA$$

where σ_{ij} is stress, ε_{ij} is strain, u_i is displacement, t_i is traction, Γ is a path around the crack tip, A is the area enclosed by Γ and the crack surface, and a comma indicates the partial differentiation with respect to the subsequent coordinate.

Weld Applications

Kevin L. Kenney,[1] Walter G. Reuter,[1] Harold S. Reemsnyder,[2] and David K. Matlock[3]

FRACTURE INITIATION BY LOCAL BRITTLE ZONES IN WELDMENTS OF QUENCHED AND TEMPERED STRUCTURAL ALLOY STEEL PLATE

REFERENCE: Kenney, K. L., Reuter, W. G., Reemsnyder, H. S., and Matlock, D. K., **"Fracture Initiation by Local Brittle Zones in Weldments of Quenched and Tempered Structural Alloy Steel Plate,"** Fatigue and Fracture Mechanics: 28th Volume, ASTM STP 1321, J. H. Underwood, B. D. Macdonald, and M. R. Mitchell, Eds., American Society for Testing and Materials, 1997.

ABSTRACT: The heat-affected zone (HAZ) embrittlement of an API 2Y Grade 50T quenched and tempered offshore structural steel plate, welded by the submerged-arc process at a heat input of 4.5 kJ/mm, was investigated from the viewpoint of identifying the local brittle zone (LBZ) microstructure and the metallurgical factors associated with its formation. Microstructural and fractographic analysis showed the LBZ microstructure to be dual phase martensite-austenite (M-A) constituent. The formation of M-A constituent was found to be related to microstructural banding of the hot-rolled base plate. When the banded base plate was welded, M-A constituent formed only within the band microstructure which penetrated the intercritically-reheated coarse-grain HAZ (IRCGHAZ). The chemistry of the band microstructure in conjunction with the thermal cycle of the IRCGHAZ provided the critical conditions for the formation of M-A constituent in the API 2Y Grade 50T steel investigated. The influence of local brittle zones (i.e., M-A constituent) on the HAZ fracture toughness was evaluated by means of Crack-Tip Opening Displacement (CTOD) tests. These tests showed the steel to suffer embrittlement when the fatigue precrack sampled an intercritically-reheated coarse-grain HAZ which contained M-A constituent, confirming that M-A constituent is the major microstructural factor controlling the HAZ toughness of this particular steel.

KEY WORDS: Local Brittle Zone (LBZ), Heat-Affected Zone (HAZ), Unaltered Coarse-Grain Heat-Affected Zone (UACGHAZ), Fine-Grain Heat-Affected Zone (FGHAZ), Intercritically-Reheated Coarse-Grain Heat-Affected Zone (IRCGHAZ), Subcritically-Reheated Coarse-Grain Heat-Affected Zone (SRCGHAZ), Crack-Tip Opening Displacement (CTOD)

[1]Idaho National Engineering Laboratory, Idaho Falls, ID 83415, USA.

[2]Bethlehem Steel Corporation, Bethlehem, PA 18016, USA.

[3]Department of Metallurgical and Materials Engineering, Colorado School of Mines, Golden, CO 80401, USA.

INTRODUCTION

Offshore activities in oil exploration and recovery in the North Sea and Arctic Ocean place critical demands on steel performance in harsh environments. User requirements for increased weldability and improved heat-affected zone (HAZ) resistance to hydrogen-induced cold cracking and stress corrosion cracking, have necessitated reduction of the carbon equivalent for offshore-grade structural steels [1]. Consequently, new classes of low-carbon microalloyed steel, which exhibit excellent combinations of high strength and toughness, have been developed for use in modern offshore structures.

Evaluations of HAZ toughness have revealed that the appropriate combinations of steel chemistry and welding variables can significantly alter the characteristically high fracture toughness of low-carbon microalloy steels. The deterioration of toughness has been correlated with small regions of poor fracture toughness, referred to as local brittle zones (LBZ's), which form in the HAZ during multipass welding. Complicating the LBZ issue is the fact that not all offshore-grade structural steels produce LBZ's under the same welding conditions [2]; rather, LBZ formation requires weld thermal cycles appropriate for the local steel chemistry.

Due to the heterogeneous nature of a weld HAZ and the narrow, discontinuous nature of individual HAZ regions, identification of LBZ's and quantifying their role in the fracture process is difficult. Therefore, the vast majority of LBZ studies have utilized weld thermal-cycle simulation techniques to develop a larger volume of uniform microstructure suitable for performing fracture toughness testing of a particular HAZ region. In comparison, few studies have been performed on full-thickness multipass welds. Weld simulation data generally present a pessimistic view of structural integrity since only a single homogeneous microstructure is sampled, whereas, in a real weld HAZ, a microstructural gradient exists, and therefore, a variety of microstructures is sampled by the crack-front [3].

The present study was developed to assess the effects of local brittle zones on HAZ cleavage fracture in multipass welds of a 108-mm thick API 2Y Grade 50T quenched and tempered steel plate. This was accomplished with a two-phase approach which, together, identified the metallurgical factors associated with LBZ formation and determined the relationship between LBZ's and the initiation of cleavage fracture. Phase I consisted of a failure analysis of broken fracture toughness specimens. Utilizing both microstructural and fractographic analysis, the critical microstructure responsible for fracture initiation was identified. Having identified the critical microstructure, a fracture toughness test program (Phase II) was implemented to quantitatively evaluate the effects of the critical microstructure on the fracture behavior of the HAZ in specially designed tests.

BACKGROUND

Prior to the conception of the current research program, testing was performed to characterize the heat-affected zone fracture toughness of full-thickness weld sections of a 108-mm thick API 2Y Grade 50T quenched and tempered steel plate. A total of six Crack-Tip Opening Displacement (CTOD) tests were performed at -10°C using full-thickness, square (BxB, B = 102-mm) single edge-notched bend specimens (SE(B) specimens) with a through-thickness notch and fatigue precrack sampling the coarse-grain regions in the areas of HAZ overlap and extending halfway through the specimen width (i.e., a normalized crack length, a/W equal to 0.5). The specimen thickness was nominally equal to the plate thickness of the original weldment. The six CTOD tests produced three δ_c values of 0.234, 0.320 and 0.389-mm and three δ_u values of 0.592, 1.29 and 1.88-mm.

Materials and Welding

The material investigated in this study was a 108-mm-thick plate of API 2Y Grade 50T steel (hereafter referred to as API 2Y-50T), whose chemical composition in weight percent is 0.087C - 1.45Mn - 0.019P - 0.005S - 0.30Si - 0.32Ni - 0.027Cr - 0.20Cu - 0.010Ti - 0.016Nb - 0.017Al - 0.003V - 0.001B - 0.0054N - <0.02Mo. This steel was ingot-cast, hot-rolled to plate of 108-mm thickness, and subsequently quenched and tempered to meet API Specification 2Y [4].

A single-bevel configuration (Figure 1) was used for fabrication of two test welds (referred to as weld #1 and weld #2) from the same API 2Y-50T steel plate. Multipass welding was performed using an automated submerged-arc welding (SAW) process under the weld parameters listed in Table 1, and two combinations of welding current and travel speed were chosen to produce welds at a constant heat input. Although the welding current and the travel speed were adjusted so that the heat input remained constant, these parameters change the base metal dilution, and therefore change the size and shape of the HAZ [5]. Although the two weldments are not identical, the HAZ microstructures and the associated HAZ fracture toughness of each weldment are assumed to be representative of a 4.5 kJ/mm weld of the API 2Y-50T steel plate, and the two welds are therefore considered to be analogous for the purpose of fracture toughness testing. The broken full-thickness CTOD specimens obtained from previous testing for failure analysis in Phase I of the current program are associated with weldment #1. The sub-size CTOD specimens tested in Phase II of the current program are associated with weldment #2. Additional distinction of the two welds will be made when applicable.

The base metal and weld metal tensile data are listed in Table 2. The material yield strengths indicate that both weldment #1 and weldment #2 are overmatched by 32% and 22%, respectively, at room temperature, and 22% and 24%, respectively, at -10°C.

PHASE I: FAILURE ANALYSIS OF CTOD SPECIMENS

The current study sought to identify the metallurgical factors responsible for the reduced-toughness δ_c behavior of the full-thickness CTOD specimens by analyzing the two broken specimens which exhibited the lowest toughness (δ_c equal to 0.234-mm and 0.320-mm). Based on other reports which have shown that low toughness in the coarse-grain regions of similar offshore structural steels is related to local brittle zones

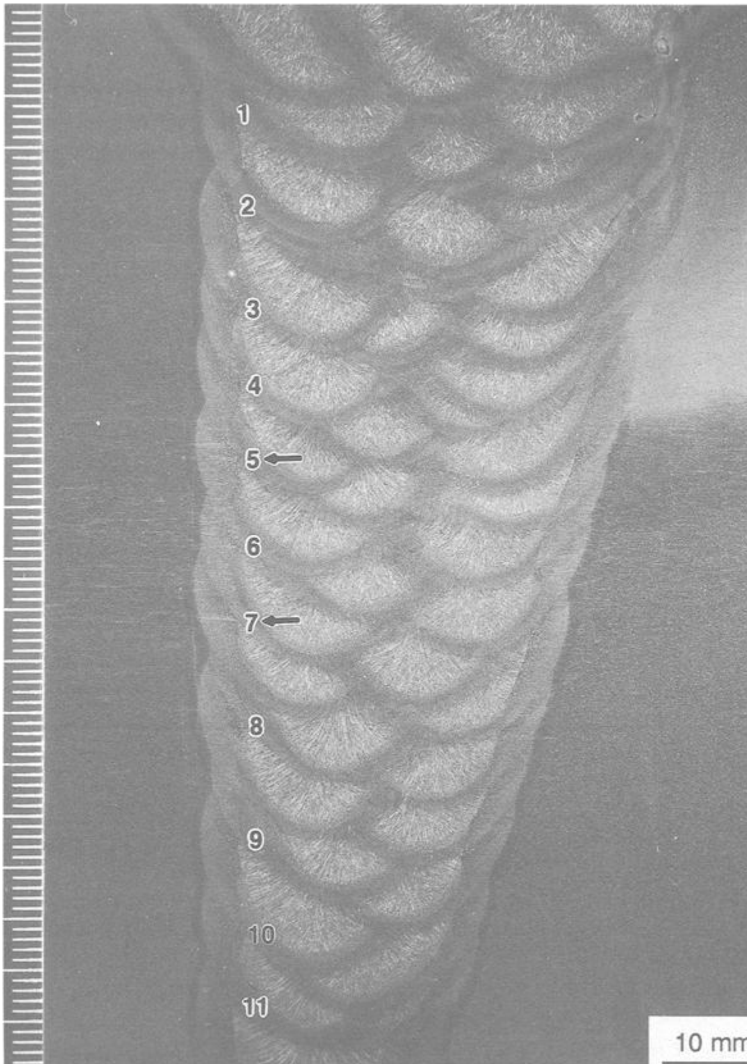

FIG. 1--Photomacrograph of a multipass weld of the API 2Y-50T plate. 5% Nital etch

(LBZ's), a microstructural investigation was initiated with the suspicion that LBZ's played a contributing role. The specific tasks involved identification of the LBZ microstructure, classification of the LBZ distribution throughout the full-thickness weld HAZ, identification of the metallurgical factors which contribute to LBZ formation and evaluation of the relationship between LBZ's and the initiation of cleavage fracture.

Table 1 -- Welding parameters used in the preparation of test welds

Weld #	Welding Process	Consumables		Heat Input (kJ/mm)	Volt.	Amps	Travel Speed (mm/min)	Temperature (°C)	
		Wire	Flux					Pre-Heat	Inter-pass
1	SAW-DC+	OE-SD3 (Ø 4.0 mm)	OP-121-TT	4.5	30	660	264	250	250
2						700	279		

Table 2 -- Tensile properties at the ¼-thickness and transverse to the rolling direction

Material		Test Temp. (°C)	Yield Strength (MPa)	Tensile Strength (MPa)	Reduction in Area (%)	Elongation in 25.4 mm (%)
Base Metal		RT	355	486	81.0	40.9
		-10	369	514	79.3	40.0
Weld Metal	Weld #1	RT	470	518	79.8	35.0
		-10	449	553	76.0	33.8
	Weld #2	RT	437	525	79.3	29.0
		-10	459	554	78.1	30.5

Experimental Techniques

Microstructural Analysis--A photograph of a polished and etched longitudinal section of one of the broken CTOD specimens is shown in Figure 2. In the orientation shown, the matching fracture surfaces are facing each other and the direction of crack propagation is into the plane of the photograph. The HAZ microstructures contained on the weld metal half of the broken specimen were examined in this analysis. This narrow band of HAZ microstructures, bound by the fusion zone on one side and the fracture surface on the other, consisted of the HAZ regions which formed immediately adjacent to the fusion zone (i.e., the UACG, FG, IRCG and SRCG zones).

The samples were nickel-coated for improved edge retention and were prepared for microstructural analysis using standard metallographic techniques. The full-thickness (102-mm) HAZ microstructures were etched with either 4% Picral, 5% Nital or LePera's Reagent [6] and examined by light microscopy and scanning electron microscopy (SEM). Furthermore, Energy Dispersive Spectroscopy (EDS) was utilized for chemical analysis. A schematic of the full-thickness fracture section is shown in Figure 3. This schematic illustrates the orientation, with respect to the fracture surface, of the surface which was examined (i.e., the plane of examination). The plane

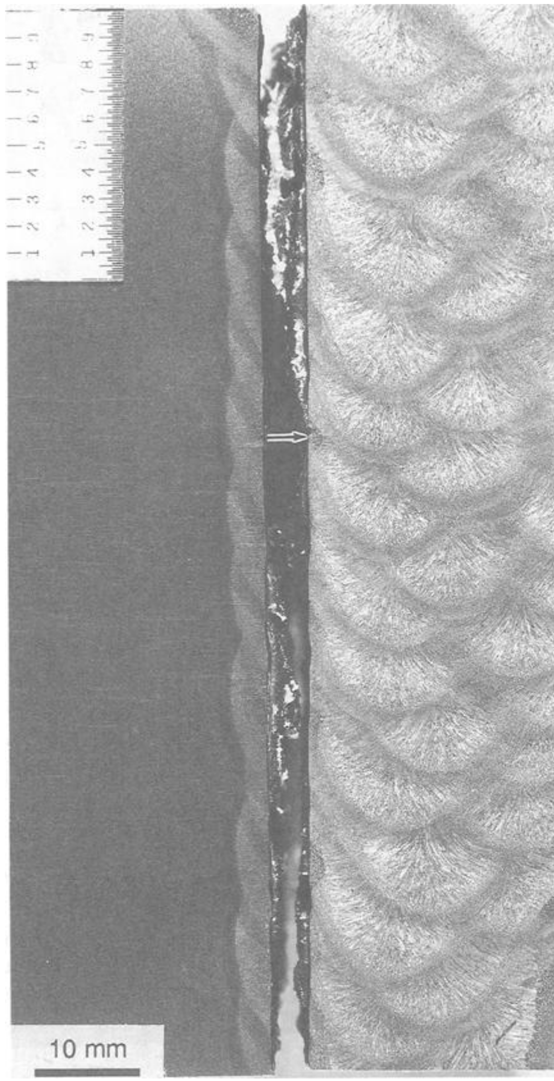

FIG. 2--Photomacrograph of the weld structure of a broken full-thickness CTOD specimen. 5% Nital etch

of examination can be described as a transverse view of a longitudinal section of the fracture specimen.

Fractographic Analysis--The macroscopic fracture initiation sites were identified for each of the two broken full-thickness CTOD specimens by visual examination of the matching fracture surfaces. This examination revealed a single initiation site for

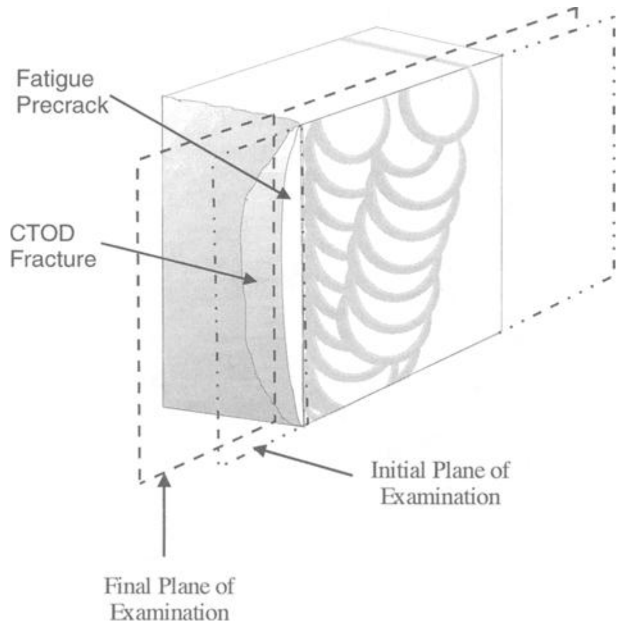

FIG. 3--Schematic drawing of the weld side of the broken full-thickness CTOD specimen showing the surface which was subjected to microstructural evaluation.

each of the two broken specimens. The macroscopic initiation site of the broken CTOD specimen which exhibited the lowest toughness (δ_c = 0.234-mm) was examined with a scanning electron microscope (SEM) to assess the fracture mode, to locate the local initiation site(s) and to identify the microstructural constituents (e.g., M-A islands, MnS inclusion, etc.) which may have played a role in fracture initiation.

Results and Discussion

Microstructures--The base metal and HAZ microstructures of full weld sections were thoroughly characterized since the details of these microstructures ultimately determine the HAZ toughness. To facilitate the analysis of the base metal and weld metal microstructures presented in the following sections, the weld schematic shown in Figure 4 is used to emphasize the important features of the weld section shown in Figure 1. The three primary areas of interest illustrated in the weld schematic are (1) the short, discontinuous bands which are evident within the base plate, (2) the base metal microstructure away from the bands and (3) the overlap region of the HAZ where the coarse-grain regions are located.

The base plate exhibits microstructural banding which is often typical of hot-rolled steel plate. The microstructural bands appear as discontinuous streaks which, depending on lighting and magnification, appear either lighter or darker than the surrounding matrix. When viewed macroscopically, the bands appear light as shown

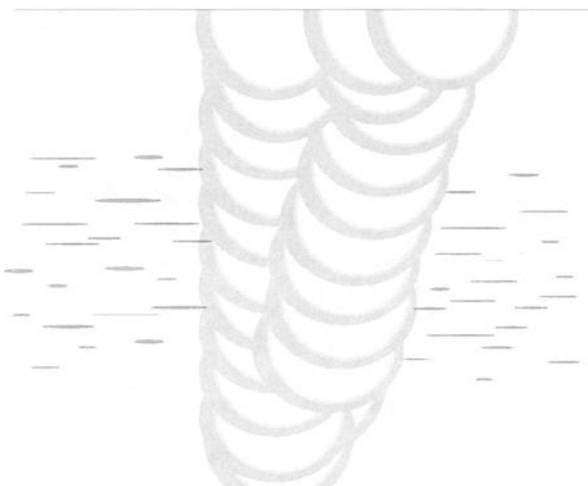

FIG. 4--Schematic diagram of a single-bevel, multipass weld joint of the 108-mm API 2Y-50T steel plate.

in Figure 1. The banding is concentrated within the central half of the plate thickness as shown in the weld joint photograph (Figure 1) and illustrated in the weld joint schematic (Figure 4). When viewed at higher magnification in a light metallograph, the bands appear dark; the matrix and band microstructures are shown in Figures 5a and 5b, respectively. It is apparent from these micrographs that the microstructural banding in this steel differs from the alternating ferrite/pearlite banding typical of most banded microstructures [7]. Both the band microstructure and the matrix microstructure consists mainly of ferrite with small colonies of pearlite/bainite intermixed. However, several features are apparent from the micrographs which distinguish the band microstructure from the matrix microstructure:

1. The ferrite grain size is much finer than that of the matrix microstructure.
2. The volume fraction of pearlite/bainite appears to be higher than in the matrix microstructure.
3. There appears to be a much higher distribution of precipitate particles (appear as black dots in the micrographs) than in the matrix microstructure. Chemical analysis via EDS showed the precipitate particles to contain Nb, although some particles also contained Ti in addition to Nb. The Nb-containing particles which did not contain Ti are presumably Nb(C,N) precipitates. The Ti/Nb-containing particles presumably result from TiN particles which formed in the steel during solidification. The Nb could be dissolved in the TiN particles or could be a Nb(C,N) precipitate on an existing TiN particle [8]. The refined grain structure

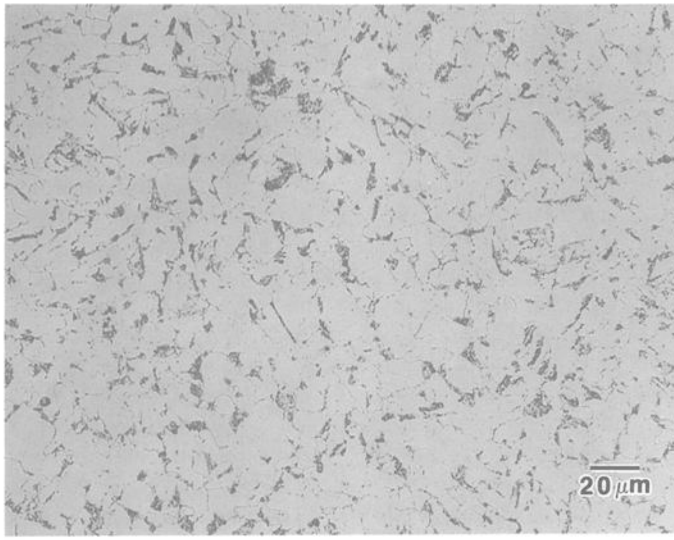

(a)

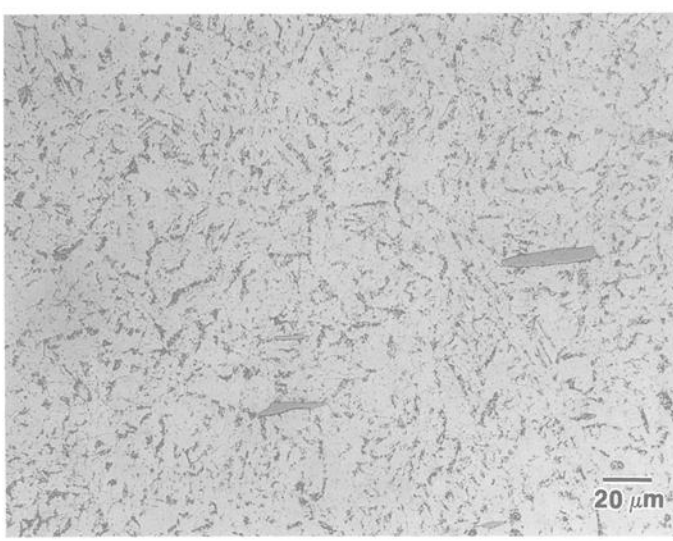

(b)

FIG. 5--Base metal light micrographs (a) away from the dark etching band and (b) in the dark etching band. 4% Picral etch

of the band microstructure is most likely the result of microalloy precipitation effects.

4. The band microstructure generally contains stringer inclusions, identified by EDS to be manganese-sulphide inclusions.

A total of four weld cross-sections, two sections from weldment #1 and two from weldment #2, were examined for characterization of the HAZ microstructures. Light microscopy of the full-thickness straight-side HAZ microstructures revealed many small (sub-micron to approximately 2.5 microns in size) islands only in very specific regions of the HAZ. These islands, shown in Figure 6, appear white due to etching with LePera's Reagent and are accordingly interpreted to be M-A constituent. In each case, the M-A constituent formed within an IRCG zone, but not all IRCG zones contained M-A constituent. For example, the weld section shown in Figure 1 includes ten IRCG zones, numbered as shown. However, only the two identified by arrows contained M-A constituent. Figure 7a shows the microstructure of an IRCG zone which contains M-A constituent and Figure 7b shows the typical microstructure of an IRCG zone which does not contain M-A constituent. Comparison of the two shows the distinguishing feature to be the dark-etching band in the IRCG of the former. The IRCG region shown in Figure 7a corresponds to region #7 in Figure 1. Note from the photomacrograph in Figure 1 that microstructural bands, which have a light-etching appearance, penetrate both IRCG region #7 and IRCG region #5. Further investigation revealed the dark-etching band in Figure 7a to correspond to the banding of the base plate microstructure. In each of the IRCG zones exhibiting M-A formation, the M-A constituent was entirely localized within similar dark-etching bands, and none existed in the surrounding IRCG microstructure.

FIG. 6--Light micrograph of M-A constituent (white islands) in the band microstructure which penetrated the intercritically-reheated coarse-grain (IRCG) HAZ. LePera's reagent

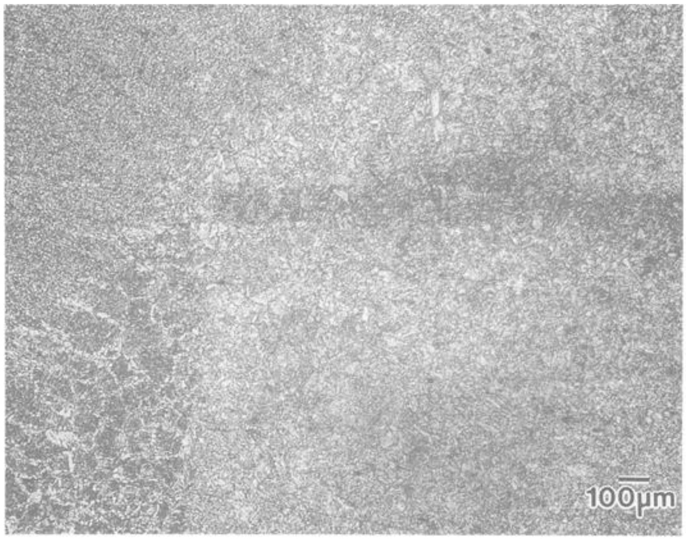

(a)

(b)

FIG. 7--Light micrograph of (a) an IRCG region which contains M-A constituent (not visible at this magnification) and (b) an IRCG region which does not contain M-A constituent. 5% Nital etch

Based on the apparent association of M-A constituent with the band microstructure, the HAZ microstructures were examined to identify all microstructural bands in the HAZ. This examination revealed that only the bands which lay within the IRCGHAZ contained M-A constituent. Bands which intersected the HAZ at locations other than in the IRCGHAZ did not contain M-A constituent.

Fractography--The fracture surface of the weld metal half of the broken specimen shown in Figure 2 is shown in Figure 8. The small area marked "F" is the fatigue precrack, the dark area "A" is the heat-tinted unstable crack extension concomitant with the achievement of the critical CTOD toughness, and the area "B" is the post-test final fracture at liquid nitrogen temperature. A single macroscopic fracture initiation site (marked by the arrow) was identified on this fracture surface (as well as on the matching fracture surface) by the chevron marks which radiate outward from the fracture origin.

SEM fractography of the macroscopic crack origin identified in Figure 8 showed the fracture mode to be dominated by cleavage with occasional ductile tearing along small shear ridges where multiple cleavage cracks unite. A montage of an area (measuring approximately 1.5x0.8-mm) which encompassed the entire macroscopic crack origin was constructed from a set of SEM fractographs (at a magnification of 750x) to aid in the examination of the crack origin. The cleavage river patterns visible in the montage were analyzed and the indicated direction of crack growth was marked in the corresponding cleavage facet on the montage. This analysis revealed a crack initiation region, approximately 300 μm in diameter, from which the river patterns, and hence the cleavage cracks, radiated. The identified crack origin, superimposed on the SEM fractograph, is illustrated in Figure 9. The arrows indicate the direction of crack growth as revealed by the cleavage river patterns. Many local initiation sites were evident within the initiation region.

Evaluation of Initiation Microstructure[1]--The location of the crack origin with respect to the weld/HAZ structure of the broken specimen is illustrated by the arrow in Figure 2. It is apparent from the photograph that the crack origin is associated with the region of HAZ overlap of two successive weld passes. The microstructure in the HAZ overlap region identified by the arrow in Figure 2 is shown in Figure 10. The large dark area "A" is the weld metal, the lighter area "B" is the HAZ, and the free surface is a face of the fatigue precrack which extends into the plane of the photograph. Note that the successive weld pass in this case lies above the micrograph. Of particular interest in this micrograph is the two dark-etching bands which appear to penetrate the intercritically-reheated coarse-grain HAZ (IRCGHAZ) from the fracture surface. As expected, based on the previously observed trend of M-A formation in microstructural bands which penetrate the IRCGHAZ, M-A constituent was identified

[1]Note: Two CTOD specimens were subjected to microstructural evaluation to identify the initiation microstructure, but the evaluation of only one of the two was discussed. A microstructural analysis was also conducted on the second specimen, and the conclusions are identical.

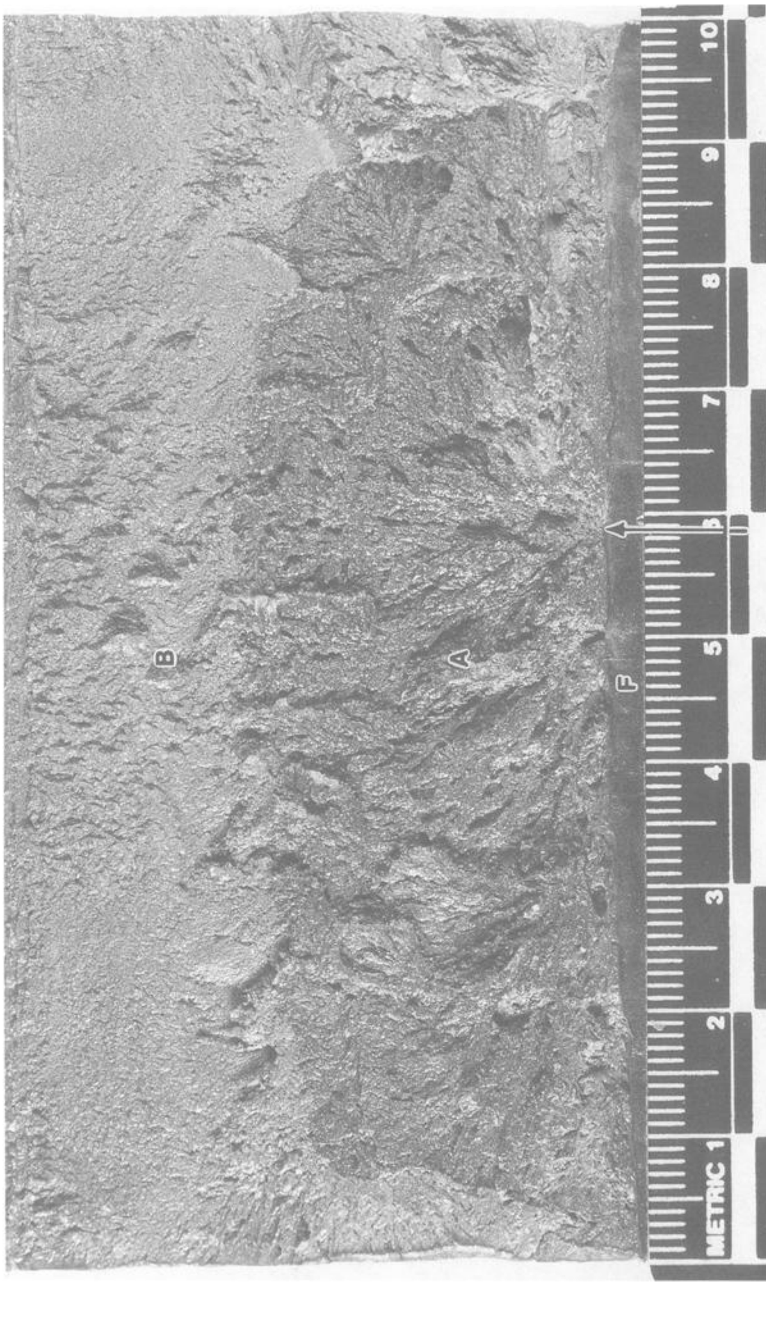

FIG. 8--Photograph of the fracture surface of a full-thickness CTOD specimen.

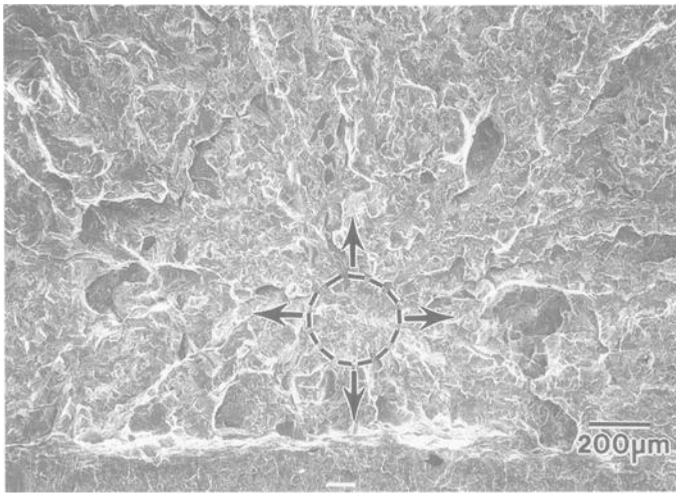

FIG. 9--SEM fractograph of macroscopic initiation site with the boundary of the identified crack initiation region superimposed. The arrows indicate the direction of cleavage crack propagation from the initiation region.

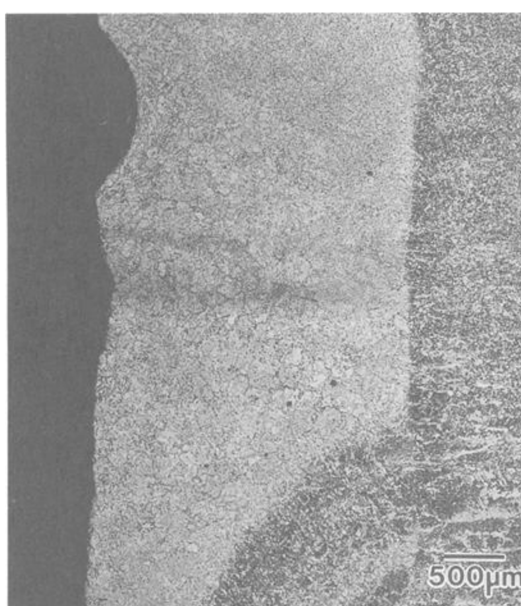

FIG. 10--Light micrograph of the initiation microstructure. 5% Nital etch

(with the aid of LePera's Reagent) within the bands shown in Figure 10. These M-A islands were similar in both size and morphology as those shown in Figure 6.

To verify the correlation between the M-A constituent and the fracture initiation region, a scribe mark was placed in the edge of the specimen to coincide with the location of the microstructural bands shown in Figure 10. The specimen was then examined in the SEM to inspect the location of the scribe mark in relation to the initiation region. It is apparent from this SEM micrograph in Figure 11a that the scribe mark (indicated by the vertical arrow) is coincident with the location of M-A containing bands which appear as a light area (bounded by the arrowheads). While in

(a)

(b)

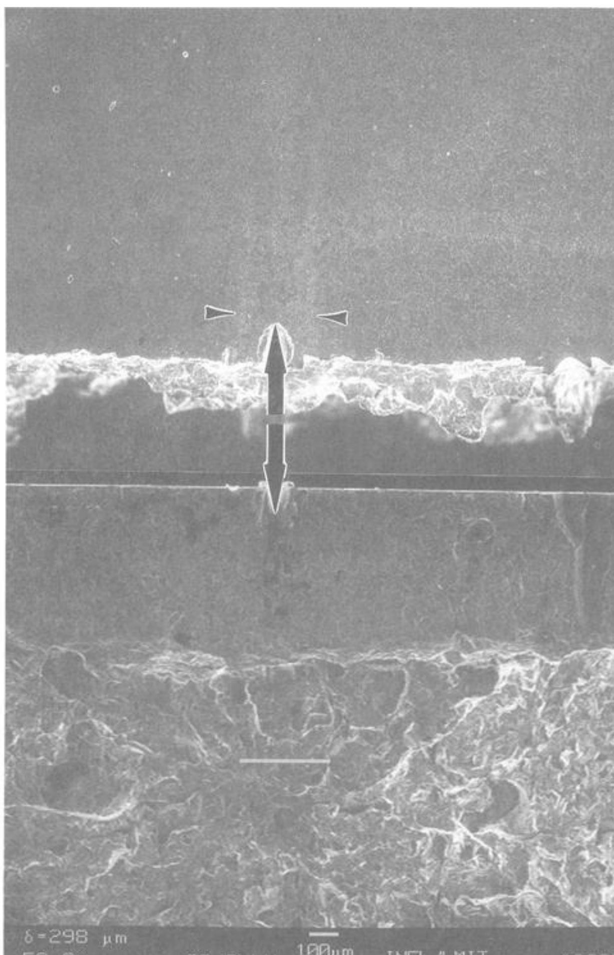

FIG. 11--SEM photographs which show the correlation between (a) the M-A containing bands visible on the polished and etched (5% Nital etch) and (b) the initiation region identified on the fracture surface.

the SEM chamber, the sample was rotated 90° to view the fracture surface. It is apparent from the fractograph in Figure 11b that the plane of the scribe mark (identified by an arrow) approximately bisects the initiation region. (A bar was superimposed on the fracture surface to span the width of the initiation region). It is also significant to note that the distance from the edge of one band to the edge of the next measures approximately 300 μm, which is the same as the diameter of the initiation region.

In order to determine if the fatigue precrack sampled any other regions which contained M-A constituent, all of the HAZ microstructures sampled by the fatigue precrack were examined with the aid of LePera's Reagent. This examination is important from the standpoint that if additional M-A containing regions are identified, it must be determined why they did not also initiate local cleavage. This examination revealed that M-A constituent formed only within the single IRCG region detailed above.

The following microstructures or microstructural constituents have been identified as potential LBZ's [2]: large grain size, upper bainite, microalloy precipitates and high-carbon martensite islands. With the exception of strain aging, each of these were found to exist throughout the straight-side HAZ microstructures of the microalloyed steel investigated in this study. However, since the unique feature of the initiation microstructure was the presence of M-A islands, it is concluded that M-A constituent was the local brittle zone which initiated cleavage fracture in these particular API 2Y-50T weldments.

Mechanisms of M-A Formation--The micrographs in Figure 5 showed that the band microstructure contained more pearlite/bainite as well as more Nb(C,N) precipitates and Ti/Nb-containing precipitates than the matrix microstructure. The elevated volume fraction of pearlite/bainite is the result of microchemical banding of manganese which was detected by EDS. Similarly, the elevated volume fraction of microalloy precipitates is apparently the result of microchemical banding of Nb and possibly Ti. Microchemical banding of manganese resulted in the formation of pearlite which provided the carbon required for the formation of M-A constituent. Similarly, the microchemical banding of microalloy elements provided additional carbon as well as nitrogen which became available by dissolution of microalloy precipitates during welding. Accordingly, the hardenability was locally elevated within microstructural bands of the base plate. Consequently, these bands were susceptible to the formation of M-A constituent during welding. Based on the observed localization of M-A constituent within these regions, it is concluded that the chemistry of the band microstructure in conjunction with the thermal cycle of the IRCGHAZ provide the critical conditions for the formation of M-A constituent in the API 2Y Grade 50T steel investigated. The conditions for M-A formation and the mechanisms of M-A formation related to this study are discussed in much greater detail in Reference [9].

PHASE II: FRACTURE TOUGHNESS TESTING

The Phase I analysis identified the relationship between M-A constituent, the band microstructure and the intercritically-reheated coarse-grain HAZ. Furthermore, Phase I showed that M-A constituent was responsible for the initiation of cleavage fracture which resulted in the reduced fracture toughness of two full-thickness CTOD specimens. Based on these results, the Phase II test program was initiated to quantitatively assess the embrittling effect of M-A constituent by comparing the fracture behavior of HAZ microstructures which contained M-A constituent to similar HAZ microstructures which did not contain M-A constituent.

Following the completion of the full-size CTOD test program discussed in the Background section, approximately 75-mm of the weld ends remained untested. This limited supply of material prevented the use of full-size CTOD specimens for testing in the current research program and necessitated the use of a sub-size specimen geometry. The concern associated with the use of a sub-size specimen geometry is that the lack of crack-tip constraint in sub-size specimens, relative to that in full-size specimens, may result in an elevated level of toughness which underestimates the effect of LBZ's in fracture initiation. However, finite element modelling (FEM) performed at the INEL demonstrated that a BxB geometry, where B = 25-mm, would adequately represent the crack-tip conditions experienced by the much larger full-size specimen where B = 102-mm. FEM demonstrated that approximately the central half of the specimen thickness of a 25x25-mm SE(B) specimen experiences plane strain conditions. Furthermore, FEM showed that the crack-tip constraint (defined as the ratio of hydrostatic stress to the equivalent von Mises stress) within the plane strain region of a 25x25-mm specimen is nearly identical to the crack-tip constraint in the plane strain region of a much larger 102x102-mm. This suggests that if the low-toughness microstructure is placed within approximately 5-mm of the specimen centerline of a 25x25-mm specimen, it will be in the plane strain region and will, therefore, experience the same magnitude of crack-tip constraint as if it were in the plane strain region of a full-size (102x102-mm) specimen. Consequently, specimen geometry effects will not alter the crack-tip stress fields and any differences in crack initiation behavior between full-size and sub-size specimens must be attributed to metallurgical factors.

Experimental Techniques

Specimen Design and Preparation--Two CTOD specimens were designed for testing in this phase of the research program. Both specimens were of the geometry shown in Figure 12 and differed only in the HAZ microstructure sampled by the fatigue precrack. The square-section (BxB, B = 25.4-mm) single edge-notched bend specimens (SE(B) specimens) were fatigue precracked to give a normalized crack length, a/W, of 0.60. The specimen axis was oriented perpendicular to the weld axes and the plate rolling direction, and the precrack was oriented parallel to the weld and plate rolling direction (T-L orientation).

The two square-section CTOD specimens were extracted from the weld section shown in Figure 1. One of the CTOD specimens sampled IRCG region #7 which was

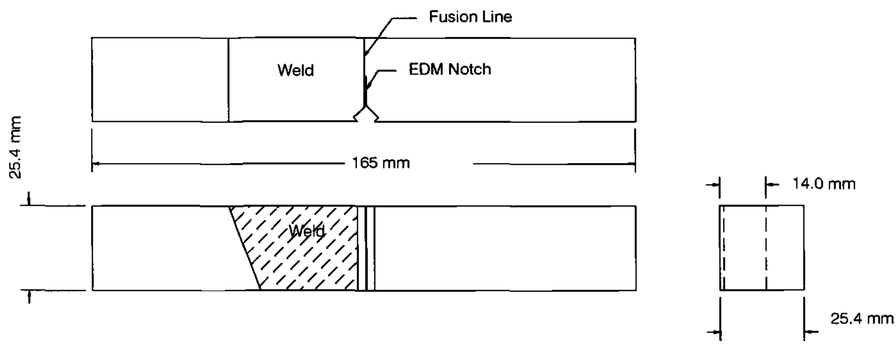

FIG. 12--Schematic drawing of the SE(B) specimen used for CTOD testing in Phase II of the research program.

"contaminated" with M-A constituent in a single microstructural band, whereas the other sampled IRCG region #3 which was not "contaminated" with M-A constituent. Accordingly, these specimens are referred to as the "contaminated specimen" and the "uncontaminated specimen," respectively. Figure 13 illustrates the placement of the two CTOD specimens relative to the IRCGHAZ microstructures of interest. The contaminated specimen was extracted from the full weld section such that the band which contained M-A constituent was located along the specimen centerline and the corresponding IRCGHAZ spanned the specimen width at mid-length. Similarly, the uncontaminated specimen was extracted from the full weld section such that a uncontaminated IRCGHAZ spanned the specimen width at mid-length.

Prior to notching, the CTOD specimens were machined to final size and, subsequently, one of the longitudinal-transverse surfaces (the surface corresponding to the front view of Figure 12) of each of the two specimen blanks was polished and etched to reveal the weld and HAZ microstructures. A scribe mark was placed along the straight-side HAZ to approximately bisect the particular IRCGHAZ microstructures of interest as well as the neighboring FG, SRCG and UACG regions. Subsequently, a stepped-width electro-discharge machine (EDM) notch was placed with its centerline coincident with the scribe mark on the specimen surface.

Prior to fatigue precracking, each specimen was locally compressed [10], resulting in a through-thickness plastic deformation of 1.0% (nominally 0.5 % each side), to ensure adequate crack-front straightness by relieving the welding residual stresses. Following the lateral compression procedure, a single reverse bend cycle was applied to each specimen as a means of promoting early fatigue crack initiation. Fatigue precracking was performed at room temperature, and fatigue crack extension was monitored using a DC potential drop system [11]. In addition, a light scribe line was placed on each side of the specimen corresponding to the minimum allowed length of the fatigue crack and, therefore, crack extension was also visually monitored on the specimen surface. After fatigue precracking, the specimens were side-grooved (to 5% of the original thickness on each side) to prevent tunneling of the crack as it grew during testing.

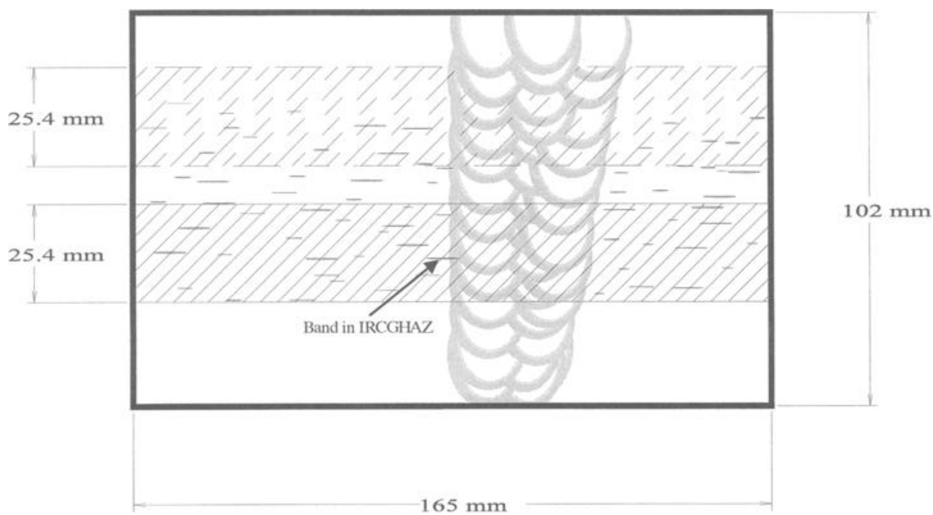

FIG. 13--Schematic diagram of sub-size CTOD specimen location in the full-thickness weld section.

CTOD Testing--The SE(B) specimens were tested in accordance with ASTM Test Method for Crack-tip Opening Displacement (CTOD) Fracture Toughness Measurement (E 1290-93). The one modification to the standard test method was the use of four-point bending rather than three-point bending. The K-solution for a four-point-loaded beam [12] was incorporated into the CTOD inference equations. The CTOD tests were performed at a temperature of -10°C, and a DC potential drop system [12] was used to monitor crack growth during testing.

After completion of each test, the specimen was again subjected to cyclic loading to produce a post-test fatigue crack which distinguished the fatigue precrack and CTOD fracture from the final fracture. Subsequently, each specimen was broken open at liquid nitrogen temperature. After testing, each specimen was metallographically prepared, etched with LePera's Reagent, and examined by light microscopy to characterize the microstructure sampled by the fatigue precrack and to evaluate the initiation microstructure.

Results and Discussion

CTOD Test Results--A comparison of the applied load-displacement (both crack-opening displacement and load-line displacement) records obtained from the CTOD tests indicates a clear distinction between the fracture behavior of the contaminated specimen and that of the uncontaminated specimen.

The test records of the uncontaminated specimen, shown in Figure 14, indicate that the fracture was dominated by slow stable crack growth interrupted by the

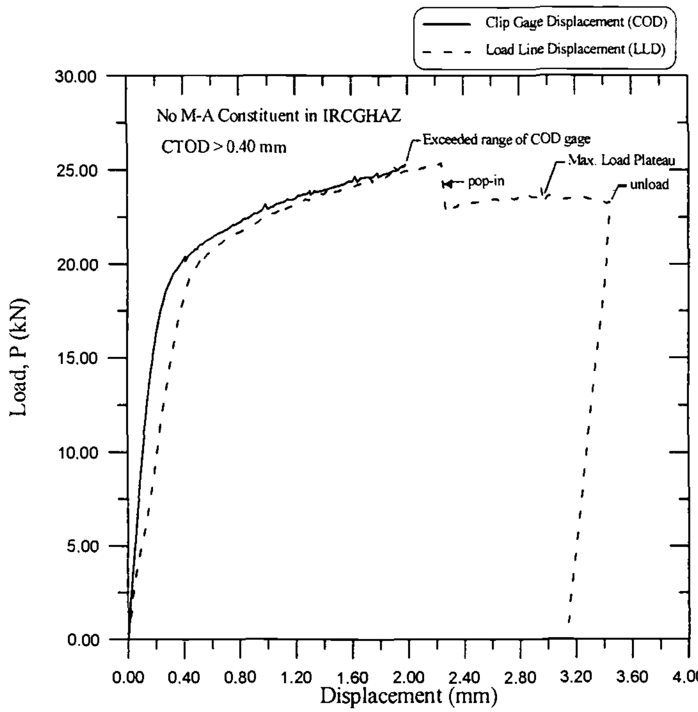

FIG. 14--Load-displacement test records of CTOD specimen which did not contain M-A constituent.

arrested, unstable fracture concomitant with pop-in. The pop-in is significant in light of the criteria of ASTM E 1290. The significant amount of slow stable crack growth (approximately 1.3-mm) prior to the (arrested) unstable crack extension defines the critical CTOD as a δ_u value. Since the crack-opening displacement exceeded the range of the clip gage, δ_u at pop-in is not known, and it must suffice to conclude that δ_u was greater than 0.40-mm.

The test records of the contaminated specimen, shown in Figure 15, indicate a significant pop-in during which the load dropped to 40% of its value at pop-in. The pop-in was attributed to an arrested unstable crack extension of approximately 1.8-mm in the plane of the fatigue precrack. The critical CTOD at the onset of unstable crack extension was estimated (from COD measurements) to be 0.185-mm. Since no significant slow stable crack growth (i.e., stable crack growth less than 0.2-mm) occurred prior to unstable crack extension, the CTOD is defined as a δ_c value.

Fractography--Macroscopic examination of the fracture surface of the contaminated specimen showed that some areas failed by cleavage fracture while others failed by ductile rupture. Post-test examination by light microscopy was conducted to characterize the microstructure sampled by the fatigue precrack and to correlate the HAZ microstructures with the observed fracture mode. The areas of

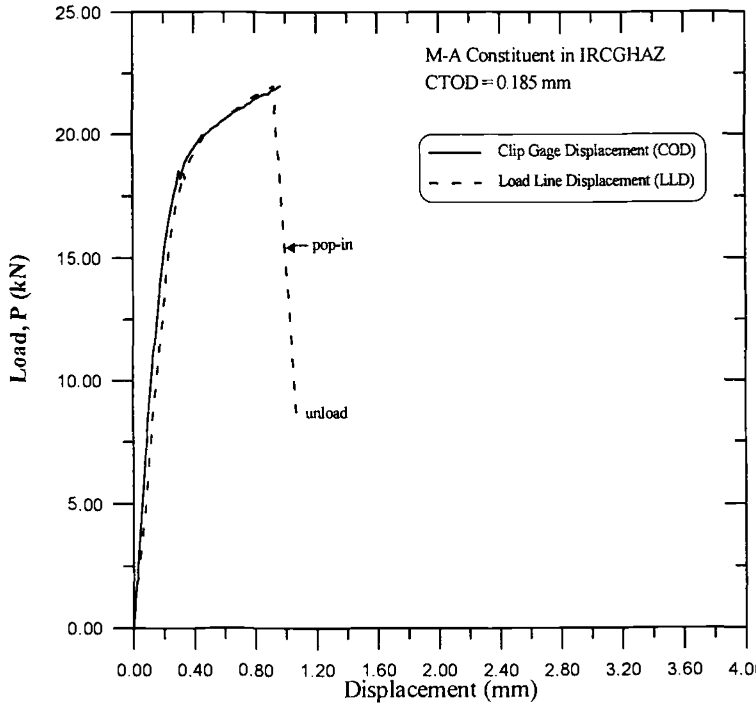

FIG. 15--Load-displacement test records of the CTOD specimen which contained M-A constituent.

cleavage fracture were shown to correspond to the UACG, IRCG and SRCG regions of the HAZ, whereas the areas of ductile rupture were shown to correspond to the FGHAZ regions. Furthermore, the examination of the IRCG zone at the center of the specimen confirmed the presence of M-A constituent. The morphology and distribution of the M-A islands is consistent with Figure 6.

Macroscopic examination of the fracture surface of the uncontaminated specimen showed the fracture mode to be dominated by ductile rupture, although a small area at the edge of the specimen failed by cleavage fracture. It is likely that the pop-in observed on the test record is related to this small area of cleavage fracture. Light microscopy confirmed the absence of M-A constituent in the microstructures sampled by the fatigue precrack of this specimen. The examination also showed the area of cleavage fracture to correspond to a IRCG zone, but this zone did not contain M-A constituent.

The difference between the fracture toughness and the mode of fracture between a specimen with M-A constituent in the crack-tip microstructure and a specimen without M-A constituent in the crack-tip microstructure verifies that M-A constituent is responsible for the reduced toughness behavior.

CONCLUSIONS

Local brittle zone (i.e., M-A constituent) formation in the HAZ of a 108-mm plate of API 2Y Grade 50T steel was shown to be related to the microstructural banding of the hot-rolled base plate. Due to microchemical segregation of manganese and niobium, the hardenability was locally elevated within the band microstructure, making these areas susceptible to the formation of M-A constituent. When the banded base plate was welded, M-A constituent formed within the band microstructure which penetrated the intercritically-reheated coarse-grain HAZ (IRCGHAZ). It is clear based on the microstructural evaluations presented in this paper, that the chemistry of the band microstructure in conjunction with the thermal cycle of the IRCGHAZ provide the critical conditions required for the formation of M-A constituent in the particular steel investigated in this study.

Since the formation of M-A constituent is contingent upon the chance that a locally altered band of material penetrates a particular HAZ region, it is apparent that LBZ formation, as well as the possibility of a LBZ-related failure, is a statistical phenomenon. The present study has demonstrated that M-A constituent did initiate cleavage fracture, and therefore the consequences of LBZ embrittlement are significant. The severity of M-A embrittlement is demonstrated by the fact that, for the two full-thickness CTOD specimens examined, cleavage fracture initiated from a locally embrittled region which occupied approximately 300-μm of the 102-mm wide crack-front in one specimen and approximately 100-μm of the 102-mm wide crack-front of the other specimen; this amounts to approximately 0.3% and 0.1% of the crack-tip microstructure, respectively.

ACKNOWLEDGMENTS

Finite element modelling was performed by Rich Williamson at the Idaho National Engineering Laboratory using ABAQUS finite element program. This work was supported in part by the U.S. Department of Energy, Office of Energy Research, Office of Basic Energy Sciences, and Office of Industrial Technology under DOE Idaho Field Office Contract DE-AC07-94ID13223.

REFERENCES

[1] M. Ramberg, O.M. Akselsen and O. Grong, "Embrittlement Phenomena in the Intercritical HAZ of Boron Containing Low Carbon Steels," *Advances in Welding Science and Technology, ASM International Conference Proceedings*, 1986, 679-684.

[2] D.P. Fairchild, "Local Brittle Zones in Structural Steels," in *Welding Metallurgy of Structural Steels*, J.Y. Koo, Ed., TMS, Warrendale, PA, 1987, 303-318.

[3] C.L. Davis and J.E. King, "Cleavage Initiation in the Intercritically Reheated Coarse-Grained Heat-Affected Zone: Part I. Fractographic Evidence," *Metallurgical Transactions A*, 25A, 1994, 563-573.

[4] API Specification 2Y (Spec 2Y), "Specification for Steel Plates, Quenched-and-Tempered, for Offshore Structures," API, Washington, DC, 1987.

[5] P.L. Harrison and P.H.M. Hart, "HAZ Toughness of Thick Section Structural Steels," *International Conference on Weld Failures,* Nov. 1988, 185-201.

[6] F. LePera, "Improved Etching Technique to Emphasize Martensite and Bainite in High-Strength Dual-Phase Steels," *Journal of Metals*, 1980, 38-39.

[7] S.W. Thompson and P.R. Howell, "Factors Influencing Ferrite/Pearlite Banding and Origin of Large Pearlite Nodules in a Hypoeutectoid Plate Steel," *Material Science and Technology*, 8, 1992, 777-784.

[8] Y. Shen, private communication, 1995.

[9] K.L. Kenney, "Heat-Affected Zone Embrittlement by Local Brittle Zones: A Case Study," *Master's Thesis*, Department of Metallurgical and Materials Engineering, Colorado School of Mines, Sept. 1996.

[10] H.S. Reemsnyder, H.G. Pisarski, and M.G. Dawes, "Residual Stresses and Fatigue Precracking Techniques for Weldment Fracture Toughness Specimens," *Journal of Testing and Evaluation*, 20(6), Nov. 1992, 416-423.

[11] J.K. Donald and J. Ruschau, "Direct Current Potential Difference Fatigue Crack Measurement Techniques," in Fatigue Crack Measurement: Techniques and Applications, K. J. Marsh, R. O. Ritchie and R. A. Smith, Eds,., 1990.

[12] H. Tada, P.C. Paris, and G.R. Irwin, "The Stress Analysis of Cracks Handbook," 2nd Ed., Del Research Corporation., Hellertown, PA, 1973.

Richard Yee[1], Lalit Malik[1], and Jack Morrison[2]

EFFECT OF WELD METAL MISMATCH ON JOINT EFFICIENCY AND MEASURED FRACTURE TOUGHNESS

Reference: Yee, R., Malik, L., and Morrison, J., **"Effects of Weld Metal Mismatch on Joint Efficiency and Measured Fracture Toughness"**, Fatigue and Fracture Mechanics: 28th Volume, ASTM STP 1321, J. H. Underwood, B. D. Macdonald, and M. R. Mitchell, Eds., American Society for Testing and Materials, Philadelphia, 1997.

Abstract: Fracture toughness tests of deep-notched and shallow-notched SENB specimens at various sub-zero temperatures were conducted to study the effect of weld metal mismatch on measured fracture toughness. Tensile tests of cross-weld tensile specimens were also conducted to study the effect of weld metal mismatch on joint efficiency. These specimens were machined from butt welds that were fabricated with the same welding consumable and welding procedure using HSLA 100 steel plates heat treated to different tensile strengths. No significant differences were found between the joint efficiencies and ductilities of the cross-weld tensile specimens with overmatching weld metal and those of specimens with up to 9% weld metal undermatch in terms of yield strength (3% in terms of ultimate tensile strength). Furthermore, 100% joint efficiency was still achieved in the cross-weld tensile specimens with intact reinforcements and 17% undermatching weld metal in terms of yield strength (9% in terms of ultimate tensile strength). No correlation was found between the degree of weld metal mismatch and the measured fracture toughness of the SENB specimens.

Keywords: mismatch, HSLA-100, weld metal, CTOD, J, joint efficiency

---

[1] Fleet Technology Limited, 311 Legget Drive, Kanata, Ontario, Canada, K2K 1Z8.

[2] Esquimalt Defence Research Detachment, CFB Esquimalt, Building 199, Victoria, B.C., Canada, V9A 7N2.

INTRODUCTION

Modern high strength steels such as HSLA-100 have excellent fracture toughness and resistance to cold cracking in the heat affected zone, even when they are welded without pre-heat. Unfortunately, welding consumables with comparable tensile strength, fracture toughness, and resistance to cold-cracking are not yet commercially available. As a result, fabricators are unable to fully exploit the cost advantages of welding such steels at this time. A potential solution is to weld the steels with undermatching consumables that have a lower yield strength but higher fracture toughness than the base metal. Although plastic strains tend to localize in the undermatching weld metal, this strain concentration is mitigated by strain hardening of the weld metal and by the constraint of the surrounding base metal. Furthermore, the higher intrinsic fracture toughness of the undermatching weld metal counters to some extent the higher driving force for fracture initiation in the weld metal. Hence, a certain degree of undermatching can be tolerated without a significant reduction in overall ductility and load capacity. While many applications of undermatching weld metal have been approved on a case by case basis, there has been a general reluctance to accept this practice until the effects of undermatching on the measured fracture toughness and load capacity of welded joints is better understood.

In the present investigation, five series of butt welded joints with varying degrees of mismatch between the yield strengths of the weld metal and base metal were fabricated from 15 mm thick HSLA-100 steel plate. This mismatch was achieved by using the same weld metal but heat treating the base metal to different yield strengths. Single edge notch bend (SENB) specimens were machined from these welds, and fracture toughness tests were conducted with these specimens at various sub-zero temperatures to investigate the effects of weld metal mismatch on the measured fracture toughness in terms of J and the crack tip opening displacement (CTOD). Tensile tests were also conducted with cross-weld tensile specimens machined from the welds to assess the effects of weld metal mismatch on joint efficiency, herein defined as the ratio of the ultimate tensile strength of the joint to the ultimate tensile strength of the base metal. Since the intrinsic fracture toughness and strain hardening of the weld metal were the same in each joint, any effects of mismatch on the measured fracture toughness and joint efficiency could be attributed to variations in constraint.

EXPERIMENTAL METHOD

Test Specimens

The same shielded metal arc welding process (Figure 1) and the same welding consumable (4 mm diameter E10018 - M1 electrodes) were used to produce multiple-pass butt welds in five 15 mm thick × 400 mm wide × 750 mm long steel plates. The five base plates were machined from the same parent plate, which was rolled to specifications for HSLA-100 steel, and then welded in the same direction as the rolling direction of the parent plate. However, four of the five base plates were aged at 650°C for different durations (1, 2, 6.5, and 72 hours) prior to welding, whereas the remaining base plate was welded in the as-received condition.

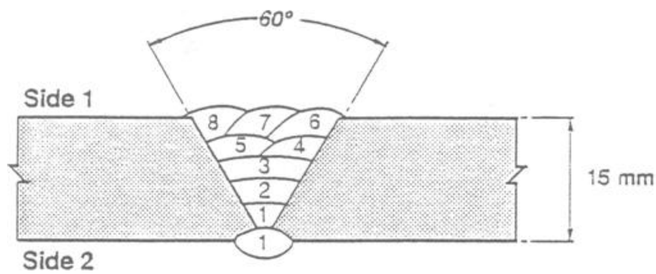

Material Specification:	HSLA 100
Welding Process:	Manual SMAW
Position of Welding:	1G
Filler Metal:	E10018M-1 Alloy Rods, 4 mm Dia.
Single or Multipass:	Multipass
Single or Multiple Arc:	Single (170 Amps, 22 Volts)
Preheat Temperature:	66° C
Interpass Temperature:	100° C
Preheat Method:	Propane Torch
Travel Speed:	130 - 200 mm/min.

Figure 1: Welding procedure for butt welds.

The chemical composition and tensile properties of the five base metals and weld metal are summarized in Tables 1 and 2, respectively. The properties of each base metal were obtained from tensile tests of two or three flat full-thickness specimens that were machined from the base plate with their longitudinal axes perpendicular to the rolling direction, whereas the properties of the weld metal were obtained from tensile tests of four 4 mm thick specimens that were machined from the fusion zones of test welds with their longitudinal axes parallel to the welding direction. As evident in Table 3, the mismatch between the average measured yield strength of the weld metal (σ_{Wy}) and the average measured yield strength of each base metal (σ_{By}) relative to the latter ranged from -0.30 to +0.15, whereas the mismatch between the average measured ultimate tensile strength of the weld metal (σ_{Wu}) and the average measured ultimate tensile strength of each base metal (σ_{Bu}) relative to the latter ranged from -0.22 to +0.18.

Table 1: Chemical composition of base metal and weld metal.

element	wt%	
	base metal	weld metal
C	0.04	0.04
Mn	0.92	1.20
P	0.007	-
S	0.002	-
Cu	1.15	0.17
Si	0.25	0.32
Ni	1.65	1.80
Cr	0.58	0.10
Mo	0.40	0.27
V	0.004	-
Ti	0.002	-
Nb	0.032	-
Al	0.019	-

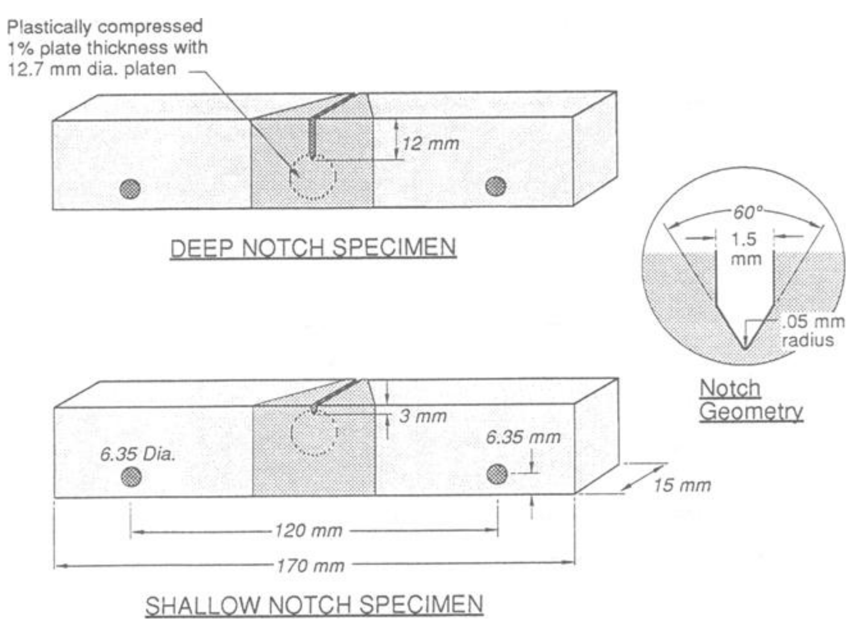

Figure 2: Geometry and dimensions of SENB specimens.

Table 2: Tensile properties of steel plates.

Material	Specimen No.	0.2% Offset Yield Strength (MPa)	Ultimate Tensile Strength (MPa)	Uniform Elongation (%)
Base Plate As-received Condition	1	822	862	8.3
	2	825	869	7.4
	3	820	863	8.9
Base Plate Aged for 1 hour @ 650°C	1	701	748	9.1
	2	686	735	9.4
Base Plate Aged for 2 hours @ 650°C	1	650	698	8.2
	2	648	698	8.6
	3	637	677	10.1
Base Plate Aged for 6.5 hours @ 650°C	1	603	662	9.7
	2	564	636	12.2
Base Plate Aged for 72 hours @ 650°C	1	512	573	12.4
	2	509	569	13.4
	3	482	567	12.1
Weld Metal	1	569	659	20.4
	2	589	677	19.6
	3	575	678	21.0
	4	589	672	19.3

Table 3: Degree of mismatch between yield strength of weld metal (σ_{Wy}) and yield strength of base metal (σ_{By}) and degree of mismatch between ultimate tensile strength of weld metal (σ_{Wu}) and ultimate tensile strength of base metal (σ_{Bu}).

Butt Weld Series No.	Base Metal Heat Treatment	$\frac{\sigma_{Wy} - \sigma_{By}}{\sigma_{By}}$	$\frac{\sigma_{Wu} - \sigma_{Bu}}{\sigma_{Bu}}$
1	None	-0.297	-0.220
2	Aged for 1 hour @ 650°C	-0.167	-0.091
3	Aged for 2 hours @ 650°C	-0.104	-0.025
4	Aged for 6.5 hours @ 650°C	-0.007	+0.038
5	Aged for 72 hours @ 650°C	+0.154	+0.183

18 to 20 SENB specimens were machined from each series of butt welds (94 specimens total). The dimensions of these specimens and the orientation of the weld metal in these specimens are shown in Figure 2. A 12 mm deep notch was machined in the weld metal of half of the specimens from each joint, while a 3 mm deep notch was machined in the remaining specimens from each joint. These through-thickness notches were cut with a slitting wheel that produced the geometry shown in the inset of Figure 2.

In addition to the SENB specimens, three 75 mm wide × 15 mm thick cross-weld tensile specimens were machined from each series of butt welds. The reinforcements in two of the three specimens were machined off, while the reinforcement in the third specimen was left in the as-welded condition.

Test Procedure

The cross-weld tensile specimens were pulled at room temperature at a displacement rate of 0.05 mm/s in a Baldwin servo-hydraulic test machine. An extensometer with a 50 mm gauge length was installed on each specimen to permit the determination of the yield strength corresponding to a 0.2% strain offset. The tests were interrupted at the peak load to record the uniform elongation over the 50 mm gauge length.

A 2 to 3 mm deep fatigue crack was initiated at the notch tip of each SENB specimen by cyclically loading the specimen in three-point bending. This pre-cracking was performed in a Pegasus servo-hydraulic test machine at an R-ratio of 0.1. Prior to this operation, the notch tip was plastically compressed in the through-thickness direction (1% plastic strain) with a 12.7 mm diameter platen. The maximum applied loads for the shallow-notched specimens and deep-notched specimens were initially maintained at 24.7 kN and 10.4 kN, respectively, until a 0.5 mm deep fatigue crack was visually detected at the edges of the starter notch. The maximum applied loads for the shallow-notched specimens and deep-notched specimens were then reduced to 19.1 kN and 7.9 kN, respectively, for the next 0.5 to 1.0 mm of fatigue crack growth. The maximum applied loads for the shallow-notched specimens and deep-notched specimens were maintained at 13.6 kN and 5.4 kN, respectively, for the final 1.0 to 1.5 mm of fatigue crack growth. The latter loads produced a maximum stress intensity factor of 22 MPa$\sqrt{m}$ at the final crack tip.

Fracture toughness tests were conducted with the SENB specimens immersed in an alcohol bath. These tests were performed under displacement control in a Baldwin servo-hydraulic test machine with a three-point bending fixture. The load-line displacement rate (quasi-static) was approximately 0.5 mm per minute. The deep-notched specimens were tested at -10°C, -30°C, -40°C, and -60°C, while the shallow-notched specimens were tested at -40°C and -60°C (see Table 4 for test matrix). These temperatures were obtained by cooling the alcohol bath with dry ice to a temperature 3°C below the desired test temperature.

Table 4: Number of specimens allotted to each series in test matrix.

$\frac{\sigma_{Wy} - \sigma_{By}}{\sigma_{By}}$	Shallow-Notched SENB		Deep-Notched SENB			
	-40°C	-60°C	-10°C	-30°C	-40°C	-60°C
-0.295	5	4	-	3	3	3
-0.165	5	4	3	-	3	3
-0.088	5	5	3	1	3	3
-0.019	5	5	-	4	3	3
+0.156	5	4	1	2	3	3

Three quantities were monitored during each test: applied force (F), crack mouth opening displacement (CMOD), and load-line displacement (LLD). Load-line displacement, which was defined as the vertical displacement of the notch mouth relative to a comparator bar, was measured with a proximity probe. Crack mouth opening displacement was measured with an extensometer that was attached to knife edges at the mouth of the starter notch. Applied force was measured with a load cell in series with the loading ram and hydraulic actuator. Data from these transducers were collected with a 16 bit data acquisition system at a sampling rate of 3 Hz. Each test was terminated when the applied force either reached a maximum plateau or abruptly decreased by more than 5%. In every case, a plateau or peak in the applied force was reached before a pop-in occurred, where a pop-in was defined as a less than 5% drop in the applied force followed by an increase in the applied force to a level at least as high as the applied force at the start of the load drop.

Once the fracture toughness tests were completed, the SENB specimens were soaked in liquid nitrogen and broken apart by rapidly loading them in the Baldwin's three-point bending fixture. The final fracture surfaces of the specimens were then examined under a stereomicroscope to identify the mode of failure.

RESULTS

Cross-Weld Tensile Tests

Figure 3 is a plot of the joint efficiency (σ_u/σ_{Bu}) of each cross-weld tensile specimen versus its degree of weld metal mismatch in terms of yield strength; where σ_u is the specimen's ultimate strength based on the measured ultimate load and initial cross-sectional area of the base plate, and σ_{Bu} is the average measured ultimate strength of the base metal. The specimens with overmatching weld metal and the specimens with up to 9% weld metal undermatch all failed in the base metal, and Figure 3 shows that the joint efficiencies of these specimens fell within a narrow range (1.02 to 1.05) regardless of the degree of weld metal mismatch and the condition of the weld reinforcement. In contrast, all but one of the specimens with greater than 9% weld metal undermatch failed in the weld metal. Furthermore, the joint efficiencies of these specimens tended to decrease with increasing weld metal undermatch, and the joint efficiencies of the specimens without reinforcements decreased at a greater rate than the joint efficiencies of the specimens with intact reinforcements. However, joint efficiencies exceeding 0.9 were still achieved in the specimens with 30% weld metal undermatch and machined-off weld reinforcements, and 100% joint efficiency was still achieved in the specimen with 17% weld metal undermatch and intact weld reinforcements.

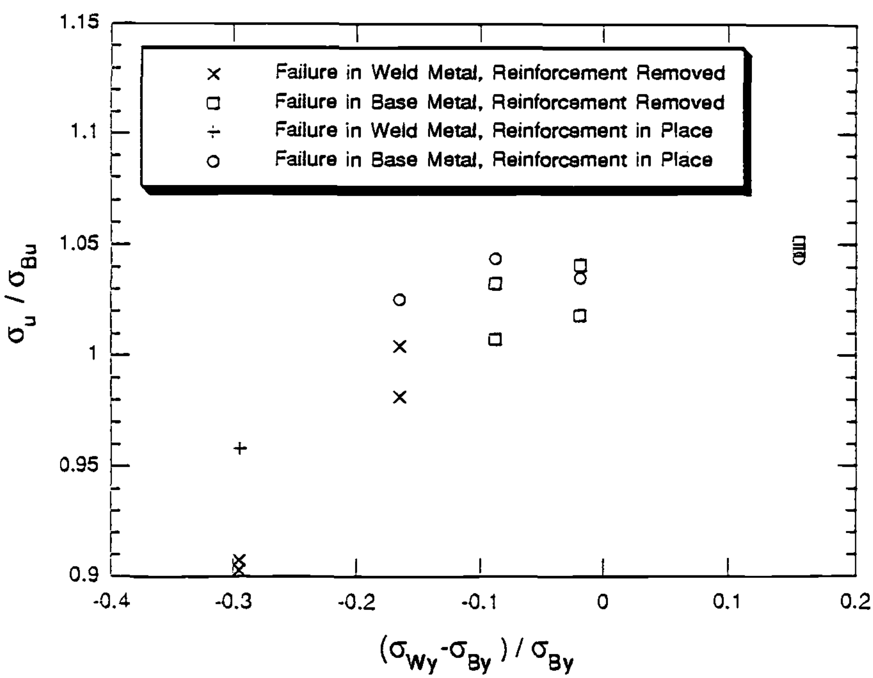

Figure 3: Joint efficiency versus weld metal mismatch in cross-weld tensile specimens.

Figure 4 is a plot of the elongation of each cross-weld tensile specimen versus its degree of weld metal mismatch in terms of yield strength. There is considerable scatter in this plot, and the only observable trend is that the minimum and maximum measured elongations of the specimens with 30% weld metal undermatch were lower than the corresponding elongations of the specimens with either overmatching weld metal or less than 30% weld metal undermatch.

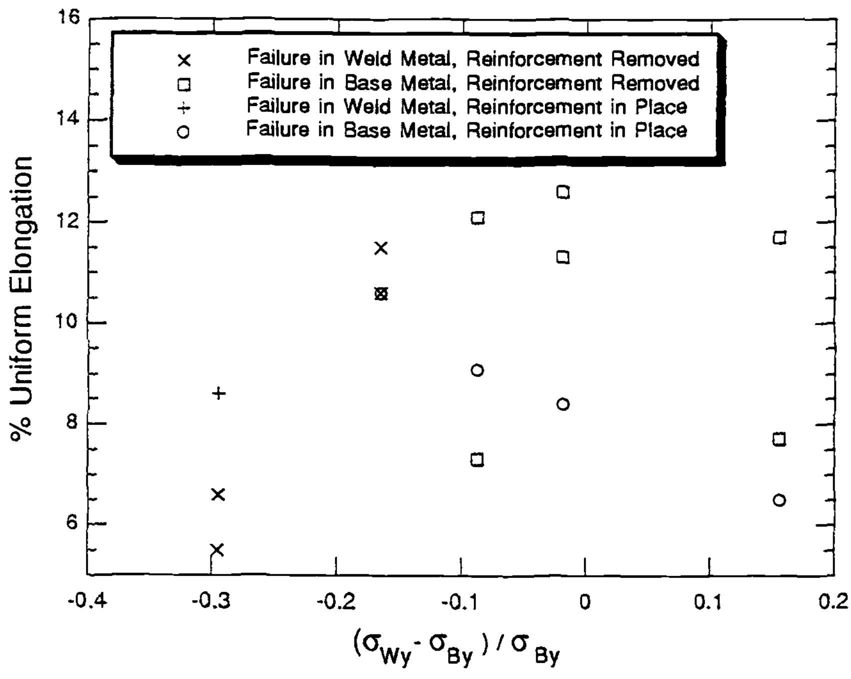

Figure 4: Elongation versus weld metal mismatch in cross-weld tensile specimens.

Fracture Toughness Tests

The SENB specimens failed by one of three basic modes:

1. arrested unstable cleavage,
2. stable ductile tearing followed by arrested unstable cleavage, or
3. stable ductile tearing.

These three modes are herein referred to as Mode c, Mode u, and Mode m failures, respectively.

As stated earlier, each test was terminated when the applied force either reached a maximum plateau, or peaked and then abruptly decreased by more than 5%. In every case, a plateau or peak in the applied force was reached before a pop-in had occurred, a pop-in being defined as a less than 5% drop in the applied force followed by an increase in the applied force to a level at least as high as the applied force at the start of the load drop. The peak forces coincided with the onset of unstable cleavage in Mode c and Mode u failures, whereas the force plateaus were reached in Mode m failures. The force peak in a Mode c or Mode u failures is herein referred to as F_c or F_u, respectively, while the maximum force in a Mode m failure is herein referred to as F_m.

Equations 1 and 2 from BS 7448 [1] were used to calculate the crack driving force ($CTOD_{standard}$ and $J_{standard}$) in the deep-notched specimens, while recommended equations by Wang and Gordon [2] were used to calculate the crack driving force ($CTOD_{CMOD}$ and J_{CMOD}) in the shallow-notched specimens (Equations 3 and 4) :

$$CTOD_{standard} = \frac{K^2(1-\nu^2)}{2\sigma_{YS}E} + \frac{0.4(W - a_o)CMOD_p}{0.4(W - a_o) + 0.6a_o + z} \tag{1}$$

$$J_{standard} = \frac{K^2(1-\nu^2)}{E} + \frac{2A_{LLD}}{B(W-a_o)} \tag{2}$$

$$CTOD_{CMOD} = \frac{K^2(1-\nu^2)}{2\sigma_{YS}E} + \frac{\eta_{C\text{-}C}A_{CMOD}}{\sigma_{YS}B(W-a_o)} \tag{3}$$

$$J_{CMOD} = \frac{K^2(1-\nu^2)}{E} + \frac{\eta_{C\text{-}C}A_{CMOD}}{B(W-a_o)} \tag{4}$$

where

$$K = \frac{4F}{BW^{.5}} - \frac{3\left(\frac{a_o}{W}\right)^{.5}\left[1.99 - \frac{a_o}{W}\left(1-\frac{a_o}{W}\right)\left(2.15 - \frac{3.93a_o}{W} + \frac{2.7a_o^2}{W^2}\right)\right]}{2\left(1+\frac{2a_o}{W}\right)\left(1-\frac{a_o}{W}\right)^{1.5}} \tag{5}$$

$$\eta_{C\text{-}C} = 4.292 - 1.667\left(\frac{a_o}{W}\right) + 0.304\left(\frac{\sigma_{Wu}}{\sigma_{Wy}}\right)^2 - 2.0\left(\frac{\sigma_{Wu}}{\sigma_{Wy}}\right) \tag{6}$$

$$\eta_{J\text{-}C} = 3.5 - 1.4167\left(\frac{a_o}{W}\right) \tag{7}$$

a_o = the depth of the fatigue pre-crack and its starter notch
F = applied load
B = specimen thickness
W = specimen width
z = the distance from the mouth of the starter notch to the point of attachment between the extensometer and its knife edges
ν = Poisson's ratio
E = modulus of elasticity
σ_{Wy} = yield strength of weld metal
σ_{Wu} = ultimate tensile strength of weld metal
A_{LLD} = the area under the plastic component of the applied force versus load-line displacement curve
A_{CMOD} = the area under the plastic component of the applied load versus crack mouth opening displacement
$CMOD_p$ = the plastic component of the crack mouth opening displacement

For the purposes of this study, the Poisson ratio (ν) and modulus of elasticity (E) of the weld metal were assumed to be 0.3 and 207 GPa, respectively, while the yield strength and ultimate tensile strength of the weld metal were taken as the averages of the measurements in Table 2. The average crack depth of the fatigue pre-crack and its starter notch was based on nine equally-spaced measurements across the crack front with a traveling microscope. A Simpson's rule algorithm (1% convergence tolerance) was used to numerically evaluate the areas under the applied load versus crack mouth opening displacement curves and applied load versus load-line displacement curves, while the areas under the elastic unloading lines were calculated analytically. The slopes of the elastic unloading lines were derived from empirical solutions for the elastic compliances of the SENB specimens in their initial configuration .

The measured fracture toughness (i.e., the calculated values of CTOD and J corresponding to F_c, F_u, or F_m) of the SENB specimens are plotted against temperature in Figures 5 and 6. The following comments can be made about the data in these figures:

1. The measured fracture toughness values of the shallow-notched specimens tended to increase with increasing temperature. The majority of these specimens failed by Mode u. Of the remaining specimens, only one failed by Mode m and only three failed by Mode c. This indicates that the two test temperatures for the

shallow notch specimens (-40°C and -60°C) were well within the ductile-brittle transition region for these specimens.

2. The measured fracture toughness values for the deep-notched specimens tested at -30°C, -40°C, and -60°C tended to increase with increasing temperature, while the measured fracture toughness values for the deep-notched specimens tested at -10°C were similar to the measured fracture toughness values for the deep-notched specimens tested at -30°C. All of the specimens that were tested at -10°C failed by Mode m, whereas the specimens that were tested at -30°C failed by either Mode u or Mode m. Furthermore, most of the specimens that were tested at -60°C failed by Mode c; the remainder of these specimens failed by Mode u. This indicates that the start of the upper shelf for the fracture toughness of the deep-notched specimens was somewhere between -10°C and -30°C, while the lower part of the ductile-brittle transition region for these specimens was located near -60°C.

3. For a given temperature, the fracture toughness values for the shallow-notched specimens were generally higher than the fracture toughness values for the deep-notched specimens. This geometry dependence is related to the lower constraint in the shallow-notched specimens, which promoted crack initiation by ductile tearing rather than brittle cleavage.

4. The fracture toughness values for the shallow-notched specimens were much more variable than the fracture toughness values for the deep-notched specimens. In addition, the fracture toughness values in the upper ductile-brittle transition region of the deep-notched specimens appeared to be more variable than the upper shelf fracture toughness values for these specimens. These differences can be attributed to two factors. First, the dominant mode of failure in these specimens was ductile crack initiation followed by brittle cleavage (i.e., Mode u). The measured fracture toughness values were associated with the onset of brittle cleavage. Second, cleavage in a Mode u failure occurs when the stress field ahead of the initial growing crack samples a critical particle. Therefore, the onset of cleavage is influenced by statistical sampling effects.

The average, maximum, and minimum fracture toughness values for different combinations of notch depth and temperature are also plotted against the degree of weld mismatch in Figures 7 and 8. None of these figures show an obvious relationship between the measured fracture toughness and the degree of weld metal mismatch, and statistical analyses of all the data failed to isolate any such relationship from the experimental scatter.

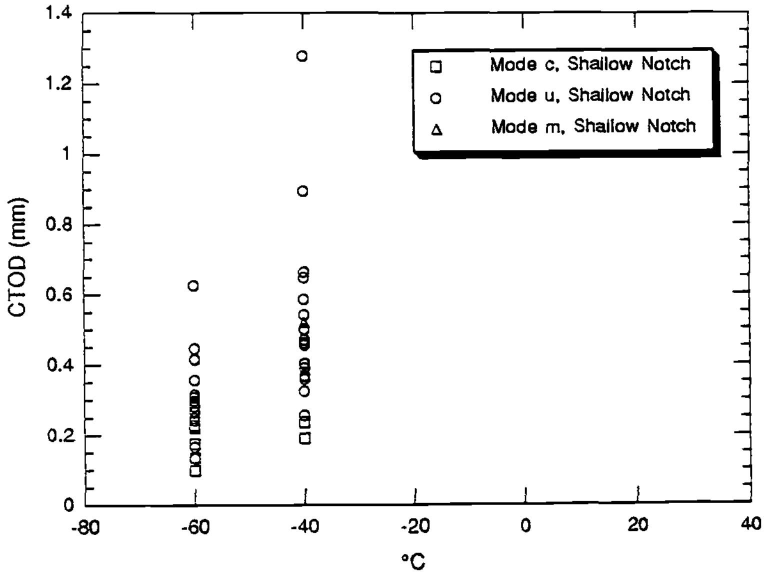

Figure 5a: Measured fracture toughness (CTOD) versus test temperature for shallow notch specimens.

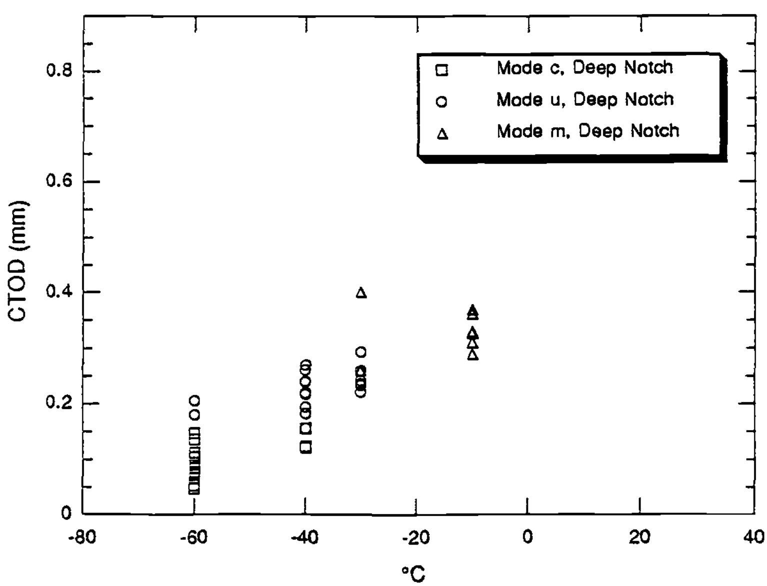

Figure 5b: Measured fracture toughness (CTOD) versus test temperature for deep notch specimens.

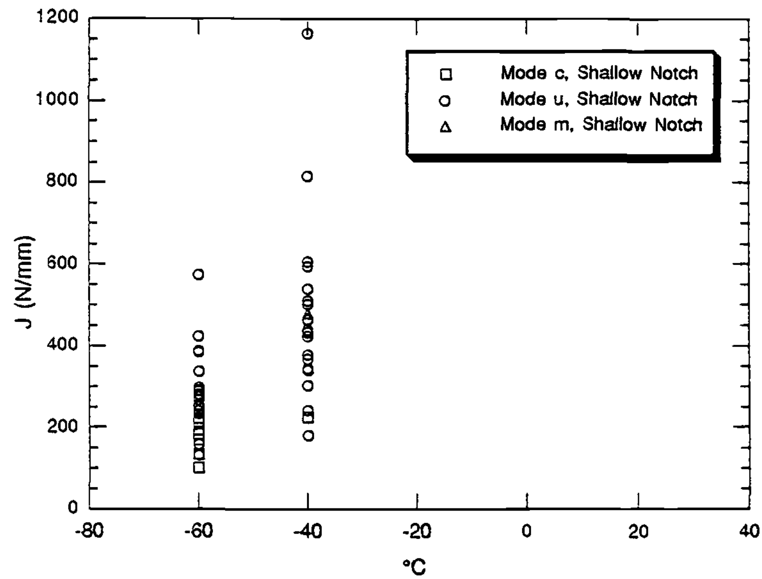

Figure 6a: Measured fracture toughness (J) versus test temperature for shallow notch specimens.

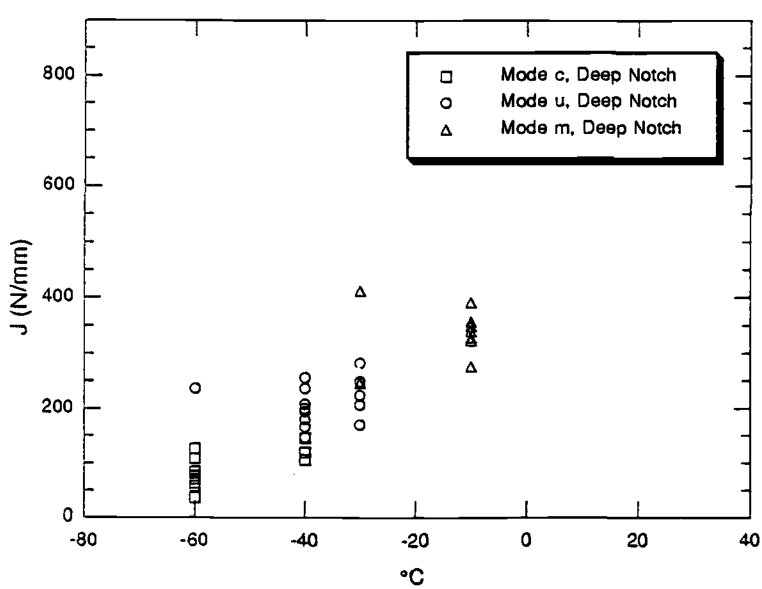

Figure 6b: Measured fracture toughness (J) versus test temperature for deep notch specimens.

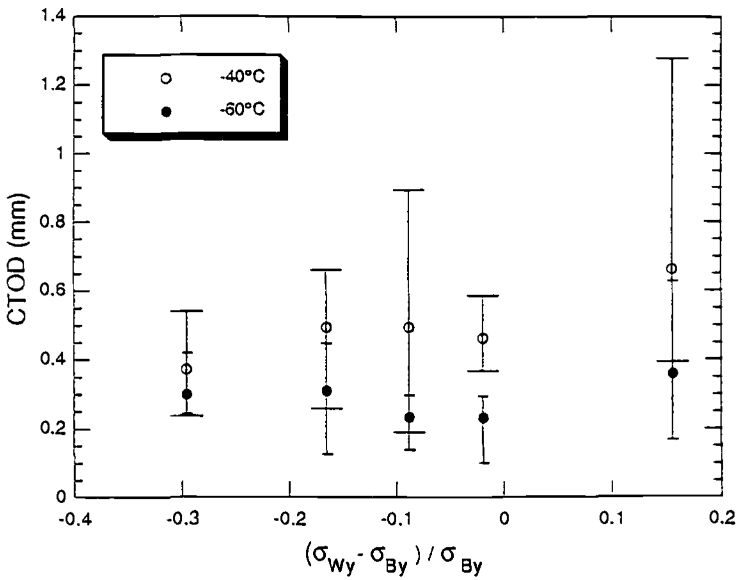

Figure 7a: Minimum, maximum, and average of measured fracture toughness (CTOD) versus degree of weld metal mismatch for shallow notch specimens.

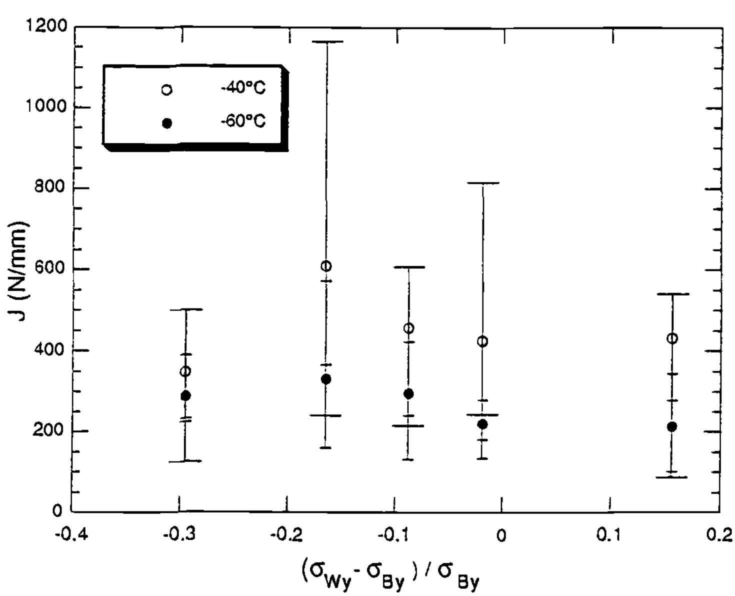

Figure 7b: Minimum, maximum, and average measured fracture toughness (J) versus degree of weld metal mismatch for shallow notch specimens.

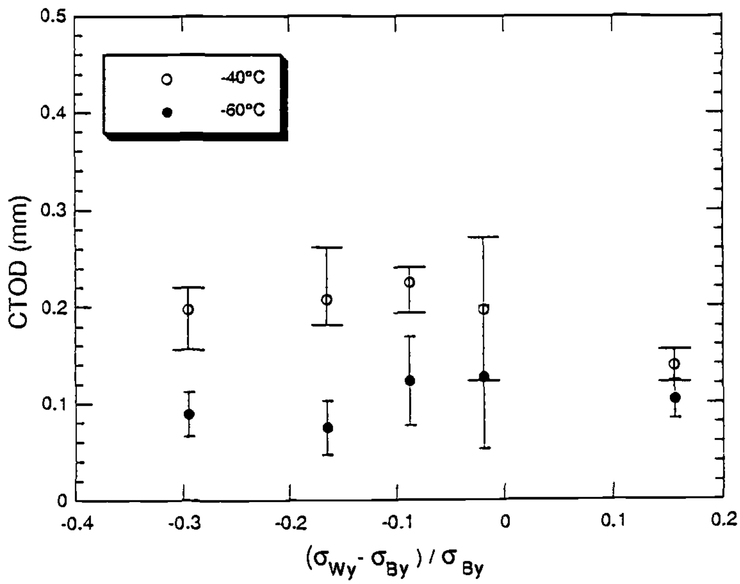

Figure 8a: Minimum, maximum, and average of measured fracture toughness (CTOD) versus degree of weld metal mismatch for deep notch specimens.

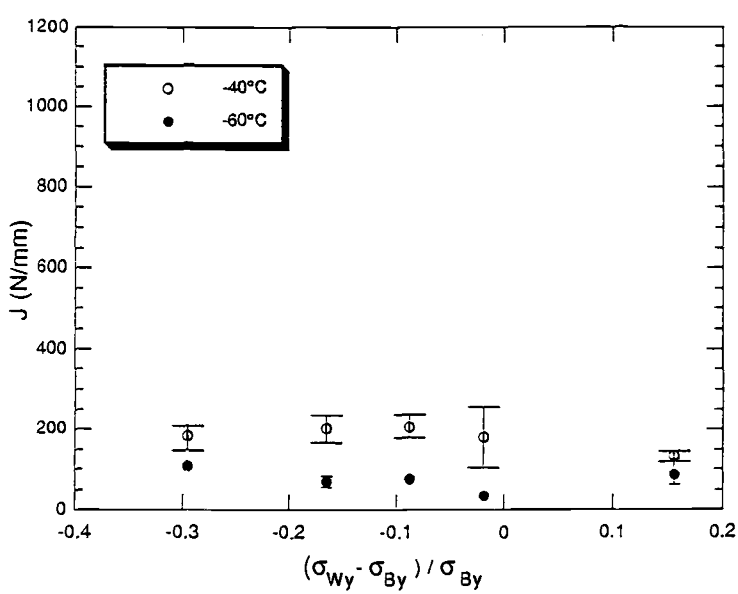

Figure 8b: Minimum, maximum, and average measured fracture toughness (J) versus degree of weld metal mismatch for deep notch specimens.

DISCUSSION

The width of the cross-weld specimens was five times their thickness. According to Satoh [3], this ratio should be sufficient to simulate reasonably the constraint in a wide plate. The joint efficiency and ductility of the cross-weld tensile specimens with up to 9% weld metal undermatch in terms of yield strength (3% in terms of ultimate tensile strength) were comparable to those for the cross-weld tensile specimens with overmatching weld metal regardless of whether the weld reinforcement was machined-off or intact. Furthermore, 100% joint efficiency was still achieved in the cross-weld tensile specimens with intact reinforcements and 17% weld metal undermatch in terms of yield strength (9% in terms of ultimate tensile strength). These results are comparable to results from other studies. For example, Satoh et al [3] investigated the effect of weld metal mismatch on the joint efficiency and ductility of transverse butt welds with intact reinforcements in 500 mm wide × 70 mm thick HT80 steel plates. They concluded that joint efficiency and ductility comparable to those of joints with overmatching weld metal can be guaranteed in sufficiently wide joints with undermatching weld metal provided the tensile strength of the weld metal is no less than 90% of the tensile strength of the base metal. In another study, Dexter and Ferell [4] investigated the effect of weld metal mismatch on the joint efficiency and ductility of transverse butt welds with ground-off reinforcements in 610 mm wide × 9, 13, or 25 mm thick HSLA 100 steel plates. They concluded that up to 12% weld metal undermatch in terms of actual yield strength could be tolerated without a significant loss of ductility and joint efficiency, provided the ratio of plate width to plate thickness is at least 12.

Equations 1-4 for estimating the crack driving force in SENB specimens are empirical and have been calibrated against experimental data for homogeneous test specimens. The first set of equations is only intended for a_0/W ratios between 0.45 and 0.55, whereas the second set of equations is applicable to a_0/W ratios between 0.1 and 0.6. For the same base metal, specimen geometry, and applied load, the plastic strain distribution and the limit load of test specimens with either undermatching or overmatching weld metal differ from that in homogeneous test specimens. Therefore, in principle, the equations should not be applied to test specimens with mismatched weld metal. However, recent elasto-plastic finite element analyses by Kirk and Dodd [5] have indicated that the aforementioned equations are sufficiently accurate for SENB specimens with up to +/-20% mismatch between the yield strengths of the weld metal and base metal. The results of this study seem to support this conclusion.

SUMMARY

Five series of butt welded joints with varying degrees of mismatch between the yield strengths of the weld metal and base metal were fabricated from 15 mm thick HSLA-100 steel plate. This mismatch was achieved by using the same weld metal but heat treating the base metal to different yield strengths. 94 SENB specimens were machined from these welds, and fracture toughness tests were conducted with these specimens at various sub-zero temperatures to investigate the effects of weld metal mismatch on the measured fracture toughness in terms of J and the crack tip opening displacement (CTOD). Tensile tests were also conducted with cross-weld tensile specimens machined from the welds to assess the effects of weld metal mismatch on joint efficiency.

No significant difference was found between the joint efficiency and ductility of the cross-weld tensile specimens with overmatching weld metal and the joint efficiency and ductility of the cross-weld tensile specimens with up to 9% weld metal undermatch in terms of yield strength (3% in terms of ultimate tensile strength). Furthermore, 100% joint efficiency was still achieved in the cross-weld tensile specimens with intact reinforcements and 17% undermatching weld metal in terms of yield strength (9% in terms of ultimate tensile strength).

Standard equations [1] were used to estimate the crack driving force in the deep-notched SENB specimens, while equations recommended by Wang and Gordon [2] were used to estimate the crack driving force in the shallow-notched SENB specimens. No correlation was found between the degree of weld metal mismatch and the measured fracture toughness (i.e., crack driving force corresponding to the applied force at the onset of unstable cleavage or the attainment of a force plateau associated with stable tearing). This implies that the aforementioned equations are essentially independent of weld metal mismatch over the range of mismatch considered in this study (-30% to +16% in terms of yield strength), since the test specimens had the same weld metal and therefore the same intrinsic fracture toughness.

REFERENCES

1. BS 7448: Part 1: 1991, "Fracture Mechanics Toughness Tests. Method for the Determination of K_{IC}, Critical CTOD, and Critical J Values of Metallic Materials."

2. Wang, Y.Y. and Gordon, J.R., "The Limits of Applicability of J and CTOD Estimation Procedures for Shallow-Cracked SENB Specimens", Proc. of Conference on Shallow Crack Fracture Mechanics, Toughness Tests, and Applications, Sept. 23-24, 1992, The Welding Institute, Paper 28.

3. Satoh, K. et al., "Joint Strength of Heavy Plates With Lower Strength Weld Metal", Welding Journal, Vol. 54, No. 9, September 1975, pp 311s-319s.

4. Dexter, R.J. and Ferrell, M., "Optimum Weld Metal Strength for High Strength Steel Structures", Ship Structure Committee Report SSC 383, July, 1995.

5. Kirk, M.T. and Dodds, R.H., " Effect of Weld Strength Mismatch on Elasto-Plastic Fracture Parameters", University of Illinois, Civil Engineering Studies, Structural Reserach Series No. 570, Report UILU-ENG-92-2008, Aug., 1992.

AKNOWLEDGEMENTS

The authors of this paper are grateful to Canada's Department of National Defence for funding this study.

Yong-Yi Wang[1], Harold S. Reemsnyder[2], and Mark T. Kirk[3]

INFERENCE EQUATIONS FOR FRACTURE TOUGHNESS TESTING: NUMERICAL ANALYSIS AND EXPERIMENTAL VERIFICATION

REFERENCE: Wang, Yong-Yi, Reemsnyder, Harold S., and Kirk, Mark T., **"Inference Equations for Fracture Toughness Testing: Numerical Analysis and Experimental Verification,"** Fatigue and Fracture Mechanics: 28th Volume, ASTM STP 1321, J. H. Underwood, B. D. Macdonald, and M. R. Mitchell, Eds., American Society for Testing and Materials, 1997.

ABSTRACT: The currently codified fracture toughness testing procedures, e.g., ASTM E 813, E 1152, E 1290, and BSI 7448:Part 1 use a set of inference equations to obtain J and CTOD from the measurements of global displacement and load. These inference equations were originally developed by assuming homogeneous and perfectly plastic material properties. Inaccurate results may be obtained when these inference equations are applied to non-homogeneous specimens and materials with strain hardening.

A systematic study of the relationship between crack driving force (J and CTOD) and the remote load and displacement is conducted using finite element method. The relationship derived from the study is compared with the inference equations used in the current standards. The analyzed geometry is a single-edge notched bend specimen, or SE(B), with a parallel-sided weld at the center. By varying the strength ratio between the weld and the base metal, a range of non-homogeneity is achieved. Other variables studied include crack depth, weld width, and strain hardening level.

The accuracy of the currently codified J and CTOD inference equations and those proposed in recent years (i.e., new equations) is examined. Compared with the codified inference equations, the new equations can be applied to a wide range of crack depth ($0.1 \leq a/W \leq 0.5$). The new CTOD inference equations provide much more accurate CTOD values for high strain hardening material than is possible using the current standards. The

[1]Senior Research Engineer, Technical Division, Edison Welding Institute, 1250 Arthur E. Adams Dr., Columbus, OH 43221

[2]Senior Research Consultant, Bethlehem Steel Corporation, Homer Research Laboratories, Bethlehem, PA 18016

[3]Industry Team Leader, Energy and Chemicals, Edison Welding Institute, 1250 Arthur E. Adams Dr., Columbus, OH 43221

accuracy of the codified inference equations and the new equations is expressed in terms of weld width, strain hardening rate, and mismatch levels.

The CTOD inference equations are tested through corroboration with experimentally measured values of CTOD in an unwelded HSLA structural steel. Interrupted fracture tests were performed at several temperatures. Subsequently the specimens were sectioned in the plane of the mid-thickness and quarter-thickness for measurement of the residual plastic component of CTOD. These experimentally measured values of CTOD were compared with those derived from the codified and the new inference equations. The new equations provide better agreement with the experimental measurements than the codified equations.

INTRODUCTION

Fracture assessments of structures require accurate fracture toughness values which are usually obtained using standardized testing procedures. The currently codified fracture toughness testing procedures, e.g., ASTM E 813, E 1152, E 1290, and BSI 7448:Part 1 [1-4], use a set of inference equations to obtain J and CTOD from the measurements of global displacement and load. These inference equations were originally developed by assuming homogeneous and perfectly plastic material properties. Inaccurate results may be obtained when these inference equations are applied to non-homogeneous specimens and materials with strain hardening. One such example is a typical weld toughness test specimen in which the weld metal, the heat-affected zone (HAZ), and the base metal have different properties.

This paper presents a systematic finite element study to derive the relationship between crack driving force (J and CTOD) and the remote load and displacement for typical weldment testing specimens. The relationship is then compared with the inference equations used in the current standards. The specimen is a single-edge notched bend (SE(B)) geometry with a parallel-sided weld at the center. The study includes a number of parameters: strength ratio between the weld and the base metal, crack depth, weld width, and strain hardening level. The new inference equations proposed in recent years are examined based on the same finite element studies. The CTOD inference equations are tested through corroboration with experimentally measured values of CTOD in an unwelded HSLA structural steel.

FINITE ELEMENT ANALYSIS

Geometry and Material Property

A typical SE(B) test specimen is chosen for the analysis, see Fig. 1. The specimen has a thickness of 25-mm, a width of 50-mm (Bx2B), and a nominal span between the rollers of 200-mm. The parallel-sided weld, shown as darkened area, has a range of thickness h/W=0.1 to 1.5. The crack depth of the specimen ranges from a/W=0.1 to 0.5.

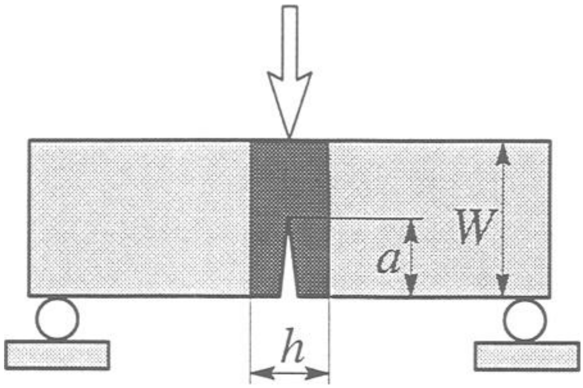

Fig. 1 The SE(B) geometry and the associated parameters

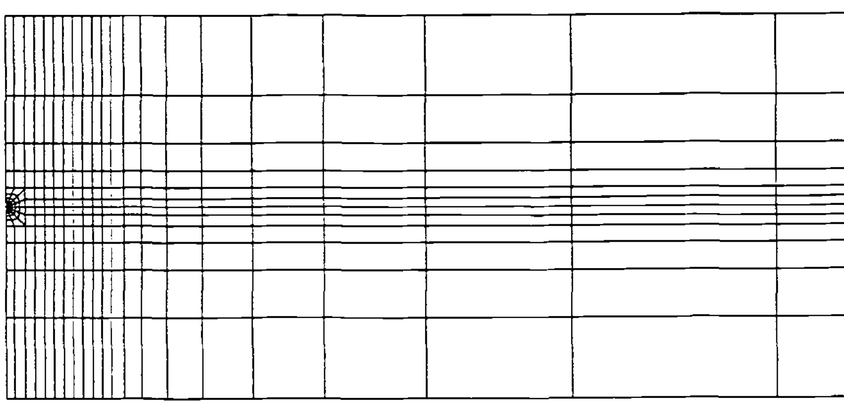

Fig. 2 A typical FE mesh for deeply-cracked SE(B) specimen

Fig. 2 shows a typical finite element (FE) mesh of a SE(B) specimen with a/W = 0.5. Due to the symmetry conditions along the crack plane, only one half of the specimen is modeled. There are 16 rings of elements around the crack tip. The typical size of the crack tip elements is on the order of $10^{-3}a$. Each model has about 400 8-node quadratic plane-strain elements with reduced integration (ABAQUS® Type CPE8R). The refinement of the mesh at the cracked-side specimen is not necessary. However, it is done to simplify the mesh generation.

The stress-strain relations of the base metal and the weld metal are modeled using a Ramberg-Osgood power law strain-hardening relationship:

$$\frac{\epsilon}{\epsilon_0} = \frac{\sigma}{\sigma_0} + \alpha\left(\frac{\sigma}{\sigma_0}\right)^n \tag{1}$$

where σ and ε are engineering stress and engineering strain, respectively, σ_0 is the reference yield stress, $\epsilon_0=\sigma_0/E$ is the reference yield strain, E is Young's modulus, α is a dimensionless material parameter, and n is the strain hardening exponent. Using the yield stress from the Ramberg-Osgood stress strain relations, the mismatch level is defined as follows:

$$M = \frac{(\sigma_0^W - \sigma_0^B)}{\sigma_0^B} \times 100\% \tag{2}$$

where σ_0^B is the yield stress of the base metal, and σ_0^W is the yield stress of the weld metal. Most of the analyses have strain hardening rates of n=20 and n=5. A small portion of the analyses has a wider range of strain hardening rates, n=4, 5, 10, 20, 50. In all cases, the strain hardening exponents of the base metal and weld metal are assumed to be the same. In many practical applications, the strain hardening rates of base metal and weld metal are different. The current simplification is done to focus on the strength mismatch between the base metal and the weld metal. The yield stress of the weld metal is fixed at 586 MPa (85ksi). The yield stress of the base metal is adjusted to give two undermatching (M=-25% and -50%), matching and two overmatching (M=25% and 50%) conditions.

Analysis Procedures

All the FE analyses are performed using ABAQUS® assuming small strain formulation and deformation theory of plasticity. Values of J-integral are obtained using the domain integral method as provided by ABAQUS. The difference in J values among the different contours is less than 0.5%. All the contours are located inside the weld. The crack tip opening displacement (CTOD) is calculated using the 45° interception definition on the crack-tip deformation fields.

EXPERIMENTS

Background

Interrupted fracture toughness tests were performed on eight unwelded 3x3-in SE(B) fatigue-cracked fracture toughness specimens with nominal aspect ratios a/W of 0.5 at 71, 50, 25, 0, -22, -25, -50, and -75°F. Five additional interrupted fracture tests were performed at room temperature on one specimen with a nominal a/W of 0.3 and two at each of a/W of 0.57 and 0.7.

All tests followed the ASTM Standard for CTOD testing E 1290 [4] and utilized the computer-controlled single-specimen compliance method. Each test was halted when compliance indicated that the stable crack extension Δa reached a value on the order of 0.2-mm (0.008-in.). The details of the tests are given in [5].

Materials

All SE(B) specimens were taken from an unwelded 88.9-mm (3¼-in.) quenched and tempered structural plate (API 2Y Grade 60T, 414 MPa (60 ksi) nominal yield strength) developed for offshore welded applications [6]. The chemical composition is shown in Table 1.

TABLE 1--Chemistry, weight percent, taken at mid-thickness [5]

C	Mn	P	S	Si	Ni	Cr	Mo	Cu	Nb
0.076	1.37	0.014	0.006	0.24	0.58	0.023	0.11	0.25	0.011

The engineering and true stress-strain curves were developed from tension specimens oriented transverse to the plate rolling direction and thus parallel to the principal stresses in the SE(B) specimens. Tensile test specimens were taken at both the quarter- and mid-thickness and tested at all of the temperatures at which interrupted fracture tests were performed. The strain-hardening exponents were determined from the true stress-strain curves according to ASTM E 646 [7].

The engineering yield and tensile strengths, respectively, σ_{ys} and σ_{uts}, and the strain-hardening exponents N_{meas} at mid-thickness are listed in Table 2 for the various temperatures of the interrupted fracture tests. Note $1/N_{meas}$ is typically different from the strain hardening exponent n in the Ramberg-Osgood stress-strain relation when such a relation is fitted to the experimental data.

CTOD Measurements

After the interrupted fracture tests were performed, each specimen was sectioned at a quarter-thickness and at the mid-thickness. The plastic component of CTOD δ_p and the crack-length a_f were measured in each crack-tip exposed by the sectioning using a tool-maker's microscope at 30X, see Table 2. The plastic component δ_p was defined as the hypotenuse of the customary 45°-45°-90° triangle with the crack-opening stretch (COS) as the altitude of that triangle. The initial crack length, a, is the difference between a_f (a_f is the apparent crack length) and the weighted CTOD/2, i.e.,

$$a = a_f - \frac{\delta_p^{mid\text{-}thick} + 2\times\delta_p^{1/4\text{-}thick}}{6} \tag{3}$$

The sections of two specimens, nominal a/W of 0.5 and tested at 71 and 50°F, were thermally stress-relieved at 1100°F for 30 minutes and the measurements of δ_p and a_f were repeated.

TABLE 2--Material properties and measured plastic components of CTOD, δ_p [5]

Specimen Mark	Test Temp. °F	Nom. a/W	B, in	W, in	σ_{ys}, ksi	σ_{uts}, ksi	N_{meas} —	a_f, in	measured δ_p mid-thick	measured δ_p 1/4-thick.	a, in
388G6012	71	0.5	3.000	2.999	60.1	75.9	0.1616	1.549	0.0224	0.0224	1.538
stress relieved									0.0221	0.0223	1.538
388G601	50	0.5	3.001	2.999	60.4	77.1	0.1641	1.549	0.0236	0.0221	1.538
stress relieved									0.0233	0.0226	1.538
388G602	25	0.5	3.000	2.987	61.5	78.7	0.1689	1.540	0.0222	0.0203	1.530
388G6011	0	0.5	3.001	3.000	62.8	80.6	0.1706	1.550	0.0205	0.0228	1.539
388I601	-22	0.5	3.000	3.000	64.0	82.7	0.1686	1.548	0.0133	0.0138	1.541
388G6014	-25	0.5	3.001	2.999	63.5	81.4	0.1752	1.549	0.0165	0.0166	1.541
388I603	-50	0.5	3.000	3.000	65.9	84.4	0.1782	1.545	0.0117	0.0121	1.539
388I605	-75	0.5	3.000	3.001	67.3	86.4	0.1823	1.544	0.0064	0.0063	1.541
388I607	71	0.3	3.001	3.002	59.9	76.1	0.1521	0.909	0.0017	0.0822	0.908
388I608	72	0.57	3.001	3.002	59.9	76.1	0.1521	1.757	0.0201	0.0194	1.747
388I6010	71	0.57	2.997	3.001	59.9	76.1	0.1521	1.741	0.0020	0.0025	1.740
388I6011	72	0.7	3.001	3.001	59.9	76.1	0.1521	2.136	0.0174	0.0171	2.128
388I6013	71	0.7	3.001	3.000	59.9	76.1	0.1521	2.132	0.0180	0.0186	2.122

J INFERENCE EQUATIONS

Codified *J* Inference Equation

In the presently codified procedures, J is given as:

$$J = \frac{K^2(1-\upsilon^2)}{E} + \frac{\eta_p U_{pl}}{B(W-a)} \tag{4}$$

where K is stress intensity factor, E is Young's modulus, ν is Poisson's ratio, and U_{pl} is the plastic component of the area under the load vs. load-line displacement (LLD) record. In the current ASTM and BSI standards [1,2,4] η_p is equal to 2.

Fig. 3 shows the average errors in estimated J values by using the ASTM J inference equation (Eq. (4)) for deeply-cracked mismatched SE(B) specimens with low strain hardening (n=20). The average error is calculated as:

$$Err_{avg} = \frac{\Sigma_{i=1}^{i=N} \left[(J^i_{cal} - J^i_{est})/J^i_{cal} \right]}{N} \tag{5}$$

where J_{est} is the estimated J from Eq. (4), and J_{cal} is the calculated J directly from the domain integral, respectively. The total number of data points, N, represents the number of load increments in a FE analysis which give J > 100 N/mm. Data points at smaller values of J were neglected because η_p did not approach a constant value until large plasticity was developed. Fig. 4 shows the average errors for SE(B) specimens with high strain hardening (n=5). For overmatched SE(B)s, the ASTM equation over-predicts the J values; i.e., a non-conservative J estimate for a fracture toughness specimen. For undermatched SE(B)s, the ASTM equation generally under-predicts or slightly over-predicts the J values. The error is largest at the mid-range h/W.

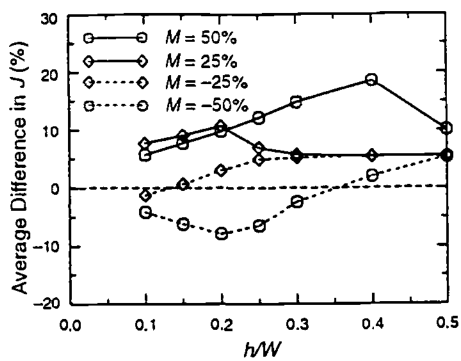

Fig. 3 Expected difference when ASTM procedure is applied to deeply-cracked SE(B)s with low strain hardening (n=20)

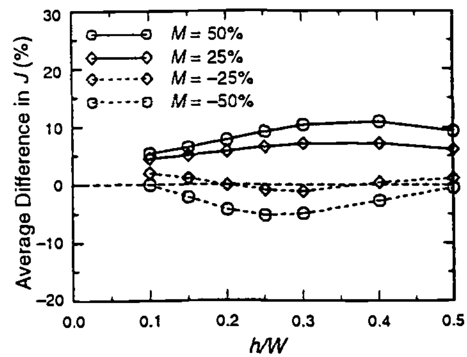

Fig. 4 Expected difference when ASTM procedure is applied to deeply-cracked SE(B)s with high strain hardening (n=5)

It is assumed in Eq. (4) that η_p is independent of the magnitude of deformation once plasticity dominates the deformation. Our FE results indicate slight variation of η_p with respect to deformation level. The variation is generally within 3-4% once the plasticity is fully developed. Therefore, an error (or difference) in estimated J of 3-4% should be viewed as insignificant and within the accuracy of the analysis procedures.

Non-Codified J Inference Equations

Sumpter [8] first proposed to use the plastic component of the area under load vs. crack mouth opening displacement (CMOD) record (A_{pl}) to calculate the plastic component of J. Kirk and Dodds [9] proposed the following formula using A_{pl},

$$J = \frac{K^2(1-\nu^2)}{E} + \frac{\eta_c A_{pl}}{B(W-a)} \tag{6}$$

where

$$\eta_c = 3.785 - 3.101\left(\frac{a}{W}\right) + 2.018\left(\frac{a}{W}\right)^2 \tag{7}$$

Wang and Gordon [8] proposed a slightly different η_c expression:

$$\eta_c = 3.50 - 1.42\left(\frac{a}{W}\right) \tag{8}$$

Part of the difference between Kirk and Dodds and Wang and Gordon is attributed to the value at which η_c was taken. The η_c values from Kirk and Dodds were taken at a higher value of J than that of Wang and Gordon. As indicated in the previous section, a small variation of η_c exists over a loading range from small scale yielding to large plasticity. It should be emphasized that Eqs. (7) and (8) provide essentially the same values of η_c in the range of a/W=0.1-0.5 with a maximum difference of about 3%. Indeed, even at a/W=0.7, the difference between Eqs. (7) and (8) is less than 4%.

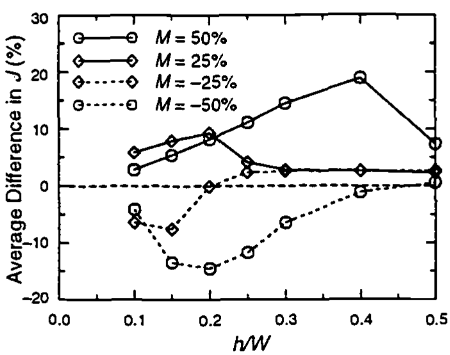

Fig. 5 Expected difference when η_c of Kirk and Dodds [9] is applied to deeply-cracked SE(B)s with low strain hardening (n=20)

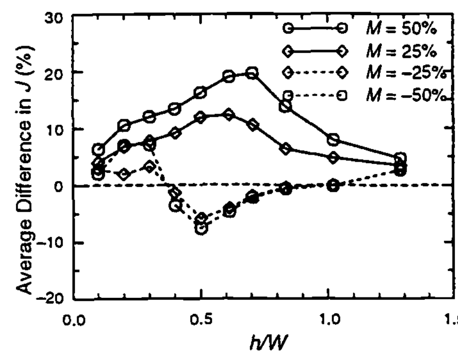

Fig. 6 Expected difference when η_c of Kirk and Dodds [9] is applied to shallow-cracked SE(B)s with low strain hardening (n=20)

Potential errors introduced by using the non-codified J inference equations are evaluated. Fig. 5 shows the variation of the average error with respect to weld width for deeply-cracked SE(B)s with low strain hardening (n=20) using Eq. (7). The average error is calculated using Eq. (5) with the usual limitation on the range of J values. For overmatched SE(B)s, Kirk and Dodds' equation over-predicts the J values (a non-conservative J estimate). For undermatched SE(B)s, the equation under-predicts the J values (a conservative J estimate). The maximum error is about one-third of the degree of mismatch. For instance, if the overmatch is 50%, the maximum over-prediction by using Eq. (7) is about 50/3=17%. The error produced for shallow-cracked SE(B) specimens with low strain hardening (n=20), shown in Fig. 6, is similar to that of deeply-cracked SE(B)s. The SE(B)s with low strain hardening were chosen since the mismatch effect is more pronounced in such materials than high strain hardening materials. The averaged error introduced by Wang and Gordon's expression [Eq. (8)] is similar to that of Kirk and Dodds.

CTOD INFERENCE EQUATIONS

Codified CTOD Inference Equation

The procedure of calculating CTOD (δ) [3,4] adopted by both ASTM and BSI testing standards is to partition the total CTOD into small-scale yielding and fully plastic components:

$$\delta = \frac{K^2(1-\upsilon^2)}{2E\sigma_{ys}} + \frac{r_p(W-a)V_p}{r_p(W-a)+a+z} \tag{9}$$

where V_p is the plastic component of CMOD measured at knife-edge height z, r_p is the plastic rotational factor, and σ_{ys} is the yield stress. The ASTM E 1290 specifies a plastic rotational factor of 0.44, whereas BSI 7448 specifies a r_p value of 0.4.

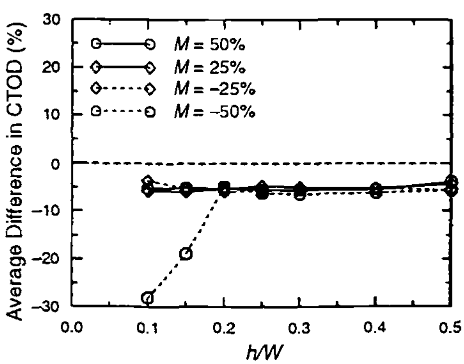

Fig. 7 Expected difference when ASTM procedure is applied to deeply-cracked SE(B)s with low strain hardening (n=20)

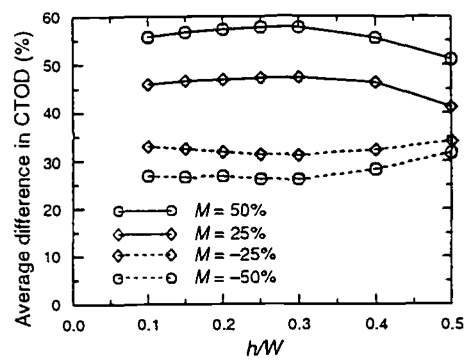

Fig. 8 Expected difference when ASTM procedure is applied to deeply-cracked SE(B)s with high strain hardening (n=5)

When applied to welds, the accuracy of the codified CTOD inference equations depends on crack depth, level of weld metal mismatch, weld width, and strain hardening level. Figs. 7 and 8 show the average errors in estimated CTOD values produced by using the ASTM CTOD inference equation (Eq. (9) and r_p=0.44) for deeply-cracked mismatched SE(B) specimens with low and high strain hardening, respectively. The average error is calculated as:

$$Err_{avg} = \frac{\sum_{i=1}^{i=N}\left[(\delta^i_{cal} - \delta^i_{est})/\delta^i_{cal}\right]}{N} \tag{10}$$

where δ_{est} is the estimated CTOD using the ASTM equation, δ_{cal} is the CTOD calculated from crack tip deformation using the 45^0 interception definition. The number of data points, N, represents the number of loading increments in the FE analysis with CTOD greater than 0.05 mm. In general, the ASTM equation is quite accurate for the SE(B) specimens with low strain hardening. The average error is independent of weld width and mismatch level except for the 50% undermatched specimen with $h/W < 0.2$. In contrast, the ASTM equation significantly over-predicts the CTOD values for SE(B) specimens with high strain hardening (n=5), as shown in Fig. 8. The average error is slightly dependent on weld width, but strongly dependent on the mismatch level. Higher overmatch levels produce higher over-predictions. The averaged error produced by the

BSI equation (Eq. (9) and r_p=0.40) for deeply-cracked mismatched SE(B) specimens is similar to that of the ASTM equation.

The standard CTOD inference equation, Eq. (9), is premised on the existence of a plastic hinge at the position $r_p(W-a)$ ahead of a crack. This hinge mechanism is strictly valid for perfectly plastic materials with a deep crack under predominantly bending loads. For materials with low to moderate strain hardening and a deep crack, the plastic hinge assumption is approximately accurate. However, such a plastic hinge does not exist at a fixed location ahead of a crack in a high strain-hardening material. Consequently, a significant error can be introduced when Eq. (9) is applied to high strain-hardening materials [9, 10]. Fig. 9 shows the relationship between the plastic component of CTOD ($CTOD_p$) and the plastic component of CMOD ($CMOD_p$) for homogeneous SE(B)s. The existence of a plastic hinge predicts a linear relation between the $CTOD_p$ and $CMOD_p$. It is apparent that this linear relation does not exist for high strain hardening materials. In Fig. 9, the linear relations between $CTOD_p$ and $CMOD_p$ associated with r_p = 0.44 [3] and r_p = 0.40 [4] are also shown. These lines are close to the n=50 line. Therefore, Eq. (9) should only be used for deeply-cracked specimens with low to moderate strain hardening.

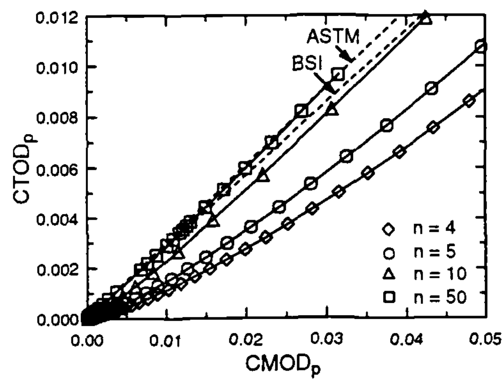

Fig. 9 The effect of strain hardening on the relationship between plastic components of CTOD and CMOD.

Non-Codified CTOD Inference Equations

Another method of obtaining the plastic component of CTOD is to use the plastic area under the load vs. CMOD record (A_{pl}) [9,10]:

$$\delta = \frac{K^2(1-\nu^2)}{2E\sigma_{ys}} + \frac{\eta_{ct}\, A_{pl}}{\sigma_{ys}B(W-a)} \tag{11}$$

The CTOD may also be calculated using its relation to J [8]:

$$\delta = \frac{J}{m_{ys}\sigma_{ys}} \tag{12}$$

where m_{ys} is a dimensionless factor relating J and CTOD.

The CTOD inference equation based on the plastic component of the area under the load vs. CMOD record, i.e., Eq. (11), has been found to be suitable to calculate CTOD of SE(B) with a large range of a/W ratio and strain-hardening rate. However, such equation is less accurate than the J to CTOD conversion procedure, i.e., Eq. (12), at small values of CTOD [10].

An m_{ys} expression was proposed by Wang and Gordon [10]:

$$m_{ys} = -0.0757 + 0.802\frac{a}{W} + 1.317R \tag{13}$$

Combining the current FE results and those in [9], Kirk and Wang [11] found slightly different coefficients for Eq. (13):

$$m_{ys} = -0.111 + 0.817\frac{a}{W} + 1.360R \tag{14}$$

For Ramberg-Osgood material, R can be calculated as [9]:

$$R = \left(\frac{500}{2.718 \times n}\right)^{1/n} \tag{15}$$

For a non-Ramberg-Osgood material, R can be taken as the ratio of tensile strength to yield stress.

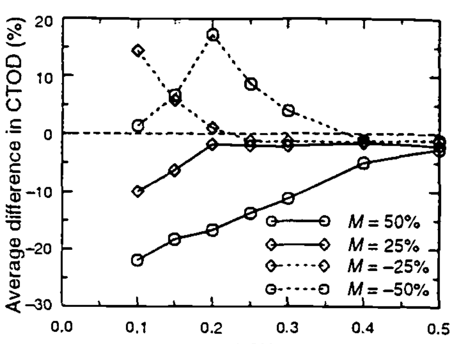

Fig. 10 Expected difference when the new procedure is applied to deeply-cracked SE(B)s with low strain hardening (n=20)

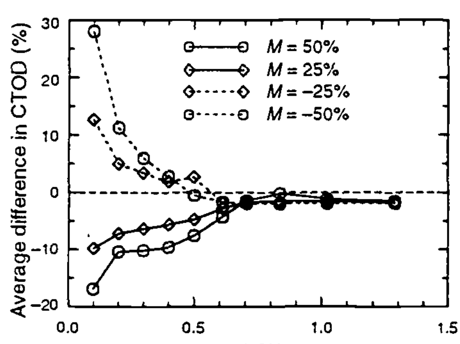

Fig. 11 Expected difference when the new procedure is applied to shallow-cracked SE(B)s with low strain hardening (n=20)

Potential errors introduced by the J to CTOD conversion procedure for mismatched SE(B)s are shown in Figs. 10 and 11. The average error is calculated using Eq. (10) where δ_{est} is from Eqs. (6), (8), (12), (14). For overmatched SE(B)s, the procedure generally under-predicts the CTOD values (conservative CTOD estimates). For undermatched SE(B)s, the procedure over-predicts the CTOD values (non-conservative). Similar trends are evident in Fig. 11 for shallow-cracked SE(B)s with low strain hardening. Our analysis also showed that the J to CTOD conversion procedure provides more accurate CTOD estimation for materials with higher strain hardening then those with low strain hardening.

An alternative to Eq. (12) was proposed by Kirk and Wang [12]:

$$\delta = \frac{J}{m_{flow}\sigma_{flow}} \tag{16}$$

where the flow stress, σ_{flow} , is defined as

$$\sigma_{flow} = \frac{\sigma_{ys} + \sigma_{uts}}{2} \tag{17}$$

and m is expressed as

$$m_{flow} = 1.221 + 0.793\frac{a}{W} + 2.75\frac{1}{n} - 1.418\frac{a}{W}\times\frac{1}{n} \tag{18}$$

The use of Eqs. (16)-(18) is illustrated in the following section.

COMPARISON OF CTOD BETWEEN EXPERIMENTAL MEASUREMENTS AND CALCULATION

The use of Eq. (18) requires the determination of strain hardening exponent n. Reemsnyder provides an empirical 3rd-order polynomial fit [13],

$$N_{poly} = 1.724 - \frac{6.098}{R} + \frac{8.326}{R^2} - \frac{3.965}{R^3} \tag{19}$$

where R is the ratio of tensile strength to yield stress.

The J to CTOD conversion [Eqs. (12) and (16)] CTOD may be written in a more general form,

$$\delta = \frac{J}{m\sigma_{nom}} \tag{20}$$

where σ_{nom} is either yield stress on flow stress and m is the associated conversion factor. The conversion factor m may be computed using either Eq. (14) or Eq. (18). In this section, we compute CTOD using a various combination of m and σ_{nom}. The plastic component of the computed CTOD, δ_p^{esti}, is then compared with the measured CTOD, δ_p^{meas}. The difference is computed as,

$$diff = \frac{\delta_p^{meas} - \delta_p^{esti}}{\delta_p^{meas}} \quad (21)$$

In the computation of δ_p^{esti} using the non-codified equations, J is taken from Eqs. (6) and (8). The difference is summarized in Table 3. The strain hardening exponent in Eq. (13) is approximated by $1/N_{meas}$ or $1/N_{poly}$. The weighted plastic component of CTOD is defined as

$$\delta_p^{weighted} = \frac{\delta_p^{mid\text{-}thick.} + 2\times\delta_p^{1/4\text{-}thick.}}{3} \quad (22)$$

Table 3 shows that the current ASTM and BSI test standards overestimate δ_p. However, the BSI estimates are closer to the measured values than the ASTM estimations, i.e., -13.2 versus -21.2%. This difference can be attributed to the different values of r_p. The negative values indicate the estimation is non-conservative.

TABLE 3--Summary-average percent differences [5]

Case	m from	σ_{nom} taken as [Eq. (20)]	Average Percent Difference, δ_p		
			1/4-thick.	mid-thick.	wtd. ave.
E 1290	...	...	-19.6	-24.6	-21.2
BS 7748	...	...	-11.7	-16.4	-13.2
3	N_{meas} [Eq. (18)]	σ_{ys}	-12.0	-16.1	-13.3
4	σ_{uts}/σ_{ys} [Eq. (14)	σ_{ys}	-6.7	-10.5	-7.9
5	N_{poly} [Eq. (18)]	σ_{ys}	-13.5	-17.6	-14.9
6	N_{meas} [Eq. (18)]	σ_{flow}	1.5	-2.1	0.3
7	σ_{uts}/σ_{ys} [Eq. (14)]	σ_{flow}	5.5	2.1	4.4
8	N_{poly} [Eq. (18)]	σ_{flow}	0.1	-3.6	-1.1

The non-codified CTOD inference equations require some estimate of strain hardening behavior. The experiemental data in Table 3 indicates that the agreement between the measured δ_p and the δ_p estimated using σ_{flow} was superior to that by using σ_{ys}. However, such a difference can be within the accuracy of FE techniques and experimental measurement. As indicated in the previous sections, our FE analysis is only accurate to about 3-4% difference. Indeed, if one to examine Case 4 and 7, their difference is within the accuracy of the FE techniques.

For the non-codified equations, the parameter m is function of the aspect ratio a/W and either the strain-hardening exponent n or the tensile to yield ratio R. The agreement between the measured δ_p and δ_p estimated using N_{meas} (Case 6) was superior to that using either R (Case 7) or N_{poly} (Case 8). Also, estimates of δ_p using N_{poly} (Case 8) were superior to those using R (Case 7). The ranges in percent differences were similar for all three cases.

DISCUSSION

The values of J-Integral computed from the non-codified equation utilizing the area under the load versus plastic component of CMOD are compared to the values computed according to ASTM E 813 [1] in Fig. 12. The average percent difference between the two values is 1.1% with a range of -10.2 to +23.5%. The latter value applies to the test on the specimen with nominal a/W of 0.3 that was interrupted prematurely. Here, the δ_p was very small and difficult to measure. If this specimen is omitted from the analyses, the average percent difference is -0.8% with a range of -10.2 to +5.4%. If the E 813-estimated values of J-integral were corrected for load-point deformations, the differences would be less.

The values of δ_p measured before and after thermal stress-relief at 1100°F were not significantly different. Therefore, it may be concluded that either:

(1) the crack-tip residual stresses present after plastic deformation were relieved by the sectioning of the specimens, or

(2) the crack-tip residual stresses present after plastic deformation were of small magnitude and were not affected by either sectioning or subsequent thermal stress-relief.

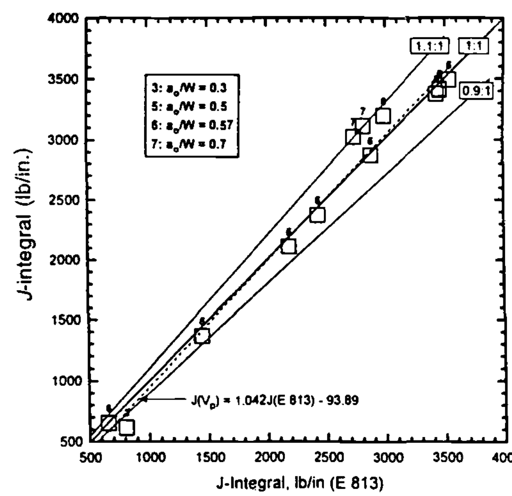

Fig. 12 Comparison of J from ASTM and that from Eqs. (6) & (7)

CONCLUDING REMARKS

The accuracy of the codified J inference equation depends on mismatch level, weld width, and strain hardening rates. The equation generally underestimates J (conservative) for undermatched specimens and overestimates (non-conservative) for overmatched specimens. The maximum overestimation is about one-third of the mismatch level. As a first order correction to the mismatch effect, one may correct the J value by one-third of the mismatch level for overmatched specimens. No such correction is needed for undermatched specimens if conservative toughness value is desired.

The major advantage of using the non-codified J inference equation is that it may be applied to shallow-cracked as well as deeply-cracked specimens. For deeply-cracked SE(B)s, the error in the non-codified equation is comparable to that of the codified equation. Good agreement has been obtained between the J computed using the non-codified equation and that using the codified equation for the experimentally tested specimens.

The codified CTOD equation can significantly overestimate the toughness value for high strain hardening materials. For SE(B)s with low strain hardening, the codified equation is accurate for mismatch levels from 50% undermatch to 50% overmatch. The non-codified CTOD equations, based on J to CTOD conversion, provide much better CTOD estimation for both high strain hardening and low strain hardening SE(B)s.

Experimental measurement of residual CTOD at the crack tip shows the non-codified equations are superior to the codified equation for the material tested. The codified equations overestimate CTOD by 9 to 15% as compared to the measured values. Using the tensile to yield ratio and Eq. (15), one may find that the strain hardening exponent of the tested material is about n=11. Referring to Figs. (7) and (8), the estimation error is expected to be within the bounds set by n=20 and n=5. Therefore, the inaccuracy of the codified equation may be attributed to strain hardening of the tested material.

More experimental tests are needed to conclusively determine which of the non-codified equations is the most accurate. The extensive finite element studies conducted in [11,12] indicated Eqs. (12) and (14) are the most accurate inference equations. The accuracy of these equations is expected to be more sensitive for high strain hardening materials. This, in addition to the expected highly non-conservative CTOD estimation by the codified equation, makes the tests of high strain hardening material extremely attractive.

ACKNOWLEDGMENT

The work at EWI was supported by an internal EWI Cooperative Research Program and several EWI and TWI member companies. The experimental work was supported by Bethlehem Steel Corporation.

REFERENCES

[1] ASTM E813-89, Standard Test for J_{Ic}, a Measure of Fracture Toughness.

[2] ASTM E1152-87, Standard Test Method for Determining *J-R* Curves.

[3] ASTM E1290-89, Standard Test Method for Crack-Tip Opening Displacement (CTOD) Fracture Toughness Measurement.

[4] BS7448:Part 1:1991, Fracture Mechanics Toughness Tests, Part 1, Method for the Determination of K_{Ic}, Critical CTOD and Critical J Values of Metallic Materials.

[5] H. S. Reemsnyder, The Experimental Measurement of the Plastic Component of Crack-Tip Opening Displacement and Comparison with Analytical Estimations, Bethlehem Steel Corporation, Bethlehem, Pa., April 22, 1996.

[6] Specification for Steel Plates, Quenched and Tempered, for Offshore Structures, API Specification 2Y (Spec 2Y), Third Edition, July 1, 1993, American Petroleum Institute, Houston.

[7] ASTM E 646-91, Standard Test Method for Tensile Strain-Hardening Exponents 9n-Values) of Metallic Sheet Materials, Section 3, Annual Book of ASTM Standards, American Society for Testing and Materials, Philadelphia.

[8] Sumpter, J. D. G., *Jc* Determination for Shallow Notch Welded Bend Specimens, *Fatigue and Fracture of Engineering Materials and Structures*, Vol. 26, No. 6, pp. 479-493, 1987.

[9] Kirk, M. T. and Dodds, R. H., *J* and CTOD Estimation Equations for Shallow Cracks in Single Edge Notch Bend Specimens, *Journal of Testing and Evaluation*, Vol. 21, No. 4, July 1993.

[10] Wang, Y.-Y. and Gordon, J. R., The Limits of Applicability of *J* and CTOD Estimation Procedures for Shallow-Cracked SENB Specimens, in *Shallow Crack Fracture Mechanics, Toughness Tests and Applications*, M. G. Dawes, Eds., Cambridge, UK, September 23-24, 1992.

[11] M. T. Kirk and Y-Y Wang, A Review of CTOD Estimation Formulas for SE(B)Specimens, Presented at the meeting of ASTM Task Group E08.08.06, Phoenix, Arizona, November 14, 1994.

[12] M. T. Kirk and Wang, Y.-Y., Wide Range CTOD Estimation Formulae for SE(B) Specimens, *Fracture Mechanics, 26th Volume*, ASTM STP 1256, W. G. Reuter, J. H. Underwood, and J. C. Newman, Jr., Eds., ASTM, Philadelphia, 1995.

[13] H. S. Reemsnyder, Determination of Strain-Hardening Exponent fromYield and Tensile Strengths, Bethlehem Steel Corporation, Bethlehem, Pa., October 11, 1994

Janis A. Keeney,[1] B. Richard Bass,[1] and Wallace J. McAfee[1]

FRACTURE ASSESSMENT OF WELD MATERIAL FROM A FULL-THICKNESS CLAD RPV SHELL SEGMENT

REFERENCE: Keeney, J. A., Bass, B. R., and McAfee, W. J., "**Fracture Assessment of Weld Material From a Full-Thickness Clad RPV Shell Segment,**" Fatigue and Fracture Mechanics: 28th Volume, ASTM STP 1321, J. H. Underwood, B. D. Macdonald, and M. R. Mitchell, Eds., American Society for Testing and Materials, 1997.

ABSTRACT: Fracture analysis techniques were evaluated through applications to full-thickness clad beam specimens containing shallow cracks in material for which metallurgical conditions are prototypic of those found in reactor pressure vessels (RPVs) at beginning of life. The beam specimens were fabricated from a section of an RPV wall (removed from a canceled nuclear plant) that includes weld, plate, and clad material. Metallurgical factors potentially influencing fracture toughness for shallow cracks in the beam specimens include gradients of material properties and residual stresses due to welding and cladding applications. Fracture toughness estimates were obtained from load vs load-line displacement and load vs crack-mouth-opening displacement data using finite-element techniques and estimation schemes based on the η-factor method. One of the beams experienced a significant amount of precleavage stable ductile tearing. Effects of precleavage tearing on estimates of fracture toughness were investigated using continuum damage models. Fracture toughness results from the clad beam specimens were compared with other deep- and shallow-crack single-edge notch bend (SENB) data generated previously from A 533 Grade B plate material. The range of scatter for the clad beam data is consistent with that from the laboratory-scale SENB specimens tested at the same temperature.

KEYWORDS: reactor pressure vessel, full-thickness clad beams, shallow-crack, single-edge notch bend specimens, constraint, η-factor method, J-Q methodology, crack-tip stress triaxiality, precleavage tearing, continuum damage models

Evaluations of reactor pressure vessel (RPV) integrity under pressurized-thermal shock (PTS) loading are based on the Marshall flaw distribution [1], U.S. Nuclear Regulatory Commission (NRC) Guide 1.154 [2], and data from deep-crack fracture toughness specimens. The Marshall flaw distribution predicts more small (shallow) than large (deep) flaws, while NRC Regulatory Guide 1.154 requires that all flaws be

[1]Engineers, Oak Ridge National Laboratory, P. O. Box 2009, Oak Ridge, TN 37831-8056.

considered as surface flaws. Probabilistic fracture-mechanics (PFM) analyses of RPVs indicate that a high percentage of the cracks that initiate in cleavage, initiate from shallow flaws [3]. Because the postulated existence of shallow flaws has a dominant influence on the results of PFM analyses and, ultimately, the conditional probability of vessel failure in a PTS evaluation, the shallow surface crack is of major importance in RPV structural integrity assessments.

Fracture analysis techniques were used to investigate results from a Heavy-Section Steel Technology (HSST) testing program designed to quantify fracture toughness for shallow cracks in weld material for which metallurgical conditions are prototypic of those found in RPVs at beginning of life. In the first phase of the investigation, five full-thickness clad beam specimens taken from the RPV of a canceled nuclear plant were fabricated at Oak Ridge National Laboratory (ORNL) and tested at the National Institute for Standards and Technology (NIST), Gaithersburg, Maryland. These tests were performed to determine the influence of material properties gradients, weld inhomogeneities, weld defects and the cladding process on the fracture toughness of material containing shallow cracks. Through-clad shallow cracks in these beams were machined in the weld material joining together two plate material shell segments. Comparison of results from these tests with those from homogeneous shallow-crack test specimens [4] provide an opportunity to quantify effects of some near surface conditions on fracture toughness. Also, the clad beam data were used to evaluate the stress-based constraint characterizations developed by O'Dowd and Shih [5-7].

FULL-THICKNESS CLAD BEAM TESTING PROGRAM

Details of Test Specimen

The full-thickness clad beam specimens were fabricated from an RPV shell segment that was available from a canceled pressurized-water reactor plant (the plant was canceled during construction, and the vessel was never in service). The RPV material is A 533 B steel with a stainless steel clad overlay on the inner surface. The shell segment contains three submerged-arc welds (two circumferential welds and one longitudinal weld). The plate material, clad overlay, and weldment are completely prototypic of a production-quality RPV.

Because the first series of five specimens was intended to investigate the fracture behavior of the longitudinal weld material, the test beams were cut in the circumferential direction of the shell. A sketch of the specimen geometry is shown in Fig. 1. The specimen was designed to be tested in three-point bending. The flaw was machined in the beam using the wire electro-discharge machining process and extended from the shell inner surface, that is, the clad surface, to predetermined depths into the beam. The final dimensions for each clad beam specimen are shown in Table 1. One deep-flaw specimen (CB-1.1) and four shallow-flaw specimens (CB-1.2 – CB-1.5) were produced.

Impact and tensile data were used to develop a consistent set of material properties needed for the clad beam test data evaluation and the finite-element analyses. These properties are listed in Table 2. The tabulated yield strength for the weld material is 36% higher than the yield strength for the base material.

Test Procedures and Results

The full-thickness clad beam tests were instrumented with crack-mouth-opening displacement (CMOD) and load-line displacement (LLD) gages and tested in three-point bending. Each specimen was cooled to the test temperature [T=–25°C (T-NDT=25°C)] and then loaded to fracture in displacement control. Details of the test procedures are described in Refs. 8 and 9. The load (P) vs displacement curves for each of the five beams are

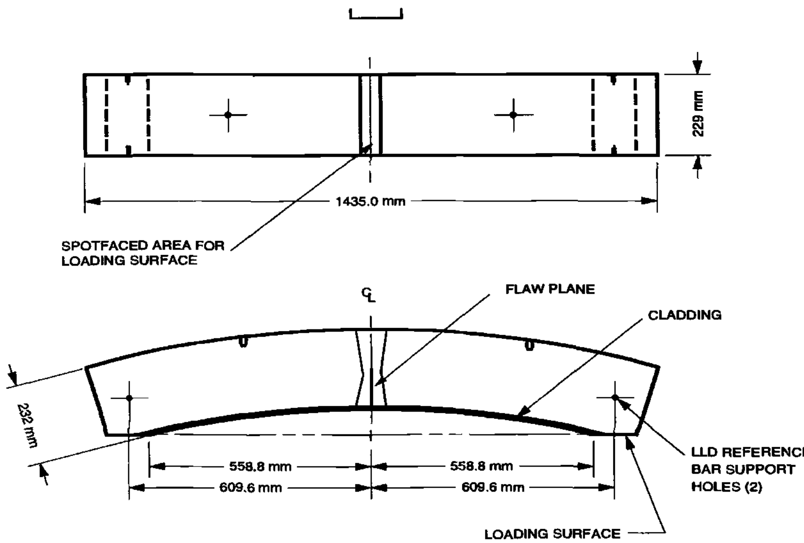

FIG. 1--Sketch of full-thickness clad beam specimen.

TABLE 1--Parameters defining specimen geometry of full-thickness clad beam specimens.

	CB-1.1[a]	CB-1.2	CB-1.3	CB-1.4	CB-1.5
Load span, S (mm)	1219.2	1219.2	1219.2	1219.2	1219.2
Thickness[b], B (mm)	230.2	230.2	229.6	229.1	231.6
Width, W (mm)	225.7	224.3	224.3	228.9	225.0
Crack depth[c], a (mm)	117.5	10.8	23.7	22.6	12.1
Ratio, a/W	0.50	0.05	0.10	0.10	0.05

[a] Used as development beam.
[b] Width includes ~5 mm of clad overlay.
[c] Final depth after fatigue precracking.

TABLE 2--Material properties[a] at test temperature of –25°C

	Base metal	Weld metal	Cladding
Modulus of elasticity (E), MPa	200,000	200,000	152,000
Poisson's ratio (ν)	0.3	0.3	0.3
Yield strength (σ_0), MPa	440	599	367
Ultimate strength (σ_u), MPa	660	704	659

[a] RT_{NDT} is –23°C for the weld metal, and
NDT is –50°C for the weld metal and –34°C for the base metal.

shown in Fig. 2(a) for LLD and in Fig. 2(b) for CMOD, respectively. These curves depict the inelastic behavior in the shallow-crack specimens as fracture conditions are approached as compared to the near elastic conditions for the deep-crack specimen. The conditions of each specimen at failure are listed in Table 3, including the plastic component of the area under the P vs displacement curve (defined as U_{pl} for LLD and A_{pl} for CMOD).

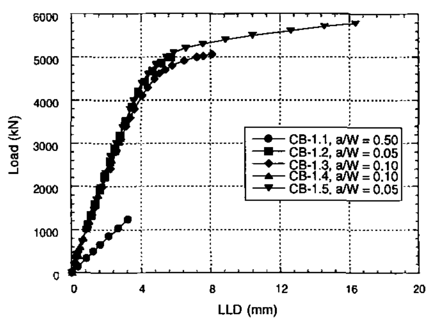

(a)

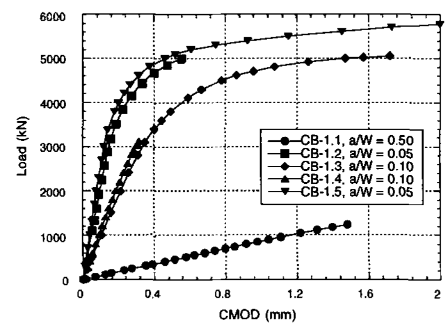

(b)

FIG. 2--Load vs displacement response for clad beam specimens: (a) LLD and (b) CMOD.

TABLE 3--Summary of results from the full-thickness clad beam testing program.

	CB-1.1	CB-1.2	CB-1.3	CB-1.4	CB-1.5
a/W	0.50	0.05	0.10	0.10	0.05
Temperature, °C	-25.5 ± 1.0	-25.0 ± 1.0	-25.0 ± 1.0	-25.3 ± 1.0	-25.9 ± 1.0
Stroke Rate, mm/min.	2.49	8.38	6.89	3.76	8.76
Time to Failure, s	230	366	440	309	556
Failure conditions					
P, kN	1232.5	5002.3	5060	3114	5783
LLD, mm	3.236	5.767	8.083	2.825	16.396
CMOD, mm	1.485	0.567	1.718	0.318	1.998
U_{pl}, kN-mm	135	6427	16879	93	—[a]
A_{pl}, kN-mm	88	1473	5486	79	—[a]

[a]Not calculated since CB-1.5 underwent precleavage ductile tearing and toughness was not estimated using η-factors.

CLAD BEAM POSTTEST ANALYSES

Finite-Element Analysis

Two different analysis techniques were used to generate finite-element solutions for the full-thickness clad beam tests. In clad beam tests CB-1.1 – CB-1.4, the cracks initiated in cleavage thus allowing the use of static analysis techniques. The CB-1.5 specimen experienced ~2.6 mm of stable ductile tearing prior to initiation of cleavage fracture. Recent studies indicate that the onset of stable ductile tearing leads to crack-tip fields ahead of the growing crack and crack-tip profiles that differ from those of a stationary crack. Stable ductile tearing exposes additional volumes of material to elevated stresses as the crack advances, which alters the sampling of potential cleavage initiation sites on the microstructural level. Also, measured cleavage fracture toughness values for these specimens will be influenced by changes in crack-tip constraint conditions that occur with prior stable crack growth. The analysis of CB-1.5 utilized the Gurson-Tvergaard (G-T) dilatant plasticity model [10] for void growth and element extinction capability for modeling crack growth.

Cleavage Model--Two-dimensional (2-D) plane-strain elastic-plastic analyses were performed on the clad beam specimens (CB-1.1 – CB-1.4) using ABAQUS [11]. A one-half section of the complete clad beam specimen illustrated in Fig. 1 is represented in the 2-D finite-element model of Fig. 3 (a/W = 0.10). The model in Fig. 3 incorporates the curvature of the plate and the flat cut-out where the specimen is supported during loading. The model has a highly refined mesh in the crack-tip region [Fig. 3(c)] to provide resolution of stress fields in front of the crack. The model consists of 3630 nodes and 1105 eight-node isoparametric elements with reduced integration. Collapsed-prism elements arranged in a focused fan configuration at the crack tip are used to produce a 1/r strain singularity appropriate for inelastic analysis. The finite-element model is loaded by a distributed pressure load over four elements on the outer edge [see Fig. 3(b)].

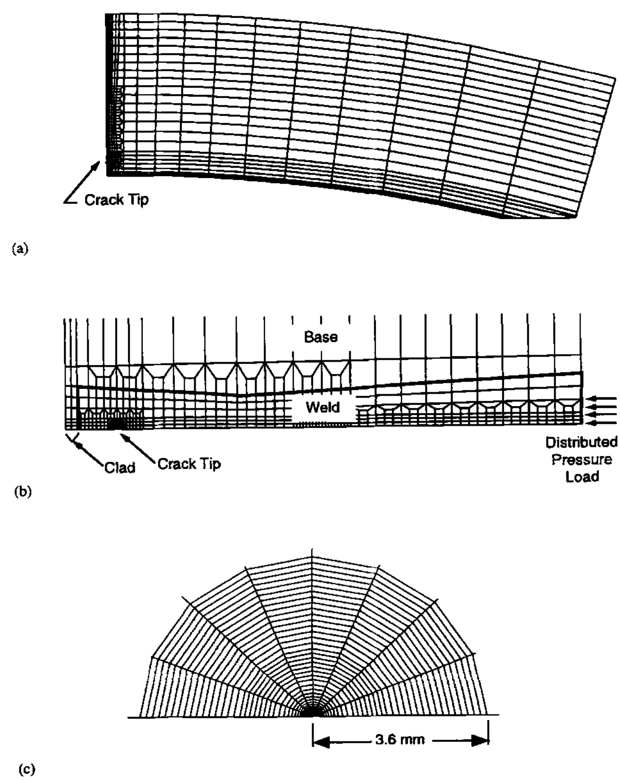

FIG. 3--(a) Finite-element mesh of clad beam specimen with a/W = 0.10, (b) crack-plane region, and (c) crack-tip region

Precleavage Ductile Tearing Model--The finite-element model shown in Fig. 4 was employed to perform plane-strain, nonlinear analyses of the clad beam specimen CB-1.5 (a/W = 0.05) which had a small amount of precleavage ductile tearing (~2.6 mm). The finite-element computer code WARP3D [12] was used to perform the analysis. For 2-D plane-strain analyses, the WARP3D code utilizes a 3-D model with one layer of elements in the thickness direction with plane-strain constraints imposed in the thickness direction on all nodes. The G-T model implemented in WARP3D incorporates void nucleation and growth ahead of a stably tearing crack into a finite-element model using computational cells with explicit length scales. In Fig. 4, the model has 2706 nodes and 1248 elements (8-node bricks). Symmetry about the crack plane permits modeling of one half of the specimen. Square elements in the crack-tip region and along the crack plane are defined to permit uniform increments of crack extension. The crack-tip element size is 100 μm (chosen from prior analytical experience in Ref. 13) for adequate resolution of the crack opening profile and stresses ahead of the growing crack.

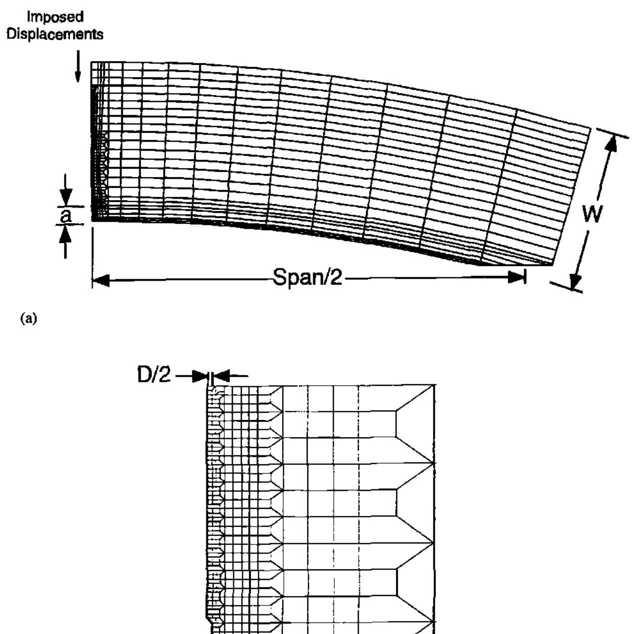

FIG. 4--(a) Finite-element mesh of clad beam specimen CB-1.5 (a/W = 0.05), and (b) crack-plane region

The finite-element model is loaded by displacement increments imposed on six centerplane nodes (the two end elements) as shown in Fig. 4(a). The Gurson constitutive model is used for the elements along the crack plane where ductile tearing occurs, and the rest of the model uses the von Mises constitutive relation. Two principal input parameters for the G-T model are the initial void volume fraction, f_0, and the characteristic length, D, associated with the G-T crack plane elements. According to theory, these parameters are dependent only on the material and not on specimen geometry. Experimental J-Δa curves obtained from compact specimens can be used to calibrate f_0 and D for the test material. In the absence of these data, a parametric study was performed to obtain the initial volume fraction f_0 and displacement increment which would reproduce the experimental load vs CMOD curve for CB-1.5. The value of f_0 used in the final analysis was 0.006 with a displacement increment of 0.00215 in. The explicit length scale D was set at 200 μm (since the crack-tip element size is 100 μm). The critical volume fraction, set at $f_f = 0.15$, is when void coalescence occurs. Full interpretation of the test results from CB-1.5 has not been completed. Additional work is on-going as noted later in this paper.

Material properties used for the posttest analyses of the clad beam specimens were taken from Table 2 and from the multilinear true stress vs true plastic-strain curves given in Fig. 5 (generated in the HSST program at ORNL).

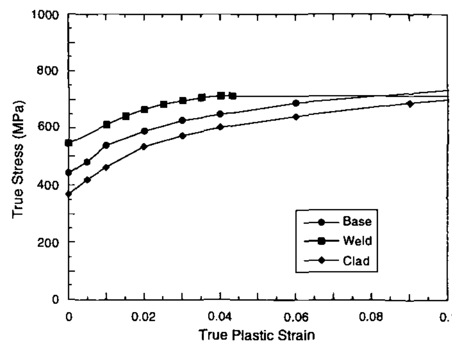

FIG. 5-- Material representation for clad beam at T = –25°C

Finite Element Results

Results from the posttest analyses of the clad beam tests are summarized in Fig. 6(a) and (b). Comparison of the measured and calculated P vs displacement responses provides a way to interpret the accuracy of the analysis results and to establish confidence in the calculated fracture mechanics parameters. The calculated P vs LLD curves are compared with measured data for each test in Fig. 6(a). For the shallow-crack specimens,

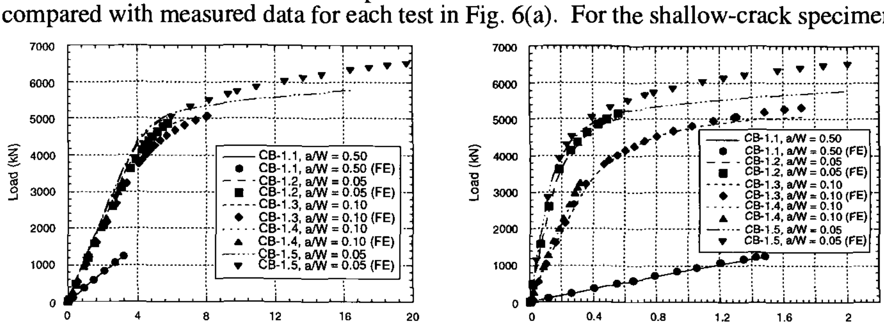

(a) (b)

FIG. 6--Comparison of calculated and measured displacements for clad beam specimens: (a) LLD and (b) CMOD.

calculated LLD values at a given load were greater than measured values for the full range of loading, except CB-1.5 where the measured values of LLD are greater than the calculated values at a given load over the plastic range of loading. Comparisons of calculated and measured P vs CMOD in Fig. 6(b) show good agreement for CB-1.1 – CB-1.4. To match the measured CMOD for CB-1.5, the load had to be increased by 12%. A higher load had to be used because the 3-D plane-strain model is too stiff for an exact comparison between measured and calculated P vs CMOD. Analysis results of CB-1.5, shown in Fig. 7, indicate that the crack began tearing at a load of 5659 kN (J value of 373 kN/m). The crack extended 2.6 mm with an end load of 6497 kN and J value of 1083 kN/m.

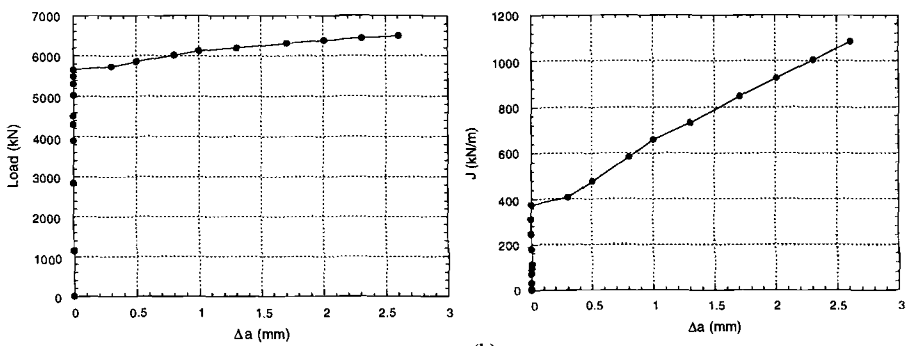

(a) (b)

FIG. 7--Analysis results for clad beam specimen CB-1.5: (a) L vs Δa and (b) J vs Δa.

Toughness Estimation Techniques

The two techniques [4, 14, and 15] used to determine the critical J-integral for CB-1.1 – CB-1.4 (initiated in cleavage) are based on the "work" at the crack tip as measured by the area under the load–displacement curves. The methods require an η-factor, which relates work at the crack tip to the plastic portion of the crack-driving force. The first method of estimating J uses the P vs LLD test record. The J-integral is divided into elastic and plastic terms given by

$$J = J_{el} + J_{pl} \ , \tag{1}$$

where

$$J_{pl} = \left(\eta_{pl}^{\ell}\, U_{pl}\right) / Bb, \tag{2}$$

and U_{pl} is the plastic component of the area under the P vs LLD curve, B is specimen thickness, b is the remaining ligament (W-a), and η_{pl}^{ℓ} is the dimensionless constant relating the area term (U_{pl}) to J_{pl}. Finite-element analysis provides values of η_{pl}^{ℓ} as a function of U_{pl} for each loading and specimen configuration. The U_{pl} value from the measured P vs LLD curve and the corresponding value of η_{pl}^{ℓ} for each test at cleavage initiation are included in Table 4. The value of η_{pl}^{ℓ} is expected to be ~2.0 for deep-crack bend

TABLE 4--Summary of analysis results from the full-thickness clad beam testing program.

	CB-1.1	CB-1.2	CB-1.3	CB-1.4	CB-1.5
a/W	0.50	0.05	0.10	0.10	0.05
η-factors					
η^{ℓ}_{pl}	1.37	0.79	1.05	1.69	—
η^{c}_{pl}	2.26	4.16	4.08	2.82	—
Fracture toughness					
Elastic component					
J_{el}, kN/m	131.3	110.6	230.5	73.52	151.6[a]
K_I, MPa$\sqrt{m}$	173.0	154.5	223.1	126.0	180.9
P vs CMOD					
J_{pl}, kN/m	8.1	124.7	486.0	4.69	
Total J, kN/m	139.4	235.3	716.5	78.21	1082.5[b]
K_{Jc}, MPa$\sqrt{m}$	173.5	225.4	393.3	130.0	483.5
P vs LLD					
J_{pl}, kN/m	7.4	103.8	384.8	3.31	—
Total J, kN/m	138.7	214.4	615.3	76.83	—
K_{Jc}, MPa$\sqrt{m}$	173.1	215.2	364.5	128.8	—

[a]Static analysis for crack depth location after ductile tearing (a ~ 14.7 mm).

[b]Gurson-Tvergaard plasticity model for void growth and element extinction for crack growth.

specimens at initiation [ASTM Standard Test Method for J_{Ic} (E 813)] but was determined to be 1.37 from the finite-element calculations. The low η^{ℓ}_{pl} value at initiation may be the result of overestimating the measured LLD, which would lead to a larger value of U_{pl} and ultimately a smaller value for η^{ℓ}_{pl}. The second technique for determining the critical J-integral [16] uses the plastic component of the area under the P vs CMOD curve (A_{pl}) to calculate J_{pl}. The values of A_{pl} (from measured P vs CMOD data) and η^{c}_{pl} for each test at initiation are listed in Table 4. The critical J-integral values were converted to critical elastic-plastic, stress-intensity factors (K_{Jc}), using the plane-strain formulation.

The values of J calculated from the two η-factor techniques are compared to J determined from finite-element analyses for specimens CB-1.1 – CB-1.4 in Fig. 8(a)–(d). In Fig. 8(a), the P vs J curve for CB-1.1 from the finite-element analysis is above the curves generated from toughness estimation techniques. This may be related to the variation of η_{pl} with increasing plastic area for the CB-1.1 specimen, while a constant value of η_{pl} is used in the estimation techniques. For the shallow-crack specimens, there was generally good agreement between experimental and finite-element analysis determined values of J. Although, like CB-1.1, the analysis results exhibited a stiffer response than was indicated from the experimental data.

Residual Stresses

An analytical study was carried out to estimate the effects of residual stresses on measured cleavage fracture toughness data obtained from the full-thickness clad beam specimens CB-1.1 through CB-1.4. A thermal gradient method (TGM) was used to generate stress distributions in the beams that approximate the residual stresses. These estimates of stress distribution were based on previous residual stress studies conducted at

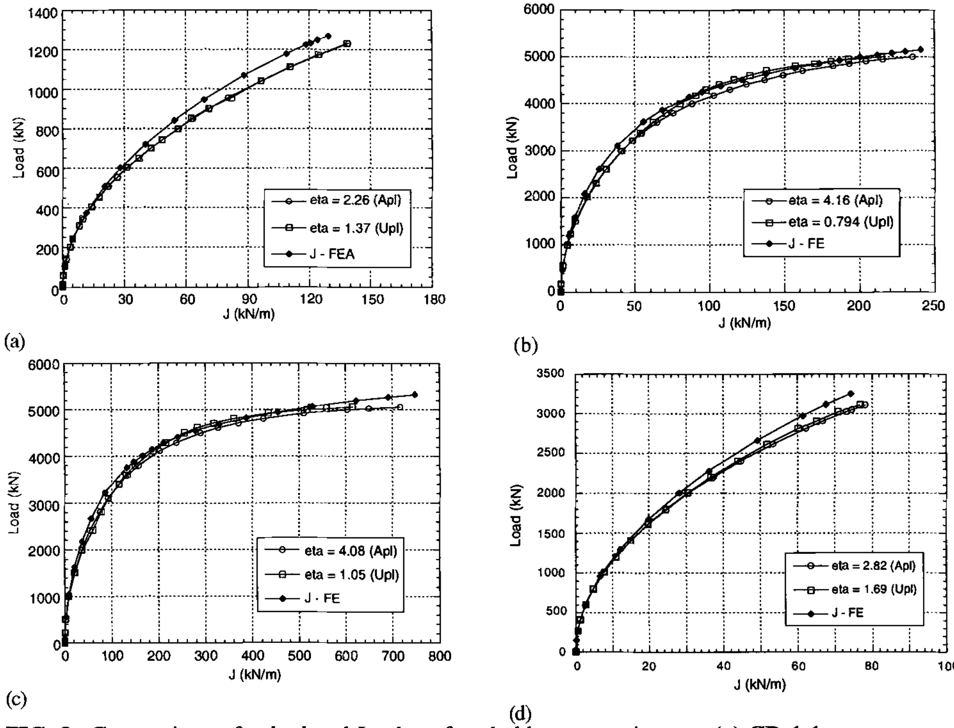

FIG. 8--Comparison of calculated J values for clad beam specimens: (a) CB-1.1, (b) CB-1.2, (c) CB-1.3, and (d) CB-1.4.

ORNL and published in Ref. 17. In the latter studies, the TGM was based on application of a temperature distribution in the form of a cosine function through the thickness of the beam. The temperature distribution was adjusted such that the generated stresses in the beam would cause the opening displacements of a pre-crack notch in the beam to match those recorded during the wire electro-discharge machining of the notch. These fictitious thermal stresses were then imposed as initial stresses on each of the clad beam models containing fatigued through-flaws. It should be noted that residual stress values may be larger in the RPV shell segment from which the clad beam specimens were fabricated. A previous study [18] has shown that the stress level in a specimen cut from a plate is lower than the stress level in the uncut plate, because the stresses in the specimen were allowed to relax when the restraining effects of the plate were removed.

Estimates of residual stress effects on cleavage fracture toughness values measured in each of the four tests are summarized in Table 5. Columns (1) and (2) provide estimates of fracture toughness based on CMOD η-factors (Table 4) that exclude and include, respectively, the effects of residual stresses. Residual stresses were shown to have a measurable effect only on the shallow flaw toughness data.

Fracture toughness data from the HSST clad beam and shallow-crack SENB programs are shown in Fig. 9 as a function of relative temperature (T-NDT). The lower bound curve in Fig. 9 is an exponential fit to the deep-crack data. Figure 9 indicates an increase in mean toughness and data scatter with decreased constraint associated with shallow crack testing in the transition temperature region. The range in scatter for data obtained from the clad beam specimens is consistent with that from the laboratory-scale SENB specimens tested at the same temperature. Note that the minimum toughness value from the clad beam specimens was provided by a shallow-crack beam, not by the single deep-cracked beam tested in this series.

TABLE 5--Summary of residual stress results from the full-thickness clad beam testing program.

Test	a/W	K (MPa$\sqrt{m}$) (1) Without Residual Stress	K (MPa$\sqrt{m}$) (2) With Residual Stress
CB-1.1	0.50	174	174
CB-1.2	0.05	225	243
CB-1.3	0.10	393	411
CB-1.4	0.10	130	155

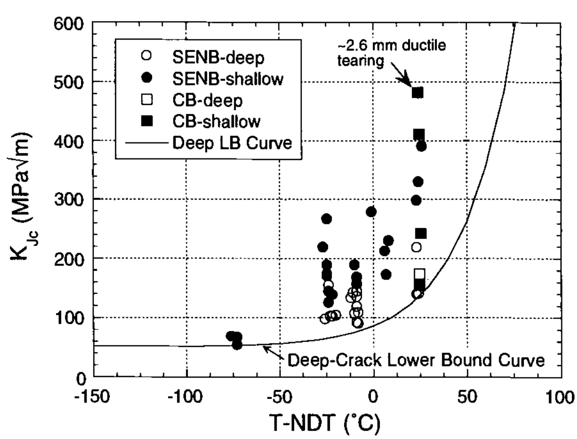

FIG. 9--Fracture toughness as function of normalized temperature T – NDT.

Constraint Analyses

The J-Q methodology [5-7] was used to assess crack-tip stress triaxiality in the clad beam specimens which experienced cleavage initiation. The coefficient Q measures the departure of the opening-mode stress from the reference plane-strain small-scale yielding (SSY) solution, normalized by the yield strength. In these analyses, results for the deep-crack specimen (CB-1.1) are employed as an approximation to the SSY reference solution. Analyses [4] have shown that Q ≈ 0 for the deep-crack specimens under these loading conditions. This observation is supported by results shown in Fig. 10(a) for the normalized opening-mode stress (σ_{yy}/σ_0) distributions vs $\bar{r}$ [$r/(J/\sigma_0)$] for the deep-crack specimen CB-1.1. The opening-mode stresses ahead of the crack tip for the shallow-crack specimens, shown in Fig. 10(b), exhibit an essentially uniform deviation from the approximated SSY solution (CB-1.1) over a distance of $2 \leq \bar{r} \leq 10$ (i.e., spatially uniform). From Fig. 10(b), the clad beam specimen CB-1.4 has a Q value of about –0.36 at failure (for $\bar{r}$ = 2), whereas CB-1.2 and CB-1.3 had Q values of –0.78 at failure (a significant loss of constraint). The coefficient Q, although found to be independent of $\bar{r}$, was formally defined at $\bar{r} = 2$, which falls just outside the finite strain blunting zone. This moderate loss of constraint in the CB-1.4 specimen is due primarily to the relatively lower failure load observed in the test.

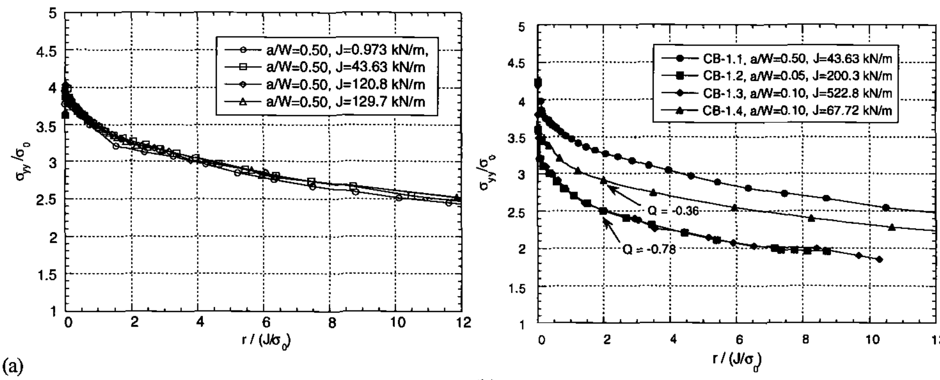

FIG. 10--Distributions of normalized opening-mode stress for clad beam specimens as a function of applied J: (a) a/W = 0.50, (b) at a/W of 0.50, 0.05, and 0.10.

SUMMARY AND FUTURE PLANS

Beam specimens, which incorporate RPV fabrication welds, base plate, and weld-overlay cladding, are providing fracture toughness data for shallow cracks in material for which metallurgical conditions are prototypic of those found in RPVs. Factors influencing the fracture toughness of RPV material containing shallow cracks include metallurgical gradients, weld inhomogeneities, weld defects, the cladding process, and residual stresses.

In the first testing phase, five full-thickness clad beam specimens were fabricated with through-thickness cracks in weld metal that ranged in depth from 10 to 114 mm ($0.05 \leq a/W \leq 0.5$). These specimens were tested in three-point bending at temperatures in the transition region of the weld metal fracture toughness curve ($T - NDT \approx 25°C$). Fracture toughness estimates were obtained from P vs LLD and P vs CMOD data using finite-element techniques and estimation schemes based on the η-factor method. The cleavage toughness data were compared with other shallow- and deep-crack uniaxial beam data generated previously from A 533 B plate material. The range in scatter for data obtained from the clad beam specimens is consistent with that from the laboratory-scale SENB specimens tested at the same temperature. Determining conditions in the weld and base metal regions near the cladding is important for interpreting the shallow-crack test results and, consequently, should be included in the HSST Program plan for future work.

In the HSST Program, initial studies of ductile tearing models have focused on the Gurson-Tvergaard (G-T) dilatant plasticity model for void growth and an element extinction capability for modeling crack growth. Two principal input parameters for the G-T model are the initial void volume fraction, f_0, and the characteristic length, D, associated with the G-T crack plane elements. According to theory, these parameters are dependent only on the material and not on specimen geometry. To evaluate this model, the following steps will be taken:

- Generate ductile crack growth data from side-grooved compact tension (CT) specimens taken from the weld material.

- The parameters f_0 and D will be selected for the material to get agreement with load versus CMOD and crack growth data from the CT specimens. Metallography may also provide some estimates of initial porosity and inclusion spacing in the weld, which could be compared with values assigned to parameters f_0 and D.
- The same values of these parameters from the CT specimen analyses will then be used to analyze the full-thickness clad beams to determine if they predict the observed responses.
- If the analytical and experimental responses match then the toughness values will be used, but if the responses do not match then the model will have to be reevaluated.

Additional full-thickness clad beams have been tested and results are being evaluated to complete the investigation of fracture toughness of shallow cracks located in prototypical full-thickness plate material. Shallow-crack fracture toughness results from these specimens should provide additional data that are essential to a better understanding of the effects of metallurgical conditions in the region of the clad HAZ.

ACKNOWLEDGMENTS

Research sponsored by the Office of Nuclear Regulatory Research, U.S. Nuclear Regulatory Commission under Interagency Agreement 1886-8011-9B with the U.S. Department of Energy under Contract DE-AC05-96OR22464 with Lockheed Martin Energy Research Corp. The submitted manuscript has been authored by a contractor of the U.S. Government No. DE-AC05-96OR22464. Accordingly, the U.S. Government retains a non-exclusive, royalty-free license to publish or reproduce the published form of this contribution, or allow others to do so, for U.S. Government purposes.

REFERENCES

[1] W. Marshall et al., "An Assessment of the Integrity of PWR Pressure Vessels," UKAEA Study Group Reports, March 1982.

[2] U. S. Nuclear Regulatory Commission Regulatory Guide 1.154, "Format and Content of Plant-Specific Pressurized Thermal Shock Safety Analysis Reports for Pressurized Water Reactors", January 1987.

[3] R. D. Cheverton and D. G. Ball, Martin Marietta Energy Systems, Inc., Oak Ridge Natl. Lab., "Pressurized-Thermal-Shock Evaluation of the Calvert Cliffs Nuclear Power Plant," pp. 201-244, NUREG/CR-4022, (ORNL/TM-9408), September 1985.

[4] T. J. Theiss, D. K. M. Shum, and S. T. Rolfe, Martin Marietta Energy Systems, Inc., Oak Ridge Natl. Lab., "Experimental and Analytical Investigation of the Shallow-Flaw Effect in Reactor Pressure Vessels," NUREG/CR-5886, (ORNL/TM-12115), July 1992.

[5] N. P. O'Dowd and C. F. Shih, "Family of Crack-Tip Fields Characterized by a Triaxiality Parameter: Part I - Structure of Fields," *J. Mech. Phys. Solids* 39, 989-1015 (1991).

[6] N. P. O'Dowd and C. F. Shih, "Family of Crack-tip Fields Characterized by a Triaxiality Parameter: Part II - Fracture Applications," *J. Mech. Phys. Solids* 40, 939-963 (1992).

[7] N. P. O'Dowd and C. F. Shih, Naval Surface Warfare Center, "Two Parameter Fracture Mechanics: Theory and Applications," USNRC Report NUREG/CR-5958 (CDNSWC/SME-CR-16-92), February 1993.

[8] J. A. Keeney et al., Martin Marietta Energy Systems, Inc., Oak Ridge Natl. Lab., "Preliminary Assessment of the Fracture Behavior of Weld Material in Full-Thickness Clad Beams," NUREG/CR-6228, (ORNL/TM-13091), October 1994.

[9] J. A. Keeney, B. R. Bass, and W. J. McAfee, "Fracture Analysis of Full-Thickness Clad Beam Specimens," Fracture Mechanics: 27th Volume, ASTM STP 1296, Robert S. Piascik, James C. Newman, Jr., and Richard P. Gangloff, Eds., American Society for Testing and Materials, Philadelphia, 1996.

[10] A. L. Gurson, "Continuum Theory of Ductile Rupture by Void Nucleation and Growth: Part I – Yield Criteria and Flow Rules for Porous Ductile Media," Journal of Engineering Materials and Technology, Vol. 99, pp. 2-15, 1977.

[11] *ABAQUS Theory Manual*, Version 5–3, Hibbit, Karlson, and Sorensen, Inc., Providence, R. I., 1993.

[12] K. C. Koppenhoefer, A. S. Gullerud, C. Ruggieri, R. H. Dodds, Jr., and B. E. Healy, Department of Civil Engineering, University of Illinois, "WARP3D: Dynamic Nonlinear Analysis of Solids Using a Preconditioned Conjugate Gradient Software Architecture," UILU-ENG-94-2017, November 1994.

[13] C. Ruggieri and R. H. Dodds, Jr., Department of Civil Engineering, University of Illinois, "Constraint and Ductile Tearing Effects in Statistical Analyses of Cleavage Fracture," UILU-ENG-95-2011, October 1995.

[14] T. J. Theiss et al., Martin Marietta Energy Systems, Inc., Oak Ridge Natl. Lab., "Initial Results of the Influence of Biaxial Loading on Fracture Toughness," NUREG/CR-6036, (ORNL/TM-12349), June 1993.

[15] B. R. Bass et al., Martin Marietta Energy Systems, Inc., Oak Ridge Natl. Lab., "Biaxial Loading and Shallow-Flaw Effects on Crack-Tip Constraint and Fracture Toughness," NUREG/CR-6132, (ORNL/TM-12498), January 1994.

[16] M. T. Kirk and R. H. Dodds, Jr., Department of Civil Engineering, University of Illinois, "J and CTOD Estimation Equations for Shallow Cracks in Single Edge Notch Bend Specimens," USNRC Report NUREG/CR-5969 (CDNSWC/SME-CR-17-92), July 1993.

[17] J. A. Keeney, Martin Marietta Energy Systems, Inc., Oak Ridge Natl. Lab., "Residual Stress Analysis of Full-Thickness Clad Beam Specimens," ORNL/NRC/LTR-94/37), August 14, 1995.

[18] E. F. Rybicki, J. R. Shadley, and A. S. Sandhu, The University of Tulsa, Mechanical Engineering Associates, Inc., "Experimental Evaluation of Residual Stresses in a Weld Clad Plate and Clad Test Specimens," NUREG/CR-4646, MEA-2145, October 1986.

Panagiotis Michaleris,[1] Mark Kirk,[2] William Mohr,[3] and Tom McGaughy[4]

INCORPORATION OF RESIDUAL STRESS EFFECTS INTO FRACTURE ASSESSMENTS VIA THE FINITE ELEMENT METHOD

REFERENCE: Michaleris, P., Kirk, M., Mohr, W., McGaughy, T., **"Incorporation of Residual Stress Effects into Fracture Assessments via the Finite Element Method"**, Fatigue and Fracture Mechanics: 28th Volume, ASTM STP 1321, J. H. Underwood and B. D. Macdonald, M. R. Mitchell, Eds., American Society for Testing and Materials, 1997.

ABSTRACT: This paper presents a finite element methodology for the incorporation of residual stress effects into fracture assessments of pressure vessel and piping components. The residual stress is determined through improved welding simulations. Following the welding simulation, interpolation is used to transfer the computed residual stresses onto fine meshes for the evaluation of J integrals. The finite element fracture assessment methodology is used as a baseline to evaluate several approximations to the residual stress field and appropriate analytic solutions for a 15.875 mm (5/8 in.) thick pipe with R/t=10, 25, and 50. The remote yield level approximation is found to be overconservative while the best approximation is the bending moment fit to the residual stress distribution.

KEYWORDS: residual stress, fracture assessment, welding simulation

[1]Senior Research Engineer, Engineering Section, Edison Welding Institute, 1100 Kinnear Road, Columbus, Ohio 43212.

[2]Section Manager and Senior Research Engineer, Edison Welding Institute, 1100 Kinnear Road, Columbus, Ohio 43212.

[3]Senior Research Engineer, Edison Welding Institute, 1100 Kinnear Road, Columbus, Ohio 43212.

[4]Marketing Development Manager and Research Engineer, Edison Welding Institute, 1100 Kinnear Road, Columbus, Ohio 43212.

1.0 INTRODUCTION

One of the major problems associated with incorporating residual stresses into a fracture assessment is the selection of a representative through-thickness distribution of residual stress. In the absence of definitive measurements, it is common practice to assume that residual stress in an as-welded structure is tensile, of yield strength magnitude, and uniform across the thickness. These assumptions may lead to extremely conservative assessments. This paper presents a finite element (FE) methodology for the incorporation of residual stress effects into fracture assessments of pressure vessel and piping components.

Early efforts to evaluate residual stress in piping components involved imposing on a cylinder the residual stress profile generated by a similar weld in a plate using shell theory [1, 2]. A difficulty of implementing such techniques is obtaining an estimate or measurement of residual stress for an equivalent weld in a plate. Furthermore, in multi-pass welds, the development of residual stress is coupled with the increasing structural resistance of the shell as the weld is deposited. Additional passes tend to impose axial compression over the residual stress pattern of the initial passes. Therefore, the applicability of these techniques is limited to thin-walled pipes with a few passes.

Computational approaches to determine welding residual stress developed over the last fifteen years include elasto-plastic welding simulations. Most notable is the work of Rybicki [3] involving an analytical thermal model which serves as input to a mechanical model based on FEs. The limitation of these models is the use of approximate analytical solutions for the thermal history. Such approximations overpredict the temperature in the weld region and ignore the effects of the latent heat of fusion. Furthermore, the mechanical models lump multiple weld passes into one, resulting in a fundamentally different weld being modelled than the one of interest.

Previous efforts to improve the accuracy with which residual stress is accounted for in fracture assessments involved generating a stress field similar to stresses measured on a component [4, 5, 6]. Rybicki and his coworkers [4] use linear elastic fracture mechanics to perform a fracture assessment with residual stress. They impose the residual stress on the fracture assessment model and determine the stress intensity factor by a crack closure integral. The residual stress is determined by a welding simulation. The model inherently accounts for any stress relaxation due to crack opening. However, it is unclear how Rybicki, et al., [4] imposed the residual stress on the fracture assessment model.

Finch and Burdekin [5, 6] use a similar approach as Rybicki. They impose the residual stress, which is assumed to be known, on a fracture assessment model either as an initial condition or as a thermal load. They evaluate the J-integral using the commercial code ABAQUS. They also consider elastic-plastic fracture. The difficulty in this approach lies in determining the residual stress. Several residual stress measurements through-thickness for each component assessed are required. Additionally, potential residual stress relaxation due to crack growth may not be considered. Finally, significant trial and error effort is required to determine a temperature load that creates a stress pattern similar to that of the residual stress.

The present work offers improved procedures for incorporating residual stress into a fracture assessment by addressing the following objectives:

- Development and validation of a FE procedure to evaluate residual stress in multi-pass welds.
- Development of an improved FE fracture assessment procedure to include residual stress effects in a fracture assessment.
- Verification of simplified fracture assessment procedures to include residual stress effects.

An improved welding simulation is developed to determine the residual stress. The procedure is presented in detail in [7] along with a compendium of residual stress distributions for several girth welds. The improved thermal input models used on plates [8, 9, 10] are applied to the modelling of pipes.

The fracture assessment is performed following the welding simulation, using interpolation to transfer the computed residual stresses onto fine meshes. The approach is both consistent and efficient. The redistribution of residual stress as a crack opens is inherently accounted for by the FE model. The efficiency of this procedure is improved since residual stress measurements are no longer required. The use of interpolation further improves computational efficiency since a relatively coarse mesh can be used for the welding simulation and several fine meshes for appropriate crack sizes and locations.

The FE fracture assessment methodology is used as a baseline to evaluate several approximations to the residual stress field and appropriate analytic solutions. Here, membrane and bending fits to the residual stress distributions computed by the welding simulation are evaluated.

2.0 RESIDUAL STRESS EVALUATION

The residual stress produced by welding is determined by two-dimensional thermo-elasto-plastic welding simulations using the commercial code ABAQUS. The procedure is presented in detail in Michaleris [7], along with experimental validation and a partial compendium of residual stress distributions for girth welds. In the welding simulation, the welding conditions and joint configuration are the input to the thermal analysis, where the heat flow is simulated. The heat input is modelled by using the double ellipsoid heat input model developed by Goldak [8]. In the mechanical analysis, which follows the thermal analysis, the elastic-plastic deformations are determined. The temperature history and the weld joint configuration are used as input. The distortion and residual stresses are output from the mechanical analyses.

3.0 FRACTURE ASSESSMENT METHOD VIA FE METHOD

A consistent fracture assessment FE methodology is developed here and illustrated in Fig. 1. The residual stress and corresponding displacement and deformation fields are determined by the welding simulation. All fields are then interpolated onto a fracture assessment model using the REZONE option of ABAQUS. A relatively coarse mesh is used for the welding simulation, and several fine meshes for the crack sizes and crack locations of interest. Furthermore, the redistribution of residual stress as a crack opens is inherently accounted for by the modelling procedure. All fields, including the plastic strain field caused by welding, are considered in the fracture assessment. The only current limitation of the interpolation approach is the restriction to linear elements imposed by ABAQUS.

The crack driving force can be evaluated by either the J-integral or the crack tip opening displacement (CTOD). The J-integral is path independent for paths that enclose any plastic wake on the crack faces. If the crack face is opened gradually (i.e., node by node) starting from the surface, a plastic wake is developed on the crack faces and the J-integral becomes path dependent. In this case, the crack driving force can be expressed only as a CTOD. In this work, in order to facilitate the comparison of the FE results to approximate analytical models, the crack driving force is evaluated as J-integral which is computed by opening the crack faces at once.

3.1 Implementation and Verification

The interpolation technique of the residual stress, displacement and plastic strain fields into the fine mesh is verified on a welded pipe with an internal circumferential crack of 20% of the wall thickness (Fig. 1). A welding simulation on a coarse mesh with axisymmetric four-noded elements is initially performed (Fig. 1, residual stress mesh). A pipe thickness of 10 mm (0.394 in.) is assumed with an internal radius of 100 mm (3.94 in.) (R/t=10). An autogenous weld is modelled. The welding simulation results are then interpolated to a mesh which is a focused at 20% of the thickness (Fig. 1, interpolation mesh). Finally, the nodes on the crack face are released (Fig. 1, fracture assessment mesh), and a J-integral is computed and plotted (Fig. 2, four-node rezone). To verify the interpolation, the welding simulation is performed on the focused mesh, then the crack face is opened and the J-integral computed (Fig. 2, four-node). The result is almost identical to that provided by interpolation. To determine the influence of element type, the welding simulation is performed on the same focused mesh, but with mid-side nodes included. Then the crack face is released, and the J-integral computed (Fig. 2, eight-node). The average of the J-integral for the first five rings is within 10% of the four-node element calculations.

The FE fracture assessment approach is demonstrated on a 15.875 mm (5/8 in.) thick pipe with three radius-to-thickness ratios, namely, 10, 25, and 50 (see Fig. 3). A lumped welding simulation model is used for simplicity, as shown in Fig. 4. The welding conditions are listed in Table 1. A mild steel, such as 1020, is assumed. The computed residual stresses are illustrated in Figs. 5 through 8. Three crack depths at the weld centerline are investigated at 10, 25 and 50% of wall thickness. The computed J-integrals generated by the residual stress are plotted in Fig. 9. The stress intensity factor for the residual stress ($K_{I(FEA)}$) is determined by assuming plane strain conditions at the crack tip as follows:

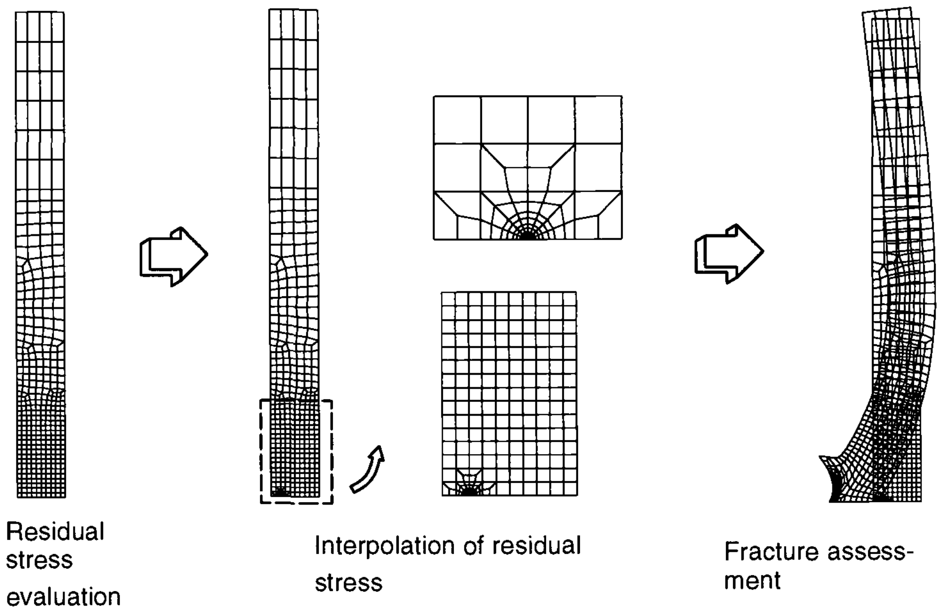

FIG. 1. Illustration of Finite Element Fracture Assessment Procedure.

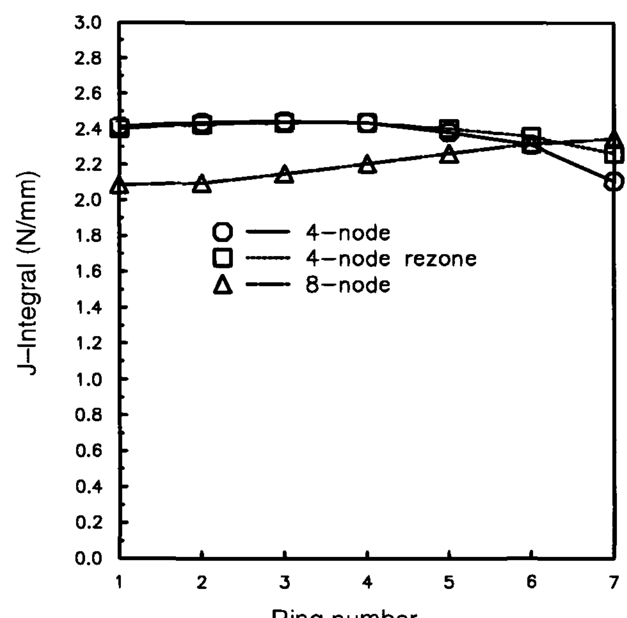

FIG. 2. Verification of Fracture Assessment Through Interpolation of Residual Stress

$$K_{I(FEA)} = \sqrt{\frac{JE}{(1-\nu^2)}} \tag{1}$$

TABLE 1--Welding conditions of 15.875 mm (5/8 in.) thick pipe with a single-V weld.

Pass	Volts (V)	Amps (A)	Travel speed (in./min)	Heat Input (kJ/in.)
1	20	83	9.5	10.5
2	30	166	9.5	31.5
3	30	166	7.5	39.84
4	30	166	7.5	39.84
5-8	25	133	4.8	41.6

4.0 APPROXIMATE FRACTURE ASSESSMENT MODELS

The FE fracture assessment approach of Section 3.0 is both accurate and computationally efficient. However, it is not suited as a general fracture assessment tool because it requires the generation and the analysis of several FE meshes. To this end, simplified approximate fracture assessment models are required. The accuracy of such models can be investigated using the FE solution as a baseline. The following approximations of the residual stress distribution are evaluated here on the ⅝-in. thick pipe:

1) Membrane stress of yield level magnitude
2) Membrane stress of magnitude equivalent to the peak axial residual stress at the crack cross section estimated by the FE process simulation
3) A stress distribution having both membrane and bending components fit to the residual stress estimated by the FE process simulation.

The computed residual stress through the pipe thickness at the weld centerline along with the approximate residual stress distributions are illustrated in Figs. 6, 7, and 8 for the 15.875 mm (5/8 in.) thick pipes with an R/t of 10, 25 and 50, respectively. To compute the stress intensity factor, the following solution models were evaluated:

1) Buchalet [11] series solution (available only for R/t=10)
2) Curve fit to FEA solutions model of Gordon [12]

The Buchalet [11] solution is as follows:

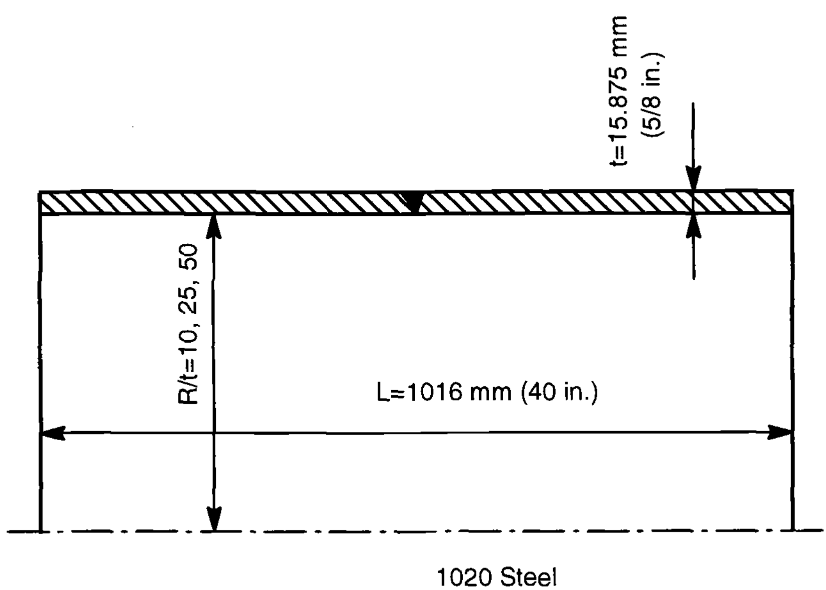

FIG. 3. Pipe Geometries Used in the Fracture Assessment

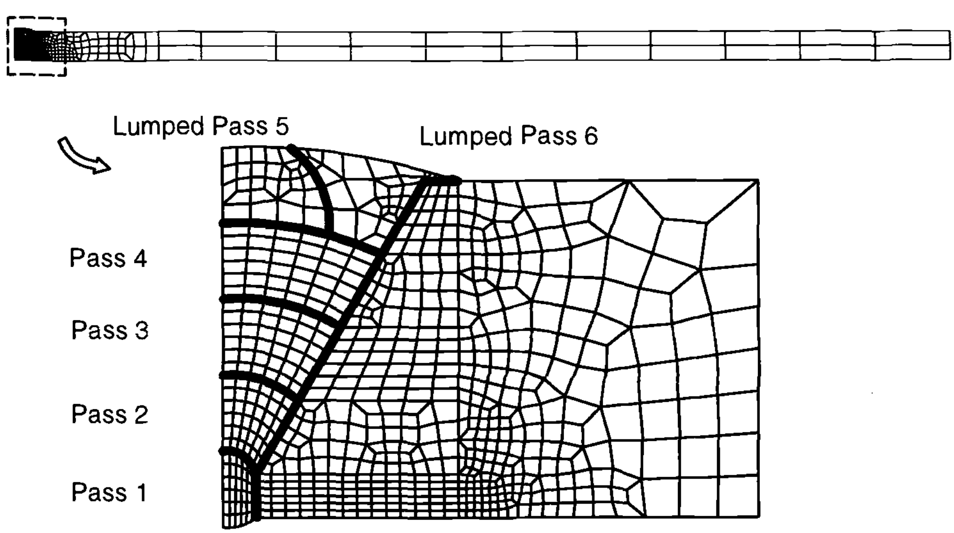

FIG. 4. Finite Element Mesh of the Welding Simulation with Lumped Final Passes.

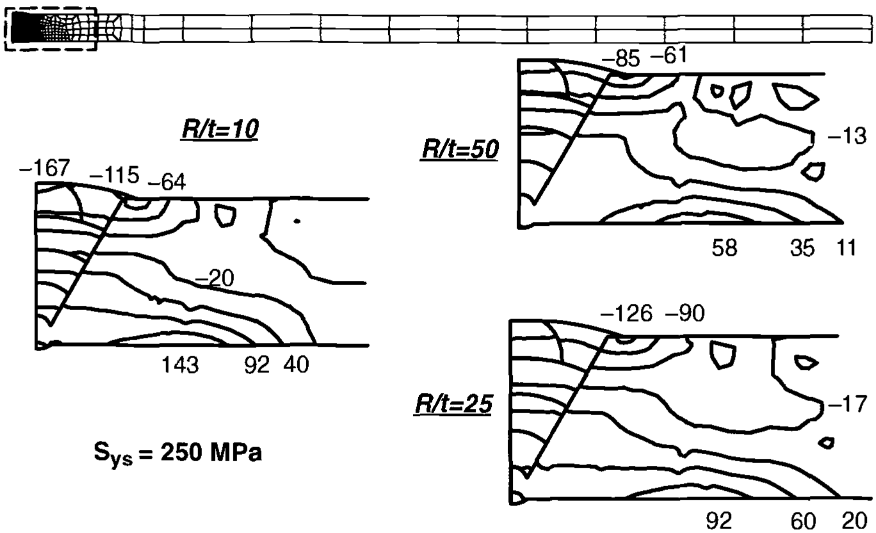

FIG. 5. Axial Residual Stress Distributions (MPa)

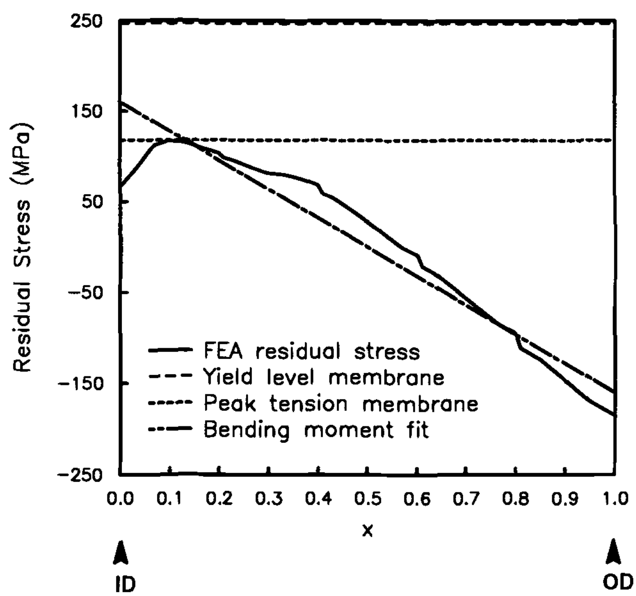

FIG. 6. Through Thickness Residual Stress Distribution and its Approximations for the 15.875 mm (5/8 in.) Thick pipe with R/t=10.

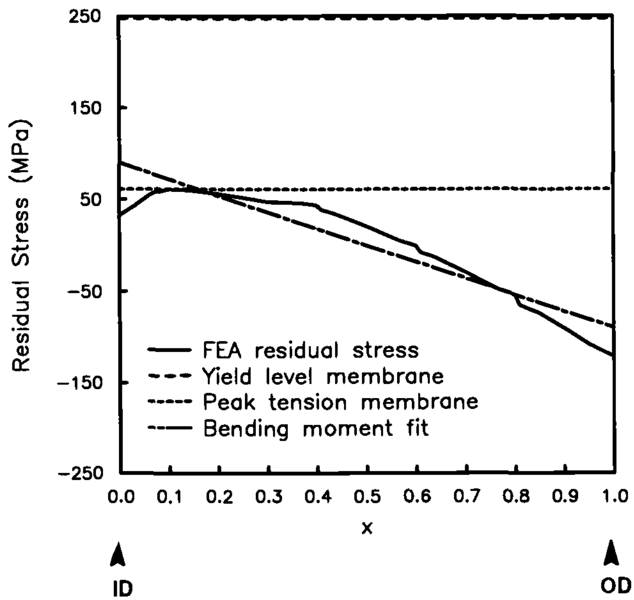

FIG. 7. Through Thickness Residual Stress Distribution and its Approximations for the 15.875 mm (5/8 in.) Thick pipe with R/t=25.

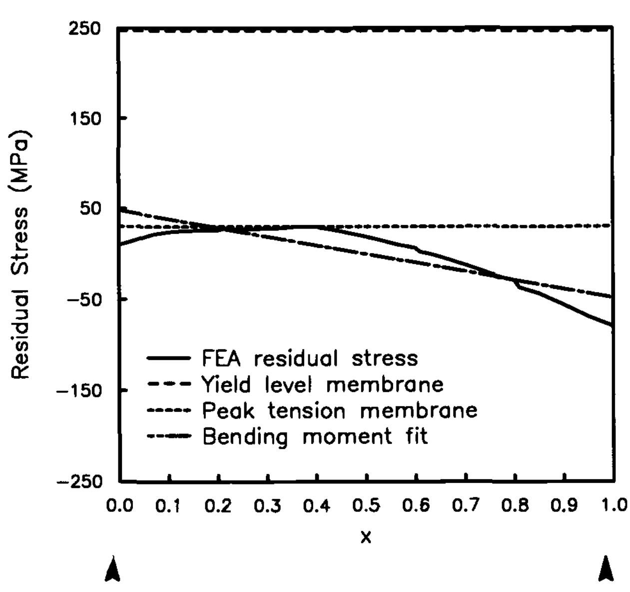

FIG. 8. Through Thickness Residual Stress Distribution and its Approximations for the 15.875 mm (5/8 in.) Thick pipe with R/t=50.

$$K = \left\{ \sum_{i=0}^{3} \sigma_i \; G_i \right\} \sqrt{\pi a} \tag{2}$$

where σ_i are the coefficients of the stress polynomial describing the axial stress σ defined as follows:

$$\sigma = \sum_{i=0}^{3} \sigma_i \left\{ \frac{x}{t} \right\} i \tag{3}$$

and

$$G_i = \sum_{i=0}^{3} A_i \left\{ \frac{a}{t} \right\} i \tag{4}$$

where the values of A_i are for a pipe with an R/t=10 are listed in Table 2.

TABLE 2--Interpolation coefficients of Buchalet [11] solution for pipes with R/t=10.

i	G_0	G_1	G_2	G_4
A_0	1.12	0.	0.	0.
A_1	-4.8966E-02	0.6657	3.3841E-02	0.
A_2	2.9276	2.6455E-02	0.21786	2.9355E-02
A_3	-0.5849	0.9368	0.7269	0.1920
A_4	0.	0.	0.	0.5099

The model of Gordon, et al., [12], offers stress intensity factors for full circumferential cracks of arbitrary depth and on arbitrary R/t ratios under remote arbitrary membrane loading. The model is derived from interpolation of FE solutions. For a membrane stress, s_b, the model of Gordon [12] computes the stress intensity factor K as follows:

$$K = s_b \sqrt{\pi a} \; \left\{ 1.1 + A [6(a/t)^B + (a/t)^C] \right\} \tag{5}$$

$$A = -.5087 + .4782 \left(\frac{d}{t} \right)^{0.2} \tag{6}$$

$$B = 1.519 + 2.573 \times 10^{-2} \left(\frac{d}{t} - 20\right)^{0.6} \tag{7}$$

$$C = 2.972 + .5780 \left(\frac{d}{t} - 20\right)^{0.25} \tag{8}$$

where $\boldsymbol{d}$ is the pipe diameter, $\boldsymbol{t}$ is the pipe wall thickness, and $\boldsymbol{a}$ the crack length. To obtain bending solutions, the solution of Gordon [12] is adjusted for bending according to the solution of Buchalet [11]. The adjustment assumes that linear and higher terms of the Buchalet [11] solution do not depend on R/t. Therefore, the constant term (membrane) of the Buchalet [11] solution is substituted by the Gordon [12] solution, and $\boldsymbol{K}$ is calculated as follows:

$$K = K_{Gordon} + s_{bending}\sqrt{\pi a}\left[0.6657\left(\frac{a}{t}\right) + 0.02646\left(\frac{a}{t}\right)^2 + 0.9368\left(\frac{a}{t}\right)^3\right] \tag{9}$$

Table 3 lists the stress intensity factors computed by the approximate models. The table also lists the FE solution for the actual residual stress distribution. Figs. 10 and 11 illustrate stress intensity factors computed by the Gordon [12] solution using the remote yield level approximation and bending fit approximation, respectively, as compared to the FE solution. Based upon these results, the following observations are made:

1) The Buchalet [11] solution is, in general, in close agreement to the FE results, but slightly less than the solution of Gordon [12].

2) The remote yield level approximation is overconservative for all cases. The overestimation increases with increasing a/t and R/t. This is attributed to the lack of residual stress relaxation in the approximate models as the crack opens and to the deceasing residual stress as R/t increases.

3) The uniform membrane approximation of magnitude peak axial residual stress at the crack cross section underpredicts the stress intensity factor for shallow cracks (a/t=0.1), and overpredicts for deep cracks (a/t=0.5).

4) The best approximation is the bending moments fit to the actual residual stress distribution.

5) The Gordon [12] $\boldsymbol{K}$ solution loaded by a bending moment which best approximates the FE computed residual stress distribution is the best approximation to the FE solution of Section 3.

TABLE 3--Approximate fracture assessment solutions.

Load		R/t	a/t	K_I ($N/mm^{3/2}$)		
Membrane (MPa)	**Bending (MPa)**			**Buchalet, 76**	**Gordon, 93**	**FEA***
247	0	10	0.1	631	643	*333**
247	0	10	0.25	1118	1195	*521**
247	0	10	0.5	2164	2348	*753**
247	0	25	0.1	-	641	*202**
247	0	25	0.25	-	1221	*323**
247	0	25	0.5	-	2599	*547**
247	0	50	0.1	-	637	*106**
247	0	50	0.25	-	1229	*196**
247	0	50	0.5	-	2786	*308**
117.5	0	10	0.1	300	306	*333**
117.5	0	10	0.25	532	569	*521**
117.5	0	10	0.5	1029	1117	*753**
60.9	0	25	0.1	-	158	*202**
60.9	0	25	0.25	-	301	*323**
60.9	0	25	0.5	-	641	*547**
30.25	0	50	0.1	-	78	*106**
30.35	0	50	0.25	-	151	*196**
30.5	0	50	0.5	-	341	*308**
0	160	10	0.1	360	368	*333**
0	160	10	0.25	518	568	*521**
0	160	10	0.5	672	792	*753**
0	90	25	0.1	-	206	*202**
0	90	25	0.25	-	329	*323**
0	90	25	0.5	-	536	*547**
0	48	50	0.1	-	109	*106**
0	48	50	0.25	-	177	*196**
0	48	50	0.5	-	323	*308**

* FEA results are computed using the actual residual stress distribution

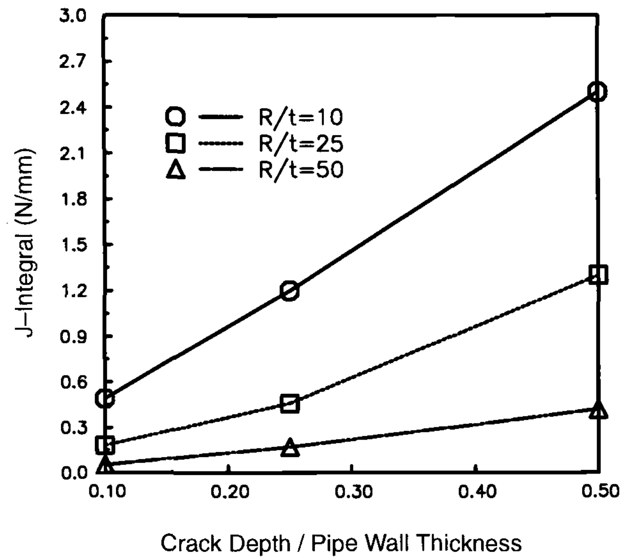

FIG. 9. J–Integral Calculations for 15.875 mm (5/8 in.) Wall Pipe Thickness with Lumped Pass Model.

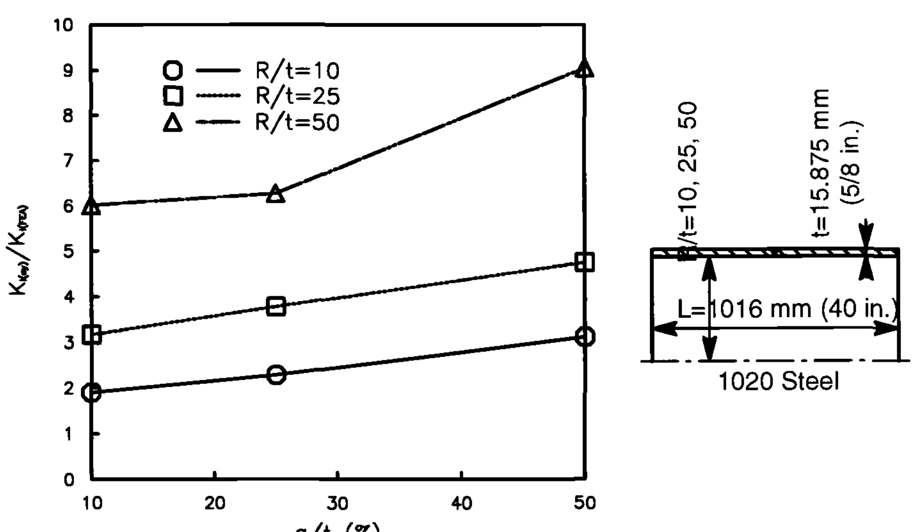

FIG. 10. Comparison of Stress Intensity Factor Using Remote Yield Stress Assumption ($K_{I(sy)}$) and the Actual Residual Stress Distribution ($K_{I(FEA)}$).

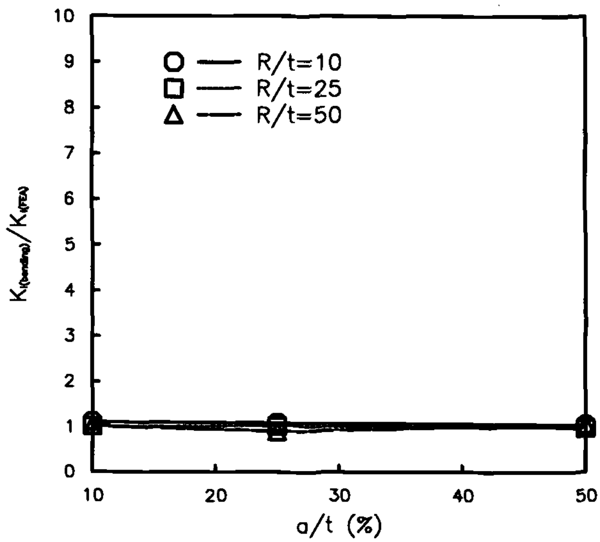

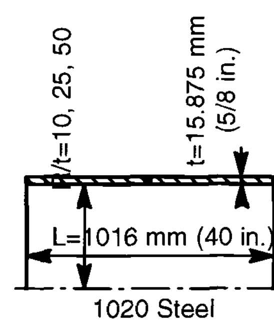

FIG. 11. Comparison of Stress Intensity Factor Using Remote Linear Approximation to Residual Stress ($K_{I(bending)}$) and the Actual Residual Stress Distribution ($K_{I(FEA)}$).

5.0 CONCLUSIONS AND RECOMMENDATIONS

A FE procedure has been developed to incorporate the effects of welding residual stress into fracture assessments. The residual stress is determined through improved welding simulations and interpolation is used to transfer the computed residual stresses onto fine meshes for the evaluation of *J*-integrals. The approach is both consistent and efficient. The redistribution of residual stress as a crack opens is inherently accounted for by the FE model. The efficiency of this procedure is improved since residual stress measurements are no longer required. The use of interpolation further improves computational efficiency since a relatively coarse mesh can be used for the welding simulation and several fine meshes for appropriate crack sizes and locations.

The FE fracture assessment methodology is used as a baseline to evaluate several approximations to the residual stress field and appropriate analytic solutions for a 15.875 mm (5/8 in.) thick pipe with R/t=10, 25, and 50. The remote yield level approximation is overconservative for all cases (ranging from 2× for a/t=0.1 and R/t=10, to 9× for a/t=0.5 and R/t=50. The best approximation is the bending moment fit to the actual residual stress distribution.

Future work on the methodology presented in this paper can address the following issues:

- The welding simulations in this work are performed on the plane perpendicular to the welding direction. This approach does consider in the residual stress the effects of start and stop of welding. These effects can be investigated by three dimensional simulations.
- The crack driving force is determined here as J-integral which is computed by opening the crack faces at once. If the crack has grown gradually, the crack driving force can be computed by the crack tip opening displacement.
- It has been demonstrated that a bending fit to the residual stress distribution is effective for thin pipes. However, for thick pipes where the through thickness residual stress distribution is more complex, higher order terms may be required for approximate solutions.

6.0 ACKNOWLEDGEMENTS

This project has been sponsored by the Edison Welding Institute (EWI) Cooperative Research Program. The authors would also like to thank Dr. Andrew DeBiccari, EWI, for the discussions and suggestions regarding the REZONE option of ABAQUS, and Dr. YongYi Wang, EWI, for the discussions regarding the evaluation of the crack driving force in the presence of a residual stress field.

7.0 REFERENCES

[1] Vaidyanathan, S., Todaro, A. D., and Finniew, I., "Residual Stresses Due to Circumferential Welds," Journal of Engineering Materials and Technology, Transactions of the ASME, 233-237, 1973.

[2] Fujita, Y., Nomoto, T., and Hasegawa, H., "Method of Thermal Elasto-Plastic Analysis (4th Report)," J.S.N.A. Japan, 146: 164-174, Dec. 1979.

[3] Rybicki, E. F. and Stonisifer, R. B., "Computation of Residual Stresses due to Multipass Welds in Piping Systems," *Journal of Pressure Vessel Technology*, Transactions of the ASME, 101: 149-154, May 1979.

[4] Rybicki, E. F., Stonisifer, R. B., and Olson, R. J. "Stress Intensity Factors due to Residual Stresses in Thin-Walled Girth-Welded Pipes," *Journal of Pressure Vessel Technology*, Transactions of the ASME, 103: 66-75, Feb. 1981.

[5] Finch, D. M. and Burdekin, "Effects of Welding Residual Stresses on Significance of Defects in Various Types of Welded Joint," Engineering Fracture Mechanics, 41(5): 721-735, 1992.

[6]Finch, D. M., "Effects of Welding Residual Stresses on Significance of Defects in Various Types of Welded Joint-II," Engineering Fracture Mechanics, 42(3): 479-500, 1992.

[7] Michaleris, P., "Residual Stress Distributions for Multi-Pass Welds in Pressure Vessel and Piping Components, to be presented at the 1996 PVP conference, ASME, 1996.

[8] Goldak, J., Chakravarti, A., and Bibby, M., "A New Finite Element Model for Welding Heat Sources," Metallurgical Transactions B, 15B:299-305, Jun. 1984.

[9] Das, S., Upadhya, G. Chandra, Kleinosky, M. J., and Tims, M. L., "Finite Element Modeling of a Single-pass GMA Weldment," in Piwonka, T. S., Voller, V., and Katgerman, L., (eds.), Modeling of Casting, Welding and Advanced Solidification Processes VI, 593-600, Palm Coast FL, 1993.

[10] Michaleris, P., Tortorelli, D. A., and Vidal, C. A., "Analysis and Optimization of Weakly Coupled Thermo-Elasto-Plastic Systems with Applications to Weldment Design," *International Journal for Numerical Methods in Engineering*, 38: 1259-1285, 1995.

[11] Buchalet, C. B. and Bamford, W. H., "Stress Intensity Factor Solutions for Continuous Surface Flaws in Reactor Presssure Vessles, " Mechanics of Crack Growth, ASTM STP 590, American Society of Testing and Materials , 1976, pp. 385-402.

[12] Gordon, J.R., Wang, Y.Y., and Dong, P., "The Development of Fitness-For-Purpose Flaw Acceptance Criteria For Sleeve Connections," Proceedings of the *Eighteenth Symposium on Line Pipe Research*, Houston, Texas, Sep. 1993.

Hugo Irizarry-Quiñones[1], Bruce D. Macdonald[1], and Wallace J. McAfee[2]

ANALYSIS OF UNCLAD AND SUB-CLAD SEMI-ELLIPTICAL FLAWS IN PRESSURE VESSEL STEELS

REFERENCE: Irizarry-Quiñones, H., Macdonald, B. D., and McAfee, W.J., "**Analysis of Unclad and Sub-clad Semi-Elliptical Flaws in Pressure Vessel Steels**", Fatigue and Fracture Mechanics: 28th Volume, ASTM STP 1321, J.H. Underwood, B.D. Macdonald, and M.R. Mitchell, Eds., American Society for Testing and Materials, 1997.

ABSTRACT: This study was conducted to support warm prestress experiments on unclad and sub-clad flawed beams loaded in pure bending. Two cladding yield strengths were investigated: 0.6 Sy and 0.8 Sy, where Sy is the yield strength of the base metal. Cladding and base metal were assumed to be stress free at the stress relief temperature for the 3D elastic-plastic finite element analysis. The model results indicated that when cooled from the stress relief temperature tensile residual stresses were generated in the cladding due to its greater coefficient of thermal expansion. The magnitude of the residual stresses depended on the amount of cooling and the strength of the cladding relative to that of the base metal. During loading, the sub-clad flaw elastic-plastic stress intensity factor, $K_I(J)$, was at first dominated by crack closing force due to tensile residual stresses in the cladding. After the cladding residual stress were overcome by the applied bending stresses, $K_I(J)$ gradually increased as if it were an unclad beam. A combination of elastic stress intensity factor solutions was used to approximate the effect of cladding in reducing the crack driving force along the flaw. This approximation was quite in keeping with the 3D elastic-plastic finite element solution for the sub-clad flaw.

Finally, a number of sub-clad flaw specimens not subjected to warm prestressing were thought to have suffered degraded toughness caused by locally intensified strain ageing embrittlement due to welding over the preexisting flaw.

KEYWORDS: Warm prestress, cladding, semi-elliptical flaws, sub-clad flaws, stress intensity factors, cladding residual stresses, locally intensified strain ageing embrittlement

The purpose of this study was to calculate stress intensity factors along the crack front of sub-clad and unclad four-point bend beams to support the interpretation of warm prestress (WPS) experiments. WPS is defined as an experimental observed phenomenon where a flawed component which was pre-loaded at a higher temperature experiences an enhancement of the fracture resistance at lower temperatures [1]. The WPS experiments

1. Lockheed Martin Corporation, PO Box 1072, Schenectady, NY 12309-1072
2. Oak Ridge National Laboratory, PO Box 2009, Oak Ridge, TN 37831-8056

were performed at Oak Ridge National Laboratory for Lockheed Martin Corporation [2]. Appendix A provides a summary of the experiments and a description of the specimens.

This paper describes the analyses performed to model the stress relieving process and the loading to failure. Stress intensity factors were obtained using finite element methods for different clad materials, test temperatures, and applied loads. The stress intensity factors were calculated using both linear-elastic and elastic-plastic fracture mechanics methods. Elastic-plastic fracture mechanics methods were used to model the stress relieving process applied to the WPS specimens after welding but prior to loading.

FINITE ELEMENT MODELING

As explained in Appendix A, the full beam configuration for the unclad WPS test specimens beams was 864 mm long, 102 mm high, and 127 mm wide. The full beam configuration was a composite design in which only the test section was fabricated from pedigreed material. The test section was 76 mm long, 102 mm high, and 127 mm wide. Test sections were taken from an ASTM A508 Class 2 steel pressure vessel cylinder. Reusable extension arms were electron-beam welded to the ends of the test section to form the full beam configuration.

The WPS specimen was modeled using quarter symmetry. Two finite element models were created using the PATRAN preprocessor [3]. Figure 1 shows the resulting unclad WPS specimen finite element model which was 432 mm long, 102 mm high, and 64 mm wide. Figure 2 shows a detail of the resulting clad WPS specimen finite element model which had an additional layer 6 mm thick to simulate the cladding.

The unclad WPS specimen finite element model had 626 elements and 3 188 nodes. The sub-clad WPS specimen finite element model had 922 elements and 4 543 nodes. The cladding was modeled using two planes of elements 3 mm thick each added to the top of

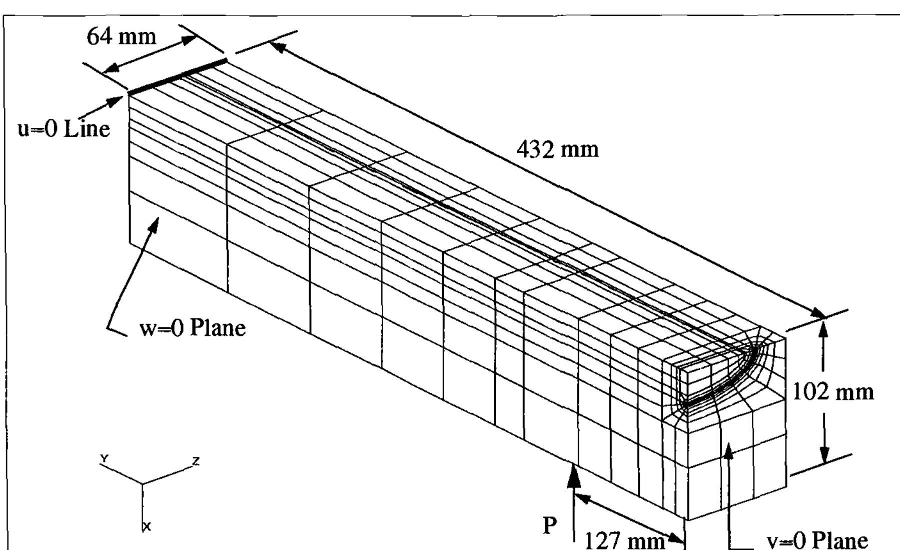

FIGURE 1. Quarter Symmetry Finite Element Model for Unclad WPS Model.

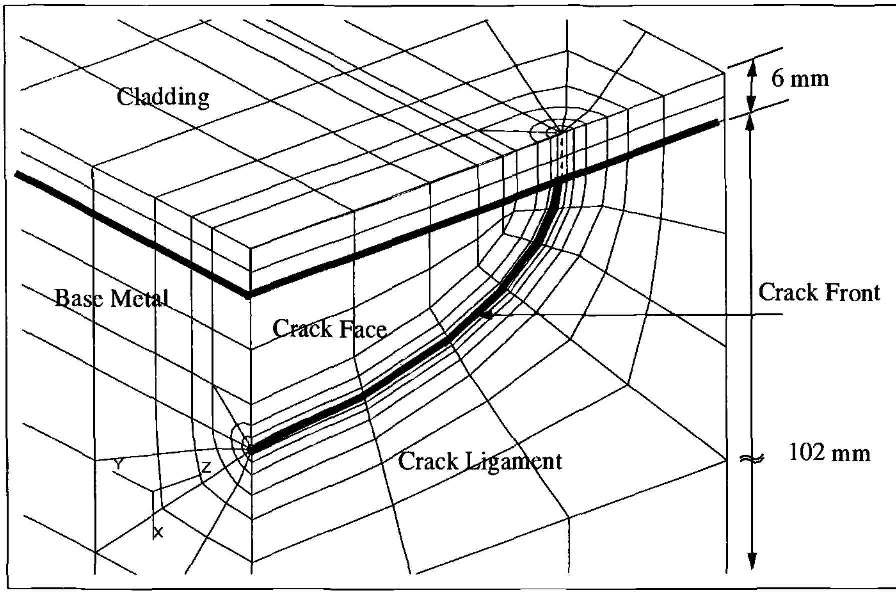

FIGURE 2. Crack Front on Quarter Symmetry Finite Element Model for Clad Model.

the unclad model. The modeled flaw was a semi-elliptical flaw 80 mm long and 21 mm deep. Figure 2 also shows the details of the modeled crack front.

All the elements of the finite element model were 20-noded hexahedron three-dimensional solid elements with the exception of the degenerate hexahedron elements along the crack front. All elements used the 2x2x2 Gaussian integration scheme. The finite element mesh along the crack front was created such that elements had a $1/\sqrt{r}$ singularity (i.e., quarter-point elements). Preliminary analyses using different flaw sizes revealed that the difference between the stress intensity factors obtained with a flaw 21 mm deep and those obtained using a flaw 19 mm deep was less than five percent for the unclad WPS specimens. Hence, the 21mm selected flaw depth was considered appropriate for this analysis since it would provide reasonable stress intensity factors. The flaw region was modelled using six elements along the crack front, four rings of elements around the crack front, and six $1/\sqrt{r}$ singularity elements surrounding the crack tip. A comparison analysis using nine elements along the crack front, six rings of elements around the crack front, and six $1/\sqrt{r}$ singularity elements surrounding the crack tip resulted in less than one percent difference in the stress intensity factors on an unclad WPS finite element model. Consequently the simpler crack front finite element model was used.

To enforce the quarter symmetry of the finite element model, two of the vertical faces had the normal displacements (v and w) set equal to zero. On the flaw plane, including the cladding but not the crack face region, the global Y displacement (v) was set equal to zero. No displacement boundary conditions were imposed on the crack face. Along the beam's length centerline, the global Z displacement (w) was set equal to zero. These faces are labeled v=0 and w=0 in Figure 1. To simulate the four-point beam reaction loads, the finite element model was supported across the top edge, 432 mm from the flaw plane, by setting the global X displacement (u) equal to zero. A point load was applied 127 mm from the flaw plane along the bottom of the finite element model. Constraint equations were used in the finite element analysis program to ensure that the displacements in the global X direction (u) for the nodes along the loading edge were equal to the node displacement where the point load was applied. To simulate the quarter symmetry of the loading, the magnitude of the point load was one-quarter of the actual load applied.

MATERIAL PROPERTIES

The base metal on the WPS test block was modeled using A508 Class 2 low alloy steel properties. With one exception, the cladding was modeled using 3-wire 308-309 stainless steel cladding (SS30X) properties. The remaining analysis was performed using Inconel EN82 cladding properties. Material properties at test temperatures (i.e., −129°C, −18°C, and 149°C) were obtained as part of the WPS test program. Material properties at high temperatures (from 149°C up to 677°C) were obtained from a previously established high temperature material properties database [4]. Table 1 shows the material properties for cladding and base metal used in this analysis. Poisson's ratio, ν, was assumed to be 0.3 for all materials and temperatures.

TABLE 1. Material properties used in finite element analysis.

	SS30X Clad			EN82 Clad			A508 Cl2 Base Metal			
Temp. (C)	Sy (MPa)	E (GPa)	$\alpha_{(mean)}$ (E-06 1/C)	Sy (MPa)	E (GPa)	$\alpha_{(mean)}$ (E-06 1/C)	Sy (MPa)	E (GPa)	$\alpha_{(mean)}$ (E-06 1/C)	Source Ref. #
-129	391	301	18.05	568	284	14.90	710	351	10.94	2
-18	363	279	18.62	447	223	15.40	558	276	11.54	2
149	315	262	19.46	403	201	16.15	503	249	12.44	2
260	197	178	20.03	334	174	16.64	382	189	13.05	4
399	166	167	20.73	320	164	17.27	346	178	13.80	4
538	135	155	21.44	307	154	17.89	310	167	14.55	4
677	103	143	22.14	293	145	18.51	274	157	15.31	4

Figure 3 shows engineering stress-strain curves for the three materials at 149°C. Stress-strain curves at other temperatures followed similar trends.

In this analysis the reference temperature (i.e., stress free temperature) was assumed to be 621°C. This provided the means to obtain an estimate of the residual stresses on the cladding which was judged to be reasonable. Kinematic strain hardening plasticity model was selected to represent the base metal and cladding material responses.

The material properties of the high strength A533 steel extension arms were assumed to be elastic and constant for the proposed temperature range. The Modulus of Elasticity, E, used was 210 MPa. The thermal expansion coefficient, $\alpha_{(mean)}$, was 8.3×10^{-6} °C^{-1}.

To assist the model construction, cladding elements were created on the extension arms. But, since there was no cladding on the extension arms of the WPS specimen, the cladding elements over the extension arms were assumed to be linear-elastic and very flexible; the Modulus of Elasticity used was 7 KPa. No thermal expansion was allowed for these elements.

METHODOLOGY FOR COMPUTING STRESS INTENSITY FACTORS

Since the experiments involved loading, unloading, and reloading, J-integral calculations were valid for only the initial loading. Thereafter, due to changes in the ratios of the principal stresses, the correspondence between deformation theory and flow theory became nonexistent. Consequently, approximations were needed to estimate the crack driving force of the test specimens after unloading occurred.

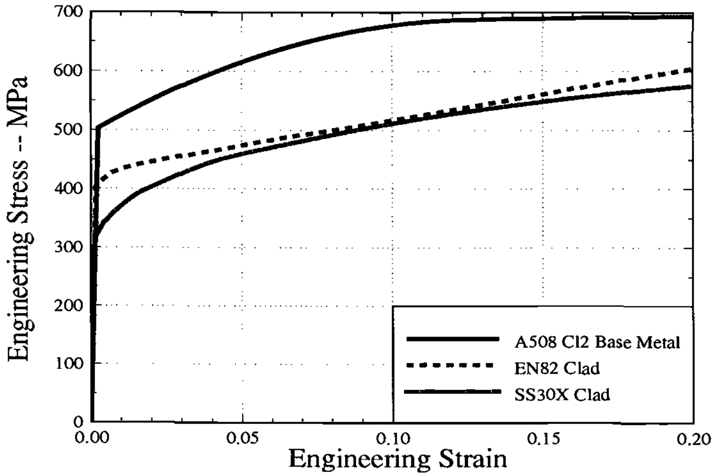

FIGURE 3. Engineering Stress-Strain Curves Used in Finite Element Analysis for Cladding and Base Metal Materials at 149°C.

An in-house linear-elastic fracture mechanics code was used to calculate elastic stress intensity factors, K_I, along the crack front on the WPS finite element model. K_I was calculated using the crack front element gauss point stresses [5]. K_{eff}, the plane strain plastic zone corrected value of K_I [6], was calculated using the following equation:

$$K_{eff} = \frac{K_I}{\sqrt{1 - \frac{K_I^2}{6\pi a S_y^2}}} \tag{1}$$

where a is the flaw depth, and Sy is the yield stress at the WPS temperature.

An in-house elastic-plastic fracture mechanics code was used to calculate the energy release rate, G, along the crack front on the WPS finite element model. G was calculated using the virtual crack extension method [7][8]. G is equivalent to J, provided that path independence is demonstrated [9]. Path independence means that the energy release rate is nearly identical for different paths around the crack tip on a partition. A partition is defined as a surface that is topologically normal to the crack front containing either corner-nodes or mid-nodes of a crack front element. A path is roughly analogous to a J-integral contour around the crack tip. $K_I(J)$, the elastic plastic stress intensity factor was calculated using the following equation:

$$K_I(J) = \sqrt{E'G} = \sqrt{E'J} \tag{2}$$

given that G is path independent, and where

$$E' = \frac{E}{1 - \upsilon^2} \tag{3}$$

for plane strain conditions, where E is the Modulus of Elasticity and ν is Poisson's ratio.

The WPS finite element models used for this analysis had 13 partitions (i.e., six elements) along the crack front. Seven paths were used for partitions passing through corner-nodes and six paths were used for partitions passing through mid-nodes. The energy release rate calculation was performed in a partition-by-partition fashion, with each partition treated as a 2D plane.

WPS EXPERIMENTS

Displacement Matching

Figure 4 shows that the crack mouth opening displacement for the clad and unclad WPS beam experiments matches those obtained from the finite element models. Thus, the modeling efforts were considered to be accurate. The presence of cladding on the WPS model caused a reduction of the crack mouth opening displacements when compared to the unclad model. This suggests a significant cladding benefit.

Unclad Beam Results

Table 2 shows various estimates of the crack driving force for six of the WPS tests.

TABLE 2. Stress intensity factors for several unclad WPS beams.

Spec. ID	WPS Load (kips)	WPS Load (KN)	K_I MPa$\sqrt{m}$	K_{eff} MPa$\sqrt{m}$	$K_I(J)$ MPa$\sqrt{m}$	% Diff. between K_{eff} & $K_I(J)$
U01	148.9	662	87	90	89	-1.6
U02	149.3	664	87	90	89	-1.2
U13	175.1	779	102	108	110	2.5
U17	176.7	786	103	109	112	3.1
U27	192.1	854	112	119	130	9.1
U19	193.3	860	112	120	133	10.6

This table shows minimum and maximum stress intensity factors for three representative WPS load values. These stress intensity factors bound the results of the remaining samples. K_{eff} results were up to 10% lower than the $K_I(J)$; the larger difference occurring at the higher WPS loads. A comparison between the K_I from this analysis and the K_I calculated using the Newman-Raju elastic solution [10] showed good agreement even at the maximum load. Both K_I values were 112 MPa$\sqrt{m}$ at the deepest point of the flaw.

In addition, path independence was demonstrated for this model. Figure 5 shows that, for a given load step and partition, the energy release rate, G, values are nearly identical for two different paths around the crack tip.

Clad Beam Stress Relieving and Cooldown Process

Due to the higher coefficient of linear expansion of the cladding compared to that of the base metal, cooling from the stress relief temperature to room temperature caused residual stresses in the cladding and in the neighboring base metal. The residual stresses were tensile in the cladding and compressive in the neighboring base metal.

At room temperature the thermally induced tensile stresses in the cladding were higher in the SS30X cladding model than in the EN82 cladding model. This was due to the larger

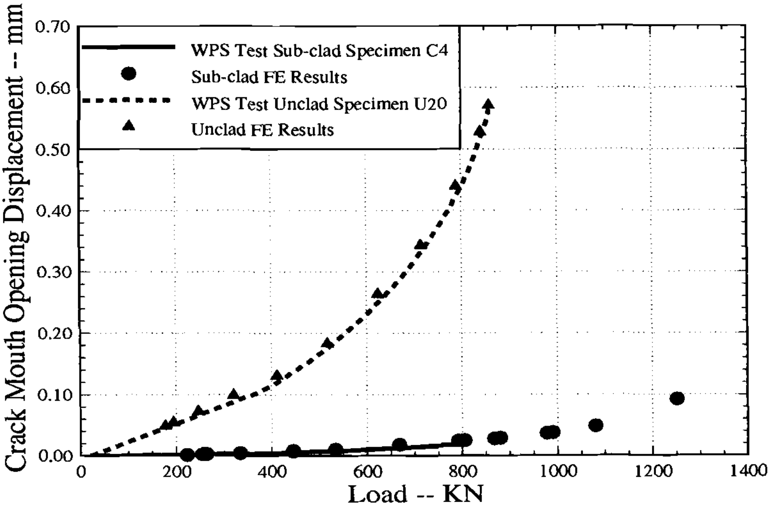

FIGURE 4. Crack Mouth Opening Displacement for Clad and Unclad Tests and Finite Element (FE) Results.

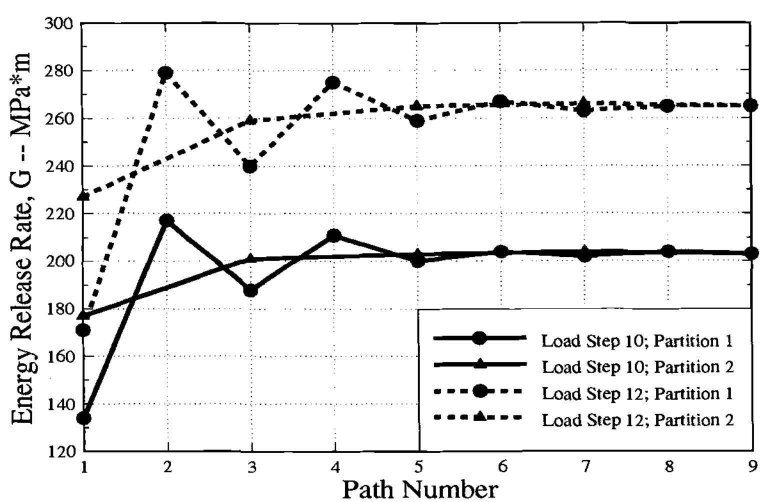

FIGURE 5. Variation of the Energy Release Rate, G, by Path for a Given Partition to Demonstrate Path Independence of G Results on Finite Element Model. (Note: Step 10 and 12 denote increasing load steps used in the analysis.)

coefficient of thermal expansion for the SS30X when compared to the EN82. As a result, the SS30X cladding (which has a yield stress of 328 MPa) yielded almost completely due to cooling following stress relief. On the other hand, the EN82 cladding (which has a yield stress of 430 MPa) yielded only near the free surface. As a consequence of the lower yield strength of the SS30X cladding, the compressive stresses in the neighboring base metal were lower than those associated with the EN82 cladding. Hence the expectation was that the fracture loads would be lowest for the unclad beams, somewhat higher for the SS30X clad beams, and highest for the EN82 clad beams.

Figure 6 shows the effect of cladding residual stresses at the deepest point of the flaw, and the edge of the flaw at the clad-base metal interface. As one might expect, the compressive stresses in the base metal are more significant at the edge of the flaw (dashed line) than at the depth (solid line). This effect diminishes with increasing load.

Effectiveness of Cladding Regarding Crack Driving Force

Figure 7 shows $K_I(J)$ at the deepest point of the flaw as a function of applied WPS load for a surface flaw and its Newman-Raju elastic solution, for the SS30X clad beam, and for the EN82 clad beam at 149°C. The results for the surface flaw serve to verify the modeling and to indicate the extent of the influence of plasticity. When subjected to the applied bending stress, $K_I(J)$ was at first dominated by crack closing force due to tensile residual stresses in the cladding. Upon further loading, the cladding completely yielded in tension and could supply no additional closing force. The cladding ligament causes the initial response to resemble that of a buried defect. The strength of the EN82 cladding was higher than the SS30X, and therefore caused the greatest departure from the surface flaw response as yielding in the cladding became more pronounced.

Figure 8 shows $K_I(J)$ at the deepest point of the flaw as a function of applied load for the SS30X clad model at three different temperatures. These curves show that as temperature decreases and cladding strength increases, the crack driving force is more greatly diminished in a manner similar to that shown in Figure 7.

Next, the responses of the unclad and sub-clad flaws are compared to show how the cladding effect can be modeled with elastic solutions. Figure 9 shows the effect of cladding on the crack driving force as a function of applied load. When the cladding has completely yielded, the sub-clad flaw response becomes offset below the unclad flaw

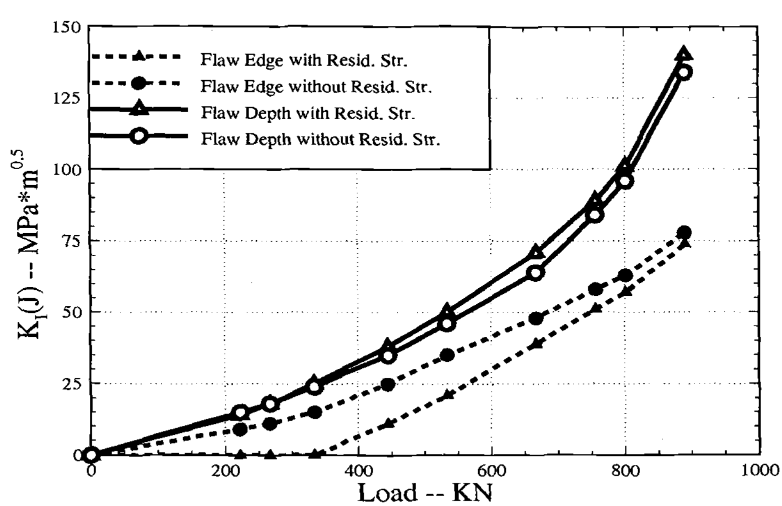

FIGURE 6. Effect of Cladding Residual Stresses on $K_I(J)$ at Depth and Edge of Sub-clad Flaw.

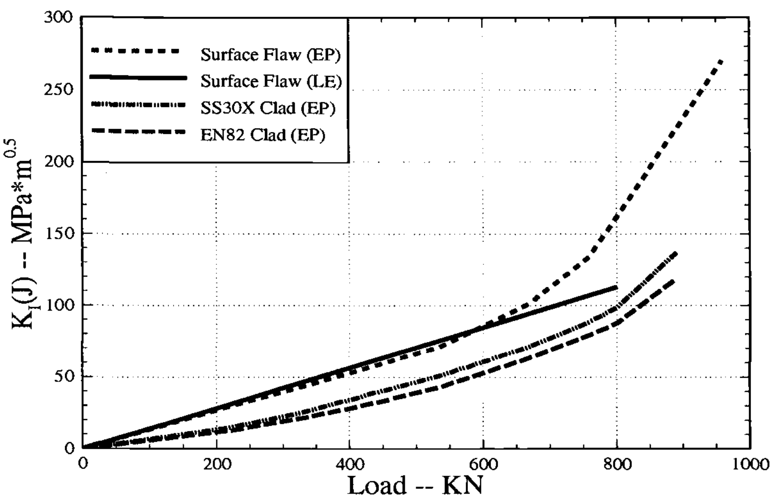

FIGURE 7. Stress Intensity Factors versus Applied Load for Three Clad Conditions (Note: EP = Elastic-Plastic Analysis; LE = Linear Elastic Analysis)

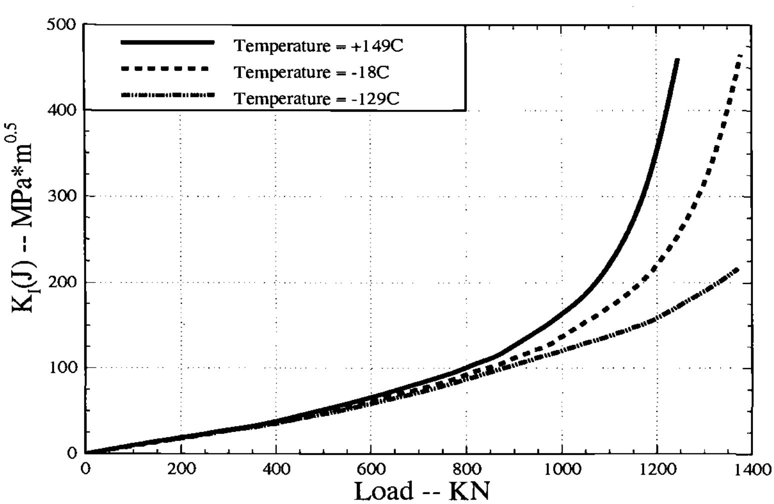

FIGURE 8. Stress Intensity Factors versus Applied Load for SS30X Clad Model at Three Temperatures.

response by a constant value. This suggests that if $K_I(J)$ for the unclad flaw is known, using for example the Newman-Raju elastic solution with a plastic zone correction, $K_I(J)$ for the sub-clad flaw can be obtained by subtracting some crack closure force $K_I(J)$ value due to the presence of the cladding.

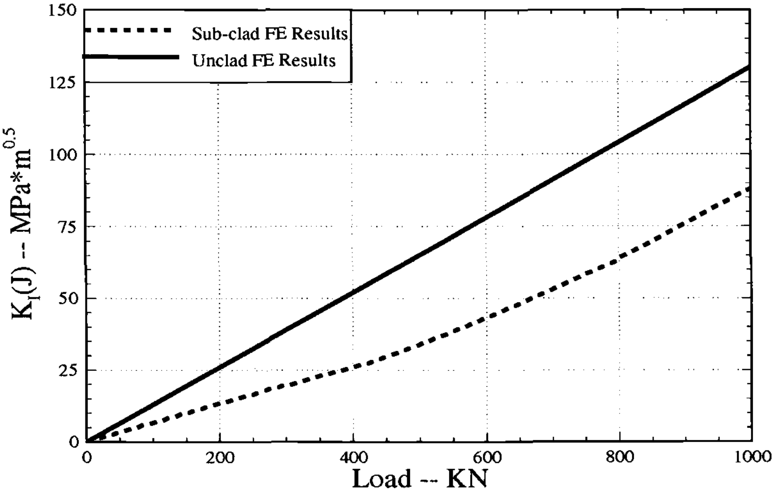

FIGURE 9. Effect of Cladding on Warm Prestress Beam Crack Driving Force From Finite Element (FE) Results.

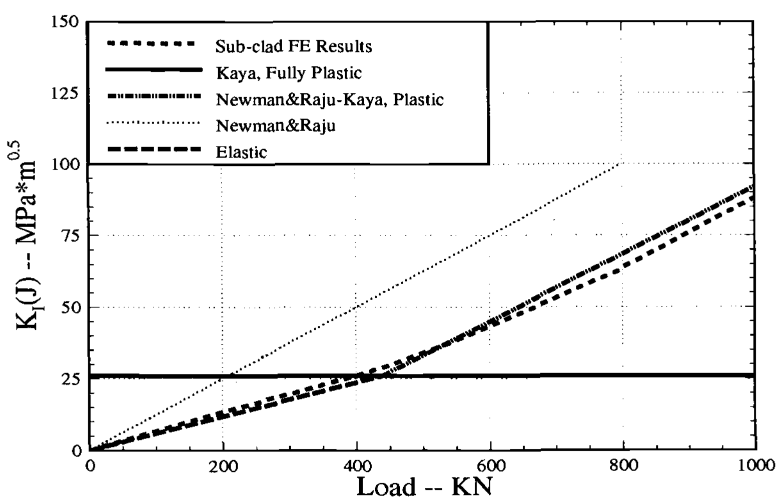

FIGURE 10. Elastic Estimates of the Effects of Cladding on Warm Prestress Beam Crack Driving Force.

Figure 10 shows a combination of elastic solutions that approximate the trends lines from Figure 9. The approximation to the cladding crack closure forces were determined from existing elastic solutions. The Kaya-Erdogan [11] solution for an edge crack loaded by opposing forces at its free edge was used to represent the fully plastic cladding crack closure force estimate. The SS30X yield stress was used to calculate the force for this "fully plastic" estimate. The flaw depth was set equal to that of the surface elliptical flaw. The fully yielded cladding result was obtained by subtracting the "fully plastic" Kaya-Erdogan solution at yield load from the plastic zone corrected Newman-Raju solution for the surface flaw. This estimate was discontinued at the "fully plastic" estimate, and an elastic estimate was obtained by extending a straight line from this point to the origin. Figure 10 suggests that the combination of these solutions provides a reasonable estimate of the elastic-plastic sub-clad flaw response.

LOCALLY INTENSIFIED STRAIN AGEING EMBRITTLEMENT

Mylonas and Rockey [12] and others, and most recently Dawes [13] have commented on the occurrence of abnormally low toughness near welded over notches. Apparently the thermal strains associated with welding are amplified by the presence of the notch at temperatures in the strain ageing regime, resulting in degraded toughness. One of the more dramatic examples of this locally intensified strain ageing embrittlement was the 1943 complete amidships fracture of the new tanker SS Schenectady while tied up at the dock at night in calm weather [13]. On a less grand scale, the manufacturing procedure for the sub-clad flaw specimens provided all the key ingredients for locally intensified strain ageing embrittlement as noted in Appendix A. Figure 11 shows $K_I(J)$ for sub-clad and surface flawed WPS beams tested at -129°C without prior WPS. The variability of $K_I(J)$ for the sub-clad specimens indicates toughness degradation.

The trend lines in Figure 11 are those seen in Figure 9 for sub-clad and unclad flawed beams. Perhaps the most clear indication of locally intensified strain ageing embrittlement is provided by comparing the filled and open circles. The filled circle represents a sub-clad flawed specimen which had the cladding removed prior to testing. The open circles represent surface flaw specimens. The toughness degradation due to welding over the flaw appears to be significant. However, the sparseness of the data for the unclad case precludes their quantitative assessment. The x's represent sub-clad flawed beams with the same

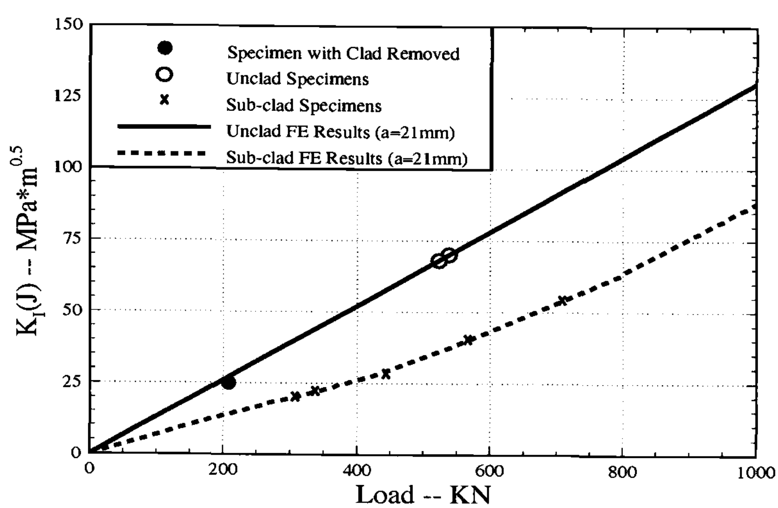

FIGURE 11. Effect of Locally Intensified Strain Aging Embrittlement on Flawed WPS Beams at −129°C Without Prior Warm Prestressing.

nominal flaw size which were expected to carry far more load at failure than their surface flawed counterparts. That was the case in only one instance, and in that case the apparent toughness was still degraded. Data presented by Macdonald, et al. [2] showed that the WPS evolution was effective in removing the toughness distinction between the sub-clad and unclad flawed beams as the sub-clad beams behaved like the unclad beams as long as the cladding remained intact.

COMPARISON WITH OTHER INVESTIGATORS

The conclusions reached in this report are in agreement with those presented by Miyazaki, et al. [14]. Although their work was based in terms of the stress triaxiality near the crack tip, they predicted that a clad material with a higher yield stress enhances the fracture toughness of a base material. Similar behavior was observed for the EN82 cladding model when compared to the SS30X cladding model, and for the −129°C SS30X cladding model when compared to the 149°C SS30X cladding model. In both of these cases the applied stress intensity factor is less for a given load, which would translate to an enhancement of the fracture toughness.

The overall behavior of the structure was well modeled and it follows the prediction by Keeney, et al. [15] (i.e., the effect of the clad material on an underclad flaw is to suppress crack opening). This is also supported by similar work performed by Electricité de France and analyzed by Keeney [16]. Although differences in finite element models, material properties, and boundary conditions prevent a direct comparison of the data and results, the analysis process used in this report agrees with that presented by Keeney.

Other work dealing with sub-clad flawed beams was also reviewed for their potential applicability to this work. Reference 17 included an assessment of cladding effects on finite element cracks due only to a pressurized thermal shock. Although thermal effects were considered in this analysis, they were not the only source of loading. Reference 18 included a 2D analysis used to determine fracture toughness estimates using the η-factor method. In addition, the Reference 18 finite element model was refined enough to provide information about the crack tip stress triaxiality using the J-Q Methodology. Unfortunately the model in this work was intended to generate stress intensity factors only and constraint was not considered. Therefore, direct comparison with Reference 18 is not possible. Finally, Reference 19 included the evaluation of stress intensity factors for semi-elliptical flaws using stress intensity factor influence coefficients. Although a number of models with different geometric ratios were presented, a direct comparison with the finite element model used in this work was not possible. The geometric ratios of the finite element model used in this work were not explicitly presented in Reference 19.

SUMMARY

Three-dimensional elastic-plastic finite element techniques were applied to detailed linear-elastic and elastic-plastic fracture mechanics of WPS experiments using clad and unclad beams in four-point bending. Comparison of crack mouth opening displacements showed good agreement between the experiments and analyses which indicate the adequacy of the finite element models. Comparison of linear-elastic with the Newman-Raju approximation also revealed good agreement. Comparison of K_{eff} and $K_I(J)$ also showed the adequacy of the finite element model and the computational techniques.

CONCLUSIONS

When modeling the stress relieving process, the cooldown to room temperature caused metal contraction which induced tensile residual stresses on the cladding and compressive residual stresses on the neighboring base metal due to a greater coefficient of thermal expansion for the cladding than for the base metal. Larger cooldowns created larger tensile residual stresses on the cladding and the compressive residual stresses on the neighboring base metal. The influence of the residual stresses on the crack driving force diminished as the distance from the clad-base metal interface increased. During loading, $K_I(J)$ increased due to the applied tensile bending stress. At first, however, $K_I(J)$ was dominated by crack closing force due to tensile residual stresses in the cladding. Further loading caused the cladding to yield completely and not supply additional closing force. The trends of $K_I(J)$ versus applied load curves were below the unclad $K_I(J)$ curve, with the EN82 cladding curve the lowest of the two. Similarly, $K_I(J)$ versus load curves as a function of temperature followed the expected trend Lower temperatures experienced reduced $K_I(J)$ values supporting the influence of increased lower yield strength at lower temperatures.

A combination of elastic stress intensity factor solutions was used to approximate the effect of cladding in reducing the crack driving force along the flaw. This approximation was quite in keeping with the 3D elastic-plastic finite element solution for the sub-clad flaw.

Finally, a number of sub-clad flaw specimens not subjected to warm prestressing were thought to have suffered toughness degradation caused by locally intensified strain ageing embrittlement due to welding over the preexisting flaw.

ACKNOWLEDGMENTS

The authors wish to acknowledge the following individuals for their assistance with this work: P.D. Vozzola and W.W. Wilkening for their input to and review of finite element models and techniques used in this analysis; G.T. Embley and P.D. Smith for providing insight into the WPS phenomena; and J.W. Wuthrich for his help with the details of the WPS Test Program.

REFERENCES

1 Chell, G.G., Haigh, J.R., and Vitek, V., "A Theory of Warm Prestressing: Experimental Validation and the Implications for Elastic Plastic Failure Criteria", CERL Report No. RD/L/N 63/79, 1979.

2 Macdonald, B.D., et al., "Analysis of Warm Prestress Data", Fatigue and Fracture Mechanics: 27th Volume, ASTM STP 1296, 1995.

3 PATRAN Version 2.5 and P3 Version 1.4 Users Manual, MacNeal-Schwendler Corporation, PDA Engineering, 1994.

4 Wilkening, W.W. and Snow, J.L., "Analysis of Welding-Induced Residual Stresses with the ADINA System", Computers and Structures, Vol. 47, No. 4/5, 1993, pp 767-786.

5 Irwin, G.R., "Analysis of Stresses and Strains near the End of a Crack Traversing a Plate", Journal of Applied Mechanics, Vol. 24, 1957, pp. 361-364.

6 Irwin, G.R., "Plastic Zone Near a Crack and Fracture Toughness", Sagamore Research Conference Proceedings, Vol. 4, 1961.

7 deLorenzi H.G., "On the Energy Release Rate and the J-Integral of 3-D Crack Configurations", International Journal of Fracture, Vol. 19, 1982, pp. 183-193.

8 deLorenzi H.G., "Energy Release Rate Calculations by the Finite Element Method", Engineering Fracture Mechanics, Vol. 21, 1985, pp.129-143.

9 Rice J.R., "A Path Independent Integral and the Approximate Analysis of Strain Concentrations by Notches and Cracks", Journal of Applied Mechanics, Vol. 35, 1968, pp. 379-386.

10 Newman, J.C. and Raju, I.S., "Analysis of Surface Cracks in Finite Plates Under Tension or Bending Loads", NASA Technical Paper 1578, December 1979.

11 Tada, H., Paris, P. C., and Irwin, G.R., The Stress Analysis of Cracks Handbook, 2nd Edition, Paris Production Incorporated (and Del Research Corporation), 1985, pp. 2.25.

12 Mylonas, C., and Rockey, K.C., "Exhaustion of Ductility by Hot Straining —An Explanation of Fracture Initiation Close to Welds", Welding Journal, Vol.40, No. 7, Research Supplement, 1961, pp 306s-310s.

13 Dawes, M.G., "Significance of Locally Intensified Strain Ageing to the Fracture Toughness of Welded Steel Structures", Fracture Mechanics, 26th Volume, ASTM STP 1256, 1995.

14 Miyazaki, N., Ikeda, T., and Ochi, K., "Constraint Effects of Clad on Underclad Crack", Fatigue and Fracture Mechanics in Pressure Vessel and Piping, PVP-Vol. 304, ASME, 1995, pp. 313-318.

15 Keeney, J.A., Bass, B.R., and Pennell, W.E., "Evaluation of the Effects of Irradiated Cladding on the Behavior of Shallow Flaws Subjected to Pressurized Thermal Shock Loading", Transactions of the 11th International Conference on Structural Mechanics in Reactor Technology, Vol. G, 1991, pp. 195-200.

16 Keeney, J.A., "Cleavage Fracture Analysis of the French Clad Beam Experiments", ORNL/NRC/LTR-94/24, Oak Ridge National Laboratory, October 1994.

17 Keeney, J.A., Bass, B.R., Sievers, J., and Xiaoming, L., "Analysis of a Pressurized Thermal Shock Experiment for Assessing Cladding Effects on Finite Element Cracks", Fatigue, Flaw Evaluation and Leak Before Break Assessments, PVP-Vol. 280, ASME, 1994, pp. 45-50.

18 Keeney, J.A., Bass, B.R., and McAfee, W.J., "Fracture Analysis of Full Thickness Clad Beams Specimens", Fatigue and Fracture Mechanics: 27th Volume, ASTM STP 1296, 1995.

19 Keeney, J.A. and Bryson, J.W., "Stress Intensity Factor Influence Coefficients for Semielliptical Inner Surface Flaws in Clad Pressure Vessels", Fracture Mechanics: 26th Volume, ASTM STP 1256, 1995.

Appendix A

SUMMARY OF KAPL/ORNL WARM PRESTRESSING EXPERIMENTS

Introduction

The unclad warm-prestress (WPS) experimental program consisted of a total of 38 tests in two groups. The first group was a control matrix of 6 specimens tested under isothermal conditions at three different temperatures, −129°C, −73°C, and −18°C. These tests were conducted to provide a baseline for evaluation of the fracture toughness. The second group, the WPS tests, consisted of 32 tests. Three types of WPS load/temperature scenarios were used. These are shown schematically in Figure A1 and were defined as Load-Unload-Cool-Fracture (LUCF), Load-Cool-Unload-Fracture (LCUF), and Load-Linear Cool and Unload-Fracture (LIN).Data for the unclad WPS tests is shown in Table A1.

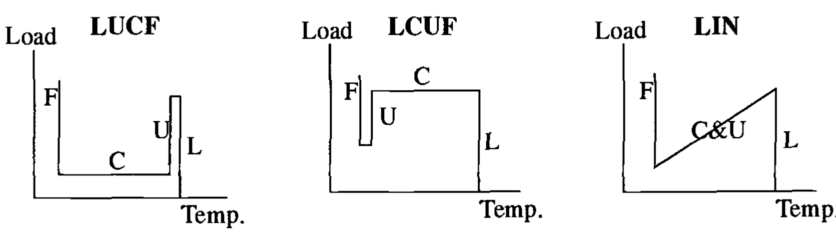

FIGURE A1. WPS Load/Temperature Scenarios.

TABLE A1. WPS test matrix and results for unclad flawed beams.

Specimen	WPS Load (kips)[a]	Minimum Load (kips)[a]	Fracture Temp. (°F)[b]	Fracture Load (kips)[a]
		Load - Unload - Cool - Fracture		
U01	148.9	37.5	−200	161.4
U29	175.8	115.4	−200	195.1
U22	192.6	78.7	−200	222.2
U08	150.4	115.9	−100	183.1
U14	176.1	78.3	−100	219.9
U20	193.0	39.7	−100	228.8
U06	150.4	78.5	0	252.8
U12	176.2	40.1	0	236.3
U27	192.1	115.4	0	231.7

TABLE A1. WPS test matrix and results for unclad flawed beams.

Specimen	WPS Load (kips)[a]	Minimum Load (kips)[a]	Fracture Temp. (°F)[b]	Fracture Load (kips)[a]
		Load - Cool - Unload - Fracture		
U07	150.2	115.4	−200	171.9
U13	175.1	79.1	−200	212.3
U19	193.3	38.8	−200	216.8
U05	149.5	77.9	−100	175.2
U11	175.9	39.0	−100	208.8
U26	193.2	114.8	−100	237.5
U03	157.0	39.0	0	224.0
U18	175.6	114.8	0	206.1
U24	192.5	78.4	0	221.5
		Load - Linearly Cool and Unload - Fracture		
U04	149.1	78.9	−200	172.7
U10	176.1	40.4	−200	161.2
U25	193.1	114.9	−200	231.9
U02	149.3	39.5	−100	200.0
U17	176.7	114.4	−100	207.3
U23	193.0	76.4	−100	217.7
U09	149.7	115.8	0	173.4
U15	175.9	77.5	0	224.7
U28	192.4	37.5	0	217.1

a. 1 kip = 1000 lbf; 1 lbf = 4.448 N
b. °C = (°F-32)/1.8

The sub-clad WPS experimental program consisted of a total of 8 tests. WPS beams with sub-clad flaws were similarly tested with similar load/temperature scenarios. The data is shown in Table A2.

TABLE A2. WPS test matrix and results for sub-clad flawed beams.

Specimen	WPS Load (kips)[a]	Minimum Load (kips)[a]	Fracture Temp. (°F)[b]	Fracture Load (kips)[a]
		Load - Unload -Cool - Fracture		
C2	178.0	59.0	0	242.8
C4	180.0	120.0	0	281.4
C1	179.0	58.0	−200	193.3
C3	179.0	120.0	−200	220.6
		Load - Cool - Unload - Fracture		
C6	181.0	57.0	0	222.4
C8	181.0	120.0	0	219.8
C5	180.0	60.0	−200	228.4
C7	180.0	120.0	−200	224.6

a. 1 kip = 1000 lbf; 1 lbf = 4.448 N
b. °C = (°F-32)/1.8

Specimen Fabrication

The unclad test specimens were beams 864 mm long, 102 mm high, and 127 mm wide. They were of a composite design in which only the test section was fabricated from pedigreed material. The dimensions and general layout of the test sections are shown in Figure A2. Blanks for the test sections were taken from an ASTM A508 Class 2 steel pressure vessel cylinder.

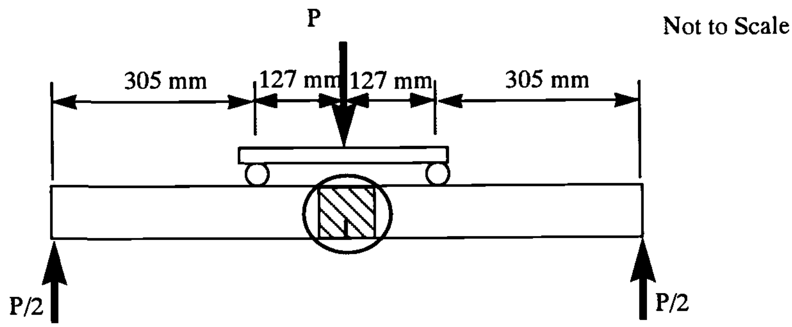

FIGURE A2. Schematic of WPS Test Beams

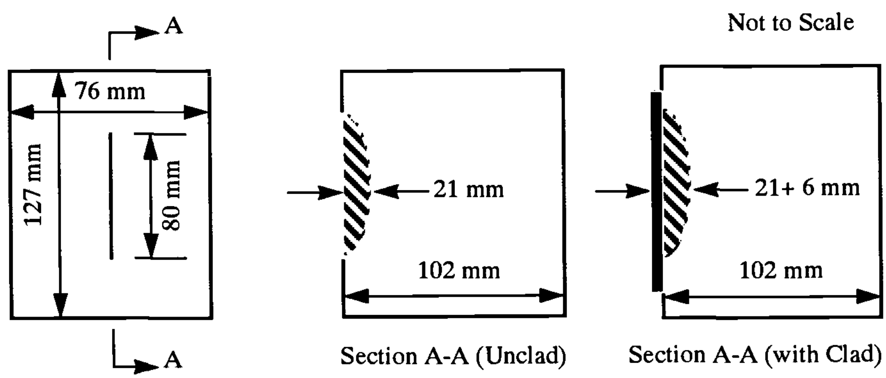

FIGURE A3. WPS Test Sections Schematic for Unclad and Sub-clad Beams

The unclad blanks were machined into test sections with final dimensions as shown in Figure A3. The flaw was ram electron discharge machined into the top surface of the test section in the shape of a semi-ellipse 76 mm long and 19 mm deep prior to fatigue pre-cracking. After machining, the test sections were post-weld-heat-treated in Argon at 621°C for 30 hours. This heat treatment was added to simulate the processing environment of the later sub-clad beams. Reusable A533 steel beam extension arms were electron-beam welded to the ends of the test section to form the full beam configuration. After electron beam welding the extension arms onto the test section, final machining was performed to remove the electron beam weld buildup.

The clad specimens were of the same geometry as the unclad with the exception of an additional 6 mm layer of cladding which was deposited after fatigue pre-cracking. The cladding was a either 3-wire 308-309 stainless steel (SS30X) or Inconel EN82 weld deposit.

Instrumentation

Each beam was instrumented to measure crack mouth-opening-displacement, surface strain, and temperature. Stroke, or test machine actuator movement, was measured through the test machine controller to obtain an indication of load-line displacement for the beam. On the isothermal tests, a linearly variable differential transducer was mounted to measure the load line displacement directly. However, for the WPS tests, the entire beam was fully enclosed in an environmental chamber, so direct measurements of load line displacement could not be made. The clad beams included additional instrumentation to track cladding deformation.

Temperatures were measured using contact thermocouples. Eight thermocouples were mounted on the surface of the test section. An additional thermocouple was inserted into the center of the test section through a side hole. This thermocouple made contact with the material near the center of the block and was used for control of the experiment.

Test Procedure

The procedures contained in ASTM Standard Test Method for Plane-Strain Fracture Toughness of Metallic Materials (E 399) were used as guidelines for these tests, although they do not apply explicitly to the semi-elliptic flaw configuration. After the specimen was instrumented, it was mounted in a four-point bend test fixture, as shown schematically in Figure A2. The specimens were fatigue precracked at room temperature using change-in-compliance measurements to determine the amount of crack growth. Development tests were performed to establish the final test procedures to yield about 2 mm of crack growth needed to obtain a final flaw about 80 mm long and 21 mm deep. As noted earlier, the 6 mm layer of cladding was deposited after fatigue pre-cracking the clad beams.

After fatigue pre-cracking, in situ instrumentation checks were performed, and the specimen was prepared for the fracture portion of the test. For the control matrix tests, the specimen was cooled to the test temperature and held for a minimum of 20 minutes to establish isothermal conditions in the test section. The specimen was then loaded to failure.

The WPS tests varied from this procedure because of additional equipment requirements. After fatigue pre-cracking, electric heaters were mounted on the specimen, a liquid nitrogen manifold was installed, and an environmental chamber that completely enclosed the specimen was put in place. The specimen was aligned and pre-loaded to 22-kN. Holding the load constant, the specimen was heated to the WPS temperature of 149°C. For a Load-Unload-Cool-Fracture test, a stable WPS temperature was established and the specified load-unload cycle was applied at a rate of 0.003 Hz using a test machine generated displacement haversine function. Using load-control, the specimen was cooled to the fracture temperature, and the load increased until fracture occurred. For a Load-Cool-Unload-Fracture test, the specimen was loaded using a load-control ramp function. The load was held constant during cool-down to the fracture temperature. The load was then lowered to the pre-load value, and the load increased until fracture occurred. For the Load-Linear Cool and Unload-Fracture test, the WPS and failure sequences of the test were the same as for the Load-Cool-Unload-Fracture. However, the Load-Linear Cool and Unload-Fracture test utilized a controller that maintained a linear relationship between the specimen temperature change and the applied load change.

Fracture Analysis

Pauline H. Davies[1]

PREDICTING CRACK INSTABILITY BEHAVIOUR OF BURST TESTS FROM SMALL SPECIMENS FOR IRRADIATED Zr-2.5Nb PRESSURE TUBES

REFERENCE: Davies, P.H., "**Predicting Crack Instability Behaviour of Burst Tests from Small Specimens for Irradiated Zr-2.5Nb Pressure Tubes,**" Fatigue and Fracture Mechanics: 28th Volume, ASTM STP 1321, J.H. Underwood, B.D. Macdonald, and M.R. Mitchell, Eds., American Society for Testing and Materials, 1997.

ABSTRACT: A scaling approach, based on the deformation J-integral at maximum load obtained from small specimens, is proposed for predicting the crack instability behaviour of burst tests on irradiated Zr-2.5Nb pressure tubes. An assessment of this approach is carried out by comparison with other toughness criteria such as the modified J-integral and the plastic work dissipation rate approach. The largest discrepancy between the different parameters occurs for materials of intermediate toughness which exhibit the most stable crack growth and tunnelling up to maximum load. A study of one material of intermediate toughness suggests crack-front tunnelling has a significant influence on the results obtained from the 17-mm-wide specimens. It is shown that for a tube of intermediate toughness the different approaches can significantly underpredict the extent of stable crack growth before instability in a burst test even after correcting for tunnelling. The usefulness of a scaling approach in reducing the discrepancy between the small- and large-scale specimen results for this material is demonstrated.

KEY WORDS: Fracture toughness, Zr-2.5Nb, pressure tubes, crack growth resistance (J-R) curve, constraint, geometry effects, burst test, crack-front tunnelling.

The determination of the critical crack length (CCL) of a CANDU®[2] reactor pressure tube is an important element in establishing the flaw tolerance of the primary containment vessel and in establishing the ability of such a tube to leak rather than break, i.e. to meet the leak-before-break criterion [1]. Values of the CCL of such tubes (nominally 6.3 m long, 103 mm diameter and 4.2 mm thick) may be determined from burst tests on 500 mm long tube sections of irradiated pressure tube material [2-4]. However, estimates of CCL may also be obtained from small (17-mm-wide curved compact) specimens machined directly from the tube material [5,6], these specimens generally producing conservative results [3]. Recently there has been considerable interest in obtaining more realistic estimates of CCL from the small specimens with a view to applying a probabilistic approach to leak-before-break for an entire reactor core of tubes, each of which may exhibit significant tube-to-tube variability in toughness.

[1] Research Scientist, AECL, Chalk River Laboratories, Chalk River, Ontario, Canada, K0J 1J0.
[2] ®CANDU: CANada Deuterium Uranium; registered trademark.

In previous work [7] an experimental programme was undertaken to study the relationship between the toughness (CCL) derived from the two different specimen configurations using material from irradiated Zr-2.5Nb pressure tubes removed from the Pickering Nuclear Generating Station (PNGS) A Unit 3 and 4 reactors after 18 years operation and irradiation to a fast neutron fluence of 1 x 10^{26} $n \cdot m^{-2}$ (E > 1 MeV). Such material is known to exhibit a wide variation in toughness due to variations in the chlorine, carbon and phosphorus concentrations of the source ingots [8-10]. Crack growth resistance or deformation J-R (J-integral versus crack extension) curves were obtained in the operating temperature regime (250°C) using the d.c. potential drop method to measure stable crack growth. In this previous study, emphasis was placed on establishing the failure mechanism of the material by means of detailed fractographic studies. By applying scaling factors based on a volume-controlled fracture model for bend-type specimens, good agreement was obtained between scaled values of the maximum-pressure/load toughness derived from the two different specimen configurations.

The current work updates the previous study and then extends it by investigating the validity of applying scaling factors to the deformation J-integral in the light of other toughness criteria such as the modified J-integral approach of Ernst [11] and the plastic work dissipation approach of Turner [12,13]. The scaling approach is assessed by comparing the different J-type parameters from the small specimens. The largest discrepancy between the parameters occurs for materials of intermediate toughness which exhibit the most stable crack growth and crack-front tunnelling. An assessment of tunnelling on the results for one material of intermediate toughness suggest such effects can have a significant influence on the toughness obtained from the 17-mm-wide specimens. Finally, the relative usefulness of the different approaches is studied using the corresponding R-curves to predict the crack growth behaviour of a burst test conducted on the same material of intermediate toughness.

TOUGHNESS RESULTS FROM SMALL- AND LARGE-SCALE SPECIMENS

A review and update of recent work [7] on the link between toughness results from the small- and large-scale specimens is given as a necessary background to the current study. The review includes test results on three additional tubes of high toughness (P4J17, P4N07, P4C17) not reported in the earlier paper.

Material

Table 1 summarises the different full length tubes of irradiated Zr-2.5Nb pressure tube material used in the study. All tubes were fabricated in the late 1960's as standard cold-worked (about 26%), Zr-2.5Nb pressure tubes and operated for about 18 years in PNGS A Units 3 and 4. Such tubes can exhibit significant variability in toughness due to the presence of microsegregated species (Zr-Cl-C complex) and particles (carbides and phosphides) [8-10]. The eighteen tubes showed a wide variation in toughness principally as a result of variations in the chlorine and phosphorus concentrations (Table 1). Six of the tubes (from fuel channels P4J17, P4L17, P3R13, P4N07, P4Q17, and P4C17, respectively) were fabricated from ingots with a very low concentration of chlorine

(< 1 wt ppm). These tubes all exhibited high toughness. The fast-neutron fluence of the tube sections used for the mechanical tests varied from 9.0 to 11.1 x 10^{25} n·m^{-2} and the irradiation temperature varied from 257 to 279°C. All tests were conducted at the same test temperature of 250°C (lowest irradiation temperature for PNGS A tubes) to avoid annealing out any irradiation damage. Finally, the maximum total equivalent hydrogen concentration (hydrogen + 0.5 deuterium concentration in wt fraction) of the tube sections was sufficiently low such that the hydrogen isotopes would have been in solution during testing at 250°C.

TABLE 1--*Chemical analysis results of PNGS A Unit 3 and 4 tubes used in study.*

Fuel Channel	Tube ID	Ingot	Cl ppm	P ppm
P3M11	98	375195	10/8/10	15/12/13
P3J17	544	377088	8	15
P3K05	7	374951	9	20
P3M12	256	375790	8	34
P3L03	95	375195	10	15
P3O07	258	375790	8	34
P3M03	65	375044	12/8[a]	20/19[a]
P3H07	1963	390597	6	13
P3M09	119	375392	10/9[a]	12/11[a]
P3N07	92	375583	10/9[a]	30/26[a]
P3S13	682	377607	5/4[a]	19/18[a]
P3N08	323	376210	0.9	57
P4J17	774	377884[b]	<0.1	41
P4L17	491	376914[b]	0.2/0.16[a]	57/39[a]
P3R13	566	377325[b]	0.4	42
P4Q17	508	376914[b]	0.1/0.2[a]	57/13.5[a]
P4C17	226	375506[b]	0.6	12
P4N07	A	UGINE[c]	0.8	2

All ingots fabricated by Teledyne Wah Chang, Albany unless stated otherwise.
[a] Repeat analysis
[b] Ingot fabricated from 100% recycled material, i.e. chlorine concentration < 1 wt ppm
[c] Ingot fabricated by Ugine, % recycled material unknown.

Large-Scale Specimen Tests

Standard burst tests were carried out on 500 mm long sections of tube using a through-wall, axial crack about 55 mm long (after fatigue precracking) sealed with a patch. After fatigue precracking by pressure cycling at the hot cell temperature (about 25 to 30°C) using water, each section was heated to 250°C, soaked at the test temperature for one hour and then pressurised monotonically to failure with argon gas at a rate corresponding to an initial rate of increase of the stress intensity factor of about 0.75 MPa$\sqrt{m}$·s^{-1}. The d.c. potential drop method was used to monitor any stable crack growth during testing. The current and voltage lead positions were such as to produce a linear relationship between the change in voltage and change in crack length based on standard calibration notches. However, it was not possible to calibrate the crack extension behaviour of the materials of different toughness on an individual basis as in the case of the small specimens (see next section). Further experimental details, as well as a photograph of the experimental equipment in-cell, are provided elsewhere [7].

The Dugdale strip yield equation for an axial, through-wall defect in a pressurised tube was used to calculate a crack growth resistance (J-R) curve in each case [14]:

$$J = \frac{K_I^2}{E} = \frac{8}{\pi}\frac{\sigma_f^2}{E} a \ln\left[\sec\left(\frac{\pi}{2}\frac{M \cdot \sigma_h}{\sigma_f}\right)\right] \tag{1}$$

where: σ_f = flow stress (mean of the yield stress and ultimate tensile strength),
E = Young's modulus,
2a = total crack length,
σ_h = hoop stress, $p \cdot r_i/t$,
p = internal pressure,
r_i = internal radius,
t = wall thickness, and
M = Folias bulging correction factor [15], given approximately by [14]:
M = $\sqrt{[1 + 1.255(a^2/(r_m \cdot t)) - 0.0135(a^4/(r_m \cdot t)^2)]}$, where r_m is the mean radius.

Finite element analyses support the use of this equation for calculating the fracture toughness for hoop stresses up to approximately 70 to 80% of the plastic collapse level [16].

Small-Scale Specimen Tests

After a burst test two curved compact specimens and two transverse tensile specimens were machined from each section for testing at 250°C. The latter were enlarged-end specimens machined from pressure tube blanks with a parallel length of 10 mm and a rectangular cross-section with a width (axial direction) of 4 mm and a final thickness (radial direction) of 2 mm. The 17-mm-wide curved compact specimens were spark-machined directly from the tube sections using a cookie cutter electrode, with each specimen oriented for crack growth in the axial direction on the radial-axial plane [5,6]. The tests were conducted following the standard method for fracture toughness testing of CANDU reactor pressure tubes [6]. Each specimen was fatigue precracked at a low level of stress intensity factor to produce an initial relative crack length, a_o/W, of 0.5. Specimens were then heated to the test temperature in an air furnace and loaded in stroke control at a constant displacement rate of 0.5 $mm \cdot min^{-1}$ corresponding to an initial rate of increase of stress intensity factor of about 1 $MPa\sqrt{m} \cdot s^{-1}$. The d.c. potential drop method was used to monitor any stable crack growth, with each test terminated after about 3 to 4 mm of crack growth to achieve a final relative crack length, $a_f/W \leq 0.75$. Finally the specimens were partially unloaded and heat tinted to mark the crack extension zone before breaking open. The measured crack extension was then used to calibrate the potential drop method on an individual basis by matching to the change in voltage signal, previous work having shown an approximate linear relationship between the voltage and crack length over the crack size range of interest, a/W of 0.5 to 0.75 [6]. Finally, the J-R curves were calculated following the procedures in [6] which uses the equation for a standard compact specimen recommended in the ASTM Standard Test Method for Determining J-R Curves (E 1152).

Results

Pressure versus crack extension and J-R curves showing the range in results obtained for the different tube materials are shown in Figures 1 and 2. Although the current tests used a standard initial crack size of about 55 mm, previous burst test results from tube sections with different starting crack sizes (30 to 80 mm) indicated little effect of initial crack length on the J-R curves for material from a tube of low toughness (P3L03) or from a tube of intermediate toughness (P3N08) [7]. A similar crack-size-effect study remains to be performed on material from a tube of high toughness.

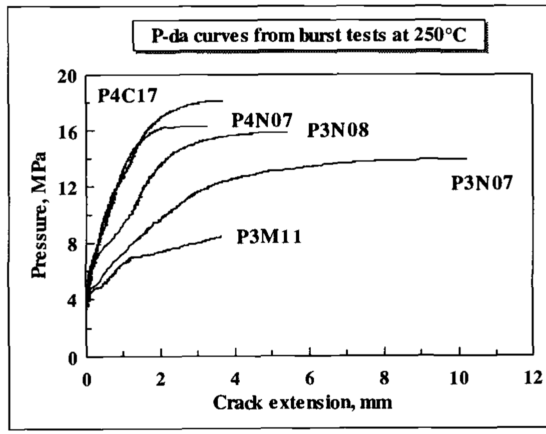

FIGURE 1--*Pressure versus crack extension curves for burst test specimens of different toughness (250°C).*

Key experimental results are listed in Table 2, including the transverse flow stress, the maximum-pressure toughness based on the instantaneous crack size, J_{mpi}, from each burst test and the average maximum-load toughness, J_{ml}, from the two small specimens. Compared with the previous work [7], the current results include those from three additional tubes of high toughness P4J17, P4N07 and P4C17.

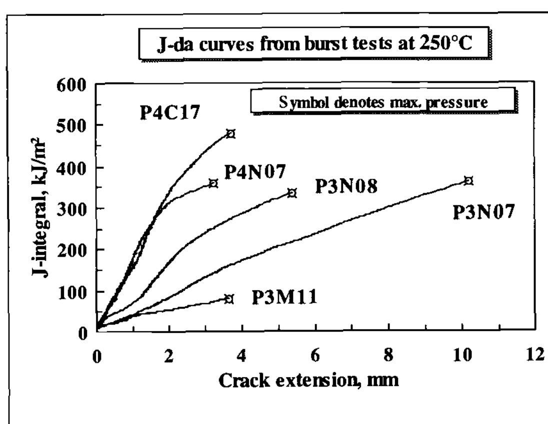

FIGURE 2--*Crack growth resistance (J-R) curves for burst test specimens of different toughness (250°C).*

The irradiated, cold-worked Zr-2.5Nb material has a high transverse tensile strength, in the range of 770 to 900 MPa at 250°C (Table 2), and the low work-hardening rate of this material results in simliar values for the 0.2% offset yield stress, flow stress and the ultimate tensile strength. Table 2 reveals that the normalised burst stress, σ_{mp}/σ_{plc} of the different tubes varied from 0.30 (lowest toughness tube P3M11) to 0.72 (highest toughness tube P4C17), i.e. the maximum burst stress was generally less than 70% of the plastic collapse stress. This supports the use of the small-scale yielding equation based on the Dugdale strip yield model (equation 1) for the analysis of the burst test results.

TABLE 2--*Summary of results from burst test and curved compact specimens tested at 250°C.*

Tube ID	σ_f	Burst Tests			Curved Compact Specimens		
		Δa_{mp}[a]	σ_{mp}[b]$/\sigma_{plc}$[c]	J_{mpi}	Δa_{ml}[d]	p_{ml}/p_{ll}[e]	J_{ml}
	MPa	mm		kJ·m^{-2}	mm	pl. stress	kJ·m^{-2}
P3M11	896	3.65	0.301	80.5	1.03	0.595	24.5
P3J17	886	3.82	0.331	97.2	1.38	0.747	40.1
P3K05	843	9.00	0.446	186	1.49	0.843	46.0
P3M12	876	11.7	0.460	239	1.91	0.944	48.6
P3L03	870	5.96	0.424	159	1.63	0.786	39.2
P3O07	881	6.51	0.433	181	1.27	0.654	36.2
P3M03	827	9.39	0.469	220	1.51	0.916	51.0
P3H07	794	9.88	0.512	244	1.24	0.895	55.8
P3M09	735	7.44	0.546	231	1.65	1.031	56.8
P3N07	847	10.2	0.583	363	1.64	0.887	46.8
P3S13	771	6.75	0.647	361	1.25	1.008	66.2
P3N08	862	5.40	0.599	336	1.07	0.950	84.8
P4J17	863	5.17	0.618	389	1.01	0.990	99.8
P4L17	867	5.38	0.626	398	0.716	1.020	103
P3R13	840	3.94	0.617	353	0.830	1.007	88.5
P4N07	823	3.24	0.642	361	0.601	1.055	130
P4Q17	852	3.99	0.671	458	0.619	1.113	156
P4C17	814	3.72	0.715	480	0.603	1.280	169

[a] Δa_{mp} = average stable crack growth per crack tip at maximum pressure
[b] σ_{mp} = hoop stress at maximum pressure
[c] σ_{plc} = hoop stress at plastic collapse based on instantaneous crack size at maximum pressure, i.e. $\sigma_{plc} = \sigma_f/M$
[d] Δa_{ml} = crack extension at maximum load
[e] p_{ml}/p_{ll} = maximum load/limit load based on instantaneous crack size.

In contrast, the normalised maximum load, p_{ml}/p_{ll}, for the small specimens varied from 0.60 (P3M11) to 1.28 (P4C17) based on the plane-stress limit-load. (Use of the plane-strain limit load would reduce these values by about 14%). Thus, the small specimens of highest toughness failed at or beyond the estimated limit load. In fact, the cracking behaviour of the small specimens from the tube of highest toughness (P4C17) loaded to the highest load levels was unusual, with evidence of significant load drops after about 1.5 mm stable crack growth, resulting in premature termination of the test after about 2.5 mm crack growth. This has been associated with the initiation of secondary shear cracks from the compressive zone at the back face of the specimen, with crack growth on planes at 45° to the radial-axial and transverse-axial planes [17]. Such load drops result in a discontinuous increase in the slope of the J-R curve due to the large reduction in elastic displacement which more than offsets any reduction in J due to crack extension. Since such J-R curves have a potential for producing non-conservative estimates of toughness, the results for these two specimens were corrected, as indicated in Figure 6 later. (No correction was made to the crack extension measurements since after matching the total change in potential drop voltage to the final measured crack extension, the resulting calibration factor was very similar to that obtained for small specimens from other high toughness tubes P4N07 and P4Q17).

A comparison of the J-R curves obtained from the corresponding matched sets of burst and compact specimen tests are given in Figures 3 to 6. Here the changing pattern of agreement between the J-R curves from the two different specimen configurations is revealed as follows:

a) for tubes of low to intermediate toughness (P3M11 to P3H07), the small-specimen J-R curves are generally well below those from the burst tests with little or no agreement over any significant range of crack extension (see Figure 3 for P3M11),
b) for tubes of intermediate to higher toughness (P3M09 to P3R13), the small-specimen J-R curves remain below those from the burst tests but there is increasing agreement over a limited initial crack extension range of about 1 to 1.5 mm (see Figure 4 for P3N08),
c) for tubes of high toughness (P4Q17 and P4N07), the agreement between the J-R curves from the two different specimen configurations is excellent over the majority of the crack extension range of

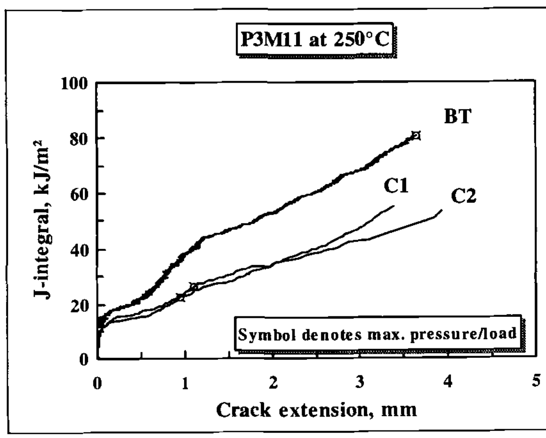

FIGURE 3--*Comparison of J-R curves from burst test and curved compact specimens (lowest-toughness tube P3M11, 250°C).*

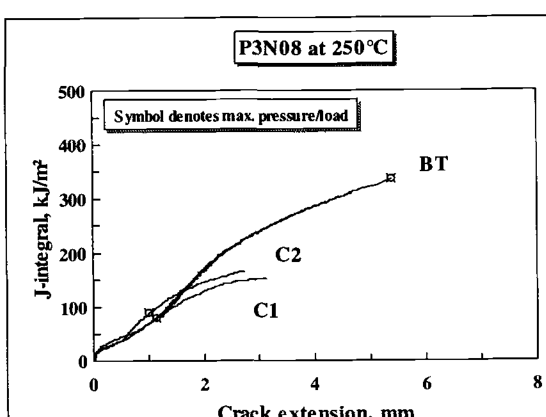

Figure 4--*Comparison of J-R curves from burst test and curved compact specimens (intermediate-toughness tube P3N08, 250°C).*

2.5 to 3 mm (see Figure 8 in [7] for P4Q17 and Figure 5 here for P4N07), and

d) for the tube of highest toughness (P4C17), the small-specimen J-R curves are higher than that of the burst test over the limited crack extension range of these specimens of about 2.5 mm (see Figure 6).

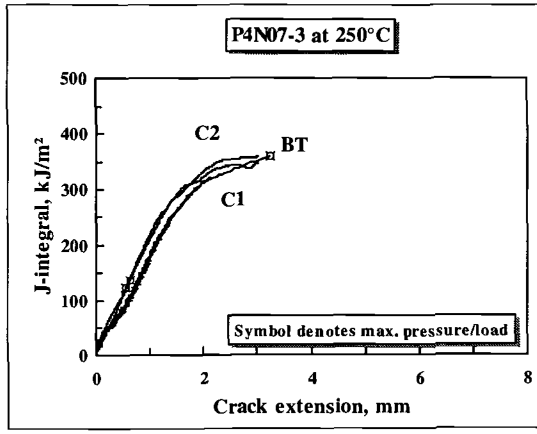

FIGURE 5--Comparison of J-R curves from burst test and curved compact specimens (high-toughness tube P4N07 (250°C).

Thus the overall trend is one of improved agreement between the J-R curves from small- and large-scale specimens at shorter crack extensions and higher-toughness levels. This is demonstrated in Figure 7 which shows a plot of the J value taken at the intersection of the 3.0 mm offset line and J-R curve, $J_{3.0}$,. Here the toughness has been normalised to produce an equivalent parameter, the plane-stress plastic zone size, $r_{3.0}$, where the latter is taken as $\pi E \cdot J_{3.0}/8\sigma_f^2$ based on the Dugdale small-scale yielding expression for consistency with the strip-yield equation 1. There is a trend of increasing deviation between the $r_{3.0}$ values for the two different types of specimens which is reversed when moving above the level of the intermediate-toughness material, for which the stable growth at instability is a maximum value. Such tubes appear to exhibit the maximum deviation from both small-scale and fully-plastic yielding conditions for J-controlled crack growth [7].

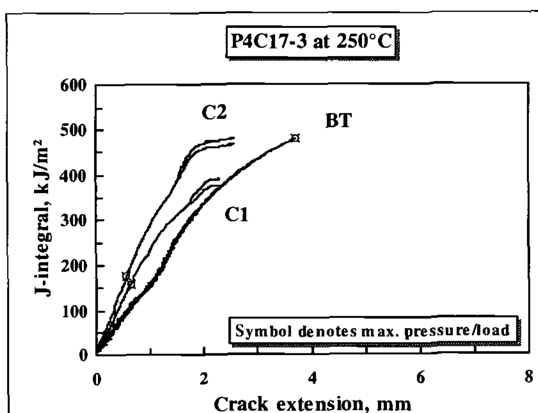

FIGURE 6--*Comparison of J-R curves from burst test and curved compact specimens (highest-toughness tube P4C17 (250°C).*

In contrast, a plot of the calculated plastic zone size at maximum pressure, r_{mpi}, versus the equivalent parameter at maximum load from the small specimens, r_{ml}, (Figure 8) reveals a steadily diverging trend in the parameters from the two different specimens but with evidence of a transition in crack growth behaviour for tubes of intermediate toughness. However, at higher toughness levels such results do not revert to a 1:1 correspondence due to the different crack extensions observed up to the maximum-pressure/load toughness. The increased scatter observed in Figure 8 for tubes of intermediate toughness is significant and reflects the uncertainty in defining a true crack instability condition when the pressure versus crack extension curves exhibit an extended region of stable crack growth at constant pressure (e.g. results for tube P3N07 in Figure 1).

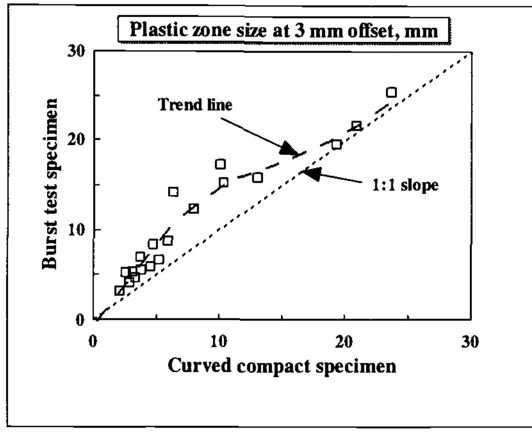

FIGURE 7--*Comparison of plastic zone size at 3mm offset ($r_{3.0}$) from burst tests and curved compact specimens (250°C).*

In the previous study [7], fractographic evidence was presented showing that crack instability in the burst test sections is controlled by the geometric requirement of a change in fracture plane from the radial-axial plane (normal to the hoop-stress direction), to a plane closer to 45° to the radial-axial and transverse-axial planes, i.e. planes of maximum shear stress for plane-stress fracture. This occurred as the crack front tunnelled forward at the highly-constrained mid-section and shear or slant fracture developed in the lower constraint region at the specimen surface with increasing crack length. The development of an angled fracture with a sufficiently high proportion of slant fracture (between 50% and 80%) appeared sufficient to precipitate this shear or "sliding-off" mechanism. Tube sections of intermediate toughness (e.g. P3N07) developed this fracture mode at larger crack extensions, consistent with the extended plateaus observed with the pressure versus crack extension curves.

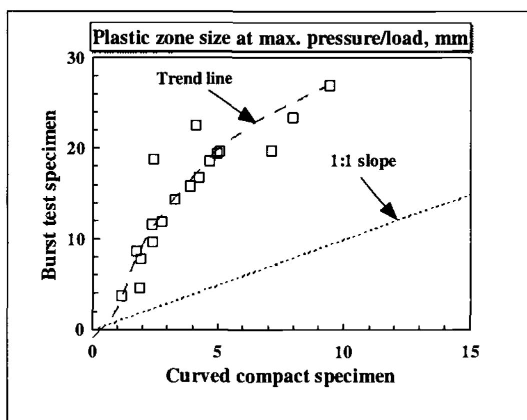

FIGURE 8--*Comparison of plastic zone size at maximum pressure/load (r_{mpi}, r_{ml}) from burst tests and curved compact specimens (250°C).*

The observed geometry effects were shown to be due to variations in the energy-absorbing capacity and relative proportions of three different fracture modes:

a) low energy-absorbing, flat-fracture zone at the mid-section in the region of highest constraint (stage 1),

b) high energy-absorbing, transition-fracture zone consisting of a flat/cup-shaped fracture between the mid-section and surface in the region of intermediate constraint (stage 2), and
c) low energy-absorbing, shear or slant-fracture zone at the surface in the region of lowest constraint (stage 3).

A larger proportion of highly-constrained, flat fracture was generally produced with the small, bend-type specimen than with the burst test specimen. However, the good correspondence between the J-R curves obtained from the two different specimens of tube P4Q17 tested previously was due to the dominance of the transition-fracture mode in this case. The fracture surfaces from the present additional tubes of high toughness material (P4J17, P4N07 and P4C17) exhibited features consistent with these observations [7] with the exception of the small specimens from tube P4C17 mentioned previously.

Volume-Controlled Fracture Model/Scaling Fracture-Toughness Parameters

Assuming the toughness of thin-walled Zr-2.5Nb pressure tube material to be governed mainly by the development of the high energy-absorbing, transition zone, it was shown [7] that the majority of test results could be rationalised in terms of a volume-controlled fracture model developed originally by Turner [18] for deeply-cracked bend specimens. The model showed that at a given level of toughness, dJ/da, the plane-stress plastic zone size, r_y, is limited by both the wall thickness, B and the size of the remaining ligament, b, as follows [18]:

$$\frac{dJ}{da} = \frac{2\gamma_{vol} \cdot r_y^2}{B \cdot b} \tag{2}$$

where: γ_{vol} = work per unit volume.

The validity of the model was demonstrated in an earlier study [19] on compact specimens of different widths of unirradiated Zr-2.5Nb pressure tube material, where it was shown that, for a given toughness level, the calculated value of the square of the plane-stress plastic zone radius, r_y^2 taken as $(E \cdot J/2\pi\sigma_f^2)^2$, was directly proportional to $(b \cdot B)$ or b, since the specimen thickness was not varied. Further support for the model came from the experimental results from the 34-mm-wide curved compact specimen [4], which were also generally consistent with a b dependence.

By using $\sqrt{(b \cdot B)}$ as a scaling factor for the small specimen results, it was subsequently shown [7] that good agreement could be obtained between scaled values of the plastic zone size at maximum load, $r_{ml}/\sqrt{(b \cdot B)}$, for the small specimens and scaled values of the plastic zone size at maximum pressure, $r_{mpi}/\sqrt{(2r_m \cdot t)}$, for the burst tests. The range of agreement corresponded to a range of normalised plastic zone size of about 0.4 to 1.0, based on the Dugdale small-scale yielding expression, $\pi E \cdot J/8\sigma_f^2$ for consistency with equation 1. The selection of the scaling factor, $\sqrt{(2r_m \cdot t)}$, for normalising results from the burst tests was primarily based on the earlier crack-size-effect study [7] which demonstrated the absence of any significant effect of initial crack size on the J-R curves for toughness levels up to that of the tube of intermediate toughness, P3N08. This suggested the use of a scaling factor related to dimensions such as the radius, r and wall thickness, t, with the parameter, $\sqrt{(2r_m \cdot t)}$, providing the best fit over the maximum range. It was considered a measure of the degree of constraint resulting from biaxial stress and/or bulging effects, the latter being proportional to $\sqrt{(r \cdot t)}$ [15].

The previous results are shown in Figure 9 which includes the present results from tubes P4J17, P4N07 and P4C17, the 34-mm-wide curved compact specimen using irradiated material from tube P3L03 tested at 250°C, and the 17- and 34-mm-wide curved compact specimens from unirradiated tube C70 tested at room temperature [4]. Thus the results continue to support the use of the volume-controlled fracture model over a normalised plastic zone size of about 0.4 to 1.0, with deviations at both lower and higher levels of toughness. At the lower toughness level, the experimental results diverge from the linear elastic regime at a normalised plastic zone size close to the limiting level for a valid linear elastic fracture toughness as provided in the ASTM Standard Test Method for Plane-Strain Fracture Toughness of Metallic Materials (E 399); i.e. $K_I \leq \sigma_y\sqrt{(B/2.5)} \leq 35$ MPa$\sqrt{m}$ or equivalently, $J = K^2(1-\nu^2)/E \leq 11$ kJ·m^{-2} or $r_{ml}/\sqrt{(b \cdot B)}$, ≤ 0.1. At higher levels of toughness the results from tubes P4N07 and P4C17 are in good agreement with those obtained previously for tube P4Q17, showing divergence from the model at values of $r_{mpi}/\sqrt{(2r_m \cdot t)}$ or $r_{ml}/\sqrt{(b \cdot B)} > 1$.

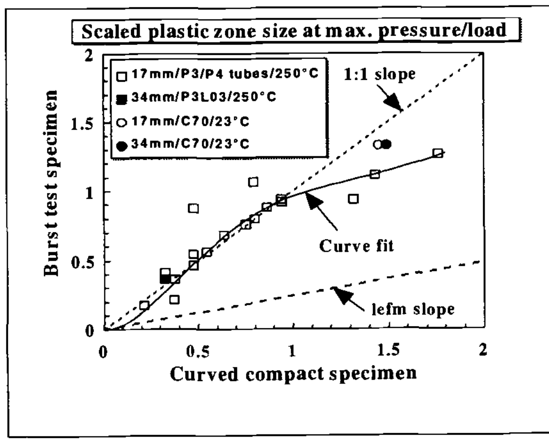

FIGURE 9--*Comparison of scaled plastic zone size at maximum pressure/load (r_{mpi}, r_{ml}) from burst tests and curved compact specimens (250°C).*

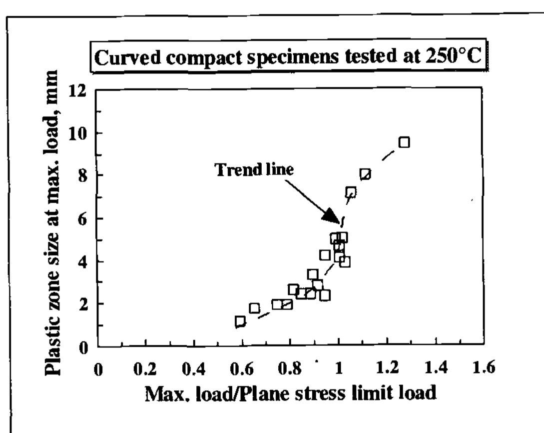

FIGURE 10--*Plastic zone size at maximum load (r_{ml}) versus normalised maximum load (p_{ml}/p_{ll}) for curved compact specimens (250°C).*

In the previous work [7], it was suggested that the deviation of results from the model at high toughness could be due to either the onset of a crack-size dependency with the burst test as a result of increased bulging or a change in the ligament dependency for the small specimen. Although the former cannot be ruled out, the present results from tube P4C17 confirm that the deviation is partly due to a reduction in crack-tip constraint in the small specimen at high nominal stress levels. This change in constraint is reflected in the plot of the plastic zone size at maximum load, r_{ml}, versus the normalised maximum load, p_{ml}/p_{ll}, for the small specimens, Figure 10, where there is a significant change in slope at stress levels above the plane-stress limit load. (A similar plot for the burst tests is not shown since the equivalent parameters (r_{mpi}, σ_h/σ_{plc}) are not measured independently, see equation 1).

A similar effect is noted in Figure 11 which shows a plot of the ratio of the plastic zone size to the crack extension at maximum pressure for the burst tests versus the equivalent parameter at maximum load for the small specimens. Such results indicate the scale of yielding with respect to the crack growth or "embedment" at the maximum-load-bearing condition, tubes of higher toughness clearly exhibiting more extensive embedment ($r_{mpi}/\Delta a_{mpi} > 5$) than tubes of lower toughness ($r_{mpi}/\Delta a_{mpi} < 2$). The relationship suggests that the plastic zone size at maximum load generally resulted in increased embedment of the crack at higher toughness levels in the small specimens compared with the burst tests by a factor of about 2, with a further deviation at the highest toughness level for tube P4C17.

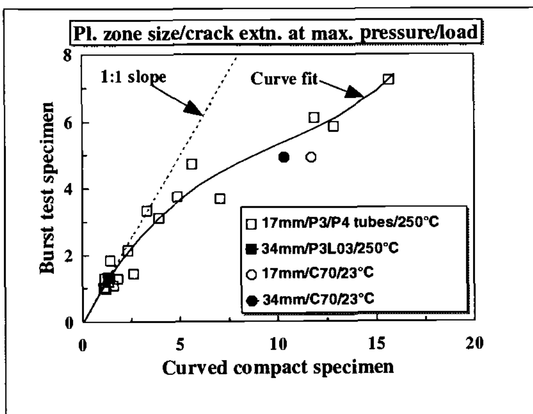

FIGURE 11--*Comparison of plastic zone size/crack extension ($r_{mpi}/\Delta a_{mpi}$, $r_{ml}/\Delta a_{ml}$) at maximum pressure/load from burst tests and curved compact specimens (250°C).*

Finally, although the results from the two different widths of small specimen are in good agreement for both material conditions (Figure 11), the higher results obtained for the unirradiated compared with the irradiated material suggest the range of applicability of the model depends on material condition. This is not unexpected given the dependence of geometry or constraint effects on nominal stress level [20-24]. It suggests that the breakdown from the proposed model occurs at lower nominal stress levels (lower values of normalised plastic zone size) for irradiated than for unirradiated material due to the increase in crack-tip stress associated with irradiation hardening, as well as the reduction in work-hardening capacity, which is not accounted for in the macroscopic model.

COMPARISON OF DEFORMATION J WITH OTHER J-TYPE PARAMETERS

The material dependence of the extent of geometry independence of the J-R curves is consistent with the known validity requirements for J-controlled crack growth (JCCG);

i.e. for a Hutchinson, Rice and Rosengren (HRR) deformation-type stress and strain field to be maintained at the crack tip [25,26]. For example, the requirement that the increase in external load be sufficiently large for the plastic strain increments to be predominantly proportional (ω parameter = b·dJ/da/J > 10 for bend-type specimens) could only be met over a reasonable J- or crack-extension range for the compact specimens of highest toughness, i.e. tubes having a toughness level greater than or equal to that of tube P3N08 (Figure 4). These are tubes for which the extent of embedment, $r_{mpi}/\Delta a_{mpi}$ or $r_{ml}/\Delta a_{ml}$ is ≥ 3 (Figure 11). In addition, there is a requirement on the maximum crack extension range for JCCG to ensure limited unloading at the crack tip (α parameter = $\Delta a/b < 0.06$ to 0.10, e.g. 0.85 mm crack growth for 17-mm-wide compact specimen). Thus, although there was good agreement between the small- and large-scale specimens over a crack extension range of up to 2.5 mm (about 30% of the remaining ligament) for the tubes of higher toughness (e.g. P4N07 and P4Q17), the present results for the tube of highest toughness (P4C17) suggests that this was fortuitous, merely reflecting a changing pattern in crack-tip constraint of the two specimens at high nominal stress.

The question arises as to the significance of the scaling factors obtained from the maximum-pressure/load toughness parameters given the limitations on the use of the deformation J-integral equation. For example, for the majority of small specimens the maximum load toughness, J_{ml}, occurred at crack extensions > 0.85 mm (Table 2), i.e. above the maximum α value of 0.1 for JCCG. Therefore it is appropriate to examine the use of other toughness criteria such as the modified J-integral approach of Ernst [11] and the plastic work dissipation approach of Turner [12,13] for comparison with the current values of deformation J_{ml}. The equations for these parameters are given below.

<u>Deformation J Parameter</u>

The recommended equation for calculating the deformation J-integral for a standard compact specimen in ASTM E 1152 splits the J-integral into an elastic component, J_e, and a plastic component, J_p, as follows:

$$J_d = J_e + J_p = \frac{K^2}{E}(1-\nu^2) + J_p \tag{3a}$$

where: K = elastic stress intensity factor,
E = Young's modulus, and
ν = Poisson's ratio.

The following incremental expression is then used for J_p:

$$J_{p,i} = [J_{p,i-1} + \frac{\eta \cdot \Delta U_p}{B \cdot b_i}][1 - (\frac{\gamma}{b_i})\Delta a] \tag{3b}$$

where: $J_{p,i}$ = plastic component of J after the ith increment of crack growth,
ΔU_p = increment of strain energy under the load-plastic displacement curve between lines of constant plastic displacement, u_p, at i-1 and i,

η = geometric constant, $2.0 + 0.522b_i/W$,
γ = geometric constant, $1.0 + 0.76b_i/W$,
B = thickness,
b_i = instantaneous remaining ligament, $W-a_i$, and
Δa = crack extension, a_i-a_{i-1}.

Equation 3b is based on the original strain energy rate expression for the deformation J-integral of Rice [27], i.e. $J_d = -(\partial U/B\partial a)_u$, which is strictly valid only up to crack initiation. It incorporates a correction for crack growth in the second or "γ" term.

Modified J Parameter

Ernst [11] defined a modified J-type parameter, J_m, with the aim of extending the useful crack extension range of deformation J-integral values obtained from laboratory specimens beyond the JCCG regime:

$$J_m = J_d - \int_{a_o}^{a_f} \left(\frac{\partial (J_d - G)}{\partial a} \right)_{u_p} da \tag{4a}$$

The form of the equation is such as to ensure consistency with the linear elastic strain energy release rate, G, in the linear elastic regime and to satisfy the Rice, Drugan and Sham (RDS) [28] requirement for a J-type parameter which, in contrast to J_d, is not an explicit function of crack extension as the limit of rigid plastic behaviour is approached. An incremental form [11] may be used to calculate the modified J from the deformation J:

$$\Delta J_m = \Delta J_d + \frac{\gamma}{b} J_{dp} \Delta a \tag{4b}$$

where: J_{dp} = plastic component of the deformation J-integral.

R and Dissipation J Parameter

More recently, Turner has [12,13] proposed the use of the plastic work dissipation rate, D_{dis}, as a more fundamental parameter for characterising toughness:

$$R = \frac{1}{B}\frac{d(W - U_e)}{da} + D_f = D_{dis} + D_f \tag{5}$$

where: R = total plastic work dissipation rate,
W = external work,
U_e = elastic strain energy,
D_{dis} = plastic work dissipation rate, and
D_f = fracture dissipation rate, generally up to initiation since separation is not possible from D_{dis} during stable crack growth.

With increasing crack extension, R increases in contained yield but decreases in uncontained yield situations [12,13], in sharp contrast to the deformation J or modified J parameters which always increase with crack growth. The difference arises from R being a more fundamental "internal energy" based parameter which is obtained directly from an energy balance, rather than a "work" based parameter as in the case of J_d or J_m. Thus at large crack extensions the zone of active plastic dissipation decreases in size as the ligament reduces until R reaches an equilibrium or steady-state value, R_{ss}.

Other than Turner's work, only limited data has been analysed using this approach (e.g. [29]) these results demonstrating decreasing R-curves for uncontained yield. The lack of data analysed by this method is surprising given that after crack initiation, R is a more correct representation of toughness as the combined energy growth rate for fracture and associated plasticity. Such a parameter is then equated with an equivalent "crack driving" parameter for the structure to determine the conditions for crack propagation and instability, as described in [13]. This is in contrast to J_d, which because of its inclusion of elastic terms, does not represent the true irreversible work during crack growth.

For consistency and comparison with the large body of J-R curve data Turner has re-formulated equation 5 into a rising J-type parameter, termed J_{dis}:

$$J_{dis} = J_i + \sum_{initiation}^{final} \frac{\eta \cdot \Delta(W - U_e)}{B \cdot b} = J_i + \sum_{initiation}^{final} \frac{\eta \cdot D_{dis} \Delta a}{b} \qquad (6a)$$

where: J_i = deformation J at crack initiation, and

η = geometric constant relating the strain energy to the change in strain energy with crack extension , $-(b/U)/(\partial U/\partial a)_u$; taken as $(2 + 0.522\ b/W)$ following ASTM E 1152.

This equation is strictly only applicable for large ω, since the plastic portion of the total strain energy then dominates the $W\text{-}U_e$ term. However, for the deeply-cracked compact specimen the η factors for the elastic and plastic regimes are similar (approximately 2) so that equation 6a should be applicable for the entire range of toughness levels. When this is not the case the following alternative formulation is recommended [13]:

$$J_{dis} = J_i + \sum_{initiation}^{final} \frac{\eta \cdot \Delta(W - U_e)}{B \cdot b} = J_i + \sum_{initiation}^{final} \left(\frac{\eta_e G \Delta a}{b} + \frac{\eta_p \cdot \Delta U_p}{B \cdot b}\right) \qquad (6b)$$

where: η_e = geometric constant relating the elastic strain energy to the change in elastic strain energy with crack extension , $-(b/U_e)/(\partial U_e/\partial a)_u$, and may be calculated for a given geometry from $(b/C)/(dC/da)$, where C is the elastic compliance, u_e/P,

η_p = geometric constant relating the plastic strain energy to the change in plastic strain energy with crack extension , $-(b/U_p)/(\partial U_p/\partial a)_u$, and may be calculated for a given geometry from $-(b/p_{ll})(\partial p_{ll}/\partial a)_u$, where P_{ll} is the limit load.

As stated by Turner [12], equation 6 provides an alternative J-type parameter, J_{dis}, which is physically meaningful but retains the necessary attributes of the modified J mentioned previously, i.e. it reduces to the elastic G parameter in the linear elastic regime but still meets the RDS requirement in the fully plastic regime of not being an explicit function of the crack growth.

Application of J-Type Parameters to Irradiated Zr-2.5Nb Pressure Tube Material

Equation 4b for the modified J parameter and equation 6a for the dissipation J parameter were used to re-analyse all the previous small specimen test results in the form of J-R curves. A comparison with the previous deformation J-R curves are shown in Figures 12, 13 and 14 for a specimen from tube P3M11 (low toughness), tube P3H07 (intermediate toughness) and tube P4N07 (high toughness), respectively. (Note that for consistency the value for J_i in equation 6a was taken as the J value at the intersection of the J-R curve and 0.2 mm offset line, i.e. engineering definition of crack initiation. A smoother transition in the J_{dis}-R curves at crack initiation could be obtained by selecting a slightly lower J value. This was done for illustrative purposes only in Figures 12 and 13. However, for Figure 14 no smooth transition at crack initiation could be produced and the resulting discontinuity at the $J_{0.2}$ value can be seen. In this case it could be argued that J_i should correspond to the J value at the limit of JCCG (about 0.85 mm crack extension), i.e. above the J at maximum load. For the purposes of the present discussion such differences are minor.)

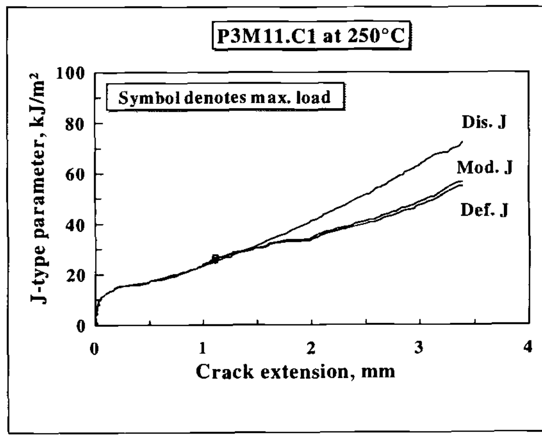

FIGURE 12--*Comparison of different J-type parameters for curve compact specimen C1 from lowest-toughness tube P3M11 (250°C).*

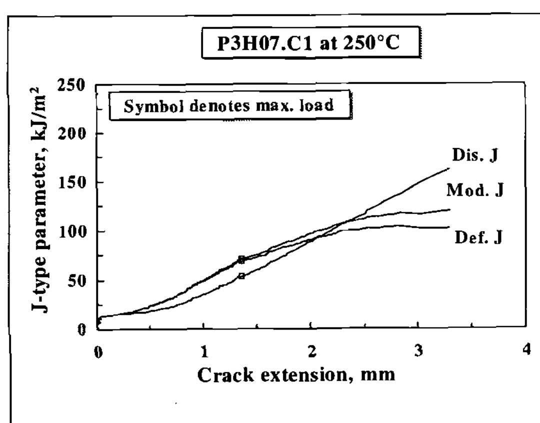

FIGURE 13--*Comparison of different J-type parameters for curved compact specimen C1 from intermediate-toughness tube P3H07 (250°C).*

Figures 12 to 14 indicate the significant differences in the different J-type parameters at large crack extensions, with the dissipation J producing higher values than the deformation or modified J parameters. However, at smaller crack extensions the differences are much reduced. For example, at maximum load the modified J was within 3% of the deformation J value at all toughness levels due to the short crack extension and relatively low contribution of the plastic component to J, i.e. the ratio of the plastic to the elastic component of J, J_p/J_e was ≤ 1.0. There was also good agreement between the dissipation J and deformation J at short crack extensions (< 1 mm) for tubes of lower (P3M11, Figure 12) and higher (P4N07, Figure 14) toughness. Figure 13 indicates that the largest difference between J_{dis} and J_d at maximum load was for the specimen from tube P3H07 of intermediate toughness, with dissipation J predicting lower values of toughness than deformation J.

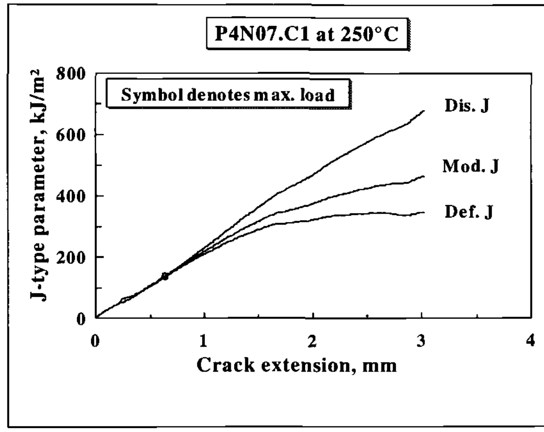

FIGURE 14--*Comparison of different J-type parameters for curved compact specimen C1 from high-toughness tube P4N07 (250°C).*

This trend is demonstrated more clearly in Figure 15 which summarises the average values obtained for each parameter from the two small specimens tested from each tube. Results obtained from the 34-mm-wide specimens from tube P3L03 tested at 250°C as well as from the 17- and 34-mm-wide specimens from unirradiated tube C70 tested at 23°C are also included. The results confirm that the maximum difference between the dissipation J and deformation J parameters at maximum load (up to 25%) occurs for specimens from tubes of intermediate toughness, with results at lower and higher toughness levels generally lying within the 10% scatter bands. Figure 16 shows that the difference between the two parameters is related to the extent of stable crack growth up to the load maximum. This is because an increase in crack extension increases both the elastic component of the deformation J as well as the "γ" term in equation 3b. However, since these specimens also exhibit the most crack-front tunnelling, some consideration of the effect of tunnelling on the magnitude of the calculated J parameters is also required.

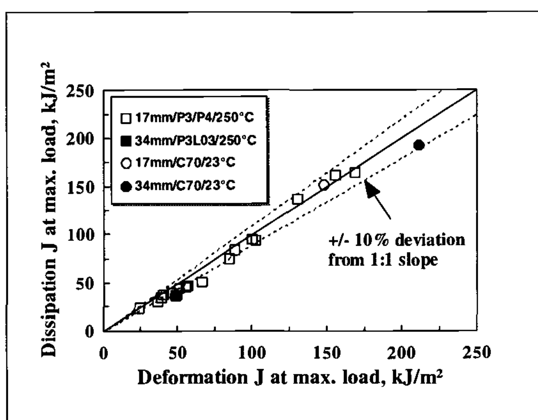

FIGURE 15–*Comparison of dissipation J with deformation J parameter at maximum load for curved compact specimens of different toughness (250°C).*

Crack-Front Tunnelling

A multiple heat tint/partial unloading technique has been developed to investigate the development of the crack front shape during small specimen testing as well as to determine more accurate calibrations for assessing the "true" toughness of the material. This work is on-going but some limited results are included here to indicate the sensitivity of the different J-type parameters to tunnelling.

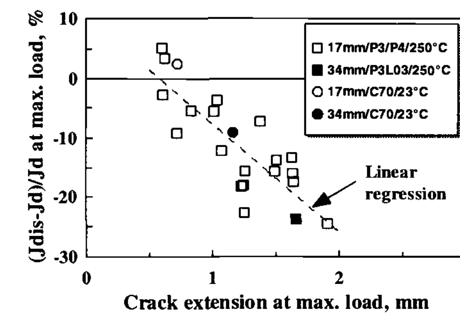

FIGURE 16--*Difference between dissipation J and deformation J parameter at maximum load versus crack growth at maximum load for curved compact specimens of different toughness (250°C).*

The technique involves the use of multiple loadings of an individual specimen to different crack extensions, partial unloading by 15% of the instantaneous load, heat tinting under load, partial unloading an additional 15% of the instantaneous load and reloading. Using a test temperature of 250°C the duration of the heat tint cycles was decreased by approximately 20 min. between each loading to ensure a sufficient difference in oxide formation and delineation of the different crack growth zones. Thus for six unloadings (seven cycles including the final crack growth zone) the duration of the heat tinting was 140, 120, 100, 80, 60, 40 and 30 min. After testing each fracture surface was photographed and the average crack extension measured at the different crack front positions. The initial elastic compliance was determined for each cycle on reloading after careful study of the load-displacement-voltage records to avoid crack closure effects. Such a technique is preferred to the use of multiple specimens to avoid problems associated with specimen-to-specimen variability.

Two sets of results have been obtained from an unirradiated tube 669 and irradiated tube P3H07 tested at 250°C. Tube 669 was selected as having a similar toughness to that of unirradiated archive material from tube P3H07, i.e. the toughness approximately corresponds to that of tube P3H07 before irradiation. The resulting potential drop and elastic compliance calibrations for the tunnel-shaped cracks are shown in Figures 17 and 18. In Figure 17 a two-dimensional analogue method [30] was used to determine the potential drop calibration for a straight crack-front. In Figure 18 an initial increase in elastic compliance was noted in the early stages of loading up to a crack extension of about 0.3 mm (relative crack extension, $\Delta a/W$, of about 0.02) and this maximum compliance was used to normalise the subsequent results after matching it to the standard elastic compliance equation in ASTM E 1152 for a specimen with a straight crack-front. This maximum compliance deviated from the ASTM value by 6 to 7% for tube 669 and by 12 to 13% for tube P3H07. The origin of this increase is currently being investigated but is believed to be associated with initial crack-tip blunting and fatigue crack-front curvature effects. After normalisation the results in Figures 17 and 18 from the two different specimens from each material are in good agreement with each other, with both sets of results lying below the corresponding calibrations for the straight crack-front. This reflects the shift in the stress distribution at the crack tip as the crack front tunnels forward at the mid-section (producing an underestimate in crack extension in Figure 17) and an increased proportion of the load is supported by the near-surface regions (producing a reduction in elastic compliance in Figure 18). The lower results observed for the irradiated material are indicative of the increased tunnelling observed with this material compared with the unirradiated material

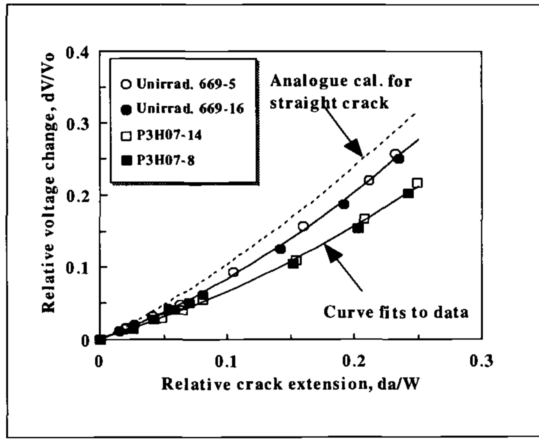

FIGURE 17--*Potential drop calibrations for tunnel-shaped cracks in curved compact specimens of unirradiated tube 669 and irradiated tube P3H07(250°C).*

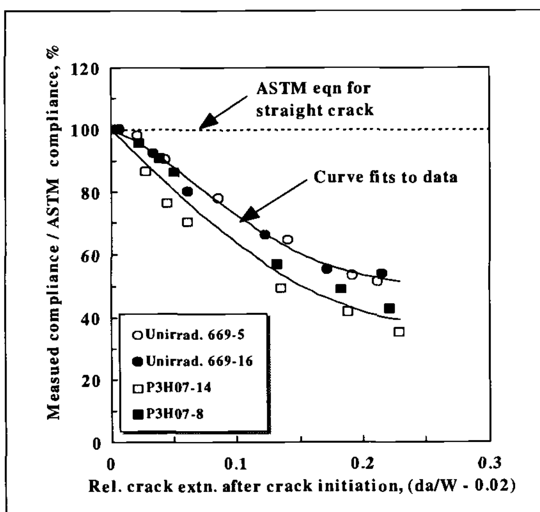

FIGURE 18--*Elastic compliance calibrations for tunnel-shaped cracks in curved compact specimens of unirradiated tube 669 and irradiated tube P3H07 (250°C).*

Using polynomial curve fits to the results in Figure 18, an estimate of the reduction in elastic stress intensity factor and the corresponding η_e factor for the tunnel-shaped crack was obtained as indicated in Figures 19 and 20, respectively. Again, comparison is made with the equivalent results for a straight crack-front as provided in ASTM E 1152. The η factor in ASTM E 1152 (η = 2+ 0.522b/W) is strictly based on an approximation of the plastic η factor, η_p, calculated from the Merkle-Corten limit analysis [31,32]. Therefore, the corresponding elastic η factor, η_e, calculated from standard elastic compliance and stress intensity factor relationships for the compact specimen with a straight crack-front is included for comparison with the present elastic results. Figure 19 shows that as tunnelling occurs the elastic stress intensity factor decreases to 40 to 50% of the value for a straight crack-front of equivalent crack length, the extent of the reduction being higher for the irradiated material which exhibited more tunnelling. Such results are generally consistent with trends previously established by finite element analyses of tunnel-shaped cracks [33,34]. The combined effect of the reduction in elastic compliance and stress intensity factor produces a reduction in the η_e factor to about 22 to 40% of the η_e value for a straight crack-front of equivalent crack length (Figure 20) .

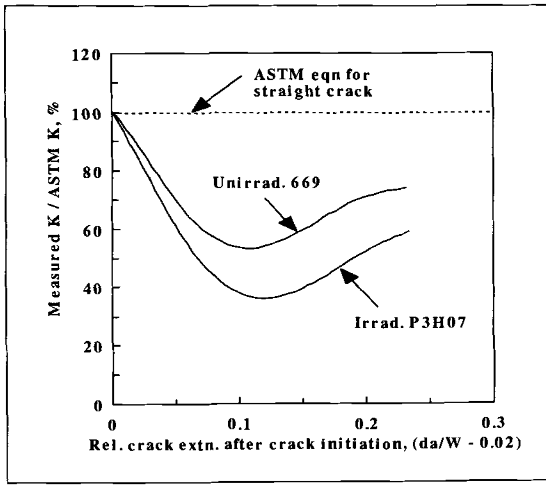

FIGURE 19--*Elastic stress intensity factor calibrations for tunnel-shaped cracks in curved compact specimens of unirradiated tube 669 and irradiated tube P3H07 (250°C).*

Sensitivity of J-Type Parameters and Scaling Factors to Crack-Front Tunnelling

Using appropriate polynomial curve fits to the previous calibrations established for the tunnel-shaped cracks in small specimens from tube P3H07, the different J-type parameters were re-calculated for small specimen C1. The results obtained at maximum load are tabulated in Table 3 according to the following four corrections carried out on a step-by-step basis to reveal the sensitivity of the different relationships:

a) potential drop calibration,
b) potential drop and elastic compliance calibrations,
c) potential drop, elastic compliance and stress intensity factor calibrations, and,
d) potential drop, elastic compliance, stress intensity factor and η_e calibrations,

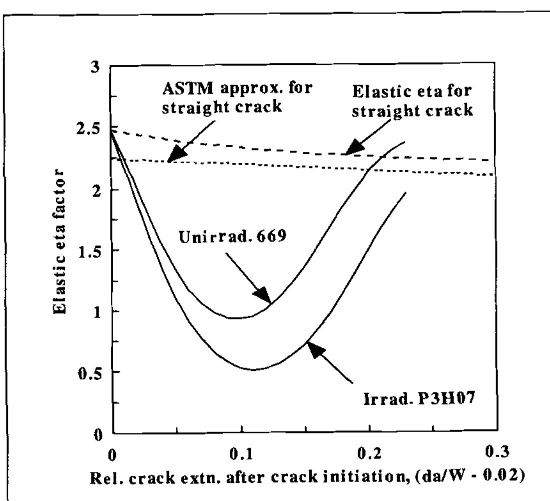

FIGURE 20--*Elastic η factors for tunnel-shaped cracks in curved compact specimens of unirradiated tube 669 and irradiated tube P3H07 (250°C).*

Table 3 reveals that correcting the potential drop calibration factor for tunnelling has little effect on the experimental results at maximum load. This is because the analogue calibration for a straight crack-front is not used in the standard test procedure , but rather a linear fit is assumed between the change in voltage and change in crack extension for each individual test specimen. Thus any error is due to the difference between this linear fit and the actual potential drop calibration which is nearer a curve fit (Figure 17). This results in a small underestimate in crack length at maximum load of about 0.23 mm, and a corresponding increase in the elastic component of J, elastic compliance and hence a reduction in the plastic component of J and the plastic strain energy. The overall effect is an increase in deformation J and modified J of 1% and a reduction in dissipation J of 6%.

TABLE 3--*Comparison of different J-type parameters at maximum load from curved compact specimen P3H07.C1 after correcting for crack-front tunnelling.*

Parameter at Max. Load	Original Value	a. Corrected Value (Pot. drop)	b. Corrected Value (Pot. drop and elastic compliance)	c. Corrected Value (Pot. drop, elastic compliance and SIF)	d. Corrected Value (Pot. drop, elastic compliance SIF and η_e)
Δa_{mt}, mm	1.36	1.59	1.59	1.59	1.59
J_e, $kJ \cdot m^{-2}$	46.4	51.8	51.8	11.2	n/a
J_p, $kJ \cdot m^{-2}$	22.4	17.7	41.7	41.7	n/a
J_p/J_e	0.48	0.34	0.81	3.67	n/a
J_d, $kJ \cdot m^{-2}$	68.8	69.5	93.5	52.9	n/a
J_m, $kJ \cdot m^{-2}$	70.8	71.3	97.6	57.0	n/a
W, N·mm	1082	1082	1082	n/a	1082
U_e, N·mm	601	651	469	n/a	469
W-U_e, N·mm	481	431	613	n/a	613
(W-Ue)/U_e	0.80	0.66	1.31	n/a	1.31
$\Sigma \Delta J_{dis}$, $kJ \cdot m^{-2}$	40.5	37.4	53.2	n/a	51.8
J_i, $kJ \cdot m^{-2}$	13.0	13.0	13.0	n/a	13.0
$J_{dis} = J_i + \Sigma \Delta J_{dis}$, $kJ \cdot m^{-2}$	53.5	50.4	66.2	n/a	64.8
D_{dis}, $kJ \cdot m^{-2}$ Max. load and max. value	----	----	169/177	n/a	n/a
$R = J_i + D_{dis}$, $kJ \cdot m^{-2}$ Max. load and max. value	----	----	182/190	n/a	n/a

In contrast, the correction for the reduction in elastic compliance associated with a tunnel-shaped crack produces a significant increase in all three J-type parameters due to the increase in the plastic component of J. For deformation and modified J it is clear that such a correction must be coupled with the corresponding reduction in the stress intensity factor to reduce the elastic component of J and avoid non-conservative values of total J. Thus, although correcting for the latter increases the ratio of the plastic to the elastic component of J, J_p/J_e, to 3.7 compared with the original value of 0.48, the final calculated values of deformation and modified J are lower than the original J values by 23% and 19%, respectively. In comparison, the dissipation J parameter shows less sensitivity to changes in the elastic strain energy with a much smaller reduction in final J value after correcting for the new η_e factor. This results in an overall increase in dissipation J of 21% compared with the original value.

The fully corrected J-R curves are shown in Figure 21, where an additional comparison is made for the dissipation J-type parameter using equation 6a (single η factor) compared with 6b (separate η_e and η_p factors). Comparison of the original J-R curves in Figure 13 with the corrected curves in Figure 21 reveal the foregoing trend, with the dissipation J results for the tunnel-shaped crack now lying above those based on the deformation and modified J parameters at all crack extensions. The importance of using equation 6b for the dissipation J (rather than 6a) when there is a significant difference in the elastic and plastic η factors is also apparent from the reduction in the dissipation J-R curve at larger crack extensions using equation 6b compared with 6a.

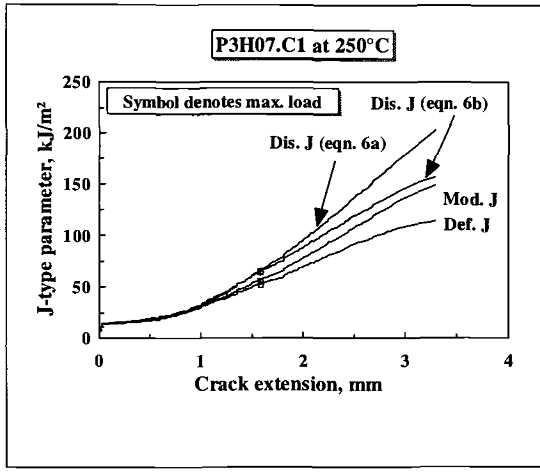

FIGURE 21--*Comparison of different J-type parameters for curved compact specimen C1 from intermediate-toughness tube P3H07 after correcting for crack-front tunnelling (250°C).*

For comparison with the J-type parameters, Figure 22 and Table 3 include results obtained using equation 5 for the plastic work dissipation parameter, D_{dis} and the total plastic work dissipation rate, R. Figure 22 shows a rising R-curve characteristic of contained yield up to a point close to the maximum load, followed by a falling R-curve characteristic of uncontained yield. The maximum value of D_{dis} (or R) may be considered the maximum achievable toughness for the particular ligament size and is anticipated to increase with increase in remaining ligament, as the maximum plastic zone size increases, in a manner similar to J_{ml}. However, the maximum values of D_{dis} and R are approximately 3 times the deformation J values at maximum load either before or after correcting for tunnelling.

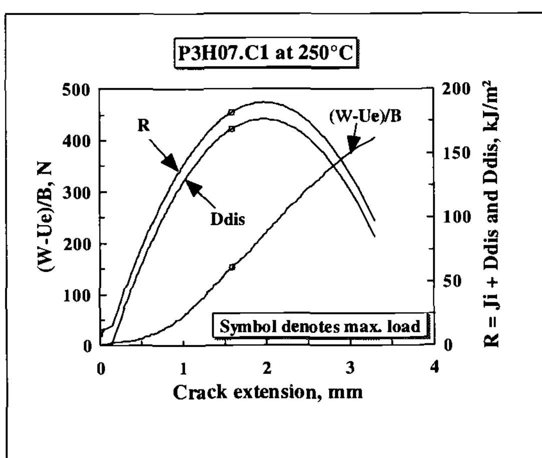

FIGURE 22--*Determination of the plastic work dissipation parameter (D_{dis}) and the total plastic work dissipation rate (R) for curved compact specimen C1 from intermediate-toughness tube P3H07 (250°C).*

The implication of the foregoing is that the scaling factor used to produce good agreement between the small- and large-scale specimens in the intermediate toughness regime is specific to the method of analysis employed, i.e. the use of deformation J values following ASTM E 1152 with no correction for crack-front tunnelling. Thus correcting for tunnelling for specimen P3H07.C1 would increase the scaling factor for the deformation J from $\sqrt{(2r_m t)}$ to about $1.8\sqrt{(r_m t)}$. In comparison, use of the modified J, dissipation J or R would change the scaling factor to values of about $1.7\sqrt{(r_m t)}$, $1.5\sqrt{(r_m t)}$ and $0.5\sqrt{(r_m t)}$, respectively. Such results suggest only minor increases in the scaling factor if a J-type parameter is used but a major reduction in scaling factor if a more meaningful toughness parameter such as R is used. Further study of other specimens and materials is required to confirm this. From an applications viewpoint such differences may not matter provided the selected parameters are used consistently. The main advantage of R is that it is physically meaningful, raising the possibility of determining scaling factors of more fundamental significance.

COMPARISON OF DIFFERENT TOUGHNESS PARAMETERS WITH J-R CURVE RESULTS FROM BURST TESTS

A comparison of the different R-curves calculated for small specimen P3H07. C1 with that from the corresponding burst test is given in Figure 23. It is clear that none of the different toughness parameters produce R-curves similar to those of the burst test even after correcting for tunnelling, and that they all underestimate the extent of stable crack growth.

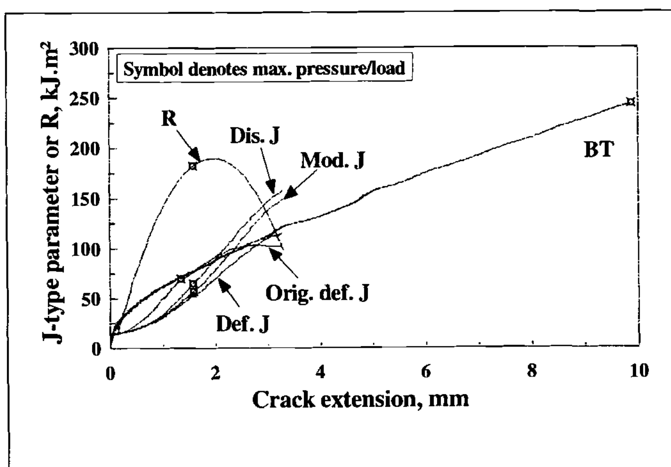

FIGURE 23--*Comparison of different crack growth resistance curves for curved compact specimen C1 from intermediate- toughness tube P3H07 with results from burst test (250°C).*

Under such circumstances the use of scaling factors on both the ordinate (J value) and the abscissa (crack extension) as suggested previously by Turner [18] are worthy of investigation. Different scaling factors were calculated for each axis based on polynomial curve fits to the relationships between the J value at maximum-pressure/load and the crack extension at maximum-pressure/load as shown in Figures 9 and 11, respectively. These variable scaling factors were then applied to each original deformation J and crack extension value on a point-by-point basis to produce a scaled J-R curve. The results are shown in Figure 24, where a scaled J-R curve based on the average results obtained from small specimens C1 and C2 are compared with the J-R curve obtained from the burst test. In applying the curve fits from Figures 9 and 11, it is assumed that such scaling factors, based solely on the maximum load-bearing capacity of the two different specimen geometries, are applicable to the entire J-R curve up to maximum load.

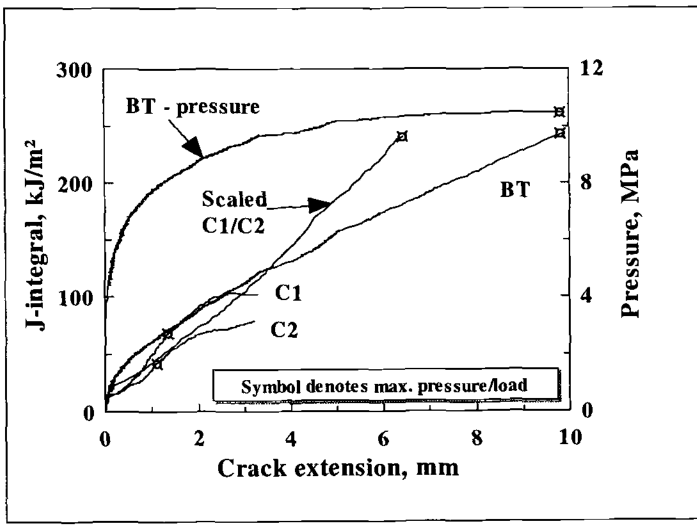

FIGURE 24--*Comparison of average scaled J-R curve for curved compact specimens C1 and C2 from intermediate-toughness tube P3H07 with results from burst test (250°C).*

Figure 24 indicates that the scaled J-R curve from the small specimen lies below that from the burst test at short crack extensions but rises above the J-R curve from the burst test at intermediate crack extensions, in a manner similar to that of both the modified J and dissipation J parameters (Figure 23). However, scaling the crack extension axis improves the stable crack extension to about 6.3 mm compared with about 3 mm for the other J-type parameters. Further significant improvements in the scaling approach for predicting the J-R curve behaviour of burst tests, such as those shown in Figure 24 for tube P3H07, appear unlikely due to the unpredictability of the extent of the slope reduction in the J-R curve at larger crack extensions. This slope reduction corresponds to the onset of the plateau region in the pressure versus crack extension curve, also shown in Figure 24, and is believed to be associated with an increase in the out-of-plane bending (bulging) at larger crack extensions just before failure. Such an effect is highly variable as revealed by the variation in the maximum-pressure toughness parameter, J_{mpi}, for the tubes of intermediate toughness noted previously (Figure 8). In addition, there is some uncertainty in the true crack extension measured in the burst test due to the difficulty of individual calibration of the potential drop method. Under such circumstances the current scaling approach is reasonable but probably requires either truncation of the scaled J-R curve or a small safety factor to avoid non-conservative estimates of stable crack growth and critical crack length when based on the initial (rather than the instability) crack size. However, further work is required to determine the true limits of applicability of the scaling approach over the full range of J-R curve behaviour.

SUMMARY AND CONCLUSIONS

A scaling approach, based on the deformation J-integral at maximum load obtained from small specimens, has been proposed for predicting the crack instability behaviour of burst tests on irradiated Zr-2.5Nb pressure tubes. An assessment of this approach has been carried out by comparison with other toughness criteria such as the modified J-integral of Ernst and the plastic work dissipation rate approach of Turner. The main conclusions may be summarised as follows:

1. For tubes of lower and higher toughness there is little difference between the deformation J, modified J and dissipation J parameters at maximum load primarily due to the small crack extensions exhibited by the 17-mm-wide curved compact specimen up to the maximum load. Tubes of intermediate toughness show the largest discrepancy between the different parameters since they exhibit the most stable crack growth and tunnelling up to maximum load.

2. Scaling factors determined on the basis of the deformation J-integral at maximum load are dependent on the method of analysis used, mainly because of the sensitivity to the toughness of the intermediate toughness tubes.

3. For a tube of intermediate toughness the different approaches can significantly underpredict the extent of stable crack growth before instability in a burst test even after correcting for tunnelling. Application of a scaling approach reduces the discrepancy between the small- and- large-scale specimen results.

4. The use of the total plastic work dissipation rate parameter, R, of Turner requires further study. It is physically meaningful, raising the possibility of determining scaling factors of more fundamental significance. The current limited work suggests the existence of a maximum R value for a given small specimen similar to the R value obtained at maximum load.

ACKNOWLEDGEMENTS

Thanks are due to R.S,W. Shewfelt and his team for providing burst test results and to G.R. Brady and D.D. Himbeault for supplying the matching small specimen results. The technical assistance of J.M. Smeltzer in conducting the interrupted small specimen tests is also gratefully acknowledged. The author thanks the CANDU Owners Group (COG) for funding this work under Work Package 2-31-6536.

REFERENCES

1. Moan, G.D., Coleman, C.E., Price, E.G., Rodgers, D.K. and Sagat, S., International Journal of Pressure Vessels and Piping, Vol. 43, 1990 pp. 1-21.

2. Langford, W.J. and Mooder, L.E.J., International Journal of Pressure Vessels and Piping, Vol. 6, 1978, pp. 275-309.

3. Chow, C.K., Coleman, C.E., Hosbons, R.R., Davies, P.H., Griffiths, M., and Choubey, R., Zirconium in the Nuclear Industry: Ninth International Symposium, ASTM STP 1132, American Society for Testing and Materials, 1992, pp. 246-275.

4. Davies, P.H. Shewfelt, R.S.W. and Järvine, A.K., Constraint Effects in Fracture: Theory and Applications, ASTM STP 1244, American Society for Testing and Materials, 1995, pp. 392-424.

5. Chow, C.K. and Simpson, L.A., Fracture Mechanics: Eighteenth Symposium, ASTM STP 945, American Society for Testing and Materials, 1988, pp. 419-439.

6. Simpson, L.A., Chow, C.K., and Davies, P.H., AECL/COG Non-Proprietary Report No. COG-89-110-I, AECL, September.

7. Davies, P.H. and Shewfelt, R.S.W., Paper presented at ASTM Eleventh International Symposium on Zirconium in the Nuclear Industry, September, 1995, Garmisch-Partenkirchen, Germany. Accepted for publication in ASTM STP1295.

8. Davies, P.H., Hosbons, R.R., Griffiths, M. and Chow, C.K., Tenth International Symposium on Zirconium in the Nuclear Industry ASTM 1245, American Society for Testing and Materials, 1995, pp. 135-167.

9. Davies, P.H., Aitchison, I., Himbeault, D.D., Järvine, A.K. and Watters, J.F., Fatigue and Fracture of Engineering Materials and Structures, Vol. 18, 1995, pp. 789-800.

10. Aitchison, I. and Davies, P.H., Journal of Nuclear Materials, Vol. 203, 1993, pp. 206-220.

11. Ernst, H.A., Elastic-Plastic Fracture: Second Symposium, Volume I, ASTM STP 803, American Society for Testing and Materials, 1983, pp. I-191-I-213.

12. Turner, C.E., Fracture Mechanics: Twenty-Second Symposium (Volume I), ASTM STP 1131, American Society for Testing and Materials, 1992, pp. 71-92

13. Turner, C.E., Fracture Mechanics: Twenty-Fourth Volume, ASTM STP 1207, American Society for Testing and Materials, 1994 pp 447-463.

14. Kiefner, J.F., Maxey, W.A., Eiber, R.J. and Duffy, A.R., Progress in Flaw Growth and Fracture Toughness Testing, ASTM STP 536, American Society for Testing and Materials, 1973, pp. 461-481.

15. Folias, E.S., International Journal of Fracture Mechanics, 1965, Vol. 1, No. 2, pp. 104-113.

16. Mok, D.H.B., and Scarth, D.A., 1992, Unpublished, Ontario Hydro Technologies, Toronto, Ontario, Canada.

17. Chow, C.K., and Himbeault, D.D., Unpublished, 1995, AECL, Whiteshell Laboratories, Pinawa, Manitoba, Canada.

18. Turner, C.E., Size Effects, Mechanical Engineering Publications, London, 1986, pp. 25-31.

19. Davies, P.H. and Smeltzer, J.M., Fracture Mechanics: Twenty-Second Symposium, ASTM STP 1131, American Society for Testing and Materials, 1992, pp. 93-104.

20. Shih, C.F., O'Dowd, N.P., and Kirk, M.T., Constraint Effects in Fracture, ASTM STP 1171, American Society for Testing and Materials, 1993, pp. 2-20.

21. Hancock, J.W., Reuter, W.G., and Parks, D.M., Constraint Effects in Fracture, ASTM STP 1171, American Society for Testing and Materials, 1993, pp. 21-40.

22. Brocks, W. and Schmitt, W., Constraint Effects in Fracture, ASTM STP 1171, American Society for Testing and Materials, 1993, pp. 64-78.

23. O'Dowd, N.P, Engineering Fracture Mechanics, Vol. 52, 1995, pp. 445-465.

24. Yuan, H., Lin, G., and Cornec, A., International Journal of Fracture, 1995, Vol. 71, pp. 273-291.

25. Hutchinson, J.W., Journal of Mechanics and Physics of Solids, Vol. 16, 1968, pp. 13-31 and pp. 337-347.

26. Rice, J.R. and Rosengren, G.F., Journal of Mechanics and Physics of Solids, Vol. 16, 1968, pp. 1-12.

27. Rice, J.R. Journal of Applied Mechanics, Transactions of the ASME, Vol. 35, 1968, pp. 379-386.

28. Rice, J.R., Drugan, W.J., and Sham, T.L., Fracture Mechanics: Twelfth Conference, ASTM STP 700, American Society for Testing and Materials, 1980, pp. 189-221.

29. Memhard, D., Brocks, W. and Schmitt, W., Fatigue and Fracture of Engineering Materials and Structures, Vol. 16, 1993, pp. 1109-1124.

30. Hicks, M.A., and Pickard, A.C., International Journal of Fracture, 1982,Vol. 20, pp.91-101.

31. Clarke, G.A., and Landes, J.D., Journal of Testing and Evaluation, Vol. 7, 1979, pp. 264-269.

32. Merkle, J.G., and Corten, H.T., Journal of Pressure Vessel Technology, Trans. ASME, Vol. 96, 1974, pp. 286-292.

33. Neale, B.K., International Journal of Fracture, 1976, Vol. 12, pp. 499-502.

34. Towers, O.L., and Smith, A.P., International Journal of Fracture, 1984, Vol. 25, pp. R43-R48.

Anthony T. Chang[1] and Jennifer A. Cordes[1]

Predicting Fracture Behavior Of Aluminum Alloys

Reference: Chang, A.T., Cordes, J.A., "**Predicting Fracture Behavior Of Aluminum Alloys**", *Fatigue and Fracture Mechanics, ASTM STP 1321,* J.H. Underwood, B.D. Macdonald, and M.R. Mitchell, Eds., ASTM, 1997.

Abstract: A computational method has been developed to predict the material fracture failure process in flawed or cracked specimens. This method does not require experimental material fracture data. Finite element technique is employed to model the physical shape of the specimen. Nonlinear spring elements are introduced to model the material damage behavior near a flaw or a crack tip. Crack initiation and crack propagation conditions are developed to predict the crack initiation load, the extent of material damage, and the crack growth behavior. The introduction of nonlinear spring elements and the development of crack initiation and crack growth conditions are unique features for fracture prediction with the development of this method. To prove the feasibility of the method, two types of specimen made by two aluminum alloys with similar material stress-strain data were studied. Fracture predictions by this method are comparable to experimental data.

KEY WORDS: Fracture, aluminum, crack propagation, ductile fracture, finite element analysis, failure prediction, stable tearing.

Most fracture predictions rely on material fracture data extracted from laboratory tests and comparison of the experimental data to a calculated fracture value. If the calculated value exceeds the critical experimental data, the material fracture is then predicted to occur. A fracture value such as stress intensity factor (K), crack-tip-opening-displacement (CTOD), or *J*-integral is usually selected for comparison. This standard single value approach to fracture predictions can be misleading if the state of stress at the material crack tip does not match those under experimental conditions. The discrepancy could be due to the following factors: when the size or geometry of the specimen differs from that of the experimental sample, when there is significant material plasticity, when multiple damage sites are present, when crack growth is significant, or when the fracture takes place in a corrosive environment.

[1] Department of Mechanical Engineering, Stevens Institute of Technology, Hoboken, NJ 07030 USA

There are several methods [1] proposed to correct fracture parameters for size or geometry effects. Two continuum methods, K-T and J-Q methods, were reviewed in depth by Anderson, Vanaparthy, and Dodds [2]. These methods require a fracture data (K or *J*) and a correction for the state of stress near the crack tip.

Panotin and Sheppard [3] investigated the accuracy of two theories for predicting crack initiation in steel panels. They are the critical strain criteria by Mackenzie, Hancock, Brown [4] and the void growth geometry criteria by Rice and Tracey [5]. Both approaches require material stress-strain data and two experimental fracture data.

The δ_5 parameter method, proposed by Schwalbe and others, bases fracture predictions on crack tip opening displacements measured 2.5 mm above or below the original crack tip. Schwalbe [6] reported that the experimental δ_5-R curves are less geometry-dependent than *J-R* curves. Newman, Dawicke, Bigelow, Crews [7,8] and others have used crack tip opening angle (CTOA) as a single material fracture parameter to predict stable crack growth under large-scale material plasticity. This parameter is relatively independent of geometry for thin structures with significant material damage. Both the δ_5 parameter and the CTOA approaches require displacement measurements near the crack tip.

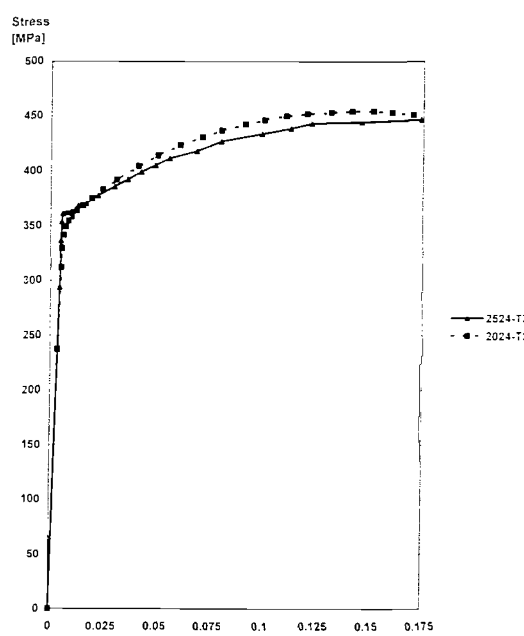

Figure 1: Stress-Strain Data 2524-T3 and 2024-T3

Cordes, Chang and Nelson [9] proposed a computational method to simulate fracture failure behavior based only on material stress strain data. The method is unique in that it does not require experimental fracture data. This paper presents improvements to the previous method. Improvements include a more sophisticated finite element model with nonlinear spring elements, a less restrictive crack initiation criteria allowing for fracture evaluation of either cracks or notches, and a more accurate crack growth criteria based on irreversible plastic strain energy near a crack or a flaw.

Specimens made from two aluminum alloys 2024-T3 and 2524-T3 (formally known as C188-T3) were selected to demonstrate the feasibility of the predictive method. Alloy 2024-T3 is the incumbent material for aircraft fuselage sheet applications. Alloy 2524-T3, a derivative of 2024-T3, has been recently developed by Alcoa to have superior fatigue and fracture toughness properties. These two alloys were chosen for their similar material properties (see the stress-strain data in Figure 1 provided by Alcoa). For each alloy, two types of specimen in the L-T orientation were tested by Alcoa. The first type was a center cracked rectangular panel (508 mm x 160 mm) with fatigue pre-cracked tip (a/W ≈ 0.25) [10]. The second type was the Kahn specimen used by Alcoa [11] for simplified fracture verifications. The Kahn specimen (Figure 2) is side notched. Its crack tip is machined, not fatigue-cracked. All test specimens were 1.6 mm thick. The fracture predictions calculated by this computational method are comparable to that of the experimental results obtained by Alcoa. This method is able to predict differences in fracture behavior for materials with similar stress strain properties.

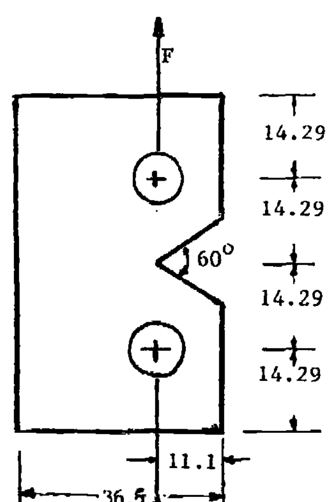

Figure 2: Kahn Specimen
Reaction Force and displacement measured from the ends of the loading pins (diameter 7.95 mm)

Fracture Prediction Method

Finite Element Model

The finite element model for predicting specimen fracture does not require special purpose finite elements such as singularity elements. All calculated examples in this study uses standard mesh with 4-node planar finite elements to model the geometry. The damage zone in front of a crack or a flaw is modeled by nonlinear spring elements. Duplicate grid points are inserted into the finite element mesh in the direction of assumed crack growth. The damage zone is represented by nonlinear springs attached between the grid point pairs. When activated, the springs act as a cohesive stress zone near the crack tip. The length of the cohesive zone is automatically determined during the finite element computation. This approach is an improvement to the Dugdale's cohesive zone model [12].

The nonlinear springs are activated only when the stress in front of a crack reaches the material proportional limit. Once activated, the springs operate between the material proportional strength limit and the ultimate strength. The nonlinear spring stiffness is derived from the material stress strain data. Spring forces are calculated from material strength, specimen thickness, and finite element mesh size. The spring displacements are assumed to behave proportional to material plastic strains. Once the springs are activated, they also represent the dissipated plastic strain energy in front of a crack. After reaching crack initiation, the first spring at the crack tip is removed and crack growth equal to one finite element length is assumed to occur. It is assumed that the amount of plastic strain energy in the damage zone determines the amount of crack growth.

The finite element model may be loaded under displacement control or load control. As the loading of the specimen is increased, crack growth is simulated by removing nonlinear springs in sequence. At each step, crack growth, damage, and reaction forces can be determined. The accuracy of the fracture prediction depends on an accurate calculation of the amount of irreversible strain energy required to advance the crack.

Crack Initiation Criterion

The critical plane strain stress intensity factor, K_{IC}, is assumed to be the indicator for crack initiation. The accepted test method to determine K_{IC} in the laboratory has been set forth by the American Society for Testing and Materials (ASTM) under Standard E399 [13]. There are stringent requirements on specimen geometry and loading condition. For most ductile materials, a valid K_{IC} test can be difficult to perform due to size requirements.

A computational method using the finite element model with nonlinear springs is developed to determine the material K_{IC} value. Plane strain finite elements are employed to simulate brittle fracture. All size and loading in the finite element model are according to ASTM specifications. The K_{IC} value is calculated based on the ASTM procedure. The ASTM procedure specifies that on the calculated load-deflection curve, draw a secant line through the origin with a slope that is 5% less than the tangent to the initial part of the curve. The load P_Q, used to calculate K_{IC}, is defined as the load at the intersection of the secant line with the original load-deflection curve. For a compact tension type specimen, the critical plane-strain stress intensity factor, K_{IC}, is calculated by the equation

$$K_{IC} = \frac{P_Q}{B \cdot W^{1/2}} f(a/W) \qquad (1)$$

where B is the specimen thickness,
W the width of the specimen,
a the crack length.

This approach determines K_{IC} numerically. The quality of the calculated K_{IC} value depends on the ability of the computational model to simulate the nonlinear stiffness of an actual specimen. The nonlinearity in the load-deflection curve of the specimen is caused by material plasticity, subcritical crack growth, or both. Material plasticity is accounted for in the computational model by the elastic-plastic material property. Physical crack growth is not. However, numerical studies have indicated that the softening in stiffness due to subcritical crack growth can be approximated by the softening effect of the one-dimensional nonlinear springs in the finite element model. This approximation is acceptable provided the amount of actual crack growth at the critical stress intensity level is small. This is a reasonable assumption for a specimen which satisfies all ASTM size requirements.

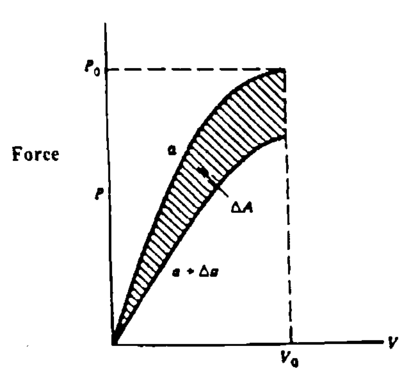

Figure 3: Determination of J Integral
Based on Displacement Control

For elastic-plastic fracture, J-integral value is considered a better indicator of material resistance to crack growth. Analogous to K_{IC} one may define the value J_{IC} which characterizes the toughness of a material near the onset of crack extension. J_{IC} is determined from the K_{IC} value by

$$J_{IC} = K_{IC}^2(1 - \nu^2)/E \quad (2)$$

It should be noted J_{IC} is sometimes defined as the J-value corresponding to minimal (0.2 mm) crack extension while in the present application it corresponds to 2% apparent crack extension.

Crack initiation is assumed to occur when J-integral of the actual component equals the J_{IC} value determined by the standard ASTM specimen. The J-integral value of an actual component may be calculated using an equivalent definition of J developed by Rice [14] who defined J as the difference of pseudo-potential energy between two identical bodies possessing slightly different crack lengths (Δa). Comparing the load versus load-line-displacement curves, the change in strain energy associated with an incremental crack advance, Δa, is the area ΔA, portrayed in Figure 3. This leads to the J value under a certain load or load-line-displacement as

$$J = \Delta A/(B \cdot \Delta a) \quad (3)$$

where B is again the specimen thickness.

Crack Propagation Criterion

In reference [9] the crack-tip-opening-displacement (CTOD) criteria was used to simulate crack growth. The required CTOD for advancement of the crack was

$$CTOD_i = CTOD_{i-1} + CTOD_I \quad (4)$$

where $CTOD_{i-1}$ was the plastic wake displacement after the previous increment of crack growth, Δa_{i-1}, and $CTOD_I$ was the crack-tip-opening-displacement at crack initiation. This approach was found not to be very accurate for some specimens.

After some parametric studies using different parameters, it was determined that the irreversible strain energy which is represented by energies of activated nonlinear springs in the finite element model provided a more accurate criteria for crack growth. The strain energy E_i required to advance a crack is

$$E_i = E_{i-1} + E_I \quad (5)$$

where E_{i-1} is the total strain energy in the springs after the previous increment of crack growth, Δa_{i-1}, and E_I is the incremental plastic strain energy required to advance the crack by the length of one finite element mesh. Equation (5) is a self-generating crack propagation criteria. As the crack growth increases, E_{i-1} dominates E_1. Nevertheless, it is important to obtain an accurate assessment of the incremental strain energy, E_1, because it determines the crack growth behavior during the initial stage of crack propagation. If E_1 is not properly assessed, the fracture prediction will be in error.

Numerical studies have indicated that the correct incremental strain energy, E_1, in equation (5) is equal to the irreversible strain energy in the nonlinear springs at the instant of crack initiation, provided the crack tip strain at this instant is above the material yield strain. The condition to reach the material yield strain may be considered a mesh size problem of the finite element model. A finer mesh will lead to a more accurate strain distribution near the crack tip and in most cases a higher crack tip strain.

If the crack tip strain corresponding to initiation is less than the yield strain, it is assumed that the mesh is too coarse to trap the singularity. In this case, a mesh refinement simulation is required. The mesh refinement simulation reduces the cohesive stress in steps and simulates a smaller amount of crack growth at each step. The procedure is as follows. After reaching crack initiation, the first spring is released slowly in several, (i), steps. This is done by replacing it with an equivalent force and checking the crack tip strain energy, $E_{t,i}$ at each step

$$E_{t,i} = E_{t,i-1} + E_{t,1} \qquad (6)$$

where $E_{t,i-1}$ is the crack tip strain energy from the previous step and $E_{t,1}$ is the initiation strain energy in the springs divided by the number of steps. At each step, the equivalent force is reduced to reflect the increased damage in front of the crack tip. This process is repeated until the crack tip strain reaches the yield strain. At this instant, the difference in irreversible strain energies required to advance the crack is E_1. The energy criteria given in equation (5) is then used to determine subsequent crack growth. Computation with a fine mesh is time consuming and expensive. Almost all calculated examples in this paper had one or two slow releasing nodes before reaching E_1. Examples which did not require the mesh refinement simulation can be found in Reference [15].

The computational procedure to simulate fracture behavior consists of a series of load or load-line-displacement increases and changes in boundary conditions due to crack front node release. These steps are repeated until no equilibrium is found.

Examples

The fracture predictive method proposed in this paper requires only material stress-strain data which are independent of component geometry. Fracture parameters or K_R-curves are not needed. Geometry and loading effects are automatically incorporated in the finite element model. To demonstrate the method it was applied to predict fracture behavior of two types of specimen made by two similar aluminum alloys. Table 1 summarizes the material strength data for the 2524-T3 and 2024-T3 sheet used in this study. Included are J_{IC} values determined by the method described in the section on crack initiation criterion. The general purpose finite element program, ABAQUS [16], was used to perform the calculations.

Table 1: Material Properties of 2524-T3 and 2024-T3

	Yield Strength MPa (kpsi)	Ultimate Strength MPa (kpsi)	Strain at Failure mm/mm	Calculated J_{IC} MPa·mm (kpsi·in)
2524-T3	362.7 (52.6)	446.8 (64.8)	0.173	17.69 (0.101)
2024-T3	349.6 (50.7)	455.0 (66.0)	0.149	14.54 (0.083)

For the particular lots of material used in this study, the yield strength for 2524-T3 was 3.7 % higher than for 2024-T3 and the ultimate tensile strength is 1.8 % lower. Stress-strain diagrams are shown in Figure 1. Although the stress-strain diagrams are similar, 2524-T3 is more resistant to fracture as reflected in the J_{IC} values. All demonstration examples were thin panels (thickness 1.6 mm). Standard four-node plane stress elements were used to model panel geometry.

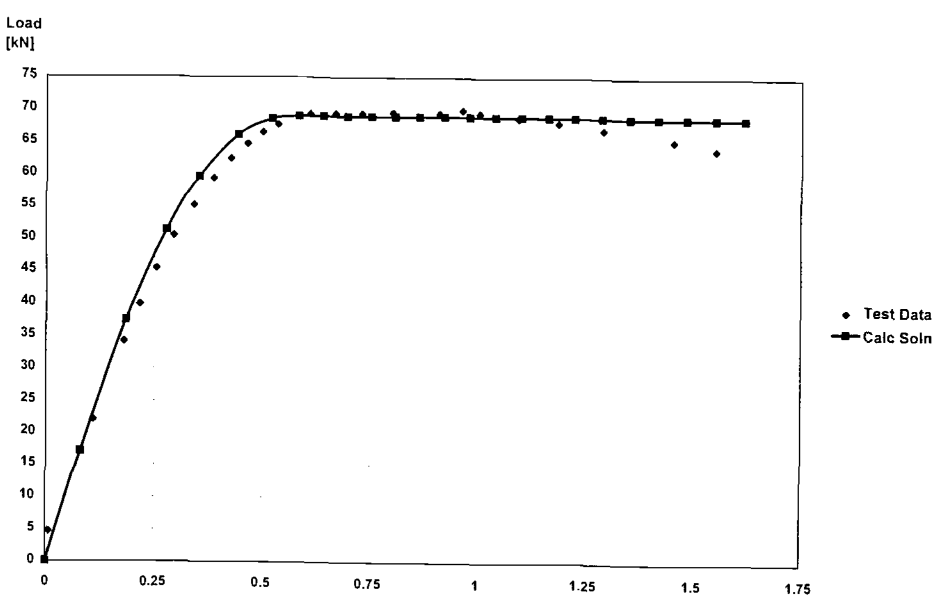

Figure 4: Center Cracked Panel, 508 mm x 160 mm, 2524-T3

Center Cracked Panel

To compare fracture behavior of the two materials, Alcoa conducted tests with 508 mm x 160 mm center cracked rectangular panels loaded under displacement control. The initial crack lengths were slightly different. Crack tips were fatigue pre-cracked. Reaction forces and gage displacements at gage span of 21.1 mm were recorded. Results are listed in Table 2 and compared with computational predictions in Figure 4 and 5. Crack initiation was determined by the *J*-integral approach. Also listed in Table 2 are the calculated load-line-displacements and the damage zone sizes corresponding to crack initiation. The calculated damage zone sizes are between Dugdale predictions based on the proportional limit strength and Dugdale predictions based on yield strength. The calculated crack growth corresponding to the peak load is larger for the 2024-T3 alloy.

Table 2: Center Cracked Panel, 508 mm x 160 mm

	Width mm	Original Crack Length mm	Load-Line-Displacement* mm	Damage Zone Size* mm	Peak Load kN	Calculated Peak Load kN
2524-T3	160	41.66	1.1176	5.486	70.02	69.24
2024-T3	160	41.02	0.9398	6.172	65.07	67.26

*at crack initiation

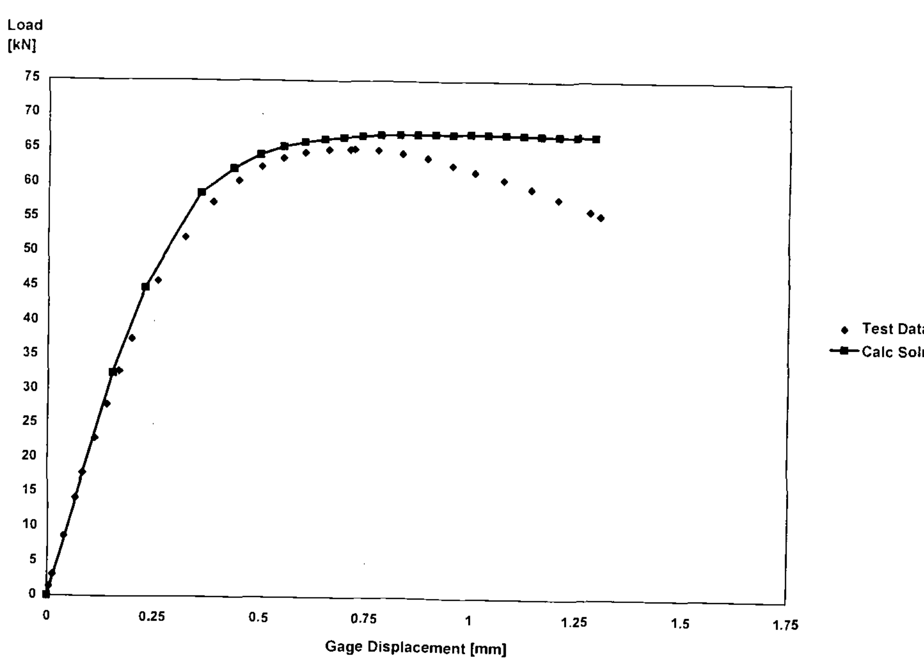

Figure 5: Center Cracked Panel, 508 mm x 160 mm, 2024-T3

Peak loads were quite accurately predicted (maximum error 3.4%) and they occur approximately at the same gage displacements as measured by testing. The computational method was able to predict the higher fracture resistance of 2524-T3. The calculated forces for the 2024-T3 specimen after the peak load as shown in Figure 5 were too high and further investigations are planned. For both materials, the calculated crack initiation loads were approximately 50% lower than the peak loads. If fracture or crack growth is not considered (standard stress analysis), the specimen will fail by plastic collapse and peak loads will occur at the maximum load-line-displacement. Specimens of these two materials will have almost identical stress distributions.

The higher strains in the specimen were located along the nonlinear springs. As enforced displacements were increased each spring reached its highest strain level just before it was removed to simulate crack growth. The maximum strain never reached the material failure strain given in Table 1, indicating that the stress-strain relation near the 'knee' of the curve has a greater effect on fracture resistance than ultimate tensile strength.

Kahn Specimen

Testing of large specimens is often impractical due to material availability, test machine capability, and/or cost. This has led to the use of smaller, less expensive tests for fracture toughness characterization. Kahn specimen is small as shown in Figure 2 and is inexpensive to test. It has a 60° notch whose tip is not fatigue pre-cracked. Material J_{IC} are the same as given in Table 1. Calculated results are listed in Table 3 and compared with experimental data in Figure 6 and 7.

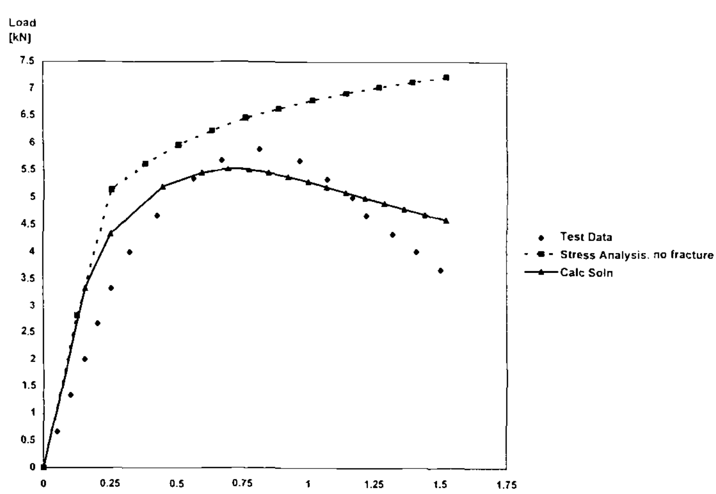

Figure 6: Kahn Specimen, 2524-T3

Table 3: Kahn Specimen

	Load-Line Displacement* mm	Damage Zone Size* mm	Load* kN	Peak Load kN	Calculated Peak Load kN
2524-T3	0.1575	3.676	3.34	5.88	5.52
2024-T3	0.1411	4.122	2.96	5.08	4.88

*at crack initiation

The applied load resulted in both tension and bending stresses in the specimen. There was substantial amount of back-side yielding during the fracture process. Due to these complications peak loads were not predicted as accurately (maximum error 6.1%).

Again the present method was able to predict the higher fracture resistance of 2524-T3. Calculated crack initiation loads were approximately 60% of peak loads which is a higher ratio compared with center cracked panel. This reflects the difference in the shape of the tip. Kahn specimen has a notched tip which is more resistant to crack initiation than a fatigue cracked specimen. The computational method was able to predict the fracture behavior during load increase quite accurately. Included in Figure 6 and 7 are results of finite element computations without considering crack growth (standard stress analysis). Without crack growth, the load versus load-line-displacement curves of these two materials are almost identical, reflecting the overall similarity in stress-strain diagrams.

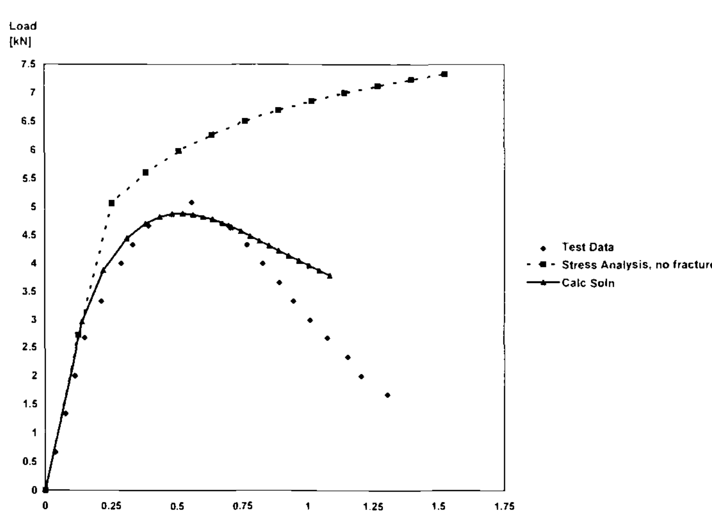

Figure 7: Kahn Specimen, 2024-T3

Conclusions

A computational method to predict the fracture behavior of thin panels with different geometry and material property was described in this paper. The method was applied to two types of specimen with two aluminum alloys having very similar stress-strain diagrams. It was able to show differences in fracture behavior due to slight differences in stress-strain diagrams. With the same material the two types of specimens did not have the same crack-tip-opening-displacement or the damage zone size in front of the crack at crack initiation. Also the fracture resistance, K_R, as function of crack growth is expected to be different. These are indications that fracture behavior is specimen geometry dependent.

Benefits of the method are summarized as follows:

- The material ranking based on fracture toughness was correct and valid for both types of specimen studied.
- The fracture behavior was predicted with the stress-strain diagram as the only material data.
- Since the load versus compliance can be determined from finite element analysis, K_R-curves can be generated by computation using this method.
- The region of the stress-strain diagram with the greatest effect on fracture behavior can be determined. This may be useful for designing new alloys for special applications.

Discussions

1) This method is based on finite element analysis. Geometry and loading effects are included. It has the potential to predict crack growth and progressive damage of complicated structural components.
2) Flawed structures operating in high temperatures experience changes in the stress-strain behavior. These changes can be described by material creep laws. With additional creep laws the present method can be applied to study creep-fracture [17].
3) Corrosion fracture is another area for future studies. Corrosion is due to pitting and oxidation of aging material. It results in time-dependent stress-strain behavior. Stress-strain diagrams can be determined from aged samples. Using stress-strain diagrams from degraded material, the residual strength of the component can be evaluated by this method.
4) The present method can also be used to study fatigue failure. Traditional fatigue prediction relies on experimental data extracted from standard specimens. It assumes that the state of stress at the crack tip is the same regardless of component geometry, loading condition, and damage history. Fatigue failure is a fracture problem. A fatigue prediction method based on computational fracture mechanics was developed by the authors [18]. It

employs finite element analysis, elastic-plastic fracture theory, and an energy approach to predict fatigue behavior.

5) This paper presents fracture predictions of thin sheet panels. Plane stress finite elements were used to model the actual specimen. Thicker panels might require three dimensional finite element analysis. The approach of the proposed method for fracture prediction, however, could remain applicable.

Acknowledgment

This paper summarizes the work sponsored by an Alcoa Foundation Science Support Grant which was awarded to Stevens Institute of Technology in June of 1995. In addition to the financial contribution we gratefully acknowledge the support feedback, and experimental data supplied by Alcoa. We also wish to thank Dr. Gary Bray for his expertise and many helpful discussions on the fracture resistance of aluminum.

References

[1] *Constraint Effects In Fracture, ASTM STP 1171*, E.M. Hackett, K.-H. Schwalbe, and R.H. Dodds, Eds, American Society for Testing and Materials, Philadelphia, 1993.

[2] Anderson, Vanaparathy, N.M.R., and Dodds, R.H., Jr, "Predictions Of Specimen Size Dependence on Fracture Toughness for Cleavage and Ductile Tearing," *Constraint Effects In Fracture, ASTM STP 1171*, E.M. Hackett, K.-H. Schwalbe, and R.H. Dodds, Eds, American Society for Testing and Materials, Philadelphia, pp. 473 -491, 1993.

[3] Panontin, T.L. and Sheppard, S.D., "The Relationship Between Constraint and Ductile Fracture Initiation as Defined by Micromechanical Analyses," *Fracture Mechanics: 26th Volume, ASTM STP 1256*, Walter G. Reuter, John H. Underwood, and James C. Newman, Jr., Eds., American Society For Testing And Materials, Philadelphia, pp. 54-85, 1995.

[4] Mackenzie, A.C.,, Hancock, J.W., and Brown, D.K., "On the Influence of State of Stress on Ductile Failure Initiation in High Strength Steels," *Engineering Fracture Mechanics*, Vol. 9, pp. 167-188, 1977.

[5] Rice, J.R., and Tracey, D.M., "On the Ductile Enlargement of Voids in Triaxial Stress Fields", *Journal of Mechanics and Physics of Solids*, Vol. 17, pp. 201-217, 1969

[6] Schwalbe, K-H, "Introduction of δ_5 as an Operational Definition of CTOD and its Practical Use", *Fracture Mechanics: 26th Volume, ASTM STP 1256*, Walter G. Reuter, John H. Underwood, and James C. Newman, Jr., Eds., American for Testing and Materials, pp. 763-777, 1995.

[7] Newman, J.C., Jr., Dawicke, D.S., and Bigelow, C.A., "Finite-Element Analysis and Fracture Simulation in Thin-Sheet Aluminum Alloy", NASA Technical Memorandum 107662, NASA Langley Research Center, Hampton VI 23665-5225, 1992.

[8] Newman, J.C., Jr., Crews, J.H., Jr., Bigelow, C.A., and Dawicke, D.S., "Variations of a Global Constraint factor in Cracked Bodies under Tension and Bending Loads", *Constraint Effects In Fracture, ASTM STP 1171*, E.M. Hackett, K.-H. Schwalbe, and R.H. Dodds, Eds, American Society for Testing and Materials, Philadelphia, pp. 21-42, 1993.

[9] Cordes, J., Chang, A., Nelson, N., Kim, Y., "A Computational Method to Predict Elastic-Plastic Fracture," *Engineering Fracture Mechanics,* Vol. 51, No. 1, pp. 151-159, 1995.

[10] Bray, G.H. and Yeh, J.R., "Evaluation of R-Curve Prediction Methodology for thin products," Report No. ED.-96-02, Alcoa Technical Center, 100 Technical Drive, Alcoa Center, PA. 15069-0001.

[11] Yeh, J.R., Bray,, B.H., Bucci, R.J., "Prediction of R-Curves from Small Coupon Tests," *FAA/NASA International Symposium on Advanced Structural Integrity Methods for Airframe Durability and Damage Tolerance*, edited & reviewed by C.E. Harris of NASA, NASA Conference Publication 3274, September 1994.

[12] Dugdale, D.S., "Yielding of Steel Containing Slits," *Journal of Mechanics and Physics of Solids,* 8, 1960, p.8.

[13] *Annual Book of ASTM Standards,* Section 3 Metals Test Methods and Analytic Procedures, Vol. 03.01, American Society for Testing and Materials, Philadelphia, 1995, pp. 412-442.

[14] Rice, J.R. "A Path Independent Integral and the Approximate Analysis of Strain Concentration by Notches and Cracks." *Journal of Applied Mechanics*, Vol. 35, 1968, pp. 145-386.

[15] Cordes, J.A., Chang, A.T., "Predicting Fracture Behavior in Aluminum Panels using Stress/strain Diagrams", Project Report Number Sitme-005-Alcoa, Stevens Institute of Technology, 1995.

[16] ABAQUS, Hibbitt, Karlson & Sorensen, Inc., Pawtucket, R.I.

[17] Chang, A., and Kim, Y., "Creep Fracture by Finite Element Method," Proceedings of the Joint FEFG/ICF International Conference on Fracture of Engineering Materials & Structures, Singapore, 6-8 August 1991, pp. 605-610.

[18] Chang, A., Nelson, N., Cordes, J., and Kim, Y., "Fatigue Prediction Based on Computational Fracture Mechanics," *Third Symposium on Advances in Fatigue Lifetime Predictive Techniques, 3rd Volume, ASTM STP 1292*, M.R. Mitchell and R.W. Landgraf, Eds., American Society for Testing and Materials, 1996, pp. 100-115.

Francis I. Baratta[1]

THE EFFECT OF CRACK INSTABILITY/STABILITY ON FRACTURE TOUGHNESS OF BRITTLE MATERIALS

REFERENCE: Baratta, F. I., **"The Effect of Crack Instability/Stability on Fracture Toughness of Brittle Materials,"** Fatigue and Fracture Mechanics: 28th Volume, ASTM STP 1321, J. H. Underwood, B. D. Macdonald, and M. R. Mitchell, Eds., American Society for Testing and Materials, 1997.

ABSTRACT: This paper summarizes three recent experimental works coauthored by the present author regarding the effect of crack instability/stability on fracture toughness, and also includes the necessary formulae for predicting stability.

Two recent works have shown that unstable crack extension resulted in apparent increases in fracture toughness compared to that determined during stable crack growth. In the first investigation a quasi–brittle polymer, polymethylmethacrylate, was examined. In the second, a more brittle metallic material, tungsten, was tested. In both cases the transition from unstable to stable behavior was predicted based on stability analyses. The third investigation was conducted on a truly brittle ceramic material, hot pressed silicon nitride. These three papers showed that fracture toughness test results conducted on brittle materials vary according to whether the material fractures in an unstable or stable manner. Suggestions for achieving this important yet difficult phenomenon of stable crack growth, which is necessary when determining the fracture toughness variation occurring during unstable/stable crack advance, are presented, as well as recommendations for further research .

KEYWORDS: Unstable/stable crack growth, stability criteria, compliance, fracture, fracture toughness, polymethylmethacrylate, tungsten, hot pressed silicon nitride

---

INTRODUCTION

Stable crack extension is difficult to obtain for very brittle materials in many of the loading geometries for which a straight through crack extends into an increasing stress intensity field. For ceramic materials with flat R–curves, stability is all but unattainable when testing under conventional conditions. Yet it appears that stable crack extension would be desirable when testing brittle materials and even necessary for well controlled fracture experiments, such as fracture toughness, R–curve, and fatigue crack growth measurements. The implicit question here is whether or not the results obtained from tests with stable crack extension differ from those obtained when only the onset of unstable fracture is experienced.

There have been only a few experimental papers in the literature concerning the subject of stable fracture of quasi–brittle and brittle materials. These papers pertinent to the present work are discussed in the following paragraphs to provide background to the subject, as well as those dealing with crack

[1]Consultant, 138 Ridge Street Arlington, MA 02174-1737

stability prediction.

Nakayama [1], who defined effective fracture energy as that energy required to separate the test piece, used effective fracture energy data to show that the energy values for stable fracture of plate glass were much lower than those for semistable fracture. Stable fracture was obtained using a stiff testing system. The results of Cooper's study of rock materials [2] agreed with the general trend shown in [1]. It was also realized in [2] the importance of the loading system stiffness in attaining stable crack growth, as well as providing a suitable starter notch. Margolis et al. [3], showed a similar trend in the determination of fracture toughness of polymethylmethacrylate (PMMA),which is a material used in one of the studies summarized in this paper. Reddy et al. [4] , in their study of fracture toughness of glass and glass-ceramics noted the same trend.

At the time Nakayama [1] published his paper an analysis which could predict stable fracture for brittle materials was not available. Subsequently, other researchers have defined stable and unstable fracture in terms of the beam geometry, material and testing machine parameters. All of these papers utilized energy considerations, i.e., energy release rate, which was the basis for prediction of stability given in these studies presented here.

Several papers: Clausing [5], Bluhm [6], and Schimmoeller[7] have provided theoretical crack stability analyses applied to linear elastic systems all based on similar principles. In [5] the compliances of beam and compact specimens were theoretically determined and were applied toward the formulation of stability criteria. Elegant stability formulations [6] were provided for a bend specimen having a chevron notch (CV) or a straight through crack (STC), which was motivated by an alternative approach to instability through the use of the "work of fracture" (WOF) specimen, proposed by Tattersall and Tappin [8]. Such stability criteria for the three-dimensional CV and WOF specimens were able to be provided [6] because of a previous paper intended for that purpose by Bluhm [9]. In this latter paper an approximate two dimensional "slice synthesis" technique aided in analytically describing the compliance of a three dimensional geometry. A displacement-controlled closed loop testing system was considered in [7]. Stability enhancement was predicted for the improved system response due to the addition of closed loop considerations. All three authors of [5 - 7], as well as the authors of [1] and [2], realized the important role of the testing system compliance or stiffness in attaining stability during fracture. Also, it was noted in [5] and [6] that under no circumstances would a load-controlled STC beam system display stable crack growth.

Later Sigl [10] advanced the theoretical analyses mentioned above where stability criteria of everyday testing situations were explored. This author examined the stability of three-point flexure STC and CV specimens under constant-load and constant displacement rate-loading of the testing machine, taking into account the load cell compliance in a closed loop testing arrangement under constant deflection. This latter situation enhances stability in beam flexure systems, which was also reported [7].

Recent progress has been made in introducing controlled cracks in ceramic beam specimens such that the difficulties described by the authors of [1] and [6], have been greatly mitigated. Nose and Fujii successfully introduced straight through precracks using the "bridge indentation" method [11] to obtain fracture toughness of brittle materials. In this technique, the specimen is initially flawed by microindentation and then compressed between two anvils, one of which is bridged, thus creating a short pop-in crack. Bar-On and co-workers [12], as well as Choi et al. [13], used this technique to evaluate the effect of the precracking parameters on crack emplacement of beam specimens of various ceramics including hot pressed silicon nitride (HPSN), which was also the material used in one of the studies summarized in this paper. The bridge indentation method (or double anvil geometry) was also employed in this same work to initiate and control precracks of desired length to explore the effect of crack growth stability (or lack thereof) on fracture toughness of brittle materials.

The more recent works of Baratta and Dunlay [14] and that of Underwood et al. [15], have shown that unstable crack extension resulted in an apparent increase in fracture toughness compared to that determined during stable crack growth of a quasi–brittle polymer, PMMA [14], and a more brittle metallic material, tungsten [15]. In both cases the transition from unstable to stable behavior was predicted based on stability analyses. A further investigation of this important phenomenon was conducted by Bar-On et al. [16], on a brittle ceramic material, HPSN, which corroborated the trend shown in [14] and [15]. These three investigations, which have shown that fracture toughness of brittle materials is dependent upon unstable/stable crack advance, are the basis for this paper and are described and summarized in that which follows. Suggestions for achieving stable crack growth during fracture testing of brittle materials, as well as suggested further research are presented

THEORETICAL ANALYSES

Previous work [14] demonstrated that the three–point loaded beam tended to be more stable than the constant moment beam. For this reason only the three-point loaded beam with a STC is considered in the stability analysis. Nevertheless, experimental data taken from [14], which includes that which is applicable to the four-point loaded beam, as well as the three-point loaded beam are presented later. In addition, a straight through-cracked-three-point loaded round beam is also considered. Therefore, the nomenclature for the three-point loaded and four-point loaded rectangular beams; and the three-point loaded round beam is shown in Figs. 1a, 1b and 1c, respectively.

Stability considerations are well presented elsewhere [5 - 7, 10] and therefore a general derivation is not repeated here. However, some comments are appropriate: The general stability equation that is used here, (as well as those papers that are summarized) taken from [6], presumes that an idealized testing system is utilized when determining fracture toughness of a brittle material. It is inferred that constant crosshead displacement is employed and that rigid body motion occurs between the crosshead of the testing machine and at the point of load application to the specimen, i.e., the deflection of the load cell is ignored.

The analysis presented in [10] comes closest to defining the actual test set–up, yet in order to apply such a formulation additional measurements beyond the usual monitoring of load and displacement would have had to be made during testing. Thus, the more idealized analysis in [6] was chosen in all three of the subject papers to guide the experiments that are later described. Only the stability formulation under constant crosshead displacement or stroke rate of the testing machine was considered. The applicable general equation, taken from [6] for arbitrary kinds of specimens, is:

$$S = d^2(\delta_s/P)/dA^2 - (2/\delta_t/P)(d(\delta_s/P)/dA)^2/\ d(\delta_t/P)/dA \tag{1}$$

Where δ_s and δ_t represent the load-point displacement of the specimen and the total load-point displacement, respectively, A is the crack area, δ_s/P is the specimen compliance and δ_t/P is the total compliance, which includes the compliance of the specimen, the testing machine and the fixtures. It is noted that the above stability equation is applicable only to those materials exhibiting flat R–curve behavior.

If for specific types of specimens, such as those in [14 - 16], and considered here, the term $1/d(\delta_t/P)/dA$ does not change sign during the process of crack extension, then this parameter can be ignored, see Quizi and Xuefu [17], so that Eq. 1 reduces to:

$$S = d^2(\delta_s/P)/dA^2 - (2/\delta_t/P)(d(\delta_s/P)/dA)^2 \tag{1a}$$

If the beam is rectangular in cross–section, then the stability equation for this specific case can be

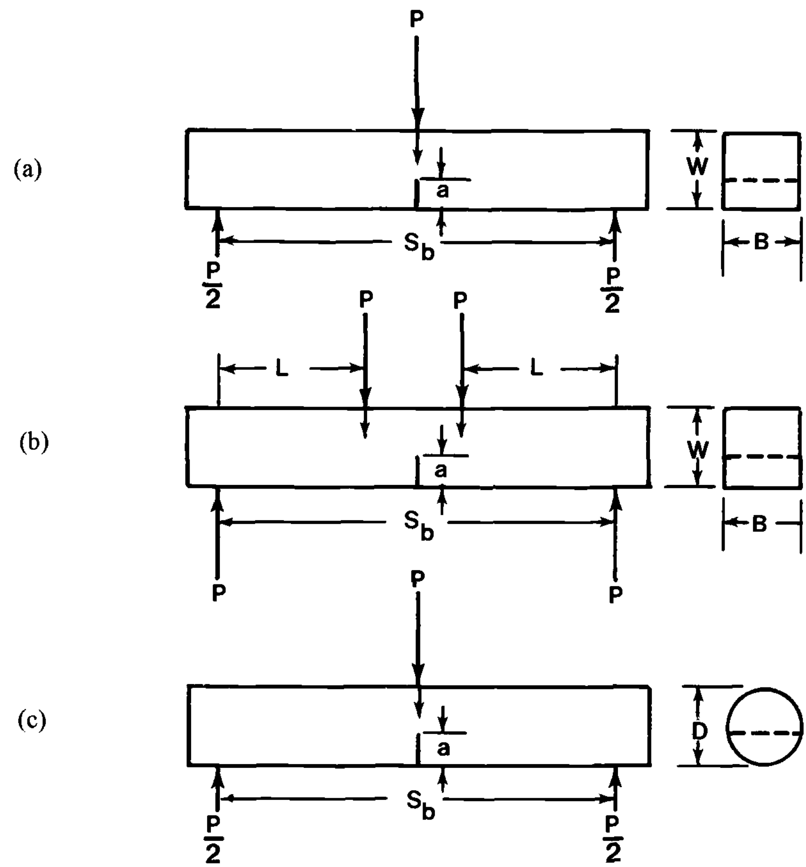

Fig. 1 -- (a) Three-point loaded rectangular beam , (b) a four-point loaded rectangular beam, and (c) a three-point loaded round beam.

further simplified to:

$$S = d^2\lambda_s/d\alpha^2 - (2/\lambda_t)(d\lambda_s/d\alpha)^2 \tag{2}$$

Where λ_s and λ_t are the normalized compliances, i.e., $\lambda_s=(\delta_s/P)EB$, $\lambda_t=\lambda_s+\lambda_m$, and $\lambda_m=(\delta_m/P)EB$. Also α is the normalized crack length a/W, (see Fig. 1), W is the beam height, E is the modulus of elasticity of the material and B is the beam width.

According to [6] the more negative S becomes the greater the probability of achieving stability. Note that all that is required in the above stability equations is the knowledge of the compliance of both the specimen (as a function of α) and the testing machine, including the fixtures. The compliance of the test set-up is usually obtained by experimental means, and the compliance of the specimen can be determined by theoretical considerations, see [14 - 16]. The nondimensional plane stress compliance of the cracked three-point loaded beam of rectangular cross-section, shown in Fig. 1a, is:

$$\lambda_s = 2(S_b/2W)^2\{S_b/2W+[2.85/(S_b/2W)-0.42/(S_b/2W)^2]/4 + 9\int\alpha[f(\alpha)]^2d\alpha\} \tag{3}$$

It is noted here the plane stress condition is considered more appropriate because: When the crack is small the contribution to the beam deflection (the last factor in Eq. 3) is also small, even though the volume of material in front of the cracked portion experiences a plane strain condition. When the crack is large, intact material in front of the crack still experiences a plane strain condition but this relatively small volume of material provides little contribution to the beam deflection. Therefore, plane stress is considered the more appropriate condition rather than plain strain used in [14 - 16] and is adopted here.

In Eq. 3, S_b is the beam support length (see Fig. 1), and $[f(\alpha)]$ is the polynomial expression for the rectangular three-point loaded beam, which is also incorporated in the following stress intensity factor relationship:

$$K_I = (6Ma^{1/2}/BW^2)[f(\alpha)] \tag{4}$$

Where M is the applied moment and $[f(\alpha)]$ represents the following polynomial:

$$[f(\alpha)] = A_0+A_1\alpha+A_2\alpha^2+\ldots+A_n\alpha^n \tag{5}$$

The coefficients used in Eq. 5 and subsequently in Eq. 6 are given below (Table 1) for the beam span ratios presently applied in each of the subject papers and were obtained in this work by matching the numerical data of Freese [18], (who claims an accuracy of better than 1 percent) to an accuracy of less than ½ percent. These data were obtained by a weight function argument and a boundary collocation technique. Because the formulation in [18] accounted for the applied load contact stress on the stress intensity factor associated with the centrally loaded beam and the experimental results deal with short crack lengths (as well as long); Eqs. 4 and 5 are adopted for use here.

The stability of the rectangular beam systems can be determined by substituting the first and second derivatives of the compliance obtained from Eq. 3 into Eq. 2, and normalizing by

$$\Phi = 18(S_b/2W)^2\alpha[f(\alpha)]^2 \tag{6a}$$

This gives the following nondimensional stability equation defined by $S_s = S/\Phi$ for the rectangular three-point loaded beam:

$$S_s = 2(d[f(\alpha)]/d\alpha)/[f(\alpha)] + 1/\alpha - 36(S_b/2W)^2[f(\alpha)]^2/\lambda_t \tag{6}$$

The compliance of a beam of round cross-section, as shown in Fig. 1c, can also be represented by a polynomial:

$$\lambda_s = (\delta_R/P)ED = [f(\beta)] = B_0 + B_1\beta + B_2\beta^2 + B_3\beta^3 + B_4\beta^4 \qquad (7)$$

Where δ_R is the load-point displacement, D is the beam diameter and β is the normalized crack length a/D. The coefficients for the above polynomial equation were developed by Baratta [19] from the data of Qizhi [20], who utilized the slice synthesis method [9]. In the above equation, β is valid between 0 and 0.70. The coefficients in Eq. 7 are given for the beam span ratios (Table 2) used in this present work and are considered more appropriate than those previously determined in [15].

TABLE 1-- Coefficients for the polynomial equation, Eq. 5[1].

S_b/W	4	5	6	6.88	7	8
A_0	1.8936	1.9179	1.9235	1.9323	1.9323	1.8931
A_1	-2.2743	-3.6206	-2.1704	-2.0826	-2.0825	-2.2644
A_2	6.2146	33.1919	6.1548	5.5327	5.5327	6.1442
A_3	11.6445	-165.7795	11.1950	13.2536	13.2536	11.8603
A_4	-43.6094	-42.9833	471.4846	-45.7716	-45.7716	-43.9867
A_5	46.3885	45.9773	-632.9601	47.4841	47.4841	46.5384
A_6	0	0	332.5167	0	0	0

[1]Equation 5 is valid between 0 and 0.70 for all S_b/W's except S_b/W of 5, which is valid between 0 and 0.80.

TABLE 2 -- Coefficients for the polynomial equation, Eq. 7.

S_b/D	4	5	6	6.67	8
B_0	31.5777	64.9668	98.3463	133.3696	226.2232
B_1	-18.5004	-29.3125	-40.2379	-48.8498	-66.9530
B_2	338.1554	547.7236	758.5683	930.0268	1305.6520
B_3	-867.6517	-1367.2980	-1870.7580	-2264.9250	-3101.8690
B_4	1430.6820	2288.2580	3149.2430	3845.0760	5374.2430

Again, the term $1/d(\delta_t/P)/dA$ can be ignored in Eq. 1 since it does not change sign during crack extension for a round beam of the material considered in this study. Thus Eq. 1a was employed to obtain the stability parameter, η, for the round three-point loaded beam in terms of the nondimensional crack length β, as given below (see [15] for details):

$$\eta = (d^2[f(\beta)]/d\beta^2)/[\beta(1-\beta)^{1/2}] - (d[f(\beta)]/d\beta)(1-2\beta)/[4\beta(1-\beta)^2] - (d[f(\beta)]\beta/d\beta)^2/[\beta(1-\beta)\lambda_t], \qquad (8)$$

(a)

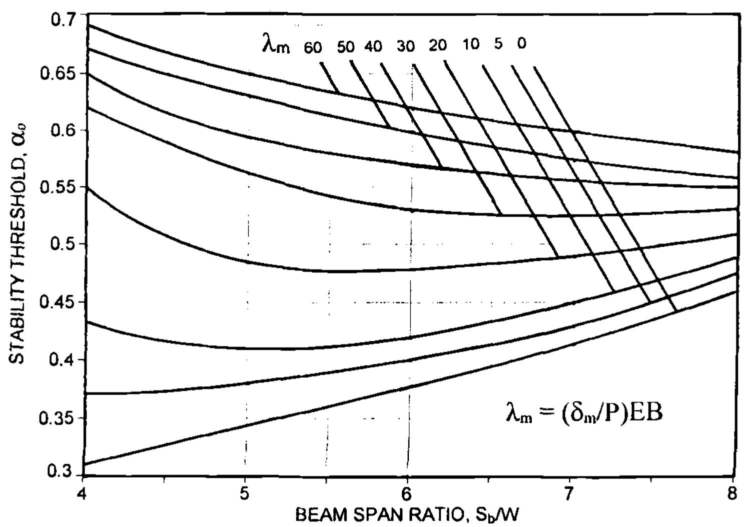

(b)

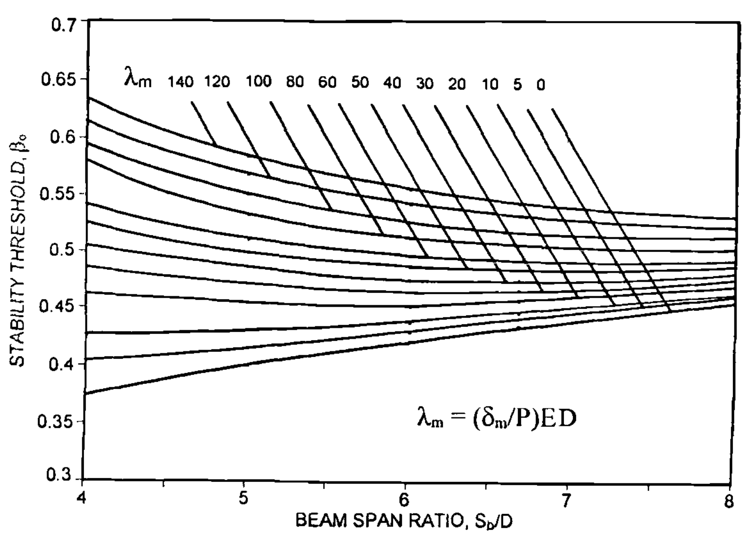

Fig. 2 -- Threshold of stability for a three-point loaded (a) rectangular beam and (b) a round beam.

Where $\beta = a/D$, $\lambda_t = \lambda_s + \lambda_m$, $\lambda_s = (\delta_R/P)ED$, and $\lambda_m = (\delta_m/P)ED$.

The wide range stress intensity factors utilized here for the round bend bar under three-point loading for S_b/D ratios from 3.0 to 8.0 were also developed By Baratta [21] from the data supplied in [20]. In addition, for the specific span ratio of 3.87 used here, the following normalized wide range stress intensity factor in the form of a simple fourth order polynomial is considered more appropriate than that given previously in [15]:

$$(K_I D^{5/2}/PS_b)(1-\beta)^2/\beta^{1/2} = 3.82 - 10.21\beta + 14.91\beta^2 - 8.98\beta^3 + 1.68\beta^4 \tag{9}$$

Where β can range from 0 to 1.00

The specimen compliance for span–to–width ratios ranging from 4 to 8 for the rectangular cross-sectioned beam was determined from Eq. 3 as previously described. These results were in turn programmed into Eq. 6 to obtain the stability parameter, S_s as a function of beam span ratios and machine compliances. By determining when S_s becomes zero, the threshold of stability for the rectangular beam, termed here α_0, can be obtained. These results are shown in Fig. 2a.

Polynomial equations of the form given in Eq. 7 for the compliance of a round beam having beam span ratios of 4 to 8 were operated on according to Eq. 8 to obtain the stability parameter η. Again by determining when η becomes zero the threshold of stability, β_0, can be realized. The effect of machine compliance, which was varied from 0 to 140, on the threshold of stability as a function of S_b/D, is shown in Fig. 2b.

Figures 2a and 2b, where $\alpha_0 = a/W$ and $\beta_0 = a/D$, provide guidance for stable fracture toughness testing of three-point loaded rectangular and round beams, respectively. Appropriate comments on this subject are subsequently presented.

MATERIALS

The materials used in the three independent studies for stability and fracture toughness tests were PMMA, tungsten, and HPSN; their nominal values of physical and mechanical properties are available below (Table 3.). For additional detailed information see [14 - 16].

BEAM GEOMETRIES

The pertinent dimensions and geometric parameters for the three systems examined are given in tabular form (Table 4) below.

MACHINE COMPLIANCES

Stability calculations were used in all three papers to provide guidance for designing test systems that would be stiff enough so that quasi-static crack advance could be attained where possible. Not only is the stiffness of the test system important but also the modulus of elasticity as well. For example, when testing beam specimens of PMMA [14] no special fixturing was required and thus it was not difficult to accomplish stable crack growth with specimens having large crack lengths, because the modulus of elasticity of PMMA was relatively low. However, when testing tungsten or HPSN considerable effort was required, regardless of the crack length, to realize stable crack advance. The values of each of the system compliances, which includes the testing machines, the load cells and fixturing arrangements, were determined by experimentally measuring the displacements using uncracked specimens. These measured compliances corresponded to the dimensionless machine compliances for each of the systems that were examined; they are shown below (Table 5). Also shown are the predicted threshold of stability ratios α_o and β_o, obtained as previously mentioned, for the rectangular and round beams, respectively.

TABLE 3 -- Physical and mechanical properties of test materials.

	Tensile Strength MPa	Elastic Modulus GPa	Hardness ---	Density g/cm^3	Fracture Toughness MPa m$^{1/2}$	Grain size mm
PMMA[1]	65	3.2	n/a	---	1.13[2], 1.61[3]	---
Tungsten[4]	1400	345	400 HB[5]	19	60	---
HPSN[6]	825 $\pm$ 137[7]	320	16 GPa[8]	3.25	4.0 to 4.9[9]	3

[1]See [22]. [2]Stable fracture, see [3]. [3]Unstable fracture, See [3]. [4]Data and material supplied by GTE Products Corp. , Towanda, PA. [5]Brinell hardness. [6] NC 132 manufactured by Norton Co., Worcester, MA. [7]Modulus of rupture. [8]Vickers hardness. [9]See [16] and Table 7.

TABLE 4--Beam geometries.

	PMMA 3-Pt	PMMA 4-Pt.	Tungsten (3-Pt.) Rectangular	Tungsten (3-Pt.) Round	HPSN (3-Pt.) Rectangular
W, mm	11.63	11.63	28.0	---	8.0
B, mm	8.13	8.13	14.0	---	6.0
D, mm	---	---	---	32.8	---
S_b/W	6.88	6.88	4.0	---	5.0
S_b/D	---	---	---	3.87	---
L_l/S_b	---	3/8	---	---	---

EXPERIMENTAL METHODS

The experimental work described in this section was accomplished by three different investigators at three different laboratories, i.e.,the PMMA, tungsten, and HPSN tests were conducted at the: Army Research Laboratory, Watertown, MA; Army Armament RD&E Center, Watervliet, NY and Worcester Polytechnic Institute, Worcester, MA, respectively.

PMMA

Starter cracks were produced in the beams, whose sides were polished, by first introducing a shallow notch, then a crack was initiated at the base of the notch using a razor blade and was extended to the desired depth by a wedge opening technique. The three-point loaded beams were centrally loaded and the four-point beams were loaded at the distances L, where $L/S_b = 3/8$, see Fig. 1b. To minimize the effect of the environment on the experimental results, the beams were loaded as rapidly as practicable in stroke control at a cross-head speed of 5 mm/min.

Experimental determination of stability was accomplished by evaluating load-displacement curves of quasi-brittle beams of PMMA having starter crack length ratios α, ranging from approximately 0.1 to 0.9. These ratios were designed to yield unstable and stable fracture based on the predicted threshold of stability crack ratio α_o for the examined beam configurations.

TABLE 5 -- Nondimensional machine compliances and predicted stability ratios for test systems.

		Rectangular		Round	
		3-Pt	4-Pt.	3-Pt.	
	λ_m	α_o		λ_m	β_o
PMMA	5.2	0.42	0.52	---	---
Tungsten	28	0.61	---	59	0.54
HPSN	59	0.65	---	---	---

The critical stress intensity was calculated by two different methods, see [14]: In the first method, K_{Ic} was obtained in the conventional manner. The second method, which was deemed more accurate than the first (this is discussed later), was calculated by utilizing the area under the load-displacement curve to determine the energy of fracture, then this was divided by the cracked area, which yielded the critical strain-energy-release rate G_{Ic}. The well known relationship between fracture toughness and critical strain-energy-release rate was employed. However, the elastic modulus E, which was needed to determine G_{Ic} and the resulting K_{Ic}, was obtained by using a beam compliance method and was found to be 3.17 GPa. This compared well with data in the literature (Table 3).

Tungsten

Rectangular beam specimens were removed from the round bars, see Fig. 1a. Fatigue cracking and fracture toughness testing was accomplished according to ASTM Standard Test Method for Plane-Strain Fracture Toughness of Metallic Materials (E-399), except bottom surface displacement, through a formulation given in [15], as opposed to crack-mouth displacement, was used on all beam configurations. However, special precautions were necessary to successfully precrack the specimens. That is by carefully controlling and monitoring the fatigue loads successful variations in the crack lengths were attained. Thus five specimens having crack length ratios α, varying from 0.500 to 0.664 were successfully fatigue cracked and fracture tested. As previously mentioned, the range of the crack length ratio was designed to result in both unstable and stable fracture.

The specimen configuration for the round bar fracture toughness tests and analysis is shown in Fig. 1c. Six specimens having crack length ratios varying from 0.519 to 0.685 were successfully fatigue cracked and fracture tested. This round bar configuration is well-suited to fracture tests in the L-R orientation shown in the figure, i.e., with the crack plane perpendicular to the longitudinal axis of the bar and crack growth in the radial direction. This configuration is particularly useful for round bar samples of high strength materials that are difficult to machine, such as the tungsten alloy tested here and structural ceramic materials in the form of round bars. Machined flats at the ends of the bar (not shown in Fig. 1c) were added to facilitate the test set-up and to eliminate the point loads that would occur between specimen and support rollers with no flats present, see [15].

The fracture toughness tests were conducted wherever possible, in accordance with ASTM E-399, except that a convenient span ratio of 3.87 rather than 4.0 was used for the round beams.

HPSN

The specimens were cut from a 3/4 inch thick (19.1 mm) plate with the hot pressing direction perpendicular to the long direction of the specimen and parallel to the crack growth direction. All specimens were carefully polished on the side and top surfaces. Again as in the above mentioned studies the span of the crack length ratio was designed to explore both the unstable and stable fracture regions.

The specimens were indented with a Vickers indenter using loads ranging from 69 to 490 N. These specimens were then loaded in a bridge indentation compression fixture [11] creating straight precracks. Precrack lengths were used for fracture toughness calculations and were measured from the surfaces of the broken specimens. Seventeen specimens with α ranging from 0.26 to 0.78 were successfully precracked using the bridge indentation method and fracture tested. Experimental evaluation of the theoretical predictions of stability was determined from the measured load-point displacement. One specimen with a crack length of $\alpha = 0.75$ was tested on a more compliant articulating fixture; the reason for this will be discussed later.

RESULTS

PMMA

Typical load displacement curves of each failure mode are shown in Fig. 3. Examination of the shape of these curves readily allowed detection of unstable/stable crack growth during fracture. Cross-head displacement was utilized for the displacement of the beam specimens. Two distinct modes of failure were observed. For small initial crack length ratios α, the crack extended in an unstable manner characterized by a reasonably linear loading curve followed by a nearly instantaneous crack extension through the entire cross section and corresponding vertical drop in the load curve. Above a threshold value of α_o, failure occurred in a stable fashion. The crack would extend rapidly at first but then slow exponentially, even though the compliance of the beam increased.

The predicted values (Table 5) of α_o are 0.42 and 0.52 for the three-point and four-point loaded beams, respectfully, which are higher than the corresponding experimental values determined to be 0.36 and 0.46. This was not unexpected, because some plasticity will occur at the crack tips of a quasi-brittle material such as PMMA, enhancing stable crack growth and thus lowering the threshold of stability.

The method by which crack starters were initiated gave rise to cracks that were not completely flat-fronted; indeed many were not within the requirement specified by ASTM E-399, which led to inaccuracy in the determination of fracture toughness. This also led to a greater degree of scatter compared to the energy method. Therefore, crack lengths were alternatively determined by using the functional relationship between crack depth and specimen compliance, which inherently resulted in an integrated average of the crack lengths after taking account of the compliance of the testing machine, load cell, and test fixtures. This resulted in a decrease in scatter for the data. Thus, only the energy method results as applied to all of the specimens that failed in a stable manner, as well as those that did not, are reported here. However, the energy method can be validly applied only to specimens that have failed stably, because the area under the load-displacement curve for unstable failure includes the energy of fracture plus excess energy that manifests itself in the form of kinetic energy in the broken parts. The energy method results for unstable specimens cannot be considered as completely accurate, the error, nevertheless, is considered small because the specimens were not highly unstable. These fracture toughness results are are shown in Fig. 4a and 4b for the three-point and the four-point loaded beams, respectively, as well as α_0, the predicted stability threshold, shown by the vertical line.

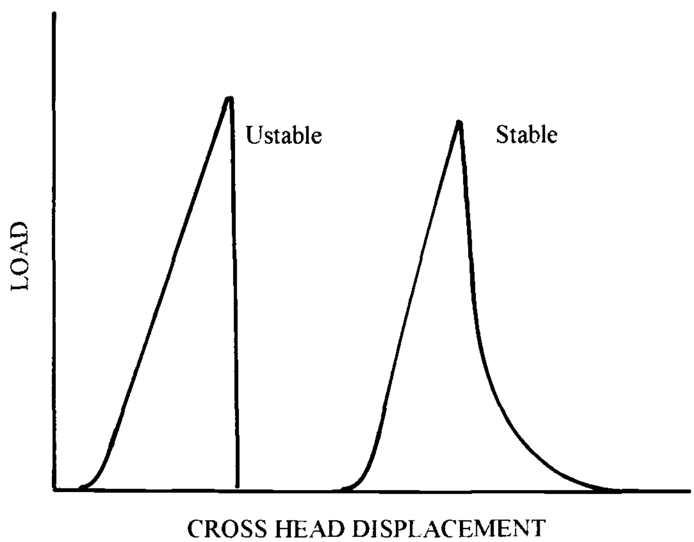

Fig. 3 -- Typical unstable and stable load-point displacement for PMMA.

Notice the definite downward trend of the K_{Ic} data in both Figs. 4a and 4b as the initial crack length increases. The vertical line in each figure indicates the predicted value of the threshold of stability. The range in fracture toughness, as shown in Fig. 4a and Fig. 4b, goes from a high of 1.38 to a low of 0.97 MPa $m^{1/2}$, and from a high of 1.24 to a low of 0.94 MPa $m^{1/2}$, respectively.

Presented below (Table 6) for comparison are the results shown in Fig. 4a and 4b. The means and the standard deviations of the unstable and stable fracture toughness results for the two specimen types are compared including their percent difference , as well as their combined mean. The K_{Ic} mean for the unstable and stable three-point loaded PMMA test specimens are shown as 1.25 and 1.06 MPa $m^{1/2}$, respectively, representing a difference of 18 percent; the combined mean is given as 1.14 MPa $m^{1/2}$. The K_{Ic} mean for the unstable and stable four-point loaded test specimens are shown as 1.15 and 1.06 MPa $m^{1/2}$, respectively, representing a difference of 8 percent; and the combined mean is given as 1.09 MPa $m^{1/2}$. Notice that the stable fracture toughness for both specimen types is the same, i.e., 1.06 MPa $m^{1/2}$. The combined K_{Ic} mean for both specimen types agree quite well with each other, when considering their standard deviations, and the data available in the literature [3].

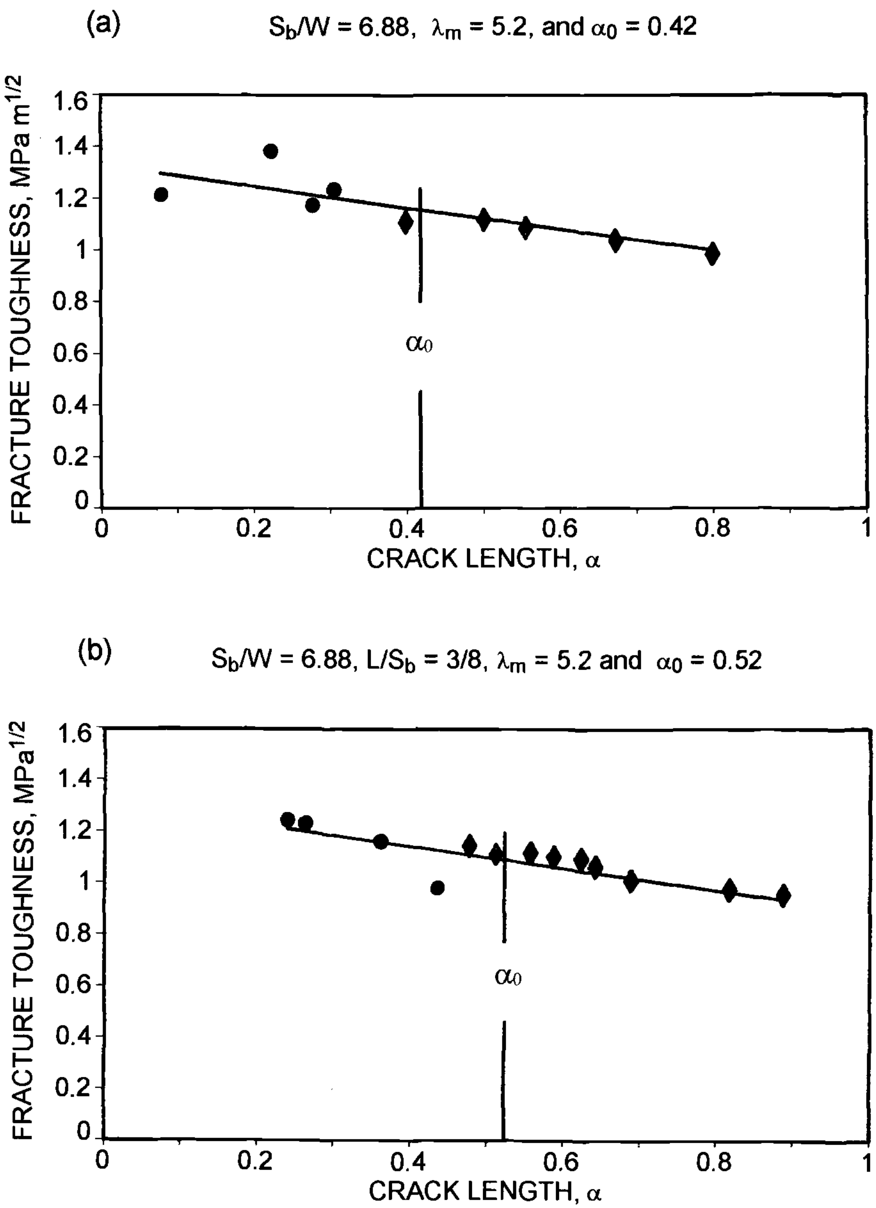

Fig. 4 -- Fracture toughness for PMMA (a) three-point and (b) four-point loaded beams; ● = unstable and ♦ = stable.

Tungsten

The numbers of fracture toughness tests of rectangular and round specimens were not large enough to statistically represent adequate sample sizes. Nevertheless, several general observations can be gleaned from the results shown (Table 6). The raw data given in [15] shows that the ranges of measured fracture toughness for the two specimens types overlap, and the difference between the combined mean of the three-point rectangular beam and that of the round beam is approximately 7 percent, as indicated (Table 6). The first two rectangular results are in the unstable range, where α for each was less than α_o of 0.61 (Table 5). Their average of 70.0 MPa $m^{1/2}$ is 11 percent greater than the fracture toughness of the remaining three stable specimens, which is 63.0 MPa $m^{1/2}$. The reduction from unstable to stable fracture confirms the earlier suggestion that a condition of unstable crack growth can cause an apparent increase in fracture toughness.

TABLE 6 --Summary of mean fracture toughness data for PMMA, tungsten and HPSN (NC-132).

PMMA
Mean (MPa $m^{1/2}$)

Type Specimen	Unstable	Stable	% Difference	Combined Mean
Three-point	1.25 ± 0.08[1] (4)[2]	1.06 ± 0.12 (5)	18	1.14 ± 0.10 (9)
Four - Point	1.15 ± 0.21 (4)	1.06 ± 0.19 (9)	8	1.09 ± 0.10 (13)

Tungsten
Mean (MPa $m^{1/2}$)

	Unstable	Stable	% Difference	Combined Mean	% Difference[3]
Three-point Rectangular	70 ± 2.7 (2)	63.0 ± 4.6 (3)	11	65.8 ± 5 (5)	
			3[4]		7
Three-point Round	---	61.4 ± 3.7 (6)	14[5]	---	

HPSN
Mean (MPa $m^{1/2}$)

	Unstable	Semistable	Stable including pop-ins	Semistable plus stable	% difference[6]	Combined Mean
Three-point Rectangular	4.54 ± 0.11 (7)	4.23 ± 0.13 (5)	4.18 ± 0.12 (5)	4.20 ± 0.12 (10)	8	4.34 ± 0.20 (17)
α	0.26-0.56	0.53-0.65	0.64-0.78	0.53-0.78		

[1]Standard deviation. [2]Number of specimens. [3]Percent difference between the three-point rectangular combined mean and the three-point round stable mean. [4]Percent difference between the stable round specimens and the stable rectangular specimens. [5]Percent difference between the three-point unstable rectangular specimens and the stable round specimens. [6]Percent difference between the unstable and semistable plus stable specimens.

The experimental demarcation between unstable and stable fracture was not clearly delineated for the round beam results indicated in [15]. It is pointed out that there is an uncertainty in the prediction of α_0 [19] using the results of [20] based on the two dimensional slice synthesis approach obtained from [9] which approximates a three dimensional case. Nevertheless, the the predicted α_0 value of 0.54 (Table 5) is not that much greater than the smallest crack length ratio tested, which was 0.52; moreover there was little difficulty encountered when precracking the round beam specimens. Notice that the mean fracture toughness of the round specimens that failed stably, which was 61.4 MPa $m^{1/2}$, is within 3 percent of the stable rectangular results of 63.0 MPa $m^{1/2}$ (Table 6). Thus it appears that all of the round beam specimens fractured in a stable manner. Further, the generally large values of crack growth for the round specimen, as compared to that of the rectangular specimen, is a clear indication of crack growth stability during fracture, see [15]. Additionally ,the mean fracture toughness of the stable round specimens is 14 percent lower than that of the unstable rectangular specimen.

The results of the analysis, summarized by Eqs. 6 and 8 for the rectangular and round beam are shown in Fig 2a and 2b for a range of S_b/W and S_b/D for both specimen types. The threshold of stability parameters α_0 and β_0, describing values of crack depth relative to specimen size above which crack growth stability is predicted, are plotted as a function of λ_m, S_b/W and S_b/D. Notice that the larger values of machine compliance, λ_m, result in decreased stability. It is also interesting to note in Fig 2a and 2b the significantly greater stability of the round beam compared to the rectangular beam. Even though the machine compliance value, λ_m, of 59 for the round beam is greater than that of the rectangular beam, i.e., 28, the threshold of stability for the round beam is less than that of the rectangular beam, i.e., 0.54 compared to 0.61, respectively (Table 5). This prediction of instability for some of the rectangular tests was also supported by the test results. It was noted that the rectangular specimens failed in fatigue cracking and showed less crack growth before abrupt failure, see [15].

HPSN

The stability analysis predicted the stability threshold to be 0.65 (Table 5) for the normalized compliance determined for the test set up. Correspondingly, the load displacement records clearly differed for different crack length regimes, even though the crack length regimes overlapped somewhat. Figure 5a and 5b portray typical load-displacement records for silicon nitride specimens exhibiting unstable and stable fracture, respectively. Figure 5a exhibits unstable and semistable fracture, and are so designated. Figure 5b shows two types of stability designated by "pop-in" and "stable".

The load-versus-displacement record was essentially linear to the point of fracture, as shown in Fig. 5a (unstable) for crack lengths ($0.26 < \alpha < 0.56$) far below the threshold level of 0.65. Fracture occurred instantaneously across the whole cross section as shown in the fractographic example in Fig. 6a.

Some stable crack extension occurred (see Fig. 5a–semistable) prior to either fracture or a large crack jump for crack lengths close to the critical crack length ($0.53 < \alpha < 0.67$). This is documented on the load-displacement record as non–linearity near the maximum load, followed by a steep load drop to a low load level.

A completely stable load displacement curve is shown in Fig 5b–stable, and a more typical curve as shown in Fig 5b (pop-ins) was observed for specimens with very long cracks ($0.62 < \alpha < 0.78$). This latter curve shows significant non linearity or several short crack pop–in jumps followed by one or several larger pop–in jumps. The larger crack jumps differ from those observed in the previous group, however, in that they exhibit clear crack arrest at some intermediate load value. Evidence of semistable crack propagation (crack jumps) can be observed on the fracture surface as shown in Fig. 6b, which is the specimen corresponding to the load displacement record shown in Fig. 5b–with pop–in.

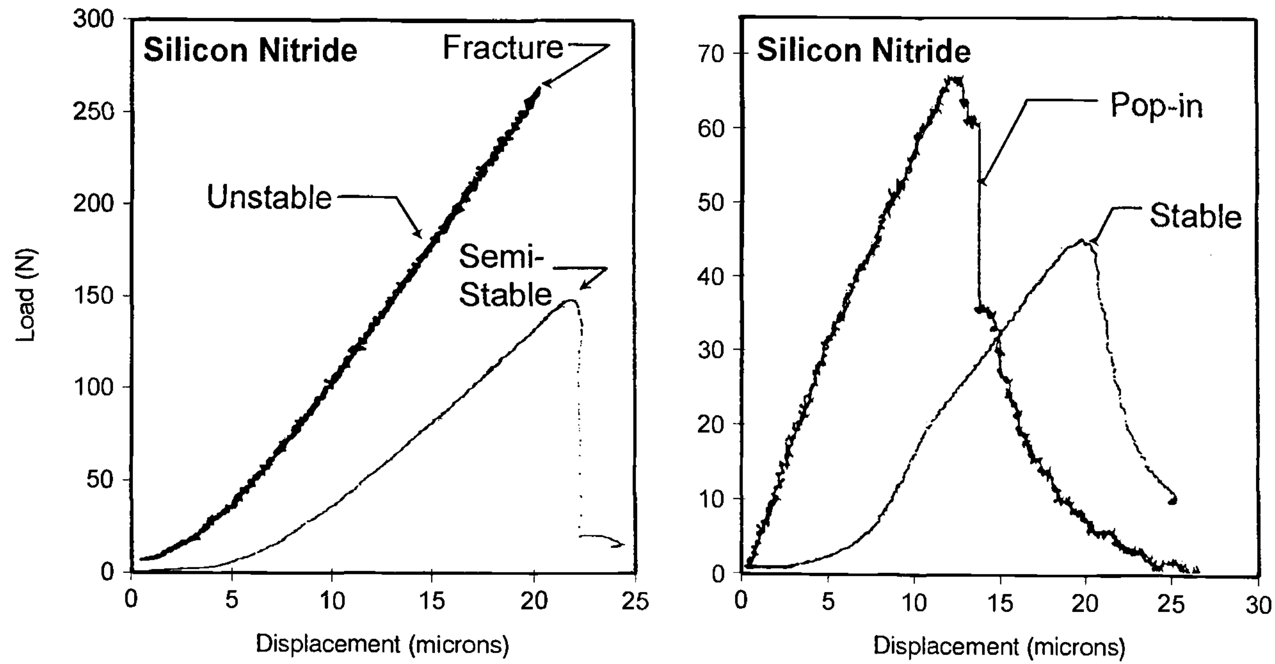

(a) (b)

Fig. 5 -- Load-displacement records for HPSN (NC-132) specimens showing (a) unstable and semistable fracture; and (b) stable fracture with and without pop-in.

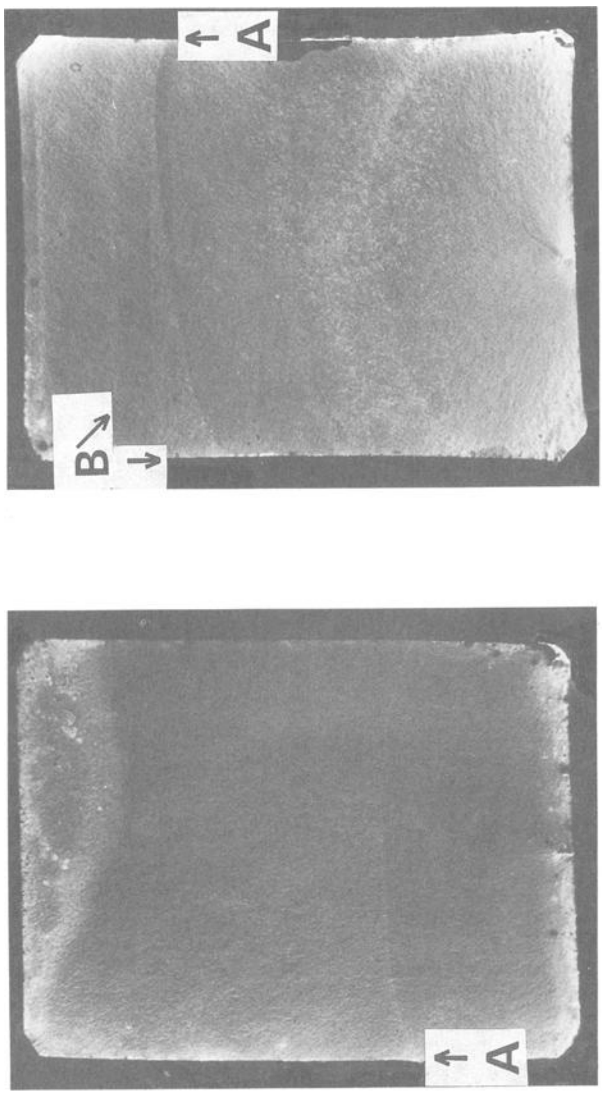

(a) (b)

Fig. 6 -- Typical fractograph (magnification 11.5x) showing stable crack front at A and pop-in crack(s) at B for unstable and (b) stable fracture.

Fracture toughness as a function of precrack length is shown in Fig 7; also shown is the predicted critical crack length for which the transition from unstable to stable behavior should occur, as indicated by the vertical line. It can be seen that the predicted crack length (α_0 = 0.65) agrees well with the transition observed in the experiments.

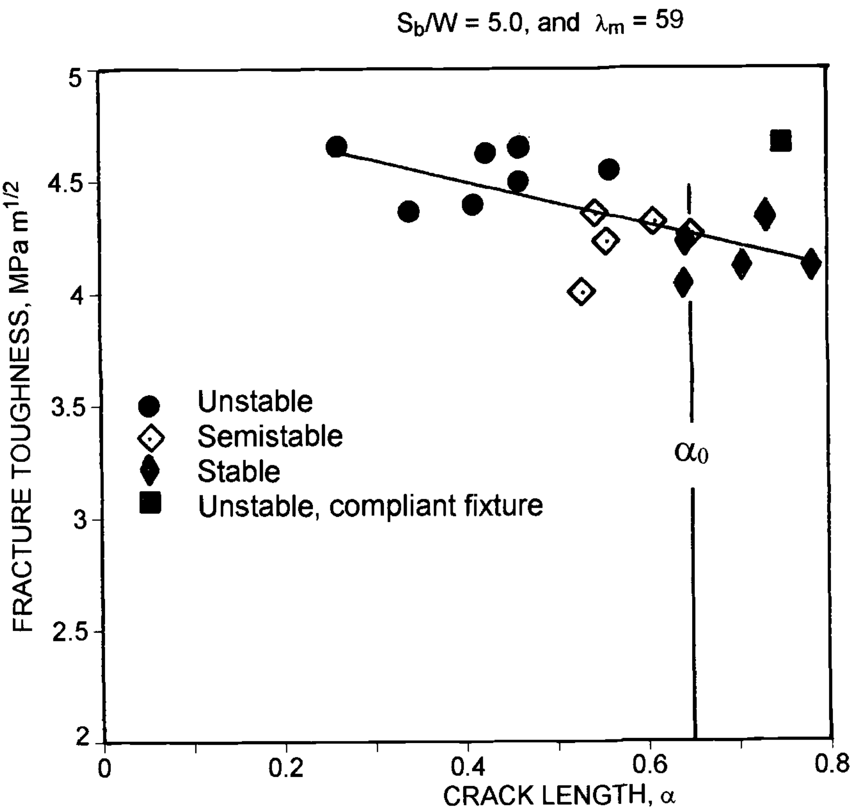

Fig. 7 -- Fracture toughness measured for specimens of various precrack lengths. The solid line indicates the analytically determined crack length which separates the unstable regime (shorter precracks) from the stable regime.

The fracture toughness data are summarized (Table 6) and are grouped by the crack advance mode. In this table and Fig. 7 are shown the results of testing seven unstable specimens with short cracks, five semistable specimens with intermediate crack lengths and five stable specimens with relatively long crack lengths. It is shown that the mean fracture toughness of 4.20 MPa $m^{1/2}$ measured for the onset of semistable and stable fracture is about 8 percent lower than that of 4.54 MPa $m^{1/2}$ measured from those specimens having unstable propagating cracks. This trend agrees with previous observations mentioned for PMMA and tungsten. In addition, a test of means was performed in order to determine if the difference between the stable and unstable fracture toughness values was significant. For this statistical test the fracture toughness of the five semistable specimens and of the five stable specimens was combined for the calculation of their mean. This combined mean was then compared to the mean of the seven unstable specimens. The rationale for this was that the mean of the fracture toughness of the semistable specimens was slightly higher than that of the stable specimens and their combined mean, and when compared to that of the unstable specimens, should provide a more conservative result. It was determined that the mean of the fracture toughness of the unstably fractured specimens differed significantly from that of the combined mean of the semistable and stable fractured specimens at the 99.5 percent confidence level.

One specimen with a relatively long crack ratio was tested on a more compliant fixture. Using the more compliant fixture increased the overall machine compliance to a value much above 59. For higher machine compliances the analysis predicted a larger threshold crack length (Fig. 2a) or complete instability. Thus this set up was expected to result in unstable fracture. This was born out by the observed load–displacement trace and a high fracture toughness of 4.65 MPa $m^{1/2}$. This result is indicated by the filled square in Fig. 7. All other specimens were tested on a much stiffer fixture. The specimen tested in the more compliant fixture had a relatively long crack ratio of 0.75 compared to those specimens tested in the stable regime. Regardless, the load-displacement curve indicated unstable crack advance and a high fracture toughness, which was greater than that exhibited by the stable specimens and slightly higher than the the largest unstable fracture toughness shown in Fig. 7. In addition, this data point is within the fracture toughness range obtained for the unstable test data gleaned from the literature shown below (Table 7).

The fracture toughness of HPSN- NC132 has been determined by several comparable techniques and typical results are summarized below (Table 7). The fracture toughness associated with the first three methods listed, undoubtedly occurred under unstable conditions; these results ranging from 4.6 to 4.9 MPa $m^{1/2}$ are in general agreement with the mean of the unstable fracture data found in this study, which was 4.54±0.11 MPa $m^{1/2}$. The last test method listed in the table, the constant-moment double cantilever beam test, which provided stable crack advance during fracture, resulted in a single value of fracture toughness of 4.0 MPa $m^{1/2}$. This and the mean value result obtained from the present work of 4.18±0.12 MPa $m^{1/2}$ are in close agreement.

TABLE 7 -- Fracture toughness of HPSN-NC 132 measured by several methods.

Test Method	K_{Ic} (MPa $m^{1/2}$)	References
Controlled flaw (surface crack in flexure)	4.6	Quinn et al.[23]
Chevron notch	4.7	Salem et al.[24]
Double torsion	4.9	Evans and Charles[25]
Constant -moment double cantilever beam	4.0	Freiman et al.[26]

It could be argued that the difference in measured fracture toughness between the shorter and longer cracks is due to the residual tensile stress field caused by the indent. Several researchers have pointed out that such an effect might exist [27 , 28]. However, if a correction for residual stress had been included the difference between the fracture toughness measured from cracks propagating under stable and unstable conditions would have been even more pronounced. The reader is referred to [16] for the details of this analysis.

DISCUSSION

The family of curves shown in Fig. 2a and 2b, which can be considered generally applicable to brittle materials, shows the threshold stability parameters, α_o and β_0, as a function of span ratio, S_b/W and S_b/D, and normalized machine compliance, λ_m. These results can be generalized to provide guidance for realizing stable fracture toughness tests for brittle materials. It appears from the family of curves in Fig. 2a and 2b, applicable to the three-point loaded rectangular and round beams, that a span ratio of 4 to 6 is workable; anything less will result in difficulty in achieving stable fracture, and anything greater will be impractical with regard to minimizing specimen deflection and optimizing specimen volume. The strategy outlined below takes advantage of the lowest possible threshold of stability ratios for those brittle materials examined herein, i.e., tungsten and HPSN, within attainable machine compliances.

Tungsten

As mentioned previously, difficulty was experienced in precracking the rectangular specimens even though λ_m was a relatively small value of 28 for the testing system and beam geometry employed. Nevertheless, it is believed that a reduction of the normalized machine compliance could have been attained for the tungsten material and testing system used in this study. Recalling that $\lambda_m = (\delta_m/P)EB$, and by reducing the B dimension from 14 mm to 10 mm, which results in λ_m of 20, and according to ASTM E 399 the beam height, W, would then be 20 mm. Data taken from Fig. 2a for $\lambda_m = 20$ and S_b/W from 4 to 6 can provide guidance for stable fracture toughness testing of tungsten rectangular beams. The recommended beam geometries are summarized below (Table 8), with what is believed to be attainable normalized compliances to ensure stable fracture and starter crack length ratios for the tungsten material examined in this work . These starter crack length ratios are considered practical and at the same time will allow stable crack advance during fracture testing.

TABLE 8 -- Recommended beam geometries and crack starter length ratios.

	Tungsten - Rectangular S_b/W					Tungsten - Round S_b/D			
	4	5	6	W (mm)	B (mm)		4	5	6	D (mm)
λ_m	α_0					λ_m	β_0			
20	0.55	0.49	0.48	20	10	46	0.52	0.49	0.48	25.4
						23	0.47	0.46	0.45	12.7

	HPSN - Rectangular S_b/W					HPSN - Round S_b/D			
	4	5	6	W (mm)	B (mm)		4	5	6	D (mm)
λ_m	α_0					λ_m	β_0			
40	0.65	0.59	0.57	8	4	42	0.51	0.49	0.47	25.4
30	0.62	0.56	0.53	8	3	22	0.47	0.46	0.46	12.7

The round beam geometry tends to be more stable than the rectangular beam compared on a S_b/D to S_b/W basis and for the same λ_m; compare Fig. 2a and Fig. 2b. The round beam fractured in a stable manner even though λ_m for the tungsten round beam was 59. As in the case of the rectangular beam, a span ratio range of between 4 to 6 appears to be practical. Recalling that $\lambda_m = (\delta_m/P)ED$ for the round beam, and by reducing D, the normalized machine compliance of the system can also be reduced. Since the diameter of the tested beams were quite large (32.8 mm) a further reduction can be realized; for example a diameter of 25.4 mm or even 12.7 mm will reduce λ_m from 59 to 46 or 23, respectively. Startercrack length ratios gleaned from Fig. 2b for these attainable machine compliance ratios and the aforementioned beam span ratios are shown (Table 8) for the tungsten round beam specimens.

HPSN

When testing rectangular beams of HPSN difficulty was experienced in realizing a test system machine compliance λ_m of less than 59 for the test system employed. Nevertheless, it is believed that a normalized machine compliance of 40 or 30 is attainable for the HPSN material and testing system used in this study by reducing the B dimension from 6 mm used in this work to 4 mm and 3mm, resulting in a beam cross section of 8 mm x 4 mm or 8 mm x 3 mm[1], respectively, i.e., W/B, of 2 or 2.67. It is expected that a normalized machine compliance of less than 30 will be difficult to achieve in a practical manner for most structural ceramic materials that have a large Young's modulus and that also require a relatively stiff testing system having a low capacity load range with correspondingly improved load resolution. Therefore, only data taken from Fig. 2a for $\lambda_m = 40$ and 30, and with S_b/W ranging from 4 to 6 are included (Table 8). This table summarizes the recommended rectangular beam geometries and approximate starter crack length ratios to ensure stable fracture for the ceramic material examined.

The round beam is more stable than the rectangular beam and can be used as an alternative fracture toughness test specimen for a brittle ceramic such as HPSN. The data taken from Fig. 2a and Fig. 2b, assuming D is also 25.4 mm or 12.7 mm, resulting in λ_m of 42 and 22, respectively for the test system used in this work are summarized (Table 8). This table shows approximate starter crack length ratios that are considered practical and at the same time will allow stable crack advance during fracture testing.

SUMMARY

Nakayama [1] has suggested an explanation of a similar phenomenon of his analogous work in the determination of fracture energies of brittle materials. The mechanism presented [1] was based on energy considerations, where the total elastic energy stored in the system at the time of fracture is composed of both the energy in the specimen and the energy in the testing apparatus. Since the elastic energy stored at the time of fracture is dissipated by the fracture process, the difference in energy obtained by subtracting the effective fracture energy, defined as the energy required to separate the test piece from the total energy in the system at the time of fracture, provides a criterion for the mode of fracture. When this difference is greater than zero, the mode of fracture is catastrophic because the excess energy must be consumed by other forms of energy, e.g., the kinetic energies of fragments. Alternatively, if the energy stored is not enough to complete the fracture process and additional external work is required, the mode of fracture may then be stable. It was further stated [1]: "The exact measurement of the effective fracture energy is valid only for perfectly stable fractures", and an analogy is advanced to aid the reader in understanding this phenomenon by stating: "The present method resembles the Charpy impact test in which the entire energy consumed in bending fracture is measured by a decrease in the maximum height of swing of the pendulum after it has broken the specimen. The mechanism in this test, however, is dynamic and the fragments of the specimen, after fracture, carry considerable excess kinetic energy. Separation of the effective energy from the kinetic energy is impossible in the Charpy test. The present method corresponds in principle to the Charpy test in that the impacting speed of the pendulum is extremely small and the mass is quite large. The accuracy of measurement in such an extreme situation is very low in the Charpy test."

There are additional reasons that can be proposed regarding the apparent increase in fracture

[1]These latter dimensions may require improved load resolution since the fracture load will be small.

toughness occurring during unstable crack advance as compared to that during stable crack growth:

(a) The three materials examined here all have exhibited an apparent increase in fracture toughness that may be due to material behavior such as crack velocity dependence or dynamic loading. For example PMMA shows a decided increase in toughness due to crazing and crack acceleration [3]. Although there is little data available in the literature regarding dynamic fracture toughness of tungsten, it is well known that high strength metallic materials exhibit an increase in fracture toughness when experiencing dynamic loading, for example see Kendall [29]. Suresh et al., [30] have also shown a similar trend when dynamically testing ceramic materials.

(b) The testing systems used in the subject studies were all suitable for testing only in the quasi-static regime and the response of these systems may not have been adequate to accurately detect and couple the dynamic peak load to the instantaneous crack length. Because of limited dynamic response of the test systems and associated instrumentation, it would seem reasonable to presume that in such situations the peak loads could be overestimated, resulting in overestimates of critical stress intensity factors.

(c) The possibility exists that the slow crack growth fracture phase of the experiments could have been affected by the environment. Polymers are well known to be sensitive to their environment, particularly relative humidity. The PMMA tests reported here were not conducted in a controlled atmosphere. Regarding the tungsten tests, they were conducted in a controlled atmosphere thus eliminating the possibility of the presence of stress corrosion cracking. It has been reported in a limited number of references [31 - 33] that there is a a trace amount of slow crack growth at room temperature that is water driven when stressing HPSN. The HPSN specimens examined in this work were precracked and tested in an air conditioned laboratory having a 50% relative humidity and thus this could possibly lower fracture toughness during stable quasi-static crack growth.

It does not seem plausible that this particular mechanism (in (c) above) is present in all three materials to a similar extent such that they exhibit the same general fracture toughness variation as a function of initial crack length. Nevertheless, the fracture toughness determined in these studies during unstable/stable crack advance is herein labeled "apparent", because the causes that result in the variation in fracture toughness are unknown. Until such time as this conundrum can be resolved it is suggested that those practitioners who wish to determine fracture toughness of brittle materials test in the stable regime so as to realize conservative results.

CONCLUSIONS

1. Threshold of stability parameters were calculated using a plane stress condition for the rectangular four-point loaded beam and for both the rectangular and round beams loaded in three point bending as a function of normalized machine compliances. Beam span ratios ranging from 4 to 8 were considered.

2. Stability threshold crack lengths, α_0 and β_0, were successfully predicted for the three test materials, PMMA, tungsten and HPSN with their respective machine compliances and beam geometries. Transition from unstable to stable crack extension during fracture was observed to be in agreement with the theoretical predictions.

3. In general, the average fracture toughness determined for each of the three materials agreed with the data available in the literature.

4. Fracture toughness results, determined at three different laboratories by three independent researchers, for the three materials examined showed the same general trend. In each instance stable fracture resulted in a lowering of K_{Ic} as compared to that obtained during unstable fracture. The mean fracture toughness during stable crack extension of the PMMA three-point loaded and four-point loaded specimens was 18 and 8 percent lower than that of the unstable specimens, respectively. The mean fracture toughness during stable crack extension of the tungsten rectangular specimens was approximately 11 percent lower than that of the unstable specimens and that of the tungsten round specimens was approximately 14 percent lower compared to that of the unstable tungsten rectangular specimens.

5. The stable tungsten round specimen results agreed with the stable rectangular results to within 3 percent.

6. The mean of the fracture toughness of the combined semistable and stat ly fractured HPSN specimens was lower by 8 percent from that of the unstably fractured specimens; this difference was found to be significant at the 99.5 percent confidence level.

7. The fracture toughness results attributed to unstable and stable fracture compared quite well to that data available in the literature.

RECOMMENDATIONS

It is recommended that:

1. Further research be accomplished to determine why brittle materials exhibit such a variation of fracture toughness as a function of unstable/stable crack advance as described in this work.

2. Examination of other structural ceramics materials as well as brittle metallic materials be conducted to determine fracture toughness in both the unstable and stable regime.

3. In order to attain stable fracture when testing beams of brittle materials the following parameters should be considered: Initial threshold crack length ratios. machine compliances, specimen geometries and specimen materials, i.e., Young's Modulus of elasticity.

REFERENCES

[1] Nakayama, J., "Direct Measurement of Fracture Energies of Brittle Heterogeneous Materials," Journal of the American Ceramic Society., Vol. 48, No. 11, 1965, pp. 583-587.

[2] Cooper, G. A. "Optimization of the Three-Point Bend Test for Fracture Energy Measurement," Journal of Material Sciences, Vol. 12, 1977, pp. 277-289.

[3] Margolis, R. D., Dunlap, R. W., and Marovitz, H., "Fracture Toughness Testing of Glassy Plastics," in ASTM Spec. Tech. Pub. 601, 1976, p 391, American Society for Testing and Materials.

[4] Reddy, K. P. R., Fontana, E. H., and Helfinstine, J. D., "Fracture Toughness Measurement of Glass and Ceramic Materials Using Chevron-Notched Specimens," Journal of the American Ceramic Society, Vol. 71, No.6, 1988, C-310-C313.

[5] Clausing, D. P., "Crack Stability in Linear Elastic Fracture Mechanics," International Journal of Fracture Mechanics, Vol. 5, No. 3, 1969, pp. 211-226.

Fracture Mechanics, Vol. 5, No. 3, 1969, pp. 211–226.

[6] Bluhm, J. I., "Stability Considerations in the Three Dimensional Work of Fracture Specimens," Proceedings of the Fourth International Conference on Fracture, 1977, pp. 409–17, University of Waterloo Press, Waterloo, Ontario, Canada.

[7] Schimoeller, H .A., "An Elastic–Quasistatic Crack Stability Criterion of Fracture Mechanic Specimens Investigated by Displacement–Controlled Closed Loop Testing Systems," International Journal of Fracture, Vol. 12, No. 3, 1976, pp. 481–484.

[8] Tatersall, H. G., and Tappin, G. J., "The Work of Fracture and its Measurement in Metals, Ceramics and Other Materials," Journal of Material Sciences, Vol. 1, 1960, pp. 296–301.

[9] Bluhm, J. I., "Slice Synthesis of a Three Dimensional 'Work of Fracture' Specimen," Engineering Fracture Mechanics, Vol. 7, 1975, pp. 593–604.

[10] Sigl, L. S., "On the Stability of Cracks in Flexure Specimens," International Journal of Fracture, Vol. 51, 1991, pp. 241–254.

[11] Nose, T., and Fujji, T., "Evaluation of Fracture Toughness for Ceramic Materials by a Single–Precracked Beam Method," Journal of the American Ceramic Society, Vol. 71, No. 5, 1988, pp. 328–333.

[12] Bar–On, I., Beals, J. T., Leatherman, G. L., and Murray, C. M., "Fracture Toughness of Precracked Bend Bars," Journal of the American Ceramic Society, Vol. 73, No. 8, 1990, pp. 2519–2522.

[13] Choi, S. R., Chulya, A., and Salem, J. A., "Analysis of Precracking Parameters for Ceramic Single–Edge–Precracked–Beam Specimens", Fracture Mechanics of Ceramics, 1992, Vol. 10, pp. 73–78, Plenum Press, New York.

[14] Baratta, F. I., and Dunlay, W. A.,"Crack Stability in Simply Supported Four–Point and Three–Point Loaded Beams of Brittle Materials," Mechanics of Materials, Vol. 10, 1990, pp. 149–159.

[15] Underwood, J. H., Baratta, F. I., and Zalinka, J. J., "Fracture–Toughness Tests and Displacement and Crack–Stability Analyses of Tungsten Round Bend Specimens," Experimental Mechanics, Vol. 31, No. 4, 1991, pp. 353–359.

[16] Bar-On, I., Baratta, F. I., and Kyu Cho, "Crack Stability and its Effect on Fracture Toughness of Hot Pressed Silicon Nitride Beam Specimens," Journal of the American Ceramic Society, 1996, Vol. 79, No. 9, pp 2300-2308.

[17] Qizhi, W., and Xuefu, X., "Compliance and Stability Factors of an Edge-Cracked Three-Point-Bend Round Bar Specimen," International Journal of Fracture, Vol. 50, 1991, R61-R67.

[18] Freese, C. E., Formerly of the Army Research Laboratory, Watertown, MA, "Single Edge-Crack Stress Intensity Solutions," To be published.

[19] Baratta, F. I., "Stability Revisited for a Straight-Fronted Edge Crack in a Three-Point Loaded Round Bend Bar," International Journal of Fracture, Vol. 62, 1993, R29-R35.

[20] Qizhi, W., "Wide Range Compliance of Edge-Cracked Three-point Bend Round Bars Based on

[21] Baratta, F. I., "Wide Range Stress Intensity Factors for a Straight Fronted Edge Crack in a Three-Point Bend, Round Bar Specimen," International Journal of Fracture, Vol. 60, 1993, R59-R63.

[22] Van Krevelen, D. W.,Properties of Polymers, Elsevier Scientific Publishing Co., Amsterdam, 1976.

[23] Quinn, G. D., Kubler, J. J., and Gettings, R. J., "Fracture Toughness of Advanced Ceramics by the Surface Crack in Flexure (SCF) Method: A VAMAS Round Robin," VAMAS Report No. 17, National Institute of Standards and Technology, Gaithersburg, MD, 1994.

[24] Salem, J. A., Shannon, J. L., Jr., "Fracture Toughness of Si_3N_4 Measured with Short Bar Chevron Notched Specimens," Journal of Material Science, Vol. 22, 1987, pp. 321-324.

[25] Evans, A. G., and Charles, E. A., "Fracture Toughness Determination by Indentation," Journal of the American Ceramic Society, Discussion and Notes, Vol. 59, No.7-8, 1976, pp. 371-372.

[26] Freiman, S. W., Williams, A., Mecholsky, J. J., and Rice, R. W., "Fracture of Si_3N_4 and SiC," Ceramic Microstructures 76, Westview Press, Boulder, CO, 1977, pp. 824-834.

[27] Warren, R., and Johannesson, B., "Creation of stable cracks in Hardmetals Using 'Bridge' Indentation," Powder Metallurgy, Vol. 27, No. 1, 1984, pp. 25-29.

[28] Nishida, T., Shiono, T, and Nishikawa, T., "On Fracture Testing of Pollycrystalline Alumina Measured by SEPB Method," Journal of the European Ceramic Society, Vol. 5, 1989, pp. 379-383.

[29] Kendall, D. P., "The Effect of Loading Rate and Temperature on Fracture Toughness of High Strength Steel,"Materials Research and Standards, Vol. 10, No. 12, 1970.

[30] Suresh, S., Nakamura, T., Yeshurun Y., Yang K.-H., and Duffy, J., "Tensile Fracture Toughness of Ceramic Materials: Effects of Dynamic Loading and Elevated Temperatures," Journal of the American Ceramic Society, Vol. 73, No. 8, 1990, pp. 2457-2466.

[31] Gulden M. E., and Metcalf A. G., "Stress Corrosion of Silicon Nitride," Journal of the American Ceramic Society, Vol. 59, No. 9-10,1976, pp.391-396.

[32] McHenry K. D., Yonushonis T., and Tressler R. E., "Low Temperature Subcritcal Crack Growth in SiC and Si_3N_4," Journal of the American Ceramic Society, Vol. 59, No. 5-6, 1976, pp. 262-263.

[33] Jakus, K., Ritter, J.,Weinraub, W.,and Drooks, W. S., "Effects of Preoxidation on the Strength and Fatigue of Hot Pressed Silicon Nitride," Surfaces and and Interfaces in Ceramic and Ceramic Metal Systems, Plenum Press, 1981.

DEDICATION:

This paper is in honor of the memory of a past colleague, Joseph I. Bluhm, who initiated stability analyses of brittle materials at the former installation, The U.S. Army Research Laboratory, located at Watertown, Massachusetts.

G. N. Vigilante[1], J. H. Underwood[1], D. Crayon[1], S. Tauscher[1], T. Sage[1], E. Troiano[1]

Hydrogen Induced Cracking Tests of High Strength Steels and Nickel-Iron Base Alloys Using the Bolt-Loaded Specimen

REFERENCE: G. N. Vigilante, J. H. Underwood, D. Crayon, S. Tauscher, T. Sage, E. Troiano, **"Hydrogen Induced Cracking Tests of High Strength Steels and Nickel-Iron Base Alloys Using the Bolt-Loaded Specimen"**, Fatigue and Fracture Mechanics: 28th Volume, ASTM STP 1321, J. H. Underwood, B. D. Macdonald, and M. R. Mitchell, Eds., American Society for Testing and Materials, 1997.

ABSTRACT:

Hydrogen induced cracking tests were conducted on high strength steels and nickel-iron base alloys using the constant displacement bolt-loaded compact specimen. The bolt-loaded specimen was subjected to both acid and electrochemical cell environments in order to produce hydrogen. The materials tested were A723, Maraging 200, PH 13-8 Mo, Alloy 718, Alloy 706, and A286, and ranged in yield strength from 760-1400 MPa. The effects of chemical composition, refinement, heat treatment, and strength on hydrogen induced crack growth rates and thresholds were examined. In general, all high strength steels tested exhibited similar crack growth rates and threshold levels. In comparison, the nickel-iron base alloys tested exhibited up to three orders of magnitude lower crack growth rates than the high strength steels tested. It is widely known that high strength steels and nickel base alloys exhibit different crack growth rates, in part, because of their different crystal cell structure. In the high strength steels tested, refinement and heat treatment had some effect on hydrogen induced cracking, though strength was the predominant factor influencing susceptibility to cracking. When the yield strength of one of the high strength steels tested was increased moderately, from 1130 MPa to 1275 MPa, the incubation times decreased by over two orders of magnitude, the crack growth rates increased by an order of magnitude, and the threshold stress intensity was slightly lower.

KEYWORDS: threshold stress intensity, hydrogen induced cracking, hydrogen cracking, hydrogen embrittlement, environmental fracture, environmental cracking, crack growth rates, high strength steels, nickel-iron base alloys

[1] Mechanical Engineer, research engineer, mechanical engineer, metallurgist, mechanical engineering technician, and mechanical engineer, respectively, Army Armament RD&E Center, Benét Laboratories, Watervliet, NY, 12189.

Introduction

Hydrogen induced cracking failures have been a particular problem in applications involving high strength materials in aggressive service environments, including armament applications. Recently, a 1.7 m long crack was found at an outside diameter keyway of a gun tube. An investigation concluded that hydrogen stress cracking occurred at a location of tensile residual stress after being exposed to an aggressive electropolish solution [1]. Also, higher energy propellants have been shown to increase the risk of hydrogen damage to bore coatings, liners, and the underlying steel substrate [2]. In addition, Troiano et al. [3] have concluded that premature seal failures in armament were likely caused by the hydrogen rich by-products of the combustion environment.

In this work, a fracture mechanics approach was used to measure the hydrogen induced cracking threshold of various steels and nickel-iron base alloys at various yield strength levels. The effects of refinement were also examined for one of the steels tested. The constant displacement bolt-loaded compact sample (Figure 1), henceforth referred to as the bolt-loaded sample, was used in the testing because it provides quantitative information on the crack growth rate, da/dt, and the threshold stress intensity, K_{IHIC}, in a simple test. K_{IHIC} is the threshold stress intensity under which no cracking will occur in a given material in a hydrogen environment. As a crack grows in a bolt-loaded specimen, the load, and therefore the stress intensity, decreases until K_{IHIC} is reached. This test is fundamentally different from constant load tests, where K_{IHIC} is found by testing several specimens at various initial stress intensities until no cracking occurs. One disadvantage of the bolt-loaded specimen is that long test times (up to 10,000 hours) may be necessary when testing insensitive materials, non-aggressive environments, and when testing at low initial stress intensities. This problem may be mitigated by first testing a sample at a high initial stress intensity level approaching K_{IC}. This will aid in determining the material susceptibility and the initial applied stress intensity levels for subsequent tests. There

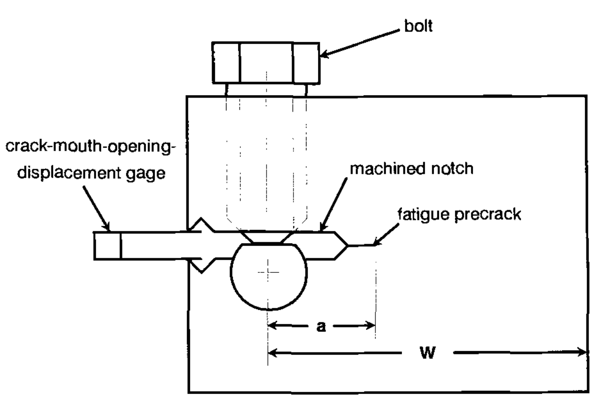

FIG. 1 - Schematic of the bolt-loaded test specimen.

is currently no recognized standardization of the bolt-loaded specimen; however, an ASTM committee is engaged in incorporating a bolt-loaded compact specimen standard with the recently adopted ASTM standard E 1681-95 on environment-assisted cracking.

Materials and Environments

Materials

The materials used in this investigation consisted of martensitic and austenitic forged alloys with yield strengths ranging from 760 MPa-1400 MPa. The martensitic alloys used have a body center cubic (BCC) crystal structure and the austenitic materials have a face centered cubic (FCC) crystal structure. The materials investigated were A723, Maraging 200, and PH 13-8 Mo steels, Alloy 718 and Alloy 706 nickel-iron base alloys, and A286 iron-nickel base alloy. A723, Maraging 200, and PH 13-8 Mo were chosen for their high strength and toughness properties (in air). Alloys 718 and 706 were chosen for their high strength, crystal structure, and hydrogen induced cracking resistance (as compared to the steels tested) [4, 5]. A286 was chosen for its well known resistance to hydrogen induced cracking [6, 7]. Some pertinent mechanical/material properties for the tested materials are listed in Table 1.

A723 is a Ni-Cr-Mo quenched and tempered steel. Both A723 Grade 1 and Grade 2 compositions were evaluated to determine the effects of strength, composition, and refinement on da/dt and K_{IHIC}. All A723 materials tested had an ASTM grain size of 11.8. A723 Grade 1 material was electric furnace melted and vacuum

TABLE 1-*Mechanical/material property information on the materials tested.*

Material	**Yield Strength (MPa)**	**Fracture Toughness (MPa√m)**	**Crystal Structure**
A723 Grade 1	1160	125	BCC
A723 Grade 2 (ESR)	1130	175	BCC
A723 Grade 2 (ESR)	1275	125	BCC
A723 Grade 2 (VIM-VAR)	1275	170	BCC
Maraging 200	1400	175	BCC
PH 13-8 Mo	1275	145	BCC
PH 13-8 Mo	1035	125	BCC
Alloy 718 (Direct Aged)	1150	135	FCC
Alloy 718	1115	145	FCC
Alloy 706	1110	180	FCC
A286	760	125	FCC

degassed (EFM-VD). A723 Grade 2 material was either electric furnace melted and electro-slag remelted (EFM-ESR) or vacuum induction melted and vacuum arc remelted (VIM-VAR). Both the ESR and VIM-VAR refinement methods increase the homogeneity of the microstructure and reduce the amount of sulfur (S) and phosphorus (P) present as compared to the EFM-VD condition. The levels of S and P in the Grade 1, Grade 2 (ESR), and Grade 2 (VIM-VAR) steels were 0.005/0.006, 0.002/0.005, and 0.0007/0.005, respectively. Additionally, the Grade 2 material contains slightly more Ni to improve fracture toughness. Maraging 200 is an 18Co-8Ni steel which was conventionally austenitized and aged to promote strengthening by Ni_3[Ti, Mo, Al] precipitates. The Maraging 200 material tested had an ASTM grain size of 13.5. PH 13-8 Mo is a 13Cr-8Ni-2Mo martensitic stainless steel which was heat treated to two standard overaged conditions. PH 13-8 Mo is strengthened by NiAl precipitates during the ageing process. The ASTM grain size of the PH 13-8 Mo material investigated was 8.6. Alloy 718 is a 52Ni-19Cr-19 Fe superalloy which was tested in the direct aged condition for maximum strength and a standard heat treatment condition for maximum ductility and impact strength [8]. Alloy 718 receives it strength from Ni_3Nb (γ'') precipitates. Alloy 718 in the direct aged condition had an ASTM grain size of 8.6 while the conventionally processed 718 had a grain size of 7.0. Alloy 706 is a 41Ni-38Fe-16Cr superalloy tested in a standard heat treated condition to maximize ductility and impact strength, and to promote formation of Ni_3[Nb, Ti, Al] (γ') precipitates [9]. The Alloy 706 material tested had an ASTM grain size of 5.3. A286 is an Fe-25Ni-15Cr superalloy which was tested in a standard heat treatment condition. A286 is also precipitation strengthened by γ'. The ASTM grain size for the A286 material tested was 10.6. Table 2 lists the various heat treatments of the materials tested.

TABLE 2 - *Heat Treatments of Materials Tested.*

Materials	**Heat Treatment**
A723 Grade 1 @ 1160 MPa YS	843°C 1 hour Water Quench, Temper 582°C 4 hours Air Cool
A723 Grade 2 @ 1130 MPa YS	843°C 1 hour Water Quench, Temper 627°C 4 hours Air Cool
A723 Grade 2 @ 1275 MPa YS	843°C 1 hour Water Quench, Temper 524°C 4 hours Air Cool
PH 13-8 Mo @ 1275 MPa YS	927°C 1/2 hour air cool, Refrigerate -73°C, 2 hours Air Warm, Age 556°C 4 hours Air Cool
PH 13-8 Mo @ 1035 MPa YS	927°C 1/2 hour air cool, Refrigerate -73°C, 2 hours Air Warm, Age 579°C 4 hours Air Cool
Maraging 200	816°C 1 hour Water Quench, Age 482°C 3 hours Air Cool
Alloy 718 Direct Aged	718°C 8 hours Furnace Cool to 621°C 18 hours Air Cool
Alloy 718	1038°C 1/3 hour Air Cool, Age 760°C 11 hours Furnace Cool to 649°C 9 hours Air Cool
Alloy 706	982°C 1 hour Air Cool, Age 718°C 8 hours Furnace Cool 38°C/hour to 621°C 8 hours Air Cool
A286	816°C 1 hour Water Quench, Age 718°C 16 hours Air Cool

Environments

All tests were conducted in either electrochemical cells or in concentrated acid solutions with the exception of A723 Grade 1 (1160 MPa YS) and Grade 2 (1130 MPa YS) and Alloy 706 which were tested in both environments. All tests were conducted at ambient temperature.

The electrochemical cell tests were conducted using a platinum anode and specimen cathode in a 3.5% aqueous NaCl solution. As_2O_3 was used as a "poison" to limit the combination of nascent hydrogen to the diatomic gas [10]. All specimens tested using this method were pre-charged at a current density of 40 ma/cm^2 for eight hours prior to load application. A current density of 40 ma/cm^2 was also applied during testing. This current density was maintained at a constant value using a current controlling power source and by keeping the exposed surface area of the specimen constant throughout the test. The NaCl solution volume was monitored on a daily basis in order to ensure a constant current density and replaced weekly to ensure a constant reservoir chemistry.

All acid cracking tests were conducted in a concentrated 50% sulfuric acid and 50% phosphoric acid solution (by volume). This solution is identical to that used in previous tests [1].

Test Procedure

All bolt-loaded test specimens were taken in the C-R orientation as described in ASTM E 399. All tests were conducted following interlaboratory guidelines on the bolt-loaded specimen from Wei and Novak [11]. All A723 steels tested in acid were tested in triplicate for each test condition. All bolt-loaded tests were tested at an initial stress intensity of 55 MPa$\sqrt{m}$ with the exception of one Alloy 706 specimen which was tested at 110 MPa$\sqrt{m}$. The low stress intensities of 55 MPa$\sqrt{m}$ were chosen from previous experience in order to avoid the problem of a deep crack growing too near to the back edge of the specimen. All tests were conducted in acid or in an electrochemical cell as described in the preceding section. The stress intensity in the bolt-loaded sample is related to the mouth opening through the following relationship [1]:

$$K_{applied}=f(a/W)\,Ev(1-a/W)^{1/2}\ /\ W^{1/2}$$

$$f(a/W)=0.654-1.88(a/W)+2.66(a/W)^2-1.233(a/W)^3$$

where v is mouth opening and E is Young's Modulus. This K expression is valid for $0.3 \leq a/W \leq 1$. For the acid cracking tests the acid was introduced to the crack tip prior to load application in order to expose fresh surfaces produced by the subsequent loading. The crack extension of the specimens was monitored optically on both specimen sides on a regular basis in order to determine $K_{applied}$ as a function of time and to obtain da/dt information. The mouth opening of the test specimen and the solution pH were checked frequently to ensure no relaxation or solution contamination, respectively. The duration of the tests depended on the material tested and its yield strength. Typically, tests were conducted for durations ranging from 1500-6000 hours. After test termination the final crack length was measured to determine if the test conformed to plain strain test conditions and the fracture surface was examined visually and by scanning electron microscopy to determine the fracture morphology. From previous experience it is believed that all materials would easily conform to plane strain conditions because of low hydrogen induced cracking threshold values.

Results and Discussion

In general, the body center cubic materials tested exhibited similar cracking characteristics. Both da/dt and K_{IHIC} information were similar, though both the PH 13-8 Mo materials tested had lower crack growth rates and slightly higher K_{IHIC} than the average BCC materials tested. With the face centered cubic materials tested, the crack growth rate was lower than with the BCC materials. This was expected in part because diffusivity of hydrogen through an open cell BCC structure is higher than through a closed cell FCC structure. In the technical literature, crack growth rates have been shown to be orders of magnitude less in FCC structures than in BCC structures, e.g. Ritchie et al. [12].

In the following sections, discussion of the results from the various materials is given. Table 3 shows a summary of the results of the hydrogen induced cracking tests conducted on all materials.

A723 Steel

The hydrogen induced cracking tests conducted on A723 steels in acid

TABLE 3 - *Summary of K_{IHIC} test results*

Material	Yield Strength (MPa)	K_{IHIC} (MPa√m)	Test Environment
A723 Grade 1	1160	16/10	acid/cell
A723 Grade 2 (ESR)	1130	16/16	acid/cell
A723 Grade 2 (ESR)	1275	10	acid
A723 Grade 2 (VIM-VAR)	1275	11	acid
Maraging 200	1400	12	cell
PH 13-8 Mo	1275	17	cell
PH 13-8 Mo	1035	19	cell
Alloy 718	1150	11	cell
Alloy 718	1115	-	cell
Alloy 706	1110	-	acid/cell
A286	760	-	cell

environments showed dramatic results when plotted as applied stress intensity versus time (Figure 2). Figure 2 shows the trend of the data, illustrating the incubation time, subsequent crack growth, and threshold. Though the Grade 1 and Grade 2 materials were tested at about the same yield strength level (1160 and 1130 MPa, respectively), the incubation time increased from approximately from 200 hours to over 2000 hours. Additionally, when the yield strength of the Grade 2 material was increased 13% from 1130 MPa to 1275 MPa, the incubation time decreased over two orders of magnitude from over 2000 hours to less than 12 hours. After the incubation time was exceeded, the crack grew until K_{IHIC} was reached. Incubation time has been observed to decrease with an increase in strength or applied stress, for example as cited by Steigerwald et al. [13] and Jones [14]. However, both the strength and applied stress intensity levels were nearly identical in the lower yield strength Grade 1 and Grade 2 materials tested. This suggests that the local crack tip chemistry may have been the controlling factor. Therefore the longer incubation time of the lower strength Grade 2 material may be attributed to the refinement and increased Ni content as compared to the Grade 1 material.

The crack growth rates of the A723 steels conducted in acid are shown in Figure 3. A five point moving average was used to analyze the data. This curve shows the stage I and a portion of the stage II crack growth regimes. For the lower

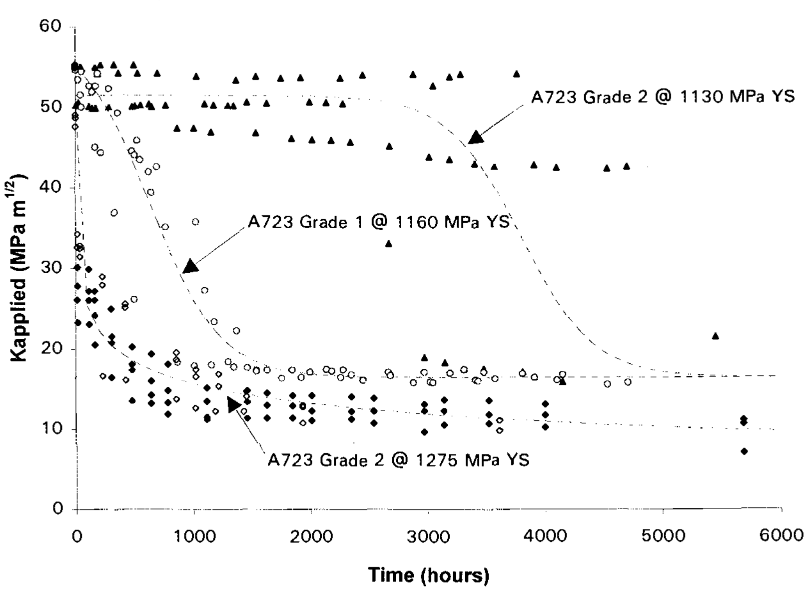

FIG. 2 - Applied K versus time for A723 steels exposed to a 50% sulfuric - 50% phosphoric acid solution.

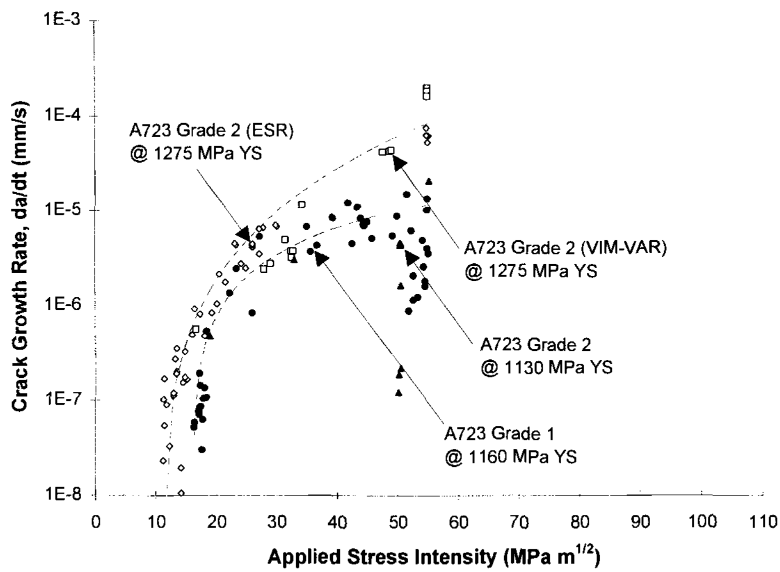

FIG. 3 - Crack growth rate versus applied K for A723 steel exposed to a 50% sulfuric - 50% phosphoric acid solution.

strength Grade 1 and Grade 2 steels, da/dt in the stage II regime appears to be constant at approximately 10^{-5} mm/s, the same as that found by Underwood et al. [1]. The constant da/dt data in the stage II regime for the lower strength steels are independent of K and are solely a result of diffusion controlled crack growth. For the higher strength Grade 2 steel, the da/dt in the stage II regime was approximately an order of magnitude higher (10^{-4} mm/s). Note the wide scatter in both of the lower strength steels at the initial applied stress intensity of 55 MPa√m. This scatter occurred during the incubation period when little or no crack growth was observed. After incubation the crack grew significantly and the scatter was eliminated.
The average K_{IHIC} for the lower strength Grade 1 steel was approximately 16 MPa√m. The average K_{IHIC} for the higher strength ESR and VIM-VAR processed Grade 2 materials was approximately 10 and 11 MPa√m, respectively.

The electrochemical cell tests on the lower strength Grade 1 and Grade 2 steels exhibited incubation times of approximately 325 and 450 hours, respectively, then cracked rapidly and reached K_{IHIC} levels of approximately 10 and 16 MPa√m, respectively. Figure 4 shows the applied stress intensity as a function of exposure time for all materials tested in the electrochemical cell tests. In the electrochemical cell tests, there was little distinction in the incubation time between the Grade 1 steel and the Grade 2 steel tested. It is believed that the high current density liberated more hydrogen than the acid tests thereby increasing the severity of cracking in both steels and reducing the incubation time in the Grade 2 steel. If the current density was

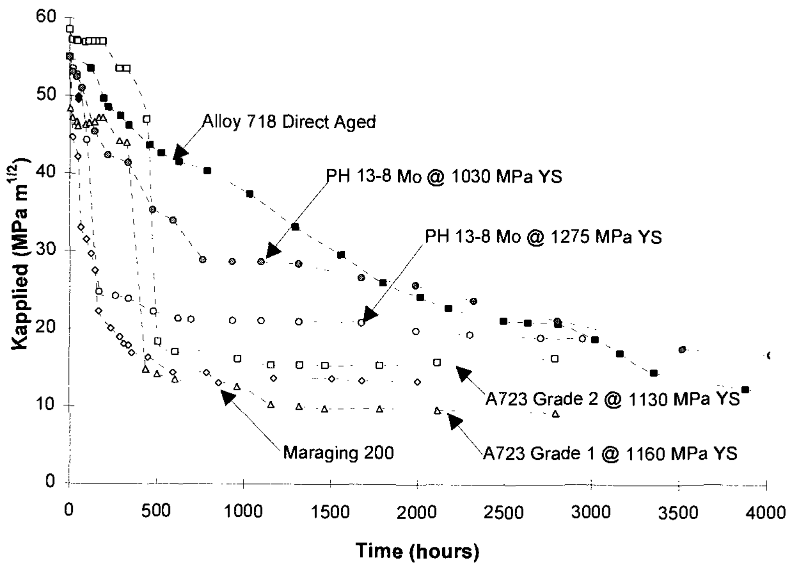

FIG. 4 - Applied K versus time for high strength steels and nickel-iron base alloys tested in an electrochemical cell.

decreased significantly, a more notable distinction may have been apparent. It is also interesting to note that only the A723 steels tested in the electrochemical cell exhibited a classical incubation period. This appears to more than just a strength effect since the 1035 MPa yield strength PH 13-8 Mo material tested did not exhibit an incubation time.

The crack growth rates of the A723 steels tested in the electrochemical cell were approximately 10^{-5} mm/s as can be seen in Figure 5. A five point moving average was used to plot the data. In Figure 5 the initial scatter was omitted from the A723 steels for clarity.

The fracture surface near the crack tip of the higher strength ESR processed Grade 2 material is shown in Figure 6a. In this figure the intergranular fracture morphology is evident as is the chemical attack of the fracture surface caused by the acid solution. Much more chemical attack was observed a lower a/W values as would be expected due to longer exposure to the acid. The remaining ligament of this specimen was forced open by tensile overload after testing was completed. Figure 6b shows a predominantly ductile fracture morphology of microvoid coalescence. However, notice the island of intergranular fracture. This intergranular area resulted from the remaining ligament being embrittled by hydrogen during immersion in the acid solution. When the tensile load was applied to break the remaining ligament, a portion of it failed in a brittle intergranular manner.

In the A723 steels examined, there were little differences in the S and P

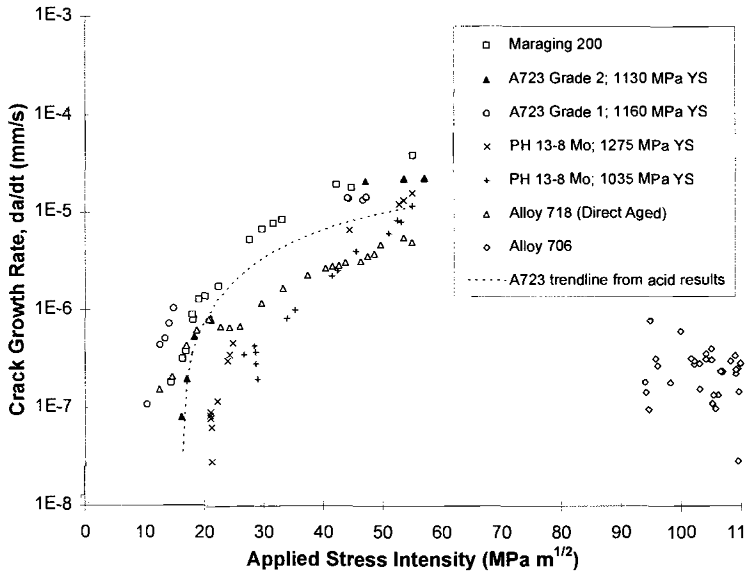

FIG. 5 - Crack growth rate versus applied K for high strength steels and nickel-iron base alloys tested in an electrochemical cell.

content between the EFM-VD and EFM-ESR refinement methods. The VIM-VAR processed steel contained approximately the same amount of P and much less S than either the VD or ESR processed steels. Because the S is "tied up" as manganese sulfide stringers in A723 steels and the P content remained essentially constant, there is no direct correlation which can be made here on the effects of these impurities on incubation time, da/dt, or K_{IHIC}. Previous studies have shown no strong effect of impurities on hydrogen induced cracking of high strength steels with yield strength greater than 1250 MPa [15].

PH 13-8 Mo

The PH 13-8 Mo material tested in the 1275 MPa yield strength condition resulted in a K_{IHIC} of approximately 17 MPa√m. The material tested at a lower yield strength level of 1035 MPa resulted in a K_{IHIC} of approximately 19 MPa√m. It was surprising that the lower yield strength condition did not provide a more improved K_{IHIC}. More dramatic threshold results may have been evident if the PH 13-8 Mo material was tested in a peak aged and an overaged condition rather than two overaged conditions, since the mechanical properties from a highly overaged condition result in lower strength but also lower toughness due to precipitate incoherency. Fracture toughness tests by Young et al. [16] on H charged PH 13-8 Mo specimens at a yield strength level of 1275 MPa show results similar to those obtained in these tests.

Maraging 200

The Maraging 200 material tested in the electrochemical cell exhibited a K_{IHIC} value of approximately 13 MPa√m.

Alloy 718

The Alloy 718 material tested in the direct aged condition exhibited no distinctive incubation time. As seen in Figure 4, the crack grew much slower and did not exhibit any gross crack advances as with the BCC materials, an advantage attributed to the lower diffusivity of H through the FCC crystal structure. However, K_{IHIC} for the direct aged Alloy 718 specimen was similar or less than that of the BCC materials tested. The lower than expected yield strength and low K_{IHIC} values are believed to be attributed to an undesirable δ phase present at the grain boundaries [17]. Figure 7a shows the fracture surface in the cracked portion of the Alloy 718 material tested in the direct aged condition. The fracture surface is entirely intergranular in nature with evidence of the second phase present at the grain boundaries. Figure 7b shows the fracture surface of the ruptured remaining ligament. The fracture morphology is brittle, containing both quasi-cleavage and intergranular fracture.

The Alloy 718 material heat treated to provide maximum ductility and impact strength exhibited no appreciable cracking after 5000 hours of exposure. Though the test is ongoing, the K_{IHIC} of Alloy 718 in this condition could be as high as 42 MPa√m based on environmental fracture tests conducted by Walter and Chandler [4].

Alloy 706

After over 3000 hours in acid and 5000 hours in the electrochemical cell, no appreciable cracking has been observed in the Alloy 706 specimens at both the 55 MPa√m and 110 MPa√m initial applied stress intensity levels. For example, after 5000 hours of exposure in the electrochemical cell at an initial applied stress intensity of 110 MPa√m the current applied stress intensity is 90 MPa√m which corresponds to crack growth of only approximately 3.7 mm. It is believed that the K_{IHIC} of Alloy 706 will be higher than that of Alloy 718 because slow strain rate notched tensile tests conducted on both alloys [18] showed a higher notched tensile strength ratio for Alloy 706 than for Alloy 718. The slow strain rate notched tensile tests were conducted on specimens which were hydrogen charged and compared to control specimens tested in laboratory air. The notched tensile strength ratio of the Alloy 706 specimens were 0.91 as compared to 0.84 for the Alloy 718 specimens. High pressure hydrogen notched tensile tests also showed a higher ratio for Alloy 706 than for Alloy 718 [4].

A286

After over 2300 hours in the electrochemical cell, no visible cracking has occurred with the A286 material. The K_{IHIC} is expected to be higher than that of Alloys 718 and 706 because slow strain rate notched tensile tests conducted [18]

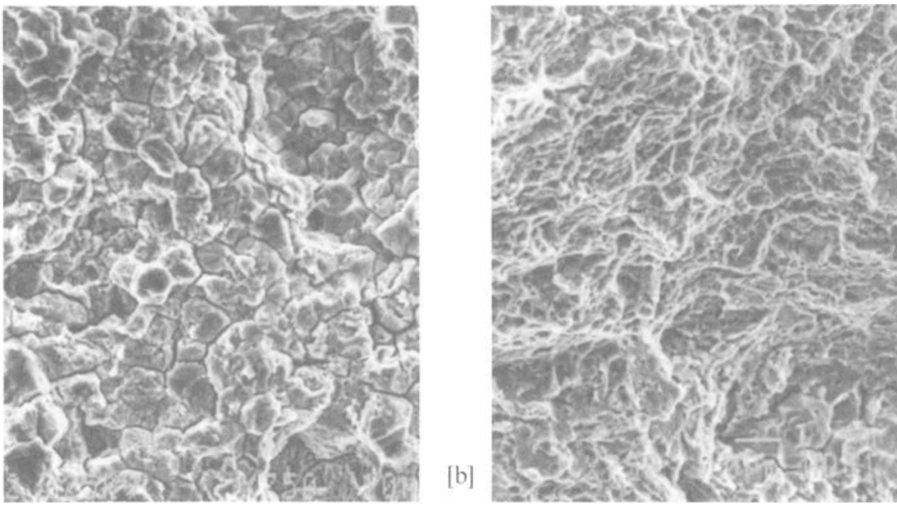

FIG. 6 - SEM fractographs of a 1275 MPa YS A723 steel exposed to an acid solution for 1100 hours; 750x magnification: [a] intergranular cracking near the crack tip and [b] microvoid coalescence in the ruptured remaining ligament.

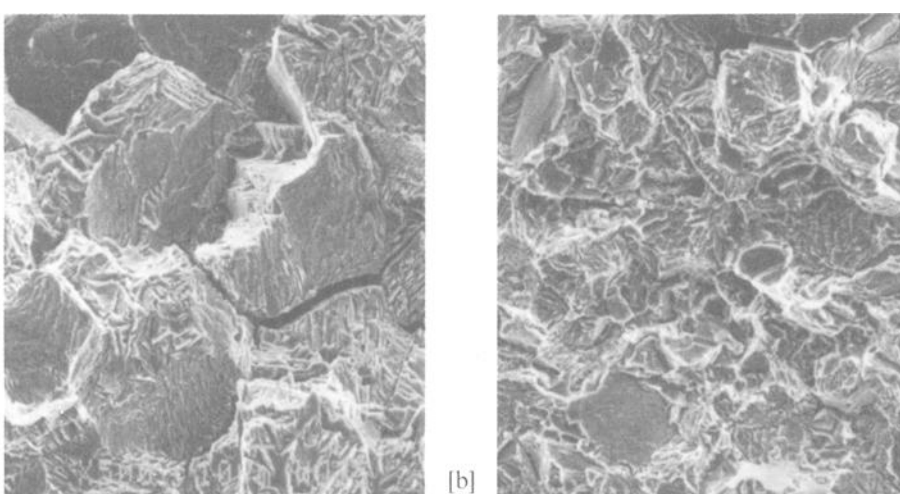

FIG. 7 - SEM fractographs of direct aged Alloy 718 tested in an electrochemical cell; 500x magnification: [a] intergranular cracking in the cracked portion of the specimen and [b] mixed mode failure in the ruptured remaining ligament.

showed a ratio of 0.98 for A286 as compared to 0.84 and 0.91, respectively. High pressure hydrogen notched tensile tests conducted on A286 also showed an improved resistance to hydrogen as compared to Alloys 718 and 706 [4].

Summary and Conclusions

1. Hydrogen induced cracking studies were conducted on A723, Maraging 200, PH 13-8 Mo, Alloy 718 Direct Aged, Alloy 718, Alloy 706, and A286 alloys using the constant displacement bolt-loaded compact specimen. All tested were conducted in either 50% sulfuric-50% phosphoric acid solutions or in electrochemical cells at room temperature. All tests, with the exception of Alloy 706, were conducted at initial stress intensities of 55 MPa√m. Information on crack growth rates and hydrogen induced cracking threshold stress intensities (with the exception of Alloys 718, 706, and A286) were obtained from these tests.

2. The bolt-loaded specimen has provided closely repeatable hydrogen induced cracking tests and allows for accurate crack growth rate and threshold measurement.

3. With the lower strength A723 steels tested in an acid environment, an incubation period was observed followed by crack growth and asymptotic approach of a threshold. At the lower strength levels (e.g. 1130 MPa YS) refinement and alloying had an effect on the hydrogen induced cracking susceptibility of A723; however, at high strength levels (1275 MPa YS) there was no apparent benefit. In A723, yield strength had the most pronounced effect on hydrogen induced cracking susceptibility. As the strength of A723 increased, the incubation time and K_{IHIC} decreased while the crack growth rate increased. Crack growth rates in the Stage II cracking regime for the lower strength A723 Grade 1 steel were approximately 10^{-5} mm/s. Crack growth rates in the Stage II regime for the higher strength Grade 2 steels were about an order of magnitude larger.

4. The electrochemical tests were more severe than the acid cracking tests for A723 steel. A shorter incubation time was observed for the A723 Grade 2 steel and a lower threshold was evident for both Grade 1 and Grade 2 steels tested in the electrochemical cell.

5. Alloy 718 tested in the direct aged condition had a low K_{IHIC} value of 11 MPa√m, due to a deleterious δ phase present at the grain boundaries. Alloy 718 tested under a standard high ductility heat treatment condition appears to be much more resistant to hydrogen induced cracking since no cracking has been observed after 5000 hours of exposure.

6. A286 and Alloy 706 have not exhibited any measurable crack growth in bolt-loaded tests conducted at 55 MPa√m after 2400 and 3000 hours of exposure, respectively. Though Alloy 706 tested at 110 MPa√m has shown some small amount of crack extension after 5000 hours of exposure it has proven to be very resilient to hydrogen induced cracking.

7. The martensitic materials tested in this investigation exhibited similar crack growth rates and hydrogen induced cracking threshold stress intensity values with the exception of the two PH 13-8 Mo specimen tested at 1130 MPa YS and 1275 MPa YS which had slightly lower crack growth rates.

8. The austenitic materials tested in this investigation exhibited up to three orders of magnitude lower crack growth rates than the martensitic materials tested.

Aknowledgements

Thanks to Mr. A. Kapusta for fractography of the bolt-loaded specimens.

References

[1]Underwood, J. H., Olmstead, V. J., Askew, J. C., Kapusta, A. K., and Young, G. A., "Environmentally Controlled Fracture of an Overstrained A723 Steel Thick-Wall Cylinder", *ASTM STP 1189*, 1993, pp. 443-460.

[2] Dalley, A.M., Buckman, R.W. Jr., and Bagnall, C., "Physical and Chemical Interactions at the Bore Surface of a Ta-10W Gun Barrel Liner", *MPIF-APMI International Conference on Tungsten and Refractory Metals, Their Alloys, Composites and Carbides*, Washington D.C., November 1995.

[3] Troiano, E., Underwood, J. H., Scalise, A., O'Hara, G. P., and Crayon, D., "Fatigue Analysis of a Vessel Experiencing Pressure Oscillations", *Fatigue and Fracture Mechanics: 28th Volume, ASTM STP 1321*, J. H. Underwood, B. D. MacDonald, M. R. Mitchell, Eds., American Society for Testing and Materials, 1997.

[4] Walter, R. J. and Chandler, W. T., "Influence of Gaseous Hydrogen on Inconel 718", *Hydrogen in Metals*, 1974, pp. 515-524.

[5] *Handbook of Corrosion Data*, ASM International Materials Data Series, 1989, p. 333.

[6] Thompson, A. W. and Brooks, J. A., "Hydrogen Performance of Precipitation-Strengthened Stainless Steels Based on A-286", *Metallurgical Transactions A*, Volume 6A, July 1975, pp. 1431-1442.

[7] Papp, J., Hehemann, R. F., and Troiano, A. R., "Hydrogen Embrittlement of High Strength FCC Alloys", *Hydrogen in Metals*, 1974, pp. 657-669.

[8] Product Literature on Inconel Alloy 718, Inco Alloys International, 1968.

[9] Product Literature on Inconel Alloy 706, Huntington Alloys, Inc., 1974.

[10] Spencer, G.L., "Hydrogen Embrittlement of Gun Steel", Master's Thesis,

Rensselaer Polytechnic Institute, Troy, NY, August 1987.

[11] Wei, R.P. and Novak, S.R. "Interlaboratory Evaluation to KISCC and da/dt Determination Procedures for High-Strength Steels", *Journal of Testing and Evaluation*, Vol. 15, No. 1, Jan. 1987.

[12] Ritchie, R. O., Castro Cedeño, M. H., Zackay, V. F., and Parker, E. R., "Effects of Silicon Additions and Retained Austenite on Stress Corrosion Cracking in Ultrahigh Strength Steels", *Metallurgical Transactions A*, Vol. 9A, 1978, pp. 35-40.

[13] Steigerwald, E. A., Schaller, F. W., and Troiano, A. R., "The Role of Stress in Hydrogen Induced Delayed Failure", *AIME Transactions*, Vol. 218, October 1960, pp. 832-841.

[14] Jones, D. A., *Principles and Prevention of Corrosion*, Prentice Hall, Inc., Saddle River, NJ, 1996, p. 249.

[15] Craig, B., "Limitations of Alloying to Improve the Threshold for Hydrogen Stress Cracking of Steels", *Hydrogen Effects on Material Behavior*, 1989, pp. 955-963.

[16] Young, L. M., Eggleston, M. R., Solomon, H. D., and Kaisand, L. R., "Hydrogen-assisted cracking in a precipitation hardening stainless steel: effects of heat treatment and displacement rate", *Materials Science and Engineering*, 1995, pp. 377-387.

[17] Vigilante, G. N. and Fusco, D. R., "Evaluation of High Strength Materials for the Regenerative Liquid Propellant Gun Program", Army Armament Research Development and Engineering Center Technical Report #95035, Watervliet, NY, 1995.

[18] Tauscher, S. and Sage, T., Unpublished Research, 1995.

Susumu Machida[1], Hitoshi Yoshinari[1], and Shuji Aihara[2]

COMPUTER SIMULATION OF FAST CRACK PROPAGATION AND ARREST IN STEEL PLATE WITH TEMPERATURE GRADIENT BASED ON LOCAL FRACTURE STRESS CRITERION

REFERENCE: Machida, S., Yoshinari, H., and Aihara, S., "**Computer Simulation of Fast Crack Propagation and Arrest in Steel Plate with Temperature Gradient Based on Local Fracture Stress Criterion**", Fatigue and Fracture Mechanics: 28th Volume, ASTM STP 1321, J.H. Underwood, B.D. Macdonald and M.R. Mitchell, Eds., American Society for Testing and Materials, 1997.

ABSTRACT: A fracture mechanics model for fast crack propagation and arrest is proposed based on the local fracture stress criterion. Dynamic fracture toughness (K_D) for a propagating crack is calculated as a function of crack velocity and temperature. The model is extended to incorporate the effect of unbroken ligament (UL) formed near the plate surfaces and crack-front-tunneling. The model simulates acceleration, deceleration and arrest of a crack in a ESSO or a double-tension test plate with temperature-gradient. Calculated arrested crack lengths compare well with experimental results. It is shown that the conventional crack arrest toughness calculated from applied stress and arrested crack length depends on temperature-gradient and the toughness is not a unique material property.

KEYWORDS: dynamic fracture, stress intensity factor, arrest toughness, shear lip, crack velocity.

INTRODUCTION

The concept of crack arrestability has been successfully applied to such welded steel structures as ships and storage tanks for ensuring safety against catastrophic failure by brittle crack propagation. The crack arrest toughness, K_{ca}, is measured by using double tension test

[1] Department of Naval Architecture and Ocean Engineering, Univeristy of Tokyo.
[2] Nagoya R&D Laboratories, Nippon Steel Corporation.

or ESSO test[1] with temperature-gradient in the specimen[1]. Value of K_{ca} is compared with stress intensity factor, K, which is calculated from applied stress and possible maximum length of a propagating crack in the structure considered. If K_{ca} is greater than K, then crack arrest is ensured. Alternatively, K_{ca} value required for steel is determined so that K_{ca} is greater than K. Because this criterion is based on the static approximation, it might possibly fail to predict the actual crack arrest behavior. The behavior of fast crack propagation and arrest is far from complete understanding.

The fast crack propagation is intrinsically dynamic. The dynamic effect is two fold; one is a mechanical effect, simply expressed as inertial effect, and the other is a material response to high strain rate, especially dependency of yielding behavior on strain rate [2]. The latter is especially important for ferritic steels because their yield stress depends on strain rate strongly. Moreover, a propagating crack accompanies shear-lips near plate surfaces. In addition, the propagating crack front is not straight but tunnels in the middle of the plate; there exist a distribution of K and crack velocity normal to the crack front. All these factors have influences on the crack propagation and arrest behavior.

Kanazawa et al. [1] showed that K_{ca} values obtained from the standard size (W=0.5m) double tension tests and that from very wide (W=2.0m) duplex-type ESSO tests did not coincide. The reason of the discrepancy was presumed to be a lack of dynamic consideration. They conducted dynamic elastic analyses using FEM and obtained dynamic fracture toughness as a function of crack velocity and temperature based on the energy balance concept. In spite of their full dynamic analyses, the experimental crack propagation and arrest behavior was not completely explained. Importance of the influence of the shear-lips was pointed out. They also noted that the energy criterion is only a *necessary* condition and local criterion is necessary.

The authors proposed a fundamental crack propagation model based on the local fracture stress criterion [3]. This model is outlined in the present paper and then the model is extended to simulate the crack propagation and arrest behavior in a specimen with temperature-gradient (extended model). Factors influencing K_{ca} are discussed based on the model.

FUNDAMENTAL MODEL (DETERMINATION OF DYNAMIC FRACTURE TOUGHNESS)

Theory

Brittle-cleavage fracture initiation of steel is stress-controlled. Transition behavior of cleavage initiation toughness, K_c or K_{IC}, can be predicted from local fracture stress, σ_F, and temperature dependency of yield stress (the RKR model [4]). σ_F is a parameter which is insensitive to temperature and stress triaxiality [5]. It is presumed that σ_F is insensitive to strain rate and a local fracture model similar to the RKR model can be applied to a crack propagating dynamically in a brittle-cleavage manner in steel. We assume that a crack continues to propagate with tensile stress ahead of the crack-tip exceeding σ_F within a characteristic distance, r_c, see Fig.1.

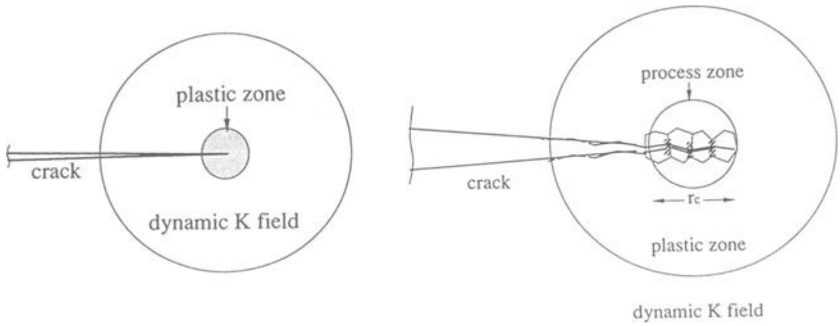

FIG.1--Deformation and stress field around a propagationg crack-tip, schematic.

$$\sigma_{yy}[r_c,0] = \sigma_F \tag{1}$$

where, $\sigma_{ij}[r,\theta]$ is stress component, (r, θ) is polar coordinate with origin at the crack-tip and θ =0 for crack advancing direction.

A complete solution for stress field around a dynamically propagation crack-tip in elastic-plastic solid has not been available, yet. Achenbach et al. [6] obtained an asymptotic solution for elastic linear strain-hardening solid. Their solution does not give absolute stress values but gives a stress singularity and relative stress distribution in a circumferential direction as a function of crack velocity and tangent modulus, E_t. They also found that upper limit crack velocity coincides with the Rayleigh wave speed calculated using E_t, instead of Young's modulus, E. We use their results. Referring to the HRR field for a stationary crack [7], we assume that the stress field for a dynamically propagating crack is expressed by,

$$\sigma_{ij}[r,\theta] = \sigma_Y \left\{ (1-\nu^2)\left(\frac{K_d}{\sigma_Y}\right)^2 \frac{1}{r} \right\}^{-s} \Sigma_{ij}[\theta, V] \tag{2}$$

where K_d is dynamic stress intensity factor, ν is Poisson's ratio, σ_Y is yield stress, $\Sigma_{ij}[\theta,V]$ is a non-dimensional function of θ and V and nearly equal to 4 for $V/c_R<0.5$ under plane-strain condition, V is crack velocity, c_R is elastic Rayleigh wave speed and "s" is a stress singularity parameter. Achenbach et al. [6] calculated "s" as a function of α and β, s[α, β], where α =

E_t/E and β is crack velocity normalized by the bar-wave velocity, $\beta = V/(E/\rho)^{1/2}$, ρ is density of solid, as shown by the symbols in Fig.2. It is noted that the stress singularity vanishes at $\beta = 0.57\ \alpha^{1/2}$ and there is no solution beyond that velocity and also the dependency of "s" on α for $\beta = 0$, $s_{\beta=0}[\alpha]$, coincides with that obtained by Amazigo and Hutchinson [8]. We assume, for simplicity, that $s[\alpha, \beta]$ is approximated by $s_{\beta=0}[\alpha]$ but $(\alpha-(\beta/0.57)^2)/(1-(\beta/0.57)^2)$ is used instead of α for the argument of $s_{\beta=0}$,

$$s[\alpha,\beta] = s_{\beta=0}\left[\frac{\alpha - (\beta/0.57)^2}{1-(\beta/0.57)^2}\right] \quad . \tag{3}$$

Lines in Fig.2 are graphical expressions of Eq.(3).

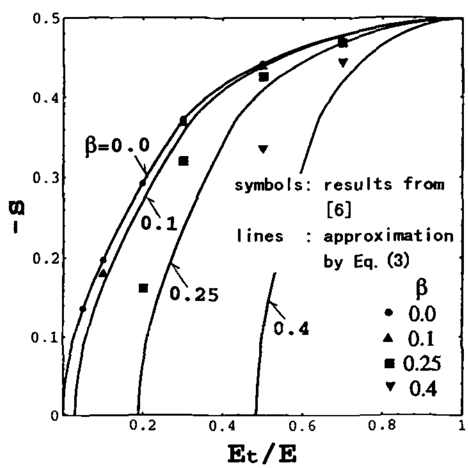

FIG.2--Stress singularity exponent based on Achenbach's model.

Strain-hardening behavior of most metals is better approximated by power-hardening law ($\varepsilon_e = \sigma_Y/E\ (\sigma_e / \sigma_Y)^n$, for $\sigma_e > \sigma_Y$) and instantaneous hardening rate depends on equivalent strain ε_e, or equivalent stress, σ_e. Instantaneous tangent modulus is expressed by,

$$E_t = \frac{d\sigma_e}{d\varepsilon_e} = \frac{1}{n}E\left(\frac{\sigma_e}{\sigma_Y}\right)^{-(n-1)} \tag{4}$$

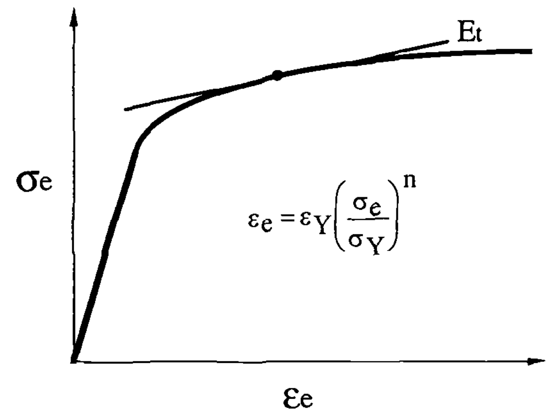

FIG.3--Relation between strain hardening and tangent modulus.

where n is reciprocal of strain-hardening exponent, see Fig.3. E_t in Eq.(4) is applied to Eq.(3). Analogously to Eq.(2), σ_e in Eq.(4) is expressed by,

$$\sigma_e[r,\theta] = \sigma_Y \left\{ (1-\nu^2) \left(\frac{K_d}{\sigma_Y} \right)^2 \frac{1}{r} \right\}^{-s} \Sigma_e[\theta, V] \tag{5}$$

where $\Sigma_e[\theta,V]$ is a non-dimensional function of θ and V and equal to unity for $\theta = 0$. It should be noted here that Eq.(4) is evaluated at $r=r_c$. Eq.(2) is based on a constant E_t throughout the plastic zone. However, in a power-hardening material, instantaneous tangent modulus changes with "r". Strictly, varying E_t cannot be applied in Eqs.(2) and (3). However, our concern is the stress level at $r=r_c$ only but not stress distribution throughout the plastic zone. In this sense, application of Eq.(4) seems to be a reasonable approximation.

As noted earlier, yield stress of steel has a strong dependency of strain-rate, $\dot{\varepsilon}$. Dependence of yield stress on $\dot{\varepsilon}$ and temperature is expressed as a sum of thermally activated and phonon drag components [9]. We use the following expression,

$$\sigma_Y = \sigma_{Y0} + (9.0\text{x}10^{-4}) T_0 E \left(\frac{\sigma_{Y0}}{E} \right)^{-1/2} \\ \text{x} \left\{ \frac{1}{T \ln[10^8 / \dot{\varepsilon}_e]} - \frac{1}{T_0 \ln[10^8 / \dot{\varepsilon}_{e0}]} \right\} + \eta \dot{\varepsilon}_e \tag{6}$$

where, T is temperature in Kelvin, T_0=293K, $\dot{\varepsilon}_{e0}=10^{-4}s^{-1}$, σ_{Y0} is yield stress at T_0 and $\dot{\varepsilon}_{e0}$.

We use a value η=2.0 x 10^{-3}MPa.s in the phonon drag term determined experimentally for mild steel [10]. This term is especially important at high strain-rate encountered in the plastic zone of a propagating crack-tip. Figure 4 shows a graphical expression of Eq.(6).

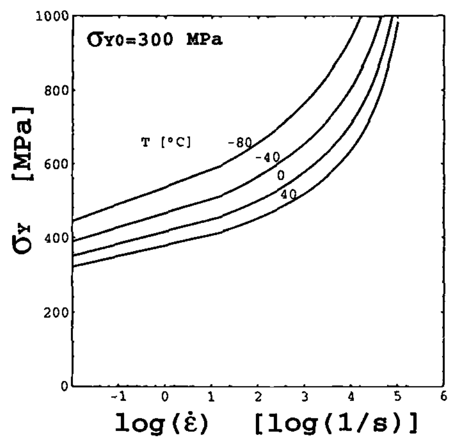

FIG.4--Dependence of yield stress on strain rate and temperature.

Assuming a steady state crack propagation, $\dot{\varepsilon}_e$ is expressed as,

$$\dot{\varepsilon}_e = \frac{\dot{\sigma}_e}{E_t} = -\frac{\sigma_Y}{E_t} V \quad s\left\{(1-\nu)^2 \left(\frac{K_d}{\sigma_Y}\right) \frac{1}{r}\right\}^{-s} r^{-1} \Sigma_e[\theta, V]. \tag{7}$$

Eq.(7) is applied at $r=r_c$.

Inserting Eq.(2) into Eq.(1), inserting Eq.(5) into Eq.(4), and rewriting Eq.(7), we obtain three simultaneous equations. In these equations, σ_Y is expressed by Eq.(6). Unknown parameters are $\dot{\varepsilon}_e$, α, V and K_d. If any one of them is given, other parameters are determined by solving the non-linear equations simultaneously. Value of K_d determined in this manner is the dynamic fracture toughness and denoted K_D. K_D is expressed as a function of V and T, K_D[V, T] for given material parameters.

Results

Figure 5 shows calculated K_D, where σ_{Y0}=300MPa, n=5 and r_c=0.3mm. Process zone size for a propagating crack has not been examined in detail, yet. The authors examined a distribution of tear-ridges behind the tip of a crack arrested in a CTOD test specimen of HT50 steel. The tear-ridges were observed as far as 1mm behind the crack-tip. It is not unreasonable, therefore, to assume r_c value of an order of 0.1 to 1mm. Also, σ_F value was

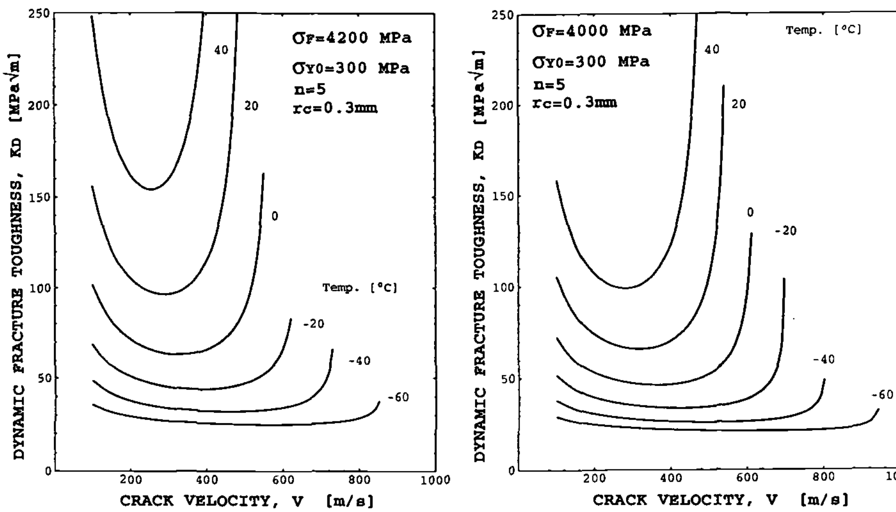

(a) σ_F=4200MPa (b) σ_F=4000MPa

FIG.5--Calculated dynamic fracture toughness.

determined so that realistic K_D value was obtained (see below for more detail). Under a constant temperature, K_D once decreases, shows a minimum and then increases with V. The initial decrease is due to the increased strain-rate and elevated yield stress. The increase at high V is due to the reduced stress singularity. K_D diverges at a certain crack velocity, which coincides with c_R calculated using E_t instead of E. With increasing temperature, equivalent strain at $r=r_c$ increases for compensating lower initial yield stress with increased strain-hardening, thereby decreasing instantaneous strain-hardening rate. Therefore, the upper limit crack velocity decreases with increasing temperature. Although theoretical upper limit crack velocity in elastic solid is c_R [2] (2950m/s for E=200GPa and ν=0.3), that obtained in experiments is much lower than c_R [1]. This is because of the plastic deformation at the crack-tip. Trend that the calculated upper limit crack velocity decreases with increasing temperature compares well with experiment [1]. Only a slight decrease in σ_F, from 4200MPa to 4000MPa, produced considerably large decrease in K_D; equivalent temperature shift is approximately 20deg.C.

EXTENDED MODEL (SIMULATION OF CRACK PROPAGATION AND ARREST)

Theory

Figure 6 shows configuration of a typical double tension test specimen. Temperature distribution, T[x], is given in the specimen width direction, x. The crack initiated at the chilled sub-loading part is propagated into the main plate and is finally arrested at high temperature region. The present extended model simulates the crack propagation and arrest behavior in this kind of the test.

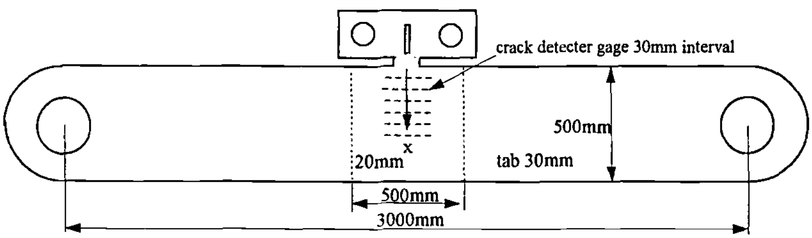

FIG.6--Typical double tension test specimen.

Figure 7 schematically shows a fracture surface. Because of low stress-triaxiality near the plate surfaces, brittle fracture does not take place there; unbroken ligaments (UL) are formed. Because the UL exhibits plastic deformation with crack advancement, tensile stress approximately equal to yield stress acts on it. The UL is plastically elongated and finally fractures in ductile manner; the shear-lips form. Inside the shear-lips, there exists brittle fracture surface.

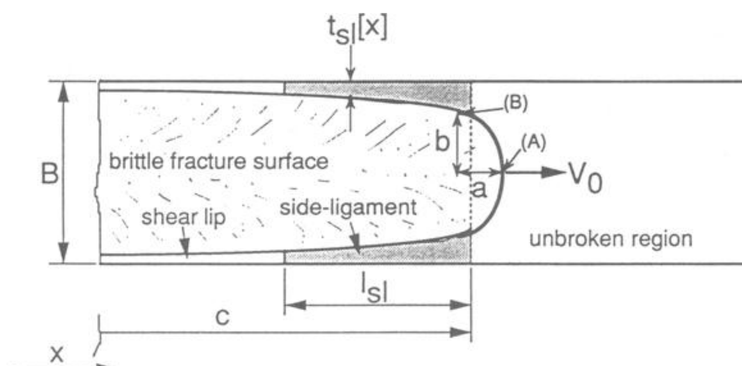

FIG.7--Fracture surface of a propagating crack, schematic.

The crack front tunnels in the middle of the plate thickness. At each point along the crack front, there is a pair of the values of dynamic stress intensity factor and crack velocity normal to the crack front. Fundamentally, the pair of these values is assumed to lie on the $K_D[V,T]$ curve determined in the fundamental model. In the extended model, however, the crack front shape is assumed to be semi-elliptical, for simplicity, and the above assumption is assumed to hold only at mid-thickness point, (A), and nearest-the-surface point, (B). At point (A), normal crack velocity is equal to macroscopic crack velocity, V_0. Although normal crack velocity at point (B) is mathematically zero, a brittle crack cannot propagate in steel at very low speed [1]. Here, we assume that lower limit crack velocity, V_{min}, exists, which cannot be determined from the present model and is assumed to be equal to 100m/s, tentatively. From the balance between K_d and K_D at point (A) and (B), we obtain,

$$K_{d(A)} = K_D[V_0, T[x]] \quad (8)$$

$$K_{d(B)} = K_D[V_{min}, T[x]] \quad (9)$$

where $K_{d(A)}$ and $K_{d(B)}$ are dynamic stress intensity factors at point (A) and (B), respectively.

Plastic zone size corresponding to $K_{d(B)}$ is formally calculated as,

$$r_p = \frac{1}{6\pi}\left(\frac{K_{d(B)}}{\sigma_Y}\right)^2 . \quad (10)$$

As a point approaches from the mid-thickness point (z=0) to plate surface (z=B/2), stress triaxiality decreases. Weiss and Senguputa [11] showed that thickness of the region where the stress triaxiality falls from that of the plane-strain condition is proportional to r_p. It is assumed that brittle fracture cannot take place within this region; the UL is formed. Therefore, the UL thickness, t_{sl}, is simply expressed as,

$$t_{sl} = k_{sl}\, r_p \quad (11)$$

where, we set the value of the proportionality factor, $k_{sl}=2$, referring to Weiss and Senguputa's result, and r_p is expressed by Eq.(10). Because $K_{d(B)}$ (Eq.(9)) and σ_Y (a constant strain-rate, $10^3 s^{-1}$, in the UL is assumed for simplicity) are expressed as functions of T[x], t_{sl} is also a function of T[x] and therefore a function of x and does not depend on V_0 in the present model, as shown in Fig.8.

The above aspects of the crack propagation are difficult to formulate fully three-dimensionally. Here, the model is simplified into the two-dimensional model. The effect of the UL is represented by crack-closure stress, $\sigma_{sl}[x]$, imposed on the crack faces behind the crack-tip, see Fig.8. Stress acting on the UL is assumed to be equal to σ_Y and $t_{sl}[x]$ is averaged in the thickness direction, i.e.

$$\sigma_{sl} = \sigma_Y \frac{2t_{sl}}{B} \quad (12)$$

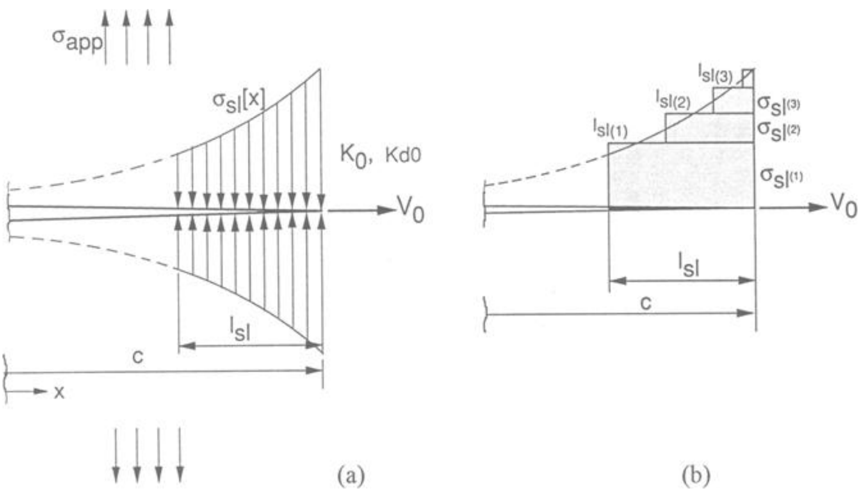

FIG.8--Two dimensional modeling of a propagating crack.

where, B is plate thickness.

Dynamic stress intensity factor for a crack of length 2c with constant remote stress, σ_{app}, and a constant crack-closure stress, σ_{sl}, over a length l_{sl} behind the crack-tip is expressed as [12],

$$K_{d0} = f_K[V_0]K_0 = f_K[V_0]\sigma_{app}\sqrt{\pi c}\left\{1-\frac{2}{\pi}\frac{\sigma_{sl}}{\sigma_{app}}\cos^{-1}\left[\frac{c-l_{sl}}{c}\right]\right\} \tag{13}$$

where, K_0 is static stress intensity factor, $f_K[V_0]$ is ratio of dynamic to static stress intensity factor and a function of V_0 [2]. Non-uniform crack-closure stress, $\sigma_{sl}[x]$, is discretized into constant crack-closure stresses and Eq.(13) is superimposed for each discretized crack-closure stress (see Fig.8-(b)). It should be mentioned that Eq.(13) is valid for infinite plate with constant σ_{app}. In the real specimen, however, the specimen width is finite and also load drop may take place during crack propagation. Influence of the finite width may not be significant for crack length to width ratio less than about 0.7. Also, in a specimen with large pin-to-pin length to the width ratio, e.g. larger than 3, all the crack propagation process is expected to finish before the stress wave reflected at the pin comes back to the center of the specimen. In this case, the influence of the load drop can be neglected.

The UL exhibits 45 degree slip deformation and finally fractures in shear, see Fig.9. Therefore, the critical opening displacement for the ductile shear fracture of the UL is expressed as,

$$2u_y[c-l_{sl}] = k_s t_{sl}[c-l_{sl}]\varepsilon_F \tag{14}$$

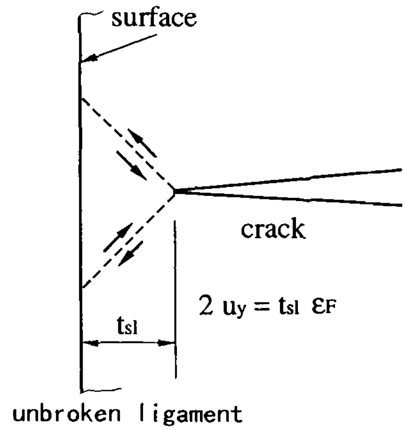

FIG.9--Plastic deformation at the unbroken ligament, cross secion.

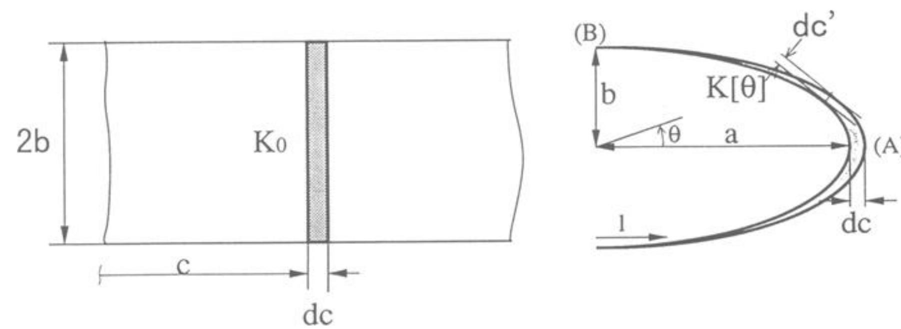

FIG.10--Conversion of stress intensity factor of the straight crack to semi-elliptical crack.

where, $u_y[x]$ is crack opening displacement as a function of x, the left hand side of the equation is crack opening displacement at the end point of the UL, i.e. $x=c-l_{sl}$, k_s is a constant and assumed to be equal to unity, and ε_F is critical strain for ductile fracture. $u_y[x]$ was obtained from reference [13].

Influence of the crack-tunneling is simplified into the two-dimensional model, as follows. $K_{d(A)}$ and $K_{d(B)}$ are assumed to be proportional to K_0,

$$K_{d(A)} = f_K[V_0]f_{e(A)}[b/a]K_0 \tag{15}$$

$$K_{d(B)} = f_K[V_{min}]f_{e(B)}[b/a]K_0 \tag{16}$$

where, $f_{e(A)}$ and $f_{e(B)}$ are functions of the aspect ratio of the semi-elliptical crack front, b/a, and determined so that the energy release rate integrated along the crack front with infinitesimal crack growth are equal for the two dimensional straight crack and for an elliptical crack in an infinite solid, see Fig.10.

$$dR_{(straightcrack)} = \frac{1-\nu^2}{E}K_0{}^2Bdc \tag{17}$$

$$dR_{(ellipticalcrack)} = \int_0^L \frac{1-\nu^2}{E}K[\theta]^2\,dc'dl \tag{18}$$

By using the formula of stress intensity factor for elliptical crack and equating Eq.(17) and (18), we obtain,

$$f_{e(A)} \equiv \frac{K_{(A)}}{K_0} = (b/a)^{1/2} f_{e(B)} \tag{19}$$

$$f_{e(B)} \equiv \frac{K_{(B)}}{K_0} = \left[\int_0^{\pi/2}\left\{1-(1-b^2/a^2)^{1/2}\cos[\theta]^2\right\}^{1/2}\cos[\theta]d\theta\right]^{-1/2} \tag{20}$$

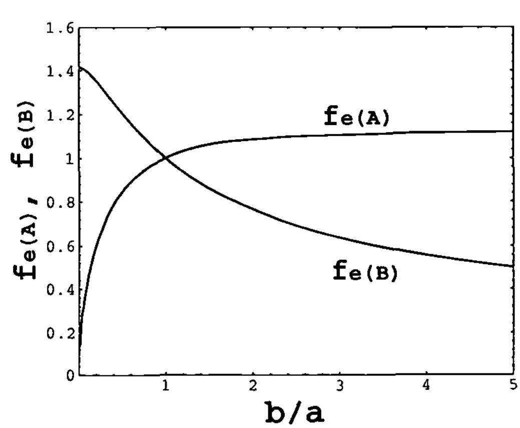

FIG.11--Functions $f_{e(A)}$ and $f_{e(B)}$.

Figure 11 shows functions $f_{e(A)}$ and $f_{e(B)}$. The above formulation is based fundamentally on static consideration and also the stress intensity factor distribution along the crack front is based on the elliptical crack in an *infinite* solid. Although more sophisticated formulation is desirable, the present formulation may be a rough but a good approximation.

Eqs.(19) and (20) are inserted into Eqs.(15) and (16), respectively, which in turn are inserted into Eqs.(8) and (9), respectively. Equations (8), (9) give crack propagation condition at the crack front, and Eq.(14) gives ductile fracture condition of the UL. In these equations, σ_{sl}, t_{sl} etc. are expressed by Eqs.(10) through (13). Those three equations constitute overall fracture conditions, where V_0, b/a and l_{sl} are unknown parameters. For a given value of c, value of these parameters are determined by solving the non-linear equations simultaneously.

Results

Some of the present authors previously conducted a series of double tension tests [14], which are computer-simulated by the present model. The steels tested are two kinds of 20mm thick mild steels, steel-A and steel-E, for ship structures with practically the same yield strength, approximately 300MPa, and different toughness. Specimen width, W, was 0.5m and pin-to-pin length was 3.5m. Figure 12 shows temperature distributions targeted in the experiment and assumed in the simulation. By changing σ_{app} and temperature distribution, arrest crack length, c_a, was changed. Arrest toughness, K_{ca}, is empirically calculated from σ_{app} and c_a by using the tangent formula [15],

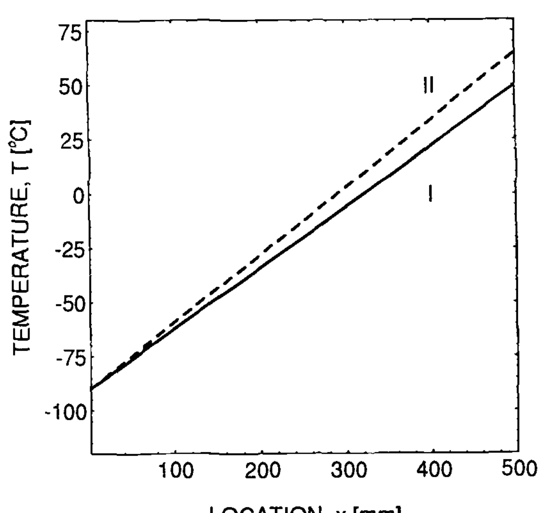

FIG.12--Assumed temperature distribution.

$$K_{ca} = \sigma_{app}\sqrt{2W\tan[\pi c_a / 2W]}\,. \tag{21}$$

Results are shown in Table 1 together with the calculated results. Figures 13-(a) and (b) show observed histories of V_0 measured by crack-detector gages for steel-A and steel-E, respectively.

TABLE 1--Results of temperature-gradient type arrest tests.

steel	σ_{app} (MPa)	Temp. Type	experiment c_a (mm)	experiment arrest temp. (deg.C)	experiment K_{ca} (MPa/m)	calculation c_a (mm)	calculation arrest temp. (deg.C)	calculation K_{ca} (MPa/m)
A	78	I	367	12	118	343	8	107
"	"	II	292	6	90	303	4	93
"	98	I	366	15	147	382	17	157
"	118	I	446	29	284	407	24	215
E	98	I	298	-6	114	308	-4	118
"	118	I	319	1	147	336	4	157
"	137	I	360	13	200	357	10	198
"	157	I	371	16	239	373	14	242

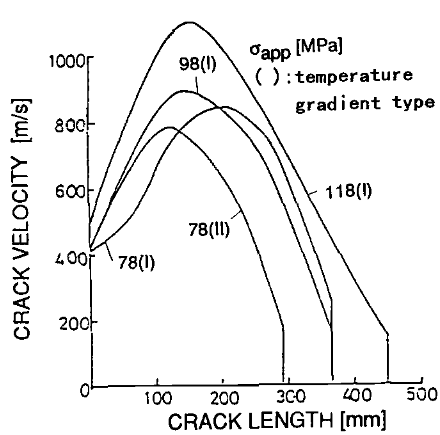

(a) Steel-A

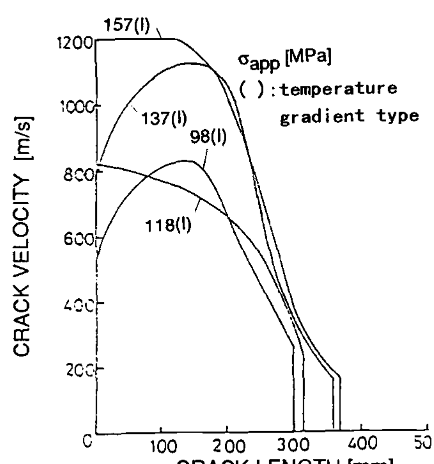

(b) steel-E

FIG.13--History of crack velocity, experiment[14].

In the simulation, we use the same values of material parameters shown in Fig.5. In addition, we set ε_F=0.1. Values of σ_F for the both steels were determined so that the calculated c_a for the lowest σ_{app} roughly agreed with the experiments: σ_F=4000MPa for steel-A and 4200MPa for steel-E.

Figure 14 shows calculated t_{sl} for steel-A (corresponding to temperature distribution I and II in Fig.12) and steel-E (temperature distribution I). Associated σ_{sl} is

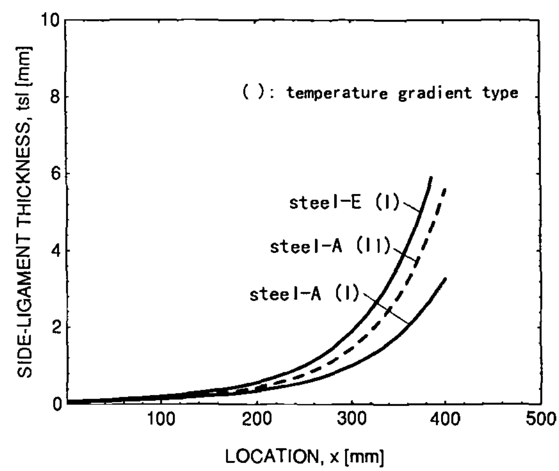

FIG.14--Calculated thickness of unbroken ligament.

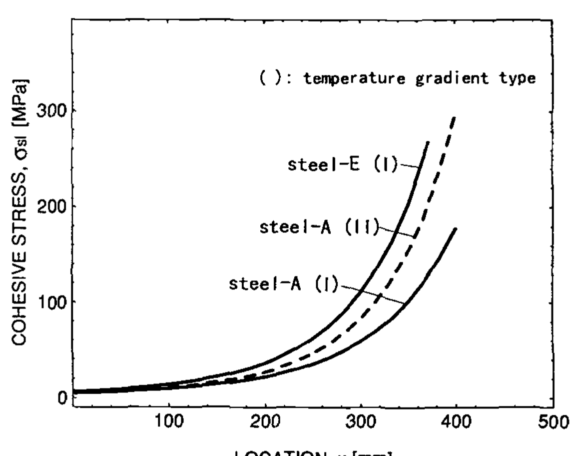

FIG.15--Calculated distribution of crack-closure stress.

shown in Fig. 15. The UL increases its thickness steeply with increasing crack-tip location due to the rise in temperature. Steel-E has thicker UL than steel-A due to higher σ_F. The UL thickness also depends on the temperature distribution.

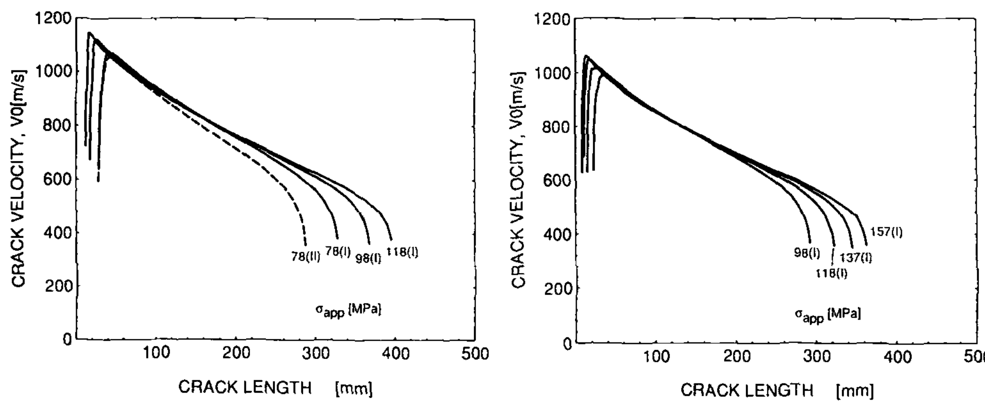

(a) steel-A (b) steel-E

FIG. 16--Caclulated history of crack velocity.

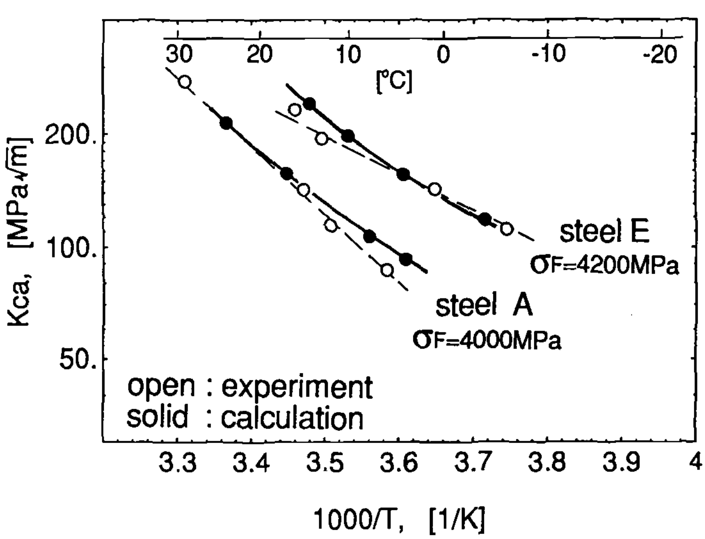

FIG. 17--Comparison between calculated and experimental arrest toughness.

Figures 16-(a) and (b) show calculated histories of V_0. V_0 increases steeply just after crack initiation, attains a maximum, decreases and the crack is finally arrested. Although there is a discrepancy at the very initial stage of the crack propagation, calculated histories of V_0 compare well with the experiment. Table 1 also compares measured and calculated c_a. c_a increases with increasing σ_{app}. History of V_0 and c_a depend on the temperature distribution, as well: lower V_0 and smaller c_a for the temperature distribution II than I.

Figure 17 shows measured and calculated K_{ca} for the two steels. Considering the possible deviation of temperature distribution from the target (Fig. 12), the calculated K_{ca} compare well with the measured K_{ca}. Although a parameter which depends on temperature is yield stress only in the present model, calculated temperature dependency of K_{ca} are well reproduced.

Figure 18 shows calculated fracture surfaces at crack arrest. With increasing σ_{app}, c_a increases and also t_{sl} at crack arrest increases. Length of the UL at crack arrest also increases

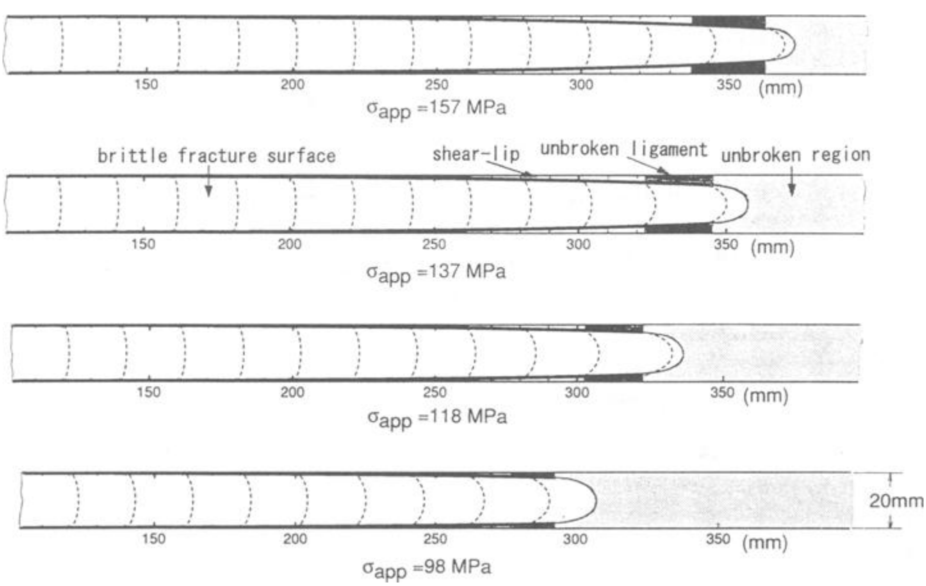

FIG.18--Calculated fracture surface profiles, steel-E.

with increasing σ_{app}. This is because larger crack opening displacement at the end point of the UL is necessary for the thicker UL in order to satisfy the ductile fracture criterion, see Eq.(14). Unfortunately, record of the fracture surfaces in the experiment is not available. Thus, we refer to the fracture surface observations by Akita et al. [16] for different series of the temperature-gradient type ESSO tests and compare them with the present calculation, only qualitatively. Figure 19 is a redrawing from the fracture surface photographs [16]. Only the arrest crack-tip region is shown and the actual arrest crack length changed with σ_{app}. With increasing σ_{app} and increasing arrest temperature, thickness of the UL at crack arrest increased (distinction between UL and shear-lip is impossible) and the crack front tunneling became more pronounced. This tendency compares well with the calculation shown in Fig. 18.

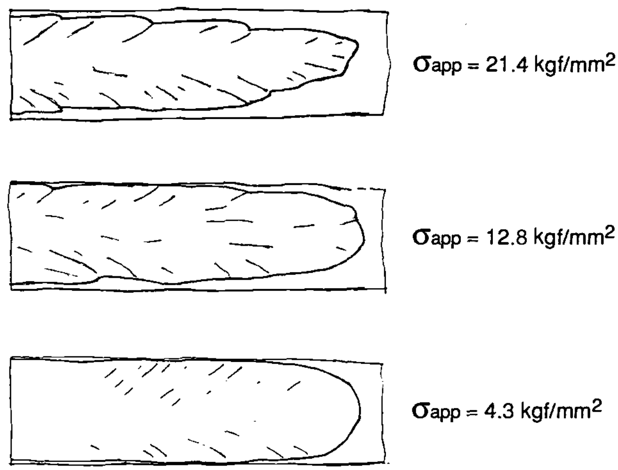

FIG.19--Fracture surface profiles, redrawing from [16].

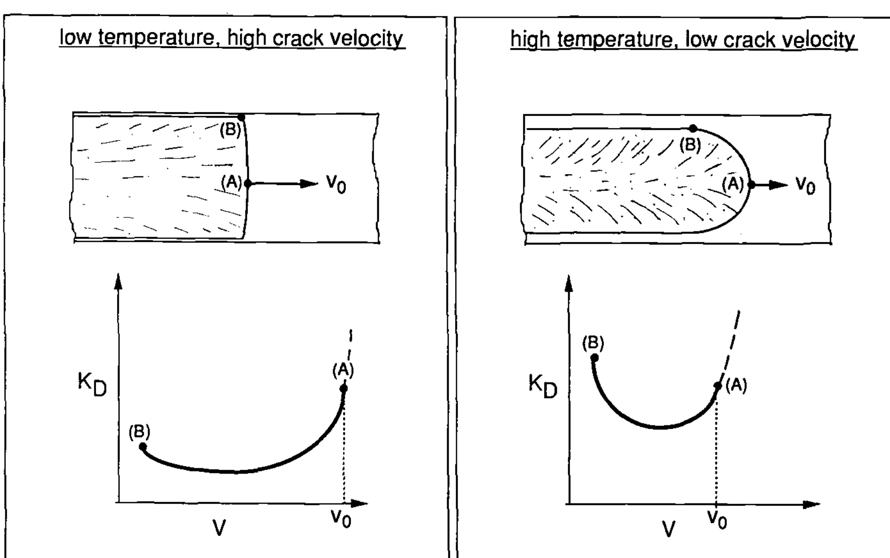

FIG.20--Relation between crack front shape and dynamic fracture toughness.

Figure 18 also shows that the crack front shape during propagation is straighter for lower temperature and higher V_0. This tendency has been observed empirically but no explanation has been made. Change in the crack front shape with temperature and V_0 is schematically explained by Fig.20. At low temperature, K_D depends on V weakly except near the upper limit velocity (left side of the Figure). In addition, V_0 tends to be high at low temperature, closer to the upper limit velocity. At this circumstance, $K_{D(A)}$ tends to be larger than $K_{D(B)}$. Because K_d is equal to K_D at both points, crack front shape becomes straighter so that $K_{d(A)}$ is larger than $K_{d(B)}$. Conversely, $K_{D(A)}$ tends to be lower than $K_{D(B)}$ at high temperature and low V_0, and the crack front tunneling becomes more pronounced (right side of the Figure). Even at low temperature, crack front tunneling becomes pronounced at low crack velocity, especially just before crack arrest.

Figures 21-(a) and (b) show changes in stress intensity factors with crack propagation for the lowest and highest σ_{app} in steel-E. K_s is apparent static stress intensity factor, $\sigma_{app}(\pi c)^{1/2}$, $K_{s(tan)}$ is apparent static stress intensity factor by the tangent formula. K_d is apparent dynamic stress intensity factor, calculated as $f_K[V_0]K_s$. K_{d0} and $K_{d(A)}$ are defined in Eq.(13) and (15), respectively. Deviation of K_{d0} from K_d is due to the crack-closure effect by the UL. Amount of the deviation increases with increasing crack length because of the increased thickness and length of the UL. It is clearly seen that the effect of the UL is more pronounced at higher arrest temperature. Reason for the drop in $K_{d(A)}$ with increasing crack length is two-fold; one is the crack-closure effect by the UL and the other is the effect of the crack-tunneling. As explained above, the crack-tunneling becomes pronounced just before crack arrest. Thus, $K_{d(A)}$ falls rapidly just before crack arrest.

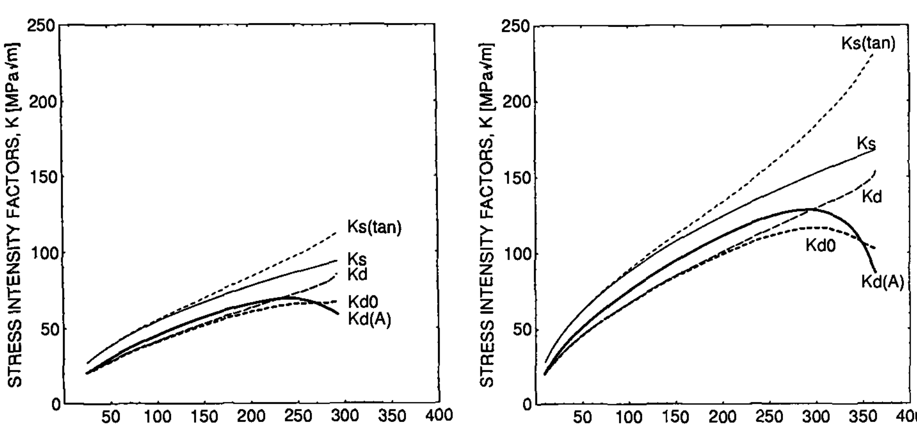

(a) steel-E, σ_{app}=98Mpa (b) steel-E, σ_{app}=157MPa

FIG.21--Calculated stress intensity factors.

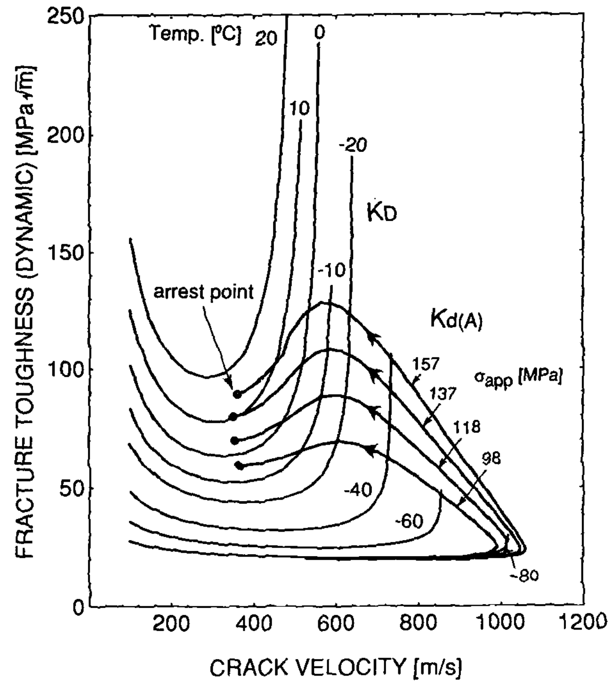

FIG.22--History of dynamic stress intensity factor and crack velocity at mid-thickness point, steel-E.

Figure 22 shows change of $K_{d(A)}$ with V_0 for steel-E. $K_D[V,T]$ curves are also plotted. After accelerated at low temperature, the crack is decelerated, while $K_{d(A)}$ increases. In turn, $K_{d(A)}$ begins to decrease with K_d continuing to increase. This is due to the double effects mentioned above. At the minimum $K_D[V,T]$ point, it becomes no longer possible to maintain the equality between $K_{d(A)}$ and $K_D[V,T]$; the former tends to decrease and the latter tends to increase and the crack is arrested. The crack is not arrested with V_0 continuously decreasing down to zero, but there is a lower limit. Calculated lower limit V_0 ranges from 300 to 350m/s and measured lower limit V_0 ranges from 200 to 300m/s (Fig.13). Considering the difficulty in measuring the crack velocity and its accuracy, especially just before crack arrest, the present model reproduces the crack arrest behavior well. It should be emphasized here that the lower limit crack velocity assumed in Eq.(9) is the *local* lower limit crack velocity and is not the same as the *macroscopic* lower limit crack velocity discussed here.

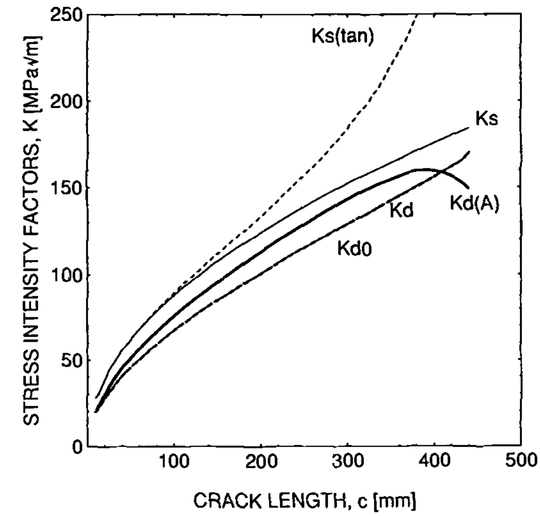

FIG.23--Calculated stress intensity factors, steel-E, σ_{app}=157MPa, without UL.

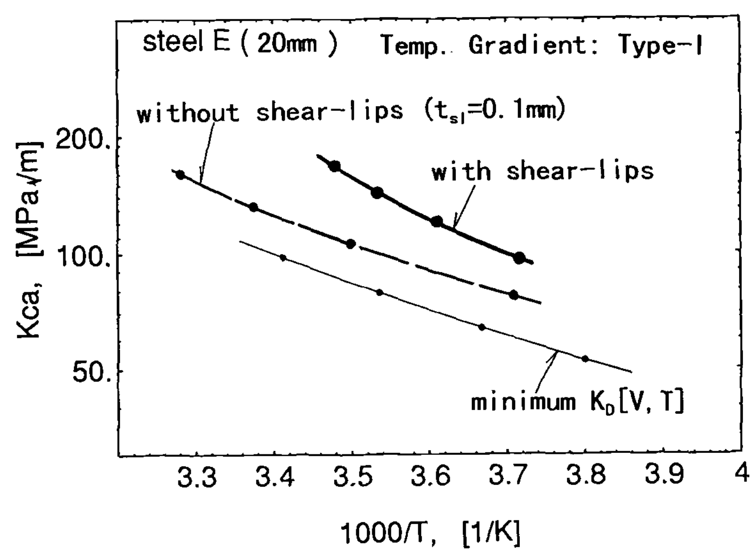

FIG.24--Calculated influence of UL on arrest toughness, steel-E.

The effect of the UL is further studied. A simulation was conducted without UL (for the sake of the computer program, we set t_{sl}=0.1mm). Figure 23 shows changes of stress intensity factors. K_d coincide with K_{d0} throughout the crack propagation process. Drop of $K_{d(A)}$ just before crack arrest is small. As a result, arrest crack length becomes longer than that with UL.

Figure 24 shows a comparison between K_{ca} with UL, K_{ca} without UL (t_{sl}=0.1mm). K_{ca}(without UL) is considered to be plane-strain arrest toughness. Minimum K_D at each temperature (Fig.5) is plotted for a reference. Note that Eq.(21) is not used for calculating K_{ca} but the formula for an infinite plate is used, instead. Difference between K_{ca}(with UL) and K_{ca}(without UL) is significantly large, especially at high temperature. Temperature dependence of K_{ca}(without UL) is milder than that of K_{ca}(with UL) and that of measured K_{ca}. It is indispensable to take account of the effect of the UL for predicting the actual temperature dependency of the arrest toughness.

DISCUSSION

It has been shown that the present model reproduces actual crack propagation and arrest behavior well. Considering the possible experimental errors, the present model predicts arrest crack length and arrest toughness with a reasonable accuracy.

σ_F was determined so that calculated arrest crack length agreed with the measured value at a certain experimental condition. At this moment, however, it is impossible to determine σ_F value experimentally. The assumed value of σ_F is rather high as compared with σ_F of brittle cleavage crack initiation in steel [17]. While brittle microphase has a significant influence on cleavage crack initiation, its effect is not so significant for crack propagation [18]. In addition, tear-ridges are formed on the propagating crack surface. The tear-ridges connect the crack faces behind the crack-tip and may have the crack-closure effect in the microscopic level. These factors may justify the assumed high value of σ_F for crack propagation.

Importance of the UL has been pointed out in the present model. Even with the same $K_D[V,T]$ values, K_{ca} can be varied by a change in the UL formation. Hence, the effect of the temperature-gradient was studied. Temperature-gradient for the standard (W=0.5m) and wide plate (W=2.0m) specimen was changed, while the temperatures at both sides were kept unchanged, T_0=-90deg.C and T_1=50deg.C. Figure 25 shows calculated apparent arrest toughness, K_{ca}. Higher K_{ca} value for the wide plate specimen (mild temperature- gradient) than that for the standard specimen (steep temperature-gradient) is obtained. This means that K_{ca} is not a unique material parameter describing the arrest resistance of steel, but depends on temperature-gradient. Although the change in K_{ca} becomes larger with larger value of assumed ε_F, it is not very significant. It should be mentioned that K_{ca} obtained from a specimen with steep temperature-gradient is a lower bound value and may be regarded as a conservative estimation [19].

For a tough material, it is sometimes difficult to obtain plane-strain arrest toughness. Side-grooves may be applied to suppress the formation of the UL or shear-lips [20]. If the effect of the UL is estimated accurately, plane-strain arrest toughness may be predicted from the arrest test accompanying the UL based on the present theory. This is subject to a future

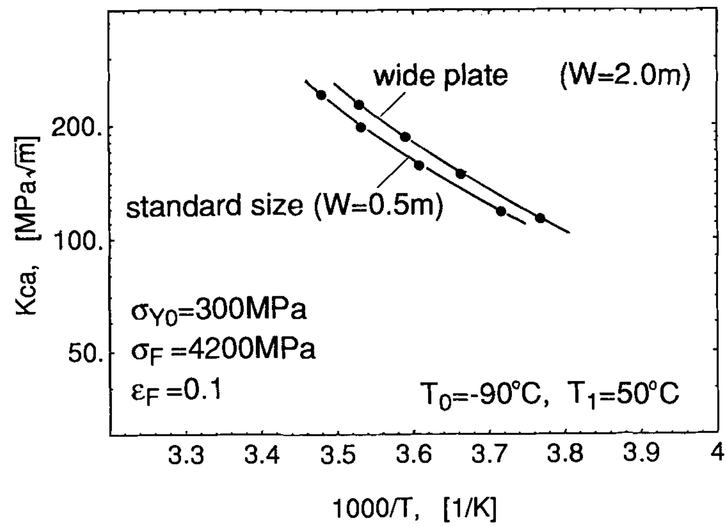

FIG.25--Calculated influence of temperature-gradient on arrest toughness.

work.

CONCLUSIONS

(1) Dynamic fracture toughness, K_D, is calculated from fundamental material parameters based on the local fracture stress criterion. K_D is expressed as a function of crack velocity and temperature.

(2) K_D has a minimum with respect to crack velocity and diverges at an upper limit crack velocity, which is related to the Rayleigh wave speed for plastic deformation and decreases with increasing temperature.

(3) A model is proposed which takes account of the unbroken-ligament formed near the plate surface and of the crack-front-tunneling in the middle of the plate thickness. The model simulates crack propagation and arrest behavior in a specimen with temperature-gradient. By assuming a suitable value of local fracture stress, calculated arrest length and apparent arrest toughness agree well with results from experiment.

(4) The effect of the unbroken-ligament is significant in suppressing the crack propagation. It changes with temperature-gradient. Arrest toughness calculated from applied stress and arrest crack length is not a unique material parameter but depends on the temperature-gradient, although weakly.

REFERENCES

[1] Kanazawa, T., Machida, S., Teramoto, T. and Yoshinari, H., "Study on Fast Fracture and Crack Arrest", Experimental Mechanics, Feb. 1981, pp 79-88.

[2] Freund, L. B., Dynamic Fracture Mechanics, Cambridge University Press, 1990.
[3] Machida, S. Yoshinari, H., Yasuda, M., Aihara, S. and Mabuchi, H., "Fracture Mechanical Modeling of Brittle Crack Propagation and Arrest of Steel", Proceedings of the 1995 Joint ASME/JSME Pressure Vessels and Piping Conference, PVP-vol.300, p 183-195, ASME, 1995.
[4] Ritchie, R. O., Knott, J. F. and Rice, J. R., "On the Relationship between Critical tensile Stress and Fracture Toughness in Mild Steel", J. Mechanics and Physics of Solids, vol.21, 1973, pp 395-410.
[5] Miyata, T., Ohtsuka, A., Mitsubayashi, M., Haze, T. and Aihara, S., "Prediction of Fracture Toughness by Local Fracture Criterion", ASTM STP 1074, 1990, p 361-377.
[6] Achenbach, J. D., Kanninen, M. F. and Popelar, C. H., "Crack-Tip Fields for Fast Fracture of an Elastic-Plastic Materials", J. Mechanics and Physics of Solids, vol.29, 1981, pp 211-225.
[7] Hutchinson, J. W., "Singular Behaviour at the End of a Tensile Crack in a Hardening Material", J. Mechanics and Physics of Solids, vol.16, 1968, pp 13-31.
[8] Amazigo, J. C. and Hutchinson, J. W., "Crack-Tip Fields in Steady Crack-Growth with Linear Strain-Hardening", J. Mechanics and Physics of Solids, vol.25, 1977, pp 81-97.
[9] Sundararajan, G. and Shewmon, P. G., "The Use of Dynamic Impact Experiments in the Determination of the Strain Rate Sensitivity of Metals and Alloys", Acta Metallurgica, vol.31, 1983, pp 101-109.
[10] Campbell, J. D. and Ferguson, W. G., "The Temperature and Strain-Rate Dependence on the Shear Strength of Mild Steel", Philosophical Magazine, vol.21, 1970, pp 63-82.
[11] Weiss, V. and Senguputa, M., "Ductility, Fracture Resistance and R-Curves", ASTM STP 590, 1976, p 194-207.
[12] Freund, L. B., "Crack Propagation in an Elastic Solid Subjected to General Loading -II, Non Uniform Rate of Extension", J. Mechanics and Physics of Solids, vol.20, 1972, pp 141-152.
[13] Embley, G. T. and Sih, G. C., "Plastic Flow Around an Expanding Crack", Engineering Fracture Mechanics, vol.4, 1972, pp 431-442.
[14] Kanazawa, T., Machida, S., Teramoto, T., Yoshinari, H. and Miyahara, T., "Study on Fast Fracture and Crack Arrest (5th Report)", Journal of Society of Naval Architects of Japan, vol.150, 1981, p 504-510.
[15] Tada, H., Paris, P. C. and Irwin, G. R., Stress Analysis of Cracks Handbook, Hellertown: Del research Corporation, 1973.
[16] Akita, Y. and Ikeda, K., "On the Brittle Crack Propagation and Arrest with Special Reference to ESSO Test with Temperature Gradient", Journal of Society of Naval Architects of Japan, vol.112, 1962, p 153-162.
[17] Bowen, P., Druce, S. G. and Knott, J. F., "Effects of Microstructure on Cleavage Fracture in Pressure Vessel Steel", Acta Metallurgica, vol.34, 1986, pp 1121-1131.
[18] Aihara, S., "Influence of HAZ Microstructure on Brittle Fracture Initiation and Arrest Toughness", CAMP-ISIJ, vol.7, 1994, p.843.
[19] Mimura, H., "Method to Estimate Kca from K1a", J. High Pressure Institute, Japan, vol.31, 1993, pp 58-64.
[20] ASTM E 1221-88, "Standard Test Method for Determining Plane-Strain Crack-Arrest Fracture Toughness, K_{Ia}, of Ferritic Steels", 1988.

Pir M. Toor[1]

STRESS INTENSITY MAGNIFICATION FACTORS FOR FULLY CIRCUMFERENTIAL CRACKS IN VALVE BODIES (THICK CYLINDERS)

REFERENCE: Toor, P. M. ''**Stress Intensity Magnification Factors for Fully Circumferential Cracks in Valve Bodies (Thick Cylinders)**'', Fatigue and Fracture Mechanics: 28th Volume, ASTM STP 1321, J. H. Underwood, B. D. Macdonald, and M. R. Mitchell, Eds., American Society for Testing and Materials, 1997.

ABSTRACT:

The stress intensity solutions presented herein were obtained using an energy method in conjunction with a two-dimensional finite element program in order to explicitly account for curvature effect for fully circumferential cracks. The magnification factors for a specific crack depth were calculated by successively loading the crack surface by a uniform, linear, quadratic, and a cubic loading distribution. The magnification factors can be used to calculate the stress intensity factors by superposition method.

The functions for each load condition in terms of radius to thickness ratio (R/t) and a fractional distance in terms of crack depth to thickness ratio (a/t) were developed. The validity of these function is $R/t = 1.5$ to 10.0 and for $0.0125 \leq a/t \leq 0.8125$. The functions agree to within 1% of the finite elements solutions for most magnification factors.

KEYWORDS: cylinders, curvature constraint, continuous circumferential cracks, finite element, stress, energy, magnification factors, stress intensity factors

[1]Bettis Atomic Power Laboratory, P.O. Box 79, West Mifflin, PA 15122.

INTRODUCTION

Fatigue crack growth and brittle fracture evaluations are often carried out using stress intensity factor solutions developed for crack-like surface defects in flat plates. The stress intensity factor solutions are expressed in terms of membrane and bending stress intensity magnifications factors calculated for plates that are subject to no geometric constraints. The lack of geometric constraint maximizes the crack opening at the crack tip and assures that the calculated stress intensity factors are conservative.

However, stress intensity factors for cracks in geometrically complex structures are often calculated by explicit finite element methods. The magnitude of stress intensity factor depends upon the location, shape, and orientation of the crack as, well as upon the geometry of the component. In real structures the application of flat plate stress intensity factor solution to structures with significant wall curvature, such as valves, results in overly conservative crack growth predictions. The curvature produces a less compliant structure than a flat plate in the presence of a crack and, due to reduced opening of the crack-tip, the resulting stress intensity factor is less than that of a flat plate.

The effect of curvature constraint on stress intensity factor is maximized when continuous cracks are considered. In this case curvature inhibits bending deformation in the uncracked ligament; no such constraint exists for the flat plate case. When the crack configuration is that of a part-through semielliptical surface crack, an inherent restraining effect due to the adjacent uncracked section inhibits bending deformation. Therefore, separate constraint mechanisms exist for semielliptical part-through and continuous surface cracks in terms of bending deformation. In this paper, magnification factors are developed for a fully circumferential crack for numerous values of curvature (R/t) and relative crack depth (a/t), where R is the inside radius of the cylinder, t is the cylindrical wall thickness, and a is the crack depth.

Several analytical procedures are available in the literature to calculate elastic stress intensity factors for complex structures using finite element analysis. For conditions of plane stress or plane strain, the potential energy (G) of the structure released as a result of crack extension can be related to the stress intensity factor (K_I), Reference (1). The advantage of using the energy-based finite element procedure is that it does not utilize any special treatment of the mechanical response in the immediate vicinity of the crack tip.

The energy method in conjunction with a two-dimensional elastic finite element program was used to expeditiously evaluate the curvature effect for fully circumferential cracks in thick-walled and thin-walled cylinders. The results were verified using other published numerical solutions for internally pressurized cylinders with continuous cracks.

STRESS INTENSITY FACTORS K_I

Calculation of Strain Energy Rebase Rate, G

The 2-dimensional elastic finite element program was used in conjunction with the automated evaluation of stress intensity factors for continuous cracks in planar or axisymmetric structures, to calculate the change in potential energy due to a unit increase in crack length for plane strain and plane stress conditions. The energy release rate method for calculating stress intensity factors is described as:

$$G\,\delta a = \int_{a}^{a+\delta a} \sigma_1 \;\; U_1 \;\; dx \tag{1}$$

where σ = stress distribution ahead of crack length a,

U_1 = crack surface displacement.

G is related to K_I by Reference (1):

$$K^2 = E'G \tag{2}$$

where E' is $\begin{cases} E \text{ for plane stress, and} \\ E/(1 - \nu^2) \text{ for plane strain} \end{cases}$

Procedure to Determine K_I

The procedure used to calculate the stress intensity factor solution consists of applying the superposition principle in the loading of the finite element model and in expressing the stress in terms of the coefficients of a third order polynomial representing the stress profile perpendicular to the section of the structure.

Superposition Principle

The superposition method is illustrated in Figure 1. The stress intensity factor K_I for the crack in Section A-A of the structure, subjected to a remote loading (F, M) represented by a force F and a moment M, is equal to the stress intensity factor K_I for the same crack in Section A-A of the structure, where the crack surface is subjected to a stress profile $\sigma(x)$ identical to the stress profile developed perpendicularly to the uncracked Section A-A by the remote loading (F, M).

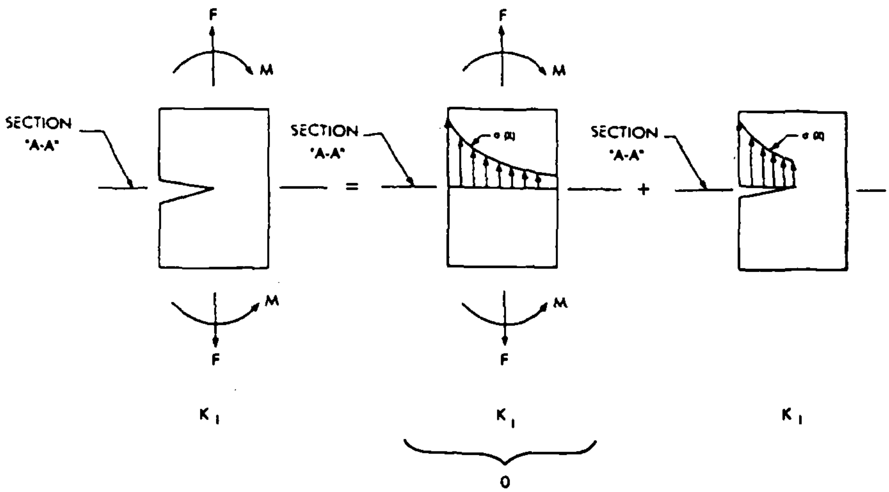

Figure 1: Superposition Principle

The stress profile $\sigma(x)$ perpendicular to Section A-A of the structure during a transient in the absence of a flaw, can be fitted, by least squares regression, to a third degree polynomial as:

$$\sigma = A_0 + A_1 x + A_2 x^2 + A_3 x^3 \qquad (3)$$

where A_0, A_1, A_2, A_3 are coefficients of the polynomial representing the stress profile $\sigma(x)$ in the uncracked Section A-A.

If a continuous flaw is now assumed to be present in Section A-A during the transient considered, the stress intensity factor is normally expressed as:

$$K_I = \sqrt{\pi a}\left[A_0 G_0 + A_1 G_1 + A_2 G_2 + A_3 G_3\right] \qquad (4)$$

where: a = the crack depth

G_0, G_1, G_2, and G_3 = magnification factors corresponding to the geometry and the crack depth.

In the above equation, the magnification factors G_0, G_1, G_2, and G_3 are functions of the crack geometry and are independent of the magnitude of loading. Therefore, the magnification factors can be calculated using any arbitrary stress profile applied to the crack surface. In this paper, the magnification factors for a specific crack depth were calculated by successively loading the crack surface as follows:

(1) a uniform loading distribution ($\sigma = A_0$)
(2) a linear loading distribution ($\sigma = A_1x_1$)
(3) a quadratic loading distribution ($\sigma = A_2x^2$)
(4) a cubic loading distribution ($\sigma = A_3x^3$)

The above procedure is then applied to many combinations of crack depth and wall curvature to determine the variation of the magnification factors G_0, G_1, G_2, and G_3 with the crack depth to thickness ratio (a/t) for various radius to thickness ratios (R/t).

The various stress distributions applied to the crack surface are shown in Figure 2 and the magnification factors are calculated as:

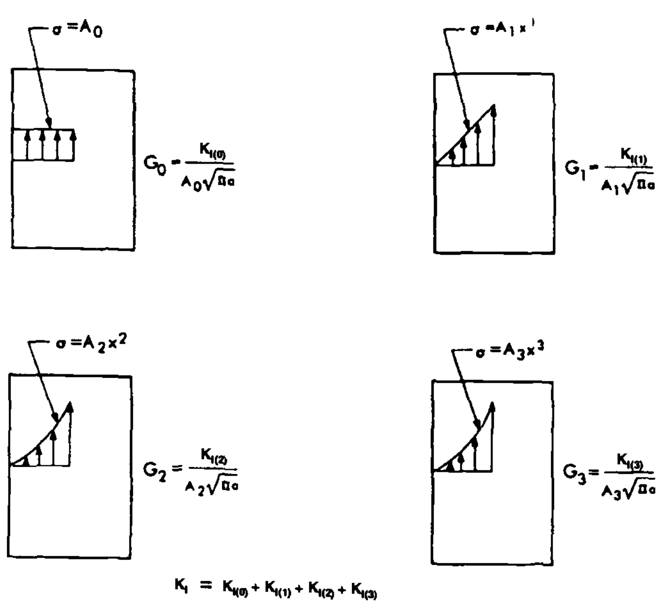

Figure 2: Magnification Factors Determination

$$G_0 = \frac{K_{I(0)}}{A_0 \sqrt{\pi a}} \qquad \text{(uniform loading)} \qquad (5)$$

$$G_1 = \frac{K_{I(1)}}{A_1 \sqrt{\pi a}} \qquad \text{(linear loading)} \qquad (6)$$

$$G_2 = \frac{K_{I(2)}}{A_2 \sqrt{\pi a}} \qquad \text{(quadratic loading)} \qquad (7)$$

$$G_3 = \frac{K_{I(3)}}{A_3 \sqrt{\pi a}} \qquad \text{(cubic loading).} \qquad (8)$$

In this paper stress intensity factors were calculated using the strain energy release rate method described above.

FULLY CIRCUMFERENTIAL INSIDE SURFACE CRACK IN CYLINDERS

Geometry

A typical circumferential cracked cylinder in tension is shown in Figure 3. The symbols R_i and R_o represent the inside and outside radius of the cylinder, respectively, t is the cylinder thickness (R_o - R_i), and a is the crack size.

The thickness of the cylinder was kept constant and the inside radius, R_i, was varied to determine various R_i/t ratios. The height of the cylinder was kept ten times the thickness to ensure the infinite nature of the cylinder.

Finite Element Mesh

Grid points and two free bodies (SA and SB) and the finite element mesh of a fully circumferential part-through crack in a cylinder are shown in Figure 4. By symmetry only one half of the specimen was modeled. The boundary conditions are zero surface tractions everywhere but on grid points 3 to 4 where the condition that displacement in the normal direction be zero is imposed. The model was loaded by specifying and applying load between grid point 2 and 3 on the crack surface. The enlarged finite element mesh near the crack is also shown in Figure 5.

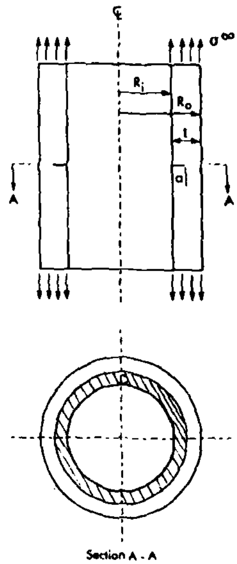

Figure 3: Fully Circumferential Crack in a Cylinder

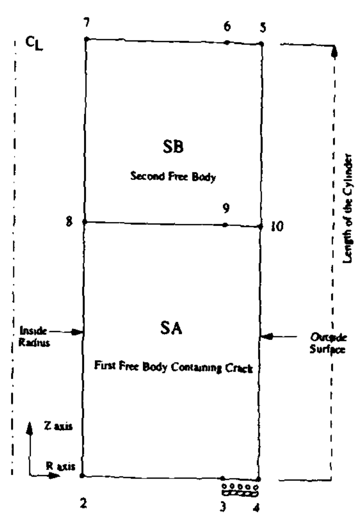

Figure 4: Grid Points and Two Free Bodies (SA and SB) for Fully Circumferential Crack

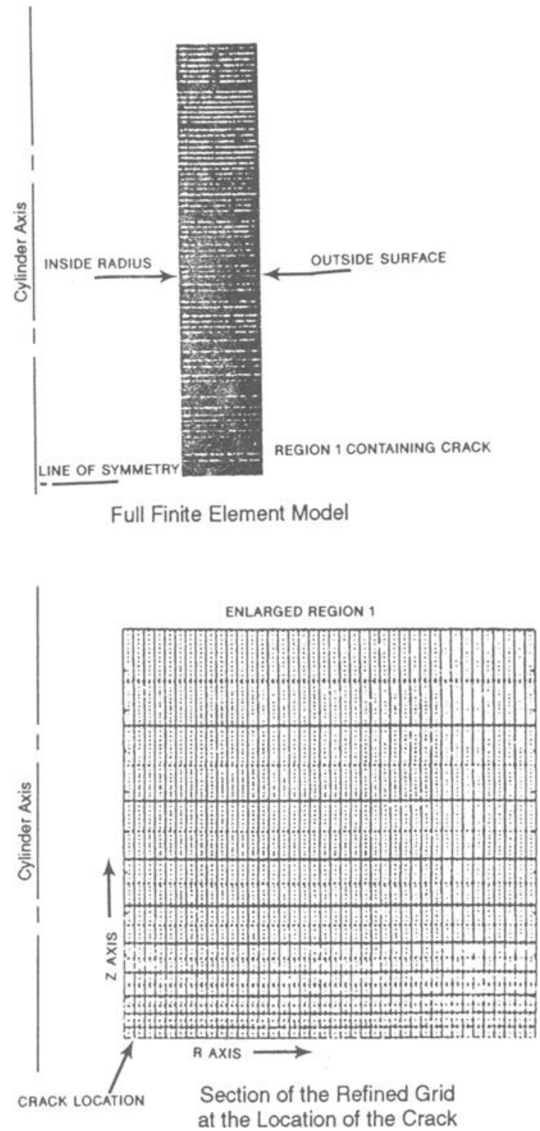

Figure 5: <u>A Two-Dimensional Finite Element Model Having a Fully Circumferential Crack</u>

Applied Loads

The magnification factors G_0, G_1, G_2, and G_3 in Equation 20 are functions of the crack geometry and the cylinder curvature and are independent of the magnitude of loading. Therefore, the magnification factors can be determined using any arbitrary loading profile applied to the crack surface. The magnitude of load in this example was one ksi. The magnification factors (G_0, G_1, G_2, and G_3) relative to a given crack depth, a, were determined by successively loading the crack surface to uniform ($\sigma = A_0$), linear ($\sigma = A_1x$), quadratic ($\sigma = A_2x^2$), and cubic ($\sigma = A_3x^3$) stress profiles.

These stress distributions were applied as piecewise linear over the 39 elements.

The various magnification factors as functions of a/t and R_i/t with the crack depth to thickness ratio (a/t) were established. Figure 3 shows the application of four loading conditions applied to the surface of the crack and equations used in each case for the corresponding magnification factor.

Boundary Conditions

By symmetry only one half of the structure was modeled. The boundary conditions are zero surface tractions everywhere but on grid points 3 to 4 where the conditions where displacement in the normal direction be zero are imposed. The crack surface was successively loaded as described above.

Mesh Sensitivity Evaluation

In order to determine the adequacy of the finite element mesh, elastic solutions were obtained to investigate the effects of several parameters (i.e. number of elements in the mesh along the thickness of the model, radial spacing of the elements, and the length of the specimens in the analytical model) on the computed stress intensity factor along the crack length. In order to achieve an optimum finite element mesh, several finite element models were developed. The final stress intensity factors for the circumferential crack model are based on two free bodies. There were forty (40) equally spaced elements along the thickness direction including 39 elements over the cracked area. The first free body (SA) has ten (10) elements in the length direction with an element size ratio of one to ten. Similarly the second free body SB has ten elements with an element size ratio of twenty. The largest element adjoining to the first free body (SA). The element ratios between 10 to 50 did not change the results as shown in Figure 6.

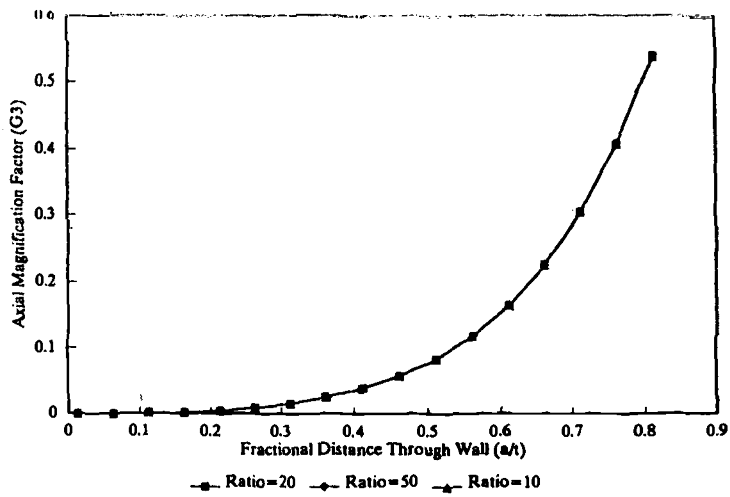

Figure 6: Finite Element Ratio Study

Determination of Magnification Factors

The magnification factors were calculated using the energy method. As discussed in previous sections the available energy (G) for unit crack extension is related to stress intensity factors (K_I). For a specified load condition, the stress intensity factor K_I for two-dimensional analysis was calculated. The input to computer code was modified to accept a linear, non-linear, and cubic load distribution at the crack surface. The stress intensity factors were obtained for crack depths up to 80 percent of the wall thickness. The magnification factors (G_0, G_1, G_2, and G_3) were calculated using Equation 12.

Verification of Fully Circumferential Magnification Factors for R/t = 10

The magnification factors for a circumferential inside surface crack in a cylinder developed in this report, using the energy method (Toor) are compared with the Buchalet and Bamford, Reference (2) and Zahoor's, Reference (3) finite element solutions for R/t=10. The comparison is shown in Figures 7-10.

Magnification Factor G_0--The magnification factor G_0 is due to a uniform stress distribution over the crack depth. Figure 7 compares three solutions. It is observed in this figure that References (2) and (3) solutions cross over at a/t = 0.5. The energy method magnification factors agree with Burchalet solution up to a/t = 0.3 but are consistently above Buchalet and Zahoor's solution up to a/t = 0.8. For deeper crack a/t = 0.8, the energy solutions are 15 percent higher than the other two solutions.

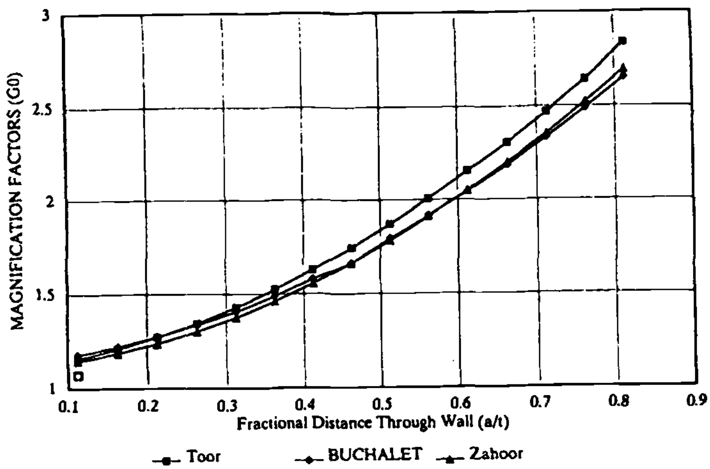

Figure 7: Fully Circumferential R/T = 10 Verification of Magnification Factor, G_0

Magnification Factor G_1--The magnification factor G_1 is associated with linear stress distribution over the crack depth. Figure 8 compares three solutions (Toor, Buchalet, and Zahoor). Again, the energy method solution results are slightly higher than the other two solutions.

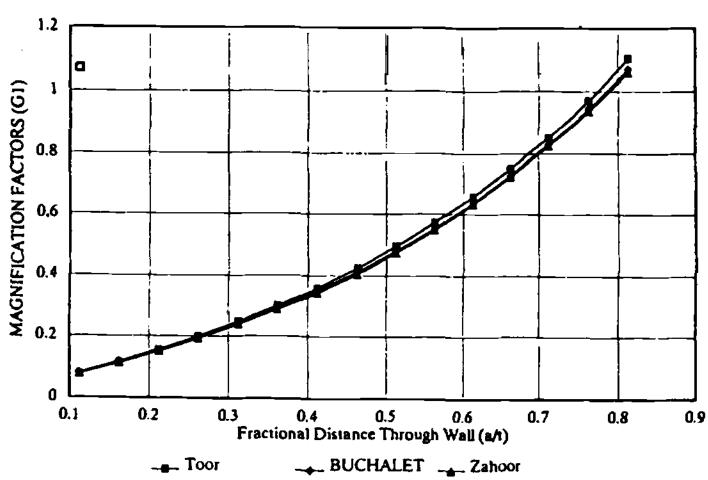

Figure 8: Fully Circumferential Crack R/T = 10 Verification of Magnification Factor, G_1

Magnification Factor G_2--The magnification factor G_2 is associated with quadric stress distribution over the crack depth. Three solutions are compared in Figure 9. It is observed from this figure that energy method values of the magnification factor are higher than the other two solutions.

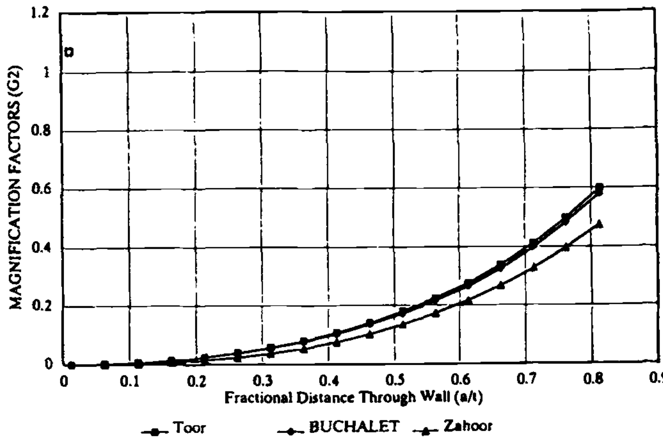

Figure 9: Fully Circumferential Crack R/T = 10
Verification of Magnification Factor, G_2

Magnification Factor G_3--The magnification factor G_3 is due to a cubic form of stress distribution over the crack depth. The comparison of the solution is displayed in Figure 10. It is again observed that Toor and Buchalet solution agree well over a/t range from 0 to 0.8. Zahoor's solutions are consistently lower bound and for deeper crack the difference between Zahoor and Toor solution increases.

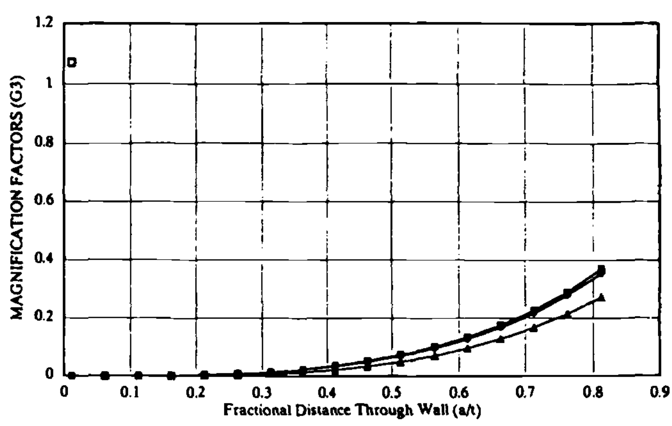

Figure 10: Fully Circumferential Crack R/T = 10
Verification of Magnification Factor, G_3

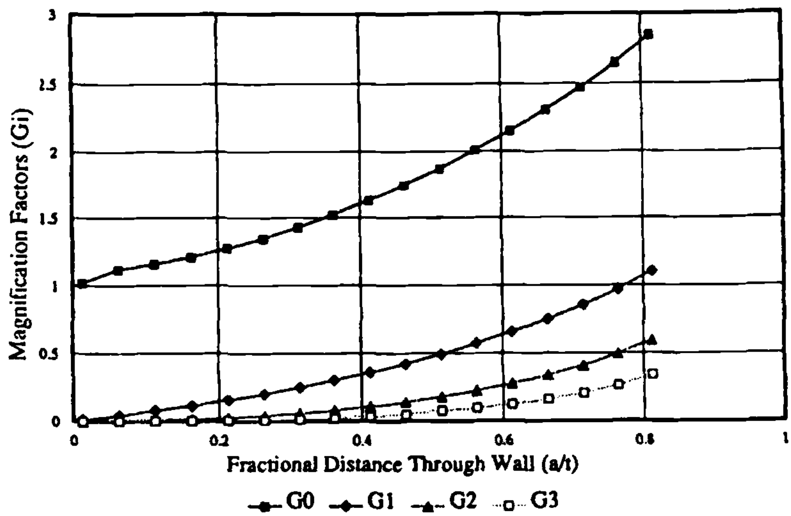

Figure 12: <u>Fully Circumferential Crack Magnification Factors for R/T = 10</u>

<u>Functional Form of the Magnification Factors</u>--The SOLO statistical package, "version 4" Reference (5) was used to fit the model to the finite element generated magnification factors for R/t = 1.5, 2, 2.5, 3, 5, 10. For each R/t four magnification factors (G_0, G_1, G_2, and G_3) were available from the finite element results in a tabular form. The non-linear least square fit procedure produced the following function for various types of loading.

<u>Uniform Loading</u>--The magnification factor associated with uniform loading is defined as G_0. The functional form of G_0 from the non-linear least square fit is as follows:

$$G_0 = a_0 (1 - a/t)^{b_0} \exp[c_0 (a/t)] \tag{9}$$

where:

$a_0 = 1.078 (R/t)^{0.003} \exp[-0.009 (R/t)]$,

$b_0 = -0.648 (R/t)^{-0.357} \exp[-0.106 (R/t)]$ and

$c_0 = 3.739 - 4.502 (R/t)^{-0.175} \exp[-0.013 (R/t)]$.

<u>Linear Loading</u>--The magnification factor associated with linear loading is defined as G_1. The functional form of G_1 is as follows:

$$G_1 = a_1 (a/t)^{b_1} \exp[c_1 (a/t)] \tag{10}$$

where:

$a_1 = 0.248\ (R/t)^{0.259}$,

$b_1 = 0.594\ (R/t)^{0.163}$ and

$c_1 = 1.465\ (R/t)^{-0.090}\ \exp[0.010\,(R/t)]$.

Quadratic Loading--The magnification factor associated with quadratic loading is defined as G_2. The functional form of G_2 is as follows:

$$G_2 = a_2\,(a/t)^{b_2}\ \exp[c_2\,(a/t)] \qquad (11)$$

where:

$a_2 = 0.115\ (R/t)^{0.285}\ \exp[0.020\,(R/t)]$,

$b_2 = 1.259\ (R/t)^{0.095}\ \exp[0.009\,(R/t)]$ and

$c_2 = 1.984\ (R/t)^{-0.098}\ \exp[-0.012\,(R/t)]$.

Cubic Loading--The magnification factor associated with cubic loading is defined as G_3. The functional form of G_3 is as follows:

$$G_3 = a_3\,(a/t)^{b_3}\ \exp[c_3\,(a/t)] \qquad (12)$$

where:

$a_3 = 0.063\ (R/t)^{0.276}\ \exp[0.042\,(R/t)]$,

$b_3 = 1.945\ (R/t)^{0.063}\ \exp[0.011\,(R/t)]$ and

$c_3 = 2.393\ (R/t)^{-0.060}\ \exp[-0.031\,(R/t)]$.

Conclusions

The magnification factors developed for fully circumferential part-through crack for R/t = 10 are compared with finite element results of two known solutions in the literature (References (8) and (9)). It is concluded that magnification factors developed using the energy method agree reasonably well for a/t = 0.3, and are conservative relative to the two other solutions for a/t from 0.3 to 0.8 for a cylinder having R/t = 10. The finite element generated magnification factors for each load distribution on the crack face in tabular form were utilized to develop the functional form of these magnification factors. The statistically generated functions and the tabular values agree within 1%. The advantage of these functions is the convenience of incorporating them in any crack growth computer program within the given applicability. This eliminates the cumbersome interpolation of the functions for a specific R/t and a/t values. The validity of these functions is $1.5 \leq R/t = 10$ for 0.0125 $a/t \leq .8125$.

ACKNOWLEDGEMENT

The author would like to thank R. J. Pierotti for his encouragement during the development of this work. The author wishes to acknowledge the help of Dr. L. C. Allison in the use of COMAND2 to generate the finite element mesh. Numerous discussions with Drs. E. Friedman, D. P. Jones, and W. K. Wilson on stress intensity factor solutions are greatly appreciated. Dr. W. J. Beggs' help in generalizing the influence functions is also appreciated. The author is also thankful to Bernadette Holly for her help in preparing the Tables and Figures. Mary Jean Molinaro's help in making numerous computer runs is very much appreciated.

REFERENCES

(1) Irwin, G. R., "Analysis of Stresses and Strains Near the End of a Crack Traversing a Plate", Appl. Mech. Vol. 24, Trans. ASME 79, PP 361-364, 1957.

(2) Buchalet, C. B. and Bamford, W. H. "Stress Intensity Factors for Continuous Surface Flaws in Reactor Pressure Vessels," ASTM STP 590, 1976, PP 385-402.

(3) Zahoor, A. Ductile Fracture Handbook, Vol. 2, Electric Power Research Institute, June 1989.

(4) Andrasic, C.P. and Parker, A. P., "Dimensionless Stress Intensity Factors for Cracked Thick Cylinders Under Polynomial Crack Face Loadings, Engineering Fracture Mechanics, Vol. 19, No. 1 (1986), PP 187-193.

(5) Solo Statistical Package, Version 4, BMDP Statistical Software, Inc; Los Angeles CA.

Wei Zhao,[1] Michael A. Sutton,[1] and James C. Newman, Jr.[2]

K3D - A PROGRAM FOR DETERMINING STRESS INTENSITY FACTORS OF SURFACE AND CORNER CRACKS FROM A HOLE

REFERENCE: Zhao, W., Sutton, M. A., and Newman, J. C., Jr., "**K3D - A Program for Determining Stress Intensity Factors of Surface and Corner Cracks from a Hole,**" Fatigue and Fracture Mechanics: 28th Volume, ASTM STP 1321, J. H. Underwood, B. D. Macdonald and M. R. Mitchell, Eds., American Society for Testing and Materials, 1997.

ABSTRACT: K3D is a computer program for determining stress intensity factors of semi-elliptical surface cracks and quarter-elliptical comer cracks emanating from a hole in a wide plate. The loading conditions considered fall into two categories: (a) pre-defined loads, which include biaxial loading with arbitrary biaxial load ratio, remote tension, remote bending (corner cracks only), and wedge loading in the hole and (b) user-defined loads, which allow users to analyze any loading conditions of interest, provided that the pertinent uncracked stress distributions can be fitted to a given functional form. K3D uses an accurate and efficient PC-based weight function algorithm, which requires no pre- or post-processing. The efficiency of the algorithm makes it possible to get a solution in a few seconds on computers equipped with an 80486 microprocessor. The program is described in some detail, following a brief introduction of the theoretical background. An example is given to illustrate its use.

KEYWORDS: stress intensity factor, surface crack, corner crack, weight function method, stress concentration

---

The stress intensity factor is a key parameter in damage tolerance analysis. It is of practical interest to be able to determine stress intensity factors (SIF) for various three-

[1] Adjunct Professor and Professor, respectively, Mechanical Engineering Department, University of South Carolina, Columbia, SC 29208.

[2] Senior Scientist, Mechanics of Materials Branch, NASA Langley Research Center, Hampton, VA 23681-0001.

dimensional (3D) crack configurations both accurately and efficiently. Previous evaluation and applications [1] have shown that the 3D weight function method (WFM) developed by the authors and their colleagues possesses such desirable features. In addition, the method has the following advantages: (1) requiring less or no 3D reference SIF, (2) dealing with complex loading conditions easily (including bi-variant stress fields), and (3) providing SIF along the entire crack front.

It is felt that the 3D WFM is an ideal complement to various sophisticated 3D numerical techniques in routine damage tolerance analysis of typical 3D crack configurations under various loading conditions. To facilitate the application of the method, a computer program, K3D, has been developed. This is a PC-based weight function algorithm, which requires no pre- or post-processing. The efficiency of the algorithm makes it possible to obtain a solution in a few seconds on computers equipped with an 80486 microprocessor. The K3D program is described in some detail, following a brief introduction of the theoretical background . An example is given to illustrate its use.

THEORETICAL BACKGROUND

The 3D WFM is based on three previous developments, as shown in Fig.1. The

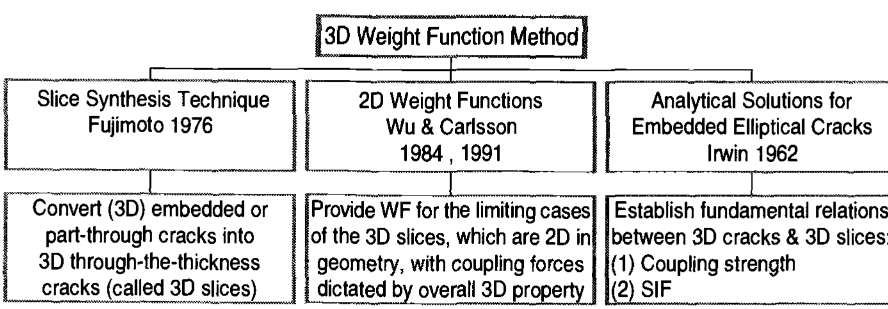

FIG. 1--Fundamentals of the 3D weight function method.

first is the slice synthesis technique proposed by Fujimoto [2]. The second is the general weight function expressions for two-dimensional (2D) crack configurations by Wu [3], and Wu and Carlsson [4]. The third is the analytical solutions for an embedded elliptical crack in an infinite body by Irwin [5]. The slice synthesis technique [2] is the starting point. It converts embedded or part-through cracks into 3D through-the-thickness cracks, called 3D slices. The 2D weight functions [3,4] provide weight functions for the limiting cases of the 3D slices. The analytical solutions [5] are used to establish fundamental relations between 3D cracks and 3D slices. To illustrate the idea, let us briefly look at corner cracks emanating from a hole, as shown in Fig.2. The 3D cracked body is decomposed into two series of 3D slices of infinitesimal thickness. Figures 3(a) and (b) show the layout of the slices. The typical slices are shown in Figs. 3(c) and (d).

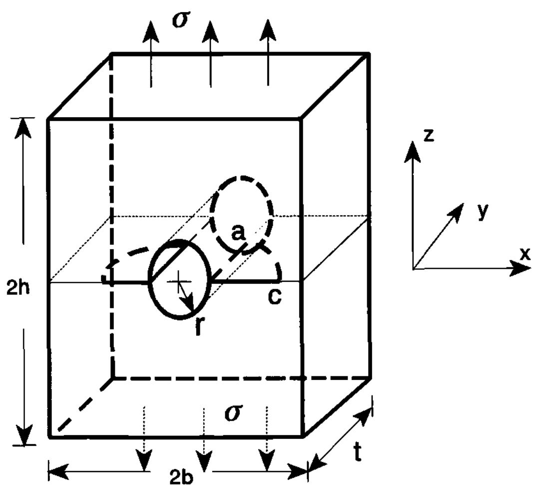

FIG. 2-- Double corner cracks at a hole under remote tension.

The slices parallel with the a-axis of the crack are called a-slices, and a subscript "a" is attached to quantities related to the a-slices. Similarly, a subscript "c" is used for c-slices, which are parallel with the c-axis of the crack. The a-slices as shown are also called basic slices, because they have the same elastic modulus, E, as the 3D cracked body and subjected to the same applied load. In contrast, the c-slices as shown are also called spring slices, because they have a different elastic modulus, E_s, called coupling strength, and subjected to a different load. In addition to the applied load, the slices are subject to two other actions: (1) P(x,y) (see Figs. 3(c) and (d)), an unknown distributed pressure on the crack surface, called spring force; (2) the restraining springs on their boundaries towards which the crack extends. The P(x,y) is an equivalent representation for the internal forces present on the slices' surfaces. The restraining springs are used to simulate the restraining effect due to the uncracked area outside the sliced regions, as denoted by R_a and R_c in Figs. 3(a) and (b). The stiffnesses of the restraining springs, k_a and k_c, are unknown functions of the restraining area. These slices can then be formulated using the 2D weight function theory [3,4]. The coupling strength and the relationship between the 3D cracks and the 3D slices are determined with the aid of the analytical solutions for an embedded elliptical crack in an infinite body [5]. For a detailed description of the 3D WFM, please refer to References [6-8].

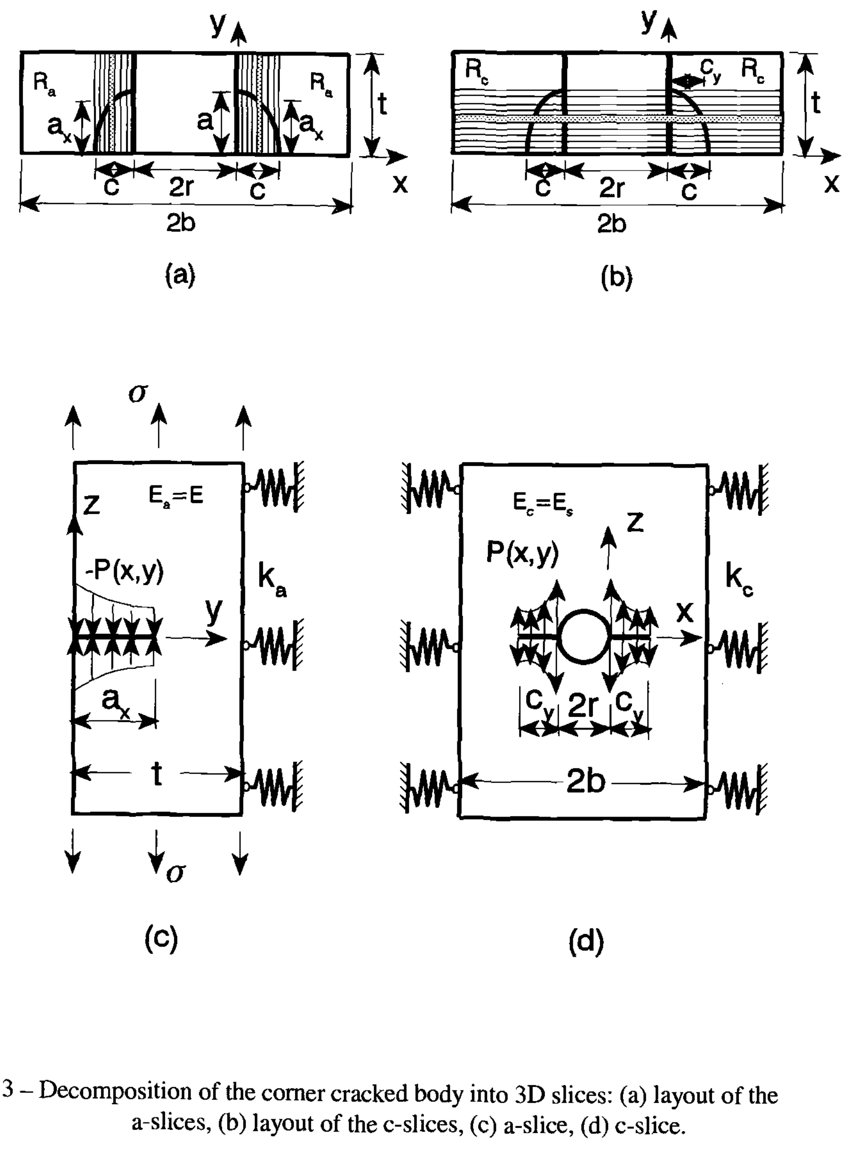

FIG. 3 – Decomposition of the corner cracked body into 3D slices: (a) layout of the a-slices, (b) layout of the c-slices, (c) a-slice, (d) c-slice.

SCOPE OF K3D

Configurations

Currently, K3D contains the following four crack configurations (see Fig.4): (1) a single surface crack from a hole, (2) two symmetric surface cracks from a hole, (3) a single corner crack from a hole, and (4) two symmetric corner cracks from a hole. The applicable ranges of the weight functions are $a/t \leq 0.9$, $c/r \leq 2$ and $(c+r)/b < 0.2$. There is no practical restriction on the a/c and r/t ratios.

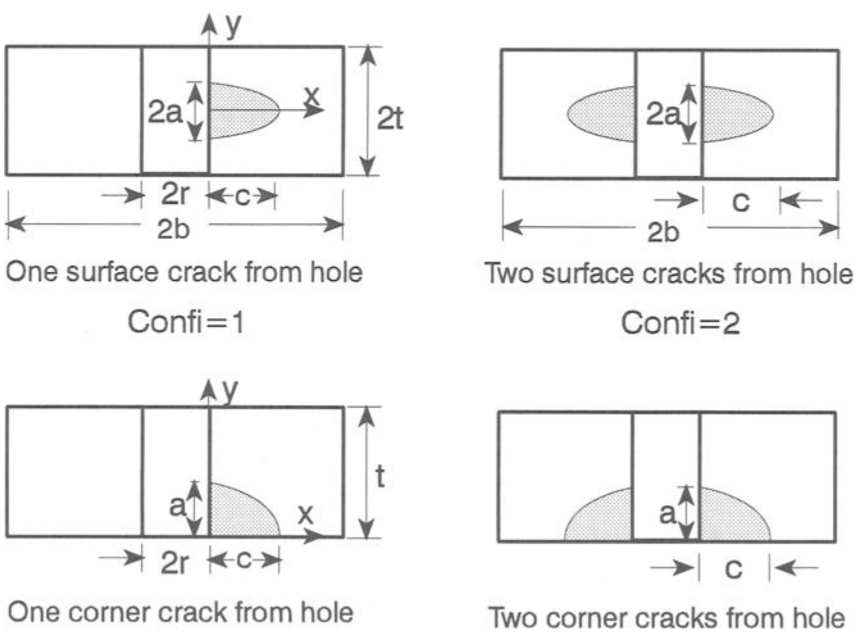

FIG. 4--Configurations considered in K3D.

Loading

The loading conditions considered fall into two categories: pre-defined loads and user-defined loads. The pre-defined loads include commonly encountered cases, such as biaxial loading with arbitrary biaxial load ratio, remote tension, remote bending (corner cracks only), and wedge loading in the hole. Typical load cases are shown in Fig.5, where λ is the biaxial load ratio to be entered by user, S_n is the hole-bearing pressure, and M is the remote bending moment.

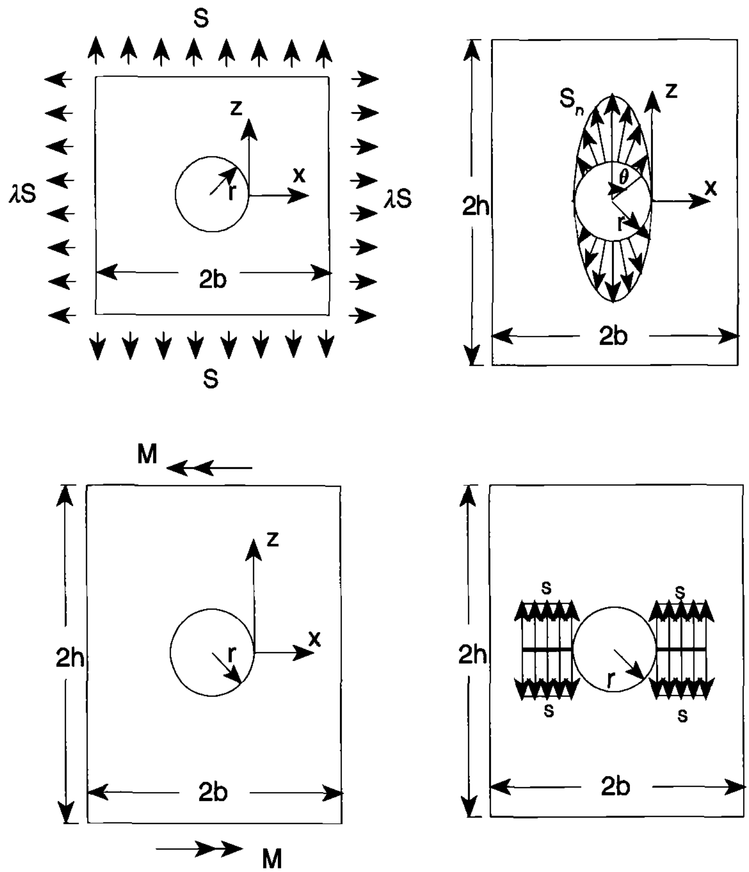

FIG. 5--Typical pre-defined loads in K3D.

The user-defined load allows analyst to describe any loading condition of interest, provided that the pertinent uncracked stress distributions can be represented by Eq.(1),

$$S(x,y)/S_0 = \sum_{i=1}^{I}\sum_{j=1}^{J} e_{ij}\left(\frac{x}{r}+1\right)^{2-2i}\left(\frac{y}{t}\right)^{q} \tag{1}$$

where S(x, y) is the normal stress distribution induced by the applied load at the crack location in the same body but without crack; S_0 is a reference stress; e_{ij} are fitting coefficients with q=2j-2 for symmetric loading such as remote tension or wedge loading, and q=2j-1 for anti-symmetric loading (e.g. remote bending).

K3D FLOW CHART

A flow chart of K3D is given in Fig.6, which emphasizes input and output (shown as solid blocks). The first input sets the configuration parameter CONFI corresponding to the four configurations shown in Fig.4. The second input describes the dimensionless geometry parameters for hole radius, crack aspect ratio and crack depth. The third input

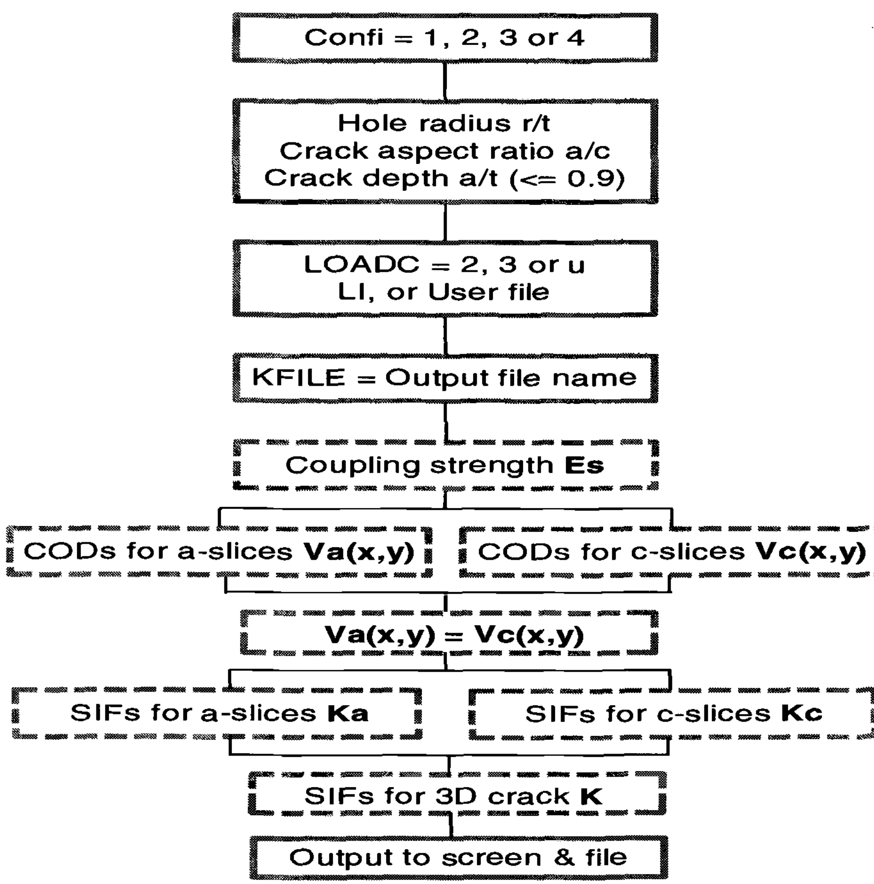

FIG. 6--A flow chart of K3D.

sets the load type, which can be either a pre-defined load or a user-defined load. The last input prescribes a file name to be used for storage of the computed stress intensity factors. Having entered the above parameters, K3D initially calculates the coupling strength, E_s. Then, numerical integration is performed to determine crack opening displacements (COD) for a-slices, $V_a(x, y)$, and for c-slices, $V_c(x, y)$. After computing COD for a- and c-slices, simultaneous equations, $V_a(x, y)= V_c(x, y)$, are solved for the coupling spring force, which is used to determine SIF for a-slices, K_a, and for c-slices, K_c. Finally, the SIF for the 3D crack, K, is obtained by using K_a and K_c along the entire crack front.

AN EXAMPLE

In the following, an example for two corner cracks under remote bending is given to illustrate the use of K3D. The screen display is shown in Italics with user input distinguished using bold face.

Type K3D and press RETURN key, the following is shown on the screen:

```
*********************************************************************
* NASA 3-D STRESS INTENSITY FACTORS FOR CRACKED HOLES  -- K3D --    *
*********************************************************************



        **     **  *******  *****
        **    **   *******  ******
        **   **         **  **    **
        **  **          **  **     **
        ****       *******  **     **
        ****       *******  **     **
        **  **          **  **     **
        **   **         **  **    **
        **    **   *******  ******
        **     **  *******  *****     VERSION-1.0



*********************************************************************
* by W. ZHAO, M.A. SUTTON and J.C. NEWMAN, Jr.    07-14-94          *
*********************************************************************
```

Then, the user is prompted to enter the configuration parameter:

Confi=Crack Configuration Analyzed:

Confi=1 ---- One Surface Crack at Hole

2 ---- Two Surface Cracks at Hole

3 ---- One Corner Crack at Hole

4 ---- Two Corner Cracks at Hole

Enter your Confi= ***4***

Here, "***4***" is entered for two corner cracks at hole. The next line is an input echo, which also says "*r/b = 0*", reminding that a very large b is assumed, such as $r/b \leq 0.2$.

**** 2 CORNER CRACKS AT HOLE r/b = 0 ****

The following line is a reminder for load input. Since 3D stress distributions are specific to r/t ratios, this line indicates, before inputing geometry parameters, what r/t ratios have 3D stress distributions available.

For 3D-Stress: Choose r/t = 0.1, 0.25, 0.5, 1, 1.5 or 2.5

Then, the user is prompted to input dimensionless geometry parameters for hole radius, r/t, crack aspect ratio, a/c, and crack depth, a/t, in that order.

Enter Geometry Parameters: r/t, a/c, and a/ t= ***.5 2 .8***

Here, ***.5 2 .8*** are entered for r/t = 0.5, a/c = 2.0 and a/t = 0.8. What follows is the prompt for input of load. It has two steps. First, enter load category LOADC, which takes the value of 2, 3 or U, representing that the uncracked stress distribution is from 2D analysis, 3D analysis, or a user-defined load, respectively. The 2D uncracked stress distribution does not consider stress variations along the plate thickness. It is the same for all r/t ratios. The 3D uncracked stress distribution reflects the true behavior of stress distribution near stress concentrations. It is a function of r/t ratios. For user-defined load, K3D will read an input file containing corresponding coefficients of Eq. (1). Depending on the input, corresponding options will be displayed. In the following, we choose LOADC=*3*.

Enter 2, 3 or U for 2D, 3D or User-defined Stress: LOADC= ***3***

The corresponding options are listed:

LI=Load Identifier:

LI=54 : 3D Bending, r/b=0.2, r/t=0.50

64 : 3D Tension, r/b=0.2, r/t=0.50

74 : 3D Wedge Load: Cos, r/b=0.2, r/t=0.50

ENTER YOUR LI= ***54***

Here, "***54***" is entered for remote tension with r/t=0.5. The following is input echo.

3D BENDING, r/b=0.2, r/t=0.50

e00= 1.036 e10= .000 e20= .763 e30= .000 e40= -.818

e01= -1.999 e02= -.235 e03= -.235 e04= 2.137

e11= .000 e21= -4.048 e12= .000 e22= 7.400

r/t= .500 a/c= 2.000 a/t= .800

Then, the following is prompted, and "***khc05208.tb3***" is entered in reply.

Enter data file name for Stress Intensity Factors: KFILE= ***khc05208.tb3***

Evaluating Integrals for Displacements ....

Within a few seconds, the results are obtained and displayed on the screen:

**** TWO CORNER CRACKS AT HOLE r/b=0 ****

r/t= .50 a/c= 2.00 a/t= .80

3D BENDING, r/b=0.2, r/t=0.50

e00= 1.036 e10= .000 e20= .763 e30= .000 e40= -.818

STANDARD DEVIATION% = .209 b.s.//a-axis

*NORMALIZED STRESS INTENSITY FACTOR: F=K/[S(pi*a/Q)^.5]*

No.	*2phi/pi*	*b.s.//a-axis*
1	.001	.8564
2	.063	.7541
3	.125	.6501
4	.188	.5534
5	.250	.4587
6	.313	.3648
7	.375	.2736
8	.438	.1881
9	.500	.1107
10	.563	.0424
11	.625	-.0169
12	.688	-.0682
13	.750	-.1128
14	.833	-.1655
15	.917	-.2178
16	.958	-.2425
17	.999	-.2672

Here, the "*b.s.//a-axis*" stands for "basic slices parallel to the a-axis of the crack' Please refer to Reference [6] for detail. The following table lists dimensionless SIF as a function of normalized parametric angles. The dimensionless SIF is defined as

$F=K/[S(\pi a/Q)^{0.5}]$, where Q is the shape factor of an elliptical crack. The normalized parametric angle is defined as $2\phi/\pi$, see Fig. 7.

*NORMALIZED STRESS INTENSITY FACTOR: F=K/[S(pi*a/Q)^.5]*

No.	*2phi/pi*	*b.s.//a-axis*
1	*.001*	*1.5210*
2	*.063*	*1.4875*
3	*.125*	*1.4534*
4	*.188*	*1.4347*
5	*.250*	*1.4302*
6	*.313*	*1.4424*
7	*.375*	*1.4738*
8	*.438*	*1.5208*
9	*.500*	*1.5756*
10	*.563*	*1.6332*
11	*.625*	*1.6974*
12	*.688*	*1.7809*
13	*.750*	*1.8966*
14	*.833*	*2.0995*
15	*.917*	*2.3793*
16	*.958*	*2.5981*
17	*.999*	*2.8169*

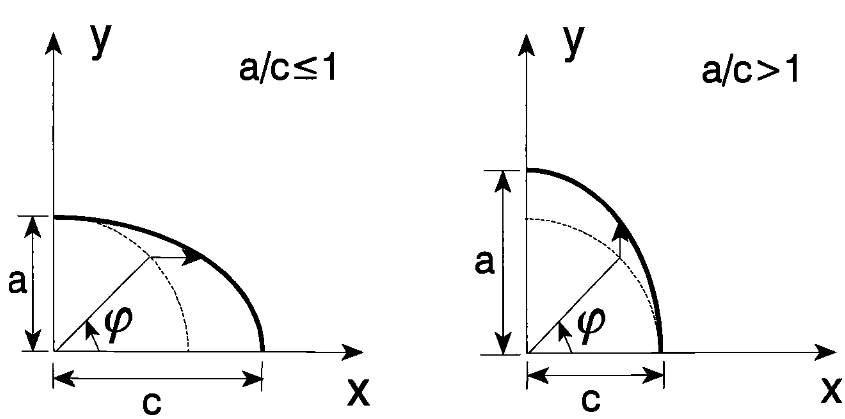

FIG. 7-- Definition of parametric angles.

The above results are also output to file "***khc05208.tb3***". A comparison with the finite element solution [9] is shown in Fig. 8. Now, K3D asks if you want to consider another case. Here, we enter "*N*" to terminate the program.

CONSIDER ANOTHER CASE ? (YES OR NO Y/N): AGAIN=N
Stop - Program terminated.

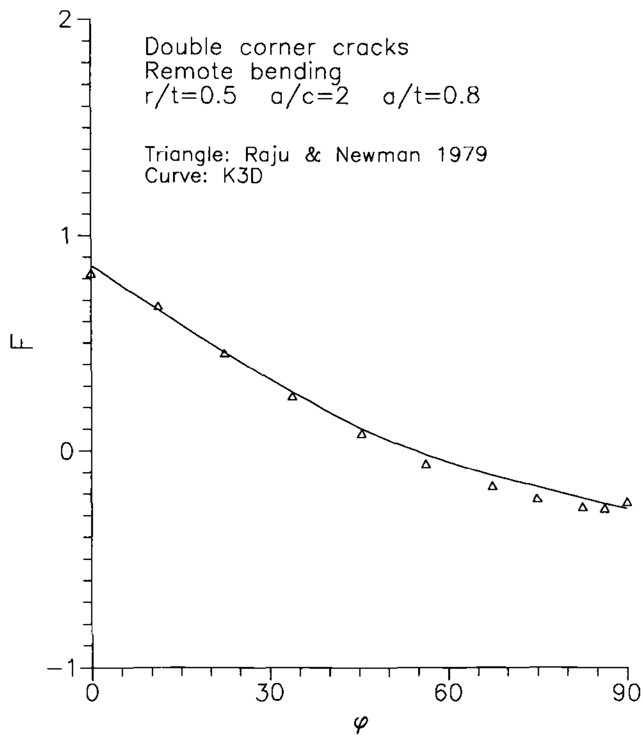

FIG. 8—Comparison of the K3D result with the finite element solution [9].

LIMITATIONS

The weight functions and uncracked stress distributions used in K3D are for a wide plate. Therefore, use of K3D for $(c+r)/b > 0.2$ is not recommended. The crack size limitations are $a/t \leq 0.9$, and $c/r \leq 2$. Since this covers crack depth up to 90% of plate thickness, and crack length up to two times of hole radius, it normally will not pose any practical restrictions. There are no restrictions on weight functions in terms of r/t and a/c ratios. However, the applicable ranges of K3D may be limited by the available 3D uncracked stress distributions. This can be overcome by developing user-defined loading conditions.

CONCLUDING REMARKS

The main features of K3D program have been described. It determines SIF for surface and corner cracks emanating from a hole in a wide plate. It covers various loading conditions with the flexibility to include user-defined loadings. The crack sizes which can be analyzed range from virtually zero to nearly through the plate thickness. The ability to deal with small cracks is particularly useful in durability and small crack studies. Being based on an accurate and efficient weight function algorithm, it is expected that K3D will become a powerful complement to various 3D numerical methods in routine damage tolerance analysis of typical 3D crack configurations.

REFERENCES

[1] Zhao, W., Newman, J. C., Jr., and Sutton, M. A., "A Three-Dimensional Weight Function Method -- Evaluation and Applications," Fatigue and Fracture Mechanics: 27th Volume, ASTM STP 1296, R. S. Piascik, J. C. Newman, Jr., R. P. Gangloff, and N. E. Dowling, Eds., American Society for Testing and Materials, 1996.

[2] Fujimoto, W. T., "Determination of Crack Growth and Fracture Toughness Parameters for Surface Flaws Emanating from Fastener Holes," Proceedings of the AIAA/ASME /SAE 17th Structures, Structural Dynamics, and Material Conference, King of Prussia, Pa., 1976, pp 522-531.

[3] Wu, X. R., "Approximate Weight Functions for Center and Edge Cracks in Finite Bodies," Engng. Fracture Mech. Vol.20, 1984, pp 35-49.

[4] Wu, X. R., and Carlsson, J., Weight Functions and Stress Intensity Factor Solutions, Pergamon press, 1991.

[5] Irwin, G. R., "Crack Extension Force for a Part-Through Crack in a Plate," J. Appl. Mech. Vol.29, 1962, pp 651-654.

[6] Zhao, W., Wu, X. R., and Yan, M. G., "Weight Function Method for Three Dimensional Crack Problems-I. Engng. Fracture Mech. Vol.34, 1989, pp 593-607.

[7] Zhao, W., Newman, J. C., Jr., Sutton, M. A., Wu, X. R., and Shivakumar, K. N., "Analysis of Corner Cracks at Hole by a 3-D Weight Function Method with Stresses from Finite Element Method," NASA TM-110144, 1995.

[8] Zhao, W., Newman, J. C., Jr., Sutton, M. A., Shivakumar, K. N., and Wu, X. R., "Analysis of Surface Cracks at Hole by a 3-D Weight Function Method with Stresses from Finite Element Method," NASA TM-110145, 1995.

[9] Raju, I.S. and Newman, J.C., Jr., "Stress intensity factors for two symmetric corner cracks," Fracture Mechanics: 11th Volume, ASTM STP 677, C.W. Smith, Ed., American Society for Testing and Materials, 1979, pp 411-430.

Yisheng Wu[1], Jingshen Wu[2] and Yiu-Wing Mai[1]

FINITE ELEMENT ANALYSIS ON THE FRACTURE OF RUBBER TOUGHENED POLYMER BLENDS

REFERENCE: Wu, Y. S., Wu, J. S., and Mai, Y-W., **"Finite Element Analysis on the Fracture of Rubber Toughened Polymer Blends,"** Fatigue and Fracture Mechanics: 28th Volume, ASTM STP 1321, J. H. Underwood, B. D. Macdonald and M. R. Mitchell, Eds., American Society for Testing and Materials, 1997.

ABSTRACT: The effect of rubber particle volume fraction on the constitutive relation and fracture toughness of polymer blends was studied using elastic-plastic Finite Element Analysis (FEA). The effect of rubber particle cavitation on the stress-strain state at a crack tip was also investigated. Stress analysis reveals that because of the high rubber bulk modulus, the hydrostatic stress inside the rubber particle is close to that in the adjacent matrix material element. As a result, the rubber particle imposes a severe plastic constraint to the surrounding matrix and limits its plastic strain. Rubber particle cavitation can effectively release the constraint and enable large scale plastic strain to occur. Different failure criteria were used to determine the optimum rubber particle volume fraction for the polymer blends studied in this paper.

KEYWORDS: polymer blends, rubber cavitation, plastic constraint, matrix shear yielding, hydrostatic stress, fracture toughness, finite element analysis

---

It is well known that brittle polymers can be toughened by blending with rubber particles. The mechanisms of rubber toughening have been studied extensively in the past decade and several toughening mechanisms have been proposed [1-7]. The most popular is that of rubber particle cavitation induced matrix shear yielding [1-3]. This mechanism emphasises the functional relationship between rubber cavitation and matrix shear yielding. It is postulated that the triaxial tension associated with the crack tip must be relieved by cavitation of the rubber particle before massive shear deformation in the matrix can occur. Experimental evidence in support of this proposed mechanism was reported [1-3, 8-9].

---

[1]Visiting Scholar and Professor, respectively, Centre for Advanced Materials Technology, Department of Mechanical and Mechatronic Engineering, University of Sydney, Sydney, NSW 2006, Australia
[2]Lecturer, Centre for Advanced Engineering Materials, Department of Mechanical Engineering, Hong Kong University of Science & Technology, Hong Kong

On the other hand, numerical results from early Finite Element Analysis (FEA) [4-5] showed that solid non-cavitied rubber particles behave no differently to empty voids. The soft rubber particles merely act as stress concentrators to enhance the stress state in the matrix near the particles and to introduce shear yielding between neighboring particles. Rubber particle cavitation and matrix shear yielding can take place independently. There was no evidence from the FEA simulation showing that cavitation must occur first in order to trigger massive shear yielding in the matrix.

Obviously, the variance between the reported experimental evidence and the computational results of the FEA simulation suggests that more research on this issue is needed. In the present paper, the results of FEA under both uniaxial and triaxial stress states were reported. The effects of rubber particle volume fraction and rubber particle cavitation on the stress-strain distribution around a crack tip and toughening mechanisms were investigated. Stress analysis was carried out under triaxial stress state. Several failure criteria were employed to predict the fracture toughness of polymer blends with different amount of rubber particles.

FINITE ELEMENT ANALYSIS

Two elastic-plastic finite element analysis (FEA) models based on ABAQUS were conducted in the present study:

FEA-1, FEA of Stress-Strain Relation of Polymer Blends under Uniaxial Loading

In FEA-1, the basic stress-strain relation of the polymer blends with different rubber particle volume fraction was studied. A 2D plane-strain FEA model under uniform uniaxial tension was adopted, which is similar to that used by Huang and Kinloch [5], Fig. 1. The diameter of the rubber particle, D, was 5μm. The ligament length between the edges of the particles, L, was changed according to the volume fraction of rubber particle. L/D was varied from 3.0 to 0.25 corresponding to a rubber particle volume fraction between 5% and 50%. 2D plane-strain and four side, four node iso-parametric elements were adopted. The boundary constraints shown in Fig. 1 were used to retain the periodic symmetry of the microstructure. These conditions are prescribed by: (1) a displacement being applied on boundary CD, (2) boundary BD being kept parallel to its original position with no transverse constraint, (3) boundaries AB and AC are constrained in the Y and X directions, respectively. The matrix was assumed to be elastic-perfectly plastic. The elastic modulus was 3500 MPa, Poisson's ratio was 0.35 and the yield stress was 80 MPa. These mechanical properties are typical of epoxy resins. The rubber particle was treated as an elastic material with an elastic tensile modulus 2 MPa [5], a bulk modulus of 2000 MPa, and a rubber cavitation stress between 8 and 20 MPa as suggested by Bucknall and co-workers [6-7]. The stress-strain relation obtained in this part of the study was used in the subsequent finite element analysis, FEA-2.

FEA-2, FEA of Crack Tip-Paricle Problem

Crack tip analysis was carried out using a 2D plane strain FEA model similar to that

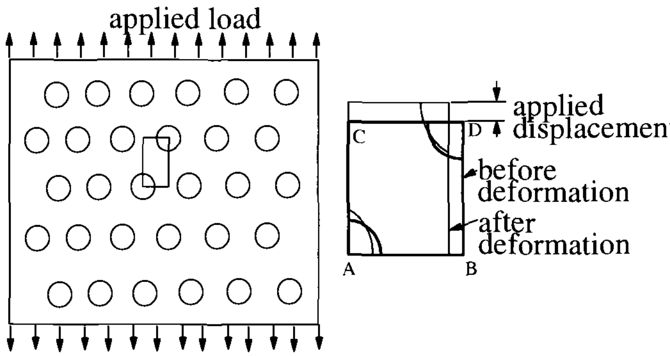

Fig.1 Two-dimensional plane strain model for rubber-modified epoxy.

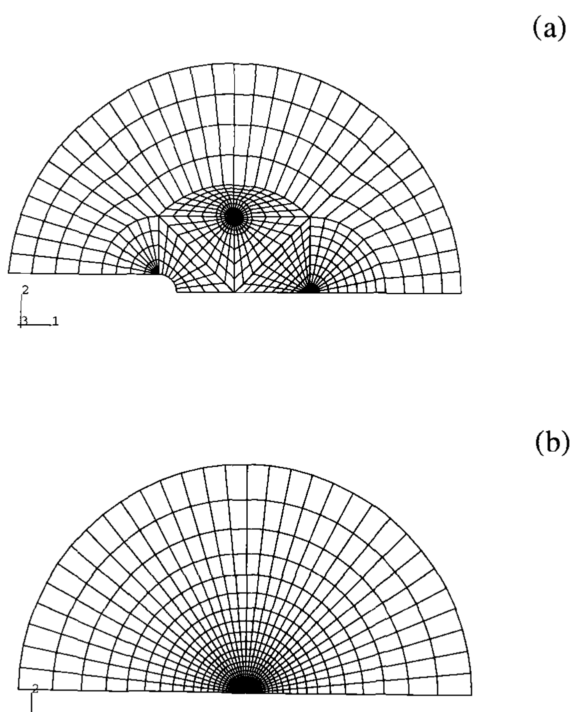

Fig.2 FEA mesh of one rubber particle at 45° to the crack tip: (a) finite element mesh in the near crack tip region (b) finite element mesh surrounding the crack tip region.

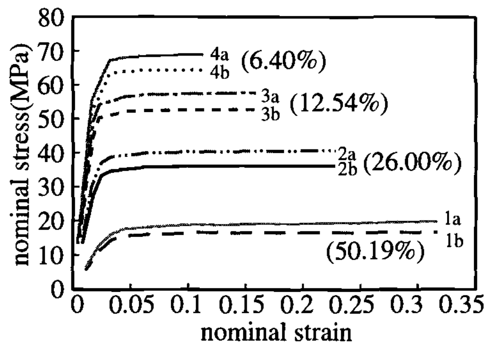

Fig.3 Nominal stress - strain curves of matrix/rubber and matrix/void systems. Number in parenthesis indicates volume fraction of particles or voids:- 1a,2a, 3a,4a for matrix/rubber particle system and 1b,2b,3b,4b for matrix/void system.

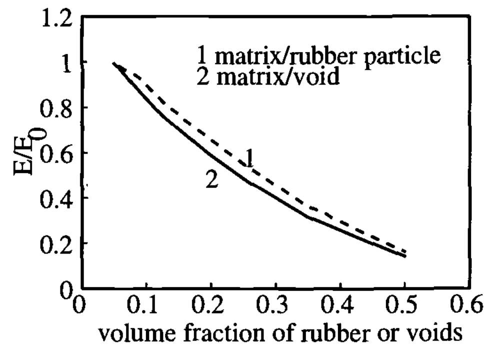

Fig.4 Effect of volume fraction of rubber particle or void on elastic modulus of blends.

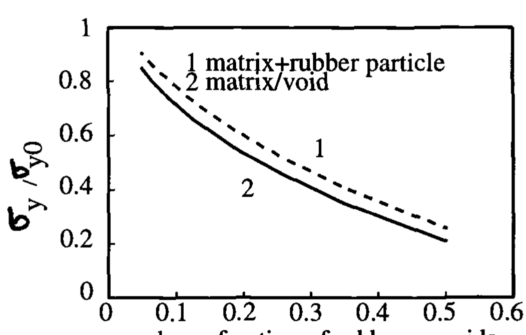

Fig.5 Effect of volume fraction of rubber particle or void on yielding stress of blends.

used by Aravas and McMeeking [10]. Two situations were considered in FEA-2: (1) a rubber particle was placed at 45° to the crack line in the crack tip area; and (2) the particle was replaced by a void at the same position. Matrix deformation before (case 1) and after (case 2) rubber particle cavitation is therefore simulated. A crack tip with the same radius as the rubber particle was assumed and the distance between them was changed within the same range as in FEA-1. The finite element meshes in the near crack tip and surrounding regions are shown in Figs. 2a and 2b, respectively. The relative distance of the boundary between "outer" regions and "inner" regions is 100 times, that is 15mm and 0.15mm, respectively. The total number of elements was 1600 and the total number of nodes was 1843. The displacement boundary conditions in the outer boundary are given by linear elastic fracture mechanics (LEFM), ie:

$$u = \frac{K_I}{G}\left(\frac{r}{2\pi}\right)^{1/2}\cos\left(\frac{\theta}{2}\right)\left[1 - 2\nu + \sin^2\left(\frac{\theta}{2}\right)\right]$$

$$v = \frac{K_I}{G}\left(\frac{r}{2\pi}\right)^{1/2}\sin\left(\frac{\theta}{2}\right)\left[2 - 2\nu + \cos^2\left(\frac{\theta}{2}\right)\right]$$

where u and v are displacements in 1 and 2 directions, r and θ are the polar coordinates, K_I is the opening stress intensity factor, and G is the shear modulus. Because the outer boundary is far away from the crack tip plastic zone, the use of LEFM is justified. The same material properties for the matrix and rubber particles as in FEA-1 were used in the inner region. In the outer region the equivalent stress-strain relation obtained from FEA-1 was utilised.

RESULTS AND DISCUSSION

FEA-1

The stress-strain curves obtained from FEA-1 for the matrix/rubber particle and matrix/void systems are shown in Fig. 3. As expected, both elastic modulus (Fig. 4) and yield stress (Fig. 5) of the blends decrease with increasing volume fraction of rubber particles or voids. The matrix/rubber particle system shows higher values for both elastic modulus and yield stress than the matrix/void system, but the difference is not significant. Due to the constraint from the elastic rubber particles, a slight plastic hardening can be seen with the matrix/rubber particle system.

FEA-2

The deformation and plastic strain distributions in the central zone around a crack tip are shown in Figs. 6a-b, the contour plot is for the equivalent plastic strain distribution. In Fig. 6a, localised plastic deformation only forms at the crack tip region before rubber cavitation. However, after the rubber particle has cavitated the matrix/rubber particle system behaves like the matrix/void system. A plastic shear band between the crack tip

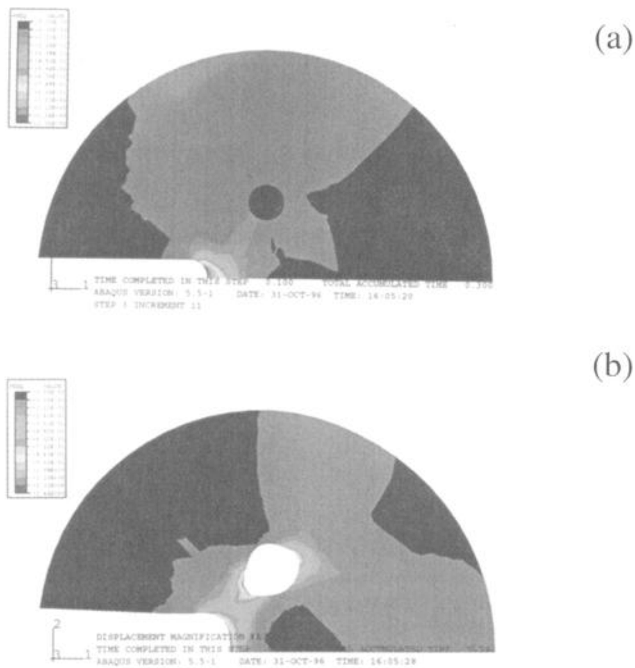

Fig.6 Localized plastic shear band between crack tip and particle or void. (a) Matrix/rubber particle, and (b) matrix/void systems.

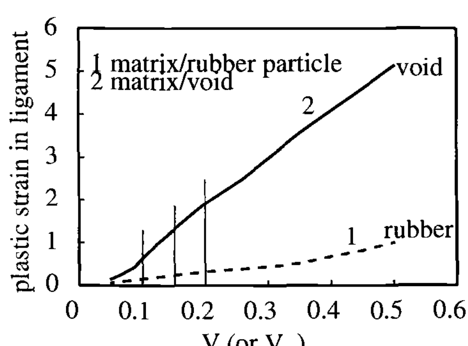

Fig.7 Effect of volume fraction of rubber particle or void on plastic strain in ligament at K=10.

and the void is developed and large scale plastic straining can be clearly seen in the ligament (Fig. 6b). A comparison between the two systems in terms of equivalent plastic strain at the centre of the ligament is shown in Fig. 7. Obviously, at all rubber particle volume fractions, the equivalent plastic strain in the ligament before rubber particle cavitation is much smaller than that after cavitation. These results show that the solid non-cavitied rubber particle in the triaxial tension area near a crack tip would have a strong constraint effect on the plastic deformation of the matrix around the rubber particle and in the localised shear band.

Some previous analyses [4,5,11] suggest that the stresses in the rubber particle are several orders smaller than those in the matrix due to the very low tensile modulus of the rubber particle. Therefore, according to these analyses, the constraint effect from the rubber particle is negligible. The resulting stresses in the matrix are similar regardless of the state of the rubber particle. This is correct only if uniaxial tension is considered. In the actual fracture process, the material element located in the area of a crack tip is always under *triaxial* tension. Hence, the bulk modulus, rather than the uniaxial tensile modulus, plays a more important role in the determination of the stress state of the element. Consequently hydrostatic stresses in the matrix and the rubber particle are of particular importance in fracture analysis. The present study shows that for a blend with 10% rubber particles, at a given stress intensity factor level, K=10, the hydrostatic stress inside the rubber particle is -90 MPa, which is close to the hydrostatic stress in the ligament between the crack tip and solid rubber particle (-100 MPa). Here K is the non-dimensional stress intensity factor, $K=K_I/(\sigma_y * a_0^{1/2})$ with K_I the stress intensity factor, σ_y the yield stress and a_0 the radius of the rubber particle. In these calculations it is assumed that the model rubber particle is "super strong" and does not cavitate at this hydrostatic stress level. In fact, since the difference in bulk modulus is not as large as that in tensile modulus between rubber particle and matrix, the small difference in hydrostatic stress between the rubber particle and matrix, and the high plastic constraint from the rubber particle, are not surprising.

After cavitation, the constraint imposed by the rubber particle is relieved, the hydrostatic stress in the surrounding matrix drops significantly. Plastic deformation in the ligament becomes much easier. In Fig. 9, it is shown that for a blend with 10% rubber particle the hydrostatic stress in the matrix drops from -100 MPa to -73 MPa after rubber particle cavitation. This reduction in hydrostatic stress results in a 4-times increase in the plastic strain in the ligament, as shown in Fig. 7. At even higher rubber particle volume fractions the increase in plastic strain becomes more significant. For instance, at 15% rubber particle volume fraction, there is a 6-times increase in plastic strain after rubber particle cavitation, Fig. 7.

From the above discussion, it is clear that solid non-cavitied rubber particles impose severe plastic constraint to the surrounding matrix material; and the rubber cavitation process relieves the plastic constraint and causes an extensive increase in plastic deformation in the ligament between the particle and the crack tip.

Failure Criteria

In FEA-2 presented above no failure criteria have been applied to consider the sequence

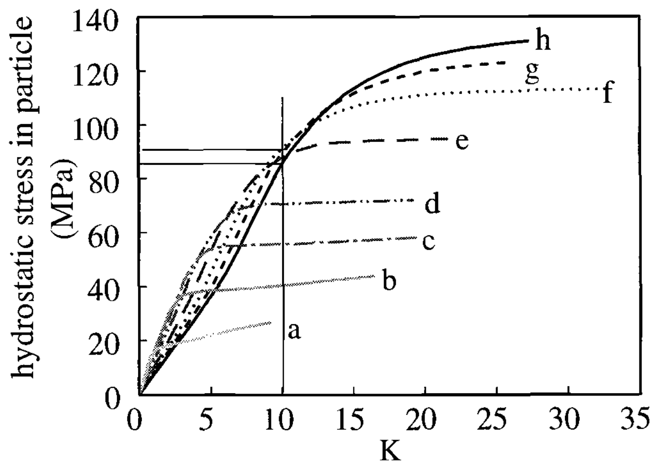

Fig.8 Effect of volume fraction of rubber particle on hydrostatic stress in rubber particle. (Rubber content: a-50.19%, b-34.91%, c-26.00%, d-19.61%, e-12.54%, f-8.71%, g-6.40%, h-4.90%)

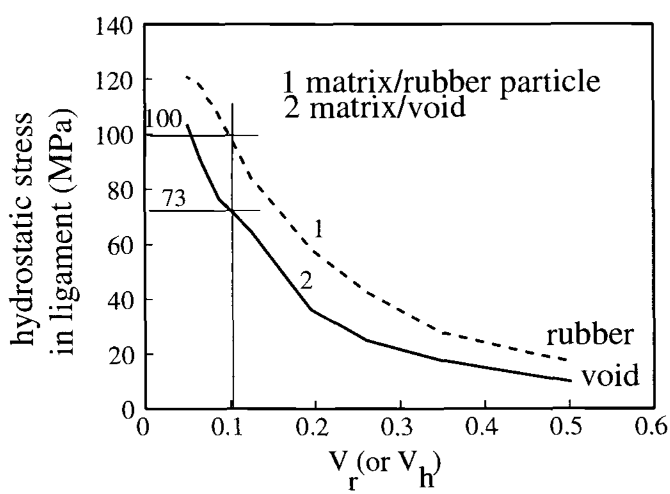

Fig.9 Effect of volume fraction of rubber particle or void on hydrostatic stress in ligament at K=10.

of deformation events, ie rubber cavitation and matrix shear yielding, or indeed their competition. Only the elastic-plastic stress strain fields and the hydrostatic stresses have been calculated depending on whether the rubber particle is assumed cavitated or not. Hydrostatic stress is considered because it is the single predominant factor for rubber cavitation. To clarify the rubber cavitation/matrix shear yielding phenomena three failure criteria are discussed below.

A. Critical tensile stress criterion

It is well known that brittle fracture occurs when the principal stress, σ_{22} , in the material under examination reaches its critical tensile stress before the material's yield point [12]. Fig. 10 shows the variation of σ_{22} in the centre of the ligament between a crack tip and a cavitied rubber particle (void) against the non-dimensional stress intensity factor K.

If the critical tensile stress for matrix to fracture is taken as 100 MPa, from Fig. 10, it is found that σ_{22} increases with increasing non-dimensional stress intensity factor, K, before generalised yielding of the ligament occurs. The blends containing more than 9% rubber particles yield before σ_{22} reaches the critical stress level. No brittle failure is predicted. On the other hand, for the blends with less than 9% rubber particles brittle fracture of the ligament occurs at K=4.95 (corresponding to K_C=0.58 MPa$\sqrt{}$m).

The effect of rubber particle cavitation on σ_{22} at a given K level is illustrated in Fig. 11. The effectiveness of rubber particle cavitation in reducing the principal stress is clearly shown. For instance, when the critical tensile stress is again taken as 100 MPa, for those blends containing 12% or less rubber particles the σ_{22} values are higher than the critical tensile stress if rubber particle cavitation is assumed not to occur. However, with rubber particle cavitation included, an addition of 6% rubber particles can effectively bring σ_{22} down to the critical tensile stress level at the same K level. This means that the cavitation process makes rubber particle toughening more effective. Therefore, fewer rubber particles are needed to achieve a required fracture toughness. Toughened blends can hence be obtained with higher yield stresses and elastic moduli.

B. Critical plastic strain criterion

When the rubber particle volume fraction is higher than a certain value the material element under examination reaches its yield stress before the critical tensile stress. Failure of the element is not dictated by the critical tensile stress but by the critical plastic strain. Ductile fracture of the element occurs only when the equivalent plastic strain of the element exceeds the critical plastic strain.

As shown in Fig. 12, the equivalent plastic strain at the centre of the ligament between the crack tip and the rubber particle increases with increasing K value at all rubber particle volume fraction. However, it is noted that the blends with a higher rubber particle volume fraction reaches a given critical plastic strain (*e.g.* 100%) at a lower K value. This indicates that excessive rubber particle can be harmful since ductile failure due to large plastic strain may occur at a low level of stress intensity factor, leading to a low fracture toughness.

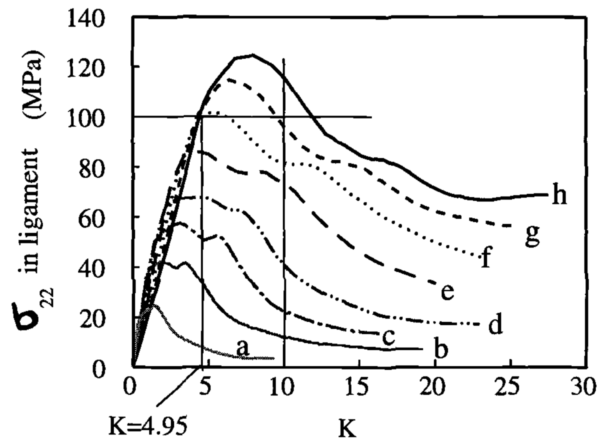

Fig.10 Effect of volume fraction of rubber particle on principal stress in ligament. (Rubber content: a-50.19%, b-34.91%, c-26.00%, d-19.61% e-12.54%, f-8.71%, g-6.40%, h-4.90%)

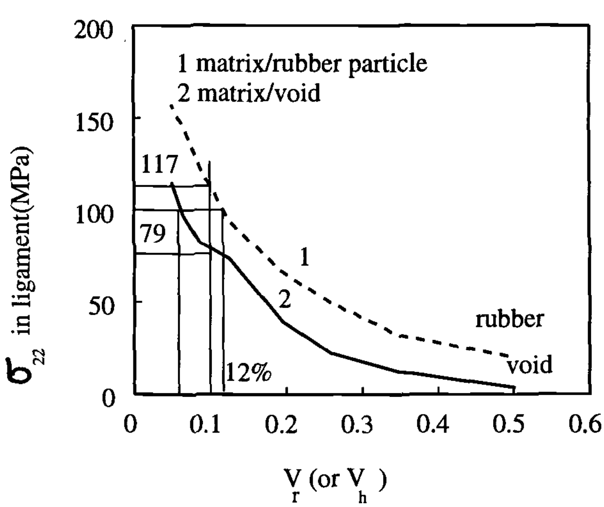

Fig.11 Effect of volume fraction of rubber particle V_r or void V_h on principal stress in ligament at K=10.

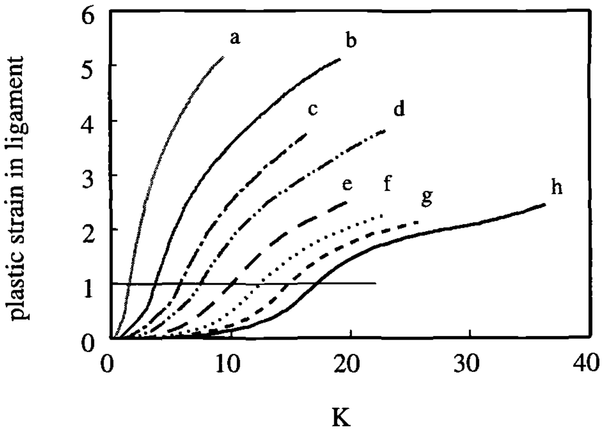

Fig.12 Effect of volume fraction of rubber particles on equivalent plastic strain in ligament. (Rubber content: a-50.19%, b-34.91%, c-26..00%, d-19.61%, f-8.71%, g-6.4%, h-4.9%)

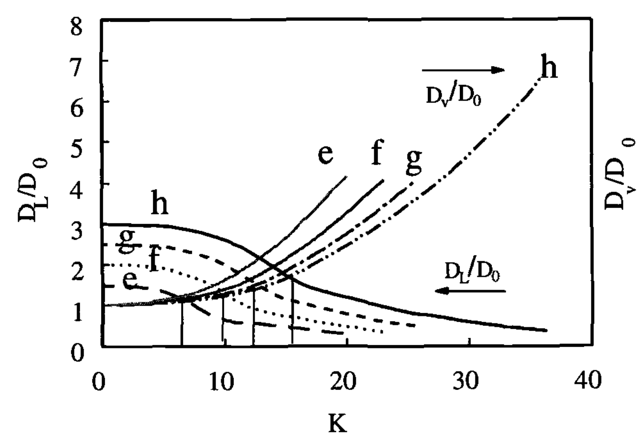

Fig.13 Variation of ligament width and void diameter with K after rubber cavitation. (Rubber content: e-12.54%, f-8.71%, g-6.40%, h-4.90%)

C. Critical ligament size criterion

Besides failures induced by a critical tensile stress and a critical plastic strain, the fracture of the ligament between the crack tip and the rubber particle can also occur when the ligament width decreases to a certain value below the critical ligament width.

The results of the present study show that with increasing stress intensity factor, K, the diameter of the void D_v, increase gradually but the ligament width D_L, decreases, as shown in Fig. 13. If it is assumed that the coalescence of the crack tip and the void takes place when the ligament size is equal to the void diameter and the fracture of the ligament occurs via the coalescence, then from Fig. 13, it can be seen that for the blends with a higher rubber particle content, the crack tip-void coalescence and the ligament fracture happen at a lower K level, resulting in a low fracture toughness. This trend is similar to that found with the critical plastic strain criterion discussed above.

In summary, the critical non-dimensional stress intensity factor obtained using the three failure criteria, K_c, is plotted against the rubber particle volume fraction in Fig. 14. According to the critical tensile stress criterion the rubber particle volume fraction should not be lower than 9% (critical tensile stress = 100 MPa and rubber cavitation occurs at early stage of loading). Otherwise brittle fracture may occur. When the critical ligament width criterion is taken into account together with the critical tensile stress criterion, the optimum rubber particle volume fraction for this particular material system is found at about 10%. Use of more than 10% rubber particles may lower the fracture toughness K_c because of easy coalescence of the crack tip and the void.

For some material systems, ductile fracture of the ligament may occur before the crack tip-void coalescence. Here, the critical plastic strain criterion is applicable. The optimum rubber particle volume fraction can be determined by the criteria of critical tensile stress and critical plastic strain, as shown in Fig. 14. Note that at a given rubber particle volume fraction, the critical non-dimensional stress intensity factor is higher using the plastic strain criterion (critical plastic strain = 100%) than that with the critical ligament width criterion.

CONCLUSIONS

1. The elastic modulus and yield stress of blends decrease with increasing rubber particle volume fraction. The cavitation of rubber particle has no significant effect on the stress-strain relation under uniaxial tension. The matrix/rubber particle system is found to be stronger than the matrix/void system. A slight plastic hardening due to the rubber particle imposed constraint is observed with the matrix/rubber system.

2. The hydrostatic stress level inside a rubber particle under triaxial tension is very close to that in the matrix element adjacent to the particle. As a result, the solid non-cavitied rubber particle imposes severe constraint on the surrounding matrix and limits the plastic strain of the matrix material.

3. The cavitation of rubber particle relieves the constraint to the adjacent matrix element and effectively lowers the hydrostatic and principal stresses in the area of the crack tip and enables large scale plastic strain in the ligament between the crack tip and the rubber particle to occur, resulting in a high fracture toughness.

4. The optimum rubber volume fraction may be determined using failure criteria

based on the critical tensile stress, critical plastic strain and critical ligament width. For the blends with rubber particle volume fraction lower than a minimum value, brittle fracture may occur due to the maximum principal stress at the crack tip being higher than the critical tensile stress. On the other hand, use of excessive rubber particles may induce unstable plastic deformation and crack tip-void coalescence at a low stress intensity level, leading to a low fracture toughness. There is an optimum rubber content that maximises the fracture toughness.

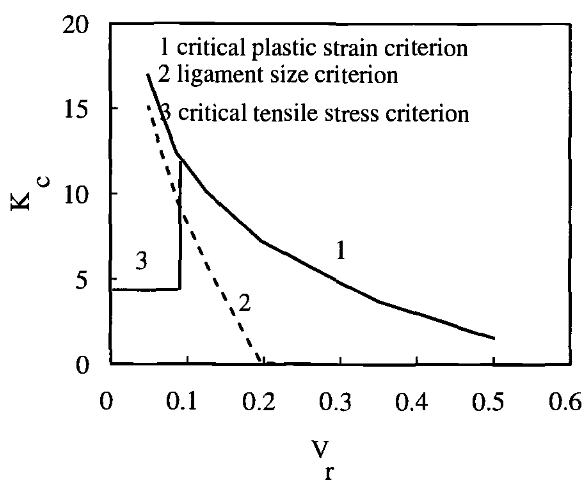

Fig.14 Dependence of critical non-dimensional stress intensity factor on fracture criteria

ACKNOWLEDGMENTS

The authors would like to thank the Australian Research Council (ARC) for the continuing support of the polymer blends projects. One of us (YSW) is funded by the ARC as a Visiting Scholar to the Centre for Advanced Materials Technology at the University of Sydney.

REFERENCES

[1] Yee, A. F. and Pearson, R. A., "Toughening Mechanisms in Elastomer-Modified Epoxies, Part 1, Mechanical Studies," Journal of Materials Science, Vol. 21, 1986, pp 2462-2474.

[2] Pearson, R. A. and Yee, A. F., " Toughening Mechanisms in Elastomer-Modified Epoxies, Part 2, Microscopy Studies," Journal of Materials Science, Vol. 21, 1986, pp 2475-2489.

[3] Parker, D. S., Sue, H-J., Hang, J., and Yee, A. F., "Toughening Mechanisms in Core-Shell Rubber Modified Polycarbonate, Polymer, Vol. 31, 1990, pp 2267.

[4] Guild, F. J. and Young, R. J., "A Predictive Model for Particulate Filled Composite Materials, Part 2, Soft Particles," Journal of Materials Science, Vol. 24, 1989, pp 2454-2460.

[5] Huang, Y. and Kinloch, A. J., "Modelling of the Toughening Mechanisms in Rubber-Modified Epoxy Polymers, Part 1, Finite Element Analysis Studies," Journal of Materials Science, Vol. 27, 1992, pp 2753-2762.

[6] Bucknall, C. B., Karpodinis, A., and Zhang, X. C., "A Model for Particle Cavitation in Rubber-Toughened Plastics," Journal of Materials Science, Vol. 29, 1994, pp 3377-3383.

[7] Lazzeri, A. and Bucknall, C. B., "Dilatational Bands in Rubber-Toughened Polymers," Journal of Materials Science, Vol. 28, 1993, pp 6799-6808.

[8] Wu, J. S. and Mai, Y.-W., "Fracture Toughness and Fracture Mechanisms of PBT/PC/IM Blends, Part 2, Toughening Mechanisms," Journal of Materials Science, Vol. 28, 1993, pp 6167-6177.

[9] Li, D., Yee, A. F., Chen, I.-W., Chang, S.-C., and Takahashi, K. "Fracture Behaviour of Unmodified and Rubber-Modified Epoxies under Hydrostatic Pressure," Journal of Materials Science, Vol. 29, 1994, pp 2205-2215.

[10] Aravas, N. and McMeeking, R. M., "Finite Element Analysis of Void Growth Near a Blunt Crack Tip," Journal Mechanics Physics of Solids, Vol. 33, 1985, pp 25-49.

[11] Huang, Y, Hunston, D. L., Kinloch, A. J., and Riew, C. K., "Mechanisms of Toughening Thermoset Resins, in Rubber Toughened Plastics I, Advances in Chemistry Series 233, ed. C. K. Riew and A. J. Kinloch, Washington D. C., USA, 1993, pp 1-35.

[12] Knott, J. F., Fundamentals of Fracture Mechanics, p 180, Butterworth, London, 1973.

Author Index

Subject Index